Shear strength of structural elements in high performance fibre reinforced concrete (HPFRC)

Lionel Moreillon

UNIVERSITÉ PARIS-EST

THESE DE DOCTORAT

Présenté pour l'obtention du grade de

Docteur de l'Université Paris-Est

Spécialité : Structures et Matériaux

PAR

Lionel MOREILLON

Shear and punching shear behaviour of structural elements in High Performance Fibre Reinforced Concrete

Thèse préparée à l'Ecole d'ingénieurs et d'architectes de Fribourg, Suisse,
présentée le 19 mars 2013
à l'Ecole Nationale des Ponts et Chaussées, Champs-sur-Marne, France

acceptée sur proposition du jury

Pr. Aurelio MUTTONI	*Ecole Polytechnique Fédérale de Lausanne, Suisse*	Rapporteur
Pr. Emmanuel FERRIER	*Université Lyon 1 – INSA Lyon, France*	Rapporteur
Pr. Ahmed LOUKILI	*Ecole Centrale de Nantes, France*	Examinateur
Dr. François TOUTLEMONDE	*UPE-IFSTTAR, France*	Examinateur
Dr. Christian CLERGUE	*Vicat - Sigma béton, France*	Examinateur
Jacques RESPLENDINO	*SETEC TPI, France*	Examinateur
Pr. René SUTER	*Ecole d'ingénieurs et d'architectes de Fribourg, Suisse*	Co-directeur de thèse
Pr. Robert LE ROY	*ENSA Paris-Malaquais, France*	Directeur de thèse

Préface

Durant les années 2003 à 2006, Lionel Moreillon a fait ses études d'ingénieur civil à l'Ecole d'ingénieurs et d'architectes de Fribourg. Pour son travail de diplôme, il a souhaité faire un projet de portée internationale, le projet du Pont sur le Bras de la Plaine (Ile de la Réunion). Avec le soutien et l'encadrement très précieux de Jacques Combault, ancien directeur scientifique de l'entreprise GTM/Dumez, il a réalisé un excellent travail de diplôme qui fut qualifié par les experts de la note maximale.

Après l'obtention de son diplôme, Lionel Moreillon a travaillé sous ma direction dans le cadre d'un important projet de recherche sur les *«Bétons à hautes performances, renforcés de fibres métalliques»*, un projet soutenu par le Fonds National Suisse de la Recherche Scientifique ainsi que par de différents partenaires industriels.

En été 2008, Lionel Moreillon a décidé de suivre un cours de Master recherche en Mécanique des Matériaux et des Structures à l'Ecole des Ponts Paristech (Université Paris-Est). La qualité de son travail de thèse de Master, basé sur les études expérimentales à Fribourg, lui a ouvert la possibilité de poursuivre sa formation par une thèse de doctorat. L'Ecole d'ingénieurs et d'architectes de Fribourg a ainsi mis au point un cadre de collaboration avec l'Université Paris-Est en définissant les différentes questions techniques, administratives et financières.

Au printemps 2009, Lionel Moreillon a entamé les travaux pour l'obtention du grade de Docteur de l'Université Paris-Est. Il fut convenu que Lionel Moreillon effectue les études théoriques et expérimentales à l'Ecole d'ingénieurs et d'architectes de Fribourg sous la direction commune de Robert Leroy, professeur à l'Université de Paris Est, directeur de thèse, et de René Suter, co-directeur de thèse. Le travail de Lionel Moreillon traite les problèmes du cisaillement et du poinçonnement de dalles en béton fibré à hautes (BFHP) et à ultra-hautes performances (BFUP). Il y décrit les influences de la qualité du béton, du dosage en fibres métalliques, du ratio de l'armature passive et d'une éventuelle précontrainte sur le comportement aux états limites de service et ultime de structures en béton hautes performances.

Dans le cadre de son travail de thèse, Lionel Moreillon a effectué plusieurs séries d'essais sur des éléments de poutres ou de dalles en béton afin de pouvoir étalonner les modèles théoriques. Il a eu l'occasion de présenter ces études à des séminaires et des conférences en suisse et à l'étranger. Le 19 mars 2013, Lionel Moreillon a défendu avec succès son travail de doctorat.

Ce travail a pu être mené à bien grâce à une collaboration positive des différents participants. Je tiens donc à remercier les représentants de l'Université Paris-Est et de l'Ecole d'ingénieurs et d'architectes de Fribourg pour leur attitude très positive à cette collaboration. Je remercie tout particulièrement le professeur Robert Le Roy, directeur de thèse, le professeur Ahmed Loukili, président du jury, les professeurs Emmanuel Ferrier et Aurelio Muttoni, rapporteurs ainsi que Messieurs Christian Clergue, Jacques Resplendino et François Toutlemonde, membres du jury.

Aussi, je tiens à soulever la collaboration très agréable et positive avec Lionel Moreillon et je le félicite très cordialement pour l'accomplissement de son travail.

René Suter

Remerciements

Cette thèse de l'Université Paris-Est a été dans sa plus grande partie réalisée au sein de l'Ecole d'ingénieurs et d'architectes de Fribourg (EIA-FR) en Suisse. Je tiens particulièrement à remercier René Suter sans qui ces travaux n'auraient jamais pu être effectués. Pour m'avoir soutenu et encadré depuis l'obtention de mon diplôme d'ingénieur en génie civil en 2006 jusqu'à la fin de ce travail, pour m'avoir transmis ses nombreuses connaissances techniques et scientifiques, pour m'avoir transmis la passion des études expérimentales dans le domaine des structures pour m'avoir toujours mis en avant lors de congrès nationaux et internationaux. Mes remerciements vont également à Robert Le Roy qui a encadré cette thèse au sein du Laboratoire Navier- équipe Matériaux et Structures Architecturés (MSA). Ses nombreux conseils avisés lors de nos intenses séances parisiennes, son œil critique parfois, son appui technique et scientifique ainsi que sa relecture attentive du manuscrit m'ont motivé et m'ont été d'une grande aide.

Je tiens également à remercier le jury, Aurelio Muttoni, Emmanuel Ferrier, Ahmed Loukili, François Toutlemonde, Christian Clergue et Jacques Resplendino, pour avoir consacré de leur temps et mis à disposition leurs expertises à ce travail, j'en suis très honoré.

Je souhaite remercier, la direction de l'Ecole d'ingénieurs et d'architectes de Fribourg pour le soutien apporté à cette thèse. Merci, à André Oribasi ancien chef de l'Institut de l'environnement et de la construction (iCEN) et Alain Rime responsable de la filière du génie civil. Merci également à Karam Sab directeur du Laboratoire Navier pour m'avoir encouragé à continuer sur une thèse à la suite du Master.

Un grand merci aux différents partenaires industriels pour leurs soutiens financiers et/ou matériels aux études expérimentales, Bekaert Schweiz AG, Creabeton Matériaux AG, Element AG, Elkem, Sika Schweiz AG, Holcim Schweiz AG, Vicat - Sigma béton et Vigier – Vibeton AG. Les contacts rapprochés avec l'industrie m'ont particulièrement enrichi au niveau de ma manière de concevoir.

Un grand merci à tous mes collègues et amis, en particulier, les collaborateurs scientifiques de l'EIA-FR qui m'ont aidé dans le cadre des études expérimentales, Jérôme, Marino, Granit, Raja et Laurent. Merci à toute l'équipe technique du Laboratoire des structures pour votre aide à ce programme expérimental ambitieux aussi pour m'avoir aidé à ramasser tous les morceaux se trouvant à travers le laboratoire, Yanis, Lukas, Arthur et Jean-Paul. Sans oublier pour leur soutien mes (ex) collègues, Emmanuelle et Olivier ainsi que les professeurs de l'EIA-FR, Fabienne, Nicolas et Jean-Marc. J'ai eu un énorme plaisir à travailler et échanger avec vous tous dans une très bonne ambiance.

Je tiens à remercier tout particulièrement Joanna Nseir de l'ESIB, Liban, que j'ai eu le plaisir à encadrer pour son travail de Master et qui m'a beaucoup apporté, entre autre au niveau de la programmation d'Excel et des simulations numériques. Et qui, à la suite de son travail de Master, a débuté une thèse réalisée partiellement à Fribourg. Merci, pour ton amitié, pour ton aide, pour nos discussions, pour ton soutien, pour la correction de mon anglais, etc. Je te souhaite plein de réussite pour ta thèse.

Merci également à Miguel Fernández Ruiz, Stefano Campana,Thibault Clément et Luis Felipe Maya Duque du Laboratoire de construction en béton de l'EPFL (IBETON) pour les discussions et échanges à propos de mes résultats ainsi que sur les modèles développés à l'IBETON.

Mes remerciements vont également à Eugen Brühwiler du Laboratoire de maintenance des structures de l'EPFL pour les discussions et échanges à propos des BFUP ainsi que pour m'avoir intégré au sein du groupe de travail SIA sur les BFUP.

Un grand merci également à Hughes Somja professeur de l'INSA de Rennes pour ces précieux conseils et l'aide apportée pour les simulations numériques avec *FINELg*.

Je tiens à remercier mes amis hors cadre professionnel qui ces derniers temps ne m'ont pas beaucoup vu et m'ont pris parfois pour un fou. Promis, nous rattraperons ces belles randonnées en montagne, ces journées de ski endiablées, ces voyages au bout du monde, etc.

Et pour finir, je tiens à remercier tout particulièrement mes parents, Françoise et Daniel, ma sœur, Sandra, pour leurs soutiens durant ces longues années d'études. En lisant ces quelques phrase, vous vous remémorez peut être qu'à l'école obligatoire ce n'était pas gagné d'avance, que j'avais plutôt un profil d'artiste que de scientifique, mais je vous ai montré qu'avec passion tout était finalement possible. Je vous en suis infiniment reconnaissant pour m'avoir permis d'atteindre cet objectif et m'avoir toujours soutenu dans mes choix.

Résumé étendu

Contexte

L'effort tranchant et le poinçonnement sont des modes de rupture souvent déterminants pour assurer la résistance des structures en béton armé ou précontraint. Pour des éléments ne comportant pas d'armatures de cisaillement, ces modes de rupture sont généralement fragiles entraînant l'effondrement partiel voire total de la structure sans signes avant-coureurs. Dès les premiers développements des bétons de fibres, la réduction voire la suppression totale des armatures dites secondaires dans les éléments de structure s'est avérée être une solution technique intéressante sous certaines conditions. Malgré de nombreux avantages techniques et économiques, particulièrement pour la préfabrication, ce type d'application est resté marginal principalement dû aux manques d'un cadre normatif et de règles de dimensionnement adaptées. D'où la nécessité de développer de tels modèles à destination des ingénieurs de la pratique.

Ces dernières années, les Bétons Fibrés Ultra-Performants (BFUP) connaissent un essor grandissant dans les domaines des ouvrages d'art et du bâtiment. Les réalisations remarquables en BFUP témoignent des très bonnes caractéristiques mécaniques et rhéologiques de ce matériau. En particulier, celui-ci est adapté à la réalisation d'éléments minces, aux formes complexes et aux textures travaillées. Les BFUP sont caractérisés par une compacité nettement supérieure aux bétons conventionnels ce qui leur permet d'atteindre une résistance en compression souvent supérieure à 150 MPa et une perméabilité très faible donc une durabilité élevée. Les BFUP ont souvent un dosage en fibres métalliques important leurs permettant de s'affranchir d'armatures conventionnelles pour des sollicitations modérées, et notamment celles de cisaillement. L'importante résistance en traction post-fissuration et la ténacité des BFUP autorise aux éléments de structure d'atteindre des résistances ainsi qu'une capacité de déformation au cisaillement nettement supérieures en comparaison avec des bétons de fibres de résistances ordinaires.

Les BFUP, peut être par effet de mode ou par méconnaissance des professionnels de la construction, occultent un large éventail de bétons de fibres présentant des caractéristiques intéressantes pour des applications structurales. L'emploi des BFUP est justifié si celui-ci répond à plusieurs exigences simultanées qu'elles soient rhéologiques, mécaniques et de durabilité. L'utilisation des BFUP n'étant pas toujours justifiée, la nécessité d'investiguer des bétons fibrés entre les bétons de fibres de classes ordinaires et les BFUP s'avère une opportunité intéressante d'un point de vue technique, économique et vis-à-vis du développement durable. Ce type de béton, nous l'appelons dans le cadre de ce travail Bétons Fibrés à Hautes Performances (BFHP). Par rapport au BFUP, les BFHP se distinguent par une moindre quantité de fibres, une granulométrie plus grossière et des résistances mécaniques plus faibles mais suffisante dans beaucoup d'applications structurales. Pourquoi, la haute performance est-elle nécessaire ? Car, les Bétons à Hautes Performances (BHP) utilisent pleinement les performances du ciment d'une part, et les propriétés mécaniques élevées permettent de réduire les dimensions des éléments de structures d'autre part. De plus, l'augmentation de la résistance de la matrice permet d'obtenir un meilleur ancrage de la fibre dans la matrice.

Les processus industriels d'une usine de préfabrication permettent l'emploi de tels bétons en vomparaison aux coulages réalisés in situ. Actuellement, des bétons autoplaçants de classes C50/60 à C80/95 sont largement employés en préfabrication. Le prochain pas de cette industrie est d'intégrer les

BFHP et les BFUP à l'échelle industrielle. Dans le but d'obtenir des éléments de structure plus légers, plus résistants, plus durables, plus innovants, etc. que ce qui se fait actuellement et permettre de se démarquer des méthodes traditionnelles du béton armé in situ.

Travail de thèse

Dans le cadre de cette thèse, plusieurs études expérimentales sur différents éléments de structures, poutres et dalles en BFHP et BFUP sans armatures de cisaillement, ont été effectuées dans le but d'analyser leur comportement vis-à-vis de l'effort tranchant et du poinçonnement, d'une part, et de proposer des règles de vérification pour les ingénieurs de la pratique, d'autre part. Parallèlement aux essais de structures, les propriétés mécaniques des BFHP et BFUP utilisés dans ce travail et plus particulièrement la réponse post-fissuration, ont été déterminées au moyen de nombreux échantillons. Les lois de comportement ont ensuite été identifiées et comparées sur la base de différents modèles proposés dans la littérature. La liaison entre les méthodes de caractérisation du matériau et le comportement au niveau de la structure s'avère être un problème clé et délicat. Cet état de fait provient principalement du caractère anisotrope de ces matériaux et des difficultés à maitriser l'orientation des fibres.

Les éléments préfabriqués de structure en béton armé ou précontraint sont caractérisés par leur haute qualité (finitions, etc.) et les délais réduits de construction sur le chantier. La large gamme d'éléments produits permet de répondre à toutes sortes de structures, particulièrement pour des applications commerciales et industrielles. Selon les normes nationales et internationales, les âmes des poutres doivent comporter une armature minimale d'effort tranchant. En préfabrication, cette armature est composée d'étriers ou de treillis spéciaux façonnés. Cette armature mobilise de l'espace pour sa production et son stockage, complique sensiblement la production des éléments précontraints par pré-tension et impose des contraintes géométriques aux sections. Le remplacement de cette armature, dite secondaire, par un BFHP s'avère une solution technique et économique intéressante pour cette industrie. De plus, la suppression de cette armature permet de s'affranchir des contraintes géométriques (enrobages minimals, façonnage, etc.) d'où un pas important vers le développement d'éléments plus fins, triangulés, allégers, etc.

Dans une première campagne expérimentale, six poutres de 5.60 m et deux poutres de 12.40 m de longueur ont été testées afin d'évaluer le comportement à la flexion et la résistance à l'effort tranchant d'éléments précontraints par pré-tension en BFHP sans armatures de cisaillement. Le paramètre principal entre les éléments d'essai était le dosage en fibres. Dans le cadre de cette étude, cinq compositions de BFHP adaptées à la préfabrication ont été développées. Les recettes se distinguaient par leur dosage en fibres et présentaient les caractéristiques suivantes ; béton autoplaçant (SCC), une résistance à la compression de 100 MPa, utilisation de granulats locaux de diamètre 0 à 16 mm et un dosage en fibres allant jusqu'à 80 kg/m^3.

Figure 1: Essais de charge sur les poutres courtes et longues en BFHP

Les essais de charges réalisés sur les poutres de 3.00 m de portée ont mis en évidence la contribution bénéfique des BFHP sur le comportement et la résistance à l'effort tranchant d'éléments précontraints, d'une part, et la capacité des fibres métalliques à remplacer l'armature minimale de cisaillement, d'autre part. Les poutres en BFHP présentaient une rigidité plus élevée en présence des fissures diagonales d'effort tranchant en comparaison aux éléments en BHP. Les fibres, si elles sont en quantité suffisante, contrôlent efficacement le développement des fissures critiques de cisaillement. Dans la configuration testée, une quantité de fibres de seulement 40 kg/m^3 a permis de retarder significativement l'apparition de la fissure critique grâce au développement d'un réseau de plusieurs fissures diagonales et atteint une résistance similaire à la poutre de référence en BHP comportant l'armature minimale d'effort tranchant. Les deux essais sur les poutres de 12.00 m de portée ont confirmé ces effets avec une rupture brutale par cisaillement de l'élément en BHP sans fibres et une rupture en flexion sans fissures diagonales de la poutre en BFHP avec 60 kg/m^3 de fibres métalliques. Cette étude a clairement mis en évidence le potentiel d'un BFHP à remplacer l'armature secondaire en usine de préfabrication.

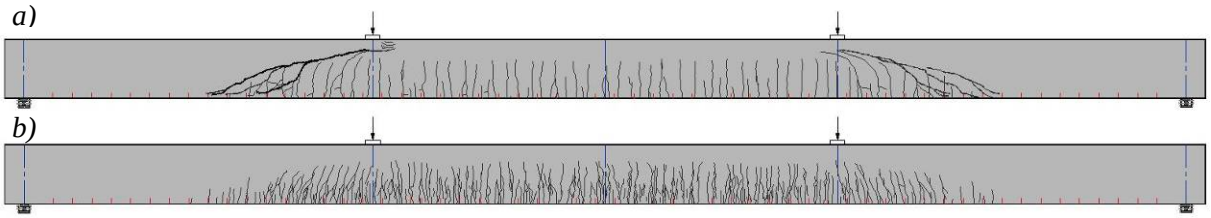

Figure 2: Aspect de la fissuration à la rupture des deux poutres de 12m de portée, AF-1 sans fibres a), AF-2 avec fibres 60 kg/m^{3}b)

Les dalles et les plaques sont des éléments redondants des structures en béton armé et précontraint. Cependant, malgré leur grande utilisation à travers le monde, le comportement et la résitance à la flexion et au poinçonnement des plaques en béton armé demeurent un problème complexe. Ceci pour des raisons de non linéarité des matériaux et de fissuration. Les bétons de fibres sont bien adaptés aux dalles dû à la capacité de redistribution de celles-ci et la propension des fibres à ponter des fissures par rapport à des armatures placées orthogonallement. Le recours à des BFHP ou des BFUP associés ou non à des armatures passives ou précontraintes permet la réalisation de plaques minces destinées par exemple à des planchers, des tabliers de ponts ou des façades. A nouveau, le poids propre des éléments de structures peut être sensiblement réduit par l'utilisation de ces matériaux.

Dans une seconde partie, comprenant deux campagnes expérimentales, ont été testées 20 dalles carrées en BFHP armées et précontraintes pour la première ainsi que 19 dalles carrées en BFUP avec et sans armatures passives. Le but principal était d'évaluer le comportement à la flexion et au

poinçonnement des dalles en BFHP et en BFUP. Dans la première étude, les paramètres principaux distanguant les éléments d'essai étaient : le dosage en fibres, le taux d'armatures passives et l'intensité de la force de précontrainte. Les dimensions des dalles carrées étaient 1240 mm de côté pour une épaisseur de 120 mm. Pour cette étude, cinq compositions de BFHP ont été développées. Les recettes se distinguaient par leur dosage en fibres et présentaient les caractéristiques suivantes : une résistance à la compression de 100 MPa, utilisation de granulats locaux de diamètre 0 à 8 mm et un dosage en fibres allant jusqu'à 80 kg/m^3.Pour la seconde étude, les paramètres étaient, le dosage en fibres, l'épaisseur et le taux d'armatures passives. Les dimensions des dalles carrées étaient 960 mm de côté pour une épaisseur variant de 30 à 80 mm. Le BFUP utilisé dans le cadre de cette étude était le Béton Composite Vicat Structure (BCV) avec des taux volumiques de fibres de 1 et 2%.

Figure 3: Essai de poinçonnement sur les dalles en BFHP et en BFUP

Pour des dalles en béton armé conventionnel sans armatures transversales, il a été montré que la résistance au poinçonnement est inversement proportionnelle à la capacité de déformation. Autrement dit, pour des dalles présentant les même caractéristiques (béton, épaisseur, système statique), plus le taux d'armature augmente plus la résistance au poinçonnement augmente. Par contre la capacité de déformation diminue. En observant les résultats le constat est similaire pour les dalles en BFHP et en BFUP mais à des niveaux de charges et de déformations plus importants. Au niveau du comportement à l'état de service, les dalles avec du béton fibré montraient une rigidité plus élevée et une fissuration mieux répartie avec des ouvertures plus faibles que les dalles en béton sans fibres.

Les essais ont mis en évidence la contribution importante des fibres métalliques sur la résistance au poinçonnement des dalles. En quantité suffisante, les fibres permettaient même d'atteindre la capacité flexionnelle de l'élément sans rupture prématurée par poinçonnement. Toute les dalles avec fibres présentaient une résistance au poinçonnement plus élevée ainsi qu'une capacité de déformation plus importante en comparaison aux dalles sans fibres. Par conséquent, le poinçonnement qui est souvent caractérisé comme un mode de rupture fragile devient plus "ductile" avec l'ajout de fibres ou autrement dit, intervient sous de plus importantes déformations.

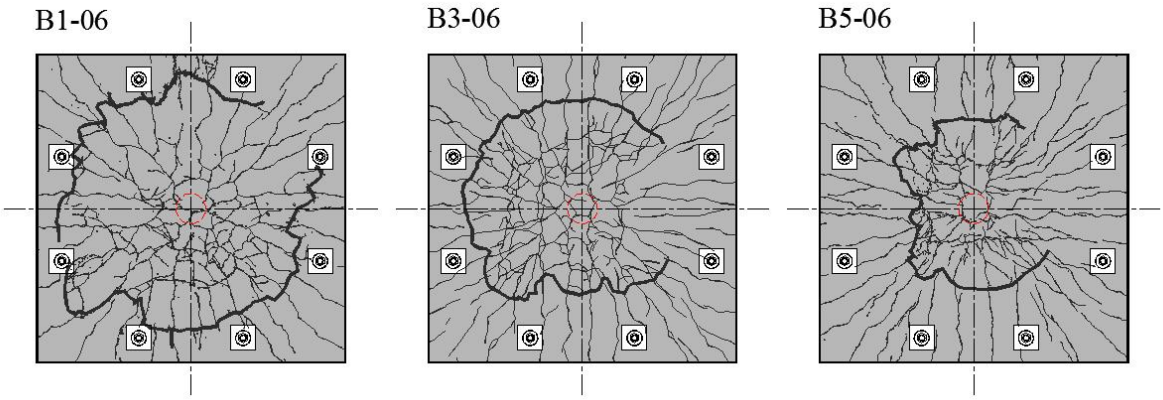

Figure 2: Aspect de la fissuration à la rupture de dalles en BFHP avec armatures, B1-06 sans fibres, B3-06 avec fibres 40 kg/m^{3}et B3-06 avec fibres 80 kg/m^3

A l'heure actuelle, les bétons de fibres structurels ne sont pas encore intégrés dans de nombreuses normes nationales et internationales de construction comme par exemple les Eurocodes. Mais, la tendance évolue dans le bon sens avec la publication récente du *fib* Model Code 2010 qui intègre les bétons fibrés ou certaines recommandations comme celles de l'AFGC sur les BFUP. Ces documents sont de bonnes bases pour les ingénieurs de la pratique mais ont encore un potentiel de développement et d'améliorations surtout au niveau des modèles de cisaillement. Prenons, l'exemple du *fib* Model Code 2010, les modèles proposés pour la résistance à l'effort tranchant des éléments en béton fibré sont basés sur des formulations empiriques alors que dans le même document de nouveaux modèles physiques plus précis sont proposés pour le béton armé. A noter que ces modèles sont déjà adoptés par les normes de construction en béton Canadienne et Suisse. Alors pourquoi ne pas avoir harmonisé les modèles du béton fibré ! Ceci, améliorerait la compréhension des ingénieurs de la pratique et favoriserait l'emploi de ces matériaux. Au niveau des modèles de poinçonnement pour les bétons de fibres peu, voire aucunes règles n'existent dans les normes et recommandations actuelles.

Dans le cadre de ce travail, des modèles de calcul pour la vérification à l'effort tranchant et au poinçonnement d'éléments de structures en BFHP et en BFUP à destination des ingénieurs de la pratique sont proposés et validés sur la base des différentes études expérimentales. Ces propositions se basent principalement sur des modèles existants robustes tel que la théorie de la fissure critique pour le poinçonnement ou la théorie des champs de compression modifiés pour l'effort tranchant et font intervenir les contributions de la matrice $V_{R,c}$ et des fibres $V_{R,f}$. Ces modèles supposent que la résistance au cisaillement de la matrice est une fonction de l'ouverture et de la rugosité de la fissure critique.
La part des fibres correspond quant à elle, à la composante verticale de l'intégrale des contraintes de traction sur le plan de rupture. La distribution de l'ouverture de fissure est considérée linéaire le long du plan. En ayant préalablement identifié la loi de comportement contrainte – ouverture de fissure $\sigma(w)$ sur la base d'essais de caractérisation du matériau, la distribution des contraintes de traction est définie le long du plan de rupture. Etant conscient qu'il s'agit d'un niveau de vérification élevé, des modèles simplifiés considérant une valeur de référence déterminés sur la base d'essais de caractérisation sont aussi proposés et validés.

Conclusions

En conclusion, l'utilisation des matériaux cimentaires à hautes et ultra-hautes performances renforcés de fibres métalliques offrent de nouvelles perspectives pour le développement de systèmes porteurs plus innovants et durables. Ceci peut être atteint, en réduisant les sections, en plaçant le bon et la bonne quantité de matériau au bon endroit ou encore en combinant différents matériaux. L'utilisation de tels bétons est parfaitement adaptée à la préfabrication et permettra sûrement à cette industrie de se démarquer et reconquérir des parts de marché par rapport aux techniques de construction en béton in situ. Les craintes récurrentes des ingénieurs praticiens au niveau des connexions entre éléments préfabriqués sontaussi balayées par l'utilisation de connexion en BFUP coulé in situ permettant ainsi d'obtenir des structures monolithiques.

Abstract

For members and flat slabs without shear reinforcement, the shear and punching shear strength are often the determining design criteria. These failure modes are characterized by a brittle behaviour implying possible partial or total collapse of the structure. Despite extensive research in this field, shear and punching shear in reinforced and prestressed concrete structures, remain complex phenomena so much that the current approach is often empirical or simplified. The ability of Steel Fibre Reinforced Concrete (SFRC) to reduce shear reinforcement in reinforced and prestressed concrete members and slabs, or even eliminate it, is supported by several experimental studies. However its practical application remains marginal mainly due to the lack of standard, procedures and rules adapted to its performance.

The stationary processes in precast industry offer optimal possibilities for using high performance cementitious materials such as Self Compacting Concrete (SCC) and High Strength Concrete (HSC). The combination of High Performance Concrete and steel fibres is the following step in the development and the optimization of this industry. The High Performance Fibre Reinforced Concrete (HPFRC) stands between conventional SFRC and Ultra-High Performance Fibre Reinforced Concrete (UHPFRC). The HPFRC exhibiting a good strength on cost ratio is, thus, an alternative of UHPFRC for precast elements.

The principal aim of this work was to analyse the shear and punching shear behaviour of HPFRC and UHPFRC structures without transversal reinforcement and to propose recommendations and design models adapted for practitioners. Several experimental studies on structural elements, i.e. beams and slabs, were undertaken for this purpose.

Firstly, an original experimental campaign was performed on pre-tensioned members made of HPFRC. A total number of six shear-critical beams of a 3.6 m span each, and two full scale beams of a 12 m span each, were tested in order to evaluate the shear and flexural strength. The principal parameter between the specimens was the fibres content. Five HPFRC mixes adapted for precast industry were developed and were distinguished by their fibres content. The material properties, particularly the post cracking response were identified by a large number of specimens. The tests have highlighted the beneficial contribution of HPFRC on shear capacity and the ability of steel fibres to replace the minimum shear reinforcement. The HPFRC beams exhibited higher stiffness in presence of diagonal shear cracks. The fibres controlled the development of the diagonal cracks, with either a low or high content. For HPFRC members, from a fibres quantity of 40 kg/m^3, the formation of critical shear cracks was significantly delayed due to the formation of a secondary cracking pattern. The full scale beam AF-1 in High Strength Concrete failed in shear, while the HPFRC members exhibited a flexural failure.

Secondly, two original experimental studies were performed on thin slabs made out of HPFRC and UHPFRC with and without reinforcement. A total number of twenty square slabs in HPFRC and nineteen slabs in UHPFRC were tested in order to evaluate the punching shear strength and the flexural behaviour. The material properties were identified by a large number of specimens.The principal parameters of the HPFRC slabs were the fibres quantity, the reinforcement ratio and the intensity of axial forces applied by post-tensioning. The principal parameters of the UHPFRC slabs were the fibres dosage, the reinforcement ratio and the thickness. Tests results have highlighted the

beneficial contribution of HPFRC and UHPFRC on punching shear capacity. They have also shown an increased deformation capacity at failure state. The increased serviceability behaviour of the HPFRC and UHPFRC slabs has shown less cracking, reduced crack width and smaller deformations.

In order to develop harmonized models, the proposals for the assessment of shear and punching shear strength are based on the latest developments concerning this topic, respectively the Critical Shear Crack theory. The proposed models involve the matrix contribution $V_{R,c}$ and the fibres contribution $V_{R,f}$. The failure criterion presented a good agreement compared to the different test results. Simplified models were also proposed based on reference values identified on specimens.

Keywords: shear and punching shear strength, pre-tensioned members, RC slabs, post-tensioned slabs, precast industry, high strength concrete, steel fibres, UHPFRC, flexural behaviour, full scale tests, design guideline, rules.

Résumé

Pour les poutres et les dalles ne comportant pas d'armatures de cisaillement, la résistance à l'effort tranchant ou au poinçonnement est souvent un critère important de dimensionnement. Ce type de rupture est caractérisé par un comportement fragile pouvant conduire à l'effondrement partiel voir total de la structure. Malgré de nombreuses recherches dans ce domaine, la résistance à l'effort tranchant et au poinçonnement des structures en béton armé ou précontraint demeure un phénomène complexe et dont l'approche normative est souvent empirique et simplifiée. La capacité des bétons renforcés de fibres métalliques à réduire voire à remplacer totalement les armatures de cisaillement des structures en béton armé et précontraint a été mise en évidence par plusieurs études expérimentales. Cependant, et malgré ses nombreux atouts, l'application à l'échelle industrielle des bétons de fibres est restée marginal, principalement due au manque d'un cadre normatif cohérent et reconnu.

Les processus fixes d'une usine de préfabrication d'éléments en béton offrant des possibilités optimales pour utiliser des matériaux cimentaires à hautes performances tel que les bétons autoplaçant, les bétons à hautes résistances, etc. L'utilisation de bétons à hautes performances renforcés de fibres métalliques est le pas de développement et d'optimisation pour cette industrie. Les Bétons Fibrés à Hautes Performances (BFHP) reprennent une matrice similaire aux Bétons à Hautes Performances (BHP) auxquels est ajoutée une certaine quantité de fibres métalliques conférant au matériau un comportement au niveau de la structure exploitable dans le dimensionnement. Les BFHP présentent un ratio résistances/coûts intéressant ainsi qu'une alternative aux Bétons Fibrés Ultra-Performants (BFUP) pour certaines applications.

L'objectif principal de ce travail est d'analyser le comportement au cisaillement et au poinçonnement d'éléments de structures en BFHP et en BFUP sans armatures de cisaillement et de proposer des recommandations et des règles de dimensionnement adaptées aux ingénieurs de la pratique. Pour répondre à cet objectif plusieurs études expérimentales sur des éléments de structures, poutres et dalles ont été réalisées.

Premièrement, une campagne expérimentale originale sur des poutres en BFHP précontraintes par pré-tension a été effectuée. Six poutres courtes de 3.6 m de portée ainsi que deux longues poutres de 12 m de portée ont été testées dans le but d'évaluer le comportement flexionnel et la résistance à l'effort tranchant. Le principal paramètre distinguant les éléments était le dosage en fibres métalliques. Cinq compositions de BFHP autoplaçant avec une résistance en compression de 100 MPa ont été développées. Les compositions étaient différenciées par leur dosage en fibres. Les caractéristiques mécaniques, particulièrement la résistance en traction post-fissuration, ont été identifiées par de nombreux essais sur des échantillons. Les essais de charges ont mis en évidence l'effet bénéfique des fibres métalliques sur la résistance à l'effort tranchant et la capacité des fibres à remplacer le pourcentage minimum d'armatures de cisaillement. Les poutres en BFHP ont montré une rigidité plus élevée que les poutres en BHP en présence de fissures diagonales de cisaillement. Les fibres, même en quantité limitée, permettent de contrôler efficacement le développement des fissures de cisaillement. Pour les poutres longues, l'élément sans fibres a eu une rupture soudaine à l'effort tranchant, alors que l'élément en BFHP a eu une rupture en flexion sans la formation de fissures diagonales.

Deuxièmement, deux études expérimentales originales sur des dalles minces en BFHP et en BFUP avec et sans armature et précontrainte ont été réalisées. Un total de 20 dalles en BFHP et 19 dalles en

BFUP ont été testées dans le but d'évaluer le comportement flexionnel et la résistance au poinçonnement. A nouveau, les propriétés mécaniques des différents bétons ont été identifiées à travers de nombreux essais sur échantillons. Les paramètres principaux distinguant les dalles en BFHP étaient, la quantité de fibres, le taux d'armatures passives et l'intensité de l'effort normal induit par la précontrainte. Pour les dalles en BFUP, les paramètres étaient : la quantité de fibres, l'épaisseur et le taux d'armatures passives. Les résultats des essais de chargement ont mis en évidence l'effet bénéfique des BFHP et des BFUP sur la résistance au poinçonnement des dalles. Ils ont aussi montré une capacité de déformation plus importante des dalles avec des fibres. De plus, à l'état de service les dalles en BFHP et en BFUP présentaient des fissures mieux réparties avec de faibles ouvertures ainsi que des déformations réduites.

Dans le but de développer un modèle harmonisé avec les derniers développements sur la résistance à l'effort tranchant et au poinçonnement des structures en béton armé et précontraint, les modèles proposés sont basés sur la théorie de la fissure critique (CSCT). Les modèles proposés font intervenir la contribution de la matrice $V_{R,c}$ et la contribution des fibres $V_{R,f}$. Les différents critères de rupture présentent une bonne corrélation avec les résultats expérimentaux. Des modèles de dimensionnement simplifiés sont aussi proposés sur la base de valeurs caractéristiques identifiées au moyen d'essais sur des échantillons normalisés.

Mots clés : Bétons fibrés à hautes performances BFHP, bétons fibrés à ultra-performants BFUP, formulation, propriétés, résistance post-fissuration, résistance à l'effort tranchant, résistance au poinçonnement, éléments préfabriqués, poutres, dalles, armature passive, précontrainte, essais de charge, modèles de dimensionnement.

List of abbreviations

AFGC	Association Française de Génie Civil
BCV	Béton Composite Vicat
CMOD	Crack Mouth Opening Displacement
COD	Crack Opening Displacement
CSCT	Critical Shear Crack Theory
ECC	Engineered Cementitious Composites
fib	International Federation for Structural Concrete
HPC	High Performance Concrete
HPFRC	High Performance Fibre Reinforced Concrete
HSC	High Strength Concrete
LC	Lightweight Concrete
LVDT	Linear Variable Differential Transducer
PT	Post-tensioning
RC	Reinforced Concrete
RILEM	International union of laboratories and experts in construction materials, systems and structures
SFRC	Steel Fibre Reinforced Concrete
SIA	Swiss Society of Engineers and Architects
SIFCON	Slurry Infiltrated Fibre Concrete
SCC	Self Compacting Concrete
SLS	Serviceability Limit State
MCFT	Modified Compression Field Theory
NSC	Normal Strength Concrete
UHPFRC	Ultra-High Performance Fibre Reinforced Concrete
UHPC	Ultra-High Performance Concrete
ULS	Ultimate Limit State
VEM	Variable Engagement Model

A	volume of air
A_c	cross-section area of concrete
A_p	cross-section area of prestressing steel
A_s	cross-section area of steel reinforcement
C_{eq}	equivalent mass of cement
E	Young's modulus
F	force, load
$F_{p,0}$	initial prestressing force
G_F	fracture energy
K	fibre orientation coefficient
L	span
M	moment
P	load
P_z	mass of pozzolan
R_c	cement compressive strength on ISO mortar

V_f	volume fraction of fibre
V_{flex}	flexural capacity
V_R	shear and punching shear strength
$V_{R,c}$	shear and punching strength carried by the concrete
$V_{R,s}$	shear and punching strength carried by the transversal reinforcement (stirrups, etc.)
$V_{R,f}$	shear and punching strength carried by the fibres
W	volume of water
a	crack length; shear span
b	width
b_0	section or perimeter of control for shear and punching shear
c	compression depth
d	effective depth
d_f	diameter of fibre
d_g	maximum aggregate size
d_{g0}	reference aggregate size
f_c	concrete compressive strength
$f_{c,cube}$	concrete compressive strength on cube
f_{ct}	concrete tensile strength
f_{Fts}	serviceability residual strength
f_{Ftu}	ultimate residual strength
$f_{fct.L}$	Limit Of Proportionality *(LOP)*
f_{matrix}	compressive strength of cementitious matrix
f_{paste}	compressive strength of cementitious paste
$f_{p0,1}$	yield limit of prestressing steel at 0.1%
f_{py}	yield limit of pretressing steel
f_{Ri}	values of residual tensile strength
$f_{s0,2}$	yield limit of reinforcement steel at 0.2%
f_{sy}	yield limit of reinforcement steel
f_u	ultimate strength of reinforcement or prestressing steel
g	volume of aggregates in a unity of concrete volume
g^*	compactness of aggregates
h	thickness
h_n	depth in the notched cross-section
k	reactive coefficient of the pozzolan addition
l_c	characteristic length
l_f	length of fibre
m	moment per unit length
q	distributed load
r_q	radius of the load application
r_c	radius of the column
r_s	radius of the slab
s	non-linear hinge length; length of failure plan
s_{rm}	average crack spacing
w	crack opening
w_0	crack opening, non-linear distribution
w_u	ultimate crack opening

α	angle of compression strut
β	coefficient taking into account the orthogonal arrangement of the reinforcement
β_u	angle of compression strut
χ	curvature
ε	strain
δ	deflection at centre
ϕ	diameter
κ	coefficient relating the rotation to the critical shear crack opening
ρ	density, reinforcement ratio
θ	rotation, angle of compression strut
σ	stress
σ_{cp}	uniform compressive stress in concrete due to prestressing
σ_{eq}	equivalent bending stress
τ	tangential stress
ψ	slab rotation
ν	Poisson's ratio
ζ	depth

Table of content

1 Introduction

1.1 Framework

From the beginning of the 20th century, Reinforced Concrete structures experienced a rapid development and became an indispensable building technology in our modern society. The concrete technology has continuously evolved, due to active research in this field. The advanced knowledge in cementitious materials has led to the development of concrete having particular properties and increasingly high performances, in term of the mechanical properties, the rheology and the durability. Since 1980, High Performance Concrete (HPC) was used at a large scale for buildings and bridges. Important knowledge about the formulation, the properties and the implementation process were developed. In comparison with the conventional concrete, HPC showed several advantages from a technical and an economical point of view.

In parallel, the progress in Steel Fibre Reinforced Concrete (SFRC) has led to the development of Ultra-High Performance Fibre Reinforced Concrete (UHPFRC). The UPHFRC is characterized by its high tensile toughness and compressive strength. Since 2000, UHPFRC knew several structural applications and highlighted the numerous advantages of using steel fibres in cementitous materials. However, the high properties and mainly the high cost of the material itself, restrained its applications only for thin and highly stressed elements. For numerous applications like the recovery of secondary stresses (shear and punching shear), the UHPFRC performances are not necessary. A High Performance Fibre Reinforced Concrete (HPFRC) with less fibres content is technically sufficient and is less expensive or has a lower cost compared to UHPFRC. Moreover, This HPFRC shows the same properties of a HPC but the main difference between them is the ductile character provided by the steel fibres.

The shear and punching shear failure mode of reinforced concrete members and slabs without transversal reinforcement is characterized by a fragile behaviour implying possible, partial or total collapse of the structure. Despite extensive research in this field, shear and punching shear in reinforced concrete structures remain complex phenomena. Subsequently, the current approach is often empirical or simplified. However, recent developments in shear and punching shear approaches based on physical model with the Modified Compression Field Theory and the Critical Shear Crack Theory gave accurate predictions. Thanks to this high tensile toughness, the High Performance Fibre Reinforced Concrete (HPFRC) can increase the shear and punching shear capacity. Steel fibres offer themselves as an alternative reinforcement possibility particularly in precast industry.

The ability of Steel Fibre Reinforced Concrete (SFRC) to reduce shear reinforcement of reinforced concrete members or even eliminate it, is supported by several experimental studies. However this practical application remains marginal mainly due to the lack of an accurate and harmonized design model. Currently, design codes or recommendations were developed for SFRC having a normal strength and for UHPFRC. A rather huge gap exists between these two classes and is not integrated yet. Therefore the use of HPFRC is limited despite its numerous advantages. This is mainly due to the lack of knowledge concerning its properties and its structural behaviour.

1.2 Objectives

The main objectives of this thesis were;

- to evaluate the flexural, shear and punching shear behaviour at the Service Limit State SLS and the Ultimate Limit State ULS of HPFRC structures (beams and slabs) without transversal reinforcement,
- to propose accurate shear and punching shear strength model and design rules for elements in HPFRC intended for practionners,
- to determine the principal mechanical properties of HPFRC, particularly the post-cracking response,
- to demonstrate that the production of HPFRC structural elements is feasible at competitive costs in precast industry.

In order to respond to these objectives the following theoretical and experimental studies were performed;

- a High Performance Fibre Reinforced Concrete with the Self Compacting criterion and a compressive strength around 100 MPa was formulated,
- the post-cracking response of HPFRC mixes used in the different experimental studies were determined using several testing methods,
- six shear beams and two full scale beams were tested in order to evaluate the possibility of the HPFRC to substitute the minimum transverse reinforcement,
- twenty HPFRC slabs and nineteen UHPFRC slabs were tested in order to evaluate the punching shear phenomenon and the flexural behaviour.
- an harmonized model based on the last development in shear and punching shear design of reinforced concrete structure was adapted for HPFRC structures.

1.3 Thesis organisation

This thesis is divided into six chapters including the introduction. This structure chronologically follows the works performed during this thesis and leads the reader to a good understanding of the topic. In Chapter 3 to 5, an introduction reminds the reader about the specific problem statement and the objectives.

In Chapter 2, the literature survey is presented and is divided into three parts mainly focusing on the High Performance Concrete, the Steel Fibre Reinforced Concrete material properties and the shear and punching shear strength of reinforced and prestressed concrete structure including several theoretical and experimental studies (which are reviewed and discussed).

In Chapter 3; the formulation of a HPFRC with the SCC criterion is detailed, the principal mechanical properties and corresponding testing methods of HPFRC and UHPFRC mixes used in Chapter 4 and 5 are also presented to then identify and compare the post-cracking response of a HPFRC and a UHPFRC through different models.

In Chapter 4, the results of an experimental research program on pre-tensioned precast members in HPFRC are presented. The test results were compared to several shear strength models for FRC

elements which were available in the literature. A numerical analysis and a simplified model are also presented.

In Chapter 5, the results of two originally experimental research programs on the flexural and punching shear strength of thin HPFRC and UHPFRC slabs are presented. A numerical analysis of the slabs based on the last development on punching shear design of reinforced concrete structure- particularly the Critical Shear Crack Theory (CSCT) is detailed.

And finally, the Chapter 6 presents the conclusions, recommendations and prospects for further research about the shear and punching shear strength of HPFRC structures.

Three appendices are added to this document: Appendix A1 A2 and A3, presenting the results of the experimental research on beams and slabs.

2 Literature survey

This literature survey is divided in three parts corresponding to Chapters 3 to 5. The first part relates the material technology of High Performance Concrete (HPC) and Steel Fibres Reinforced Concrete (SFRC); the components, the mix proportioning methods and the principal mechanical properties including the testing methods are reviewed. In the second part, the shear behaviour and models of reinforced and prestressed concrete members is investigated. Moreover several similar works on shear strength of SFRC members are detailed. And finally in the third part, the punching shear behaviour and models of reinforced concrete slabs are studied. Several similar works on punching shear strength of SFRC slabs are also detailed. The topic of this thesis is large, therefore only relevant and original works are listed.

2.1 From Normal Strength Concrete to Ultra-High Fibre Reinforced Concrete

2.1.1 Development and definition

2.1.1.1 Generalities

The Concrete technology was already known by the Roman. The Pantheon in Rome is the finest example. After the Roman Empire, the use of concrete became scarce. The Concrete technology was re-pioneered in the mid-19th century by Louis Vicat and Joseph Aspdin with the development of modern cement. From the beginning of the 20thcentury, the Concrete technology knew a rapid expansion due to the development of Reinforced Concrete. Currently, concrete is a material largely used around the world due to its economical components locally-available in large quantities.

Figure 2-1: From the first Concrete Bridge (L. Vicat 1855) to the Burj Khalifa Tower (2008)

Concrete is composed of different phases; the aggregate, generally more rigid and resistant compared to the other components; the solid products of the hydration reaction; one part of cement that has not completely reacted and continues slowly the hydration reaction; a certain volume of pores, empty or partially filled with water. The advanced knowledge in cementitious materials has sets its qualities, but also its weaknesses. Active research in this field, particularly on cement hydration process, additives and optimization of the packing density has led to the development of concrete with particular

properties and high performance. The performance term is not limited to only the mechanical properties but also include the rheology and the durability.

2.1.1.2 High Strength Concrete – High Performance Concrete

The first development and implementation of High Strength Concrete (HSC) were carried out at Chicago for several tower constructions in 1960's. The HSC exhibited a modest compressive strength, around 60 MPa, but was two times higher compared to the ready mix concrete of the time. The principal benefit was the decrease of the columns' cross-sections therefore a gain of space. The compressive strength increase is correlated to the development of modern superplasticizer and the use of silica fume from 1980's. Hans Hendrik Bache [BAC1991] was a pioneer in the development of ultra-high fine particle based materials. The UHPC developed by Bache reached a compressive strength of 280 MPa with a water-on-binder ratio of 0.16 and a special curing treatment. However, this concrete was an academic material. During this time, several developments were undertaken in bridge engineering, particularly in France by Malier and Richard [AIT2001]. Yves Malier was the first to introduce the term High Performance Concrete because the performances are not limited only to the strength but also include high durability, rapid strength development, rapid development of creep and shrinkage, etc. The company Bouygues, under the leadership of Pierre Richard, has used High Performance Concrete at large-scale with Ile de Ré Bridge, Arche de la Défense and Sylans and Glacière Viaducts (Figure 2-2) [AIT2001]. Since the 1990's, HPC were used inter alia for Normandie Bridge, Confederation Bridge, several offshore oil platforms in North Sea, Millau Viaduct and Burj Khalifa Tower. Important knowledge about the concrete mix design, the properties and implementation process were developed in France [LOU1996] [ROY1996] [LAR2000] [BHP2000] [TOU2003]. Currently in Europe, HPC with a compressive strength around 60 to 80 MPa is widely used in precast industry but still stay uncommonly casted in-situ.

Figure 2-2: Ile de Ré Bridge under construction and Glacières Viaducts on highway A40 France

According to the *CEB-fip* Model Code 1990 [CEB1993], a concrete is considered as a HPC if the compressive strength on cylinder is in excess of 60 MPa at 28 days. In the North American practice [ACI1992], High strength concretes are those reaching a compressive strength of at least 41 MPa on cylinders at 28 days. Currently, HPC with a compressive strength up to 100 MPa is integrated in several standards [EC22005] [SIA262].

2.1.1.3 Fibre Reinforced Concrete

The first research on Fibre Reinforced Concrete (FRC) was performed by Romualdi in 1960's [ROM1964]. His works were based on the idea that discrete fibres randomly distributed throughout the concrete mass can control the cracking process. FRC was subjected to several experimental and

industrial developments in the recent years. However structural use of FRC remains limited to specific applications like pavements, tunnel segment and shotcrete for walls and tunnels [ROS1998] [ROS2002] [SUT2005a] [SUT2005b]. Important knowledge of the interaction between fibres and matrix has been in a constant development [NAA2012]. FRC with high fibre volume ratio was developed like the Slurry Infiltrated Fibre Concrete (SIFCON) and Engineered Cementitious Composites (ECC). These materials exhibit a higher toughness compared to conventional FRC. From his initial works on Ultra-High Performance Concrete, Bache focused on combination of high volumes of fibres and high steel reinforcement ratios, for slender structures. In order to avoid the splitting effect due to the bars for this structure, he proposed to add a sufficient amount of fine steel fibres to UHPC. In 1990's, Pierre Richard developed the Reactive Powder Concrete (RPC) [RIC1995]. The RPC was the base of modern Ultra-High Performance Fibre Reinforced Concrete (UHPFRC) [BEH1996]. In 1997, the first remarkable structural application of UHPFRC was the Sherbrooke Footbridge [AIT1998]. Since the 2000's, UHPFRC knows an important development along with several applications [TOU2011] (Figure 2-3), while FRC stays an unusual material.

Figure 2-3: Seonyu Footbridge in Korea and roof covering of Millau Viaduct toll-gate in France

2.1.1.4 Self-Consolidating Concrete

The Self-Consolidating Concrete, also known as Self-Compacting Concrete (SCC) was first developed in Japan by several researchers, led by Okamura and Ozawa, at the University of Tokyo in 1980's. This highly workable concrete places itself without mechanical vibration (Figure 2-4). Therefore SCC does not require as many workers for its placement and the environmental impact (noise) due to the vibration is eliminated. SCC mixes are characterized by their flowability, passing ability and segregation resistance. Advancement in SCC technology was primarily possible due to the introduction of new generation of chemical admixtures. SCC technology can be applied from Normal Strength Concrete to Ultra-High Performance Concrete. Since the 1990's in Europe, Japan and USA, SCC mixes have replaced conventional concrete in a number of precast concrete plants and are used in situ particularly for constructions in cities [SKA2000].

Figure 2-4: SCC in precast industry and Slump Flow Test

Several tests at fresh state were developed in order to characterize SCC. The flowability is determined through the Slump Flow test and the V-Funnel test. According to the French recommendation on SCC [AFGC2008] the target slump is between 550 to 850 mm depending to the class. The passing ability is tested by J-Ring test, L-Box test, U-Box test or Kajima Box test (Figure 2-5). The segregation may be esteemed visually by Slump Flow test or determined by Segregation Column test and also the Sieve Segregation test [SKA2000] [BAR2002] [AFGC2008].

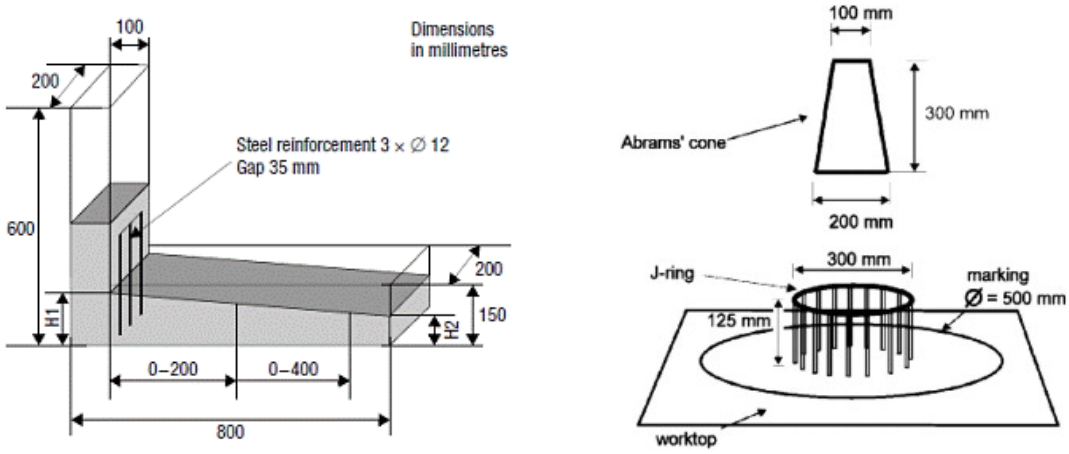

Figure 2-5: Principe of L-Box test and J-Ring test

2.1.2 Mix Design of High Performance Concrete

Originally, the concrete was composed of three components: cement, aggregates, and water. Over the years, the number and the diversity of available components have noticeably increased, enabling the production of tailor made concrete. The term 'tailor made concrete' defines concrete with specified properties like mechanical properties, rheology and durability.

Compared to Normal Strength Concrete (NSC), High and Ultra-High Performance Concrete (HPC - UHPC) cannot be produced without particular attention to the different components and their content. The choice of the different components depends principally on availability, cost and targeted performances. The components of HPC and UHPC are similar to those used for NSC. The Portland cement is the most widely used cement due to its commercial availability and relatively low cost. In France and Switzerland, cement type CEM I 52,5R is commonly used for HPC and UHPC mixes. The cement content is < 350 kg/m^3 for NSC, 350 – 500 kg/m^3 for HPC and 600 – 1000 kg/m^3 for UHPC. Supplementary reactive cementitious materials such as fly ash, silica fume, ground blast furnace slag

or natural pozzolan are often used due to both technical and economical advantages. They can be divided in two categories following their reaction type; hydraulic or pozzolanic. Hydraulic materials react directly with water and form cementitious compounds, while pozzolanic materials chemically react with calcium hydroxide to form compounds possessing cementitious properties. Fly ash, slag and silica fume are communally used for high performance materials. The typical content is between 20 – 50% by cement mass for fly ash, 30 – 85% for ground blast furnace slag and 5 – 10% for silica fume. The benefits of supplementary reactive cementitious materials include: improving workability of fresh concrete, limiting heat of hydration, reducing the free lime content, mitigating alkali-aggregates reaction, etc. Moreover the reaction between the cement and these materials refine the pore structure and reduce the permeability of hardened pastes. It's also interesting to combine different additive in ternary or quaternary systems. Compared to the other reactive cementitious materials, the silica fume shows a reactive coefficient higher than that of cement and a kinematic hardening effect on early age strength, therefore it is commonly used for HPC and UHPC mixes.

For each strength level there is an optimum size for coarse aggregate that will yield the greatest compressive strength per unit mass of cement. In general, smaller size aggregate will result in higher compressive strength, but the use of largest size aggregate allows a higher Young's modulus and a better creep and shrinkage behaviour [ROY1996]. The concept of Maximum Paste Thickness (MPT) was introduced by de Larrard and Tonda [LAR2000]. On the basis of several mixes, de Larrard highlighted the effect of the distance between two coarse aggregates, named MPT, on concrete compressive strength. A decrease of MPT results in an increase of the strength, this can be done by reducing the maximum size of aggregates. However, for compressive strength > 80 MPa the strength of aggregates can control the strength of concrete. For UHPC extra-hard aggregates and sands are needed, like calcined bauxite or granite. The packing density of aggregate influences the concrete properties. According to de Larrard [LAR2000] the denser packing density exhibits the better workability and compressive strength. The application of densified mixture design like BétonlabPro [LAR1999] which includes all particles (cement, supplementary cementitious materials, sand, coarse aggregates) is needed for compressive strengths higher than 80 MPa.

The compressive strength depends on water to cement ratio or water to binder ratio. A high W/C ratio is detrimental to the mechanical properties, deformation and durability of concrete. However, a low W/C ratio is detrimental to viscosity. The use of superplasticizers is essential to achieve high strength and good workability. Other chemical admixtures can be used like air entrainment agents, retarding agents, accelerating agents, shrinkage reducing agents, antiwashout, steel corrosion inhibitors, etc. The compatibility between cement and chemical admixtures should be determined by laboratory experiments. Chemical admixtures can influence the compressive strength and its development with time. For HPC de Larrard [LAR2000] recommends a saturation dosage of superplasticizers in order to obtain a stable workability with time.

Discontinuous fibres for cementitious materials can be characterized by several parameters. First of all and according to the nature of fibre: natural such as bamboo, jute, cellulose, rock-wool, etc.; metallic such as steel, stainless steel, titanium, etc.; synthetic such as PVA, PP, PE, glass, carbon etc. Secondly, according to the geometrical properties: length, diameter, cross sectional shape, longitudinal shape. Thirdly, according to their mechanical properties such as the tensile strength, the Young's modulus, the surface adhesion properties, the ductility, etc. Fourthly, according to their physical and chemical properties such as density, surface roughness, chemical stability, fire resistance, etc. Following their length and diameter, we can distinguish macro-fibres $l_f > 20$ mm $d_f > 0.2$ mm and micro-fibres $L_f < 10$ mm $d_f < 0.1$ mm [ROS1998]. Steel fibres are communally used for structural applications, while

synthetic fibres are used for non-structural applications such as increasing the concrete fire resistance or reducing the cracking effect of early age shrinkage, etc. According to the different manufacturers, steel fibres exhibit a large range of shape, length, diameter, strength, etc. The fibres are commonly characterized by their aspect ratio (l_f/d_f) and the selection of the fibres' type depends on the matrix strength, the maximum size of coarse aggregates and the targeted post-cracking tensile strength. Macro-fibres having shapes (hooked, twisted, crimped,…) are typically used in Normal and High-Strength Fibre Reinforced Concrete, while straight fibres is used in UHPFRC. The fibre volumetric ratio varies generally from 0.25 to 1.5% (20 – 120 kg/m^3) for Normal and High-Strength Fibre Reinforced Concrete, 1.5 to 5% (120 – 400 kg/m^3) for UHPFRC and can reach 10% (800 kg/m^3) for special mixes like the CEMTEC$_{multiscale}$®. It was shown that addition of fibres decreases the workability particularly for mixes with large coarse aggregates because the fibres disturb the packing density. This effect increases with the fibres' content and their aspect ratio (l_f/d_f). In other words, the increasing of the fibres content or the aspect ratio requires the increasing of the sand to gravel ratio and the quantity of binder paste also [MART2010].

Three methods were developed for mix design of SCC; 1) combination of superplasticizer and high content of mineral powders, 2) combination of superplasticizer and viscosity-modifying admixture with or without defoaming agents, 3) a mix of methods 1) and 2) [SKA2000]. The mix design of SCC is difficult because the filling and passing ability are antagonistic to the segregation stability. The viscosity must be optimized. Generally SCC mixes type 1 are composed of binder content in range of 500 to 700 kg/m^3 [SKA2000]. Therefore, it's relatively easy to obtain SCC criteria for HPC and UHPC thanks to their high powder and superplasticizer content. For SCC mixes with rigid fibres several researches showed the existence of critical fibres content. Once this critical content is reached, the concrete cannot flow anymore. Above this content, it was observed that fibres tend to form a "hedgehog". Most results tend to indicate that this critical volumetric fraction decreases with the volumetric fraction of coarse particles or the increase of the fibres' aspect ratio. According to Martinie [MART2010], the maximum fibre volumetric ratio in fibres reinforced mortar or UHPFRC is given by:

$$V_{f,\max} = \frac{400}{r} \cdot \left(1 - \frac{\phi_S}{\phi_m}\right) \quad \text{(in \%)} \qquad (2\text{-}1)$$

Where r is the aspect ratio, ϕ_S is the volumetric ratio of sand in the mix and ϕ_m is the maximum packing density of the sand (65% for rounded sand in first approximation).

2.1.3 Environmental impact of concrete

The building materials segment is the third-largest CO2-emitting industrial sector in the world and represents 5 to 10% of the total anthropogenic CO2 emissions [UN2010]. The principal part for this segment is related to concrete manufacturing (cement, gravel extraction, etc.). The building materials sector is also the main contributor to the natural resource consumption. Civil works and building construction activities consume 60% of materials extracted from the lithosphere. In Europe, the mineral extraction intended for buildings is about 4.8 tons per inhabitant per year. Moreover, the availability of natural aggregates used in concrete is rapidly shrinking in the areas around large cities, causing an increase in transportation distance [HAB2009].

In order to reduce the environmental impact of cement, different ways are explored by the cement industry. For example, improvements in the cement production, the use of alternative fuels and the substitution of clinker material by mineral additions, reduce the CO2 emissions.

Another option is to reduce the concrete volume needed for a given construction process by increasing the concrete performance. However, by increasing the mechanical strength, therefore the cement quantity, the CO2 emissions per cubic meter of concrete produced will also be increased, but the amount of concrete needed to build a given structural element will decrease. Habert et al [HAB2012] showed that higher strength allows for a reduction in concrete volume that compensates the CO2 increase due to this increased strength. This will lead to a net decrease in CO2 emissions. Habert et al have compared two classical executed bridges and crossing a highway having a two-lane road. The first bridge was built using traditional concrete, and the second was built with a high performance concrete (f_c around 80 MPa). The two bridges were analysed with a Life Cycle Assessment method. The analysis has highlighted that the use of high performance concrete allowed a 20% reduction in the global warming impact of the bridge life cycle. Similar study showed that high strength concrete around 100 to 120 MPa present the best compromise efficiency vs. cement quantity.

2.1.4 Mechanical properties of concrete

The design methods of reinforced or prestressed concrete structures require the constitutive relationship of each materials used (e.g., concrete, steel reinforcement, prestressing steel, etc.). The material behaviour must be known and mathematically described by constitutive curves which should be accurate and easily applicable by practitioner engineers. The parameters of the constitutive curves can be obtained directly by characterization tests or micro-mechanical models.

2.1.4.1 Compressive behaviour

The compressive strength is the principal parameter used for the characterization of ordinary concrete. The stress – strain behaviour depends on several parameters such as the aggregates type, the strength, the age, the curing and the shape of the tested specimen etc. For NSC, the behaviour is linear elastic up to 30 % of compressive strength. For higher stresses, several micro-cracks may develop up to 70 – 75 % of the compressive strength. In this phase the stiffness decreases progressively. At failure the micro-cracks form a macro-cracking. After the peak, the stress decreases with a softening behaviour. For HPC and UHPC, the matrix has fewer defaults and is more compact compared to NSC. Therefore, the behaviour of concrete approaches the stiffness of aggregates. The elastic linear portion is higher, up to 80 – 90 % of the compressive strength. Before failure, the stiffness decreases progressively. At the peak load, the failure may be brittle due to the tensile behaviour. For compressive strength higher than 70 – 80 MPa the aggregates are generally fractured. Therefore the softening behaviour is less compared to NSC due to smoother rupture surfaces. The compressive strength of HPC and UHPC is in the range of 60 – 120 MPa and 150 – 250 MPa respectively. And the Young's modulus of HPC and UHPC is in the range of 30 – 50 GPa and 40 – 70 GPa respectively. The fib Model Code 2010 [FIB2010a] proposes several constitutive laws describing the compressive behaviour.

$$\frac{\sigma_c}{f_{cm}} = -\left(\frac{k\cdot\eta-\eta^2}{1+(k-2)\cdot\eta}\right) \qquad \text{for} \qquad |\varepsilon_c| < |\varepsilon_{c,\lim}| \tag{2-2}$$

with $$\eta = \varepsilon_c / \varepsilon_{c1} \tag{2-3}$$

and $$k = E_{ci} / E_{c1} \tag{2-4}$$

Where ε_{c1} is the strain at maximum compressive stress, E_{c1} is the secant modulus from the origin to the peak compressive stress and E_{ci} is the tangent modulus.

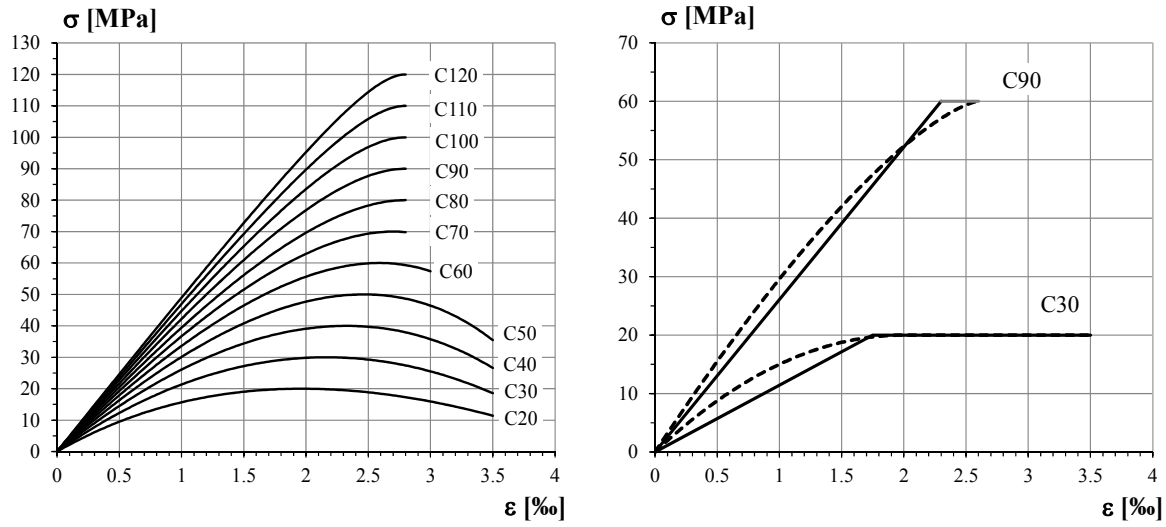

Figure 2-6: Constitutive laws in compression, a) non-linear laws for different classes, b) simplified design laws (included safety factor) for concrete of class C30 and C90

The influence of steel fibres on compressive strength is relatively low for volumetric ratio < 1 %. For higher fibres content the influence on compressive strength may be significant up to 10%. For HPC and UHPC, fibres avoid a brutal failure and confer a ductile post-peak behaviour (Figure 2-7). The slope of descending branch depends on the fibres' content.

Figure 2-7: Failure of HPC compared to HPFRC

2.1.4.2 Tensile behaviour of plain concrete

The concrete is a quasi-brittle material like mortar, rocks or timber. The cracking of quasi-brittle materials can be modelled by a micro-cracked zone, called the Fracture Process Zone (FPZ), in the front of the macro-crack [HIL1991] (Figure 2-8). The FPZ dissipates one part of the stocked energy in the structure, inducing a non-linear behaviour. The tensile strength is an important property, even though it is not explicitly used in design models. The tensile strength governs the cracking process and

is an important parameter for shear and torsion strength, splitting under concentrated load, anchorage of reinforcement, etc. In these examples, the safety of the structure depends on the tensile properties. However, the strength is not the only parameter, thus the behaviour at tensile fracture and the toughness are being also important parameters.

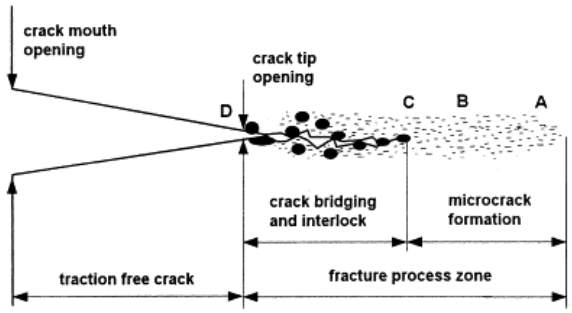

Figure 2-8: General structure of a fracture process zone in concrete [HIL1991].

The behaviour of a concrete tie is schematically showed in Figure 2-9. The behaviour is linear elastic up to 90 % of the tensile strength, the total elongation Δl corresponds to a uniform strain ε along the bar. Between this point and the tensile strength f_{ct}, a damage zone with micro-cracks begin to develop and the global stiffness decreases progressively. At the peak load, one macro-crack opens. After the peak-strength, the stress drops rapidly with a softening branch (Figure 2-9). Several "bridge" appear across the crack for small openings (0.05 to 0.15 mm) allowing the transfer of the tensile stress. The slope of descending branch is influenced by the maximum size of coarse aggregates and the matrix tensile strength. The behaviour of fracture zone is defined by a stress – crack opening relationship (σ–w) while the rest of the tie is defined by a stress – strain (σ–ε) relationship. The (σ–w) relationship may be considered constant for quasi-brittle materials and independent of the specimen size. The area under the softening curve is called fracture energy G_F, Eq. (2-5), and describes the post-cracking ductility of material. Another parameter is the characteristic length l_{ch} that corresponds to half the length of a specimen subjected to axial tension in which just enough elastic strain energy is stored to create one complete fracture surface [HIL1976]. A decrease of the characteristic length is an indication of increased brittleness.

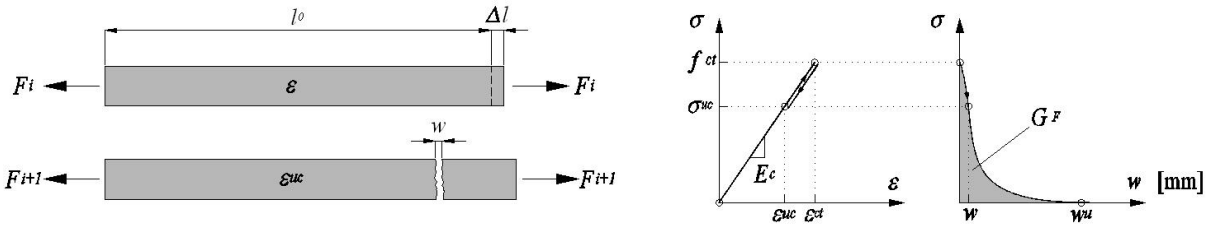

Figure 2-9: Schematic tensile behaviour of plain concrete tie

$$G_F = \int_0^{w_u} \sigma(w)dw \tag{2-5}$$

$$l_{ch} = \frac{E_c \cdot G_F}{f_{ct}^2} \tag{2-6}$$

In the absence of experimental data, the fracture energy of NSC may be estimated from the mean value of compressive strength f_{cm}, Eq. (2-7), as proposed in the *fib* Model Code 2010 [FIB2010a].

$$G_F = 73 \cdot f_{cm}^{0.18} \tag{2-7}$$

For plain concrete the tensile properties can be derived with sufficient accuracy from compression tests on cylinders or cubes. The *fib* Model Code 2010 [FIB2010a] gives the following relations:

$$f_{ctm} = 0.3 \cdot \left(f_{ck}\right)^{2/3} \quad \text{for } f_{ck} \le 50 \tag{2-8}$$

$$f_{ctm} = 2.12 \cdot \ln\left(1 + 0.1 \cdot \left(f_{ck} + 8\right)\right) \quad \text{for } f_{ck} > 50 \tag{2-9}$$

$$f_{ctk,\min} = 0.7 \cdot f_{ctm} \tag{2-10}$$

$$f_{ctk,\max} = 1.3 \cdot f_{ctm} \tag{2-11}$$

The Model Code 2010 [MC2010a] proposes a bilinear relationship $\sigma(\varepsilon)$ following by a bilinear softening branch $\sigma(w)$. The relationships are defined in Figure 2-10.

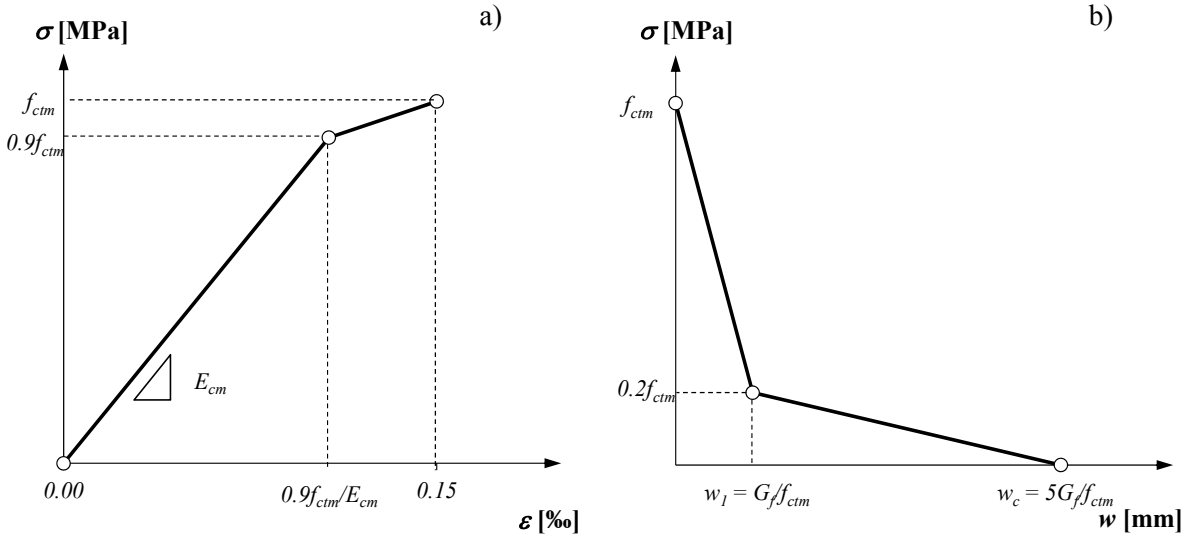

Figure 2-10: a) Pre-peak stress – strain relationship, b) post-peak stress – crack opening relationship according to [FIB2010a]

The direct tensile test is theoretically the best test for identifying the tensile properties. Unfortunately, it is difficult to perform a stable tensile and the test setup should have a high stiffness. Therefore, the properties are determined by indirect methods; 3 points bending test on notched prism, 4 points bending test on unnotched prism, splitting test or double punching test.

2.1.4.3 Tensile behaviour of fibre reinforced concrete

In Fibre Reinforced Concrete tie, different failure modes may occur, depending on the effectiveness of fibres in providing crack bridging. The effectiveness of fibres depends on several parameters such as content, shape, length, diameter, aspect ratio, strength of cementitious matrix, etc. The first crack is formed when the tensile strength of the cementitious matrix f_{ct} is reached. The fibres crossing this crack will resist to further crack openings and impose what is called crack bridging effect. If the fibres break or become pulled out during crack initiation, or if they cannot carry more stress after the development of the first crack $f_t \le f_{ct}$, the global deformation becomes governed by the opening of a single macro-crack and the fibres will be pulled out and/or broken along the crack lips. This behaviour is called tension softening behaviour. On the other hand, if the fibres are able to sustain more stress after the formation of the first crack $f_t \ge f_{ct}$, multiple micro- or macro-cracks will develop depending on the fibres' type and content. This behaviour is called tension hardening behaviour. At ultimate strain

ε_u, the hardening behaviour is followed by a softening branch. The deformation is localized on a single macro-crack (Figure 2-11).

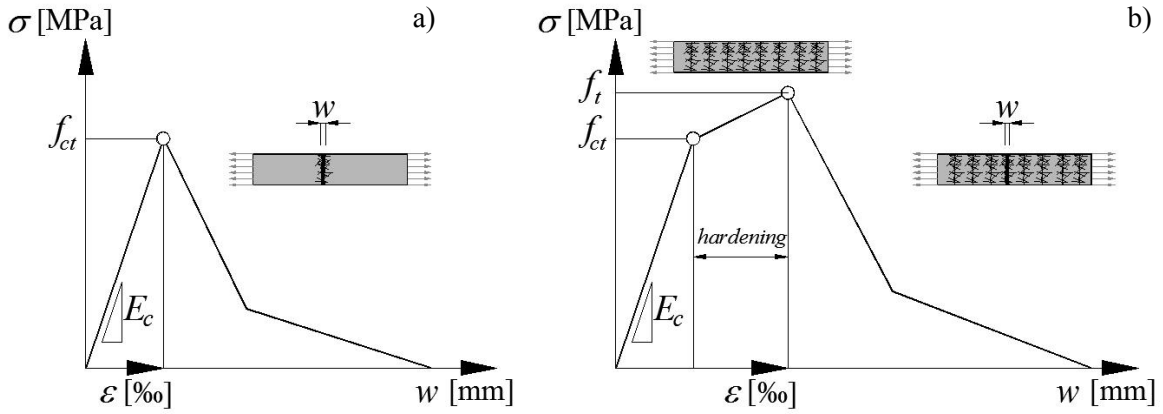

Figure 2-11: a) Tensile strain softening behaviour b) Tensile strain hardening behaviour of FRC specimens.

It's important to distinguish the hardening behaviour in tension and the hardening behaviour in bending. For structural use of FRC a hardening behaviour in bending is necessary. However, most of FRC exhibit a softening behaviour in tension but it does not mean that they cannot be used for structural applications. If this FRC is loaded in bending, structural hardening behaviour may occur, depending of the structure type (beam, slab, shell, etc.) and on the post-cracking response of the FRC. A schematic overview of the different behaviour according to structural level is given in (Figure 2-12) [FIB2010a].

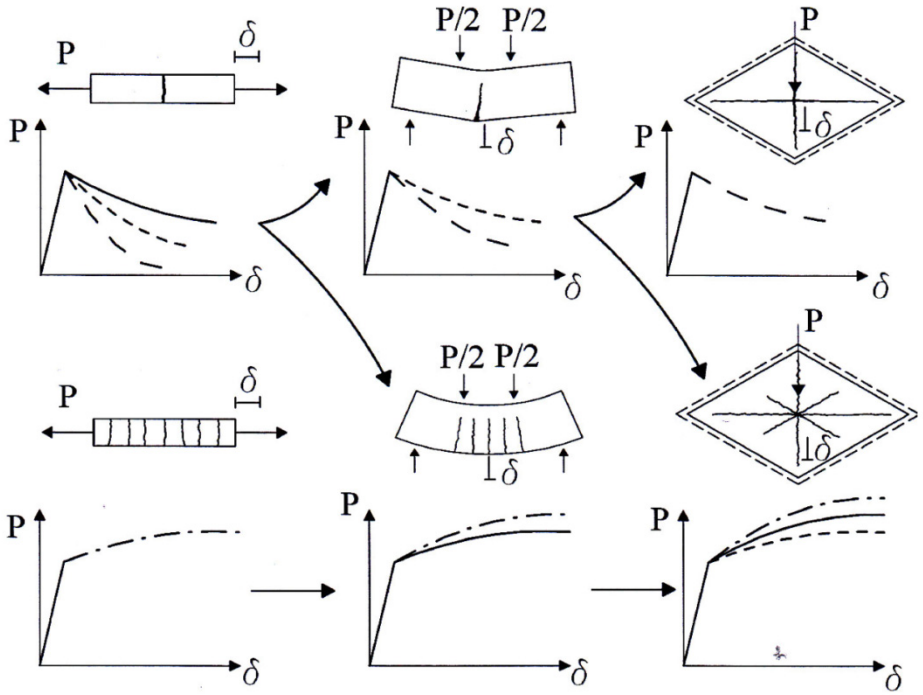

Figure 2-12: Structural behaviour of FRC according to structural level according to Di Prisco [FIB2010a]

Fibre Reinforced Concrete cannot be considered as an isotropic material. The fibres orientation is influenced by the casting process and the thickness of element. Several researches highlighted this fact, particularly for Self Compacting Fibre Reinforced Concrete (Figure 2-13 a). During the casting process the fibres close to the formwork are oriented in a parallel way to the surface (Figure 2-13 b). The affected thickness is approximately $l_f/2$. When preferential fibre orientation occurs due to casting process (e.g., SCC) or to thin thickness, more realistic tests representing the structure are recommended [GRU2001] [AFGC2002] [FIB2010a].

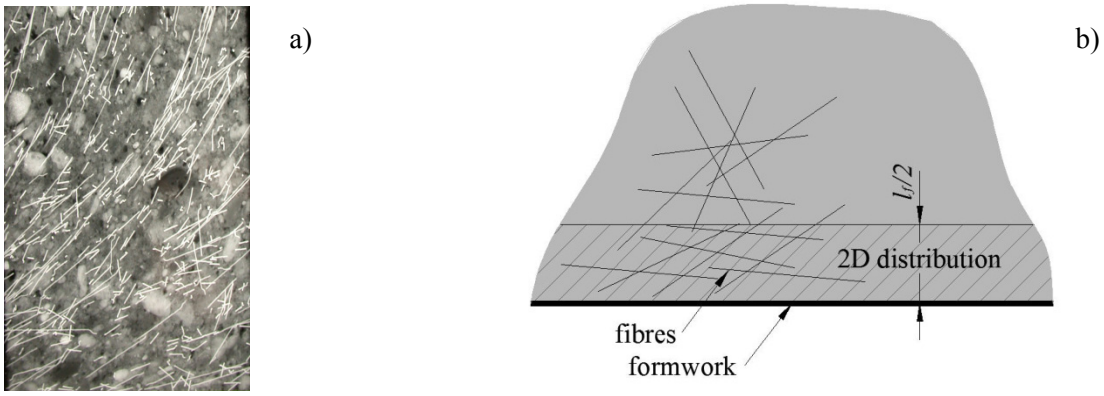

Figure 2-13: a) X-ray picture in element cast with Self-Compacting FRC [GRU2001] b) formwork effect

2.1.5 Experimental characterization of the post-cracking behaviour of SFRC

Several tests were developed in order to define the post-cracking behaviour of SFRC. On a theoretical point of view, the uniaxial tensile test is the best test for determining the behaviour. Despite its apparent simplicity, the uniaxial tensile test presents several difficulties during its execution, for concrete and SFRC. Therefore, standards methods generally require bending tests on prisms or plates. But this type of test involves structural effects and does not allow an exact and direct determination of the constitutive relationship. Concerning the characterization tests, different testing methods are being reviewed nowadays.

2.1.5.1 Uniaxial tensile test

According to Rossi [ROS1998], uniaxial tensile test is the only accurate method for determining the post-cracking behaviour. For FRC with softening behaviour in tension, the RILEM Group TC 162-TDF [RIL2002] recommend uniaxial tensile test on notched cylinder (Figure 2-14a). The standard specimen is cylindrical with a diameter and length of 150 mm. The specimens are notched at their centre with a circumferential notch of 15 mm depth. The specimen is glued to metal plates which are connected to the testing machine using rigid, bolted connections. The measured values are the applied load and the Crack Opening Displacement (*COD)*. The stress-crack opening relationship $\sigma(w)$ is obtained from a series of tests of at least 6 specimens. The cylinder may be drilled on the element or cast in a cylindrical mould.

Attar [ATT1996] investigated the effect of boundary conditions on post-cracking response. He concluded that a fixed condition is better compared to pinned conditions in order to avoid flexural effect. For FRC with hardening behaviour in tension no testing method recommendations are available. However, several studies were performed on dog-bone shaped specimens and tie-bars

(Figure 2-14b). The principal difficulties of these tests are the boundary conditions on the testing machine. The measured values are generally the applied load and the longitudinal strains. For softening branch, it is recommended to perform uniaxial tests on notched specimens [RIL2001].

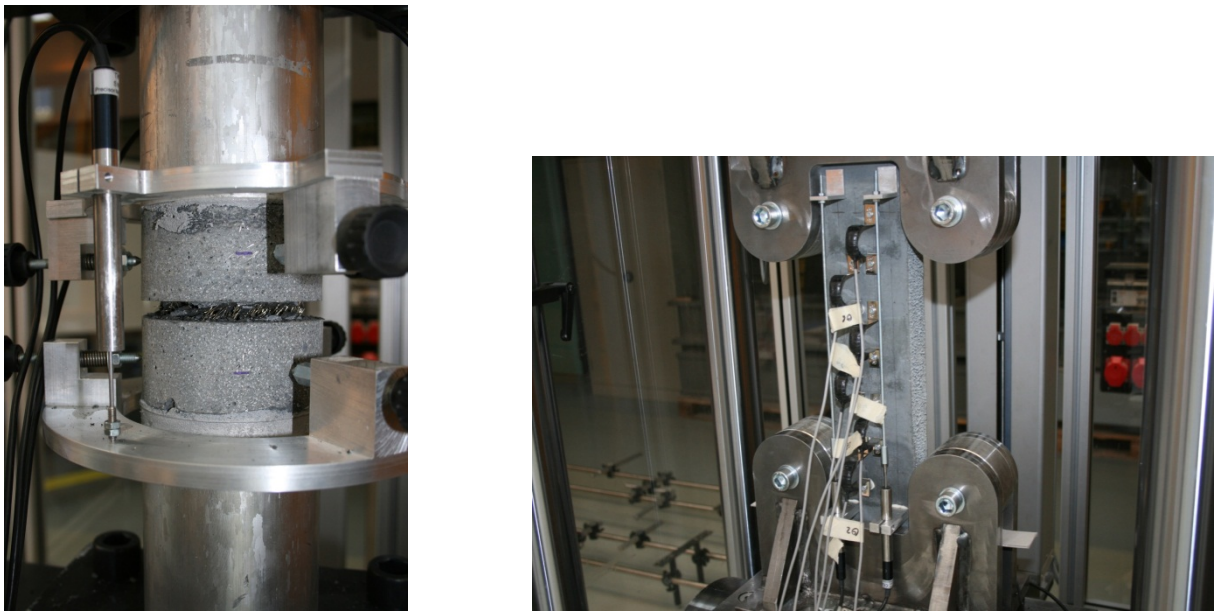

Figure 2-14: Uniaxial tensile test performed on notched core and "dog bone" element

2.1.5.2 Bending test on prisms

Bending tests on prisms are often used for the characterization of FRC. This type of test is easy to perform. Several testing methods were developed on prisms or thin plates, notched or un-notched, 4- or 3-points, casted or sawed, etc. according to the materials' properties and applications. Currently, the RILEM TC 162-TDF [RIL2003] and the Model Code 2010 [FIB2010a] propose three-points bending test on notched prisms. The specimens have a square cross section of 150 mm, a length of 550 mm and are notched at centre on a depth of 25 mm. The notch is sawn perpendicularly to the casting surface. The prisms are tested on a clear span of 500 mm. A single load is applied on centre via a steel roller. The measured values are the applied load, the Crack Mouth Opening Displacement (*CMOD)* or/and the deflection at centre. According to the European standard EN 14651 [EN14651], the Limit Of Proportionality (*LOP)* $f_{fct.L}$ and four different values of the residual strength f_{R1}, f_{R2}, f_{R3}, and f_{R4} corresponding to the different values of the *CMOD* are identified respectively through these values*:* 0.5, 1.5, 2.5 and 3.5 mm (Figure 2-15).

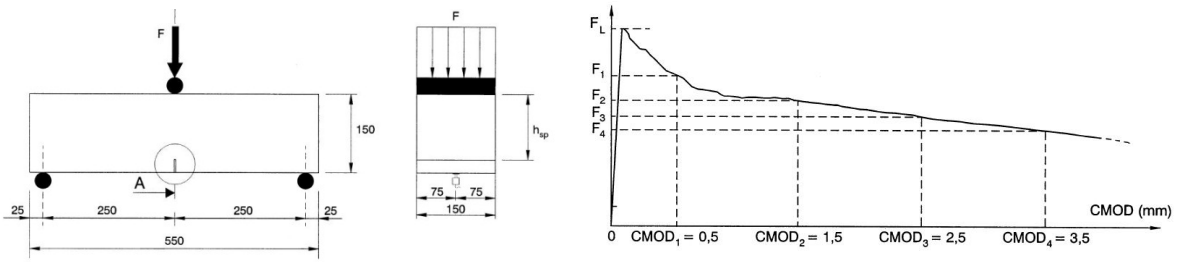

Figure 2-15: Test setup and typical response load vs CMOD [EN14651]

In the analysis of the test results, the stress distribution is assumed to be elastic even at a cracked state. The residual strengths f_{Rj} j = {1;2;3;4} are defined as follow:

$$f_{Rj} = \frac{3 \cdot F_j \cdot l}{2 \cdot b \cdot h_{sp}^2} \tag{2-12}$$

The post-cracking relationships of RILEM TC162 – TDF [RIL2003] and *fib* Model Code 2010 [FIB2010a] are identified on the basis of this test. Three-points bending tests are also proposed for thick elements in AFGC recommendations for UHPFRC [AFGC2002]. For this latter recommendation, the specimens have generally a cross-section of 100 mm, a length of 400 mm and are notched at the centre on a depth of 10 mm. The prisms are tested on a clear span of 300 mm. The Italian standards [UNI2003] proposes four-points bending tests on notched prism. The specimens have a cross-section of 150 mm, a length of 700 mm and are notched at their centre with a depth of 50 mm. The prisms are tested on a clear span of 600 mm. The German standards propose four-points bending tests on un-notched prism. For thin structures in UHPFRC, the [AFGC2002] recommends four-points bending tests on unnotched plates with the same thickness of the structure. The specimen's geometry depends on fibres' length and the slenderness criterion.

However, bending test on prism exhibits large scatter. Figure 2-16 shows the natural variation of the load-deflection curves obtained on 71 identical prisms [GOS2000]. It is seen that the scatter is quite large .The principal reason is that the load-deflection relations depend strongly on the casting technique. Moreover the fracture surface is relatively small compared to the structure. Therefore, the scatter in the tests is in general not representative of the expected scatter in the structure.

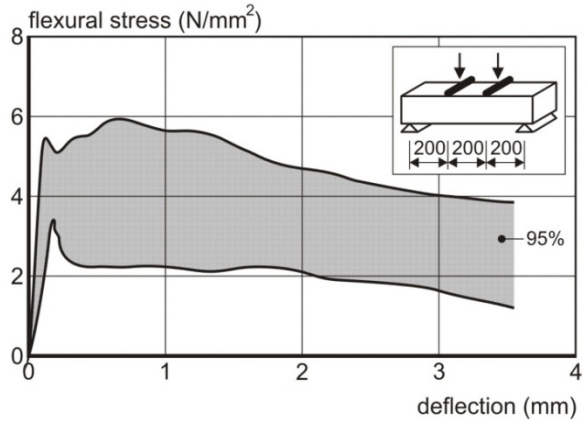

Figure 2-16: Observed load – deflection scatter on 71 identical prisms [GOS2000]

2.1.5.3 Bending tests on plates

Bending tests on square and round panels were firstly developed in order to evaluate the performance of steel fibre shotcrete in tunnel lining applications. The ASTM C1550-04 [ASTM2004] proposes tests on large round slab having a diameter of 800 mm and a thickness of 75 mm. The specimens are supported with three supports at 120 degrees and loaded at the centre by a spherical punch. In this loading configuration, the cracking pattern is easily predictable. Therefore, the post-cracking material properties can be adequately determined using yield lines model. The Swiss recommendations SIA162/6 [SIA1999] proposes tests on square or round slabs (Figure 2-17). The specimens have generally 600 mm sides for square slabs or a diameter of 800 mm for round slab with a thickness of 100 mm. The square or round slabs are simply supported along the edges on a clear span of 500 or 700 mm respectively. A single load is applied on the slab centre via a 100 mm square or round steel plate. The measured values are the applied load and the punch deflection.

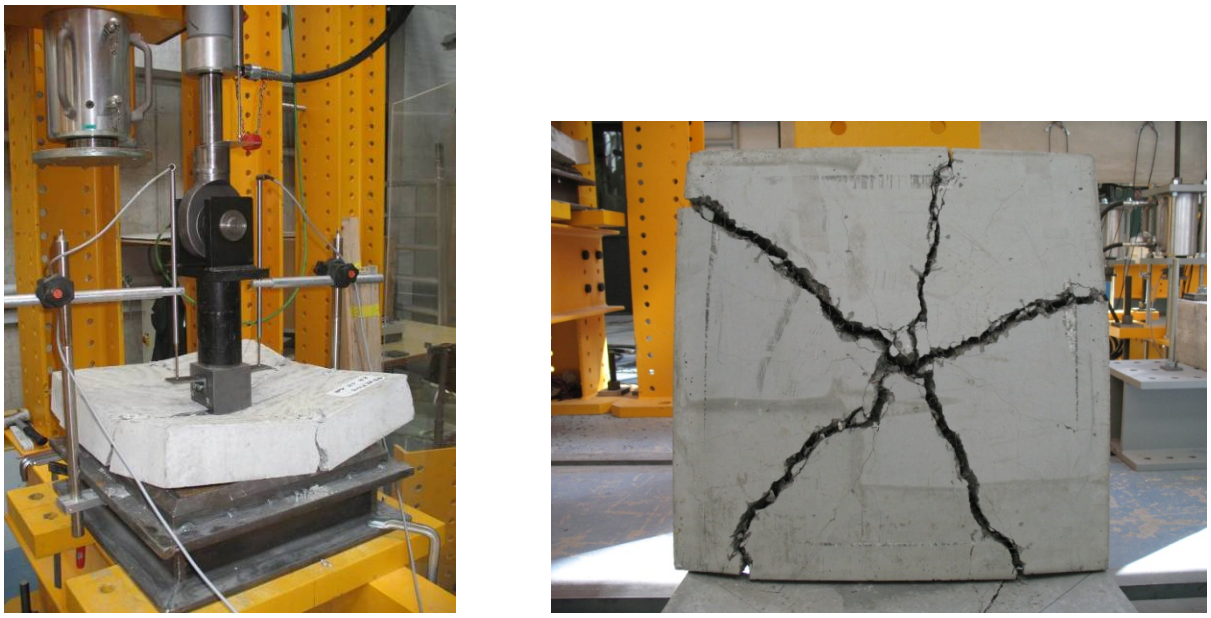

Figure 2-17: Load test on square slabs according to SIA162/6 [SIA1999] and typical cracking pattern

Tests on panels show lower scatter compared to bending test on prisms. This is due to the large length of the yield lines, which have moreover different orientations.

2.1.6 Modelling the post-cracking behaviour of SFRC for structural design purposes

For a design approach, the results of characterization tests are often not sufficient. The test results must be treated by an inverse or a direct method. In the following points different models describing the post-cracking behaviour are presented.

2.1.6.1 fib Model Code 2010

According to the fib Model Code 2010 [FIB2010a], two simplified stress – crack relationships in tension are identified from the 3-point bending test on notched prism which are performed in their turn according to the standards EN 14651 [EN14651]. A first constitutive law, rigid-plastic model (Figure 2-18 a) is defined as follow:

$$f_{Ftu} = \frac{1}{K \cdot \gamma_F} \cdot \frac{f_{R3}}{3} \tag{2-13}$$

A second constitutive law, is defined through a softening linear post-cracking model (straigth line) or a hardening (dashed line) one (Figure 2-18 b). f_{Fts} represents the serviceability residual strength and f_{Ftu} represents the ultimate residual strength. They are defined as follow:

$$f_{Fts} = \frac{1}{K \cdot \gamma_F} \cdot 0.45 \cdot f_{R1} \tag{2-14}$$

$$f_{Ftu} = \frac{1}{K \cdot \gamma_F} \cdot \left[f_{Fts} - \frac{w_u}{2.5} \cdot \left(f_{Fts} - 0.5 \cdot f_{R3} + 0.2 \cdot f_{R1} \right) \right] \geq 0 \tag{2-15}$$

Where, f_{R1} and f_{R3} are the residual strength defined from Eq. (2-12), K is the orientation factor, in general case K = 1.0 and γ_F is the partial safety factor equal to 1.5.

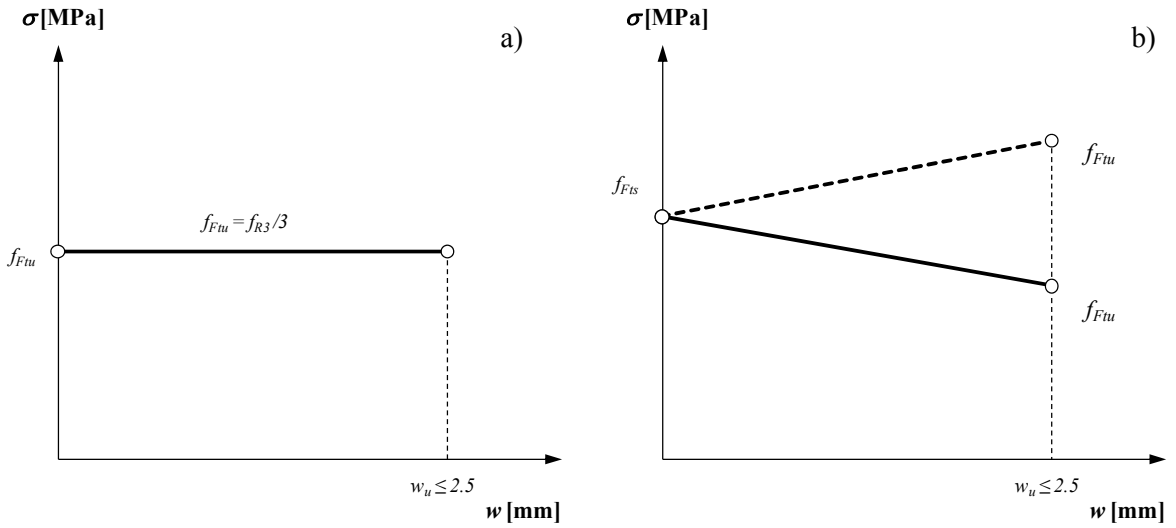

Figure 2-18: Tensile stress – crack relationships at ULS according to the fib MC2010 [FIB2010a]

For the structural design it is necessary to transform the crack opening w into strain ε. When considering softening materials, the definition of the stress-strain law is based on the identification of the crack width w and on the corresponding structural characteristic length l_{cs} of the structural element.

$$\varepsilon = w/l_{cs} \tag{2-16}$$

In structural elements with conventional reinforcement, the characteristic length may be evaluated as follows:

$$l_{cs} = \min\{s_{rm}, y\} \tag{2-17}$$

Where s_{rm} is the mean of the crack spacing and y is the distance between the neutral axis and the tensile side, evaluated in the elastic-cracked state at SLS and by neglecting the tensile strength of FRC.

For the two constitutive laws, the crack opening correponding to the ultimate limite state w_u depends on the required ductility of the structure. The ultimate crack width w_u can be calculated as follow:

$$w_u = l_{cs} \cdot \varepsilon_{Fu} \tag{2-18}$$

Where ε_{Fu} is assumed to be equal to 2% when the neutral axis is internal to the cross section and 1% when the neutral axis is external to the cross section.

For hardening materials in tension, in a first phase micro-cracking occurs, the identification of stress-strain law may be directly determined from a uniaxial tensile test.

For the Serviceability Limit State (SLS) the same constitutive relationship for plain concrete (Figure 2-10) is adopted up to the matrix strength f_{ct}. In the post cracking stage, a bilinear relation defined by f_{Fts} and f_{Ftu} is applied (Figure 2-19).

$$\varepsilon_{SLS} = 0.5/l_{cs} \tag{2-19}$$

$$\varepsilon_{SLU} = \min\{\varepsilon_{Fu}, 2.5/l_{cs}\} \tag{2-20}$$

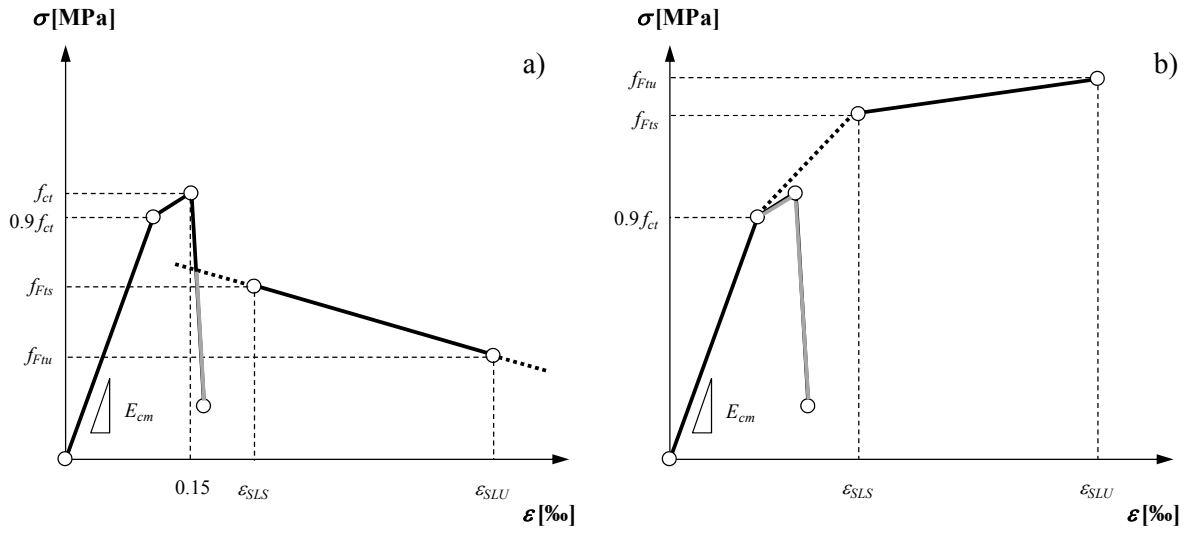

Figure 2-19: Tensile stress – strain relationships at SLS according to the fib MC2010 [FIB2010a], a) softening behaviour, b) hardening behaviour

2.1.6.2 RILEM TC 162-TDF

The Technical Committee RILEM TC162-TDF has proposed two design methods. The first one is the σ-w method [RIL2002], where the tensile relationship of FRC is formulated in function of stress versus crack opening. The second one is the σ–ε method [RIL2003], where the tension relationship of FRC is formulated in function of stress versus strain.

The design of FRC structures according to the σ–ε method [RIL2003] is based on the same fundamentals as design of conventional reinforced concrete structures in Eurocode 2. The RILEM σ–ε method is valid for concrete strengths limited to f_{ck}< 50 MPa. For concrete with a superior strength special attention should be paid to the fibres so they do not break. The model is trilinear, with σ_1 corresponding to the elastic part and σ_2 and σ_3 corresponding to the residual strengths of FRC (Figure 2-20 a). The values of σ_1 to σ_3 are derived from 3-points bending tests on notched prism according to the EN 14651. The ultimate strain ε_3 is limited to 25‰.

$$\sigma_1 = 0.7 \cdot f_{ct,L}^{f} \cdot (1.6 - d) \quad (d \text{ in [m]}) \qquad \varepsilon_1 = \sigma_1 / E_c \tag{2-21}$$

$$\sigma_2 = 0.45 \cdot f_{R1} \cdot \kappa_h \qquad \varepsilon_2 = \varepsilon_1 + 0.1‰ \tag{2-22}$$

$$\sigma_3 = 0.37 \cdot f_{R4} \cdot \kappa_h \qquad \varepsilon_3 = 25‰ \tag{2-23}$$

The model involves a size factor κ_h (Figure 2-20 b) defined as follows:

$$\left.\begin{aligned} \kappa_h &= 1 \\ \kappa_h &= 1 - 0.6 \cdot (h - 125)/475 \\ \kappa_h &= 0.4 \end{aligned}\right\} \qquad \begin{aligned} &h \le 125 \\ &125 < h < 600 \quad \text{[mm]} \\ &h \ge 600 \end{aligned} \tag{2-24}$$

Where, $f_{ct,L}^{f}$, f_{R1} and f_{R4} are the residual strengths defined from Eq. (2-12), E_c is the Young's modulus and h is the depth of the structural element.

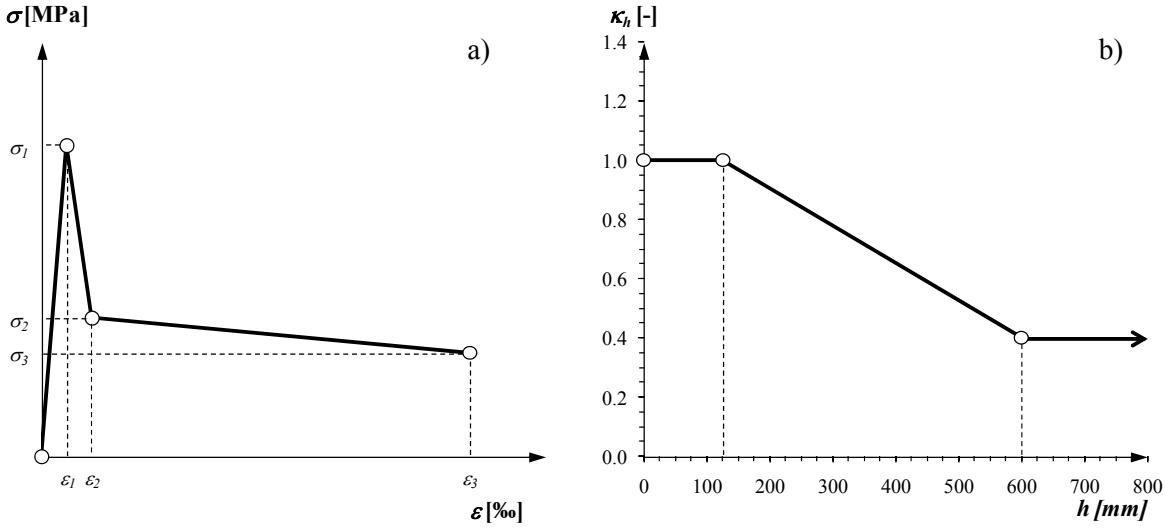

Figure 2-20: a) Tensile stress – strain relationship at ULS according to the Rilem TC162 [RIL2003], b) size factor κ_h relationship

The σ-w method [RIL2002] is based on the fictitious crack model developed by Hillerborg [HIL1980] for plain concrete. The response can be separated in two contributions, the matrix and the fibres (Figure 2-21). The matrix behaviour is modelled by a linear stress – strain relationship up to the matrix strength f_{ct}. The softening behaviour can be approached by a multi-linear relationship according to the precision level. The shape of the softening part and the values should be identified by uniaxial tensile tests on notched core. For a design approach, a bilinear relationship is considered as sufficient.

$$\sigma(w)\begin{cases} f_t - \alpha_1 \cdot w \\ \sigma_2 - \alpha_2 \cdot w \end{cases} \quad \text{for} \quad \begin{matrix} 0 \le w \le w_1 \\ w_1 < w \le w_u \end{matrix} \tag{2-25}$$

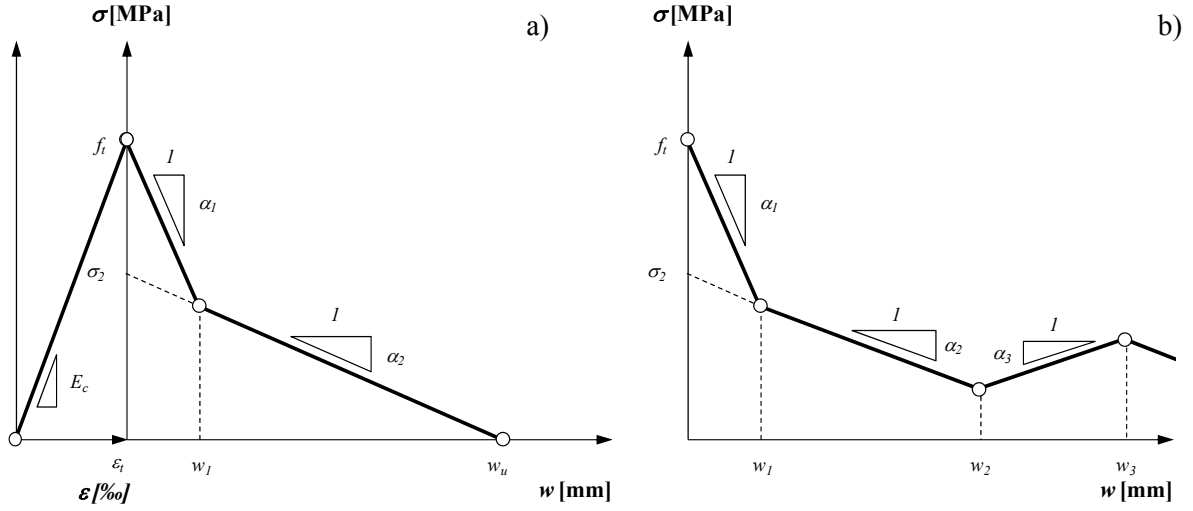

Figure 2-21: Tensile stress – crack relationships at ULS according to the Rilem TC162 [RIL2002], a) bilinear post-cracking relationship, b) multi-linear post-cracking relationship

2.1.6.3 AFGC-SETRA Recommendations for UHPFRC

In French interim recommendations for UHPFRC [AFGC2002], thick and thin elements are distinguished and the corresponding post-cracking relationships and computing methods are different.

For thick elements, ($h \geq 3l_f$), the post-cracking response is determined from 3-points bending tests on notched prisms. A multi-linear stress – crack width $\sigma(w)$ post-cracking relationship is determined on the basis of an inverse analysis on prisms test results. The factor K takes into account the orientation effects. This factor is determined experimentally from tests on prototype or in preliminary design computation, K is assumed equal to 1.25 for global effects and to 1.75 for local effects. The inverse analysis is based on the following equations:

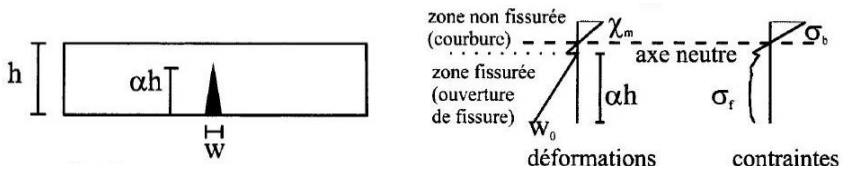

Figure 2-22: Fictitious crack model used for inverse analysis and corresponding strains, crack openings and stresses distributions [AFGC2002]

Equilibrium equations

$$N = E \cdot \chi_m \cdot \left[\frac{h^2}{2 \cdot \alpha^2} + \left(\frac{h \cdot \sigma_t}{E \cdot \chi_m} - h^2 \right) \alpha + \left(\frac{h^2}{2} - \frac{h \cdot \sigma_t}{E \cdot \chi_m} \right) \right] \tag{2-26}$$

$$M = E \cdot \chi_m \cdot b \left[\frac{h^3}{6} \alpha^3 + \frac{h^2 \cdot \sigma_t}{2 \cdot E \cdot \chi_m} \alpha - \frac{h^3}{2} \alpha + \frac{h^3}{3} - \frac{h^2 \cdot \sigma_t}{2 \cdot E \cdot \chi_m} \right] \tag{2-27}$$

In order to link the crack width to the curvature of the uncracked part, a kinematic relationship is necessary.

$$w = \left[\chi_m + 2 \cdot \chi_e \right] \cdot \frac{2 \left(\alpha \cdot h \right)^2}{3} \tag{2-28}$$

$$\text{with} \qquad \chi_e = \frac{M}{E \cdot I} \tag{2-29}$$

The tensile stress relationship (σ-w) is obtained by an iterative computation. From the computation results a simplified relationship is determined according to the UHPFRC' behaviour (Figure 2-23). The stress – crack opening relationship is transformed in stress – strain relationship with the characteristic length l_c.

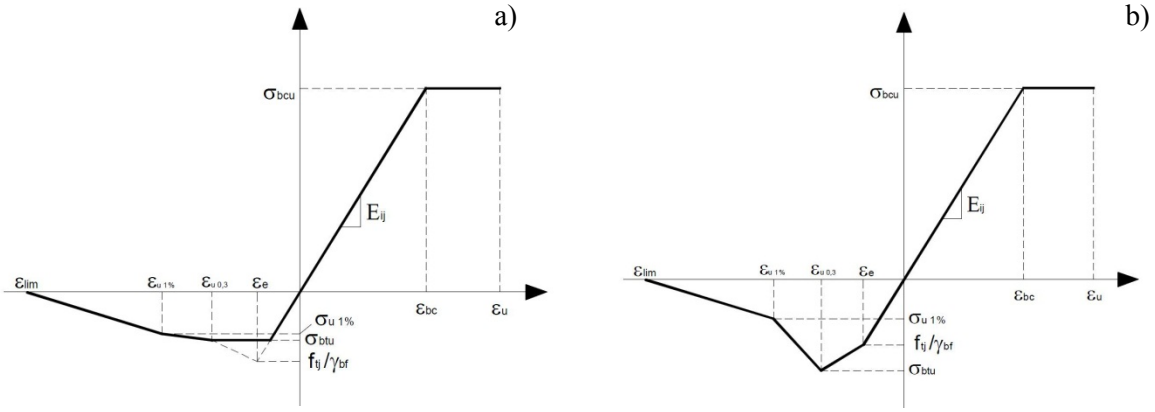

Figure 2-23: Tensile stress – strain relationships at ULS for thick element according to the [AFGC2002], a) softening behaviour, b) hardening behaviour

$$f_{tj}/\gamma_{bf} \qquad \varepsilon_e = \frac{f_{tj}}{\gamma_{bf}\cdot E_{ij}} \tag{2-30}$$

$$\sigma_{btu} = \frac{\sigma\left(w_{0,3}\right)}{\gamma_{bf}\cdot K} \qquad \varepsilon_{0,3} = \frac{f_{tj}}{\gamma_{bf}\cdot E_{ij}} + \frac{w_{0,3}}{l_c}\,(w = 0.3\ mm) \tag{2-31}$$

$$\sigma_{u1\%} = \frac{\sigma\left(w_{1\%}\right)}{\gamma_{bf}\cdot K} \qquad \varepsilon_{1\%} = \frac{f_{tj}}{\gamma_{bf}\cdot E_{ij}} + \frac{w_{1\%}}{l_c}\,(w = 0.01H) \tag{2-32}$$

$$\sigma_{\lim} = 0 \qquad \varepsilon_{\lim} = L_f/\left(4\cdot l_c\right) \tag{2-33}$$

$$\text{with} \qquad l_c = \frac{2\cdot h}{3} \tag{2-34}$$

Where H is the prism depth, h is the structure depth, f_{tj} is the matrix tensile strength, γ_{bf} is the partial safety factor ($\gamma_{bf} = 1.3$) and l_c is the characteristic length.

If the bending behaviour of a thin element is regarded, ($h<3l_f$), the standard test should be carried out on a specimen where the cross sectional height is smaller than $3l_f$. By choosing a standard bending test specimen with such a small thickness, the stress-strain relation obtained includes implicitly the effect of the fibres' alignment with the boundary conditions, which is expected to occur in the structural elements as well. In this case, a bilinear stress – strain $\sigma(\varepsilon)$ post-cracking relationship is computed from an inverse analysis (Figure 2-24).

$$Mr\left(\chi\right) = \frac{f_{tj}\cdot b\cdot h^2}{2} + \frac{E\cdot\chi\cdot b}{6}\cdot\left[\alpha\left(\chi\right)^3\cdot h^3\cdot\left(1-K\right) - 3\alpha\left(\chi\right)\cdot h^3 + 2h^3\right] \tag{2-35}$$

$$\text{with} \qquad \alpha\left(\chi\right) = \frac{1}{1\text{-}K}\cdot\left[1\text{-}\sqrt{\frac{2f_{tj}\cdot(K\text{-}1)}{E\cdot\chi\cdot h}+K}\right] \tag{2-36}$$

$$\text{and} \qquad K = \frac{f_{tuj}\text{-}f_{tj}}{E\cdot\varepsilon_u\text{-}f_{tj}} \tag{2-37}$$

Iteration on f_{tuj} is performed out until the computed maximum moment is equal to the maximum moment M_{Rmax} from the test on prism. The strain ε_u is limited to 10‰.

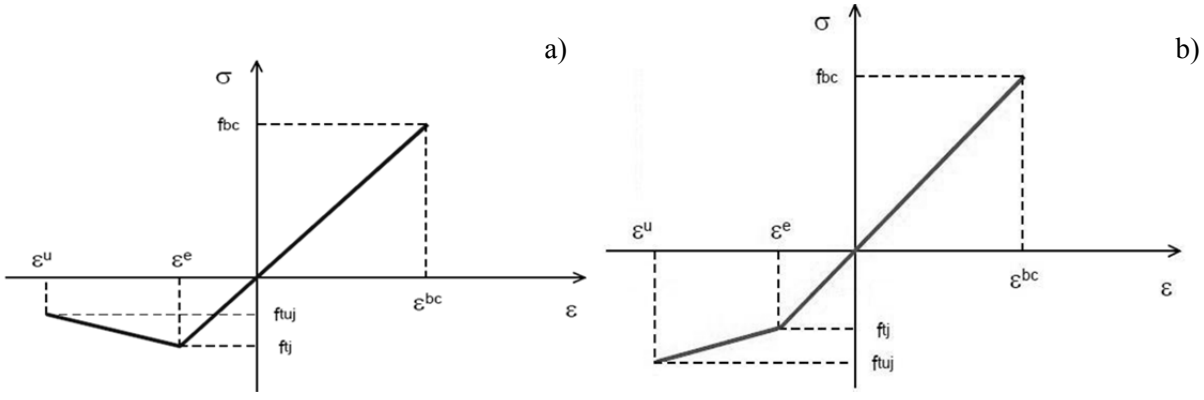

Figure 2-24: Tensile stress – strain relationships at ULS for thin element according to the [AFGC2002], a) softening behaviour, b) hardening behaviour

2.1.6.4 Variable Engagement Model VEM

The Variable Engagement Model (VEM) was developed by Voo and Foster [VOO2003a] for modelling the stress versus crack opening displacement tensile $\sigma(w)$ relationship of FRC. The bridging phenomena of fibres crossing a cracked surface are described using a modified pulley approach where the pulley is attached to the matrix via a spring (Figure 2-25). In the development of the VEM, the following assumptions are made:

- The behaviour of FRC may be obtained by a summation of the individual components, matrix and fibres, the effects of each individual fibre can be summed.
- The geometric centre of the fibres is uniformly distributed in the space and all fibres have an equal probability of being oriented in any direction.
- All fibres are being pulled out from the side of the crack with the shorter embedded length while the longer side of these fibres remains rigidly embedded in the matrix
- Displacements due to elastic strains in the fibres are small and relative to displacements resulting from a slip between the fibres and the matrix
- The bending stiffness of the fibres is small and the energy expended through the fibres' bending can be neglected.

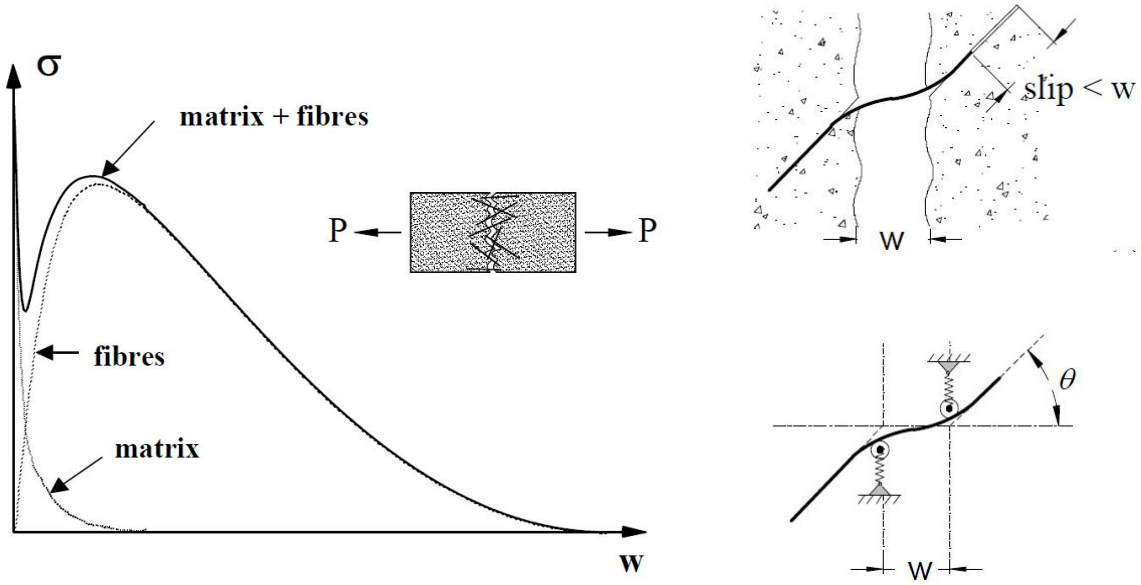

Figure 2-25: Stress vs crack opening displacement relationship of the different FRC components and modified pulley model [VOO2003a]

The tensile stress versus strain softening relationship of the matrix is given by

$$\sigma_{ct} = f_{ct} \cdot e^{-cw} \tag{2-38}$$

Where f_{ct} is the tensile strength of the matrix, w is the crack opening displacement and c is an attenuation factor taken as $c = 15$ for concrete and $c = 30$ for mortar.

The tensile stress of fibre σ_{tf} is given by

$$\sigma_{tf} = K_f \cdot K_d \cdot \frac{l_f}{d_f} \cdot \rho_f \cdot \tau_b \tag{2-39}$$

Where K_f is the global orientation factor, K_d is a factor taking into account the fibre efficiency and τ_b is the bond shear stress

The global orientation factor K_f is defined as follows:

$$K_f = \frac{\tan^{-1}(w/\alpha)}{\pi} \cdot \left(1 - \frac{2w}{l_f}\right) \quad \text{for} \quad l_f \le \frac{d_f}{2} \cdot \frac{\sigma_{fu}}{\tau_b} \tag{2-40}$$

In the formulation of Eq. (2-40), it was assumed that all fibres are pulled out

$$K_f = \frac{4}{\pi \cdot {l_f}^2} \cdot \int_0^{\theta_{crit}} \left\{\max\left(l_{a,crit} - w, 0\right)\right\}^2 d\theta \quad \text{for} \quad l_f > \frac{d_f}{2} \cdot \frac{\sigma_{fu}}{\tau_b} \tag{2-41}$$

The formulation of Eq. (2-41) includes fibres fracture but excludes strains induced by bending of the fibres.

With

$$l_{a,crit} = \min\left(l_c/2 + w_e, l_f/2\right) \tag{2-42}$$

$$w_e = \alpha \cdot \tan\theta \tag{2-43}$$

$$\alpha = d_f/3.5 \tag{2-44}$$

$$\theta_{crit} = \tan^{-1}\left(w/\alpha\right) \tag{2-45}$$

The bond stress is defined as follows:

$$\tau_b = k_b \cdot \sqrt{f_c} \tag{2-46}$$

Where k_b is a fibre shape factor

$$\rho_f = m_f/78.1 \tag{2-47}$$

The VEM has the advantage that no tests on specimen (prism, plate, etc.) are needed. The VEM was validated by Voo and Foster [VOO2003a] on several test results available in the literature. The VEM gives accurate predictions compared with the test results.

2.1.7 Behaviour of Reinforced - SFRC in tension and bending

In several structural applications, SFRC and UHPFRC are combined with conventional reinforcement and/or prestressing. SFRC structures with reinforcement in uniaxial tension or bending exhibit higher stiffness, more cracks with less space and opening and higher flexural capacity compared to conventional reinforced concrete. Moreover, the bond strength between reinforcement (rebar, strand) and concrete is enhanced with steel. The fibres contribution depends of the SFRC or UHPFRC post-cracking response [RED2009].

The tensile behaviour of a concrete tie is schematically represented in Figure 2-26. When the cracking strength F_{cr} is reached, the reinforced concrete tie exhibits a plateau with the cracking development while the steel fibres tie shows a progressive decrease of the stiffness. After this phase, the behaviour is linear up to the steel yield's limit F_y. This point is followed by the plastic plateau. The post-peak

response for SFRC or UHPFRC tie depends of several parameters like the fibres length l_f, the fibre content, the reinforcement ratio, etc.

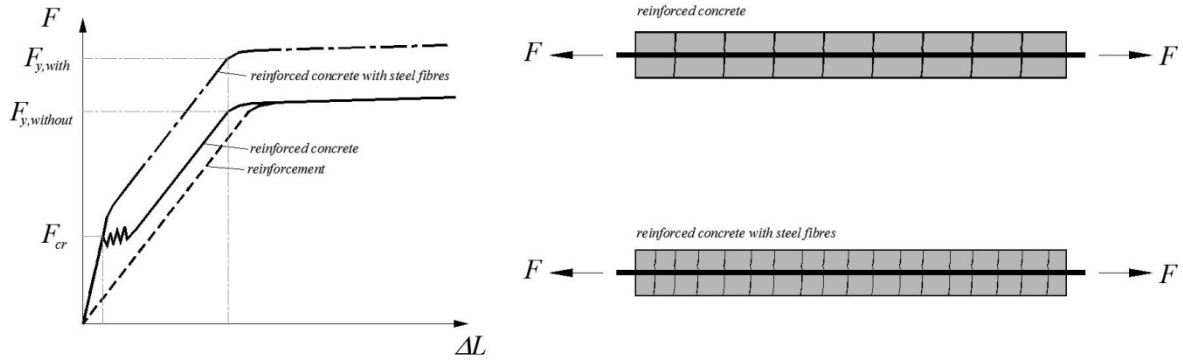

Figure 2-26: Behaviour of reinforced ties with and without steel fibres

Several experimental campaigns highlighted the fibres contribution on flexural capacity of reinforced members and are presented further. The following experimental campaign [MOR2009] was chosen to illustrate the behaviour. In this study 5 beams in UHPC and UHPFRC of 100 x 150 x 1700 mm were tested (Figure 2-27). The principal parameters distinguishing the specimens were the fibre content and the reinforcement ratio. Two beams were without reinforcement and three beams were composed of 2 rebars ϕ10 mm with an effective depth of 120 mm. The fibres volumes V_f were of 0, 1% and 2%. The beams were tested in four-point bending test on a clear span of 1350 mm.

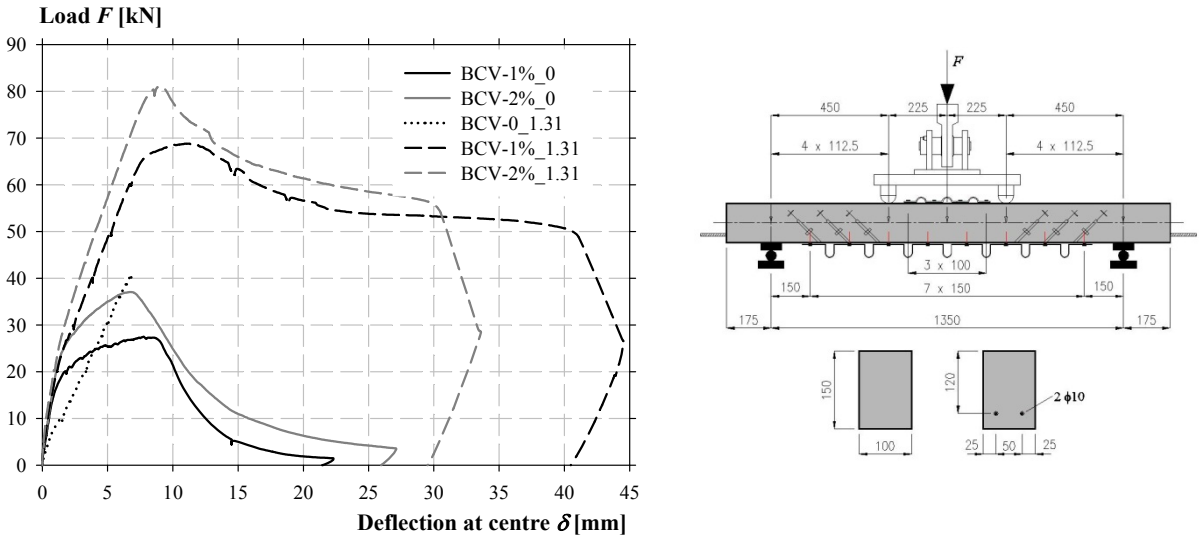

Figure 2-27: Curves load vs deflection at centre of the different specimen and loading configuration

The stiffness of specimens with fibres is clearly higher compared to the beam without fibres. The flexural capacity of beams without reinforcement is 6.17 kNm respectively 8.34 kNm for BCV-1% and BCV-2%. The moment carried by the reinforcement corresponds theoretically to $0.9 \cdot d \cdot A_s \cdot f_y$ = 9.33 kNm. The addition of reinforcement and fibres contribution gives 15.5 kNm and 17.7 kNm for BCV-1% and BCV-2% respectively and corresponds well with the test results 15.5 kNm and 18.2 kNm. Therefore fibres and reinforcement act simultaneously. Moreover, the deflection at the peak-load is increased for beams with reinforcement compared to the beams without.

2.1.8 Structural analysis of SFRC element in bending

2.1.8.1 Discrete crack approach

A cross-sectional analysis of FRC element can be carried out using a non-linear hinge model [RIL2002]. The structural element in bending is divided into a non-linear hinge of length *s* and the rest of the structure behaves in a linear elastic manner (Figure 2-28). The non-linear behaviour of the element is concentrated in the zone of the hinge. The models assume that end faces of the hinge remain plane, providing continuity with the rest of the element. The mechanical equilibrium in the cracked section is established using the tensile softening stress-crack opening relationship, while the rest of the section follows the linear-elastic material relationship (Figure 2-29). A kinematic assumption is introduced to describe the hinge zone, while the rest of the structure behaves in a linear-elastically way. Following the model, different kinematic assumptions are taken into account.

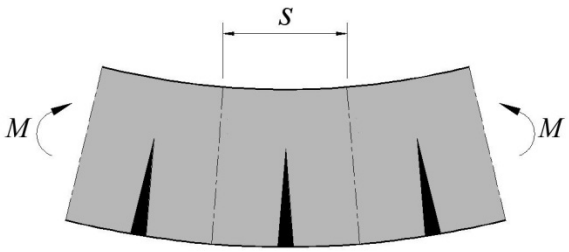

Figure 2-28: Fictitious cracks model

The classical non-linear hinge approach assumes that fictitious crack surfaces remain plane and the crack opening angle equates the overall angular deformation, as follows:

$$\varphi = \frac{w_0}{a} \tag{2-48}$$

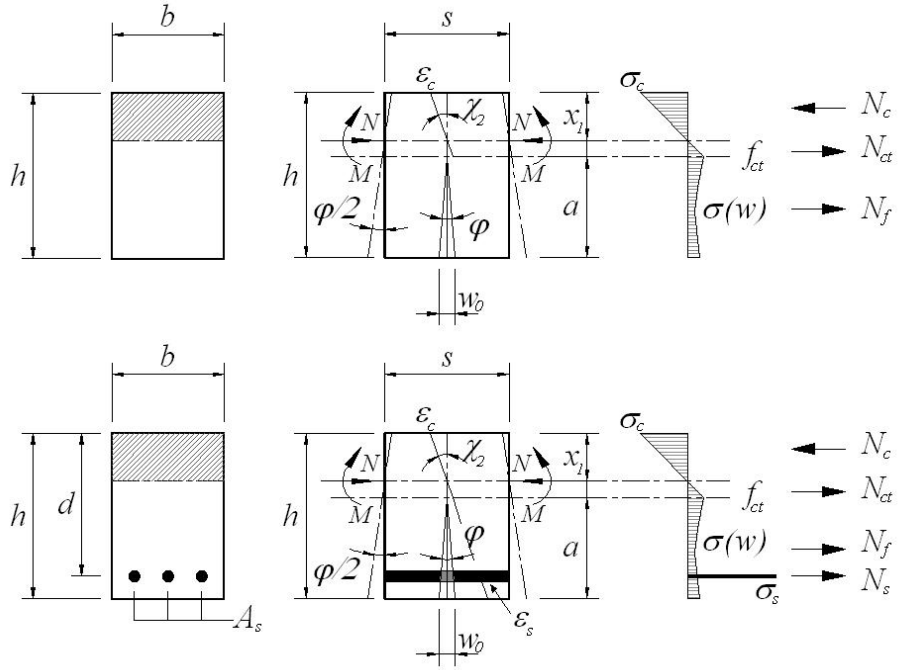

Figure 2-29: Cross sectional analysis using the discrete crack approach with and without reinforcement

In all models the average curvature of the non-linear hinge is given by:

$$\chi_m = \frac{\varphi}{s} \tag{2-49}$$

Pedersen's model

In the non-linear hinge model proposed by Pedersen [PED1996], the kinematic hypothesis assumes that the fictitious crack surfaces are plane, and that the crack opening angle is equal to the overall angular deformation of the non-linear hinge, which is related to the crack mouth opening displacement w_0, as follows:

$$h - x_1 = \frac{1}{\varphi} \cdot \left(\frac{f_{ct}}{E_c} \cdot s + w_0 \right) \tag{2-50}$$

The length of the non-linear hinge*s* is considered a fitting parameter. According to the [PED1996], it was shown that reasonable results are obtained with $s = h/2$ for plane concrete and FRC. The model allows for the application of any stress-crack opening relationship using numerical integration to obtain the solution. The analysis takes into account combined axial force N and moment M on the cross section. The equilibrium of the section is written as follows:

$$N_f + N_c + N_{ct} = N \tag{2-51}$$

$$N_f = \frac{1}{\theta} \cdot \int_0^{w_0} \sigma_w \tag{2-52}$$

$$N_c = \frac{\varphi \cdot E \cdot x^2}{2 \cdot s} \tag{2-53}$$

$$N_t = \frac{f_t^2 \cdot s}{2 \cdot \varphi \cdot E} \tag{2-54}$$

And the moment M is given by:

$$M_f + M_c + M_{ct} = M \tag{2-55}$$

Casanova and Rossi's model

Another non-linear hinge model was developed by Casanova and Rossi [CAS1996]. The assumptions of this model regarding the kinematics of the non-linear hinge are similar to those proposed by Pedersen. The fictitious crack surfaces remain plane and the crack opening angle is equal to the overall angular deformation. But two curvatures are considered in this model: the curvature in the cracked section χ_2 and the elastic curvature at the edge of the non-linear hinge χ_1. Assuming a parabolic variation of the curvature along the non-linear hinge, the average value of the curvature can be obtained as follows:

$$\chi_m = \frac{2 \cdot \chi_1 + \chi_2}{3} \tag{2-56}$$

The length of the non-linear hinge s varies with the crack depth as $s = 2a$. Finally, combining equations (2-50) and (2-56), the kinematic equation can be written as follows:

$$w_0 = 2 \cdot \chi_m \cdot a^2 \tag{2-57}$$

Massicotte's model

Massicotte et al [MAS2008] have proposed a modified form. Compared to the model proposed by Casanova and Rossi the length of the non-linear hinge s is assumed constant. The average value of the curvature χ_m is the same. The crack opening is written as follows:

$$w_0 = \left(\frac{2 \cdot \kappa_1 + \kappa_2}{3} \right) \cdot s \cdot a \tag{2-58}$$

$$s = \min \begin{cases} h/2 \\ s_m \end{cases} \tag{2-59}$$

Where s_m is the average cracks spacing.

The equations of equilibrium have the same form of the model proposed by Pederson. But the factor f/s must be replaced with κ_m. With reinforcement, the strain of steel is defined as follows:

$$\varepsilon_s = \left(d - x_1 \right) \cdot \chi_2 \tag{2-60}$$

The maximum moment M_R is obtained by iterations on the crack opening w_0.

2.1.8.2 Smeared crack approach

The second approach, named smeared crack, consists in transforming the stress – crack $\sigma(w)$ constitutive law in $\sigma(\varepsilon)$ relationship by introducing the characteristic length l_c. The cross-sectional analysis is computed in a similar manner to that of reinforced concrete (Figure 2-30). This method is more familiar for practitioners' engineers.

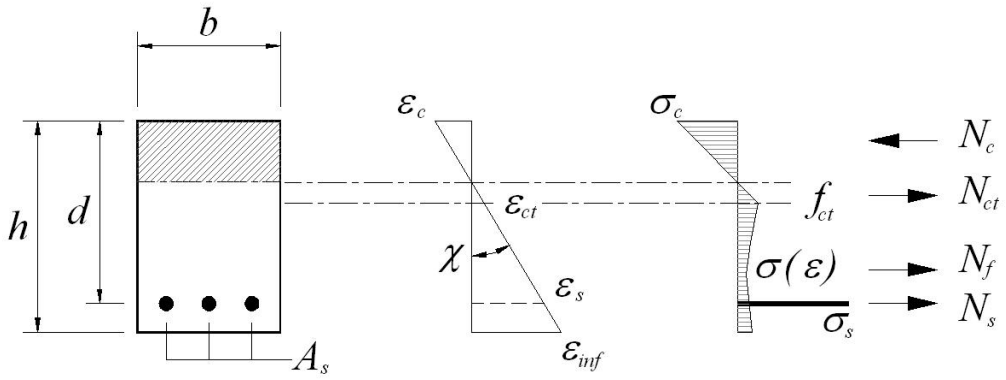

Figure 2-30: Cross sectional analysis using the smeared crack approach

The relationship $\sigma(w)$ is transformed as follows:

$$\varepsilon = \frac{f_{ct}}{E_c} + \frac{w}{l_c} \tag{2-61}$$

For rectangular or T cross-section, the characteristic length l_c is defined according to [AFGC2002] as follows

$$l_c = \frac{2 \cdot h}{3} \tag{2-62}$$

According to [FIB2010b], in structural elements with conventional reinforcement, the characteristic length may be evaluated as follows:

$$l_{cs} = \min\{s_{rm}, y\} \tag{2-63}$$

Where s_{rm} is the mean of the crack spacing and y is the distance between the neutral axis and the tensile side, evaluated in the elastic-cracked state at SLS and by neglecting the tensile strength of FRC.

The maximum moment M_R is obtained by iterations on the curvature χ.

2.1.9 Discussion

At the end of this first part of the literature survey dedicated to material properties, we have seen that High Performance Concrete (HPC) compared to Normal Strength Concrete (NSC) exhibits: higher mechanical properties allowing the development of slender structures, a higher compactness and a better homogeneity therefore a higher durability, a rapid development of shrinkage and a reduced creep, a rapid formwork removal therefore accelerated construction, etc. Moreover, HPC allows a net reduction in the environmental impact of the life cycle of the structure by limiting the materials quantities. The components of HPC are similar to those used for NSC, but HPC cannot be formulated without particular attention to their content and quality. However, HPC is characterized by a fragile behaviour in compression and the fracture of aggregates in tension.

We have also shown that steel fibres added in a cementitious matrix may confer a “pseudo-ductile” behaviour in tension. The fibres crossing this crack will resist to further crack openings and impose what is called “crack bridging effect“. Two different behaviours in tension may be identified. If the fibres cannot carry more stress after the development of the first crack, the global deformation becomes governed by the opening of a single macro-crack. This behaviour is called tension softening. If the fibres are able to sustain more stress after the formation of the first crack, multiple micro- or macro-cracks will develop depending on the fibres’ type and content. This behaviour is called tension hardening. At the ultimate strain ε_u, the hardening behaviour is followed by a softening branch. At a structural level, a SFRC with a tension softening behaviour may exhibit a hardening behaviour in bending depending on the structural level (beam, slab, shell, etc.).

The principal property of a SFRC compared with a plain concrete is its post-cracking response which can be taken into account in a structural design. Different testing methods and models were developed for its determination. The methods may be classified into two classes; based on a test (prism, plate, etc.) or based on a micro-mechanical model (e.g. VEM, etc.). For the first class, several testing

methods were developed. From a theoretical point of view, the uniaxial tensile test is the simplest test for determining the behaviour. Despite its apparent simplicity, the uniaxial tensile test presents several difficulties during its execution. That is the reason why standards methods generally require bending tests on prisms or plates. But this type of test involves structural effects and does not allow an exact and direct determination of the constitutive relationship. The second class is interesting for a first or a primary calculation if no data are available on the SFRC tensile behaviour.

For the tensile relationship of a SFRC, two approaches coexist in the various standards and recommendations: the stress vs crack opening σ-w method and the stress vs strain σ-ε. The σ-w method seems adapted for thick elements and for tensile softening material. However in structural engineering, the material laws are often expressed in term of stress vs strain. This particularity involves some difficulties but simplified cross-sectional models considering fictitious cracks were developed. *A contrario*, the σ-ε method seems adapted for thin element and for tensile hardening material particularly for Ultra-High Performance Fibre Reinforced Concrete. The σ-ε method may be used with tensile softening material but a size effect factor must be taken into account.

At a structural level, the fibre orientation is one of the most important aspects. The fibre orientation is influenced by the casting process and deviates from the uniformly distributed 3-D orientation. The AFGC-SETRA recommendations for UHPFRC [AFGC2002a] and the fib Model Code 2010 [FIB2010a] take into account this effect through a coefficient $1/K$ ($K > 1$) depending on local or global effect. However, the orientation must be identified by testing the procedure on a prototype.

The review of the different recommendations design approaches have highlighted that several codes and recommendations are adapted either for “conventional SFRC” just like the RILEM TC 162-TDF [RIL2002] [RIL2003] and the *fib* Model Code 2010 [FIB2010a] or for UHPFRC just like the AFGC-SETRA recommendations [AFGC2002a]. However, there is a large gap but also a large number of interesting applications between conventional SFRC and UHPFRC.

2.2 Shear

2.2.1 Problem statement

At the end of the 19th century, François Hennebique patented the first reinforced concrete structures. Hennebique proposed to place steel reinforcement only in zones where the concrete is in tension. According to his concept, the beams were reinforced longitudinally by steel bars and transversally by steel plates. Following the foregoing, W. Ritter [RIT1899] was the first to explain the functioning of the Hennebique's beams (Figure 2-31). His observations and explanations about the flexural and shear behaviour are still current today. On the basis of the inclined shear cracks, Ritter concluded that the reinforced concrete beams can act like a truss and the stirrups carry the shear force. His assumption, which was detailed a few years later by Mörsch [MOE1908], is still used for the design of the stirrups in reinforced concrete structures.

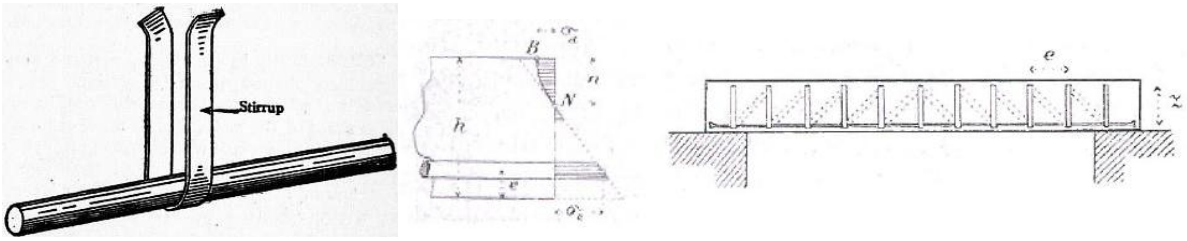

Figure 2-31: Stirrups of Hennebique and beam model of Ritter

Since the beginning of the 20th century, the reinforced concrete structures experienced an increased development with Robert Maillart, Alexandre Sarrasin, Albert Caquot and later on with Eugène Freysssinet and the prestressed concrete structures (Figure 2-32).

Figure 2-32: Salginatobel Bridge by Maillart 1930 (CH), Luzancy Bridge by Freyssinet 1947 (FR).

All linear members where the moment over the length is not constant are stressed by shear forces. For concrete, the tangential shear stresses do not constitute a cracking criterion. Therefore, these stresses influence the direction of the principal compressive and tensile stresses. Assuming a homogenous uncracked section, the principal stresses are defined according to Continuum Mechanics Theory. However, the concrete is not homogeneous.

A reinforced concrete element containing an adequate longitudinal and transverse reinforcement can be designed using a simple strut and tie model. However, a number of reinforced concrete structures are constructed without transversal reinforcement such as slabs, footings, retaining walls and secondary members. The design of these elements with a strut and tie model (Figure 2-33) results in an

unsafe solution [DRU1973]. In this model, the main assumption is that the failure occurs by yielding of the longitudinal reinforcement. But the shear failure occurs often in a sudden manner through the development of a diagonal crack without the longitudinal reinforcement having reached the steel yield limit implying possible partial or total collapse of the structure (Figure 2-34). Despite extensive research in this field, shear remains such a complex phenomenon that the current design codes approach is often empirical or simplified.

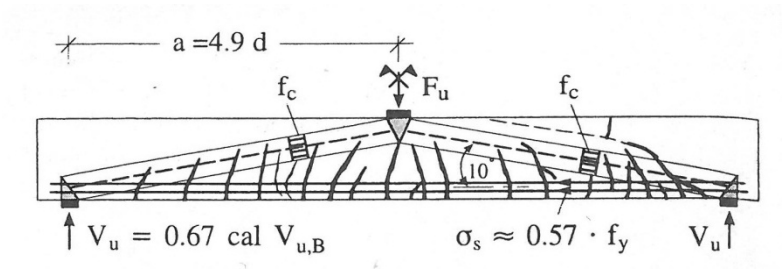

Figure 2-33: Unsafe strut and tie model proposed by Drucker [ASCE1998]

Figure 2-34: Partial collapse of reinforced concrete structures by shear failure, Air Force warehouse 1955 (USA) on left, a bridge pile after the seism in 1995 at Kobe (JPN) on right.

2.2.2 Shear transfer mechanisms in reinforced concrete beams

The reports of the ACI Committee 426 [ACI1973] and ASCE-ACI 445 [ASCE1998] describe in detail the various failure modes and shear transfer mechanisms of members with and without transversal reinforcement. In these reports, the main parameters affecting the shear strength and several empirical formulas were determined. Currently, these equations are still the basis of shear design rules in several standards.

These reports identify five shear transfer mechanisms of reinforced concrete members; (1) the interface shear transfer, (2) the dowel action of longitudinal reinforcement (3) the residual tensile stress across cracks, (4) the shear carried by the un–cracked concrete and (5) the arch action. Often the first four mechanisms are summarized in the Beam Action. These mechanisms depend on several parameters and in function of the load level influence more or less the shear strength. In reality it is a combination of the different types that allows the transfer of the shear force. For punching shear the same transfer mechanisms are present. The tri-axial state of stress, in the compression zone near the loading point, influences certainly the different failure criteria of the transfer mechanisms.

2.2.2.1 Un-cracked concrete zone

In the un-cracked part of the members, the shear force is transferred by inclined principal tensile and compressive stresses, as visualized by the principal stress-trajectories [WALT1999]. However, reinforced concrete members are often cracked. The cracks introduce a discontinuity and modify the stress-flow. But in the un-cracked compression zone, depth *x*, the elastic distribution of the shear stresses is still valid. The integration of the shear stresses over the depth gives a shear force component. The shear transferred by the un-cracked concrete depends on several parameters, like the shape of the cross-section, the member's depth or the presence of an axial force. For a first example, in the case of a slender member without axial force, the shear force carried by the compression zone does not contribute significantly to the shear capacity because the depth is relatively small. For a second example, if a prestressed T-beam is less cracked, the shear force transferred by the un-cracked concrete and the compression table is higher in this case.

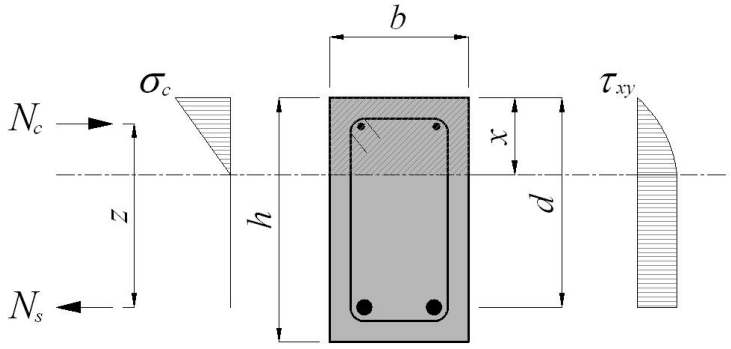

Figure 2-35: Normal and shear stresses over the depth of cracked reinforced concrete beam [WALT1999]

2.2.2.2 Interface shear transfer

The interface shear transfer can be explained by the aggregates protruding from the crack surface that provide a resistance against the slip. This mechanism is often called aggregate interlock. According to several studies, the interface shear transfer is an important mechanism in shear strength of members without stirrups. The important role of this mechanism in the redistribution of diagonal compression fields in members with stirrups is well known. The interface shear transfer capacity depends principally on the surface roughness, the crack opening and the crack sliding.

For normal strength concrete, the crack gets round the aggregates because the matrix strength is largely lower than the inclusions strength, therefore the surface is irregular (Figure 2-36). For high strength concrete and lightweight concrete, the cementitious matrix reaches the same strength as the aggregates, at cracks formation the inclusions may fracture forming a smoother surface (Figure 2-36). Push-off tests (Figure 2-37) performed by Walraven [WAL1995] have shown that shear friction capacity in plain concrete is reduced to about 35% of the value which would be obtained without particle fracture. For cracks intersected by reinforcement, the interface shear transfer capacity of high strength concrete is reduced to 55-75% of the value for normal strength concrete. The reduction in interface shear transfer resistance due to aggregate fracture is considerable. Several shear design model take this effect into account. However, experiments on push-off specimens in high strength concrete performed by Nagle & Kuchma [NAG2007] and Sagasesta & Vollum [SAG2011] have highlighted that calculated strength were generally conservative in comparison with the test results.

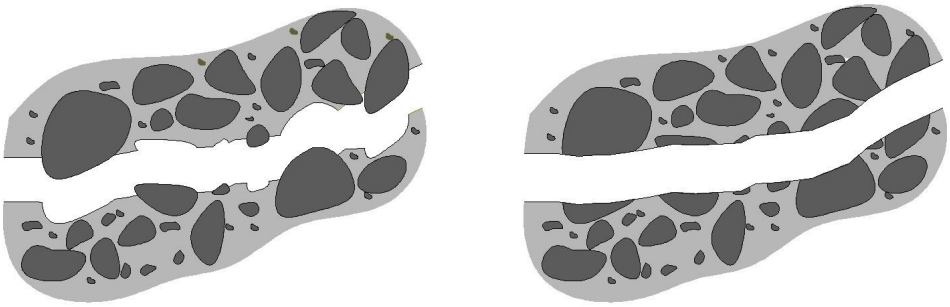

Figure 2-36: Contact surface of normal strength concrete and lightweight or high strength concrete [ASCE1998]

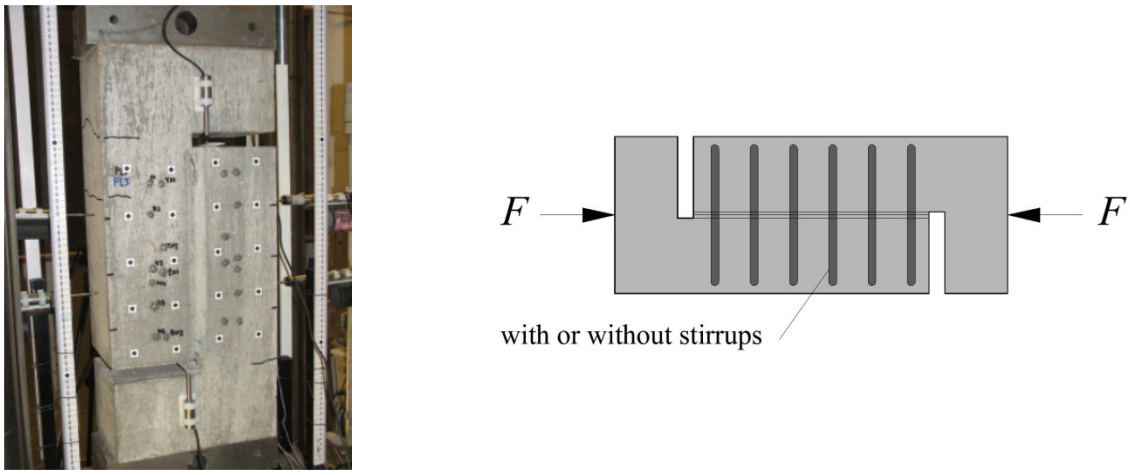

Figure 2-37: Push-off test arrangement [NAG2007]

The studies performed by Fenwick and Paulay [FEN1968] Gambarova [GAM1981], Walraven [WAL1981], Millard & Johnson [MIL1985], allowed significant progress towards understanding the aggregate interlock mechanism. The interface shear transfer capacity was extensively studied using push-off test specimens in which different ratio of reinforcement, either embedded or external, were placed in a perpendicular way to the shear plane to control the opening stiffness. The interface shear transfer resistance depends on four principal parameters; the concrete strength, the normal stress, the crack opening and the slip between the crack lips. Walraven [WAL1981] developed a model based on the probability that aggregates, idealized as spheres, will project from the crack interface. In Walraven's model the relation between the stress and the displacement depends on the concrete compressive strength, but is only valid for normal strength concrete. Other relationships have been developed by Kupfer [KUP1983], Vecchio & Collins [VEC1986], which assume that the shear that can be transferred depends on the crack opening and on the aggregates' size. Several models in shear design consider the interface shear transfer as being the principal effect like the Modified Compression Field Theory MCFT [VEC1986] or the Critical Shear Crack Theory CSCT [MUT2008a].

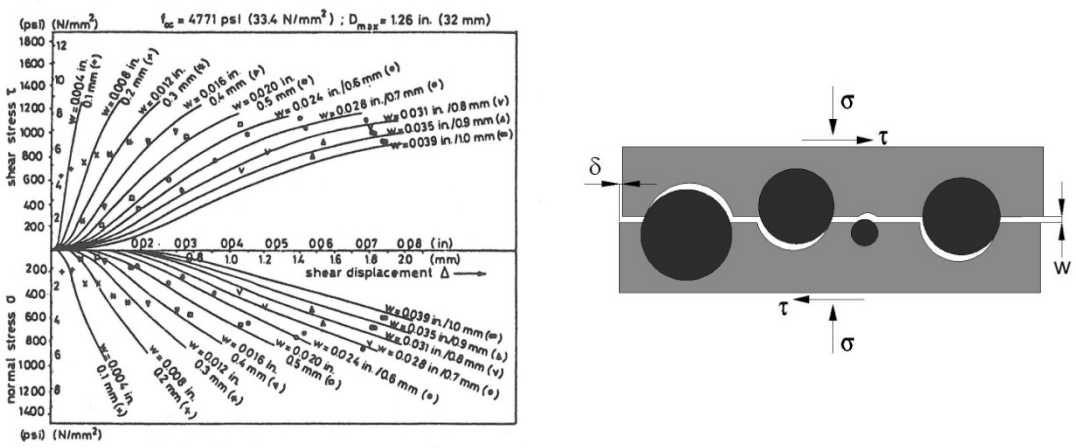

Figure 2-38: Comparison between the prediction and the test results, Walraven [WAL1981]

2.2.2.3 Dowel action of longitudinal reinforcement

The dowel action is the capacity of the longitudinal reinforcement to carry a part of the shear force (Figure 2-39). This transfer mechanism depends principally on the following parameters: the reinforcement ratio, the diameter of the bars, their space, the stress in the reinforcement, the depth of the concrete cover and the concrete tensile strength. Two failure modes may be distinguished: The first failure mode is the splitting of the concrete cover under the reinforcement (Figure 2-40 a/b). This failure can be directly linked to the concrete tensile strength. The second failure mode is the crushing of the concrete on the bar followed by the yielding of the steel bar (Figure 2-40 c). In a member without transversal reinforcement, the dowel action is relatively low, because the longitudinal rebars are not supported by the stirrups. The dowel action is more important for members with reinforcement implemented on several levels, in both directions or supported by stirrups [VIN1968].

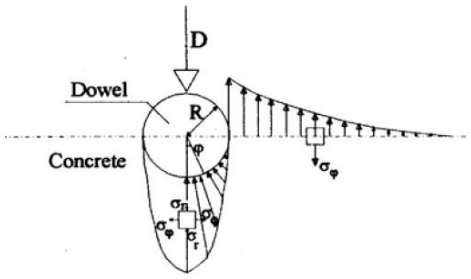

Figure 2-39: Schematic distribution of the stresses [CEB1997]

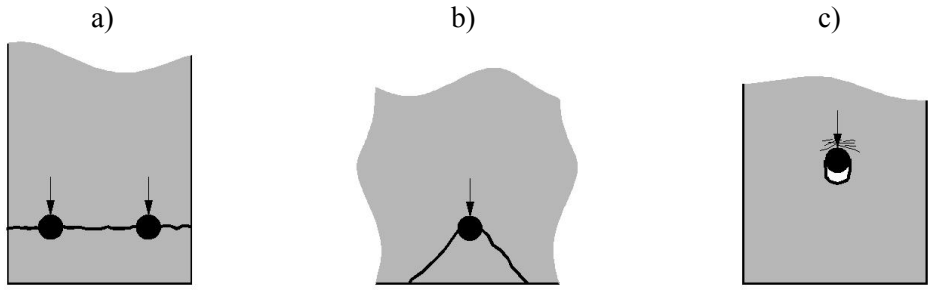

Figure 2-40: Different failure mechanisms of the dowel action

2.2.2.4 Residual tensile stresses across cracks

The tensile behaviour of concrete can be characterised by two phases. In the first phase, the behaviour is elastic linear until the tensile strength f_{ct} is reached. In the second phase, and after the peak-strength, the stress drops rapidly with a softening branch (Figure 2-41). It exists several "bridges" across the crack for small openings (0.05 to 0.15 mm), thus allowing the transfer of the tensile stress. In this second phase, the strains are localized in a small region called the fracture process zone. Therefore the response must be expressed in terms of stress – crack opening and not in terms of stress - strain [ACI1989]. The application of fracture mechanics to shear design is based on the assumption that residual tensile stress is the principal shear transfer mechanism.

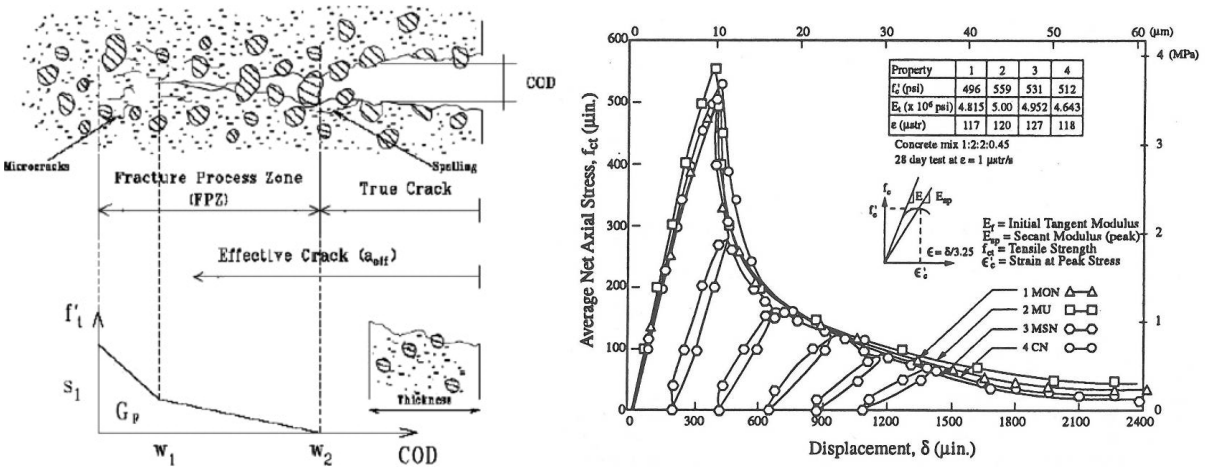

Figure 2-41: Fracture process zone and post-cracking response in tension of normal strength concrete [ASCE1998]

2.2.2.5 Beam Action

In a reinforced concrete member, the flexural cracks divide the tension zone in several blocks as proposed by Kani [KAN1964]. These blocks may be assimilated as a cantilever beam fixed in the compression zone where the different described mechanisms act (Figure 2-42). The equilibrium of one concrete tooth gives a horizontal and vertical force and a moment at the support. The external moment is in equilibrium with the internal moment. The beam action is often named cantilever action. The formation of the critical shear crack disables the transfer mechanisms of the beam action.

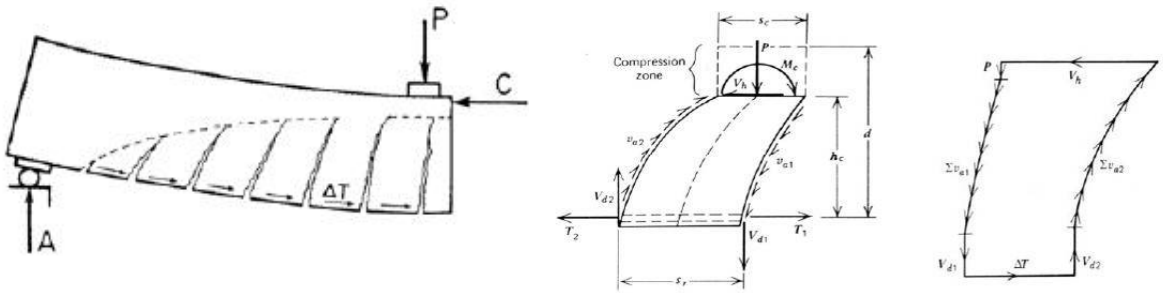

Figure 2-42: Concrete tooth model and equilibrium [ASCE1998]

2.2.2.6 Arch Action

As seen in point 2.2.2.1, the shear force is transferred from the loading point to the support by inclined principal tensile and compressive stresses. The development of the arch action requires a horizontal reaction at the support. For a simply supported beam, the horizontal reaction is carried by the longitudinal reinforcement. However, for the full development of the arch action, a perfect anchorage of the reinforcement is required. The arch action depends of on the following parameters: the slenderness or the shear span to depth ratio *a/d*, the loading arrangement, the concrete strength and the reinforcement ratio. For beams without transverse reinforcement simply supported, the arch action can be seen only if the load is applied on the top and not on the bottom of the beam.

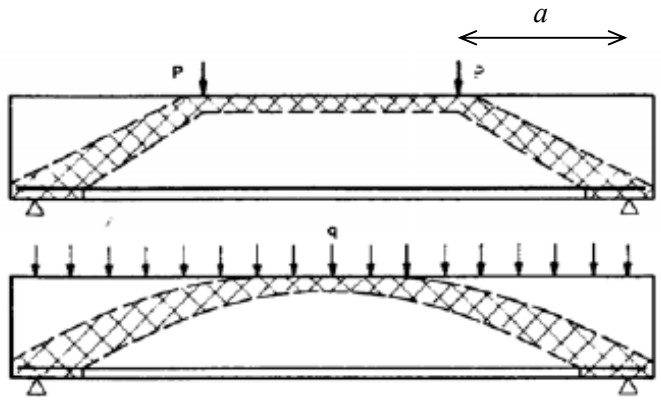

Figure 2-43: Schematic arch action according to the loading arrangement [ASCE1998]

Four arch failure modes may be identified: In the first mode, the propagation of the critical shear crack reduces the compression zone. Therefore the failure occurs by the crushing of the concrete at the root of the diagonal shear crack. This type of failure is named shear-compression. In the second mode, the failure occurs by the debonding of the compression zone. In the third mode, the failure occurs by the splitting of the strut. This type takes place for low shear to depth ratios, < 2, and presents large reserve of strength. The last mode is the debonding of the reinforcement at the supports.

2.2.3 Parameters influencing the shear strength

2.2.3.1 Shear span to depth ratio

The studies performed by Leonhardt and Walther [LEO1966] and Kani [KAN1966] [KAN1979] highlighted the influence of the slenderness of the members and the presence of different modes governing the shear failure. Kani has performed at University of Toronto 133 tests on beams without stirrups in order to establish the influence on shear strength of the shear span to depth *a/d* ratio, the concrete compressive strength and the reinforcement ratio. All beams were tested in 4-points bending and have an identical cross-section of 305 mm depth and 152 mm wide. The tests results were represented according to the ratio, moment M on the plastic moment M_u, versus the shear span to depth ratio *a/d*. This representation highlighted clearly the dependence of the slenderness on the shear strength and the presence of different failure modes.

For *a/d*< 1, the shear strength reaches the flexural capacity and the strength is governed by the yielding of the flexural reinforcement, as diagonal cracks almost do not disturb the compression strut.

For 1 <*a/d*< 2.5 – 3, the arch action is dominant. The diagonal shear crack is linear from the loading point to the support. In this configuration, the shear crack progresses in a stable manner and presents large reserve of strength. This regime is called direct strut.

For 2.5 <*a/d*< 7 – 13, the diagonal shear crack develops from an inclined flexural crack. The failure develops due to the localization of the strains and limits the strength of the inclined compression strut carrying shear.

For *a/d*> 7, the flexural capacity is dominant

The test results performed by Kani highlighted that the test moment to plastic moment ratio M/M_u reaches a minimum for a shear span to depth *a/d* ratio around 2.5 – 3. The different tests results represented in a graph according to the three parametrers *a/d,* M/M_u and ρ, draw a valley (Figure 2-45).

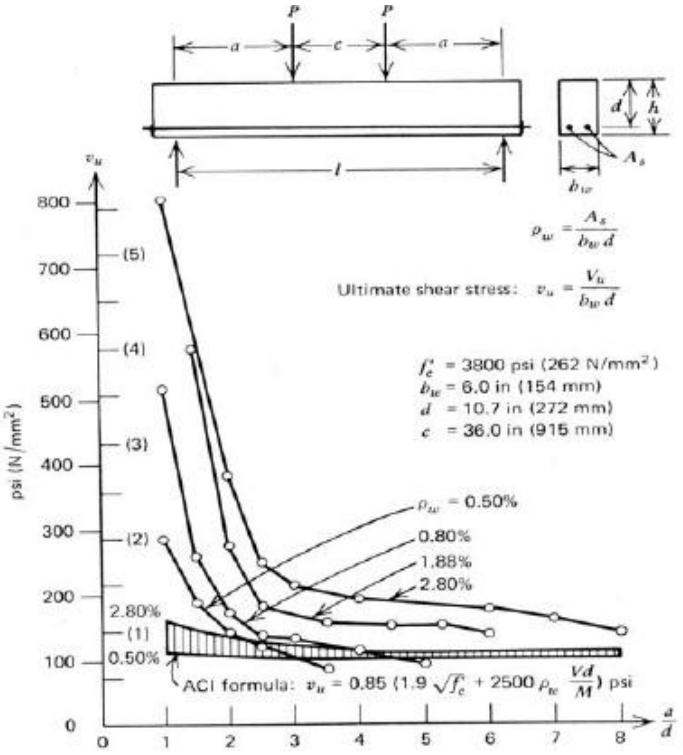

Figure 2-44: Nominal shear stress vs shear span to depth ratio of shear beams with different reinforcement ratio [ASCE1998]

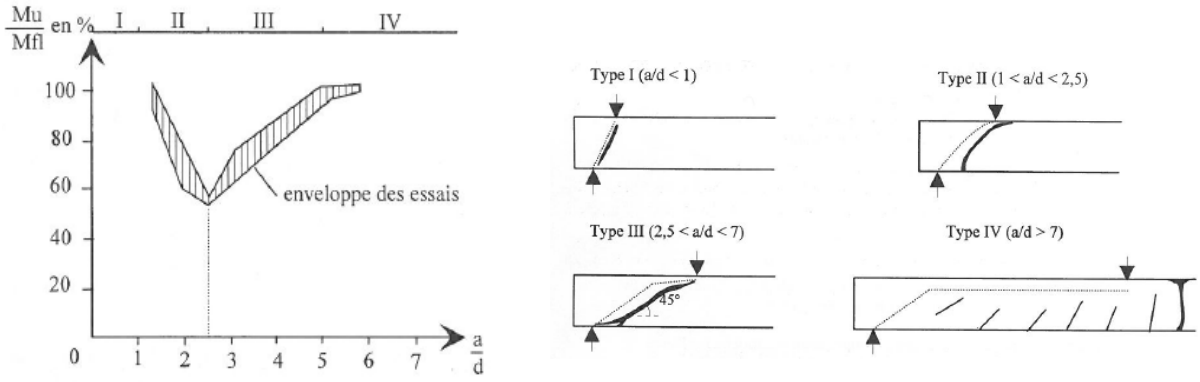

Figure 2-45: Kani's valley and the different failure modes observed [CAS1996]

2.2.3.2 Size effect or depth effect

The nominal shear strength depends linearly on the member's width and non-linearly on the member's depth. Several tests on shear behaviour were performed on relatively small beams h<500 mm. However, some structural members present higher depth like bridge girders. Tests on deep beams h> 1000 mm have highlighted that the nominal shear strength is significantly lower compared to small beams (Figure 2-46). In other words, the shear strength of members without transverse reinforcement decreases as the depth increases. The main reason for this size effect is that deep beams show larger crack width. Therefore, the interface shear transfer in deep beams is smaller. Shear tests performed by Collins [COL1993] and Frosch [FRO2000] highlighted that the size effect disappears when beams without stirrups contain well distributed longitudinal reinforcement. In fact, the cracking pattern of these beams showed better distribution and smaller cracks width.

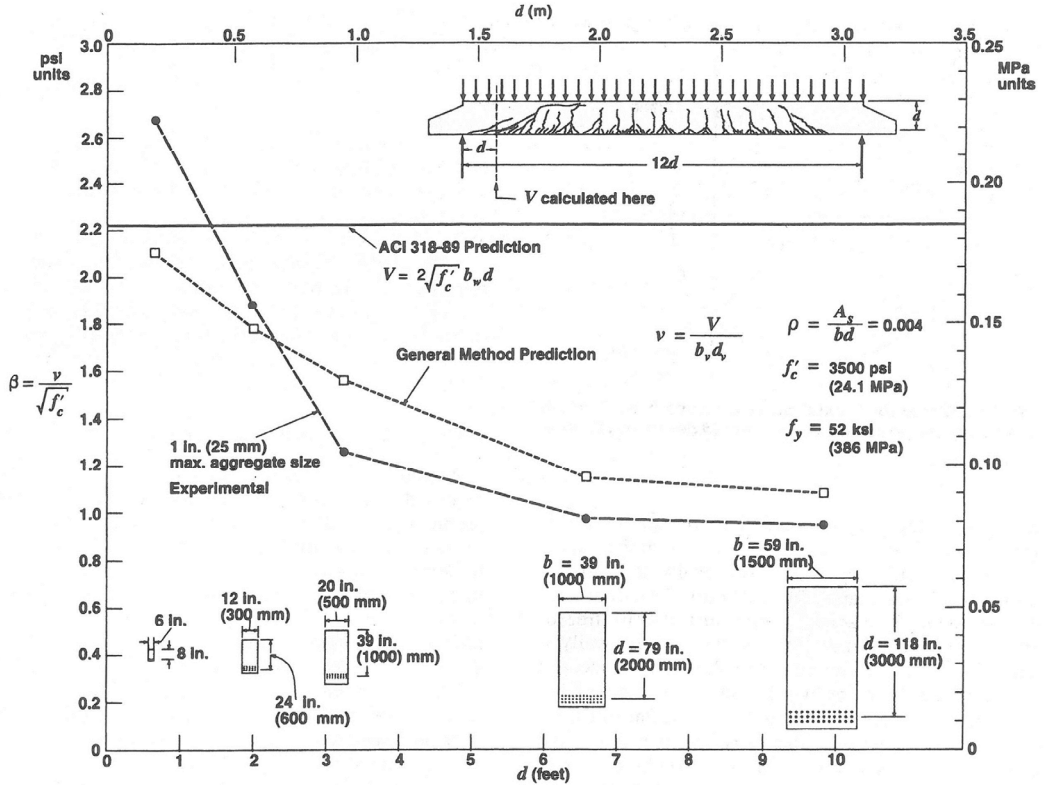

Figure 2-46: Comparison between experimental results on deep beams and computed values [COL1993].

2.2.3.3 Longitudinal reinforcement ratio and arrangement

The influence of reinforcement ratio on shear capacity was largely investigated by Kani [KAN1966]. Members with low reinforcement ratio can fail in shear at low load level. This low shear capacity can be explained by larger flexural crack widths that reduce the size of the compression zone, the dowel action and the interface shear transfer. In other words, the shear strength increases as the reinforcement ratio increases as well, however the deformation capacity decreases and the failure is more brittle and sudden.

Kuchma et al. [KUC1997] have investigated the shear behaviour of deep members with different distribution of the longitudinal reinforcement. The two tested beams have the same ratio of longitudinal reinforcement. For one beam, six rebars were uniformly distributed over the depth with a

space of 195 mm. These beams exhibited shear strength 50% higher and large deformation prior to the failure in comparison with the beam without distributed reinforcement. The beam with distributed reinforcement showed more closely spaced cracks (Figure 2-47).

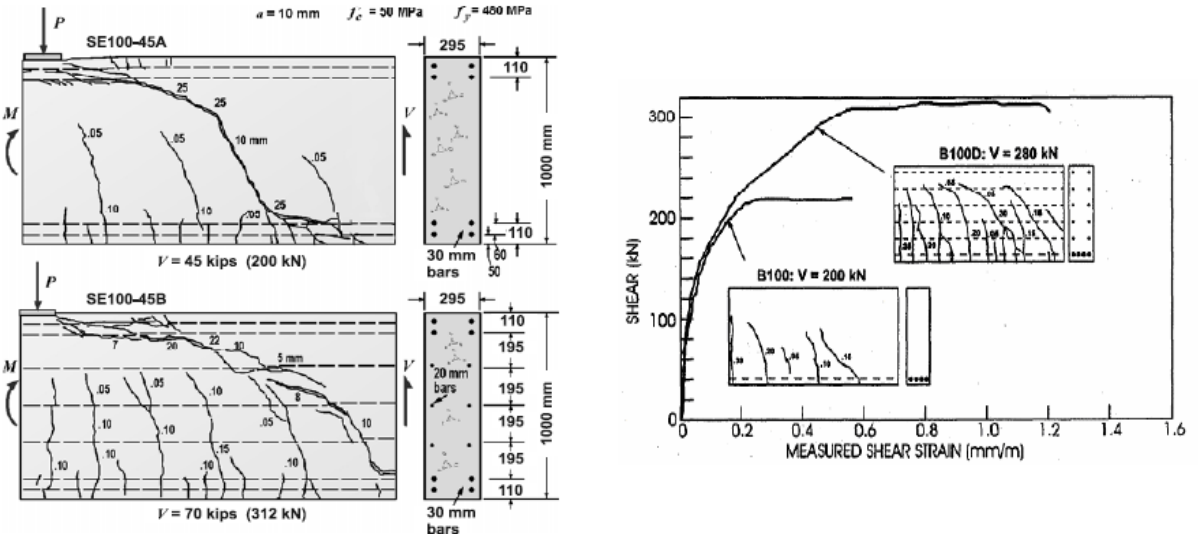

Figure 2-47: Cracking pattern and curves load vs shear strains of the Kuchma's tests [KUC1997]

A longitudinal reinforcement well distributed over the depth of the members, particularly for deep members, has an important influence on the flexural and shear cracking development. Flexural tests on large T-beams with concentrated reinforcement performed by Leohnardt [LEO1977] have highlighted the importance of minimal reinforcement on cracks pattern (Figure 2-48). Deep beams with concentrated reinforcement, present less cracks but with higher widths on the part situated above the reinforcement. In presence of shear diagonal cracks, this reinforcement can control their development; therefore the interface shear transfer mechanism is enhanced.

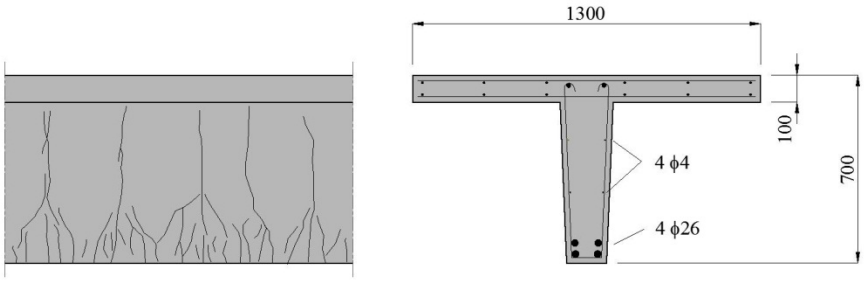

Figure 2-48: Cracking pattern of a deep T-beam described by Leohnardt [LEO1977]

2.2.3.4 Axial force

Several studies highlighted that the shear strength of members is dependent on axial force. While an axial tension decreases the shear strength, an axial compression, applied by external load or prestressing, increases the shear resistance. But the contribution of axial force on shear capacity is not clearly defined and is still subjected to research programs. A member without transverse reinforcement subjected to high compressive and shear stresses exhibits a sudden failure. Therefore, the shear design is subjected to particular attention.

Several load tests on prestressed members showed that the angles between the longitudinal axis and the diagonal shear crack are lower compared to reinforced concrete members [CEB1987]. The prestressing force delays the cracking formation. A large part of prestressed beams is un-cracked up to the failure, (*A* region). Another point of consideration, the cross-section of prestressed members exhibits often an I-shape or T-shape. These forms are more favourable to the shear strength compared to rectangular cross section. In prestressed members two shear failure modes can be distinguished. The first mode is the shear-flexure failure where the critical shear crack develops from a flexural crack. The second mode is the shear-tension failure where the principal tensile stress in the web reaches the concrete tensile strength.

In prestressed members, the effective shear span is smaller than the geometric span. This is due to the fact that the normal force does not allow the development of flexural cracks close to the support, (region A in Figure 2-49b). [FER2010].

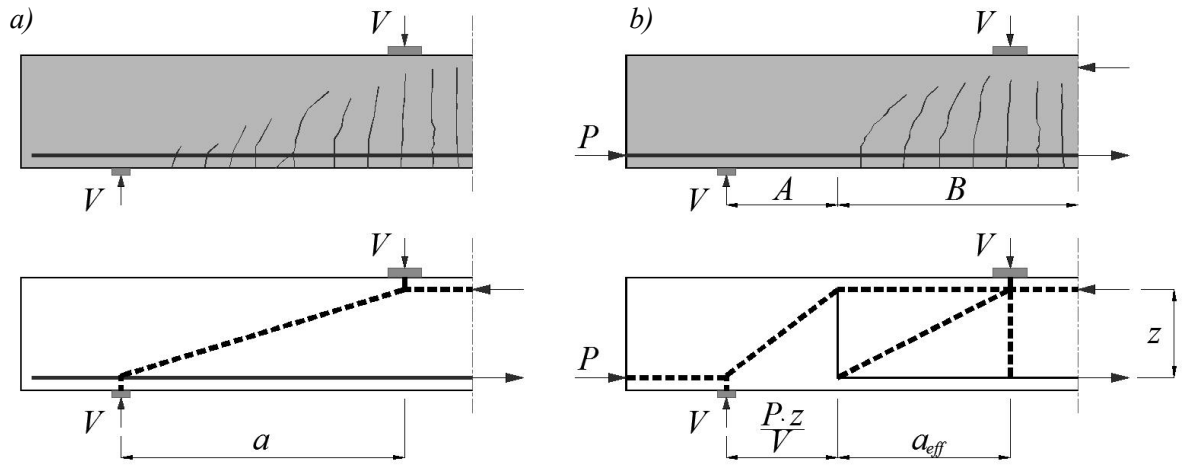

Figure 2-49: Geometric shear span in a reinforced concrete beam (a); effective shear span for a prestressed member (b) [FER2010]

The effective shear span can be calculated in the following way:

$$a_{eff} = a - \frac{P}{V} \cdot z \tag{2-64}$$

Where a is the geometric shear span, P is the normal force, V is the shear force and z is the flexural lever arm of the member, in first approximation $z = 0.9d$.

2.2.3.5 Concrete strength and aggregates size

For Normal Strength Concrete, the cracks get round the aggregates as the matrix strength is generally lower than the inclusions strength; the contact surface is then irregular. The crack path depends on the maximum aggregate size. The Figure 2-50 shows that increasing the maximum aggregate size from 10 to 50 mm is making the path of the shear crack rougher and is increasing the failure shear stress of large specimen by 33%. However in recent years, several new concrete formulations are largely used in construction as Self Compacting Concrete (SCC), Lightweight Concrete (LC) and High Strength Concrete (HSC). In comparison of vibrated concrete, SCC is composed of more cement paste. LC and HSC exhibit a matrix strength higher to the aggregate strength. Therefore, these concrete mixes show a smoother contact surface. In this case, the interface shear transfer is lower.

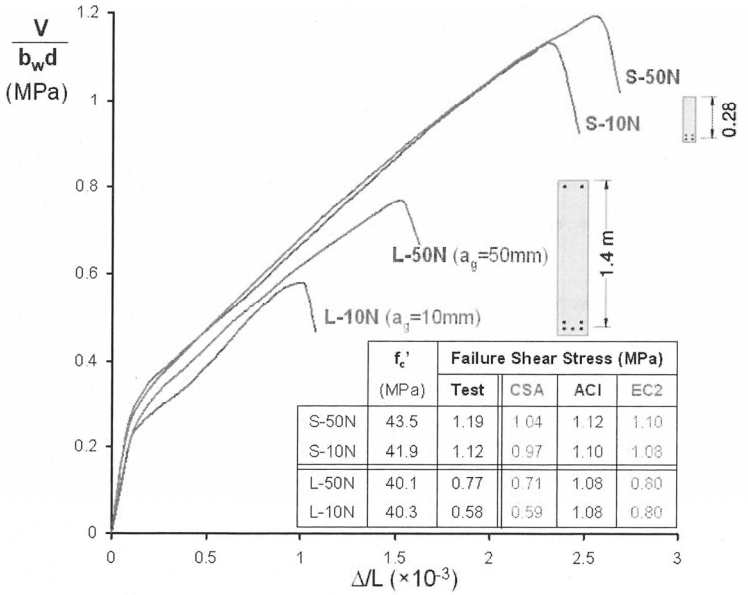

	fc' (MPa)	Failure Shear Stress (MPa) Test	CSA	ACI	EC2
S-50N	43.5	1.19	1.04	1.12	1.10
S-10N	41.9	1.12	0.97	1.10	1.08
L-50N	40.1	0.77	0.71	1.08	0.80
L-10N	40.3	0.58	0.59	1.08	0.80

Figure 2-50: Comparison between different beam and aggregate size [COL2010]

Kani [KAN1966] concluded that the nominal shear strength does not depend on the concrete compressive strength. However, he has only tested beams with concrete compressive strength in a range of 18 to 36 MPa. For these compressive strengths the effect is less noticeable and can present a large scatter. Actually, it's clear that concrete properties have a significant effect on shear capacity. The tensile strength influences the development of the cracking and the interface shear transfer mechanism. On the basis of several shear tests on high strength concrete beams, Pendyala & Mendis [PEN2000] have highlighted that shear strength does not increase significantly for concrete compressive strength in the range of 50 to 70 MPa, but increase for values between 70 and 90 MPa and appears to level off above a compressive strength of 90 MPa (Figure 2-51).

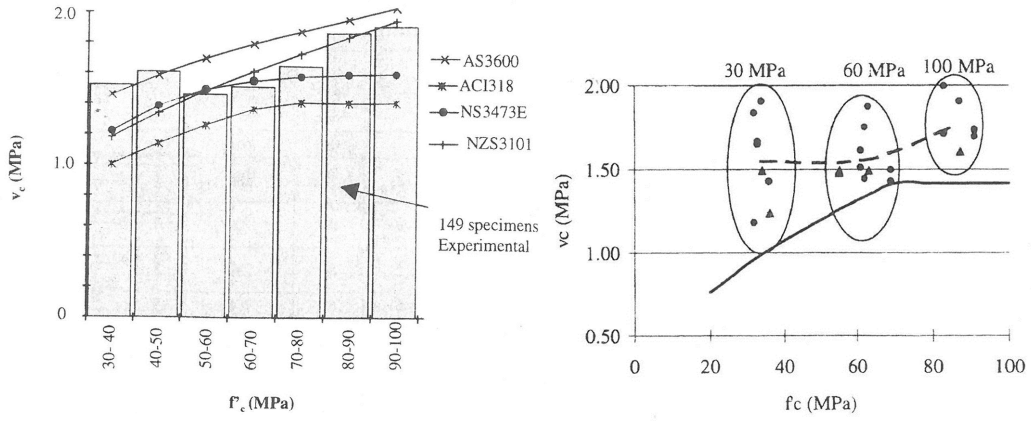

Figure 2-51: Effect of concrete compressive strength on nominal shear strength [PEN2000]

2.2.3.6 Load distribution

Loeonhard and Walter [LEO1962] have conducted several tests on members similar to the ones tested by Kani [KAN1966] with concentrated and distributed loads in order to define the effective shear span. The beams with a uniformly loading distribution showed more favourable results compared to the beams with concentrated loading. The shear span for simply supported beams with a uniformly loading distribution is considered at *L/4*.

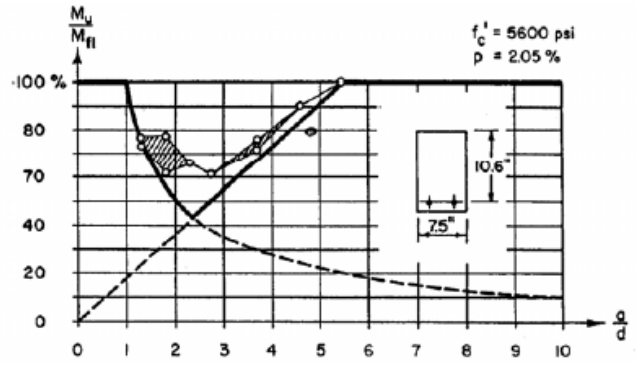

Figure 2-52: The Kani's valley for beams with uniformly distributed load [ASCE1998]

2.2.3.7 Cross section shape

The shape of the cross section influences the cracks propagation. Several tests show that diagonal shear cracks stop under the flange of T-beams and I-beams. Therefore, the compressed flange is un-cracked and can support a large part of the shear force. The flange allows a redistribution of the diagonal cracks like stirrups. Close to failure, the diagonal crack often may develop horizontally under the flange [CEB1987]. Moreover, the uncracked flange can carry a large part of the shear load ().

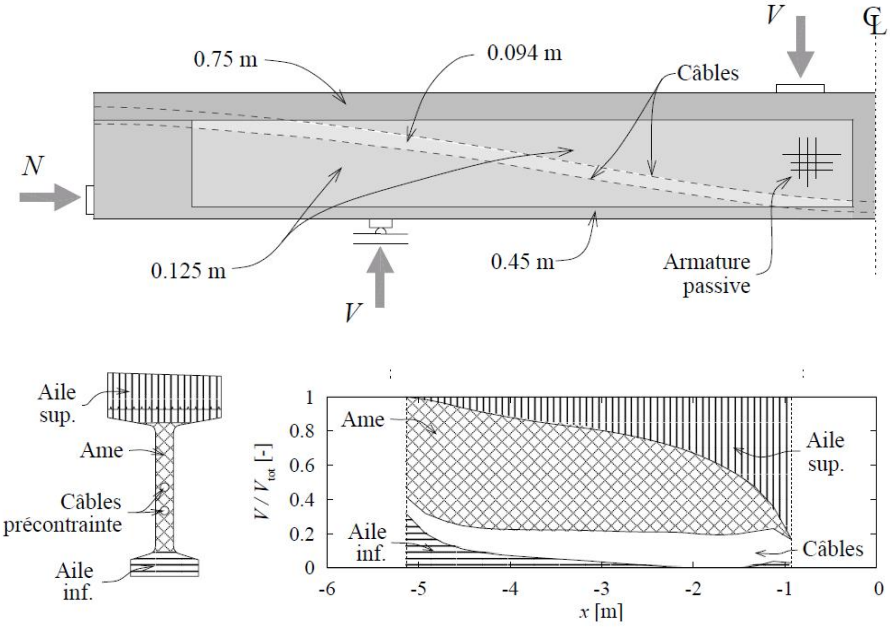

Figure 2-53: Distribution of computed shear strength (FEM) in the different element of a prestressed I-beam [FER2006]

2.2.4 Shear model for reinforced concrete member

2.2.4.1 Modified Compression Field Theory

The Modified Compression Field Theory (MCFT) was developed by Frank J. Vecchio & Michael P. Collins at University of Toronto on the basis of the Compression Field Theory (CFT) [VEC1986] [VEC1994]. The MCFT is an analytical model for predicting the load versus deflection response of reinforced concrete element simultaneously subjected in their plan to bi-axial and shear stresses. In this model, the cracked concrete is treated as a new material with its own stress – strain relationship. The model is composed of fifteen equations; five equilibrium equations, five geometric conditions and five stress - strain relationships. The stress-strain relationships are formulated in terms of average strains and stresses on the element. In comparison with the CFT, this model take into account the tensile stress across the cracks (tension stiffening) and uses average stress - strains relationships for cracked concrete. In parallel of to the MCFT development, a large experimental campaign on reinforced concrete panels has been performed at the University of Toronto in order to incorporate realistic constitutive relationships for cracked concrete.

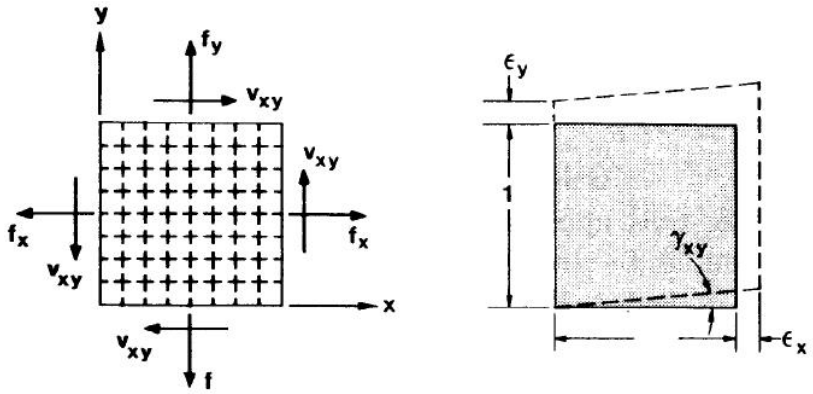

Figure 2-54: Stresses and strains in membrane element [VEC1986]

The MCFT is based on the following assumptions: uniformly distributed reinforcement, uniformly distributed and rotating cracks, uniformly applied shear and normal stresses, unique stress state for each strain state, without consideration of strain history, strains and stresses are the average over a distance including several cracks, and a uniform application of normal and shear stresses, the orientations of the principal strains and principal stress are the same, perfect bond between concrete and reinforcement, independent constitutive relationships for concrete and steel reinforcement, no shear stresses in reinforcement, no dowel effect.

Compatibility conditions

According to the assumption that steel reinforcement is perfectly anchored to the concrete, for non-prestressed reinforcement the strains of concrete and steel reinforcement are identical.

$$\varepsilon_{sx} = \varepsilon_{cx} = \varepsilon_x \tag{2-65}$$

$$\varepsilon_{sy} = \varepsilon_{cy} = \varepsilon_y \tag{2-66}$$

If the three strains components ε_x, ε_y and ν_{xy} are known then the strain in any other direction can be found geometrically with the Mohr's circle.

$$\nu_{xy} = \frac{2(\varepsilon_x - \varepsilon_2)}{\tan\theta} \tag{2-67}$$

$$\varepsilon_x + \varepsilon_y = \varepsilon_1 + \varepsilon_2 \tag{2-68}$$

$$\tan^2\theta = \frac{\varepsilon_x - \varepsilon_2}{\varepsilon_y - \varepsilon_2} = \frac{\varepsilon_1 - \varepsilon_y}{\varepsilon_1 - \varepsilon_x} = \frac{\varepsilon_1 - \varepsilon_y}{\varepsilon_y - \varepsilon_2} = \frac{\varepsilon_x - \varepsilon_2}{\varepsilon_1 - \varepsilon_x} \tag{2-69}$$

Equilibrium equations

The external forces applied in directions x and y must be in equilibrium with internal stresses of concrete and reinforcement. After ignoring the reduction of the concrete due to the reinforcement, the equilibrium equations can be written as follows:

$$f_x = f_{cx} + \rho_{sx} \cdot f_{sx} \tag{2-70}$$

$$f_y = f_{cy} + \rho_{sy} \cdot f_{sy} \tag{2-71}$$

Assuming that the steel reinforcement does not carry shear stresses;

$$\tau_{xy} = \nu_{cxy} \tag{2-72}$$

The concrete stresses can be deduced with the Mohr's circle.

$$f_{cx} = f_{c1} - \nu_{cxy} / \tan\theta \tag{2-73}$$

$$f_{cy} = f_{c1} - \nu_{cxy} \cdot \tan\theta \tag{2-74}$$

$$f_{c2} = f_{c1} - \nu_{cxy} \cdot (\tan\theta + 1/\tan\theta) \tag{2-75}$$

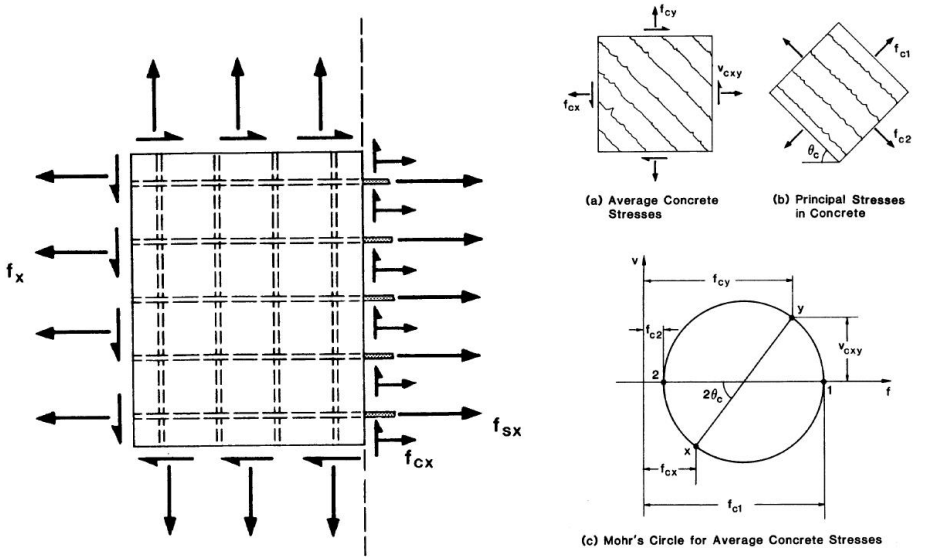

Figure 2-55: Free body diagram of part of element and stresses in cracked concrete [VEC1986]

Stress – strain relationships

Materials constitutive relationships are required in order to link the strains ε_x ε_y and ν_{xy} to the stresses f_x, f_y and τ_{xy}. Frank J. Vecchio & Michael P. Collins have tested several reinforced concrete panels subjected to normal and shear stresses. A special tests set-up has been developed. The parameters were: the applied forces, the reinforcement ratio in direction x and y and the concrete strength. The

panels have a length of 890 mm and 70 mm thick. The applied stresses (f_x, f_y and τ_{xy}) were known and the average of strains (ε_x, ε_y and ν_{xy}) was measured (Figure 2-56).

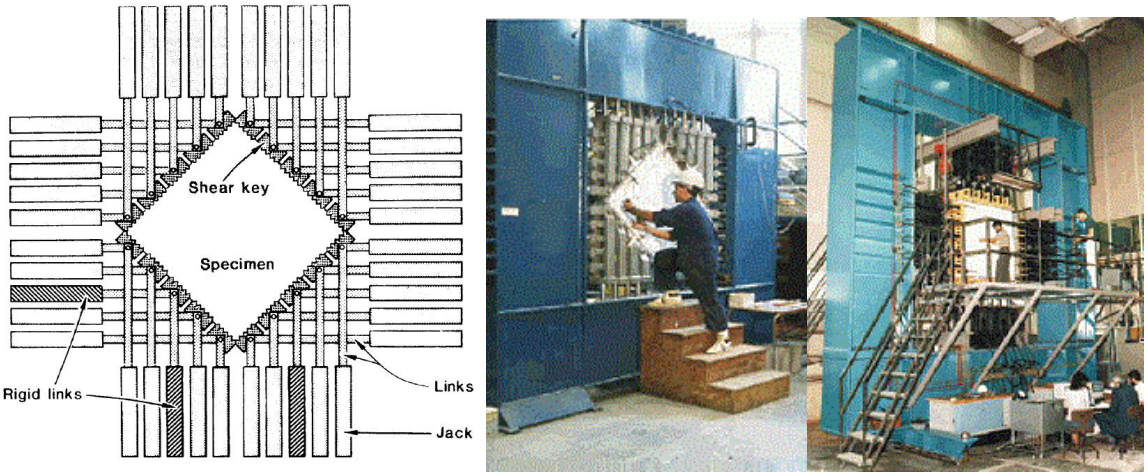

Figure 2-56: Membrane and shell elements test setup [VEC1986]

The tests results have highlighted that the principal compressive stress of concrete f_{c2} does not only depend of the principal compressive strain ε_2 but is also influenced by the principal tensile strain f_{c1}. The cracked concrete subjected to tensile stress in the normal direction presents less strength and stiffness in comparison to a simple compressive test (Figure 2-57).

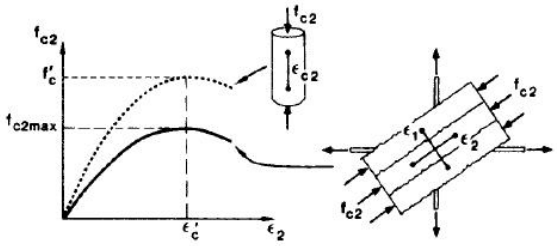

Figure 2-57: Stress – strain relationship for cracked concrete in compression

$$f_{c2} = f_{c2\max} \cdot \left[2\left(\varepsilon_2 / \varepsilon_c^{'}\right) - \left(\varepsilon_2 / \varepsilon_c^{'}\right)^2 \right] \tag{2-76}$$

$$\frac{f_{c2\max}}{f_c^{'}} = \frac{1}{0.8 - 0.34\left(\varepsilon_1 / \varepsilon_c^{'}\right)} \leq 1.0 \tag{2-77}$$

The relationship between the average principal tensile stress in the concrete and the average principal tensile strain is given by:

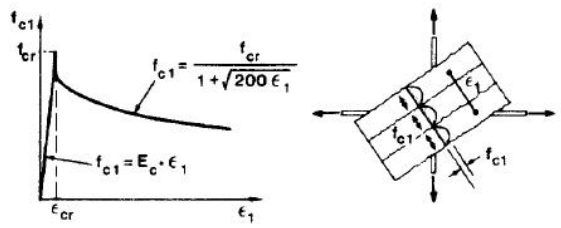

Figure 2-58: Stress – strain relationship for cracked concrete in tension

$$f_{c1} = E_c \cdot \varepsilon_1 \le f_t^{'} \qquad \text{for } \varepsilon_1 \le \varepsilon_{cr} \tag{2-78}$$

$$f_{c1} = \frac{f_t^{'}}{1+\sqrt{200\varepsilon_1}} \qquad \text{for } \varepsilon_1 > \varepsilon_{cr} \tag{2-79}$$

The behavior of steel reinforcement is represented by a bi-linear curve.

$$f_{sx} = E_s \cdot \varepsilon_x \le f_{yx} \tag{2-80}$$

$$f_{sy} = E_s \cdot \varepsilon_y \le f_{yy} \tag{2-81}$$

$$\nu_{sx} = \nu_{sy} = 0 \tag{2-82}$$

The average stress–strain relationships don't give local information. At a crack, the steel reinforcement stresses are higher than average stresses, while between two cracks the stresses are smaller. Compared to calculated average stresses, the local tensile stress is equal to zero in a crack and is higher between two cracks. These local variations are important because the ultimate strength of a bi-axial stressed element depends of on the ability of the reinforcement to transmit the tensile stress across the cracks (Figure 2-59). In order to take into account these local variations, the local stresses at cracks and the concrete average tensile stresses are limited in the model.

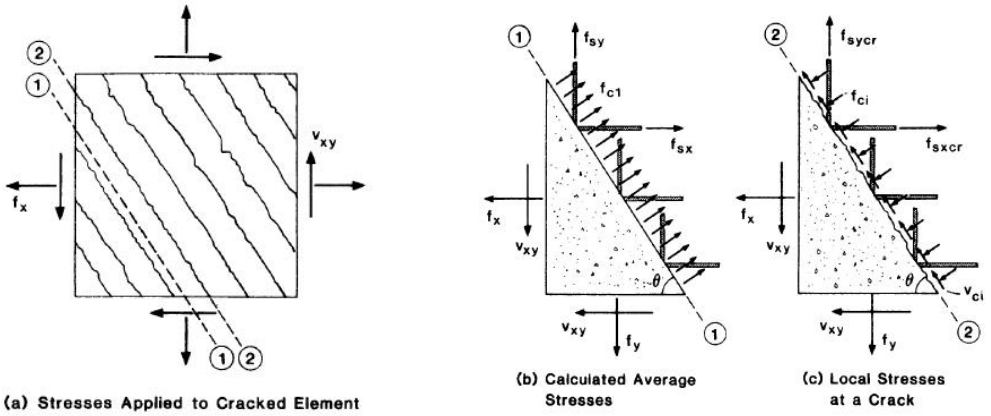

Figure 2-59: Comparison between calculated average stresses and local stresses at a crack [VEC1986]

The critical cracks direction is assumed to be normal to the principal tensile strain direction. At cracks, the concrete carries shear stresses through the interface shear transfer mechanism. By comparing the average stresses of the Plane 1 with the local stresses of the Plane 2, it's possible to write the following equations;

$$\rho_{sx} f_{sx} \sin\theta + f_{ci} \sin\theta = \rho_{sx} f_{sxcr} \sin\theta - f_{ci} \sin\theta - \nu_{ci} \cos\theta \tag{2-83}$$

$$\rho_{sy} f_{sy} \cos\theta + f_{c1} \sin\theta = \rho_{sy} f_{sycr} \cos\theta - f_{ci} \cos\theta - \nu_{ci} \sin\theta \tag{2-84}$$

$$\rho_{sx} (f_{sxcr} - f_{sx}) = f_{c1} + f_{ci} + \nu_{ci} / \tan\theta \tag{2-85}$$

$$\rho_{sy} (f_{sycr} - f_{sy}) = f_{c1} + f_{ci} + \nu_{ci} \tan\theta \tag{2-86}$$

The equilibrium between the equations (2-85) and (2-86) can be satisfied with no shear stresses and compressive stresses only if:

$$\rho_{sx} (f_{sxcr} - f_{sx}) = \rho_{sy} (f_{sycr} - f_{sy}) = f_{c1} \tag{2-87}$$

And the local reinforcement stresses f_{sxcr} and f_{sycr} cannot exceed the steel yield limit f_{sy}. However, if the calculated average stresses in reinforcement are high, the equation (2-87) is not satisfied. In this case, the equilibrium is only satisfied with shear stresses at cracks. Based on Walraven's works, the following equation was developed;

$$v_{ci} = 0.18 \cdot v_{ci\max} + 1.64 f_{ci} - 0.82 \frac{f_{ci}^2}{v_{ci\max}} \tag{2-88}$$

with $$v_{ci\max} = \frac{\sqrt{-f_c'}}{0.31 + 24 \cdot w/(a+16)} \tag{2-89}$$

The cracks openings w correspond to the average of openings on the element defined as follows;

$$w = \varepsilon_1 \cdot s_\theta \tag{2-90}$$

with $$s_\theta = \frac{1}{\frac{\sin\theta}{s_{mx}} + \frac{\cos\theta}{s_{my}}} \tag{2-91}$$

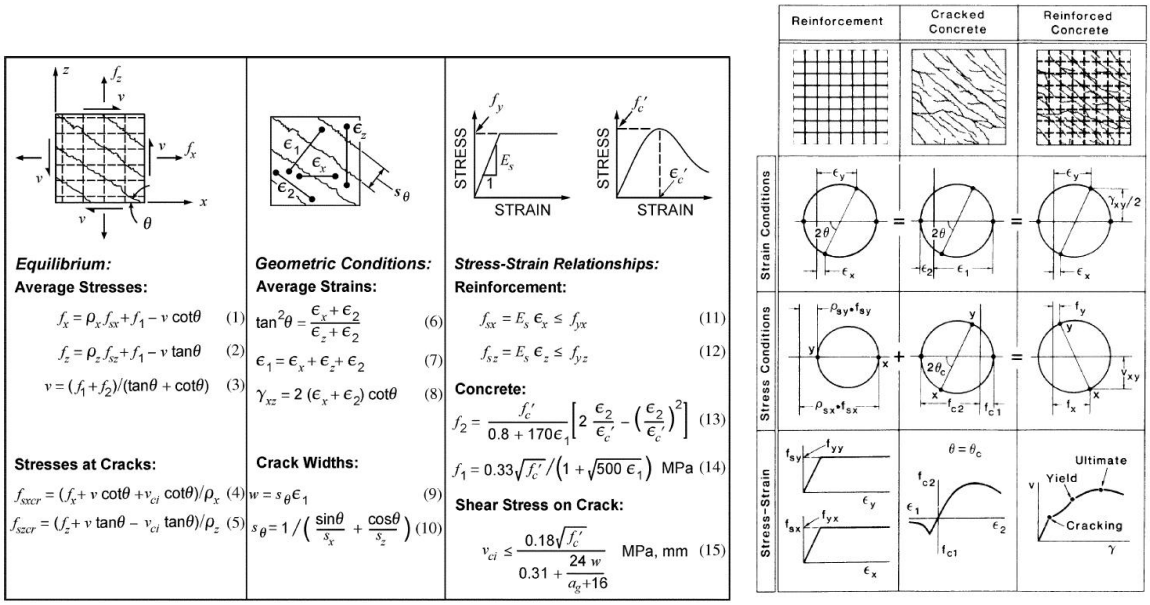

Figure 2-60: Summary of equations of the modified compression field theory [VEC1986]

To use the MCFT to predict the load-deformation response of a reinforced concrete beam, the member should be represented as a two dimensional grid of elements with the response of each element being predicted by the MCFT. This model is implemented in non-linear finite element programs such as VecTor2 [VEC2000a] or Response 2000. On the basis of the MCFT an analytical simplified model [BEN2006] was proposed. This MCFT-based sectional design model is the method used in the current Canadian Standards Association "Design of Concrete Structures" A23.3-04 [CSA2004] and the *fib* Model Code 2010 [MC2010b].

Frank J. Vecchio proposed a new model named the Disturbed Stress Field Model (DSFM) [VEC2000b] [VEC2001a] [VEC2001b]. The DSFM includes a new approach to the reorientation of concrete stress and strain fields, removing the MCFT restrictions and an improved treatment of shear stress on cracks surfaces is developed. New sets of equilibrium, compatibility and constitutive

relationships were formulated. Compared to the MCFT, the DSFM gives better results for elements without transverse reinforcement.

2.2.4.2 Critical Shear Crack Theory CSCT

A. Muttoni [MUT2008a], from Ecole Polytechnique Fédérale de Lausanne (EPFL), proposed the Critical Shear Crack Theory (CSCT) for the shear strength assessment of beams without shear reinforcement. The CSCT was developed on the basis of the following assumptions and observations. In members in bending, various shear carrying mechanisms may develop like the cantilever action, aggregate-interlock and dowel action (Figure 2-61). These shear carrying mechanisms induce tensile stresses and the cracks progress.

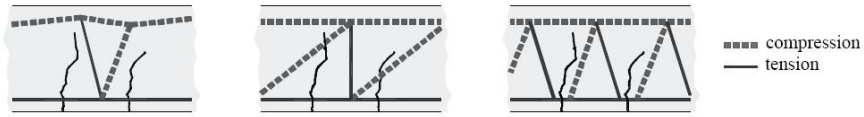

Figure 2-61: The cantilever action, the aggregate interlock and the dowel action [MUT2008a]

At a certain load level, a critical shear crack may develop. However, this does not necessarily imply the failure of the member. A new shear-carrying mechanism may be formed, the arching action. Two possibilities may occur for the development the arching action. The first one is the development of an elbow-shaped strut. The second is the development of a direct strut that activates the aggregate interlock in the critical shear crack. The model reflects the superposition of the two effects (Figure 2-62). The load carrying by aggregate interlock depends on the crack opening and the roughness.

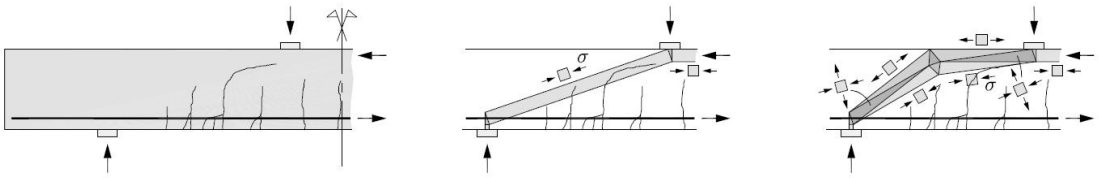

Figure 2-62: Direct strut activated by aggregate interlocking and elbow-shaped strut [MUT2008a]

The shear strength is checked in a section depending on the load configuration where the width of the critical shear crack can be adequately represented by the strain at a depth 0.6*d* from the compression face (Figure 2-63). The critical crack width *w* is proportional to the product of the longitudinal strain in the control depth equal to ε times the effective depth *d*.

$$w \propto \varepsilon d \tag{2-92}$$

Assuming that plane sections remain plane with the concrete having a linear elastic behaviour in compression (i.e. neglecting its tensile strength), the strain for rectangular members without axial forces at a depth of 0.6*d* is defined as follows:

$$\varepsilon = \frac{M}{b \cdot d \cdot \rho \cdot E_s \cdot (d - c/3)} \frac{0.6d - c}{d - c} \tag{2-93}$$

Where *c* is the compression depth

$$c = d \cdot \rho \cdot \frac{E_s}{E_c} \cdot \left(\sqrt{1 + \frac{2 \cdot E_c}{\rho \cdot E_s}} - 1 \right) \tag{2-94}$$

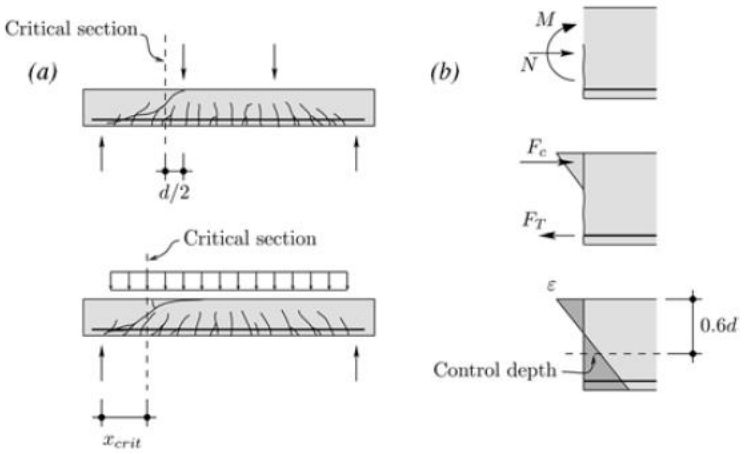

Figure 2-63: Definition of the critical section and determination of the longitudinal strain [MUT2008a]

The failure criterion is defined as follows:

$$\frac{V_R}{b \cdot d \cdot \sqrt{f_c}} = \frac{1}{6} \frac{2}{1 + 120 \cdot \left(\frac{\varepsilon \cdot d}{d_{g0} + d_g} \right)} \tag{2-95}$$

Where d_{g0} is the reference aggregate size, generally d_{g0} = 16 mm, and d_g is the maximal aggregate size. For lightweight concrete and high strength concrete (f_c> 60 MPa), d_g should be taken equal to zero because the cracking surface develops through the aggregates. Therefore the roughness would become lower.

The model was compared to 150 shear tests with concentrated loads and 16 tests with uniformly distributed loading in normal and high-strength concrete (Figure 2-64). The model gives a good agreement with the tests results.

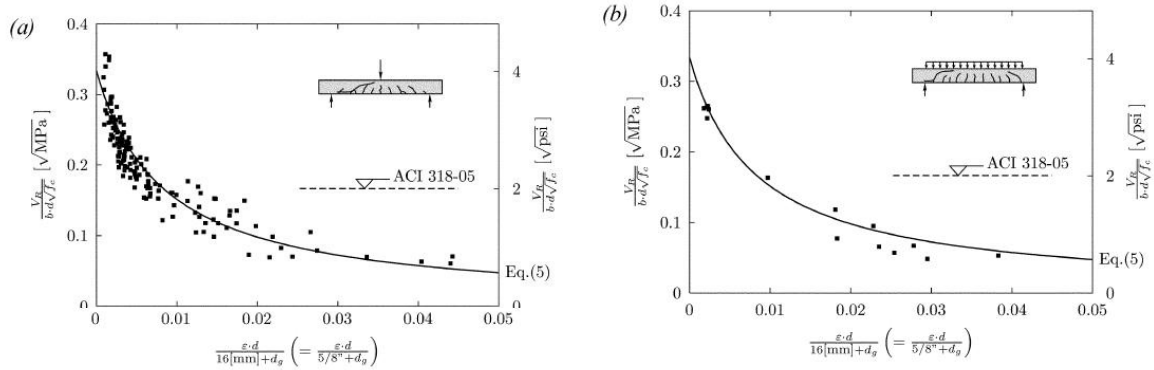

Figure 2-64: Comparison of the test results with the failure criterion, for beams with concentrated loading arrangement and beams with uniformly distributed loading arrangement [MUT2008a]

A simplified design model was proposed by the author. This simplified CSCT design model is the method used in the current Swiss Code SIA262 "Concrete Structures" [SIA2003] for assessing the shear strength of slabs without transverse reinforcement.

2.2.4.3 Stress field and strut-and-tie models

The strut-and-tie model was initiated by Ritter [RIT1899] at the beginning of the 20thcentury. Ritter concluded that the reinforced concrete beams can act like a truss with a diagonal inclination of 45° to be considered. Therefore, the stirrups must be spaced at a distance corresponding to the level arm *z* in order to carry the shear force. The Ritter's works were detailed few years later by Mörsch [MOE1908]. The latter analysed the cases of beams with longitudinal bars inclined near the supports and beams with low spacing stirrups. On the basis of several loading tests, Mörsch concluded that a large part of the shear is transmitted directly to the support by a strut and the corresponding inclination not necessarily being 45 degrees. Mörsch proposed a refined model where the Ritter's truss was replaced by a unique compression stress field (Figure 2-65). These works were extended to all reinforced concrete structures by Leonhardt and later by Schlaich [SCH1984] [REI2005]. Drucker was the first to apply the plasticity theory for beams loaded in flexure and shear. On the basis of Drucker's works, the rigid-plastic stress field model was generalized to all reinforced concrete structures by Thürlimann. Later, some considerations on the concrete behaviour and the cracking process were introduced by Muttoni.

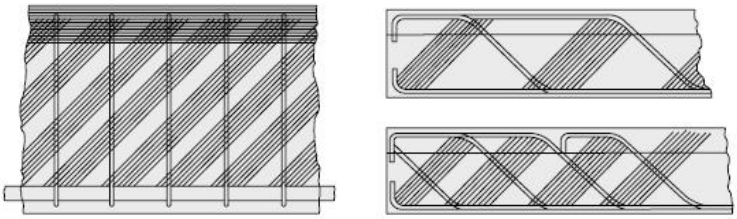

Figure 2-65: Stress field model by Mörsch [MUT2011]

For the design of reinforced concrete structure, Schlaich proposed to divide the structure into two types, firstly, where the hypothesis of Bernoulli and Navier is verified, named zone B, and secondly, the discontinuity zone (load introduction, geometry change, etc.), named D, where a strut-and-tie model is necessary (Figure 2-66).

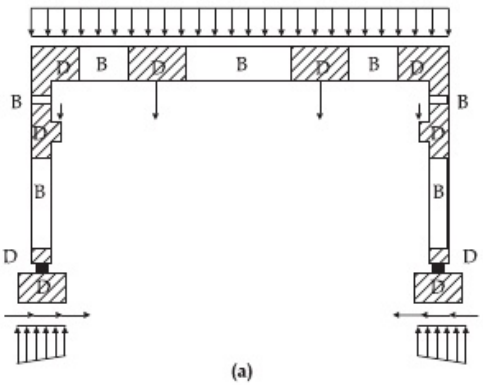

Figure 2-66: Definition of B and D zones for a reinforced concrete structure [SCH1984]

The stress field model represents the lower bound of the plasticity theory. Therefore, all loading Q_S in equilibrium with a stress field that satisfies the static condition of plasticity is a lower limit of the ultimate load Q_R. The static condition of plasticity is verified if the stresses in the concrete and rebars are inferior or equal to the yield limit of the materials.

$$Q_S \leq Q_R \tag{2-96}$$

A couple of models are available, the Elastic-Plastic Stress Field Model (EPSFM) or the Rigid-Plastic Stress Field Model (RPSFM). The use of the EPSFM requires generally a FEM analysis. As for the RPSFM, it can be computed manually, considering several assumptions and is composed of three element types, i.e, nodes, ties and concrete struts or compression fields (Figure 2-67) [FER2007] [MUT2011].

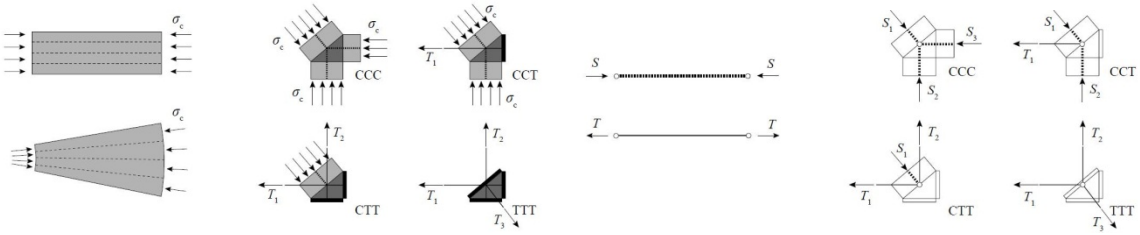

Figure 2-67: Stress field and strut-and tie elements [MUT2011]

The concrete and steel behaviours are assumed to be rigid perfectly plastic. The concrete tensile strength is neglected. Considering these assumptions it becomes possible to introduce discontinuity lines in the structure. However, the concrete is far from being a plastic material. In order to take into account the softening behaviour, the concrete strength is limited [MUT2011]. Moreover, the concrete compressive strength is also limited by the lateral strains and the cracking. According to the Swiss Code SIA 262 [SIA2003], the effective concrete strength f_{ce} is computed as follows:

$$f_{ce} = k_c \cdot \frac{\eta_{fc} \cdot f_{ck}}{\gamma_c} \tag{2-97}$$

$$\eta_c = \left(\frac{30}{f_{ck}}\right)^{1/3} \leq 1 \tag{2-98}$$

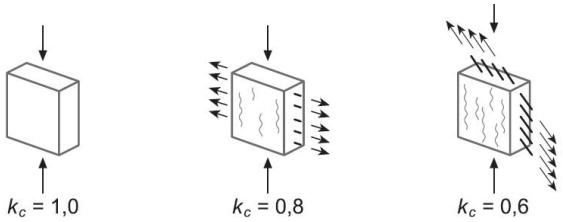

Figure 2-68: Some values of the coefficient k_c for current cases [SIA2003]

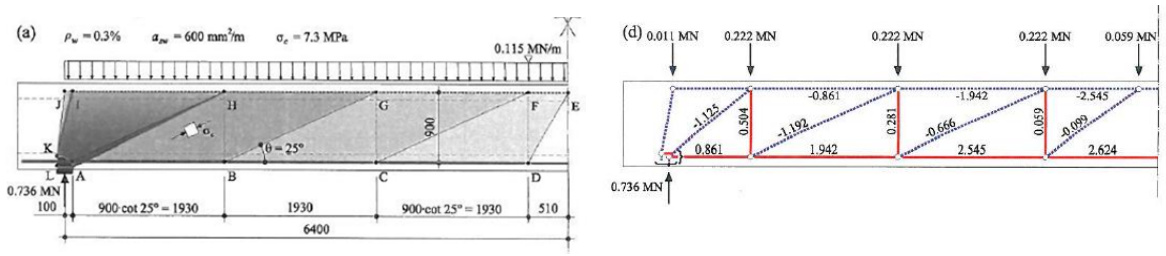

Figure 2-69: RPSFM for a uniformly loaded beam and corresponding strut-and-tie model [MUT2011]

2.2.5 Recommendations and standards, shear strength of Reinforced Concrete

2.2.5.1 EN 1992-1-1 Eurocode 2

In the Eurocode 2 [EC22005], the shear strength for members not requiring transverse reinforcement $V_{Rd,c}$ is given by:

$$V_{Rd,c} = \left[\frac{0.18}{\gamma_c} \cdot k \cdot \left(100 \cdot \rho_I \cdot f_{ck}\right)^{1/3} + 0.15 \cdot \sigma_{cp} \right] \cdot b_w \cdot d \geq \left[v_{\min} + 0.15 \cdot \sigma_{cp} \right] \cdot b_w \cdot d \qquad (2\text{-}99)$$

This formulation is fully empirical.

Where k is a factor taking into account the size effect (Figure 2-70),

$$k = 1 + \sqrt{\frac{200}{d}} \leq 2.0 \qquad (d \text{ in [mm]}) \qquad (2\text{-}100)$$

ρ_l is the tensile reinforcement ratio, which anchor beyond the section considered,

$$\rho_l = \frac{A_{sl}}{b_w \cdot d} \leq 0.02 \qquad (2\text{-}101)$$

σ_{cp} is the compressive stress in the centre of gravity of cross-section due to loading or pre-stressing. The influence of imposed deformation may be ignored,

$$\sigma_{cp} = N_{Ed} / A_c \leq 0.2 \cdot f_{cd} \qquad (2\text{-}102)$$

And v_{min} is the minimum shear strength given by:

$$v_{\min} = 0.035 \cdot k^{3/2} \cdot f_{ck}^{1/2} \qquad (2\text{-}103)$$

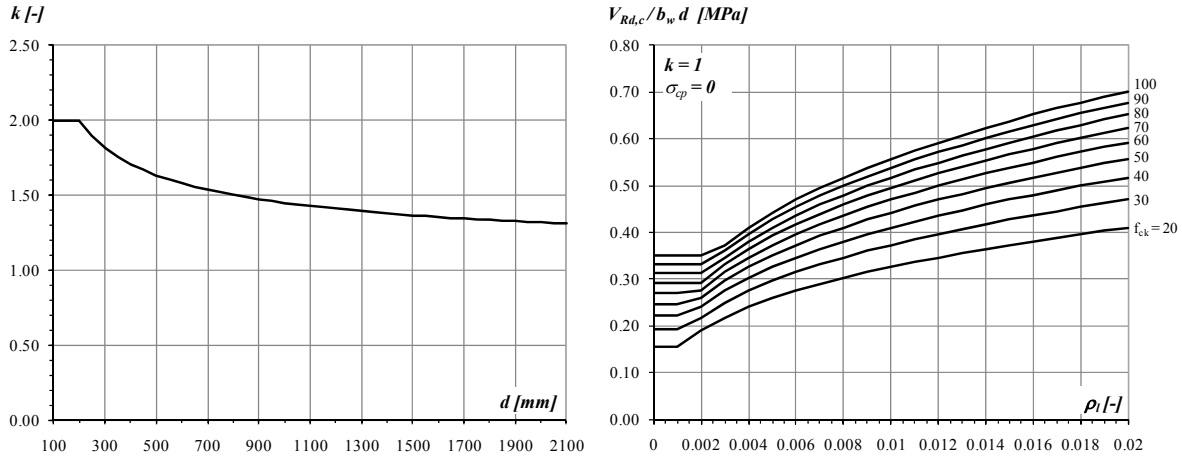

Figure 2-70: Evolution of size factor k according to the effective depth and evolution of the nominal strength according to the reinforcement ratio for different concrete compressive strengths

2.2.5.2 Swiss Code SIA 262

The shear provision for beams without transverse reinforcement in the Swiss Code SIA 262 "Concrete Structures" [SIA2003] is based on a simplified form of the Critical Shear Crack Theory [MUT2008a]. The shear strength is given by equation (2-104) general form and equation (2-105) common form;

$$\frac{V_{Rd}}{b \cdot d \cdot \sqrt{f_{ck}}} = \frac{0.3/\gamma_c}{1 + \frac{50}{16 + d_g} \cdot \frac{f_{yk}}{\gamma_s \cdot E_s} \cdot d \cdot \frac{m_{Ed}}{m_{Rd}}} \tag{2-104}$$

$$\frac{V_{Rd}}{b \cdot d \cdot \sqrt{f_{ck}}} = \frac{0.2}{1 + 0.0022 \cdot d \cdot \frac{m_{Ed}}{m_{Rd}}} \tag{2-105}$$

Where m_{Ed} is the moment in the critical section and m_{Rd} is the flexural capacity. For equation (2-105) if the stress in the reinforcement σ_s is higher or equal to f_{yk} ,the value 0.0022 is replaced by 0.003.When an axial force is applied to the member, m_{Ed} has to be replaced by ($m_{Ed} - m_{Dd}$) and m_{Rd} by ($m_{Rd} - m_{Dd}$), where m_{Dd} is the decompression moment (bending moment causing $\varepsilon_s = 0$).

2.2.5.3 fib Model Code 2010

In the *fib* Model Code 2010 [FIB2010b], four Levels of approximation (LoA) were introduced for the shear and punching shear design of reinforced concrete and prestressed concrete structures. As the LoA increases, the quality of predictions improves, but requires more complex calculation (Figure 2-71). Level I provides the simplest analysis method and is also the most conservative. Level II is intermediate in complexity and accuracy. Level III provides the most accurate and general predictions. Level IV allows the use of nonlinear finite element method.

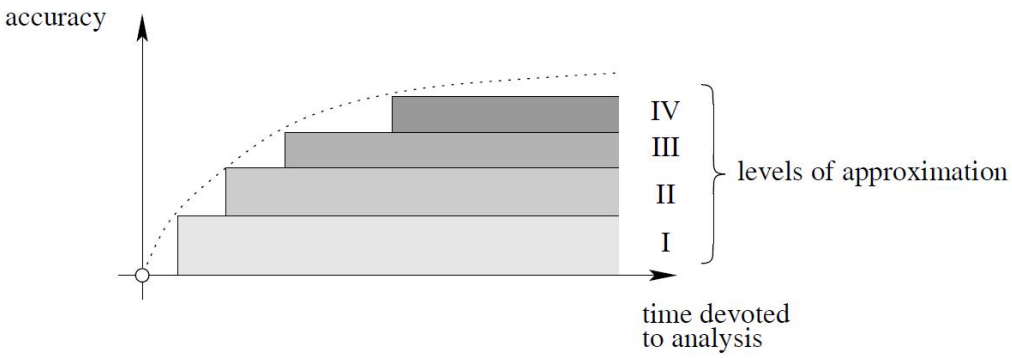

Figure 2-71: Levels of approximation [FIB2010b], graph accuracy of prediction vs time of analysis

For assessing the shear strength of reinforced concrete members, two parameters are calculated, i.e. the inclination of the stress field θ, and a coefficient for the concrete contribution k_v. The concrete contribution represents principally the shear transferred by the aggregates interlock mechanism. The complexity of the equations depends of the LoA. The shear strength V_{Rd} is the sum of the concrete contribution $V_{Rd,c}$ and the stirrups contribution $V_{Rd,s}$.

$$V_{Rd} = V_{Rd,c} + V_{Rd,s} \leq V_{Rd,\max} \tag{2-106}$$

$$V_{Rd,s} = \frac{A_{sw}}{s_w} \cdot z \cdot f_{ywd} \cdot \left(\cot\theta + \cot\alpha\right) \cdot \sin\alpha \tag{2-107}$$

$$V_{Rd,c} = k_v \cdot \frac{\sqrt{f_{ck}}}{\gamma_c} \cdot z \cdot b_w \tag{2-108}$$

$$V_{Rd,\max} = k_c \cdot \frac{f_{ck}}{\gamma_c} \cdot b_w \cdot z \cdot \frac{\cot\theta + \cot\alpha}{1 + \cot^2\theta} \tag{2-109}$$

The first LoA are based on the simplest form of the Modified Compression Field Theory [BEN2010]. The first Level may only be used for members with a characteristic concrete strength $f_{ck} \leq 64$ MPa, a characteristic steel strength $f_{yk} \leq 500$ MPa and with maximum coarse aggregate size $d_g \geq 10$ mm.

$$\theta = 45° \tag{2-110}$$

$$k_v = \begin{cases} \dfrac{200}{\left(1000 + 1.3 \cdot z\right)} \\ 0.15 \end{cases} \quad \text{if} \quad \begin{matrix} \rho_w = 0 \\ \rho_w \geq 0.08\sqrt{f_{ck}} \,/\, f_{yk} \end{matrix} \tag{2-111}$$

$$k_c = 0.5 \cdot \left(\frac{30}{f_{ck}}\right)^{1/3} \leq 0.5 \tag{2-112}$$

The second LoA is based on a strain-modified form of plasticity. It may only be used for members with transversal reinforcement. For this method, no concrete contribution $V_{Rd,c}$ is taken into account and the angle of the stress field θ can be selected between the following values:

$$k_v = 0 \tag{2-113}$$

$$20° + 10'000 \cdot \varepsilon_x \leq \theta \leq 45° \tag{2-114}$$

The third LoA is based directly on the equation of the MCFT (point 2.2.4.1)

$$\theta = 29° + 7000 \cdot \varepsilon_x \tag{2-115}$$

Where ε_x is the longitudinal strain at mid-depth of the members calculated with a plane analysis ignoring the tension stiffening, or based on the following equation resulting from a truss model of a member stressed to bending shear and axial load.

$$\varepsilon_x = \frac{M_{Ed}/z + V_{Ed} + 0.5 \cdot N_{Ed} - A_p \cdot f_{p0}}{2\left(E_s \cdot A_s + E_p \cdot A_p\right)} \qquad -0.0002 \le \varepsilon_x \le 0.0003 \tag{2-116}$$

$$k_c = 0.55 \cdot \left(\frac{30}{f_{ck}}\right)^{1/3} \le 0.55 \tag{2-117}$$

$$k_v = \begin{cases} \dfrac{0.4}{\left(1+1500 \cdot \varepsilon_x\right)} \cdot \dfrac{1300}{\left(1000 + 0.7 \cdot k_{dg} \cdot z\right)} \le 0.15 \\ \dfrac{0.4}{\left(1+1500 \cdot \varepsilon_x\right)} \end{cases} \tag{2-118}$$

$$k_{dg} = \begin{cases} \dfrac{48}{16 + d_g} \ge 1.15 & \text{if} \quad f_{ck} \le 70 \\ 3 & \quad\quad\; f_{ck} \le 70 \end{cases} \tag{2-119}$$

In precast single span members without shear reinforcement, shear failure can occur when the principal tensile stress in the web reaches the tensile strength of the concrete. This type of failure can occur in the uncracked region of the beam in flexure and is relevant especially for precast element like prestressed hollow core slabs.

For the first LoA the shear tension capacity is calculated as follow;

$$V_{Rd,ct} = \frac{I \cdot b_w}{S} \cdot \sqrt{f_{ctd}^2 + \alpha_l \cdot \sigma_{cp} \cdot f_{ctd}} \tag{2-120}$$

$$\alpha_l = l_x / 1.2 \cdot l_{bpt} \tag{2-121}$$

$$l_{bpt} = \frac{0.10 \cdot \phi_s \cdot \sigma_{pi}}{f_{ctd}} \tag{2-122}$$

Where I is the second moment of area, S is the first moment of area above and about the centroidal axis, σ_{cp} is the concrete compressive stress at centroidal axis due to prestressing.

2.2.6 Recommendations and standards, shear strength of Steel Fibre Reinforced Concrete

2.2.6.1 RILEM TC 162 TDF

In interim recommendations for FRC [RIL2003], ultimate shear strength V_R is given as the sum of concrete contribution V_c, transversal reinforcement V_w and fibres contribution V_f. The shear strength is limited at the crushing strength of the compression struts V_{Rc}. The terms V_c, V_{Rc} and V_w have the same form of Eurocode 2 [EC22005].

$$V_R = V_c + V_f + V_w \le V_{Rc} \tag{2-123}$$

The fibres contribution consists of an integration of shear strength due to fibres on the critical shear cracks. The fibres contribution is defined as follows:

$$V_f = k_f \cdot k \cdot \cos\theta \cdot \tau_{fd} \cdot b_w \cdot d \cdot \cot\theta \tag{2-124}$$

Where θ is the inclination of the compression strut and k_f is a factor taking into account the flange contribution of T-section given by:

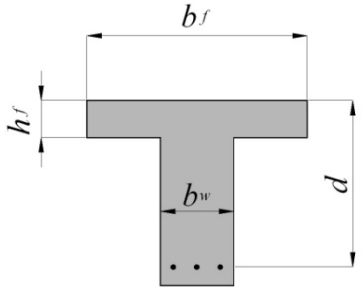

$$k_f = 1 + n \cdot \left(\frac{h_f}{b_w}\right) \cdot \left(\frac{h_f}{d}\right) \tag{2-125}$$

with $$n = \frac{b_f - b_w}{h_f} \le 3 \tag{2-126}$$

and $$n \le \frac{3 \cdot b_w}{h_f} \tag{2-127}$$

And k is a factor taking into account the size effect and τ_f is the shear strength of FRC

$$k = 1 + \sqrt{\frac{200}{d}} \le 2.0 \qquad (d \text{ in [mm]}) \tag{2-128}$$

$$\tau_f = \frac{0.18}{\gamma_c} \cdot f_{R,4} \tag{2-129}$$

Where $f_{R,4}$ is the residual tensile strength for a *CMOD* of 3.5 mm, given by flexural tests on notched prism as seen in point 2.1.5.2 (Figure 2-15).

2.2.6.2 Interim recommendations for UHPFRC AFGC-SETRA

In the French interim recommendations for UHPFRC [AFGC2002], ultimate shear strength V_u is given as the sum of concrete contribution V_c, transversal reinforcement contribution V_w and fibres contribution V_f. This model is derived from the French standards BAEL and BPEL and the model developed by Casanova [CAS1996]

$$V_u = V_c + V_f + V_w \tag{2-130}$$

The contribution of concrete V_c to shear strength is defined as follows:

$$V_c = \frac{0.21}{\gamma_c} \cdot k \cdot \sqrt{f_{ck}} \cdot b_w \cdot d \qquad \text{for reinforced concrete members} \tag{2-131}$$

$$V_c = \frac{0.24}{\gamma_c} \cdot \sqrt{f_{ck}} \cdot b_w \cdot d \qquad \text{for prestressed members} \tag{2-132}$$

where γ_c is the concrete safety coefficient, generally γ_c=*1.5, k* takes into account the effect of an axial force, $k > 1$ for compression or $k < 1$ for tension, b_w is the effective width of the web. It should be noted that the structural parameters are not taken into account in the concrete contribution.

The contribution of transversal reinforcement V_w is defined as follows:

$$V_w = z \cdot \frac{A_{sw}}{s} \cdot \frac{f_{swk}}{\gamma_s} \cdot \frac{\left(\sin\left(\alpha + \beta_u\right)\right)}{\sin\left(\beta_u\right)} \tag{2-133}$$

where z is the level arm ($z = 0.9d$), A_{sw} is the transversal reinforcement area, s is the spacing between the transversal rebars , f_{swk} is the steel yield limit and α is the inclination of transversal rebars.

On the basis of the model proposed by Casanova, the contribution of fibres V_f is defined as follows:

$$V_f = \frac{\sigma_p}{\gamma_f} \cdot \frac{1}{\tan\left(\beta_u\right)} \cdot b_w \cdot z \tag{2-134}$$

With σ_p is the average residual tensile stress transferred by the crack, defined as:

$$\sigma_p = \frac{1}{K} \cdot \frac{1}{w_u} \cdot \int_0^{w_u} \sigma(w) \cdot dw \tag{2-135}$$

And β_u *is* the angle of the compression strut, assumed to be $\pi/4$ for RC-members, determined by iteration for PT-members, $\tan(\beta_u)=2\tau_u/\sigma_c$. *K is* the fibre orientation coefficient for general effects and γ_f the partial safety factor for UHPFRC. The crack opening is limited to:

$$w_u = \max\left(2/3 \cdot h \cdot \varepsilon_u, 0.3\right) \qquad \text{and } \varepsilon_u \text{ is limited to } 3‰ \tag{2-136}$$

2.2.6.3 fib Model Code draft 2010

In the *fib* Model Code draft 2010 [MC2010b], the proposed design equation, for the shear strength of FRC members without transversal reinforcement, includes concrete toughness in the Eurocodes 2 equation for the shear strength of plain concrete members without transversal reinforcement. The fibres contribution appears not as a separate term but as a modified concrete contribution according to [MIN2005]. Therefore, the term of the longitudinal reinforcement ratio ρ_l is modified throughout a factor that includes the toughness properties of FRC and the shear span ratio *a/d*. The contribution of FRC to shear resistance of members without transversal reinforcement is defined as:

$$V_{Rd,F} = \left\{ \frac{0.18}{\gamma_c} \cdot k \cdot \left[100 \cdot \rho_l \cdot \left(1 + 7.5 \cdot \frac{f_{Ftuk}}{f_{ctk}} \right) \cdot f_{ck} \right]^{1/3} + 0.15 \cdot \sigma_{cp} \right\} \cdot b_w \cdot d \tag{2-137}$$

where f_{Ftu} is the residual tensile strength at an ultimate crack opening w_u of 1.5 mm, in first approximation $f_{Ftu} = f_{R3}/3$. The other terms are the same as in the Eurocodes 2 (point 2.2.5.1).

Like the EC2 equation, the shear strength $V_{Rd,F}$ is assumed to be not smaller than $V_{Rd,Fmin}$

$$V_{Rd,F} \geq V_{Rd,F\min} \tag{2-138}$$

$$V_{Rd,F\min} = \left(0.035 \cdot k^{3/2} \cdot f_{ck}{}^{1/2} + 0.15 \cdot \sigma_{cp}\right) \cdot b_w \cdot d \tag{2-139}$$

2.2.7 Works on shear resistance of Steel Fibre Reinforced Concrete members

A non-exhaustive list of shear tests on Fibre Reinforced Concrete members is reviewed in this point. Different concrete compressive strength, loading arrangement, reinforcement and prestressing arrangement are presented. Moreover, several models for shear strength are presented as well.

2.2.7.1 Imam's works

This experimental study was performed at the Catholic University of Leuven, Belgium [IMA1997]. Sixteen beams in high strength concrete with and without fibres were tested in order to investigate the shear behaviour. The main parameters were the shear span to depth ratio *a/d*, the longitudinal reinforcement ratio ρ and the fibres content. The beams have 3600 mm length and a cross section of 350 mm depth and 200 mm wide. The reinforcement was composed of 3 ϕ22 or 3 ϕ28 mm deformed bars with an effective depth of 300 mm (Figure 2-72). The reinforcement ratio was 1.90% and 3.08% respectively. The concrete compressive strength was around 110 MPa. The maximal aggregates size was 10 mm. Hooked-end steel fibres 60/0.8 mm (l_f/d_f) were used with a volume ratio V_f of 0.75%. The tensile properties of the HSC and HSFRC were determined using splitting tensile tests on cylinders. The beams were tested on a clear span of 3250 mm and were subjected to a two points load. The shear span varied of 525 / 750 / 1050 / 1350 mm according to the *a/d* ratio of 1.75 / 2.5 / 3.5 / 4.5 respectively.

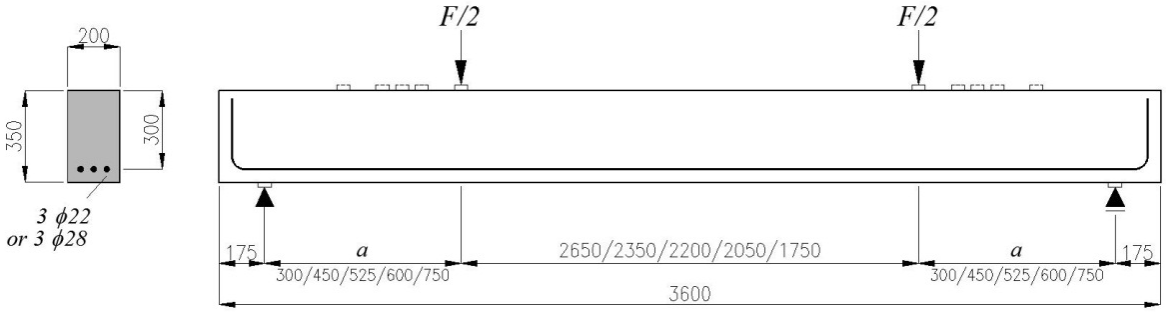

Figure 2-72: Specimens geometry and loading configuration

The test results highlighted that, the addition of steel fibres to high strength concrete increased the stiffness and the shear strength while the failure mode was more ductile. For the series with the reinforcement ratio of 1.90%, the addition of steel fibres allowed the reaching of the flexural capacity. The following graphs (Figure 2-73) highlighted the influence on the shear strength of the shear span to depth ratio.

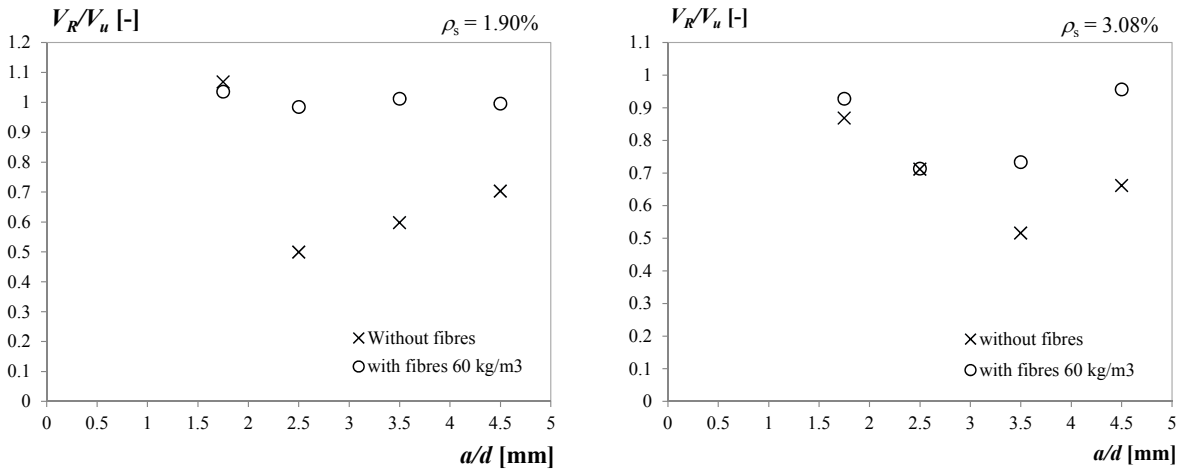

Figure 2-73: Test results represented according the shear strength to flexural capacity ratio vs the shear span to depth ratio.

Based on the tests results, Iman proposed two empirical expressions predicting the shear strength of high performance fibre reinforced concrete. The proposed equations are based on the work of Bazant and Kim on shear strength of normal strength concrete. The model proposed by Bazant and Kim assumes that the arch action and beams action mechanisms occur simultaneously. The size effect is taken into account according to the principles of the nonlinear fracture mechanics.

$$v_u = 0.83 \cdot \xi \cdot \sqrt[3]{\rho} \cdot \left[\sqrt{f_c} + 249.28 \cdot \sqrt{\frac{\rho}{(a/d)^5}} \right] \tag{2-140}$$

$$\xi = \frac{1}{\sqrt{1 + \frac{d}{25 \cdot d_g}}} \tag{2-141}$$

Iman modified the Bazant's equation by incorporating the fibres effect as follows:

$$v_u = 0.6 \cdot \xi \cdot \sqrt[3]{\rho \cdot (1 + 4 \cdot F)} \cdot \left[f_c^{0.44} + 275 \cdot \sqrt{\frac{\rho \cdot (1 + 4 \cdot F)}{(a/d)^5}} \right] \tag{2-142}$$

$$\text{with} \quad \xi = \frac{1 + \sqrt{\frac{5.08}{d_g}}}{\sqrt{1 + \frac{d}{25 \cdot d_g}}} \tag{2-143}$$

$$\text{and} \quad F = \frac{l_f}{d_f} \cdot V_f \cdot \alpha \tag{2-144}$$

Where ρ is the reinforcement ratio, d is the effective depth, d_g is the maximal aggregate size, l_f is the fibres length, d_f is the fibres diameter, V_f is volumetric ratio of fibres and α is equal to 0.5 for smooth fibres, 0.9 for deformed fibres and 1.0 for hooked fibres.

The flexural strength is determined by the following equation

$$M_{fl} = \frac{1}{2} \cdot \rho \cdot f_y \cdot b \cdot d^2 \cdot (2 - \eta) + 0.83 \cdot F \cdot b \cdot d^2 \cdot (0.75 - \eta) \cdot (2.15 + \eta) \quad (2\text{-}145)$$

with $$\eta = \frac{\rho \cdot f_y + 2.32 \cdot F}{0.85 \cdot f_c + 3.08 \cdot F} \quad (2\text{-}146)$$

2.2.7.2 Casanova and Rossi's works

This experimental campaign was performed at the French Public Works Research Laboratory LCPC, France [CAS1996]. Five large T-beams and five small beams were tested in order to investigate the shear behaviour of FRC members without transversal reinforcement. The FRC properties were largely investigated using direct tensile tests on notched cores.

The T-beams had a length of 6200 mm and 800 mm depth. The cross-section was composed of a flange of 1000 mm wide and 200 mm thick and a web 450 mm wide. The web was thinned to 150 mm wide on a length of 2600 mm. The longitudinal reinforcement was composed of 8 ϕ40 mm deformed bars in order to avoid flexural failure (Figure 2-74). The beam named BS was in plain concrete without stirrups, the beams BA1 and BA2 were in plain concrete with different ratio of stirrups and the beams BFM1 and BFM2 were in FRC without stirrups. The concrete compressive strength was 35 MPa. The beams BFM1 and BFM2 have a fibre content of 100 kg/m^3 which were hooked steel fibres with dimensions of 60/0.8 (l_f/d_f) and 30/0.5 respectively. The beams were tested in an inverted 3-points bending.

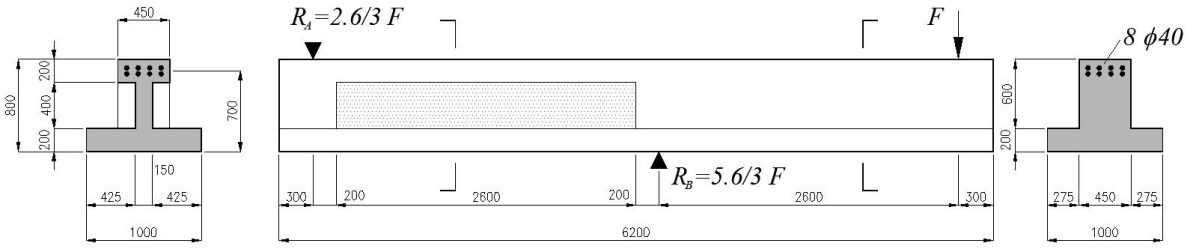

Figure 2-74: Geometry and loading configuration of the T-beams [CAS1996]

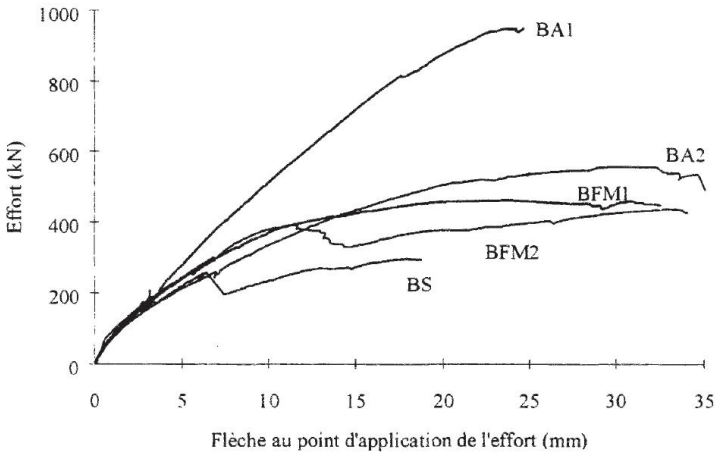

Figure 2-75: Curves load vs deflection at the load application of the T-Beams [CAS1996]

The beam BS showed a shear failure at a relatively low load level with the formation of one critical shear crack on the web panel. The beam BA-1 has reached the flexural capacity and the panel presented several thin shear cracks. The beams BA-2, BFM1 and BFM2 had similar shear strength. At the elastic-cracked state the members in FRC showed a higher stiffness. The deflection capacity of the beams BFM2 composed of steel fibres 30/0.5 was limited. This member showed a drop in the strength at a deflection of 12 mm. The conclusions of P. Casanova for this series were the following: The beams in FRC, 100 kg/m^3, exhibited a similar behaviour compared to the reinforced concrete beams HA2 composed of a transversal reinforcement ratio of 0.2%. Subsequently the FRC solution is not attractive from an economic point of vue. The size effect on the behaviour at ultimate limit state was important. The critical shear opening depends directly on the depth. Therefore the fibres effect decreases as the member depth increases. At the serviceability limit state the FRC beams exhibited a higher level compared to the reinforced concrete beams with the development of thin cracking. Therefore, it's attractive to combine FRC with stirrups, the FRC being effective during the SLS and the stirrups during the ULS.

The second test series was composed of five beams having a rectangular cross-section of 250 mm depth with a 125 mm width for a length of 2300 mm (Figure 2-76). The beams were cast in high strength concrete with a compressive strength of 90 MPa. The beams BHPA1 and BHPA2 were made out of high strength concrete without fibres and comprised stirrups with different spacing. The specimens BHPFM1, BHPFM2 and BHPFM3 were made out of FRC 100 kg/m^3, hooked steel fibres 30/0.5, without stirrups. The longitudinal reinforcement of the members was composed of 2 ϕ25 mm deformed bars and 2 ϕ20 mm for the specimen BHPFM3. The beams were tested on a clear span of 2000 mm with two points load. The shear span was 650 mm and the shear span to depth ratio a/d was 2.89.

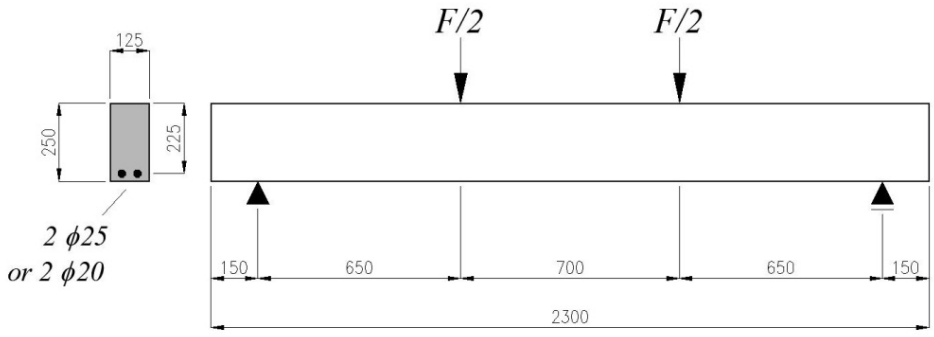

Figure 2-76: Geometry and loading configuration of the beams in High Strength Concrete [CAS1996]

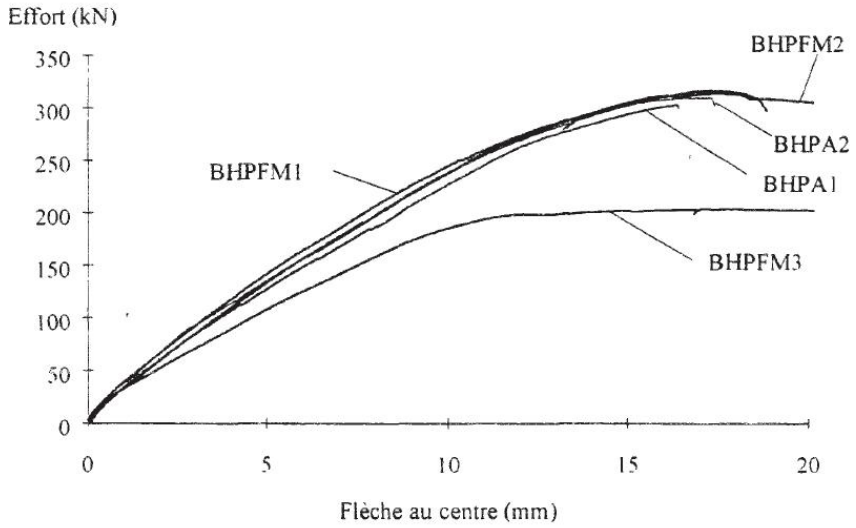

Figure 2-77: Load vs deflection at centre of the beams in High Strength Concrete [CAS1996]

The reinforced concrete beams exhibited a failure mode between shear and flexure with the yielding of the stirrups. The beams BHPFM1 and 2 having the same parameters showed a shear failure and a flexural failure respectively and at the same load level. And the beam BHPFM3 exhibited a flexural failure. The analysis and conclusions of P. Casanova were the following: The size effect on the behaviour at ultimate limit state is important. The fibres effect was more important for this experimental campaign due to the small depth and the higher post-cracking strength of HSFRC. At the serviceability limit state the HSFRC beams exhibited a higher level compared to the reinforced concrete beams with the development of thin cracks.

On the basis of the empirical model developed by Kordina [KOR1985] for reinforced concrete members, Casanova added the fibres contribution. In this model, the shear strength is the sum of the concrete, the transversal reinforcement and the fibres contributions and is defined as follows:

$$V_R = V_c + V_s + V_f \tag{2-147}$$

The contribution of the concrete V_c is defined as follow:

$$V_c = f_T \cdot \Delta\tau \cdot \sqrt[3]{\frac{A_s}{b \cdot d}} \cdot \sqrt{\frac{f_c}{0.82}} \cdot b \cdot d \tag{2-148}$$

Where f_T is form factor, ($f_T = 0.9 + b/b_w$) and $\Delta\tau$ is a coefficient equal to 0.24

The contribution of the transversal reinforcement V_s is defined as follows:

$$V_s = 0.9 \cdot d \cdot \frac{A_{sw}}{s} \cdot f_{sy} \tag{2-149}$$

The model developed by Casanova and Rossi assumes the formation of a block mechanism in a reinforced concrete beam (Figure 2-78). The contribution of fibres to the shear resistance corresponds

to the force transferred between crack faces for a certain crack mouth opening *w*. The contribution of fibres V_f is defined as follows:

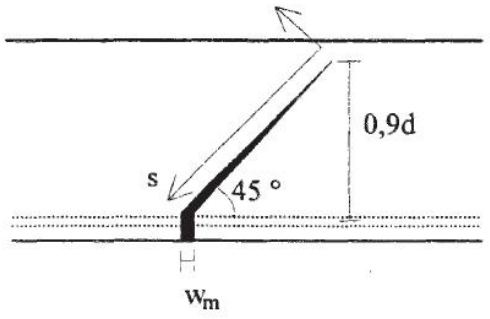

Figure 2-78: Casonava model for rectangular beams [CAS1996]

$$V_f = \int_0^{0.9 \cdot d \cdot \sqrt{2}} \sigma_f \cdot \left(\frac{s}{0.9 \cdot d \cdot \sqrt{2}} \cdot w_m \right) \cdot b \cdot \frac{\sqrt{2}}{2} \cdot ds \qquad (2\text{-}150)$$

$$\text{or} \quad = 0.9 \cdot b \cdot d \cdot \sigma_p \left(w_m \right) \qquad (2\text{-}151)$$

$$\text{with} \quad \sigma_p \left(w_m \right) = \frac{1}{w_m} \int_0^{w_m} \sigma_f \left(w \right) \cdot dw \qquad (2\text{-}152)$$

Where $\sigma_f(w)$ is the material stress-crack opening relationship, $s = 0.9\ d$ in the case of a rectangular beam. Casanova proposed to relate directly the crack opening to the longitudinal strain of the reinforcement bar, i.e. $w_m = 0.9\ d\ \varepsilon\ s$, and considered two cases: the steel's yield limit f_{sy} or $f_{s0.2}$ and the ultimate yielding strain value of 1%.

2.2.7.3 Noghabai and Gustafsson's works

This experimental study was performed at the Lulea University of Technique, Sweden [NOG2000]. Twenty beams were tested in order to investigate if steel fibres can replace stirrups as they do with the shear reinforcement in high strength concrete beams. The parameters were the types and content of steel fibres and the beams' size. Three different sizes of beams were cast, 200x250x 1500 mm, 200x500x 3600 mm and 300x700x 6000 mm in order to analyze the size effect.

The beams were made out of high strength concrete with a compressive strength on cubes around 100 to 115 MPa. The maximal aggregates size was 16 mm. Three different types of fibres were used, straight fibres 6/0.15 (l_f/d_f), hooked fibres 30/0.6 and 60/0.7. The fibres ratio V_f varied between 0.5 to 1.0%. Four beams were cast with a mix of 0.5% of 6/0.15 and 0.5% of 30/0.6. Plain concrete and fibre reinforced concrete properties were determined from compressive tests on cubes and tensile tests on notched cores (Figure 2-79).

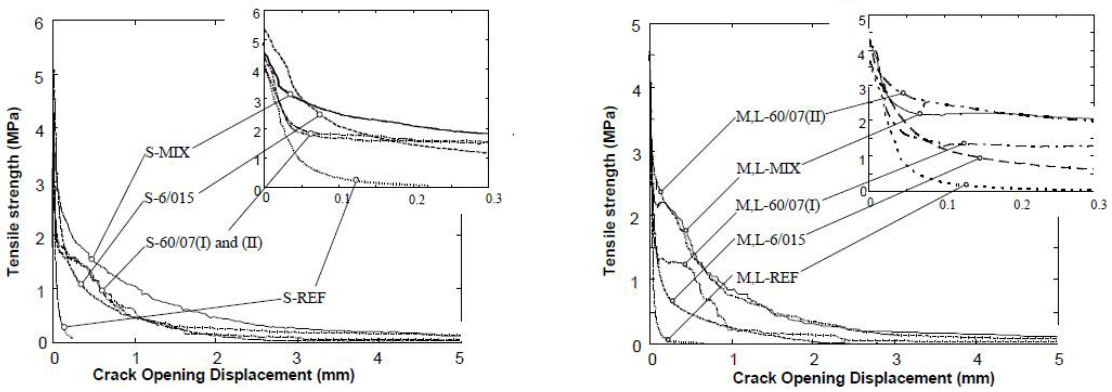

Figure 2-79: Tensile stress vs crack opening displacement for the different SFRC mixes [NOG2000]

The beams were divided into 3 series named small, medium and large (Figure 2-80). One beam in each series was composed of stirrups as shear reinforcement. For the series S and M one reference beam without shear reinforcement and fibres was tested. The reinforcement ratios were 4.47%, 3.06% and 2.87% for beams S, M and L respectively. The longitudinal reinforcement was composed of deformed bars of Swedish Grade Ks600s, with a yield limit of approximately 590 MPa. At the beam's ends, high ratio of stirrups was implemented in order to avoid anchorage failure. The shear reinforcement was composed of stirrups of Swedish Grade Ks400s, with a yield limit of approximately 400 MPa. The beams were tested on a span of 1200 mm, 3000 mm and 5000 mm for series S, M and L respectively. The loads were applied at the centre for series S and at two points with a shear span of 1250 mm and 1700 mm for series M and L respectively. The shear span-to-depth ratios *a/d* were 3.33, 3.04 and 2.98.

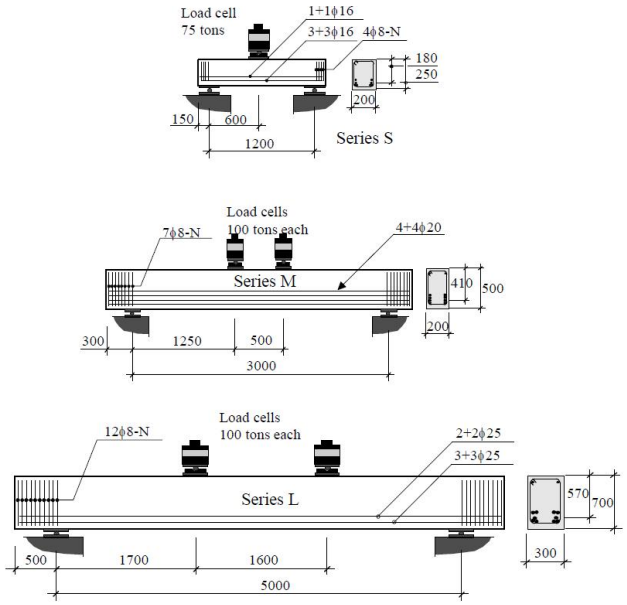

Figure 2-80: Geometry and reinforcement arrangement of the beams and loading configuration [NOG2000]

All beams exhibited a shear failure (Figure 2-81). The beams in FRC showed the same and even a higher shear strength compared to elements with stirrups. The stiffness at the elastic-cracked state of the FRC members was clearly increased. As the depth increases the failure of FRC beams was brittle.

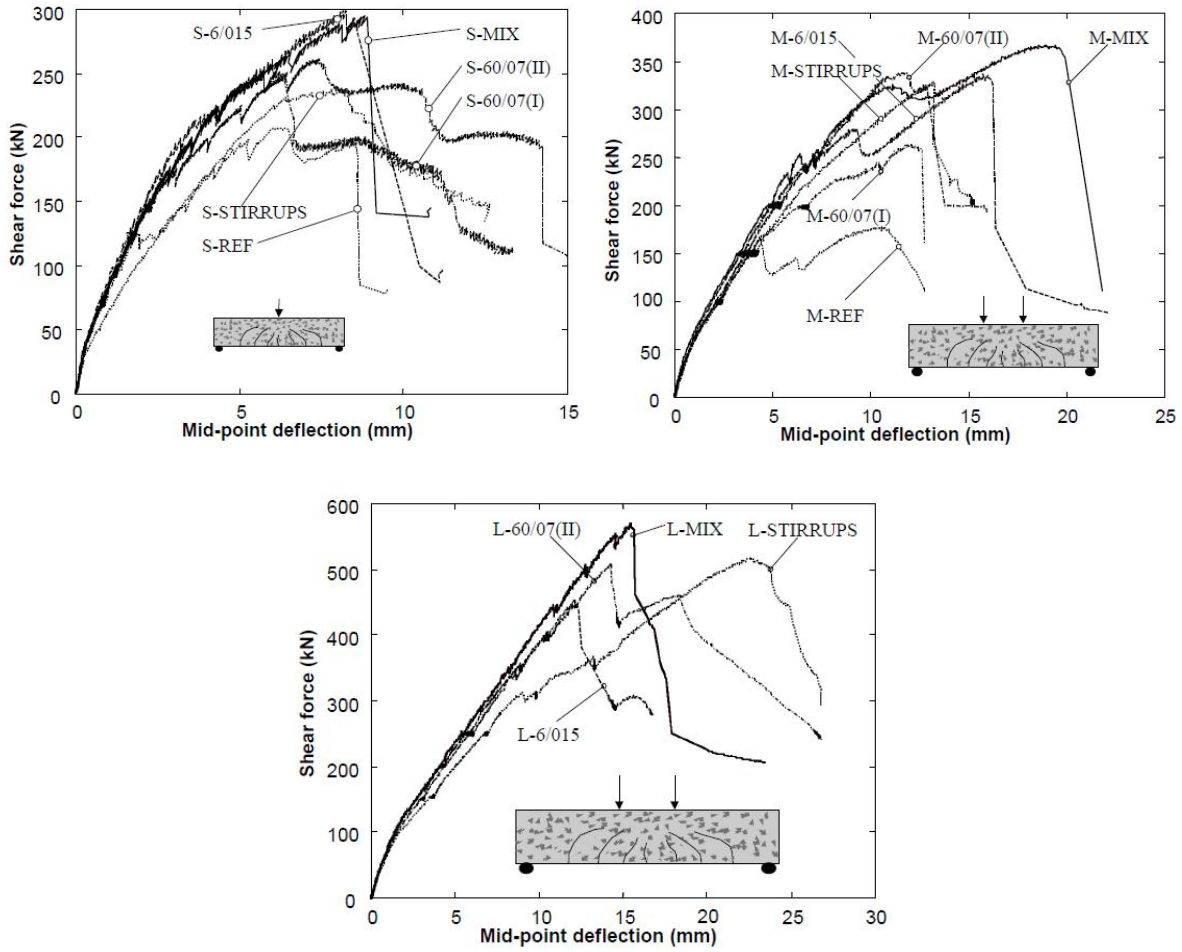

Figure 2-81: Shear force vs deflection at mid span of the series S, M and L [NOG2000]

The analysis and conclusions of authors were the following: By adding steel fibres with a low content, 1% or less, it is possible to reach the same capacity as the one of the beams with stirrups. The post-cracking response of the FRC is an important parameter, particularly the fibres type and strength. The tests highlighted that the requirements on the fibres become greater as the beam size increases. For small beams a shorter type of fibres may be sufficient, whereas for larger beams, fibres that are better anchored and have a higher strength are required. In other words, this size effect is more important for FRC compared to conventional reinforced concrete structures.

K. Noghabai developed a non-linear truss model in order to evaluate the shear strength [NOG2000]. This model gave a good correlation with small beams but a poor one for large beams.

2.2.7.4 Voo, Foster and Gilbert's works

This experimental campaign was performed at the University of New South Wales, Australia [VOO2003b]. Seven beams were tested in order to investigate the shear behaviour of UHPFRC prestressed members without transversal reinforcement. The principal parameters distinguishing the specimens were the fibre type and content and the pre-tensioning force intensity. The members had an I-shaped cross section of 650 mm depth and a length of 4500 mm. The top flange had a width of400 mm and 250 mm for the bottom flange. The width of the web was 50 mm on 400 mm depth (Figure 2-82). The reinforcement was composed of 12 strands (ϕ15.2 mm) at the bottom flange and 6 strands at the top flange with an effective depth of 600 mm. The initial prestressing force F_{p0} was 0 kN for

SB1, 1350 kN for SB2 and 675 kN for specimens SB3 to SB7. The concrete compressive strength was in the range of 150 to 170 MPa. The different FRC were composed of straight steel fibres of 13/0.2 mm (l_f/d_f) and hooked steel fibres of 30/0.5 mm. The content of steel fibres varied from 1.25 to 2.5%. The plain concrete and FRC properties was investigated using cubes, cylinders and 3-point bending test on notched prisms 150 x 150 x 550 mm. The beams were tested on a span of 4000 mm with a loading point at the centre. The shear span to depth ratio a/d ratio was 3.33.

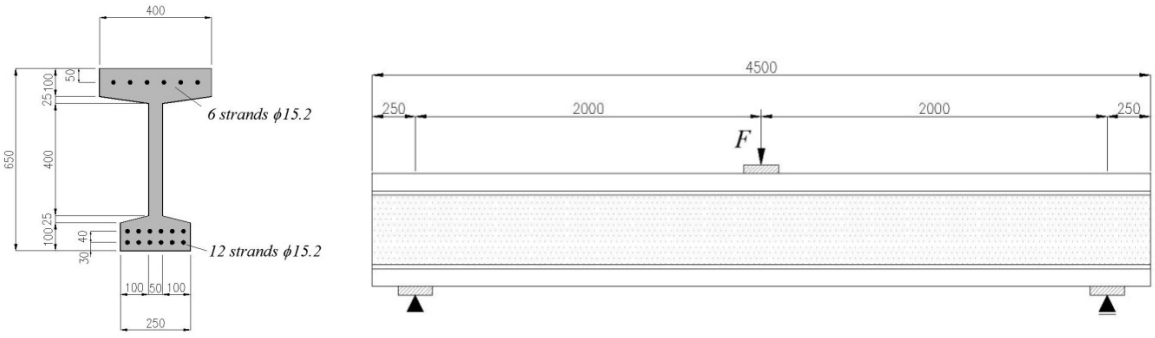

Figure 2-82: Geometry of the UHPFRC beams and loading configurations [VOO2003b]

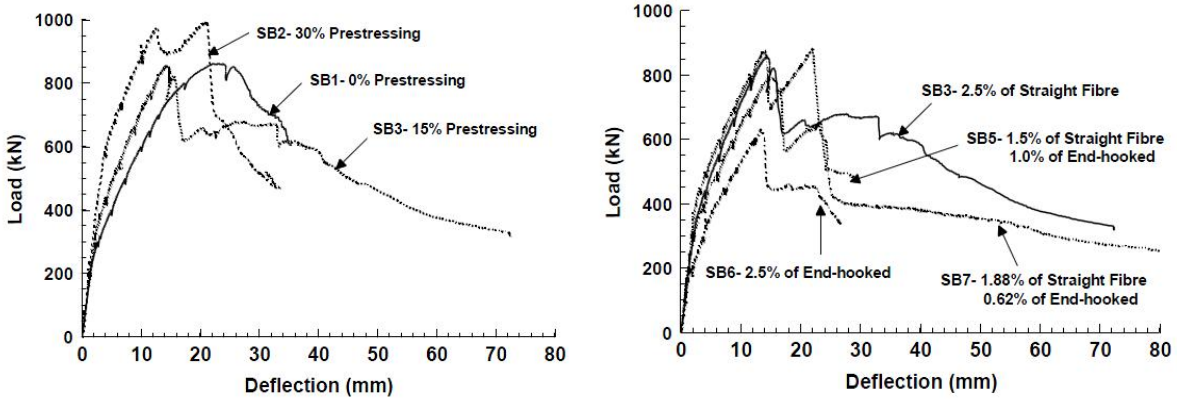

Figure 2-83: Load vs deflection at centre of the UHPFRC beams [VOO2003b]

All beams exhibited a shear failure (Figure 2-83). The analysis and conclusions were the following: In terms of prestressing effect, the comparison indicates a 15 percent variation in strength due to the effect of prestressing. The quantity and type of fibres used in the concrete mixture did not significantly affect the cracking load but had a significant influence on the rate of crack propagation and on the failure loads. At the peak load, many fine cracks were formed in the web, with the cracks well distributed through the shear spans. The failure loads were more than twice the cracking loads.

The experimental beams were analysed using a non-linear finite element model including the variable engagement model for FRC post-cracking response [VOO2003a]. The results of the FE analyses showed a good correlation with the experimental data. Two analytical models based on the upper bound theory of plasticity were proposed. The first plasticity model was based on the works of Zhang [ZHA1994] for an over reinforced rectangular beam without stirrups. The second plasticity model was based on the works of Hoang [HOA1997] for T-beams and modified herein for I-beams. In these two propositions the variable engagement model was implemented for the FRC post-cracking response.

In the case of a RC beam with two symmetrical point loads, the cracks pattern is schematically shown in Figure 2-84. The cracks start to develop in the constant moment zone and are vertical. Between the support and the load, the cracks have a curved path in the direction of the load.

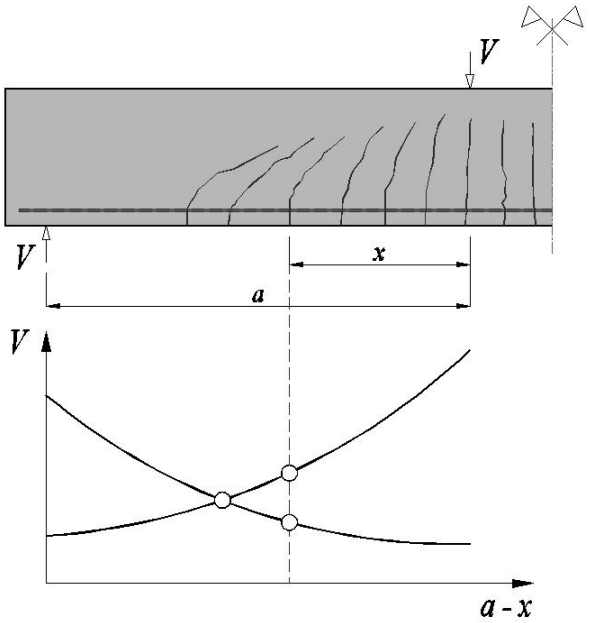

Figure 2-84: Relationship between V_u and V_{cr} according to a-x and the corresponding cracking pattern [VOO2003b]

The cracking load V_{cr} needed to develop these cracks decreases progressively by moving away from the support. The effect of an axial force can also be taken into account. Neglecting the depth of the compression zone and using an equivalent plastic stress distribution f_{tef}, the cracking load V_{cr} can be defined as follows.

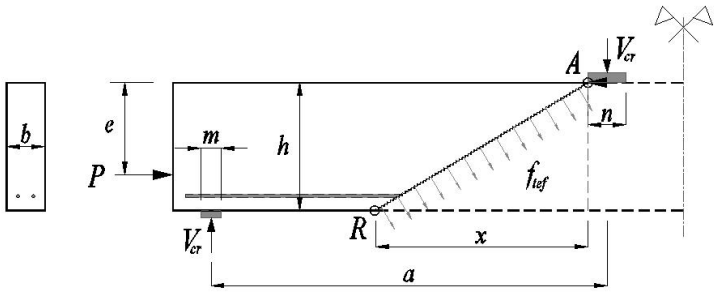

Figure 2-85: Assumed stress distribution at cracking load and parameters [VOO2003b]

$$V_{cr} = \frac{1}{2} \cdot f_{tef} \cdot b \cdot \frac{h^2 + x^2}{a - n/2} + \frac{P \cdot e}{a - n/2} \tag{2-153}$$

where $f_{tef} = 0.6 \cdot \left(\frac{h}{0.1} \right)^{-0.3} \cdot 0.26 \cdot f_c^{2/3}$ with h in [m] (2-154)

In the upper bound approach of plastic theory, a shear failure mechanism is assumed by setting up a straight yield line. The concrete is assumed as a rigid plastic material obeying to the modified Mohr-Coulomb failure criterion. The yield line, which gives the lowest load solution V_0 for un-cracked RC beams with zero tensile strength and simple span, runs from the support to the load application

(dashed line in Figure 2-86). For cracked RC beams, assuming a yield line following a diagonal crack, the ultimate shear load V_u is lower than load V_0. The shear load V_u, is obtained by equalizing the internal work and the external work of the failure mechanism. V_u can be defined as follows:

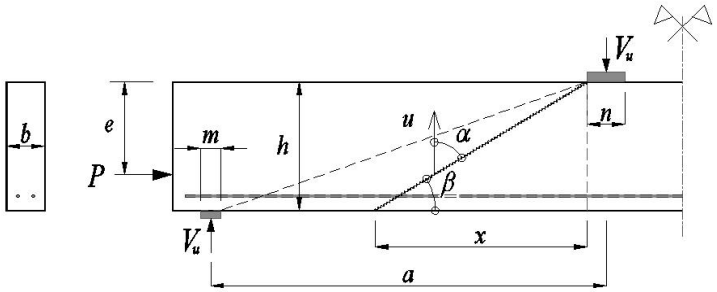

Figure 2-86: Yield line at ultimate load and parameters [VOO2003b]

$$V_u = \frac{1}{2}\cdot\nu\cdot f_c\cdot b\cdot h\cdot\left(\sqrt{1+\left(\frac{x}{h}\right)^2}-\frac{x}{h}\right) \tag{2-155}$$

where $\nu = \frac{0.88}{\sqrt{f_c}}\cdot\left(1+\frac{1}{\sqrt{h}}\right)\cdot\left(0.26\cdot\rho_s+1\right)$ for RC members (2-156)

$$\nu = \frac{1.2}{\sqrt{f_c}}\cdot\left(1+\frac{1}{\sqrt{h}}\right)\cdot\left(0.26\cdot\rho_s+1\right)\cdot\left(1+\frac{2\cdot P}{A_c\cdot f_c}\right) \quad \text{for PT members} \tag{2-157}$$

For $5 \le f_c \le 60MPa$, $\rho_s \le 4.5\%$ and $0.08 \le h \le 0.7$ m. In this study, the authors propose to consider $\nu = 0.8$

When, the two curves intersect, the crack may develop into a yield line and shear failure takes place. According to the description above, cracks with cracking load lower than the sliding resistance are not critical. Further, cracks with cracking load lower than sliding resistance cannot develop. In this case, the load carrying capacity is determined by the minimum value of the shear capacity curve.

$$\nu\cdot f_c\cdot b\cdot h\cdot\left(\sqrt{1+\left(\frac{x}{h}\right)^2}-\frac{x}{h}\right) = f_{tef}\cdot b\cdot\frac{h^2+x^2}{a-n/2}+\frac{2\cdot P\cdot e}{a-n/2} \quad \text{for } 0\le x\le\left(a-n\right) \tag{2-158}$$

According to the Variable Engagement Model, the authors propose to change the equation (2-154) in the following way:

$$f_{tef} = \upsilon_t\cdot f_{tf} = 0.8\cdot f_{tf} \tag{2-159}$$

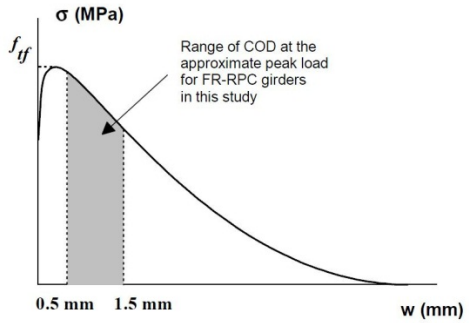

Figure 2-87: Range of tensile stress across failure surface for specimens SB1 to SB3 [VOO2003b]

2.2.7.5 Minelli's works

This experimental campaign composed of two series was performed at the University of Brescia, Italy [MIN2005]. In the first series, six pretensioned I-beams were tested in order to evaluate the possibility of substituting the minimum shear reinforcement required by Eurocode 2 [EC22005] with steel fibres in precast members. The shear behaviour was analysed both in the pretensioning transfer zone (TZ) as well as in the region where the axial force is completely diffused (DZ). The concrete compressive strength was around 85 MPa on cubes. The main variables were the fibres type and the diffusion of the prestressing force. Two beams were cast in plain concrete, I-1 and I- 2. I-1 didn't contain stirrups and I-2 was reinforced with stirrups ϕ6 @100 mm in zone TZ and mesh ϕ5 #200 mm in zone DZ. The beams I-3 and I-4 were in FRC with hooked steel fibres 45/30 with a content of 50 kg/m^3 (V_f = 0.64%). The beams I3 and I4 were without stirrups in zone DZ and were reinforced with stirrups ϕ6 @100 mm in zone TZ. And I-beams I-5 and I-6 were in FRC with hooked fibres 80/30 for content of 50 kg/m^3 (V_f = 0.64%). These two beams were without transversal reinforcement.

The I-beams 1 to 4 had a length of 9000 mm and 9900 mm for the beams 5 and 6 (Figure 2-88). These beams had two testing zones where the web was thinned on a length of 1750 mm. The cross section has I-shape with 700 mm depth and 600 mm width. The web's width was 120 mm in the testing zone and 300 mm elsewhere. The reinforcement was composed of 6 ϕ22 deformed bars placed both at top and bottom flange with 50 mm cover. The pretensioning was composed of 18 low-relaxation strands 0.6'', 15 placed at bottom flange and 3 at top. The initial tension of each strand was 1400 MPa. The beams were tested on single span of 5650 mm with one off centred point load. The load was placed at a distance of 2200 mm from the support corresponding to the side of the testing zone.

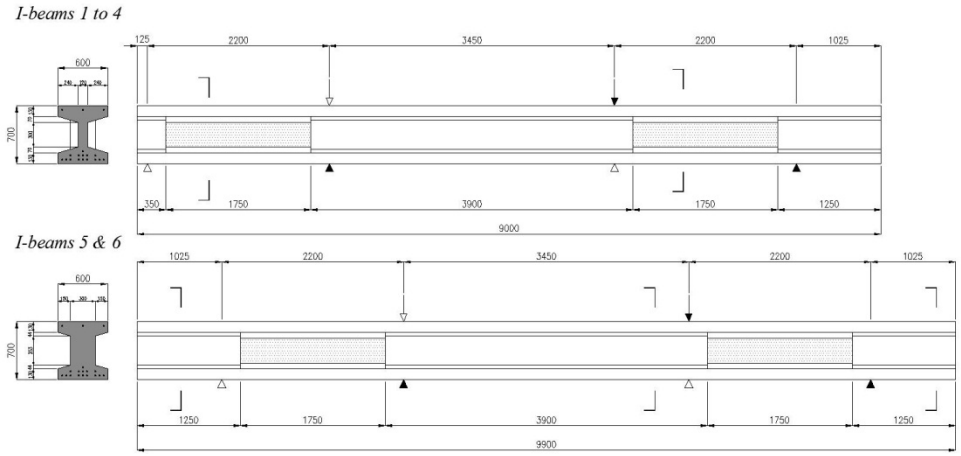

Figure 2-88: Geometry of the I-beams and loading configurations [MIN2005]

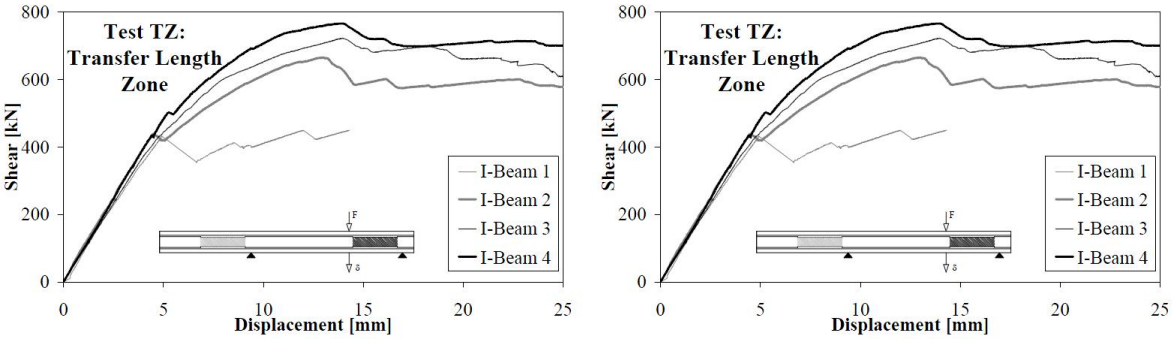

Figure 2-89: Curves load vs deflection at centre of some prestressed I-beams [MIN2005]

The experimental results showed that the FRC members had a post-cracking behaviour similar to the beams with minimal transverse reinforcement (Figure 2-89). Therefore, it's possible to replace the minimal shear reinforcement by steel fibres.

In the second series, eleven shear-critical beams were tested (Figure 2-90). The principal parameters were the fibres type, the fibres content and the concrete compressive strength. The beams had a length of 4450 mm, and a cross section of 480 mm depth and 200 mm wide. The two concrete compressive strengths were around 30 MPa and 60 MPa. For some FRC mixes, different types of fibres were mixed. The longitudinal reinforcement was composed of 2 ϕ24 mm deformed bars (ρ_s=1.04%). The bars were anchored by steel plates at the extremities in order to develop the arch action. The beams were tested on a span of 4350 mm with two load application points situated at a distance of 1090 mm from the supports.

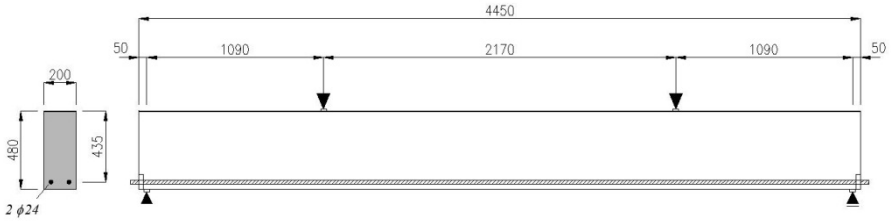

Figure 2-90: Geometry of the shear critical beams and loading configuration [MIN2005]

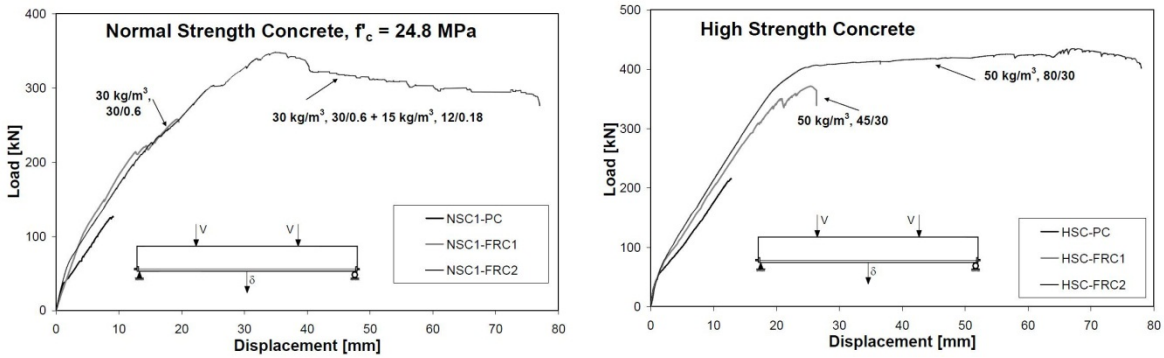

Figure 2-91: Curves load vs deflection at centre of some critical shear beams [MIN2005]

The fibres effect on the shear strength was important even with a relatively low content (Figure 2-91). Several beams had reached the flexural capacity. The fibres can substitute the minimal shear reinforcement but the fibres type had an important effect on the shear behaviour.

A non-linear numerical approach based on the MCFT and DSFM was performed. These models gave a good correlation with the test results [MIN2006]. A code like provision for assessment was proposed including the concrete toughness in the Eurocodes 2 equation. The fibres contribution do not appear as a separate term but as a modified concrete contribution. According to Minelli, the fibres act like longitudinal reinforcement distributed on the height of the cross section. Therefore, the term of the longitudinal reinforcement ratio ρ_l is modified throughout a factor that includes the toughness properties of FRC and the shear span ratio *a/d*. The contribution of FRC to shear resistance of members without transversal reinforcement is defined as:

$$V_{Rd,f} = \left\{ \frac{0.18}{\gamma_c} \cdot k \cdot \left[100 \cdot \rho_l \cdot \left(1 + \frac{a}{d} \cdot \frac{f_{eq(0.6-3)}}{f_{ct}} \right) \cdot f_{ck} \right]^{1/3} + 0.15 \cdot \sigma_{cp} \right\} \cdot b_w \cdot d \qquad (2\text{-}160)$$

Where $f_{eq(0.6\text{-}3)}$ is the equivalent stress in the Crack Tip Opening Displacement (CTOD) ranges of 0.6-3 mm on notched prism according to the Italian standard UNI 11039 [UNI2003]. The other terms are the same as in the Eurocodes 2.

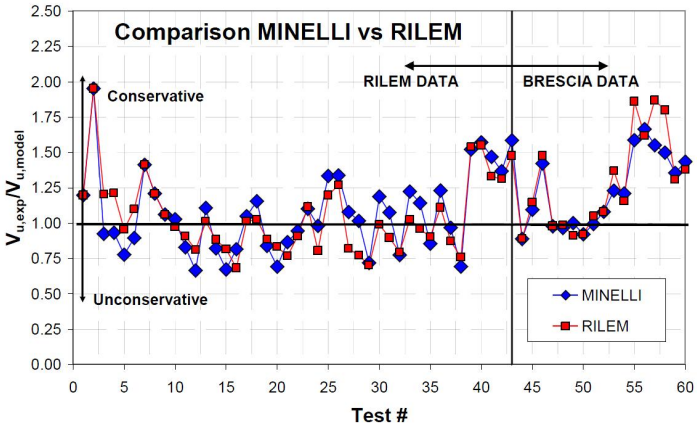

Figure 2-92: Comparison between the prediction of the Rilem model and the Minelli model and different tests [MIN2005]

The formulation proposed by Minelli gives similar predictions compared to the Rilem formulation [RIL2003]. For prestressed members the shear strength is clearly underestimated by the two models (points on right in Figure 2-92).

2.2.7.6 Dinh, Parra-Montesino and Wight's works

This experimental campaign was performed at the University of Michigan, USA [DIN2010]. Twenty-eight beams were tested in order to investigate the shear behaviour of FRC members without transversal reinforcement. The principal parameters were the fibre type and content, the member's size and the reinforcement ratio. The beams were divided into 2 series named, B18 and B27 (Figure 2-93). The beams of the series B18 had a cross-section of 455 mm depth and 152 mm width for a 2440 mm length. The longitudinal reinforcement was composed of 4 ϕ19 mm or 4 ϕ22 mm deformed bars according to the reinforcement ratio. Eight pairs of this type were cast. The beams were tested on a clear span of 2136 mm with one off centred load. The shear span of 1310 mm was without stirrups and the short shear span was reinforced transversally. The beams of series B27 have a cross-section of 685 mm depth and 205 mm width for a length of 4320 mm. The longitudinal reinforcement was composed of 5 ϕ25mm or 5 ϕ22 mm deformed bars according to the reinforcement ratio. Four pairs and four

single beams of this type were cast. The beams were tested on a span of 3558 mm with one off centred load. The shear span of 2136 mm was without stirrups and the short shear span was reinforced transversally. The *a/d* ratio was approximately 3.5. The targeted compressive strength was 41 MPa and the maximal aggregate size was 10 mm. The different FRC were composed of hooked steel fibres of 30/0.55, 30/0.38, and 60/0.75 (l_f/d_f). The volumetric ratio of steel fibres varied from 0.75 to 1.5%. The plain concrete and FRC properties was investigated using cylinders and four-point bending test on prisms with the dimensions of 150x150x510 mm.

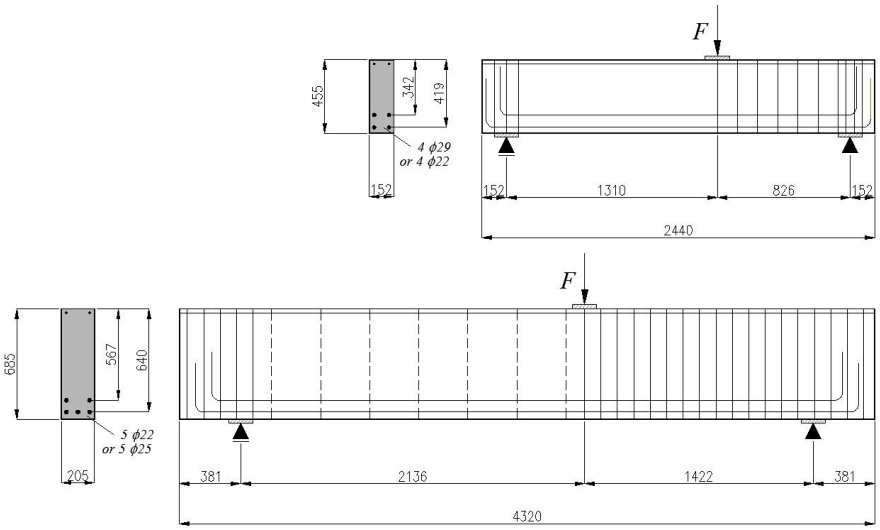

Figure 2-93: Geometry and reinforcement arrangement of the beams and loading configurations [DIN2010]

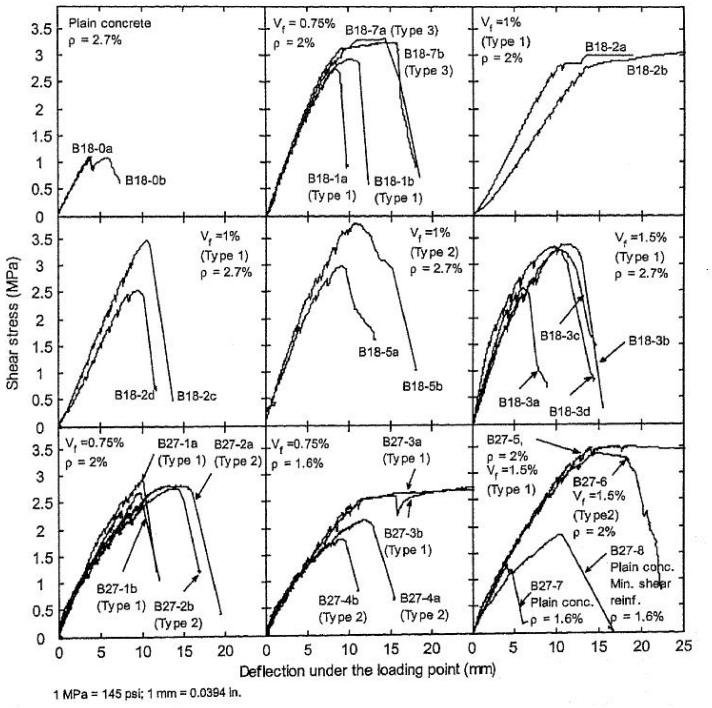

Figure 2-94: Shear stress vs the deflection under the loading point of the specimens [DIN2010]

All beams ultimately failed in shear, except one (Figure 2-94). The following conclusions were drawn by the authors from the test results; when used, in a volume fraction greater than or equal to 0.75%,

steel fibre reinforced concrete can be used in place instead of the minimum transverse reinforcement required by the American ACI Code 318. The increase in shear strength associated with an increase in fibre volumetric ratio beyond 1% was relatively small. The tested hooked steel fibres led to enhanced inclined cracking pattern and improved shear strength in beams without stirrups. Long fibres, 60 mm length, allowed a greater inclined crack opening before failure compared to the short fibres of 30 mm length. But the long fibres were difficult to implement.

2.2.7.7 Baby's works

This experimental work was performed at the French institute of science and technology for transport, development and networks IFSTTAR [BAB2010]. Eleven beams in UHPFRC were tested. The principal parameters distinguishing the specimens were the active or passive longitudinal reinforcement, the UHPFRC mix and the presence of transversal reinforcement. The beams had an I-shaped cross section of 380 mm depth, 200 mm width, and a length of 3000 mm (Figure 2-95). The top flange had a 270 mm width and the bottom flange had a 230 mm width. The width of the web was 65 mm on a 140 mm depth. The experimental studies were divided in two series. In the first series, the beams were pretensioned by 6 strands T15S (0.6'') with an effective depth of 305 mm and an initial prestressing force of 1020 kN. In the second series, the beams were reinforced by 5 ϕ20 and 1ϕ25 deformed bars with an effective depth of 305 mm. The concrete compressive strength was in the range of 160 to 200 MPa. The different UHPFRC mixes were composed of straight steel fibres with a volumetric ratio of 2% for the UHPFRC-F and 2.5% for the UHPFRC-B. Two reinforced beams were in UHPFRC-B without fibres and UHPFRC-F with organic fibres in order to evaluate the concrete contribution in shear and directly derive the fibres contribution. The beams were tested on 2000 mm span with two points load situated at 760 mm from the supports. The shear span to depth ratio a/d ratio was 2.49. The tensile post-cracking responses of the UHPFRC and the fibres orientation were well investigated using 3-point bending tests on notched prisms.

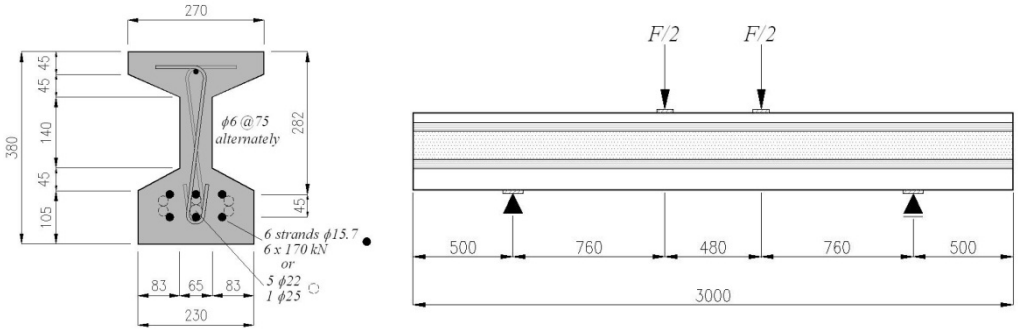

Figure 2-95: Geometry of the members and loading configuration [BAB2010]

The prestressed beams exhibited a shear failure with large plastic strains at different load levels according to the UHPFRC mix and the presence of stirrups (WS) or not (NS). The reinforced beams showed a brittle shear failure for the specimens without stirrups and fibres (NF-NS) or with organic fibres (OF-NS) (Figure 2-96). The reinforced beams in UHPFRC without stirrups had a shear failure at a load level two times higher than the beam without fibres. Part of the UHPFRC reinforced beams in with stirrups exhibited a flexural failure with large plastic deformations and yet a fully developed critical shear crack. These load tests highlighted that the contributions of fibres and stirrups can be summed.

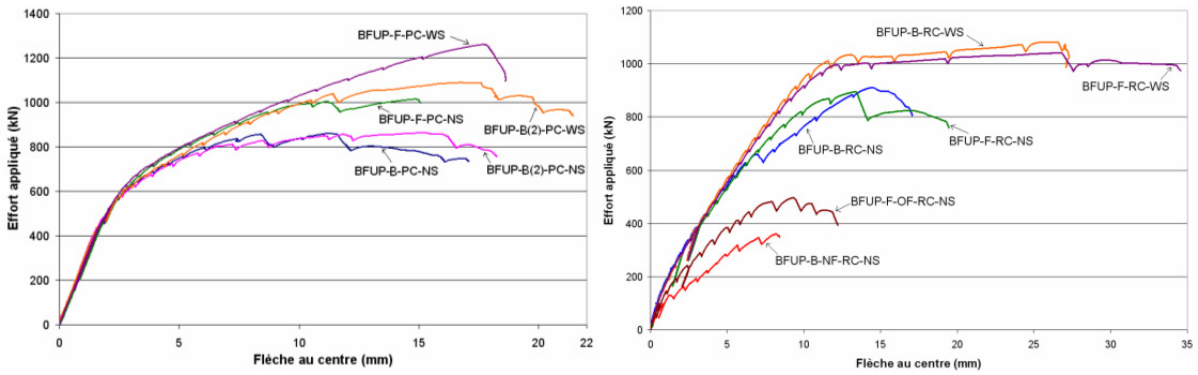

Figure 2-96: Load vs deflection at centre of the prestressed and reinforced beams [BAB2010]

In a first part, the author had compared the test results to different design approaches (Rilem TC 162-TDF, Model Code 2010 and AFGC-SETRA 2002). The different models underestimate clearly the shear capacity and the coefficients of variation are high. In a second part, two approaches types (stress-crack opening, stress-strain) were discussed for the determination of the shear capacity. A numerical analysis was also performed. The model proposed by the French recommendation [AFGC2002] was adapted to I and Π beams. This work has also highlighted the possibility to sum the UHPFRC contribution and the stirrups contribution for UHPFRC with multi-cracking behaviour.

Table 2-1: Recapitulation of reviewed works on shear resistance of Steel Fibre Reinforced Concrete members

Experimental study	Material properties	Determination of post-cracking behaviour	Cross-section	Loading configuration	Principal parameters
Imam [IMA1997]	High strength concrete f_c = 110 MPa Vf = 0 and 0.75% hooked fibres 60/0.8 mm	Splitting test on cylinder	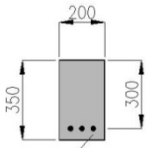	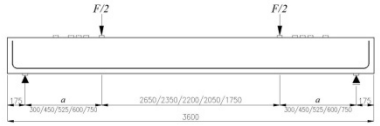	• Reinforcement ratio • Shear span • Fibre content
Casanova and Rossi [CAS1996]	Normal strength Concrete f_c = 35 MPa V_f = 0 and 100 kg/m^3 hooked fibres 60/0.8 or 30/0.5 mm High strength concrete f_c = 90 MPa V_f = 0 and 0.75% hooked fibres 30/0.5 mm	Tensile test on notched cores	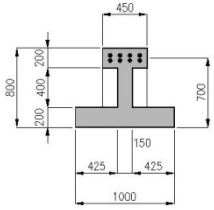 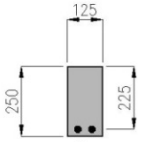	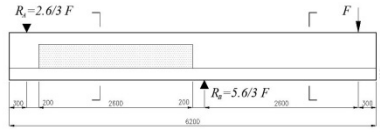 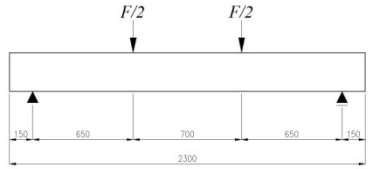	• Fibre types • Stirrups or not • Fibres type • Stirrups or not

Noghabai and Gustafsson [NOG2000]	High strength concrete f_c = 100-115 MPa V_f = 0 to 1%	Tensile test on notched cores	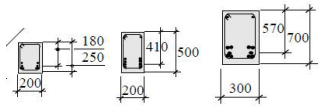	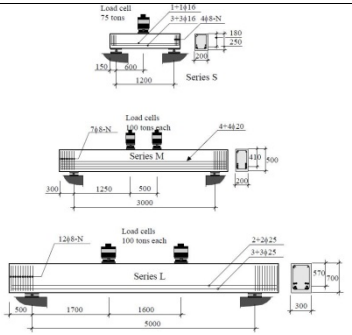	• Fibres type • Fibre content • Size of beams
Voo, Foster and Gilbert [VOO2003b]	UHPFRC f_c = 150-170 MPa V_f = 1.25 to 2.5% straight fibres 13/0.2 mm hooked fibres 30/05 mm	3-points bending test on notched prism	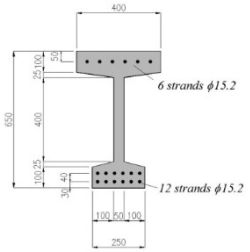	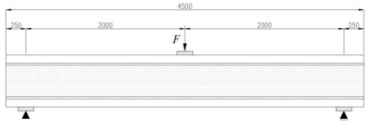	• Prestressing intensity • Fibre content • Fibres type
Minelli [MIN2005]	High strength Concrete f_c = 85 MPa V_f = 50 kg/m^3 hooked fibres 30/0.67 or 60/0.75 mm Normal or High strength Concrete f_c = 30 or 60 MPa V_f = 30/45/50 kg/m^3	4-points bending test on unnotched prism	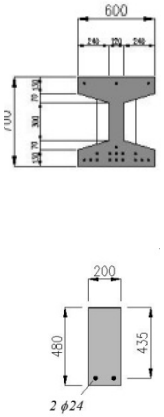	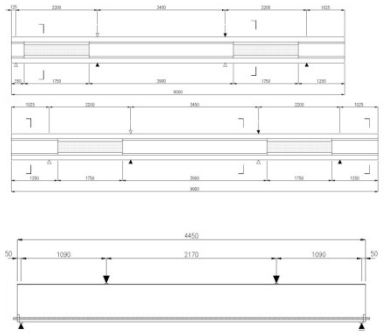	• Loading configuration • Fibres type • compressive strength • Fibre content • Fibres type • compressive strength

Dinh, Parra-Montesinos and Wight [DIN2010]	Normal strength Concrete f_c = 41 MPa V_f = 0 and 100 kg/m^3 hooked fibres 30/0.55 ; 30/0.38 ; 60/0.75 mm	4-points bending test on unnotched prism	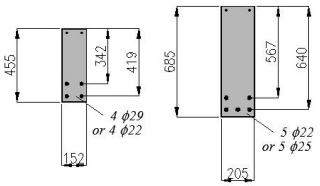	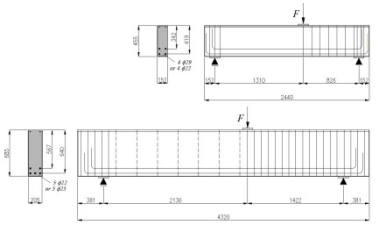	• Fibre content • Fibres type • Reinforcement ratio • Size of beam • Stirrups or not
Baby [BAB2012]	UHPFRC f_c = 160-200 MPa V_f = 2 to 2.5%	4-points bending test on unnotched prism Direct tensile test on prism	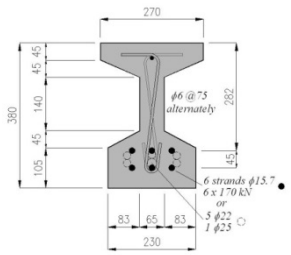	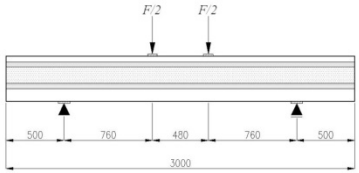	• Type of UHPFRC • Stirrups or not • Prestressing or passive reinforcement

2.2.8 Discussion

At the end of this second part of the literature survey dedicated to shear, we have seen that the shear strength of reinforced concrete members with and without transverse reinforcement is a complex phenomenon including several shear transfer mechanisms. Five shear transfer mechanisms in reinforced concrete members are identified; the interface shear transfer, the dowel action of longitudinal reinforcement, the residual tensile stress across cracks, the shear carried by the un–cracked concrete and the arch action. Often the first four mechanisms are summarized in the beam action. In reality it is a combination of the different types that allows the transfer of the shear force. The steel fibres influence positively the different shear transfer mechanisms particularly the residual tensile stress across cracks.

The shear strength of reinforced concrete members without transversal reinforcement is influenced by the following principal parameters, the shear span-to-depth ratio (*a/d*), the reinforcement ratio, the member's depth (size effect), the concrete strength and the aggregates size, the axial force, the loading configuration; etc. Different studies have highlighted the important influence of the slenderness of the members and the presence of different modes governing the shear failure. For a ratio *a/d* between 1 to 2.5 – 3, the arch action is dominant. In this configuration, the shear crack progresses in a stable manner and presents some large strength reserve. For a ratio *a/d* between 2.5 to 7 – 13, the diagonal shear crack develops from an inclined flexural crack. The failure develops due to the localization of the strains and limits the strength of the inclined compression strut carrying shear. Another interesting parameter is the beneficial effect of an axial force due to prestressing on the shear strength. The prestressing force delays the cracking formation and the angles between the longitudinal axis and the diagonal shear crack are lower compared to reinforced concrete members.

The assessment of shear resistance of reinforced concrete members with stirrups is correctly evaluated with the strut-and-tie model and the stress field model. These two models are integrated in numerous standards. The code approach for the assessment of the shear strength of members without transverse reinforcement was often empirical, e.g. the European standard EC 2 and the American standard ACI 318. Currently, recent developments in shear strength particularly the Modified Compression Field Theory and the Critical Shear Crack Theory are based on a physical model. These approaches consider the aggregates interlock as the principal shear mechanism and give accurate predictions. In these models, the opening of the critical shear crack governs the strength. Currently, the MCFT was integrated in *fib* Model Code 2010 [FIB2010b] and the Canadian standard [CSA2004].

Several experimental studies have highlighted that SFRC can reduce or substitute the shear reinforcement of reinforced and prestressed members. In comparison with plain concrete members without transverse reinforcement, SFRC beams with the same reinforcement and loading arrangements exhibit higher strength and deflection capacity. Moreover, the tests showed that the fibres contribution depends directly on the post-cracking response of a SFRC. On the basis of the test results, different empirical and mechanical models were proposed. An interesting approach is the model developed by Casanova and Rossi because of its simplicity and its rational basis. This model assumes the formation of a block mechanism and integrates the fibres, the transversal reinforcement and the concrete contribution. The contribution of fibres to the shear resistance corresponds to the force transferred between crack faces for a certain crack mouth opening *w* like the aggregates interlocking mechanism. However, in this model, the concrete contribution is fully empirical.

2.3 Punching shear

2.3.1 Problem statement

The first reinforced concrete slabs construction supported by columns and ribs was patented by Hennebique (FR) in 1862 (Figure 2-97a). In the early 20th century, Turner (USA) developed the first reinforced concrete slabs with capital for the construction of buildings. In Switzerland, Maillart submitted a patent in 1909 for a floor system supported on RC columns without ribs (Figure 2-97b). In order to solve the problems caused by the intense stress surrounding the columns, Maillart has increased gradually the slab thickness in critical areas. Since the 1930s, reinforced concrete flat slabs have experienced significant growth in the construction of buildings and bridges. Nowadays, this construction system is widely used around the world, thanks to these economic and functional benefits. But despite its simple appearance, a flat slab has a complex bending and shear behaviour [FIB2001].

a) *b)*

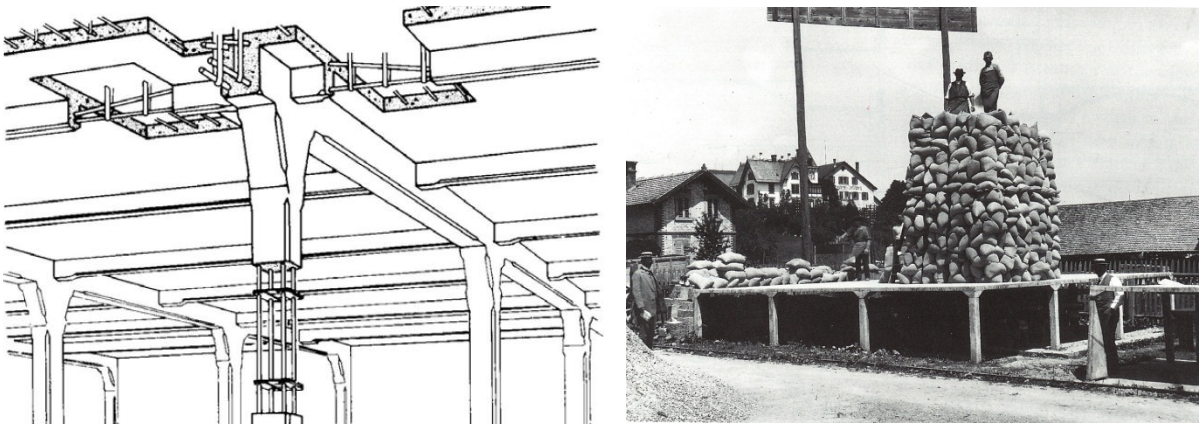

Figure 2-97: a) Floor system patented by Hennebique and b) load test performed by Maillart.

The punching shear or two ways shear is often the critical failure mode for the design of Reinforced Concrete floor and deck slabs. For RC slabs without shear reinforcement, the punching shear failure is characterized by a fragile behaviour implying possible partial or total collapse of the structure (Figure 2-99). Punching shear failure occurs where a point force is applied (e.g. column reaction, truck wheel, etc), causing a localized rupture after a penetration through the slab (Figure 2-98). This failure mechanism forms a truncated cone or a truncated pyramid separated from the rest of the slab by the shear crack. Despite extensive research in this field, punching shear remains such a complex phenomenon that the current design code approach is often empirical or simplified [POL2005].

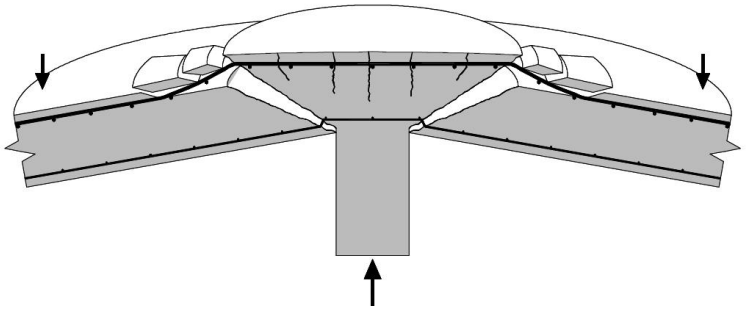

Figure 2-98: Principe of a punching shear failure mechanism in RC flat slabs

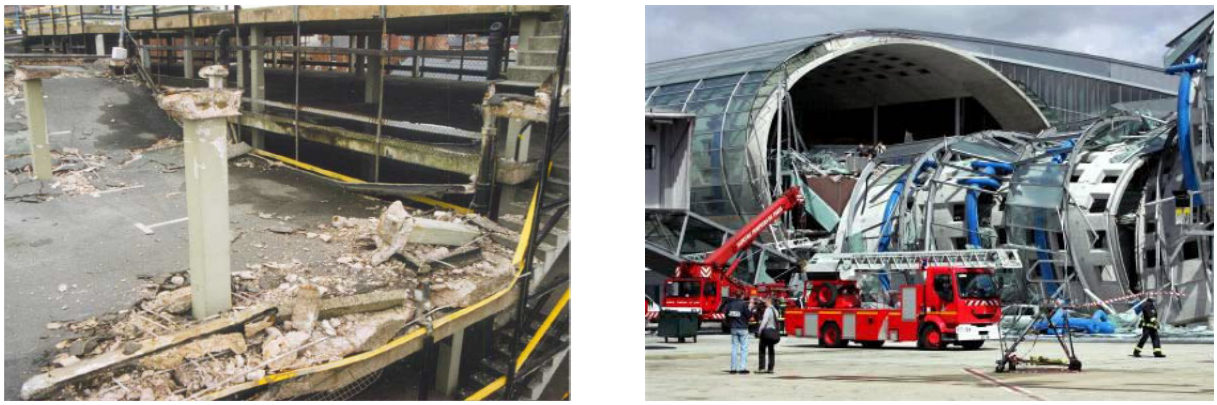

Figure 2-99: Partial collapse of the structure caused by a punching shear failure, Piper's Row car park UK, terminal 2E Roissy airport FR.

2.3.2 Punching shear model for reinforced concrete slab

2.3.2.1 Kinnunen & Nylander's model

The first mechanical model predicting the punching shear strength of reinforced concrete slabs without transversal reinforcement has been developed in the 1960s at the Royal Institute of Technology in Stockholm, by Sven Kinnunen and Henrik Nylander [KIN1960]. The model is based on tests on circular slabs supported by a short column at their centre and loaded on the perimeter. This test configuration represents the slab portion where the moment is negative. The variables of this test series were the column diameter, the arrangement of reinforcement (orthogonal or radial) and the reinforcement ratio. The observations performed on the tests, particularly the formation of punching cone, the deflections of the slabs and the concrete and reinforcement strains are the basis of this model.

The mechanical model is based on the equilibrium of forces acting on polar-symmetrical circular slabs supported in their centre by a column and loaded uniformly on the perimeter (Figure 2-100a). The model satisfies the equilibrium equations in forces and moments acting on a slab portion delimited by the shear crack and the radial cracks (Figure 2-100b). During their tests, Kinnunen and Nylander have observed that this slab segment acts like a rigid body. The slab is supported by a conical wedge that develops between the slab- column root and the tip of the shear crack. Gradually, as the load increases, the segment will have a rotation ψ. The segment is in equilibrium with the forces applied on the edges. These stresses depend on the rotation and mechanical properties of concrete and steel. Kinnunen and Nylander also observed that the tangential strains of concrete and steel are inversely proportional to the radius from the centre. The punching strength is determined using the equations of equilibrium and the failure criterion. The failure criterion involves the concrete tangential strain of the compressed face at a distance y of the column's edge (Figure 2-100c). The ultimate tangential stress, i.e. the failure criterion is calibrated on the punching shear tests results.

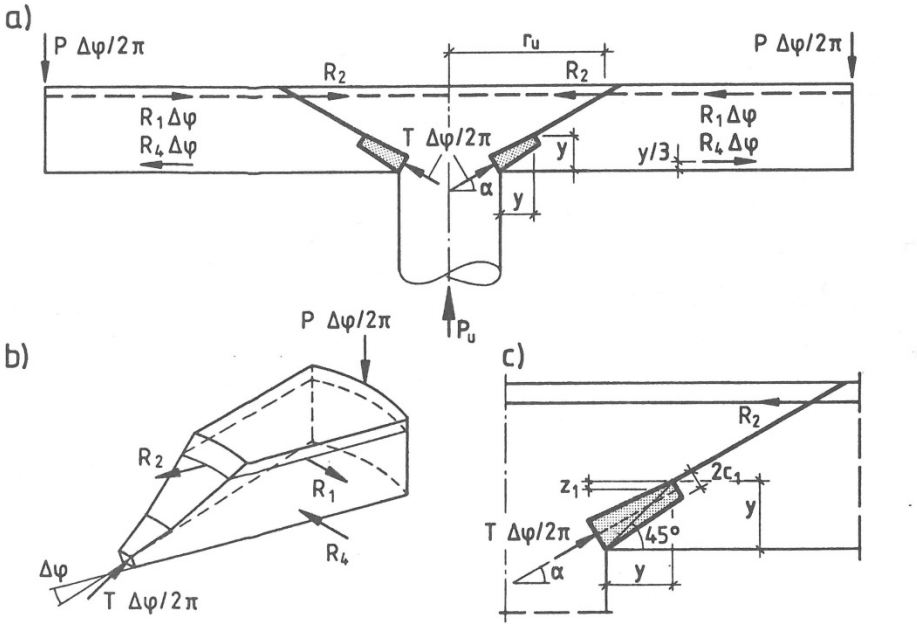

Figure 2-100: Mechanical model proposed by Kinnunen & Nylander

The equilibrium equation of the vertical forces is determined as follow:

$$P_u = k \cdot \pi \cdot \frac{B \cdot y}{d^2} \frac{(1+2y/B)}{(1+y/B)} \cdot f(\alpha) \cdot \sigma_t \cdot d^2 \tag{2-161}$$

Where B is the diameter of the column, y the distance between the compressed face and the shear crack root, $f(\alpha)$ is a function of the compressed wedge inclination, σ_t is the tangential compressive stress and d is the level arm of the reinforcement. The constant k takes into account the dowel effect of orthogonal reinforcement and is equal to 1.1. It should be noted that dowel effect is not considered differently in this model.

$f(\alpha)$ is defined as follows:

$$f(\alpha) = \sin\alpha \cdot \cos\alpha \left(1 - \tan\alpha\right) = \frac{\tan\alpha\left(1 - \tan\alpha\right)}{1 + \tan^2\alpha} \tag{2-162}$$

The angle α can be determined by the following equation.

$$\left(\frac{0.5B - B/2}{d - y/3}\tan\alpha - 1\right)\frac{1 - \tan\alpha}{1 + \tan^2\alpha} = \frac{1}{2 \cdot 2.35}\left(1 + \frac{y}{B}\right)\ln\left(\frac{0.5c/d}{0.5B/d + y/d}\right) \tag{2-163}$$

With c is the diameter of the slab where the moment is negative. For tests configuration, c is equal to the support diameter.

On the basis of the tests results, the concrete tangential stress at a distance of $r = B/2 + y$ is approximated as follows:

$$\sigma_t = 2.35 \cdot \sigma_{cT,r=B/2+y} = 2.35 \cdot E_c \cdot \varepsilon_{cT,r=B/2+y} \tag{2-164}$$

where $$E_c = 10^4\left(0.35 + 0.3\frac{f_{c,cube}}{15}\right) \tag{2-165}$$

The concrete tangential strain at ultimate load constitutes the failure criterion, calibrated on the tests results. The ultimate strain is defined as follows:

$$\varepsilon_{cT,r=B/2+y} = 0.0035\left(1-0.22\,B/d\right) \quad \text{for } B/d \le 2 \tag{2-166}$$

$$\varepsilon_{cT,r=B/2+y} = 0.0019 \quad \text{for } B/d > 2 \tag{2-167}$$

The rotation ψ of the segment delimited by the critical shear crack and radial cracks is defined as follows:

$$\psi = \left(1+0.5\,B/y\right)\cdot\varepsilon_{cT,r=B/2+y} \tag{2-168}$$

The plastic radius r_s defines the zone where the steel has reached the yield limit f_{sy}.

$$r_s = \frac{E_s}{f_s}\cdot\psi\cdot\left(1-\frac{y}{d}\right)d \tag{2-169}$$

The distance c_0 between the column centre and the shear crack in the plan of the reinforcement is approximated by:

$$c_0 = 0.5B + 1.8d \tag{2-170}$$

Moment equilibrium equations

If the plastic radius $r_s \le c_0$ then P_u is calculated as follows:

$$P_u = k\cdot 4\pi\cdot\rho\cdot f_s\cdot d\cdot r_s\left[1+\ln\left(0.5\,c/c_0\right)\right]\frac{d-y/3}{c-B} \tag{2-171}$$

If the plastic radius $r_s > c_0$ then P_u is calculated as follows:

$$P_u = k\cdot 4\pi\cdot\rho\cdot f_s\cdot d\cdot r_s\left[1+\ln\left(0.5\,c/r_s\right)\right]\frac{d-y/3}{c-B} \tag{2-172}$$

The iteration is made on the distance y with the two equilibrium equations and allows computing the ultimate load P_u. The model has been improved by several researchers, Andersson (1963), Sundquist (1977), Shehata (1985), Broms (1990), Gomes (1990) and Hallgren (1997).

2.3.2.2 Hallgren's model

On the basis of the model computed by Kinnunen & Nylander, Hallgren proposed some improvements on failure criterion. This new criterion takes better account of the size effect and the high strength concrete fragility on the punching shear strength [HAL1996]. The model is based on ten punching shear tests on circular slabs in high strength concrete and non-linear finite element analysis. The tests have highlighted that high strength concrete increases significantly the punching shear strength. However, the punching shear strength is neither proportional to the compressive and tensile strength of the concrete.

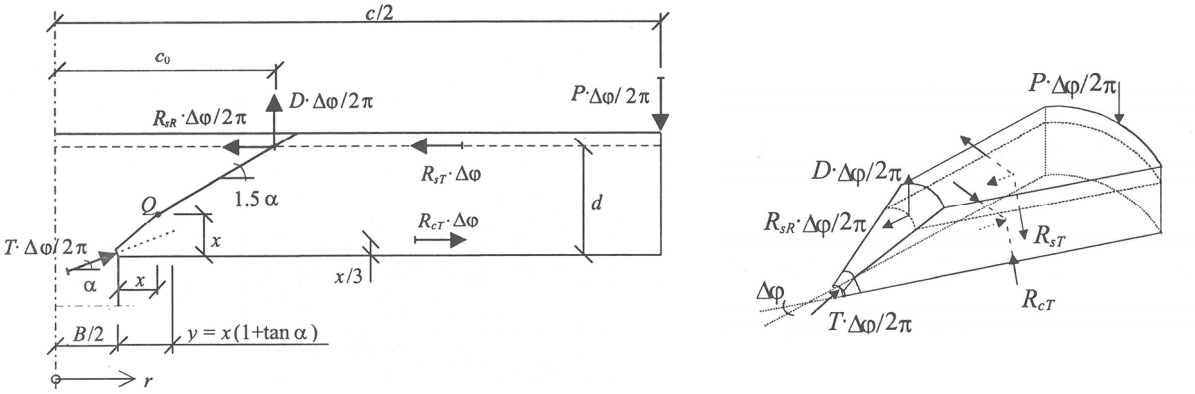

Figure 2-101: Mechanical model proposed by Hallgren [HAL1996]

Like Kinnunen & Nylander, the model proposed by Hallgren is based on the forces equilibrium acting on polar-symmetrical circular slabs supported in their centre by a column and loaded uniformly on the perimeter (Figure 2-101). The slab portion delimited by the shear critical crack and radial cracks is supported by a truncated wedge. The load carried by the compressed zone is called *T*. The length of the compressed zone is equal to $y = x\left(1+\tan\alpha\right)$, where x is the depth of the tangential compression zone and α is the inclination of the force *T*.

The radius c_0 from the column centre to the shear crack in the plan of the longitudinal reinforcement is defined as follows:

$$c_0 = \frac{B}{2} + x + \frac{d-x}{\tan\left(1.5\alpha\right)} \tag{2-173}$$

The value of 1.5α represents the angle of the critical shear crack. This value is defined on the basis of the tests results and non-linear finite element analysis. On the same basis, the tangential strains in the concrete on the compressed face and in the reinforcing steel on the tensioned side are assumed to be inversely proportional to the radius *r* from the centre. The concrete and steel relationships are represented by bi-linear curves. The depth of the tangential compression zone *x* is defined through the steel and concrete tangential strains and depends on the stress state of the materials. The strains distribution across the tangential cross section is assumed to be linear.

If the steel and the concrete are in the elastic state, *x* is defined as follows:

$$x = \rho \cdot \frac{E_s}{k_E \cdot E_c} \cdot \left(\sqrt{1 + \frac{2 \cdot K_E \cdot E_c}{\rho \cdot E_s}} - 1 \right) \cdot d \tag{2-174}$$

The factor K_E takes into account the increase of the concrete stiffness under bi-axial stresses. K_E is defined as follow:

$$K_E = \left(1 - \frac{\nu + 2 \cdot \nu^2}{2 + \nu} \right)^{-1} \tag{2-175}$$

Where ν is the Poisson's ratio.

If the concrete has reached its yield limit and the steel is in the elastic state, *x* is defined as follows:

$$x = \frac{\rho \cdot E_s \cdot \varepsilon_{cT0}}{2 \cdot \alpha_{c0} \cdot f_{cc}} \cdot \left(\sqrt{1 + \frac{4 \cdot \alpha_{c0} \cdot f_{cc}}{\rho \cdot E_s \cdot \varepsilon_{cT0}}} - 1 \right) \cdot d \tag{2-176}$$

with $$\alpha_{c0} = 1 - \frac{f_{cc}}{2 \cdot \varepsilon_{cT0} \cdot E_c} \tag{2-177}$$

At ultimate load, the concrete tangential strain at $r = c_0$ is given by the following relation:

$$\varepsilon_{cT0} = \varepsilon_{cTu} \cdot \frac{(B/2 + y)}{c_0} \tag{2-178}$$

Where, ε_{cTu} is the ultimate tangential concrete strain, i.e. the failure criterion

If the reinforcing steel has reached the yield limit f_{sy} at $r = c_0$ and the concrete is in elastic state, x is defined as follows:

$$x = \frac{2 \cdot \rho \cdot d \cdot f_{sy}}{\varepsilon_{cT0} \cdot k_E \cdot E_c} \tag{2-179}$$

If both materials have reached their yield limits, x is defined as follows:

$$x = \frac{\rho \cdot d \cdot f_{sy}}{\alpha_{c0} \cdot f_{cc}} \tag{2-180}$$

The resulting forces of concrete in compression R_{cT} and steel R_{sT} in tension are computed by integration of stresses over the slab portion. Again, the resulting forces depend on the stress states of the materials. If the concrete stress in tangential direction is in the elastic domain, then the resulting tangential concrete force at ultimate load is defined as follows:

$$R_{cT} = \frac{1}{2} \cdot E_c \cdot x \cdot \varepsilon_{cTu} \cdot \left(\frac{B}{2} + y \right) \cdot \ln \left(\frac{c}{B + 2y} \right) \tag{2-181}$$

If the concrete stress in tangential direction has reached its yield limit, then the resulting tangential concrete force at ultimate load is defined as follows:

$$R_{cT} = f_{cc} \cdot x \cdot \left[r_c \cdot \left(\frac{3}{4} + \frac{1}{2} \cdot \ln \left(\frac{c}{2r_c} \right) \right) - \left(\frac{B}{2} + y \right) + \frac{1}{4 \cdot r_c} \cdot \left(\frac{B}{2} + y \right)^2 \right] \tag{2-182}$$

Where, r_c represents the plastic radius of the concrete, defined as:

$$r_c = \frac{\varepsilon_{cTu}}{\varepsilon_{cy}} \cdot \left(\frac{B}{2} + y \right) \tag{2-183}$$

If the steel stress in tangential direction is in the elastic domain, then the resulting tangential steel force at ultimate load is defined as follows:

$$R_{sT} = \rho \cdot d \cdot E_s \cdot \varepsilon_{cTu} \left(\frac{d}{x} - 1 \right) \cdot \left(\frac{B}{2} + y \right) \cdot \ln \left(\frac{c}{2 \cdot c_0} \right) \tag{2-184}$$

If the steel stress in tangential direction exceeds the yield limit, then the resulting tangential steel R_{sT} force at ultimate load is defined as follows:

$$R_{cT} = \frac{1}{2} \cdot E_c \cdot x \cdot \varepsilon_{cTu} \cdot \left(\frac{B}{2} + y \right) \cdot \ln \left(\frac{c}{B + 2y} \right) \tag{2-185}$$

Where r_s represents the plastic radius of the steel, defined as:

$$r_s = \frac{\varepsilon_{cTu}}{\varepsilon_{sy}} \cdot \left(\frac{d}{x} - 1 \right) \cdot \left(\frac{B}{2} + y \right) \tag{2-186}$$

The tangential steel strain intersecting the shear crack at $r=c_0$ is assumed to be equal to the tangential steel strain at $r=c_0$.

$$R_{sR} = \rho \cdot d \cdot 2\pi \cdot E_s \cdot \varepsilon_{cTu} \cdot \left(\frac{d}{x} - 1 \right) \cdot \left(\frac{B}{2} + y \right) \qquad \text{If } r_s < c_0 \tag{2-187}$$

$$R_{sR} = \rho \cdot d \cdot 2\pi \cdot c_0 \cdot f_{sy} \qquad \text{If } r_s \geq c_0 \tag{2-188}$$

The dowel effect is considered on the basis of a semi-empirical expression derived from beam tests performed by Hamadi & Regan [HAM80].

$$D = 27.9 \cdot \phi^{2/3} \cdot c_0 \cdot \left(1 - 1.6 \cdot \frac{\rho \cdot d}{\phi} \right) \cdot f_{cc}^{\,1/3} \tag{2-189}$$

Where ϕ is the rebars diameter. If the steel reinforcement has yielded at $r = c_0$ then the dowel force D is set to 0.

The equilibrium equations of forces and moments can be written as follows:

$$P = \left[R_{sR} + 2\pi \left(R_{sT} - R_{cT} \right) \right] \tan \alpha + D \tag{2-190}$$

The inclination α is the iteration variable. The ultimate load P_u is reached as far as the tangential concrete strain of the compressed side at distance $B/2 + y$ reaches the ultimate tangential strain ε_{cTu} determined by the failure criterion.

The failure criterion is based on the non-linear finite element analysis and the fracture mechanics concepts. The simulation has highlighted that concrete between the tip of the shear crack and the slab-column root is in three-axial state of the compressive stress. At a distance between one and two times the depth of the tangential compression zone, the concrete is in a bi-axial state of compressive stresses in the horizontal plan and tensile stresses in vertical direction. As soon as a crack is formed in this zone, the tri-axial state is lost and the shear crack can propagate. On the basis of the numerical simulations and the tests results, the concrete in compression situated at a distance of B/2 + y is assumed to be in a bi-axial state of stresses, where the tangential strains ε_{cT} and radial strains ε_{cR} are equal. At failure load, the proposed failure criterion assumes, that the ultimate tangential strain ε_{cTu} is equal to the vertical tensile strain.

$$\varepsilon_{cTu} = \frac{3.6 \cdot G_F^{\infty}}{x \cdot f_{ct}} \cdot \left(1 + \frac{13 \cdot d_a}{x} \right)^{-1/2} \tag{2-191}$$

$$G_F^{\infty} = G_F^R \cdot \left(1 + \frac{13 \cdot d_a}{d^R} \right)^{1/2} \tag{2-192}$$

Where, G_F^R represents the fracture energy determined from tests on notched prisms, d^R is the notch depth and d_a the maximum aggregates size.

2.3.2.3 Menétrey's model

The analytical model proposed by Menétrey [MEN1996] is based on finite element analysis of the failure mechanism of reinforced concrete slabs. The load transfer from the application point up to the column is assumed to have a strut-and-tie analogy. The punching shear failure corresponds to the failure of the concrete tie which crosses the crack, so that the tie strength is equivalent to the punching shear strength. The resulting punching load F_{punch} is calculated by integrating the vertical components of the concrete tensile stresses around the punching cone and adding the contributions of each reinforcement which will be crossing the shear crack (Figure 2-103). The model is based on the non-linear fracture mechanics concepts, for which tensile stresses can still be transmitted across cracks.

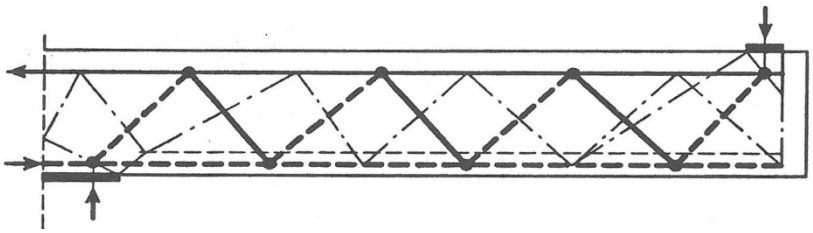

Figure 2-102: Load transfer according to the strut-and-tie model [MEN1996]

The development of the critical shear crack does not appear suddenly but is the result of micro-cracks coalescence. In the presence of transversal reinforcement, these micro-cracks activate gradually the steel. Therefore, the force carried by the transversal reinforcement can be added to the concrete tensile force as proposed by the general model.

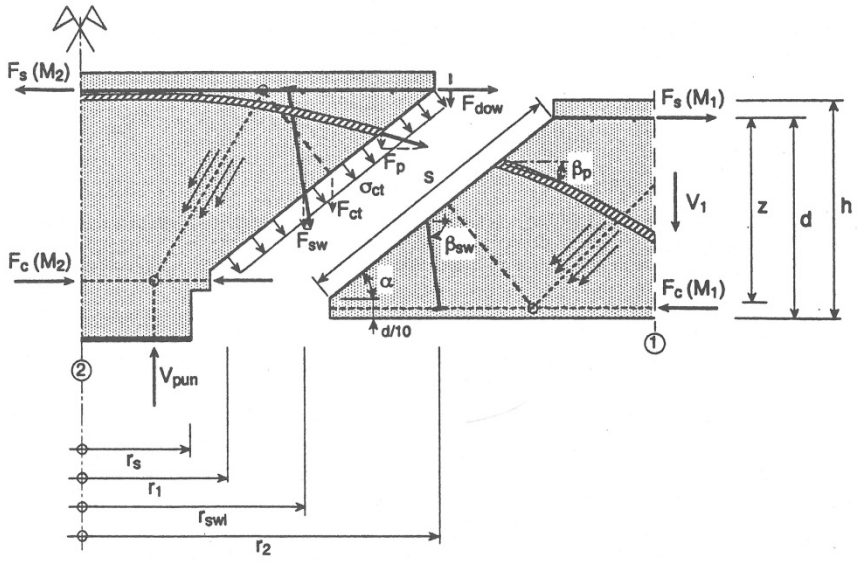

Figure 2-103: Mechanical model proposed by Menétrey [MEN1996]

The resulting punching load F_{pun} is calculated by the summation of four contributions

$$F_{pun} = F_{ct} + F_{dow} + F_{sw} + F_p \tag{2-193}$$

Where, F_{ct} is the vertical component of the concrete tensile force, F_{dow} is the dowel contribution of the flexural reinforcement, F_{sw} is the vertical contribution of the transversal reinforcement (stirrups, studs,…) and F_p is the vertical force of inclined post-tensioning

The concrete contribution is determined by vertical projection of the tensile stress around the punching cone. In this model, the aggregates interlock is not taken into account. The critical shear crack is assumed to be a truncated cone included between the radius r_1 and r_2. The concrete contribution is defined as follows:

$$F_{ct} = \pi\left(r_1 + r_2\right)\cdot s \cdot \sigma_{ct} = \pi\left(r_1 + r_2\right)\cdot s \cdot f_{ct}^{2/3} \cdot \xi \cdot \eta \cdot \mu \tag{2-194}$$

The radius r_1 corresponds to 1/10 of the reinforcement level arm d.

$$r_1 = r_s + \frac{1}{10}\frac{d}{\tan\alpha} \tag{2-195}$$

The radius $r_2$corresponds to the intersection between the longitudinal reinforcement and the critical shear crack

$$r_2 = r_s + \frac{d}{\tan\alpha} \tag{2-196}$$

s is the inclined plan length

$$s = \sqrt{\left(r_2 - r_1\right)^2 + \left(0.9d\right)^2} \tag{2-197}$$

The tensile stresses distribution σ_{ct} is assumed constant along the failure plan. Three parameters (ξ, μ, η) take into account the influences of reinforcement ratio, slab thickness and column radius on the concrete tensile strength f_{ct}.

The influence of reinforcement ratio on concrete tensile strength was determined using a finite element analysis with reinforcement ratio ρ varying between 0.2% and 2 %. It was observed that the intensity of tensile stresses and their inclinations increase with increasing reinforcement ratio.

$$\xi = \begin{cases} -0.1\rho^2 + 0.46\rho + 0.35 \\ 0.87 \end{cases} \tag{2-198}$$

The parameter μ takes into account the size effect through the level arm d and the maximal aggregates size d_a.

$$\mu = 1.6\left(1 + d/d_a\right)^{-1/2} \tag{2-199}$$

The parameter η takes into account the effect of the column radius on the critical shear crack development.

$$\eta = \begin{cases} 0.1\left(r_s/h\right)^2 - 0.5\left(r_s/h\right) + 1.25 \\ 0.625 \end{cases} \tag{2-200}$$

The contribution of the dowel effect is defined as follows.

$$F_{dow} = \frac{1}{2}\sum^{barres}\phi_s^2 \cdot \sqrt{f_c \cdot f_t \cdot \left(1 - \left(\frac{\sigma_s}{f_t}\right)^2\right)} \cdot \sin\alpha \tag{2-201}$$

Several researches have shown that dowel effect is important for orthogonal reinforcement.

The shear force carried by the dowel effect is computed by adapting the CEB-FIP model code approach [CEB1990]. The interaction between the axial stress σ_t and the dowel stresses in the

reinforcing bars is accounted for in the relation $\left(1-\left(\sigma_s/f_t\right)^2\right)$. The axial stress in reinforcement σ_s is obtained by the horizontal projection of the punching force F_{pun}.

$$\sigma_s = \frac{F_{pun}/\tan\alpha}{\sum_{barres} A_s} \tag{2-202}$$

The generalized model takes into account the contribution of transversal reinforcement. This reinforcement may be composed by stirrups, studs or bent-up bars. For slabs with transversal reinforcement, the author distinguishes the following three failure modes:

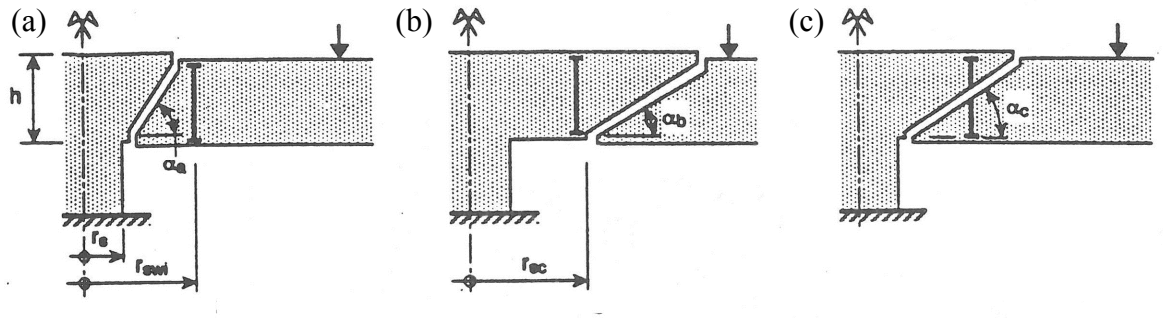

a) The shear crack is formed between the column and the first transversal reinforcement. The shear crack inclination is equal to $\alpha_a = arc\tan\left(\left(r_{swi}-r_s\right)/h\right)$

b) The shear crack is formed after the last transversal reinforcement. This failure mode is similar to the slab without transversal reinforcement but the radius r1 increases considerably

c) The shear crack is formed through the transversal reinforcement.

In the third case, it is necessary to distinguish transversal reinforcement with or without bond. Furthermore, the model is not valid for high transversal reinforcement ratio i.e. transverse steel contribution must be inferior to concrete contribution $F_{sw} < F_{ct}$, because the steel yield limit f_{sw} and the tensile strength f_{ct} won't be reached simultaneously.

The force supported by the transversal reinforcement without bound (studs) is defined as follows:

$$F_{sw} = \sum A_{sw}\cdot E_{sw}\cdot\frac{5\cdot G_f}{f_{ct}\cdot l\cdot\cos\alpha}\cdot\sin\beta_{sw} < \sum A_{sw}\cdot f_{sw}\cdot\sin\beta_{sw} \tag{2-203}$$

The shear crack opening is w_r approached by:

$$w_r \approx \frac{5\cdot G_f}{f_{ct}} \tag{2-204}$$

The force supported by the transversal reinforcement with bound (stirrups or bent-up bars) is defined as follows:

$$F_{sw} = \sum A_{sw}\cdot f_{sw}\cdot\sin\beta_{sw} \tag{2-205}$$

The model takes into account the vertical component of inclined post-tensioning in punching shear strength. The contribution F_p is defined as follows:

$$F_p = \sum^{torons} A_p \cdot \sigma_p \cdot \sin \beta_p \qquad (2\text{-}206)$$

Where, σ_p is the tensile stress of the post-tensioning including the long term effects. For bonded post-tensioning, the yield limit f_p is not considered because the deformations at failure are small. For bonded tendons, the reinforcement ratio used to compute the parameter z is increased due to the addition of the post-tensioning ratio $\rho = \rho_s + \rho_p$.

2.3.2.4 Critical Shear Crack Theory

On the basis of the test results performed by Kinunnen & Nylander [KIN1960], Muttoni & Schwartz [MUT1991] have observed that the punching shear strength decreases with increasing rotation of the slab (Figure 2-104). This has been explained as follows: the shear strength is reduced by the presence of a critical shear crack that propagates through the slab into the inclined compression strut carrying the shear force to the column. Several punching shear tests have shown that the radial compressive strain in the top face of the slab near the column, after reaching a maximum for a certain load level, begins to decrease. In certain cases, positive strains may be measured. This phenomenon can be explained by the development of an elbow-shaped strut with a horizontal tensile tie along the top face due to the development of the critical shear crack. A similar phenomenon has been observed in beams without shear reinforcement [GUA2005] [ROD2007].

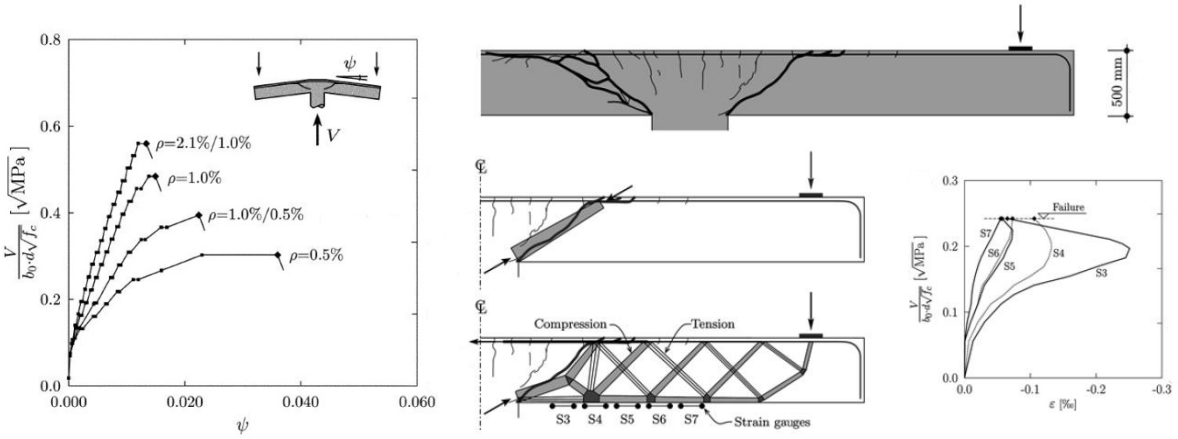

Figure 2-104: Curves nominal shear strength vs rotation fromtests performed by Kinnunen and internal cracking pattern with the measured bottom strains of slab tests by Guandalini & Muttoni [MUT2003]

Punching shear tests performed by Bollinger [BOL1985] have also highlighted the role of the critical shear crack in the punching strength. Bollinger has tested circular slabs with only rings reinforcement (Figure 2-105). According to the position of the reinforcement, the punching shear strength is considerably different. The slab with an additional ring placed close to the column has shown considerably lower punching shear strength. This ring has initiated the development of a tangential crack in this region which did reduce the shear capacity.

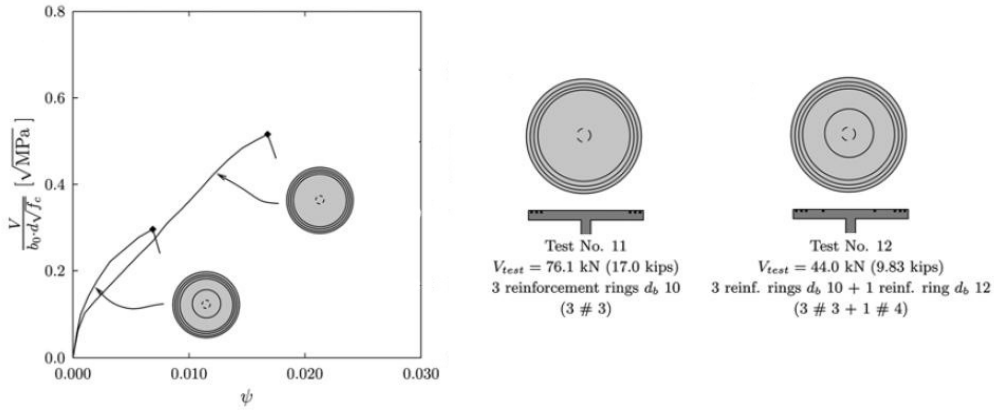

Figure 2-105: Curves nominal shear strength vs rotation, from tests performed by Bollinger, and reinforcement arrangement of the slabs [MUT2003]

On this basis, Muttoni & Schwartz [MUT1991] have formulated a semi-empirical failure criterion for punching shear. This criterion assumes that the width of the critical crack can be assumed to be proportional to the product ψd.

$$w \propto \psi \, d \tag{2-207}$$

$$\frac{V_R}{u \cdot d \cdot \sqrt[3]{f_c}} = \frac{1}{1 + \left(\frac{\psi \cdot d}{4} \right)} \tag{2-208}$$

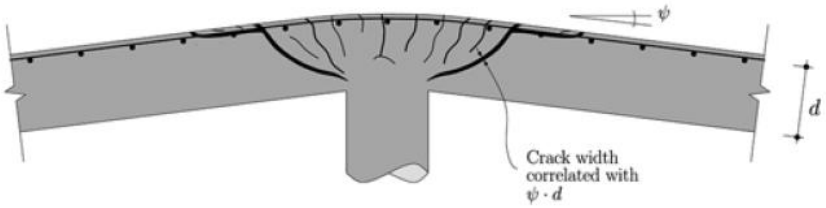

Figure 2-106: Correlation between the critical shear crack opening and the rotation [MUT2003]

In 2003, A. Muttoni [MUT2003] has proposed an improved formulation for the failure criterion on the basis of the works of Walraven and Vecchio & Collins on the aggregates interlock. The amount of shear that can be transferred across the critical shear crack depends on the roughness of the crack. This roughness is a function of the aggregate size. The capacity to carry the shear forces by the aggregates interlock is accounted by dividing the nominal crack width ψd by the aggregate sizes ($d_{g0} + d_g$), where d_g is the maximum aggregate size, and d_{g0} is a reference size equal to 16 mm. For high strength concrete and lightweight concrete, d_g is equal to zero because the cracks develop through the aggregates.

$$\tau_R = \frac{V_R}{u \cdot d} = \frac{0.3 \cdot \sqrt{f_c}}{0.4 + 0.125 \cdot \psi \cdot d \cdot \left(\frac{48}{d_{g0} + d_g} \right)} \tag{2-209}$$

Where τ_r is the nominal shear strength, u is the perimeter of the critical section for punching shear, according to the Swiss standards SIA262 [SIA2003] u is considered at a distance of $d/2$ from the support. The concrete shear strength τ_c is defined as follows:

$$\tau_c = 0.3 \cdot \sqrt{f_c} \tag{2-210}$$

The relation can be written as follows:

$$\frac{V_R}{u \cdot d \cdot \sqrt{f_c}} = \frac{3/4}{1 + 15 \cdot \left(\frac{\psi \cdot d}{d_{g0} + d_g} \right)} \tag{2-211}$$

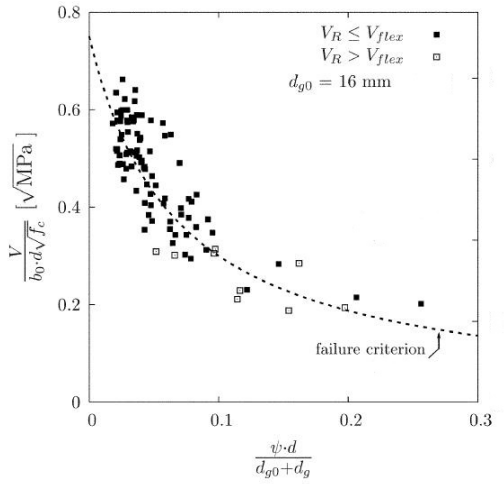

Figure 2-107: Comparison between several test results and the failure criterion [MUT2003]

In the model, the punching failure occurs at the intersection of the load-rotation curve with the failure criterion. The flexural behaviour must be known. The load – rotation relationship can be obtained by a nonlinear numerical simulation. For axisymmetric slabs, the load-rotation relationship can be obtained by an analytical model.

A simplified design model was proposed by the author. This simplified CSCT design model is the method used in the current Swiss Code SIA262 "Concrete Structures" [SIA2003] for assessing the shear strength of slabs with and without transverse reinforcement. The CSCT is also proposed in the *fib* Model Code 2010 [FIB2010b], with the rotation accuracy depending on the different Levels of approximation.

2.3.3 Recommendations and standards, punching shear strength of Reinforced Concrete

2.3.3.1 EN 1992-1-1 Eurocodes 2

In the Eurocode 2 [EC22005], the punching shear strength for slabs not requiring transverse reinforcement $V_{Rd,c}$ has the same form as the shear equation (2-99) and is given by:

$$V_{Rd,c} = \left[\frac{0.18}{\gamma_c} \cdot k \cdot \left(100 \cdot \rho_l \cdot f_{ck}\right)^{1/3} + 0.15 \cdot \sigma_{cp} \right] \cdot u \cdot d \geq \left[v_{\min} + 0.15 \cdot \sigma_{cp} \right] \cdot u \cdot d \tag{2-212}$$

Where k is a factor taking account of the size effect, see equation (2-100), and u is the critical perimeter defined at $2d$ of the column edge.

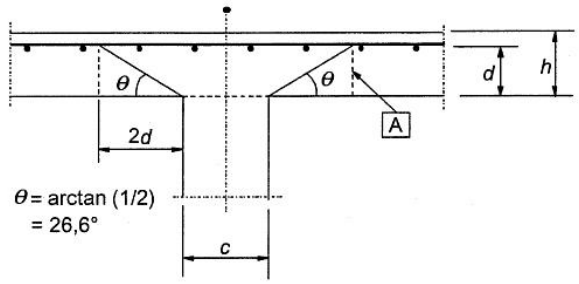

Figure 2-108: Definition of the critical perimeter for flat slabs supported on columns

ρ_l is the average reinforcement ratio, which anchor beyond the section considered,

$$\rho_l = \sqrt{\rho_{lx} \cdot \rho_{ly}} \leq 0.02 \tag{2-213}$$

σ_{cp} is the average compressive stress in the centre of gravity of cross-section due to loading or prestressing. The influence of imposed deformation may be ignored,

$$\sigma_{cp} = \left(\sigma_{cx} + \sigma_{cy}\right)/2 \tag{2-214}$$

and v_{min} is the minimum resistance, see equation (2-103).

2.3.3.2 Swiss Code SIA 262 and fib Model Code 2010

The punching shear provision for slabs without transverse reinforcement in the Swiss Code SIA 262 "Concrete Structures" [SIA2003] and *fib* Model Code 2010 [FIB2010b] is based on a form of the Critical Shear Crack Theory [MUT2008b].

$$\frac{V_{Rd}}{u \cdot d \cdot \sqrt{f_{ck}}} = \frac{2}{3 \cdot \gamma_c} \cdot \frac{1}{1 + 20 \cdot \dfrac{\psi \cdot d}{16 + d_g}} \tag{2-215}$$

$$\psi = 0.33 \cdot \frac{L}{d} \cdot \frac{f_{yk}}{\gamma_s \cdot E_s} \cdot \left(\frac{m_{0d}}{m_{Rd}}\right)^{3/2} \tag{2-216}$$

Where m_{0d} is the average bending moment in the support strip ($=V_d/8$ for inner columns) and m_{Rd} is the average flexural capacity in the support strip. When an axial force is applied to the member, m_{0d} has to be replaced by $(m_{0d} - m_{Pd})$ and m_{Rd} by $(m_{Rd} - m_{Pd})$, where m_{Dd} is the average decompression moment in the support strip (bending moment causing $\varepsilon_s = 0$).

2.3.4 Similar works

A non-exhaustive list of punching shear tests performed at the University of Applied Sciences Fribourg and elsewhere is reviewed in this point. Different concrete compressive strengths, loading arrangement, reinforcement and prestressing arrangement are presented.

2.3.4.1 Suter and Buchs' works

This experimental study was performed at the University of Applied Sciences Fribourg, Switzerland [SUT2005b]. The principal aim of this campaign was to investigate the shear strength of thin High Performance Concrete slabs aimed at replacing reinforced concrete deck of old steel bridges. The load tests were carried out on 4 ribbed slabs of 3.96 m length, 1.44 m wide and 80 mm thick (Figure 2-109). The slab included four testing parts separated by the ribs. The varying parameters among the specimens were: the fibre content, the reinforcement ratio and the intensity of the prestressing forces. According to the reinforcement ratio, the testing parts were reinforced with ϕ6 / ϕ8 / ϕ10 / ϕ12 mm rebars, 50 mm pitch and placed in both directions. The effective depth was 60 mm for all parts. The prestressed slabs were composed of four strands 0,5'' with bond in the direction *x* and five monostrands 0,6'' without bond in the direction *y*. The prestressing force was respectively, 4 x 127 kN and 5 x 180 kN and corresponded to a concrete compressive stress of 3 MPa. The concrete compressive strength was around 90 MPa. The FRC mix was composed of end-hooked fibres 30/0.375 mm (l_f/d_f) with a content of 30 kg/m^3.

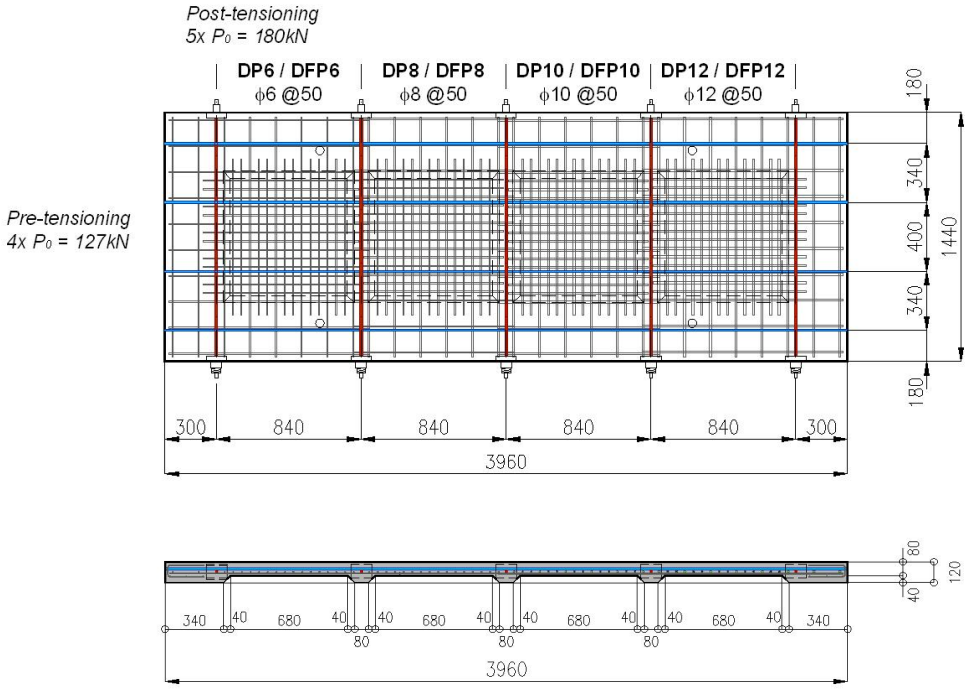

Figure 2-109: Geometry and reinforcement arrangement of slabs

The load tests were performed on a specially designed punching test setup (Figure 2-110). Four punching shear tests were performed on each testing slab. The slab was supported along the ribs. The distance between the supports was 840 mm in each direction. The load was applied at the centre point of the part through a 100 mm diameter punch. After each test, the actuator was moved.

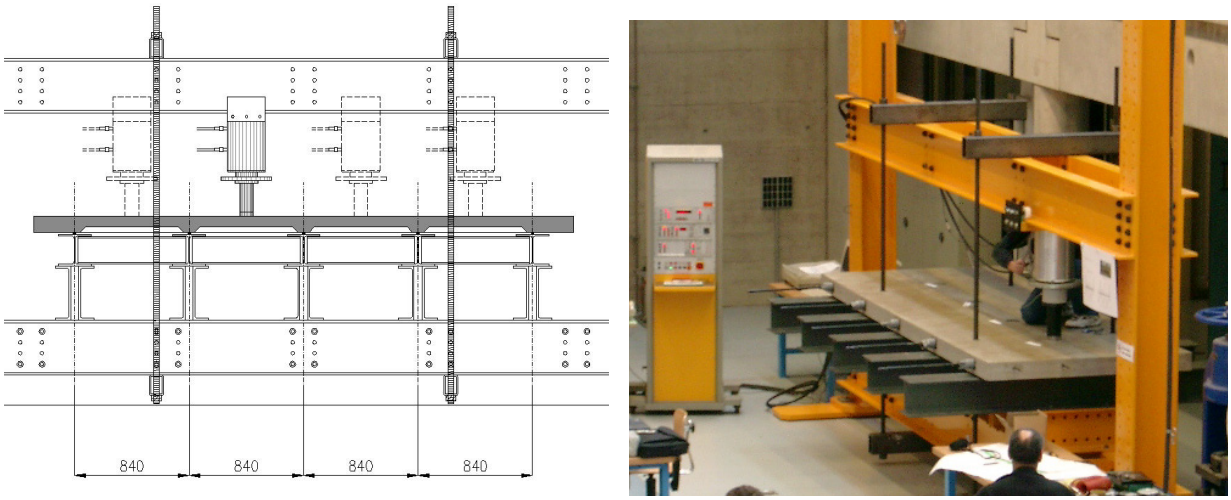

Figure 2-110: Punching shear test setup

The punching shear tests highlighted the following points: All slabs exhibited a sudden punching shear failure without large plastic strain. For HPFRC slabs, the fibre content was not sufficient for controlling the drop of strength. The HPFRC slabs showed a punching shear strength and a deflection at failure higher compared to HPC slabs for a given reinforcement ratio and prestressing force. The fibres effect decreased with the reinforcement ratio increasing. Despite a limited volume of fibre, the increase in strength and ductility is important.

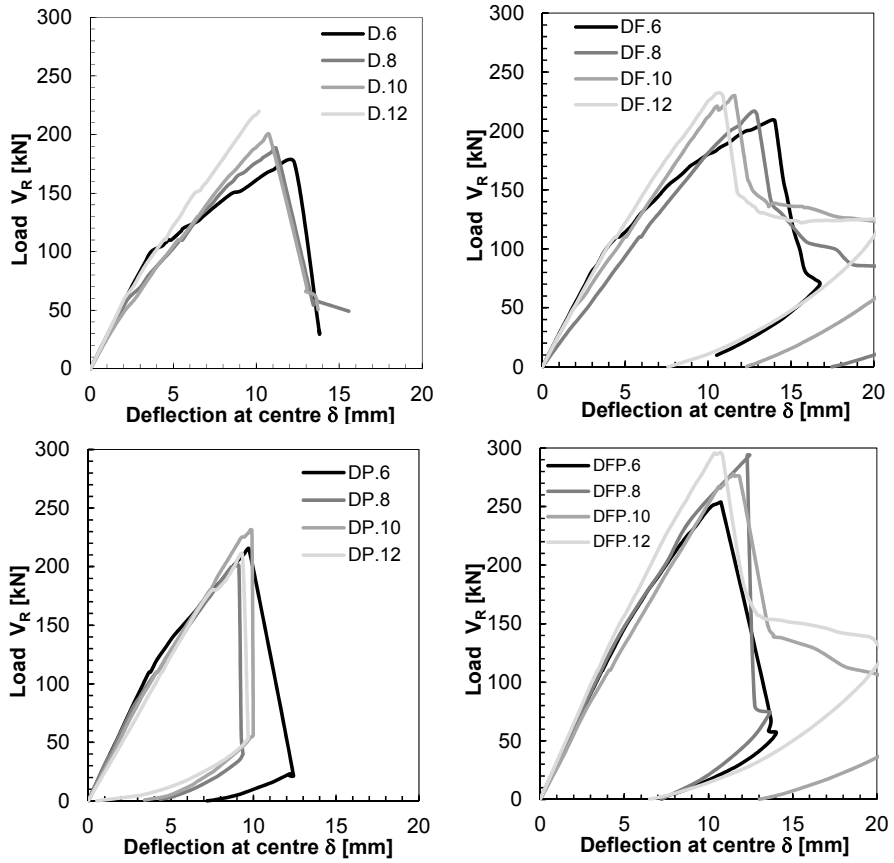

Figure 2-111: Curves load vs deflection at centre of the slabs, F with fibres, P with prestressing

Following the first series, three 3 square slabs of 2.00 m side and 80 mm thick were tested [SUT2005b]. The principal aim was to investigate the behaviour of High Performance Fibre Reinforced Concrete slabs under concentrated load. The varying parameter was the fibre content. The slabs were reinforced with 2 superposed meshes ϕ6 #100 mm with an effective depth of 64 mm. The concrete compressive strength was around 100 MPa. The FRC mixes were composed of end-hooked steel fibres 30/0.375 mm (l_f/d_f) with a content of 30 and 60 kg/m^3. The load tests were performed on a specially designed punching test setup (Figure 2-12). The slab was simply supported along the edges on a clear span of 1920 mm in each direction. The load was applied at centre by an actuator through a circular steel plate with a diameter of 200 mm.

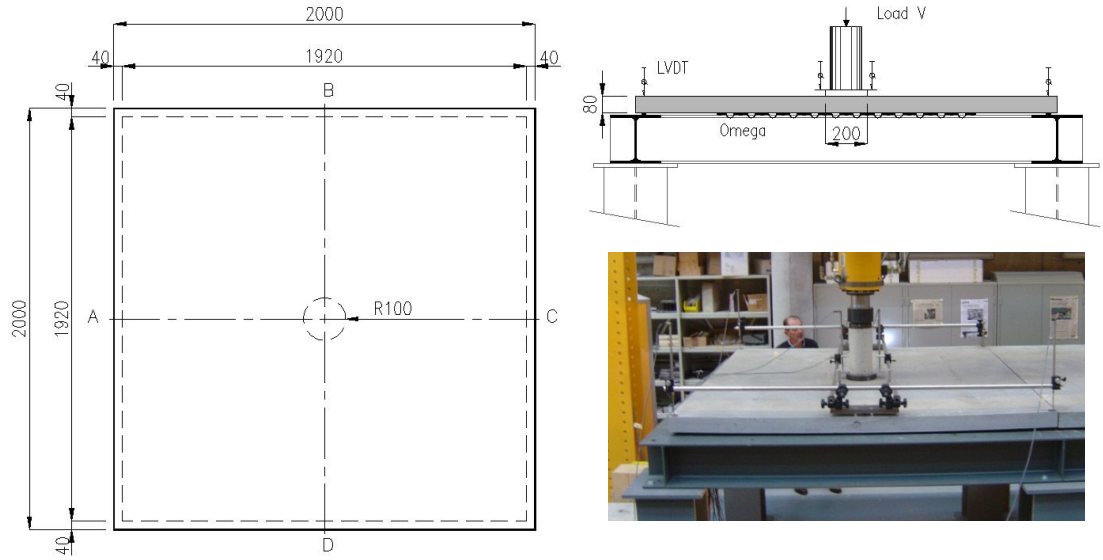

Figure 2-112: Slabs geometry and loading configuration

The loading tests highlighted the following points: The slab without fibres DA. 1 showed a punching shear failure while the HPFRC slabs DA. 5 and DA. 6 had a flexural – punching shear failure. All slabs exhibited large deflections before failure (Figure 2-113). The slabs with fibres showed a higher stiffness compared to the reference slab DA. 1.

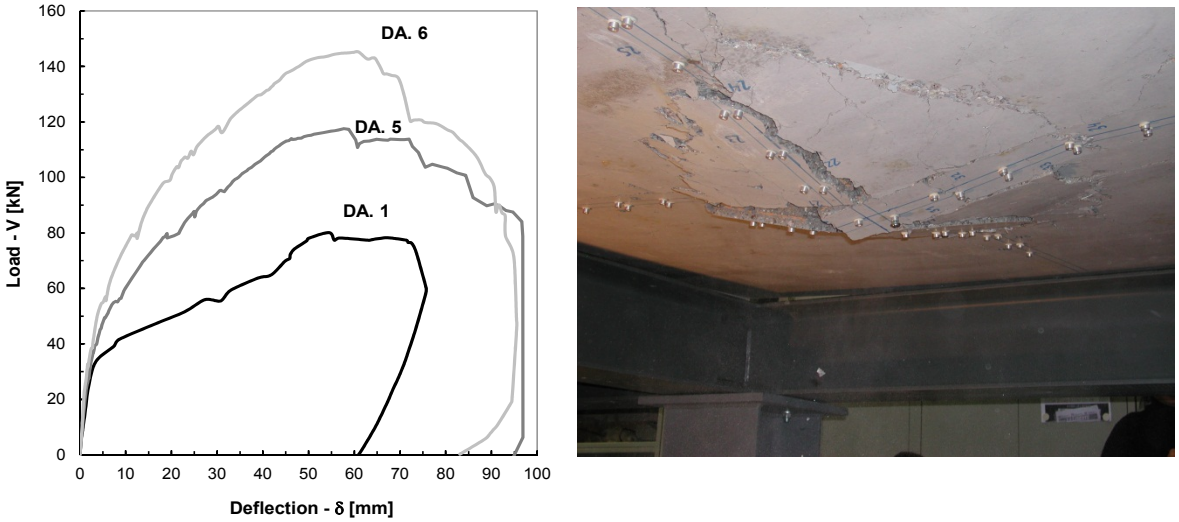

Figure 2-113: Curves load vs deflection at centre of the HPFRC slabs and view of failure

2.3.4.2 Suter and Nicolet's works

This experimental study was performed at the University of Applied Sciences Fribourg, Switzerland [SUT2007]. The principal aim was to investigate the punching shear strength of Fibre Reinforced Concrete slabs. The load tests were performed on 9 square slabs of 2.12 m side, 120 mm thick. The varying parameters were: the fibre content and the fibre type, organic or steel. The slabs were reinforced with 2 superposed meshesϕ6 #100 mm with an effective depth of 90 mm. The concrete compressive strength was around 35 MPa. The FRC mixes were composed of synthetic fibres 40/1.4 mm (l_f/w_f) or hooked steel fibres 40/0.5 mm (l_f/d_f). The fibres content were 2.30, 3.15, 4.60, 6.90 kg/m^3 for synthetic fibres and 20, 40, 60 kg/m^3 for steel fibres. The post-cracking tensile behaviour was largely investigated using 4-points bending tests on prism and flexural tests on square slabs according to the DBV method [DBV2001] and the recommendations SIA162/6 [SIA162/6] respectively.

The load tests were performed on a specially designed punching test setup (Figure 2-114). The slab was simply supported along the edges on a clear span of 2000 mm in each direction. The load was applied at centre by an actuator through a circular steel plate of 200 mm in diameter. The edges of the slab DA-fm 60 A were restrained.

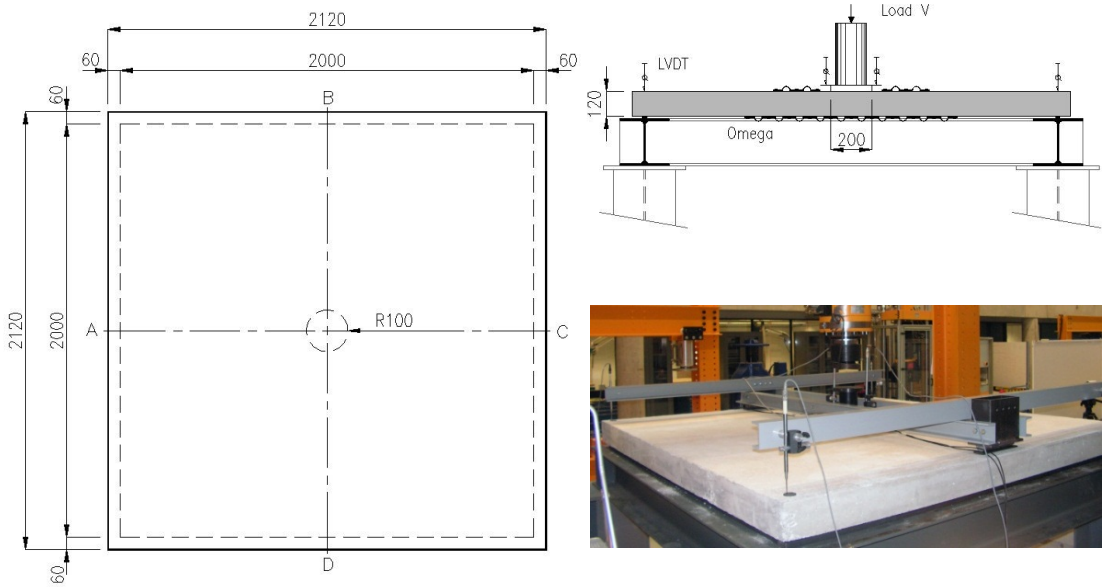

Figure 2-114: Slabs geometry and loading configuration

All slabs exhibited a punching shear failure characterized by a sudden drop of the strength (Figure 2-115). The FRC slabs showed a punching strength and a higher deflection capacity compared to the reference slab DA-0. The synthetic fibres had a lower effect on the stiffness compared to the steel fibres. All synthetic fibre mixes showed a softening behaviour in bending on prisms while the steel fibre mixes 40 and 60 kg/m^3 showed a hardening behaviour in bending on prisms (4-points bending tests).

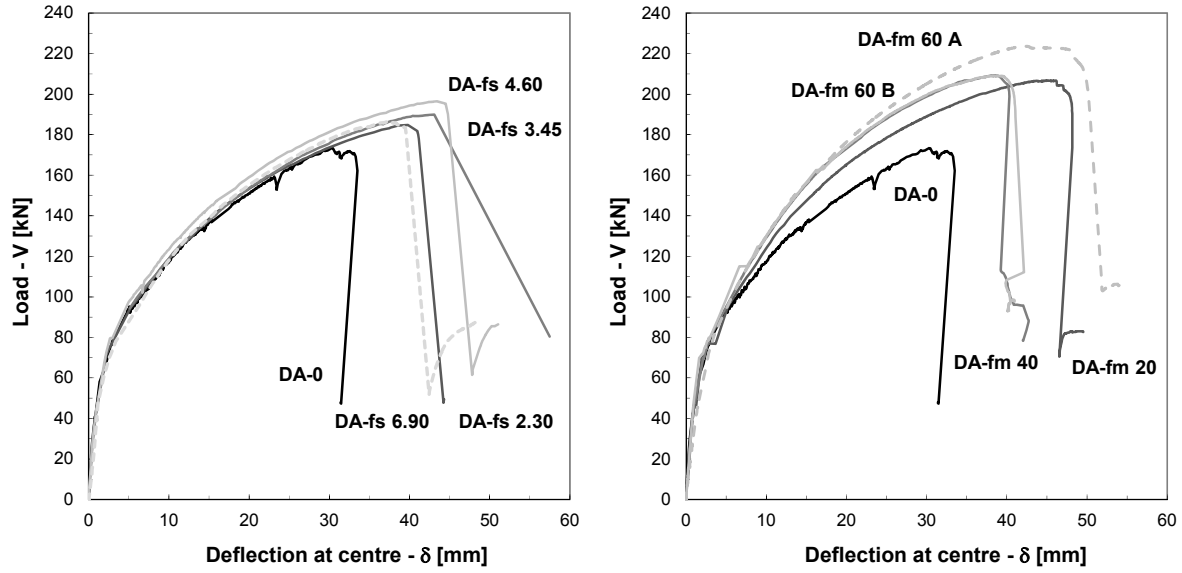

Figure 2-115: Curves load vs deflection at centre of slabs with organic fibres (on left) and steel fibres (on right)

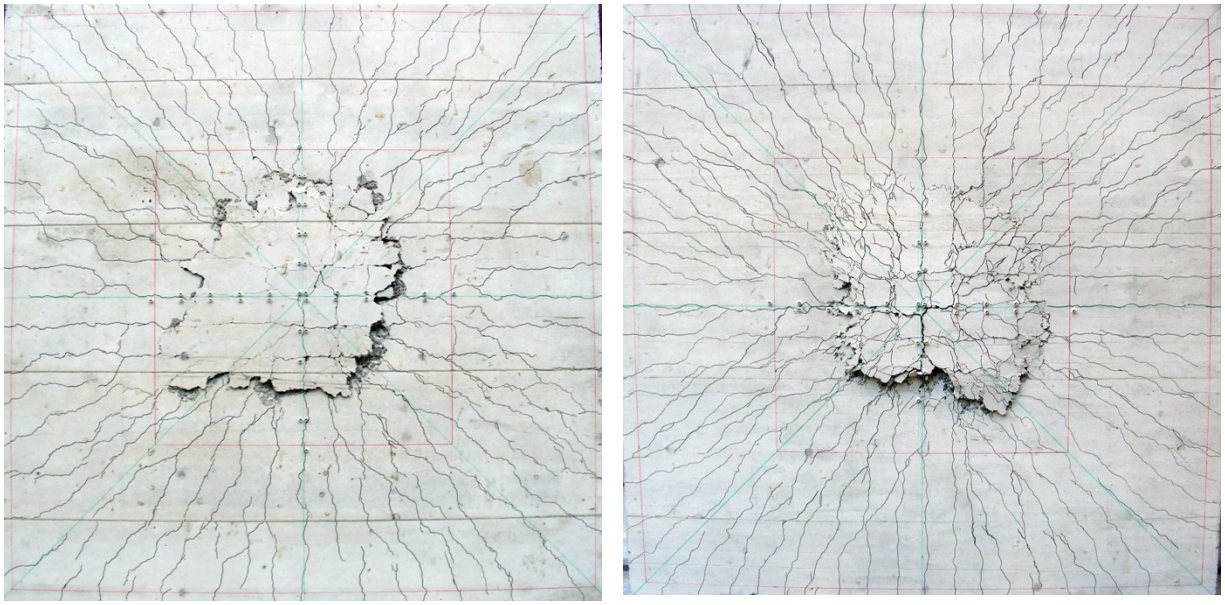

Figure 2-116: Cracking pattern of plain concrete slab DA-0 (on left) and SFRC slab DA-fm 20 (on right)

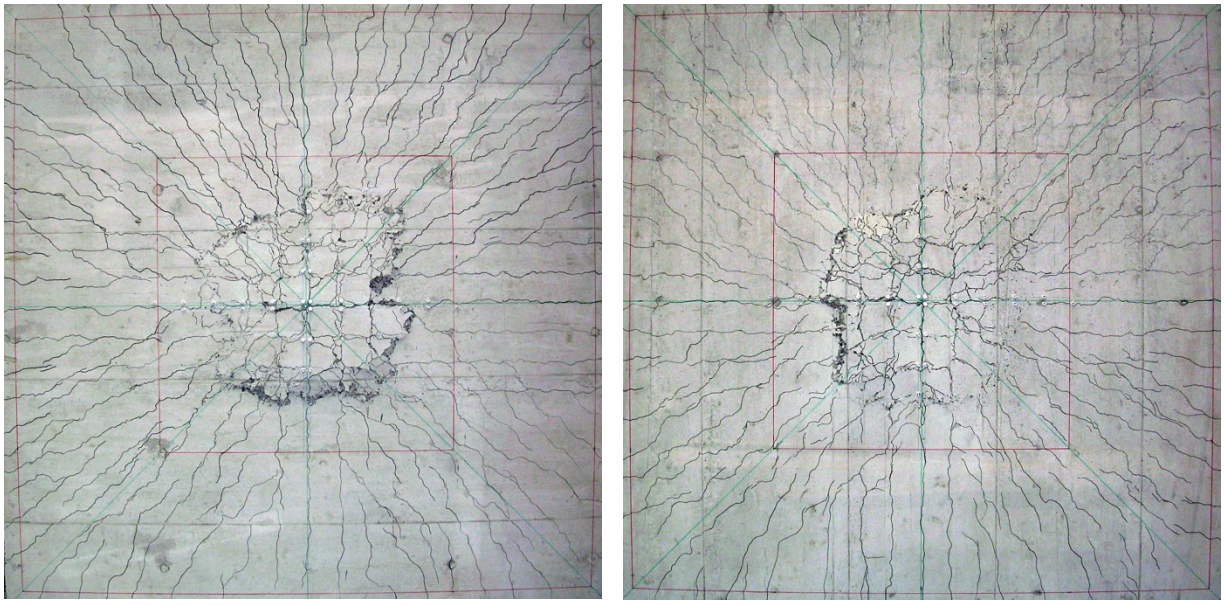

Figure 2-117: Cracking pattern of plain concrete SFRC slabs DA-fm 40 (on left) and DA-fm 60 (on right)

2.3.4.3 Harris' works

This experimental study was performed at the Virginia Polytechnic Institute, USA [HAR2005]. The principal aim was to optimize the flange thickness of precast double tee bridge girders in UHPFRC (Figure 2-118). Twelve square slabs of 1114 mm side and three large slabs of 3658 x 2134 mm were tested in order to characterize the punching shear strength (Figure 2-119). The varying parameters among the small specimens were: the thickness 51, 64 and 76 mm, and the size of the square loading plates, 25, 38, 45, 51, 64 and 76 mm. The UHPFRC mix used for this study was the Ductal with a fibres volume ratio of 2%. The slabs were without conventional reinforcement. The slabs were tested with clamped edges on a span of 990 mm.

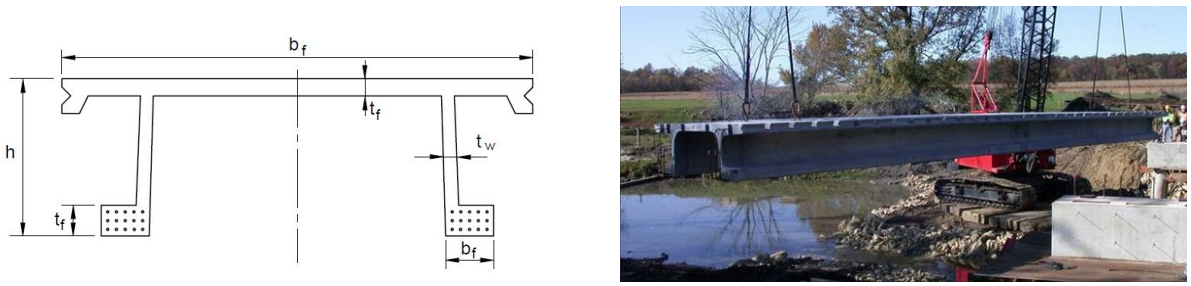

Figure 2-118: UHPFRC bridge girder and construction of Jakway Park Bridge USA

Figure 2-119: Views of loading setup of small and large UHPFRC slabs

The thin slabs 51 mm thick and the slabs loaded by small plates exhibited a punching shear failure. The other slabs showed a flexural failure with the development of yield lines. The three large slabs exhibited a flexural failure. The test results were compared to different codes and empirical models.

Table 2-2: Test results of specimen failed in punching shear

Series	Thickness h [mm]	Size of loading plate a [mm]	Shear strength V_{test} [kN]	Deflection at centre δ [mm]	τ [MPa]
1	55.1	38.1	103.6	18.4	5.0
1	58.9	50.8	121.0	20.2	4.7
1	53.8	25.4	100.5	No data	5.9
2	66.3	50.8	146.8	14.5	4.7
2	65.5	76.2	159.7	53.6	5.1
3	64.5	38.1	135.7	32.0	5.0
3	70.1	63.5	152.1	47.5	5.7

2.3.4.4 Toutlemonde's work

This experimental campaign was performed at the French Public Works Research Laboratory LCPC, France [TOU2007] in the framework of the national project MIKTI. The principal aim was to investigate the behaviour of a prototype ribbed deck slab in UHPFRC under concentrated loads (Figure 2-120) [TOU2005]. Two slab segments of 6.1 m wide and 2.5 m length, distinguished by their UHPFRC type, were tested (Figure 2-121). The ribbed slabs were pre-tensioned with two strands per rib in the transversal direction and post-tensioned by external cables in the longitudinal direction providing a uniform compressive stress of 4 MPa. The UHPFRC mixes used for this study were the Ductal and the BSI with a fibre volume ratio of 2 and 2.5 % respectively.

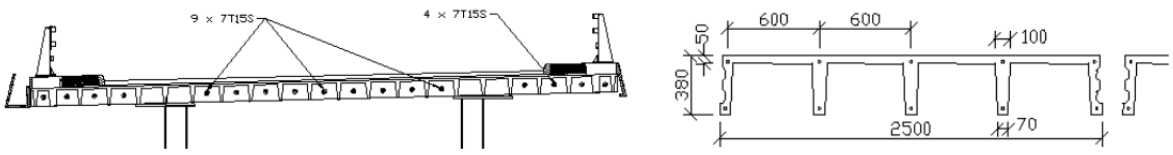

Figure 2-120: Prototype ribbed deck slab and geometry

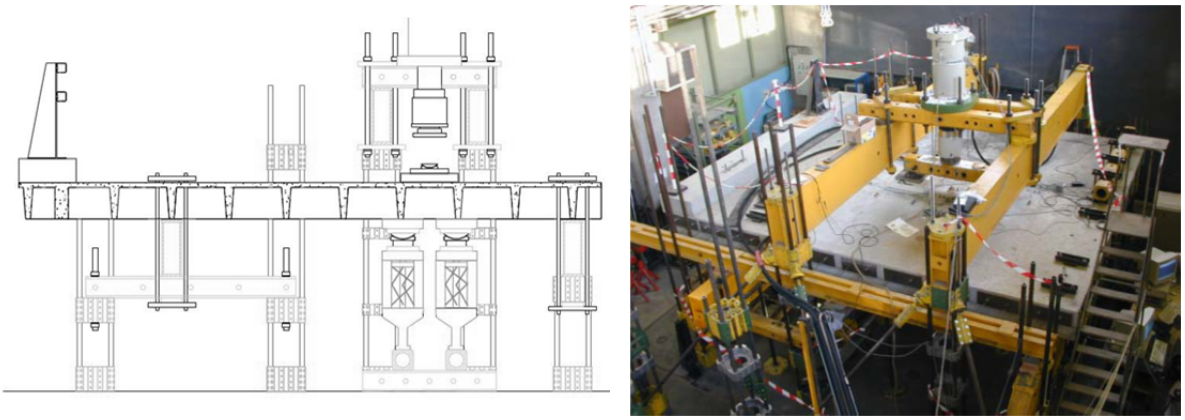

Figure 2-121: Ribbed deck slab test setup

Local bending tests were performed on several “honeycombs”. Intermediate supports at the four corners of the loaded part were implemented. Different sizes of loading steel plates were used, 400 x 400 mm and 190 x 260 mm. Moreover, square plate in polymer of 600 mm side, representative of the diffusion induced by the bituminous concrete paving layers were used. Four loading configuration were tested; 1) steel plate 400 x 400 mm + polymer plate, 2) steel plate 190 x 260 mm + polymer plate, 3) steel plate 400 x 400 mm + thin sand layer and 4) steel plate 190 x 260 mm + thin sand layer.

Only the loading configuration with the smallest loading plate and without elastomer plate exhibited a punching shear failure. However, if loading area according to the Eurocodes is considered, punching shear failure is not critical in this case.

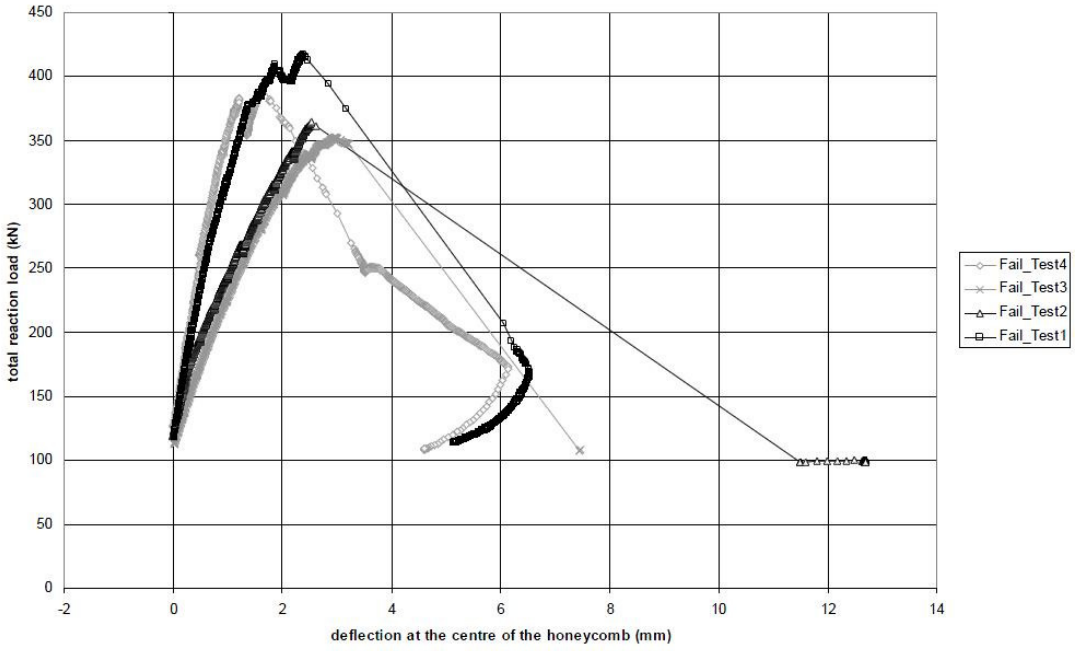

Figure 2-122: Curves load vs deflection at centre of local bending test on honeycomb.

2.3.4.5 Spasojevic's works

This experimental study was performed at the Ecole Polytechnique Fédérale de Lausanne (EPFL), Switzerland. The principal aim of this thesis work was to investigate the potential of UHPFRC in bridge design [SPA2008]. Five small UHPFRC slabs without reinforcement, of thicknesses varying from 30 to 60 mm were tested (Figure 2-123). The slabs were of constant square shape, 350 mm side length, with restrained rotations along all four edges and the loading surface was 20 x 20 mm. The UHPFRC mix used for this study was the BSI with a fibre volume ratio of 2.5 %.

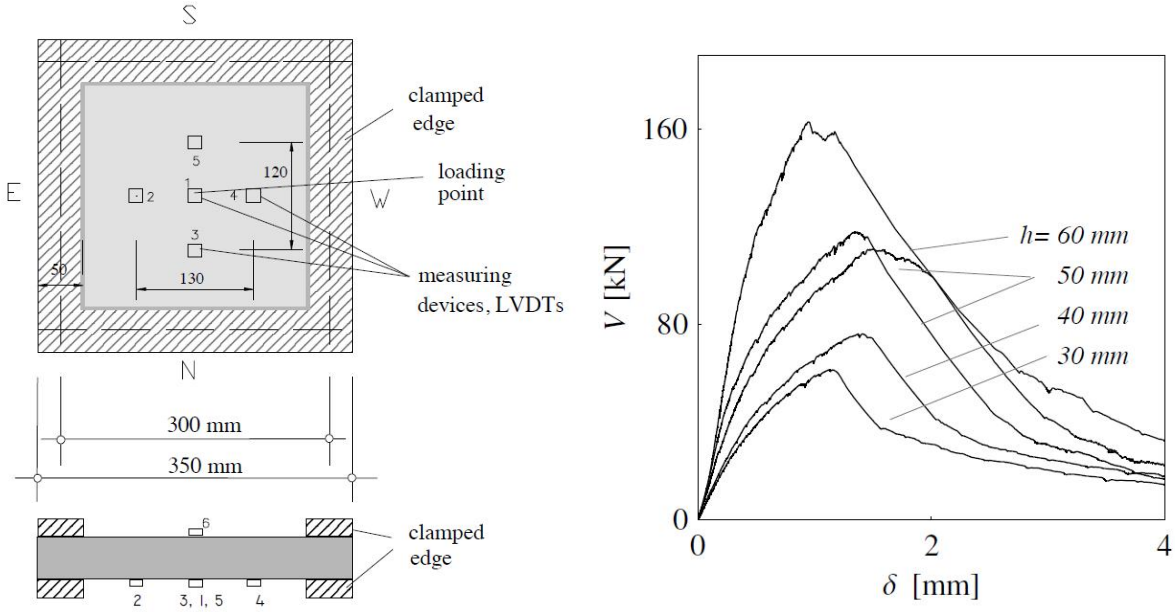

Figure 2-123: Loading arrangement and curves load vs deflection at centre of the BSI slabs

Four slabs failed in punching shear, whereas one slab PP 50b, reached the maximal force in bending, and attained the punching shear failure in the post-peak phase.

Table 2-3: Test results of the BSI slabs

Specimen	Thickness h [mm]	Shear strength V_{test} [kN]	Deflection at centre δ [mm]	τ [MPa]
PP 30	31	61.5	1.13	9.7
PP 40	38	76.2	1.37	8.6
PP 50a	51	117.7	1.37	8.1
PP 50b	50	110.7	1.51	7.9
PP 60	60	162.8	0.95	8.5

2.3.5 Discussion

At the end of this last part of the literature survey dedicated to punching shear we have seen that the punching shear strength of reinforced concrete slabs without transverse reinforcement is also a complex phenomenon including several shear transfer mechanisms and parameters. Punching shear failure occurs where a loading point is applied, causing a localized rupture after a penetration through the slab. For RC slabs without shear reinforcement, the punching shear failure is characterized by a brittle behaviour implying possible partial or total collapse of the structure

The code approach for the assessment of the punching shear strength of slabs without transverse reinforcement is also empirical, e.g. the European standard EC 2 and the American standard ACI 318. Currently, recent developments in punching shear strength particularly the Critical Shear Crack Theory (CSCT) are based on physical models. This approach considers the aggregates interlock as the principal shear mechanism and gives accurate predictions. In this model, the opening of the critical shear crack governs the strength and is correlated to the deflection capacity. Currently, a simplified form of the CSCT is integrated in the *fib* Model Code 2010 [FIB2010b] and the Swiss standards SIA 262 [SIA2003].

Several experimental studies highlighted that SFRC and UHPFRC increase the punching shear strength. In comparison with plain concrete slab without shear reinforcement, SFRC slab with the same reinforcement and loading arrangements exhibit higher strength and deflection capacity. Moreover, the tests showed that the fibres contribution depends directly on the post-cracking response of a SFRC. Currently, no standards and recommendations integrate the punching shear strength of SFRC and UHPFRC slabs. In the same trend for shear strength of members, an harmonized model for steel fibres cementitious composite based on the recent development on punching shear strength of reinforced concrete slabs is seen to be the best approach for practitioners.

3 High Performance Fibre Reinforced Concrete: Material

3.1 Problem statement

The advanced knowledge in cementitious materials has led to the development of High Performance Concrete (HPC). Compared to a Normal Strength Concrete (NSC), a HPC shows several advantages; higher mechanical properties allowing the development of slender structures, a higher compactness, a better homogeneity therefore a higher durability, a rapid development of shrinkage and a reduced creep, a rapid formwork removal subsequently the construction phases may be accelerated, etc. Several constructions around the world i.e. buildings, offshore platforms and bridges, highlighted the benefits of HPC from a technical and an economical point of view.

The steel fibres can be added starting from a NSC to an Ultra-High Performance Concrete. Different steel fibres types and shapes, adapted for each concrete strength, were developed (Figure 3-3). Since 2000, Ultra-High Performance Fibre Reinforced Concrete UHPFRC have known an important development and several applications. The UPHFRC is characterized by its high compressive strength which is superior to 150 MPa and their high fibres content often equal to 160 kg/m^3 offering a high tensile toughness. However, the high properties and the material high cost have limiting the extend of UHPFRC applications to thin and highly stressed elements or also to elements exposed to aggressive agents. For conventional applications, like beams and slabs, the combination of an HPC with less steel fibres is more suitable. The material investigated in this thesis is named High Performance Fibre Reinforced Concrete (HPFRC). HPFRC stands between conventional SFRC and UHPFRC. HPFRC is characterized by a compressive strength between 60 to 150 MPa, a matrix comprising coarse aggregates and a limited fibres dosage (Figure 3-1). However, its mechanical properties, particularly the post-cracking response, are sufficient for structural applications. Currently there are no design codes or recommendations for HPFRC. Therefore the use of HPFRC is limited despite its numerous technical and economical advantages. This fact is principally due to the lack of knowledge concerning its properties and its structural behaviour.

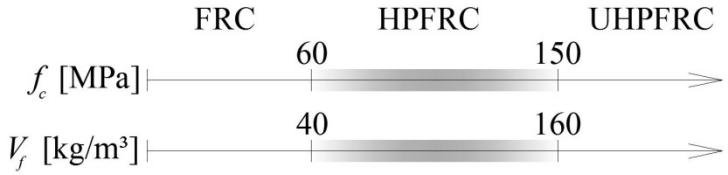

Figure 3-1: Classification according to the compressive strength and fibre content

Self-Compacting Concrete (SCC) mixes are characterized by their high workability and thus do not require mechanical vibration (Figure 3-2**)**. Therefore SCC necessitates fewer workers for its placement and the environmental impact of the vibration (i.e. the noise generated) is eliminated. SCC technology can be applied to a concrete going from a NCS to a UHPC. Currently, SCC with a compressive strength varying between 50 to 80 MPa has replaced conventional concrete in the precast industry. Moreover, the stationary processes in precast plants offer optimal possibilities for using HPC and steel fibres. The combination of HPC with SCC criterion and steel fibres is the following step in the development and the optimization of this industry.

Originally, the concrete was composed of three components: cement, aggregates, and water. Over the years, the number and the diversity of components available have noticeably increased, enabling the production of HPC and UHPC. Compared to NSC, High and Ultra-High Performance Concrete cannot be produced without a particular attention being paid to the different components and their content. The choice of the different components depends principally on the availability, the practices, the cost and the targeted performances. An important point to mention is the control of mixing and casting processes in order to reach the targeted performances of the material and the structure.

Figure 3-2: Self Compacting Concrete

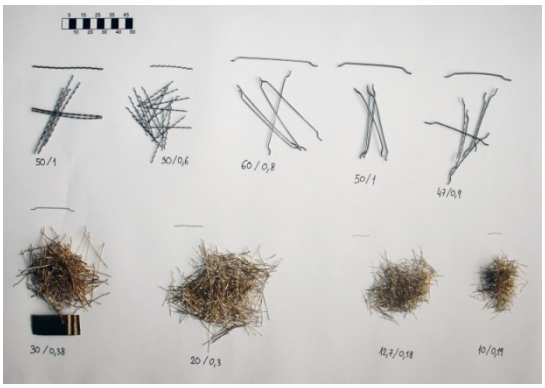

Figure 3-3: Different type of steel fibres

Compared to concrete without fibres the principal mechanical property of a SFRC is its post-cracking tensile response which depends on several parameters such as the fibres content, the fibres type, the strength of the matrix, the casting process, etc. This tensile strength may be considered in the design of the structure. However, the test for the determination of the post-cracking tensile relationship is not as easy as a simple compression test on a cube or a cylinder. Several testing methods were developed often in indirect way like bending tests on prisms or plates. These tests require some assumptions for the determination of the post-cracking tensile relationship (Figure 3-4). Moreover, the identified constitutive tensile laws may not be adequately representative of the structure response if the casting process is not considered mainly for SCC mixes.

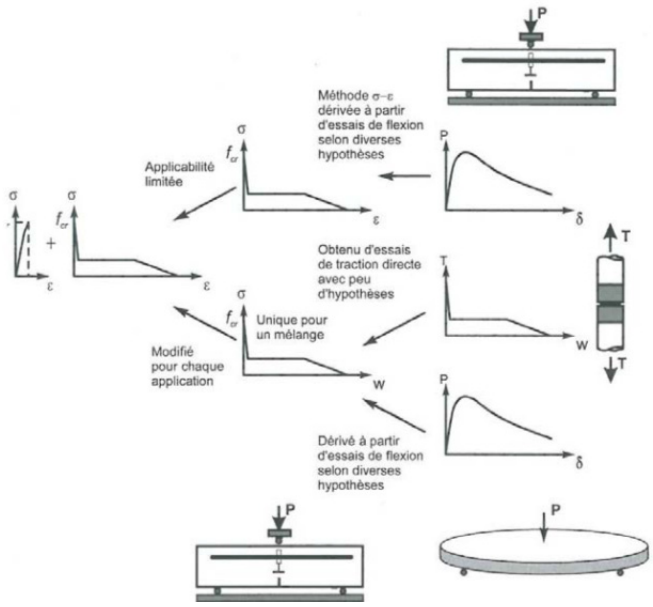

Figure 3-4: Determination of the post-cracking tensile relationship on the basis of different testing methods [MAS2008]

3.2 Program and objectives

In this study different mix design of High Performance Fibres Reinforced Concrete were developed for structural applications and used in the different studies on shear and punching shear presented in Chapters 4 and 5. An Ultra-High Performance Concrete developed by the Group *Vicat* was also used for the study on the punching shear of thin slabs in Chapter 5.

In this chapter the following points are developed: Firstly, the mix design process of a self-compacting HPFRC adapted for the precast industry is presented. Secondly, the principal mechanical properties of a HPFRC and a UHPFRC used in the different parts of this thesis are detailed. And finally, different testing methods have been used in order to identify the post-cracking relationship of HPFRC and UHPFRC. The main objectives of this study were:

- developing a High Performance Fibre Reinforced Concrete with the Self Compacting Concrete criterion and a compressive strength around 100 MPa, mainly for the precast industry,
- determining the principal mechanical properties, particularly the post-cracking response,
- comparing different models for the determination of the tensile constitutive laws.

3.3 Formulations

3.3.1 High Performance Fibre Reinforced Concrete - A

The development of a High Performance Fibre Reinforced Concrete with the SCC criterion is presented herein. This mix is used for the study on shear strength of pre-tensioned members in chapter 4. In order to join technical, economical, and casting criteria, the concrete mix design must meet the following requirements: self-compacting concrete with a minimum slump flow of 600 mm, a compressive strength on cylinder f_{cm} of 100 MPa at 28 days, use of local aggregates and different fibre contents of 0, 20, 40, 60 and 80 kg/m^3.

The preliminary works were focused on optimizing the aggregate grading and the binder composition (cement + additions) according to the works of de Larrard [LAR2000] and tests. In order to reach the Self Compacting criterion, three methods are available for the mix design; 1) combination of superplasticizer and high content of mineral powders, 2) combination of superplasticizer and viscosity-modifying admixture with or without defoaming agents, 3) a mix of methods 1) and 2). The first method was chosen because a HPC already includes a large part of powders (cement, fine sand, reactive cementitious materials, etc). According to the literature, the powder content for a SSC mix is around 450 to 600 kg/m^3. A Portland cement CEM I 52,5R of *Vigier* or *Jura Cement* was used; the aggregate grading curve is represented in Figure 3-6. The maximum cement content was limited to 500 kg/m^3 in order to limit the heat of hydration and problems with the alkali-silica reaction (ASR). Three different reactive cementitious materials were selected; fly ash (*Holcim Hydrolent*®), blast furnace slag and densified silica fume (*SikaFume® HR-TU*). The reactive coefficient *k*, determined on ISO mortar, was around 0.7 for the fly ash, 0.9 for the blast furnace slag and 1 to 1.5 for the silica fume. The water on binder ratio was selected in order to reach the targeted compressive strength. Different types of superplasticizer were selected and tested with the binder. The superplasticizer was dosed at the saturation point according to the AFREM grout method [LAR1997]. This method consists

in measuring the flow time of the grout through a March's cone and it is also possible to estimate the viscosity [ROY2004]. The strength of the paste may be evaluated with the following equations:

$$f_{paste} = 13.4 \cdot R_{c28} \cdot \left(1 + \rho_c \cdot \frac{W + A}{C_{eq}}\right)^{-2.85} \quad (3\text{-}1)$$

$$C_{eq} = C + \sum k \cdot P_z \quad (3\text{-}2)$$

Where R_{c28} is the compressive strength at 28 days of cement on ISO mortar, ρ_c the cement density, W the volume of water and A the volume of air, C_{eq} the equivalent mass of cement, k the reactive coefficient of the pozzolan addition and P_z is the mass.

The sand and aggregates came from the Fribourg region, Switzerland, and the origin was fluvioglacial. They were separated in three aggregate grading classes of 0-4 mm for the sand, 4-8 mm for the gravel and 8-16 mm for the coarse aggregates. These classes are the standards in Switzerland. It was chosen to keep the coarse aggregates (8 - 16 mm) in order to limit the shrinkage. Moreover, the coarse aggregates transmit a large part of the stress. The main properties of aggregates were defined; the density, the absorption coefficient, the aggregate grading, etc. The aggregate grading curves are represented in Figure 3-6. The aggregate grading was optimized with the software *BetonLab* developed by de Larrard [LAR2000]. In aggregate arrangement loaded in compression, the large grains are the most loaded and transmit the force. In a random arrangement, some large particles can be in direct contact. The biggest stresses are found through these points. We can make the same analogy with cement composite; the paste between two large aggregates will be highly stressed (Figure 3-5). In a given arrangement, the largest interval between two large particles is called maximal paste thickness (MPT). The MPT is defined as follows:

$$MPT = d_g \left(\sqrt[3]{\frac{g^*}{g}} - 1\right) \quad (3\text{-}3)$$

$$f_{matrix} = f_{paste} \cdot MPT^{-0.13} \quad (3\text{-}4)$$

Where d_g is the maximum aggregate size, g is the volume of aggregates in a unity of concrete volume and g^* is the compactness of aggregates.

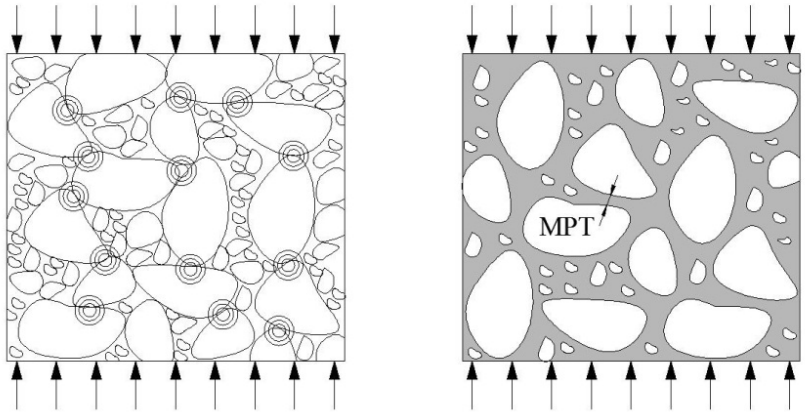

Figure 3-5: Aggregates arrangement without and with paste loaded in compression

However, for high strength concrete or lightweight concrete the strength of aggregates can limit the concrete strength. Moreover, the bond between the paste and aggregates can also limit the concrete strength. This different effect was highlighted by de Larrard [LAR2000]. The concrete compressive strength f_c may be evaluated with the following equation:

$$f_c = \frac{p \cdot f_{matrix}}{q \cdot f_{matrix} + 1} \tag{3-5}$$

Where p and q are two empirical constants depending on the aggregates. In this study they were determined on the basis of the compressive tests. For the used aggregates p = 0.671 and q = 0.002 were adopted.

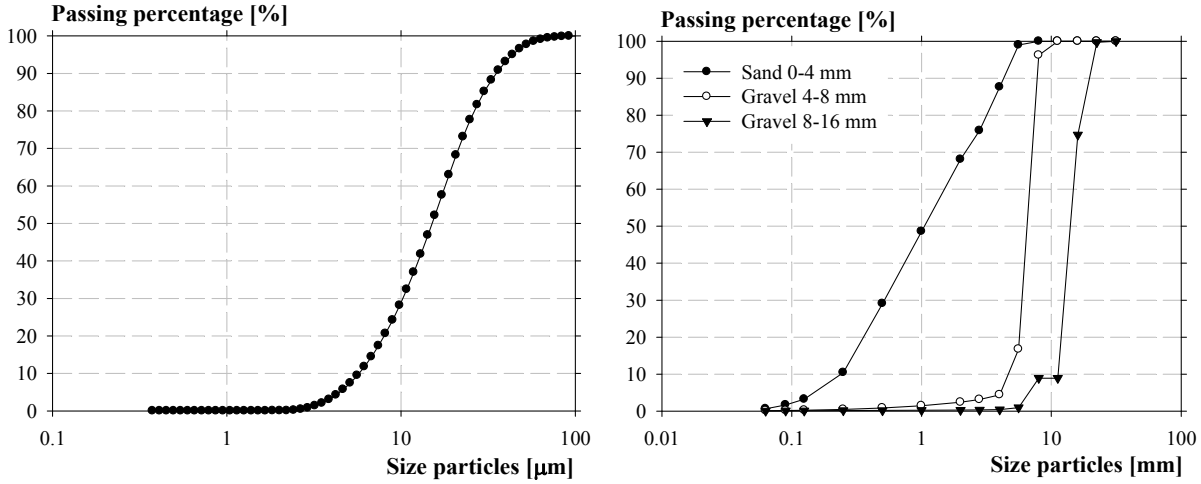

Figure 3-6: Granulometric curves of cement and aggregates

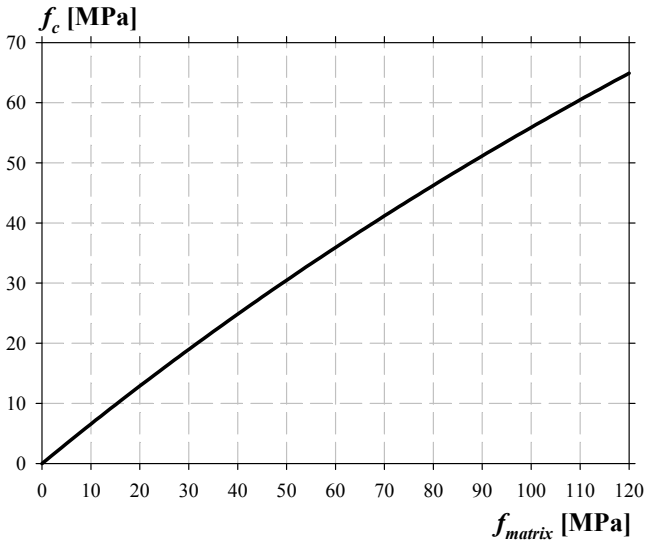

Figure 3-7: Influence of the coefficient p and q on the compressive strength

End-hooked fibres type *Bekaert Dramix RC-80/30-BP* were used. These fibres have a length of 30 mm and a diameter of 0.375 mm with a tensile strength of 2300 MPa. The fibre disturbs the arrangement of coarse aggregates (Figure 3-8). Therefore, in comparison with the optimum aggregates arrangement simulated with *BetonLab* the ratio of sand content related to aggregates was increased. The mix was

designed for a fibre content of 60 kg/m^3. Several testing batches were performed at the laboratory (Figure 3-9). Some compositions are summarized in Table 3-1.

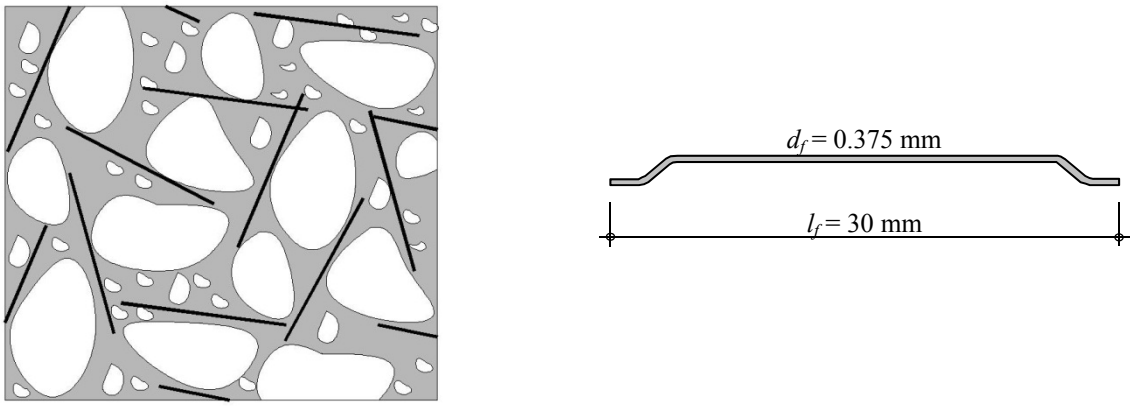

Figure 3-8: Aggregates arrangement with fibres and shape of used end-hooked fibres

Figure 3-9: Testing batches at the laboratory

Table 3-1: Mixes proportion of testing batches and corresponding compressive strength

Cement CEM I 52,5R *Jura Cement*	[kg/m^3]	450	400	400	450	450	475	450	475
Silica fume *SikaFume® HR/TU*	[kg/m^3]	-	50	50	50	50	50	50	50
Blast furnace slag	[kg/m^3]	150	150	100	100	-	-	100	75
Fly ash *Holcim Hydrolent®*	[kg/m^3]	-	-	-	-	100	-	-	-
Effective water	[kg/m^3]	155	155	160	170	160	160	160	160
Superplasticizer *Sika ViscoCrete® 20 HE*	[kg/m^3]	10	10	12.5	15.8	9	9	9	9.5
Steel fibres *Bekaert RC-80/30-BP*	[kg/m^3]	60							
Compressive strength f_{cm}	[MPa]	88 28 days	100 28 days	104 28 days	68 7 days	70 7 days	73 7 days	75 7 days	77 7 days

The mixes composed of blast furnace slag and silica fume showed better rheology and a higher strength compared to a binary binder. However, from a logistic point of view it was not possible to use a ternary binder in the ready mix concrete plant. Therefore a binder composed of cement and silica fume was chosen. After preliminary tests in laboratory, two mixes G11 and G2 were tested in a ready mix concrete plant.

Table 3-2: HPC and HPFRC first mix proportion

Composition		**G1**	**G2**
Steel fibres *Bekaert Dramix RC-80/30-BP*	[kg/m^3]	0	40
Cement CEM I 52,5R *Vigier Péry*	[kg/m^3]	475	
Silica fume *SikaFume HR/TU*	[kg/m^3]	50	
Effective water	[l/m^3]	160	
W/B ratio	[%]	0.30 *(with k=1)*	
Superplasticizer *Sika ViscoCrete®-20 PRO*	[kg/m^3]	9.5	
Sand 0-4 mm	[kg/m^3]	842 *50%*	
Coarse aggregate 4-8 mm	[kg/m^3]	166 *10%*	
Coarse aggregate 8-16 mm	[kg/m^3]	663 *40%*	

Table 3-3: Properties of HPC and HPFRC G1 and G2

Formulation	Slump flow [mm]	$f_{cm,7}$ [MPa]	$f_{cm,28}$ [MPa]	$f_{cm,cube28}$ [MPa]
G1	600	73	78	/
G2	620	66	86	99

Clearly, the mechanical properties of the first mixes were not sufficient. Moreover, the control of the effective water was complicated in comparison to the laboratory. The W/B was also too high. The densified silica fume showed a very low reactive coefficient. On the basis of this full-scale experiment, the mix was adapted. Microsilica in slurry type *Elkem EMSAC 500S* was selected. The effective water was reduced and the aggregates arrangement was adapted. Finally, five mixes were developed and were distinguished by their fibres content (Table 3–4).

Table 3-4: HPC and HPFRC final mix proportion

Composition		**A1**	**A2**	**A3**	**A4**	**A5**
Steel fibres *Bekaert Dramix RC-80/30-BP*	[kg/m^3]	0	20	40	60	80
Cement CEM I 52,5R *Vigier Péry*	[kg/m^3]	475				
Silica fume *Elkem EMSAC 500S*	[kg/m^3]	62.5 solids content				
Effective water	[l/m^3]	138				
W/B ratio	[%]	0.25 *(with k=1)*				
Superplasticizer *Sika ViscoCrete®-20 PRO*	[kg/m^3]	9.0			11.0	
Sand 0-4 mm	[kg/m^3]	732 *47%*			782 *50%*	
Coarse aggregate 4-8 mm	[kg/m^3]	197 *13%*			203 *13%*	
Coarse aggregate 8-16 mm	[kg/m^3]	608 *40%*			579 *37%*	

The properties at fresh state of HPC and HPFRC –A (Table 3-5) were directly measured at the precast plant during the casting process of the test beams (Chapter 4).

Table 3-5: Properties at fresh state of HPC and HPFRC - A

Concrete	Date of casting	Slump Flow [mm]	Density [kg/m^3]	Air Temp. [C°]	Concrete Temp. [C°]
A1	20/8/2010	600	2410	25.5	23.5
A2	27/8/2010	650	2442	26.0	27.5
A3		700	2438	26.0	27.0
A4	10/9/2010	620	2469	23.0	25.0
A5		460	2500	23.0	24.5
A1	13/9/2010	620	2405	22.0	24.0
A4	15/9/2010	650	2465	21.0	25.5

The casting process of test beams has highlighted the following points. The steel fibres decreased the workability and in presence of dense reinforcement, the aggregates were blocked due to the mesh formed by the fibres. The compositions A1 to A3 (40 kg/m^3) didn't show any problems, due to the easy flow of the material which could be cast without vibration. But for composition A4 (60 kg/m^3) and A5 (80 kg/m^3) a vibration along the reinforcement was needed.

Remarks concerning the mix design:

The SCC criterion may be easily reached for HPC due to the high powder content. The recommended minimum powder content is around 550 to 600 kg/m^3. Different reactive cementitious materials may be selected, but the silica fume shows better results. The silica fume improves the rheology and the strength. A ternary binder is also possible and allows limiting the cement content.

Different superplasticizer must be tested preliminary with the binder. The AFREM grout method for HPC [LAR1996] is appropriate in order to evaluate the binder rheology with superplasticizer. The aggregates arrangement was optimized with the software *BetonLab*. However, in comparison with the optimal aggregates arrangement simulated with *BetonLab*, the ratio sand to coarse aggregates must be increased in order to take into account the fibres.

The steel fibres disturb the aggregates arrangement and decrease the flowability. Moreover, in presence of dense reinforcement, the fibres and coarse aggregates are blocked. The critical content depends on the fibre type and the ratio length to diameter l_f/d_f [GRU2001]. In this formulation end-hooked fibres of 30 mm length and a ratio l_f/d_f of 80 were used. The observed critical content was around 60 kg/m^3. For high content, a mix of different type of fibres is possible (e.g. 50% end-hooked fibres and 50% straight fibres).

3.3.2 High Performance Fibre Reinforced Concrete - B

This HPFRC mix was developed for the study on punching shear of slabs series 1 in chapter 5. In order to meet technical, economical, and casting criteria, the composition of concrete must meet the following requirements: a compressive strength on cylinder f_{cm} of 100 MPa, use of local aggregates, and different fibres contents of 0, 20, 40, 60 and 80 kg/m^3. Five compositions were developed and were distinguished by their fibres content. The cementitious matrix was composed of Portland cement CEM II/A-D 52,5R including 8% (mass) of silica fume. The grading curve of cement is represented in Figure 3-10. The binder to cement ratio was fixed to 0.3 and the content of superplastizer was adapted depending on the fibres volume. The sand and coarse aggregates came from the Fribourg region and the origin was fluvioglacial. They were separated in two grading classes of 0-4 mm for the sand and 4-8 mm for the coarse aggregates. The grading curves are represented in Figure 3-10. End-hooked fibres type *Bekaert Dramix RC-80/30-BP* were used. For this mix, the SCC criterion was not required but with small adjustments (higher powder content) it can be reached.

Table 3-6: HPC and HPFRC compositions

Composition		**B1**	**B2**	**B3**	**B4**	**B5**
Steel fibres *Bekaert Dramix RC-80/30-BP*	[kg/m^3]	0	20	40	60	80
Cement CEM II/A-D 52,5R *Holcim Siggenthal*	[kg/m^3]	500				
Effective water	[l/m^3]	150				
W/B ratio	[%]	0.3				
Superplastizer *Sika ViscoCrete-20 HE*	[kg/m^3]	5	5.5	6.5	7	7.5
Sand 0-4 mm	[kg/m^3]	917 *50%*				
Coarse aggregate 4-8 mm	[kg/m^3]	917 *50%*				

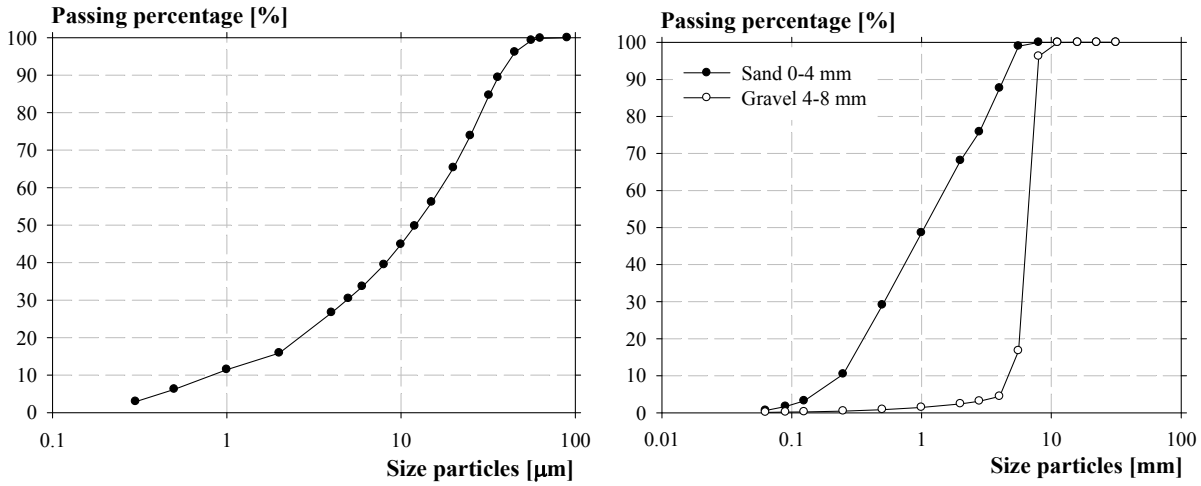

Figure 3-10: Grading curves of cement and aggregates

3.3.3 Ultra-High Performance Fibre Reinforced Concrete - BCV

This UHPFRC was used for the study on punching shear of slabs series 2 in chapter 5. The *Béton Composite Vicat BCV®* is developed by the Group *Vicat* and belongs to the family of UHPFRC as defined in the interim recommendations of the French Civil Engineering Association (AFGC) [AFGC2002]. The BCV offered particular potential in innovative achievements such as the La Chabotte's bridge on the highway A51 in France. The BCV is a self-compacting concrete but shows a high viscosity like all UHPFRC mixes. All components of the matrix are selected and strictly verified, the maximum particle size is 3 mm. For this study, two mixes were analysed, which are distinguished by their fibre volume and fibres type. The BCV-1% is only composed of short straight fibres, while the BCV-2% is composed of a mix between short and long straight fibres. The BCV-1% is not a UHPFRC as properly defined due to its lower tensile response, but from an economical point of view it's interesting to mix conventional reinforcement with a reduced fibres volume.

Table 3-7: UHPFRC compositions

Composition		**BCV-1%A**	**BCV-2%**
Steel fibres 12.7/0.175 mm	[kg/m^3]	79	52
Steel fibres 20/0.3 mm	[kg/m^3]	-	106
Premix *Vicat VPI Montluel*	[kg/m^3]	2090	
Water added	[l/m^3]	210	
W/B ratio	[%]	> 0.2	
Superplastizer *Sika ViscoCrete Tempo 10*	[kg/m^3]	28.7	

3.4 Mechanical properties

3.4.1 Compressive properties of HPC and HPFRC - A

The compressive strength f_c and the Young's modulus E_c of the HPC and the HPFRC were defined on 4 cylinders ϕ150 x 300 mm tested the same day on the corresponding beams. The Young's modulus and the compression strength tests were performed on a compression testing machine of 4000 kN capacity of the firm *Walter & Bai*. The Young's modulus was defined according to the Swiss standard SIA 262/1 [SIA262/1], the level of stress was fixed at a value of 40 MPa.

Table 3-8: Compressive strength and Young's modulus

Formulation	Beams	Fibres content [kg/m^3]	*Age*	Density [kg/m^3]	E_{cm} [GPa]	f_{cm} [MPa]
A1	AV-1	0	32	2410* *16***	37900 *840*	94.9 *1.5*
A2	AV-2	20	39	2440 *36*	40340 *1565*	91.6 *4.0*
A3	AV-3	40	39	2440 *32*	39750 *80*	97.5 *3.1*
A4	AV-4	60	39	2500 *20*	37160 *880*	102.2 *2.1*
A5	AV-5	80	40	2500 *2*	37250 *670*	100.8 *2.2*
A1	AF-1	0	78	2450 *19*	36380 *2250*	93.6 *4.0*
A4	AF-2	40	79	2475 *19*	37500 *900*	106.6 *1.9*

** Average ** Standard deviation*

Figure 3-11: HPFRC cylinders after the failure, formulations B2 to B5 and E-modulus test

The steel fibres have a limited effect on the compressive strength. The macro-fibres do not contribute to micro-cracking due to compression [ROS1998]. The compressive strength is primarily due to the compactness and the W/C ratio. At strength levels above 60 MPa, concrete shows a fragile behaviour. The fibres avoid any brutal fracturing and confer a ductile post-peak behaviour. Compared to the targeted compressive strength, the effective strength is lower. This is due to the aggregates strength and the control of the water to binder ratio in the mixing plant.

3.4.2 Compressive properties of HPC and HPFRC - B

The compressive strength f_c and the Young's modulus E_c of the HPC and the HPFRC were defined on cylinders ϕ110 x 220 mm tested at 28 days. The Young's modulus and the compression strength tests were performed on a compression testing machine of 4000 kN capacity of the firm *Walter & Bai*. The Young's modulus was defined according to the Swiss standard SIA 262/1 [SIA262/1], the level of stress was fixed at a value of 40 MPa.

Table 3-9: Compressive strength and Young's modulus

Formulation	Fibre content [kg/m^3]	Density [kg/m^3]	E_{cm} [GPa]	f_{cm} [MPa]
B1	0	2420* *13***	44200 *3300*	99 *9.0*
B2	20	2430 *14*	41500 *5200*	102 *4.6*
B3	40	2460 *22*	46800 *3200*	102 *4.9*
B4	60	2470 *20*	40200 *800*	102 *4.6*
B5	80	2500 *15*	43300 *6800*	106 *3.0*

** Average ** Standard deviation*

3.4.3 Compressive properties of UHPFRC

The compressive strength f_c and the Young's modulus E_c of the UHPFRC were defined on cylinders ϕ110 x 220 mm and cube 100 mm^3 tested the same day of the corresponding slabs. The Young's modulus and the compression strength tests were performed on the same testing machine of the HPFRC. The Young's modulus was defined according to the Swiss standard SIA 262/1 [SIA262/1], the level of stress was fixed at a value of 50 MPa.

Table 3-10: Compressive strength and Young's modulus, average values.

Formulation	Fibre content [%]	Density [kg/m^3]	E_{cm} [GPa]	f_{cm} [MPa]	f_{ccm} [MPa]
BCV-1%A	1	2480* *19***	45700 *500*	157 *3.5*	140 *4.2*
BCV-2%	2	2530 *41*	42700 *1300*	152 *8.0*	158 *4.1*

** Average ** Standard deviation*

3.4.4 Tensile properties of HPC - A

The tensile strength f_{ct} of the HPC was defined using double punch tests and 4-points bending tests. Double punch tests were performed in a compression testing machine on 8 cylinders ϕ150 x 150 mm at load rate of 0.02 MPa/s. The cylinders were loaded in compression at the centre throughout two steel punches of 37.5 mm diameter. The tensile strength was defined in the following way

$$f_{ct} = \frac{F_u}{\pi \cdot \left(0.6 \cdot b \cdot h - \left(a/2\right)^2\right)} \tag{3-6}$$

where F_u is the peak load obtained during the double punch test, b = 150 mm; h = 150 mm and a is the diameter of the punch a = 37.5 mm.

Figure 3-12: Double punching test on HPC cylinders

The four-point bending tests were carried on specimens with a square cross section of 150 mm and a length of 700 mm. They were tested in a universal testing machine. The prisms were simply supported on steel roller supports with a clear span of 600 mm. The loads were applied via steel rollers at 1/3 and 2/3 of the span. The central deflection was increased at a rate of 0.2 mm/s. Applied load P, deflection at centre δ, were monitored by the load cell and the LVDTs, respectively.

Table 3-11: Tensile strengths of HPC

Formulation	f_{ct} double punch test [MPa]	$f_{ct,flex}$ [MPa]	$f_{ct,flex}/f_{ct}$ [-]
B1	5.3* *0.26***	5.7 *0.33*	1.08

** Average ** Standard deviation*

On the basis of failure plane observations, all aggregates were broken (Figure 3-12).

3.4.5 Post cracking response of HPFRC - A

Three-point bending tests on notched prisms were carried out according to the European standard EN 14651 [EN14651] (point 2.1.5.2). The specimens had a square cross section of 150 mm and a length of 550 mm and were notched at the centre on a depth of 25 mm. They were tested in a universal testing machine. The prisms were simply supported on steel roller supports with a clear span of 500 mm. A single load was applied on the centre via a steel roller. The central deflection was increased at a rate of 0.2 mm/s. the applied load F, the deflection at centre δ and the Crack Mouth Opening Displacement $CMOD$, were monitored respectively by the load cell, the LVDTs and the strain gauge transducers (Figure 3-14).

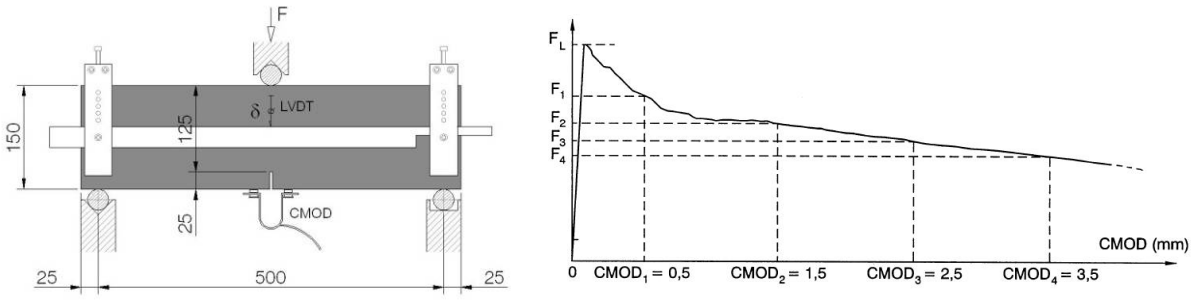

Figure 3-13: 3-points bending test setup on notched prisms and typical response with identified values

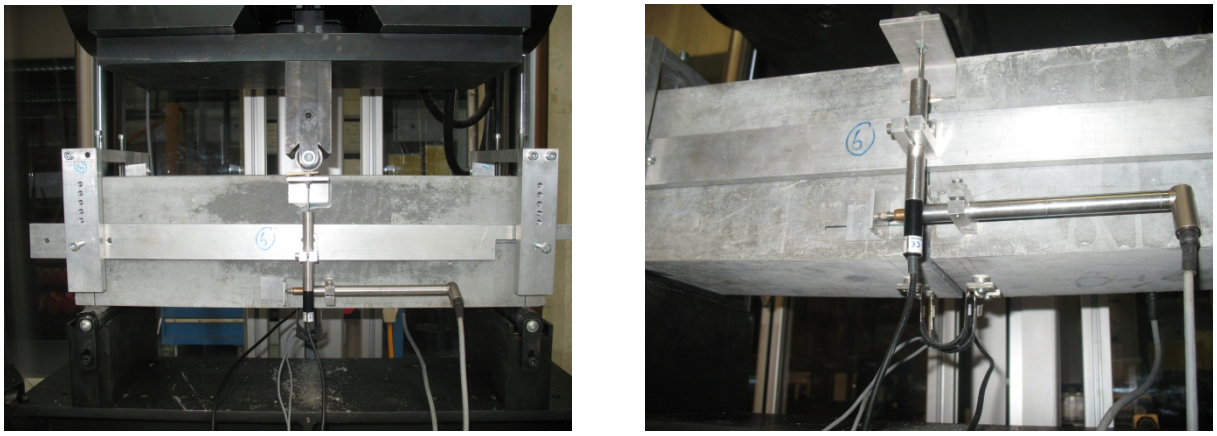

Figure 3-14: Views of loading and measurement arrangement

According to the standard EN 14651 [EN14651], the Limit Of Proportionality LOP f_{ctL} is identified and four different values of the residual tensile strength f_{R1}, f_{R2}, f_{R3}, and f_{R4} which correspond respectively to different values of the $CMOD$ = 0.5, 1.5, 2.5 and 3.5 mm (Figure 3-13). The residual strength is defined considering an elastic stress distribution as follows.

$$f_{Ri} = \frac{3 \cdot F_i \cdot L}{2 \cdot b \cdot h_n^{\,2}} \tag{3-7}$$

Where F_i is the force corresponding to different values of the $CMOD$, L the span, b the wide and h_n the depth in the notched cross-section.

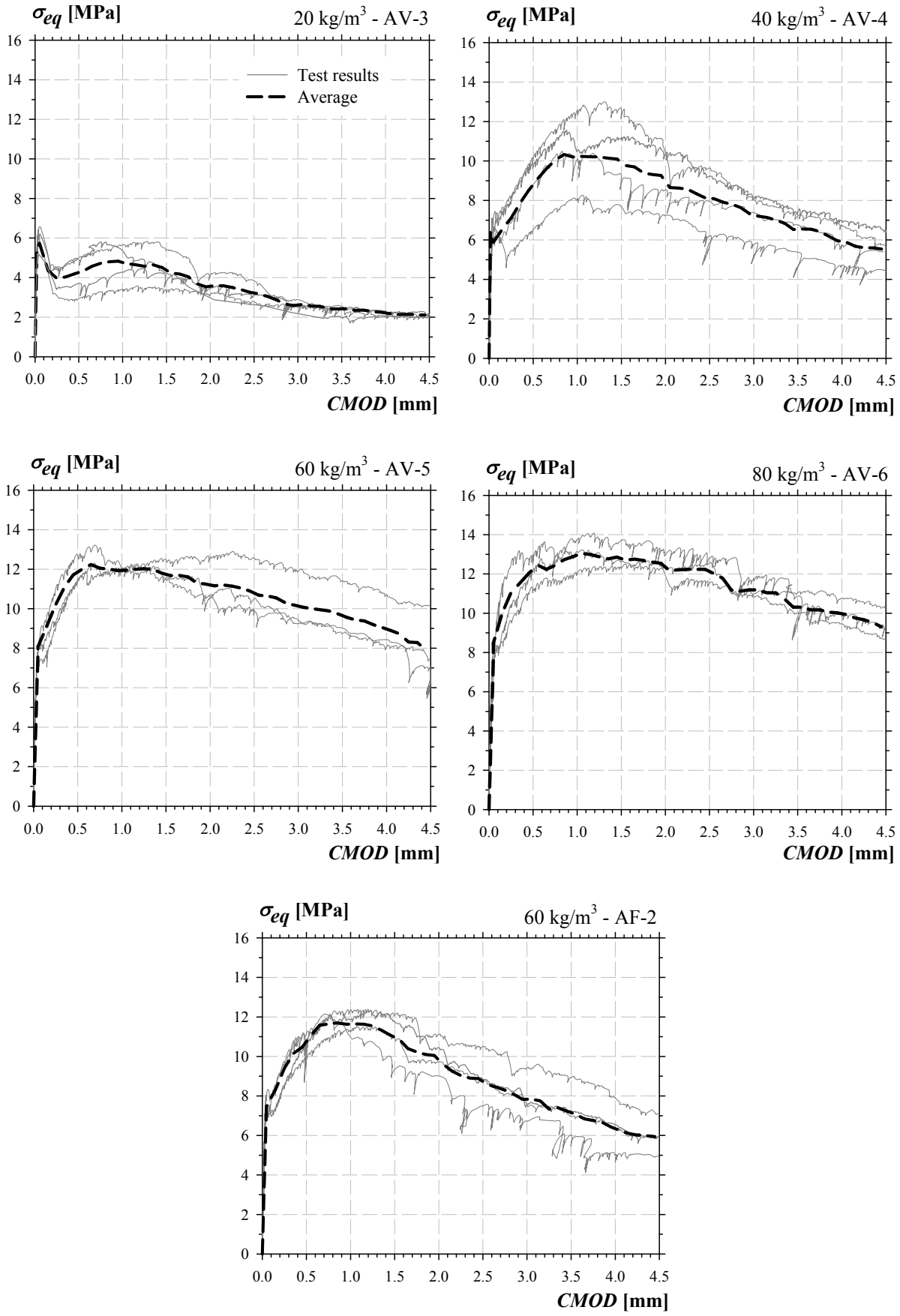

Figure 3-15: Equivalent bending stress vs crack mouth opening displacement of HPFRC-A notched prisms

Table 3-12: Post-cracking residual strengths according to EN 14651

HPFRC	Beams	Fibre content [kg/m^3]	$f^f_{ct.L}$ [MPa]	f_{R1} [MPa]	f_{R2} [MPa]	f_{R3} [MPa]	f_{R4} [MPa]
A2	AV-3	20	6.1* *0.59***	4.1 *1.02*	4.4 *0.87*	3.1 *0.58*	2.4 *0.23*
A3	AV-4	40	6.7 *0.41*	8.9 *1.65*	9.9 *2.17*	8.2 *1.68*	6.5 *1.28*
A4	AV-5	60	7.6 *0.34*	11.9 *0.66*	11.8 *0.56*	11.0 *1.38*	9.7 *1.47*
A4	AF-2	60	7.5 *0.42*	10.7 *0.50*	11.0 *1.24*	8.9 *1.24*	7.2 *1.37*
A5	AV-6	80	7.5 *0.80*	12.0 *0.75*	12.9 *0.76*	12.3 *0.69*	10.7 *0.56*

** Average ** Standard deviation*

The prisms in HPFRC A2 with only 20 kg/m^3 of fibres showed a softening behaviour in bending. Conversely, the other compositions exhibited a hardening behaviour in bending. The post cracking strength didn't increase proportionally to the fibre content. The difference in post cracking strength was important between a fibre content of 20 and 40 kg/m^3 and became lower for higher contents. These HPFRC showed a similar behaviour compared to the HPFRC-B which were developed for the slabs.

3.4.6 Post cracking response of HPFRC - B

In order to evaluate the post cracking response of the HPFRC-B, bending tests on notched prisms, uniaxial tensile tests and bending tests on square slabs were performed.

Bending tests on notched prisms

Three-point bending tests on notched prisms were carried out according to the European standard EN 14651 [EN14651]. Four prisms of each formulation were tested. The specimens and test setup was similar to HPFRC-A

Table 3-13: Post-cracking residual strengths according to EN 14651

HPFRC	Fibre content [kg/m^3]	$f^f_{ct.L}$ [MPa]	f_{R1} [MPa]	f_{R2} [MPa]	f_{R3} [MPa]	f_{R4} [MPa]
B2	20	6.1* *0.22***	4.3 *0.69*	4.2 *0.42*	2.6 *0.72*	1.8 *0.42*
B3	40	5.6 *0.34*	10.4 *1.99*	11.2 *1.28*	9.3 *1.93*	7.6 *1.59*
B4	60	6.6 *0.73*	12.5 *1.20*	12.4 *1.26*	10.2 *1.10*	8.6 *1.29*
B5	60	7.1 *0.60*	14.4 *1.25*	15.1 *1.62*	13.8 *1.81*	12.6 *1.52*

** Average ** Standard deviation*

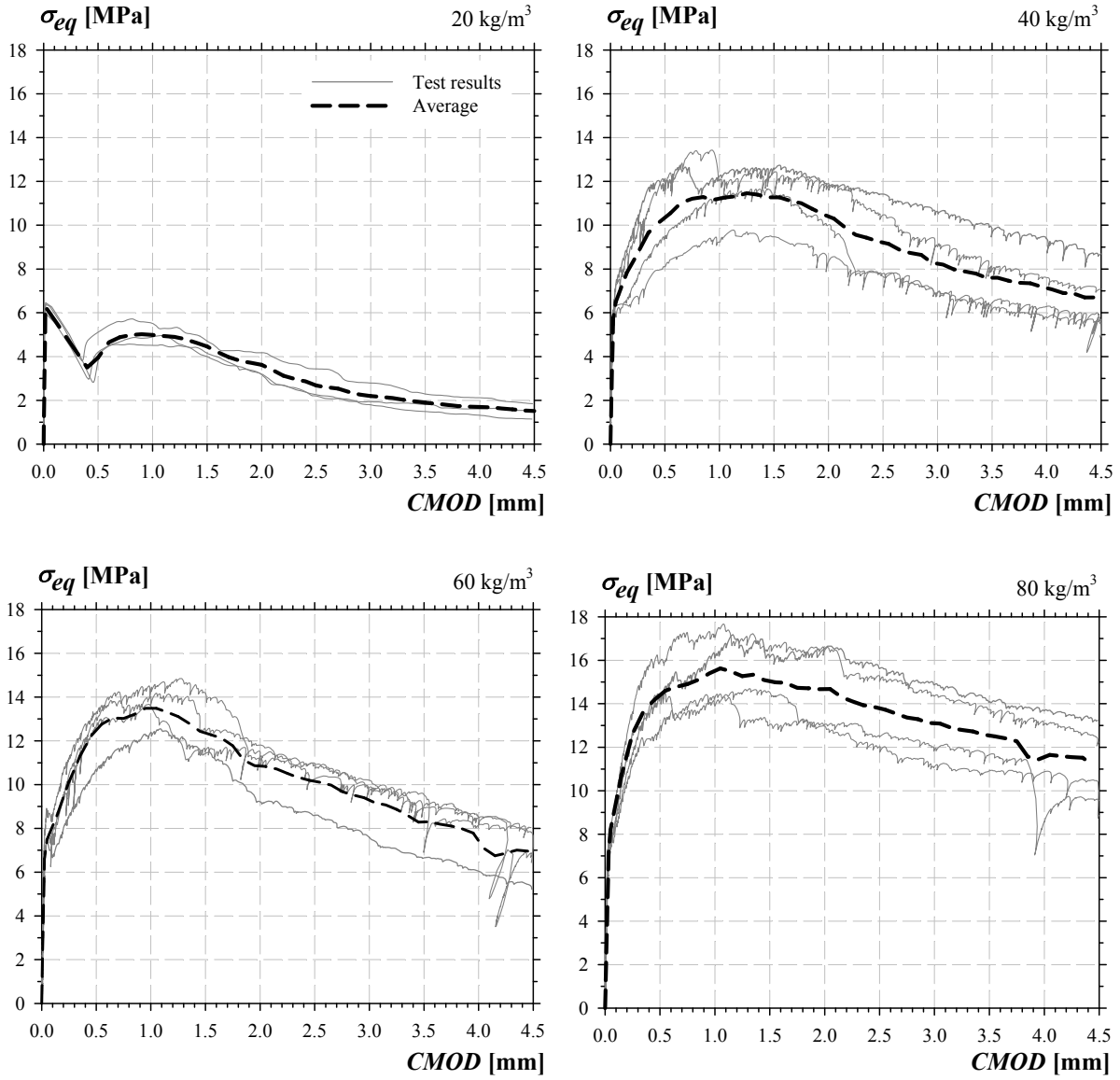

Figure 3-16: Curves equivalent bending stress vs crack mouth opening displacement of HPFRC-B notched prisms

The prisms in HPFRC B2 with only 20 kg/m^3 of fibres showed a softening behaviour in bending. Conversely, the other compositions exhibited a hardening behaviour in bending. The post cracking strength didn't increase proportionally to the fibre content. The difference in post cracking strength was important between a fibre content of 20 and 40 kg/m^3 and became lower for higher contents.

Uniaxial test

Uniaxial tests were performed on notched cores of 100 mm diameter and 100 mm high, drilled at 45° from concrete blocks cast like the slabs. The diameter in the fracture zone was 80 mm. Four cores of each formulation were tested. The tests were conducted on a universal testing machine and monitored in displacement. The cores were glued with epoxy glue between two aluminium cores. The cores were fixed to the testing machine through steel plates, no rotations were allowed. The vertical displacement was increased at a rate of 0.1 mm/s. Applied load *P* and crack opening displacement *COD*, were monitored by load cell and 3 LVDTs, respectively (Figure 3-17).

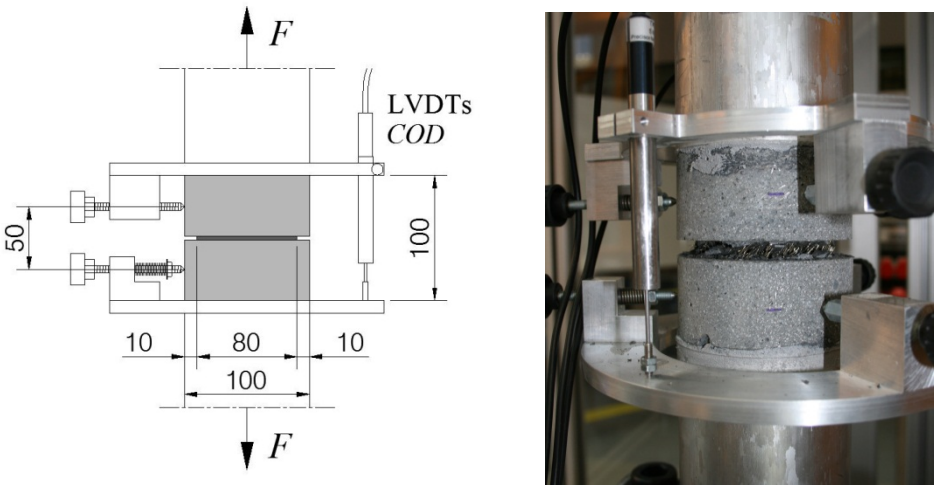

Figure 3-17: Uniaxial test setup on notched cores

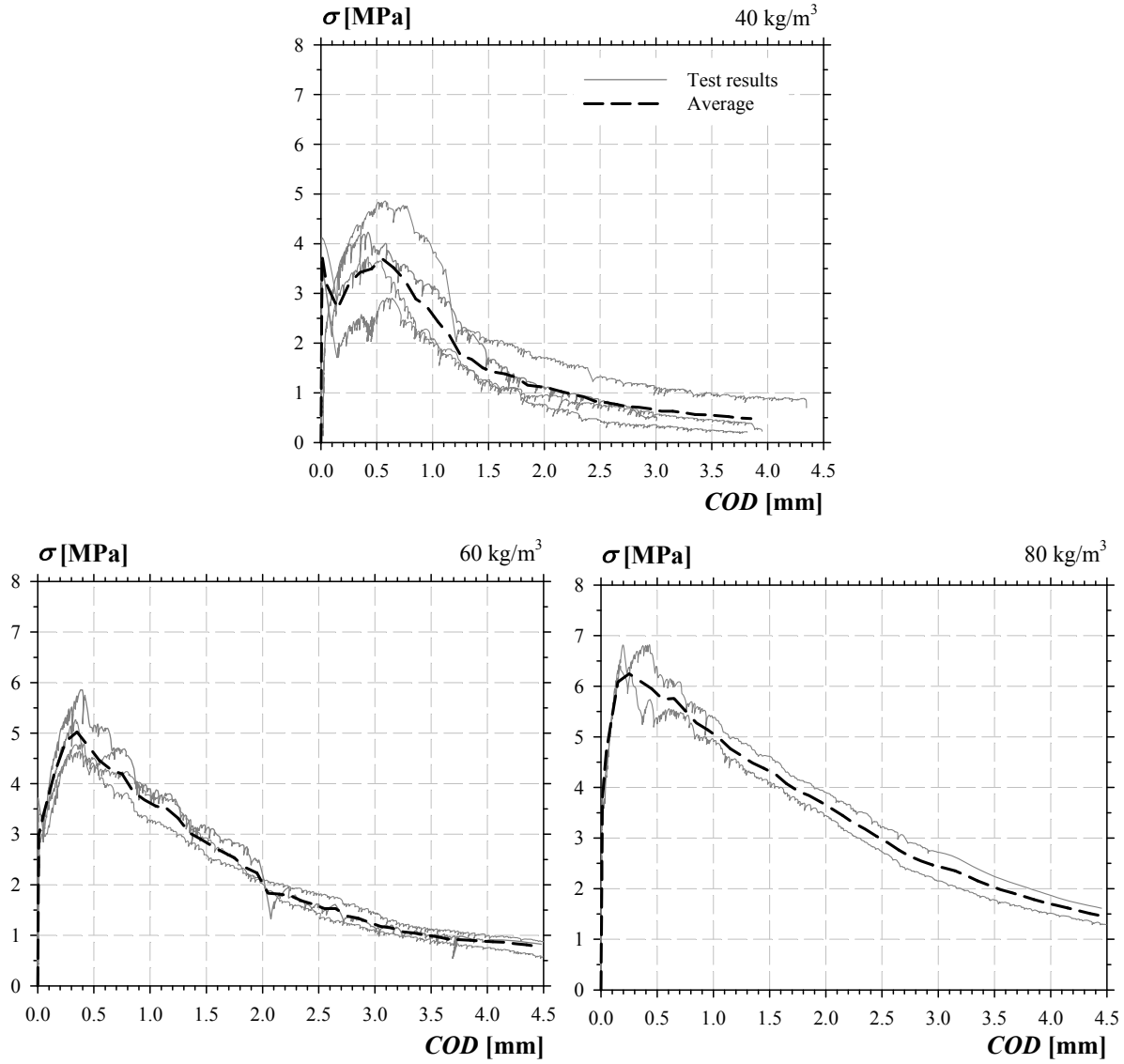

Figure 3-18: Curves stress vs crack opening displacement of the notched cores

Only the formulations B3, B4 and B5 were tested. The HPFRC B3 with a fibre content of 40 kg/m^3 exhibited a post-cracking strength inferior to the matrix strength. This HPFRC showed a drop after the cracking of the matrix following by a hardening phase and a softening branch. Conversely, the compositions B4 and B5 showed a hardening behaviour followed by a softening branch. The maximal post-cracking strength was 3.7, 5.0 and 6.2 MPa for the composition B3, B4 and B5 respectively. The strain corresponding to the maximal post-cracking strength decreased with the increasing of the fibre content.

Bending tests on square slabs

Load tests were carried out on square slabs according to the Swiss recommendation SIA162/6 [SIA1999]. Only one specimen was tested for each fibres volume. The specimens had 600 mm sides and 100 mm thick. They were tested on a rigid steel frame. The square slabs were simply supported along the edges with a clear span of 500 mm in each direction. A single load was applied on the slab centre via a square steel plate of 100 mm side. The central deflection was increased at a rate of 1.5 mm/min. Applied load P and deflection at centre δ, were monitored by load cell and LVDTs, respectively (Figure 3-19) to finally count the number of yield line n.

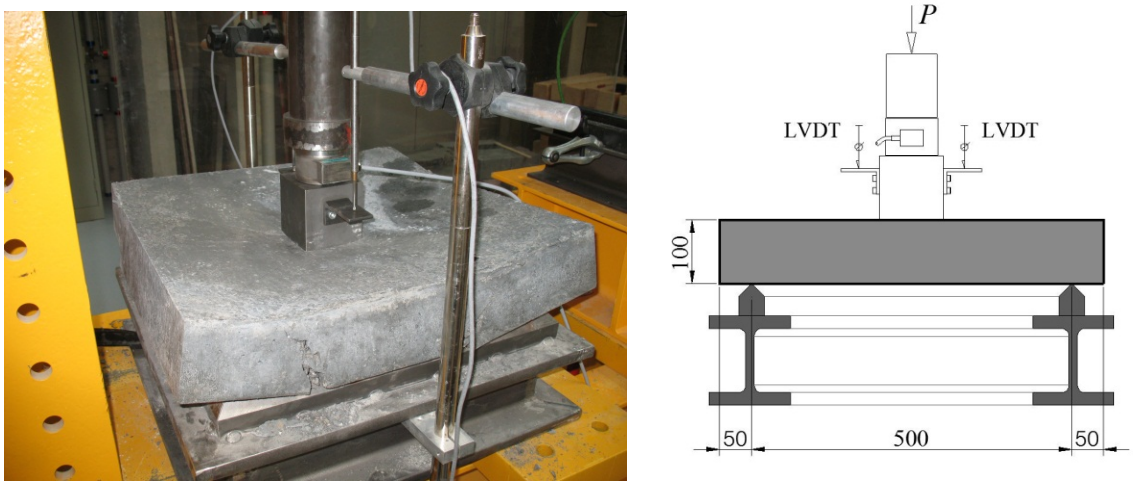

Figure 3-19: Bending test set-up on square slabs

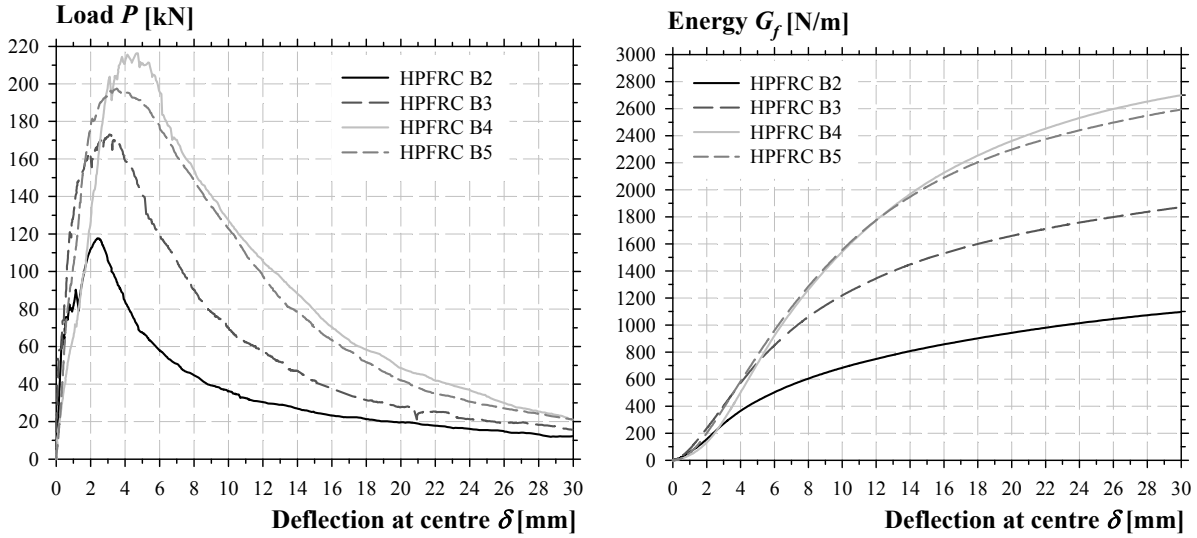

Figure 3-20: Curves Load and Energy vs deflection at centre of the square slabs

Figure 3-21: Typical cracking pattern of bending test on square slabs, n=5 and n=4

3.4.7 Post cracking response of UHPFRC

In order to evaluate the post cracking response of the UHPFRC, bending tests on prisms and uniaxial tensile tests were performed.

Bending tests on thin prism

According to the French interim recommendations for UHPFRC [AFGC2002], the post-cracking response of thin structural element is defined by bending test on prism with the same thickness. In order to evaluate the thickness influence on the post-cracking response, an experimental campaign was performed. The experimental study was composed of 32 prisms with a 200 mm wide and 700 mm length. The varying parameters were the thickness h and the fibre volume ratio V_f. The thicknesses h varied from 30 to 80 mm. The prisms were sawn on rectangular slabs of 700 x 500 x h mm and two prisms per slabs were cut. Four prisms of each formulation and thickness were tested. All slabs were cast in a similar manner without any vibration. The UHPFRC was poured in the middle of the formwork in a similar manner to the slabs for punching shear tests (Fig. 3-22).

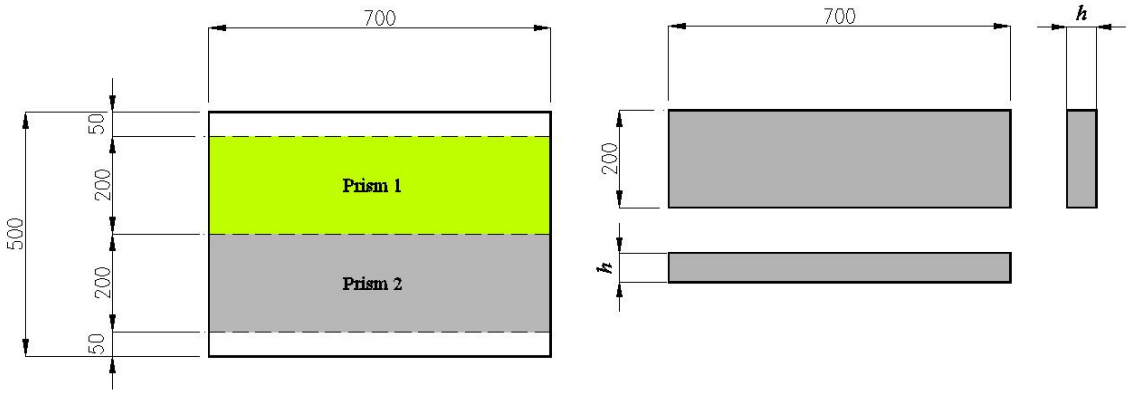

Figure 3-23: Geometry of the specimens

Figure 3-24: Casting process of the UHPFRC prisms

The prisms were tested in 3-points bending on a specially designed setup. The prisms were simply supported on steel roller supports with a clear span of 500 mm. A single load was applied on centre by a hydraulic jack via a steel roller. The tests were controlled in displacement by a servo-electronic system of the firm *Walter & Bai*. The central deflection was increased at a rate of 0.2 mm/min. The applied load P, the deflection at centre δ and the strains of the tensile face, were monitored by load cell, LVDT and strain gauge transducers Omega, respectively (Figure 3-25).

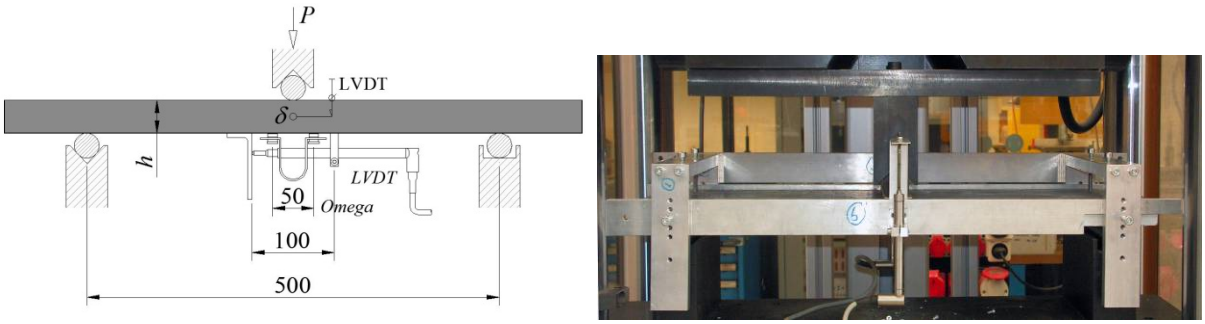

Figure 3-25: 3-points bending test setup of the UHPFRC prisms

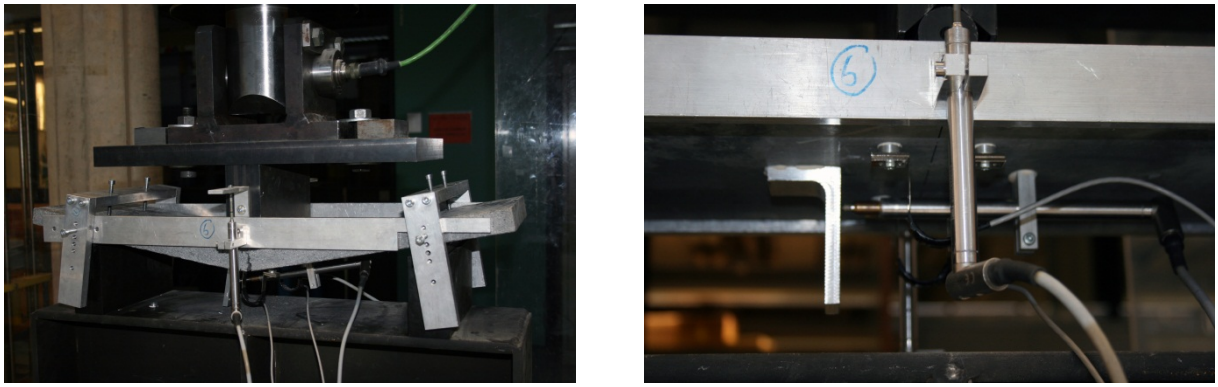

Figure 3-26: Views of the UHPFRC prisms test setup and measurement arrangement

The equivalent bending stress σ_{eq} is defined considering an elastic stress distribution even at the cracked state.

$$\sigma_{eq} = \frac{3 \cdot P \cdot L}{2 \cdot b \cdot h^2} \tag{3-8}$$

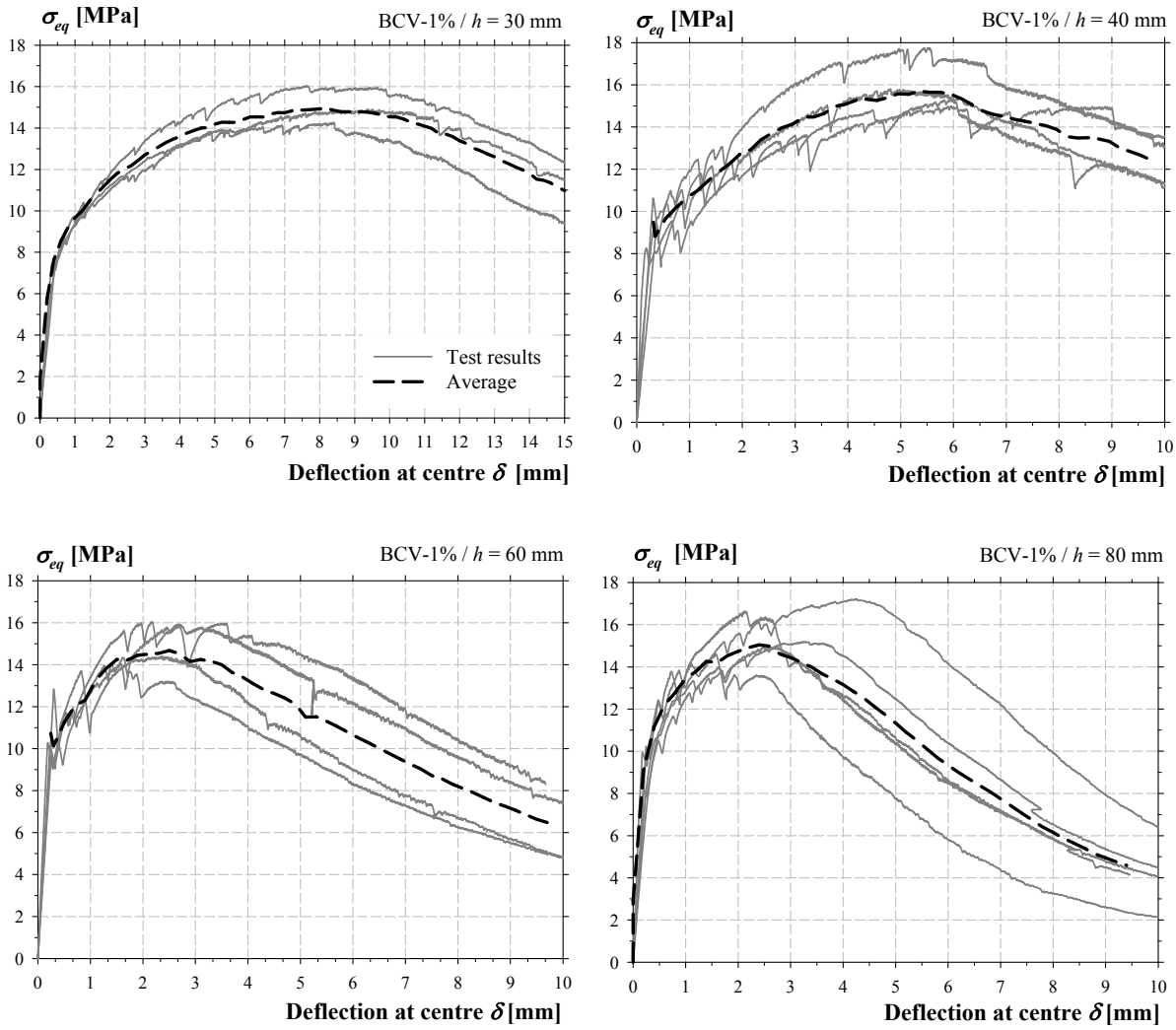

Figure 3-27: Curves equivalent bending stress vs deflection at centre of the prisms in BCV-1%

The prisms with a thichknesses of 40 to 80 mm exhibited a similar behaviour. From the cracking point to the peak load, the stiffness decreases progressively with the development of macro-cracking. Each small peaks on the curves correspond to the development of one crack. The prisms of 30 mm thick showed the development of micro-cracking. After the peak load, the deformations were concentrated on one macro-crack. The curves showed a softening branch, the load decreased progressively with the opening of the macro-crack.

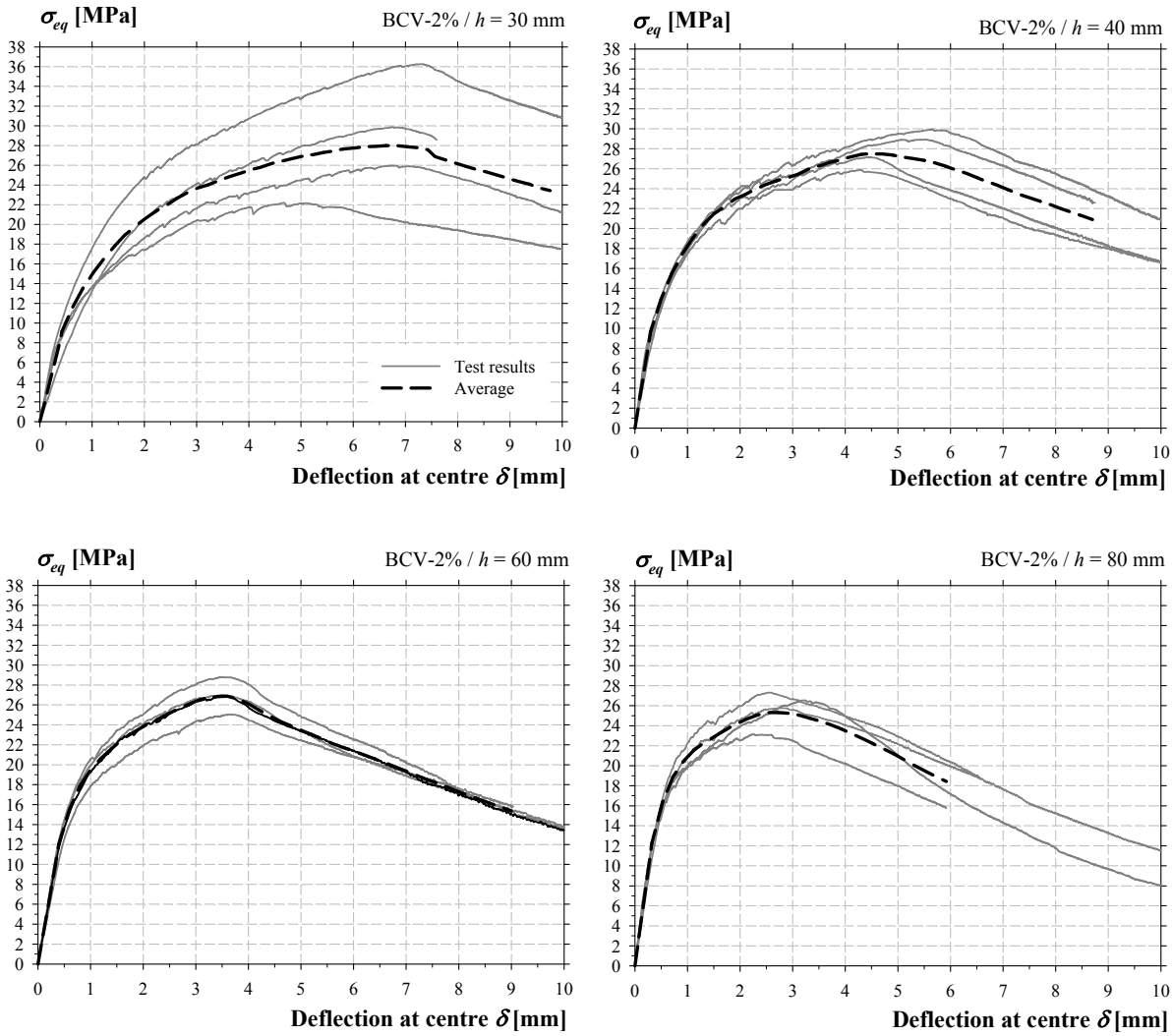

Figure 3-28: Curves equivalent bending stress vs deflection at centre of the prisms in BCV-2%

All prisms exhibited a similar behaviour. From the cracking point to the peak load, the stiffness decreased progressively with the development of micro-cracking. At the peak load, several micro-cracks formed one macro-crack. After this point, the curves showed a softening branch and the load decreased progressively with the opening of the macro-crack. The curves of the prisms with a thickness of 30 mm showed a large scatter compared to the other thicknesses.

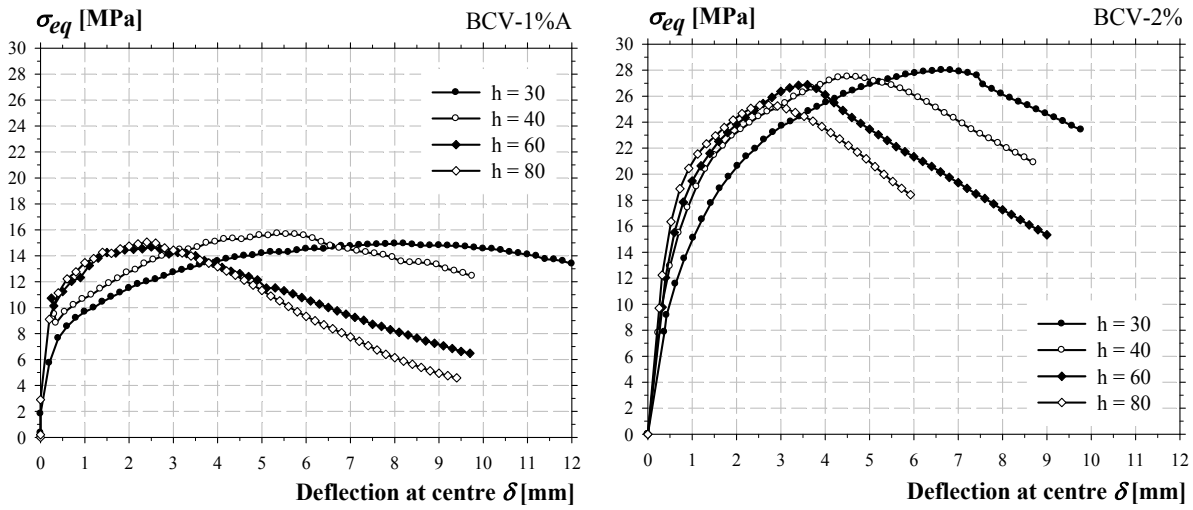

Figure 3-29: Average curves equivalent bending stress vs deflection at centre of the UHPFRC prisms

The two formulations showed a hardening behaviour in bending, with an equivalent bending stress going from 14 to 16 MPa for the BCV 1% and from 23 to 28 MPa for the BCV 2%. The bending stress was positively influenced by small thickness, especially for the BCV-2%. This fact is due to a preferential orientation of the 20 mm length fibres in thin specimens. For the BCV-1%, which was only composed of micro-fibres, this trend is not clear. The deflection capacity is inversely proportional to the thickness. The deflection capacity of thin prism in BCV-1% (h = 30 and 40 mm) is higher compared to the prisms in BCV-2%. For thick prisms the deflection capacity is similar between the mixes BCV-1% and 2%. The BCV-1% showed a cracking pattern composed of several macro-cracks. While the BCV-2% exhibited micro-cracking and one macro-crack after the peak load (Figure 3-30).

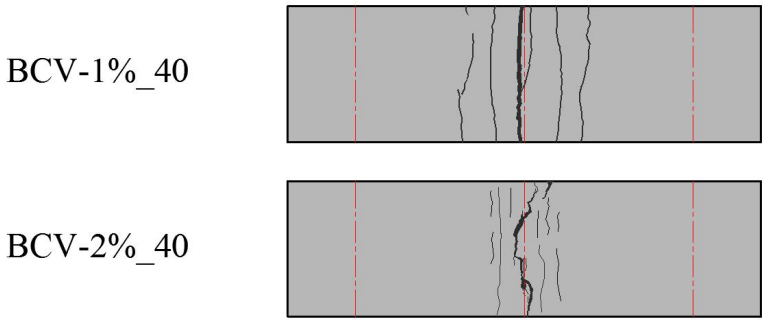

Figure 3-30: Typical cracking pattern of UHPFRC prisms, h = 40 mm

Bending test on notched prism

Three-point bending tests on notched prisms were carried out according to the French interim recommendations for UHPFRC [AFGC2002]. The specimens had a square cross section of 100 mm and a length of 400 mm and were notched at the centre on a depth of 10 mm. They were tested in a universal testing machine. The prisms were simply supported on steel roller supports with a clear span of 300 mm. A single load was applied on the centre via a steel roller. The central deflection was increased at a rate of 0.2 mm/s. the applied load P and the Crack Mouth Opening Displacement $CMOD$, were monitored respectively by the load cell and the strain gauge transducers (Figure 3-31).

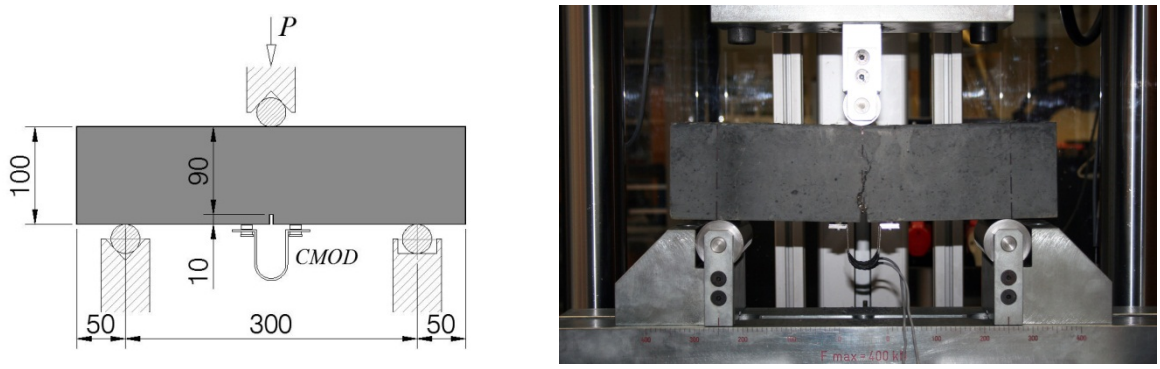

Figure 3-31: 3-points bending test setup on notched prisms in UHPFRC

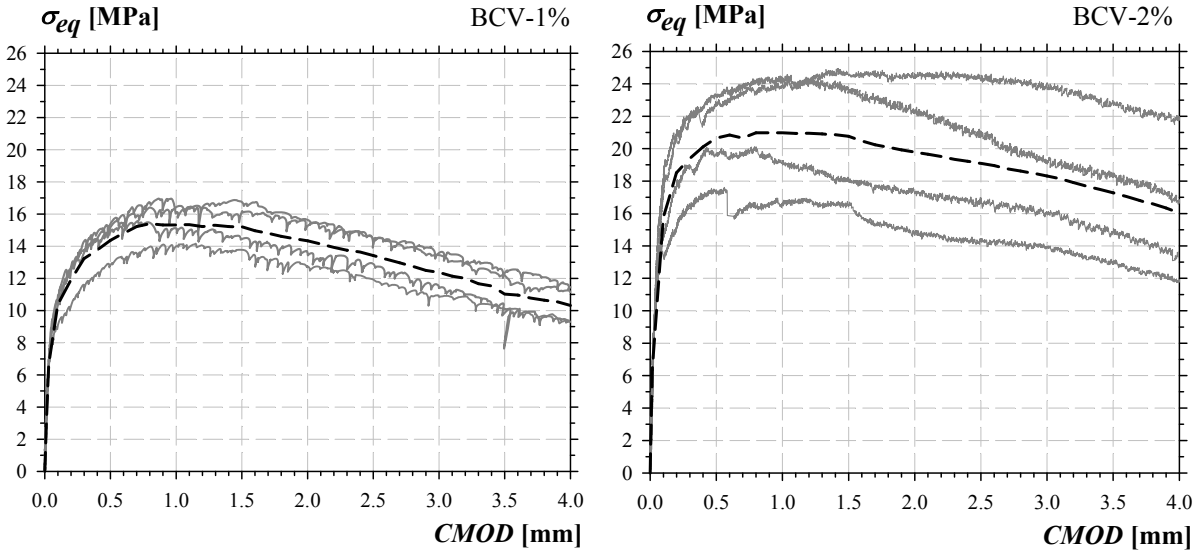

Figure 3-32: Curves equivalent bending stress vs crack mouth opening displacement of UHPFRC notched prisms

The two formulations showed a hardening behaviour in bending, with an equivalent bending stress going from 14 to 17 MPa for the BCV 1% and from 17 to 25 MPa for the BCV 2%. The test results of BCV-1% exhibited a low scatter compared to BCV-2%. In comparison with the bending test on thin un-notched prism, the equivalent bending stresses are in the same range.

Uniaxial tests

Uniaxial tests were performed on dog bone shaped specimens. The area in the fracture zone was 100 x 40 mm. Four specimens of each formulation were tested. The tests were conducted on a universal testing machine and monitored in displacement. The specimens were fixed in a specially designed setup. No rotations were allowed. The vertical displacement was increased at a rate of 0.1 mm/s. the applied load *P* and the longitudinal strains, were monitored respectively by the load cell, 4 LVDTs and 6 Omega (Figure 3-33).

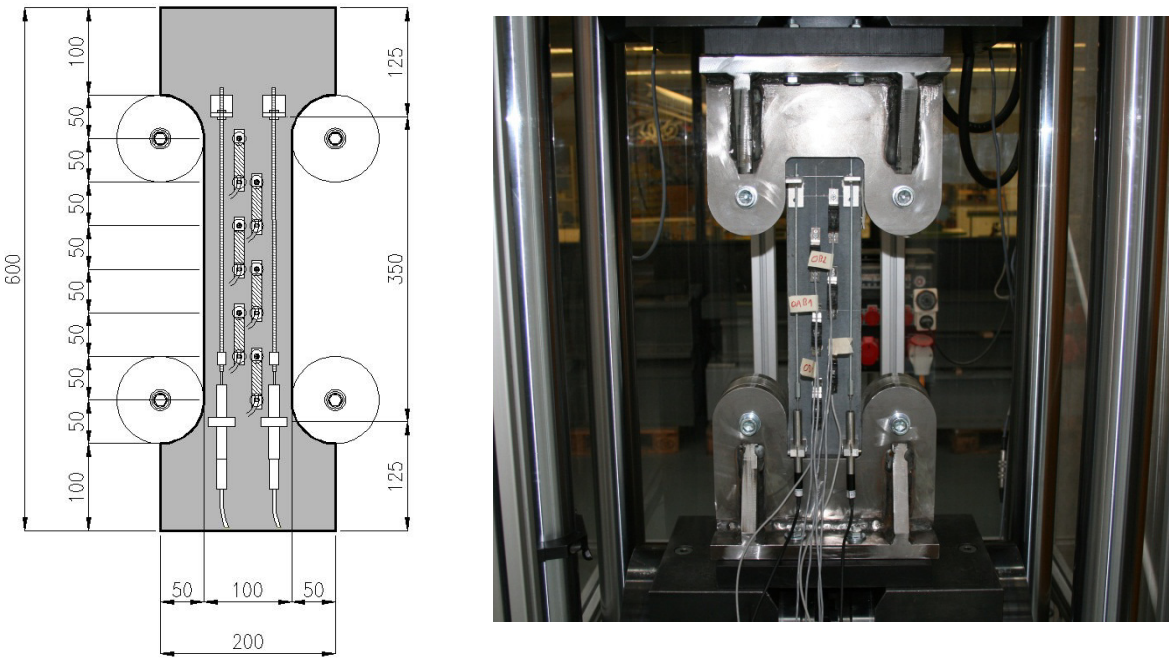

Figure 3-33: Uniaxial tensile test set-up of the UHPFRC "dog bones"

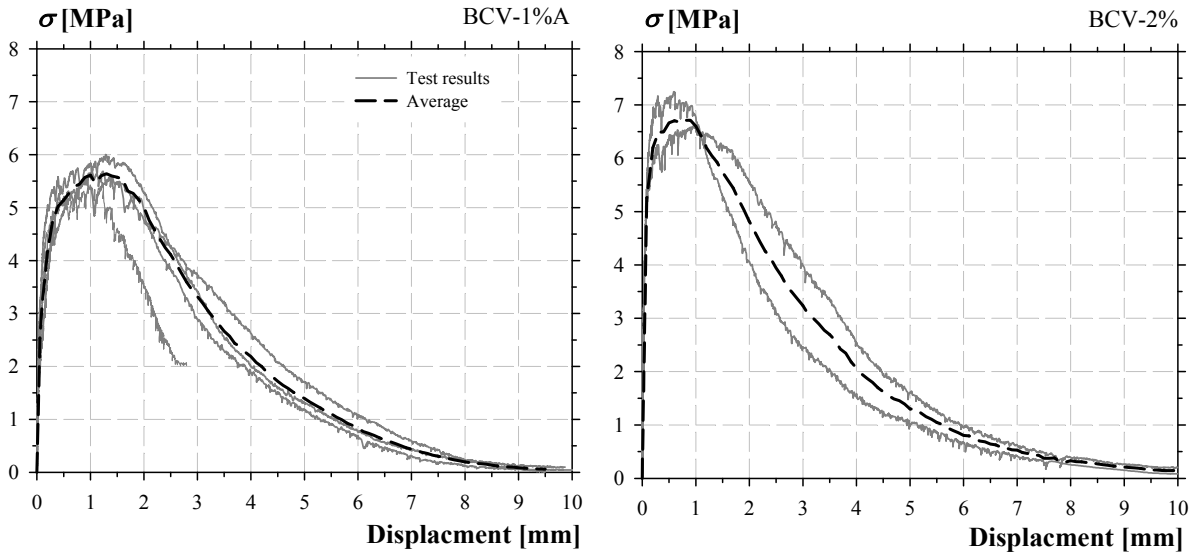

Figure 3-34: Curves stress vs total strain (LVDTs) of the UHPFRC "dog bones"

The BCV-1% showed a hardening behaviour with the development of several macro-cracks followed by a softening branch with the localisation of the strain on one macro-crack. The maximal strength is around 5.5 MPa. For the BCV-2%, only two specimens were valid, the other had important rotations. The formulation BCV-2% exhibited a hardening behaviour with the development of micro-cracking followed by a softening branch with the localisation of the strain on one macro-crack. The maximal strength was around 6.5 to 7 MPa. The ultimate strain of the micro-cracking phase measured by the Omega was around 2.5 mm/m. However more tests are necessary in order to confirm these values.

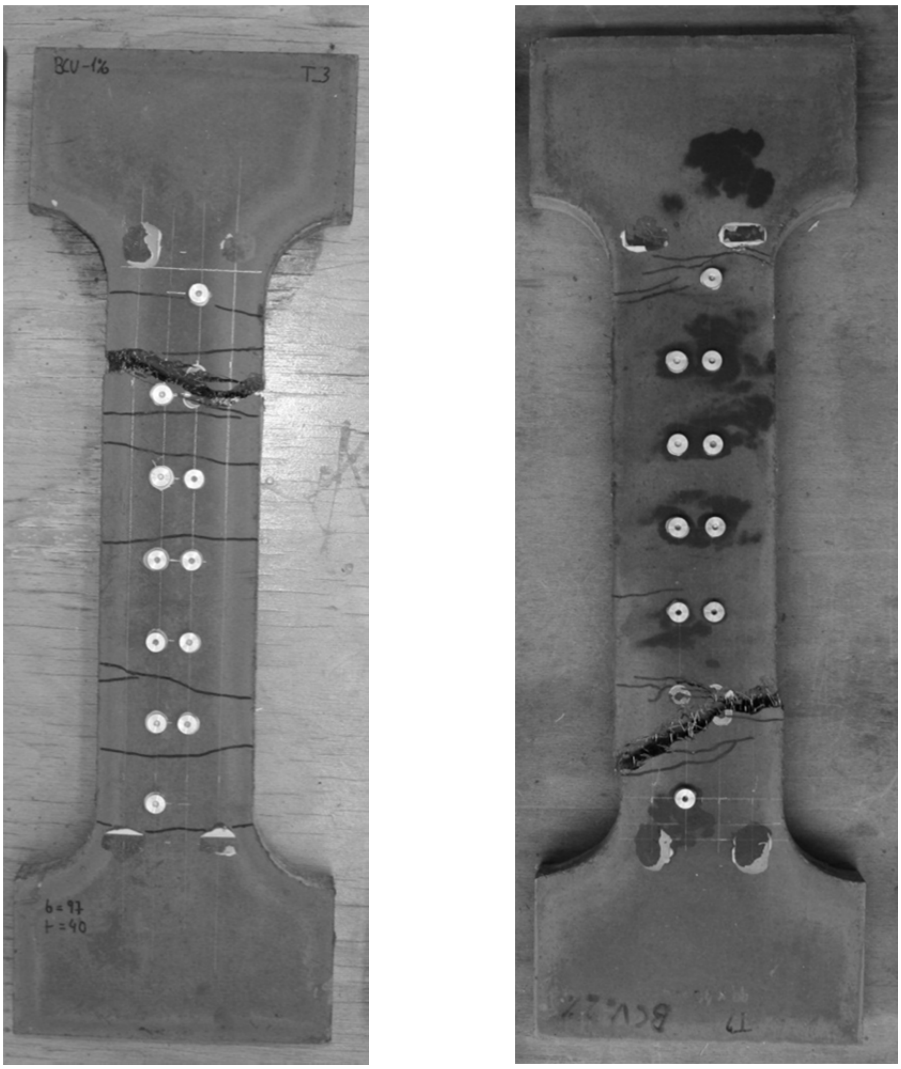

Figure 3-35: Typical cracking pattern of UHPFRC – 1% and 2%

The average cracks spacing s_m of UHPFRC – 1% was around 32 mm. This value corresponds to $2.5l_f$. The UHPFRC – 2% showed a multi-microcracking along the fracture zone. However this microcracking was difficult to observe visually.

3.5 Numerical analysis

3.5.1 Relationship based on tensile tests

The uniaxial tensile test is certainly the simplest method for determining the tensile relationship. On the basis of the average curve, a multi-linear relationship may be easily identified [RIL2002]. The ultimate crack opening w_u may be considered equal to $l_f/3$ or $l_f/2$. For HPFRC - B the ultimate crack opening was chosen to be equal to $l_f/3$ (w_u = 10 mm).

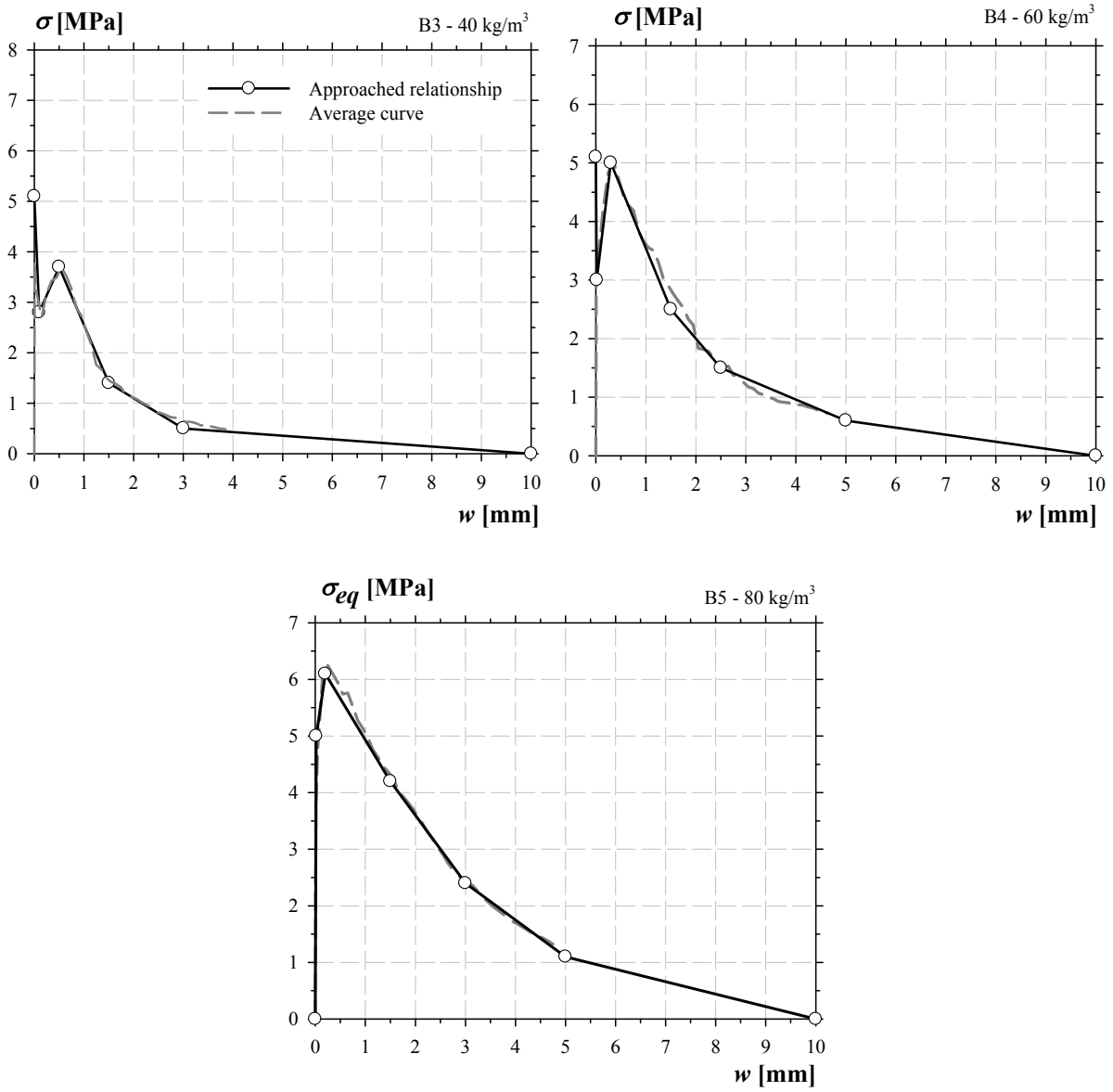

Figure 3-36: Identified multi-linear relationships of HPFRC – B

The uniaxial tensile test on UHPFRC showed a hardening behaviour with the development of several macro-cracks for BCV-1% and micro-cracking for BCV-2%. For UHPFRC-1%, the hardening phase was determined by dividing the relative displacement by the number of macro-cracks. For UHPFRC-2%, the hardening phase (pseudo-plastic phase) was identified from the strain measurement (Omega). The softening branch was approached by a multi-linear relationship. For UHPFRC the ultimate crack opening was chosen to $l_f/2$ (w_u = 6.5 mm for BCV-1% and w_u = 10 mm for BCV-2%).

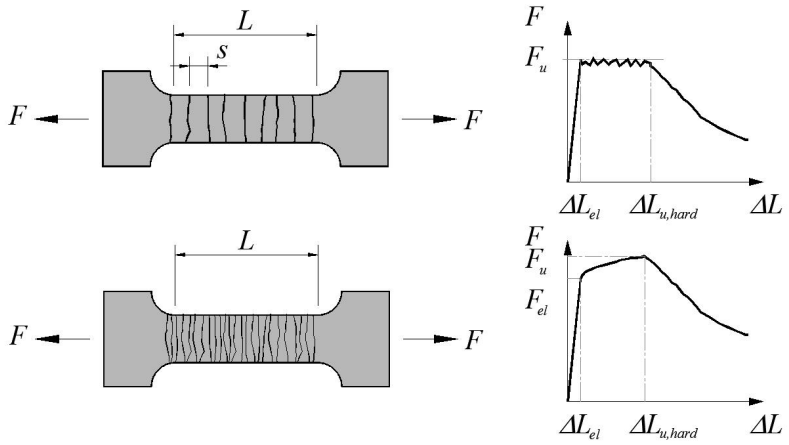

Figure 3-37: Identified values for the hardening branch of the relationship according to multi macro- or micro-cracking behaviour

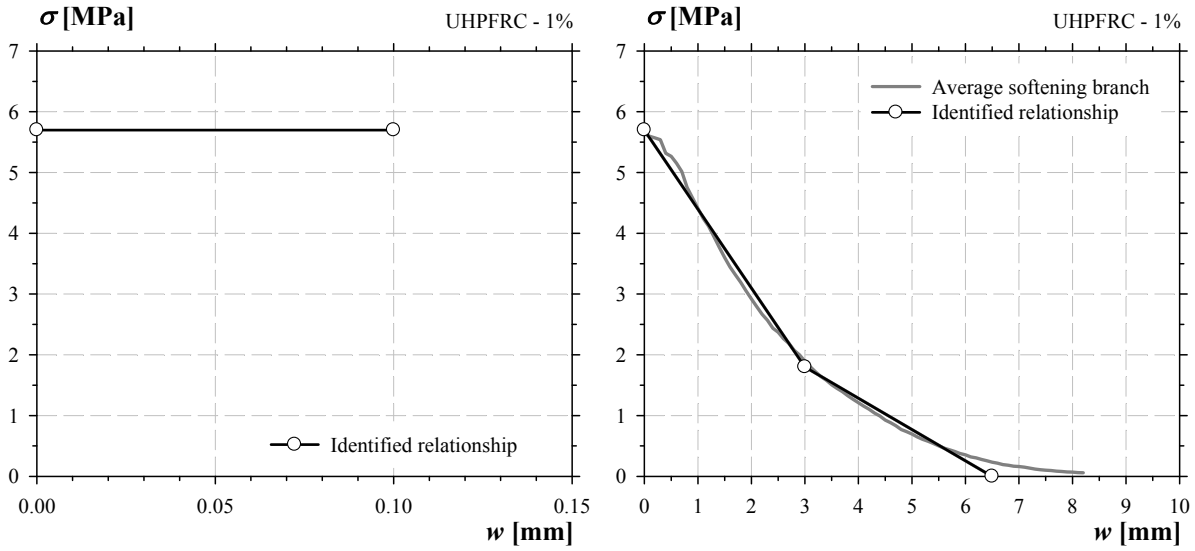

Figure 3-38: Identified multi-linear relationships of UHPFRC – 1%

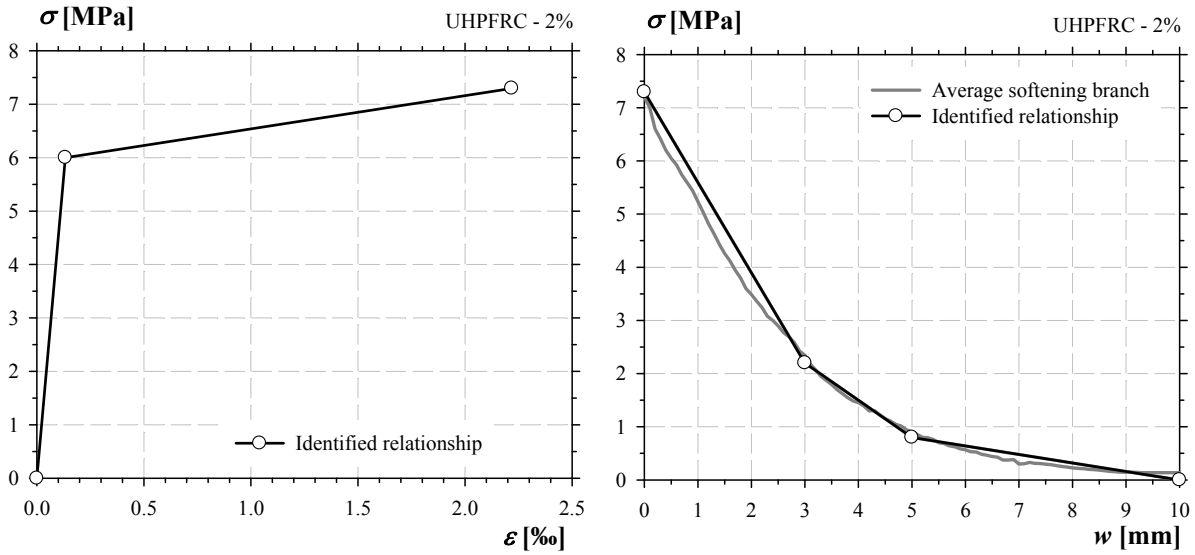

Figure 3-39: Identified multi-linear relationships of UHPFRC – 2%

3.5.2 Relationship based on inverse analysis

In French interim recommendations for UHPFRC [AFGC2002] an inverse analysis of three-points bending test on notched prism is proposed. The analysis is based on the assumption of a fictitious crack development. Two different parts are distinguished: the uncracked part where the stress distribution corresponds to linear elastic behaviour and the cracked part where stress distribution depends on the post-cracking relationship. On the basis of the equilibrium equations and a continuum relation (developed in point 2.1.5.3) the problem can be solved with an iterative process. The method was applied on average data moment - *CMOD*. For HPFRC and UHPFRC the ultimate crack opening was chosen to be equal to $l_f/3$ (w_u = 10 mm).

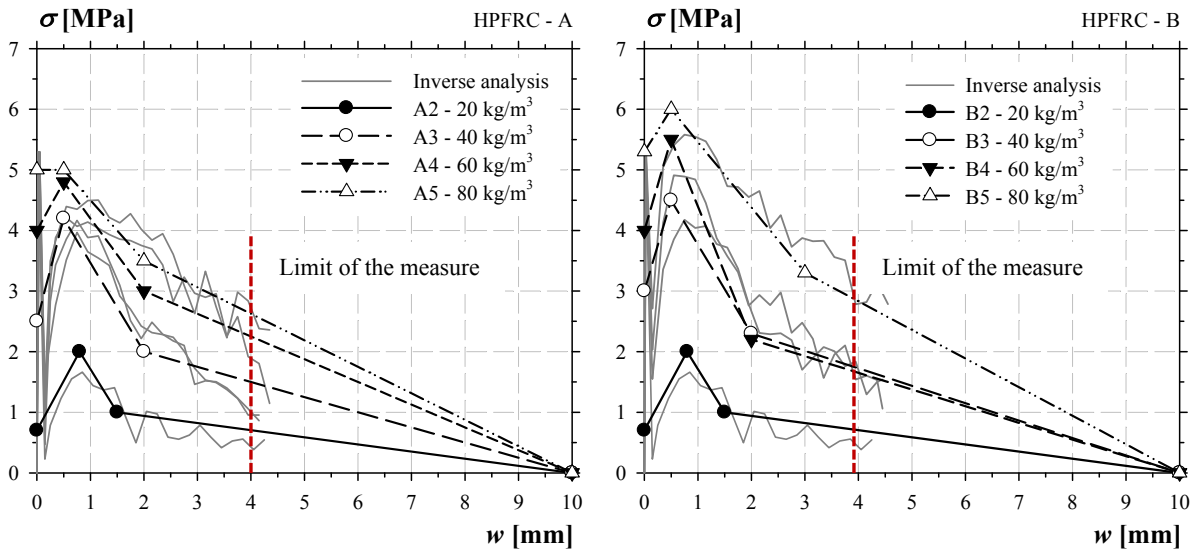

Figure 3-40: Identified relationships by inverse analysis for HPFRC - A and B

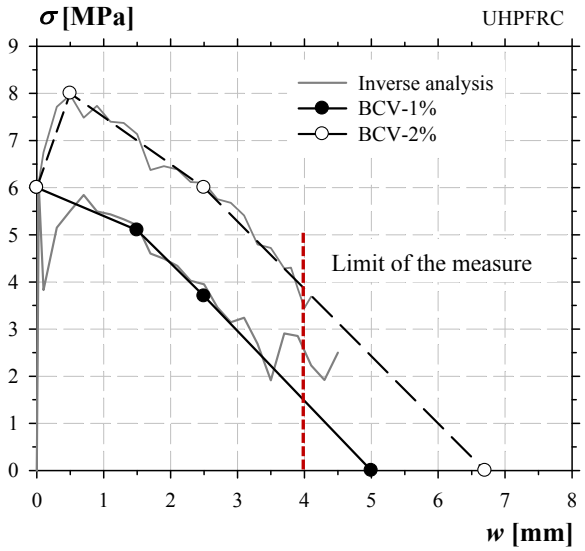

Figure 3-41: Identified relationships by inverse analysis for UHPFRC

For un-notched thin prisms in UHPFRC the French interim recommendations for UHPFRC [AFGC2002] proposed a simplified inverse analysis. A bi-linear sigma - epsilon relationship is adopted (Figure 3-42). The relation is defined by the tensile strength f_{tj} and the ultimate post-cracking

strength f_{tuj} at ε_u. Iteration on f_{tuj} is performed until the computed maximum moment will be equal to the maximum moment M_{Rmax} from the test on prism. The ultimate strain is fixed at a value of 10 ‰.

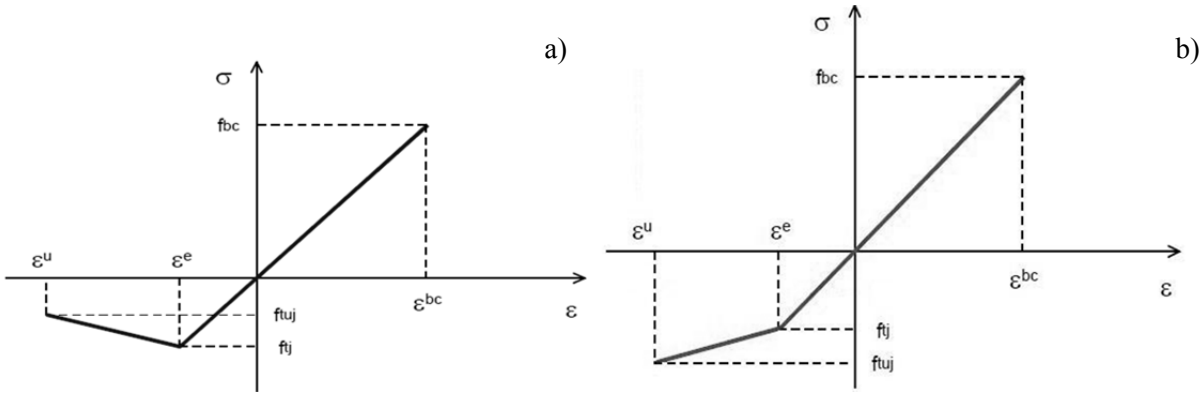

Figure 3-42: Tensile stress – strain relationships at ULS for thin element according to the [AFGC2002], a) softening behaviour, b) hardening behaviour

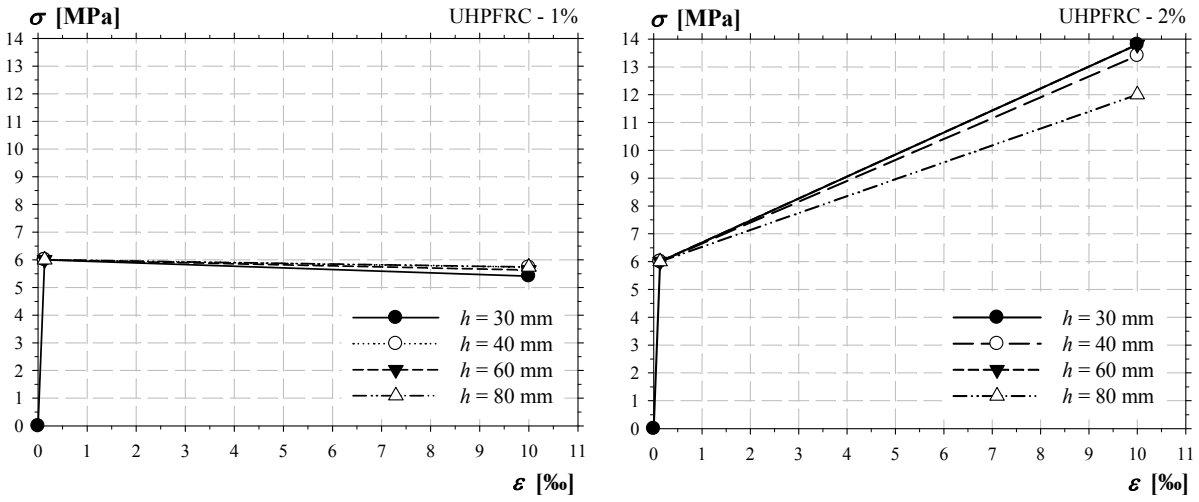

Figure 3-43: Identified relationships by inverse analysis for UHPFRC thin element, method AFGC 2002

In the revision of the French interim recommendations for UHPFRC [AFGC2012] a new method is proposed. An elastic – plastic relationship is adopted (Figure 3-44). The residual post-cracking strength f_{ctf} is determined from the maximum moment M and the corresponding deflection at centre δ. The curvature χ is defined from the deflection at centre δ considering an elastic assumption. On the basis of the equilibrium, the cracked depth α, the residual post-cracking strength f^*_{ctf} and the ultimate strain ε_{lim} can be computed. Finally the residual post-cracking strength f^*_{ctf} is corrected by a factor of 0.9.

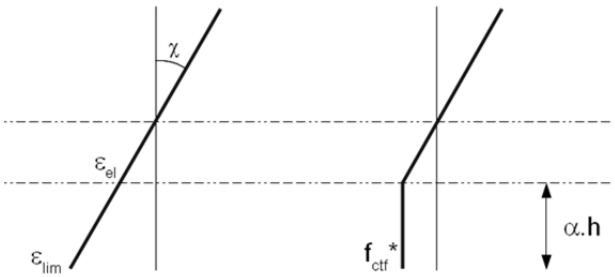

Figure 3-44: Assumed strains and stresses distribution

$$M = \left(2\alpha^3 - 3\alpha^2 + 1\right)^2 . \frac{b.h^3 \chi.E}{12} \tag{3-9}$$

$$f_{ctf}^* = -\frac{1}{2}(1-\alpha)^2 .h.\chi.E \tag{3-10}$$

$$\varepsilon_{\lim} = -\chi.\alpha.h + \frac{f_{ctf}^*}{E} \tag{3-11}$$

$$f_{ctf} = 0{,}9 \;\; f_{ctf}^* \tag{3-12}$$

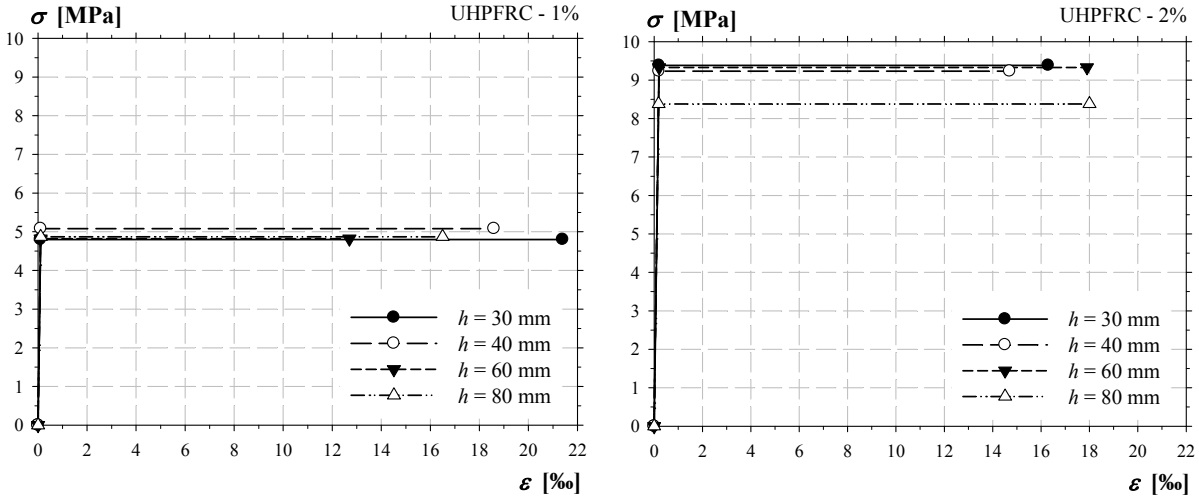

Figure 3-45: Identified relationships by inverse analysis for UHPFRC thin element, method AFGC 2012

3.5.3 Post cracking response defined by standards and recommendations

3.5.3.1 Swiss recommendation for FRC SIA 162/6

According to the standard SIA 162/6 [SIA1999], the effective flexural tensile strength f_{ctf} is determined from 4-points bending test or flexural test on square or round slab. For square slabs, the different values are defined as follows:

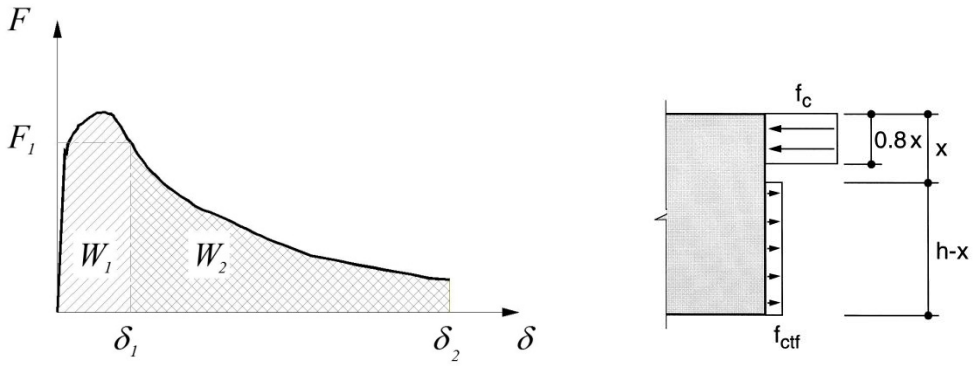

Figure 3-46: Identified values on the basis of the test results and assumed stresses distribution

$$\delta_1 = \left(0.03 \cdot n + 0.06\right) \cdot l_f \quad (d \text{ in [m]}) \tag{3-13}$$

$$W_1 = \int_0^{w_1} F \cdot d\delta \tag{3-14}$$

$$f_{ctf} = \left(0.95 - 0.06 \cdot n\right) \cdot \frac{W_1}{h^2 \cdot l_f} \tag{3-15}$$

$$\delta_2 = 4 \cdot \delta_1 \tag{3-16}$$

$$W_2 = \int_0^{w_2} F \cdot d\delta \tag{3-17}$$

$$G_f = \left(0.107 - 0.007 \cdot n\right) \cdot \frac{W_2}{h^2} \tag{3-18}$$

where n is the number of yield line

Table 3-14: Calculated values according to SIA 162/6 for HPFRC - B

Formulation		B2	B3	B4	B5
Fibres content	[kg/m^3]	20	40	60	80
f_{ctf}	[MPa]	1.10	1.83	1.92	2.02
G_f	[J]	7090	12800	19200	18500

3.5.3.2 *fib Model Code 2010*

According to the *fib* Model Code 2010 [FIB2010a], two simplified stress – crack relationship in tension for ULS are identified from 3-point bending test on notched prism performed according to the standards EN 14651 [EN14651]. A first constitutive law, rigid-plastic model is defined as follows:

$$f_{Ftu} = \frac{1}{K} \cdot \frac{f_{R3}}{3} \tag{3-19}$$

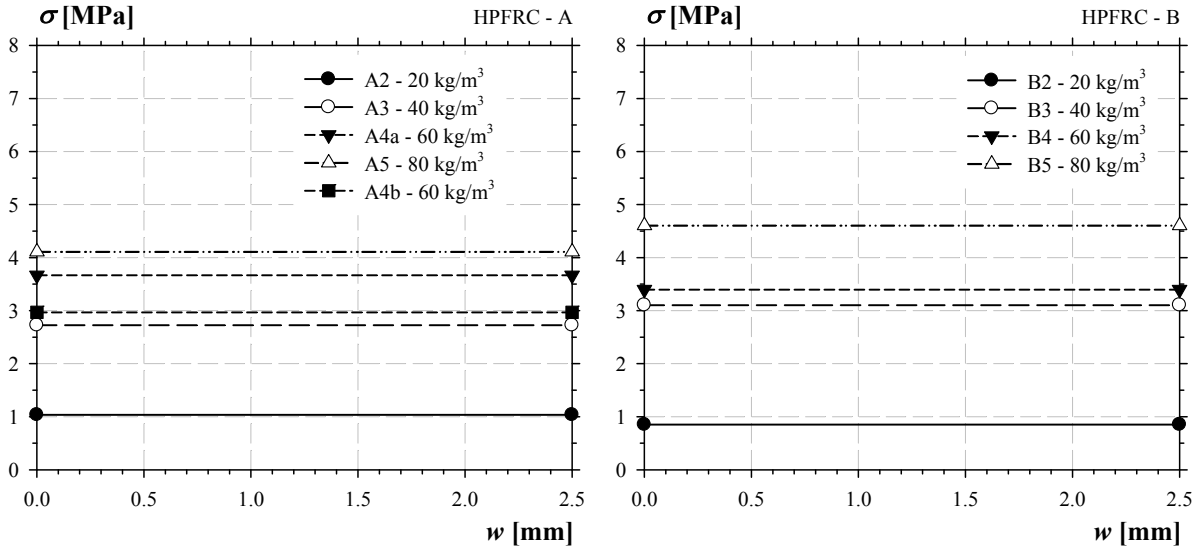

Figure 3-47: Identified rigid-plastic relationships at ULS for HPFRC - A and B

And a second constitutive law is defined with linear post-cracking model with softening or hardening behaviour. f_{Fts} represents the serviceability residual strength and f_{Ftu} represents the ultimate residual strength. The two reference values are defined as follows:

$$f_{Fts} = \frac{1}{K} \cdot 0.45 \cdot f_{R1} \tag{3-20}$$

$$f_{Ftu} = \frac{1}{K} \cdot \left[f_{Fts} - \frac{w_u}{2.5} \cdot \left(f_{Fts} - 0.5 \cdot f_{R3} + 0.2 \cdot f_{R1} \right) \right] \geq 0 \tag{3-21}$$

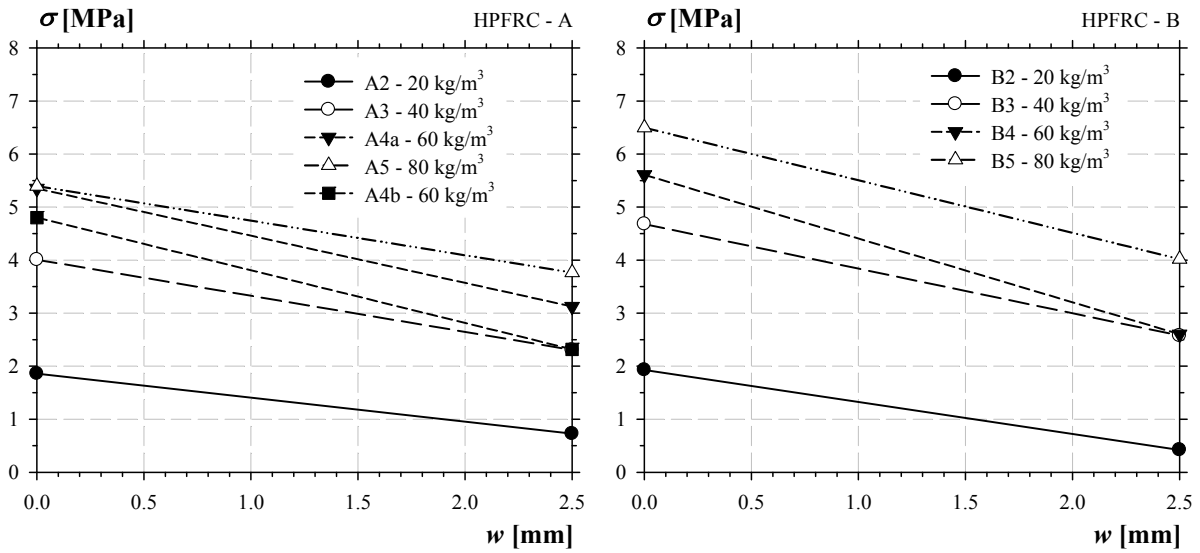

Figure 3-48: Identified linear relationships at ULS for HPFRC - A and B

For the Serviceability Limit State SLS a bi-linear relationship $\sigma(w)$ is proposed. After the cracking limit the descending branch correspond to the behaviour of plain concrete until the intersection with the residual post-cracking behaviour. When this condition does not apply, a new second branch linking the cracking limit to f_{Fts} at w= 0.5 mm is proposed.

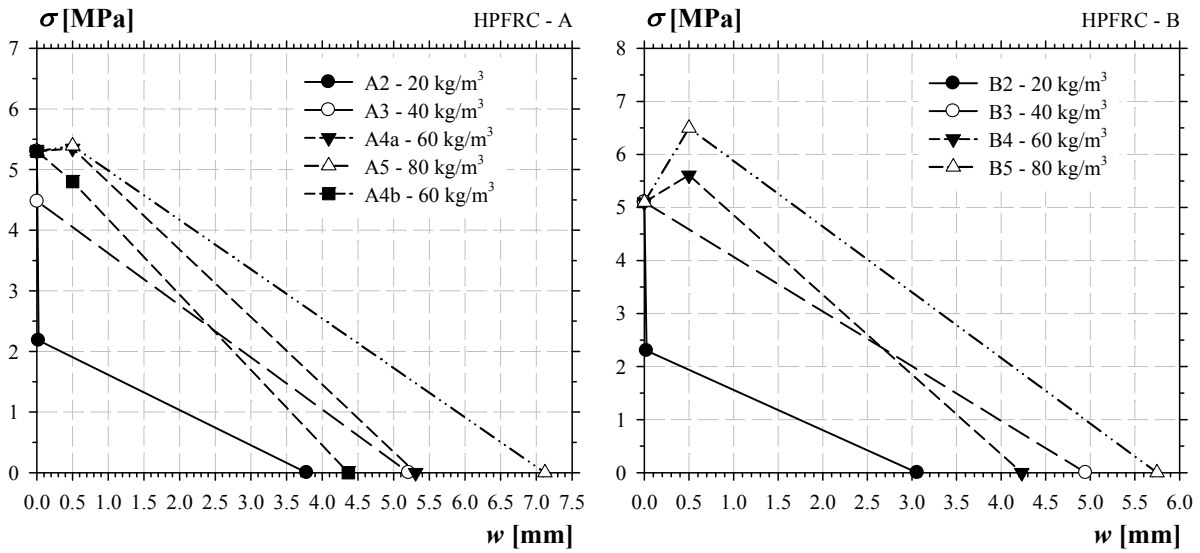

Figure 3-49: Identified relationships at SLS for HPFRC - A and B

3.5.4 Relationship based on Variable Engagement Model

The Variable Engagement Model VEM is a micromechanical model describing the tensile response of randomly oriented Steel Fibre Reinforced Cementitious Composite. This approach doesn't require preliminary tests. The VEM formulation is detailed in point (2.1.5.4). The HPFRC - A & B showed a similar matrix strength which was around 100 MPa and the computed relationships were the same because the same end-hooked fibres type was used,. The interface fibres-matrix bond strength was considered in the following manner; $\tau_b = 0.8 f_{cm}^{0.5}$ for end-hooked fibres and $\tau_b = 0.4 f_{cm}^{0.5}$ for straight fibres.

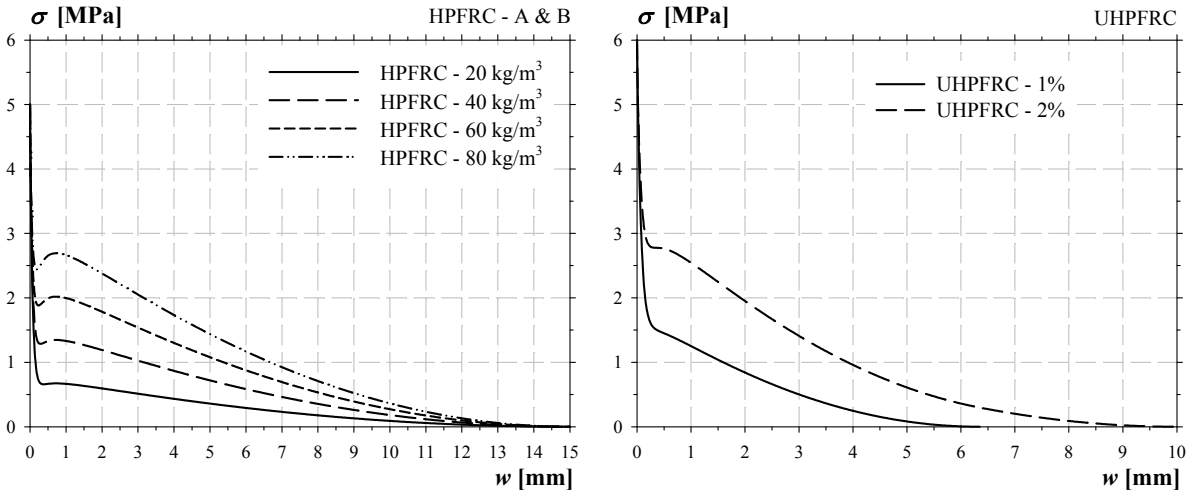

Figure 3-50: Computed relationships according the VEM for HPFRC - A & B and UHPFRC

3.5.5 Comparison and discussion

In the following graphs, the different relationships of HPFRC were compared.

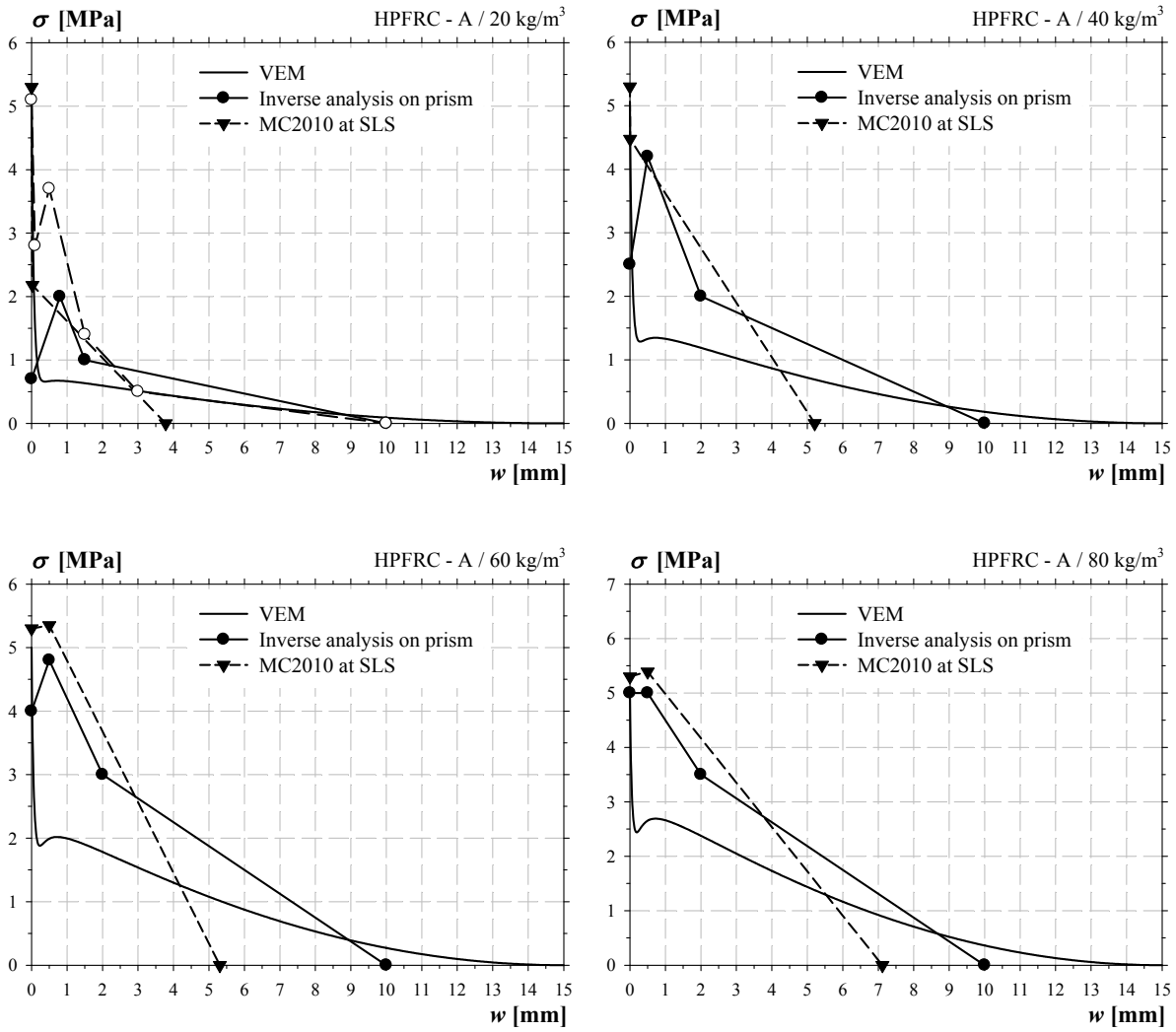

Figure 3-51: Comparison between the different identified relationships for HPFRC - A

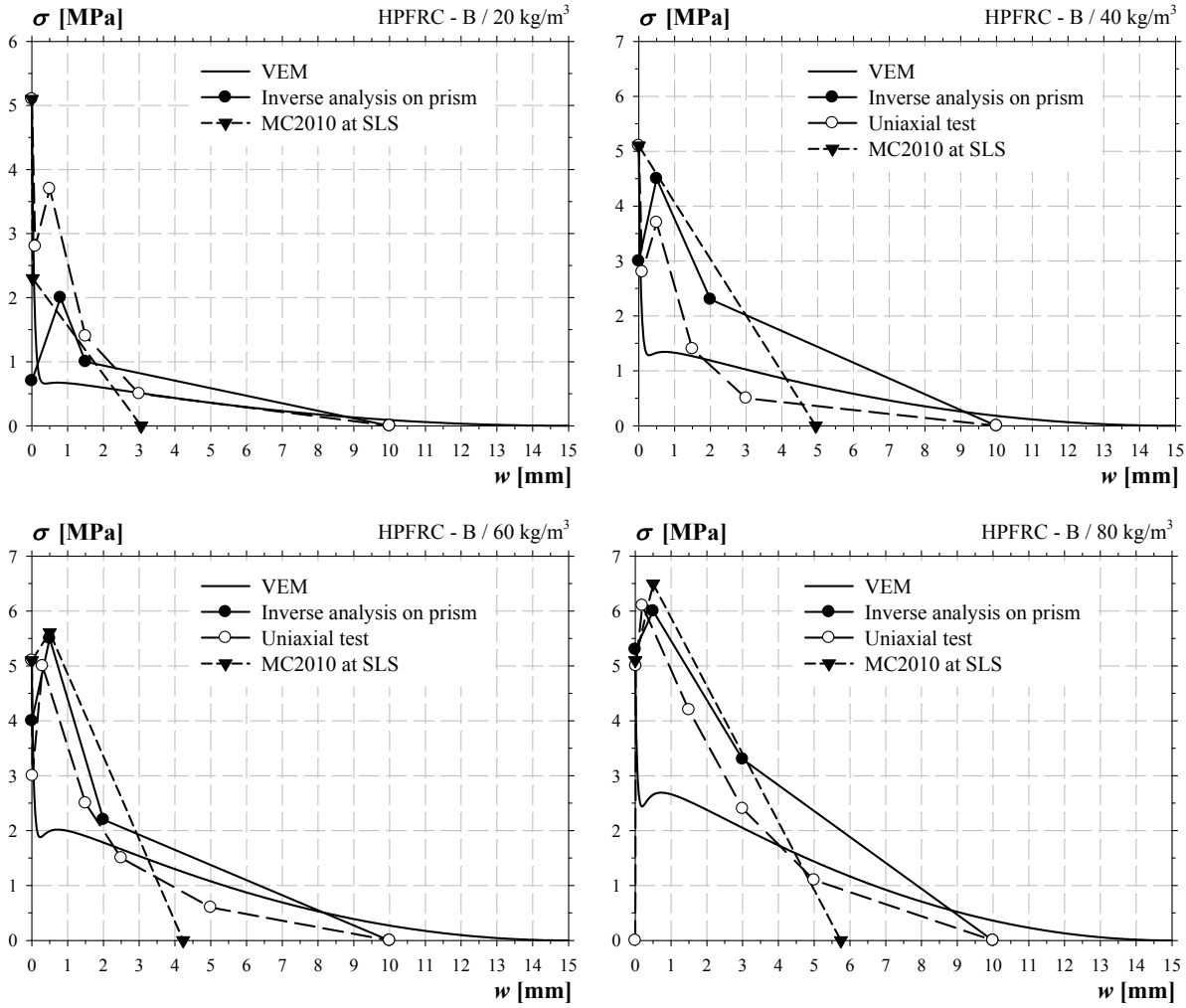

Figure 3-52: Comparison between the different identified relationships for HPFRC – B

The post-cracking relationships are significantly different according to the adopted method. In comparison with relations identified from testing methods, the VEM underestimates clearly the peak strength of HPFRC – A & B. On the other side, the peak strength of HPFRC – B is similar amongst relations determined from the inverse analysis on 3-points bending on notched prims and the uniaxial tensile test on notched cores. However, the softening branch is higher for relations identified from the inverse analysis compared to a uniaxial tensile test. This fact is principally due to the limit of the measure of the bending test on notched prisms. The simplified relation proposed at SLS by the *fib* Model Code 2010 [FIB2010a] is similar with the relation determined by inverse analysis for short crack opening. However, this simplified form disregarded large crack opening. For high fibre content, the difference between the models is reduced.

The inverse analysis proposed for UHPFRC, methods AFGC 2002 and 2012, give relationships adapted for ULS. However, these relationships are not representative of the effective tensile behaviour. Only uniaxial tests gave correct information about the tensile behaviour and the shape of the relation.

In the following graphs the stress vs *CMOD* of a notched prism was computed with a non-linear hinge model developed by Casanova and Rossi [CAS1997] considering the different relationships of HPFRC – B. The model is detailed in Chapter 2 (point 2.1.7.1).

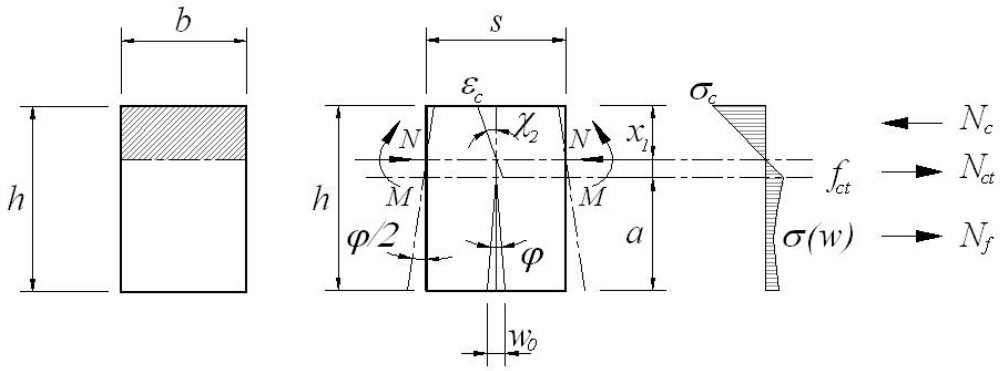

Figure 3-53: Cross sectional analysis using the discrete crack approach

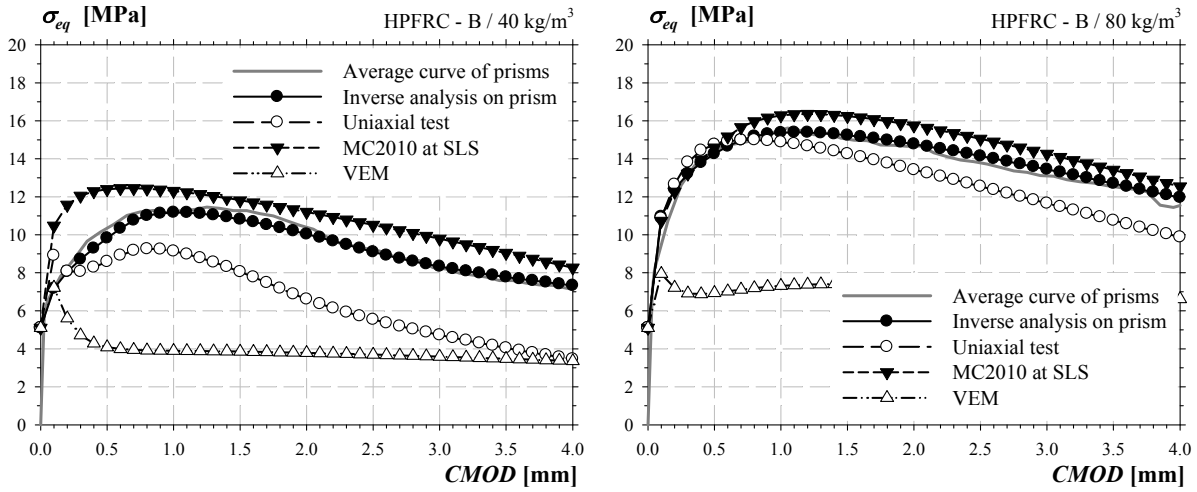

Figure 3-54: Computed curves equivalent bending stress vs CMOD according to the different relationships for HPFRC - B

At the structural level the difference between the post-cracking relationships is large. The VEM relations underestimate largely the flexural behaviour compared to other relationships. The law identified through uniaxial tensile test gives also lower response.

3.6 Conclusions

In this Chapter, ten HPFRC and two UHPFRC mixes, were used and studied for the different experimental studies on structural elements. The HPFRC – A was developed particularly for precast industry with a self-compacting criteria and a targeted compressive strength of 100 MPa. This formulation was used for the study on shear strength of pre-tensioned members which was detailed in Chapter 4. The HPFRC – B was developed for the first study on the punching shear of thin slabs (Chapter 5) with a compressive strength of 100 MPa. And finally, a UHPFRC developed by the Group Vicat, the Béton Composite Vicat BCV®, was studied and compared to the HPFRC. This UHPFRC was used for the second study on punching shear of thin slabs (Chapter 5).

The development of HPFRC – A has highlighted the possibility to design the mix proportions of a self-compacting concrete with coarse aggregates and steel fibres from the technical point of view. The targeted compressive strength of 100 MPa was reached by using local aggregates. In order to limit the cement quantity and to improve the rheology, microsilica was used. Ternary binder, composed of cement, microsilica, fly ash or blast furnace slag, was also studied with interesting results. But from a logistical point of view this type of binder was not retained for final compositions. Up to a fibres content (end-hooked fibres) of 60 kg/m^3, the self-compacting criteria was respected. However, the steel fibres decreased the workability and in presence of dense reinforcement, the aggregates were blocked due to the mesh formed by the fibres. This problem may be easily solved by adopting a larger spacing of rebars.

Compared to UHPFRC, self-compacting – HPFRC with coarse aggregate and steel fibres is more difficult to formulate and demand some compromises. Depending on the type of fibres, the coarse aggregates limit the fibre content. However, in order to limit the shrinkage and the cost of the matrix it's interesting to keep the coarse aggregates particularly for large structural elements.

The mechanical properties, particularly the compressive strength and the post-cracking response, were identified through a large numbers of specimens. Different testing methods were used and compared. For fibre reinforced cementitious composite, tensile response was often identified with an indirect way due to their ease (e.g. bending tests on prism or slab). However, these indirect testing methods required several assumptions for the determination of the tensile constitutive law. For the HPFRC-B and the UHPFRC, uniaxial tensile tests were also performed. Tensile laws determined from the indirect way, were slightly higher compared to the response generated after a uniaxial tensile response, this was probably due to the structural effect.

The uniaxial tensile test is probably the simplest test for determining the tensile law in a direct way, especially for a UHPFRC with a large hardening behaviour. However, its practical application is delicate. The bending test are simplest in practical point of view but demand several hypothesis for the analysis. Currently, several design codes and recommendations recommend bending test on notched or unnotched prisms and proposed different approaches for inverse analysis.

Finally, in this Chapter, a large data base of different test results was collected. But at this stage, no generalized method can be determined and the identification of a tensile response is clearly a function of the material itself and the corresponded structure.

4 Shear strength of pre-tensioned members in HPFRC

4.1 Problem statement

According to national and international standards, minimum shear reinforcement is required in the webs of structural members. This reinforcement, generally formed by stirrups, complicates the manufacture and increases the production costs in precast industry. In most practical applications, precast members are used for roof coverings or commercial surfaces (Figure 4-1). They are mainly subjected to distributed loads of average intensity which do not generate important shear forces. However, the shear reinforcement cannot be simply removed. The shear failure mode of reinforced or prestressed concrete members without transversal reinforcement is characterized by a fragile behaviour implying possible, partial or total collapse of the structure. Steel fibres offer themselves as an alternative reinforcement possibility in precast industry. The principal aim of this part of the thesis is to demonstrate that sufficient steel fibre content can provide an effective control of the shear cracking of prestressed members.

The precast members, compared to in-situ concrete girders, are characterized by their high quality and short time construction. The stationary processes in precast industry offer optimal possibilities for using High Performance Concrete (HPC) such as the Self Compacting Concrete (SCC) and the High Strength Concrete (HSC). Currently, the SCC with a compressive strength varying between 50 to 80 MPa is widely used in precast industry. Moreover, HSC is characterized by a brittle behaviour; the fibres addition may avoid any brutal fracturing and confer a ductile behaviour. The combination of a HPC and steel fibres (HPFRC) is a promising step in the development and the optimization of this industry.

Figure 4-1: Example of precast members and conventional steel reinforcement cage

The ability of Steel Fibre Reinforced Concrete (SFRC) to reduce shear reinforcement of reinforced concrete members or even eliminate it, is supported by several experimental studies as described in the chapter 1. In this chapter, HPFRC is investigated as an advanced cementitious material offering many technical and economic advantages; however its practical application remains marginal mainly due to the lack of standards and an adaptation period is needed to develop procedures and rules adapted to its performance.

4.2 Program and objectives

In this chapter, the results of an experimental research program on pre-tensioned members are presented. Six shear beams of 5.60 m length named AV and two full scale beams of 12.40 m length named AF were tested in order to evaluate the possibility of the high performance fibre reinforced concrete to substitute the minimum transverse reinforcement. The principal parameter distinguishing the beams was the fibre volume. The test results were compared to several shear strength models for Fibre Reinforced Concrete elements available in the literature. A non-linear finite element model analysis was performed. In a first step, the model was validated on the basis of the test results. In a second step, a parametric study was performed in order to determine the main parameters in the shear strength of pre-tensioned members in HPFRC. The main objectives of this experimental study are:

- to evaluate the flexural and shear behaviour at Service Limit State SLS and Ultimate Limit State ULS of pre-tensioned members in HPFRC without transversal reinforcement,
- to determine the influence of the fibres content on the shear strength of pre-tensioned members in HPFRC without transversal reinforcement,
- to compare the test results with several shear strength models available in the literature for FRC elements,
- to propose an accurate shear strength model and design rules for elements in HPFRC,
- to demonstrate that the production of HPFRC structural elements is feasible at competitive costs in precast industry.

4.3 Preliminary works

In 2007 a large experimental program was carried out at University of Applied Sciences Fribourg on High Performance Fibre Reinforced Concrete [SUT2009]. In one part, the possibility of substituting the minimum shear reinforcement in pre-tensioned double-tee members (Figure 4-2) was investigated. For this purpose, five shear T-beams of 5.00 m length named PV and two full scale T-beams of 13.00 m length named PF were tested (Table 4-2). The principal parameters distinguishing the shear beams were the fibre content and the pre-tensioning. The cross section was composed of a trapezoidal web of 500 mm depth and 170 mm wide surmounted by a flange of 800 mm width and 70 mm thick (Figure 4-3). The pre-tensioning was composed of 7 or 10 strands having an area of 100 mm^2. The initial tension of the strands was 130 kN each (without prestress losses). Two strands were placed at the top of the cross section in order to avoid any cracking. At the extremities, the beams had 9 stirrups ϕ12 in order to introduce the prestressing forces. In the central part, no transversal reinforcement was placed.

Figure 4-2: Double-tee beams for the construction of an industrial floor

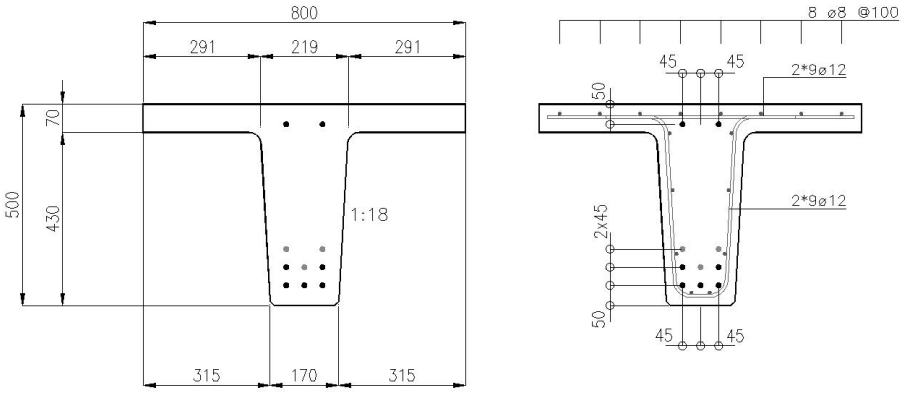

Figure 4-3: Cross section and reinforcement arrangement at the end of T-beams PV and PF

Three Self Compacting Concrete compositions were developed and distinguished by their fibres content (0, 40, 60 kg/m^3). In this study, end-hooked fibres type *Bekaert Dramix RC-80/30-BP* were used. The concrete compressive strength was around 70 MPa on cylinders and the Young's modulus was around 37 GPa. The post-cracking response (Table 4-1) was determined using 3-point bending test on notched prisms according to the European standards EN 14651 [EN14651], see point 2.5.1.2.

Table 4-1: Post-cracking residual strengths according to EN 14651 [EN14651]

Beams	Fibre content [kg/m^3]	$f_{ct.L}$ [MPa]	f_{R1} [MPa]	f_{R2} [MPa]	f_{R3} [MPa]	f_{R4} [MPa]
PV-2 **PV-4** **PF-2**	40	5.0* *0.48***	6.5 *1.42*	8.0 *1.77*	7.4 *1.62*	6.4 *1.60*
PV-3	60	5.5 *0.33*	10.5 *0.70*	11.2 *0.82*	10.6 *0.85*	9.7 *1.20*

** Average ** Standard deviation*

The five shear beams were tested in 4-points bending on single span of 3.00 m (Figure 4-4). A distance of 1.00 m at each side was kept to allow the diffusion of the pre-tension forces. The two full-scale members were tested on single span of 12.00 m with four distributed loads (Figure 4-5).

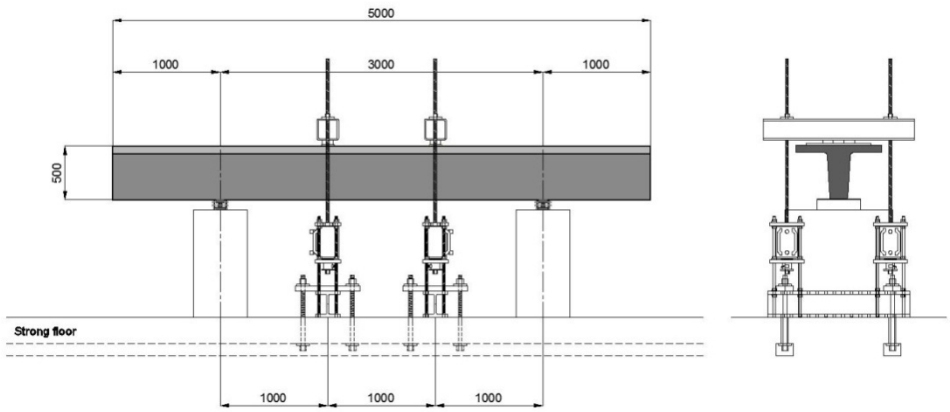

Figure 4-4: Test setup of the shear beams PV

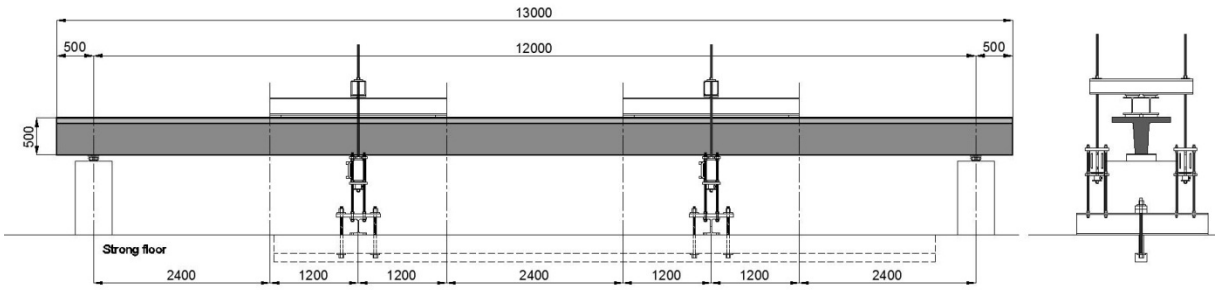

Figure 4-5: Test setup of the full-scale beams PF

At the serviceability limit state, the HPFRC beams exhibited a better behaviour compared to the beams without fibres, mainly due to the development of thin cracks. The shear beams without fibres, i.e. PV-1 and PV-4, exhibited a brittle shear failure. For members with low pre-tensioning forces, the beams PV-2 and PV-3 having respectively a fibre content of 40 and 60 kg/m^3, exhibited a flexural failure. For the elements having high pre-tensioned forces the beams PV-5 with 40 kg/m^{3}of fibres exhibited a higher shear strength and deformation capacity compared to the beam PV-4 without fibres. The two full-scale beams showed a flexural failure with large deflections at the centre (300 mm). The element AF-2 exhibited a higher stiffness and flexural strength compared to the beam AF-1 without fibres. The average crack spacing in the central part of the tested specimens was approximately 100 mm for the elements without fibres, but was reduced to only 60 mm for the specimens with fibres (Figure 4-8) [MOR2009].

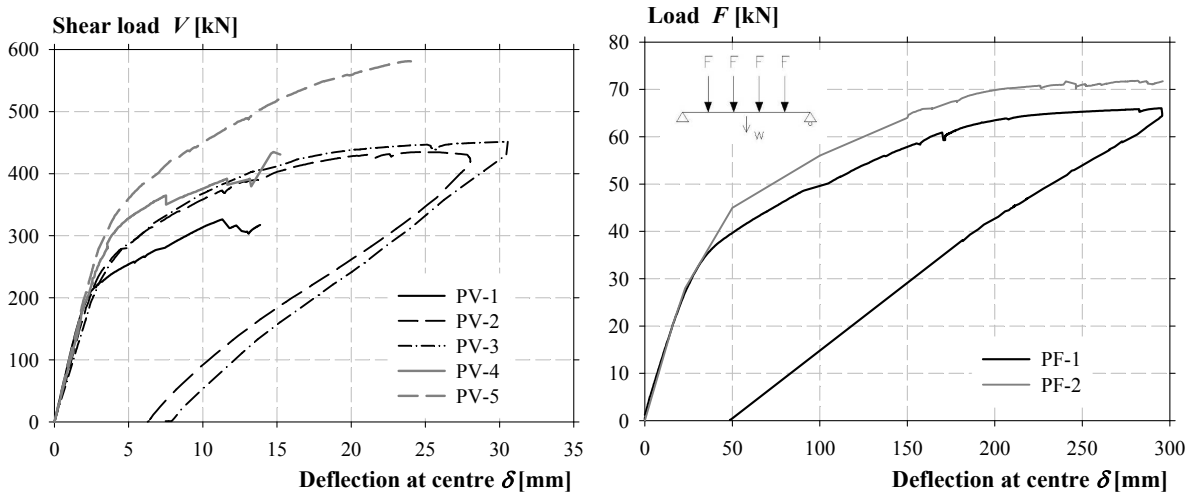

Figure 4-6: Curves load vs deflection at centre of PV and PF beams

Table 4-2: Test data of specimens PV an PF

Specimen		**PV-1**	**PV-2**	**PV-3**	**PV-4**	**PV-5**	**PF-1**	**PF-2**
Prestressing force	[kN]	930	930	930	1100	1100	1100	1100
Fibres content	[kg/m^3]	-	40	60	-	40	-	40
Failure type		shear	flexural	flexural	shear	shear	flexural	flexural
V_R	[kN]	327	435	451	435	581	132	144
δ at V_R	[mm]	14	28	30	15	24	295	282

According to the Kani's valley, see point 2.2.3.1, a ratio *a/d* of 2.5 corresponds approximately, for ordinary reinforced beams, to the limit between unstable crack propagation and direct strutting regions. This ratio corresponds also to the minimum nominal shear strength. However, in prestressed members, the effective shear span a_{eff} is smaller than the geometric one. This is due to the fact that the normal force does not allow for the development of flexural cracks close to the support and this is clearly highlighted with the cracking pattern of specimens PV and PF (Figure 4-7) (Figure 4-8). Therefore the arching action or direct strutting is predominant in this configuration. The shear span to depth ratio of the beams PV was 2.3 or 2.5 according to the pre-tensioning. It was observed experimentally that the propagation of the shear cracks was not unstable. The shape of the critical shear cracks was straight from the load application to the support. It was also observed that the critical shear cracks were stopped under the flange. Therefore, the flange carried a large part of the shear force. This study clearly highlighted that steel fibres even with a low content around 40 – 60 kg/m^3 increase the shear strength and the deflection capacity of prestressed members in the direct strutting regime. However, the reduced number of specimens which exhibited a shear failure did not allow for the development of an accurate model; therefore a new experimental study was needed.

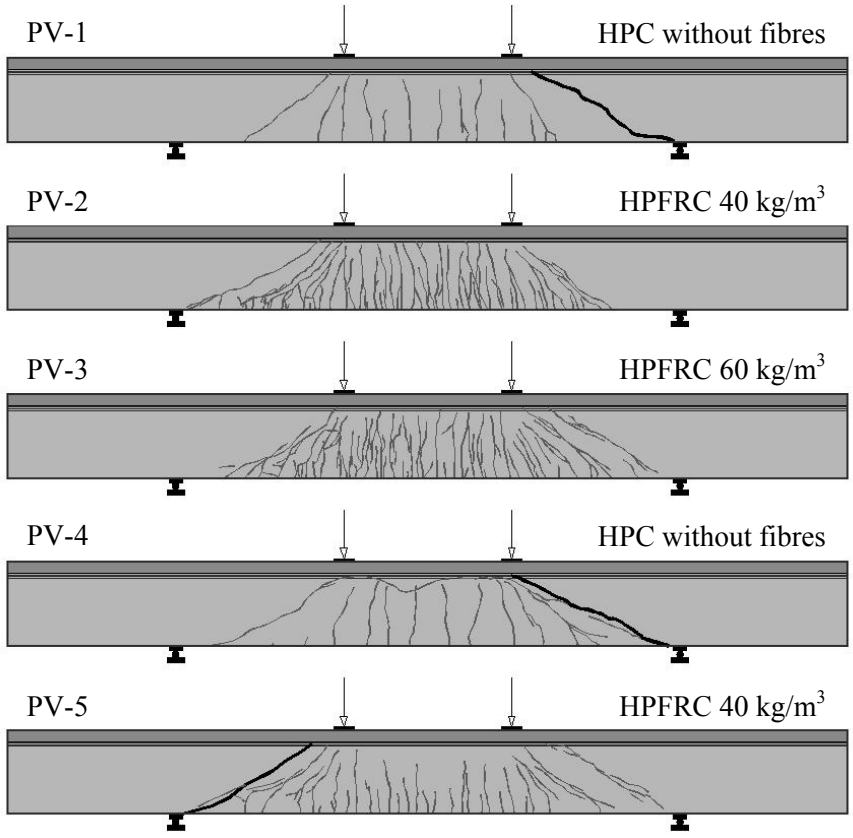

Figure 4-7: Cracking pattern of members PV-1 to PV-5

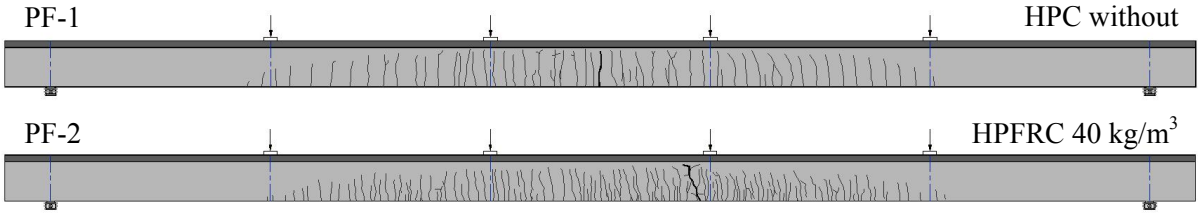

Figure 4-8: Cracking pattern of members PF-1 and PF-2

4.4 Description of the experimental studies

4.4.1 Reminder of HPC and HPFRC mechanical properties

In this point the principal properties of concrete are briefly described. More information about the formulation and the determination of the mechanical properties are given in Chapter 3. Five compositions were developed and were distinguished by their fibres content (Table 4-3). End-hooked fibres type *Bekaert Dramix RC-80/30-BP* were used. The formulation of the cement matrix was similar between the different compositions. However, from a fibre content of 60 kg/m^3, the sand ratio was increased in order to improve the rheology.

Table 4-3: HPC and HPFRC denomination and fibre content

Composition		**A1**	**A2**	**A3**	**A4**	**A5**
Steel fibres *Bekaert Dramix RC-80/30-BP*	[kg/m^3]	0	20	40	60	80

The compressive strength f_c and the Young's modulus E_c of the HPC and the HPFRC were defined on 4 cylinders ϕ150 x 300 mm tested the same day of the corresponding beams. The Young's modulus was defined according to the Swiss standard SIA 262/1 [SIA262/1]

Table 4-4: Compressive strength and Young's modulus

Beams	Formulation	Fibre content [kg/m^3]	*Age*	Density [kg/m^3]	E_{cm} [GPa]	f_{cm} [MPa]
AV-1	**A1**	0	32	2410* *16***	37900 *840*	94.9 *1.5*
AV-2	**A2**	20	39	2440 *36*	40340 *1565*	91.6 *4.0*
AV-3	**A3**	40	39	2440 *32*	39750 *80*	97.5 *3.1*
AV-4	**A4**	60	39	2500 *20*	37160 *880*	102.2 *2.1*
AV-5	**A5**	80	40	2500 *2*	37160 *670*	102.2 *2.2*
AF-1	**A1**	0	78	2450 *19*	36380 *2250*	93.6 *4.0*
AF-2	**A4**	40	79	2475 *19*	37500 *900*	106.6 *1.9*

** Average ** Standard deviation*

Bending tests on notched prisms

Three-points bending tests on notched prism were performed according to the European standard EN 14651. According to the standard EN 14651 [EN14651], see point 2.1.5.2, the Limit Of Proportionality *LOP* $f_{fct.L}$ and four different values of the residual strength f_{R1}, f_{R2}, f_{R3}, and f_{R4} corresponding to different values of the *CMOD* = 0.5, 1.5, 2.5 and 3.5 mm, respectively, are identified. The residual strength is defined considering an elastic stress distribution as follows:

$$f_{Ri} = \frac{3 \cdot F_i \cdot L}{2 \cdot b \cdot h_n^{\,2}} \tag{4-1}$$

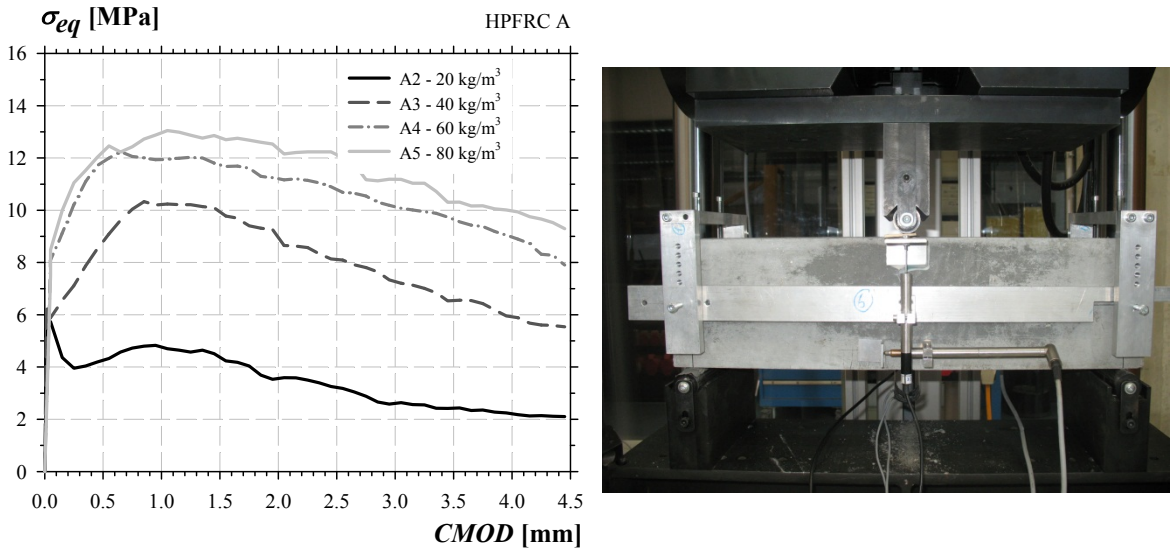

Figure 4-9: Average curves equivalent bending stress vs CMOD of HPFRC notched prisms

Table 4-5: Post-cracking residual strengths according to EN 14651

HPFRC	Beams	Fibre content [kg/m^3]	$f_{ct.L}$ [MPa]	f_{R1} [MPa]	f_{R2} [MPa]	f_{R3} [MPa]	f_{R4} [MPa]
A2	**AV-3**	20	6.1* *0.59***	4.1 *1.02*	4.4 *0.87*	3.1 *0.58*	2.4 *0.23*
A3	**AV-4**	40	6.7 *0.41*	8.9 *1.65*	9.9 *2.17*	8.2 *1.68*	6.5 *1.28*
A4	**AV-5**	60	7.6 *0.34*	11.9 *0.66*	11.8 *0.56*	11.0 *1.38*	9.7 *1.47*
A4	**AF-2**	60	7.5 *0.42*	10.7 *0.50*	11.0 *1.24*	8.9 *1.24*	7.2 *1.37*
A5	**AV-6**	80	7.5 *0.80*	12.0 *0.75*	12.9 *0.76*	12.3 *0.69*	10.7 *0.56*

** Average ** Standard deviation*

The prisms in HPFRC A2 with only 20 kg/m^3 of fibres showed a softening behaviour in bending. Conversely, the other compositions exhibited a hardening behaviour in bending. The post cracking strength didn't increase proportionally to the fibre content. The difference in the post cracking strength was important between a fibre content of 20 and 40 kg/m^3 and became lower for higher contents. The test results were treated by inverse analysis in Chapter 3.

4.4.2 Design of testing members

The geometry, the pre-tensioning and the reinforcement of the testing members were based on real precast concrete structure for an industrial hall and storage in Switzerland (Figure 4-10). The reference members had a length of 13 m and 650 mm depth (Figure 4-11). The pre-tension of these beams was composed of 10 strands. These beams usually support the roof covering, therefore they are mainly subjected to distributed loads. In this case the shear strength is not the determining criteria, but according to the Swiss Codes SIA 262 [SIA2003] these members must contain a minimum shear reinforcement which corresponds to at least 0.2% of the associated concrete cross-section. In the case of wide webs, the web width may be taken into account up to a maximum of 400 mm.

Figure 4-10: Assembly of the precast concrete structure

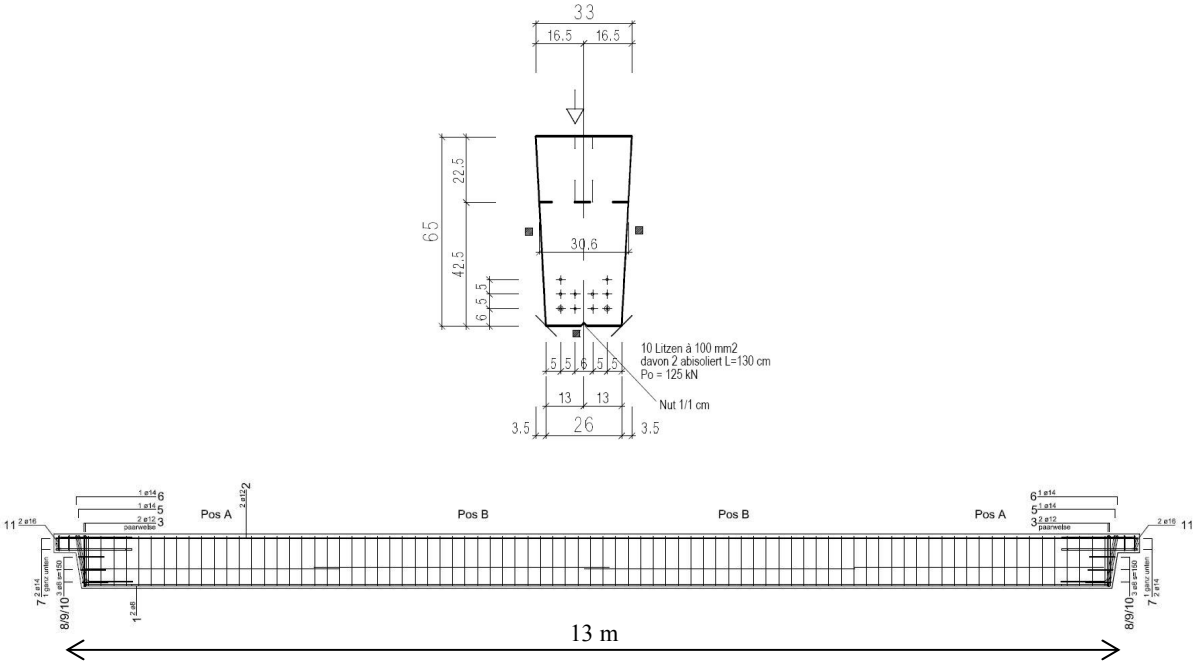

Figure 4-11: Cross section geometry and reinforcement arrangement of the full scale members

The experimental campaign was composed of six shear beams named AV and two full-scale beams named AF. The tested beams had a depth of 600 mm according to the laboratory capacity. The width was defined in order to put several rows of 3 strands and ensure a minimum concrete cover of 20 mm for the stirrups. The inclination of the faces, 1/18, was defined by the steel framework used at the

precast plant. The principal parameter among the beams AV and AF was the fibre content (Table 4-7). The concrete mixes are shown in Table 3-5 of Chapter 3.

The tested beams AV were designed in order to obtain a shear failure with a fibre content of 60 kg/m^3. The shear span a was chosen in order to obtain a truss mechanism and not a direct strutting. According to the Kani's valley, a ratio a/d of 2.5 corresponds approximately, for ordinary reinforced beams, to the limit between unstable crack propagation and direct strutting regions. However, in prestressed members, the effective shear span a_{eff} is smaller than the geometric one (Figure 4-12). This is due to the fact that the normal force does not allow for the development of flexural cracks close to the support (region A) [FER2010].

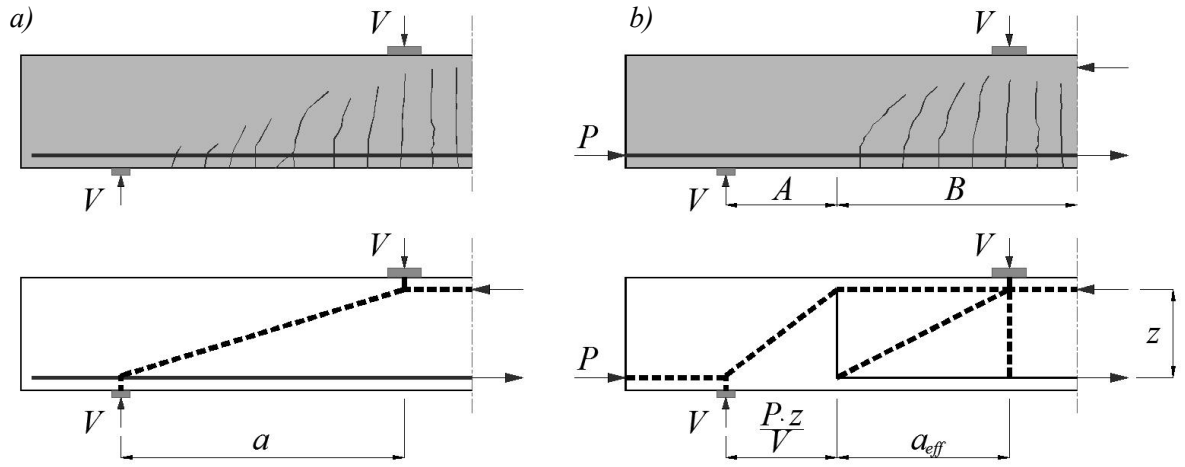

Figure 4-12: Geometric shear span in a reinforced concrete beam (a); effective shear span for a prestressed member (b) [FER2010]

The effective shear span can be calculated in the following way:

$$a_{eff} = a - \frac{P}{V} \cdot z \tag{4-2}$$

Where a is the geometric shear span, P is the normal force, V is the shear force and z is the flexural lever arm of the member, in first approximation $z = 0.9d$.

The minimum shear reinforcement for the member AV-1 was designed according to the Swiss standards SIA 262 [SIA2003] in the following way:

$$\rho_{sw,\min} \geq 0.2\% \tag{4-3}$$

$$\rho_{sw} = \frac{A_{sw}}{s \cdot b_w \cdot \sin\alpha} \tag{4-4}$$

$$\frac{A_{sw,\min}}{s} = \frac{1}{2} \cdot 0.2/100 \cdot 170 \cdot \sin\left(\pi/2\right) = 0.17 mm/m \tag{4-5}$$

With s = 150 mm, $A_{sw,min}$= 25.5 mm^2/m, therefore the choice was ϕ6 @150 mm and the effective ratio was ρ_{sw} = 0.22%.

The flexural and shear strength were evaluated using different models described in the Chapter 1 and considering the mean values of each material without safety factors.

Table 4-6: Evaluation of the flexural and shear strength

Beams	V_{flex} [kN]	V_R [kN]
AV-1	488	388
AV-5	525	488

The cross section of the shear beams AV was trapezoidal with a minimal width of 170 mm and 600 mm depth (Figure 4-13). The pre-tensioning was composed of ten low-relaxation strands (seven wires) having an area A_p of 100 mm^2. The initial tension force P_0 of 130 kN was introduced in each strand (without losses). Two strands were placed at the top of the cross section to avoid cracking. After stripping, the evaluated axial force and bending moment due to the pre-tensioning with a consideration of the elastic losses, instantaneous shortening of the concrete, were respectively 1212 kN and 145 kNm. In order to obtain a shear failure, two ϕ22 rebars were placed at the bottom of the cross-section. The effective depth d_s of theses rebars was 562 mm. The equivalent depth of the strands and rebars was 512 mm. At the extremities, the shear beams AV-1 to AV-3 had ϕ8 @150 mm stirrups in order to introduce the pre-tensioning forces. The beams AV-4 to AV-6 contained only 4 stirrups ϕ8 for the positioning of the longitudinal reinforcement. In the central part, the element AV-1 contained the minimum transverse reinforcement which consisted of ϕ6 @150 mm stirrups. For the other elements, no transversal reinforcement was placed. The geometrical properties of the cross-section are shown in Table 4-8.

Table 4-7: Properties of the specimens

Specimen	Concrete denomination fibre content	Transversal reinforcement	Length	Longitudinal reinforcement	Longitudinal Pre-tension
AV-1	HPC A1 without fibres	Stirrups ϕ6 @150 mm	5.60 m	2 ϕ22 mm d_s = 562 mm	Strands ϕ12.9 mm A_p = 100 mm^2 8 strands at bottom 2 strands at top Initial tension force $F_{p,t0}$ = 10x 130 kN
AV-2					
AV-3	HPFRC A2 20 kg/m^3	Without stirrups			
AV-4	HPFRC A3 40 kg/m^3				
AV-5	HPFRC A4 60 kg/m^3				
AV-6	HPFRC A5 80 kg/m^3				
AF-1	HPC A1 without fibres	Without stirrups	12.40 m	Without rebars	
AF-2	HPFRC A4 60 kg/m^3				

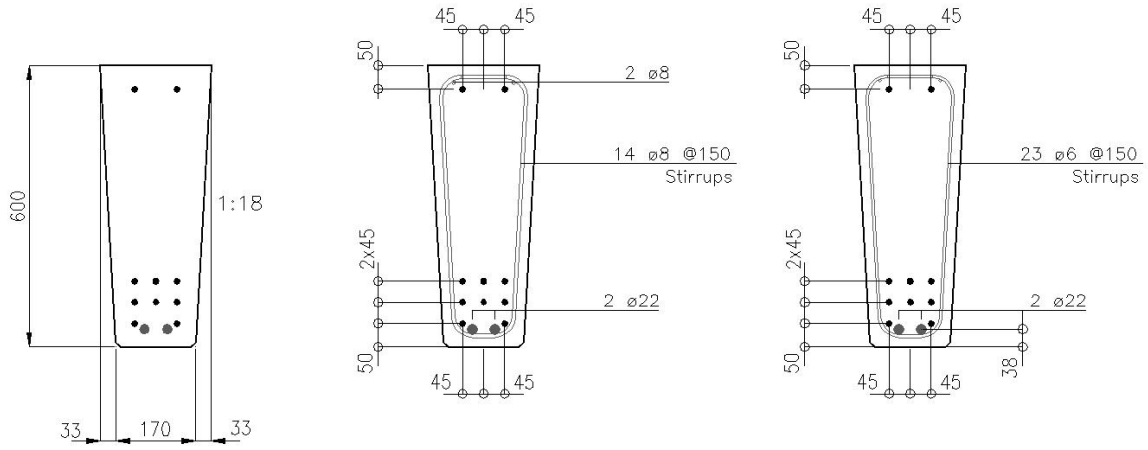

Figure 4-13: Cross section and reinforcement arrangement of the shear beams AV

Table 4-8: Cross-section properties

Area	A_c	[mm^2]	122E+3
Inertia	I_y	[mm^4]	3.627E+6
Position of the centroid from the top	z_g	[mm]	284
Axial force due to prestressing	$F_{p,t1}$	[kNm]	1212
Bending moment due to prestressing	$M_{p,t1}$	[kNm]	145
Effective depth	d	[mm]	512

Only the pre-tensioning losses at short term were considered. For pre-tensioned members, the losses due to the instantaneous shortening of the concrete during the transfer of the prestressing force were non-negligible. For beams AV, these calculated losses corresponded to 7%.

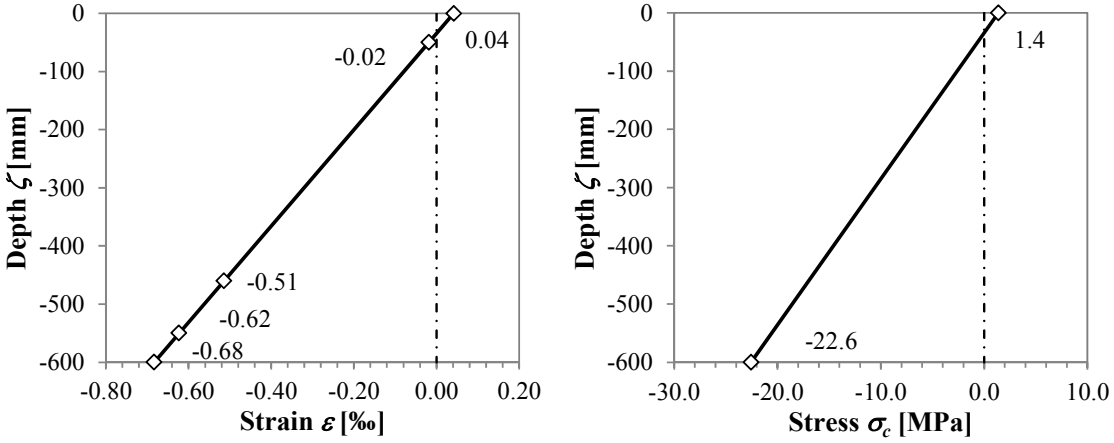

Figure 4-14: Theoretical strain and stress diagrams due to the prestressing after elastic losses

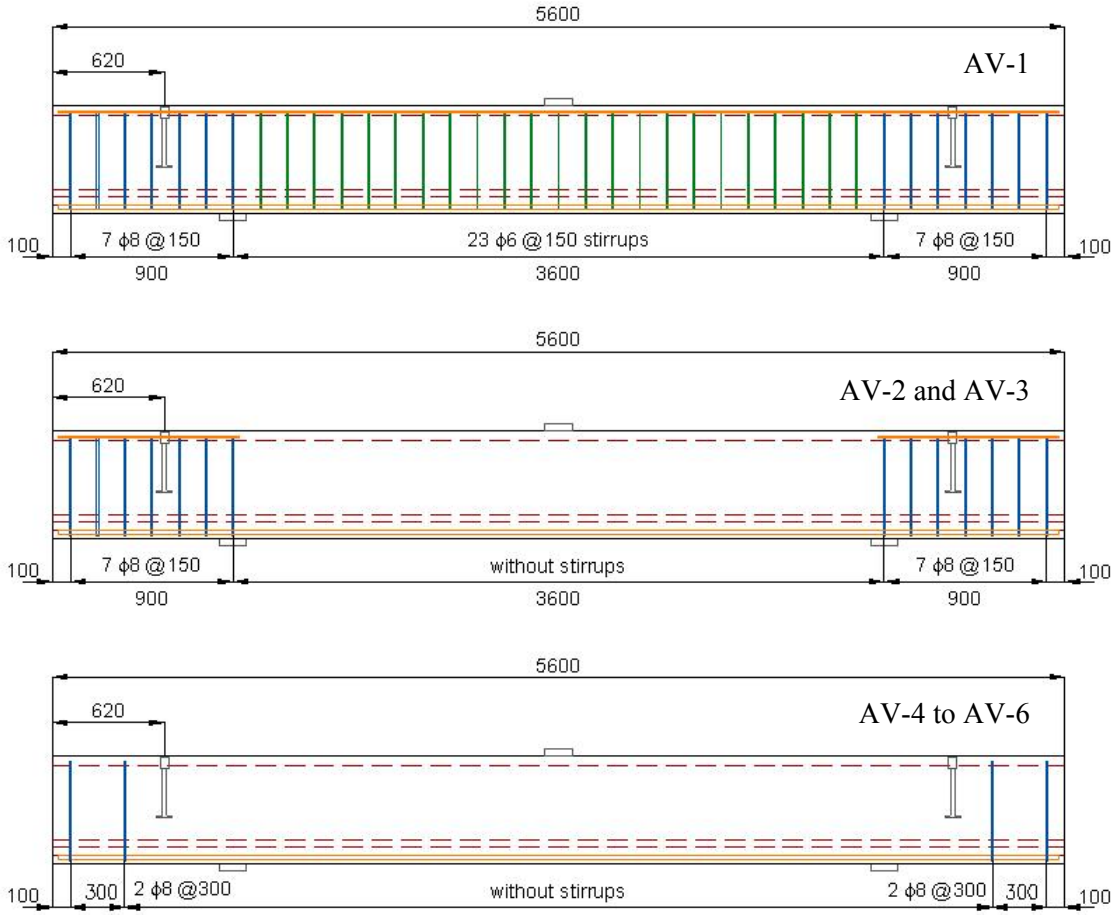

Figure 4-15: Reinforcement arrangement of the shear beams AV

The flexural beams AF had the same cross section of the shear beams AV. However, the arrangement of the pre-tensioning was different (Figure 4-16). At the extremities, the members had a reinforcement composed of stirrups and U-bars in order to introduce the pre-tension forces and support reactions. In their central part, no transversal reinforcement was placed. The axial force and bending moment due to the pre-tensioning with a consideration of the corresponded elastic losses, were respectively 1208 kN and 154 kNm. The beam AF-1 was casted with a HPC B1 without fibres and the beams AF-2 with a HPFRC B4 having a fibres content of 60 kg/m^3. The geometrical properties of the cross-section are shown in Table 4-9.

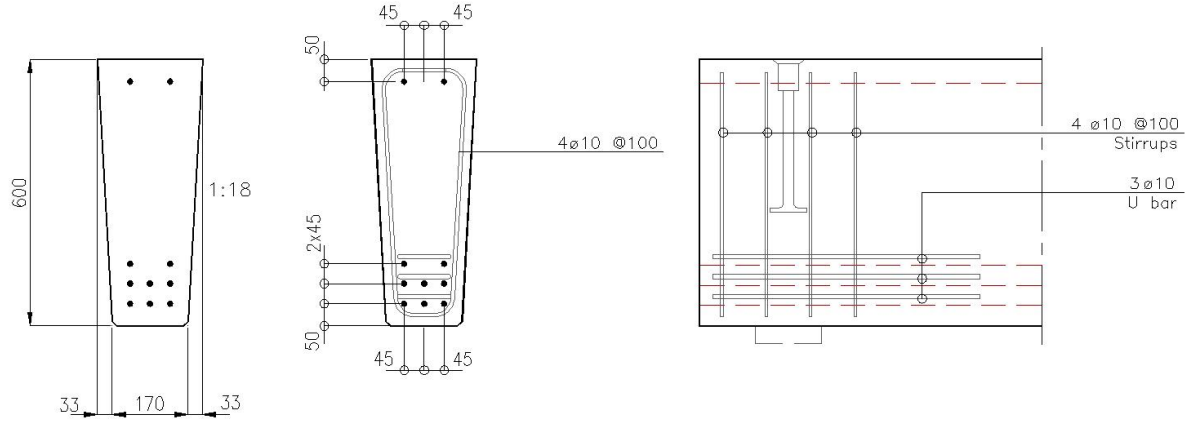

Figure 4-16: Cross section of the full scale beams AF

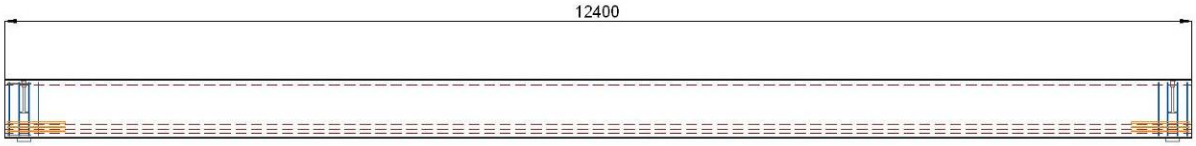

Figure 4-17: Geometry and reinforcement of the full scale beams AF

Table 4-9: Cross section properties, beams AF

Area	A_c	[mm^2]	122E+3
Inertia	I_y	[mm^4]	3.627E+6
Position of the centroid from the top	z_g	[mm]	284
Axial force due to prestressing	$F_{p,t1}$	[kNm]	1208
Bending moment due to prestressing	$M_{p,t1}$	[kNm]	154
Effective depth	d	[mm]	507

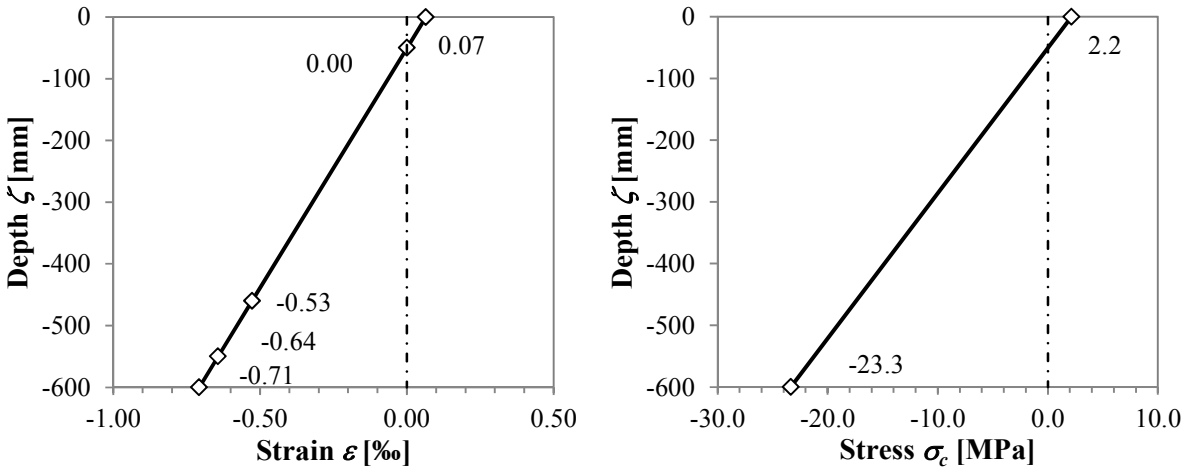

Figure 4-18: Theoretical strain plane and stresses in cross-section considering the elastic losses

4.4.3 Casting process

The members were cast in the precast plant of Element AG at Tafers, Switzerland. The beams were prestressed and removed from the framework after 3 days for type AV and after 2 days for type AF. The HPC and HPFRC were prepared in a mixing plant outside the precast plant and were transported in a mixing truck. After the slump flow test, the concrete was poured in the framework with a bucket (Figure 4-20). All beams were casted in a similar manner. The concrete was poured from one extremity to the other. Up to a fibre content of 60 kg/m^3 the compositions respected the self-compacting criteria, with a slump flow higher than 600 mm. However steel fibres decreased the workability and in presence of dense reinforcement, the aggregates were blocked due to the mesh formed by the fibres. The compositions A1 to A3 (40 kg/m^3) didn't show any problems, due to the ease of flow of the material which could be casted without vibration. Whereas the A4 (60 kg/m^3) and A5 (80 kg/m^3) compositions, they needed a vibration process along the longitudinal reinforcement. In a first casting without the vibration process, the beams AV-5 and AV-6 showed several defaults at the level of the reinforcement (Figure 4-20). These two beams were cast again. After the removal of the formwork, the beams were transported and stored outside the precast plant approximately two weeks and removed inside the laboratory.

Figure 4-19: Mixing plant and slump flow test before the casting process

Figure 4-20: Casting process and the first shear beams AV-5 and 6

For each HPC batch, the following specimens were cast:

- 8 cylinders ϕ150 x 300 mm for f_c, f_t, E_c
- 2 prisms 150 x 150 x 700 mm for $f_{t,flex}$ (only with AF-1)

For each HPFRC batch, the following specimens were casted:

- 4 cylinders ϕ150 x 300 mm for f_c, E_c
- 4 prisms 150 x 150 x 550 mm for determining the post cracking response

Table 4-10: Properties of the fresh concrete

Members	Concrete	Date of casting	Date of prestressing	Slump Flow [mm]	Density [kg/m^3]	Air Temp. [C°]	Concrete Temp. [C°]
AV-1	A1	20/8/2010	23/8/2010	600	2410	25.5	23.5
AV-2	A1						
AV-3	A2	27/8/2010	30/8/2010	650	2442	26.0	27.5
AV-4	A3			700	2438	26.0	27.0
AV-5	A4	10/9/2010	13/9/2010	620	2469	23.0	25.0
AV-6	A5			460	2500	23.0	24.5
AF-1	A1	13/9/2010	15/9/2010	620	2405	22.0	24.0
AF-2	A4	15/9/2010	17/9/2010	650	2465	21.0	25.5

4.4.4 Test setup

AV beams

The load tests were performed at the Structural laboratory of the University of Applied Sciences Fribourg. The beams were tested on a span of 3.60 m. For the shear beams, a distance of 1.00 m at each side was kept to allow the diffusion of the pre-tension forces. The load was applied at the centre of the element through a steel plate. In this load configuration, the geometrical ratio between the shear span and the effective depth ***a/d*** **was 3.52**. The loading system was composed of a steel crossbeam (2) connected to the 1000 kN actuators (5) by prestressing tie-rods (1). The two actuators were connected to a steel crossbeam anchored (7) to the strong floor (Figure 4-21). The tests were controlled in displacement by a servo-electronic system of the firm *Walter & Bai*. The displacement rate was 0.02 mm/s representing a quasi-static loading. The load was applied with increments of 20 kN until the formation of the first critical shear crack. At each step, the cracking pattern and the crack openings were plotted.

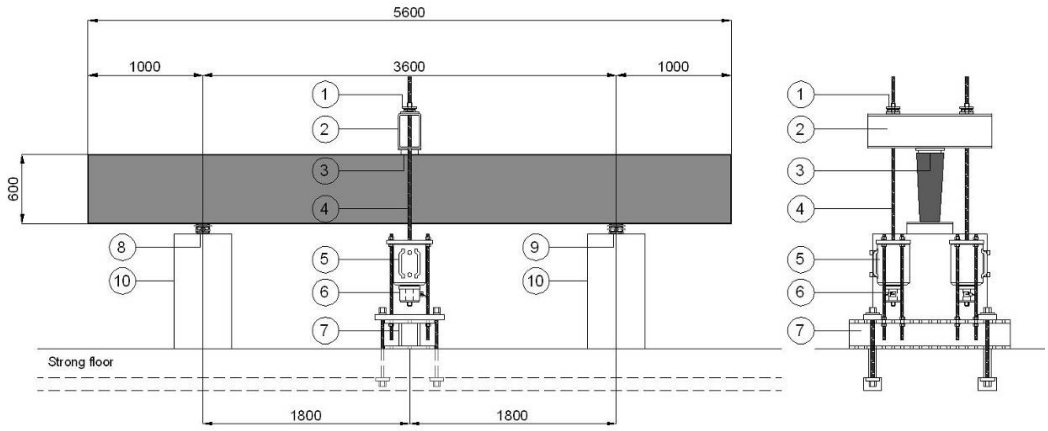

1 spherical plain thrust bearings *SKF*
2 loading crossbeam RRW 300/200/12.5
3 steel plate 200 x 150 x 15 mm on mortar layer
4 tie-rods *Stahlton-MSP* 32 mm
5 actuators *Bieri* 1000 kN/160 mm
6 load cells *HBM* 1000 kN
7 bottom crossbeam
8 pined support with introduction plate of 300 x 80 x 30 mm
9 rolled support with introduction plate of 300 x 80 x 30 mm
10 support blocks

Figure 4-21: Test setup of the shear beams AV

A total number of 40 instruments were recorded for each test (Figure 4-22). Two load cells type *HBM C6A 1000 kN* were placed between the actuators and the tie rods. Six linear variable differential transducers (LVDT) allowed the measurement of the vertical displacements of the beam and the supports. Eight LVDT were placed in diagonal with an inclination of 45° on both sides in order to measure the shear cracks openings. Eleven LVDT were arranged on the tension chord in order to measure the average of cracks openings. Four displacement transducers type *TML Omega* were placed on the top of the beam, near the load introduction in order to measure the compression strain. Nine strain gauges type *HBM LY41 50/120* were glued, two in diagonal with an inclination of 18 and 45° on compression struts and critical sections. The instruments were connected to a data acquisition system type *HBM Spider 8* with the data acquisition software *HBM Catman*. The frequency of recording was 1 Hz. The face of the beams without transducers was painted in white in order to plot the cracking pattern.

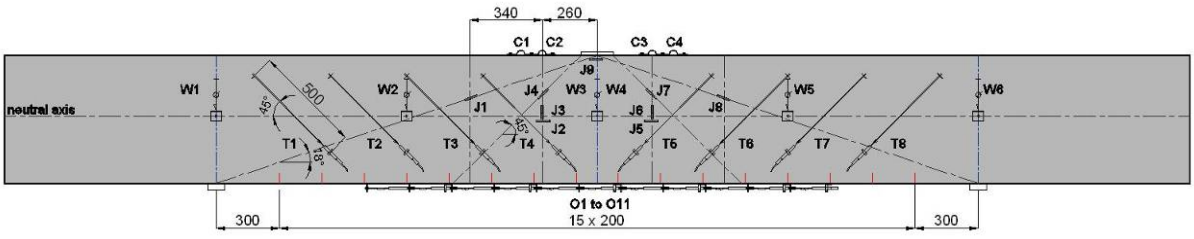

Figure 4-22: Measurement arrangement of the shear beams AV

Figure 4-23: Views of the shear beams setup and measurement arrangement

AF beams

The full scale beams were tested on a 12.00 m span. The load was applied at two points symmetrically located at a 3600 mm distance of the supports and were introduced through steel plates. In this load configuration, the geometrical ratio between the shear span and the effective depth **a/d was 7.10**. The loading system was similar to the shear beams set-up (

Figure 4-24). The tests were controlled in displacement by a servo-electronic system of the firm *Walter & Bai*. The displacement rate was 0.02 mm/s representing a quasi-static loading. The load was applied with 20 kN increments up to the failure. At each step, the cracking pattern and the crack openings were plotted.

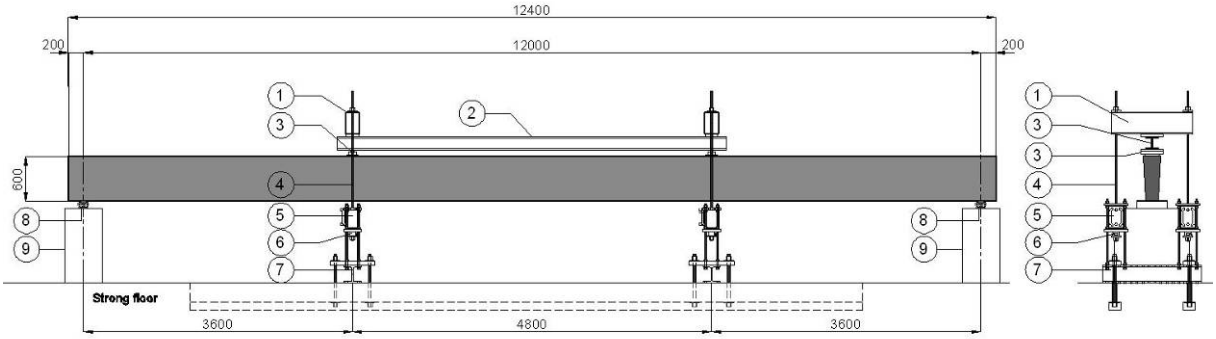

1 loading crossbeams in steel RRW 300/200/12.5
2 connecting beam HEM 160
3 supports with steel plates 200 x 150 x 15 mm on mortar layer
4 tie-rods *Stahlton-MSP* 26.5 mm
5 actuators *Bieri* 500 kN/160 mm
6 load cells *HBM* 200 or 500 kN
7 bottom crossbeams HEM 260
8 rolled support with introduction plate of 300 x 80 x 30 mm
9 support blocks

Figure 4-24: Test set-up of the full scale beams AF

A total number of 37 instruments were recorded for each test (Figure 4-25). Four load cells type *HBM C6A 200 or 500 kN* were placed between the actuators and the tie rods. Nine linear variable differential transformers (LVDT) allowed the measurement of the vertical displacements of the beam and the supports. Nineteen LVDTs were arranged on the tension chord in order to measure the average of cracks openings. Three displacement transducers type *TML Omega* were placed on the top of the beam, at the centre in order to measure the compression strain. Six strain gauges HBM type LY41 50/120 were glued horizontally under the loads, at the centre and at the critical sections. The instruments were connected to a data acquisition system type *HBM Spider 8* with the data acquisition software *HBM Catman*. The frequency of recording was 1 Hz. The face of the beams without transducers was painted in white in order to plot the cracking pattern.

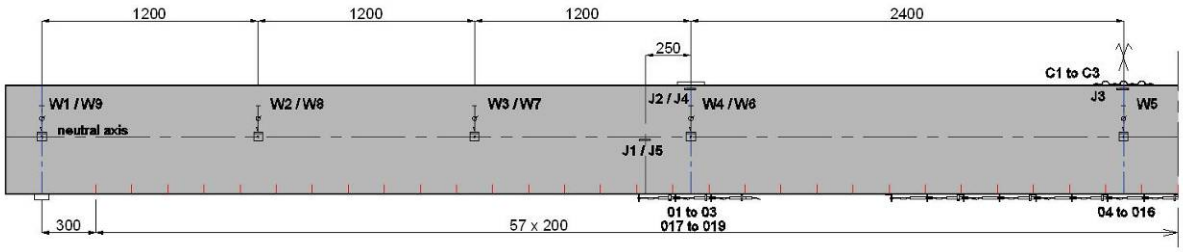

Figure 4-25: Measurement arrangement of the shear beams AF

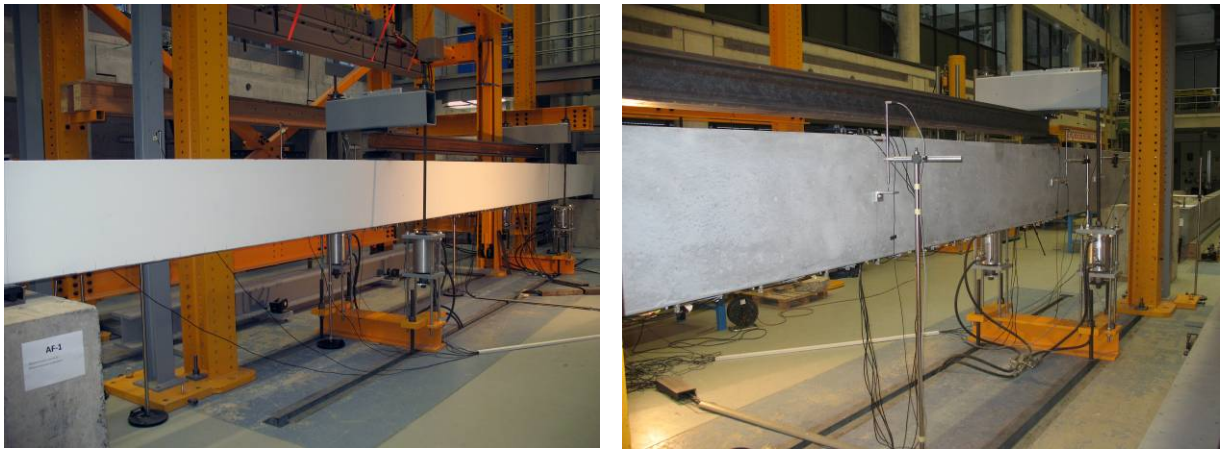

Figure 4-26: Views of the full scale beam setup and measurement arrangement

4.4.5 Tensile properties of reinforcement

The tensile properties of steel rebars and prestressing strands were defined on six bars of each diameter. The tests were performed on bars of 600 mm length in a universal testing machine of the firm *Walter & Bai* according the standards ISO 15630 parts 1 and 3 [ISO2010a] [ISO2010c].

Table 4-11: Mechanical properties of the reinforcing steel

Diameter [mm]	E_s [GPa]	$f_{s0,2}$ [MPa]	f_u [MPa]	ε_u [%]
ϕ6	202	547	630	5.4
ϕ22	200	565	674	10.4

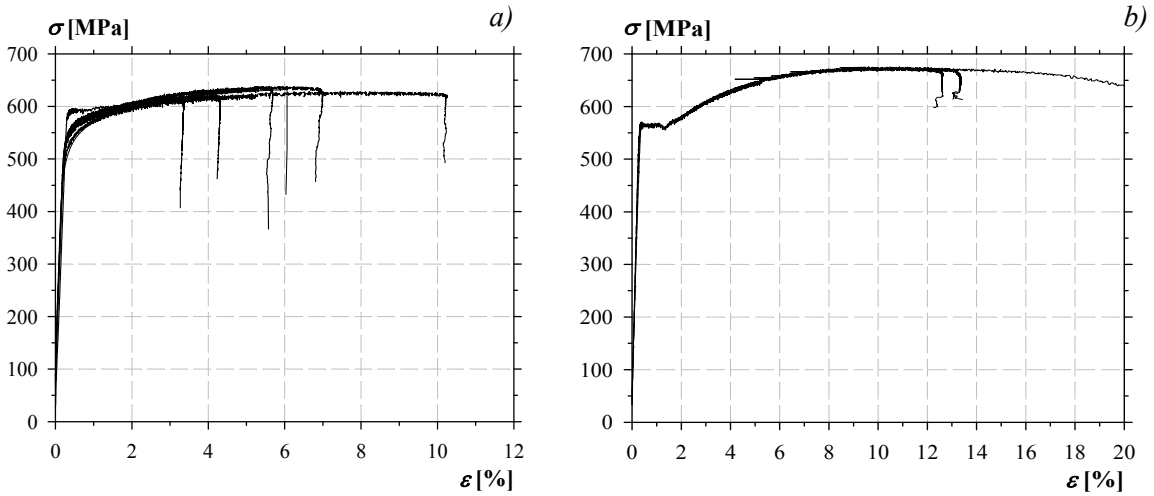

Figure 4-27: Stress-strain characteristics of the reinforcing steel, a) stirrups ϕ6 mm, b) longitudinal rebars ϕ22 mm

The reinforcing steel for the stirrups showed a hardening behaviour without yield plateau. Conversely, the rebars ϕ22 exhibited a yield plateau and large strains at the ultimate strength.

Table 4-12: Mechanical properties of the prestressing steel

E_s [GPa]	$f_{p0,1}$ [MPa]	f_u [MPa]	ε_u [%]
206	1,832	1,982	3.1

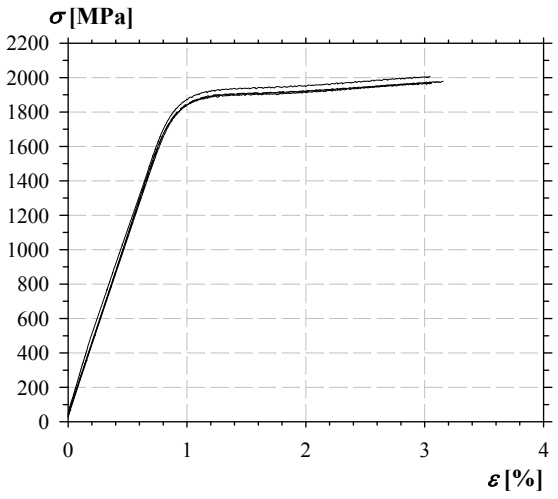

4.5 Test results

AV beams

Tests results on shear beams are presented on Figure 4-28 and Table 4-13. The first flexural cracks appeared approximately under a shear load of 190 kN. Due to the high axial force, the cracking load was difficult to identify. The content and the used type of steel fibres didn't affect the cracking load of the matrix in a significant manner, but had a considerable influence on the propagation, development and distribution of the cracks. When the fibres content was increased, the crack was discontinuous and had smaller openings.

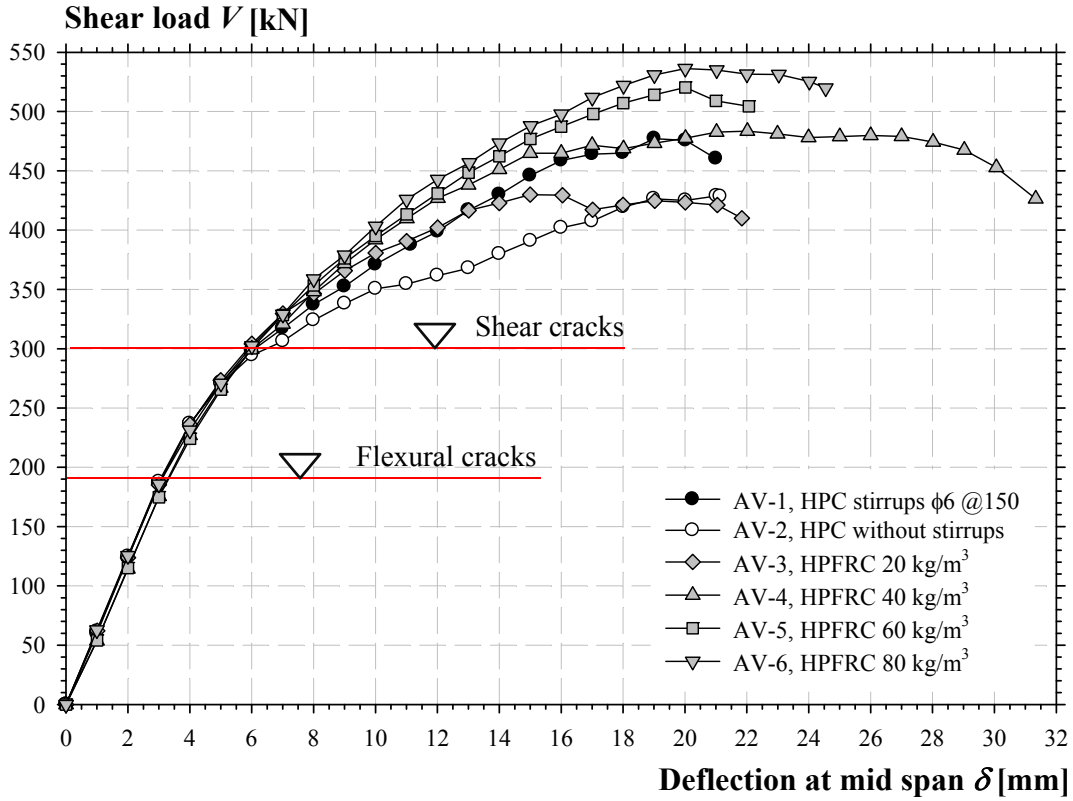

Figure 4-28: Curves shear load V vs displacement at mid span δ of the shear beams AV

Table 4-13: Test data of shear beams AV

Specimen	Fibres content [kg/m^3]	V_R [kN]	δ_{VR} [mm]	Failure mode [-]
AV-1	0	481 *112%**	19.8 *93%*	Shear - compression
AV-2 *ref.*	0	429 *100%*	21.1 *100%*	
AV-3	20	430 *100%*	15.1 *72%*	
AV-4	40	484 *113%*	21.9 *104%*	
AV-5	60	521 *121%*	20.2 *96%*	
AV-6	80	538 *125%*	20.3 *96%*	

* difference with the reference beams AV-2

Once the cracking load was reached, the stiffness decreased progressively. Several cracks were developed in the central part of the beams. Due to the high axial force and high reinforcement ratio, the fibres' effect on the beams' stiffness wasn't important. However, the cracking pattern was different amongst all the beams. After cracking has occurred, the steel fibres improved the cracking distribution by reducing spacing and by limiting the cracks' openings (Figure 4-30).

From a shear load of 300 kN, the first diagonal shear cracks appeared (Figure 4-29). In presence of these cracks, the HPFRC beams showed a higher stiffness. The diagonal cracks' developments were controlled by the fibres, and this phenomenon was absent in the high strength concrete beam without stirrups (AV-2). For HPFRC members, from a fibres content of 40 kg/m^3, the macro-shear crack development was significantly delayed due to the formation of a secondary crack network (Figure 4-30). The HPC beam without transverse reinforcement AV-2 showed a significant decrease of stiffness once the diagonal shear crack appeared, which wasn't the case with the other beams. The beam AV-2 highlighted the importance of transversal reinforcement on one hand, and the ability of fibres to replace the shear reinforcement on the other hand. The AV-2 specimen had two diagonal cracks on both sides of the load application. Despite the formation of these two diagonal cracks, the failure didn't take place in a brittle way. The beam showed a large post-cracking reserve before the failure's occurrence and this was mainly due to the high axial force.

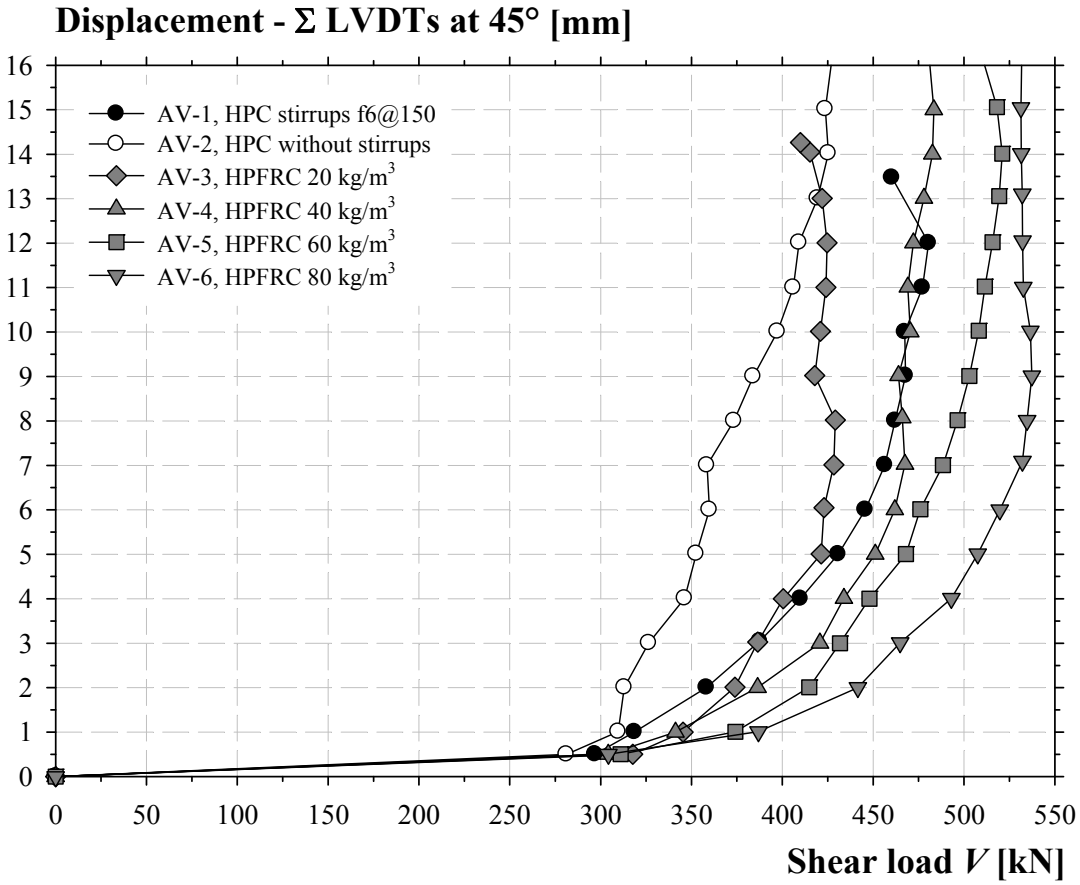

Figure 4-29: Curves shear load V vs Σ displacement at 45° of the shear beams AV

The failure mode of the six beams was similar but at different load levels. The two strands at the top of the cross section stopped the development of diagonal cracks through the compression chord. These strands had a similar effect as the compression flange of the T-section. Subsequently, the failure occurred through the crushing of the concrete at the root of a diagonal shear crack. The failure took

place after a drop in resistance followed by a separation of the specimen in two blocks. This type of failure can be named shear-compression. The appearance of the critical shear crack was increasingly delayed while the fibres content increased. The critical shear crack was dragged towards the supports due to the effect of the axial force combined with fibres (Table 4-14). Moreover, these cracks tend to straighten up with the increasing fibres content (Figure 4-30).

The test results highlighted the ability of steel fibres to replace the minimum shear reinforcement. However, the minimum fibres content depends on the properties of fibres and concrete. Based on the three-points bending tests on notched prisms, it appeared that the HPFRC, which presented a hardening behaviour in bending, was capable to control the shear cracks development.

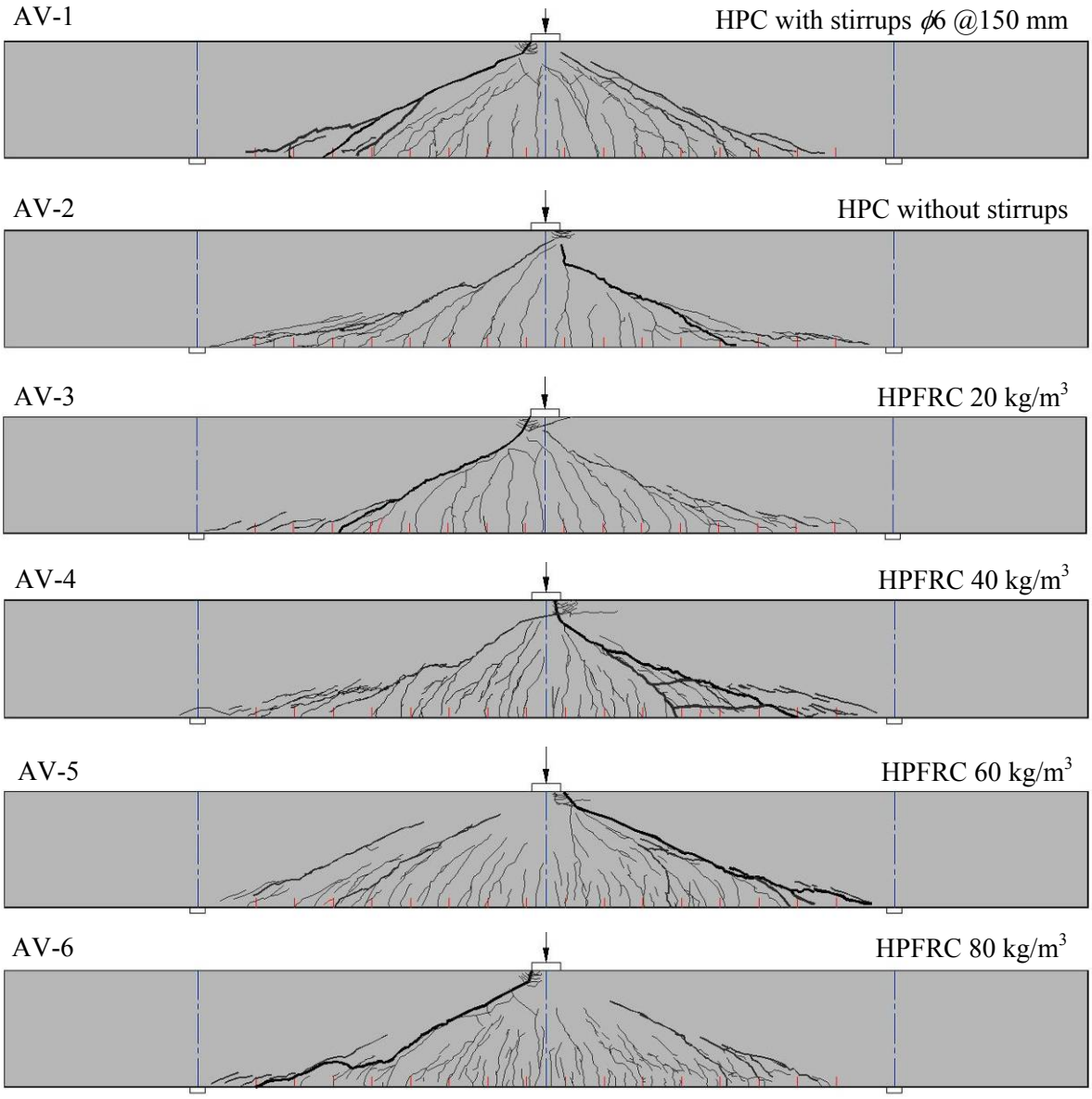

Figure 4-30: Cracking pattern of the shear beams AV-1 to AV-6

Table 4-14: Measured inclination of critical shear cracks

Beam	**AV-1**	**AV-2**	**AV-3**	**AV-4**	**AV-5**	**AV-6**
Fibre content [kg/m^3]	0 stirrups	0	20	40	60	80
Inclination of CSC* [°]	26	29	27	21	25	26

*Critical shear crack (CSC)

The analysis of the failure plan showed that all fibres were pulled out and not broken (Figure 4-31). However, all coarse aggregates were broken.

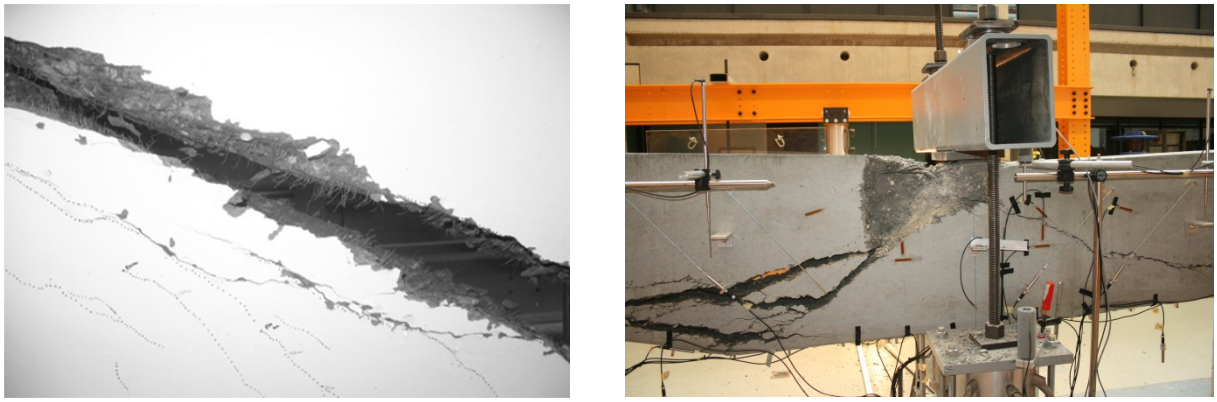

Figure 4-31: Fibres in the critical shear cracks and concrete crushing zone

Beams AF

The results obtained on full-scale beams are presented in Figure 4-32. The failure mechanism of specimen AF-1 was similar to that of the beams type AV. In a first step, several diagonal cracks were developed without causing sudden failure. The two strands placed at the top of the cross section prevented the cracks' propagation through the compression chord. In a second step, the evolution of the cracks caused the concrete crushing of the compression chord and a brittle failure took place. This type of failure can be considered as a shear-compression one.

Table 4-15: Test data of full-scale beams AF

Specimen	Fibres content [kg/m^3]	V_R [kN]	δ_{VR} [mm]	Failure mode [-]
AF-1 *ref*	0	170 *100%**	224 *100%**	Shear - compression
AF-2	60	203 *119%*	280 *125%*	Flexural

* difference with the reference beams AF-1

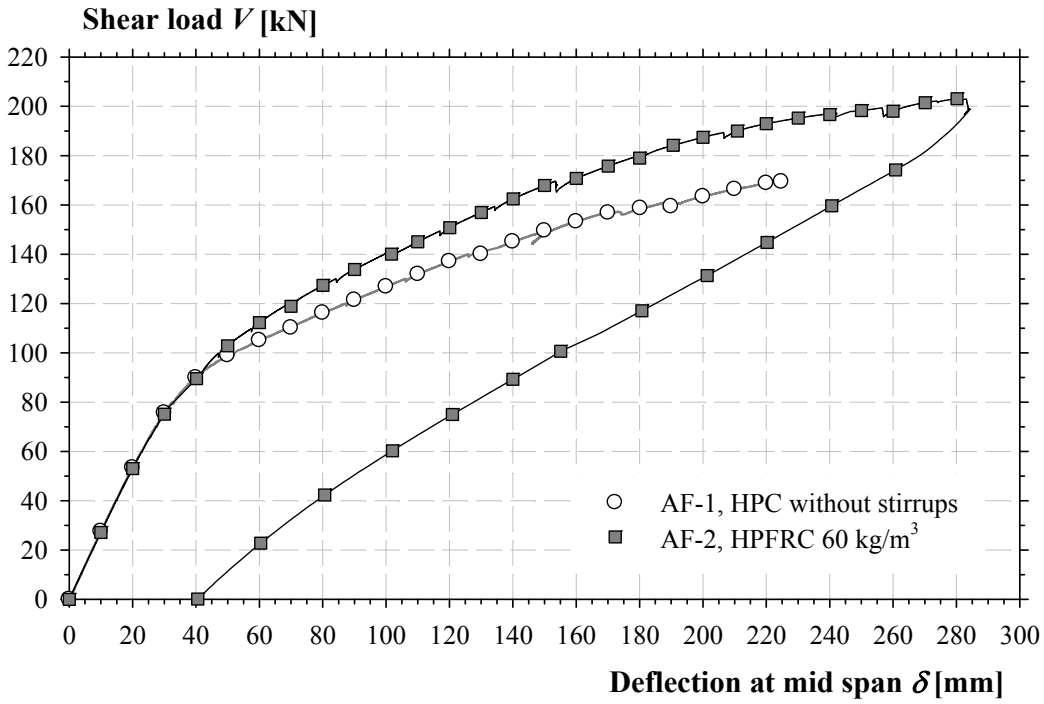

Figure 4-32: Curves shear load V vs displacement at mid span δ of the full scale beams AF

The beam AF-2 with a fibres content of 60 kg/m^3, showed a different behaviour. The test was stopped at the plateau under a deflection at mid span of 280 mm. The stiffness in state II, elastic-cracked, was higher compared to specimen AF-1. The beam presented multi-cracks spaced with a distance of about 30 mm and less than 0.3 mm openings. From a shear load of 200 kN, several cracks were joined to form one macro-crack in the central part. This element has reached its flexural capacity without the development of diagonal shear cracks (Figure 4-33).

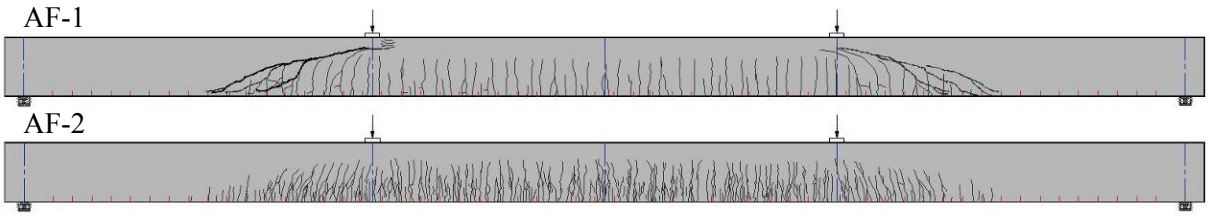

Figure 4-33: Cracking pattern of the full scale beams AF-1 and AF-2

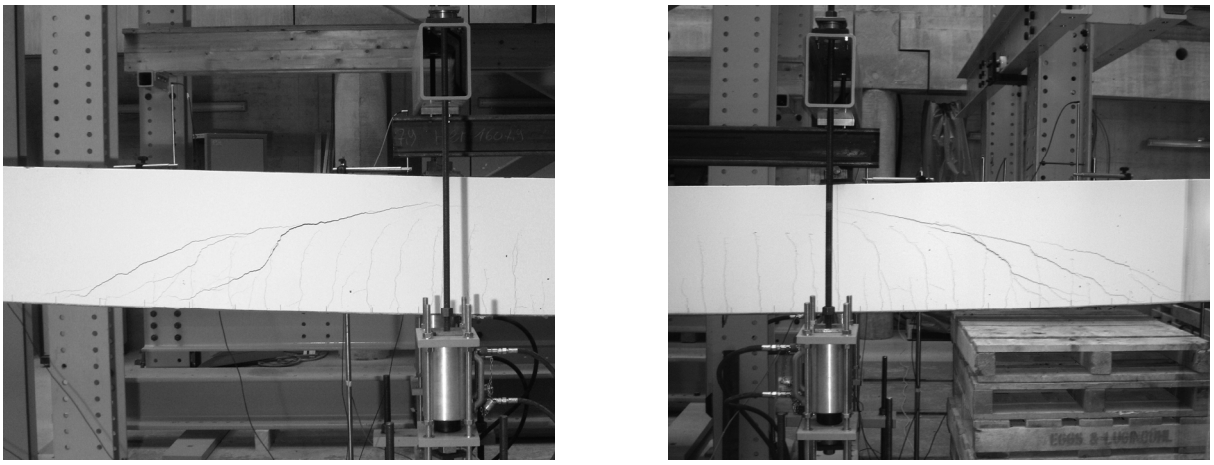

Figure 4-34: Critical shear cracks of specimen AF-1

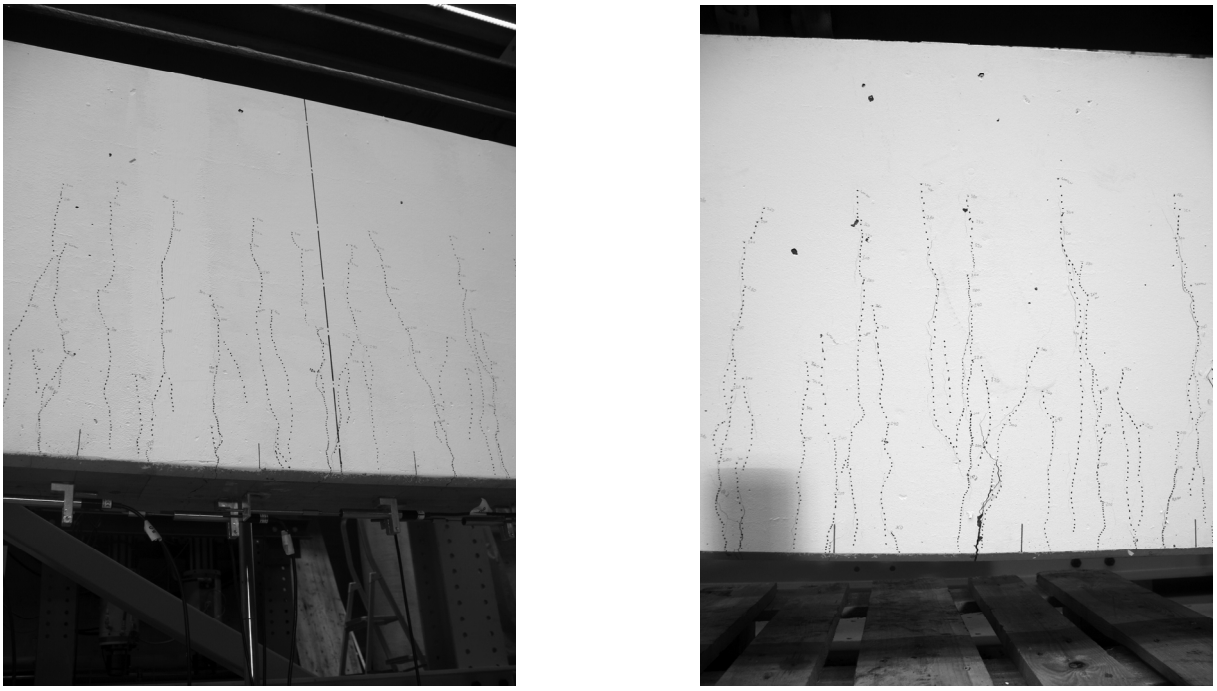

Figure 4-35: Thin cracking pattern of specimen AF-2

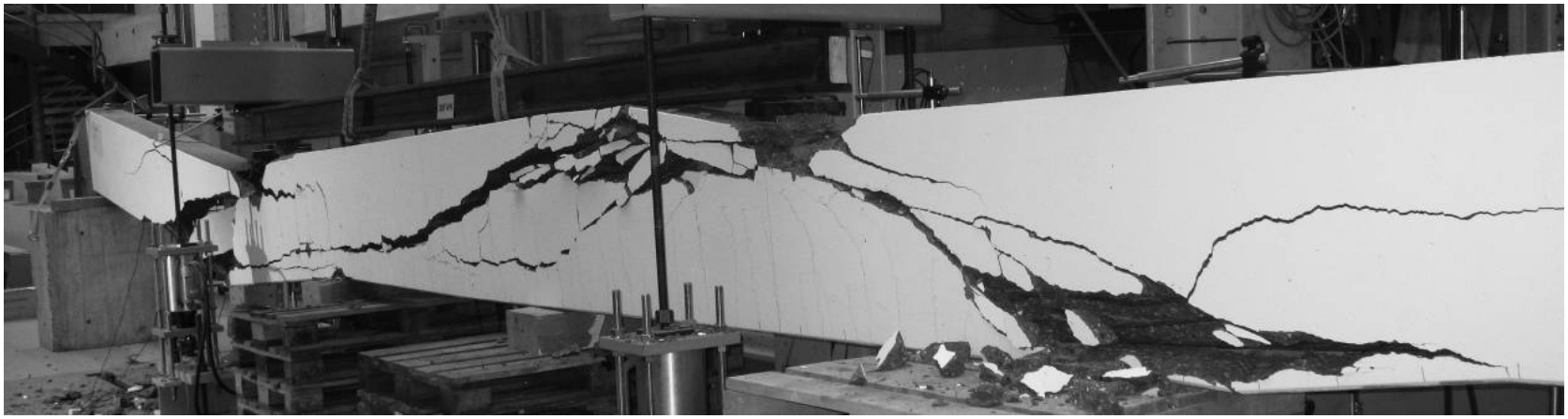

Figure 4-36: Beam AF-1 after the failure, V_R 170 kN

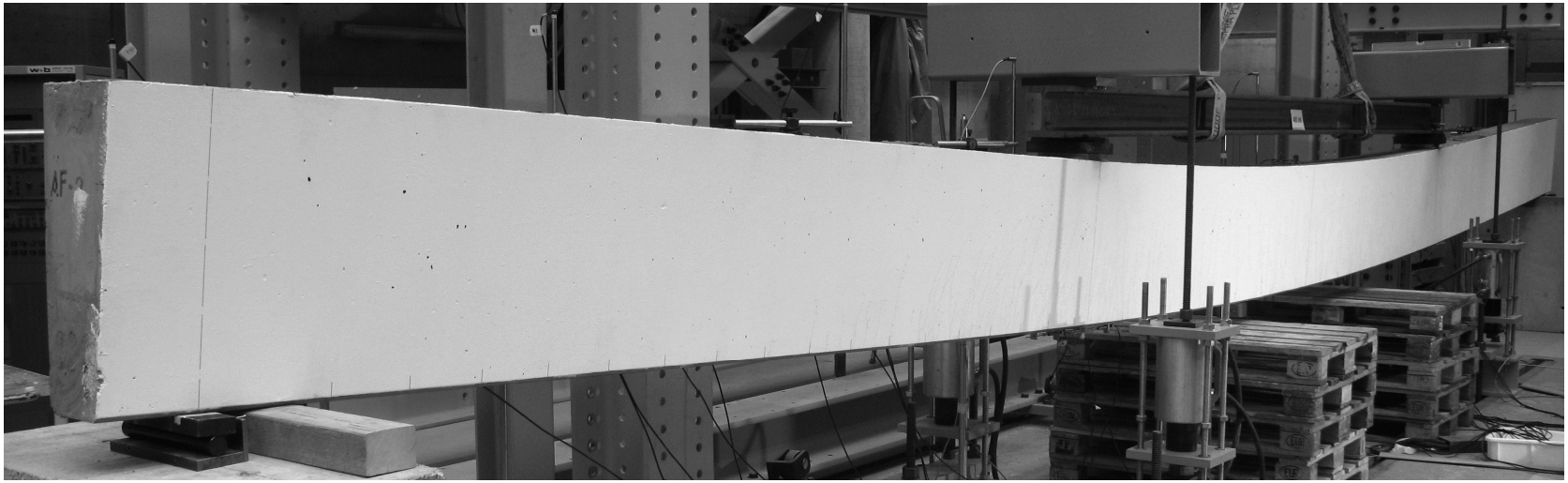

Figure 4-37: Beam AF-2 under a deflection at centre of 280 mm and a shear force V of 203 kN

4.6 Numerical analysis

4.6.1 Comparison with code formulations

The test results of points 4.3 and 4.5 were compared to the calculated values according to the shear provisions for SFRC proposed by the Rilem TC162-TDF 2003 [RIL2003] and the *fib* Model Code 2010 [MC2010b] and the AFGC – UHPFRC [AFGC2002]. The flexural strength V_{flex} was evaluated considering the tensile strength at ultimate state of the SFRC f_{Ftu} (model *fib,* see point 2.1.6.1).

$$V_{R,Rilem} = \left[\frac{0.18}{\gamma_c} \cdot k \cdot \left(100 \cdot \rho_I \cdot f_{ck}\right)^{1/3} + 0.15 \cdot \sigma_{cp} + k_f \cdot k \cdot \cos\theta \cdot \tau_{fd} \cdot \cot\theta \right] \cdot b_w \cdot d \tag{4-6}$$

$$V_{R,MC2010} = \left\{ \frac{0.18}{\gamma_c} \cdot k \cdot \left[100 \cdot \rho_l \cdot \left(1 + 7.5 \cdot \frac{f_{Ftuk}}{f_{ctk}} \right) \cdot f_{ck} \right]^{1/3} + 0.15 \cdot \sigma_{cp} \right\} \cdot b_w \cdot d \tag{4-7}$$

$$V_{R,AFGC} = \left[\frac{0.24}{\gamma_c} \cdot \sqrt{f_{ck}} + \frac{\sigma_p}{\gamma_f} \cdot \frac{0.9}{\tan\left(\beta_u\right)} \right] \cdot b_w \cdot d \tag{4-8}$$

Where β_u *is* the angle of the compression strut, assumed to be $\pi/4$ for RC-members, determined by iteration for PT-members, $tan(\beta_u)=2\tau_u/\sigma_c$.For further details on the Rilem TC162, AFGC and MC2010 shear provisions for SFRC, the models are detailed into the points 2.2.7.1, 2.2.7.2 and 2.2.7.3 respectively.

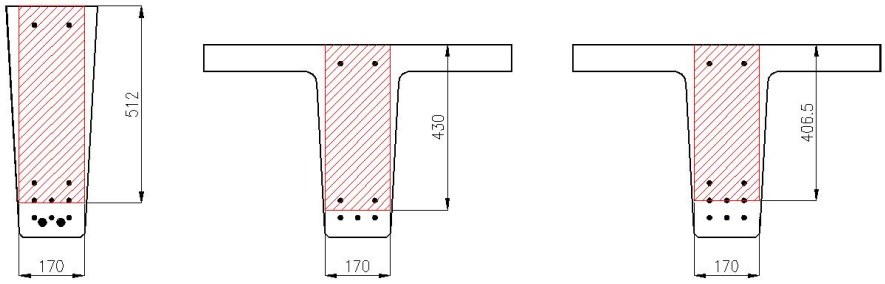

Figure 4-38: Effective cross-section considered for the shear strength

Table 4-16: Comparison between the test results and the calculated values for beams type A.

Specimen	V_{test} [kN]	V_{flex} [kN]	$V_{R,Rilem}$ [kN]	$V_{R,MC2010}$ [kN]	$V_{R,AFGC}$ [kN]
AF-1	170	194	258	294	186
AF-2	203 flexural	214	393	402	518
AV-1	481	488	388	314	321
AV-2	429	488	293	296	188
AV-3	430	502	349	356	352
AV-4	484	519	427	409	257
AV-5	521	525	488	430	573

AV-6	538	530	507	439	684
Average V_{test}/V_{calc}			1.12	1.19	1.24
Coefficient of variation			0.21	0.26	0.25

Table 4-17: Comparison between the test results and the calculated values for beams type P.

Specimen	V_{test} [kN]	V_{flex} [kN]	$V_{R,Rilem}$ [kN]	$V_{R,MC2010}$ [kN]	$V_{R,AFGC}$ [kN]
PF-1	132 flexural	146	193	193	125
PF-2	144 flexural	154	287	244	391
PV-1	327	423	155	155	132
PV-2	435 flexural	462	287	244	414
PV-3	451 flexural	480	340	259	527
PV-4	435	612	193	193	125
PV-5	581	646	294	263	391
Average V_{test}/V_{calc}			1.49	1.64	1.54
Coefficient of variation			0.38	0.35	0.36

The Rilem TC162, MC2010 and AFGC shear provisions for SFRC and UHPFRC are based on empirical formulation and are not based on the latest developments. The calculated values of shear strength are largely underestimated. This fact is due to the direct strutting failure mode, while these formulations are a truss based model.

4.6.2 Elastic Plastic Stress Fields model

Although, the shear span of the beams AV and PV was around 3.5 and 3.0 respectively, it was observed experimentally that the propagation of the shear cracks was not unstable. Moreover, the critical shear cracks were straight. The code like models developed above underestimate the failure load. This fact can be explained by the failure regime. The shear span was chosen in order to obtain a truss mechanism and not a direct strutting. According to the Kani's valley, a ratio *a/d* of 2.5 corresponds approximately, for ordinary reinforced beams, to the limit between unstable crack propagation and direct strutting regions. However, in prestressed members, the effective shear span a_{eff} is smaller than the geometric one. This is due to the fact that the normal force does not allow the development of flexural cracks close to the support (region A) (Figure 4-12).

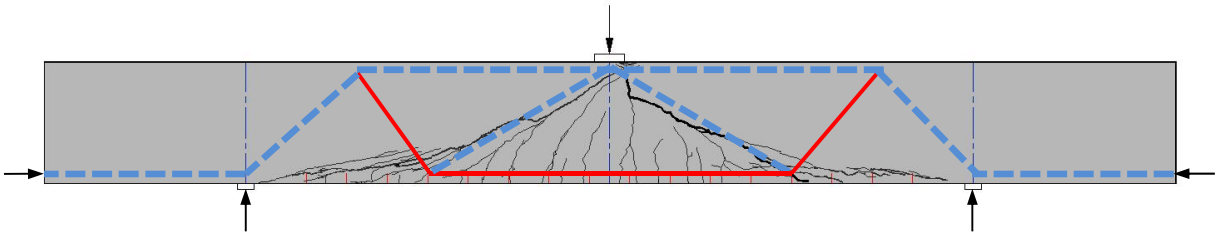

Figure 4-39: Strut and tie model for the shear beams AV, blue for compression, red for tension

For a more accurate prediction of the shear behaviour and strength in direct strutting regime, a Non Linear Finite Element Analysis with the Elastic Plastic Stress Fields (EPSF) model was performed [MUT2011]. However, only the beams without fibres may be calculated with this model. The principal hypotheses of this model are the following:

- 2D model,
- elastic – plastic behaviour of materials,
- concrete tensile strength neglected,
- aggregates interlocks resistance neglected,
- the concrete compressive strength depends on transversal strains (cracking).

The cross section was divided into several stripes in order to represent the wide variation. The pre-tensioning was replaced by horizontal forces applied on rigid plates considering the prestressing losses (Figure 4-40). The equivalent prestressing steel yield limit $f_{p,eq}$ was implemented in the following manner:

$$f_{p,eq} = f_{py} - \frac{F_{pi}}{A_{pi}} \tag{4-9}$$

Where f_{py} is the yield limit of the prestressing steel, F_{pi} is the tension in the strand after the elastic losses and A_{pi} is the section of the strand.

The load P was applied by increment up to the failure load.

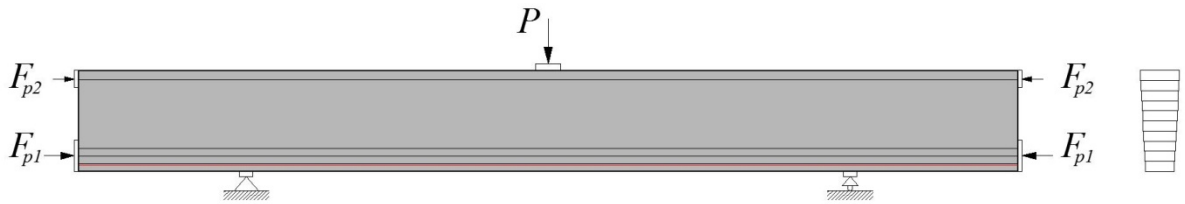

Figure 4-40: Model adopted for the EPSF analysis

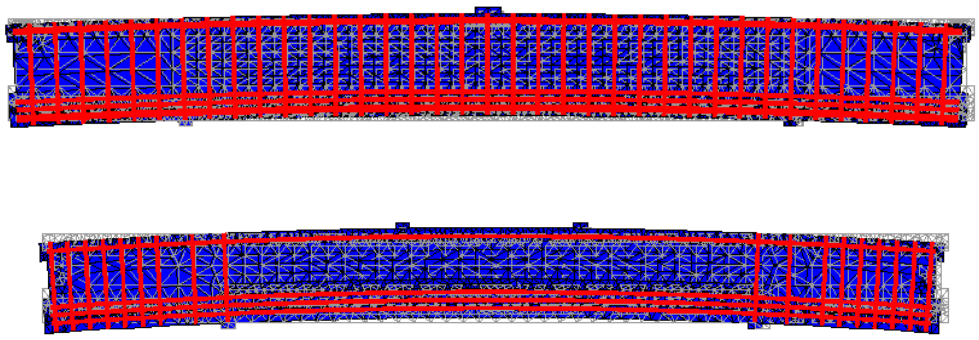

Figure 4-41: Amplified deformation of beam AV-1 and PV-4 under prestressing forces.

In the Figure 4-42, the results of the EPSF analysis at the failure load are presented. The blue lines represent the direction and the intensity of the principal compressive stresses, the red lines represent the intensity of tensile stresses in the reinforcement. The dark red shows the reinforcement plasticity and the grey to black colours in the concrete elements indicate the level of damage due to the transversal strains.

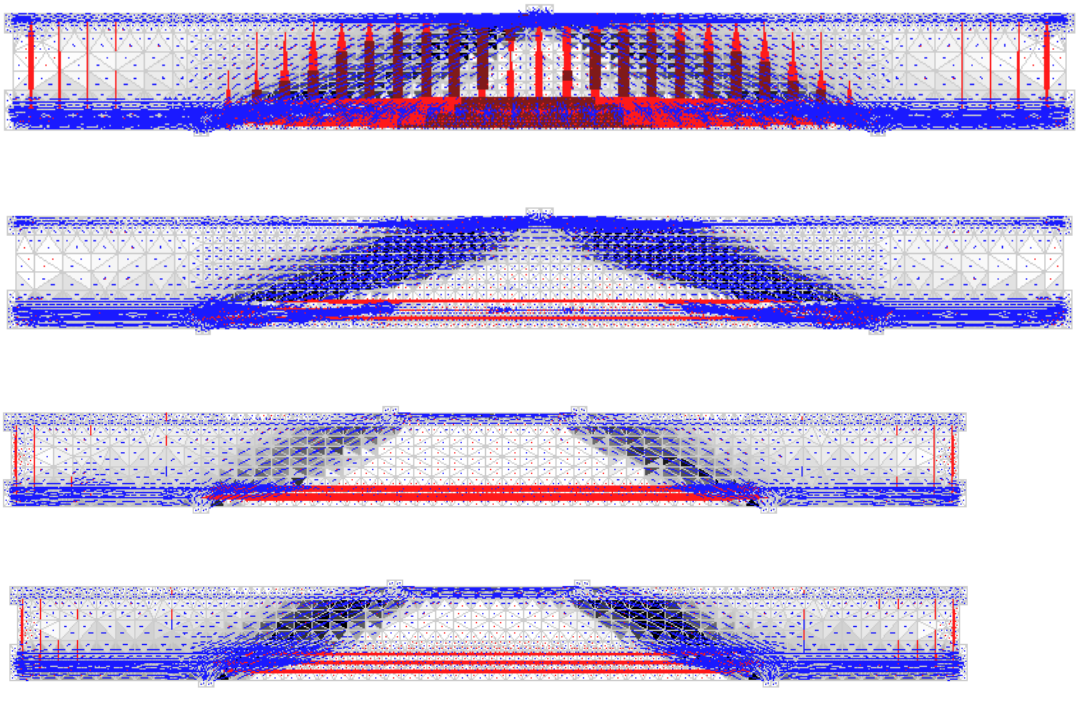

Figure 4-42: State of stresses at the failure load of pre-tensioned members in HSC without fibres

The inclinations of the compressive struts are clearly highlighted for the different pre-tensioned members. The middle zone, flexural cracking zone, corresponds to the cracking pattern. At ultimate load, the longitudinal and transversal reinforcement of the beam AV-1 reached their steel yield limit. While for other beams the steel reinforcement is always in the elastic state. The EPSF analysis adopted is able to represent the linear and non-linear behaviour of pre-tensioned members under shear loading with a good accuracy (Figure 4-43).

The ultimate loads are slightly overestimated, around 5 to 10%, except for beam AV-2. This fact is due to the important scatter associated with phenomena related to cracking in tension. The numerical simulation of beam AV-1 exhibited a flexural failure with large plastic deformation. The failure load prediction for beam AV-2 is clearly underestimated. This fact is probably due to the EPSF model assumptions; the tensile stresses and the aggregate interlocking mechanism are neglected. But in the test this beam exhibited a large reserve after the formation of the critical shear cracks certainly due to these shear transfer mechanisms.

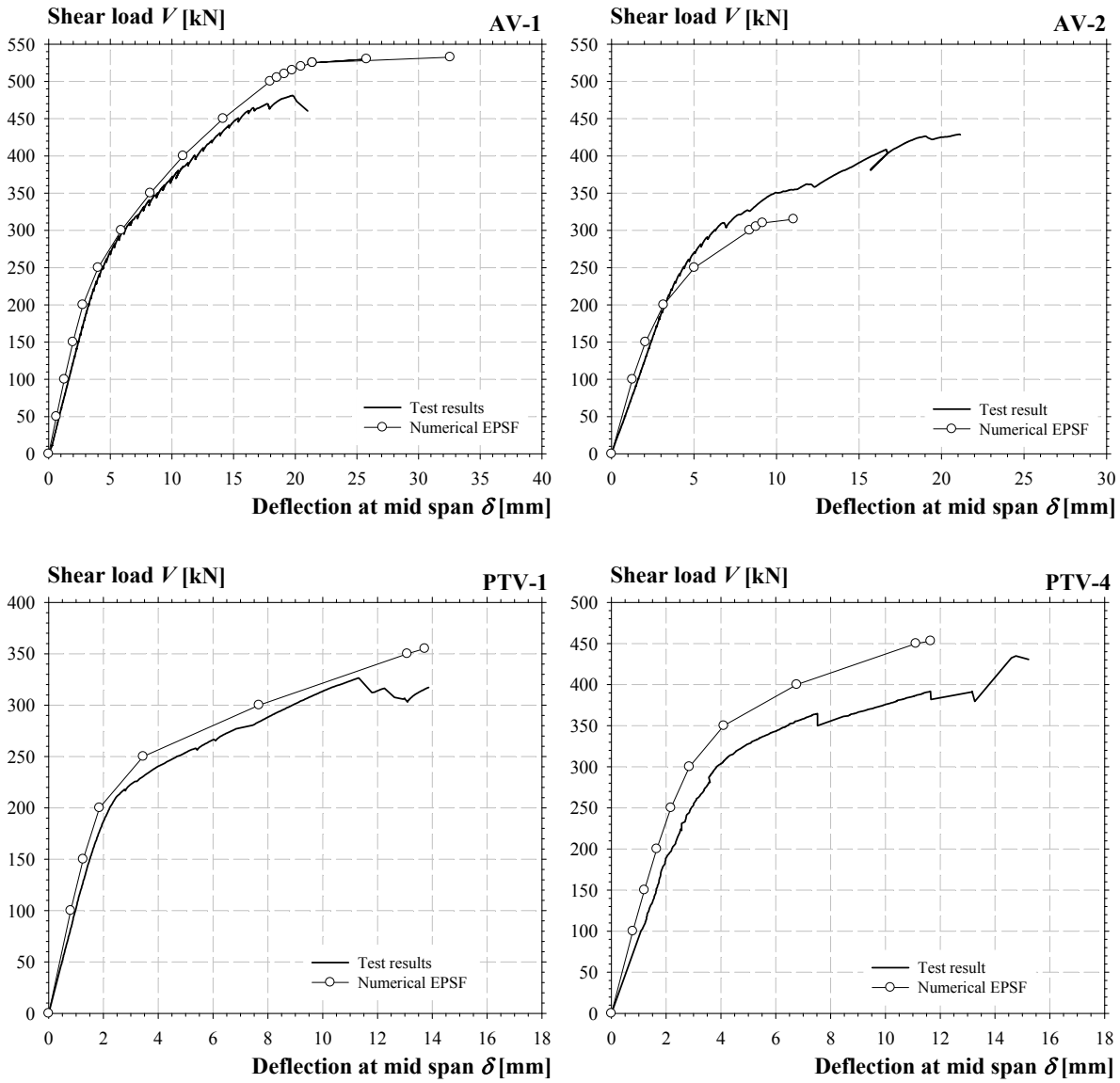

Figure 4-43: Comparison between computed curves load vs deflection and test results

Table 4-18: Comparison between the test results and the calculated values

Specimen	V_{test} [kN]	$V_{R,EPSM}$ [kN]	$V_{test}/V_{R,EPSM}$ [-]
AV-1	481	533	0.90
AV-2	429	321	1.34
PTV-1	327	355	0.92
PTV-4	435	453	0.96
Average V_{test}/V_{calc}			1.03
Coefficient of variation			0.20

4.6.3 Modified Compression Field Theory

The program Response 2000 was developed at the University of Toronto [BEN2010] and is based on the Modified Compression Field Theory MCFT (point 2.2.4.1). The program allows the analysis of simply supported beams and columns subjected to axial load and bending (moment and shear). The cracking pattern may be visualized at different load levels (Figure 4-44). The principal assumptions in the program are the following;

- 2D model,
- Bernouilli's hypothesis (plane section remain plane),
- concrete tensile strength neglected,
- perfect bond between concrete and steel,
- no transverse clamping stress across the depth.

However, the concrete tension softening in Response 2000 cannot be implemented by the user. Therefore, only the beams in plain concrete without fibres may be computed.

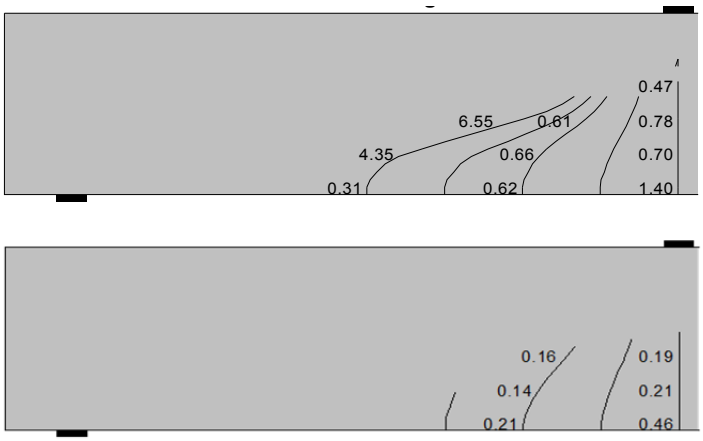

Figure 4-44: Cracking pattern at failure predicted by Response 2000 for beams AV-1 and AV-2

Except for full-scale beam AF-1, the ultimate loads of shear beams are slightly overestimated (Figure 4-45). However, the simulated load – deflection curves don't give an accurate prediction compared to the test results. The stiffness of the members is clearly overestimated.

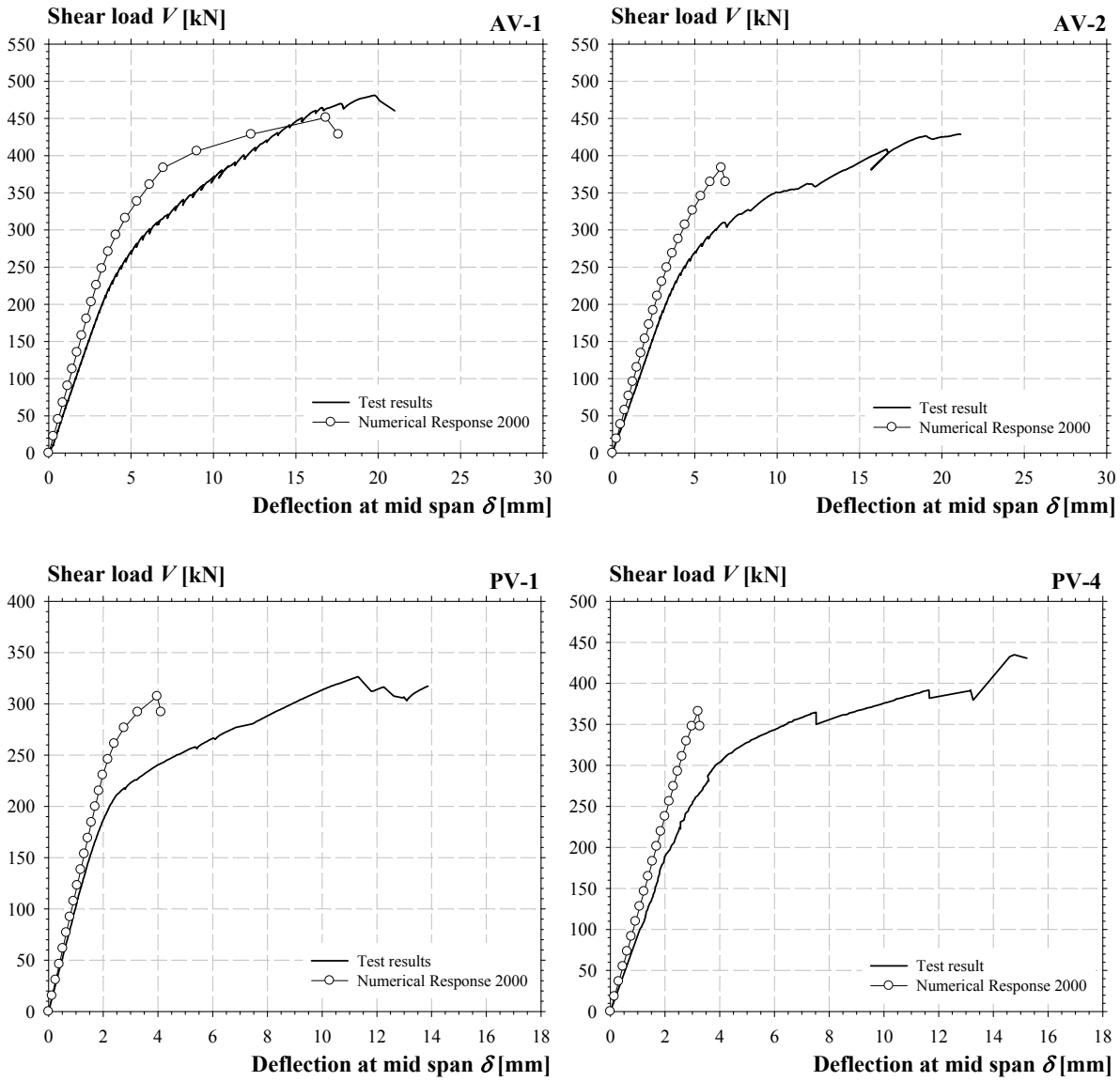

Figure 4-45: Comparison between computed curves load vs deflection and test results

Table 4-19: Comparison between the test results and the calculated values, Response 2000

Specimen	V_{test} [kN]	$V_{R,R2000}$ [kN]	$V_{test}/V_{R,R2000}$ [-]
AV-1	481	451	1.07
AV-2	429	384	1.12
AF-1	150	186	0.81
PV-1	326	307	1.06
PV-4	435	365	1.19
Average V_{test}/V_{calc}			1.05
Coefficient of variation			0.14

4.6.4 Non-linear finite element analysis (NLFEA)

In order to take into account the fibres contribution, numerical computations were performed with the use of the non-linear FEM software *FINELg* [FIN2012]. This software is continuously developed at the University of Liège and Greisch Engineering Office since 1970. It offers almost all types of FEM types of analyses such as:

- Geometrically and materially non-linear solid or structural problems under static dead loads.
- Linear and non-linear instability problems, leading to buckling loads and instability modes by eigenvalue computation.
- Dynamic problems, leading to eigenfrequencies and vibration modes with taking account, or of the internal stresses.

The numerical technique available in *FINELg* enables one to follow the behaviour of a structure under increasing external loading up to collapse or instability, and even beyond.

The external loading may consist of a series of sequences, where each load sequence, defined in sequence cards, is a combination of load cases.

Non-linear material effects are dealt with through the finite elements using either the total, the up-dated or the corotational Lagrangian formulation

Non-linear material effects are treated via the incremental plasticity theory (small strains); usual constitutive laws, such as elastic-perfectly plastic, bilinear, trilinear, Tamborg-Osgood, etc…, are included in the program

Model description

Only the members AV were analysed. The 2D model is composed of quadrangular 4-nodes shell finite elements with typical features (Corotational total Lagrangian formulation, Kirchhoff's theory for bending). These elements are rectangular and are disposed regularly. Each longitudinal stripe has a different thickness in order to represent the wide variation. The full beam was modelled (Figure 4-46).

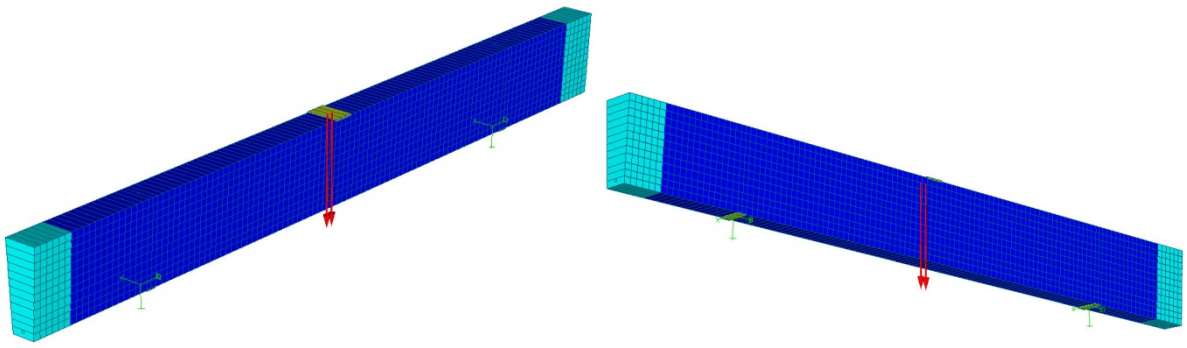

Figure 4-46: Views of model for beams AV

The prestressing strands are represented by the truss-bar element loaded by a temperature variation. Therefore, this element type cannot be loaded in compression and it doesn't have a flexural stiffness.

$$F_{p,0} \cdot \beta = E_p \cdot A_p \cdot \alpha_T \cdot \Delta_T \qquad (4\text{-}10)$$

Where β represents the prestressing losses.

The longitudinal and transversal reinforcement are represented by beam elements in order to take into account their flexural stiffness and the dowel action of longitudinal rebars. The loading plates are represented by beam elements in order to distribute the load and limit the local effects. For beams AV-2 to AV-6, the stirrups in the central part were removed (Figure 4-47).

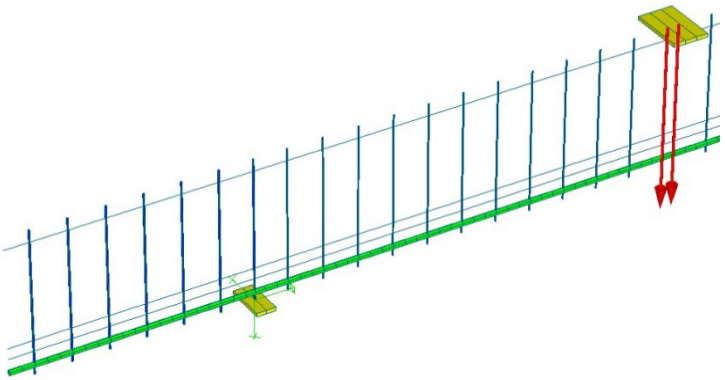

Figure 4-47: Elements type bars for reinforcement, prestressing and loading plates

For reinforcement and prestressing steel, bilinear and trilinear $\sigma - \varepsilon$ constitutive laws were adopted (Figure 4-48) considering the effective values of yield limit f_{sy} and ultimate strength f_t derived from tensile tests (point 4.4.5). A Young's modulus of 195 and 205 GPa was respectively implemented for the prestressing and the reinforcement. For the loading plate an elastic law with a Young's modulus of 210 GPa was considered.

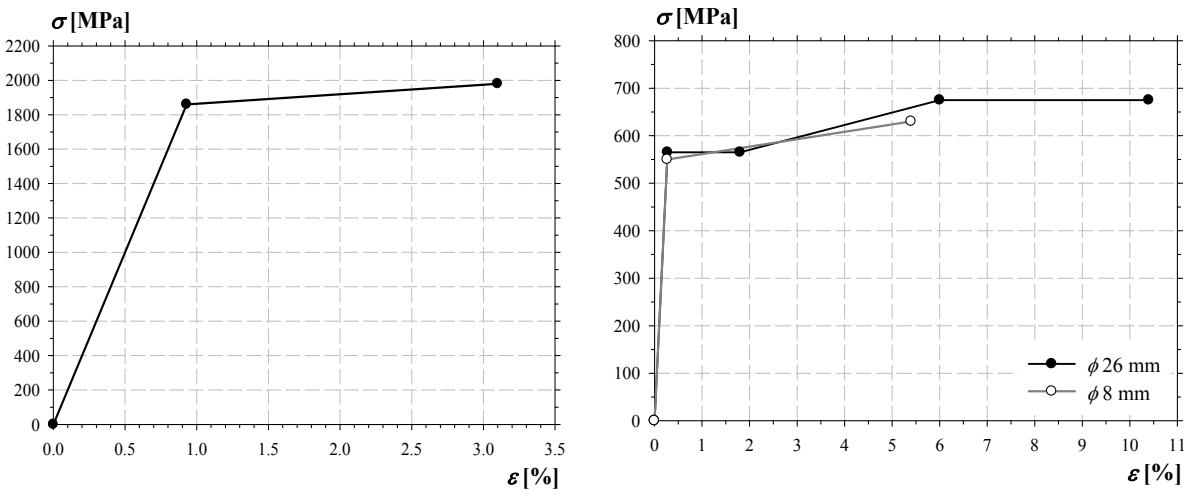

Figure 4-48: Implemented constitutive laws for prestressing steel (left) and reinforcement steel (right)

For concrete in compression, a bilinear elastic perfectly plastic law was adopted considering a compressive strength f_c of 100 MPa and a Young's modulus of 38 GPa. The plateau was limited to 3.5‰. For plain concrete in tension, a tri-linear tension stiffening law was considered with a concrete tensile strength of 5.3 MPa. For HPFRC, a new multi-linear tensile law was implemented into *FINELg,* it had been developed at the INSA-Rennes especially done for this work. Tensile laws identified by inverse analysis in Chapter 2 were considered. A critical length l_c of 400 mm corresponding to 2/3h was adopted. At the extremities, the concrete tensile strength of the first six

columns of shell elements was increased in order to avoid locally numerical problem due to the introduction of prestressing forces, (i.e. elements in light blue (Figure 4-46)).

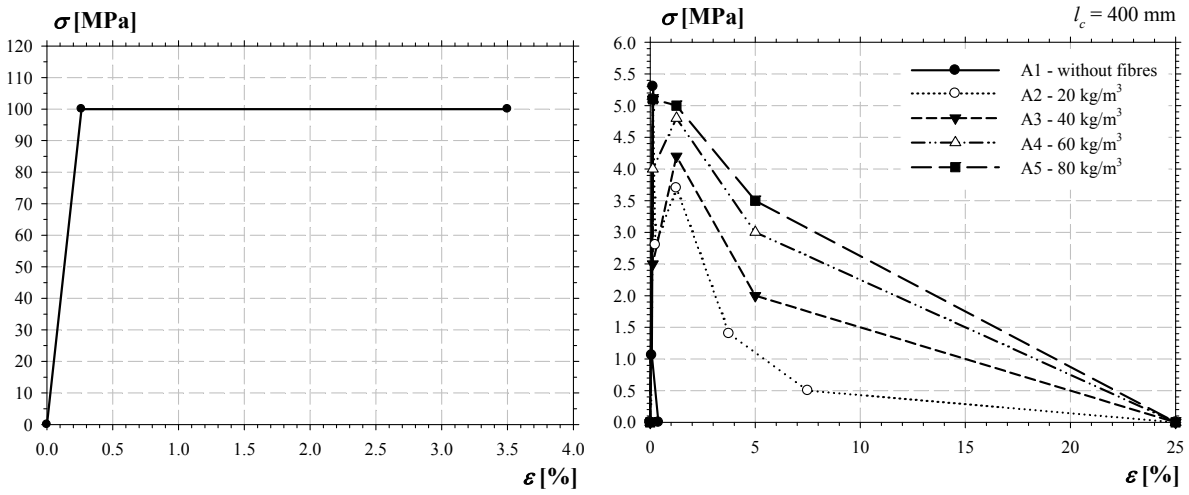

Figure 4-49: Implemented constitutive laws for concrete in compression (left) and in tension (right)

In a first sequence of calculations, the prestressing forces are applied by incremental steps and in second sequence the load was applied using the arc-length method (Figure 4-50).

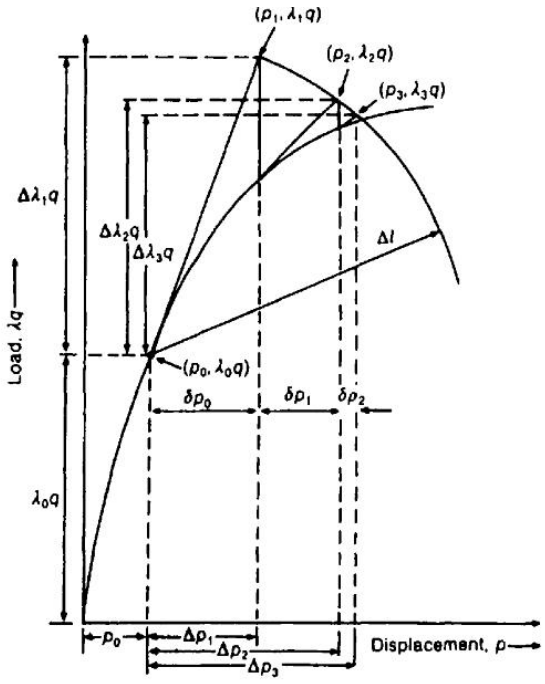

Figure 4-50: Spherical arc-length procedure and notation for one degree of freedom system

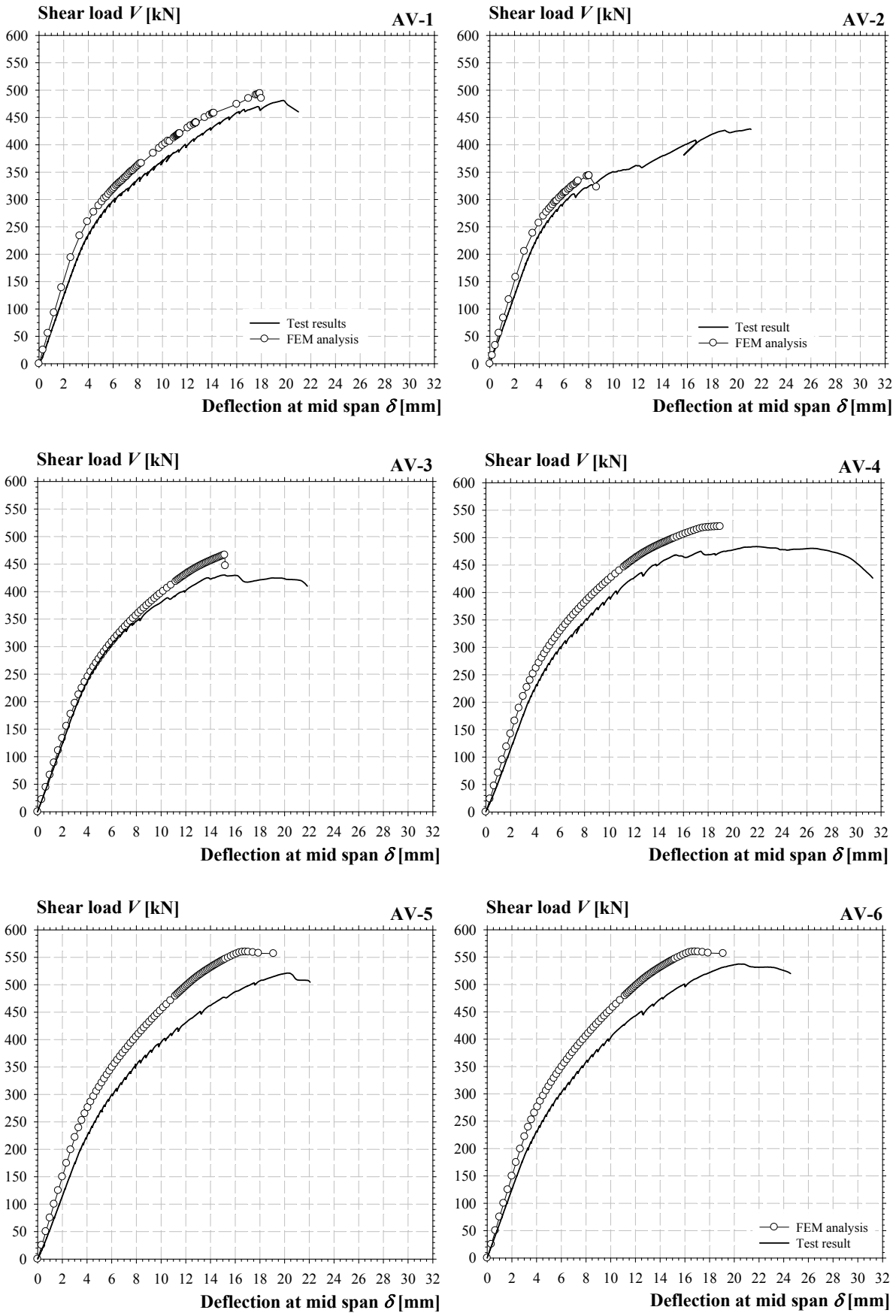

Figure 4-51: Comparison between computed curves load vs deflection and test results

Table 4-20: Comparison between the test results and the calculated values, FINELg

Specimen	V_{test} [kN]	$V_{R,FEM}$ [kN]	$V_{test}/V_{R,FEM}$ [-]
AV-1	481	493	0.98
AV-2	429	344	1.25
AV-3	430	466	0.92
AV-4	484	522	0.93
AV-5	521	559	0.93
AV-6	538	570	0.94
Average V_{test}/V_{calc}			0.99
Coefficient of variation			0.13

The simulated load – deflection curves with the NLFEA give an accurate prediction compared to the test results. Except for beam AV-2 in HSC without fibres, the ultimate loads of shear beams are overestimated. However the stiffness of members is also slightly overestimated. The numerical modelling analysis adopted is able to representing the linear and non-linear behaviour of pre-tensioned members under shear loading. It also able to predict with sufficient accuracy the failure load and the steel fibres contribution of HPFRC beams. For beams without fibres AV-2 and low fibres content AV-3, the prediction accuracy is lower. This fact is certainly due to the uncontrolled propagation of the shear crack. This previous analysis highlights the potential of FEM analysis for SFRC and UHPFRC structural elements. However, the time devoted for this analysis is high, level IV in Figure 4-52, and not adapted for common practice. Therefore it's necessary to develop code like approach for practionner.

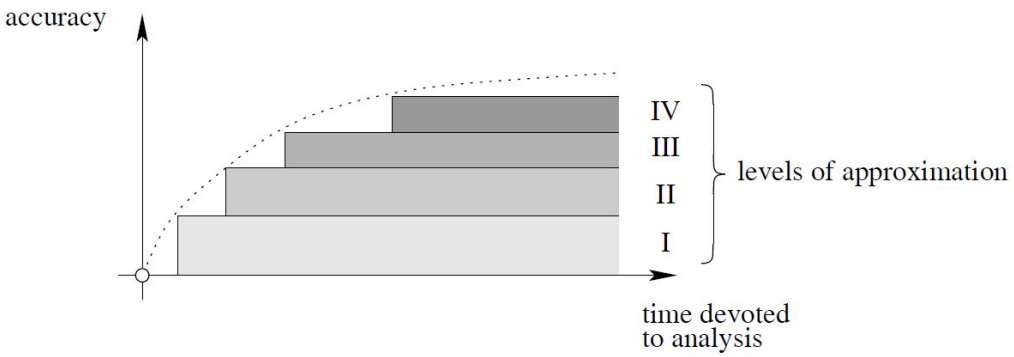

Figure 4-52: Levels of approximation [FIB2010b], graph accuracy of prediction vs time of analysis

4.6.5 Code like approach proposal

The recent models developped for the shear assessement of reinforced concrete members without shear reinforcement, as the Modified Compression Field Theory (MCFT) and the Critical Shear Crack Theory (CSCT), are based on the aggregate interlock mechanism localised on one shear crack. These models describe the beam action mechanism, see point 2.2.2.5 and not the direct strutting mechanism. However, the test performed in this thesis exihibited a direct strutting mechanism due to the high prestressing intensity. Therefore, the MCFT and CSCT give not an accurate prediction for this shear

failure mode. On the following points, we propose two models, one adapted for a localisation problem based on the CSCT and a second based on stress field model. The first model is adapted for reinforced concrete members with low fibre content (V_f < 60 kg/m^3). Whereas the second model is adapted for direct strutting mechanism, high fibre content (V_f > 60 kg/m^3).

Proposal I

As seen in Chapter 2, the Critical Shear Crack Theory (CSCT), developped by Muttoni, is an accurate model describing the shear strength of Reinforced Concrete members without transversal reinforcement [MUT2008a]. Currently, different forms of this model are adopted in the Swiss Standard SIA262 [SIA2003] and SIA269/2 [SIA2011], for the assessement of the shear strength of reinforced concrete slabs without transverse reinforcement. The amount of shear that can be transferred by the concrete across the critical shear crack depends on the roughness of the crack and its opening. This roughness is a function of the aggregate size. The shear strength is checked in a section depending on the load configuration where the width of the critical shear crack can be adequately represented by the strain at a depth 0.6d from the compression face. The critical crack width w is proportional to the product of the longitudinal strain in the control depth ε times the effective depth d. Based on these assumptions, the failure criterion is defined as follows:

$$w \propto \varepsilon d \tag{4-11}$$

$$\frac{V_{R,c}}{b_0 \cdot d \cdot \sqrt{f_c}} = \frac{1}{6} \frac{2}{1+120 \cdot \left(\frac{\varepsilon \cdot d}{d_{g0} + d_g} \right)} \tag{4-12}$$

Where $V_{R,c}$ is the shear strength, b_0 is the control section, d_g is the maximum size of the coarse aggregate and d_{g0} = 16. However, the maximum size of the coarse aggregate d_g = 0 for lightweight concrete and High Strength Concrete due to the aggregates fracture.

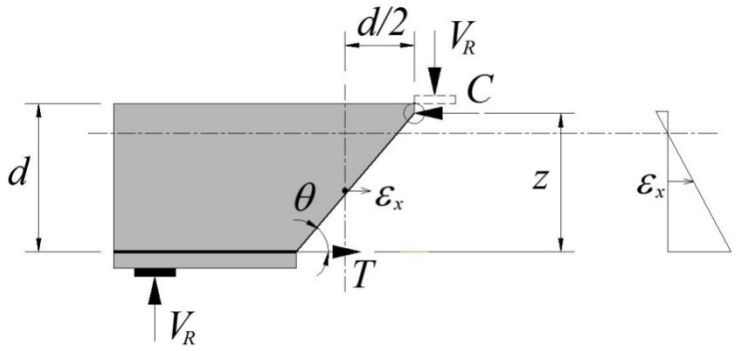

Figure 4-53: Parameters of CSCT model

In the following graphs, several test results of FRC beams well documented performed by Minelli, see point 2.2.7.5, are represented in the shear failure criterion developped for reinforced concrete. For the plotted SFRC test results, the longitudinal strain ε_x is defined considering the steel fibres as follows:

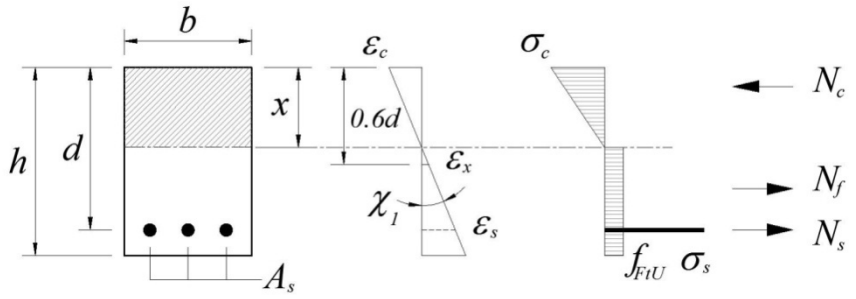

Figure 4-54: Adopted stresses distribution

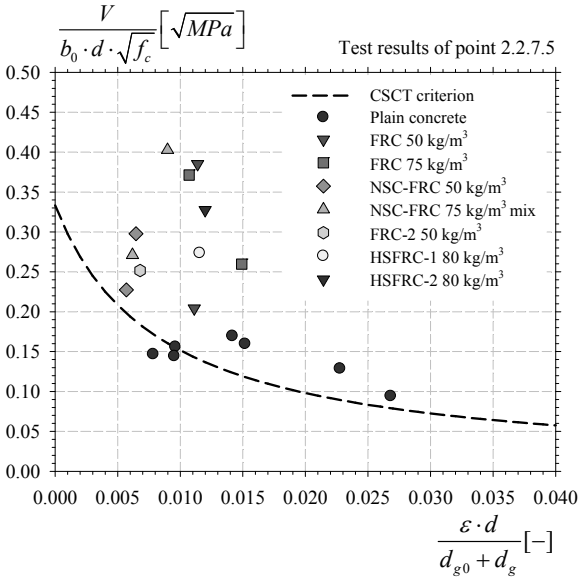

Figure 4-55: Tests results of points 2.2.7.5 represented in the failure criterion

The fibres effect acts on the flexural behaviour and the shear cracks. In order to integrate the fibre contribution to punching shear strength, the model developed by Casanova and Rossi for FRC members is recalled in this paragraph. The model assumes the formation of a block mechanism. The shear capacity is defined as the sum of concrete, fibre and stirrups contributions. The contribution of fibres to the shear resistance corresponds to the force transferred between crack faces for a certain crack opening w. The fibres contribution is computed by integration of tensile stresses across the critical crack. The tensile stresses are defined by the post-cracking relationship $\sigma(w)$ of FRC and the distribution of the opening along the shear crack. On this basis, similar assumptions may be superposed with the CSCT. The punching shear strength correspond to the sum of the concrete and the fibres contribution. This contribution corresponds to the vertical component of the integration of the tensile stresses across the failure surface A_p. The distribution of the crack opening is assumed to be linear along the failure plan and the angle is equal to $\pi/4$. With the post-cracking tensile relationship $\sigma(w)$, the distribution of the tensile stresses is defined along the failure plan. The diagonal crack opening w can be correlated to the longitudinal strain ε_x by the distance between the cracks s_x.

$$w_x = \varepsilon_x \cdot s_x \tag{4-13}$$

The fibres contribution corresponds to the vertical component of the integration of the tensile stresses across the shear plan A_p (Figure 4-56). The distribution of the crack opening is assumed to be linear along the failure plan. With the tensile stress – opening law $\sigma(w)$, the distribution of the tensile stresses

is defined along the failure plan. In order to not consider two times the tensile strength of the matrix, the softening tensile law of the matrix is subtracted from the tensile relationship. The factor K takes account of the fibres orientation.

$$V_{R,f} = \frac{1}{K} \cdot \int_{A_p} \sigma_f(w) \cdot dA_p \tag{4-14}$$

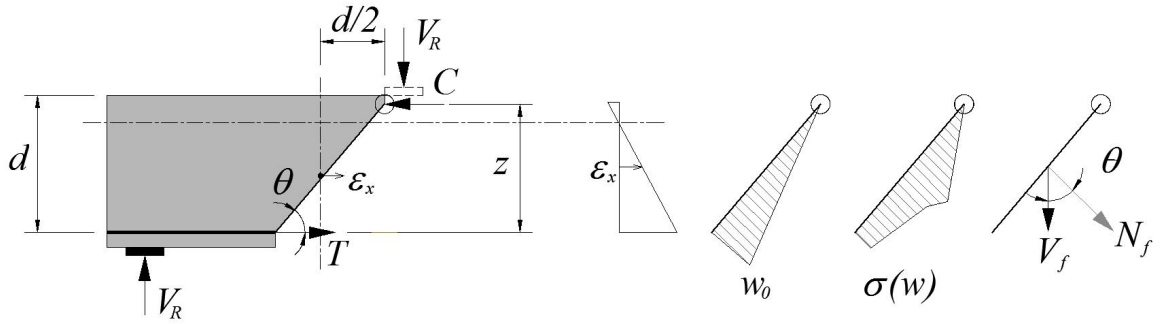

Figure 4-56: Mechanical model and parameters

We propose a simplified design model integrating the safety factors, V_R become V_{Rd}. Multi-linear relationship is not appropriate for a simplified design approach. A constant stress distribution allows a rapid and a simple computation. The fibre contribution $V_{Rd,f}$ depends on longitudinal strain ε (4-17). The punching strength V_{Rd} and the concrete contribution $V_{Rd,c}$ are defined as follows:

$$V_{Rd} = V_{Rd,c} + V_{Rd,f} \tag{4-15}$$

$$V_{Rd,c} = \frac{1}{6} \frac{2}{1 + 120 \cdot \left(\frac{\varepsilon \cdot d}{d_{g0} + d_g} \right)} \cdot b_0 \cdot d \cdot \sqrt{\frac{f_c}{\gamma_c}} \tag{4-16}$$

Where b_0 is the web width, located at $d/2$ of the edges of the loading support.

The fibre contribution $V_{Rd,f}$ is defined as follows:

$$V_{Rd,f} = \frac{1}{K} \cdot \frac{f_{Ftuk} / \gamma_F}{1 + \frac{\varepsilon \cdot d}{w_u}} \cdot b_0 \cdot z \tag{4-17}$$

Where K is the orientation factor, b_0 is the control section, w_u is the ultimate crack opening considered to 2.5 mm and z is the level arm in first approximation $z = 0.9d$.

The ultimate residual tensile strength is defined on the basis of the Model Code 2010 [FIB2010a], see point 2.1.6.1 in the following manner:

$$f_{Ftu} = 0.45 \cdot f_{R1} - \frac{w_u}{2.5} \cdot \left(0.45 \cdot f_{R1} - 0.5 \cdot f_{R3} + 0.2 f_{R1} \right) \tag{4-18}$$

In the following graph (Figure 4-57), some tests results presented in point 2.2.7.5 are presented in the simplified failure criterion. These test results were selected due to the post-cracking tensile behaviour identified on notched prisms according to the EN 14651 [EN14651].

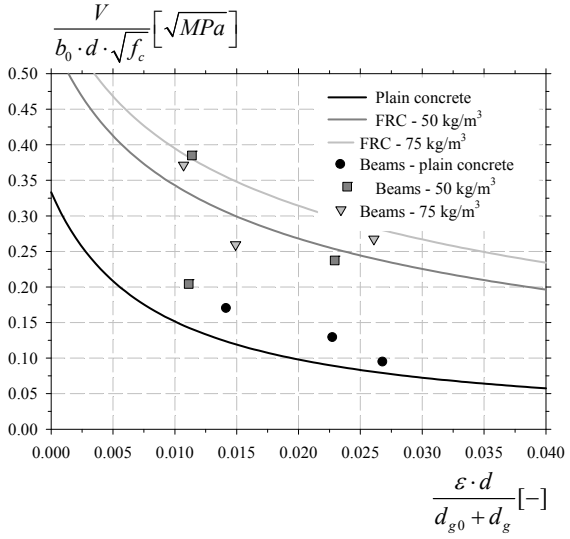

Figure 4-57: Tests results of points 2.2.7.5 represented in the modified failure criterion

The simplified model gives promising results for FRC beams. However for validating this approach, several database must be confronted. But, the recurrent problem is the identification of the post-cracking response that changes at each experimental campaign or that is not documented.

Proposal II

The shear provision for beams with shear reinforcement in the Swiss Code SIA 262 "Concrete Structures" [SIA2003] is based on a simplified form of stress field. The angle of the strut is freely chosen between $20° \leq \theta \leq 45°$. The shear is carried only by the transverse reinforcement. Moreover, the compressive strength of the concrete strut $V_{Rd,cw}$ must be verified and is limited by the lateral strains and the cracking, see point 2.2.4.3. The favourable effect of inclined prestressing, $F_p \sin(\beta_p)$, is added to the shear strength. For high fibre content ($V_f > 60$ kg/m^3) and direct strutting mechanism we proposed similar approach (Figure 4-58). The high fibre content allows stress redistribution just like the transverse reinforcement. In this model, the shear is carried only by the fibre effect considering a constant stress distribution on the failure plan.

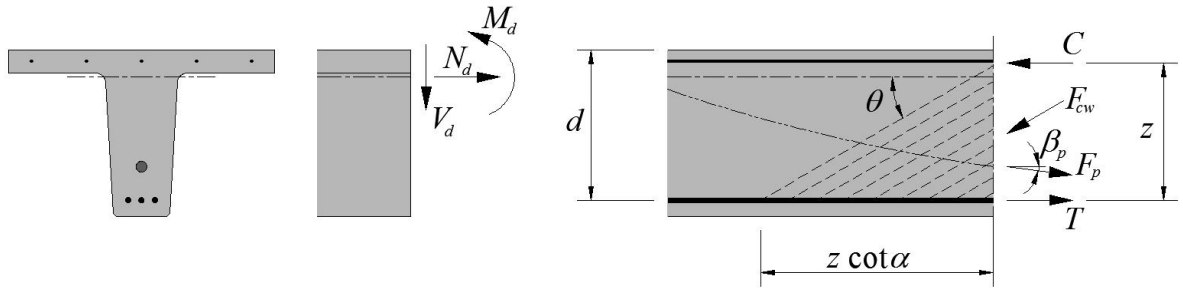

Figure 4-58: Stress field for web of structural member

$$V_{Rd,f} = \frac{1}{K} \cdot \frac{f_{Ftu}}{\gamma_f} \cdot z \cdot b_w \cdot \cot\theta \leq V_{Rd,cw} \tag{4-19}$$

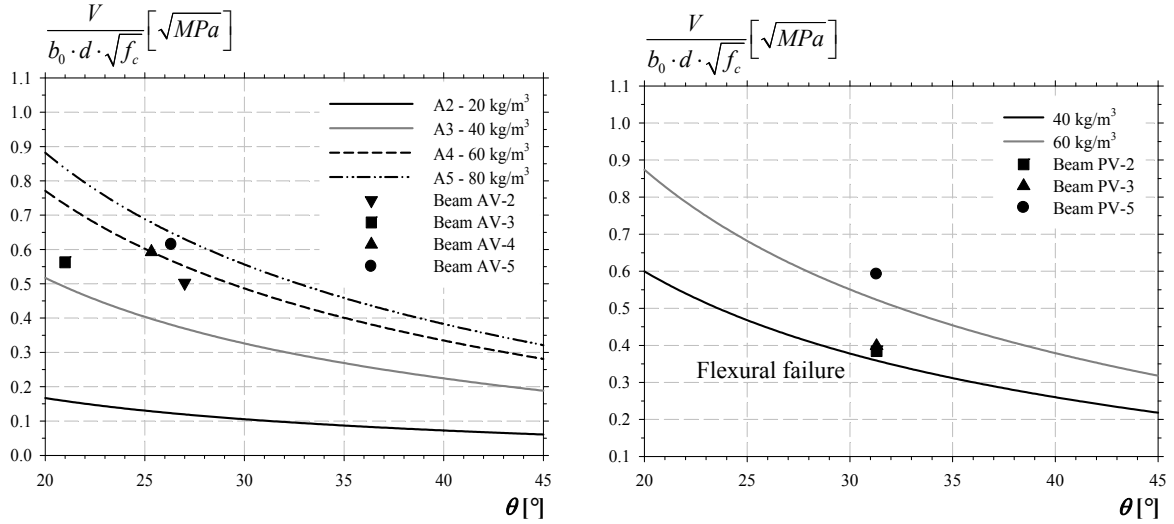

Figure 4-59: Graphs shear strength according to the inclination for beams AV (on left), beams PV (on right)

For this shear failure mechanism, the proposed approach seems adapted, except for beam AV-2 with a fibre content of 20 kg/m^3. However the choice of the inclination strut influence significantly the fibre contribution. For reinforced beams an inclination of 45° is recommanded. For prestressed beams the angle must be firstly approached by stress field model considering the prestressing force. The simplified model must be validated with several database.

4.7 Conclusion

In this Chapter, an original experimental study on pre-tensioned members in HPFRC was presented. A total number of six critical shear beams of 3.6 m span and two full scale members of 12 m span were tested in order to analyse the shear strength of HSFRC pre-tensioned members without transversal reinforcement and to propose recommendations and models. The principal parameters distinguishing the members was the fibres quantity. The material properties, particularly the post-cracking response, were identified through a large numbers of specimens.

This experimental campaign allowed the collection of a large data base concerning the shear behaviour of pre-tensioned beams in HPFRC. All measurements are presented in the testing reports in Appendix A. Tests results have highlighted the beneficial contribution of steel fibres on shear capacity and the ability to replace the minimum shear reinforcement. The failure mode of the six shear critical beams was similar but at different load levels. The failure has occurred due to the crushing of the concrete at the root of diagonal shear crack. The failure took place after a drop in resistance followed by a separation of the specimen in two blocks. This type of failure can be named shear-compression. According to the fibres content, the development and the opening of the critical diagonal crack were delayed and the inclination was smaller. From a fiber content of 40 kg/m^3 several parallel cracks were developed. A fiber content of 20 kg/m^3 was not sufficient to control the development of the shear critical cracks. A hardening behaviour of the material in bending is zhus required. For this formulation and type of fibres, a content of 60 kg/m^3 presents the best ratio cost/performance. The full scale beam AF-1 in High Strength Concrete failed in shear, while the HSFRC members exhibited a flexural failure. These beams highlighted the ability of fibres to replace the conventional shear reinforcement.

Different non-linear finite element approaches were performed and compared to the test results. The analysis with the Elastic Plastic Stress Field Model (EPSFM) and the Modified Compression Field Theory (MCFT Response 2000) represents with sufficient accurancy the behaviour and the strength of HSC members without fibres. However these software don't allow to take into account the fibres contributions. Therefore a numerical analysis with the non-linear FEM software *FINELg* was performed. The numerical modelling analysis composed of shell elements is able to representing the linear and non-linear behaviour of pre-tensioned members under shear loading. It also able to predict with sufficient accuracy the failure load and the steel fibres contribution of HPFRC pre-tensioned beams. However, the time devoted for this analysis is high and not adapted for common practice.

In order to develop a simplified code like model harmonized with conventional reinforced concrete, two approaches were proposed. The first approach, adapted for reinforced concrete members with low fibre content (V_f < 60 kg/m^3), is based on the Critical Shear Crack Theory (CSCT). This models involves the matrix contribution $V_{R,c}$ and the fibres contribution $V_{R,f}$. For the matrix contribution, it is assumed that the shear strength is carried by the shear friction and is a function of the critical crack opening depending on the sate of strain. The fibres contribution corresponds to the vertical component of the integration of the tensile stresses across the critical shear crack. The distribution of the crack opening is assumed to be linear along the failure plan. Based on the tensile stress vs crack opening law determined on specimens, the distribution of the tensile stresses is defined along the failure plan. The second approach, adapted for direct strutting reinforced concrete members with high fibre content (V_f > 60 kg/m^3), is based on stress field model. This models involves only the fibres contribution $V_{R,f}$ considering a constant distribution of the stress along the failure plan. The two approaches give promising results but may be validated on larger test series.

5 Punching shear strength of thin slabs in HPFRC and UHPFRC

5.1 Problem statement

The punching shear strength is often the critical criterion to ensure the structural safety of reinforced concrete slabs. For RC slabs without shear reinforcement, this failure mode is characterized by a fragile behaviour implying possible partial or total collapse of the structure (Figure 5-1). Punching shear failure occurs where a point force is applied, causing a localized rupture by penetration through the floor. This failure mechanism forms a cone separated from the rest of the slab by the shear crack. Despite extensive research in this field has been carried out, punching shear remains very complex, so much that the current approach is often empirical or simplified [CEB1985] [FIB2001] [POL2005] [FIB2010c]. In order to prevent a punching shear failure, the slabs can be locally thickened or reinforced by stirrups or studs. However, this type of reinforcement can be only used if the location of the point load is known (e.g. a column). Several studies highlighted that a punching shear failure can occur on bridge decks. But, for a bridge deck, a truck wheel can be anywhere, i.e the location of the punching load cannot be predicted in order to prevent a local failure caused by such cases.

Figure 5-1: Collapses of car parks by punching shear failure in New Zealand after a seism a), in Switzerland due to an overload of embankment b)

The Steel Fibre Reinforced Concrete (SFRC) provides an alternative to conventional methods. The ability of SFRC to increase the punching shear strength is supported by several experimental studies, as seen in Chapter 2. SFRC can be used in situ (e.g. localized strengthening of the slabs around the columns) or in precast industry (e.g. precast deck slabs) (Figure 5-2). Despite his high mechanical properties, the High Strength Concrete is not used at large scale mainly due to its fragile behaviour. The combination of a HPC and steel fibres (HPFRC) is a promising step in the development of innovative and light structures. Thanks to its high tensile toughness, the High and Ultra-High Performance Fibre Reinforced Concrete (HPFRC and UHPFRC) punching shear capacity is increased and allows the design of thinner slabs, panels, shell, etc. In this chapter, HPFRC is investigated as an advanced cementitious material offering many technical and economic advantages; however its practical application remains marginal mainly due to the lack of standards, and an adaptation period is needed to develop procedures and rules adapted to its performance.

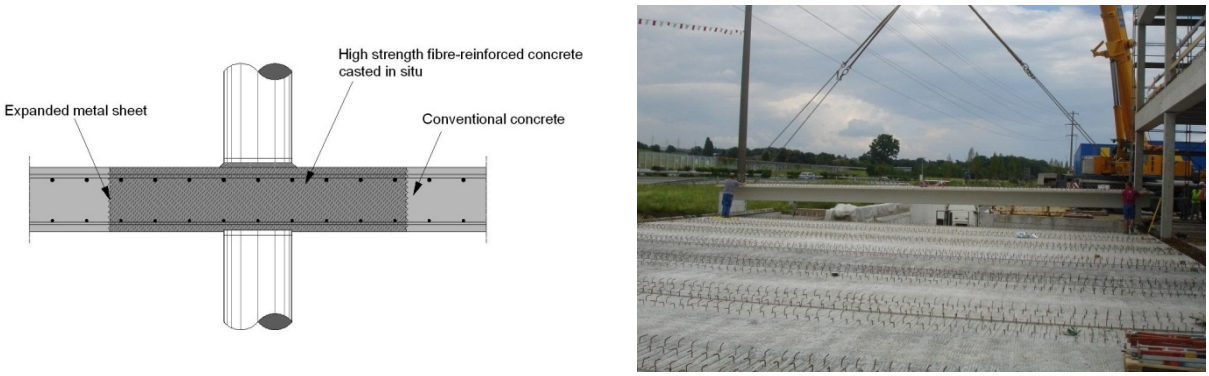

Figure 5-2: Localized strengthening of the slabs around the columns with HPFRC, commercial deck composed of precast double-T beams

5.2 Program and objectives

In this chapter, the results of two originally experimental research programs on the flexural and punching shear strength of thin slabs in High Performance Fibre Reinforced Concrete (HPFRC) and Ultra-High Performance Fibre Reinforced Concrete (UHPFRC) are presented. The first experimental study was performed on twenty square slabs in HPFRC of 1240 mm side and 120 mm thick. The varying parameters among the specimens were: the fibre volume ratio, the reinforcement ratio and the intensity of the post-tensioning forces. The second experimental study was conducted on nineteen square slabs in Ultra-High Performance Fibre Reinforced Concrete UHPFRC of 960 mm side in order to compare the punching shear behaviour with HPFRC slabs and to extend the validity domain of the developed model. The distinguishing parameters among the specimens were: the fibre volume ratio, the thickness and the reinforcement ratio. The post-cracking response of the HPFRC and UHPFRC was determined using flexural and tensile tests in order to determine the post-cracking behaviour. In order to develop an harmonized model, the analysis of the slabs is based on the latest developments in punching shear design of reinforced concrete structure, particularly the Critical Shear Crack Theory (CSCT) [MUT2008b]. This chapter presents several recommendations and rules for the punching shear design of HPFRC and UHPFRC slabs.

The main objectives of these experimental studies were:

- to evaluate the flexural and punching shear behaviour at the Service Limit State SLS and the Ultimate Limit State ULS of thin slabs in HPFRC and UHPFRC,
- to determine the influence of the different parameters on the punching shear strength of thin slabs in HPFRC and UHPFRC,
- to link the material properties defined in different types of specimen to structural behaviour and strength,
- to propose an accurate and simplified punching shear strength model and design rules for elements in HPFRC intended for practionners,

5.3 Description of experimental studies

5.3.1 Reminder of HPC and HPFRC mechanical properties

In this point the principal properties of concrete and reinforcement are briefly described. More information about the formulation and the determination of the mechanical properties are given in Chapter 3. In the first study, the test slabs were made in HPC or HPFRC. Five compositions were developed and were distinguished by their fibre content (Table 5-1). Each composition had the same cementitious matrix.

Table 5-1: HPC and HPFRC fibre content and corresponding mechanical properties

Composition		**B1**	**B2**	**B3**	**B4**	**B5**
Steel fibres *Bekaert Dramix RC-80/30-BP*	[kg/m^3]	0	20	40	60	80
E_{cm}	[GPa]	44.2	41.5	46.8	40.2	43.3
f_{cm}	[MPa]	99	102	102	102	106

Bending tests on notched prisms

Three-point bending tests on notched prisms were performed according to the European standard EN 14651 [EN14651], see point 2.1.5.2. Four prisms of each mix were tested. According to the method, the Limit Of Proportionality *LOP* $f_{fct.L}$ and four different values of the residual strength f_{R1}, f_{R2}, f_{R3}, and f_{R4} corresponding to different values of the *CMOD* = 0.5, 1.5, 2.5 and 3.5 mm, respectively, were identified.

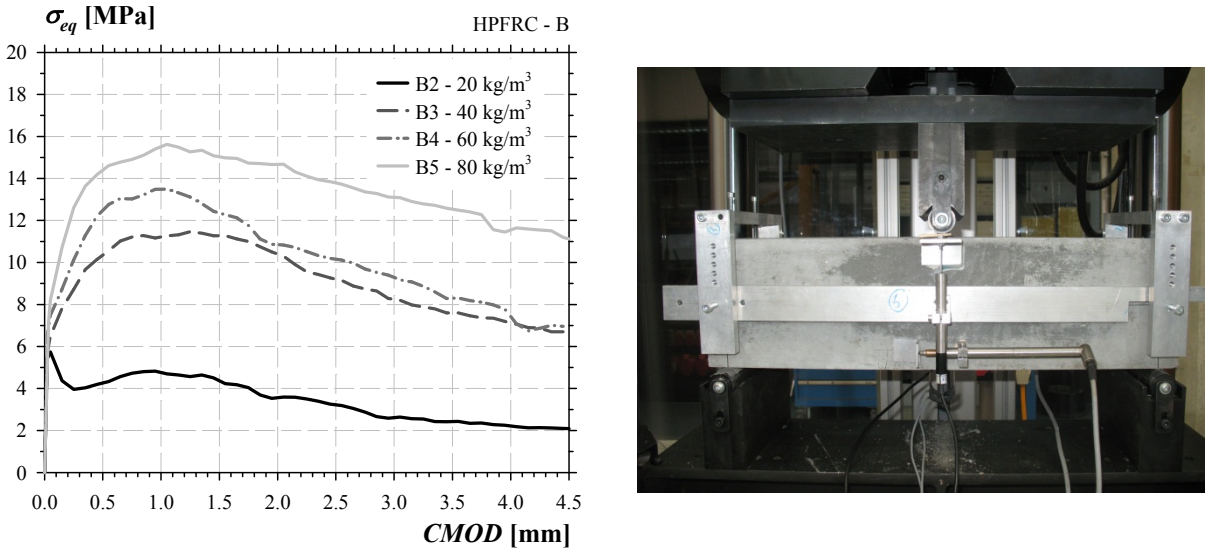

Figure 5-3: Average curves equivalent bending stress vs CMOD of the HPFRC notched prisms

Table 5-2: Post-cracking residual strengths according to EN 14651

HPFRC	Fibre content [kg/m^3]	$f'_{ct.L}$ [MPa]	f_{R1} [MPa]	f_{R2} [MPa]	f_{R3} [MPa]	f_{R4} [MPa]
B2	20	6.1* *0.22***	4.3 *0.69*	4.2 *0.42*	2.6 *0.72*	1.8 *0.42*
B3	40	5.6 *0.34*	10.4 *1.99*	11.2 *1.28*	9.3 *1.93*	7.6 *1.59*
B4	60	6.6 *0.73*	12.5 *1.20*	12.4 *1.26*	10.2 *1.10*	8.6 *1.29*
B5	60	7.1 *0.60*	14.4 *1.25*	15.1 *1.62*	13.8 *1.81*	12.6 *1.52*

** Average ** Standard deviation*

Uniaxial test

Uniaxial tests were performed on notched cores of 100 mm diameter and 100 mm high, drilled at 45° on concrete blocks cast like the slabs. The diameter in the fracture zone was 80 mm. Four cores of each formulation were tested. The cores were fixed to the testing machine through steel plates and no rotations were allowed.

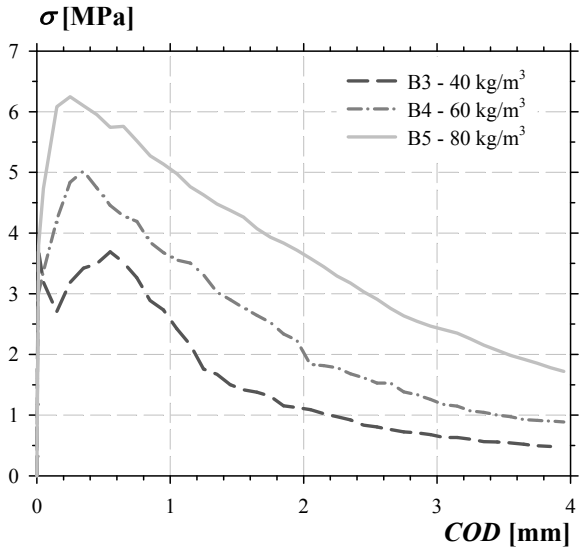

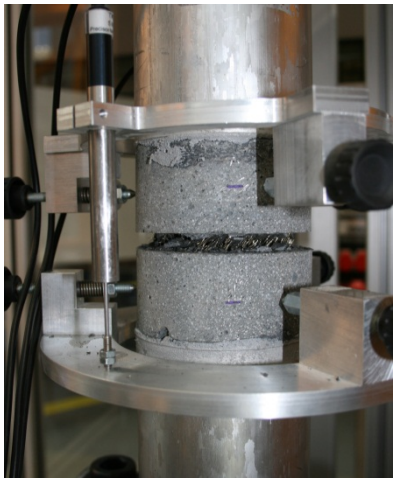

Figure 5-4: Average curves stress vs crack opening displacement of the notched cores

5.3.2 HPFRC slabs

The experimental study was conducted on twenty square HPFRC slabs of 1240 mm side and 120 mm thick in order to evaluate their flexural and punching shear behaviour. The varying parameters among the specimens were: the fibre volume ratio, the reinforcement ratio and the intensity of the post-tensioning forces (Table 5-3) (Table 5-8). The slabs were designed in order to obtain a punching shear failure.

Table 5-3: Specifications of the tested slabs

Designation of the slabs	**Bi-01**	**Bi-02**	**Bi-03**	**Bi-04**	**Bi-05**	**Bi-06**
Concrete compositions	i = 1/2/3/4/5	i = 1/3/5				
Reinforcement [mm] ratio ρ_s [%]	ϕ10 #100 *0.87*				ϕ8 #100 *0.56*	ϕ12 #100 *1.26*
Post-tensioning force [kN] $\sigma_{cp,0}$ [MPa]	0	360 2.4	540 3.6	720 4.8	0	0

According to the reinforcement ratio, the slabs were reinforced with ϕ8/10/12 mm rebars with a pitch of 100 mm and placed in both directions, with a minimum concrete cover of 20 mm. The post-tensioned slabs were reinforced with 10 mm rebars on the top and 8 mm rebars on the bottom and a 100 mm pitch in both directions. The post-tensioning was composed of 2 or 4 straight monostrands for each side located at the neutral axis (Figure 5-5). The monostrands were composed of seven wires and had an area A_p of 150 mm^2. The post-tensioning was without bond and the forces were applied to the concrete through steel plates 100 x 100 x 10 mm placed behind the anchors. According to the post-tensioning intensity, three forces were applied in both directions (x/y): 2 x 180 kN, 4 x 135 kN and 4 x 180 kN.

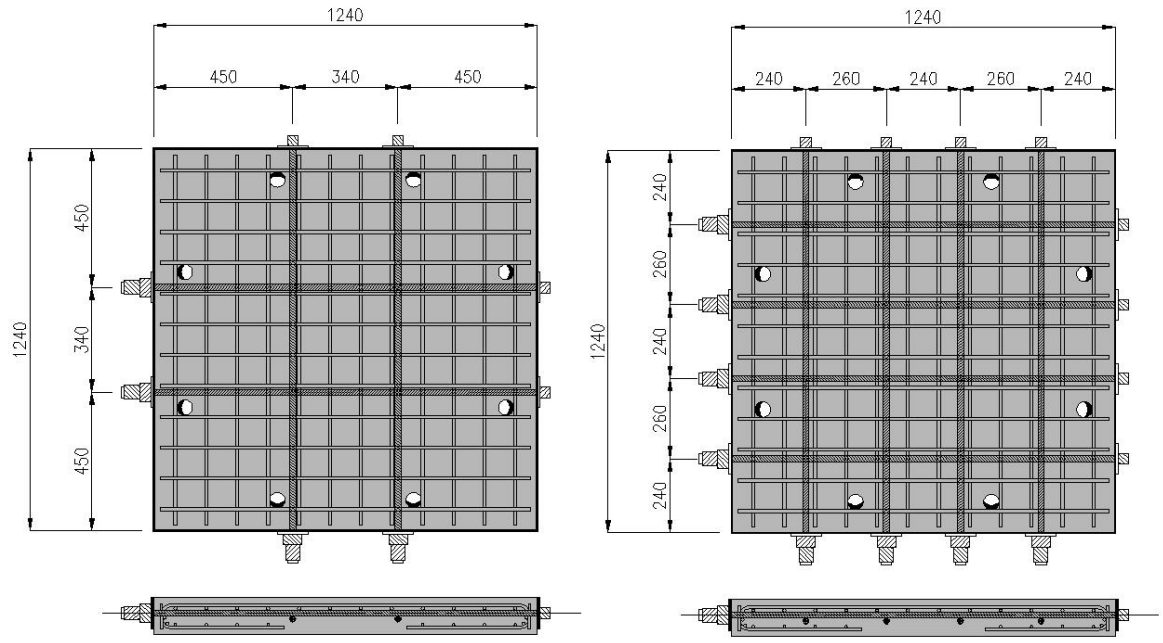

Figure 5-5: Reinforcement and post-tensioning arrangement

The slabs were made at the Structural laboratory of the University of Applied Sciences of Fribourg. The formwork was composed of wood panels and steel L profiles for the sides. The openings for the supports were realized with steel bars surrounded by insulation pipes. The concrete was realised in a lab mixer *Zyklos* with a capacity of 150 litres. Two batches of 110 litres were necessary for casting one slab. The concrete was vibrated (Figure 5-8). The slabs were removed from the framework after 3 days and stored inside the laboratory. The post-tension force was implemented few days before the tests in order to limit the prestressing losses which were controlled by load cells

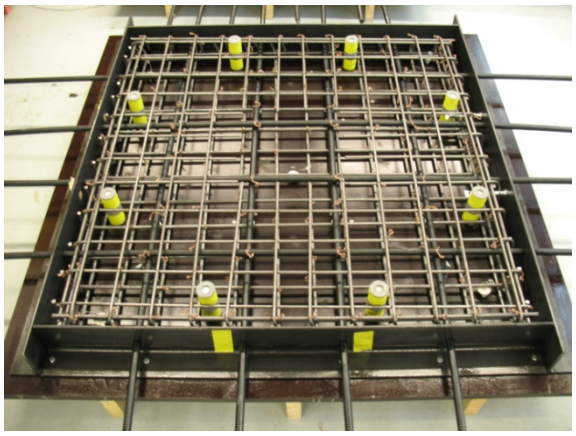

Figure 5-6: Reinforcement and monostrands

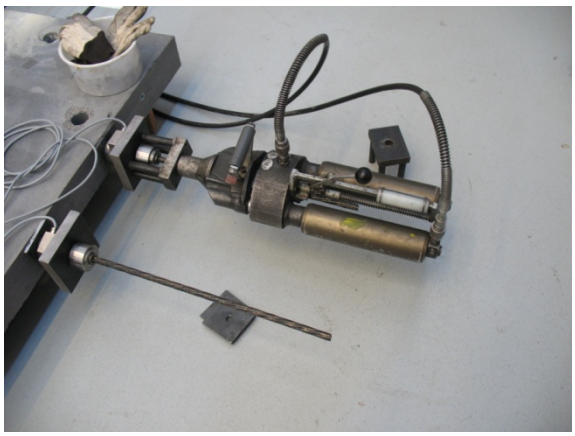

Figure 5-7: Implementation of the post-tension

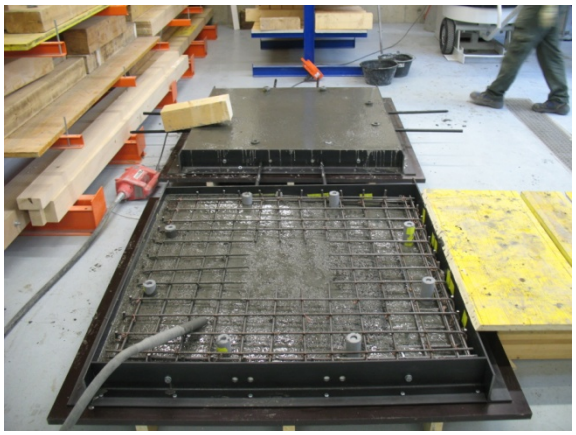

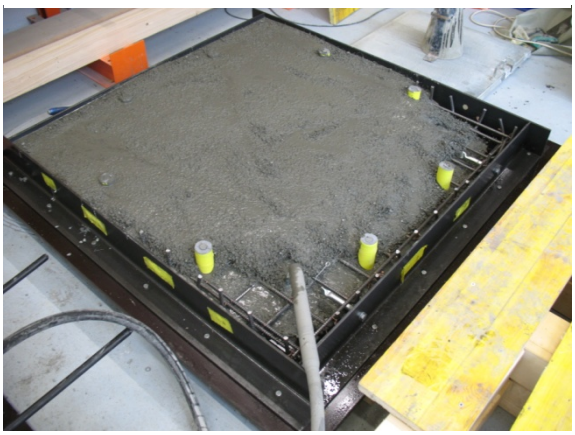

Figure 5-8: Concreting process at left and right

The load tests were performed on a punching test setup specially designed for this study (Figure 5-9) and (Figure 5-10). The load was applied with a hydraulic jack located at the centre point of the slab through a 120 mm diameter punch in steel. The slab was supported by eight steel rods M20, anchored to a steel frame which was also anchored to the strong floor. The support system described a circle with a diameter of 1130 mm. It was composed of 100 x 100 x 10 mm steel plates and spherical plain thrust bearings allowing free rotations. The tests were controlled in displacement by a servo-electronic system of the firm *Walter & Bai*. The displacement rate was 0.02 mm/s representing a quasi-static loading. The load was applied by increments until the failure load. At each step, the cracking pattern was plotted.

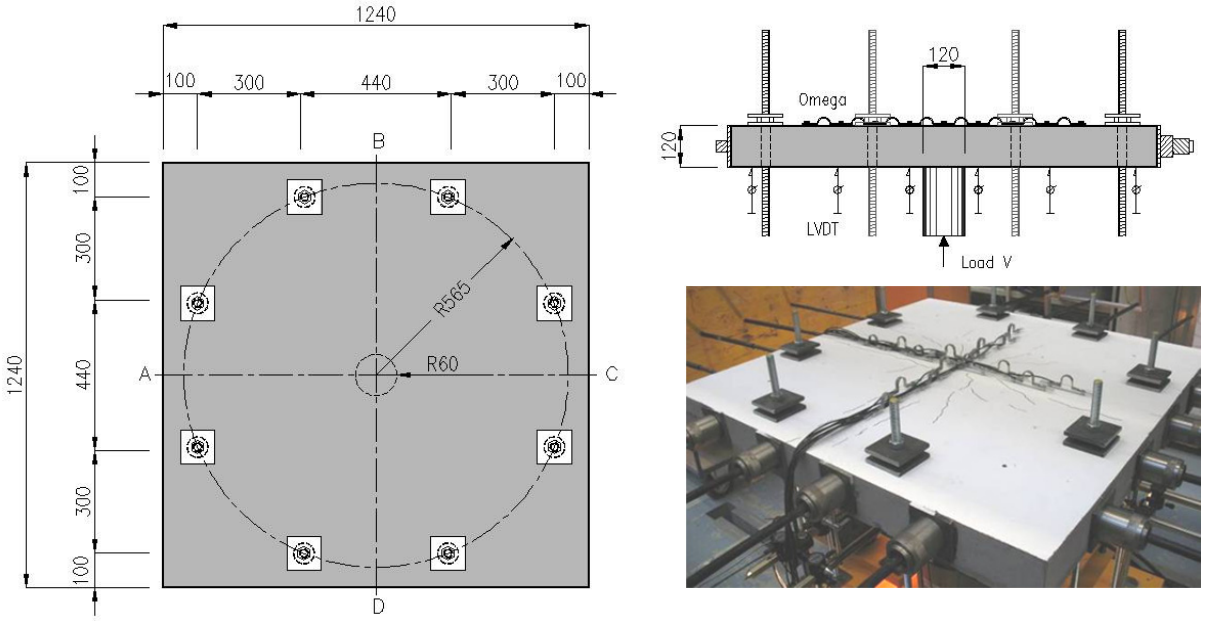

Figure 5-9: Geometry of a punching shear test of the HPFRC slabs

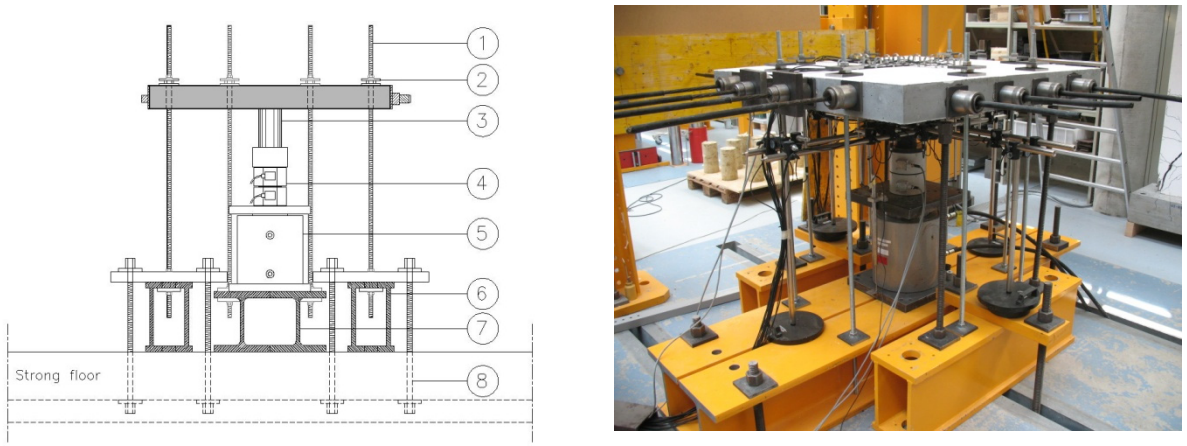

1 tie-rods M20 8.8
2 spherical plain thrust bearings SKF + steel plates 100 x 100 x 10 mm
3 steel punch ϕ120 mm
4 load cells HBM 1000 kN
5 hydraulic jack *Lukas* 4000 kN/150 mm
6 bottom crossbeam
7 bottom crossbeam HEM 280
8 tie rods *MSP* 26.5 mm

Figure 5-10: Punching shear test setup

A total number of 31 instruments were recorded for each test. Two load cells type *HBM C6A 1000 kN* were placed between the actuators and the steel punch. Fourteen linear variable differential transducers (LVDTs) allowed the measurement of the vertical displacements of the slabs and the supports. Sixteen displacement transducers type *TML Omega* were placed on the top face of the slabs in order to measure the top strains (Figure 5-11). The instruments were connected to a data acquisition system

type *HBM Spider 8* with the data acquisition software *HBM Catman*. The top face of the slabs was painted in white in order to plot the cracking pattern.

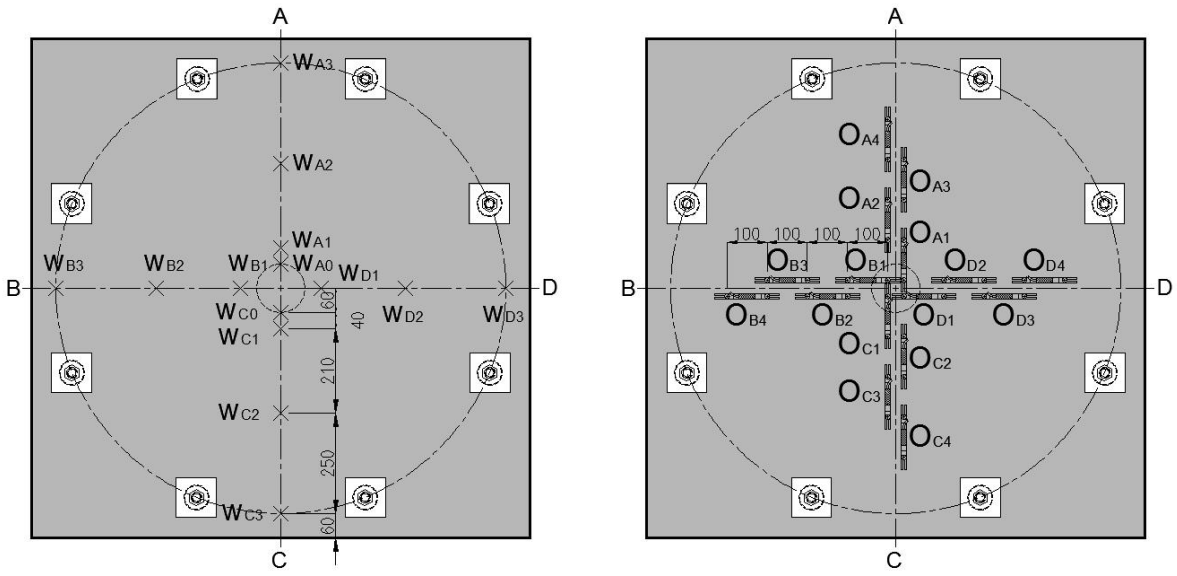

Figure 5-11: Measurement arrangement of the HPFRC slabs

Figure 5-12: Views of the deflections and top strains measurements

5.3.3 Reminder of UHPFRC mechanical properties

In this second study, the test specimens were made in *Béton Composite Vicat BCV*. Two mixes were analysed, and distinguished by the fibre volume and the fibres type. The BCV-1% was only composed of short straight fibres, while the BCV-2% was composed of a mix between short and long straight fibres (Table 5-4). Each composition had the same cementitious matrix.

Table 5-4: UHPFRC fibres content and mechanical properties

Composition		**BCV-1%A**	**BCV-2%**
Steel fibres 12.7/0.175 mm	[kg/m^3]	79	52
Steel fibres 20/0.3 mm	[kg/m^3]	-	106
E_{cm}	[GPa]	45.7	42.7

f_{cm}	[MPa]	157	152

In order to evaluate the post cracking response of the UHPFRC, bending tests on prisms and uniaxial tensile tests were performed.

Bending tests on thin prism

According to the French interim recommendations for UHPFRC, the post-cracking response of a thin element is defined by a bending test on a prism with the same thickness. In order to evaluate the thickness influence on the post-cracking response, an experimental campaign was performed. The experimental study was composed of 32 prisms with 200 mm width and 700 mm length. The varying parameters were the thickness h and the fibre volume ratio V_f. The prisms were tested in 3-point bending on a specially designed setup. The prisms were simply supported on steel roller supports with a clear span of 500 mm. A single load was applied at the centre by a hydraulic jack via a steel roller.

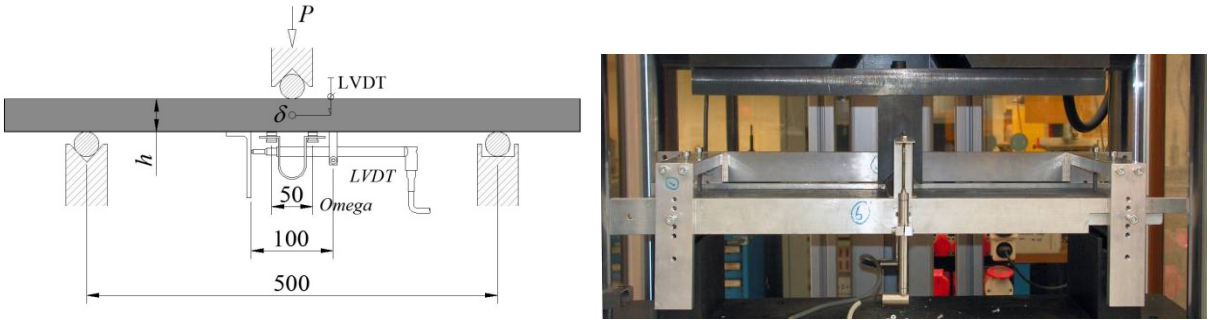

Figure 5-13: 3-points bending test setup of the UHPFRC prisms

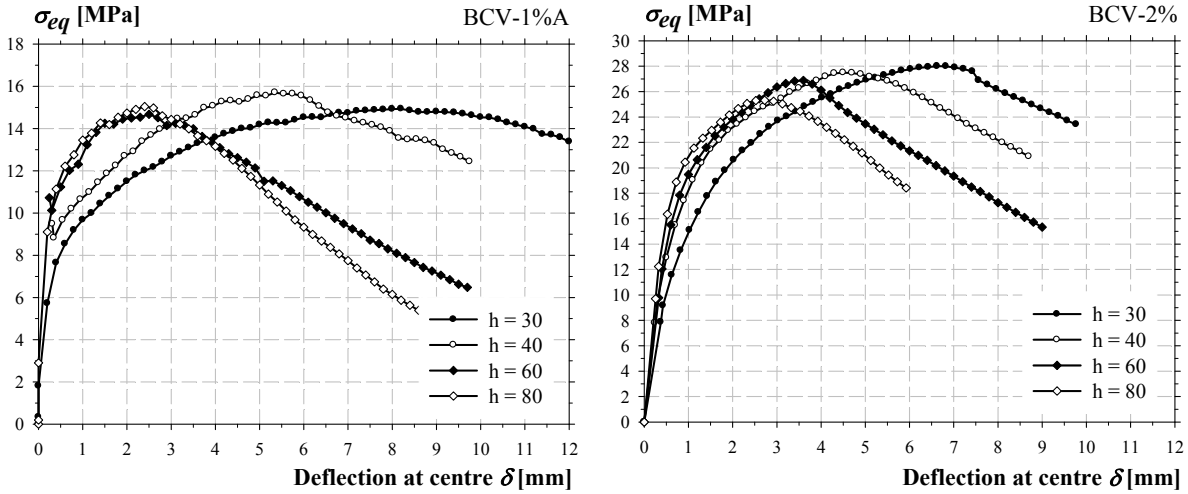

Figure 5-14: Average curves equivalent bending stress vs deflection at centre of the UHPFRC prisms

Bending test on notched prism

Three-points bending tests on notched prism were carried out according to the French interim recommendations for UHPFRC [AFGC2002]. The specimens had a square cross section of 100 mm and a length of 400 mm and were notched at the centre on a depth of 10 mm. They were tested in a universal testing machine. The prisms were simply supported on steel rollers with a clear span of 300 mm. A single load was applied on the centre via a steel roller.

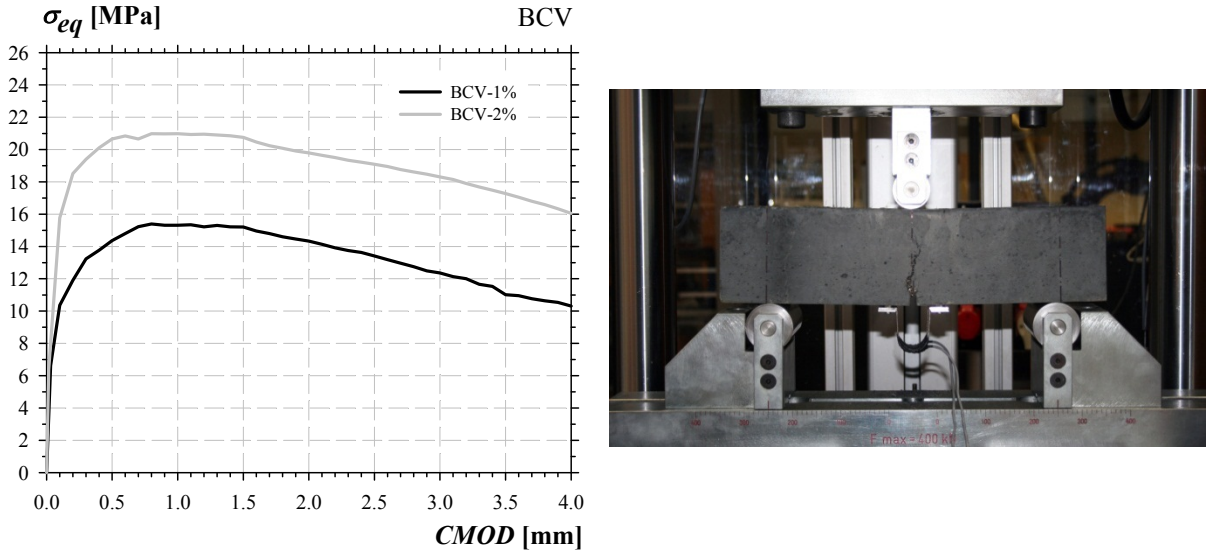

Figure 5-15: 3-points bending test setup on notched prisms in UHPFRC

Uniaxial tests

Uniaxial tests were performed on dog bone shaped specimens. The area in the fracture zone was 100 x 40 mm. Four specimens of each formulation were tested. The tests were conducted on a universal testing machine and monitored in displacement. The specimens were fixed in a specially designed setup. No rotations were allowed (Figure 5-16).

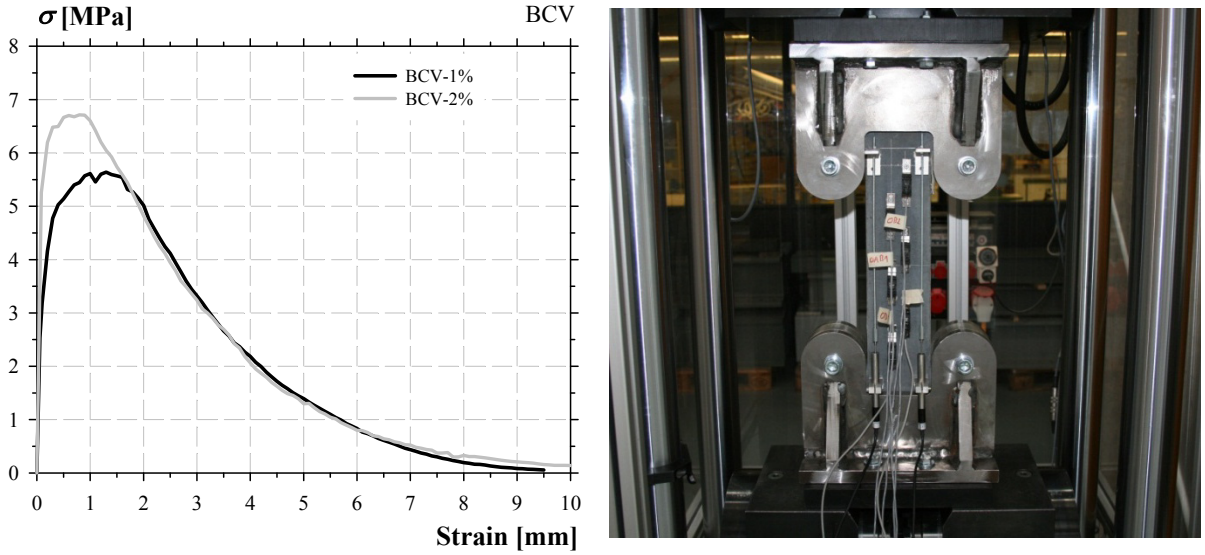

Figure 5-16: Curves stress vs total strain (LVDTs) of the UHPFRC "dog bones"

5.3.4 UHPFRC slabs

The experimental study was conducted on twenty square slabs with a 960 mm side in order to evaluate the flexural and punching shear behaviour of UHPFRC thin slabs. The varying parameters among the specimens were: the thickness h, the fibre volume ratio V_f, the reinforcement ratio ρ and the reinforcement arrangement (Table 5-5).

Table 5-5: Specifications of the test slabs

Series	Thickness h [mm]	Reinforcement ρ [%] / [mm]	Fibre volume ratio V_f [%]	Effective depth d [mm]
BCV-V_f_30_ρ	30	without	1 / 2	15
		1.36 / ϕ5 #100 A*	2	
		2.67 / ϕ7 #100 A	1	
BCV-V_f_40_ρ	40	without	2	20
		1.02 / ϕ5 #100 A	1 / 2	
BCV-V_f_60_ρ	60	without	2	40
		1.00 / ϕ7 #100 A	2	
		1.49 / ϕ9 #100 B	1 / 2	
		1.66 / ϕ9 #100 A	2	
		2.05 / ϕ10 #100 A	1	
BCV-V_f_80_ρ	80	without	2	60
		1.10 / ϕ9 #100 A	1 / 2	
		1.77 / ϕ12 #100 B	1 / 2	
		1.96 / ϕ12 #100 A	1	

** reinforcement arrangement according to Figure 5-17*

Two reinforcement arrangements were adopted (Figure 5-17). The first arrangement, type A, consisted of a regular square mesh, positioned in a way to have the centre of a cell positioned at the centre of the slab. The second arrangement, type B, consisted also of a regular square mesh, placed in a way to have the rebars positioned at the centre of the slab. This second arrangement was only applied on 4 slabs having high reinforcement ratios with 60 and 80 mm thicknesses. According to the reinforcement ratio, the steel mesh was composed of ϕ 5/7/9/10/12 diameter with a 100 mm pitch. The effective depths were 15, 20, 40 and 60 mm for the respective thicknesses of 30, 40, 60 and 80 mm

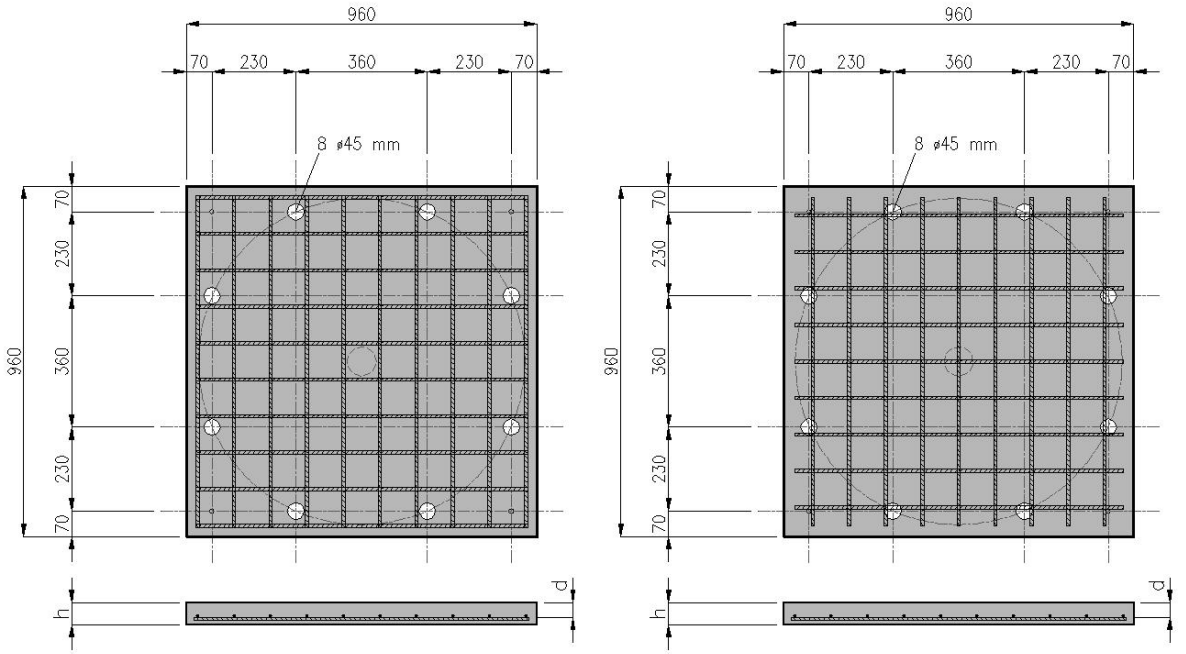

Figure 5-17: Reinforcement arrangement type Aon left and B on right

One part of the test slabs were made in a precast plant of the firm *Creabeton Matériaux* and the other part at the laboratory of UAS Fribourg. In the precast plant, the concrete was realized in a conical mixer *Kniele* with a capacity of 450 litres (Figure 5-18). All slabs were cast in a similar manner without any vibration. The UHPC was poured in the middle of the formwork (Figure 5-19). The flow was regular for the slabs without reinforcement and a little bit disturbed for the reinforced ones. They were then removed of the framework after 1 day and stored inside the plant surrounded by plastic sheet, approximately for two weeks to be then transported to the laboratory.

Figure 5-18: Mixer and formworks at Creabeton Matériaux

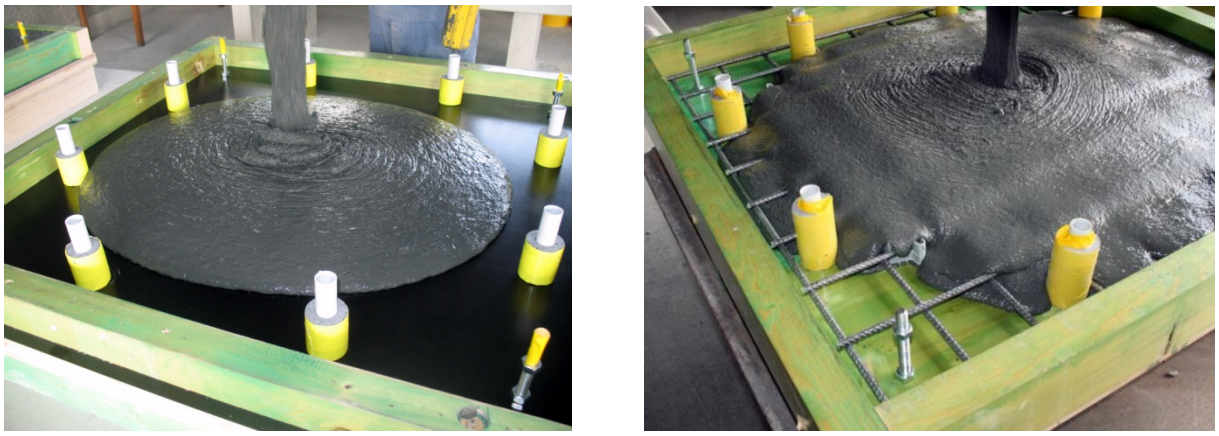

Figure 5-19: Casting process with and without reinforcement

The load tests have been carried out at the Structural laboratory of UAS Fribourg, on a punching test setup specially designed for this study (Figure 5-20) and (Figure 5-21). The load was applied with an actuator located at the centre point of the slab through a 80 mm diameter punch in steel. The slab was supported by eight steel rods M20, anchored to a steel frame. The support system described a circle with a diameter of 878 mm and spherical plain thrust bearings allowed free rotations. The tests were controlled in displacement by a servo-electronic system of the firm *Walter & Bai*. The displacement speed was 0.02 mm/s representing a quasi-static loading. The load was applied by increments until the failure load and the load increments depended on the thickness. At each step, the cracking pattern was plotted.

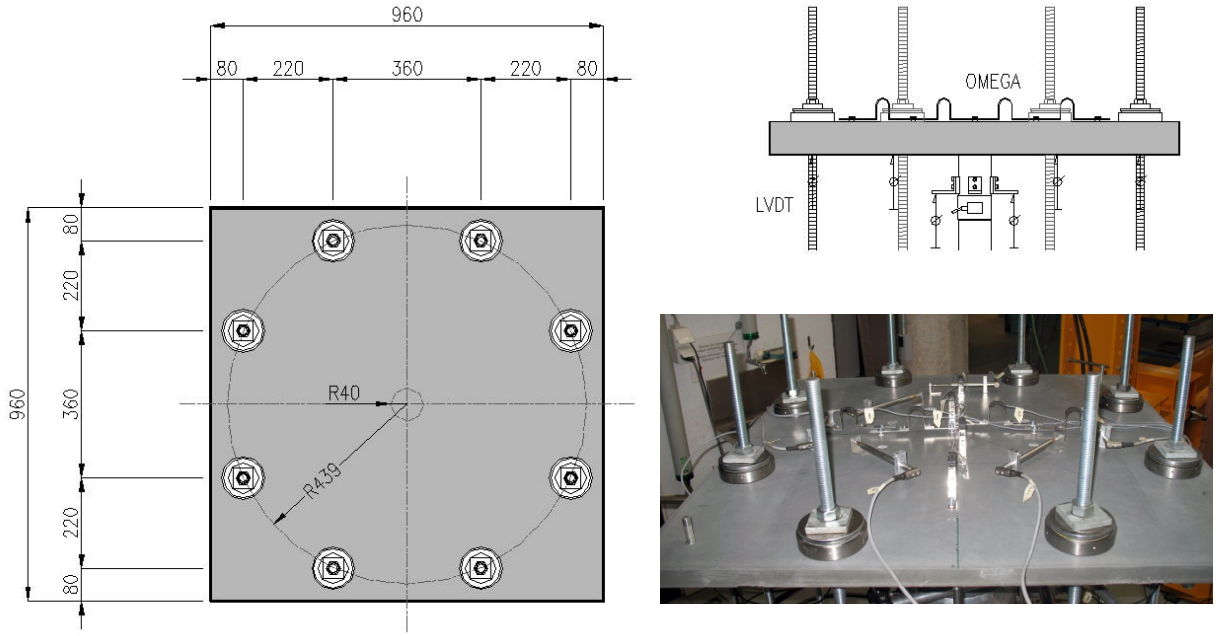

Figure 5-20: Punching shear test setup of the UHPFRC slabs

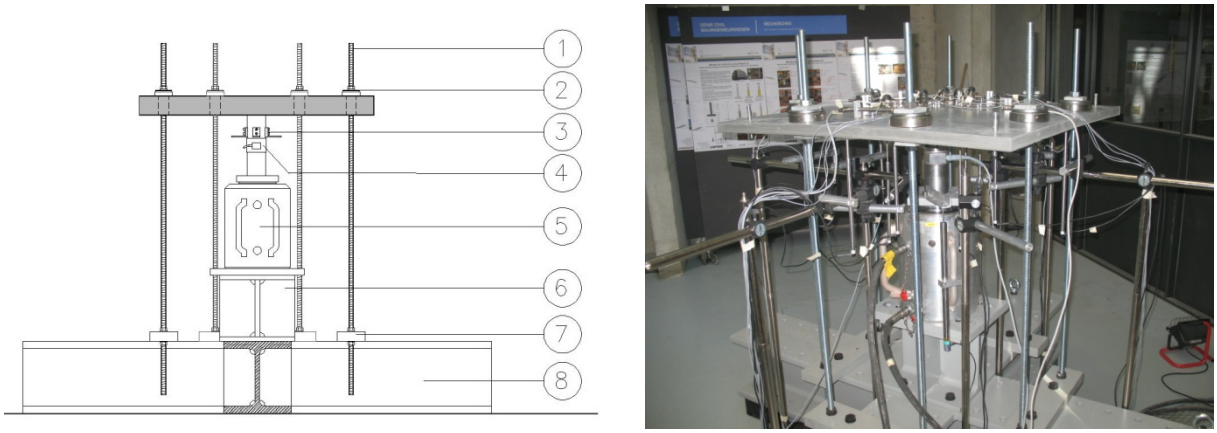

1 tie-rods M20 8.8
2 spherical plain thrust bearings SKF
3 steel punch ϕ80 mm
4 load cells HBM 500 kN
5 Hydraulic jack *Bieri* 1000 kN/160 mm
6 support HEB 300
7 steel plates 400 x 150 x 40 mm
8 bottom crossbeam HEM 280

Figure 5-21: Punching shear test setup of the UHPFRC slabs

A total number of 31 instruments were recorded for each test. One load cell type *HBM C6A 500 kN* was placed between the actuators and the steel punch. Twelve linear variable differential transformers (LVDT) allowed the measurement of the vertical displacements of the slabs and the supports. Twelve displacement transducers type *TML Omega* were placed on the top face of the slabs in order to measure the top strains. Six LVDTs were placed on the top face of the slabs for the measurement of the yield lines openings (Figure 5-22). The sensors were connected to a data acquisition system type *HBM Spider 8* with the data acquisition software *HBM Catman*. The frequency of data recording was 1 Hz.

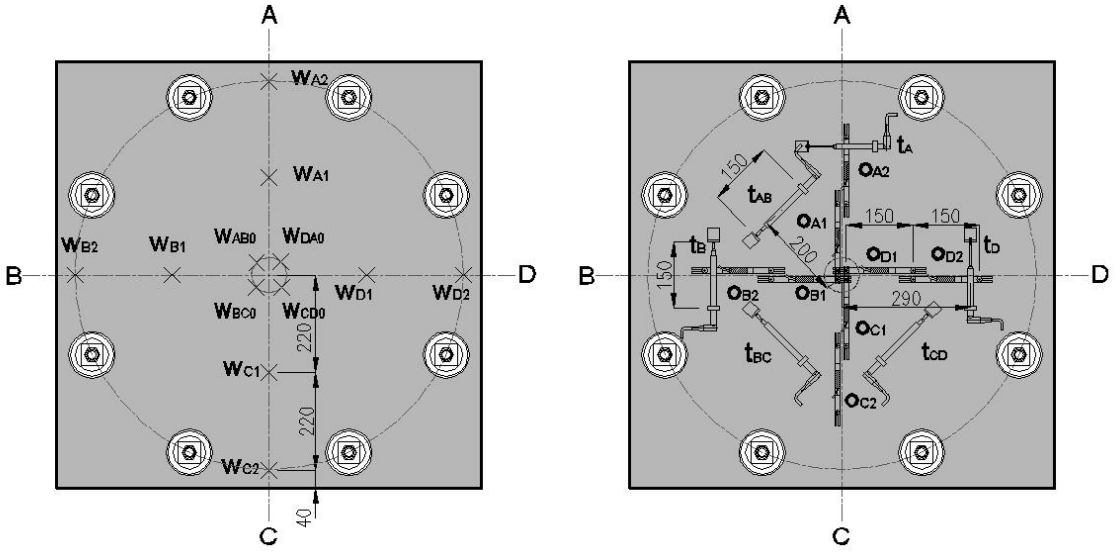

Figure 5-22: Measurement arrangement of the UHPFRC slabs

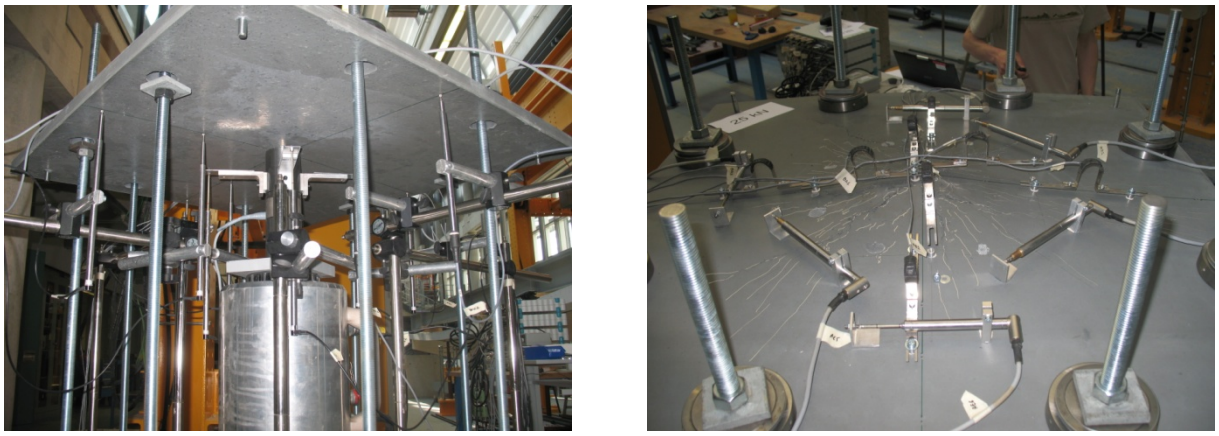

Figure 5-23: Views of the deflections and top strains measurements

5.3.5 Tensile properties of reinforcement

The tensile properties of steel rebars and prestressing strands were defined on four or six bars of each diameter. The tests were performed on bars of 600 mm length in a universal testing machine of the firm *Walter & Bai* according to the standards ISO 15630, parts 1 and 3.

Table 5-6: Mechanical properties of the reinforcing steel of HPFRC slabs

Diameter [mm]	E_s [GPa]	$f_{s0,2}$ [MPa]	f_u [MPa]	ε_u [%]
ϕ8	205	528	620	5.99
ϕ10	206	504	574	6.34
ϕ12	202	531	590	6.20

Table 5-7: Mechanical properties of the reinforcing steel of UHPFRC slabs

Diameter [mm]	E_s [GPa]	$f_{s0,2}$ [MPa]	f_u [MPa]	ε_u [%]
ϕ5	201	623	645	3.60
ϕ7	205	546	585	3.43
ϕ9	202	556	599	3.52
ϕ10	203	557	599	3.80
ϕ12	200	504	599	8.24

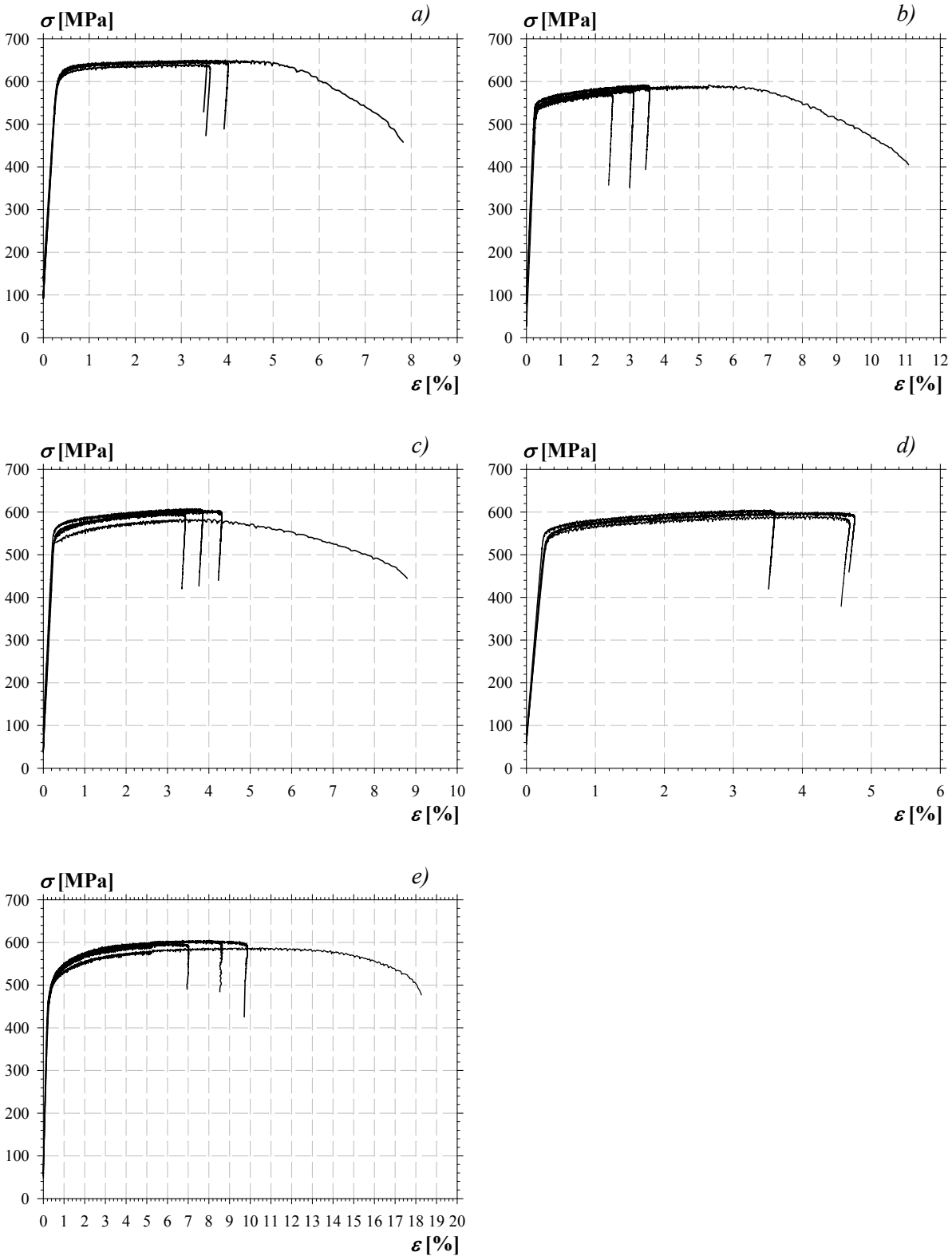

Figure 5-24: Stress-strain characteristics of the reinforcing steel of UHPFRC slabs, a) ϕ5 mm, b) ϕ7 mm, c) ϕ9 mm, d) ϕ10 mm, e) ϕ12 mm

5.4 Test results

5.4.1 Results of HPC and HPFRC slabs

Influence of reinforcement ratio and prestressing intensity

The following graphs were represented in order to highlight the influence of the reinforcement and post-tensioning on the flexural behaviour and punching shear strength (Figure 5-25). Each graph contains the load vs. deflection curves of the slabs having the same fibre content but containing different steel reinforcement ratio and post-tensioning forces.

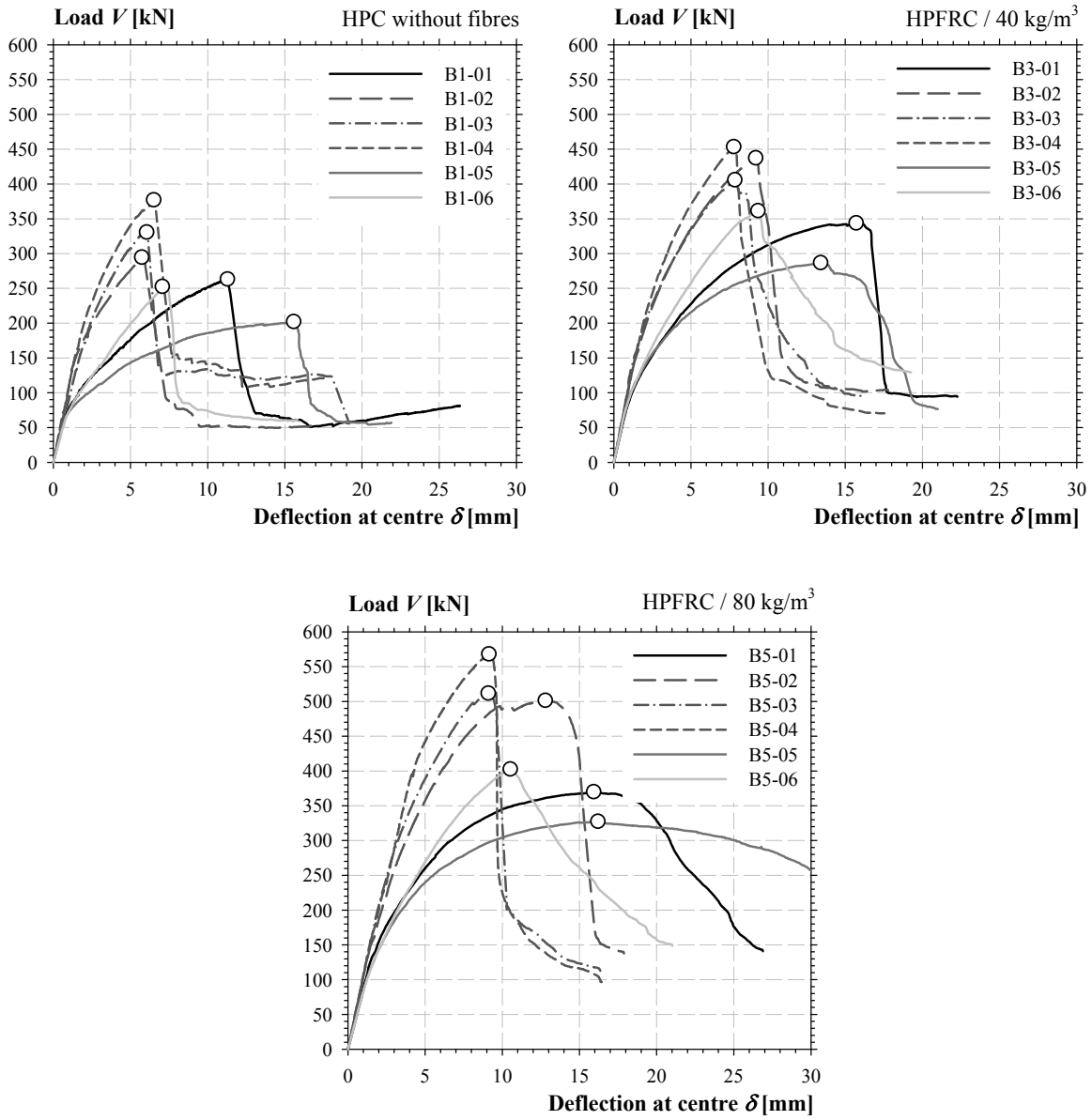

Figure 5-25: Curves load vs deflection at centre of the slabs according to the fibre content

For conventional reinforced-concrete slabs without transversal reinforcement, several experimental studies highlighted that the punching shear strength is inversely proportional to the deflection capacity as seen in chapter 2. In other words, for slabs with the same concrete composition, thickness and

loading configuration, when the reinforcement ratio and the prestressing force intensity increase, the punching shear strength increases as well, but the deformation capacity diminishes. Based on the experimental observations and results, this established fact is similar for the HSFRC slabs.

The behaviour can be divided into three parts on the basis of the observations. In the first part, the slabs were uncracked, the behaviour was linear elastic. All slabs had the same stiffness. When the tensile strength of the matrix was reached, the first cracks appeared at the centre and the stiffness decreased. For the post-tensioned slabs, the cracking load was delayed according to the prestressing force intensity. In the second part, the reinforcement was activated with the cracking development. For some slabs, especially the post-tensioned ones, the punching shear failure occurred in a sudden manner before the steel's yield limit. In the third part, the yield limit of the reinforcement was reached and the slabs had plastic strains. For some slabs, particularly the HPFRC slabs and the element with a low reinforcement ratio, the punching shear failure occurred in this part. The slabs B5-01 and B5-05 exhibited a flexural failure with the development of yield lines followed by a punching shear failure in the descending branch.

Influence of fibre content

The following graphs were represented in order to highlight the influence of the fibre content on the flexural behaviour and punching shear strength (Figure 5-26). Each graph contains the load vs. deflection curves of slabs having the same steel reinforcement ratio and post-tensioning forces but containing different fibres contents.

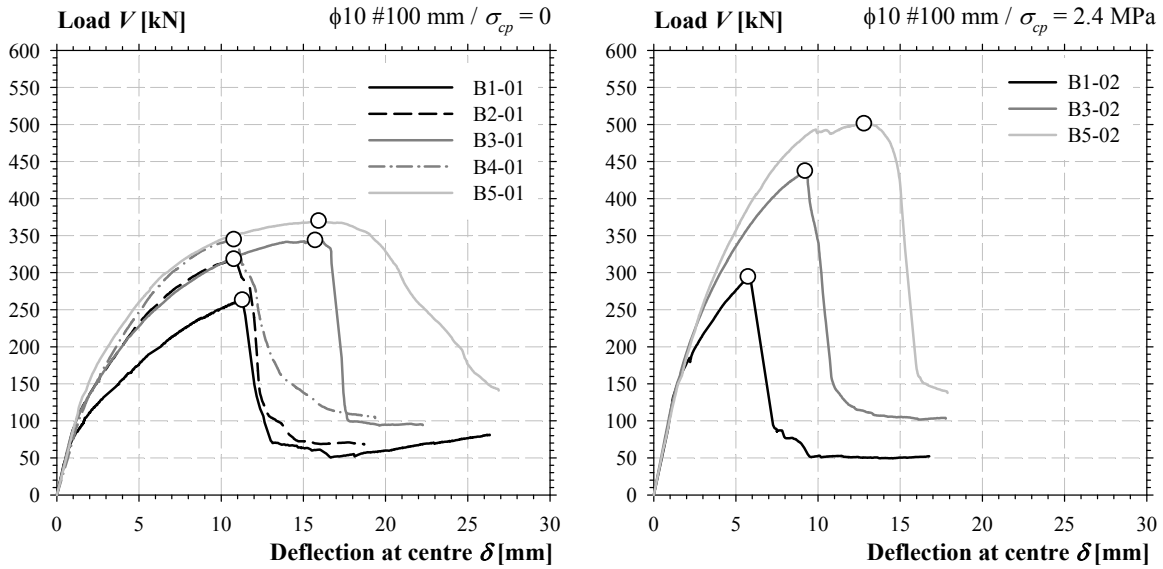

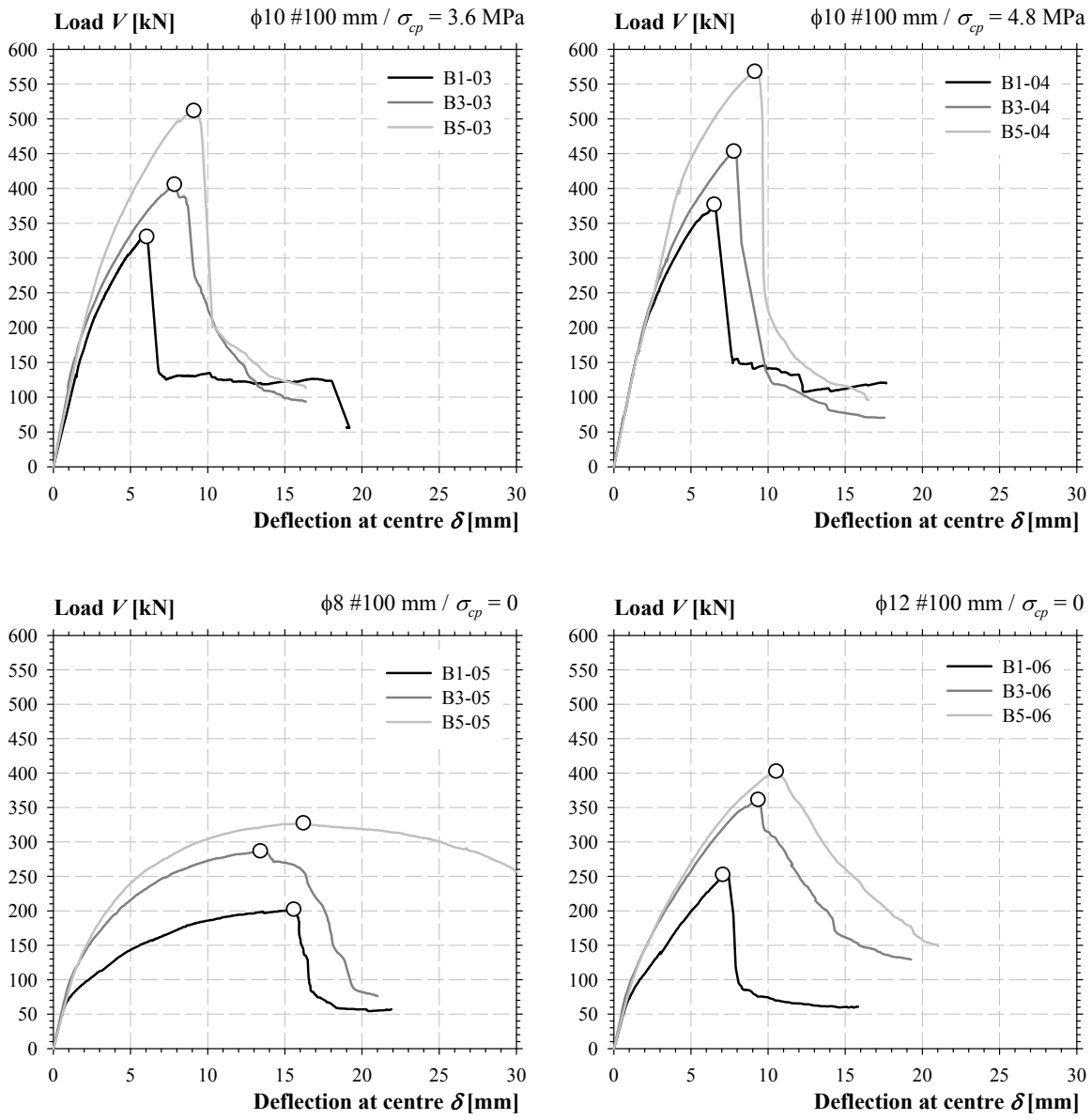

Figure 5-26: Curves load vs deflection at centre of the slabs according to the reinforcement ration and prestressing force intensity

Once the cracking load was reached, the plain concrete slabs had a significant decrease of their stiffness. The HPFRC slabs presented a more progressive decrease in stiffness, which was shown with a better-controlled cracking development. The stiffness difference in the elastic-cracked stage between the HPC and HPFRC slabs decreased when the reinforcement ratio or the post-tensioning force intensity was increased. The fibre effect is important for the slab with a low reinforcement ratio, i.e series Bi-05.

Except for slabs B5-01, B5-05 and B5-06, all specimens had a sudden drop of the strength at the failure load. The failure of the slabs without axial force is located before or after the steel's yield limit, according to the reinforcement ratio. The plastic strains were important for specimens B3-01, B5-01, B1-05, B3-05, and B5-05. These five slabs underwent important deformations before the punching shear failure. The slab B5-05 exhibited a flexural failure with the development of yield lines. For all HPFRC specimens without prestressing, the punching shear strength was increased.

The post-tensioned slabs showed a sudden drop of the load after the peak. These slabs didn't exhibit large plastic strains, except for the slab B5-02. Added to normal stress, fibres provide an increased load and deflection capacity; this has been proved for the three degrees of post-tensioning.

The evolution of the punching shear capacity according to the fibre content is not a linear function. For reinforced concrete slabs the fibre effect decreases as the reinforcement increases as well. For prestressed slabs the fibres effect tends to increase as the prestressing force increases as well.

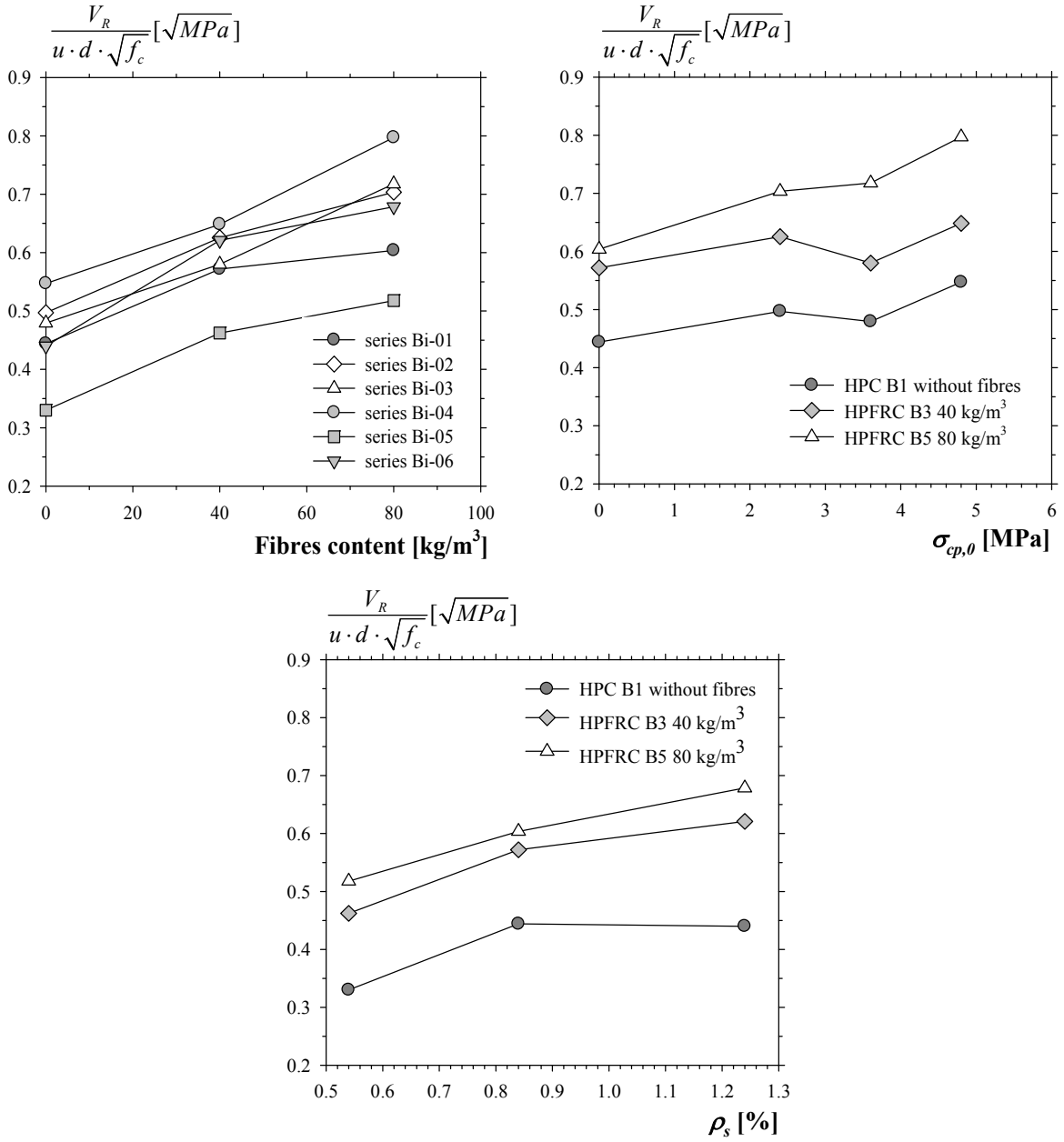

Figure 5-27: Evolution of the nominal punching shear strength according to the different parameters

The serviceability of the HPFRC slabs is higher compared to HPC specimens and the cracks were better distributed with smaller openings. Their stiffness was higher, therefore for a same load level the HPFRC specimens exhibited smaller deflections.

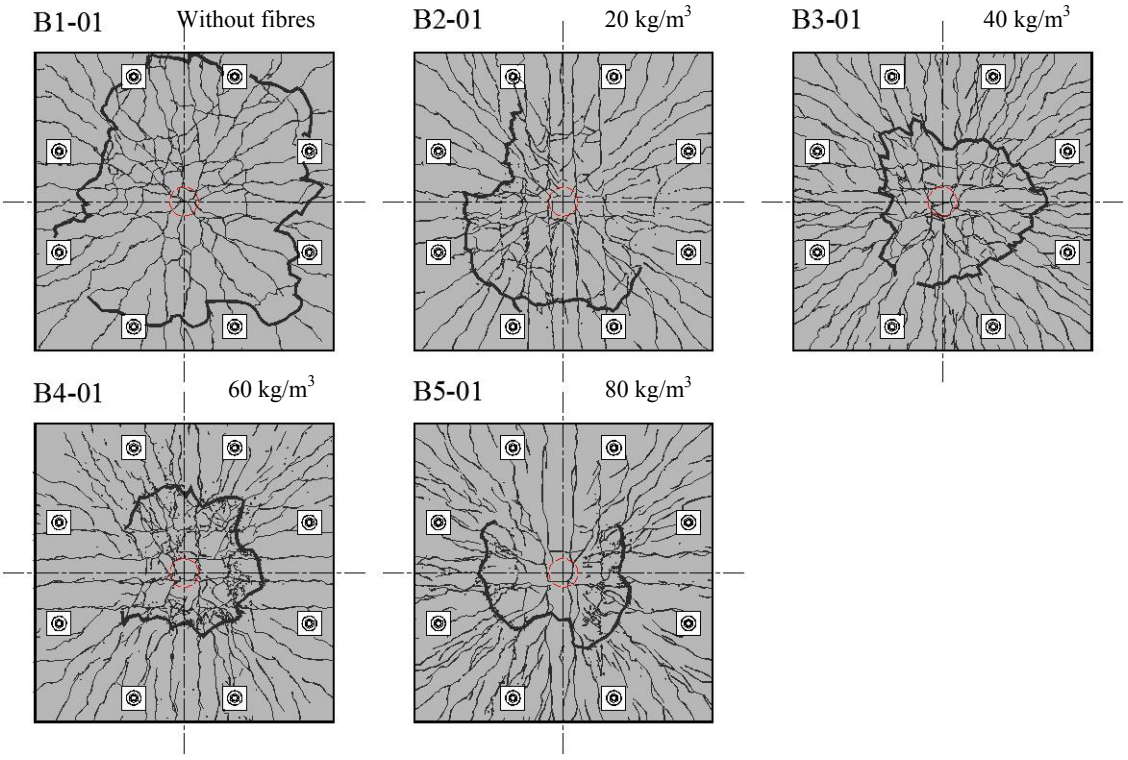

Figure 5-28: Cracking pattern of the slabs series 01, ρ_s = 0.87% - $\sigma_{cp,0}$ = 0 MPa

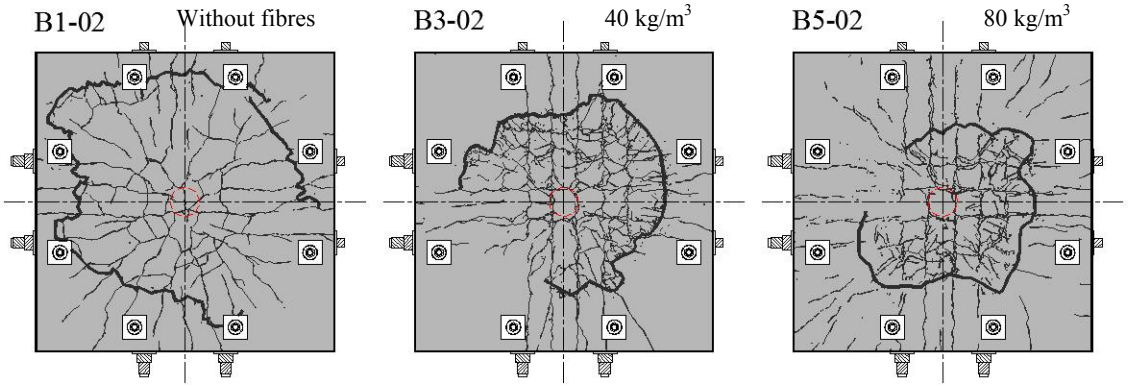

Figure 5-29: Cracking pattern of the slabs series 02, , ρ_s = 0.87% - $\sigma_{cp,0}$ = 2.4 MPa

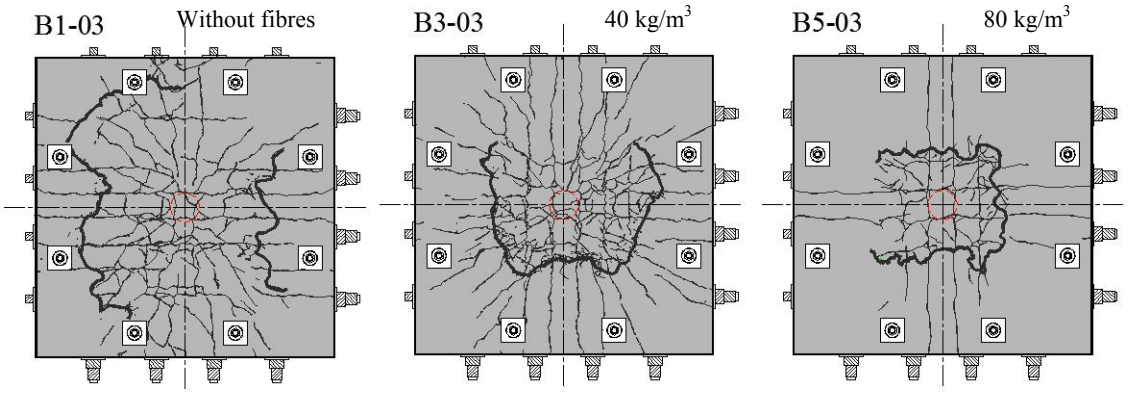

Figure 5-30: Cracking pattern of the slabs series 03, ρ_s = 0.87% - $\sigma_{cp,0}$ = 3.6 MPa

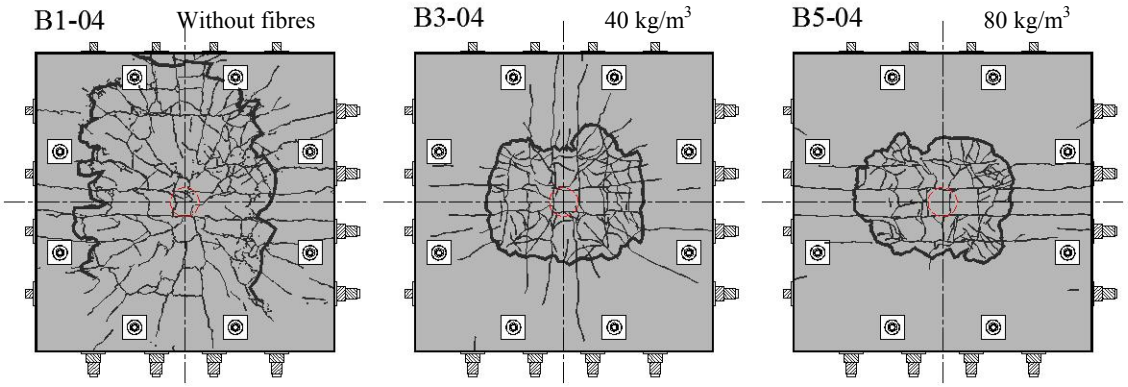

Figure 5-31: Cracking pattern of the slabs series 04, ρ_s = 0.87% - $\sigma_{cp,0}$ = 4.8 MPa

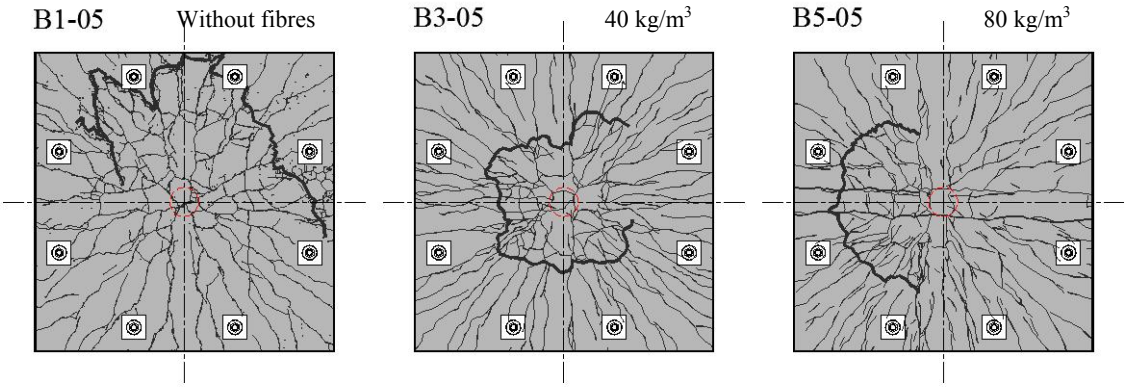

Figure 5-32: Cracking pattern of the slabs series 05, ρ_s = 0.56% - $\sigma_{cp,0}$ = 0 MPa

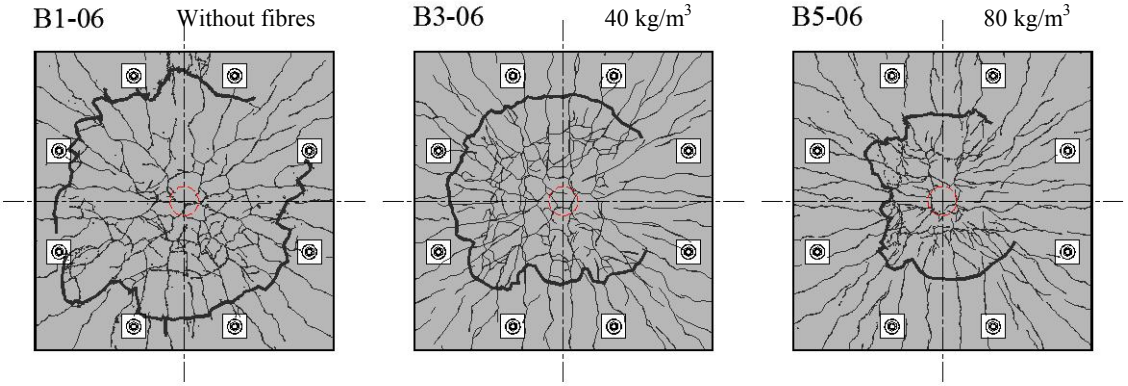

Figure 5-33: Cracking pattern of the slabs series 06, ρ_s = 1.26% - $\sigma_{cp,0}$ = 0 MPa

Table 5-8: Effective properties and tests results of the HPC and HPFRC slabs

Specimen	V_f	f_c	ρ_s	$\sigma_{cp,0}$	d	$V_{R,test}$	$\delta_{R,test}$	ψ	$\frac{V_R}{b_0 \cdot d \cdot \sqrt{f_c}}$	$\frac{\psi \cdot d}{16 + d_g}$
	[kg/m^3]	[MPa]	[%]	[MPa]	[mm]	[kN]	[mm]	[mm/m]	[$\sqrt{\text{MPa}}$]	[-]
B1-01	without fibres	99	0.84	0.00	90	262	11.3	18.9	0.44	0.07
B1-02			0.84	2.40	90	294	5.8	8.1	0.50	0.03
B1-03			0.76	3.60	100	330	6.1	8.6	0.48	0.04
B1-04			0.76	4.80	100	376	6.6	9.1	0.55	0.04
B1-05			0.54	0.00	90	201	15.6	28.4	0.33	0.11
B1-06			1.24	0.00	88	252	7.1	11.4	0.44	0.04
B2-01	20	102	0.76	0.00	100	318	10.8	17.9	0.46	0.07
B3-01	40	102	0.84	0.00	90	343	15.8	27.7	0.57	0.10
B3-02			0.76	2.40	100	437	9.2	15.4	0.63	0.06
B3-03			0.76	3.60	100	405	7.9	13.0	0.58	0.05
B3-04			0.76	4.80	100	453	7.8	12.7	0.65	0.05
B3-05			0.53	0.00	92	286	13.5	24.4	0.46	0.09
B3-06			1.24	0.00	88	361	9.4	16.7	0.62	0.06
B4-01	60	100	0.76	0.00	100	344	10.8	18.1	0.50	0.08
B5-01	80	106	0.84	0.00	90	369	16.0	27.6	0.60	0.10
B5-02			0.76	2.40	100	501	12.8	20.1	0.70	0.08
B5-03			0.76	3.60	100	511	9.1	14.1	0.72	0.06
B5-04			0.76	4.80	100	567	9.2	13.5	0.80	0.06
B5-05			0.53	0.00	92	327	16.2	28.6	0.52	0.11
B5-06			1.24	0.00	88	402	10.6	17.2	0.68	0.06

5.4.2 Results of UHPC slabs

Influence of thickness

The following graphs were represented in order to highlight the influence of the thickness on the flexural and punching shear behaviour. Each graph contains the load vs. deflection curves of slabs having different thicknesses but containing the same fibre content and the same steel reinforcement ratio.

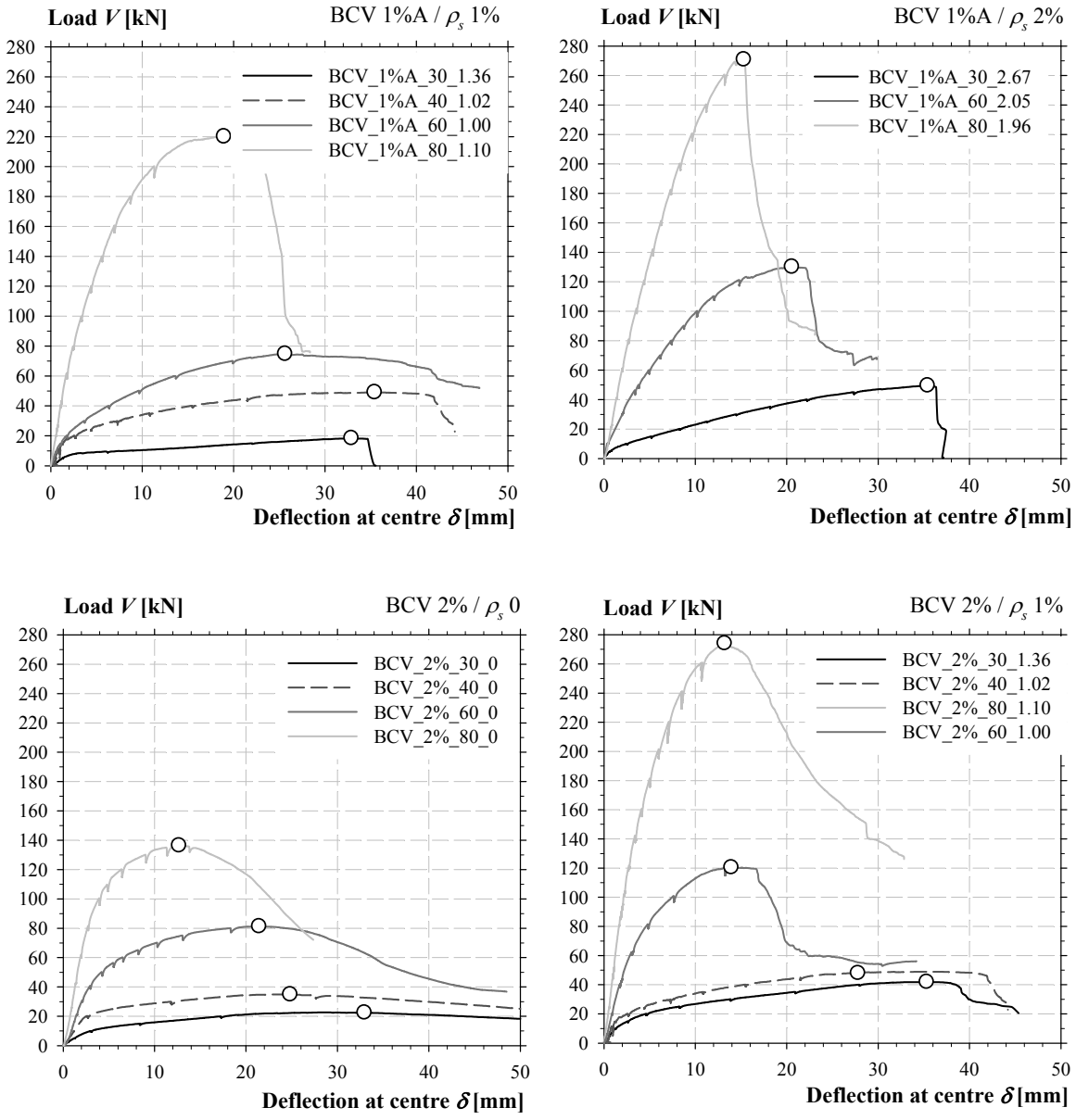

Figure 5-34: Curves load vs deflection at centre of the UHPC slabs according to the fibre content and reinforcement ratio

The behaviour of the tested slabs with and without reinforcement can be divided into several parts on the basis of the observations. In the first part, the behaviour is elastic linear and the stiffness is directly related to the thickness. When the tensile strength of the matrix is reached, the first cracks appear at the centre near the loading point. In the second part, the stiffness decreases progressively with the

cracking development. The cracks then propagate toward the ends of the slabs. For the slabs without reinforcement, this portion was extended to a load corresponding almost to 0.9 times the peak load. Before the peak load, yield lines appeared. After the peak, the load decreased progressively and the openings of the yield lines increased. The slabs without reinforcement showed a flexural failure. For these slabs, the flexural strength is not a linear function of the thickness. The ultimate load was four times higher between a thickness of 30 mm (22.6 kN) and 40 mm (34.9 kN) and their double respective thicknesses of 60 mm (81.2 kN) and 80 mm (136 kN). The slabs were cut in half. After the internal cracking analysis, no punching shear cones were developed for these specimens. The flexural strength of these slabs was moderate, therefore the punching shear strength was not determining in this studied case.

For the slabs with reinforcement, after the development of the first cracks, the rebars were activated. The behaviour was almost linear and can be classified as an elastic-cracked state. When the steel yield limit of the reinforcement was reached, the stiffness decreased. The following failure mechanisms can be identified as follows: punching shear, flexural – punching shear and flexural. The punching shear failure is characterized by a sudden drop of the load without a large plastic strain. For the flexural - punching shear failure, the flexural strength was reached but the punching shear limited the development of a plastic strain. And finally the flexural failure is characterized by large deflections with a softening branch.

As seen below with the HPFRC slabs, the flexural and punching shear strength is inversely proportional to the deflection capacity. In other words, for slabs having the same fibre content, a reinforcement ratio and a loading configuration, the flexural and punching shear strength increases while the thickness increases, but the deformation capacity diminishes.

Influence of steel reinforcement and fibre content

In this section, each graph contains the load vs. deflection curves of the slabs having the same thickness. The following graphs were represented in order to highlight the influence of the steel reinforcement, from one hand, and the influence of the fibre content, from a second hand.

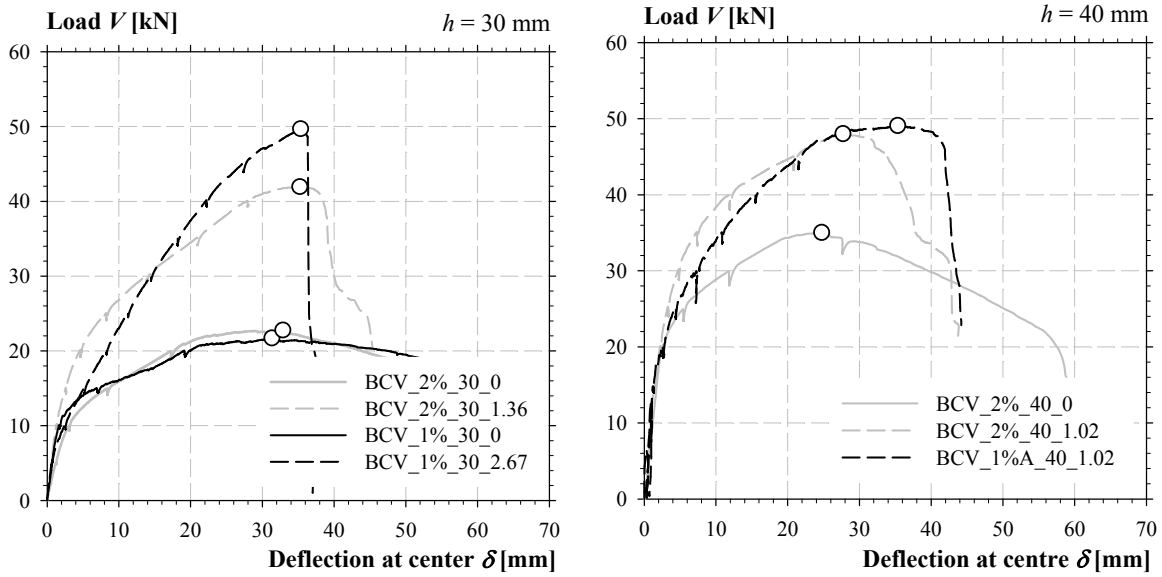

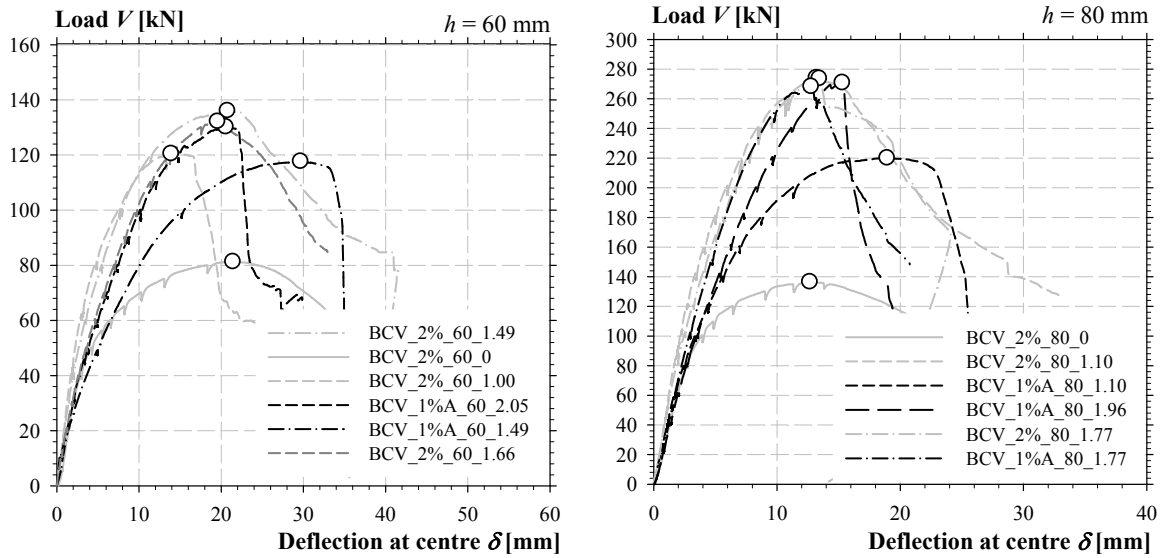

Figure 5-35: Curves load vs deflection at centre of the UHPC slabs according to the thickness

The reinforced slabs in BCV-2% showed a higher stiffness in the elastic-cracked state compared to the slabs BCV-1%A. For slabs, BCV_x_80_1.10 and BCV_x_ 60_1.49 having the same reinforcement ratio and thickness, as the fibre content increases, the flexural and punching shear strength increases as well, but the deformation capacity decreases. The slabs BCV_x_80_1.77 with the reinforcement arrangement type B exhibited the same pre-peak behaviour. These two slabs failed in punching shear, but the slab in BCV-2% showed a more ductile post-peak behaviour. For the specimens with the reinforcement arrangement B, BCV_x_ 60_1.49 and BCV_x_ 80_1.77, the dowel action of the rebars at the centre was important in the post-peak response.

As the thickness increases, the difference between the slabs with reinforcement is higher. The effective depth of the reinforcement is more efficient for thick specimens compared to the thin slabs with a reinforcement located at mid-depth. For the reinforcement arrangement type A, we distinguished two types of punching shear failure mechanisms; In the first type, the critical shear crack intercepts the rebars, resulting in the development of a large punching cone and thus the load carrying capacity was high (Figure 5-37). In the second type, the critical shear crack didn't intercept the rebars, the punching cone was restrained in a mesh's cell and the load carrying capacity was lower (Figure 5-36). The second type concerned particularly the slabs with a thickness of 30 and 40 mm. The rebars included in the punching cone allowed a better control of the shear cracks development compared to the cone formed in the slabs reinforced with the fibres alone.

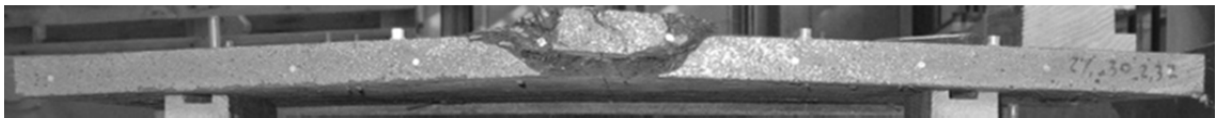

Figure 5-36: Internal shear crack of thin slab

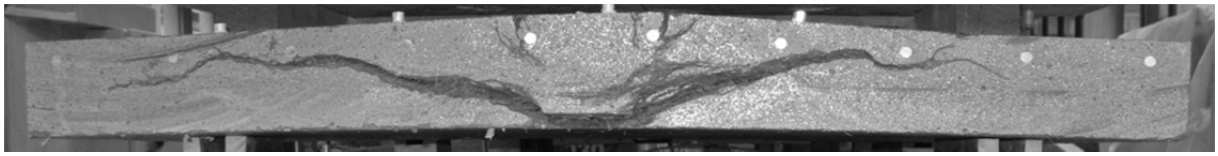

Figure 5-37: Internal shear crack of thick slab

For slabs with a thickness of 30 and 40 mm, concentric tangential cracks were developed on the compression side under large deflections. This behaviour can be assimilated to an in-plane loading of the specimen.

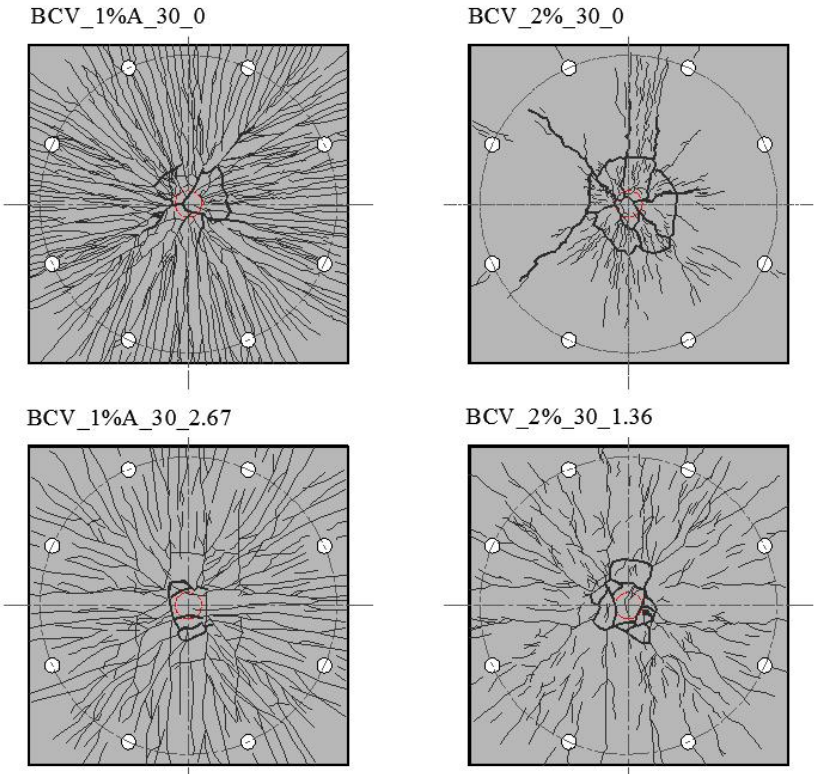

Figure 5-38: Cracking pattern of UHPFRC slabs with a thickness of 30 mm

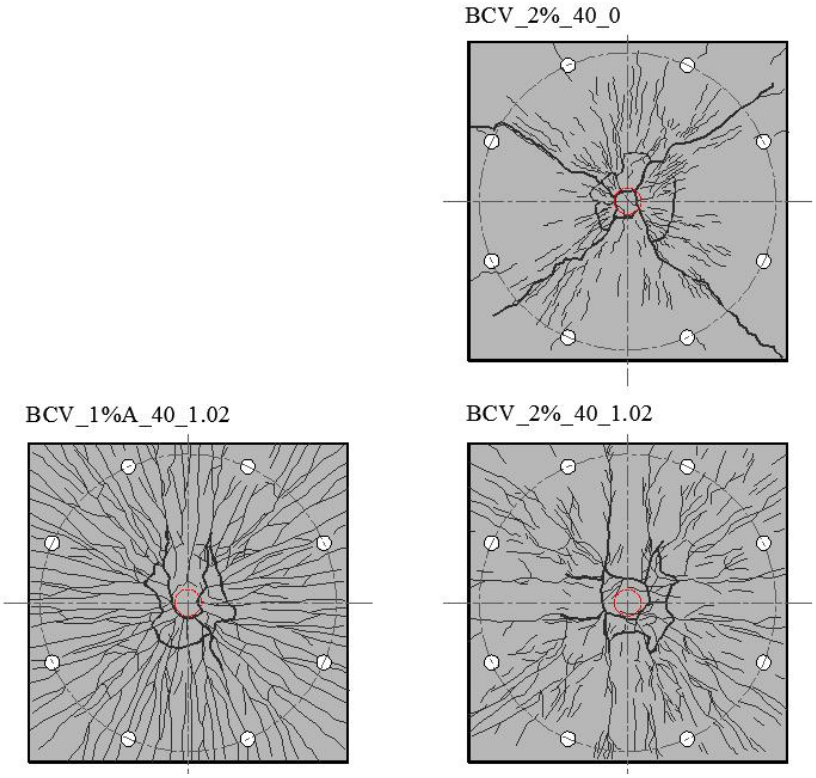

Figure 5-39: Cracking pattern of UHPFRC slabs with a thickness of 40 mm

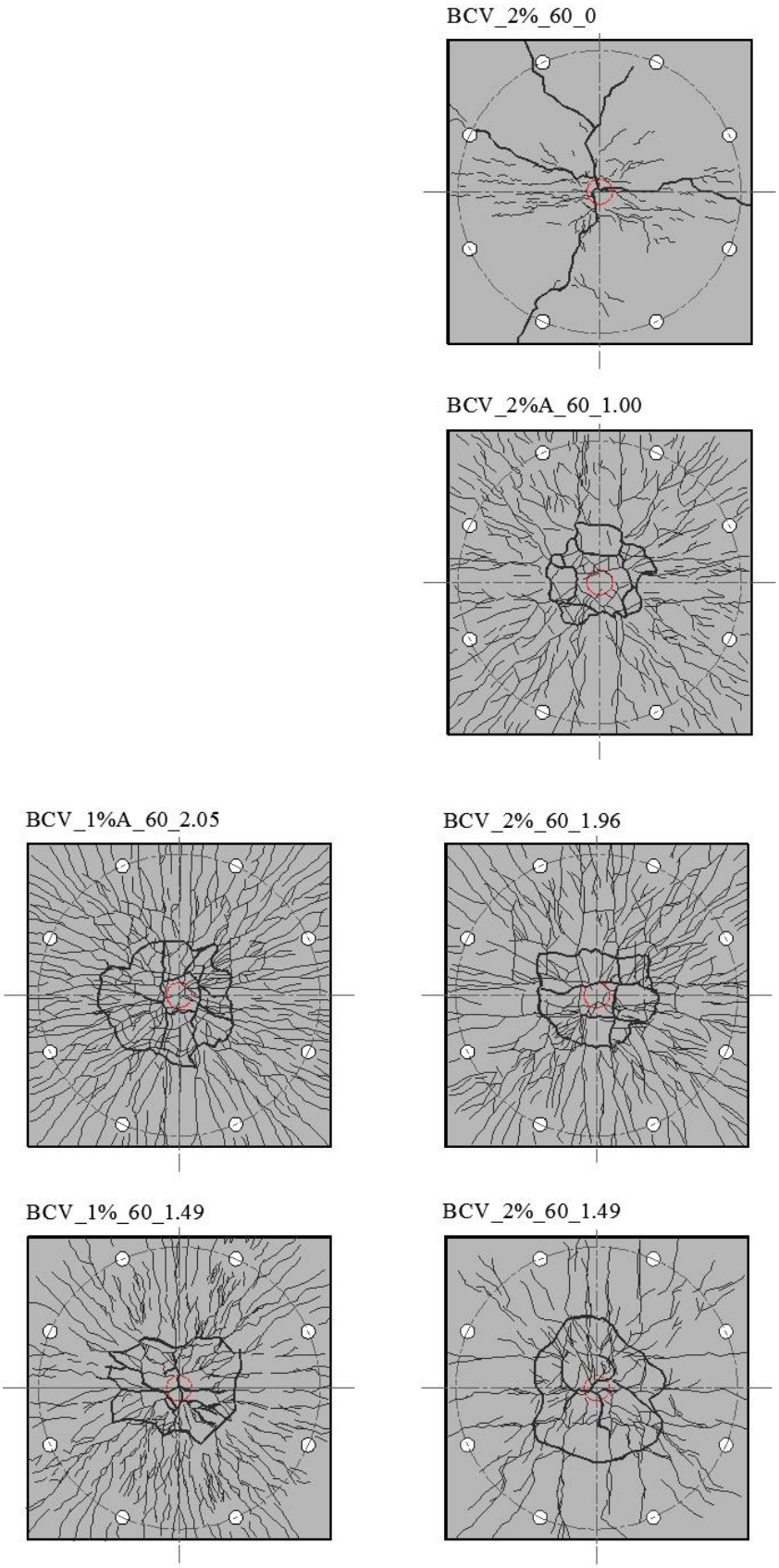

Figure 5-40: Cracking pattern of UHPFRC slabs with a thickness of 60 mm

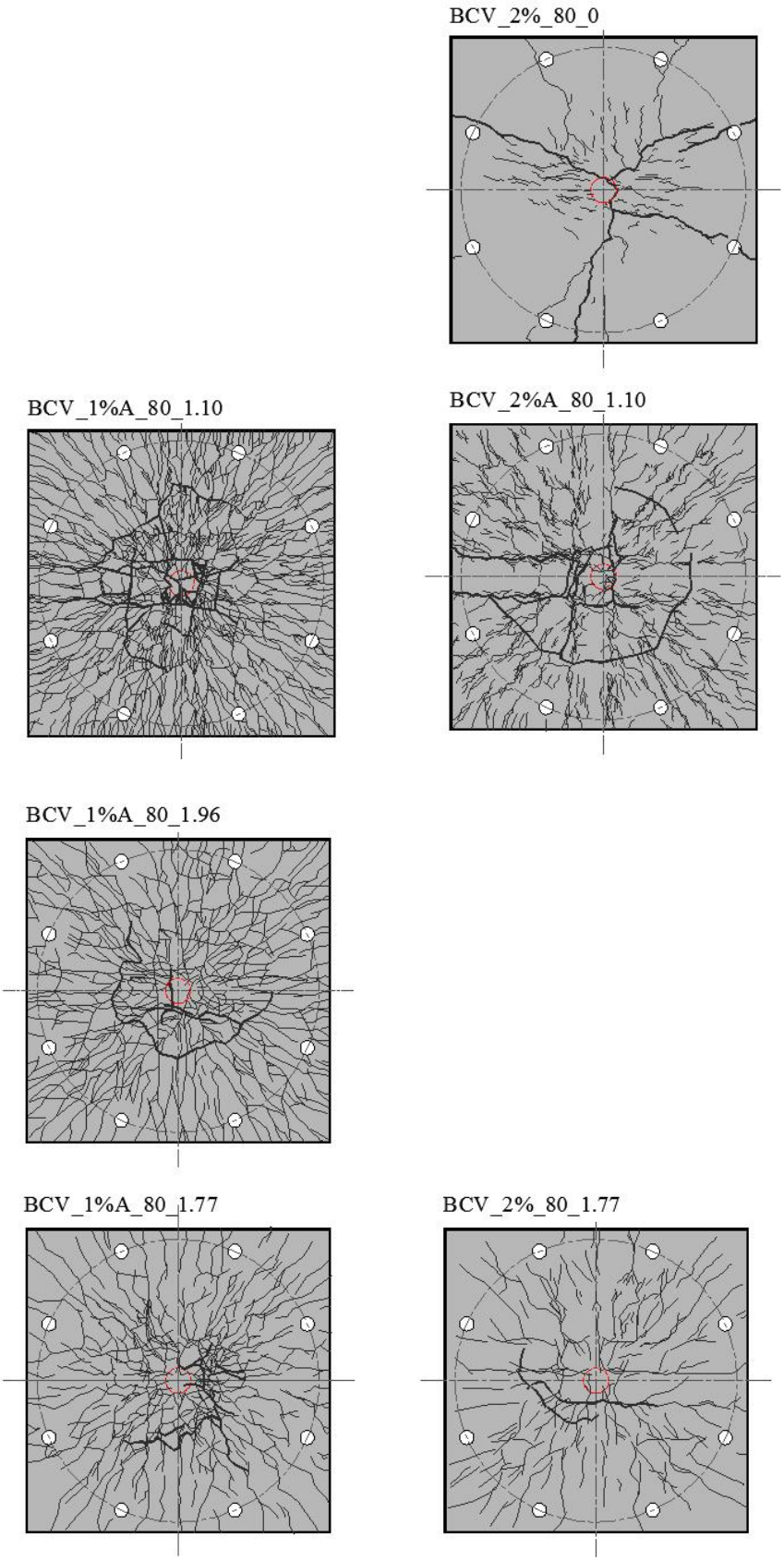

Figure 5-41: Cracking pattern of UHPFRC slabs with a thickness of 80 mm

Table 5-9: Effective properties and tests results of the UHPFRC slabs

Specimen	f_c [MPa]	h [mm]	d [mm]	Figure 5-17	$V_{R,test}$ [kN]	$\delta_{R,test}$ [mm]	ψ [mm/m]	Failure	$\frac{V_R}{b_0 \cdot d \cdot \sqrt{f_c}}$ [$\sqrt{\text{MPa}}$]	$\frac{\psi \cdot d}{16 + d_g}$ [-]
BCV-2%_30_0	143	30	30	Without mesh	22.7	33.0	63.6	F	0.18	0.12
BCV-2%_40_0		40	40		34.9	24.9	58.5	F	0.19	0.15
BCV-2%_60_0		60	60		81.2	21.5	45.3	F	0.26	0.17
BCV-2%_80_0		80	80		136	12.7	26.2	F	0.28	0.13
BCV-2%_30_1.36	156	30	15	A	41.9	35.3	82.7		0.75	0.08
BCV-2%_40_1.02		40	20		47.9	27.8	59.2		0.61	0.07
BCV-2%_60_1.00		60	40		120	14.0	29.6		0.64	0.07
BCV-2%_80_1.10		80	60		274	13.2	26.0		0.83	0.10
BCV-1%A_30_0	157	30	30	A	21.6	31.4	71.9	F	0.17	0.13
BCV-1%A_40_1.02		40	20		49	35.5	77.6		0.62	0.10
BCV-1%A_60_2.05		60	40		130	20.6	44.1	P	0.69	0.11
BCV-1%A_80_1.10		80	60		220	19.0	39.2	P	0.67	0.15
BCV-1%A_30_2.67	150	30	15	A	49.6	35.4	77.4	P	0.90	0.07
BCV-1%A_80_1.96		80	60		271	15.3	29.8	P	0.84	0.11
BCV-2%_60_1.66	152	60	40	A	132	19.6	41.5		0.71	0.10
BCV-1%A_60_1.49	149	60	40	B	118	29.7	63.5		0.64	0.16
BCV-1%A_80_1.77		80	60		268	12.8	18.4	P	0.83	0.07
BCV-2%_60_1.49	153	60	40	B	136	20.8	45.6		0.73	0.11
BCV-2%_80_1.77		80	60		274	13.5	25.7	P	0.84	0.10

5.5 Numerical analysis

5.5.1 Failure criteria

As seen in Chapter 2, the Critical Shear Crack Theory (CSCT), developped by Muttoni, is an accurate model describing the punching shear strength of Reinforced Concrete slabs [MUT2008b]. Currently, different forms of this model are adopted in the Swiss Standard SIA262 [SIA2003] and the *fib* Model Code 2010 [FIB2010b], for the assessement of the punching shear strength of RC slabs without transverse reinforcement. The amount of shear that can be transferred by the concrete across the critical shear crack depends on the roughness of the crack and its opening. This roughness is a function of the aggregate size as defined by Vecchio and Collins. The critical crack opening is assumed to be proportional to the product of the effective depth d with the slab rotation ψ. For an axysymmetric slab with a point load at centre, the deformations are concentrated in the area surrounding the loading point. The part outside the punching cone is assumed to act like a rigid body (Figure 5-42). The rotation ψ is defined as the maximum rotation of the slab. Based on these assumptions, the semi-empirical failure criterion is defined as follows:

$$w \propto \psi \, d \tag{5-1}$$

$$\frac{V_{R,c}}{b_0 \cdot d \cdot \sqrt{f_c}} = \frac{3/4}{1+15 \cdot \frac{\psi \cdot d}{16+d_g}} \tag{5-2}$$

Where $V_{R,c}$ is the punching shear strength, b_0 is the control perimeter, located at $d/2$ of the edges of the loading support, d_g is the maximum size of the coarse aggregate. However, d_g = 0 for lightweight concrete and High Strength Concrete due to the aggregates fracture.

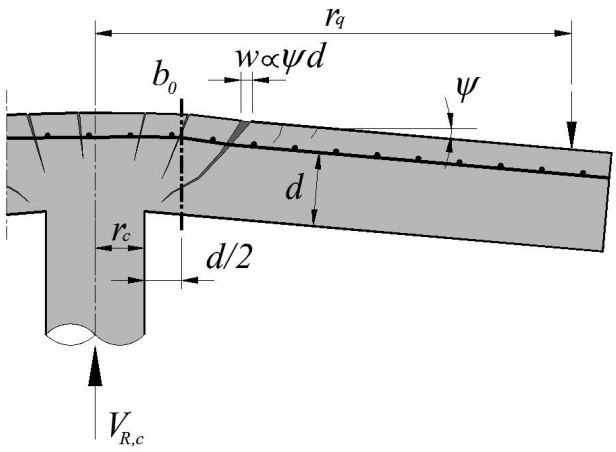

Figure 5-42: Critical shear crack with the different parameters

In the following graphs, the test results of the HPFRC and UHPFRC slabs and the test results presented in Chapter 2 are represented in the punching shear failure criterion developped for reinforced concrete. For the plotted test results, the rotation ψ outside the critical crack is defined as follows:

$$\psi = \delta \Big/ \left(r_q - r_c \right) \tag{5-3}$$

Where δ is the deflection between the support and the load application, r_q is the radius of the load application or the support, and r_c is the radius or the equivalent radius of the loading plate.

The effect of steel fibres on punching shear strength is clearly highligthed in the different graphs (Figure 5-43 to Figure 5-46). SFRC slabs exihibited a higher strength and a larger deformation at the failure compared to slabs without fibres. According to the fibres content, the SFRC results move away of the punching shear failure criterion. For test results of points 2.3.4.3 to 2.3.4.5 corresponding to UHPFRC slabs without conventional reinforcement, the plotted points are close to the failure criterion for reinforced concrete but the behaviour is more ductile.

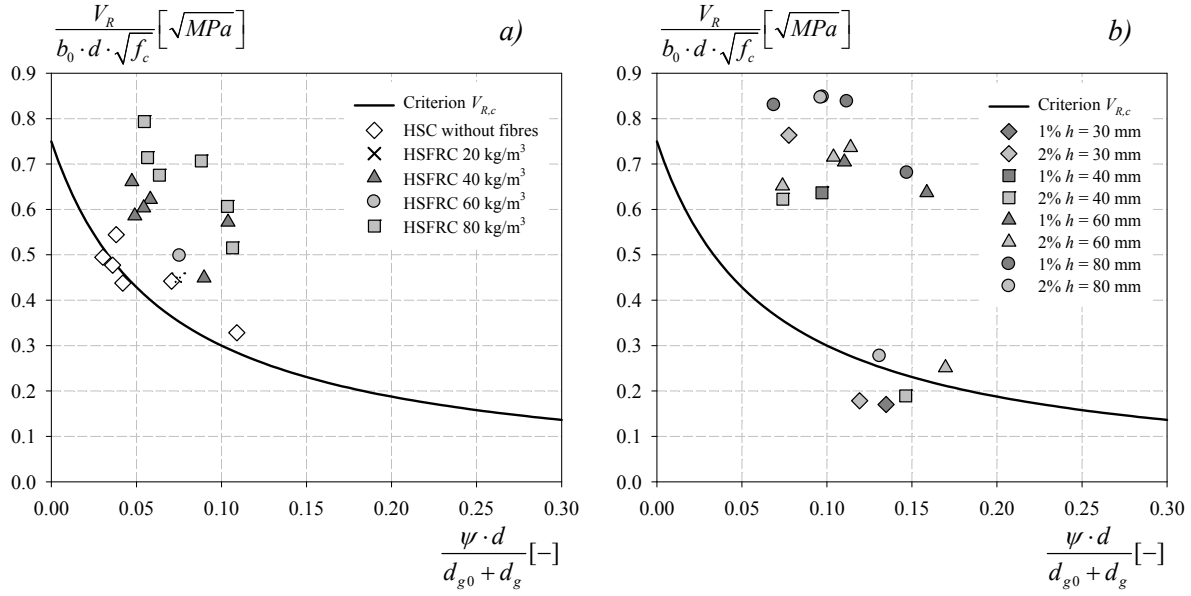

Figure 5-43: Test results represented in the failure criterion, HPFRC slabs a), UHPFRC slabs b)

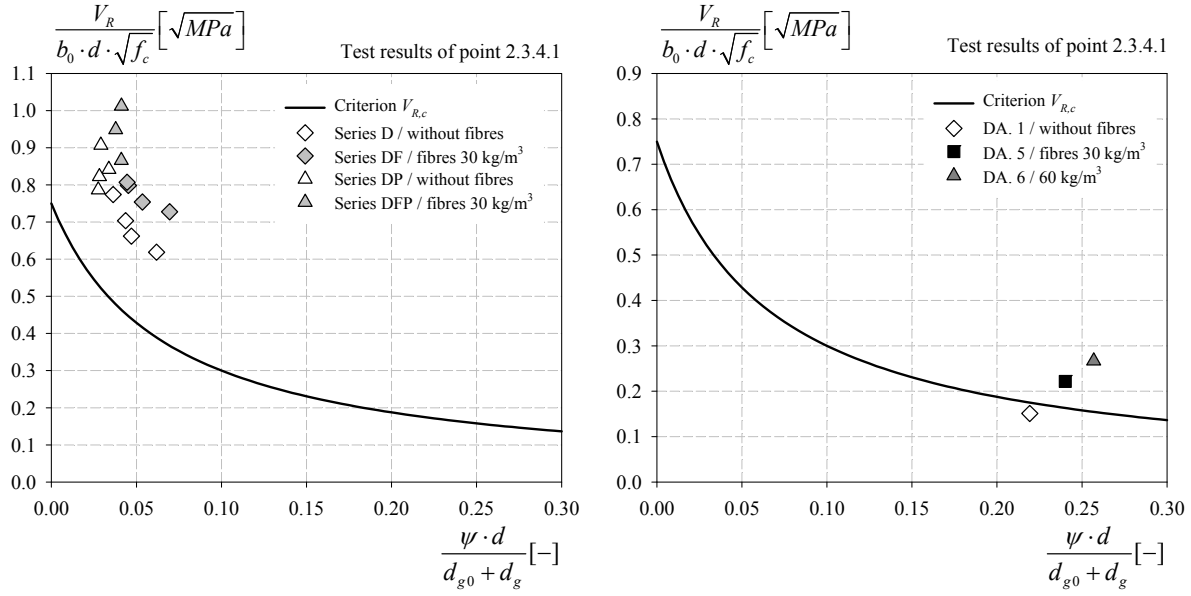

Figure 5-44: Test results of points 2.3.4.1 represented in the failure criterion

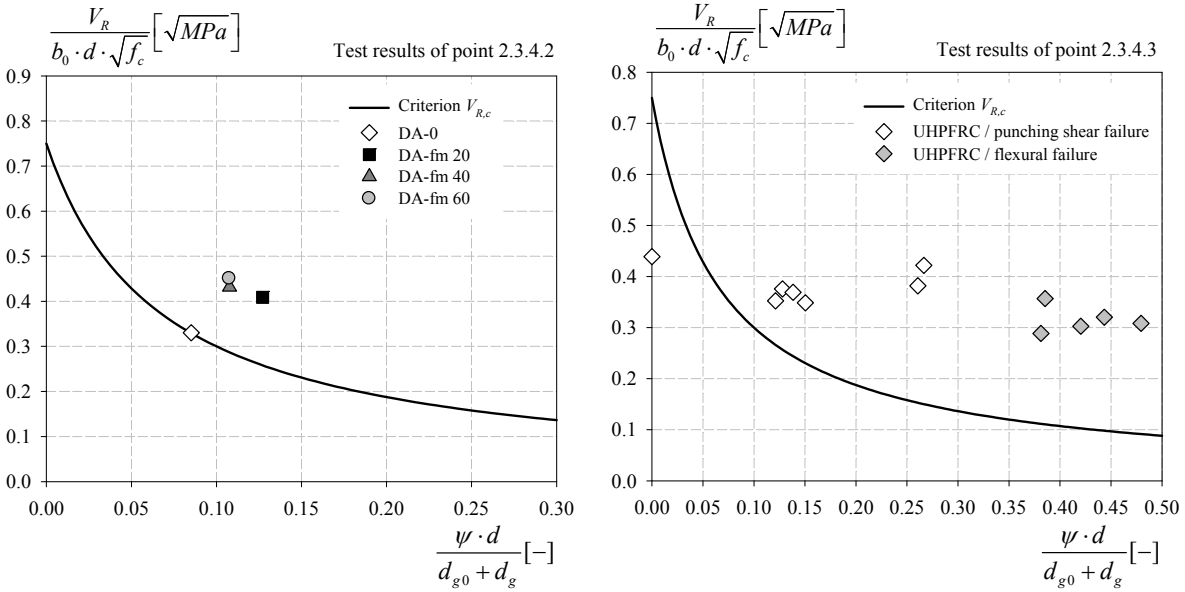

Figure 5-45: Test results of points 2.3.4.2 and 2.3.4.3 represented in the failure criterion

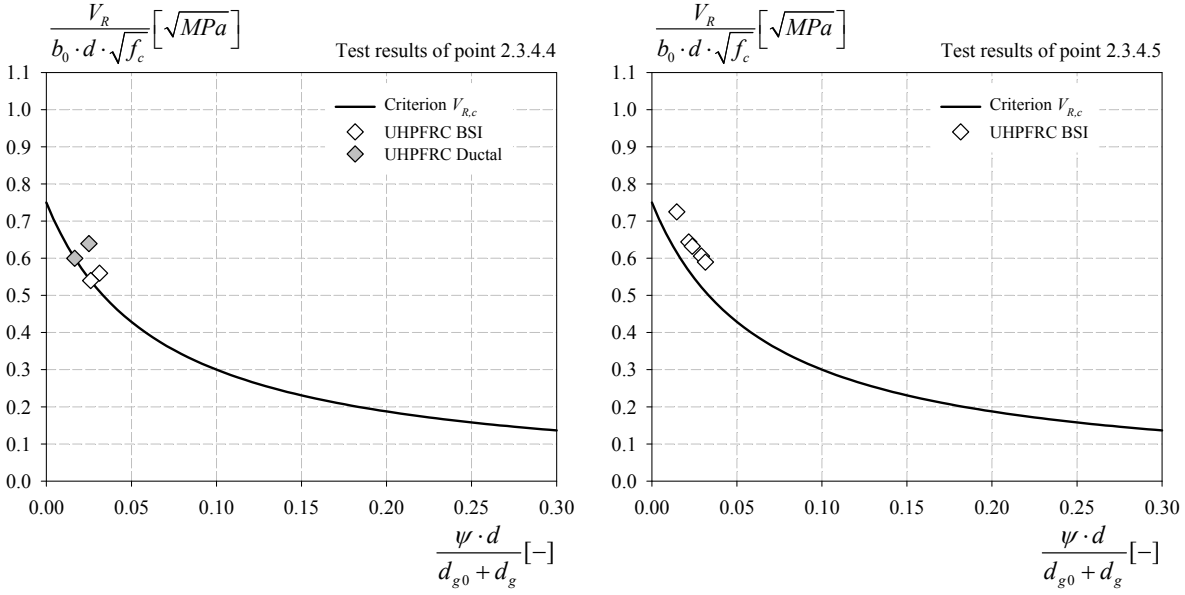

Figure 5-46: Test results of points 2.3.4.4 and 2.3.4.5 represented in the failure criterion

The fibres effect acts on the flexural behaviour and the punching shear cracks. In order to integrated the fibre contribution to punching shear strength, the model developed by Casanova [CAS1996] for FRC members is recalled in this paragraph. The model assumes the formation of a block mechanism. The shear capacity is defined as the sum of concrete, fibre and stirrups contributions. The contribution of fibres to the shear resistance corresponds to the force transferred between crack faces for a certain crack opening *w*. The fibres contribution is computed by integration of tensile stresses across the critical crack. The tensile stresses are defined by the post-cracking relationship $\sigma(w)$ of FRC and the distribution of the opening along the shear crack. On this basis, we proposed similar assumptions superposed with the Critical Shear Crack Theory. The punching shear strength correspond to the sum of the concrete and the fibres contribution. This contribution corresponds to the vertical component of the integration of the tensile stresses across the punching cone surface A_p. Two mechanical models were investigated. In the first model the compression depth was disregarded (Figure 5-47). In the

second model, the compression depth is considered, in a first approximation where $x = 0.1d$ (Figure 5-48). The distribution of the crack opening is assumed to be linear along the failure plan and the angle is equal to π/4 for both models. With the post-cracking tensile relationship $\sigma(w)$, the distribution of the tensile stresses is defined along the failure plan. Parrelely to this development, similar models were proposed by Spacojevic [SPA2008] for UHPFRC, by Muttoni and Fernández [MUT2010] and Maya et al [MAY2012] for FRC considering the Variable Engagement Model [VOO2003] for the $\sigma(w)$ relationship.

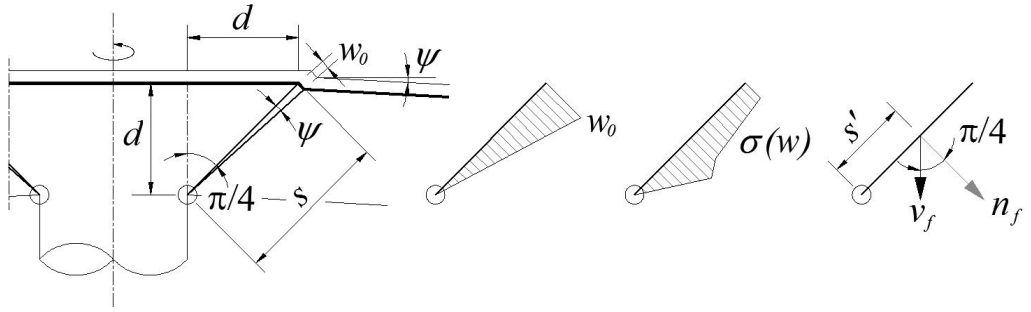

Figure 5-47: Mechanical model disregarding the compression depth, case I

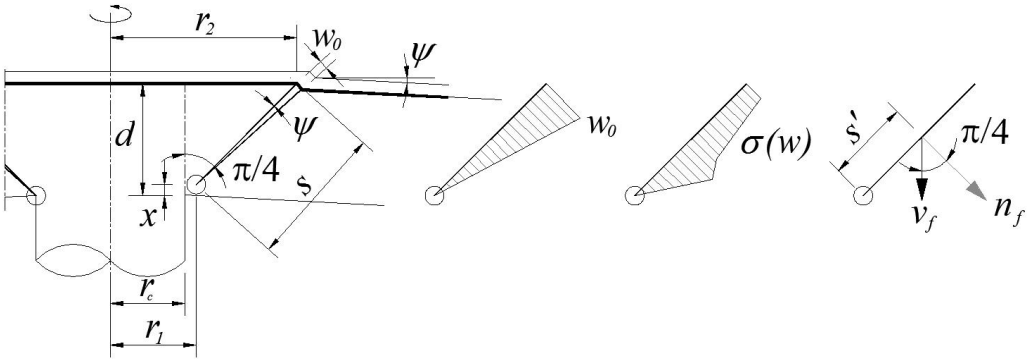

Figure 5-48: Mechanical model considering the compression depth, case II

The punching shear strength V_R, the fibre contribution $V_{R,f}$ and the maximal critical shear crack opening w_0 are defined as follows in both cases:

$$V_R = V_{R,c} + V_{R,f} \tag{5-4}$$

$$V_{R,f} = \int_{A_p} \sigma_f(w) \cdot dA_p \tag{5-5}$$

$$w_0 = \kappa \cdot \psi \cdot d \tag{5-6}$$

κ is a coefficient relating the rotation to the critical shear crack opening. A value of $\kappa = 0.5$ is proposed by Muttoni [MUT2008b] for reinforced concrete slabs with transverse reinforcement.

For the model II, the radius r_1 corresponds to 1/10 of the reinforcement level arm d.

$$r_1 = r_c + \frac{1}{10}\frac{d}{\tan\alpha} \tag{5-7}$$

And the radius r_2 corresponds to the intersection between the longitudinal reinforcement and the critical shear crack

$$r_2 = r_c + \frac{d}{\tan\alpha} \tag{5-8}$$

In model I, the inclined plan length s is defined as follows:

$$s = \frac{2}{\sqrt{2}} \cdot d \tag{5-9}$$

And in model II, s is defined as the following way:

$$s = \sqrt{\left(r_2 - r_1\right)^2 + \left(0.9d\right)^2} \tag{5-10}$$

The fibre contribution along the failure plan may be easily computed with a spreadsheet. The vertical component of the integration along the line s and the perimeter are defined as follows:

$$v_f = \frac{\sqrt{2}}{2} \cdot \int_s \sigma_f\left(w\right) \cdot ds \tag{5-11}$$

$$V_{R,f} = 2 \cdot \pi \cdot \left(r_{punch} + r_v\right) \cdot v_f \tag{5-12}$$

where r_v is the horizontal distance of the stress resultant along the line s (Figure 5-49).

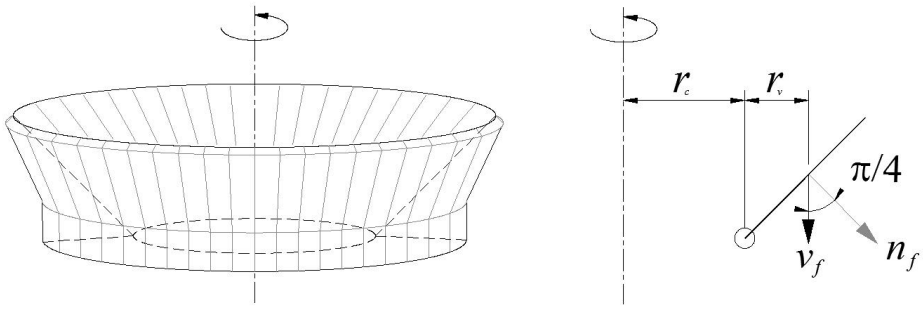

Figure 5-49: Tensile stresses across the punching cone and resultant force along the line s

In order to not consider two times the tensile strength of the matrix, the softening part of the matrix is substracted from the post-cracking tensile relationship. The softening part of the matrix may be approached by a bilinear relationship according to the Model Code 2010 [FIB2010a]:

$$w_0 = 0 \qquad \sigma_0 = f_{ct} \tag{5-13}$$

$$w_1 = G_f / f_{ct} \qquad \sigma_1 = 0.2 \cdot f_{ct} \tag{5-14}$$

$$w_2 = 5 \cdot G_f / f_{ct} \qquad \sigma_2 = 0 \tag{5-15}$$

Where the facture energy G_f is defined as follows

$$G_f = 73 \cdot f_{cm}^{\ 0.18} \tag{5-16}$$

The post-cracking tensile relationships $\sigma(w)$ of HPFRC were defined on the basis of the direct tensile tests on notched cores and inverse analysis on notched prism. For UHPFRC, the relationships $\sigma(w)$ were defined on the basis of the direct tensile tests on "dog bones" and inverse analysis on notched prisms, see Chapter 3. For both FRC composites, multi-linear laws were adopted.

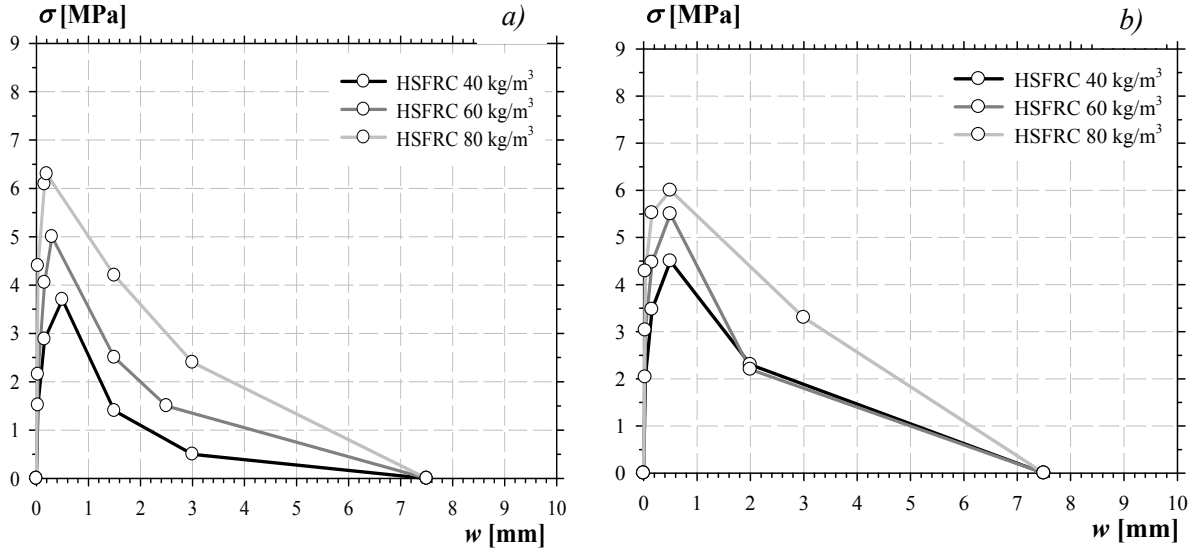

Figure 5-50: Post cracking tensile relationship σ(w) of HPFRC defined by uniaxial tensile tests a) by inverse analysis on prisms b)

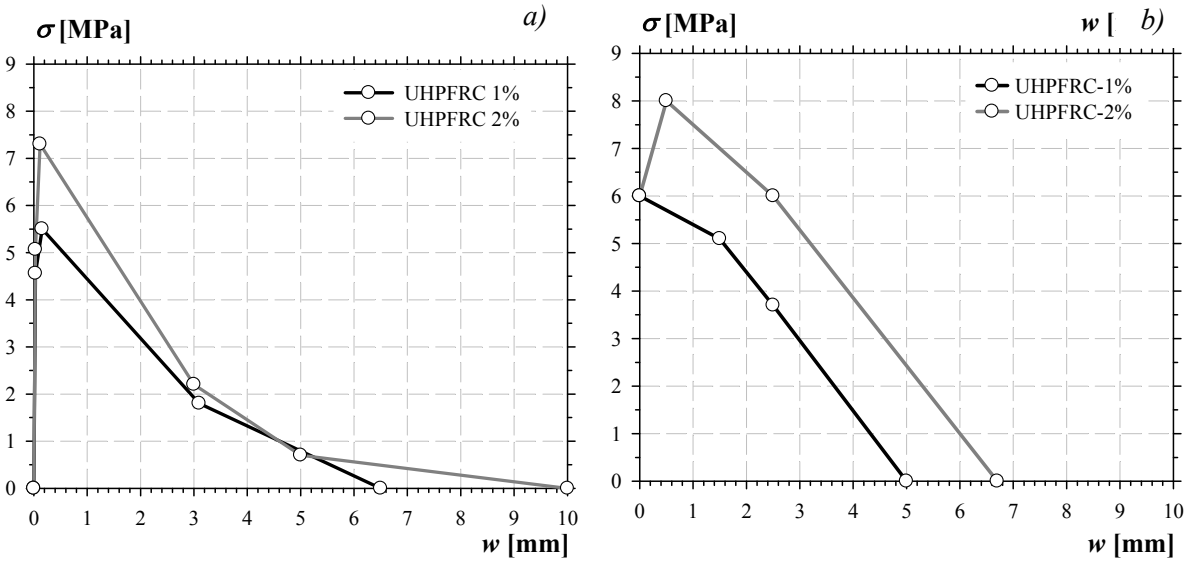

Figure 5-51: Post-cracking tensile relationship σ(w) of HPFRC defined by uniaxial tensile tests a) by inverse analysis on prisms b)

Hereafter, the influence on the failure criterion of the considered model, the adopted post cracking tensile relationship and the value of the parameter κ are investigated (Figure 5-52 to Figure 5-56).

The definition of the post-cracking tensile relationship is the most important parameter. The relationships determined on the basis of uniaxial tensile test give a better agreement compared to the relationship identified on the basis of bending tests on prisms. Moreover, the parameter κ influences strongly the slope of the criterion. The recommended value of 0.5 for κ proposed by Muttoni and

Fernandez showed often a poor agreement compared to the test results. Values of 1 and 2 gives better results depending on the adopted post-cracking relationship. The model I and II show similar results, therefore the compression depth may be reasonably disregarded.

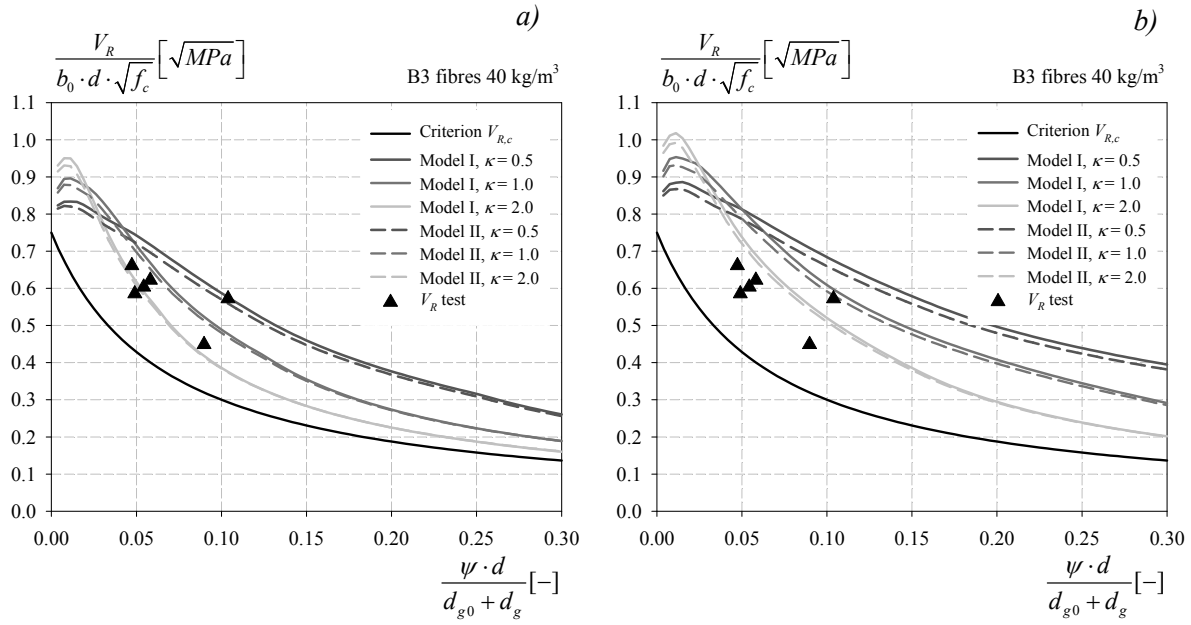

Figure 5-52: Failure criteria of HPFRC 40 kg/m^3 according to the different parameters, post-cracking tensile relationship defined by uniaxial tensile tests a) by inverse analysis on prisms b)

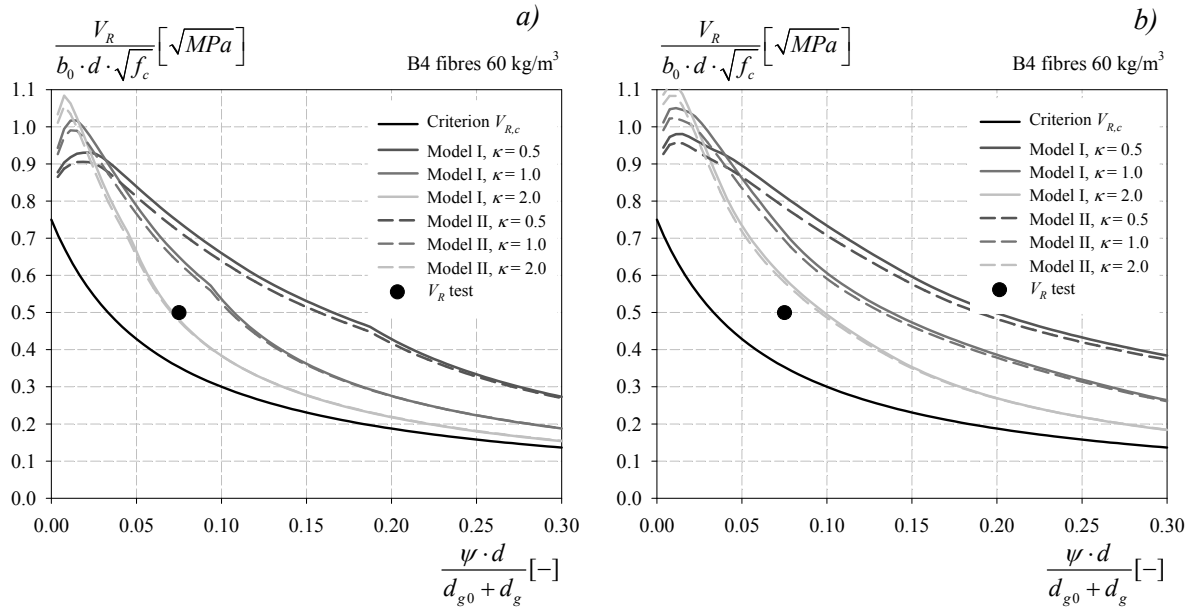

Figure 5-53: Failure criteria of HPFRC 60 kg/m^3 according to the different parameters, post-cracking tensile relationship defined by uniaxial tensile tests a) by inverse analysis on prisms b)

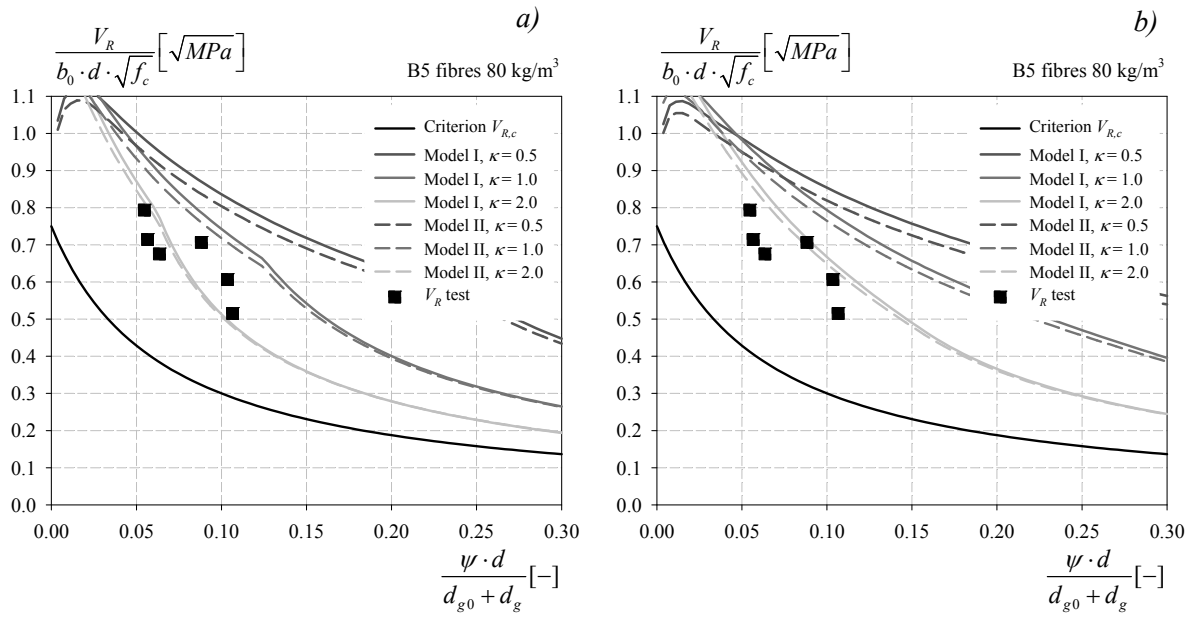

Figure 5-54: Failure criteria of HPFRC 80 kg/m^3 according to the different parameters, post-cracking tensile relationship defined by uniaxial tensile tests a) by inverse analysis on prisms b)

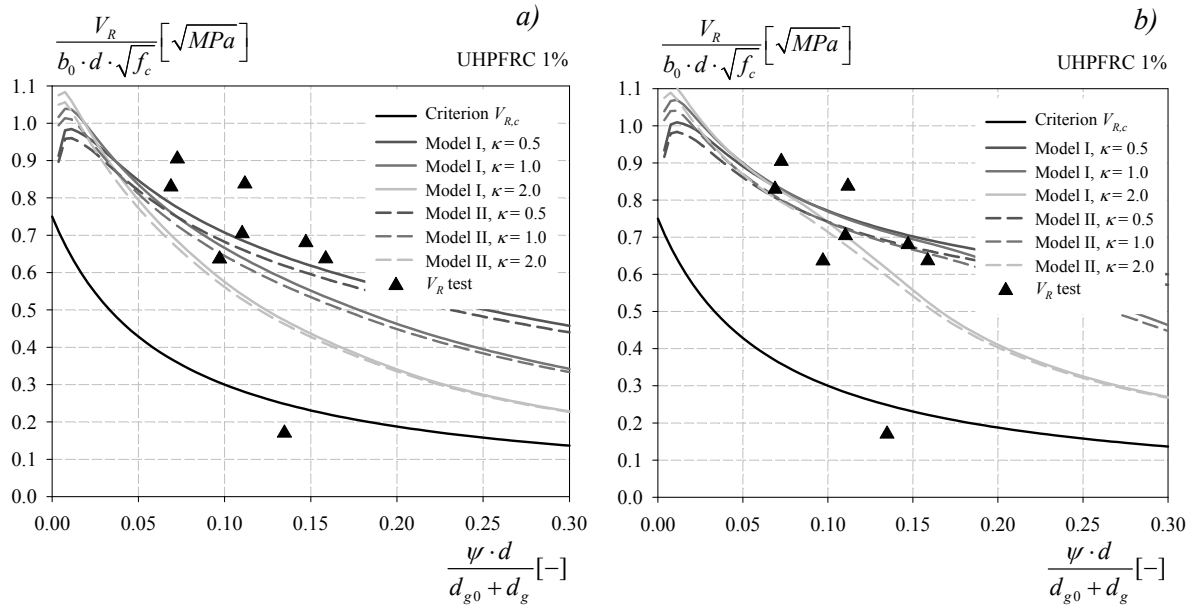

Figure 5-55: Failure criteria of UHPFRC 1% according to the different parameters, post-cracking tensile relationship defined by uniaxial tensile tests a) by inverse analysis on prisms b)

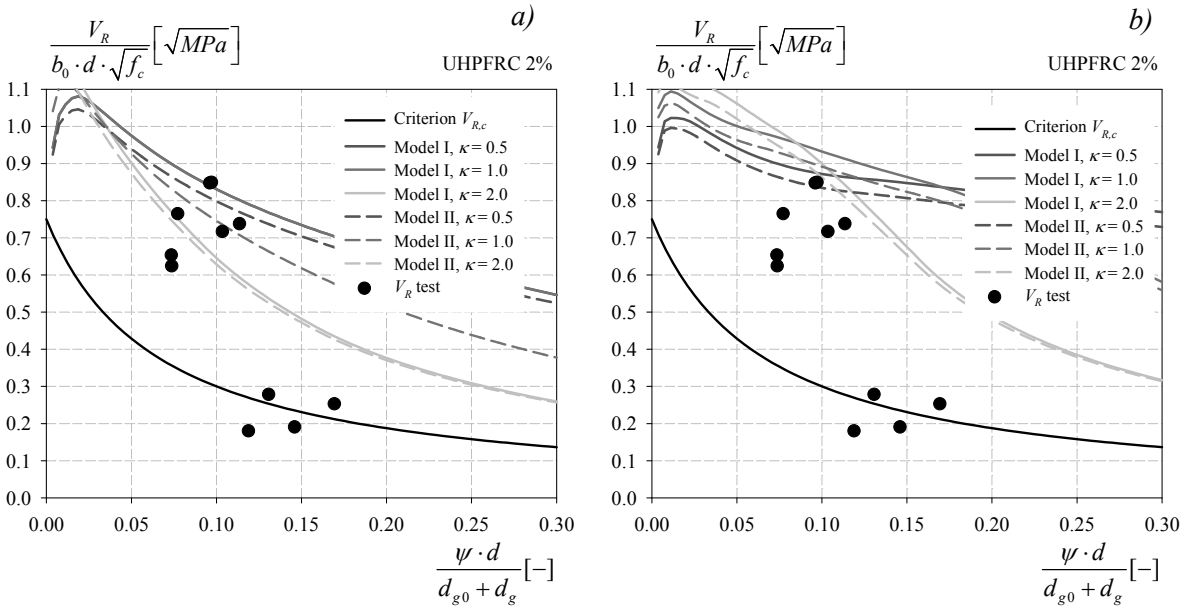

Figure 5-56: Failure criteria of UHPFRC 2% according to the different parameters, post-cracking tensile relationship defined by uniaxial tensile tests a) by inverse analysis on prisms b)

Simplified approach

In this point, we propose a simplified design model, V_R becomes V_{Rd}. Multi-linear relationship is not appropriate for a simplified design approach. A constant stress distribution allows a rapid and a simple computation. For HPFRC slabs, two simplified approaches were investigated taking into account the ultimate residual strength f_{Ftu} calculated with w_u=1.5 mm. In the first approach, the fibre contribution $V_{Rd,f}$ is assumed as a constant value (5-18). In the second approach, the fibre contribution $V_{Rd,f}$ depends on the slab's rotation ψ (5-20). For both approaches, the punching strength V_{Rd} and the concrete contribution $V_{Rd,c}$ are defined as the follows:

$$V_{Rd} = V_{Rd,c} + V_{Rd,f} \tag{5-17}$$

$$V_{Rd,c} = \frac{3/4}{1+15\cdot\left(\frac{\psi\cdot d}{d_g + d_{g0}}\right)}\cdot\frac{\sqrt{f_{ck}}}{\gamma_c} b_0 \cdot d \tag{5-18}$$

Where b_0 is the control perimeter, located at $d/2$ of the edges of the loading support.

Approach I is defined as follows:

$$V_{Rd,f} = \frac{1}{K}\cdot\frac{f_{Futk}}{\gamma_F}\cdot b_0 \cdot d \tag{5-19}$$

Approach II is defined as follows:

$$V_{Rd,f} = \frac{1}{K}\cdot\frac{f_{Ftuk}/\gamma_F}{1+\frac{\psi\cdot d}{w_u}}\cdot b_0 \cdot d \tag{5-20}$$

For both approaches the ultimate residual tensile strength is defined on the basis of the Model Code 2010 [FIB2010a], see point 2.1.6.1 in the following manner:

$$f_{Ftu} = 0.45 \cdot f_{R1} - \frac{w_u}{2.5} \cdot \left(0.45 \cdot f_{R1} - 0.5 \cdot f_{R3} + 0.2 f_{R1}\right) \tag{5-21}$$

The ultimate crack opening w_u in equations (5-20) and (5-21) was calibrated with the test results on HPFRC slabs, a value of 1.5 gives accurate results.

Table 5-10: Considered values of ultimate residual tensile strength f_{Ftu}

Concrete	B2	B3	B4	B5
f_{Ftum} [MPa]	1.02	3.42	3.80	5.01

In the following graphs, the different approaches are compared to the test results considering the mean values of the compressive strength f_{cm} and the ultimate residual tensile strength f_{Ftum}.

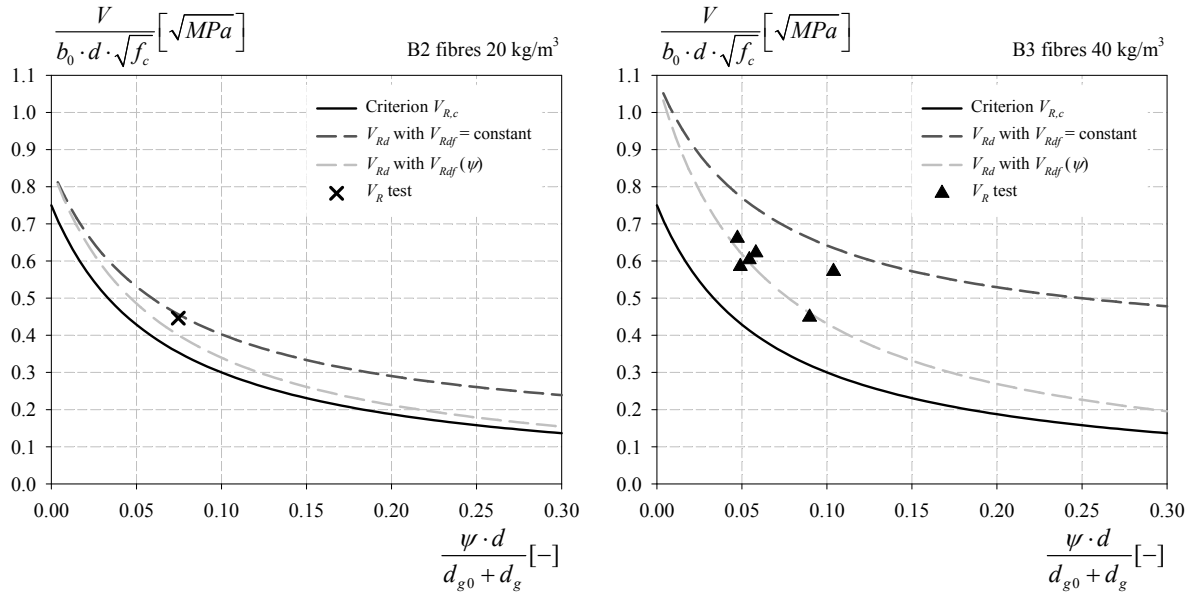

Figure 5-57: Simplified failure criterion of HPFRC slabs B2 and B3

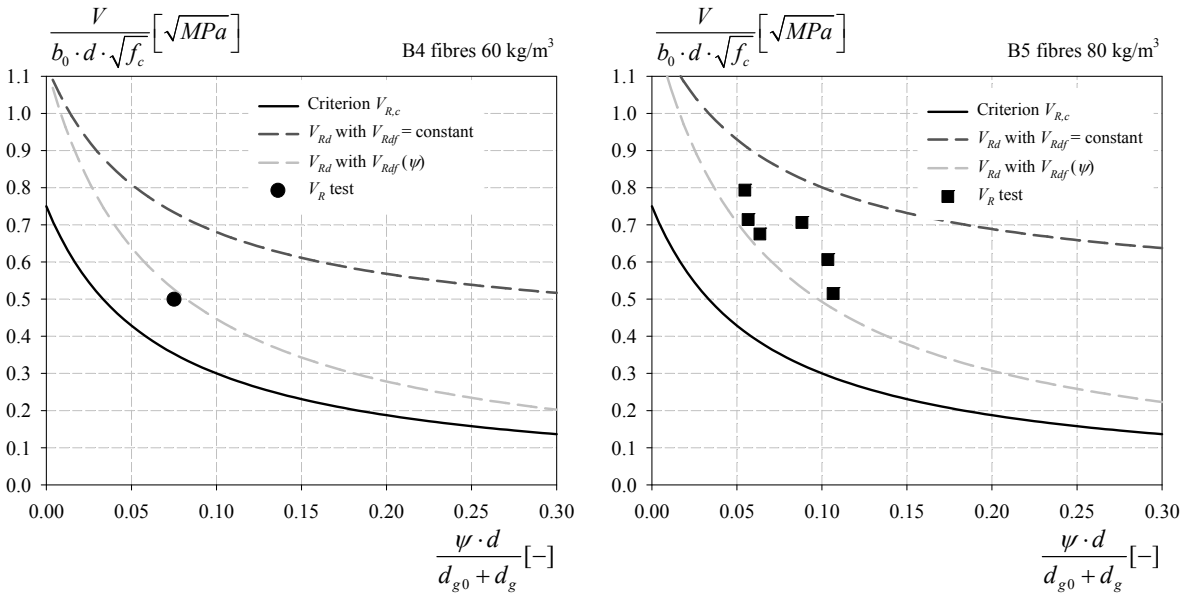

Figure 5-58: Simplified failure criterion of HPFRC slabs B4 and B5

The constant fibre contribution is not realistic. While in the second simplified form, the fact of taking into account the crack opening through the slab's rotation gives a good correlation with the test results. For a design purpose the second simplified form is recommended.

For UHPFRC, a similar approach was adopted. However, the post-cracking tensile strength is often not determined in the same way compared to HFRC. Therefore, the reference value corresponds to the post-cracking tensile strength of the UHPFRC in the pseudo-plastic plateau f_{Ut} determined on the uniaxial tensile test.

Table 5-11: Considered values of residual tensile strength f_{Ut}

UHPFRC	1%	2%
f_{Utm} [MPa]	5.7	7.5

Approach I is defined as follows

$$V_{Rd,f} = \frac{f_{Utk}}{\gamma_U} \cdot b_0 \cdot d \tag{5-22}$$

Approach II is defined as follows

$$V_{Rd,f} = \frac{f_{Utk}/\gamma_U}{1 + \frac{\psi \cdot d}{w_u}} \cdot b_0 \cdot d \tag{5-23}$$

In the following graphs the ultimate crack opening w_u is assumed to be equal to $l_f/4$ = 5 mm.

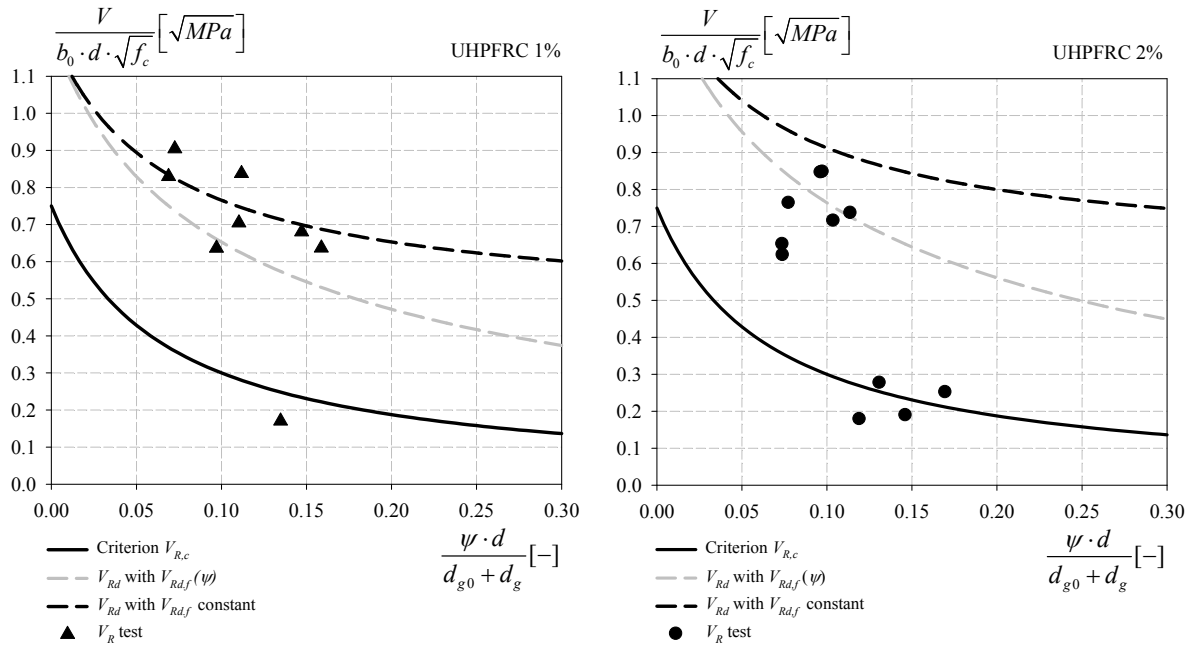

Figure 5-59: Simplified failure criterion of UHPFRC slabs 1% and 2%

The second simplified form, which takes into account the variation of the critical shear crack opening, gives a better correlation with the test results compared to the constant form. For a design purpose the second simplified form is recommended.

5.5.2 Flexural behaviour

For determining the punching shear strength, the load – rotation curve must be calculated. The relationship $V(\psi)$ can be computed by finite difference or finite element methods for a complex slab and/or a loading arrangement [MUT2008a]. The intersection between the computed curves load – rotation and the failure criterion corresponds to the ultimate punching shear strength. If the curve does not cut the criterion, the flexural capacity is critical.

Elastic behaviour

The elastic theory of plates was first developed by Cauchy and Poisson in 19th century. In 1850 Kirchhoff published an important thesis on the theory of thin plates [TIM1959]. In this thesis, Kirchhoff stated several assumptions which are now widely accepted in the thin plate theory and are known as ‘‘Kirchhoff’s hypotheses’’. The principal assumptions are the following.

- The material of the plate is elastic, homogeneous, and isotropic.
- The plate is initially flat.
- The deflection of the mid-plane is small compared to the thickness of the plate. The slope of the deflected surface is therefore small and the square of the slope is a negligible quantity in comparison with unity.
- The straight lines, initially normal to the middle plane before bending, remain straight and normal to the middle surface during the deformation, and the length of such elements is not altered. This means that the vertical shear strains *xz* and *yz* are negligible.
- The stress normal to the middle plane *z*, is small compared to the other stress components and may be neglected.

- The displacements of the plate are small.

For circular slab with a constant thickness *h* and axisymmetric boundary conditions with a loading arrangement, all points at the same radius *r* from the centre have the same displacement *δ*. Therefore the slope at all points on the same perimeter is equal. These boundary conditions and loading arrangement may be assimilated to the ones adopted for testing slabs.

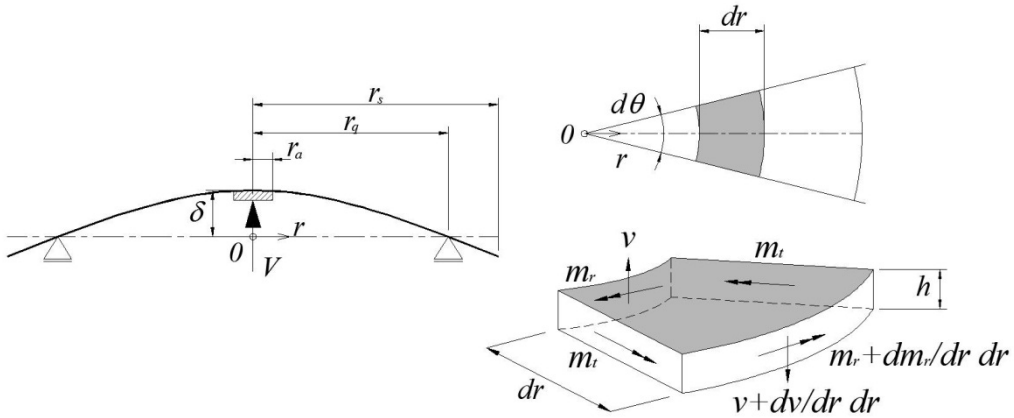

Figure 5-60: Circular slab with axisymmetric boundary conditions and equilibrium of a slab element

For small displacements, the radial curvature can be expressed as follows:

$$\kappa_r = -\frac{d^2\delta}{dr^2} = \frac{d\psi}{dr} \tag{5-24}$$

The second tangential curvature can be calculated as the following:

$$\kappa_t = -\frac{1}{r}\cdot\frac{d\delta}{dr} = \frac{\psi}{r} \tag{5-25}$$

The radial and tangential strains and the corresponding stresses on the depth *z* can be expressed as:

$$\varepsilon_r = \chi_r \cdot z \qquad \sigma_r = \frac{E}{1-\nu^2}\cdot\left(\varepsilon_r + \nu\cdot\varepsilon_t\right) \tag{5-26}$$

$$\varepsilon_t = \chi_t \cdot z \qquad \sigma_t = \frac{E}{1-\nu^2}\cdot\left(\varepsilon_t + \nu\cdot\varepsilon_r\right) \tag{5-27}$$

The radial and the tangential moments can be computed as follows:

$$m_r = \frac{E}{1-\nu^2}\cdot\int_{-h/2}^{+h/2}\left(\kappa_r\cdot z + \nu\cdot\kappa_t\cdot z\right)dz = D\cdot\left(\kappa_r + \nu\cdot\kappa_t\right) \tag{5-28}$$

$$m_t = \frac{E}{1-\nu^2}\cdot\int_{-h/2}^{+h/2}\left(\kappa_t\cdot z + \nu\cdot\kappa_r\cdot z\right)dz = D\cdot\left(\kappa_t + \nu\cdot\kappa_r\right) \tag{5-29}$$

The flexural stiffness *D* in the linear elastic regime is expressed as follows:

$$D = \frac{E \cdot h^3}{12 \cdot (1 - \nu^2)} \tag{5-30}$$

Where E is the Young's modulus and ν is the Poisson's ratio.

The equilibrium of the finite element of the slab gives the following equation:

$$(m_r + dm_r) \cdot (r + dr) \cdot d\varphi - m_r \cdot r \cdot d\varphi - m_t \cdot dr \cdot d\varphi + \nu \cdot r \cdot dr \cdot d\varphi = 0 \tag{5-31}$$

This expression may be simplified by disregarding the infinitesimally terms of a higher order.

$$m_r + \frac{dm_r}{dr} \cdot r - m_t + \nu \cdot r = 0 \tag{5-32}$$

Substituting the moment values for the linear elastic regime given by Equations (5-28) and (5-29), the equilibrium equation may be rewritten as:

$$\frac{d\delta^3}{dr^3} + \frac{1}{r} \cdot \frac{d\delta^2}{dr^2} - \frac{1}{r^2} \cdot \frac{d\delta}{dr} = -\frac{\nu}{D} \tag{5-33}$$

For axisymmetric circular slab, the shear force v acting at the radius r may be easily computed by dividing the load q by $2\pi r$. Therefore the Equation (5-33) may be rewritten as follows:

$$\frac{1}{r} \cdot \frac{d}{dr} \left\{ r \cdot \frac{1}{dr} \cdot \left[\frac{1}{r} \cdot \frac{d}{dr} \cdot \left(r \cdot \frac{d\delta}{dr} \right) \right] \right\} = \frac{q}{D} \tag{5-34}$$

For simple boundary conditions, the solution of the differential Equation (5-34) may be computed in a closed form. The testing slabs in HPFRC and UHPFRC may be assimilated to two cases: the case I where the loading zone is infinitely rigid compared to the slab and the case II where the load is uniformly applied. The shape of the deflection, the slope, the curvatures and the moments are represented in Figure 5-62. The boundary conditions for case I are:

$$\delta(r_a) = 0 \tag{5-35}$$

$$\delta'(r_a) = 0 \tag{5-36}$$

$$m_r(r_q) = 0 \tag{5-37}$$

And the boundary conditions for case II are :

$$\delta(r_0) = 0 \tag{5-38}$$

$$\delta'(r_0) = 0 \tag{5-39}$$

$$m_r(r_q) = 0 \tag{5-40}$$

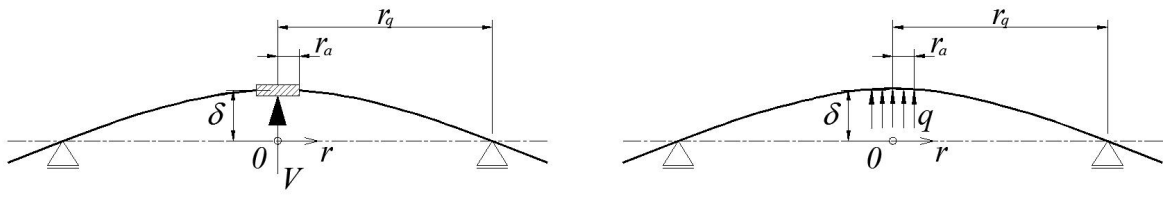

Figure 5-61: Loading arrangement of case I and II

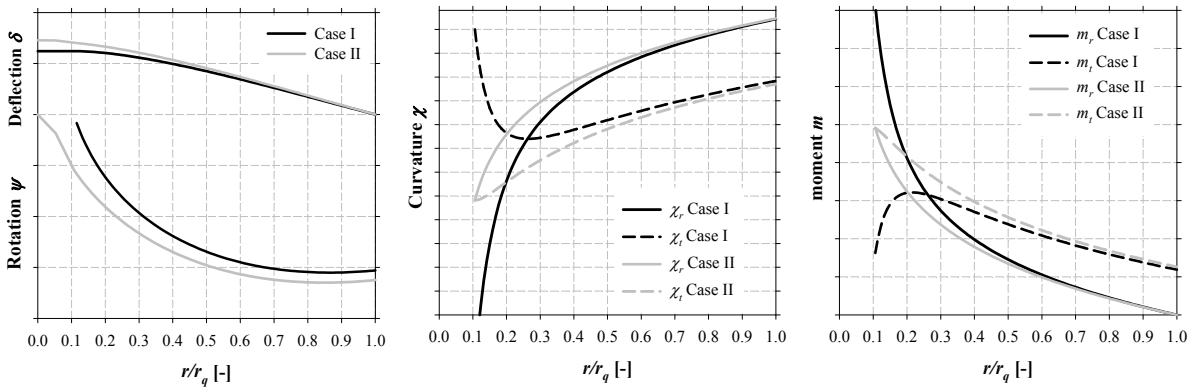

Figure 5-62: Shape along the radius of the deflection, slope, curvatures and moments according to the different loading arrangements.

Non-linear behaviour

For an axisymmetric slab with a point load at the centre, the load vs rotation behaviour may be obtained analytically after some assumptions according to the model developed by Muttoni for Reinforced Concrete slab [MUT2008b]. The radial and tangential curvatures are concentrated close to the loading point. Outside the punching cone the radial curvature decreases rapidly. Therefore, it can be assumed that the slab portion outside the punching cone follows a constant rotation.

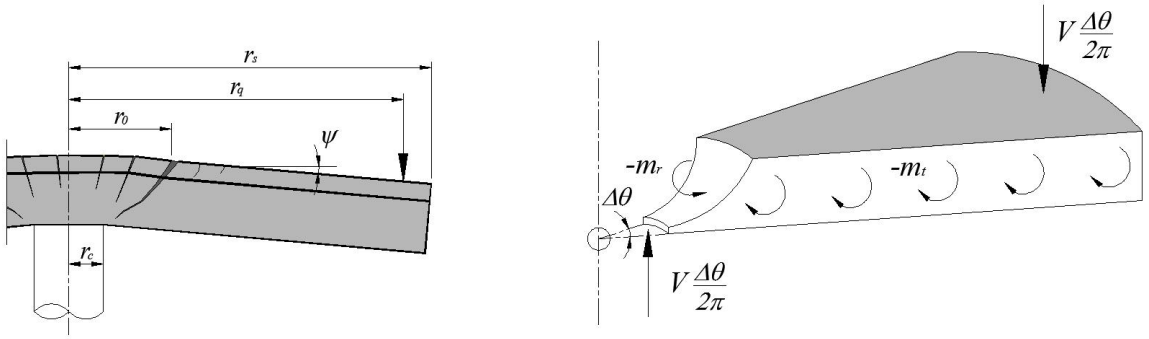

Figure 5-63: Parameters of the model and internal forces acting on portion slab [MUT2008a]

$$\chi_t = -\frac{\psi}{r} \qquad \text{for } r > r_0 \tag{5-41}$$

$$\chi_t = \chi_r = -\frac{\psi}{r} \qquad \text{for } r \le r_0 \tag{5-42}$$

With the curvature, the moment may be calculated according to the moment – curvature relationship. For reinforced concrete a quadrilinear moment – curvature relationship is proposed. This relation is defined by the stiffnesses EI_0 before and EI_1 after cracking, the cracking moment m_{cr}, the moment of flexural capacity m_R and the tension stiffening χ_{TS}.

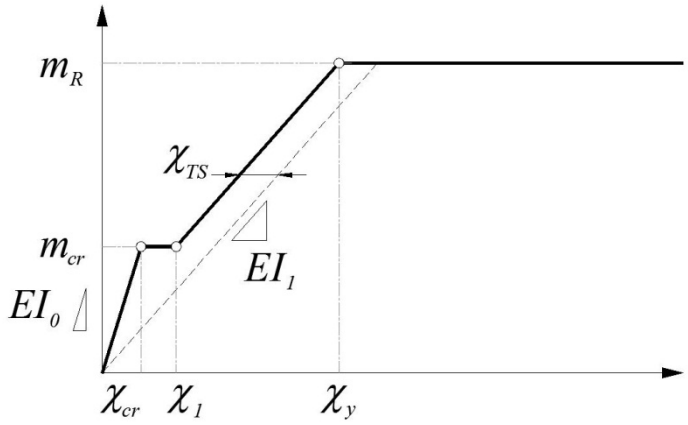

Figure 5-64: Quadrilinear moment – curvature relationship m(χ) with the different parameters [MUT2008a]

The different terms are defined as follows:

$$EI_0 = \frac{E_c \cdot h^3}{12} \tag{5-43}$$

$$m_{cr} = \frac{f_{ct} \cdot h^2}{6} \tag{5-44}$$

$$-\chi_{cr} = \frac{2 \cdot f_{ct}}{h \cdot E_c} \tag{5-45}$$

Assuming linear-elastic behaviour for the steel and the concrete after cracking, the stiffness after cracking may be calculated as follows:

$$EI_1 = \rho \cdot \beta \cdot E_s \cdot d^3 \cdot \left(1 - \frac{x}{d}\right) \cdot \left(1 - \frac{x}{3 \cdot d}\right) \tag{5-46}$$

Where x is the depth of the compression zone. On the basis of the stress equilibrium in the cross-section, x is defined as follows:

$$x = \rho \cdot \beta \cdot \frac{E_s}{E_c} \cdot d \cdot \left(\sqrt{1 + \frac{2 \cdot E_c}{\rho \cdot \beta \cdot E_s}} - 1\right) \tag{5-47}$$

Where ρ is the reinforcement ratio and β, which is equal to 0.6, is a factor taking into account the orthogonal arrangement of the reinforcement. The tension stiffening is defined as follows:

$$\chi_{TS} = \frac{f_{ct}}{\rho \cdot \beta \cdot E_s} \cdot \frac{1}{6 \cdot h} \tag{5-48}$$

Assuming a perfectly plastic behaviour of steel after yielding and a rectangular stress distribution for the concrete in the compression zone, the flexural moment is defined as follows:

$$m_R = \rho \cdot f_y \cdot d^2 \cdot \left(1 - \frac{\rho \cdot f_y}{2 \cdot f_c}\right) \tag{5-49}$$

The curvatures at the beginning and at the end of the elastic cracked state are defined in the following way:

$$-\chi_1 = \frac{m_{cr}}{EI_1} - \chi_{TS} \tag{5-50}$$

$$-\chi_y = \frac{m_R}{EI_1} - \chi_{TS} \tag{5-51}$$

The three radii delimiting the different regimes are defined as follows:

$$r_{cr} = -\frac{\psi}{\chi_{cr}} = \frac{\psi \cdot EI_0}{m_{cr}} \le r_s \tag{5-52}$$

$$r_1 = -\frac{\psi}{\chi_1} = \frac{\psi}{\frac{m_{cr}}{EI_1} - \chi_{TS}} \le r_s \tag{5-53}$$

$$r_y = -\frac{\psi}{\chi_y} = \frac{\psi}{\frac{m_R}{EI_1} - \chi_{TS}} \le r_s \tag{5-54}$$

Finally, the equilibrium equation of the slab portion (Figure 5-63) is given by Equation (5-55) and may be rewritten after integration as shown in Equation (5-56):

$$V \cdot \frac{\Delta\varphi}{2\pi} \cdot \left(r_q - r_c\right) = -m_r \cdot \Delta\varphi \cdot r_0 - \Delta\varphi \cdot \int_{r_0}^{r_s} m_\varphi \cdot dr \tag{5-55}$$

$$\begin{aligned} V = \frac{2 \cdot \pi}{r_q - r_c} \Bigg\{ & -m_r \cdot r_0 + m_R \cdot \left\langle r_y - r_0 \right\rangle + EI_1 \cdot \psi \cdot \left\langle \ln\left(\frac{r_1}{r_y}\right) \right\rangle + EI_1 \cdot \chi_{TS} \cdot \left\langle r_1 - r_y \right\rangle \\ & + m_{cr} \cdot \left\langle r_{cr} - r_1 \right\rangle + EI_0 \cdot \psi \cdot \left\langle \ln\left(\frac{r_s}{r_{cr}}\right) \right\rangle \Bigg\} \end{aligned} \tag{5-56}$$

where the operator $\langle x \rangle$ is x for $x \ge 0$ and 0 for $x < 0$

The flexural capacity V_{flex} is reached when the radius r_y is equal to the radius of the slab r_s.

$$V_{flex} = 2 \cdot \pi \cdot m_R \cdot \frac{r_s}{r_q - r_c} \tag{5-57}$$

For a design purpose, the following simplified form is proposed [MUT2008b]:

$$V = V_{flex} \cdot \frac{\psi}{1.5 \cdot \left(\frac{r_s \cdot f_y}{d \cdot E_s} \right)} \tag{5-58}$$

5.5.3 Punching shear model

Adopting this model for the slabs in High Performance Concrete without fibres, the computed curves are given in Figure 5-65. For the reinforcement, the measured steel yield limit $f_{s0.2}$ was taken into account for f_y (Table 5-6).

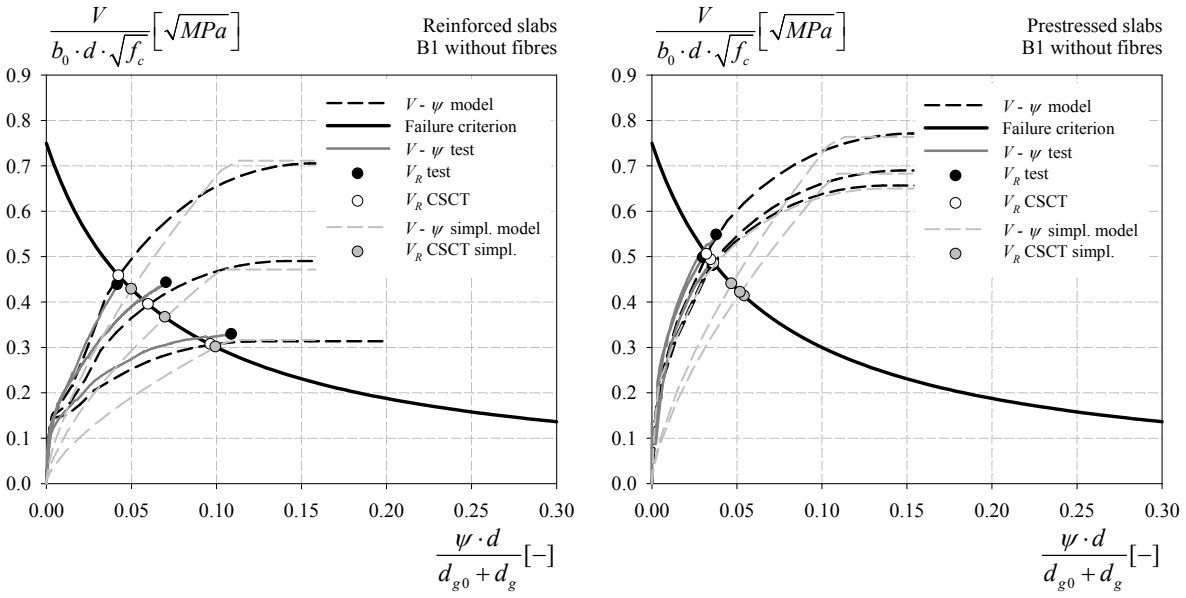

Figure 5-65: Comparison between the test results and the model for the reinforced and prestressed slabs in High Performance Concrete without B1 fibres

Table 5-12: Test data and punching shear strength predictions for the slabs made out of HPC without fibres

Specimens	ρ_s [%]	$\sigma_{cp,0}$ [MPa]	V_R [kN]	V_{CSCT} [kN]	V_R/V_{CSCT} [-]	$V_{CSCT,simpl.}$ [kN]	V_R/V_{CSCT} [-]
B1-01	0.84	0.00	262	234	1.12	217	1.21
B1-02	0.84	2.40	294	288	1.02	245	1.20
B1-03	0.76	3.60	330	340	0.97	291	1.13
B1-04	0.76	4.80	376	349	1.08	304	1.24
B1-05	0.54	0.00	201	188	1.07	184	1.09
B1-06	1.24	0.00	252	263	0.96	246	1.02
				Mean	**1.04**		**1.15**
				CoV	**0.06**		**0.07**

The model presents a good correlation with the test results. The test results and the computed curves are very close. The mean value and the coefficient of variation are inferior to 5% and 10% respectively.

We have adapted the quadrilinear moment – curvature $m(\chi)$ approach in order to take into account the fibres effect. As seen in Chapter 2, the fibres increase the tension stiffening, the stiffness after cracking EI_I and the flexural moment m_R.

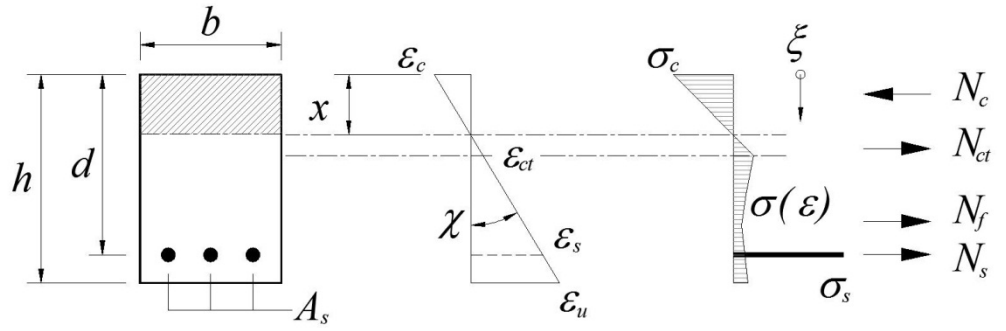

Figure 5-66: Cross sectional analysis, smeared crack approach

With the hypothesis of Bernoulli-Navier and the equilibrium equations (5-59) (5-60), the moment-curvature $m(\chi)$ relationship may be determined with a spreadsheet.

$$\int_{a_c} \sigma_c(\varepsilon)\cdot d_{a_c} + \int_{a_s} \sigma_s(\varepsilon)\cdot d_{a_s} + \int_{a_p} \sigma_p(\varepsilon)\cdot d_{a_p} + \int_{a_{ctf}} \sigma_{ctf}(\varepsilon)\cdot d_{a_{ctf}} = n \tag{5-59}$$

$$\sum \int_{a_j} \sigma_j(\varepsilon)\cdot \zeta_j \cdot d_{a_j} = m \tag{5-60}$$

In the following graphs (Figure 5-67), a bilinear relationship with a strain hardening branch for steel reinforcement and a multi-linear tensile relationship for FRC, defined by uniaxial tensile tests, were adopted.

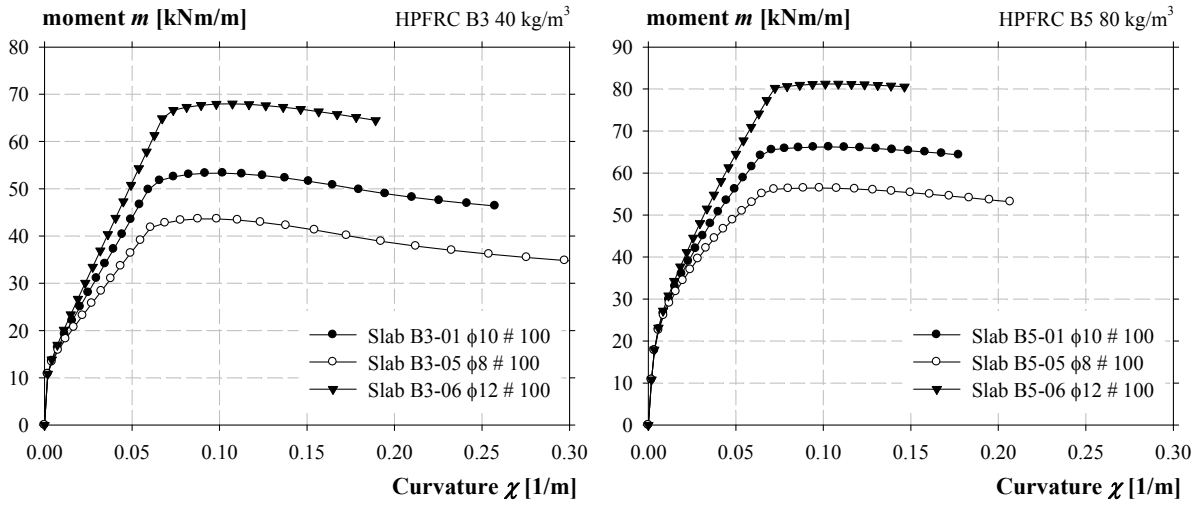

Figure 5-67: Calculated curves moment – curvature according to the different reinforcement ratio and fibres content of reinforced HPFRC slabs.

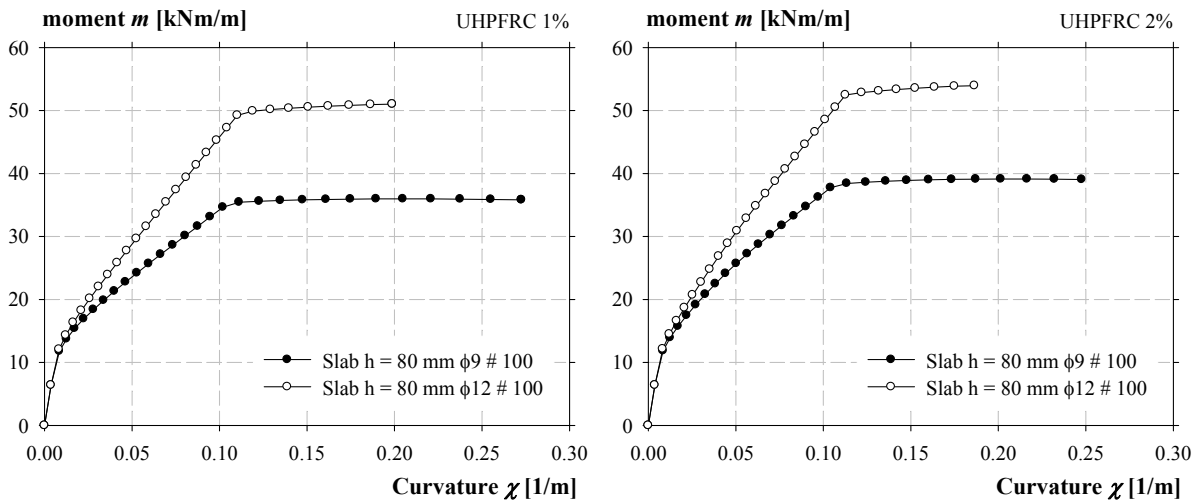

Figure 5-68: Calculated curves moment – curvature according to the different reinforcement ratio and fibres content of reinforced UHPFRC slabs 80 mm thick.

When the cracking moment m_{cr} is reached, the stiffness decreases progressively compared to the reinforced concrete members without fibres. After this state the behaviour is linear up to the steel reinforcement yield limit. Close to this point the flexural capacity moment m_R is reached. After reaching the maximum, the moment decreases progressively according to the FRC post-cracking response.

On the same basis of reinforced concrete, a trilinear or a quadrilinear moment – curvature relationship is proposed for SFRC with reinforcement. This relation is defined by the stiffnesses *EI0* before and *EI1* after cracking, the cracking moment m_{cr}, the moment of flexural capacity m_R and the tension stiffening χ_{TS}. The trilinear or quadrilinear relationship depends of the post-cracking response.

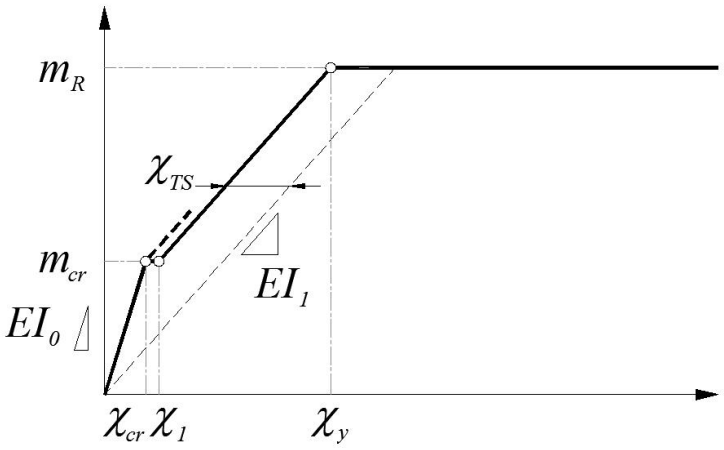

Figure 5-69: Trilinear or quadrilinear moment – curvature relationship m(χ) with the different parameters for SFRC with reinforcement

The linear elastic behaviour with a centred axial force (prestressing) is defined as follows:

$$EI_0 = \frac{E_c \cdot h^3}{12} \tag{5-61}$$

$$m_{cr} = \frac{(f_{ct} + \sigma_{cp}) \cdot h^2}{6} \tag{5-62}$$

with $$\sigma_{cp} = \frac{A_p \cdot f_p}{b \cdot h} \tag{5-63}$$

$$-\chi_{cr} = \frac{m_{cr}}{EI_0} \tag{5-64}$$

Considering the strain and stress distribution in Figure 5-70, the curvature after cracking χ_1 may be calculated with the equations of equilibrium. If no solution is possible then $\chi_1 = \chi_{cr}$.

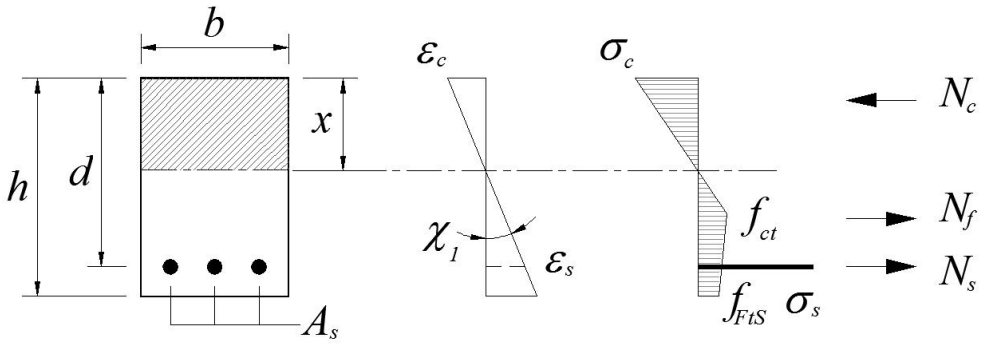

Figure 5-70: Cross section analysis considered for the cracking curvature χ_1

Considering that the flexural capacity m_R is reached when the reinforcement strain ε_s is equal to the yielding strain ε_y corrected by the factor β (β=0.6) , the curvature χ_y and the flexural capacity m_R may be calculated with the equations of equilibrium assuming the stress distribution in Figure 5-71. The flexural capacity m_R can be computed as follows:

$$m_R = \rho \cdot f_y \cdot d^2 + \kappa_F \cdot f_{Ftu} \cdot (h - x) \cdot \left(\frac{(h - x)}{2} + x \right) - \frac{x^2}{2} \cdot E_c \cdot \varepsilon_c \tag{5-65}$$

With the compression depth defined as follows:

$$x = \frac{\rho \cdot d \cdot f_y + \kappa_F \cdot f_{Ftu} \cdot h}{E_c \cdot \varepsilon_c + \kappa_F \cdot f_{Ftu}} \tag{5-66}$$

The factor $k_F < 1$ takes into account the dispersion of the post-cracking response at the structural level.

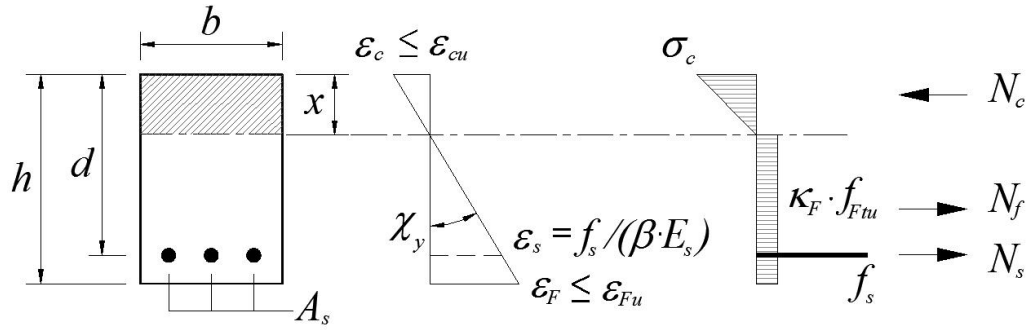

Figure 5-71: Cross section analysis considered for the flexural capacity m_R

For a design purpose the same simplified equation (5-58) for reinforced concrete is adopted considering the flexural capacity m_R with fibres.

In the following graphs, a comparison between the test results of HPFRC and UHPFRC slabs and the computed values with the complete and simplified model are presented.

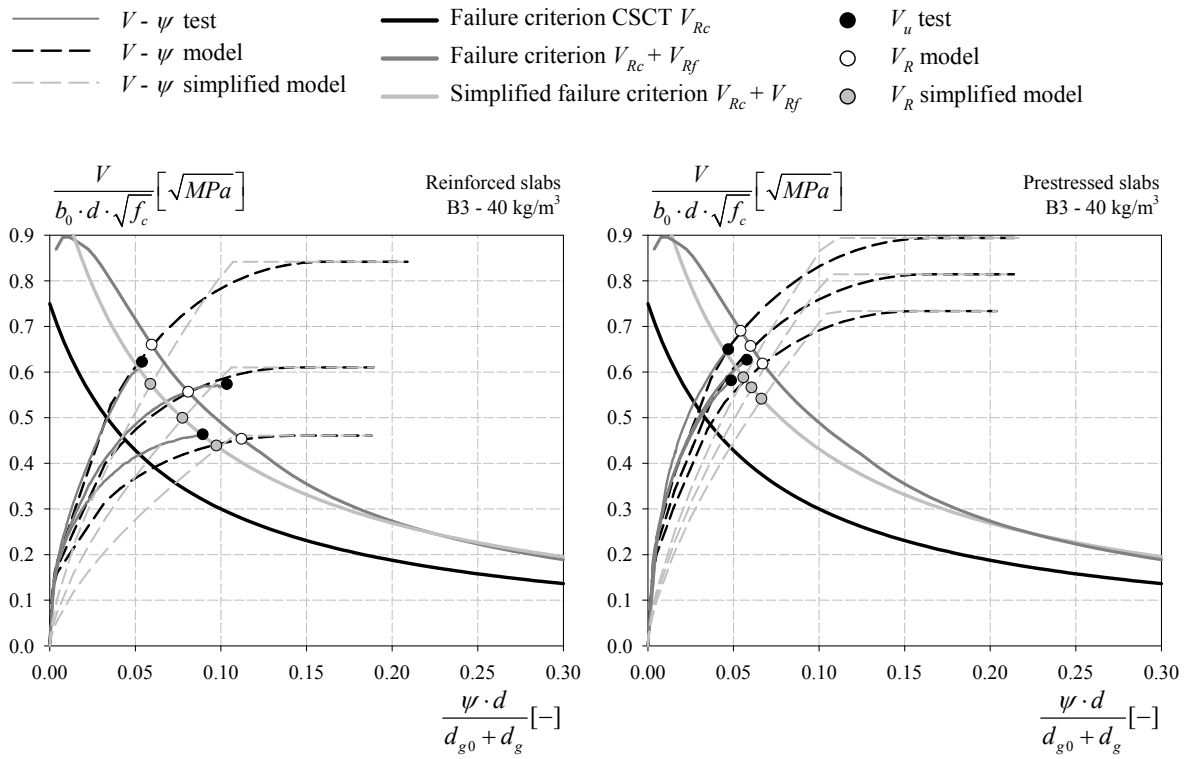

Figure 5-72: Comparison between the test results and the model for the reinforced and prestressed slabs in HPFRC with a fibres content of 40 kg/m³

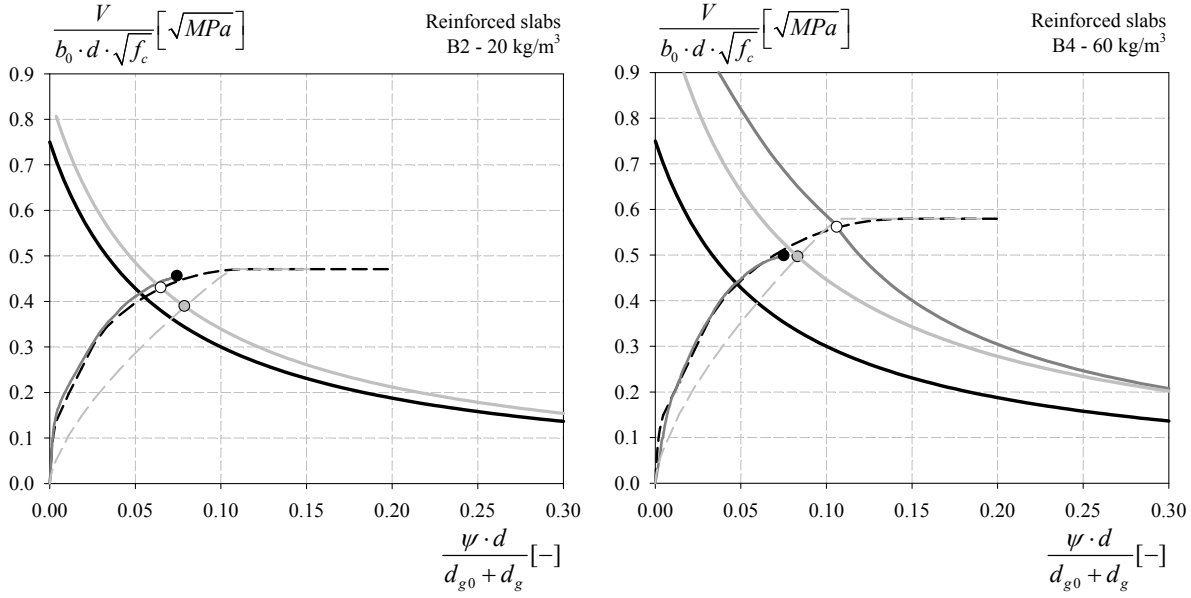

Figure 5-73: Comparison between the test results and the model for the reinforced in HPFRC with a fibres content of 20 kg/m³ and 60 kg/m³.

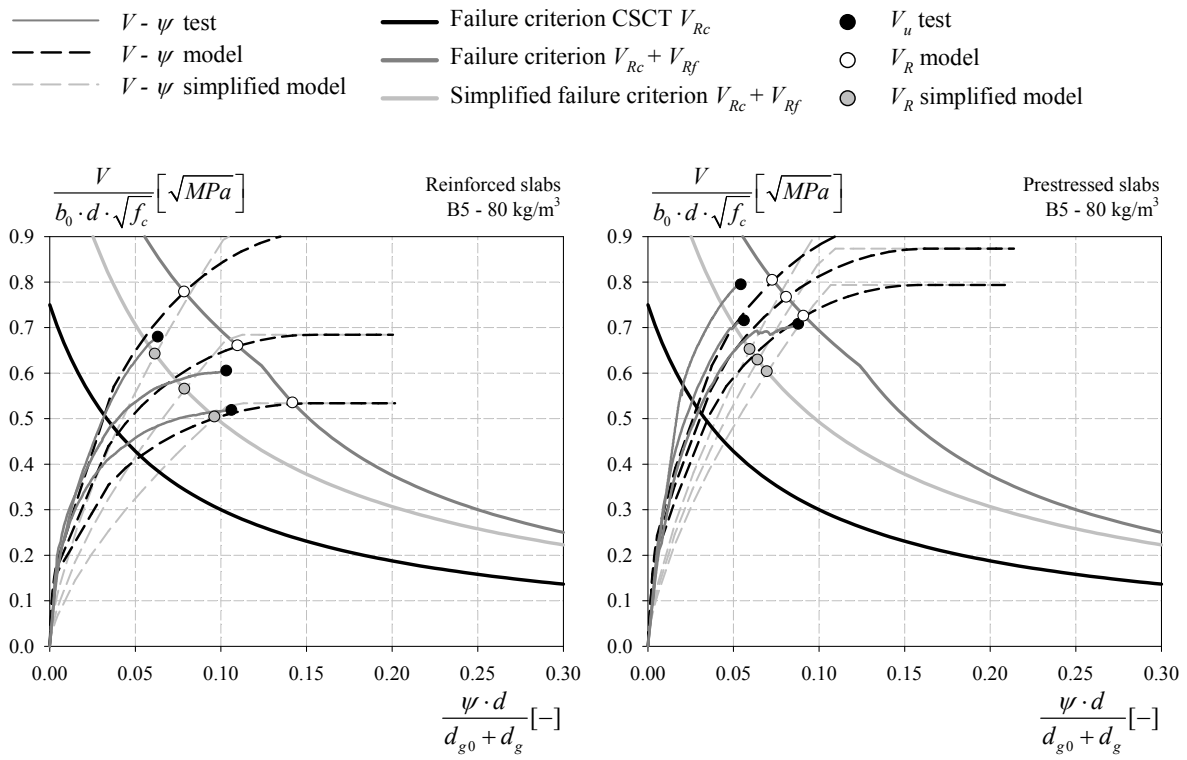

Figure 5-74: Comparison between the test results and the model for the reinforced and prestressed slabs in HPFRC with a fibres content of 80 kg/m³

Table 5-13: Summary of tests and computed values for HPFRC slabs

Specimen	V_f [kg/m³]	ρ_s [%]	$\sigma_{cp,0}$ [MPa]	V_R [kN]	V_{CSCT} [kN]	V_R/V_{CSCT} [-]	$V_{simpl.}$ [kN]	V_R/V_{simpl} [-]
B2-01	20	0.76	0.00	318	297	1.07	268	1.18
B3-01	40	0.84	0.00	343	330	1.04	296	1.16
B3-02	40	0.76	2.40	437	427	1.02	373	1.17
B3-03	40	0.76	3.60	405	453	0.89	390	1.04
B3-04	40	0.76	4.80	453	476	0.95	406	1.12
B3-05	40	0.54	0.00	286	277	1.03	268	1.07
B3-06	40	1.24	0.00	361	379	0.95	329	1.10
B4-01	60	0.76	0.00	344	387	0.89	343	1.00
B5-01	80	0.84	0.00	369	392	0.94	335	1.10
B5-02	80	0.76	2.40	501	501	1.00	417	1.20
B5-03	80	0.76	3.60	511	529	0.96	434	1.18
B5-04	80	0.76	4.80	567	555	1.02	450	1.26
B5-05	80	0.54	0.00	327	327	1.00	308	1.06
B5-06	80	1.24	0.00	402	447	0.90	369	1.09
					Mean	**0.98**		**1.12**
					CoV	**0.06**		**0.06**

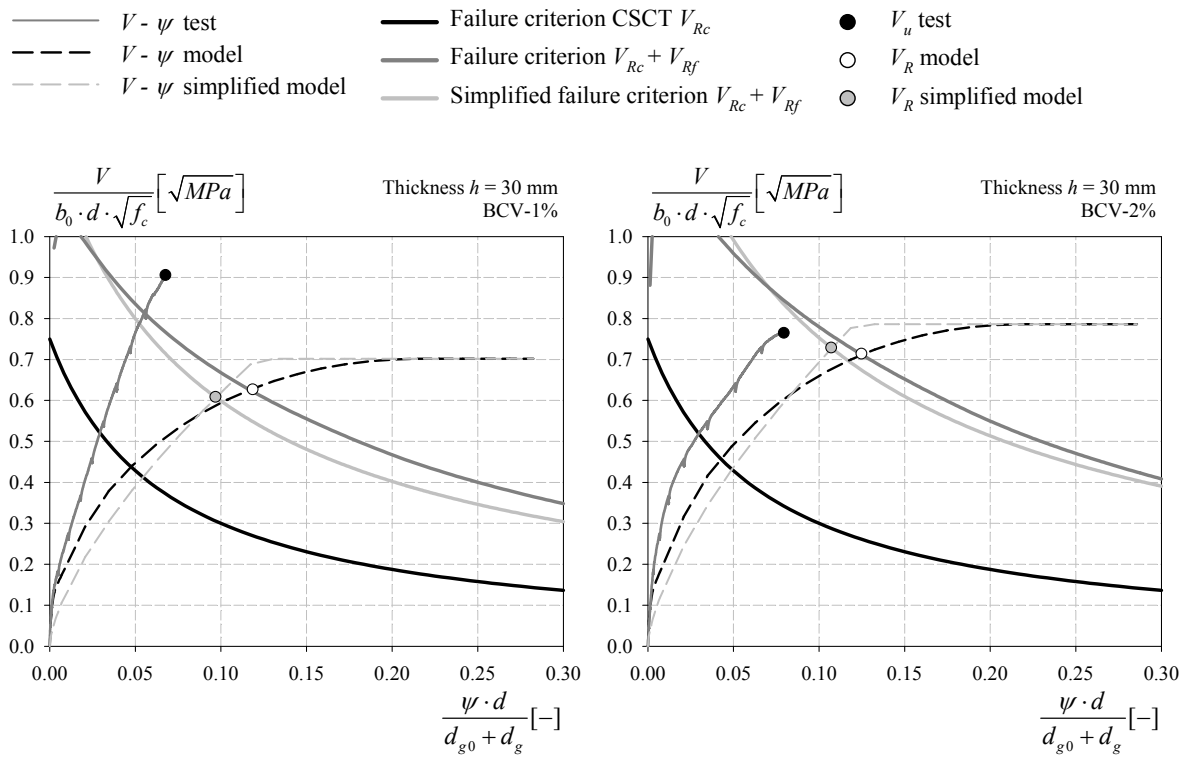

Figure 5-75: Comparison between the test results and the model for the reinforced slabs of 30 mm thick in UHPFRC with a fibre volume ratio of 1% and 2%

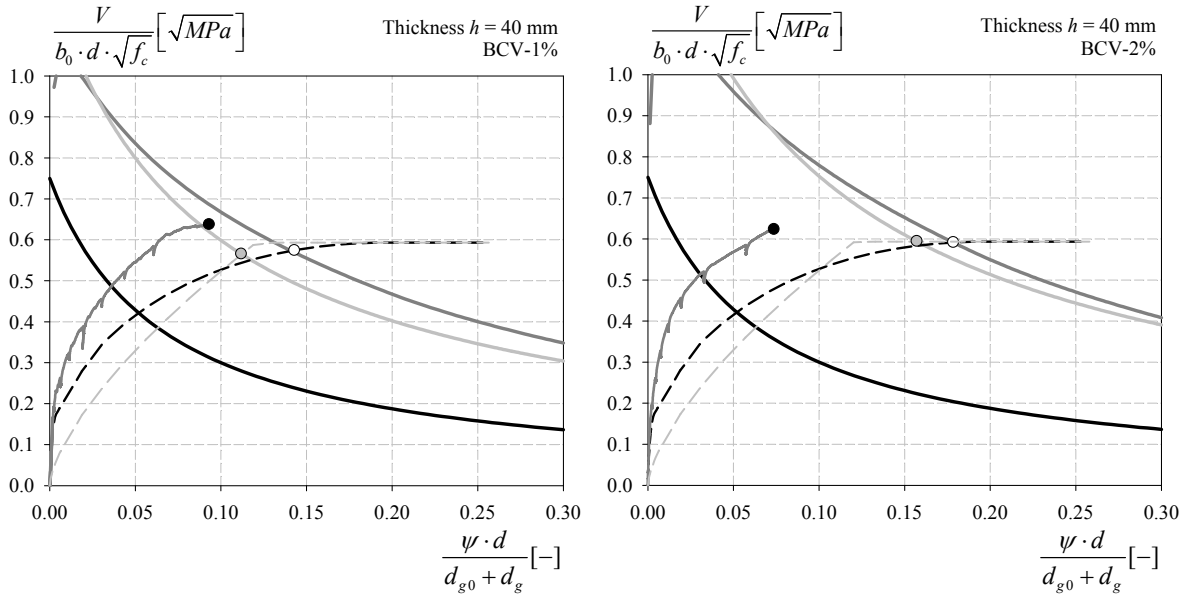

Figure 5-76: Comparison between the test results and the model for the reinforced slabs of 40 mm thick in UHPFRC with a fibre volume ratio of 1% and 2%

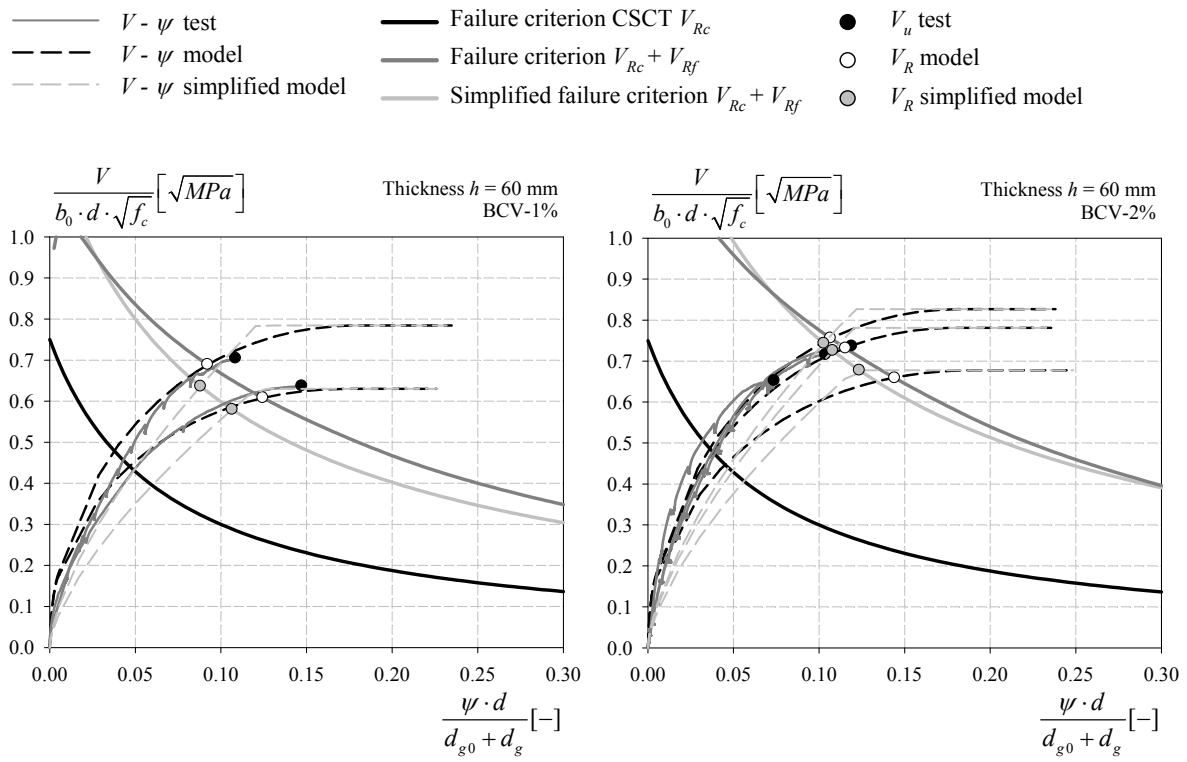

Figure 5-77: Comparison between the test results and the model for the reinforced slabs of 60 mm thick in UHPFRC with a fibre volume ratio of 1% and 2%

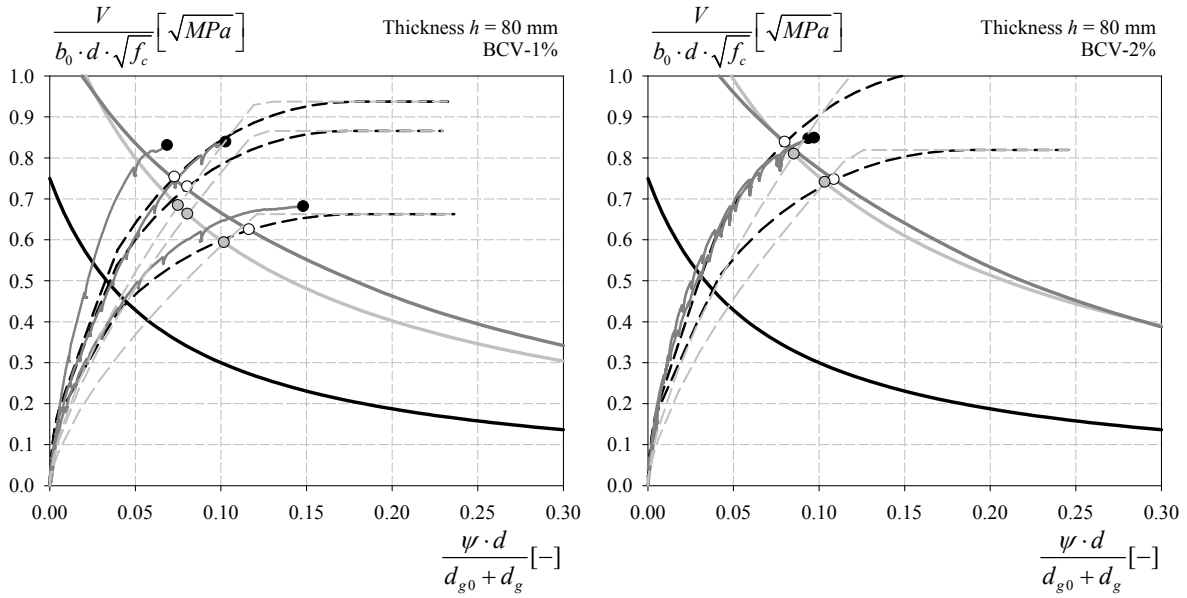

Figure 5-78: Comparison between the test results and the model for the reinforced slabs of 80 mm thick in UHPFRC with a fibre volume ratio of 1% and 2%

Table 5-14: Summary of tests and computed values for UHPFRC slabs

Specimen	V_f [%]	h [mm]	ρ_s [%]	V_R [kN]	V_{CSCT} [kN]	V_R/V_{CSCT} [-]	$V_{simpl.}$ [kN]	V_R/V_{simpl} [-]
BCV-1%A_30_2.67	1	30	2.67	49.6	34.3	1.45	33.3	1.49
BCV-1%A_40_1.02	1	40	1.02	49	44.1	1.11	43.5	1.13
BCV-1%A_60_1.49	1	60	1.49	118	112	1.05	107	1.10
BCV-1%A_60_2.05	1	60	2.05	130	127	1.02	117	1.11
BCV-1%A_80_1.10	1	80	1.10	220	202	1.09	192	1.15
BCV-1%A_80_1.77	1	80	1.77	268	236	1.14	214	1.25
BCV-1%A_80_1.96	1	80	1.96	49.6	243	1.11	221	1.23
BCV-2%_30_1.36	2	30	1.36	41.9	39.1	1.07	39.9	1.05
BCV-2%_40_1.02	2	40	1.02	47.9	45.5	1.05	49.5	0.97
BCV-2%_60_1.00	2	60	1.00	120	122	0.99	126	0.96
BCV-2%_60_1.49	2	60	1.49	136	140	0.97	137	0.99
BCV-2%_60_1.66	2	60	1.66	132	135	0.98	134	0.99
BCV-2%_80_1.10	2	80	1.10	274	241	1.14	239	1.15
BCV-2%_80_1.77	2	80	1.77	274	271	1.01	261	1.05
					Mean	**1.08**		**1.11**
					CoV	**0.11**		**0.13**

The complete and simplified models present a good agreement compared to the 28 slabs in HPFRC and UHPFRC with reinforcement and prestressing forces. The average ratio between measured-to-predicted punching shear strength with the complete model is 1.12 and 1.08 and the coefficient of variation is 0.06 and 0.11, for HPFRC and UHPFRC respectively. The average ratio between measured-to-predicted punching shear strength with the simplified model is 0.98 and 1.11 with a coefficient of variation of 0.06 and 0.13, for HPFRC and UHPFRC respectively. The proposed models are based on the post-cracking response determined on specimens. A good and representative identification of the tensile post-cracking response is the key factor of this model. For design computation, partial safety factor may be considered for the characteristic values of the material properties according to the European practice. Therefore, the mean value with a partial safety factor of 1.5 is maybe more appropriate for a slab due to the redistribution possibilities and the 3D aspect of the punching shear failure.

5.6 Conclusions

In this Chapter, two original experimental studies were presented on thin slabs in HPFRC and in UHPFRC with and without reinforcement and prestressing. A total number of twenty square slabs in HPFRC and nineteen slabs in UHPFRC were tested in order to evaluate the punching shear strength and the flexural behaviour. The material properties, particularly the post-cracking response, were identified through a large numbers of specimens. The principal parameters of the HPFRC slabs were the fibres quantity, the reinforcement ratio and the intensity of axial forces applied by a post-tensioning. The principal parameters of the UHPFRC slabs were the fibres dosage, the reinforcement ratio and the thickness.

These experimental campaigns allowed the collection of a large data base concerning the punching shear behaviour of HPFRC and UHPFRC slabs with reinforcement and prestressing forces. All measurements are presented in the test reports in Appendices B and C. Tests results have highlighted the beneficial contribution of steel fibres on punching shear capacity. They have also shown an increased deformation capacity at the failure state and a more ductile post-peak behaviour. Steel fibres in a sufficient quantity allowed reaching the flexural capacity of the slab without a punching shear failure. The minimum fibre dosage depends on the loading configuration, the thickness, the reinforcement ratio, etc. However, a punching shear failure can occur after the yielding of the reinforcement and the deformation capacity will be thus limited. The improved serviceability behaviour of the HPFRC and UHPFRC slabs has shown less cracking, reduced crack width and smaller deformations. The UHPFRC slabs without reinforcement exhibited a flexural failure with the development of yield lines. After the internal cracking analysis, no punching shear cones were developed for the elements without reinforcement. The flexural strength of these slabs was moderate, therefore the punching shear strength was not critical in this studied case.

Currently, no design models for the assessment of the punching shear strength are proposed in the different recommendations for SFRC and UHPFRC. In order to develop a harmonized model with conventional reinforced concrete, the proposal is based on the Critical Shear Crack theory (CSCT). The proposed models involves the matrix contribution $V_{R,c}$ and the fibres contribution $V_{R,f}$. For the matrix contribution, it is assumed that the punching shear strength is carried by the shear friction and is a function of the critical crack opening depending on the deformation capacity of the slab. The fibres contribution corresponds to the vertical component of the integration of the tensile stresses across the punching shear plan. The distribution of the crack opening is assumed to be linear along the failure plan. Based on the tensile stress vs crack opening law determined on specimens, the distribution of the tensile stresses is defined along the failure plan. Simplified models were also proposed based on reference values identified on specimens. To determine the punching strength, the load – rotation curve must be calculated. The relationship $V(\psi)$ can be modelled by finite difference or finite element methods. The intersection between this curve and the failure criterion corresponds to the punching shear strength.

The complete and simplified models present a good agreement compared to the results of the HPFRC and UHPFRC slabs with reinforcement and prestressing forces tested in this work. For the slabs in UHPFRC without reinforcement, this model is probably not adapted due to the lack of rebars which can control the critical shear crack development.

6 Conclusions and perspectives

6.1 Conclusions of the research

The studies performed during this research have contributed to a better understanding of the shear and punching shear behaviour of High and Ultra-High Performance Fibre Reinforced Concrete (HPFRC) (UHPFRC) structural elements. In this work, the HPFRC is investigated as an advanced cementitious material offering many technical and economical advantages. HPFRC stands between conventional Steel Fibre Reinforced Concrete and UHPFRC. HPFRC is characterized by a compressive strength between 70 to 120 MPa and a matrix composed of coarse aggregates with limited fibres content. However, its mechanical properties, particularly the post-cracking response, may be sufficient for structural applications. HPFRC studied in this work, exhibited generally a hardening behaviour in bending and a softening behaviour in uniaxial tension.

This research focuses primarily on material mix design and mechanical properties. Two HPFRC and one UHPFRC mixes with different fibre content were studied. The HPFRC formulation named A was developed particularly for precast industry with a self-compacting criteria and a targeted compressive strength of 100 MPa. This formulation was used for the study on shear strength of pre-tensioned members. The HPFRC formulation named B was developed for the first study on the punching shear of thin slabs with a compressive strength of 100 MPa. Finally, a UHPFRC developed by the Group *Vicat*, the *Béton Composite Vicat* BCV®, was studied and compared to HPFRC. This UHPFRC was used for the second study on the punching shear of thin slabs.

The developments of HPFRC have highlighted the possibility to design a self-compacting concrete with coarse aggregates and steel fibres from technical and economical points of view. The targeted compressive strength of 100 MPa was reached by using locally available components. Compared to a UHPFRC, self-compacting – HPFRC with coarse aggregates and steel fibres is more difficult to design and needs some compromises. Depending on the type of fibres, the coarse aggregates limit the fibre content. However, in order to limit the shrinkage and the cost of the matrix it's interesting to keep the coarse aggregates particularly for large structural elements.

Secondly, the mechanical properties, particularly the compressive strength and the post-cracking response, were identified through a large numbers of specimens. Different testing methods were used and compared. The uniaxial tensile test is certainly the simplest test for determining the tensile law in a direct way, particularly for a UHPFRC exhibiting a hardening behaviour. However, uniaxial tensile tests are complicated to perform, that's why tensile response was often identified with an indirect way using easier techniques and tests to perform (e.g. bending tests on prism or slab). However, these indirect testing methods required several assumptions for the determination of the tensile constitutive law. Tensile laws determined from the indirect way, were slightly higher compared to the response generated after a uniaxial tensile response, which was probably due to the structural effect. A special attention must be paid to the representativeness of the specimens at the structural level (fibre orientation, scale effect, etc.).

Thirdly, several experimental studies on structural elements, beams and slabs, were undertaken in order to analyse the structural behaviour of HPFRC and UHPFRC, particularly their behaviour in shear and punching shear. For members and flat slabs without shear reinforcement, the shear and punching shear strength were often the critical design criteria. These failure modes are characterized by a fragile behaviour implying possible partial or total collapse of the structure. Despite extensive research in this field, shear and punching shear in reinforced and prestressed concrete structures, remain complex phenomena so that the current approach in standards is often empirical or simplified. The ability of Steel Fibre Reinforced Concrete (SFRC) to reduce shear reinforcement in reinforced and prestressed concrete members and slabs, or even eliminate it, is supported by several experimental studies. However its practical application remains marginal mainly due to the lack of standard, procedures and rules adapted to its performance. The different experimental campaigns on prestressed beams and slabs have highlighted the potential of HPFRC compared to UHPFRC. In numerous structural applications, the mechanical properties of HPFRC may be sufficient.

One original experimental campaign was performed on pre-tensioned members in HPFRC. A total number of six shear-critical beams of a 3.60 m span each, and two full scale beams of a 12.00 m span each, were tested in order to evaluate the shear and flexural strength. The load tests have highlighted the beneficial contribution of HPFRC on shear capacity and the ability of steel fibres to replace the minimum shear reinforcement. The HPFRC beams exhibited higher stiffness in presence of diagonal shear cracks. The fibres controlled the development of the diagonal cracks. For HPFRC members, even with low fibres dosage, the formation of critical shear cracks was significantly delayed due to the formation of a secondary cracking pattern. The full scale beam AF-1 in High Strength Concrete failed in shear, while the HPFRC (60 kg/m^3) members exhibited a flexural failure without diagonal shear cracks. In this study, a fibre content of 50 kg/m^3 can replace the minimum shear reinforcement.

Two original experimental studies were performed on thin slabs in HPFRC and in UHPFRC with and without reinforcement and prestressing. A total number of twenty square slabs in HPFRC and nineteen slabs in UHPFRC were tested in order to evaluate the punching shear strength and the flexural behaviour. These experimental campaigns allowed the collection of a new data base concerning the punching shear behaviour of HPFRC and UHPFRC slabs with reinforcement and pre-stressing. Tests results have highlighted the beneficial contribution of steel fibres on flexural behaviour and punching shear capacity. They have also shown an increased deformation capacity at the failure state and a more ductile post-peak behaviour. Steel fibres in a sufficient quantity allowed reaching the flexural capacity of the slab without a punching shear failure. The minimum fibre dosage depends on the loading configuration, the thickness, the reinforcement ratio, etc. However, a punching shear failure can occur after the yielding of the reinforcement. In this study, with the tested configurations, a minimum fibre content of 80 kg/m^3 (V_f = 1%) seems sufficient to avoid a sudden punching shear failure. At serviceability limit state, the behaviour of the HPFRC and UHPFRC slabs has shown less cracking, reduced crack width and smaller deformations.

Theoretical studies are supported by experimental research on shear strength of pre-tensioned members and punching shear strength of thin slabs. For pre-tensioned members, we have performed a numerical analysis with non-linear FEM software. The numerical modelling analysis composed of shell elements was able to represent the linear and non-linear behaviour of pre-tensioned members under shear loading. It was also able to predict, with a good accuracy, the failure load and the steel fibres contribution of HPFRC pre-tensioned beams. In order to develop a simplified code-like such as an harmonized model with conventional reinforced concrete, we have also proposed two approaches based on the Critical Shear Crack Theory (CSCT) and stress field model depending on the loading

configuration and fibres content. The models presented a good agreement with the different test results on SFRC and HPFRC beams.

Currently, no design models for the assessment of the punching shear strength are proposed in the different recommendations for SFRC and UHPFRC. In order to develop a harmonized model with conventional reinforced concrete, we have proposed an approach based on the Critical Shear Crack theory (CSCT). The proposed models involves the matrix contribution $V_{R,c}$ and the fibres contribution $V_{R,f}$. For the matrix contribution, it is assumed that the punching shear strength is carried by the shear friction and is a function of the critical crack opening depending on the deformation capacity of the slab. The fibres contribution corresponds to the vertical component of the integration of the tensile stresses across the punching shear plan. The distribution of the crack opening is assumed to be linear along the failure plan. Based on the tensile stress vs crack opening law determined on specimens, the distribution of the tensile stresses is defined along the failure plan. We have also proposed simplified models based on reference values identified on specimens. To determine the punching strength, the load – rotation curve must be calculated. The relationship $V(\psi)$ can be modelled by finite difference or finite element methods. The intersection between this curve and the failure criterion corresponds to the punching shear strength. The complete and simplified models present a good agreement compared to the results of the HPFRC and UHPFRC slabs with reinforcement and prestressing forces tested in this work.

6.2 Perspectives for further research

High Performance Fibre Reinforced Concrete is a relatively uncommon and unknown building material, lot of subjects still need to be studied at the material and the structural levels. For Ultra-High Performance Fibre Concrete, the structural behaviour of an element having a combination of steel reinforcement and prestressing, still need to be investigated for more rational application. The following research proposals should be considered for future research.

The influence of the post-cracking response of HPFRC and UHPFRC on the reorientation of the compressive struts of beam webs and walls should be studied. The study of membrane and shell elements with different reinforcement ratios, fibre types and content, etc. tested simultaneously under normal and shear stresses would allow the investigation of this effect.

The influence of the shear span to depth ratio a/d, reinforcement ratio and fibre content on the development of shear mechanism of members should be better studied experimentally and numerically.

The analysis of structural behaviour with Non Linear Finite Element Model should be better studied. In the same subject, the characteristic length necessary to transform the stress - crack opening w relationship into a stress - strain ε relationship should be better studied.

In this thesis only axisymmetric punching shear strength was investigated. The study of non-symmetrical punching shear strength of slabs in HPFRC and UHPFRC is also necessary.

The influence of fibres type and content on the bond behaviour between steel reinforcement (rebars or strands) and High Performance Concrete should be investigated in order to assess how the bending response can be modelled.

The creep and shrinkage behaviour of HPFRC was not investigated in this work; however they are important properties for reinforced and prestressed concrete structures.

The aggregates shear transfer capacity of very High Strength Concrete is not clearly defined and therefore should be better investigated.

The performances of HPFRC and UHPFRC allow the design of slender structures in comparison with conventional reinforced concrete. Among several aspects, the effects of global and local instabilities and buckling phenomena could become crucial. The investigations of instabilities behaviour and the development of design models are necessary for the development of rational applications.

6.3 Perspectives for construction

Thanks to their high mechanical properties, High and Ultra-High Performance Fibre Reinforced Concrete have undeniable potential to allow innovative design and to improve durability of concrete structures. These materials are adapted for stationary processes in precast industry as well as for in situ process. In precast industry, the weight of the element could be sensibly reduced allowing facilities for transport and handling. Another interesting point is the reduced environmental impact of the structure and the increased durability particularly in bridge applications. HPFRC or UHPFRC should be chosen in function of the applications and the targeted performances. The following propositions should be considered for future applications.

The preparation of dedicated standards and recommendations appears as a key aspect, in order to take advantage of the full benefits of the increased performances while allowing for safe uses of these materials. A standard including models and rules for FRC to UHPFRC are preferable for practitioners.

The development of new and optimized forms adapted to the materials properties allows a reduction of the weight (hollow beams, etc). The suppression of the secondary reinforcement allows new cross-sectional design.

The combination of HPFRC and UHPFRC with different materials like steel, reinforced concrete, timber, fibre reinforced polymer, etc. offers unlimited potential for the development of light and innovative structures.

References

[ACI1992] AMERICAN CONCRETE INSTITUTE, *State-of-the-art Report on high strength concrete*, ACI 363-92, ACI, Detroit, MI, 1992, 55 p.

[ACI1992] AMERICAN CONCRETE INSTITUTE, Fracture Mechanics of Concrete: Concepts, Models and Determination of Material Properties, Report by ACI Committee 446, Fracture Mechanics. American Concrete Institute, Detroit, 1992.

[ACI2011] ACI 318-08, *Structural Concrete Building code*, American Concrete Institute, Farmington Hills, MI, 2011, 430 p.

[AFGC2002] AFGC-SETRA, *Interim recommendations and Appendices, Ultra High Performance Fibre-Reinforced Concretes*, Association française de Génie civil, Paris, 2002, 250 p.

[AFGC2008] AFGC, *Recommendation for the use of Self-Compacting Concrete*, Association française de Génie civil, Paris, 2008, 62 p.

[AIT1998] AITCIN, P.-C., LACHEMI, M., ADELINE, R., RICHRAD, P., *The Sherbrooke Reactive Powder Concrete Footbridge*, Structural Engineering International IABSE, vol. 8, no.2, 1998, pp. 140-144.

[AIT2001] AÏTCIN, Pierre-Claude, *Bétons haute performance*. Paris : Editions Eyrolles, 2001, 683 p.

[ASC1973] ASCE-ACI Committee 426. The Shear Strength of Reinforced Concrete Members,"Journal of the Structural Division, Proceedings of the American Society of Civil Engineers, Vol. 99, No. ST6, June, 1973, 1091-1187 p.

[ASTM2004] ASTM C1550-04, *Standard test method for flexural toughness of fiber reinforced concrete - using centrally loaded round panel*, ASTM International, West Conshohocken, PA, 2004, 9 p.

[BAB2010] BABY, F., BILLO, J., RENAUD, J.C., MASSOTTE, C., MARCHAND, P., TOUTLEMONDE, F., *Shear resistance of ultra-high performance fibre-reinforced concrete I-beams*, FraMCoS7, B.H. Oh et al. eds, Jeju (Korea), 23-28 May 2010, pp. 1411-1417.

[BAC1981] BACHE, Hans Hendrik, Densified cement / ultra-fine particle based materials*, in Second International Conference on Superplasticizers in Concrete*, Ottawa, Canada, June 10-12, 1981.

[BAEL1991] BAEL 91, *Règles techniques de conception et de calcul des ouvrages et constructions en béton armé suivant la méthode des états limites*, Fasc, 62, 1991

[BAEL1999] BAEL 91 révisé 99, *Règles techniques de conception et de calcul des ouvrages et constructions en béton armé suivante la méthode des états limites*, Fasc. 62, Avril 1999.

[BAZ1984] BAZANT, Z. P., KIM, I.-K., *Size effect in shear failure of longitudinally reinforced beams*, ACI Journal, Vol. 81, No 5, September-October 1984, pp. 456-468.

[BAZ1987] BAZANT, Z.P., SUN, H.H., *Size effect in diagonal shear failure: Influence of aggregate size and stirrups*, ACI Materials Journal, Vol. 84, No 4, July-August 1987, pp. 259-272.

[BAZ1991] BAZANT, Z. P., KAZEMI, M. T., *Size effect on diagonal shear failure of beams without stirrups*, ACI Journal, Vol. 88, No 3, May-June 1991, pp. 268–276.

[BARO1999] BARON, J., OLLIVIER, J., *Les bétons, Bases de données pour leur formulation*, Paris, Eyrolles, 1999, 522 p.

[BART2002] BARTOS, P.J.M., SONEBI, M., TAMIMI, A.K., *Workability and Rheology of Fresh Concrete: Compendium of Tests – Report of RILEM Technical Committee 145-WSM*. Cachan: RILEM Publications, 2002, 127 p.

[BEH1996] BEHLOUL, *Mouloud, Analyse et modélisation du comportement d'un matériau à matrice cimentaire fibrée à ultra hautes performances*, E.N.S. Cachan, thèse de doctorat, Cachan France, 1996, 182 p.

[BEH2003] BEHLOUL, M., LEE, K.C., *Ductal Seonyu footbridge*, Structural concrete, Journal of the *fib*, Vol. 4, No 4, 2003, pp. 195-201.

[BEN2006] BENTZ E.C., VECCHIO F.J., COLLINS M.P., *Simplified Modified Compression Field Theory for Calculating Shear Strength of Reinforced Concrete Elements,* ACI Structural Journal, Vol. 103, No 4, July-August, 2006, pp. 614-624.

[BEN2010] BENTZ, Evan C., *MC2010. Shear Strength of beams and implications of new approaches*, in Shear and punching shear in RC and FRC elements: Workshop 15-16 October 2010, Salò, Bulletin No 57, Fédération international de béton *fib*, 2010, pp. 15-30.

[BHP2000] *Synthèse des travaux du projet national BHP 2000 sur les bétons à hautes performances*, Paris: Presses de l'Ecole Nationale des Ponts et Chaussées, 298 p.

[BIL1989] BILLIGTON, David P., *Robert Maillart and The Art of Reinforced Concrete*, The MIT Press, Cambridge, Massachusetts, and London, England, 1989, 151 p.

[BPEL1991] BPEL 91, Règles techniques de conception et de calcul des ouvrages et constructions en béton précontraint suivant la méthode des états limites, Fasc, 62, 1991.

[BPEL1999] BPEL 91 révisé 99, *Règles techniques de conception et de calcul des ouvrages et constructions en béton précontraint suivant la méthode des états limites*, Fasc, 62, Avril 1999.

[BRU2005] BRÜHWILER, E., DENARIE, E., HABEL, K., *Ultra-High Performance Fibre Reinforced Concrete for advanced rehabilitation of bridges*. Proceedings *fib* Symposium Keep Concrete Attractive, Budapest, 2005.

[BRU2011] BRÜHWILER, E., MOREILLON, L., SUTER, R., *Bétons fibrés ultra-performants – Concevoir, dimensionner, construire,* Proceedings of UHPC symposium in Fribourg (Switzerland), October 26, 2011, Fribourg, 2011, 207 pp.

[CAS1996] CASANOVA, Pascal, *Bétons renforcés de fibres métalliques : Du matériau à la structure*. Paris : Presses du Laboratoire Central des Ponts et Chaussées, 1996, 203 p.

[CAS1997] CASANOVA, P., ROSSI, P., SCHALLER, I., *Can Steel Fibers Replace Transverse Reinforcement in Reinforced Concrete Beams?*, ACI Material Journal, Vol. 94, No. 5, September 1985, pp. 341-354.

[CEB1985] Comité Euro-international du Béton. *Punching Shear in Reinforced Concrete*, *a State of the Art Report*. Thomas Telford Publishing, Bulletin d'information N°168, Lausanne, Switzerland, 1985. 232 p.

[CEB1987] Comité Euro-international du Béton. *Shear in Prestressed Concrete Members*, *a State of the Art Report*. Thomas Telford Publishing, Bulletin d'information N°180, Lausanne, Switzerland, 1987. 144 p.

[CEB1993] Comité Euro-international du Béton. *CEB-FIP Model Code 90*. Thomas Telford Publishing, Bulletin d'information N°213 - 214, Lausanne, Switzerland, 1993. 460 p.

[CEB1997] Comité Euro-international du Béton. *Concrete Tension and Size Effect*. Bulletin d'information N°237, Lausanne, Switzerland, 1997. 258 p.

[CHA2000] CHANVILLARD, G. *Characterisation of fibre reinforced concrete mechanical properties : a review*, Fifth RILEM Symposium on Fibre-Reinforced Concertes (FRC), Lyon, 2000.

[CHO2003] CHOPIN, David, *Malaxage des bétons à hautes performances et des bétons auto-plaçants – Optimisation du temps de fabrication*, OA 41, Laboratoire Central des Ponts et Chaussées, Paris, 2003, 206 p.

[COL1993] COLLINS M.P., MITCHELL D., MACGREGOR J.G., *Structural Design Considerations for high-Strength Concrete,* ACI Concrete Int., Vol. 15, No 5, May, 1993, pp. 27-34.

[CSA2004] CSA A23.3-04, *Design of Concrete Structures,* Canadian Standards Association, Mississauga, Ontario, 2004, 204 p.

[DBV2001] DBV, Deutscher Beton- und Bautechnik-Verein E.V., *DBV-Merkblatt Stahlfaserbeton*, Berlin, 2001.

[DEL2011] DELAUZUN, O., ROGAT, D., BOUTILLON, L., LINGER, L., CLERGUE, C., *Construction of the PS34 UHPFRC Bridge, in Designing and Building with UHPFRC: State of the Art and Development*, Ed. By TOUTLEMONDE, F., RESPLENDINO, J., ISTE and Wiley, 2011, pp. 137-147.

[DEN2011] DENARIE, Emmanuel, *Formulation et propriété des BFUP – du matériau aux structures*, in Journée d'étude du 27 octobre 2011 – BFUP concevoir, dimensionner, construire, EIA-FR, 2011, pp. 49-65.

[DIN2010] DINH H., PARRA-MONTESINOS G.J., WIGHT K.J., *Shear Behavior of Steel Fiber-Reinforced Concrete Beams without Stirrup Reinforcement,* ACI Structural Journal, Vol. 107, No 5, September – October, 2010, pp. 597-606.

[DIP2010] DI PRISCO, M., PLIZZARI, G., VANDEWALLE, L., *MC2010: Overview on the shear provisions for FRC*, in Shear and punching shear in RC and FRC elements: Workshop 15-16 October 2010, Salò, Bulletin No 57, Fédération international de béton *fib*, 2010, pp. 61-76.

[EC22005] EN 1992-1-1, *Eurocode 2 — Design of concrete structures — Part 1-1: General rules and rules for buildings*, European Committee for Standardization (CEN), Brussels, 2005, 205 p.

[EN14651] EN 14651+A1, *Test method for metallic fibre concrete — Measuring the flexural tensile strength*, European Committee for Standardization (CEN), Brussels, 2007.

[FAL2006] FALKNER, H, TEUTSCH, M., *XI Stahlfaserbeton – Anwendungen und Richtlinie*, Beton Kalender, Berlin : Ernst & Sohn, 2006, pp. 667 - 703

[FAV1997] FAVRE, Renaud et al, *Dimensionnement des structures en béton*, Traité de génie civil de l'EPFL Volume 8, Presses polytechniques et universitaires romandes, Lausanne, Suisse, 1997, 612 p.

[FEN1968] FENWICK, R. C., PAULAY, T., *Mechanisms of Shear Resistance of concrete Beams*, Journal of Structural Division, ASCE, Vol. 94, No. 10, October 1968, pp. 2325-2350.

[FER2006] FERNANDEZ RUIZ, M., HARS, E., MUTTONI, A., *Résistance à l'effort tranchant des poutres précontraintes à âmes minces,* Rapport OFROU, N° 606, Bern, Switzerland, 2006, 68 p.

[FER2007] FERNANDEZ RUIZ, M., MUTTONI, A., *On Development of Suitable Stress Fields for Structural Concrete,* ACI Structural Journal, Vol. 104, No 4, July-August 2007 pp. 495-502.

[FER2010] FERNANDEZ RUIZ M., CAMPANA S., MUTTONI A., *Discussion of paper 'Influence of Flexural Reinforcement on Shear Strength of Prestressed Concrete Beams' by E. I. Saquan and R. J. Frosch,* ACI Structural Journal, November-December, 2010, pp. 907-908.

[FIB1990] FÉDÉRATION INTERNATIONALE DU BÉTON *fib*, *High Strength Concrete - State of the Art Report*, No. SR 90/1, London, Aug. 1990, 61 p.

[FIB1999a] FÉDÉRATION INTERNATIONALE DU BÉTON *fib*, *Structural Concrete – Textbook on Behaviour, Design and Performance – Updated knowledge of CEB/FIP Model Code 1990 – Volume 1*. Bulletin 1, Lausanne, 1999, 244 p.

[FIB1999b] FÉDÉRATION INTERNATIONALE DU BÉTON *fib*, *Structural Concrete – Textbook on Behaviour, Design and Performance – Updated knowledge of CEB/FIP Model Code 1990 – Volume 2*. Bulletin 2, Lausanne, 1999, 324 p.

[FIB2001] FÉDÉRATION INTERNATIONALE DU BÉTON *fib*, *Punching of Structural Concrete Slabs*, Bulletin 12, Lausanne, Switzerland, 2001, 307 pp.

[FIB2008a] FÉDÉRATION INTERNATIONALE DU BÉTON *fib*, *Constitutive modelling for high strength / high performance concrete. State-of-art report*, Bulletin 42, Lausanne, Switzerland, 2008, 130 pp.

[FIB2008b] FÉDÉRATION INTERNATIONALE DU BÉTON *fib*, *Practitioners' guide to finite element modelling of reinforced concrete structures. State-of-art report*, Bulletin 45, Lausanne, Switzerland, 2008, 344 pp.

[FIB2010a] FÉDÉRATION INTERNATIONALE DU BÉTON *fib*, *Model Code 2010 – First complete draft – volume 1*. Bulletin 55, Lausanne, 2010.

[FIB2010b] FÉDÉRATION INTERNATIONALE DU BÉTON *fib*, *Model Code 2010 – First complete draft – Volume 2*. Bulletin 56, Lausanne, 2010.

[FIB2010c] FÉDÉRATION INTERNATIONALE DU BÉTON *fib*, *Shear and punching shear in RC and FRC elements – Workshop 15-16 October 2010*, Salò. Bulletin 57, Lausanne, 2010.

[FIN2012] Non-linear finite element analysis program *FINELg*, *User's Manual, version 9.3*, ArGEnCo Department, University of Liège, Greisch Info S.A., Liège, Belgium, 2012.

[FRO2000] FROSCH, Robert J., *Behavior of Large-Scale Reinforced Concrete Beams with Minimum Shear Reinforcement,* ACI Structural Journal, Vol. 97, No 5, November-December, 2010, pp. 814-820.

[GAM1981] GAMBAROVA, Pietro Giovanni, *On Aggregate Interlock Mechanism in Reinforced Concrete Plate with Extensive Cracking*, Transactions, IABSE Colloquium Delft, 1981 on Advenaced Mechanics of reinforced Concrete, International Association for Bridge and Structural Engineering, Zurich, pp. 99-120.

[GOS2000] GOSSLA, Ulrich, *Tragverhalten und Sicherheit Betonstahlbewehrter Stahlfaserbetonbauteile*, Deutscher Ausschuss für Stahlbeton (DAfStb), Heft 501, Beuth Verlag GmbH, Berlin, 2000, 128 p.

[GOS2004] GOSSLA, Ulrich, *Decken aus selbstverdichtendem Stahlfaserbeton*, In: Qualität im Bauwesen, Heft 181, Braunschweig: IBMB, 2004, pp. 147 - 154

[GRU2001] GRÜNEWALD, S., WALRAVEN, J. C., *Parameter-study on the influence of steel fibers and coarse aggregate content on the fresh properties of self-compacting concrete*, Cement and Concrete Research, Vol. 31, No 12, December, 2001, pp. 1793-1798.

[GRUN2004] GRUNERT, J. P., STROBACH, C.-P., *Stahlfaserverstärkte Spannbetonbauteile aus SVB ohne Betonstahlbewehrung*. In: Qualität im Bauwesen. Heft 181, Braunschweig: IBMB, 2004, pp. 33-42.

[GUA2005] GUANDALINI, Stefano, *Poinçonnement symétrique des dalles en béton armé*, Thèse N° 3380, Ecole Polytechnique Fédérale de Lausanne, 2005, 179 p.

[HAB2009] HABERT, G., ROUSSEL, N., *Study of two concrete mix-design strategies to reach carbon mitigation objectives*, Cement and Concrete Composites, Vol. 31, pp. 397-402.

[HAB2012] HABERT, G., ARRIBE, D., DEHOVE, T., ESPINASSE, L., LE ROY, R., *Reducing environmental impact by increasing the strength of concrete: quantification of the improvement to concrete bridges*, Journal of Cleaner Production, Vol. 35, 2012, pp. 250-262.

[HAL1996] HALLGREN, M. *Punching Shear Capacity of Reinforced High Strength Concrete Slabs*, Ph D thesis, KTH Stockholm, Sweden, 1996. 206 p.

[HAR2005] HARRIS D. K., ROBERTS-WOLLMANN, C.L., *Characterizations of Punching Shear Capacity Of Thin UHPC Plates*, Final contract report, Virginia Polytechnic Institute and State University, June 2005, 64 p.

[HIL1976] HILLERBORG, A., MODEER, M., PETERSSON, P., *Analysis of crack formation and crack growth in concrete by means of fracture mechanics and finite elements*, Cement and Concrete Research, Vol. 6, No. 6, 1976, pp. 773-781.

[HIL1980] HILLERBORG, Arne, *Analysis of fracture by means of the fictitious crack model, particulary for fibre reinforced concrete*, The journal of Cement Composite, Vol. 2, No. 4, November, 1980, pp. 177-184.

[HIL1985] HILLERBORG, Arne, *The theoretical basis of a method to determine the fracture energy G_f of concrete*, Materials and Structures, 1985, pp. 291-296.

[HIL1991] HILLERBORG, Arne, *Application of the fictitious crack model to different types of materials*, International Journal of Fracture, 51, 1991, 95-102.

[HOA1997] HOANG, L. C., *Shear Strengths of Non-Shear Reinforced Concrete Elements, Part 2 – T-Beams*, Technical University of Denmark, Department of Structural Engineering and Materials, Report No. 29, Lyngby, 1997, 35 p.

[IMA1997] IMAM, Mahmoud, *Shear domain of fibre-reinforced high-strength concrete beams*, Engineering Structures, Vol. 19, No. 9, 1997, pp. 738-747.

[ISO2010a] ISO 15630-1:2010, Aciers pour l'armature et la précontrainte du béton - Méthodes d'essai - Partie 1: Barres, fils machine et fils pour béton armé, 2010, 20 p.

[ISO2010b] ISO 15630-2:2010, Aciers pour l'armature et la précontrainte du béton - Méthodes d'essai - Partie 2: Treillis soudés, 2010, 16 p.

[ISO2010c] ISO 15630-3:2010, Aciers pour l'armature et la précontrainte du béton - Méthodes d'essai - Partie 3: Aciers de précontrainte, 2010, 28 p.

[KAN1964] KANI, G. N. J., *The Riddle of Shear Failure and Its Solution*, ACI Journal, V 61, No. 4, April 1964, pp. 441-467.

[KAN1966] KANI, G.N.J., *Basic Facts Concerning Shear Failure*, ACI Journal, Vol. 63, June 1966, pp. 675–692.

[KAN1979] KANI, Mario W., HUGGINS, M.W., WITTKOPP, R.R., *Kani on Shear in Reinforced Concrete*, Department of Civil Engineering, University of Toronto, Toronto, 1979, 225 pp.

[KAU1998] KAUFMANN, Walter, *Strength and Deformations of Structural Concrete Subjected to In-Plane Shear and Normal Forces,* Thesis of ETH Zurich, 1998*,* 147 p.

[KIN1960] KINNUNEN, S., NYLANDER, H. *Punching of concrete slabs without shear reinforcement*. Stockholm : Transactions of the Royal Institute of Technology, 1960. 112 p.

[KOR1985] KORDINA K., BLUME, F. Empirische Zusammenhänge zur Ermittlung der Schubtragfähigkeit stabförmiger Stahlbetonelemente, Ernst & Sohn, Deutscher Ausschuss für Stahlbeton, Heft 364, Berlin, Germany, 1985. 85 p.

[KUC1997] KUCHMA, D.A., VEGH, P., SIMIONOPOULOS, K., STANIK, B. and COLLINS, M.P., *The Influence of Concrete Strength, Distribution of Longitudinal Reinforcement, and Member Size, on the Shear Strength of Reinforced Concrete Beams*, CEB-Bulletin No. 237, pp. 209-229.

[KUP1983] KUPFER, H., & al., *Failure of Shear Zone of R.C. and P.C. Girders – An analysis with consideration of interlocking of cracks (in German)*, Bauingenieur, Vol. 58, 1983, pp. 143-149.

[LAR1996] DE LARRARD, F., BOSC, F., CATHERINE, C., DEFLORENNE, F., *La nouvelle méthode des coulis de l'AFREM pour la formulation des bétons à hautes performances*, Bulletin des Laboratoires des Ponts et Chaussées, N°202, mars-avril, pp. 61-69.

[LAR2000] DE LARRARD, François, *Structures granulaires et formulation des bétons*. Paris : Presses du Laboratoire Central des Ponts et Chaussées, 2000, 414 p.

[LEO1966] LEONHARDT, F., WALTHER, R., *Wardetiger Trager*, Deutscher Ausschuss für Stahlbeton, No. 178, 1966, pp. 2325-2350.

[LOU1996] LOUKILI, Ahmed, *Etude du retrait et du fluage de Bétons à Ultra-Hautes Performances*, E.C. Nantes, Thèse de Doctorat, Nantes, France, 1996, 155 p.

[MAR1999] MARTI, Peter et al, *Harmonized test procedures of steel fiber-reinforced concrete*, ACI Materials Journal , Vol. 96, No 6, November 1999, pp. 676 à 685.

[MART2010] MARTINIE, L., ROSSI, P., ROUSSEL, N., *Rheology of fiber reinforced cementitious materials: classification and prediction*, Cement and Concrete Research, Vol. 40, No 2, February, 2010, pp. 226-234.

[MAY2012] MAYA DUQUE, L. F., FERNANDEZ RUIZ M., MUTTONI, A., FOSTER, S. J., *Punching shear strength of steel fibre reinforced concrete slabs*, Engineering Structures, Vol. 40, July, 2012, pp. 93-94.

[MIL1985] MILLARD, S. G., JOHNSON, R. P., *Shear Transfer in Cracked Reinforced Concrete*, Magazine Concrete Research, Vol. 37, No. 130, 1985, pp. 3-15.

[MIN2005] MINELLI, Fausto. *Plain and fiber reinforced concrete beams under shear loading: Structural behavior and design aspects*, Thèse de doctorat, Starrylink Editrice Brescia, Italia, 2005. 429 p.

[MIN2006] MINELLI, F., VECCHIO, F. J. *Compression Field Modeling of Fiber-Reinforced Concrete Members Under Shear Loading*, ACI Structural Journal, Vol. 103, No 2, March – April, 2006, pp. 244-252.

[MOE1908] MOERSCH, E., Der Eisenbetonbau, seine Theorie und Andwendung, 3rd Edition, verlag von Konrad Wittwer, 1908, 376 p.

[MOM2003] MOMBER, Andreas, *The efficiency of mechanical concrete comminution*, Engineering Fracture Mechanics, Vol. 70, No 1, January, 2003, pp. 81-91.

[MOR2008] MOREILLON, L., LE ROY, R., SUTER, R., *Punching shear strength of high performance fibre reinforced concrete slabs*, Proceedings of the 8th fib PhD Symposium in Kgs. Lyngby, Denmark, June 20-23, 2010, pp. 201-206.

[MOR2009] MOREILLON, L., SUTER, R., *Comportement à la flexion et au cisaillement d'éléments poutre en BFUP*, Rapport d'essais, Ecole d'ingénieurs et d'architectes de Fribourg, 2009.

[MUT1991] MUTTONI, A., SCHWARTZ, J. *Behavior of Beams and Punching in Slabs without Shear Reinforcement*, IABSE Colloquium, Vol.62, Stuttgart, Germany, 1991, pp. 703-708.

[MUT2008a] MUTTONI, A., FERNANDEZ RUIZ, M., *Shear Strength of Members without Transverse Reinforcement as Function of Critical Shear Crack Width*, ACI Structural Journal , V.105, No 2, July-August, 2008, pp. 163-172.

[MUT2008b] MUTTONI, Aurelio, *Punching Shear Strength of Reinforced Concrete Slabs without transverse Reinforcement*, ACI Structural Journal , V.105, No 2, March-April, 2008, pp. 440-450.

[MUT2011] MUTTONI, A., FERNANDEZ RUIZ, M., KOSTIC, N., *Champs de contraintes et méthode des bielles et tirants : Applications dans la conception et le dimensionnement des structures en béton armé*, IBETON-EPFL, 2011, 118 p.

[NAA1991] NAAMAN, A.E. et al, *Fiber pullout and bond slip: Experimental validation*, ASCE Journal of Structural Engineering, Vol. 117, No 9, 1991, pp. 2791-2800.

[NAA2003] NAAMAN A., REINHARDT H., *Fourth International Workshop on - High Performance Fiber Reinforced Cement Composites*, RILEM, Ann Arbor USA, 2003.

[NAA2004] NAAMAN A., REINHARDT H., *Fiber reinforced concrete - Current needs for successful implementation*, International RILEM Workshop Fiber Reinforced Concrete from Theory To practice, Bergamo, 2004.

[NAA2012] NAAMAN A., WILLE K., The path to Ultra-High Performance Fiber Reinforced Concrete (UHPC-FRC): Five Decades of Progress*, in Proceeding of Hipermat 2012 - 3rd International Symposium on UHPC and Nanotechnology for High Performance Construction Materials*, Kassel, March 7-9, 2012, pp. 3-15.

[NAG2007] NAGLE, T., KUCHMA, D.A., *Shear Transfer Resistance in High-Strength Concrete Girders*, Magazine of Concrete Research, Vol. 59, No. 8, October 2007, pp. 611 –620.

[NOG2000] NOGHABAI, Keivan, *Beams of fibrous concrete in shear and bending experiments and model*, Journal of Structural Engineering, Vol. 126, No. 2, February, 2000, pp. 243-251.

[NOS2012] NOSHIRAVANI, Talayeh, *Structural Response of R-UHPFRC – RC Composite Members Subjected to Combined Bending and Shear*, Thèse N°5246, Ecole Polytechnique Fédérale de Lausanne, Suisse, 2012, 184 p.

[PED1996] PEDERSEN, Carsten, *New production processes, materials and calculation techniques for fiber reinforced concrete pipes*, PhD thesis, Department of Structural Engineering and Materials, Technical University of Denmark, No. 14, 1996.

[PEN2000] PENDYALA R.S., MENDIS P., *Experimental Study on Shear Strength of High-Strength Concrete Beams,* ACI Structural Journal, Vol. 97, No 4, July-August, 2000, pp. 564-571.

[PFY2001] PFYL T., MARTI P., Versuche an stahlfaserverstärkten Stahlbetonelementen, Institut für Baustatik und Konstruktion, ETH Zürich, 2001.

[PFY2003] PFYL, Thomas, *Tragverhalten von Stahlfaserbeton*, Dissertation n° 15005, ETH Zürich, 2003, 140 p.

[POL2005] POLAK, Maria Anna, ed., *Punching Shear in Reinforced Concrete Slabs*, SP-232, American Concrete Institute, Farmington Hills, MI, 2005, 302 pp.

[RED2009] REDAELLI, Dario, Comportement et modélisation des éléments de structure en Béton Fibré à Ultra-Hautes Performances avec armatures passives, Thèse de Doctorat de l'EPFL, 2009, 288 p.

[REI1991] REINECK, Karl-Heinz, *Ultimate shear force of structural concrete members without transverse reinforcement derived from a mechanical model*, ACI Structural Journal, Vol. 88, No 5, 1991, pp. 592-602.

[REI2005] REINECK, Karl-Heinz, *Teil XI: Modellierung der D-Bereiche von Fertigteilen*, Beton-Kalender, Berlin, 2001, 243-296 pp.

[RIC1995] RICHARD, P., CHEYREZY, M., Composition of Reactive Powder Concretes, Cement and Concrete Research, Vol. 25, no. 7, October 1995, pp. 1501-1511.

[RIL2000] RILEM TC 162-TDF, *Test and design methods for steel fibre reinforced concrete: bending test,* Materials and Structures, Vol. 33, January-February 2000, pp. 3-5.

[RIL2001] RILEM TC 162-TDF, *Test and design methods for steel fibre reinforced concrete: Uni-axial tension test for steel fibre reinforced concrete*. Materials and Structures, Vol. 34, January-February 2001, pp. 3-6.

[RIL2002] RILEM TC 162-TDF, *Design of steel fibre reinforced concrete using the σ-w method: principles and applications*. Materials and Structures, Vol. 35, June 2002, pp. 262-278.

[RIL2003] RILEM TC 162-TDF, *Test and design methods for steel fibre reinforced concrete: sigma-epsilon-design method*. Materials and Structures, Vol. 36, October 2003, pp. 560-567.

[RIT1899] RITTER, Wilhem, Die Baueweise Hennebique, Schweizerische Bauzeitung, Zürich, Vol. 33/34, 1899 41-43 pp., 49-52 pp., 59-61 pp.

[ROM1964] ROMUALDI, J. P., MANDEL J.A. , *Tensile strength of concrete affected by uniformly distributed and closely spaced short lengths of wire reinforcement*, Journal of the American Concrete Institute, Vol. 61, No. 6, June 1964, pp. 657-671.

[ROS1998] ROSSI, Pierre, *Les bétons de fibres métalliques*, Paris : Presses de l'Ecole Nationale des Ponts et Chaussée, 1998, 309 p.

[ROS2002a] ROSSI, Pierre, *Le développement industriel des bétons de fibres métalliques*, Paris: Presses de l'Ecole Nationale des Ponts et Chaussées, 2002, 262 p.

[ROS2002b] ROSSI, Pierre, *Development of new cement composite material for construction, Innovations and Developments In Concrete Materials And Construction*, Proceedings of the International Conference, University of Dundee, Dundee, Scotland, 2002, pp. 17-29.

[ROY1996] LE ROY, Robert, *Déformations instantanées et différées des bétons à hautes performances*. Paris : Presses du Laboratoire Central des Ponts et Chaussées, 1996, 343 p.

[SAQ2009] SAQAN, E. I., FROSCH, R. J., *Influence of Flexural Reinforcement on Shear Strength of Prestressed Concrete Beams*, ACI Structural Journal, Vol. 106, No. 1, January-February 2009, pp. 60-68.

[SCH1984] SCHLAICH, J., SCHAEFER, *Teil II: Konstruieren im Stahlbetonbau*, Beton-Kalender, Berlin, 2001, 787-1005 pp.

[SIA1999] SN 562 162/6, *Steel Fibre Reinforced Concrete*, Recommendation, Swiss Society of Engineers and Architects, Zürich, 1999, 23 p.

[SIA2003] SN 505 262, *Concrete Structures*, Standard, Swiss Society of Engineers and Architects, Zürich, 2003, 94 pp.

[SIA2008] D 0226 Documentation, *Sécurité structurale des Parkings couverts*, Swiss Society of Engineers and Architects, Zürich, 2008.

[SKA2000] SKARENDAHL, A., PETERSSON, O., *Self-Compacting Concrete – State-of-the-Art report of RILEM Technical Committee 172-SCC*. Cachan : RILEM Publications, 2000, 154 p.

[SPA2006] SPASOJEVIC, Anna, *Possibilites for Structural Improvements in the Design of Concrete Bridges*, Proceedings of the 6th Int. PhD Symposium in Civil Engineering, Zurich, Switzerland, 2006.

[SPA2008] SPASOJEVIC, Anna, *Structural implications of ultra-high performance fibre-reinforced concrete in bridge design*, Thèse de l'EPFL No. 4051, Lausanne, 2008, 198 p.

[STU2008] STUERWALD, Simone, *Bending Behaviour of UHPFRC combined with Rebars*, Proceedings of the 8th fib PhD Symposium in Kgs. Lyngby, Denmark, June 20-23, 2010, pp. 261-266.

[SUT2005a] SUTER R., BUCHS P. *Voussoirs préfabriqués en béton à fibres - Etude expérimentale en vue d'une optimisation de l'armature*, Rapport de synthèse, Ecole d'ingénieurs et d'architectes de Fribourg, 2005.

[SUT2005b] SUTER, R., BUCHS, P. *Béton à hautes performances renforcé de fibres métalliques : Synthèse des études expérimentales menées de 2001 à 2005*. Rapport de synthèse, Ecole d'ingénieurs et d'architectes de Fribourg, 2005.

[SUT2007] SUTER R., NICOLET J., *Béton renforcé de fibres - Etude comparative entre fibres synthétiques et métalliques,* Rapport d'étude, Ecole d'ingénieurs et d'architectes de Fribourg, 2007.

[SUT2009] SUTER R., MOREILLON L. Bétons à hautes performances renforcés de fibres métalliques – Dalles nervurées préfabriquées, Rapport d'essai, Ecole d'ingénieurs et d'architectes de Fribourg, 2009.

[SUT2009] SUTER R., MOREILLON, L. *Bétons à hautes performances renforcé de fibres métalliques, Projet CTI 7459.2,* Rapport de synthèse, Ecole d'ingénieurs et d'architectes de Fribourg, 2009.

[TIM1959] TIMOSHENKO, S., WOINOWSKY-KRIEGER, S., *Theory of Plates and Shells,* McGraw-Hill, Second Edition, 1959, 580 p.

[TOU2003] TOUTLEMONDE, F., LEGERON, F., PIQUET A., *Valorisation des bétons à hautes et très hautes performances dans les structures d'ouvrages d'art*, Bulletin des Laboratoires des Ponts et Chaussées, No 246-247, 2003, pp. 57-72.

[TOU2007] TOUTLEMONDE, F., RENAUD, J.-C., LAUVIN, L., BRISARD S., RESPLENDINO, J., *Local bending tests and punching failure of a ribbed UHPFRC bridge deck*, Fracture Mechanics of Concrete and Concrete Structures FraMCos 2007, Editors A. Carpinteri, P. Gambarova, G. Ferro, G. Plizzari, Vol. 3, pp. 1481-1489.

[TOU2011] TOUTLEMONDE, F., RESPLENDINO, J., SORELLI, L., BOUTEILLE, S., BRISARD, S., *Innovative design of ultra-high-performance fiber reinforced concrete ribbed slab: experimental validation and preliminary detailed analyses*, Seventh International Symposium on the utilization of High-Strength/High-Performance Concrete, ACI Special Publication SP-228, Vol. 2, June 2005, pp. 1187-1205.

[TOU2009] TOUTLEMONDE, F., RESPLENDINO, J., *Designing and Building with UHPFRC: State of the Art and Development*, Proceedings of UHPFRC symposium in Marseille (France), November 17-18, 2009, London, 2011, 814 pp.

[UN2010] UNSTATS, Greenhouse Gas Emissions by Sector (Absolute Values), United Nation Statistical Division, New York, USA, 2010.

[UNI2003] UNI 11039, *Steel Fiber Reinforced Concrete – Part I: Definitions, Classification, specification and Conformity – Part II: Test Method for Measuring First Crack Strength and Ductility Indexes*, Italian Board Standardization, 2003.

[VAZ2007] VAZ RODRIGUES, Rui, *Shear strength of reinforced concrete bridge deck slabs*. Thèse N°3739, Ecole Polytechnique Fédérale de Lausanne, 2007, 289 p.

[VEC1986] VECCHIO F.J., COLLINS M.P., *The Modified Compression Field Theory for Reinforced Concrete Elements Subjected to Shear,* ACI Journal, Vol. 83, No 2, March-April, 1986, pp. 219-231.

[VEC1994] VECCHIO F.J., COLLINS M.P., ASPIOTIS J., *High-Strength Concrete Elements Subjected to Shear,* ACI Structural Journal, Vol. 91, No 4, July-August, 1994, pp. 423-433.

[VEC2000a] VECCHIO, Frank. J., *Analysis of Shear Critical Reinforced Concrete Beams,* ACI Structural Journal, Vol. 97, No 1, January-February, 2000, pp. 102-110.

[VEC2000b] VECCHIO, Frank. J., *Disturbed Stress Field Model for Reinforced Concrete: Formulation*, ASCE Journal of Structural Engineering, Vol. 126, No 9, September, 2000, pp. 1070-1077.

[VEC2001a] VECCHIO, Frank. J., *Disturbed Stress Field Model for Reinforced Concrete: Implementation*, ASCE Journal of Structural Engineering, Vol. 127, No 1, January, 2001, pp. 12-20.

[VEC2001b] VECCHIO F.J. & al, *Disturbed Stress Field Model for Reinforced Concrete: Validation*, ASCE Journal of Structural Engineering, Vol. 127, No 4, April, 2001, pp. 350-358.

[VIN1986] VINTZELOU, E. N., TASSIOIS, T. P., *Mathematical Models for Dowel Action under Monotonic Conditions*, Magazine Concrete Research, Vol. 38, No. 4, 1986, pp. 13-22.

[VOO2003a] VOO, J.Y.L., FOSTER, S.J., *Variable Engagement Model for Fibre Reinforced Concrete in Tension*, UNICIV Report R-420, School of Civil and Environmental Engineering, The University of New South Wales, Sydney, Australia, June 2003, ISBN: 85841 387 6, 86 pp.

[VOO2003b] VOO, J.Y.L, FOSTER, S.J., GILBERT, R.I., *Shear Strength of Fibre Reinforced Reactive Powder Concrete Girders without Stirrups*, UNICIV Report R-421, The University of New South Wales, School of Civil and Environmental Engineering, Kensington, Sydney, Australia, November 2003, ISBN: 85841 388 4, 131 pp.

[VOO2006] VOO, Y.L, FOSTER, S.J., GILBERT, R.I., *Shear Strength of Fiber Reinforced Reactive Powder Concrete Prestressed Girders without Stirrups*, Journal of Advanced Concrete Technology, Vol. 4, No. 1, February 2006, pp. 123-132.

[VOO2008] VOO, Y.L., FOSTER, S.J., *Shear Strength of Steel Fiber Reinforced Ultra-High Performance Concrete Beams without Stirrups*, 5th International Speciality Conference of Fibre Reinforced Materials, Singapore, 28-29 August 2008, pp. 177-184.

[WAL1981] WALRAVEN, Joost C., *Fundamental Analysis of Aggregate Interlock*, Journal of Structural Division, ASCE, Vol. 108, No. 11, November 1981, pp. 2245-2270.

[WAL2004] WALRAVEN, Joost C., *Design with ultra-high strength concrete: basics, potential and perspectives*, in Proceedings of the International Symposium on Ultra High Performance Concrete, Kassel, Germany, 2004, pp. 853-864.

[WAL1995] WALRAVEN, Joost C., *Shear Friction in High-Strength Concrete*, Progress in Concrete Research, Vol. 4, TU Delft, 1995.

[WAL2008] WALRAVEN, Joost C., *On the way to design recommendations for UHPFRC*, in Ultra-High Performance Concrete: Second International Symposium on Ultra High Performance Concrete March 05-07, 2008, Ed. By E. Fehling, M. Schmidt and S. Stürwald, Kassel, 2008, pp. 45-56.

[WALT1999] WALTHER R., MIEHLBRADT M., D*imensionnement des structures en béton – Bases et technologie*. Traité de génie civil de l'EPFL, Vol. 7, Presses polytechniques et universitaires romandes, Lausanne, Suisse 1999, 408 p.

[ZHA1994] ZHANG, J. P., *Strength of Cracked Concrete. Part 1 – Shear Strength of Conventional Reinforced Concrete Beams, Deep Beams, Corbels, and Prestressed Reinforced Concrete Beams without Shear Reinforcement*, Technical University of Denmark, Department of Structural Engineering, Report No. 311, Lyngby, 1994, 106 p.

Curriculum vitae

Name	Moreillon
First name	Lionel
Date of birth	January 24, 1981
Birthplace	Lausanne, Switzerland
Nationality	Swiss
Email	lionel.moreillon@gmail.com

Education

Ph. D. Degree, Université Paris-Est - Graduate school Sciences, Engineering and Environment, Champs-sur-Marne, France, 2013.

MSc in Mechanics of Materials and Structures, Ecole Nationale des Ponts et Chaussées, Champs-sur-Marne, France, 2008.

Diploma HES in Civil Engineering, University of Applied Sciences Fribourg, Switzerland, 2006.

Vocational Degree as Structural Drafter, Lausanne, Switzerland, 2002.

Baccalaureate degree in sciences, Pully, Switzerland, 2000.

Professional Experience

Structural engineer, INGPHI SA Lausanne, Switzerland, 2012-to present.

Environmental engineer, Ville de Pully – Swiss Confederation, Switzerland, 2012.

Research Associates, University of Applied Sciences Fribourg, Switzerland, 2008-to present.

Civil Drafter, Daniel Willi SA Montreux, Switzerland, 2000-2006.

Selected publications

Moreillon L., Nseir J., Suter R., **Le Roy R.,** *Shear strength of pre-tensioned members in high performance fibre reinforced concrete*, Proceedings of the BEFIB Symposium 2012, Guimarães, Portugal, 2012, 12 p.

Moreillon L., Suter R., **Nseir J.**, *Punching shear strength of high performance fibre reinforced concrete slabs*, Proceedings of the 3rd HiPerMat Symposium, Kassel, Deutschland, 2012, pp. 749-756.

Moreillon L., Suter R., **Le Roy R.**, *Punching shear strength of high performance fibre reinforced concrete slabs*, Proceedings of the 8th *fib*-PhD Symposium, Copenhagen, Denmark, 2010, pp. 201-206.

Suter R., Moreillon L., *Punching shear strength of high performance fiber reinforced concrete slabs*, Proceedings of the 3rd *fib*-PCI Congress, Washington, USA, 2010, pp. 2103-2113.

Languages

French, mother tongue

English, intermediate

German, intermediate

Professional Affiliations

Association française de génie civil, AFGC

International Association for Bridge and Structural Engineering, IABSE

Swiss society of engineers and architects, SIA

Swiss Engineering, UTS

Ecole d'ingénieurs et d'architectes de Fribourg
Hochschule für Technik und Architektur Freiburg

UNIVERSITÉ PARIS-EST

Navier

Ecole doctorale SIE
Science, Ingénierie et Environnement

Poutres précontraintes en BFHP

Comportement au cisaillement

Rapport des essais

Doctorant :	Lionel MOREILLON
Directeur de thèse :	Robert LE ROY
Encadrant EIA-FR :	René SUTER

Table des matières

1. Introduction

1.1. Les bétons fibrés à hautes performances

La recherche active dans le domaine des matériaux cimentaires a mené au développement des bétons à hautes et ultra-hautes performances (BHP et BUHP). Les performances de ces bétons ne se limitent pas aux seules caractéristiques mécaniques mais englobent leur comportement rhéologique ainsi que leur durabilité élevée. La connaissance de plus en plus pointue du matériau béton a permis de définir ses qualités et ses faiblesses puis de remédier à ces dernières. Par rapport aux bétons ordinaires (BN), les bétons à hautes et ultra-hautes performances présentent une homogénéité et une compacité nettement plus élevée. Au niveau du matériau ceci se traduit par une résistance à la compression et un module d'élasticité plus élevés ainsi qu'une plus grande étanchéité aux agents extérieurs. Ces caractéristiques permettent au niveau structural, une réduction de la section des éléments porteurs et par conséquent une diminution du poids propre des structures et une durabilité accrue. Ces propriétés sont atteintes en abaissant le rapport eau/liant par l'emploi d'adjuvants haut réducteur d'eau ainsi qu'en optimisant le squelette granulaire ce qui favorise une diminution des pores. La granulométrie des BHP est généralement inférieure à celle d'un béton standard alors que pour les BUHP les graviers sont totalement supprimés. La quantité de liant est souvent supérieure à 400 kg/m^3 et se compose de ciment et d'additions réactives telles que les cendres volantes, les laitiers de haut fourneau et les fumées de silice. Néanmoins, l'augmentation de la compacité et de la résistance à la compression rend ces bétons plus homogènes mais fragiles. C'est pourquoi ces bétons sont généralement armés, frettés ou renforcés de fibres [1].

Figure 1 : Pont sur le Bras de la Plaine

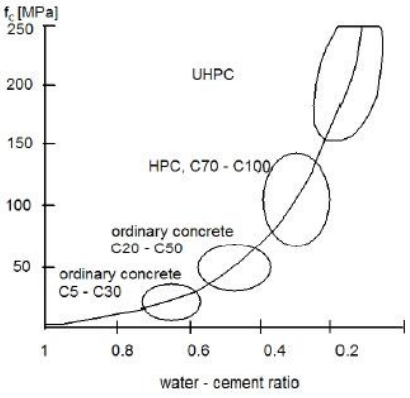

Figure 2 : Influence du rapport E/C

Depuis quelques années, les bétons à fibres (BF) sont sujets à de nombreux développements expérimentaux et industriels [18-24]. Ce matériau composite particulier présente des caractéristiques supérieures à celles des bétons ordinaires, notamment au niveau de ses résistances à la traction et au cisaillement, de sa rigidité à l'état fissuré ainsi que de sa ductilité. Les bétons à fibres se situent entre le béton non armé et le béton armé. Actuellement leurs utilisations restent cantonnées à des domaines d'applications spécifiques comme les dallages, les chaussées et le béton projeté. Les bétons fibrés à hautes performances (BFHP) reprennent une matrice cimentaire similaire au BHP, dans laquelle est ajoutée une certaine quantité de fibres métalliques. L'ajout de fibres permet aussi de rendre ces bétons plus ductiles en compression en assurant un certain frettage.

L'utilisation de bétons fibrés à hautes performances présente de nombreux avantages techniques et économiques pour tous les acteurs de la construction. Associés aux techniques de la précontrainte, ils ouvrent des voies nouvelles dans la conception de structures plus élancées et de systèmes porteurs innovants et durables. Les BFHP sont produits depuis plusieurs années en condition de laboratoire, par contre les applications pratiques restent marginales malgré leurs nombreux atouts. Les raisons de ce constat sont les suivantes : le manque de maîtrise de la production et de la mise en œuvre, la mauvaise connaissance des caractéristiques spécifiques et l'absence de règles cohérentes de dimensionnement.

1.2. Préfabrication en béton

La préfabrication en béton offre une large palette d'éléments de structure qui permettent de répondre à tout type de construction, bâtiments et infrastructures. Des temps de construction réduits, une haute qualité et une grande efficacité caractérisent les structures préfabriquées en béton. La préfabrication d'éléments béton en Suisse subi une forte concurrence du marché européen, ce qui demande des coûts et des délais de fabrication réduits afin de rester compétitifs.

Actuellement, selon les normes en vigueur, les âmes des poutres doivent être pourvues d'une armature minimale d'effort tranchant [34]. Dans la grande partie des applications pratiques, les éléments préfabriqués sont utilisés pour la couverture de toitures ou pour la réalisation de planchers commerciaux et industriels. Ils sont ainsi essentiellement soumis à des charges réparties de moyenne intensité ce qui engendre des sollicitations de cisaillement peu importantes.

L'armature d'effort tranchant complique la fabrication et augmente les coûts de production. Grâce à la ténacité non-négligeable en traction des BFHP, il serait possible de réduire l'armature d'effort tranchant voir d'y renoncer totalement [5/13/25]. Cependant, par la nature fragile d'une rupture par cisaillement et l'absence de règles établies pour les bétons fibrés, le remplacement des armatures transversales par un BFHP demande à être vérifié théoriquement et expérimentalement.

Figure 3 : Exemples de structures préfabriquées en béton

1.3. Objectifs et buts de l'étude

Dans le but d'analyser l'application de bétons fibrés à hautes performances pour la fabrication d'éléments préfabriqués précontraints sans armatures d'effort tranchant, l'Ecole d'ingénieurs et d'architectes de Fribourg (EIA-FR) a effectué des études théoriques et expérimentales. Les principaux objectifs sont les suivants :

- analyser le comportement à l'état limite de service (ELS) et à l'état limite ultime (ELU) d'éléments de structure en BFHP soumis à des sollicitations concentrées.
- modéliser le comportement au cisaillement d'éléments précontraints en BFHP sans armatures secondaires et établir des règles de dimensionnement de type ingénieur.
- montrer la faisabilité de produire, à des coûts compétitifs, des éléments de structure en BFHP dans une usine de préfabrication.

1.4. Etudes expérimentales

Les études expérimentales comprennent deux séries d'essai. Dans la première série, dénommée AV, les poutres ont une longueur de 5.6 m et sont testées en flexion 3 points sur une portée de 3.6 m. Six éléments de ce type ont été réalisé se distinguant par leurs dosage en fibres. Dans la deuxième série, dénommée AF, les poutres ont une longueur de 12,4 m et sont testées en flexion 4 points sur une portée de 12 m. Deux éléments ont été réalisés, l'un sans fibres et l'autre avec 60 kg/m^3 de fibres métalliques.

Les éléments d'essai ont une section identique d'une hauteur de 600 mm et de forme trapézoïdale. La disposition de la précontrainte et des armatures passives est par contre différente entre les poutres type AV et AF.

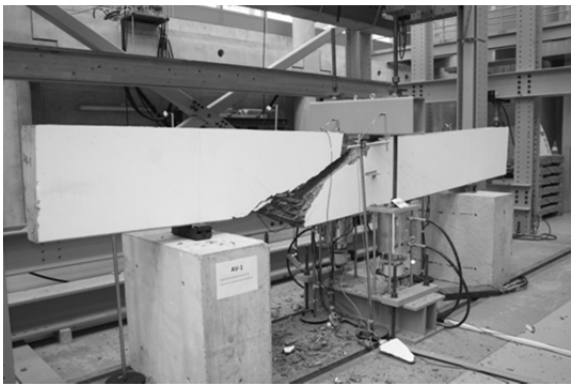

Figure 4 : Essais de charges type AV.

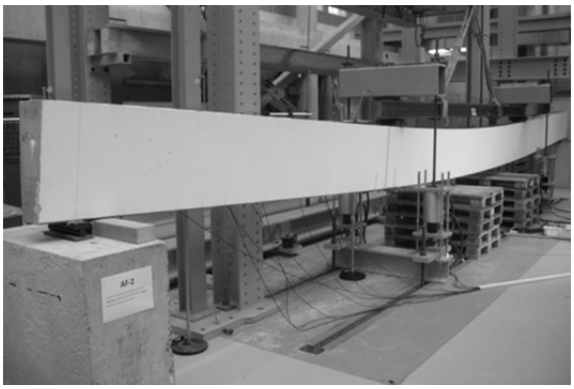

Figure 5 : Essais de charges type AF

2. Technologie des bétons

2.1. Formulations des bétons

Afin de répondre aux critères techniques, économiques et de mise en œuvre, les recettes de béton doivent satisfaire les exigences suivantes :

- résistance moyenne en compression de 100 MPa,
- bonne ouvrabilité : bétons auto-plaçant (Self Compacting Concrete)
- dosage en fibres métalliques compris entre 20 et 80 kg/m^3,
- réalisation en centrale à béton hors de l'endroit de bétonnage,
- emploi de granulats locaux utilisés par la centrale à béton.

Dans une première phase, des formulations de béton ont été développées en laboratoire. Les travaux ont porté sur l'optimisation du squelette granulaire ainsi que sur la composition du liant (ciment + additions) [3/12]. Dans une deuxième phase, des essais en centrale à béton ont été réalisés. A la suite de ces essais préliminaires, la formulation a dû être modifiée car la résistance en compression de 100 MPa n'a pas été atteinte. Le rapport E/L a été diminué et la composition du liant a été changée. La composition des bétons est similaire entre les différentes quantités de fibres. Cependant, la quantité de sables est augmentée à partir de 60 kg/m^3 de fibres afin d'améliorer la rhéologie.

Tableau 1 : Formulation des bétons

Composants		B1	B2	B3	B4	B5
Ajout [kg/m^3] / *[%v]*	Fibres métalliques Bekaert Dramix RC-80/30-BP	0	20 *0.25*	40 *0.51*	60 *0.76*	80 *1.02*
Sable 0-4 [kg/m^3]	Granulats roulés Provenance : St-Ours	732 *47%*			782 *50%*	
Gravier 4-8 [kg/m^3]	Granulats roulés Provenance : St-Ours	197 *13%*			203 *13%*	
Gravier 8-16 [kg/m^3]	Granulats roulés Provenance : St-Ours	608 *40%*			579 *37%*	
Ciment [kg/m^3]	CEM I 52,5R Vicem (Péry)	475				
Addition [kg/m^3]	Micro silice en suspension Elkem EMSAC 500S	62.5 *extrait sec*				
Adjuvant [kg/m^3]	Fluidifiant Sika ViscoCrete-20 PRO	9.0 *2.0%Cement*		11.0 *2.3%Cement*		
Eau efficace [litres/m^3]		138				
Eau ajoutée (granulats secs) [litres/m^3]		83		81		
Rapport E_{eff}/C		0.29				
Rapport E_{eff}/L		0.26				

Les fibres employées sont de type Bekaert Dramix RC-80/30-BP. Elles ont une longueur de 30 mm pour un diamètre de 0.38 mm et disposent de crochets aux extrémités. Le rapport de forme l_f/d_f est de 80. Les fibres sont composées d'un acier à haute teneur en carbone avec une résistance minimale en traction de 2300 MPa.

Les bétons ont été confectionnés en centrale dans un malaxeur à axe horizontale d'une capacité de 1.5 m^3. Des charges de 1 à 1.5 m^3 ont été réalisées selon la procédure suivante.

1 Mélange des granulats et du ciment à sec
2 Ajout de l'eau de gâchage et de l'adjuvant
3 Ajout de la micro silice en suspension
4 Malaxage de 90 secondes au minimum (éventuellement ajustement de l'eau)
5 Ajout progressif des fibres métalliques
6 Malaxage de 90 secondes

Figure 6 : Centrale à béton et transport du béton

Le béton est transporté en camion-malaxeur de la centrale à béton jusqu'à l'usine de préfabrication. Le temps de trajet est d'environ 5 minutes. Avant d'être versé dans la benne, le béton est malaxé 30 secondes à haute vitesse dans la toupie. Il est ensuite déversé dans le coffrage par une extrémité et étalé sur la longueur. Pour des quantités de fibres inférieures à 60 kg/m^3, les poutres n'ont pas été pervibrées. Pour les éléments AV-1 à AV-4, le béton s'est mis en place sans difficultés et aucuns défauts n'ont été constatés. Par contre, les poutres AV-5 et AV-6 contenant respectivement 60 et 80 kg/m^3 de fibres ont nécessité une pervibration au niveau des armatures longitudinales. Un premier coulage de ces deux éléments sans pervibration c'est traduit par un mauvais enrobage des torons et des armatures.

Figure 7 : Défauts d'enrobage poutres AV-5/6

Figure 8 : Coulage d'un élément d'essai

2.2. Caractéristiques du béton frais

Les caractéristiques des bétons frais on été analysées lors du bétonnage des éléments d'essai à l'usine de préfabrication d'Element SA à Tavel. Ces essais ont été réalisés par l'EIA-FR et comprennent, l'étalement (Slump flow), la masse volumique ainsi que la température de l'air et du béton frais.

Tableau 2 : Récapitulatif des valeurs d'essais sur béton frais

Béton	Date de confection	Dosage en fibres [kg/m^3]	Etalement final [mm]	Masse volumique [kg/m^3]	Température de l'air [C°]	Température du béton [C°]
B1a	20/8/2010	-	600	2'410	25.5	23.5
B1b	13/9/2010	-	620	2'405	22.0	24.0
B2	27/8/2010	20	650	2'442	26.0	27.5
B3	27/8/2010	40	700	2'438	26.0	27.0
B4a	10/9/2010	60	620	2'469	23.0	25.0
B4b	15/9/2010	60	650	2'465	21.0	25.5
B5	10/9/2010	80	460	2'500	23.0	24.5

L'ajout de fibres métalliques diminue l'ouvrabilité. Ceci peut être corrigé dans une certaine mesure par l'augmentation du dosage en fluidifiant. Pour des dosages en fibres métalliques supérieurs à 40 kg/m^3, le rapport sable/granulat doit être augmenté ainsi que la quantité de particules fines, ciment et/ou addition. En présence d'une densité d'armature élevée, les fibres ont tendance à créer un maillage avec l'armature, bloquant ainsi la progression des granulats. Le surdosage en adjuvant ne permet pas de résoudre ce problème. Lorsque le dosage en fibres devient important des mesures constructives doivent être prises en considération. L'enrobage et l'écartement des armatures passives devraient au moins être égaux à la longueur des fibres l_f.

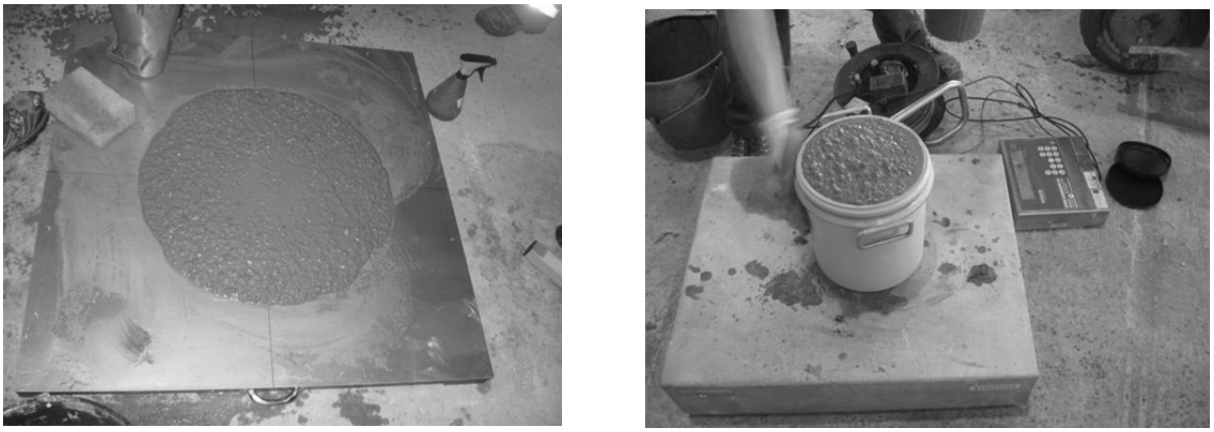

Figure 9 : Essai d'étalement Slump flow et mesure de la masse volumique

2.3. Caractéristiques mécaniques du béton

Les caractéristiques mécaniques des bétons ont été identifiées au sein du Laboratoire des Structures de l'EIA-FR. Les échantillons ont été confectionnés à l'usine d'Element SA à Tavel lors du bétonnage des éléments d'essai.

Caractéristiques en compression

Le module d'élasticité E_c et la résistance en compression sur cylindre f_c ont été déterminés à partir de quatre cylindres ϕ150 x 300 mm pour chaque type de béton. Le module d'élasticité E_c a été défini en fixant une contrainte supérieure de 40 MPa correspondant à $0.4f_{cm}$.

Tableau 3 : Caractéristiques des bétons en compression

Béton	Date du coulage	Dosage en fibres [kg/m^3]	f_{cm} [MPa]	E_{cm} [MPa]
B1a	20/8/2010	-	94.9	37'900
B1b	13/9/2010	-	93.6	36'380
B2	27/8/2010	20	91.6	40'340
B3	27/8/2010	40	97.5	39'750
B4a	10/9/2010	60	102.2	37'160
B4b	15/9/2010	60	106.6	37'500
B5	10/9/2010	80	100.8	37'250
			98.2	38'040

La résistance moyenne à la compression f_{cm} est plus faible que celle visée ceci dû principalement aux granulats. La variation de résistance entre les différents bétons est de l'ordre de 5%. Cependant, cette étude montre la faisabilité de réaliser des BHP dans des conditions pratiques. Avec une installation de malaxage moderne disposant d'un contrôle précis de l'humidité des sables et des granulats ainsi que d'un dosage automatique des additions et des fibres, ce type de béton est facilement réalisable à l'échelle industrielle.

Caractéristiques en traction du BHP

La résistance en traction f_{ct} a été déterminée au moyen d'essais de poinçonnement et de flexion 4 points. L'essai de poinçonnement ou "double punch test" consiste à soumettre un cylindre ϕ150 x 150 mm à un effort de compression concentré au travers de deux poinçons ϕ37.5 mm en acier. Ces essais ont seulement été réalisés sur la formulation B1 sans fibres.

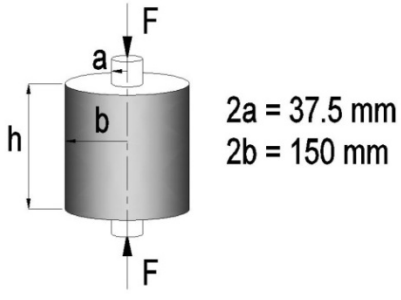

$$f_{ct} = \frac{F_u}{\pi \cdot \left(1.2 \cdot b \cdot h - a^2\right)}$$

Figure 10 : Configuration de l'essai de poinçonnement

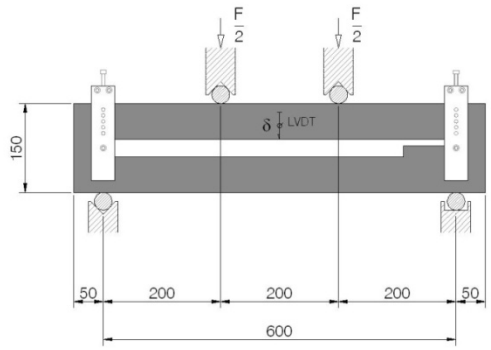

$$f_{ct}' = \frac{F_u \cdot l}{b \cdot h^2}$$

Figure 10 : Configuration de l'essai de flexion 4 points

Tableau 4 : Caractéristiques du BHP B1 en traction

Béton	Dosage en fibres [kg/m^3]	f_{ct} [MPa]	f_{ct}' [MPa]	f_{ct}'/f_{ct} [-]
B1	-	5.3	5.7	1.08

Figure 11 : Essais de poinçonnement sur cylindre

Caractéristiques en traction des BFHP

Afin de déterminer les caractéristiques en traction des bétons à fibres, les recommandations Rilem TC 162 [31/32] et *fib* Model Code 2010 [29/30] recommandent des essais de flexion 3 points sur prisme entaillé. Cet essai est normalisé par la norme européenne EN 14'651 [33]. La méthode permet de déterminer la limite de proportionnalité (LOP) ainsi qu'un ensemble de valeurs de la résistance résiduelle à la traction par flexion. Les résultats permettent de déterminer la loi de comportement intrinsèque du béton à fibres en traction en utilisant une méthode inverse.

Les prismes ont une longueur de 550 mm pour une section de 150 x 150 mm et sont entaillés au centre sur une hauteur de 25 mm. Ils sont testés en flexion 3 points sur une portée de 500 mm. L'évolution de la force, de la flèche au centre δ et l'ouverture de l'entaille *CMOD* sont mesurées. Quatre poutrelles ont été testées pour les BFHP B2 à B5.

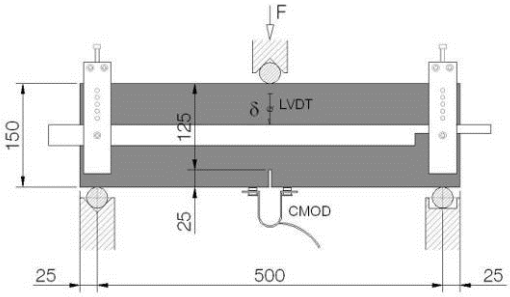

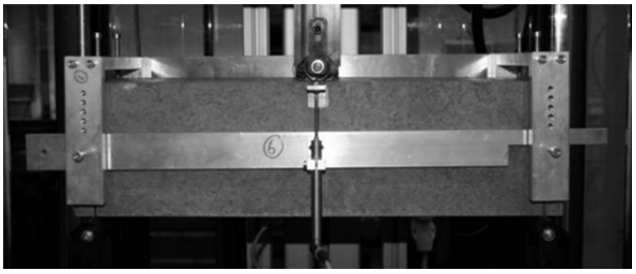

Figure 12 : Configuration de l'essai de flexion 3 points

La limite de proportionnalité (LOP) $f^{f}_{ct.L}$ correspond à la contrainte maximale pour un CMOD compris entre 0 et 0.05 mm. Les résistances résiduelles f_{Rj} correspondent aux contraintes pour un CMOD de 0.5, 1.5, 2.5 et 3.5 mm. La distribution des contraintes est admise élastique.

$$\sigma_{equ} = \frac{3 \cdot F \cdot l}{2 \cdot b \cdot h_{sp}^2}$$

Tableau 5 : Valeurs moyennes selon la norme EN 14'651

Béton	$f^{f}_{ct.L}$ [MPa]	f_{R1} [MPa]	f_{R2} [MPa]	f_{R3} [MPa]	f_{R4} [MPa]
B2	6.1	4.1	4.4	3.1	2.4
B3	6.7	8.9	9.9	8.2	6.5
B4a	7.6	11.9	11.8	11.0	9.7
B4b	7.5	10.7	11.0	8.9	7.2
B5	7.5	12.0	12.9	12.3	10.7

A partir de la relation d'essai force-ouverture de l'entaille, il est possible d'obtenir la loi intrinsèque en traction par la méthode inverse [26/27].

Equations d'équilibres

$$N = E \cdot \chi_m \cdot \left[\frac{h^2}{2 \cdot \alpha^2} + \left(\frac{h \cdot \sigma_t}{E \cdot \chi_m} - h^2 \right) \alpha + \left(\frac{h^2}{2} - \frac{h \cdot \sigma_t}{E \cdot \chi_m} \right) \right]$$

$$M = E \cdot \chi_m \cdot b \left[\frac{h^3}{6} \alpha^3 + \frac{h^2 \cdot \sigma_t}{2 \cdot E \cdot \chi_m} \alpha - \frac{h^3}{2} \alpha + \frac{h^3}{3} - \frac{h^2 \cdot \sigma_t}{2 \cdot E \cdot \chi_m} \right]$$

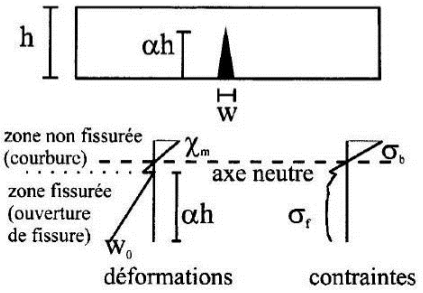

Relation cinématique

$$w = \left[\chi_m + 2 \cdot \chi_e \right] \cdot \frac{2(\alpha \cdot h)^2}{3} \quad \text{avec} \quad \chi_e = \frac{M}{E \cdot I}$$

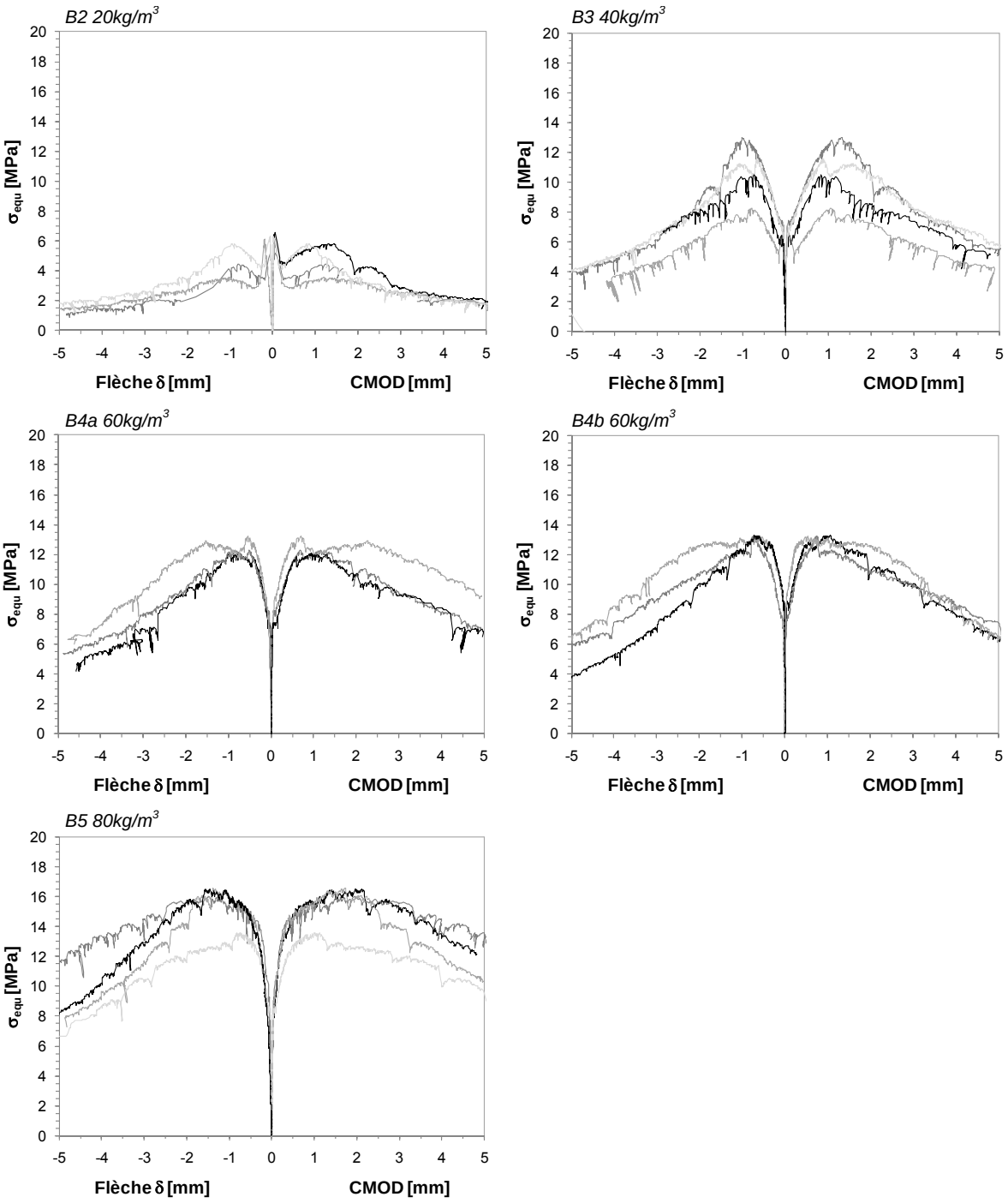

Figure 13 : Relations σ_{equ} - flèche et σ_{equ} - CMOD des essais de flexion sur prismes entaillés.

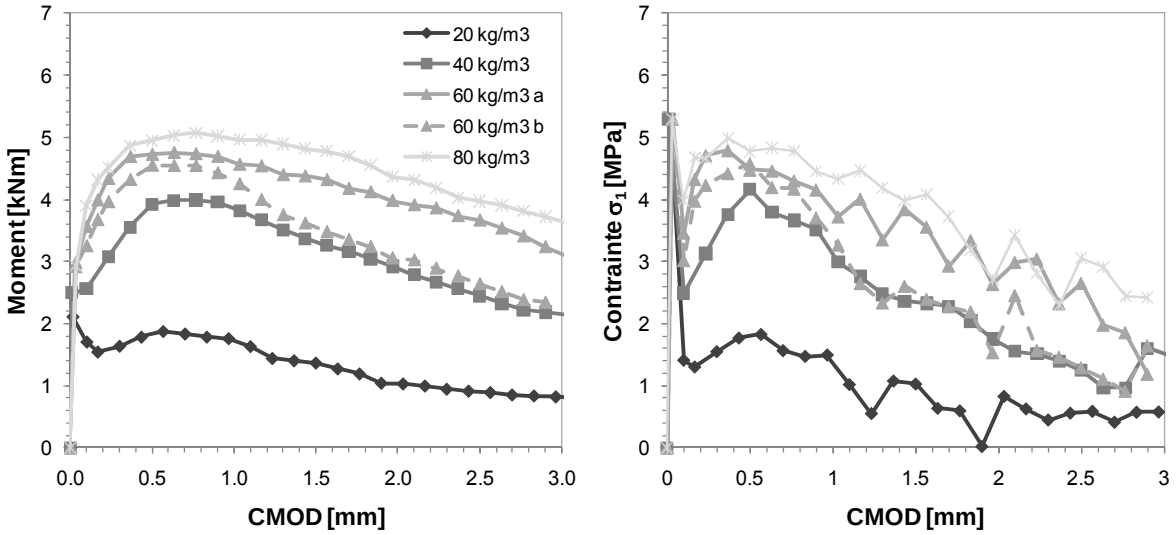

Figure 14 : Courbes moyennes Moment - CMOD des essais de flexion sur prismes entaillés et réponse de la méthode inverse contrainte - CMOD.

Les résultats des essais de flexion 3 points sur prismes entaillés montrent qu'à partir d'un dosage en fibres de 40 kg/m^3, les BFHP testés ont un comportement durcissant en flexion. C'est-à-dire que la résistance maximale post-fissuration est supérieure à la résistance de la matrice cimentaire. Le béton B2 contenant 20 kg/m^3 a un comportement adoucissant. Le gain de résistance est significatif entre les dosages en fibres de 20 et 40 kg/m^3 et devient moins importants pour les dosages supérieurs. Cependant, la dégradation de résistance est moins élevée pour une quantité de fibres importante. Pour un même dosage en fibres de 60 kg/m^3, bétons B4a et b, la variation de résistance post-pic peut être non-négligeable.

L'essai sur prisme fait intervenir un effet de structure et ne permet pas de déterminer la loi de comportement intrinsèque en traction de manière directe. Le traitement des résultats par analyse inverse est nécessaire pour obtenir la loi de comportement. Les résultats de la méthode inverse montrent que les bétons testés ont un comportement adoucissant en traction directe. La résistance maximale post-pic est atteinte pour une ouverture de fissure *w* d'environ 0.5 mm.

2.4. Caractéristiques mécaniques des aciers

Les caractéristiques mécaniques des aciers d'armature et de précontrainte ont été déterminées au sein du Laboratoire des Structures de l'EIA-FR. Les essais ont été réalisés sur 6 barres de chaque diamètre en accordance avec les normes ISO 15'630 parties 1 et 3 "*Aciers pour l'armature et la précontrainte du béton – Méthode d'essai*".

Tableau 6 : Valeurs moyennes des aciers d'armature en fonction du diamètre

Diamètre [mm]	$f_{s0,2}$ [MPa]	f_u [MPa]	ε_u [%]	E_s [GPa]
ϕ6	547	630	5.4	202
ϕ22	565	674	10.4	200

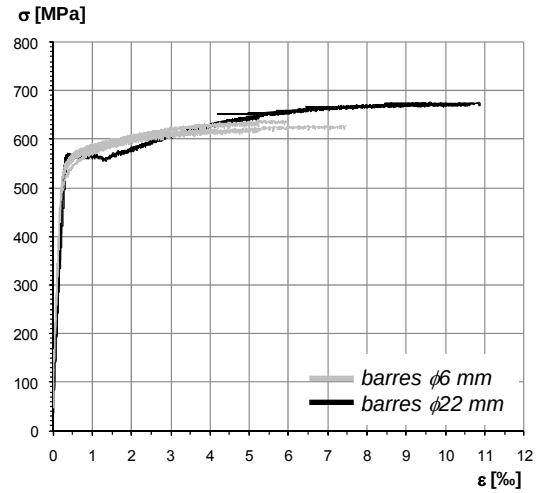

Figure 15 : Courbes contrainte – allongement des aciers d'armature

Tableau 7 : Valeurs moyennes des aciers de précontrainte

$f_{p0,1}$ [MPa]	f_u [MPa]	ε_u [%]	E_p [GPa]
1'832	1'982	3.1	206

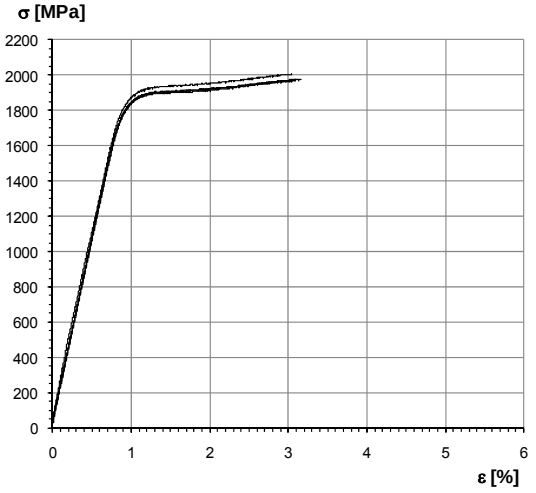

Figure 16 : Courbes contrainte – allongement des aciers de précontrainte

3. Description de l'étude expérimentale

3.1. Eléments d'essais

Poutres AV

Six éléments d'essai ont été confectionnés en usine de préfabrication. Les spécimens présentent les caractéristiques suivantes :

- longueur : 5.60 m
- hauteur : 600 mm
- largeur à la base : 170 mm
- largeur au sommet : 236 mm
- armature passive : 2 ϕ22 mm, d_s = 564 mm
- précontrainte : torons ϕ12.9 mm, A_p = 100 mm^2
  8 torons inférieurs
  2 torons supérieurs
  force de mise en tension $P_{0,tot}$ = 10x 130 kN

Les six éléments d'essai se distinguent par leur dosage en fibres métalliques.

- Poutre **AV-1** / BHP B1a sans fibres – étriers ϕ6 @150 mm
- Poutre **AV-2** / BHP B1a sans fibres
- Poutre **AV-3** / BFHP B2 20 kg/m^3
- Poutre **AV-4** / BFHP B3 40 kg/m^3
- Poutre **AV-5** / BFHP B4a 60 kg/m^3
- Poutre **AV-6** / BFHP B5 80 kg/m^3

La section est de forme trapézoïdale. Aux extrémités, les éléments d'essai AV-1 à AV-3 comprennent des étriers ϕ8 @150 mm afin d'introduire les forces de précontrainte. Les poutres AV-4 à AV-6 contiennent uniquement 4 étriers ϕ8 de positionnement des armatures longitudinales ϕ22 mm. Dans la partie centrale, l'élément AV-1 contient l'armature transversale minimale composée d'étriers ϕ6 @150 mm. Pour les autres éléments aucune armature transversale n'est disposée. L'enrobage minimal des barres est de 20 mm.

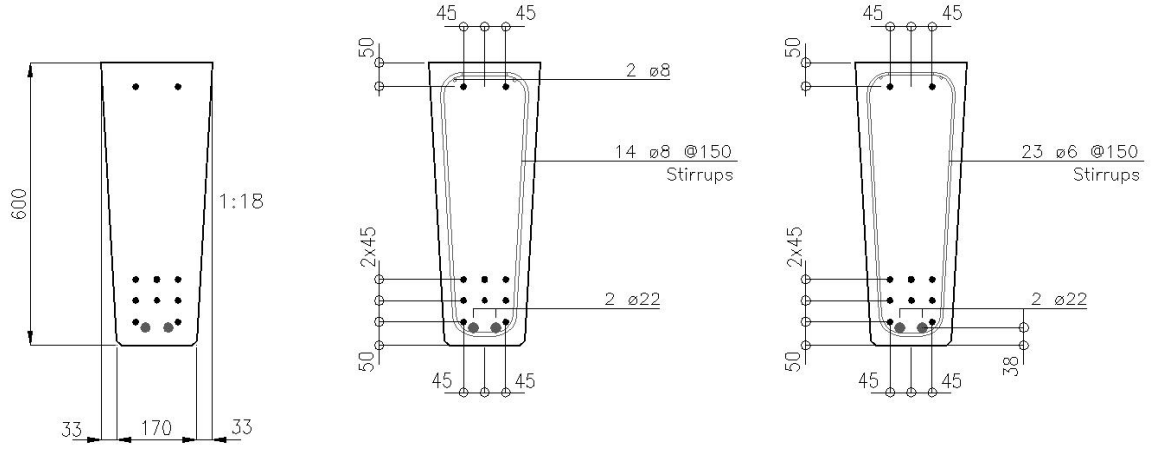

Figure 17 : Section et armatures des éléments d'essai AV

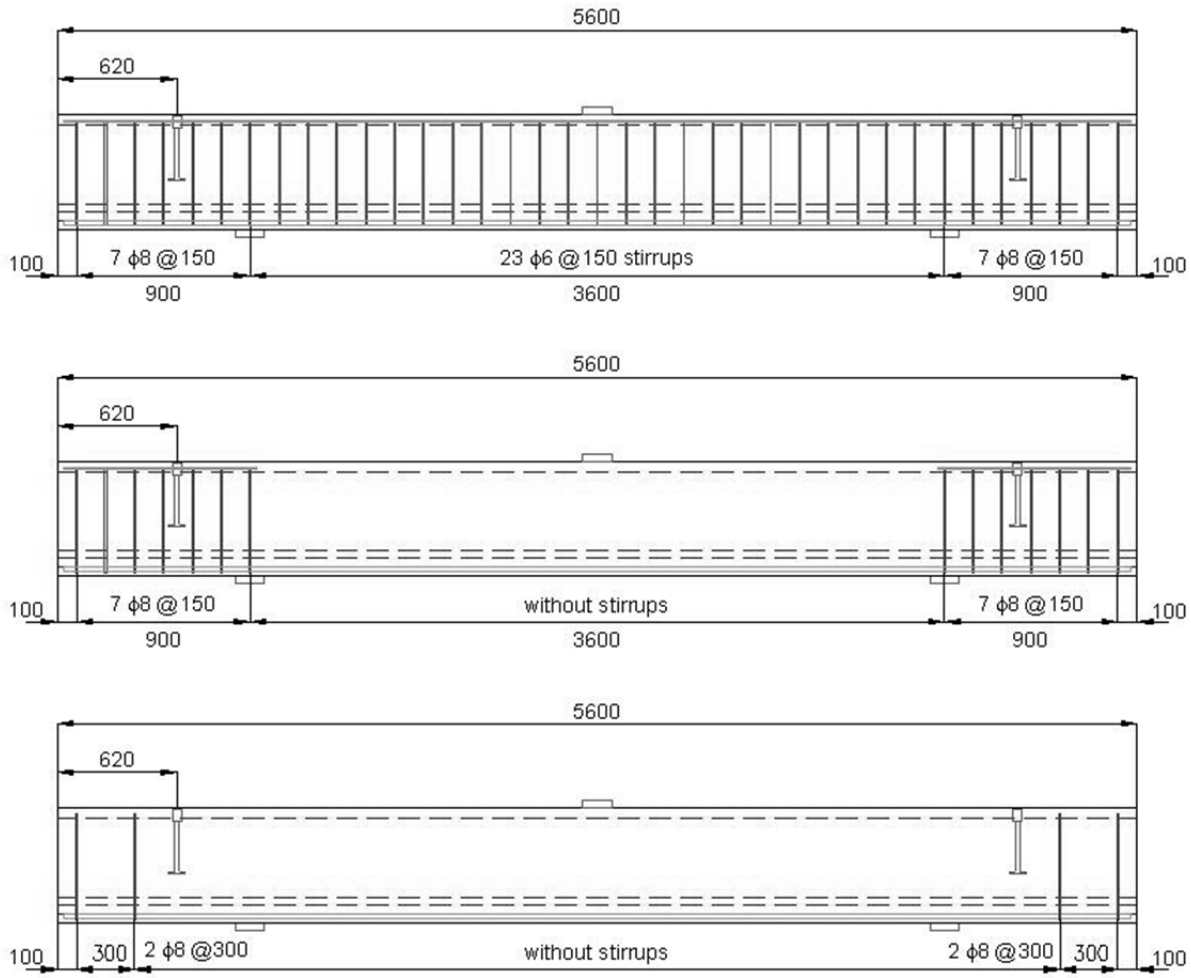

Figure 18 : Géométrie et armatures des éléments d'essai AV

Tableau 8 : Caractéristiques géométriques de la section

Aire [mm^2]	122E+3
Inertie [mm^6]	3'627E+3
Position z du centre de gravité depuis le haut de la section [mm]	284
Moment de la précontrainte [kNm]	167
Hauteur utile effective [mm]	512

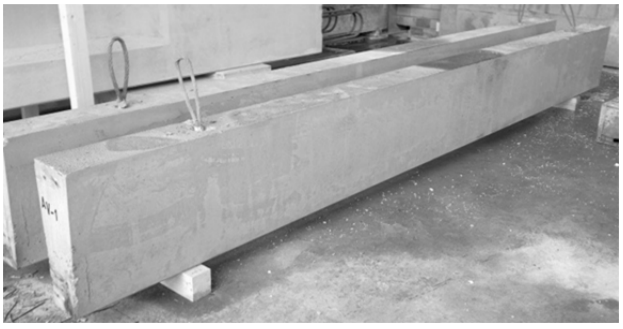

Figure 19 : Eléments AV après décoffrage

Poutres AF

Deux éléments d'essai de 12.40 m ont été confectionnés en usine de préfabrication. La section est identique aux éléments AV, par contre la disposition de la précontrainte et l'armature sont différentes. Les spécimens présentent les caractéristiques suivantes :

- longueur : 12.40 m
- hauteur : 600 mm
- largeur à la base : 170 mm
- largeur au sommet : 236 mm
- précontrainte : torons ϕ12.9 mm, A_p = 100 mm^2
  8 torons inférieurs
  2 torons supérieurs
  force de mise en tension $P_{0,tot}$ = 10x 130 kN

La poutre AF-1 est réalisée avec le BHP B1b (sans fibres) et la poutre AF-2 avec le BFHP B4b (60 kg/m^3 de fibres). Aux extrémités, les éléments d'essai comprennent une armature passive sous forme d'étriers et d'épingles afin d'introduire les forces de précontrainte et les réactions d'appui. Dans leur partie centrale, aucune armature passive n'est disposée.

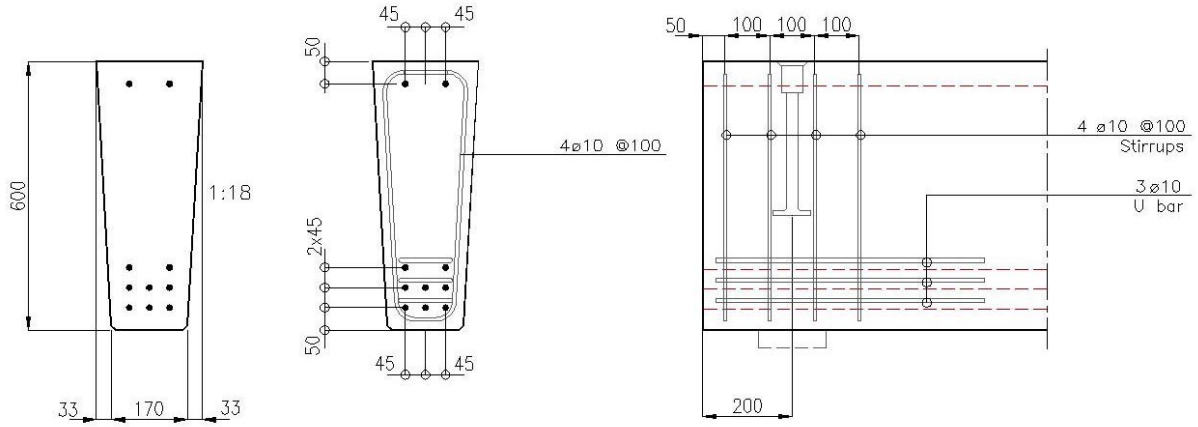

Figure 20 : Section et armatures des éléments d'essai AF

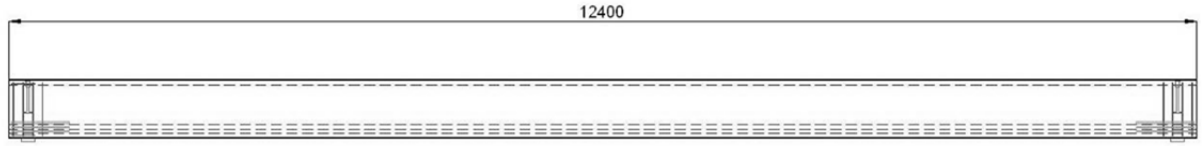

Figure 21 : Géométrie et armatures des éléments d'essai AF

Tableau 9 : Caractéristiques géométriques de la section

Aire [mm^2]	122E+3
Inertie [mm^6]	3'627E+3
Position z du centre de gravité depuis le haut de la section [mm]	284
Moment de la précontrainte [kNm]	180
Hauteur utile effective [mm]	507

3.2. Dispositifs d'essai

Poutres AV

Les essais de charge ont été effectués au sein du Laboratoire de Structures de l'EIA-FR, sur un dispositif d'essai d'une capacité totale de 2'000 kN. Les poutres sont testées sur une portée de 3.60 m. La charge est introduite au centre de l'élément. Dans cette configuration, le rapport géométrique portée de cisaillement sur hauteur utile a/d est de 3.52. Le système de chargement est composé d'un profilé creux relié aux deux vérins hydrauliques par des barres de précontrainte MSP ϕ32 mm. L'essai est dirigé en déplacement par un système d'asservissement servo-électronique reproduisant un chargement quasi-statique.

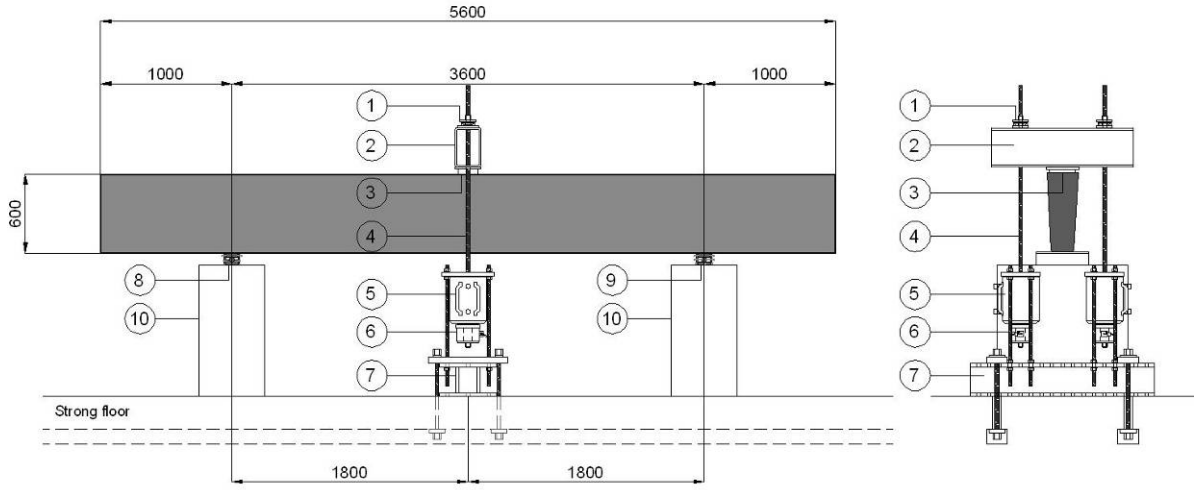

Figure 22 : Configuration des essais de charges, poutres AV

1 rotules sphériques SKF
2 profilé de chargement RRW 300/200/12.5
3 plaque de répartition en acier 200 x 150 x 15 mm callée au mortier
4 tiges de précontrainte MSP 32 mm
5 vérins à trou central Bieri 1'000 kN, course 160 mm
6 cellules de force HBM 1'000 kN
7 caisson composé-soudé d'ancrage
8 appui fixe, plaque d'introduction 300 x 80 x 30 mm
9 appui mobile, plaque d'introduction 300 x 80 x 30 mm
10 blocs d'appuis en béton

Cinq réseaux de capteurs permettent de mesurer les forces appliquées, les flèches, les allongements locaux du béton, les déformations dues au cisaillement et les allongements de la fibre tendue.

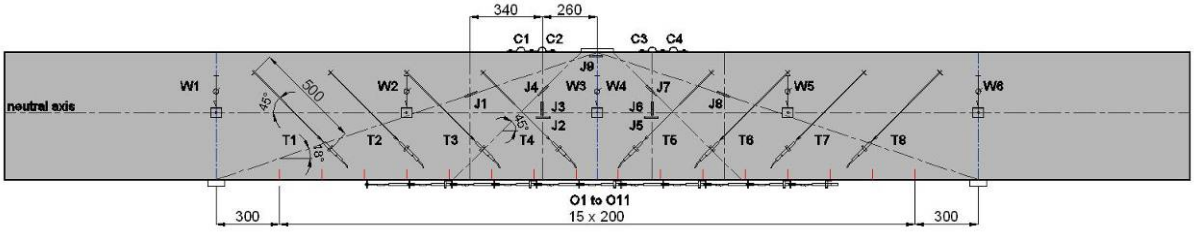

Figure 23 : Disposition et dénomination des capteurs, poutres AV

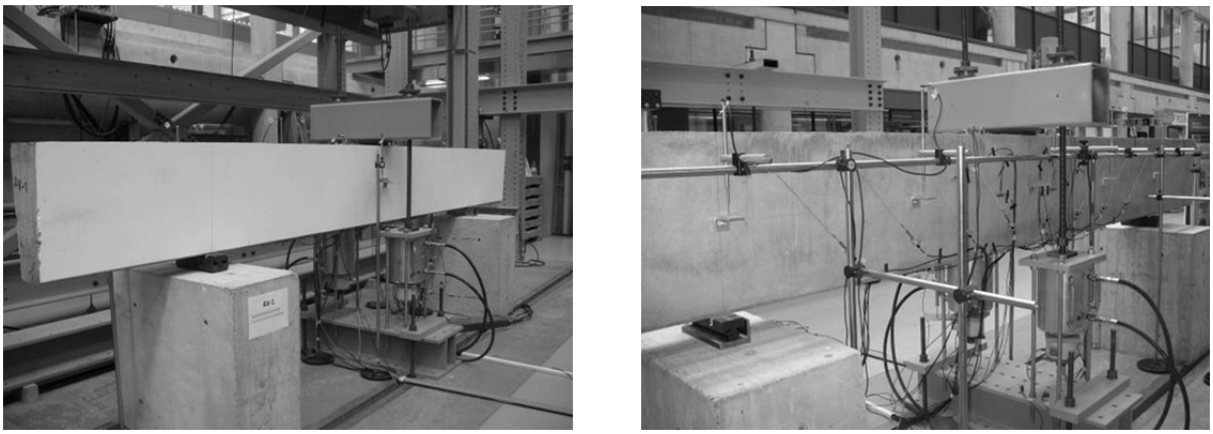

Figure 24 : Vues du dispositif d'essai et de mesures des poutres AV.

La mise en charge est appliquée par paliers de 20 kN jusqu'à la formation des premières fissures diagonales critiques. Un cycle de déchargement est effectué à une charge comprise entre 500 et 600 kN. A chaque palier, l'état de fissuration ainsi que l'ouverture la plus grande sont relevés.

Poutres AF

Les essais de charge ont été effectués au sein du Laboratoire de Structures de l'EIA-FR, sur un dispositif d'essai d'une capacité totale de 2'000 kN. Les poutres sont testées sur une portée de 12 m. La charge est introduite en deux points à une distance de 3.60 m des appuis. Dans cette configuration le rapport géométrique portée de cisaillement sur hauteur utile a/d est de 7.10. Le système de chargement est composé de profilés creux reliés aux quatre vérins hydrauliques par des barres de précontrainte MSP ϕ26.5 mm. Les deux charges sont reliées par un profilé HEM 160. L'essai est dirigé en déplacement par un système d'asservissement servo-électronique reproduisant un chargement quasi-statique.

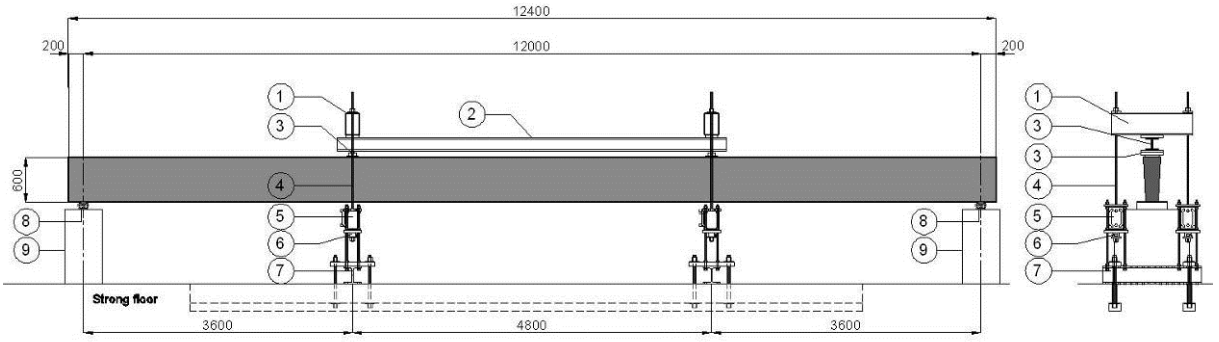

Figure 25 : Configuration des essais de charges, poutres AF

1 profilés de chargement RRW 300/200/12.5
2 profilé de liaison HEM 160
3 appuis fixes avec plaques d'introduction 200 x 150 x 15 mm
4 tiges de précontrainte MSP 26.5 mm
5 vérins à trou central Bieri 500 kN, course 160 mm
6 cellules de force HBM 200 ou 500 kN
7 profilés d'ancrage HEM 260
8 appuis mobiles, plaque d'introduction 300 x 80 x 30 mm
9 blocs d'appuis en béton

Cinq réseaux de capteurs permettent de mesurer les forces appliquées, les flèches, les allongements locaux et les allongements de la fibre tendue.

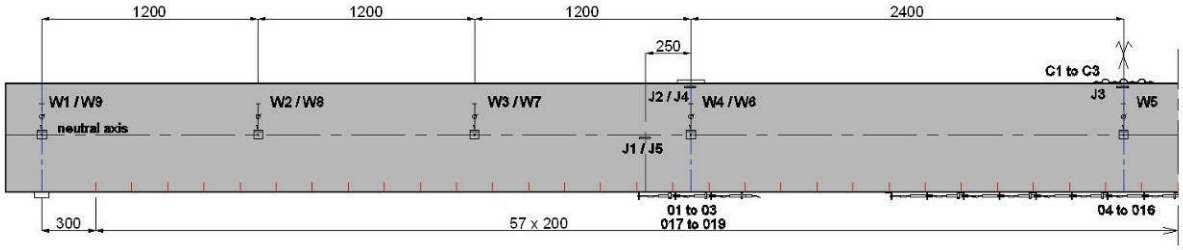

Figure 26 : Disposition et dénomination des capteurs, poutres AF

Figure 27 : Vues du dispositif d'essai et de mesures, poutres AF

La mise en charge est appliquée par paliers de 20 kN (charge totale) jusqu'à la rupture de l'élément. Des cycles de déchargement sont effectués à des charges de 200 et 280 kN. A chaque palier, l'état de fissuration ainsi que l'ouverture de la plus grande fissures sont relevés.

4. Résultats

4.1. Poutre AV-1 *(BHP sans fibres avec étriers ϕ6 @150)*

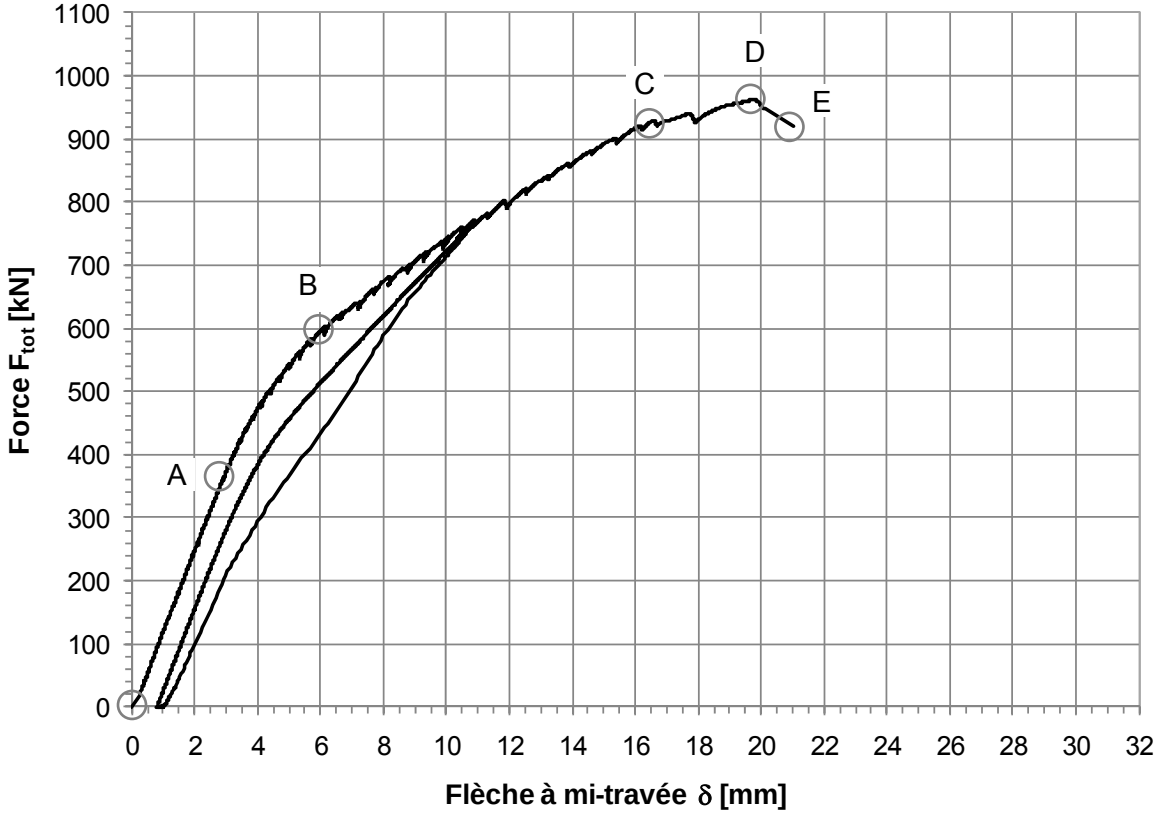

Figure 28 : Relation force-flèche à mi-travée de l'élément AV-1

Le stade I, élastique non-fissuré, s'étend entre les points 0 et A. Les premières fissures apparaissent au point A sous une charge F de 360 kN. A partir de ce point, la fissuration se développe et la rigidité diminue progressivement. Au point B, sous une charge F de 600 kN se forment les premières fissures diagonales. Entre les points B et C, plusieurs fissures diagonales se développent de part et d'autre de la charge. Le comportement reste néanmoins linéaire. Cependant, les fissures diagonales évoluent plus rapidement que les fissures de flexion. Au point C, sous une charge de 920 kN, la courbe marque un nouveau point d'inflexion indiquant la plastification des armatures transversales. A partir de ce point, les déformations se concentrent sur une seule fissure diagonale. La charge maximale de 962 kN est atteinte au point D. Le béton de la table de compression, en pointe de la fissure diagonale du côté droit, s'écrase progressivement marquant une chute de résistance. Au point E intervient brutalement la rupture de l'élément par cisaillement.

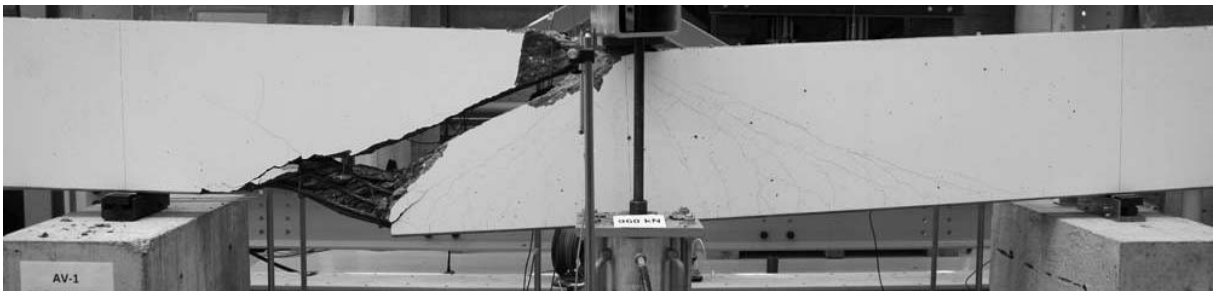

Figure 29 : Aspect à la rupture de l'élément AV-1

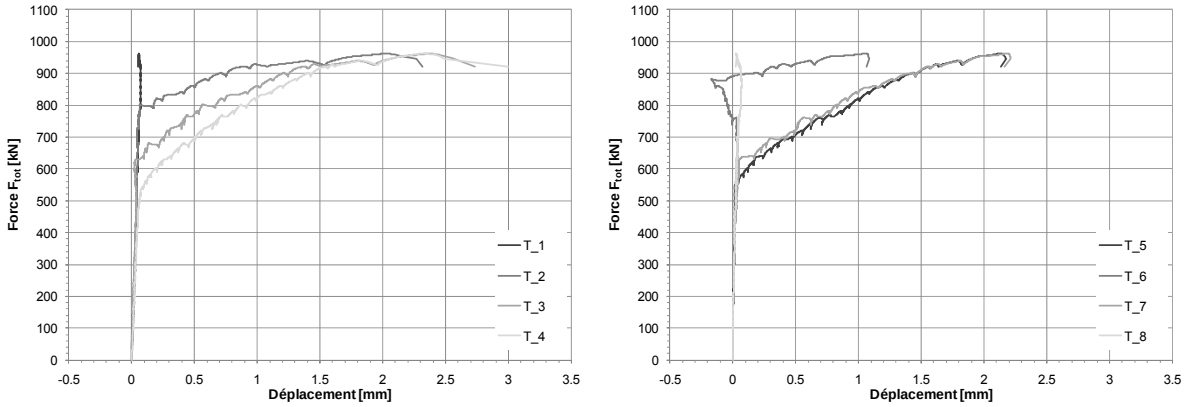

Figure 18 : Relations force - déplacement des capteurs diagonaux

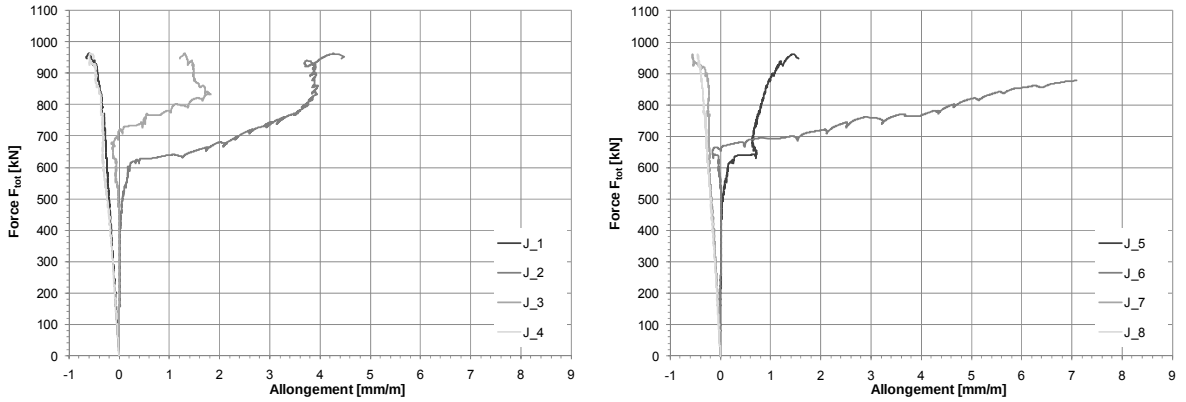

Figure 19 : Relations force - allongement des jauges extensométriques

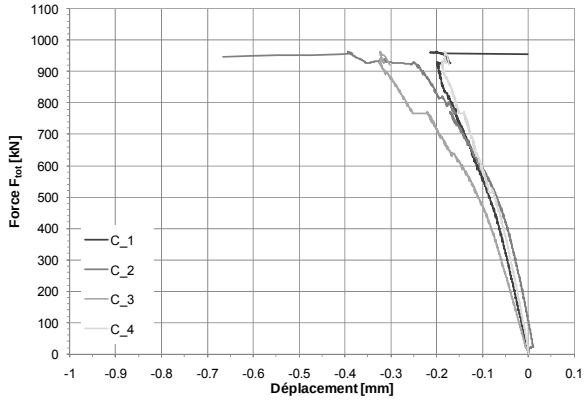

Figure 30: Relations force – déplacement des capteurs Oméga

F = 600 kN

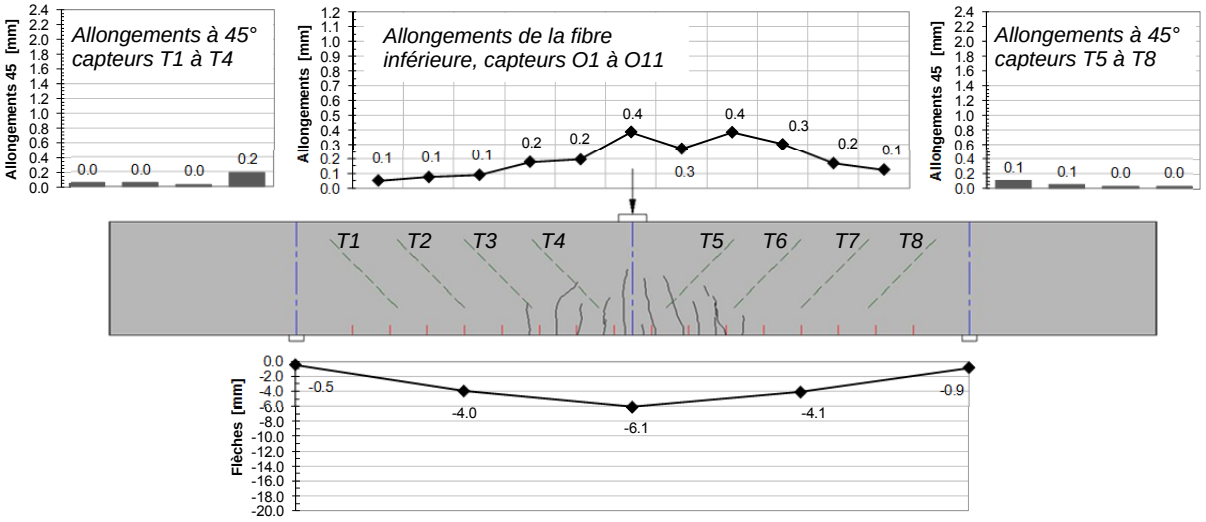

F = 700 kN

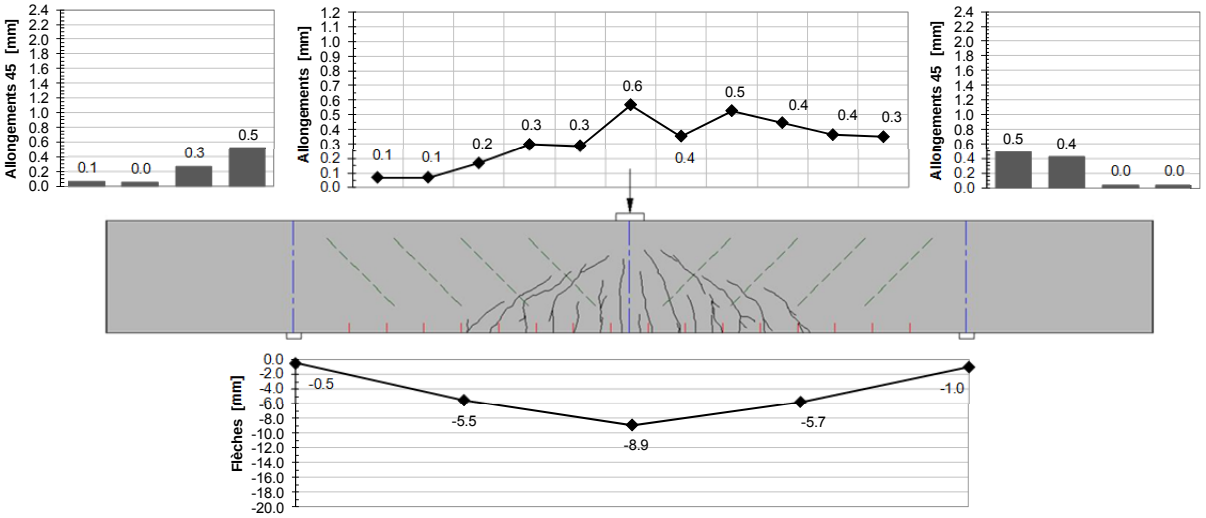

F = 800 kN

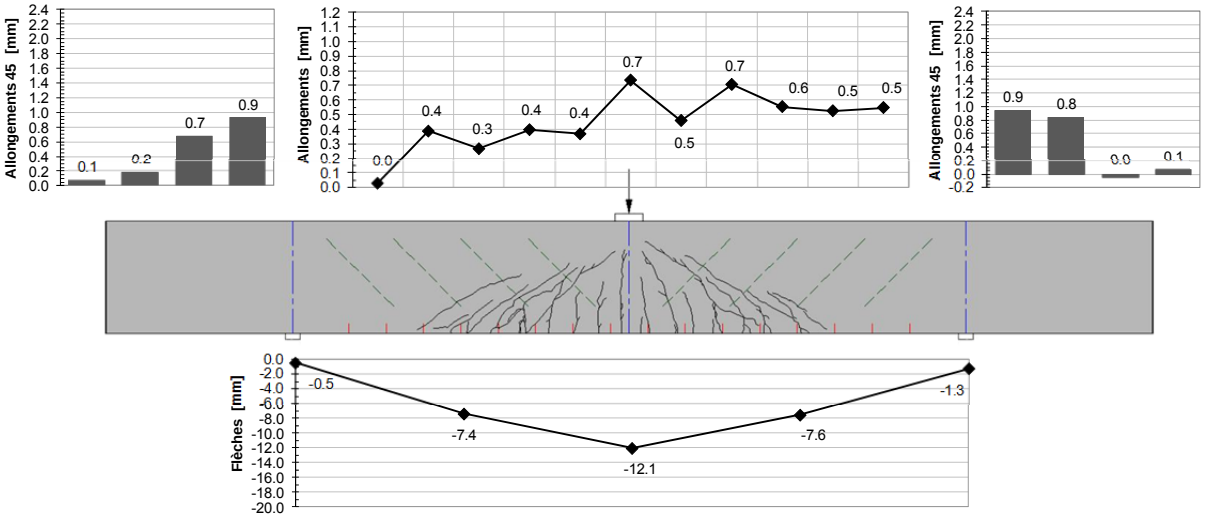

F = 900 kN

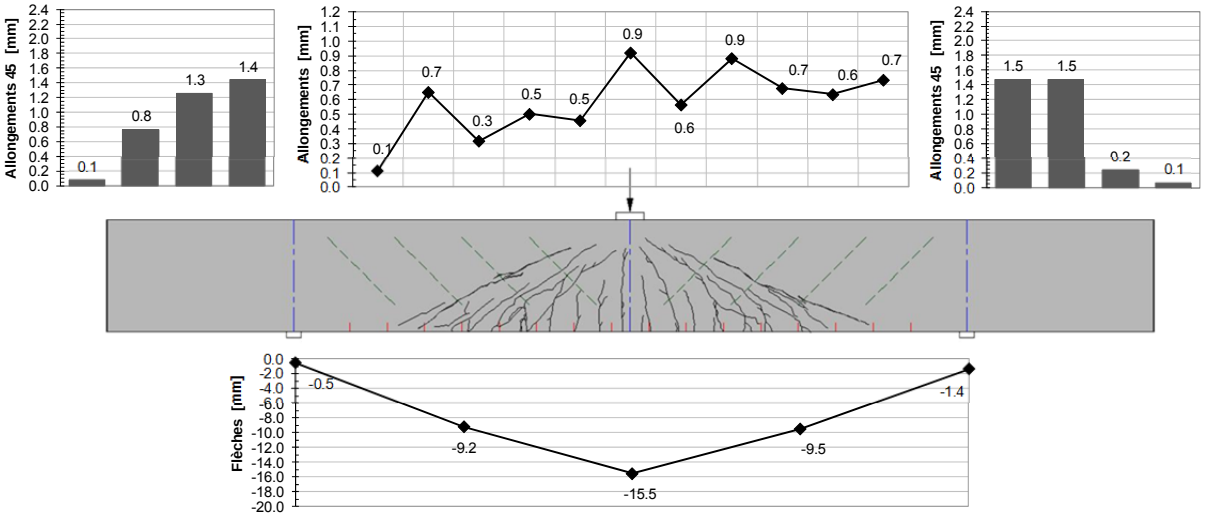

F_u = 962 kN

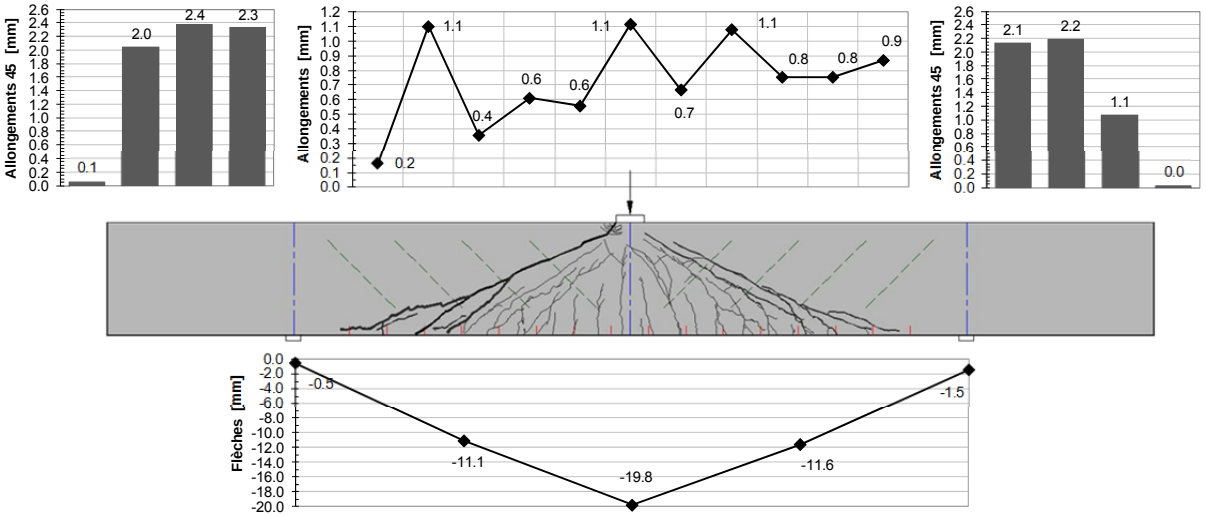

4.2. Poutre AV-2 *(BHP sans fibres)*

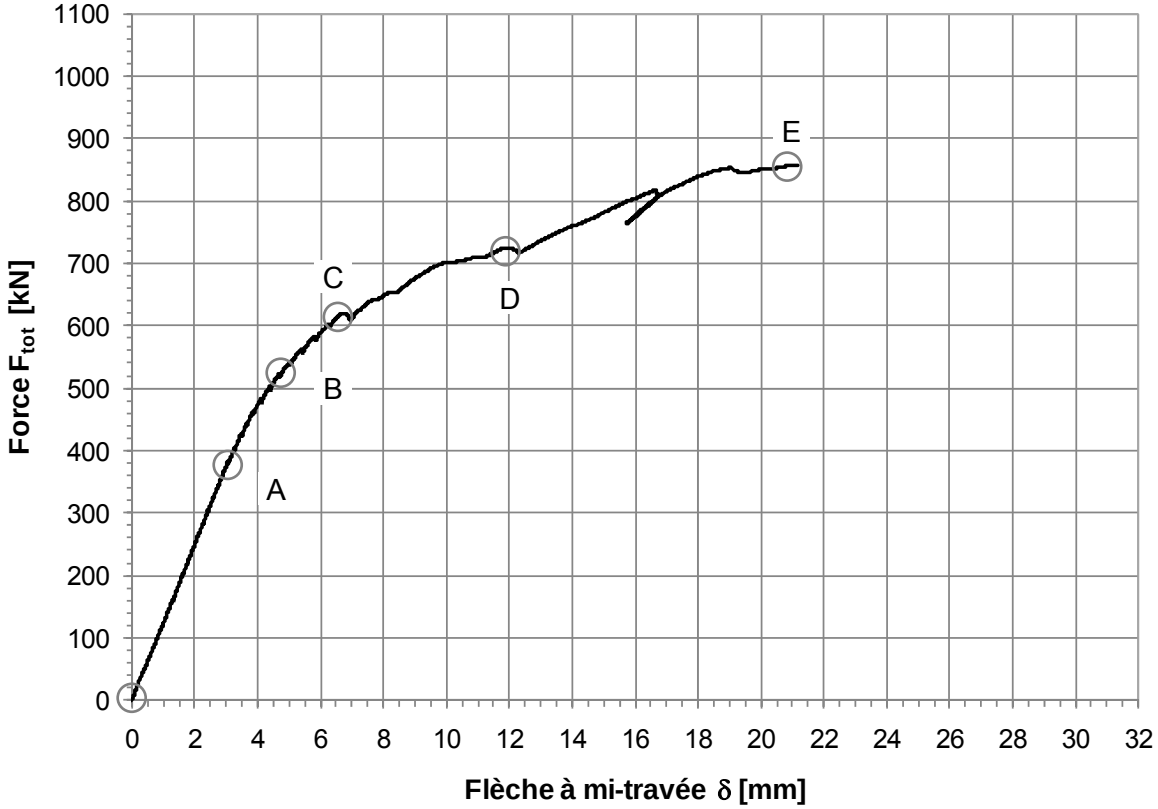

Figure 31 : Relation force-flèche à mi-travée de l'élément AV-2

Le stade I, élastique non-fissuré, s'étend entre les points 0 et A. Les premières fissures apparaissent au point A, sous une charge de 380 kN. A partir de ce point, la fissuration se développe et la rigidité diminue progressivement. Les premières fissures diagonales apparaissent au point B sous une charge de 580 kN. A partir de ce point, la fissuration de cisaillement évolue plus rapidement que les fissures de flexion. Au point C sous une charge de 620 kN, la courbe marque un point d'inflexion correspondant au développement d'une première fissure critique de cisaillement, du côté gauche. Cette fissure évolue rapidement mais ne provoque pas la rupture. La précontrainte supérieure empêche la progression des fissures diagonales à travers la membrure comprimée. Au point D, sous une charge de 720 kN la courbe marque un nouveau point d'inflexion indiquant la formation d'une deuxième fissure critique du côté droit. La rupture par cisaillement intervient brutalement au point E suite à l'éclatement du béton de la table de compression, sous une charge de 858 kN.

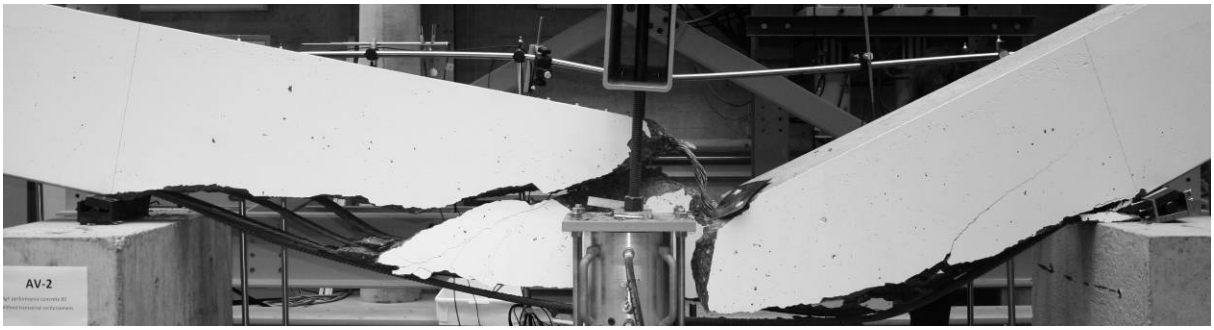

Figure 32 : Aspect à la rupture de l'élément AV-2

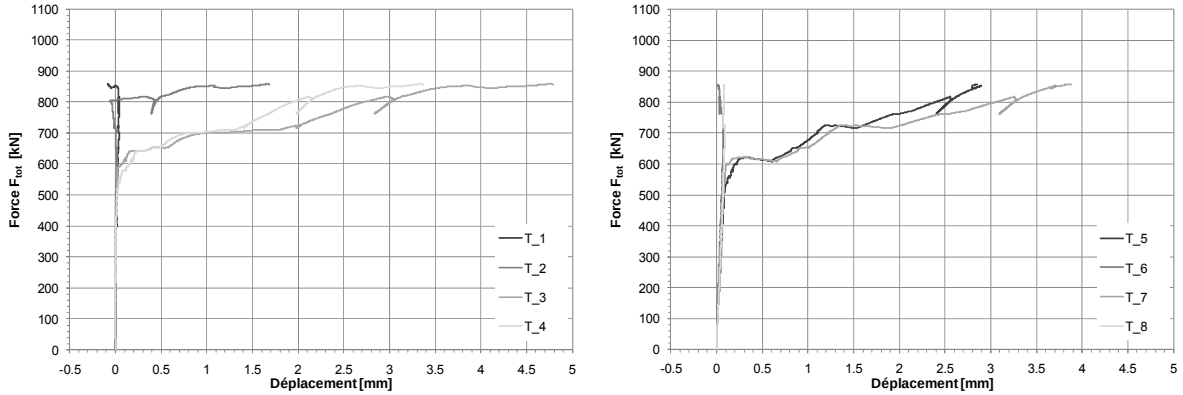

Figure18 : Relations force - déplacement des capteurs diagonaux

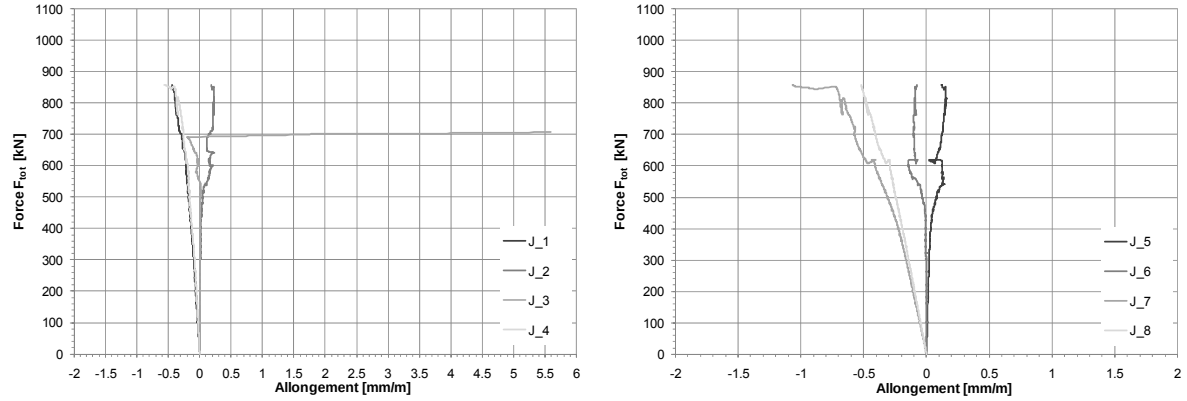

Figure 19 : Relations force - allongement des jauges extensométriques

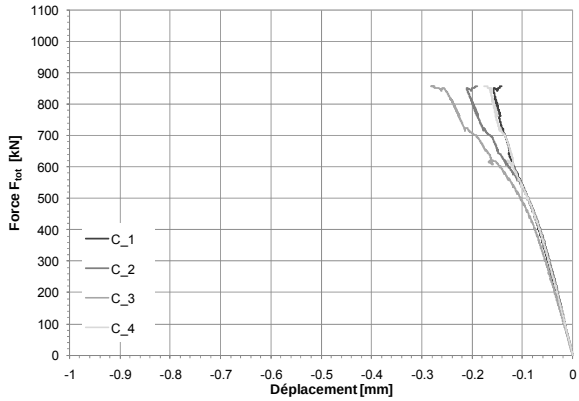

Figure 33 : Relations force – déplacement des capteurs Oméga

F = 600 kN

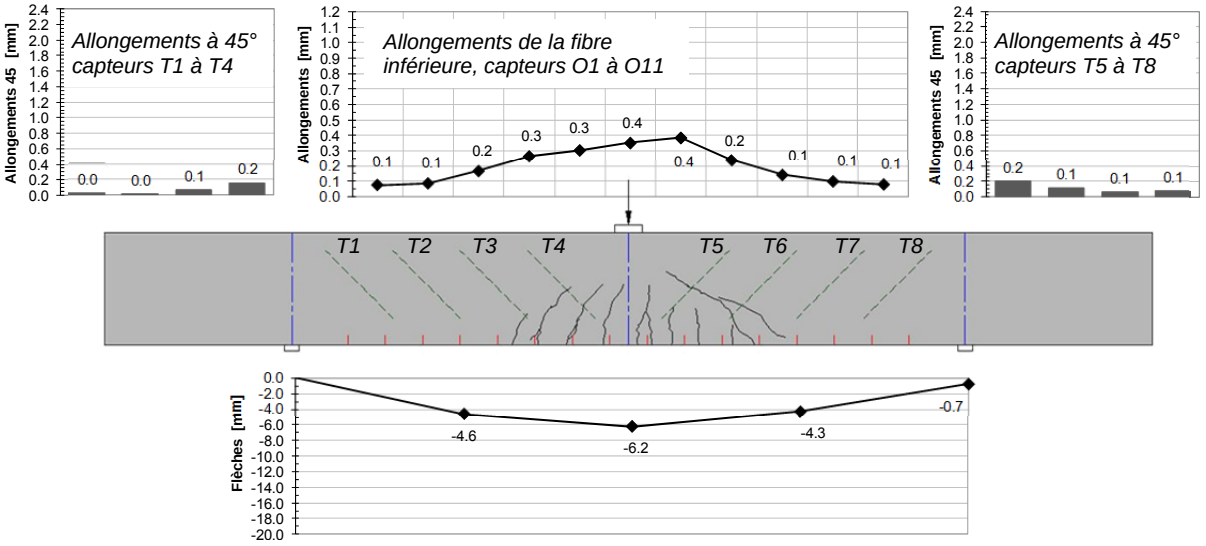

F = 800 kN

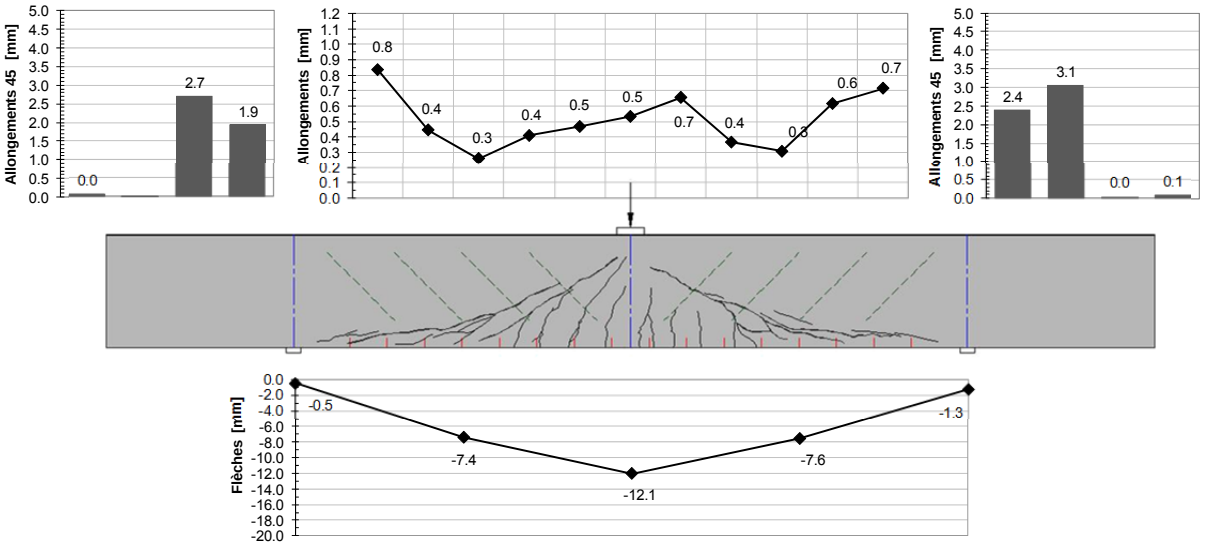

F_u = 858 kN

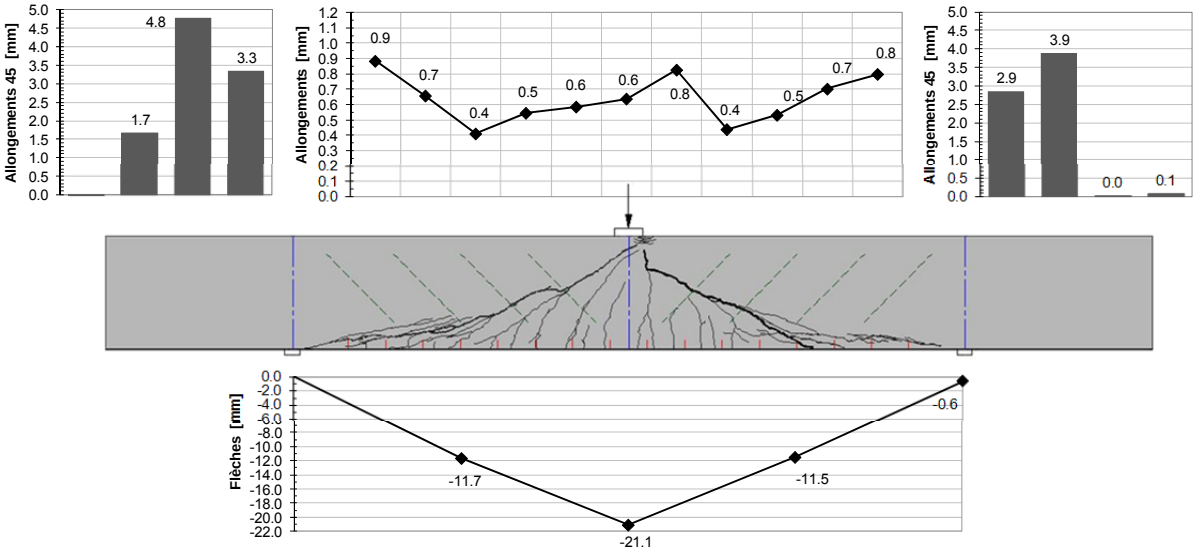

4.3. Poutre AV-3 *(BFHP avec 20 kg/m^3 de fibres)*

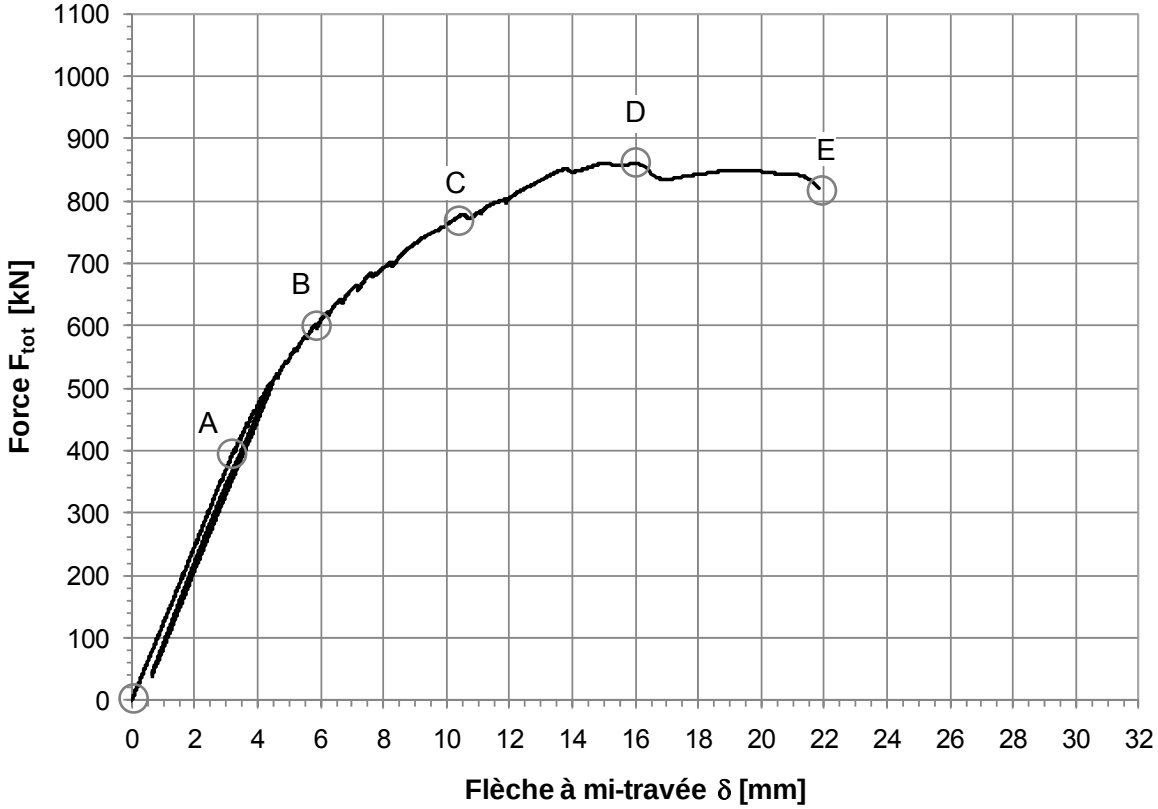

Figure 34 : Relation force-flèche à mi-travée de l'élément AV-3

Le stade I, élastique non-fissuré, s'étend entre les points 0 et A. Les premières fissures apparaissent au point A sous une charge F de 400 kN. A partir de ce point, la fissuration se développe et la rigidité diminue progressivement. Au point B, sous une charge de 600 kN, apparaissent les premières fissures diagonales. Entre les points B et C, plusieurs fissures diagonales se développent. Au point C, sous une charge de 780 kN, la courbe marque un point d'inflexion indiquant le développement d'une fissure critique de cisaillement du côté gauche. A nouveau, la précontrainte supérieure empêche la progression des fissures de cisaillement à travers la membrure comprimée. Entre les points C et D, les fissures diagonales du côté gauche s'ouvrent de plus en plus. La charge maximale de 860 kN est atteinte au point D. A partir de ce point la résistance diminue, le béton de la table de compression en pointe de la fissure diagonale s'écrase progressivement. Au point E, sous une charge de 820 kN, intervient brutalement la rupture de l'élément par cisaillement.

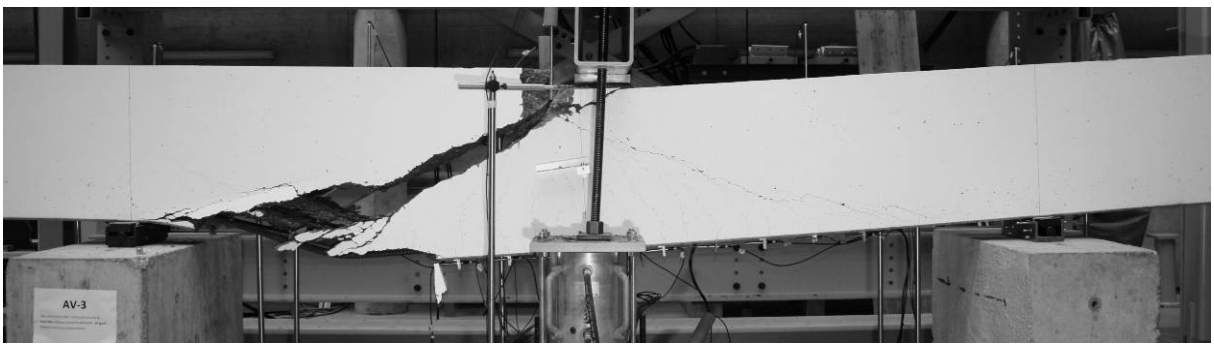

Figure 35 : Aspect à la rupture de l'élément AV-3

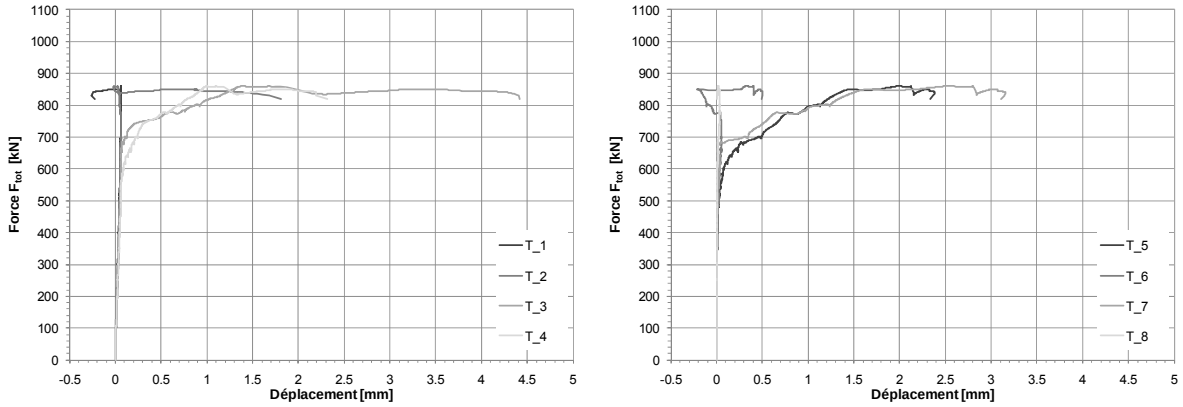

Figure18 : Relation force - déplacement des capteurs diagonaux

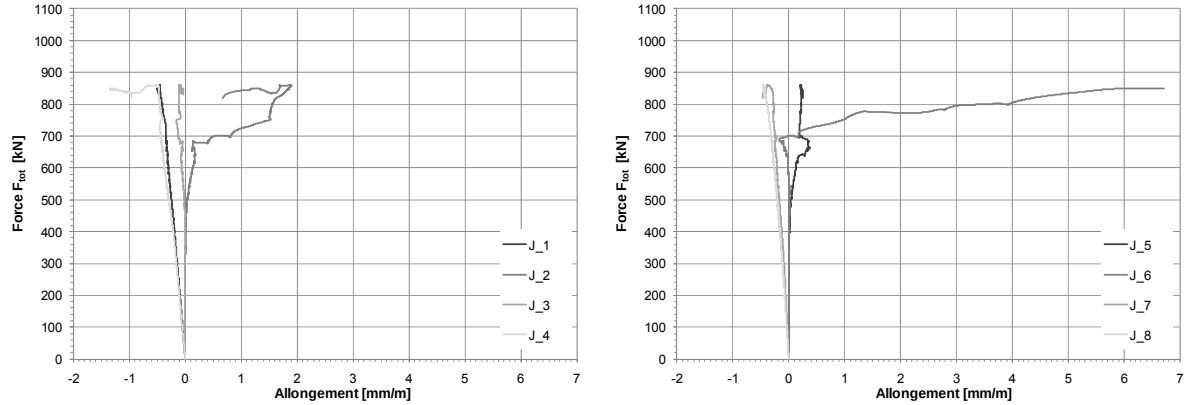

Figure 19 : Relations force - allongement des jauges extensométriques

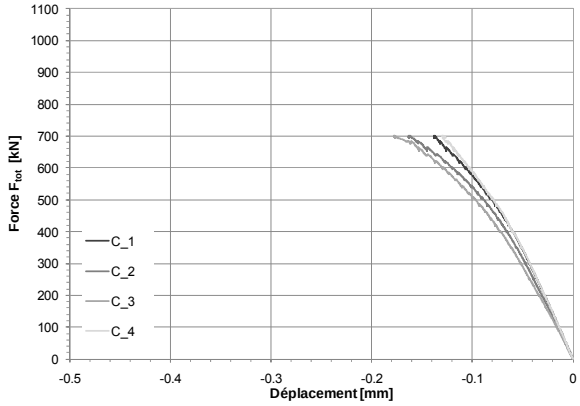

Figure 36 : Relations force – déplacement des capteurs Oméga

F = 600 kN

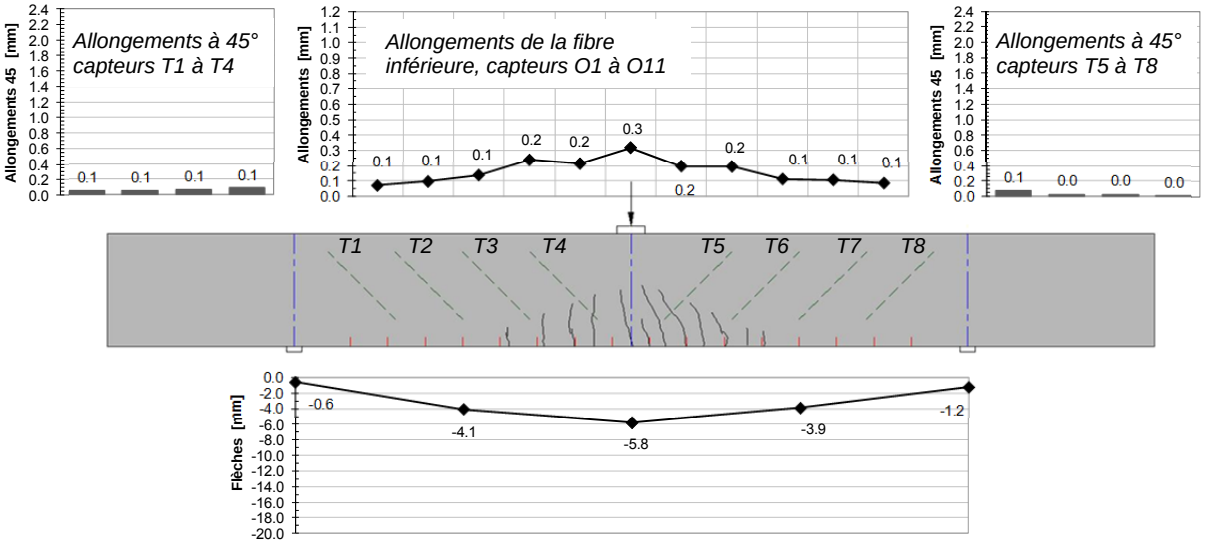

F = 700 kN

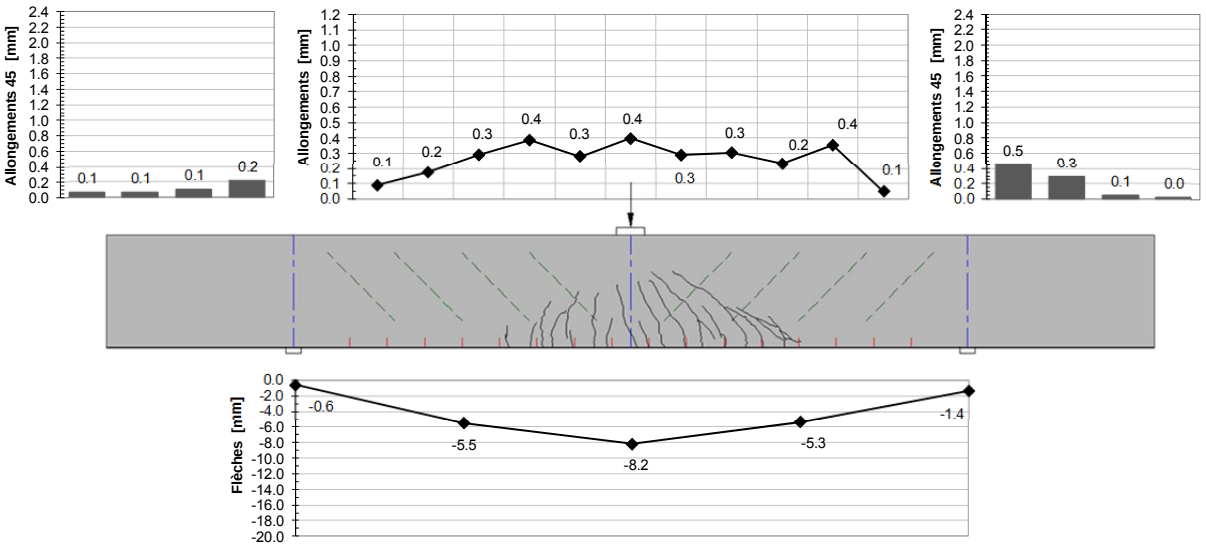

F = 800 kN

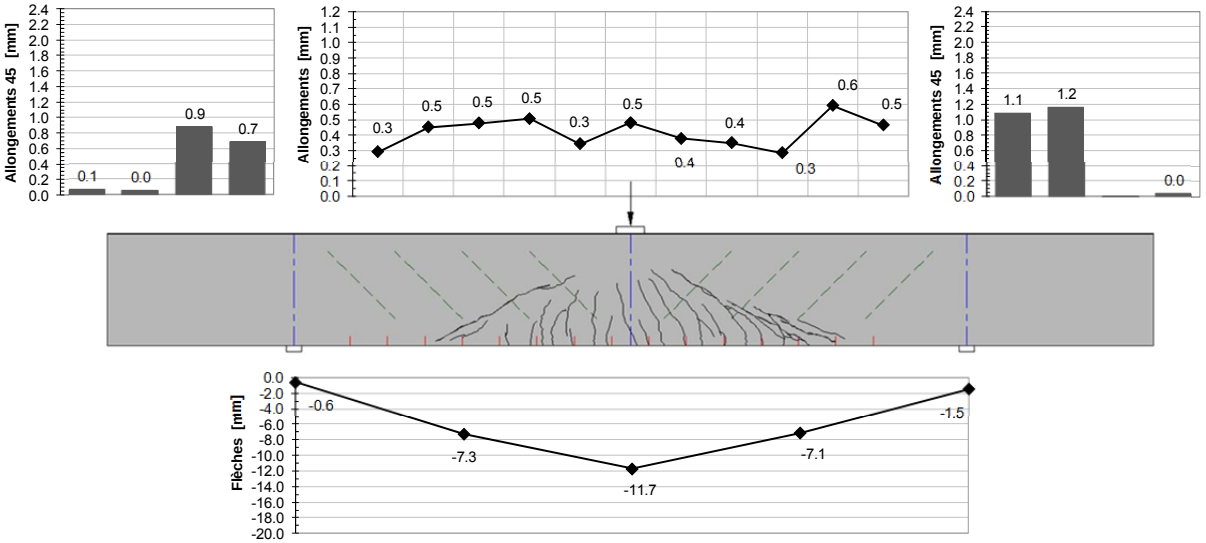

F_u = 860 kN

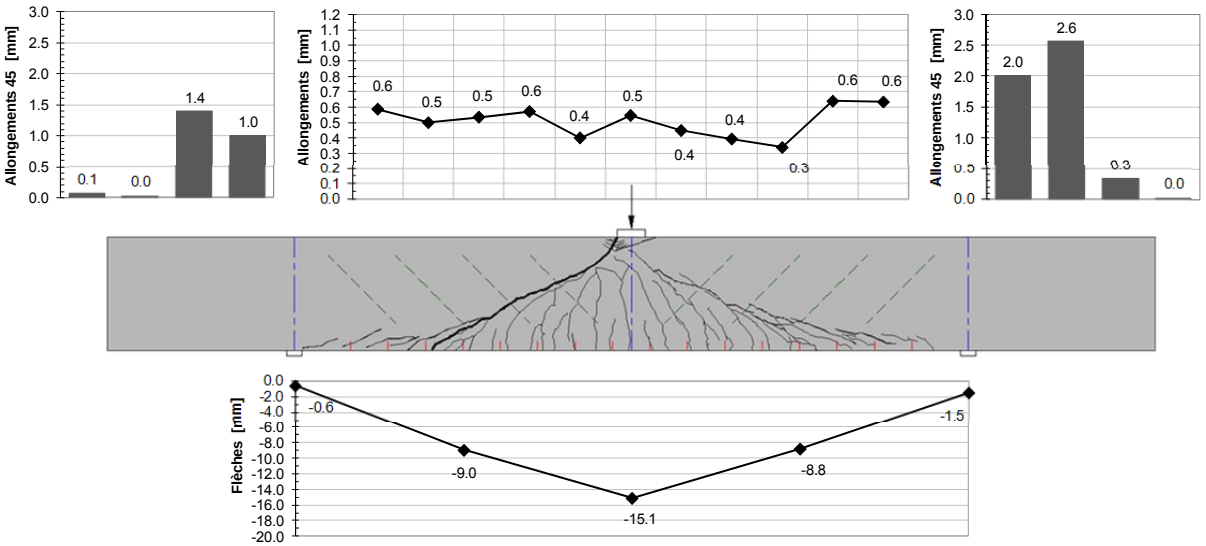

4.4. Poutre AV-4 *(BFHP avec 40 kg/m^3 de fibres)*

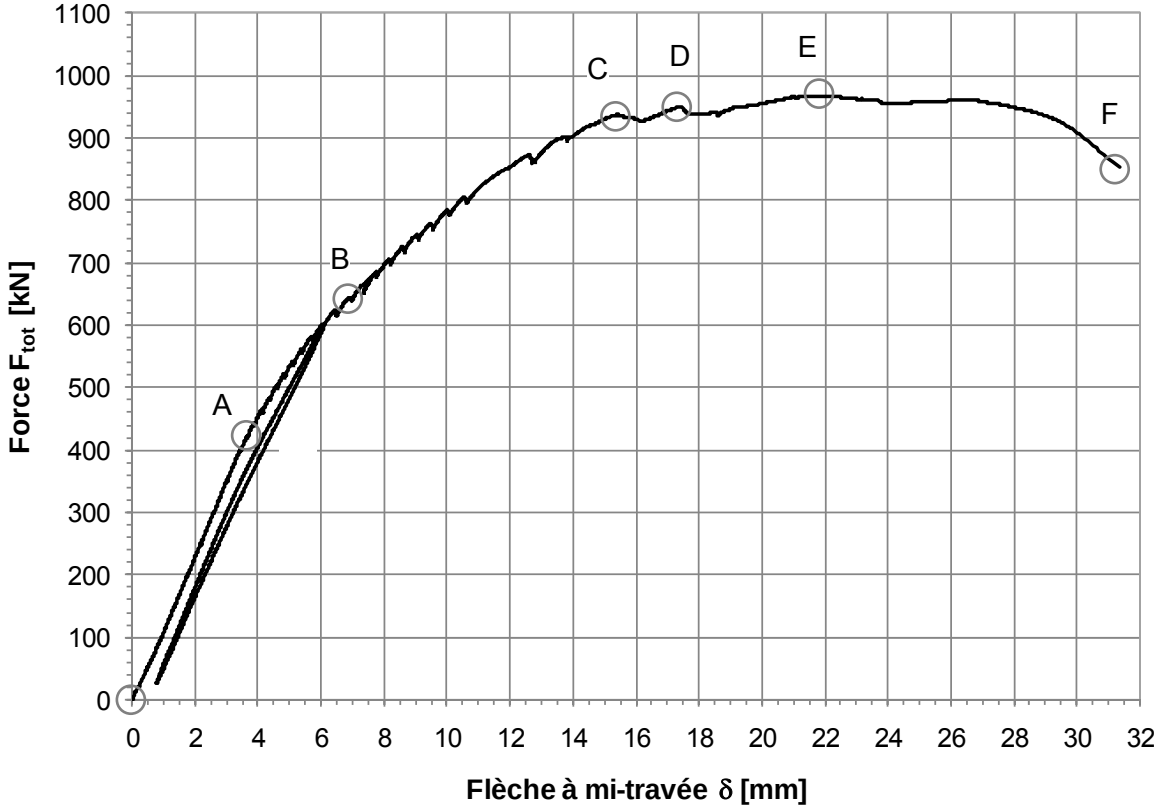

Figure 37 : Relation force-flèche à mi-travée de l'élément AV-4

Le stade I, élastique, s'étend entre les points 0 et A. Les premières fissures de flexion apparaissent au point A sous une charge de 440 kN. A partir de ce point, la fissuration se développe et la rigidité diminue progressivement. Au point B, sous une charge de 640 kN, apparaissent les premières fissures diagonales. A partir de ce point, les fissures de cisaillement évoluent plus rapidement que les fissures de flexion. Entre les points B et C, plusieurs fissures de cisaillement se forment parallèlement. Au point C sous une charge de 920 kN, une première fissure critique de cisaillement se développe du côté droit. Au point D, sous une charge de 940 kN, une deuxième fissure critique se forme du côté gauche. L'ouverture des fissures du côté droit se stabilise alors que les fissures de gauche se développent et se croisent sous l'introduction de la force. La charge maximale de 967 kN est atteinte au point E. Le béton de la table de compression en pointe de la fissure diagonale de gauche s'écrase progressivement. Au point F, intervient la rupture de l'élément par cisaillement.

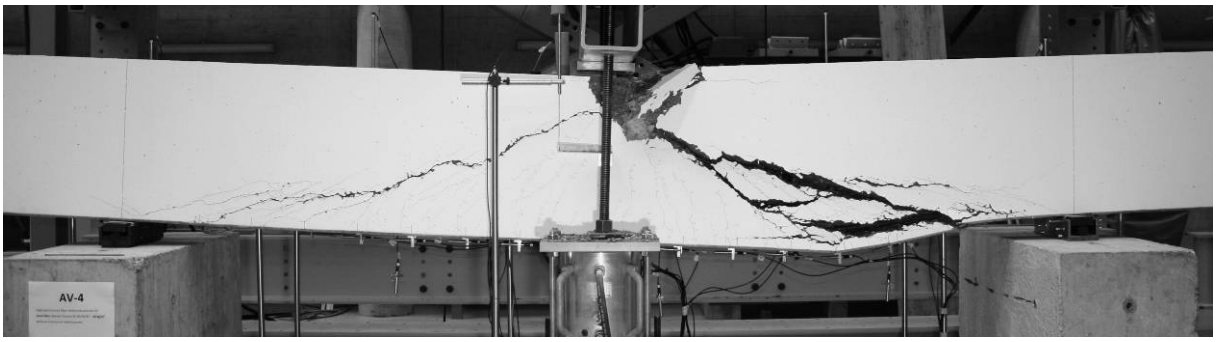

Figure 38 : Aspect à la rupture de l'élément AV-4

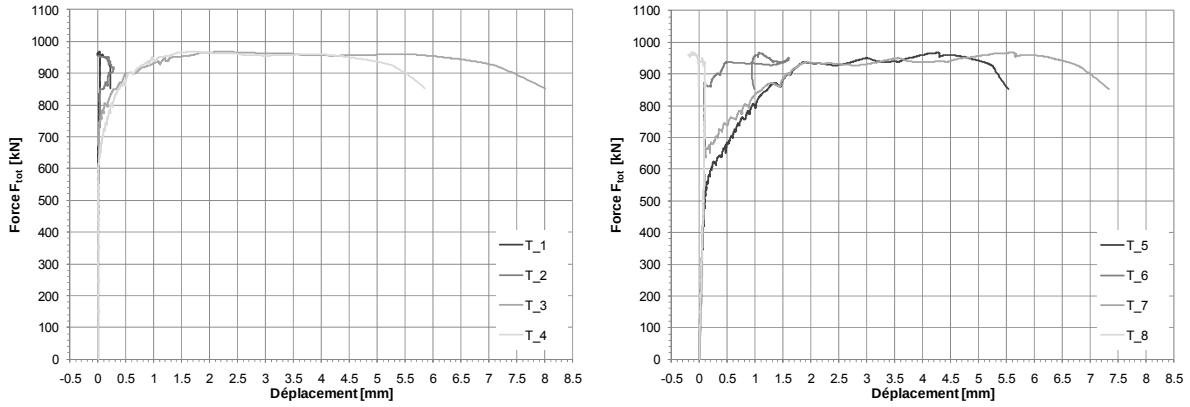

Figure18 : Relation force - déplacement des capteurs diagonaux

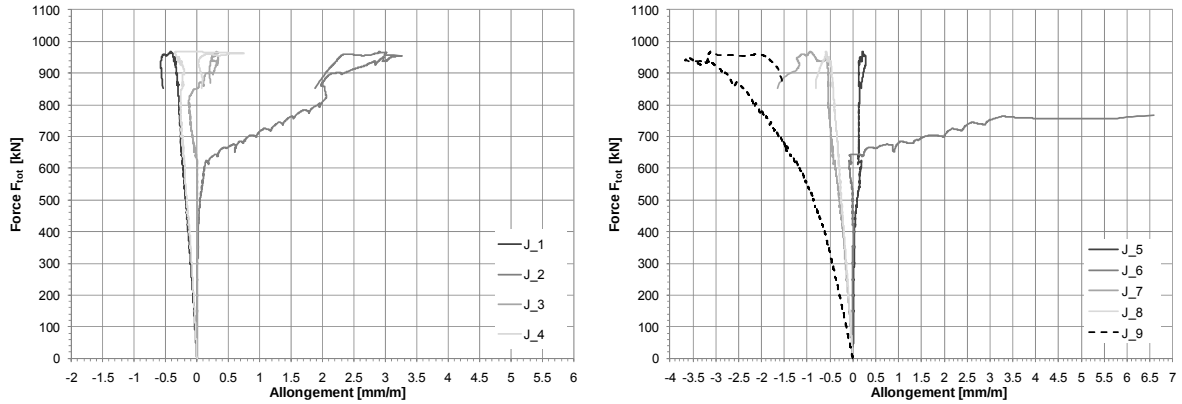

Figure 19 : Relations force - allongement des jauges extensométriques

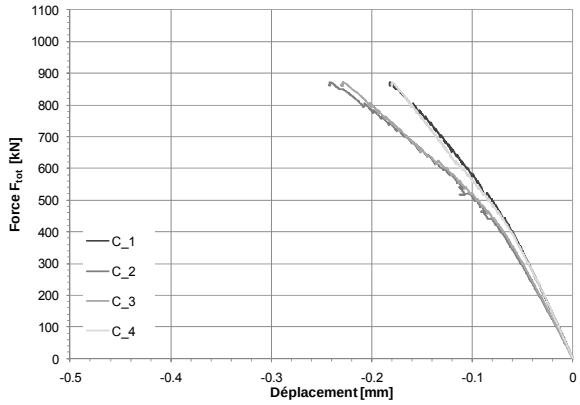

Figure 39 : Relations force – déplacement des capteurs Oméga

F = 600 kN

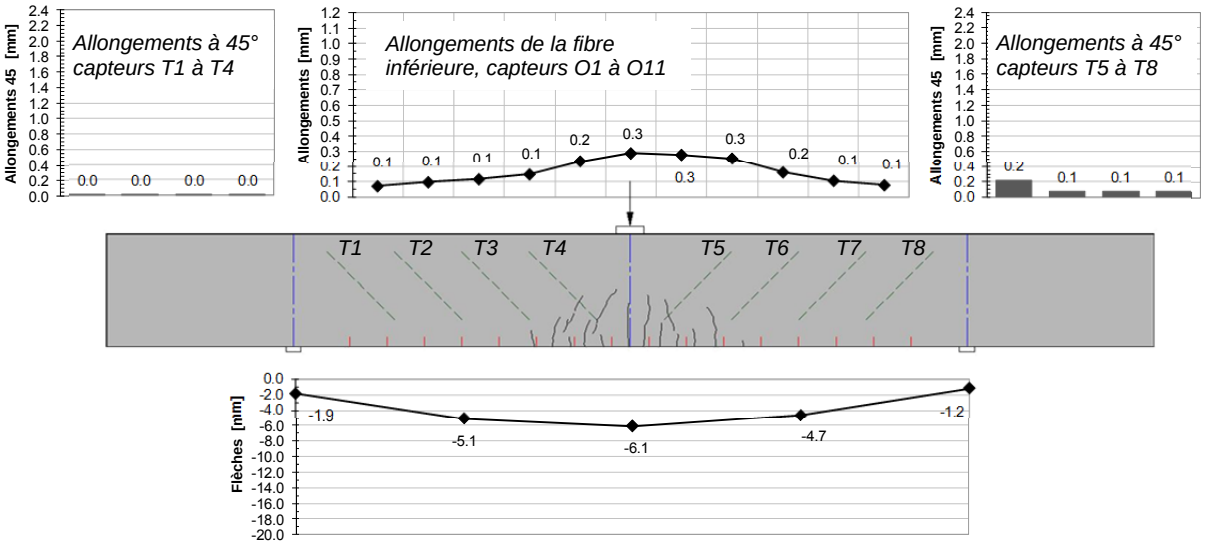

F = 700 kN

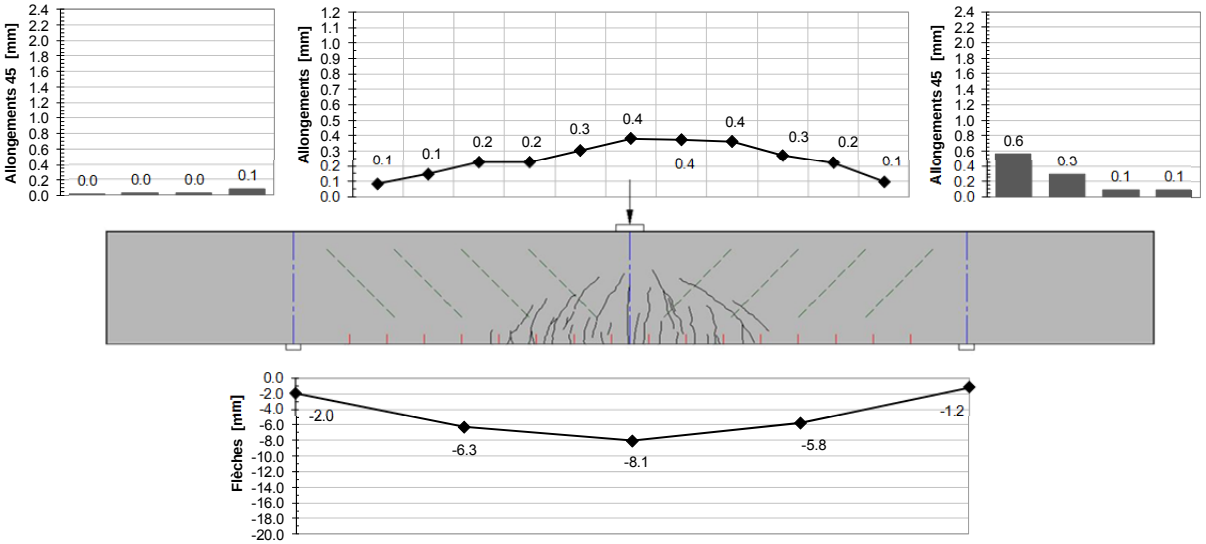

F = 800 kN

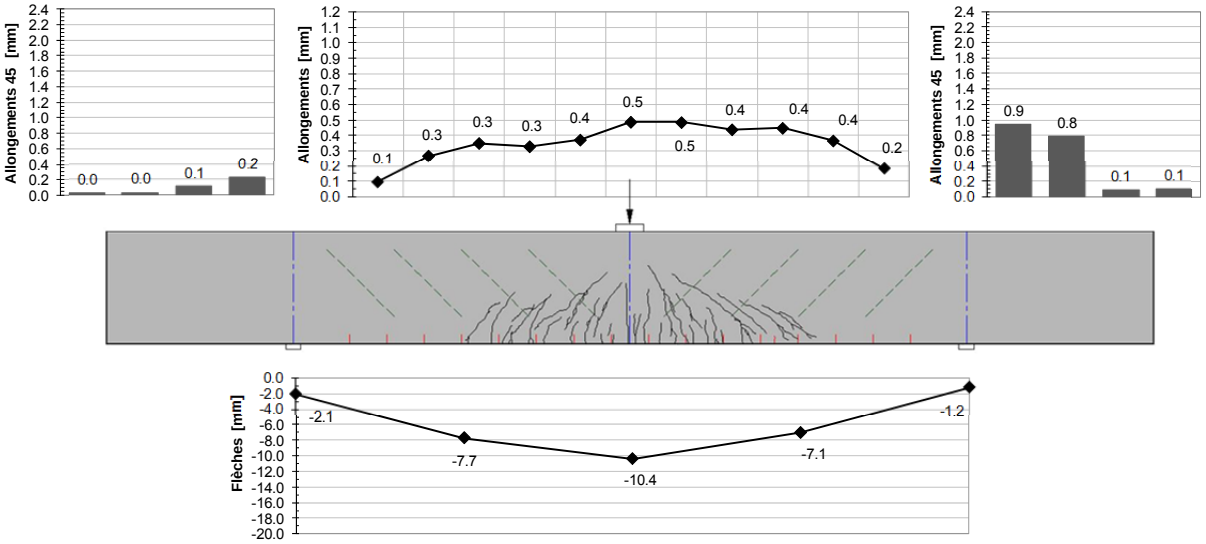

F = 900 kN

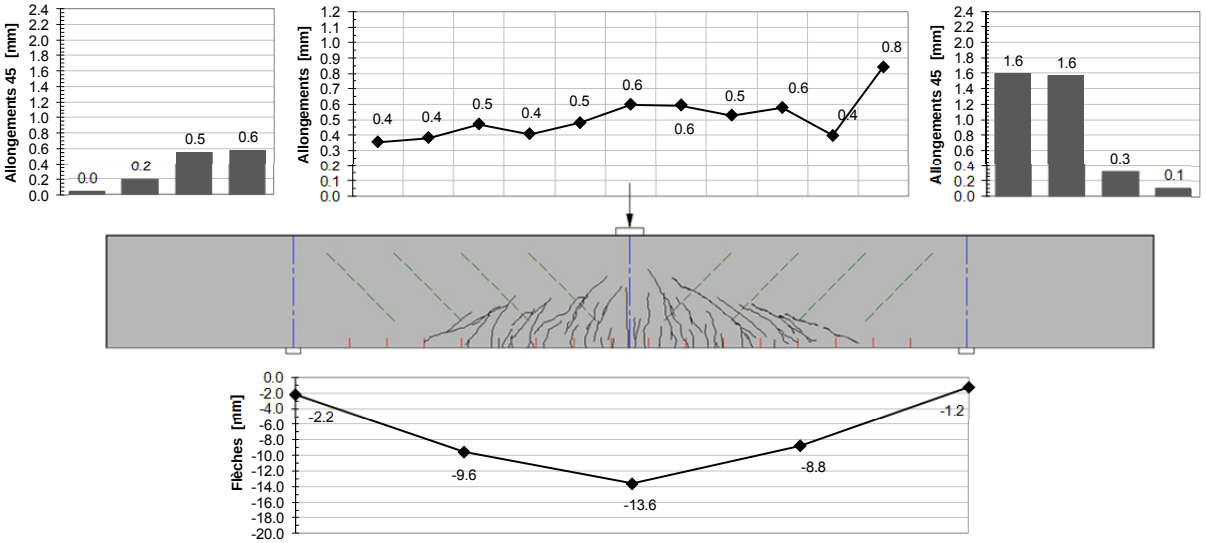

F_u = 967 kN

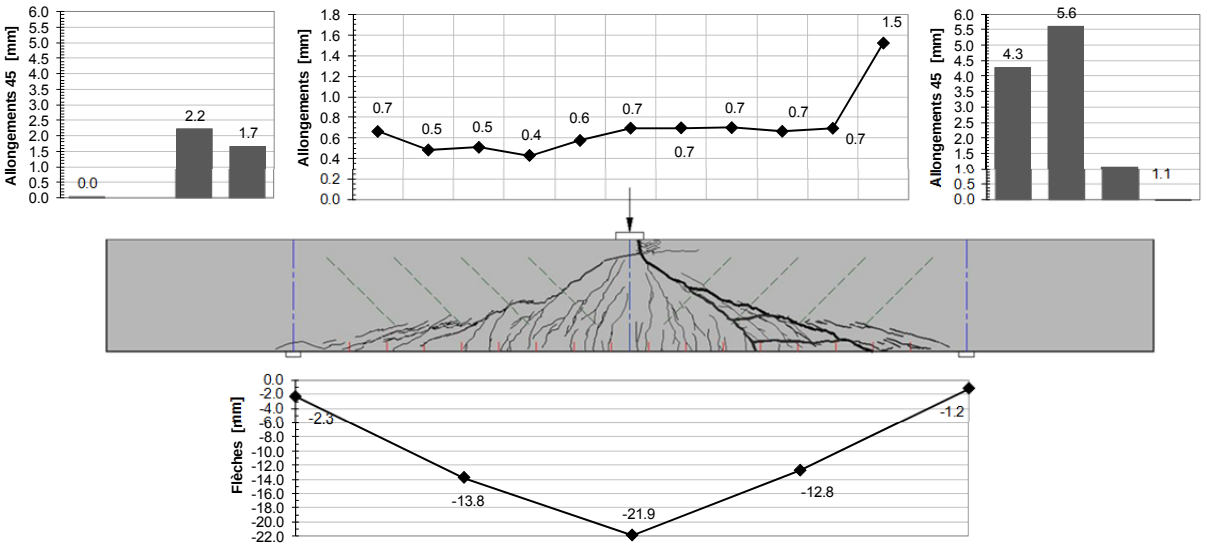

4.5. Poutre AV-5 *(BFHP avec 60 kg/m^3 de fibres)*

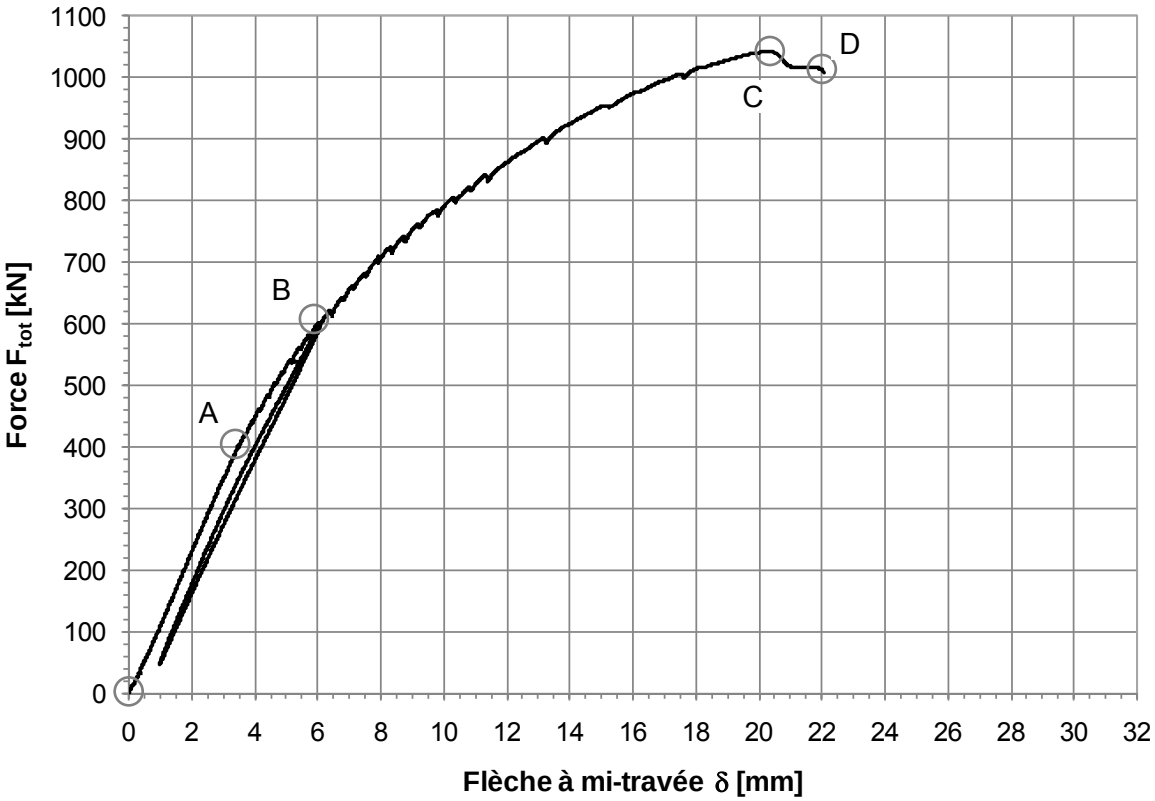

Figure 40 : Relation force-flèche à mi-travée de l'élément AV-5

Le stade I, élastique non-fissuré, s'étend entre les points 0 et A. Les premières fissures de flexion apparaissent au point A sous une charge de 400 kN. Cependant, ces fissures sont difficilement visibles. A partir de ce point, la rigidité de la poutre diminue progressivement. Au point B sous une charge de 600 kN apparaissent les premières fissures diagonales. A partir de ce point, les fissures de cisaillement évoluent plus rapidement que les fissures de flexion. La rigidité de l'élément est dirigée par l'ouverture des fissures diagonales. Entre les points B et C, une fissure critique se développe du côté droit. La charge maximale de 1'042 kN est atteinte au point C. Le béton de la membrure comprimée s'écrase progressivement et la rupture intervient brutalement au point D. L'inclinaison des fissures de cisaillement tend vers les appuis.

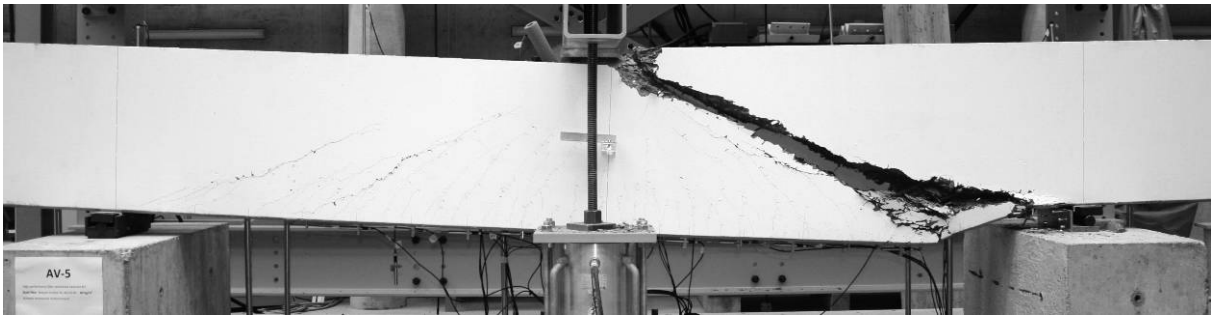

Figure 41 : Aspect à la rupture de l'élément AV-5

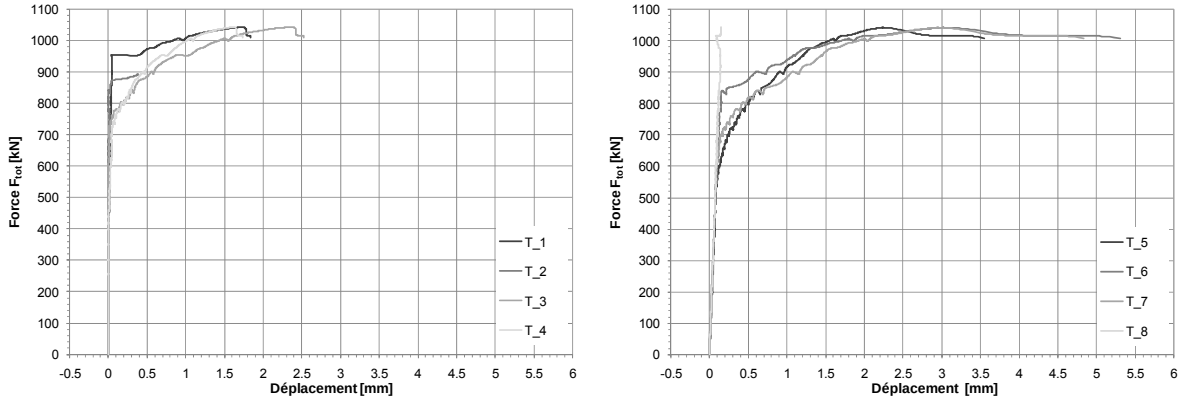

Figure18 : Relation force - déplacement des capteurs diagonaux

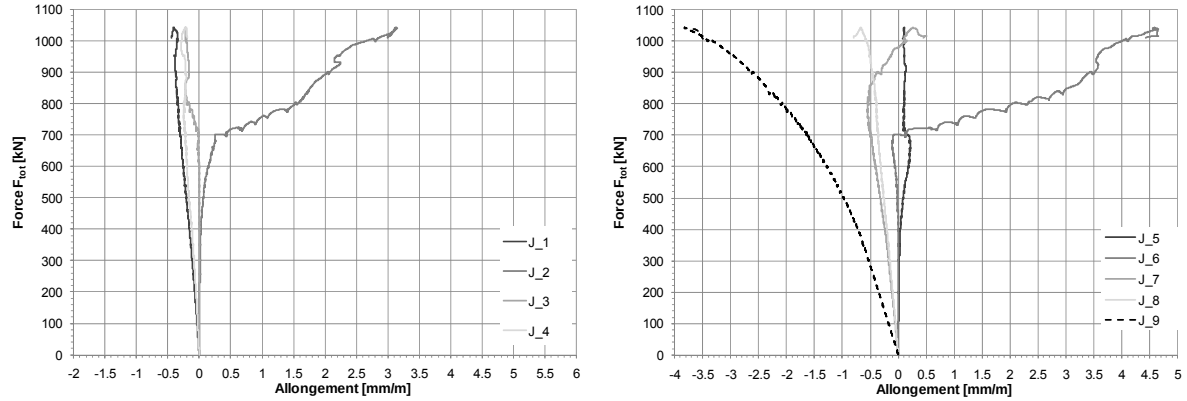

Figure 19 : Relations force - allongement des jauges extensométriques

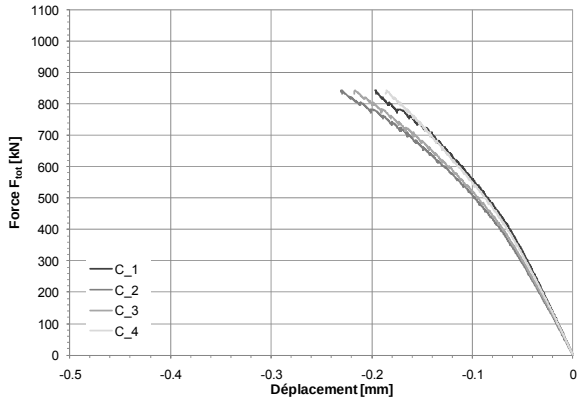

Figure 42 : Relations force – déplacement des capteurs Oméga

F = 600 kN

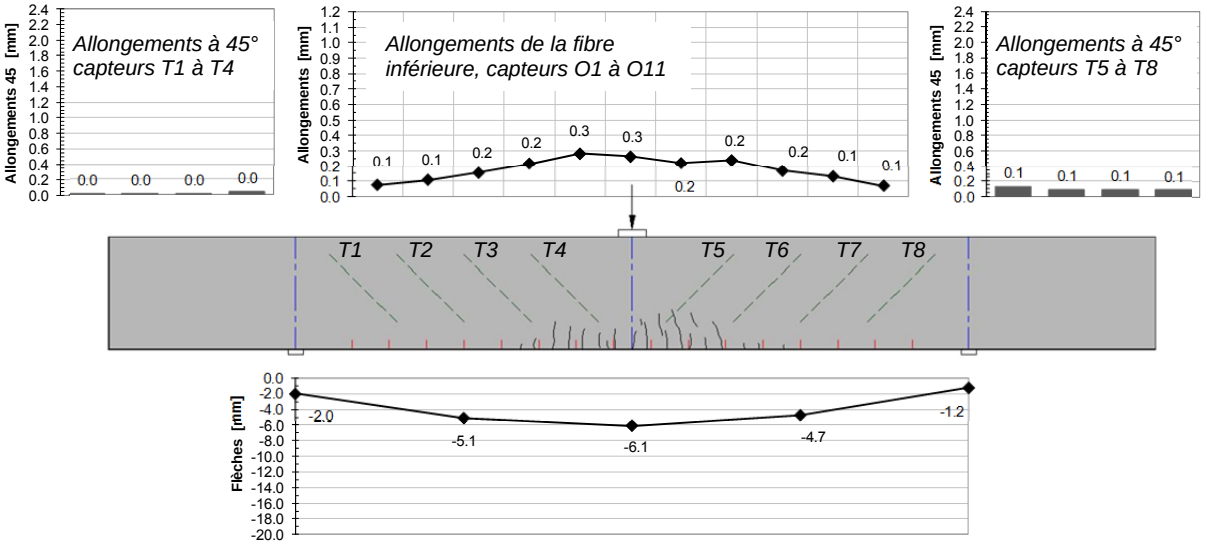

F = 700 kN

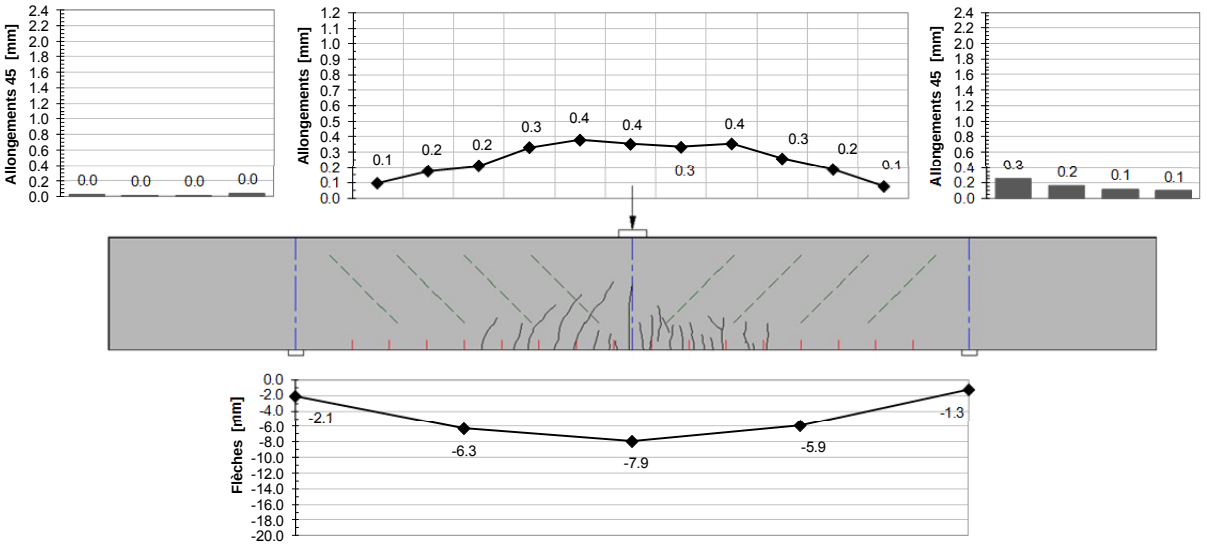

F = 800 kN

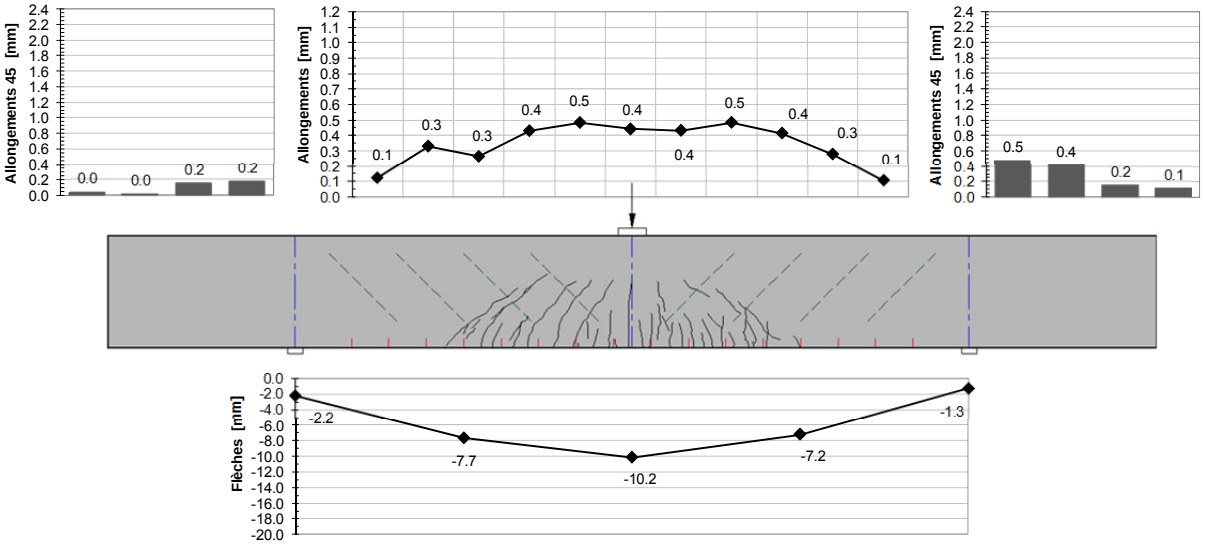

F = 900 kN

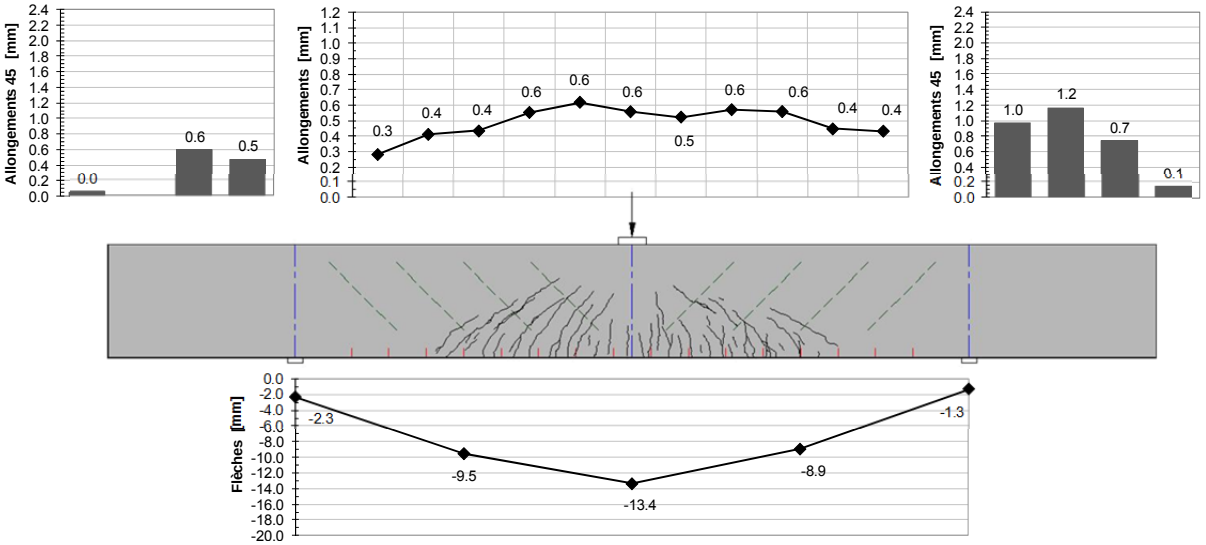

F = 1'000 kN

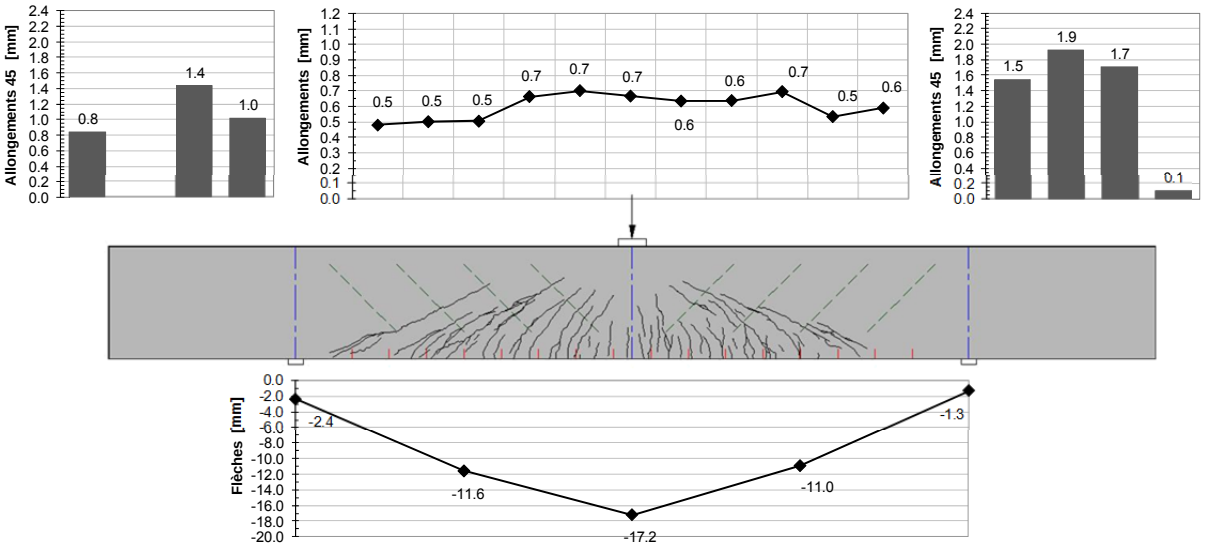

F_u = 1'042 kN

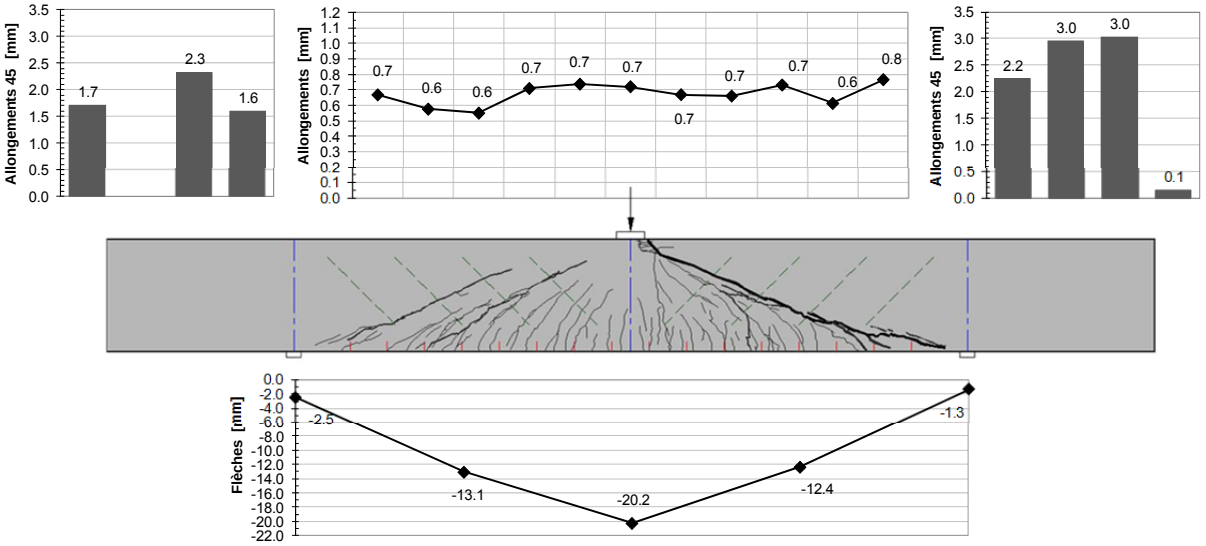

4.6. Poutre AV-6 *(BFHP avec 80 kg/m^3 de fibres)*

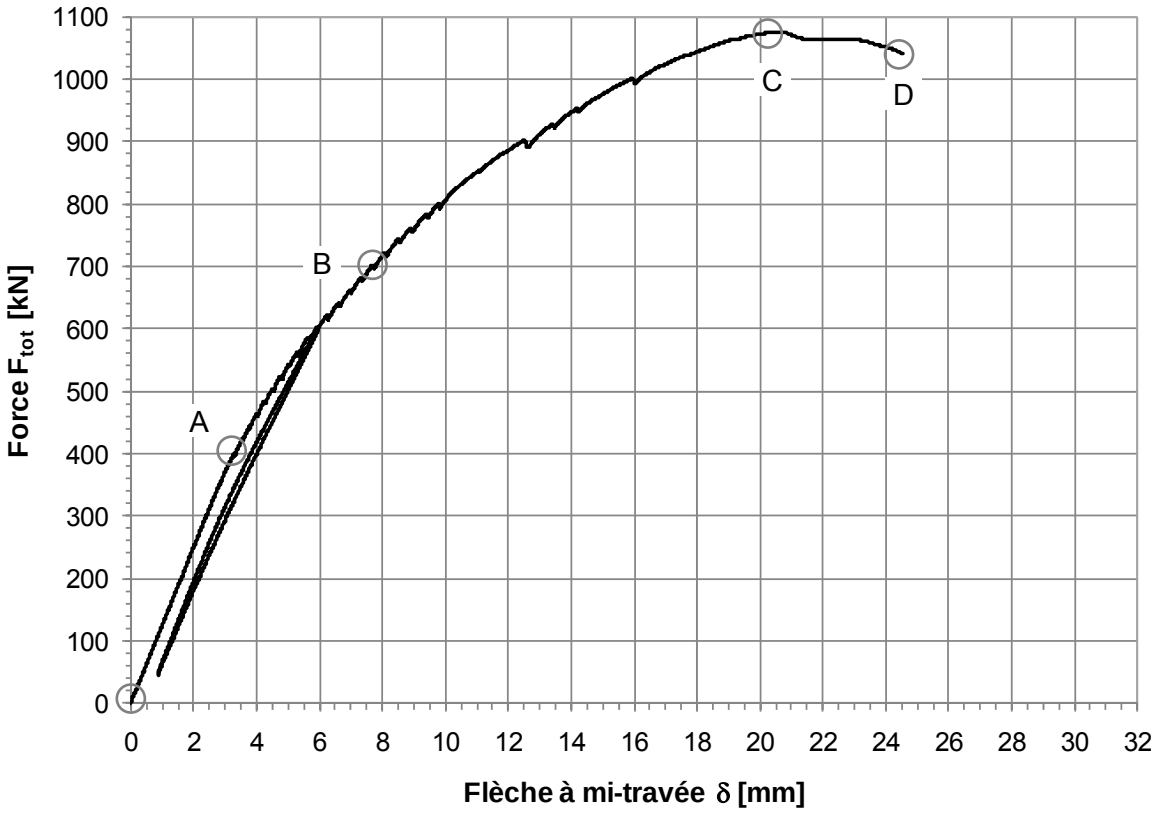

Figure 44 : Relation force-flèche à mi-travée de l'élément AV-6

Le stade I, élastique non-fissuré, s'étend entre les points 0 et A. Les premières fissures de flexion apparaissent au point A sous une charge de 400 kN. Cependant, ces fissures sont difficilement visibles. A partir de ce point, la rigidité de la poutre diminue progressivement. Au point B sous une charge de 700 kN apparaissent les premières fissures diagonales. A partir de ce point, les fissures de cisaillement évoluent plus rapidement que les fissures de flexion. Plusieurs fissures diagonales se développent en éventail. A nouveau, la précontrainte supérieure empêche une propagation des fissures à travers la membrure comprimée. La charge maximale de 1'075 kN est atteinte au point C. Suite à l'écrasement du béton de la table de compression, la rupture par cisaillement intervient au point D. A nouveau, grâce au dosage important en fibres, l'inclinaison des fissures de cisaillement tend vers les appuis.

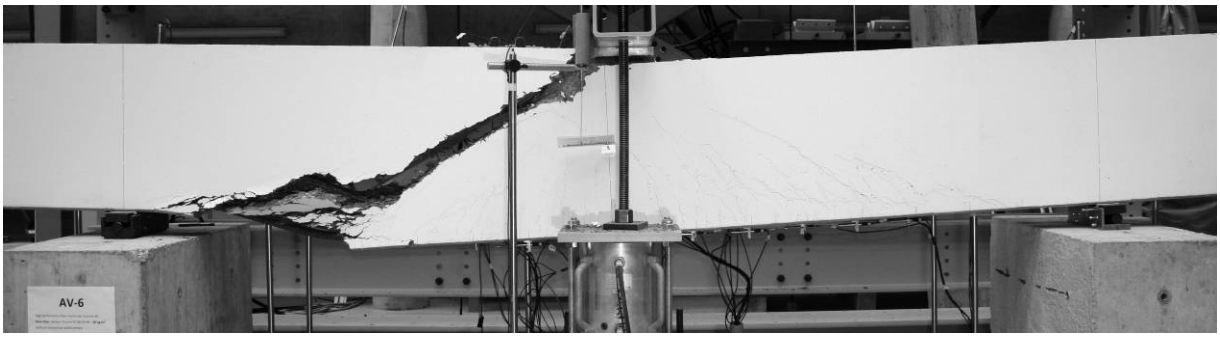

Figure 45 : Aspect à la rupture de l'élément AV-6

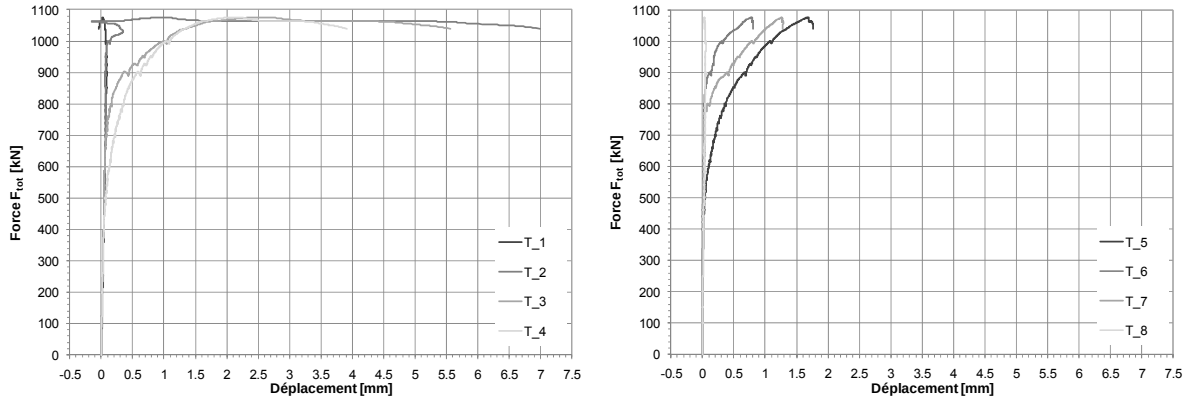

Figure18 : Relation force - déplacement des capteurs diagonaux

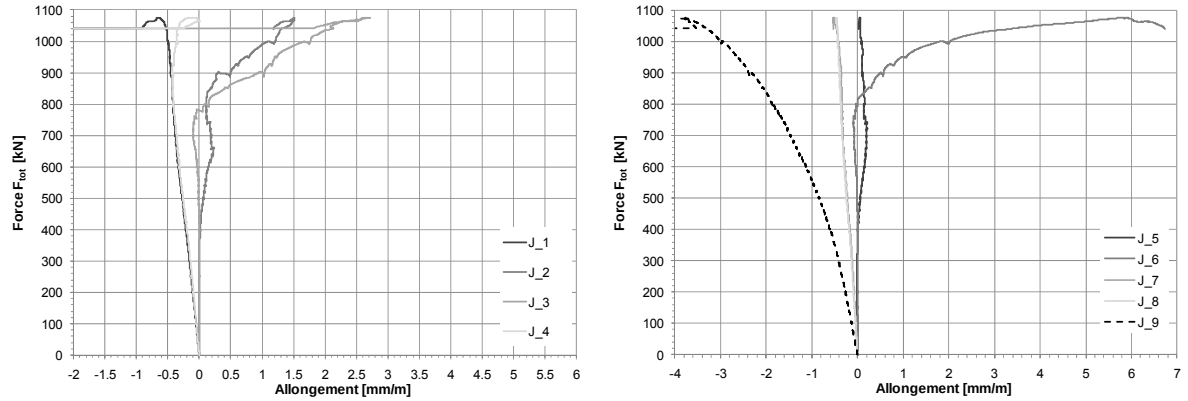

Figure 19 : Relations force - allongement des jauges extensométriques

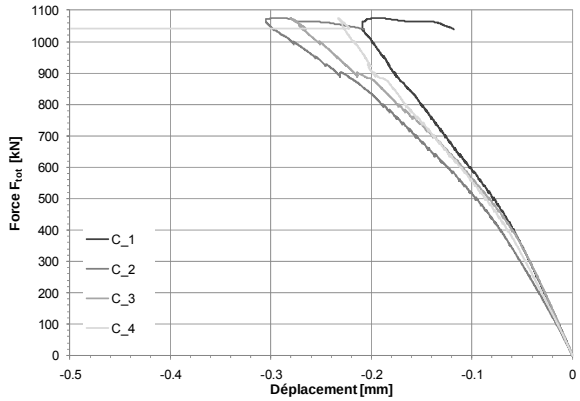

Figure 46 : Relations force – déplacement des capteurs Oméga

F = 600 kN

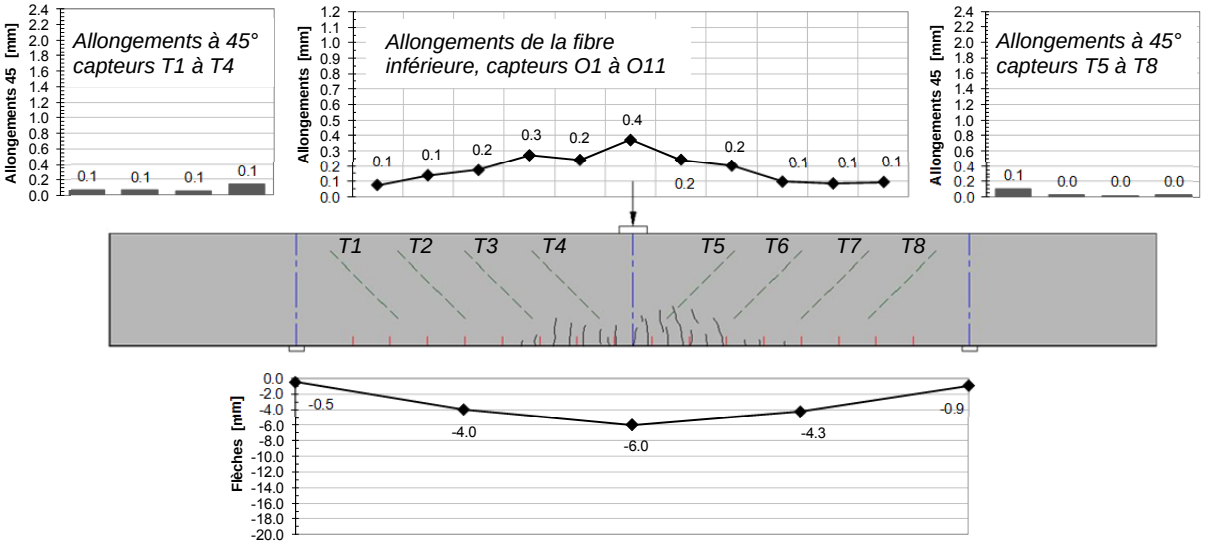

F = 700 kN

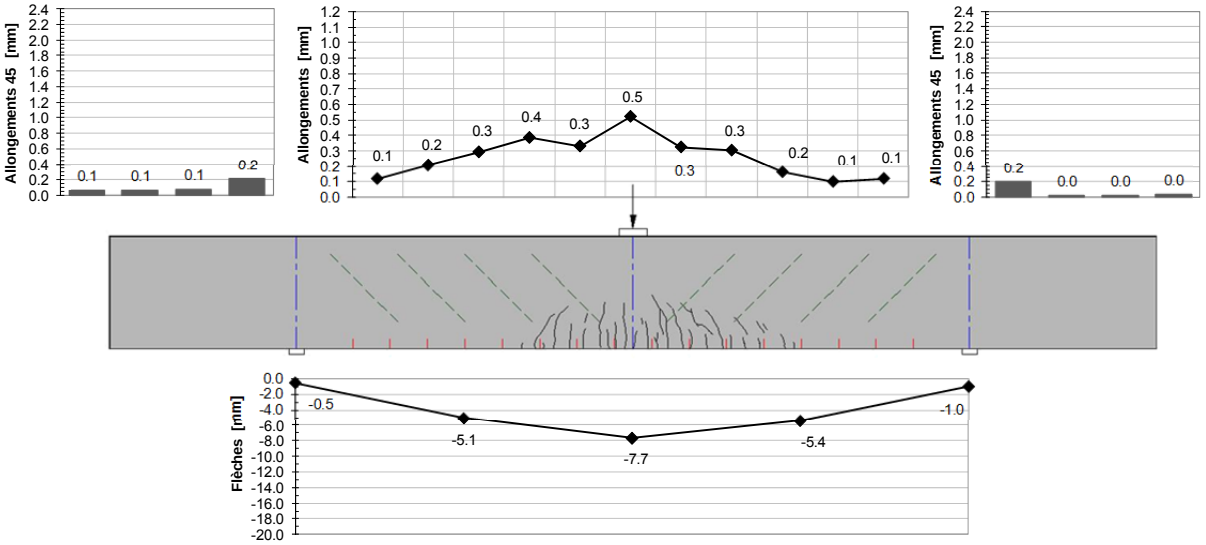

F = 800 kN

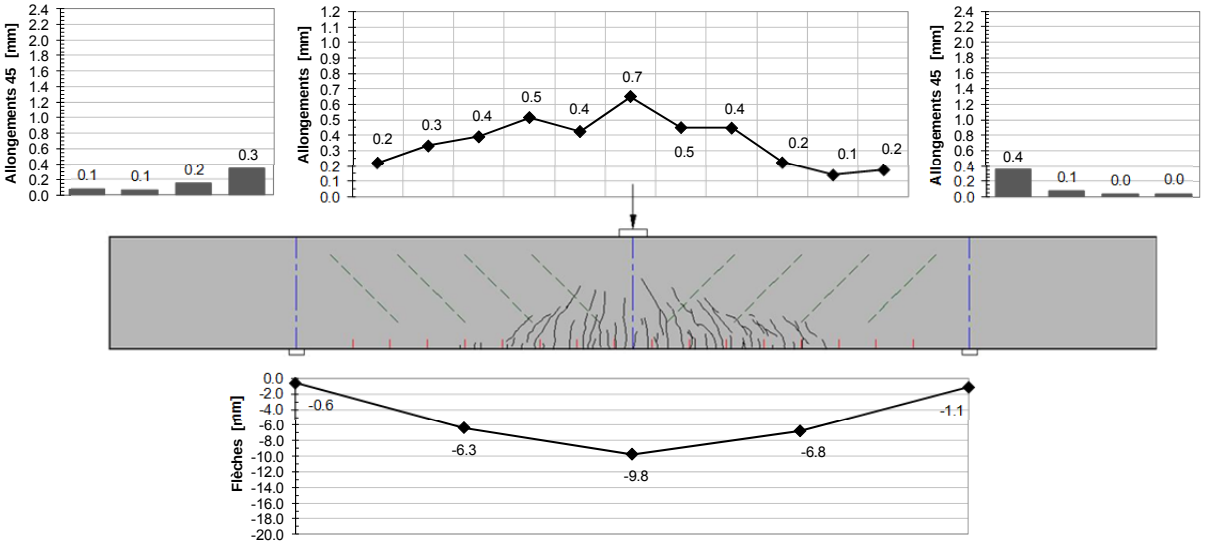

F = 900 kN

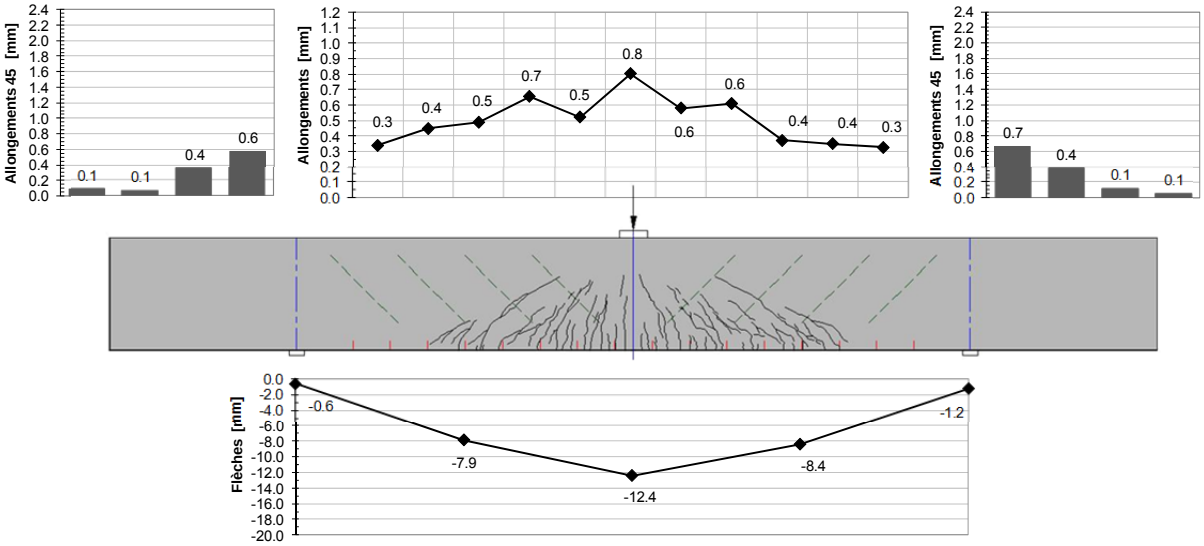

F = 1'000 kN

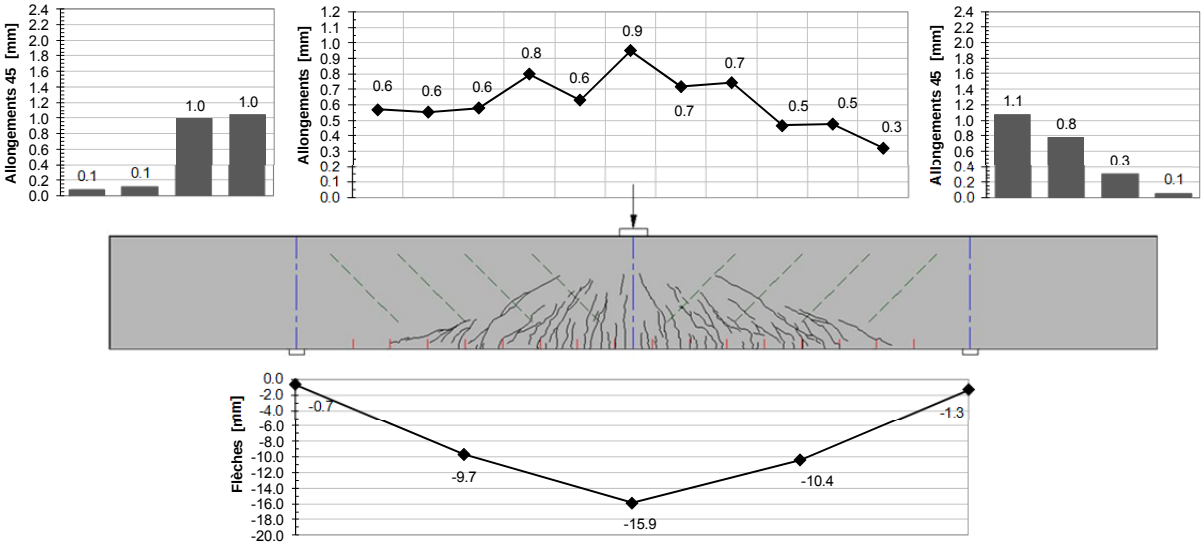

F_u = 1'075 kN

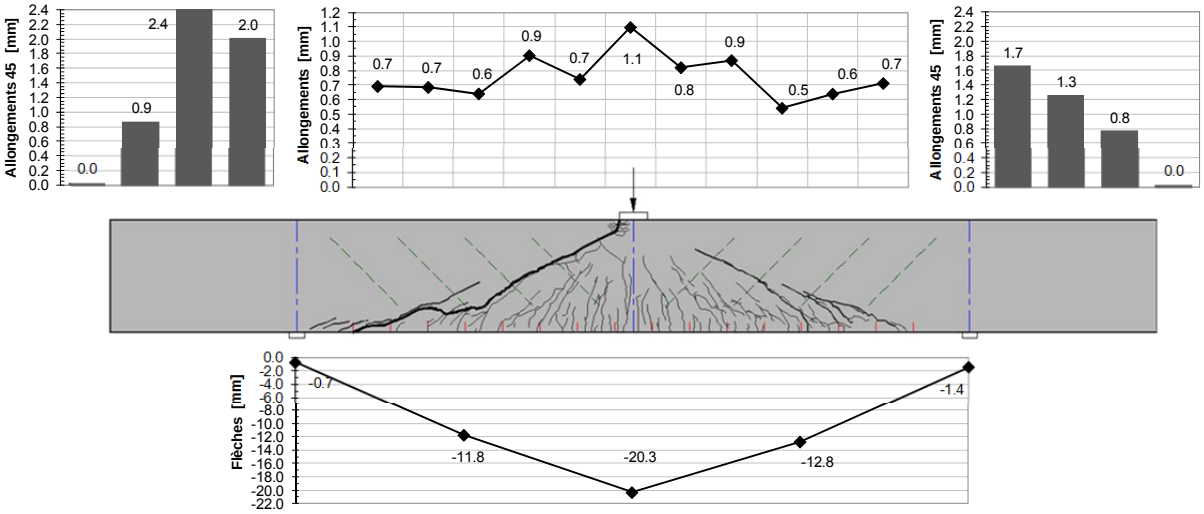

4.7. Poutre AF-1 *(BHP sans fibres)*

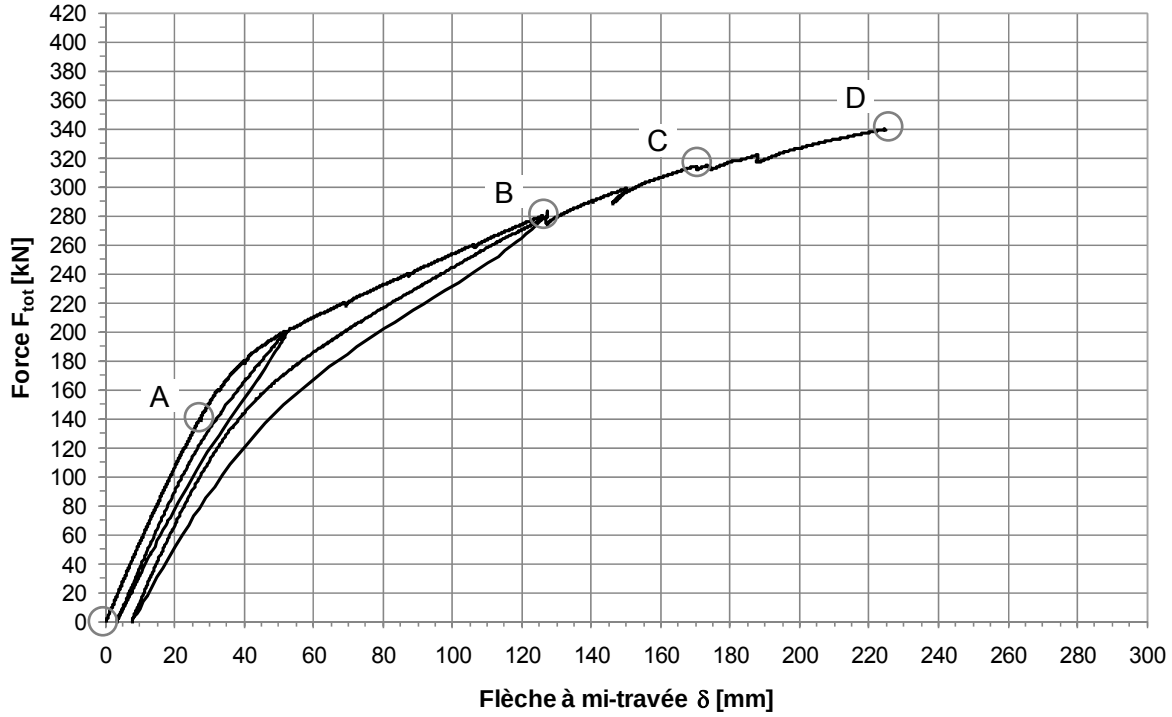

Figure 47 : Relation force-flèche à mi-travée de l'élément AF-1

Le stade I, élastique non fissuré, s'étend entre les points 0 et A. Les premières fissures de flexion apparaissent au point A sous une charge de 140 kN. A partir de ce point, la rigidité de la poutre diminue progressivement. Au point B sous une charge de 280 kN apparait une première fissure diagonale du côté droit. A partir de ce point, la rigidité diminue. Au point C, plusieurs fissures diagonales se développent successivement du côté gauche et droit. Cependant, ces fissures ne provoquent pas une rupture immédiate. Les câbles supérieurs empêchent le développement rapide des fissures de cisaillement à travers la membrure comprimée. Entre les points C et D, les fissures diagonales évoluent et leurs ouvertures augmentent. La rupture par cisaillement intervient brutalement au point D, sous une charge de 340 kN. Les fissures diagonales du côté gauche provoquent l'éclatement du béton de la membrure comprimée suivie d'une propagation de plusieurs fissures suite à l'effondrement de l'élément.

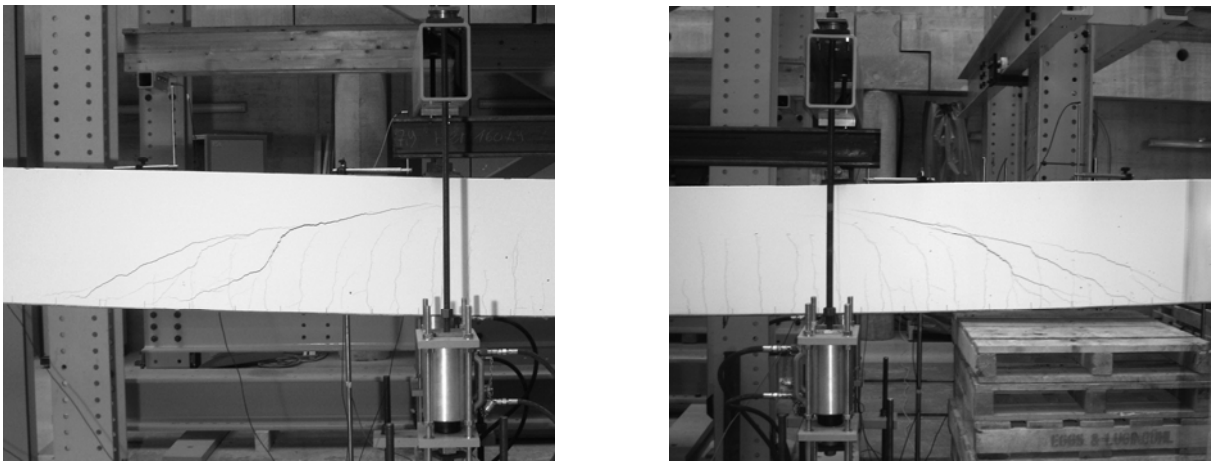

Figure 48 : Fissures diagonales des côtés gauche et droite de l'élément AF-1

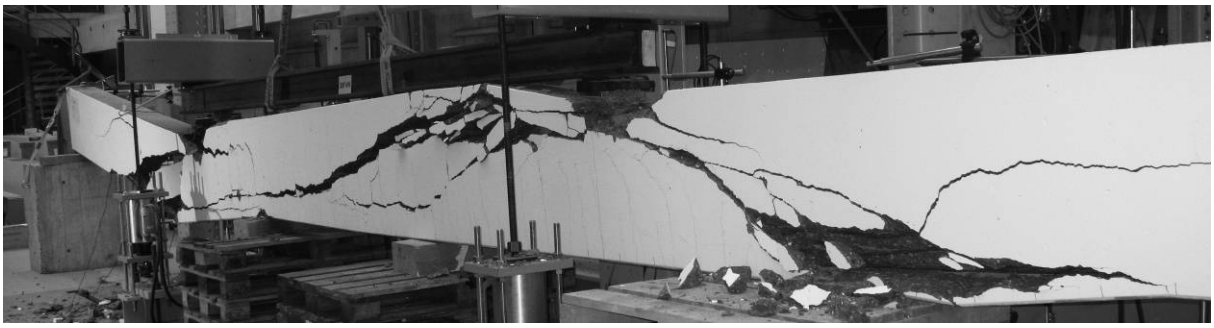

Figure 49 : Aspect à la rupture de l'élément AF-1

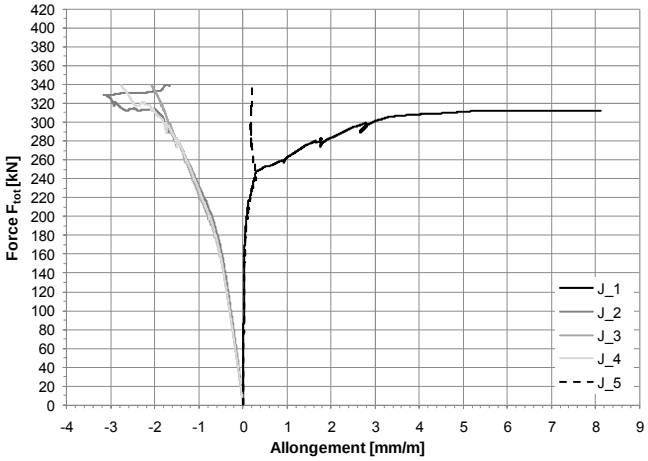

Figure 50 : Relations force – allongement des jauges extensométriques

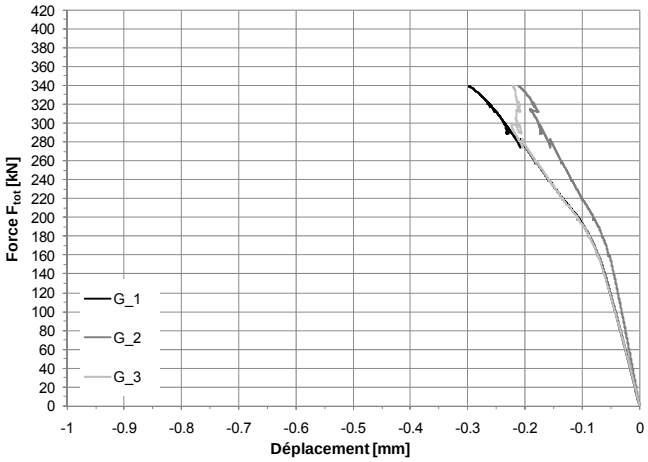

Figure 51 : Relations force – déplacement des capteurs Oméga

F = 200 kN

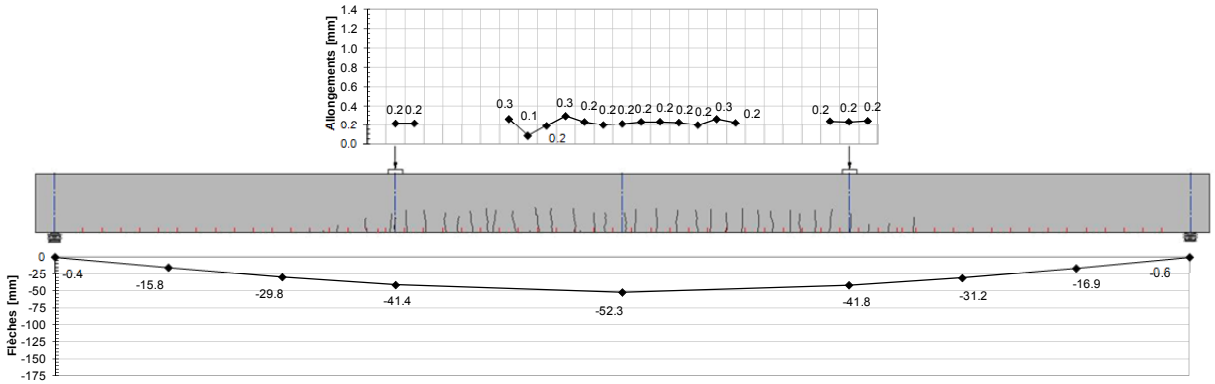

F = 220 kN

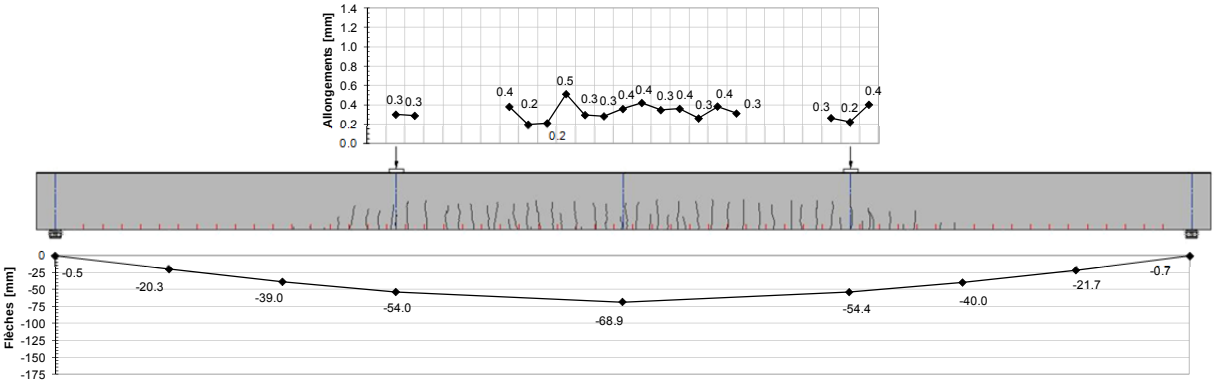

F = 240 kN

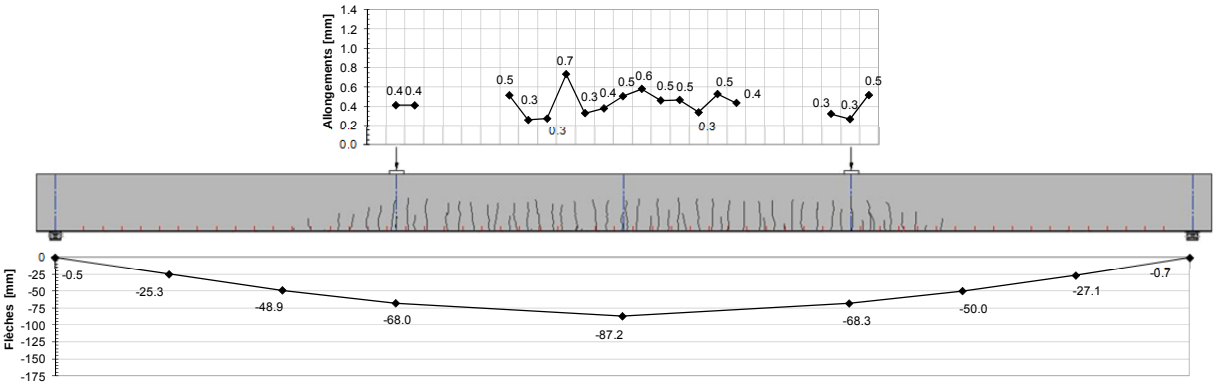

F = 260 kN

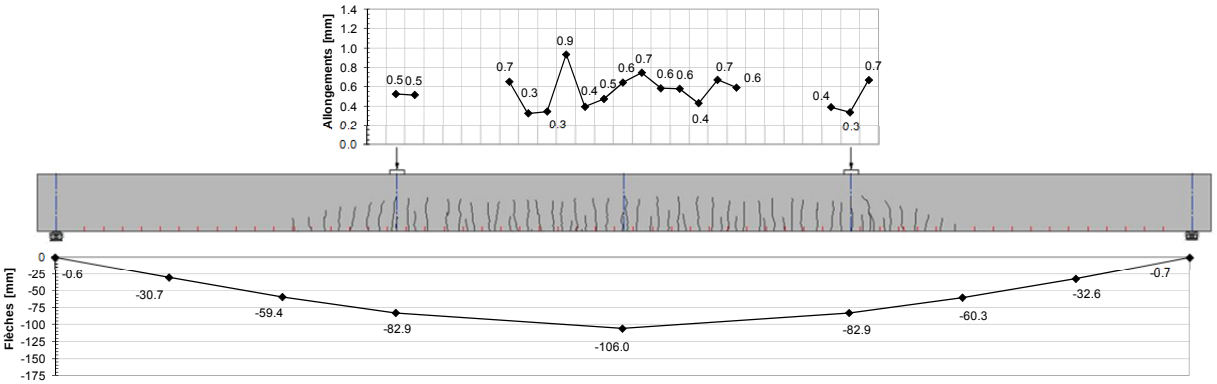

F = 280 kN

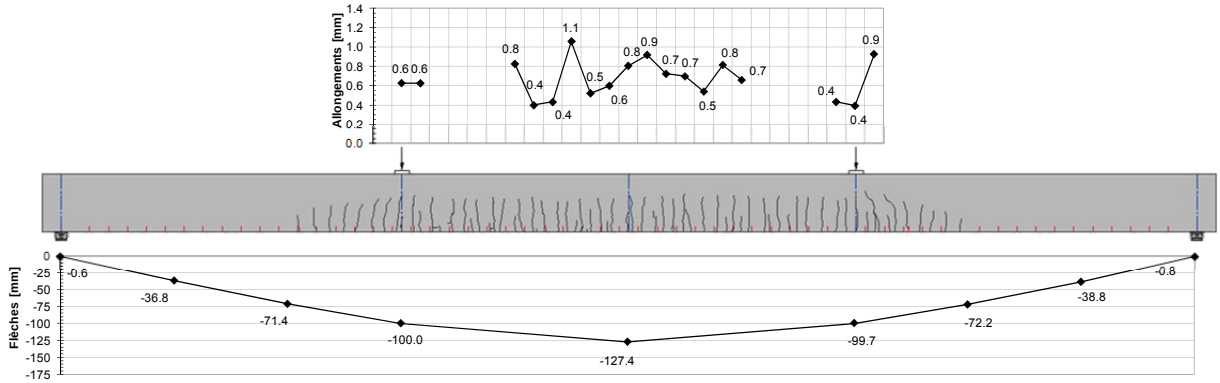

F = 300 kN

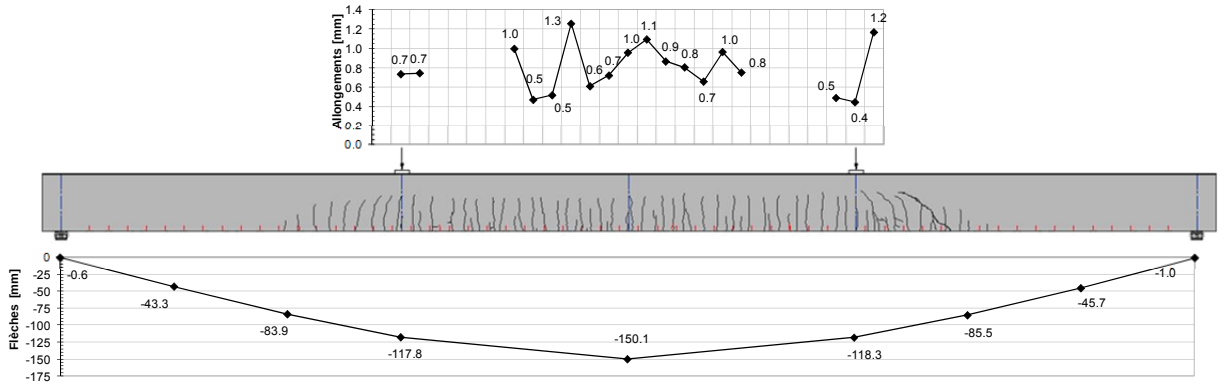

F_u = 340 kN

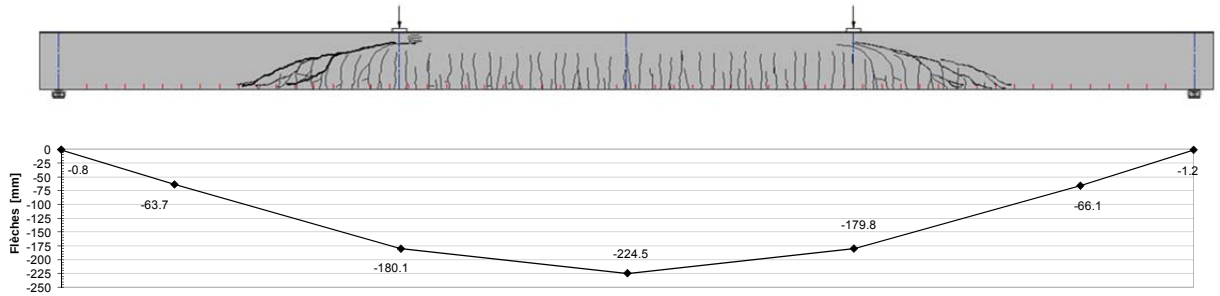

4.8. Poutre AF-2 *(BFHP avec 60 kg/m^3 de fibres)*

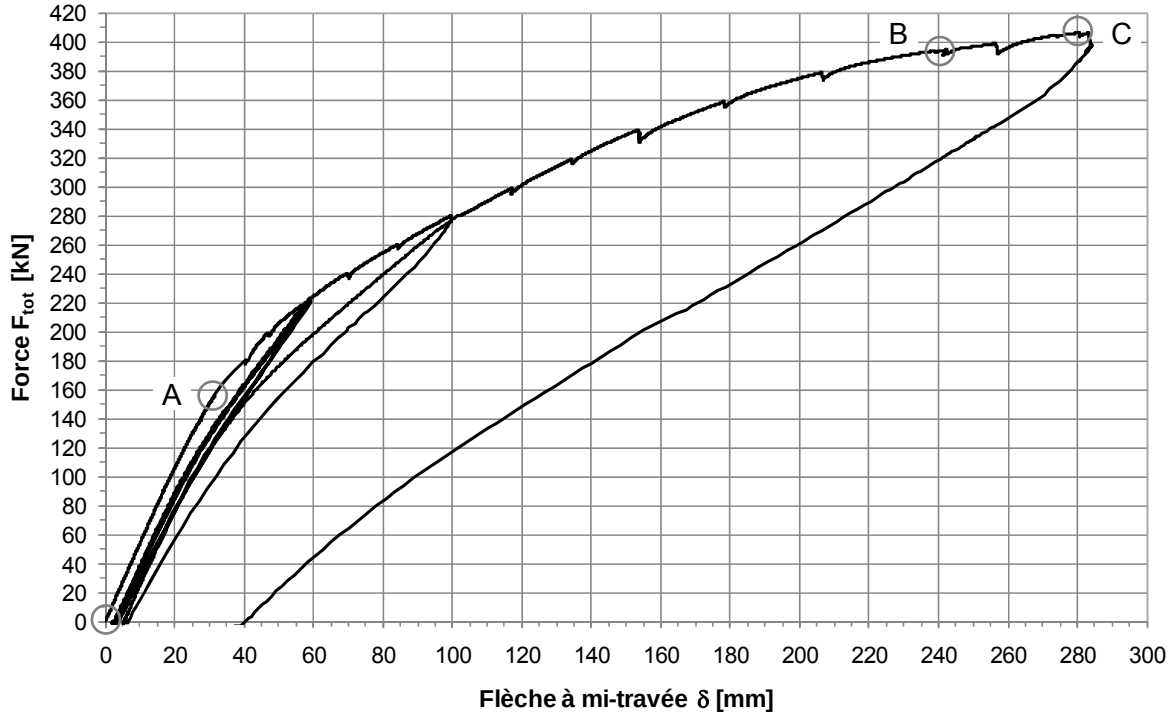

Figure 52 : Relation force-flèche à mi-travée de l'élément AF-2

Le stade I, élastique non-fissuré, s'étend entre les points 0 et A. Les premières fissures de flexion apparaissent au point A sous une charge de 160 kN. A partir de ce point, la rigidité de la poutre diminue progressivement et la fissuration se développe. Entre les points A et B s'étend le stade II, élastique – fissuré. A partir du point B, la charge plafonne alors que la déformation augmente. Proche du milieu de l'élément plusieurs fissures rapprochées forment une macro-fissure. L'essai est interrompu au point C, sous une flèche de 280 mm, afin d'éviter une rupture brutale en flexion. Aucunes fissures diagonales ne se sont développées. L'écartement entre les fissures de flexion est d'environ 30 mm et les ouvertures sont inférieures à 0.3 mm jusqu'à la localisation sur une seule macro-fissure.

Figure 53 : Multi-fissuration de flexion et localisation sur une seule macro-fissure

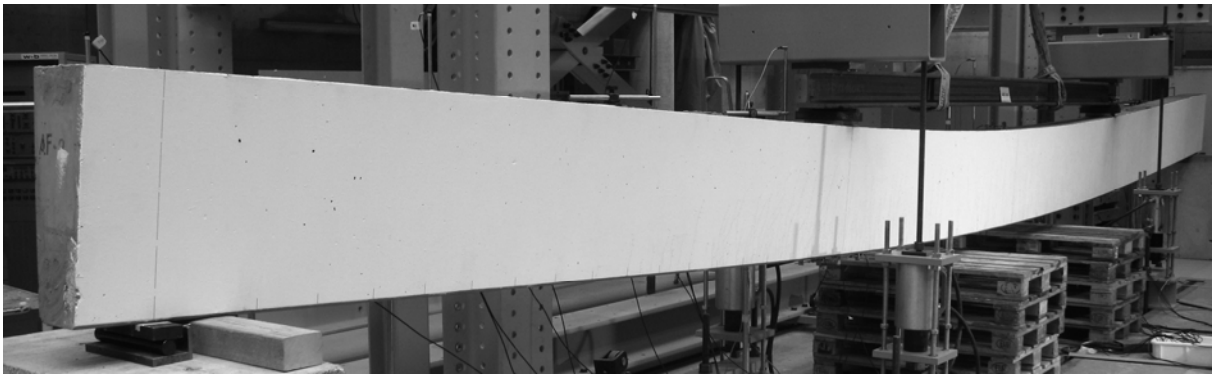

Figure 54 : Aspect de l'élément AF-2 sous une flèche de 280 mm

F = 200 kN

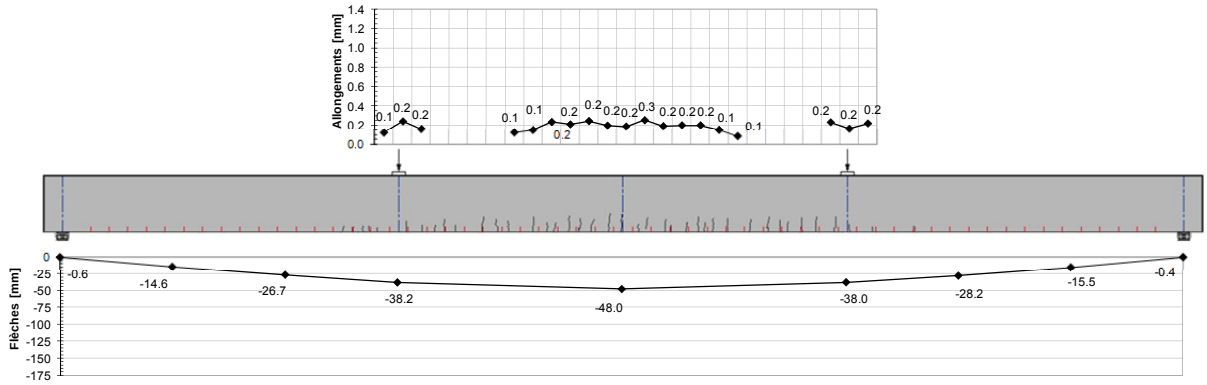

F = 220 kN

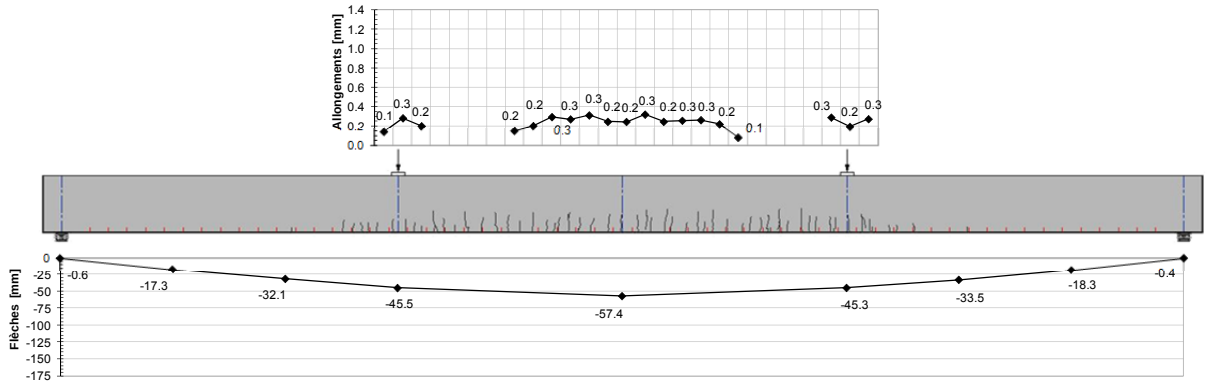

F = 240 kN

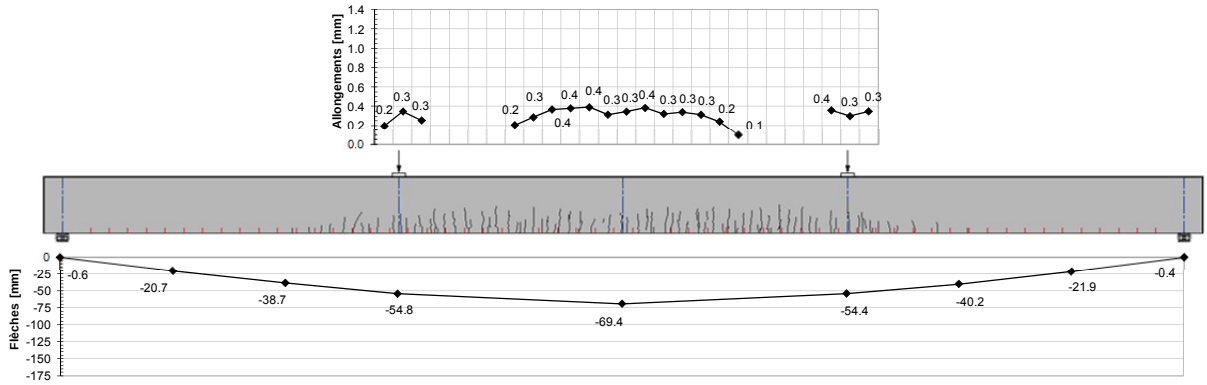

F = 260 kN

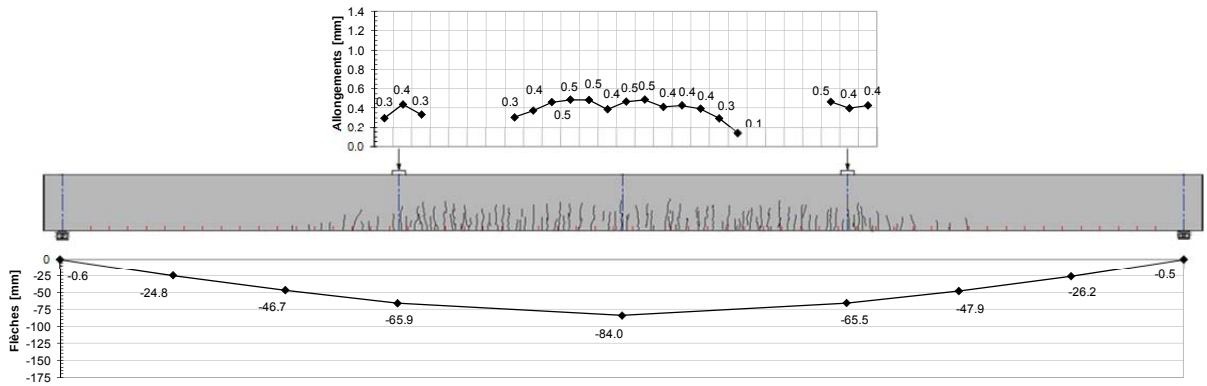

F = 280 kN

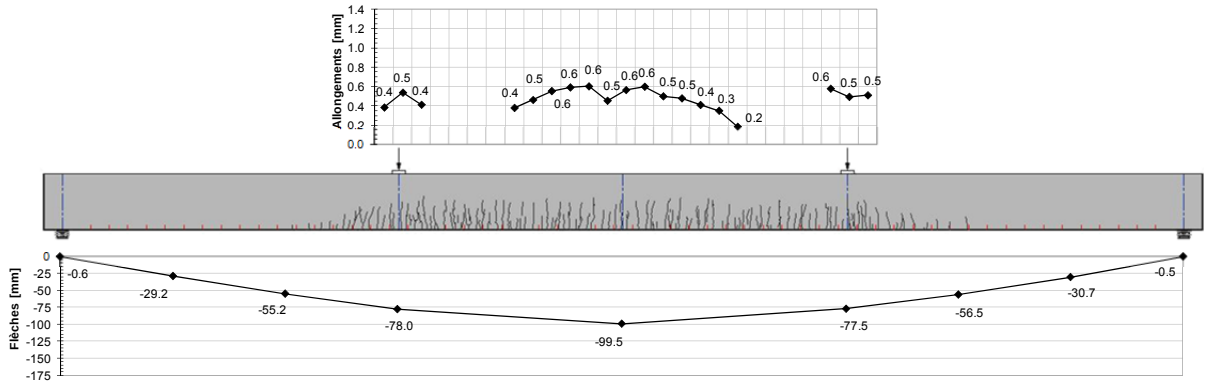

F = 300 kN

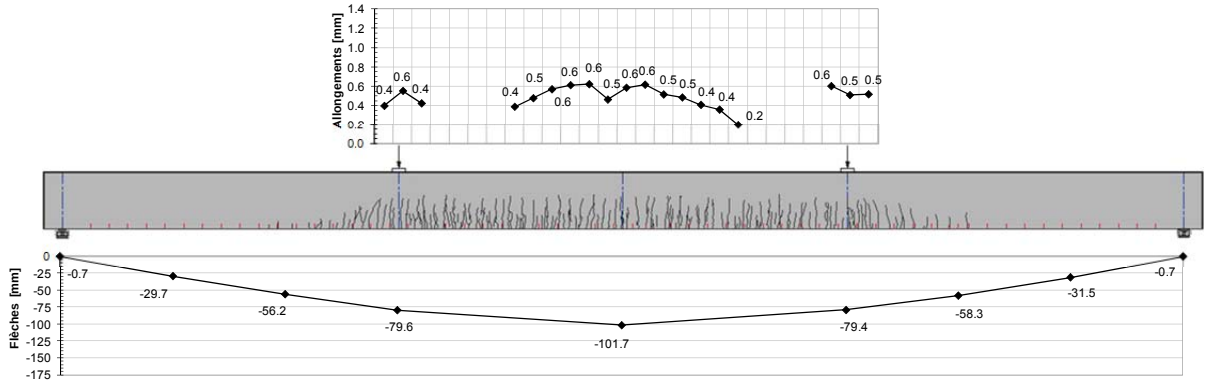

F = 400 kN

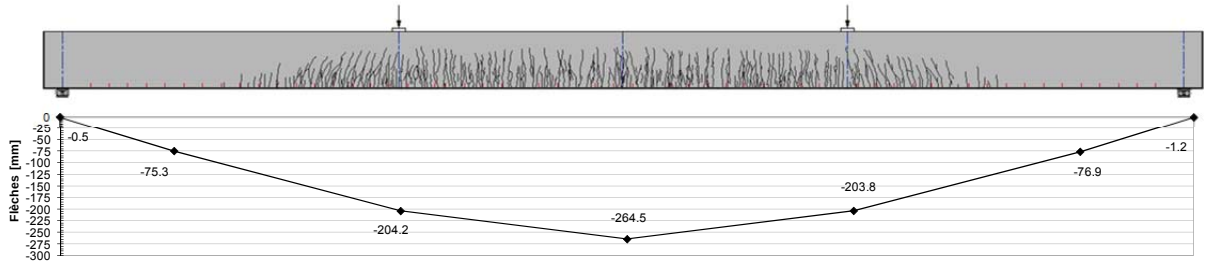

5. Analyses et Comparaisons

5.1. Poutres AV

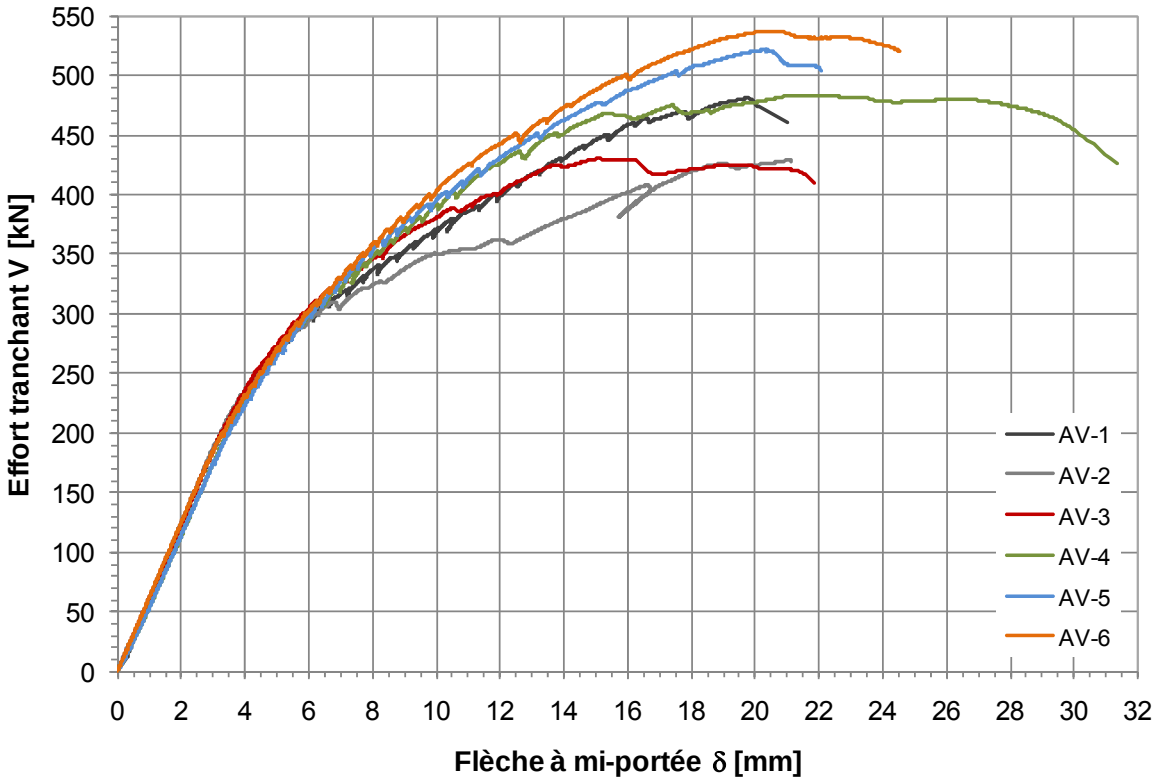

Figure 55 : Relations effort tranchant - flèches à mi-travée des poutres AV

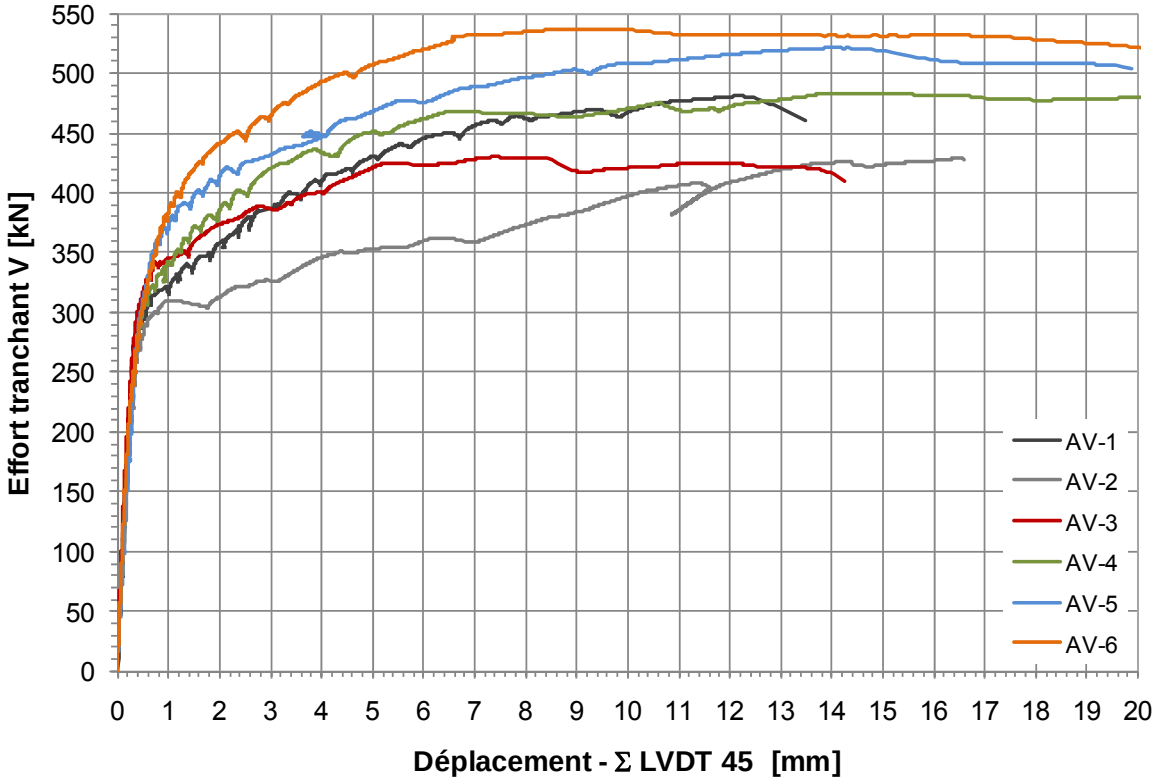

Figure 56 : Relations effort tranchant – Σ des capteurs à 45° des poutres AV

Tableau 10 : Récapitulatif des valeurs ultimes

Elément	Dosage en fibres [kg/m^3]	Charge maximale V_u [kN]	Flèche à mi-travée δ_{Fu} [mm]	Rupture [-]
AV-1	0	481 *112%*	19.8 *93%*	V
AV-2	0	429 *100%*	21.1 *100%*	V
AV-3	20	430 *100%*	15.1 *72%*	V
AV-4	40	484 113%	21.9 *104%*	V
AV-5	60	521 *121%*	20.2 *96%*	V
AV-6	80	538 *125%*	20.3 *96%*	V

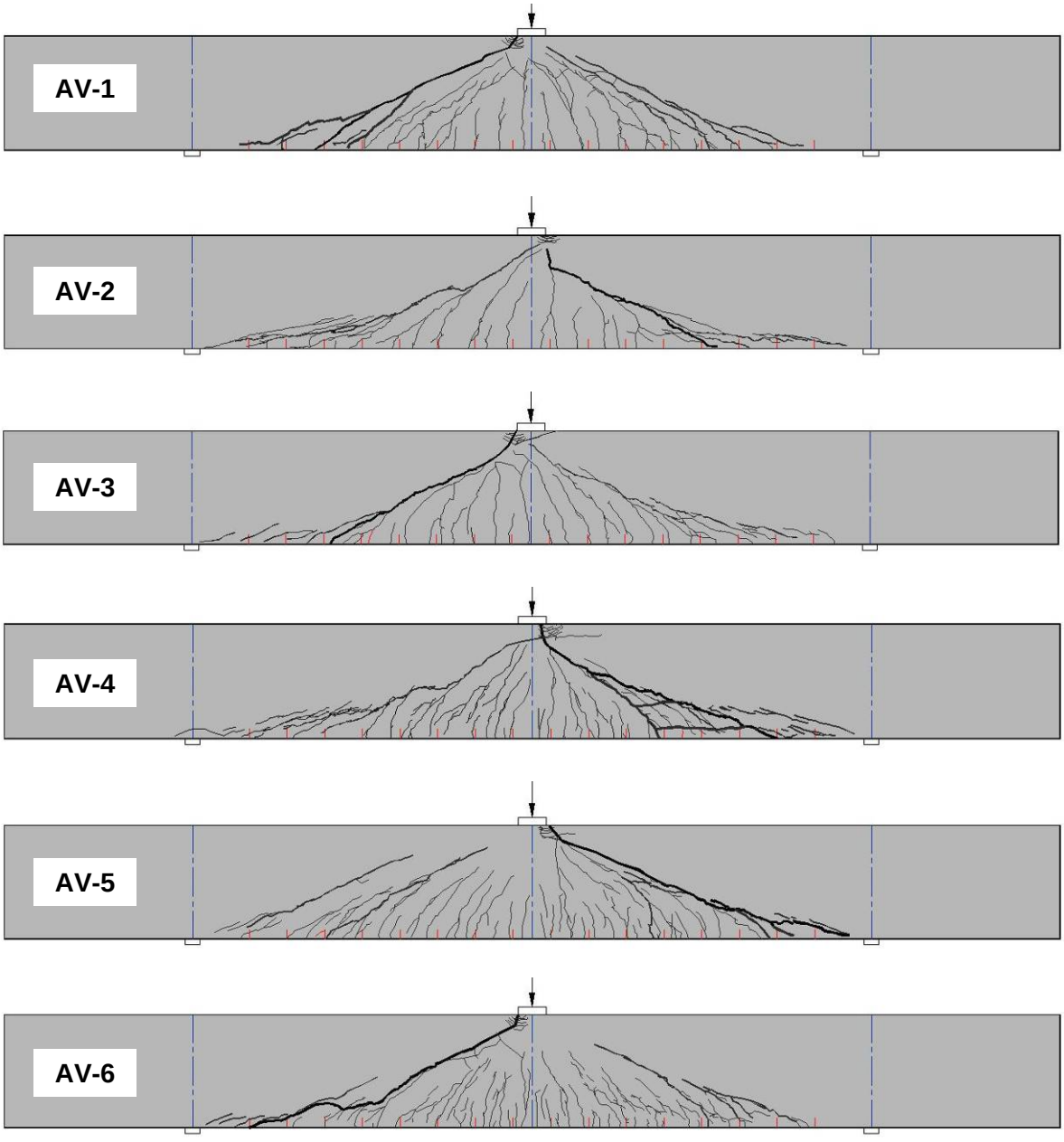

Figure 57: Distribution des fissures à la rupture des poutres AV

Le comportement en stade I est similaire entre les éléments. Les premières fissures de flexion apparaissent sous une charge de 400 kN. La quantité et le type de fibres utilisés n'affectent pas significativement la charge de fissuration de la matrice cimentaire, mais influencent la propagation et la distribution des fissures. Plus la quantité de fibres augmente, plus les fissures sont discontinues et de faible ouverture.

A partir de la charge de fissuration, la rigidité diminue progressivement et la fissuration se développe. Compte tenu de la forte précontrainte et du taux d'armature élevé, la différence de rigidité entre les poutres avec et sans fibres n'est pas importante. Cependant, la fissuration est différente. Les poutres en BFHP présentent des fissures plus rapprochées avec des ouvertures plus faibles.

A partir d'une charge de 600 kN apparaissent les premières fissures diagonales. En présence de ces fissures de cisaillement, les poutres en BFHP présentent une rigidité plus élevée. Les fibres permettent un contrôle du développement de ces fissures, par rapport à la poutre en BHP sans étriers (AV-2). Pour les éléments en BFHP, à partir d'une quantité de fibres de 40 kg/m^3, la formation des macro-fissures de cisaillement est significativement retardée par la formation d'un réseau de fissures secondaires.

La poutre AV-2 sans armatures transversales et sans fibres marque un important changement de rigidité par rapport aux autres éléments dès la formation des fissures de cisaillement. La poutre AV-2 met en évidence l'importance du renforcement transversal d'une part et l'efficacité des fibres à remplacer les armatures d'effort tranchant d'autre part. L'élément AV-2 présente deux fissures diagonales de part et d'autre de la charge. Malgré, ces deux fissures diagonales, l'élément AV-2 a une importante réserve avant la rupture en raison du degré élevé de la précontrainte.

Le mode de rupture des six éléments est similaire mais à des niveaux de charge différents. La précontrainte supérieure a empêché le développement des fissures diagonales à travers la membrure comprimée. La précontrainte supérieure a un effet comparable à une table de compression d'une section en T. Par la suite, la rupture est intervenue par éclatement ou écrasement du béton en pointe d'une fissure diagonale à la charge maximale. La rupture des éléments intervient après une chute de résistance suivie de la séparation des deux blocs au niveau de la fissure diagonale. Ce type de rupture peut être qualifié de cisaillement-compression. L'apparition de la fissure diagonale critique est de plus en plus retardée selon le dosage en fibres. L'effort axial combiné aux fibres, permet de décaler la fissure critique vers l'appui. De plus, le chemin de la force de compression tend vers une droite avec l'augmentation du dosage en fibres.

Les courbes relatives aux poutres en BFHP, mettent en évidence la capacité des fibres métalliques à remplacer l'armature minimale de cisaillement. Cependant, le dosage minimum dépend des caractéristiques des fibres et de la matrice cimentaire. Sur la base des essais de flexion 3 points sur prismes entaillés, les BFHP qui ont un comportement durcissant en flexion s'avèrent capable de contrôler le développement des fissures de cisaillement.

5.2. Poutres AF

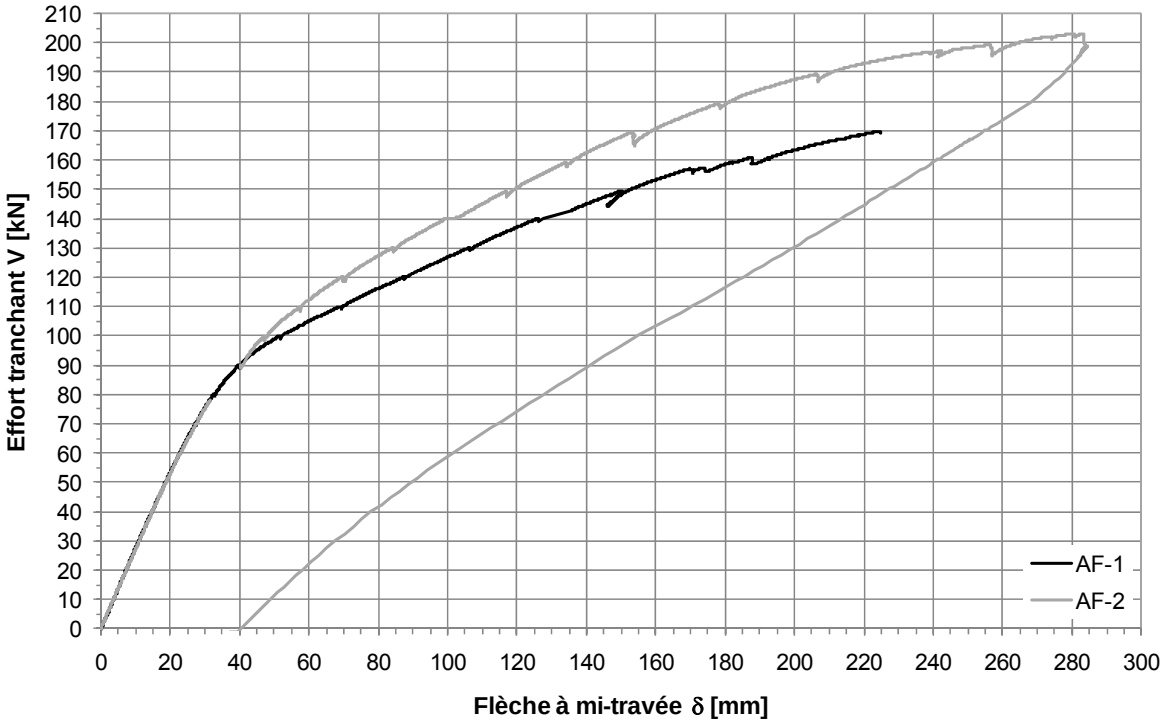

Figure 60 : Relations effort tranchant – flèche à mi travée des poutres AF

Tableau 11 : Récapitulatif des valeurs ultimes

Elément	Dosage en fibres [kg/m^3]	Essai V_u [kN]	Flèche à mi-travée δ_{Fu} [mm]	Rupture [-]
AF-1	0	170 *100%*	224 *100%*	V
AF-2	60	203 *119%*	280 *125%*	F

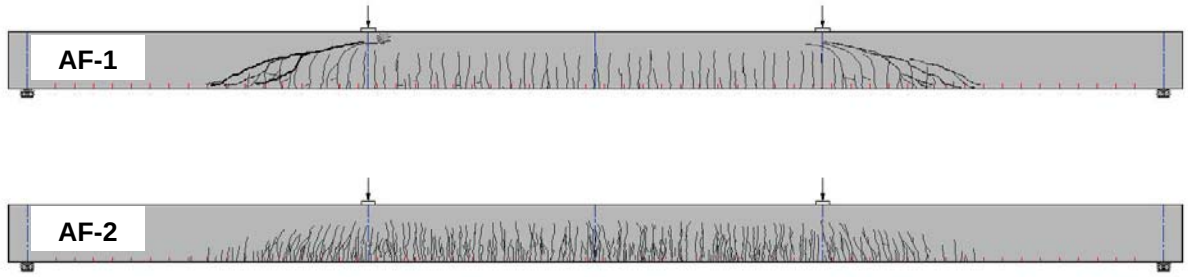

Figure 61: Distribution des fissures à la rupture des poutres AF

Le mécanisme de rupture de l'élément AF-1 est similaire à celui des poutres AV. Dans un premier temps, plusieurs fissures critiques de cisaillement se développent sans provoquer une rupture immédiate. La précontrainte supérieure empêche la propagation des fissures diagonales dans la membrure comprimée. Dans un second temps, l'évolution des fissures provoque l'éclatement du béton de la table de compression. Ce mécanisme peut être qualifié de cisaillement-compression.

La poutre AF-2, contenant 60 kg/m^3 de fibres, présente un comportement différent. La rigidité en stade II, élastique – fissuré, est nettement supérieure par rapport à la poutre AF-1 sans fibres. L'élément présente une fissuration dense avec des espacements entre fissures d'environ 30 mm et des ouvertures inférieures à 0.3 mm. A partir d'une charge F de 400 kN, plusieurs fissures rapprochées forment une macro-fissure. Cet élément a atteint sa capacité flexionnelle sans la formation de fissures diagonales de cisaillement.

Le niveau de service maximum pour les deux éléments équivaut à F_{ELS} = 200 kN (F_{flex}/ γ_{global} avec γ_{global} = 2). Compte tenu de l'intensité élevée de l'effort axial, les poutres sont peu voir pas fissurées à ce niveau de charge. Par conséquent, la contribution des fibres métalliques sur la rigidité est faible voir inexistante. Par contre à l'état limite ultime, l'effet des fibres est important en permettant d'atteindre la capacité flexionnelle de l'élément tout en évitant une rupture prématurée et brutale par cisaillement.

4. Conclusions

Les bétons fibrés à hautes performances (BFHP) se situent entre les bétons de fibres "ordinaires" (BF) et les bétons fibrés à ultra-hautes performances (BFUHP). Ces bétons reprennent une matrice cimentaire similaire aux BHP au quelle est ajouté une quantité de fibres métalliques comprise entre 40 et 160 kg/m^3 environ. Les BFHP présentent des caractéristiques mécaniques et de durabilités élevées pour des coûts de production raisonnables.

L'utilisation de ce type de béton dans l'industrie de la préfabrication présente de nombreux avantages techniques et économiques. Grâce à leur ténacité non-négligeable en traction, les BFHP permettent de supprimer partiellement voir totalement les armatures dites secondaires tels que les étriers d'effort tranchant et l'armature minimale de fissuration. La suppression de ces armatures permet un gain de temps et une simplification au niveau de la chaîne de production, d'une part, et une plus grande liberté de forme, d'autre part.

Les pannes de toiture et les poutres π sont des éléments de structures essentiellement soumis à des charges réparties de moyenne intensité ce qui engendre des sollicitations de cisaillement peu importantes. Ce type d'élément s'avère parfaitement adapté à l'emploi de BFHP. Cependant, par la nature fragile d'une rupture par cisaillement et l'absence de règles établies pour les bétons fibrés, le remplacement des armatures transversales par un BFHP demande à être vérifié théoriquement et expérimentalement.

Dans le but d'analyser l'application de bétons fibrés à hautes performances pour la fabrication d'éléments préfabriqués précontraints sans armatures d'effort tranchant, l'Ecole d'ingénieurs et d'architectes de Fribourg (EIA-FR) a effectué des études théoriques et expérimentales. Les études expérimentales comprennent deux séries d'essai. Dans la première série, dénommée AV, les poutres ont une longueur de 5.6 m et sont testées en flexion 3 points sur une portée de 3.6 m. Six éléments de ce type ont été réalisé se distinguant par leurs dosages en fibres. Dans la deuxième série, dénommée AF, les poutres ont une longueur de 12,4 m et sont testées en flexion 4 points sur une portée de 12 m. Deux éléments ont été réalisés, l'un sans fibres et l'autre avec 60 kg/m^3 de fibres métalliques.

La réalisation des bétons et des éléments d'essai, au sein de la centrale Vibéton et l'usine d'Element SA à Tavel, a permis de relever les points suivants :

- Cette étude montre la faisabilité de réaliser des BHP dans des conditions pratiques. Avec une installation de malaxage moderne disposant d'un contrôle précis de l'humidité des sables et des granulats ainsi que d'un dosage automatique des additions et des fibres, ce type de béton est facilement réalisable à l'échelle industrielle.

- De manière générale, l'ajout de fibres métalliques diminue l'ouvrabilité. Pour le type de fibres employé, un dosage de 60 kg/m^3 s'avère être la limite supérieure pour obtenir un béton auto-plaçant. L'augmentation de la quantité de sable est nécessaire pour améliorer la rhéologie.

- En présence d'une densité d'armature élevée, les fibres ont tendance à créer un maillage avec l'armature, bloquant ainsi la progression des granulats. Le surdosage en adjuvant ne permet pas de résoudre ce problème. Lorsque le dosage en fibres devient important des mesures constructives doivent être prises en considération. L'enrobage et l'écartement des armatures passives devraient au moins être égaux à la longueur des fibres l_f.

Les essais de charges effectuées au sein du Laboratoire des Structures de l'EIA-FR ont permis de relever les points suivants :

- Par rapport à un élément armé sans effort axial de compression, un élément précontraint présente une inclinaison des fissures diagonales plus faible. L'effort axial de compression permet de retarder l'apparition des premières fissures de flexion et de cisaillement et empêche le développement de fissures dans les zones proches des appuis dans le cas d'une poutre simple.

- La rupture des six éléments de 5.6 m type AV est intervenue par un mécanisme de cisaillement-compression. A la charge ultime, la table de compression s'est écrasée provoquant la séparation en deux blocs de l'élément par les fissures diagonales. L'élément de 12.4 m sans fibres AF-1 a subi une rupture par cisaillement alors que l'élément en BFHP 60 kg/m^3 AF-2 a subi une rupture par flexion.

- Deux torons ont été disposés dans la partie supérieure de la section des poutres type Av et AF afin d'éviter une pré-fissuration à vide. La présence de ces torons permet de stopper la progression de la fissure critique à travers la membrure comprimée et contribue à la formation du mécanisme de cisaillement-compression. Ceci peut être comparé à l'effet de la table de compression d'une poutre en T.

- Les éléments AV-2 et AF-1 en BHP sans fibres et sans armatures transversales ont subi une rupture très brutale par cisaillement. Dès la formation de la première fissure diagonale le comportement est devenu critique. Les plans de rupture passent à travers les granulats et présentent une surface lisse.

- L'élément AV-4, BFHP avec 40 kg/m^3 de fibres, a atteint une résistance équivalente à la poutre AV-1 armé transversalement (étriers ϕ6 @150 mm). Pour des quantités de 60 et 80 kg/m^3 de fibres, éléments AV-5 et AV-6, le gain de résistance est respectivement de 8 et 12% par rapport à la poutre AV-1.

- En fonction de la quantité de fibres, le développement et l'ouverture de la fissure diagonale critique est retardé et l'angle d'inclinaison est plus faible. A partir d'une quantité de fibres de 40 kg/m^3 plusieurs fissures diagonales se forment parallèlement.

- Dans la gamme testée, un dosage de 20 kg/m^3 de fibres n'est pas suffisant pour contrôler le développement des fissures critiques de cisaillement. Un comportement du matériau de type durcissant en flexion est nécessaire pour assurer la non-fragilité.

- Les fibres employées ont une longueur de 30 mm, un rapport de forme de 80 et une limite élastique de 2'300 MPa. L'analyse des plans de rupture montre que toutes les fibres ont subi un glissement.

- Après la fissuration, les éléments BFHP présentent une rigidité plus élevée ainsi qu'un réseau de fissures plus dense avec des ouvertures plus faibles. Cependant, ce type d'élément et fortement précontraint et s'avère peu ou pas fissuré au niveau des charges de service. Par conséquent, l'apport des fibres est négligeable à l'état limite de service ELS.

Remerciements

Les études ont été menées en collaboration et avec le soutien des entreprises Sika SA, producteur d'additifs pour le béton, Bekaert SA, fabricant de fibres métalliques, Element SA, usines de préfabrication d'éléments en béton et Vigier Béton Romandie SA, producteur de béton prêt à l’emploi. Les auteurs tiennent à remercier très sincèrement ces différentes entreprises pour leurs soutiens financiers, matériels et techniques, sans lesquels de tels projets de recherche ne pourraient être entrepris.

5. Références

[1] AÏTCIN, Pierre-Claude. *Bétons haute performance*. Paris : Eyrolles, 2001.

[2] ASCE-ACI Committee 445. Recent Approaches to Shear Design of Structural Concrete, *Journal of Structural Engineering*, Vol. 124, n°12, 1998, pages 1375 à 1417.

[3] BARON, Jacques et al. *Les bétons, Bases de données pour leur formulation*. Paris : Eyrolles, 1999.

[4] CASANOVA, Pascal. *Bétons renforcés de fibres métalliques du matériau à la structure*. Paris : Presses du Laboratoire Central des Ponts et Chaussées, 1996.

[5] DINH H., PARRA-MONTESINOS G.J., WIGHT K. J., Shear Behavior of Steel Fiber-Reinforced Concrete Beams without Stirrup Reinforcement, *ACI Structural Journal*, 2010, V. 107, pages 597 à 605.

[6] FEDERATION INTERNATIONALE DU BETON (*fib*). *Shear and punching shear in RC and FRC elements – Workshop 15-16 October 2010, Salò*. Bulletin 57, Lausanne, 2010.

[7] FALKNER, Horst / TEUTSCH, Manfred. XI Stahlfaserbeton – Anwendungen und Richtlinie, *BetonKalender*, Berlin : Ernst & Sohn, 2006

[8] HILLEMEIER, Bernd et al. IX Spezialbetone, *BetonKalender*, Berlin : Ernst & Sohn, 2006.

[9] HOLSCHEMACHER, Klaus et al. X Faserbeton, *BetonKalender*, Berlin : Ernst & Sohn, 2006.

[10] HOLCIM (Suisse) SA. *Guide pratique*, 5ème édition, 2004.

[11] HOLCIM (Suisse) SA. *Le béton autocompactant*, 1ère édition, 2009.

[12] LARRARD (de), François. *Structures granulaires et formulations des bétons*. Paris : Presses du Laboratoire Central des Ponts et Chaussées, 2000.

[13] MINELLI, Fausto. *Plain and fiber reinforced concrete beams under shear loading: structural behavior and design aspects*, PhD Thesis, Starrylink Editrice, Brescia, 2005.

[14] MUTTONI A., FERNANDEZ RUIZ M., Shear Strength of Members without Transverse Reinforcement as Function of Critical Shear Crack Width, *ACI Structural Journal,* 2008, V.105, n°2, pages 163 à 172.

[15] MUTTONI A., CAMPANA S., FERNANDEZ RUIZ M., Influence of flexural reinforcement on shear strength of prestressed concrete members*, ACI Structural Journal*, 2009, V. 106, n°1, pages 60 à 68.

[16] NAAMAN A., REINHARDT H., *Fiber reinforced concrete - Current needs for successful implementation*, International RILEM Workshop "Fiber Reinforced Concrete from Theory To practice", Bergamo, 2004.

[17] PFYL, Thomas. *Tragverhalten von Stahlfaserbeton*, Dissertation n° 15005, ETH Zürich, 2003.

[18] ROSSI, Pierre. *Les bétons de fibres métalliques*, Paris : Presses de l'Ecole Nationale des Ponts et Chaussée, 1998.

[19] SUTER R., BUCHS P. *Béton à hautes performances renforcé de fibres métalliques : Synthèse des études expérimentales menées de 2001 à 2005. Rapport de synthèse*, Ecole d'ingénieurs et d'architectes de Fribourg, 2005.

[20] SUTER R., BUCHS P. *Voussoirs préfabriqués en béton à fibres - Etude expérimentale en vue d'une optimisation de l'armature, Rapport de synthèse,* Ecole d'ingénieurs et d'architectes de Fribourg, 2005.

[21] SUTER R., MOREILLON L. *Bétons à hautes performances renforcés de fibres métalliques – Technologie des bétons, Rapport d'essai*, Ecole d'ingénieurs et d'architectes de Fribourg, 2009.

[22] SUTER R., MOREILLON L. *Bétons à hautes performances renforcés de fibres métalliques – Dalles nervurées préfabriquées, Rapport d'essai*, Ecole d'ingénieurs et d'architectes de Fribourg, 2009.

[23] SUTER R., MOREILLON L. *Bétons à hautes performances renforcés de fibres métalliques, Rapport de synthèse*, Ecole d'ingénieurs et d'architectes de Fribourg, 2009.

[24] SUTER R., NICOLET J. *Béton renforcé de fibres - Etude comparative entre fibres synthétiques et métalliques, Rapport d'étude*, Ecole d'ingénieurs et d'architectes de Fribourg, 2007.

[25] VOO J. Y. L., FOSTER S. J., GILBERT R. I., *Shear strength of fibre reinforced reactive powder concrete girders without stirrups, Test report*, University of New South Wales, 2003.

Normes et recommandations

[26] ASSOCIATION FRANCAISE DE GENIE CIVIL (AFGC). *Recommandations pour l'emploi des bétons auto-plaçant*. Paris, 2008.

[27] ASSOCIATION FRANCAISE DE GENIE CIVIL (AFGC). *Recommandations provisoires, Bétons fibrés à ultra-hautes performances*. Paris, 2002.

[28] ASSOCIATION FRANCAISE DE GENIE CIVIL (AFGC). *Recommandations provisoires, Bétons fibrés à ultra-hautes performances - Annexes*. Paris, 2002.

[29] FEDERATION INTERNATIONALE DU BETON (*fib*). *Model Code 2010 – First complete draft*. Bulletin 55, Lausanne, 2010.

[30] FEDERATION INTERNATIONALE DU BETON (*fib*). *Model Code 2010 – First complete draft*. Bulletin 56, Lausanne, 2010.

[31] RILEM TC 162-TDF, *Test and design methods for steel fibre reinforced concrete : bending test.* Bagneux : RILEM, 2002.

[32] RILEM TC 162-TDF, *Test and design methods for steel fibre reinforced concrete: sigma-epsilon-design method*. Bagneux : RILEM, 2003.

[33] NF EN 14'651+A1, Norme européenne version française. *Méthode d'essai du béton de fibres métalliques – Mesurage de la résistance à la traction par flexion (limite de proportionnalité (LOP), résistance résiduelle)*. Paris : AFNOR, 2007.

[34] SN 505-262, Norme suisse. *Construction en béton*. Zürich : Société suisse des ingénieurs et architectes, 2003.

[35] SN 505-262/1, Norme suisse. *Construction en béton – Spécifications complémentaires*. Zürich : Société suisse des ingénieurs et architectes, 2003.

[36] SN 562 162/6, Recommandation. *Béton renforcé de fibres métalliques*. Zürich : Société suisse des ingénieurs et architectes, 1999.

Ecole d'ingénieurs et d'architectes de Fribourg
Hochschule für Technik und Architektur Freiburg

MATERIAUX ET INNOVATION

Bétons à hautes performances renforcés de fibres métalliques

Projet de recherche : AGP 13'940
CTI 7'459.2
Cemsuisse 200'498

POINCONNEMENT DE DALLES

René Suter, professeur dr. sc tech.,
Lionel Moreillon, ingénieur MSc ENPC

RAPPORT D'ESSAIS

Hes·so FRIBOURG FREIBURG
Haute Ecole Spécialisée de Suisse occidentale
Fachhochschule Westschweiz

JUILLET 2009

Table des matières

1. Introduction

1.1. Les bétons fibrés à hautes performances

Le terme béton à hautes performances (BHP) englobe tous les bétons qui comportent des caractéristiques particulières. Ces particularités peuvent être aussi bien en rapport à leurs caractéristiques mécaniques, à leur ouvrabilité ou encore à leur durabilité. Par rapport aux bétons ordinaires (BN), les BHP présentent une résistance à la compression ainsi qu'un module d'élasticité plus élevés et un développement rapide du fluage. Ces caractéristiques permettent respectivement une réduction de la section des éléments porteurs et par conséquent une diminution du poids propre de la structure, un décoffrage plus rapide et une durabilité accrue. Ces propriétés sont atteintes en abaissant le rapport eau/liant, en augmentant la compacité du mélange et en utilisant des additions réactives. La granulométrie des BHP est généralement proche de celle d'un béton standard tandis que la quantité de liant est comprise entre 400 kg/m^3 et 600 kg/m^3. L'ouvrabilité du béton frais est, quand à elle, améliorée en ajoutant des fluidifiants et/ou des ajouts à haute teneur en particules fines [2]. Dans le cadre de cette étude, seules les propriétés mécaniques sont analysées. Le béton est défini à hautes performances si sa résistance en compression sur cylindre est comprise entre 60 et 120 MPa.

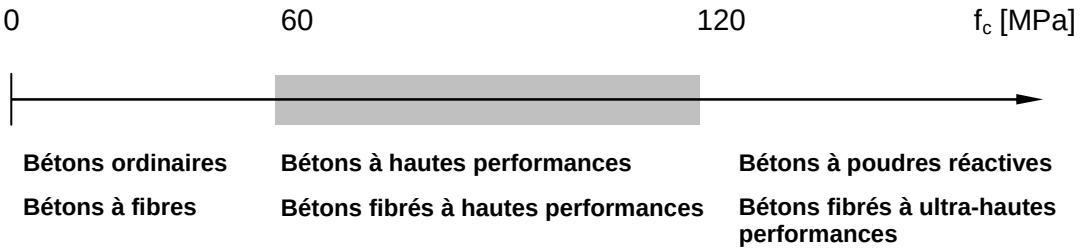

Fig. 1 : Arche de la Défense.

Fig. 2 : Pont sur le Bras de la Plaine.

Depuis quelques années, les bétons à fibres (BF) sont sujets à de nombreux développements expérimentaux et industriels. Ce matériau composite particulier présente des caractéristiques supérieures à celles des bétons ordinaires, notamment au niveau de ses résistances à la traction et au cisaillement, de sa rigidité à l'état fissuré ainsi que de sa ductilité. Les bétons fibrés se situent entre le béton non armé et le béton armé. Actuellement leurs utilisations restent cantonnées à des domaines d'applications spécifiques comme les dallages, les chaussées, certains éléments préfabriqués et le béton projeté [32]. **Les bétons fibrés à hautes performances (BFHP)** reprennent une matrice cimentaire similaire au BHP, dans laquelle est ajoutée une certaine quantité de fibres métalliques et/ou synthétiques. Cet ajout donne un caractère plus ductile au BHP qui est souvent caractérisé par un comportement fragile.

L'utilisation de bétons fibrés à hautes performances présente de nombreux avantages techniques et économiques pour tous les acteurs de la construction. Associés aux techniques de la précontrainte, ils ouvrent des voies nouvelles dans la conception de structures plus élancées et de systèmes porteurs innovants et durables. Les BFHP sont produits depuis plusieurs années en condition de laboratoire, par contre les applications pratiques restent marginales malgré ces nombreux atouts. Les raisons de ce constat sont les suivantes : le manque de maîtrise de la production et de la mise en œuvre, la mauvaise connaissance des caractéristiques spécifiques et l'absence de règles cohérentes de dimensionnement.

1.2. Projet bétons à hautes performances renforcés de fibres métalliques

L'Ecole d'ingénieurs et d'architectes de Fribourg (EIA-FR) a mené avec le soutien de l'agence pour la promotion de l'innovation CTI, un vaste projet de recherche sur les bétons à hautes performances renforcés de fibres métalliques [42-45]. Ce projet s'est effectué en collaboration avec l'industrie du ciment Cemsuisse ainsi que d'autres partenaires industriels. Les objectifs visés de la recherche sont les suivants :

- mettre au point des recettes de bétons type BFHP adaptées à des applications spécifiques ;
- déterminer les caractéristiques mécaniques de ces bétons ;
- analyser le comportement d'éléments de structures en BFHP sous l'effet de charges et déformations imposées ;
- développer des modèles de résistance permettant le dimensionnement des structures en BFHP.

1.3. Poinçonnement des dalles

Les dalles sont les éléments centraux de la construction en béton pour des planchers ou des dalles de roulement de ponts. L'utilisation de BFHP dans des constructions neuves permettrait de réaliser des systèmes porteurs innovants et durables. Ceci s'adresse particulièrement aux tabliers de ponts où les exigences concernant les caractéristiques mécaniques et la durabilité des matériaux sont élevées (fig. 3). Malgré un surcoût du matériau, des économies importantes au niveau de l'ouvrage sont effectuées notamment au niveau des fondations dû à la réduction du poids propre de la structure. Dans le domaine de la transformation ou de la rénovation de structures existantes, les BFHP ouvrent la voie à de nouvelles solutions techniques attractives (fig. 4) [39].

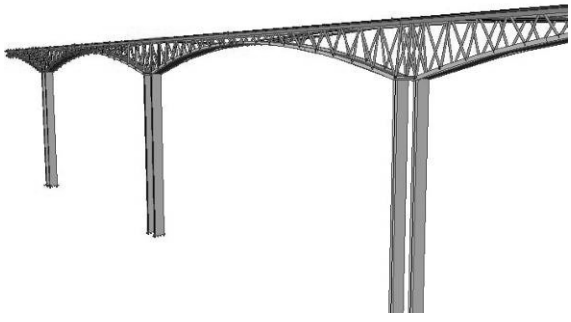

Fig. 3 : Tablier à âmes triangulées.

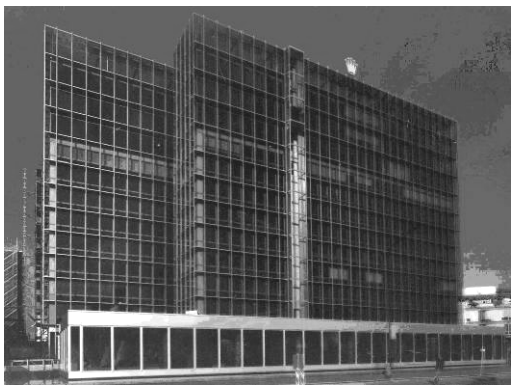

Fig. 4 : Surélévation du siège social de Rolex.

Lorsque l'épaisseur des dalles diminue, outre la flexion, le poinçonnement devient un mode de rupture déterminant. Pour des dalles ne comportant pas d'armature d'effort tranchant, ce mode de rupture est caractérisé par un comportement fragile qui généralement entraîne l'effondrement partiel ou total de la structure, comme en témoigne des accidents survenus en Suisse et à l'étranger [9]. La ruine par poinçonnement se produit à l'endroit d'une force concentrée, colonne ou charge extérieure, provoquant ainsi une rupture locale par pénétration au travers du plancher. Ce mécanisme de rupture forme un cône séparé de la dalle par la fissure de poinçonnement. Cette fissure présente une inclinaison par rapport au plan de la dalle variant entre 25° et 40° [15]. Mal gré de nombreuses recherches menées dans ce domaine, le poinçonnement reste un phénomène complexe faisant intervenir beaucoup de paramètres, dont l'approche actuelle est simplifiée.

Fig. 5 : Poinçonnement d'une dalle de parking.

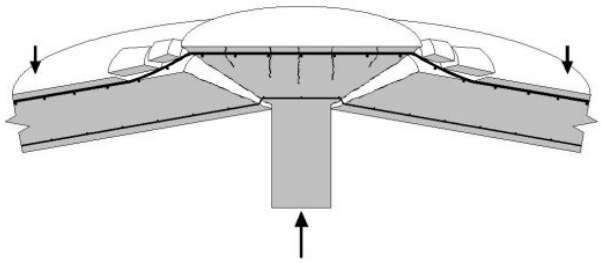

Fig. 6 : Mécanisme de rupture au poinçonnement.

1.4. Objectifs et buts de l'étude

Dans le but d'analyser l'application de bétons à hautes performances pour la fabrication de dalles minces, l'Ecole d'ingénieurs et d'architectes de Fribourg (EIA-FR) à entrepris, en 2006/7 des études théoriques et expérimentales. Ces études s'inscrivent dans le cadre d'un projet de recherche plus vaste sur les bétons à hautes performances renforcés de fibres métalliques, que l'EIA-FR mène actuellement en collaboration avec l'industrie du ciment (Cemsuisse), et d'autres partenaires industriels. Les objectifs des études théoriques et expérimentales sont les suivants :

- analyser le comportement de dalles minces, soumises à une charge concentrée,
- déterminer l'influence et les interactions de l'armature, de la précontrainte et des fibres métalliques sur la résistance au poinçonnement,
- établir des règles de dimensionnement pour des éléments en BFHP,

Dans une première phase, il s'agit de mettre au point un BFHP de classe C90/105. Au moyen de nombreux essais sur des échantillons de béton durci, les caractéristiques spécifiques sont identifiées [42].

Dans une deuxième phase, des essais de poinçonnement sont réalisés sur 20 dalles carrées en béton à hautes performances. Leurs dimensions sont de 1.24 m de côté pour une épaisseur de 120 mm. Les paramètres variant entre les éléments d'essai sont : la quantité de fibres, le taux d'armature et le taux de précontrainte.

2. Technologie des bétons

2.1. Composition des bétons

Cinq recettes de béton à hautes performances, avec et sans fibres métalliques, ont été élaborées. Afin de répondre aux critères techniques, économiques et de mise en œuvre, les recettes de béton doivent satisfaire au cahier des charges suivant :

- résistance moyenne sur cylindre à 28 jours ($f_{cm,28}$) de 100 MPa,
- compactage standard par vibration,
- emploi de granulats locaux, granularité 0-8mm,
- dosages en fibres de 0, 20, 40, 60 et 80 kg/m^3

La formulation de ces bétons est fondée sur une composition mise au point lors de recherches antérieures sur les BHP et ayant donnée satisfaction en matière d'ouvrabilité et de résistance. Il s'agit d'un micro béton car la granularité se limite à 8 mm. L'utilisation d'un ciment composé à la fumée de silice dosé à 500 kg/m^3 ainsi qu'un rapport eau/ciment bas, se sont imposés pour atteindre une résistance élevée. L'ouvrabilité du béton frais n'a pas été un point déterminant dans cette formulation compte tenu d'une mise en place par vibration.

Les fibres utilisées sont de type Bekaert Dramix® RC-80/30-BP en acier tréfilé avec crochets. Elles sont adaptées aux bétons à hautes performances avec une résistance et un rapport l_f/d_f élevés. Les principales caractéristiques techniques des fibres sont les suivantes :

- longueur l_f: 30 mm
- diamètre d_f: 0.375 mm
- rapport l/d: 80
- module d'élasticité: 210'000 MPa
- limite d'élasticité: 2'300 MPa

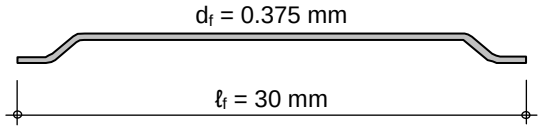

Fig. 7 : Géométrie des fibres.

Le tableau 8 comporte les indications relatives à la composition de chaque béton.

BFHP - phase II	Dénomination projet		**B2-1**	**B2-2**	**B2-3**	**B2-4**	**B2-5**
	Dénomination rapport		**B1**	**B2**	**B3**	**B4**	**B5**
Ajout [kg/m^3]	Fibres métalliques Bekaert Dramix® RC-80/30-BP		**0**	**20** V_f = 0.25%	**40** V_f = 0.5%	**60** V_f = 0.75%	**80** V_f = 1%
Sable 0-4 [kg/m^3]	Granulats roulés Provenance : Châtillon	50%	333	331	330	328	327
Gravier 4-8 [kg/m^3]	Granulats roulés Provenance : Châtillon	50%	333	331	330	328	327
Ciment [kg/m^3]	CEM II 52,5R Holcim (Siggenthal)		500	500	500	500	500
Adjuvant [% de C]	Fluidifiant Sika® ViscoCrete®-20 HE		1.0	1.1	1.3	1.4	1.5
Eau y.c. adjuvant [litres/m^3]			150	150	150	150	150
Rapport E_{tot}/C			0.30	0.30	0.30	0.30	0.30

Tab. 1 : Dénomination et dosage en fibres des différents bétons.

Les cinq recettes mises au point ont une matrice cimentaire identique. Le dosage en adjuvant et la quantité de granulats sont adapté en fonction du dosage en fibres métalliques. Aucuns essais sur bétons frais ne sont effectués sur les bétons de la phase II.

2.2. Essais sur bétons durcis

Les caractéristiques mécaniques moyennes à 28 jours sont les suivantes :

			B1	B2	B3	B4	B5
Compression sur cylindre	$f_{cm,\,28}$	[MPa]	99.0	103	108	106	107
Module d'élasticité	$E_{cm,\,28}$	[MPa]	44'200	41'500	46'800	40'200	43'300
Traction effective	f_{ctf}	[MPa]		1.1	1.9	1.9	2.0
Cisaillement par torsion	τ_{ct}	[MPa]	8.5	8.4	8.5	9.2	9.5

Tab. 2 : Caractéristiques mécaniques moyennes des différents bétons.

Dans le domaine de la construction, les bétons sont historiquement classés par leur résistance à la compression. Néanmoins cette seule caractéristique ne suffit pas à classer les bétons renforcés de fibres [2]. Pour qualifier un tel béton, il est nécessaire d'analyser ses performances en traction.

Les essais réalisés sur cylindres montrent que l'adjonction de fibres métalliques influence peu la résistance à la compression. Au dessus d'une résistance de 60 MPa, le béton a un comportement fragile. Les fibres permettent d'éviter un éclatement brutal et confèrent au béton un comportement ductile. La montée en résistance dans le temps s'effectue rapidement et évolue encore dans le temps de manière significative. L'ajout de fibres métalliques ne permet pas d'améliorer le module d'élasticité du béton. Celui-ci est principalement dirigé par les volumes et modules d'élasticité relatifs de la pâte de ciment et des granulats.

Compte tenu de sa faible valeur et de son caractère fragile, la résistance à la traction f_{ct} est en principe négligée lors du dimensionnement des ouvrages. Les fibres ne permettent pas d'augmenter cette résistance, par contre elles autorisent la reprise d'un effort de traction post-fissuration. Les essais de traction directe sur les bétons à fibres, bien que riches en enseignements, sont souvent délicats et demandent un travail de préparation important. Pour cette raison, la résistance résiduelle en traction f_{ctf} est souvent définie de manière indirecte par un essai de flexion sur prisme ou de poinçonnement sur plaque. Dans le cadre de cette étude deux différents types d'essai sont effectués : flexion trois points sur prismes entaillés selon la norme EN 14'651 [23] et poinçonnement sur plaques carrées selon la recommandation SIA162/6 [37] (fig. 8).

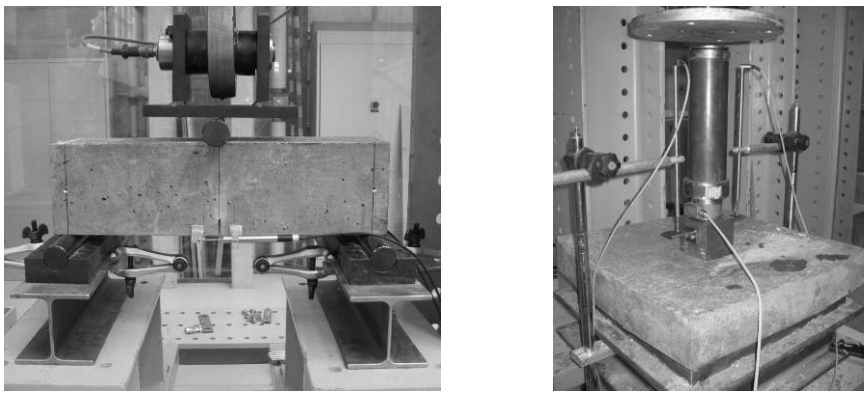

Fig. 8 : Essais de flexion 3 points et de poinçonnement.

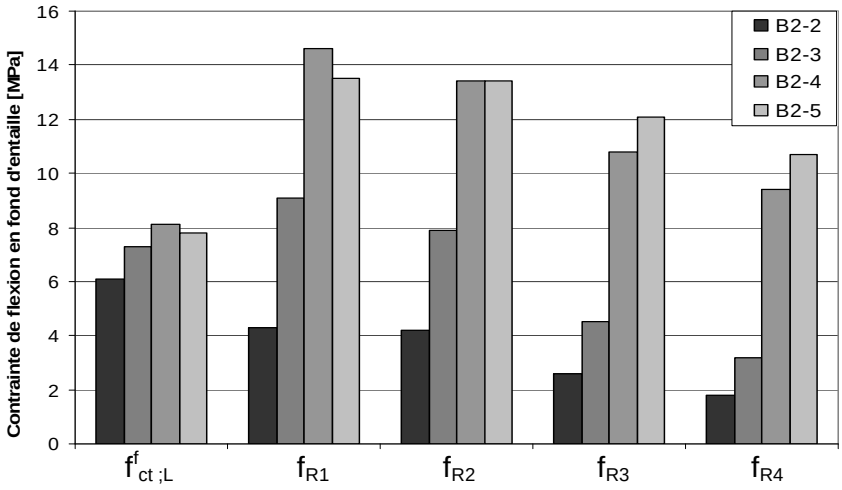

Fig. 9 : Comparatifs des valeurs d'essais de flexion sur prismes entaillés selon EN 14'651.

Les résistances résiduelles à la traction par flexion (f_{R1} à f_{R4}) sont directement influencées par le taux de fibres. Le BFHP B2 contenant 20 kg/m^3 de fibres a un comportement adoucissant en flexion. Pour des dosages en fibres plus élevé, les bétons testés ont un comportement écrouissant en flexion. Cet apport de résistance est plus ou moins marqué, le BFHP B3 contenant 40 kg/m^3 de fibres perd relativement vite la sur-résistance. Les deux BFHP B4 et B5 contenant respectivement 60 et 80 kg/m^3 de fibres permettent de garder une résistance élevée même pour des ouvertures d'entaille importante. Cet apport de résistance est très intéressant pour une structure en flexion.

Le cisaillement tel qu'il est utilisé pour le dimensionnement des structures n'a pas, à proprement dit, de représentation physique. Cette grandeur est un modèle qui, en réalité, découle des contraintes principales dans le matériau. Le cisaillement apparaît dans tous les éléments de structures fléchis ou soumis à la torsion. La résistance au cisaillement du béton n'est pas aisée à déterminer de manière expérimentale (fig. 10). L'essai de torsion développé à l'EIA-FR permet d'identifier des contraintes de cisaillement quasiment pures.

Les résultats des essais de cisaillement par torsion montrent que les résistances maximales moyennes τ_{ctm} obtenues sont proches pour les bétons analysés. Cette valeur dépend principalement de la qualité de la matrice de béton si les fibres n'apportent pas un comportement écrouissant post-fissuration. Dans ce cas, cette résistance maximale est corrélée à la résistance en traction du béton f_{ct}.

La résistance résiduelle au cisaillement par torsion ne peut pas être mesurée de manière fiable. Le dispositif permet seulement de diriger l'essai en couple et pas en déformation angulaire. Une fois la matrice fissurée, l'énergie libérée est trop importante et le contrepoint redescend trop rapidement pour permettre un enregistrement des valeurs post-fissuration.

Fig. 10 : Machine d'essai de torsion de type Amsler et prisme après essai de torsion.

3. Essais de poinçonnement

3.1. Description

La série d'essai est composée de 20 dalles carrées en béton à hautes performances. Leurs dimensions sont de 1240 mm de côté pour une épaisseur de 120 mm. Les éléments d'essai comprennent 8 réservations de diamètre 50 mm réparties sur un cercle de rayon 565 mm permettant le passage des tiges d'appui (fig. 14). Les paramètres variant entre les éléments d'essai sont : la quantité de fibres, le taux d'armature et le taux de précontrainte.

En fonction du taux d'armature passive, les dalles contiennent une armature supérieure de flexion composée de barres façonnées en acier B500B de diamètre 8/10/12 mm espacées de 100 mm et disposées orthogonalement avec un enrobage de 20 mm. Les dalles avec précontrainte contiennent une armature supérieure composée de barres de diamètre 10 mm ainsi qu'une armature inférieure composée de barres de diamètre 8 mm, espacées de 100 mm dans les deux directions. L'armature inférieure est interrompue dans la zone centrale (zone grisée) afin de ne pas influencer le poinçonnement de la dalle (fig. 11).

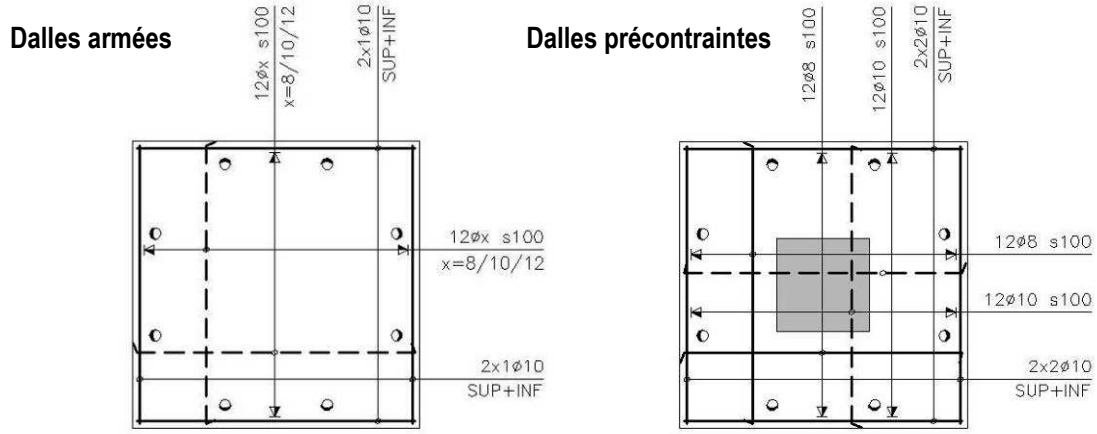

Fig. 11 : Schéma d'armature des dalles d'essai.

En fonction du degré de précontrainte les dalles contiennent deux ou quatre torons rectilignes par côté disposés à la hauteur de l'axe neutre. Il s'agit d'une précontrainte non adhérente, composée de monotorons gainés graissés de type Y1770S7-15.7 (fig. 12). L'effort de précontrainte est introduit dans le béton au travers de plaques de 120 x 120 x 20 mm en acier placées derrière chaque tête d'ancrage. Trois taux de précontrainte sont mis en œuvre dans les deux directions : 2 x 180 kN, 4 x 135 kN et 4 x 180 kN.

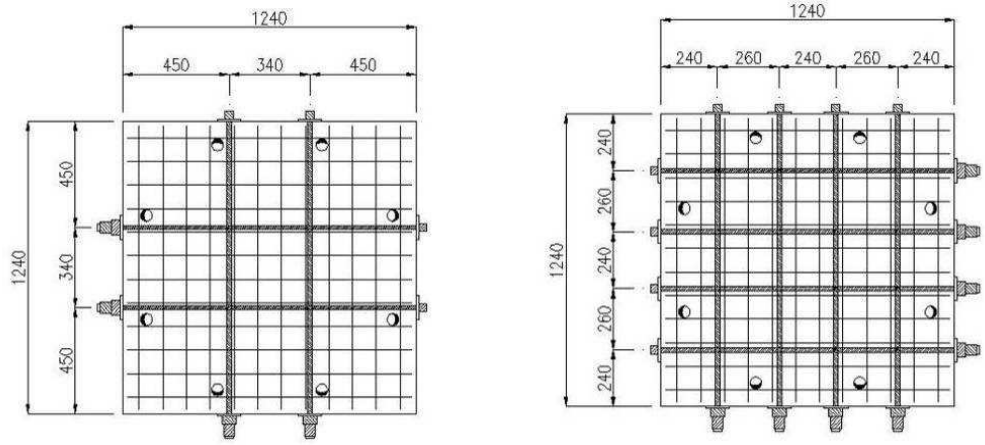

Fig. 12 : Schéma de précontrainte des dalles d'essai.

Dénomination	Dosage en fibres	Armature de flexion	Précontrainte
Bi-01	i=1 / sans fibres i=2 / 20 kg/m^3 i=3 / 40 kg/m^3 i=4 / 60 kg/m^3 i=5 / 80 kg/m^3	ϕ10 s = 100 mm ρ = 0.87%	
Bi-02	i=1 / sans fibres i=3 / 40 kg/m^3 i=5 / 80 kg/m^3		2 x 2 x 180 kN $\sigma_{cp,0}$ = 2.42 MPa
Bi-03			2 x 4 x 135 kN $\sigma_{cp,0}$ = 3.63 MPa
Bi-04			2 x 4 x 180 kN $\sigma_{cp,0}$ = 4.84 MPa
Bi-05		ϕ8 s = 100 mm ρ = 0.56%	
Bi-06		ϕ12 s = 100 mm ρ = 1.26%	

Tab. 3 : Récapitulatif des caractéristiques des éléments d'essai.

Les essais de charge sont réalisés au sein du laboratoire des structures de l'EIA-FR, sur un dispositif d'essai au poinçonnement d'une capacité de 4'000 kN (fig. 13). La mise en charge s'effectue par un vérin hydraulique placé au centre surmonté d'un poinçon de diamètre 120 mm. Le vérin est contrôlé en déplacement par un système d'asservissement servo-électronique reproduisant un chargement quasi-statique. L'élément est testé face coffrée en supérieur. La dalle est retenue par huit tiges filetées et ancrées au sol du laboratoire au travers de profilés en acier. Le système d'appui décrit un cercle de 565 mm de rayon et autorise les rotations au travers de rotules.

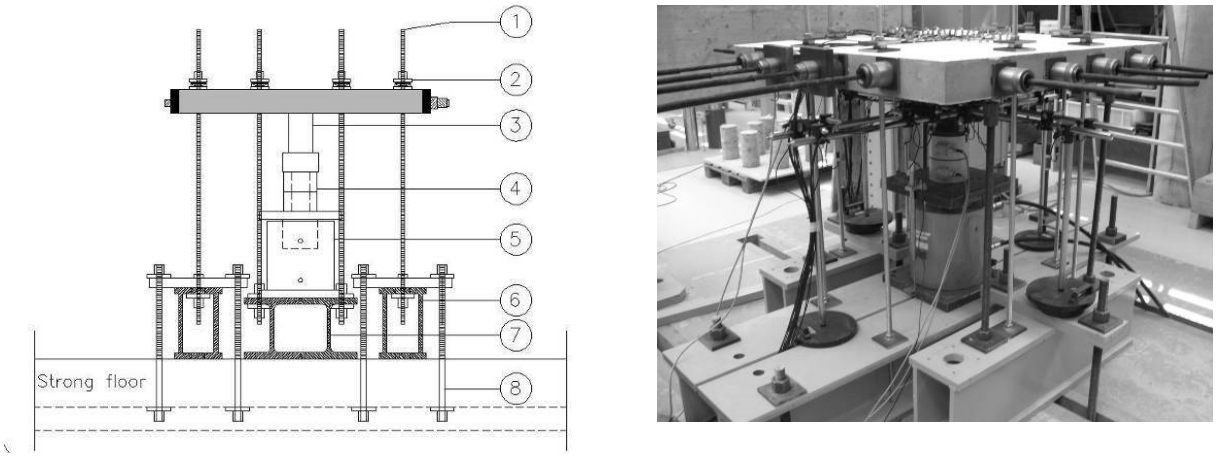

Fig. 13 : Dispositif d'essai au poinçonnement.

1 tiges filetées M20
2 rotules SKF et plaques de répartition 100 x 100 x 10 mm
3 poinçon en acier ϕ 120 mm et colonne de mise en charge
4 cellules de force HBM
5 vérin Lukas 4000 kN d=150 mm
6 caissons de retenu
7 profilé de retenu HBM 280
8 tiges d'ancrage MSP

Le système statique représente un champ de dalle central à trame régulière. La portée expérimentale de 1.13 m (diamètre du cercle d'appuis) correspond à la ligne des moments radiaux nuls (fig. 14). Le moment radial d'une dalle appuyée sur une colonne de champs intérieur est nul sur un cercle de rayon qui équivaut à 0.22 multiplié par la portée L [11]. Ceci signifie que la configuration d'essai représente une portée fictive de 2.57 m.

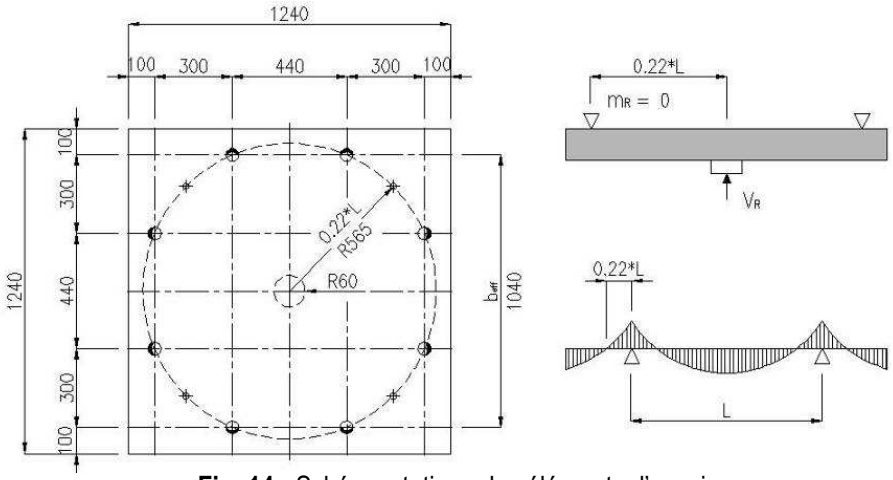

Fig. 14 : Schéma statique des éléments d'essai.

Le système de mesures est composé de trois réseaux de capteurs mesurant les forces appliquées, les flèches et l'ouverture des fissures (fig. 15).

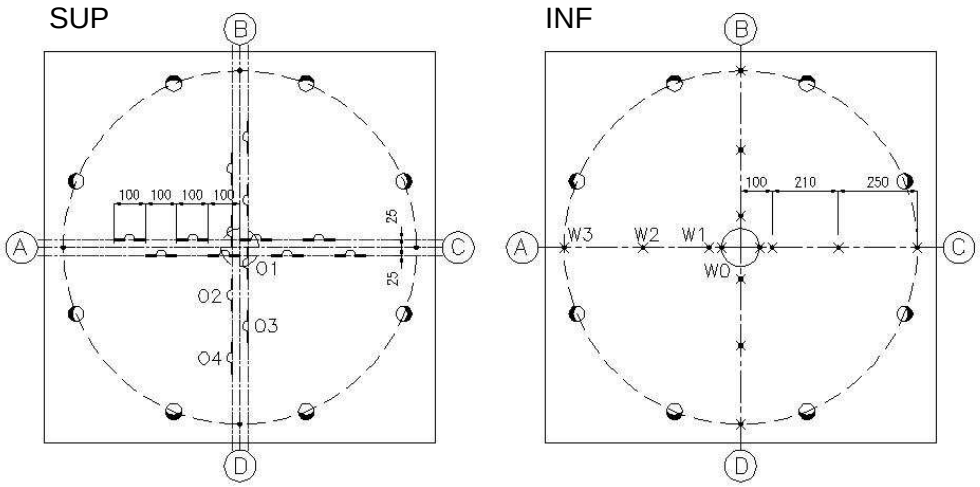

Fig. 15 : Disposition des instruments de mesures sur les dalles d'essai.

Le programme de chargement comprend trois cycles de chargement – déchargement aux niveaux des charges : de service (V_{Rd}/1.4) et de dimensionnement V_{Rd} (tab.4).

Dénomination des dalles	**Bi-01**	**Bi-02**	**Bi-03**	**Bi-04**	**Bi-05**	**Bi-06**
Charge de service V_{serv} [kN]	130	150	155	160	120	140
Charge de poinçonnement V_{Rd} selon SIA 262 [kN]	182	207	215	220	165	200

Tab. 4 : Charges de dimensionnement V_{Rd} selon la norme SIA 262.

3.2. Résultats

3.2.1. Dalle B1-01

Caractéristiques :

- Béton B1 sans fibres f_{cm} = 90 MPa
- Armature longitudinale supérieure : ϕ10 s = 100 mm (ρ = 0.87 %)

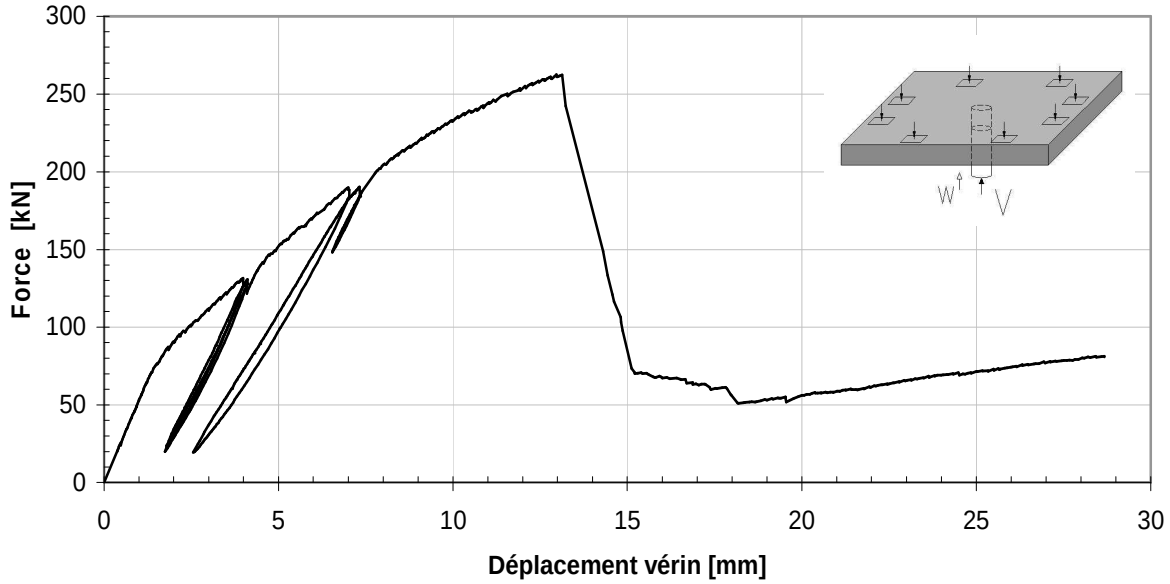

Fig. 16 : Courbe force – déplacement du vérin de la dalle B1-01.

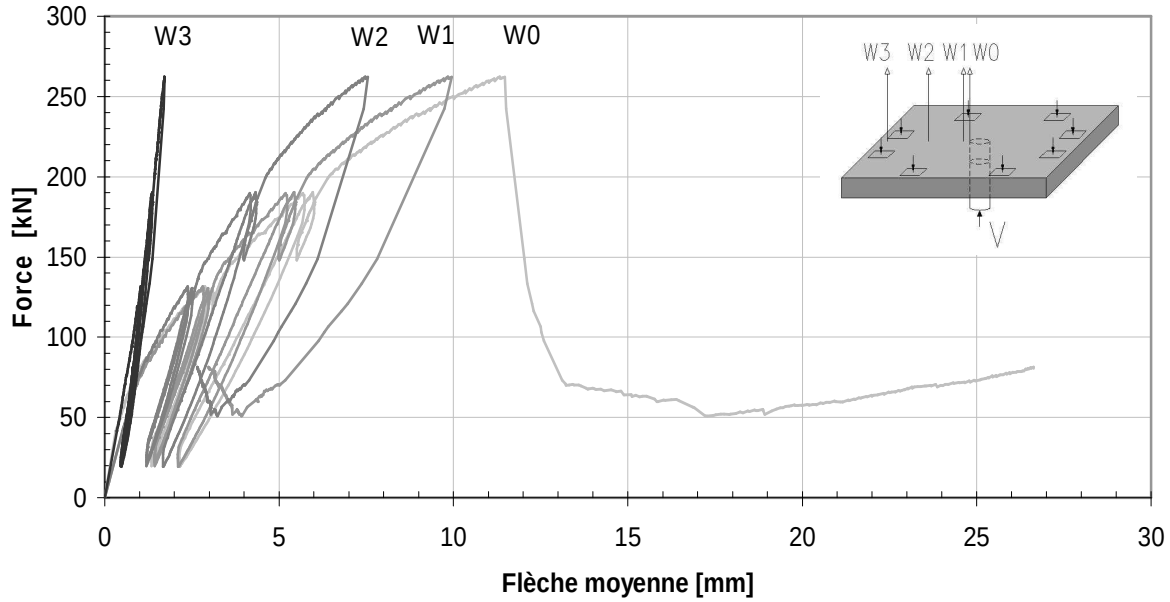

Fig. 17 : Courbes force – flèche moyenne de la dalle B1-01.

Force maximale V_{test} [kN]	Flèche au centre W_0 [mm]	Rotation ψ [‰]
262	**11.3**	**21.1**

Tab. 5 : Résultats principaux de l'essai de la dalle B1-01.

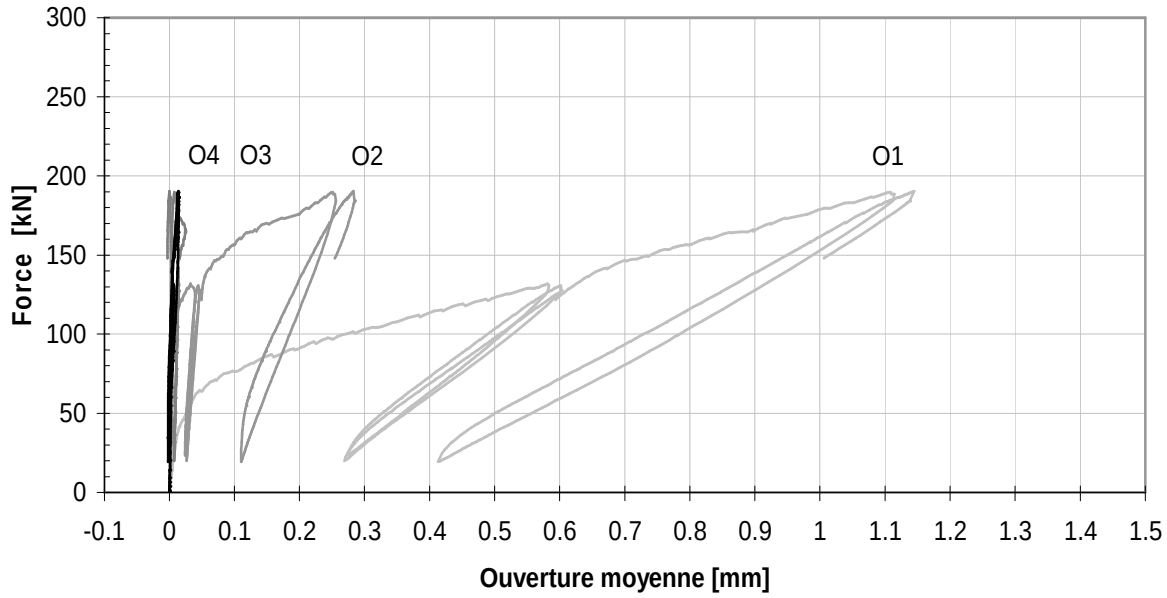

Fig. 18 : Courbes force – ouverture moyenne des fissures de la dalle B1-01.

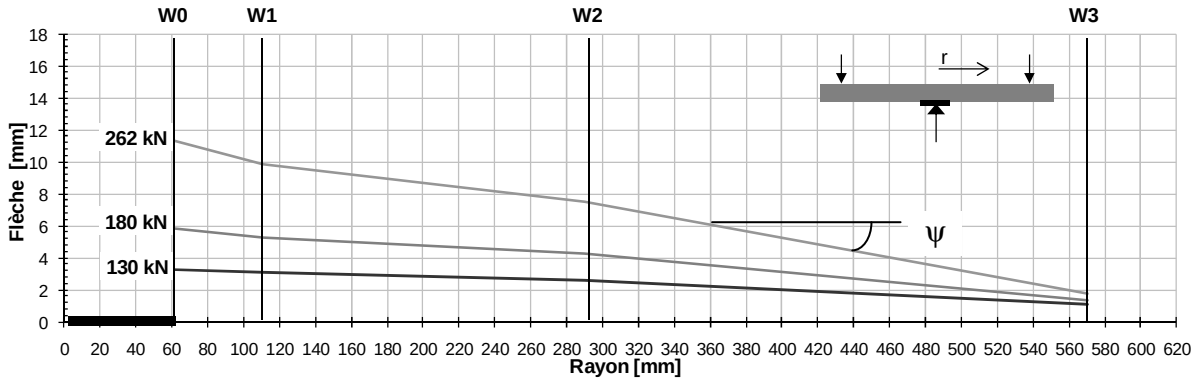

Fig. 19 : Déformation moyenne de la dalle B1-01 à plusieurs niveaux de charge.

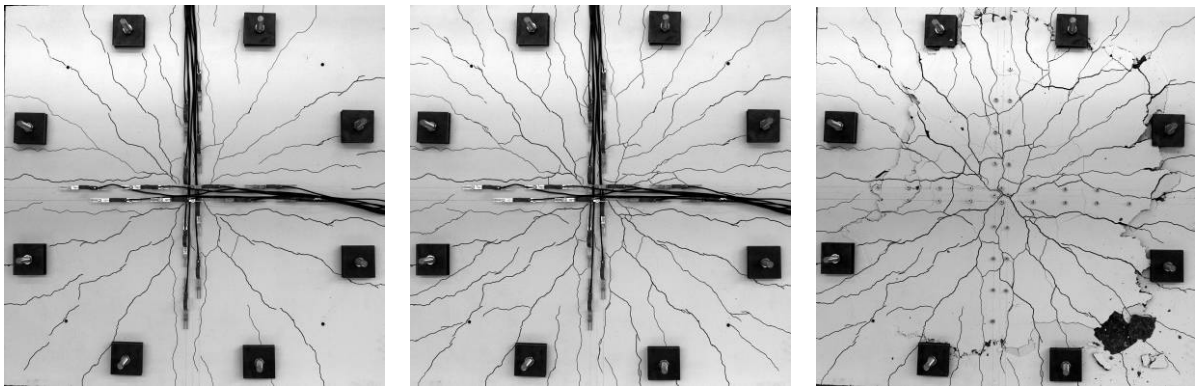

Charge de service 130 kN | Charge de dimensionnement 180 kN | Rupture

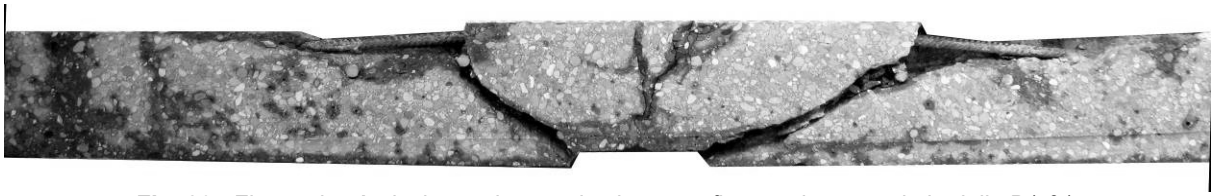

Fig. 20 : Fissuration à plusieurs niveaux de charge et fissures internes de la dalle B1-01.

3.2.2. Dalle B1-02

Caractéristiques :

- Béton B1 sans fibres f_{cm} = 90 MPa
- Armature longitudinale supérieure : ϕ10 s = 100 mm ρ = 0.87 %
- Précontrainte : 2 x 2 x 180 kN $\sigma_{cp,0}$ = 2.42 MPa

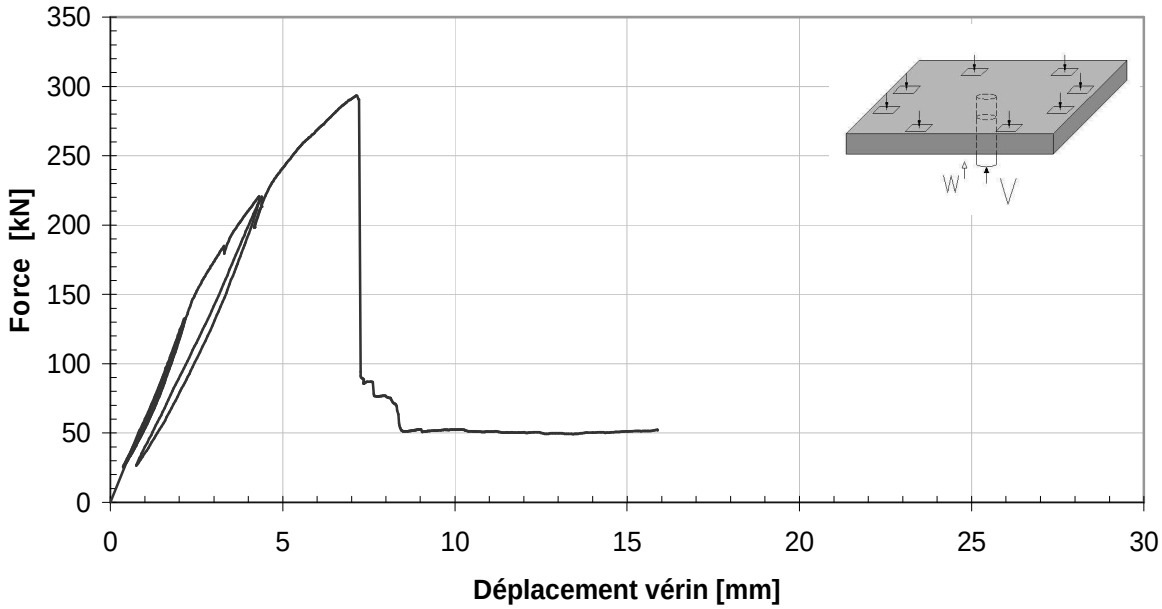

Fig. 21 : Courbe force – déplacement du vérin de la dalle B1-02.

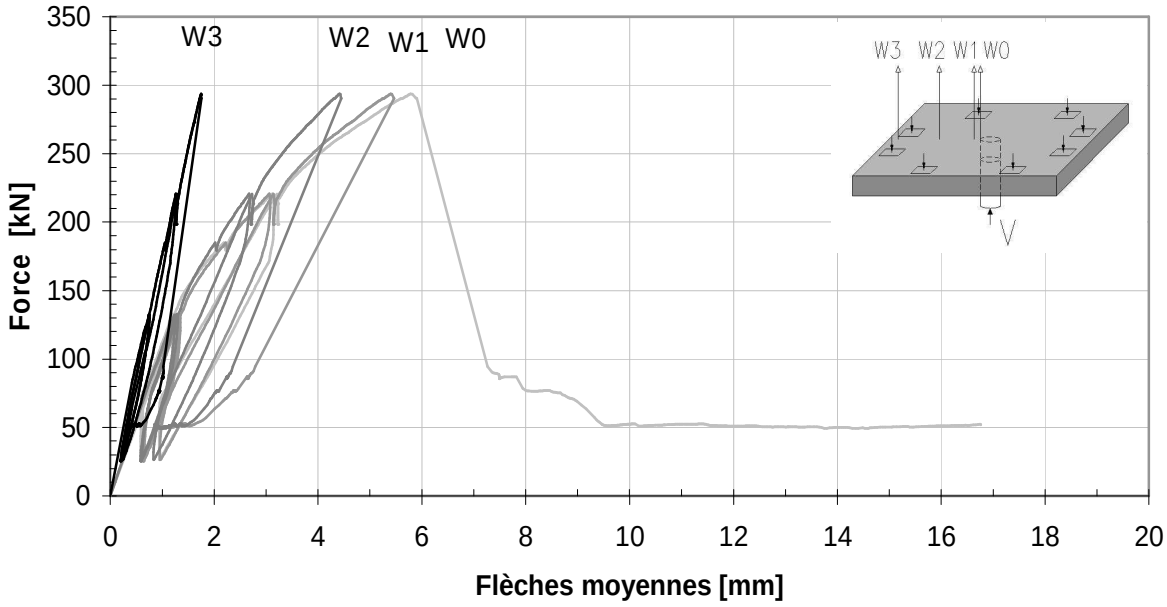

Fig. 22 : Courbes force – flèche moyenne de la dalle B1-02.

Force maximale V_{test} [kN]	Flèche au centre W_0 [mm]	Rotation ψ [‰]
294	**5.8**	**8.6**

Tab. 6 : Résultats principaux de l'essai de la dalle B1-02.

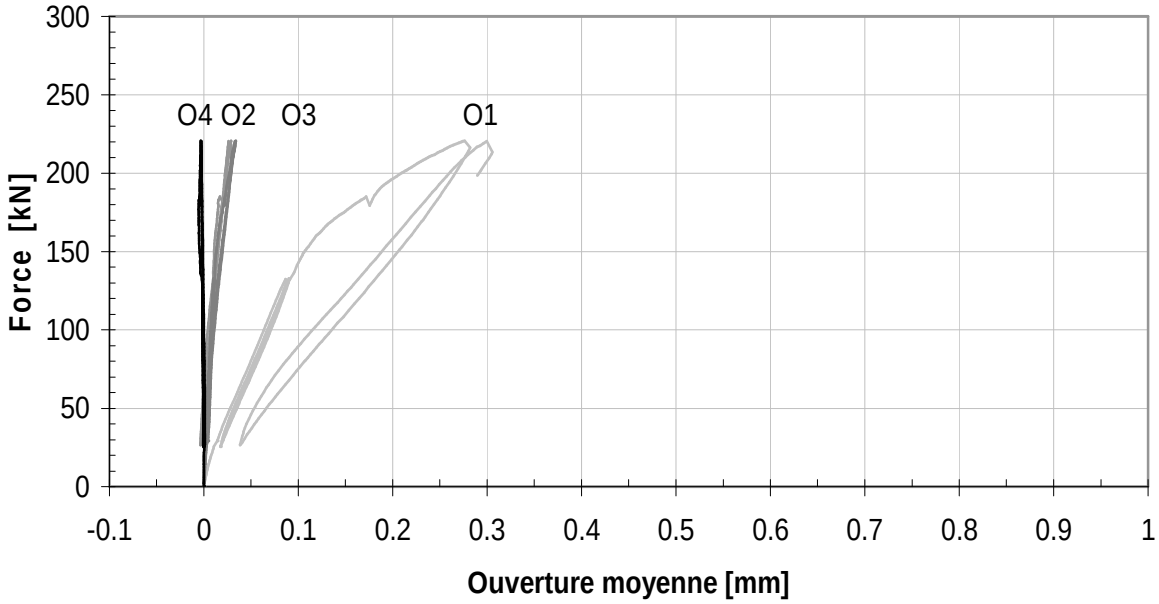

Fig. 23 : Courbes force – ouverture moyenne des fissures de la dalle B1-02.

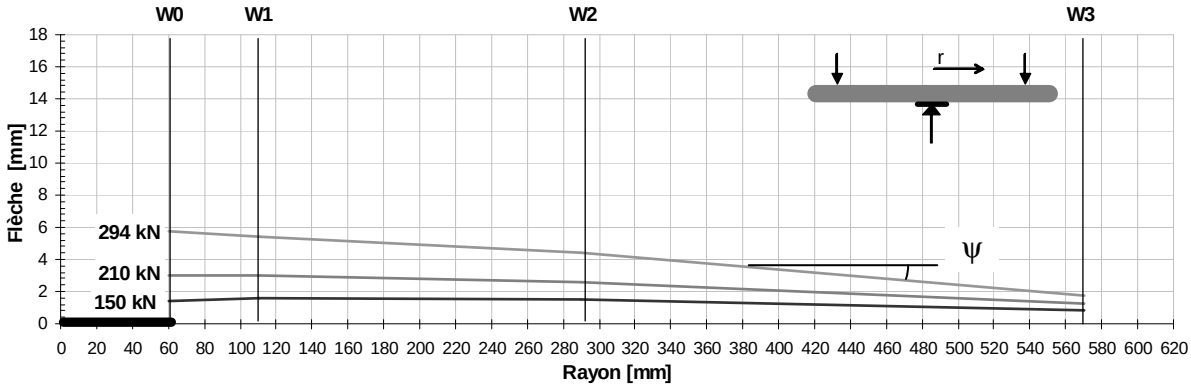

Fig. 24 : Déformation moyenne de la dalle B1-02 à plusieurs niveaux de charge.

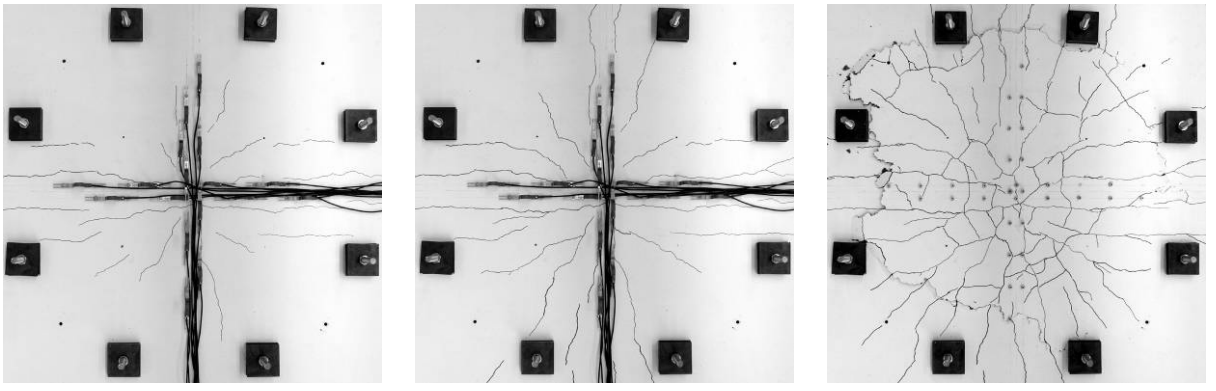

Charge de service 150 kN | Charge de dimensionnement 210 kN | Rupture

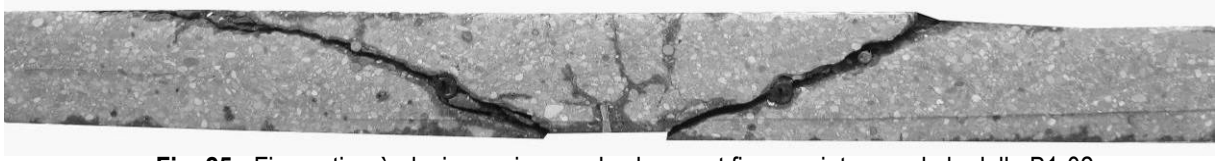

Fig. 25 : Fissuration à plusieurs niveaux de charge et fissures internes de la dalle B1-02.

3.2.3. Dalle B1-03

Caractéristiques :

- Béton B1 sans fibres f_{cm} = 90 MPa
- Armature longitudinale supérieure : ϕ10 s = 100 mm ρ = 0.87 %
- Précontrainte : 2 x 4 x 135 kN $\sigma_{cp,0}$ = 3.63 MPa

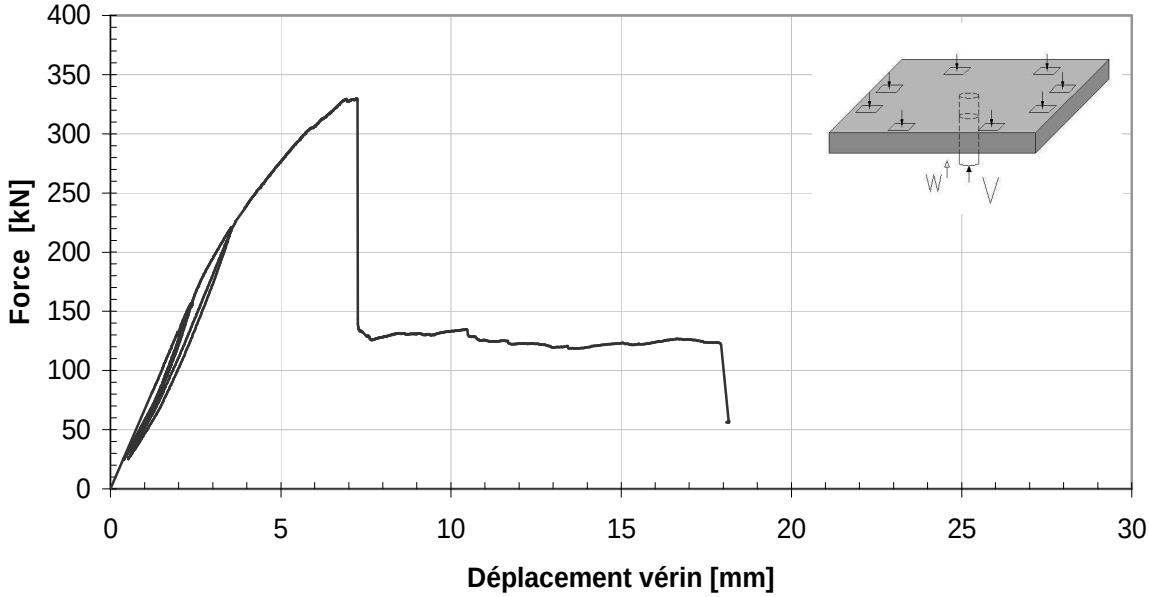

Fig. 26 : Courbe force – déplacement du vérin de la dalle B1-03.

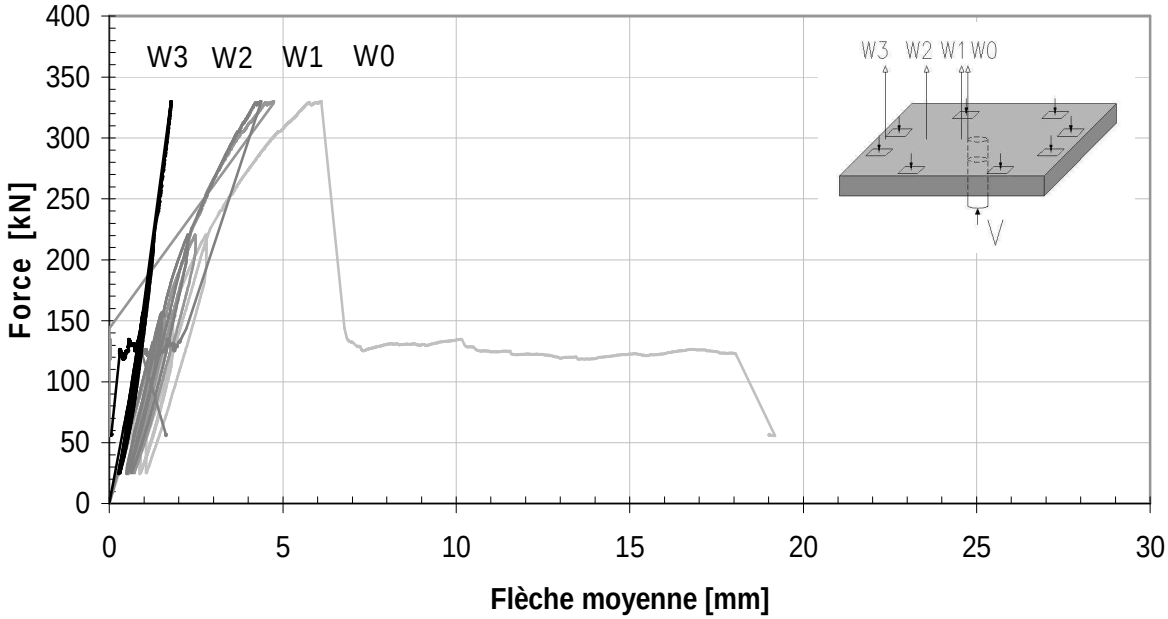

Fig. 27 : Courbes force – flèche moyenne de la dalle B1-03.

Force maximale V_{test} [kN]	Flèche au centre W_0 [mm]	Rotation ψ [‰]
330	**6.1**	**9.2**

Tab. 7 : Résultats principaux de l'essai de la dalle B1-03.

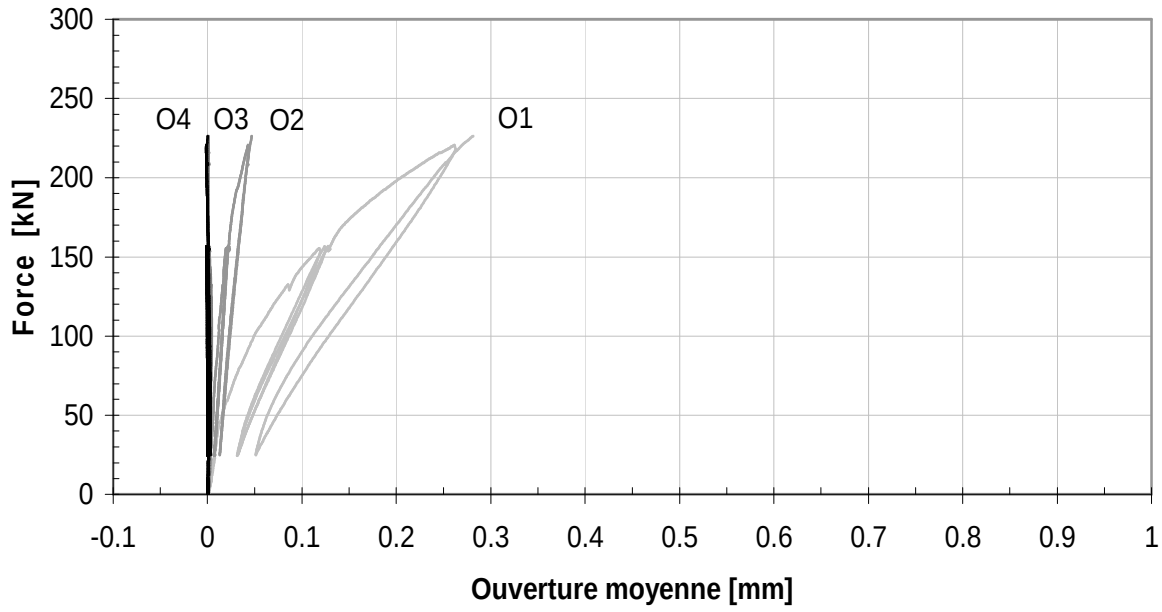

Fig. 28 : Courbes force – ouverture moyenne des fissures de la dalle B1-03.

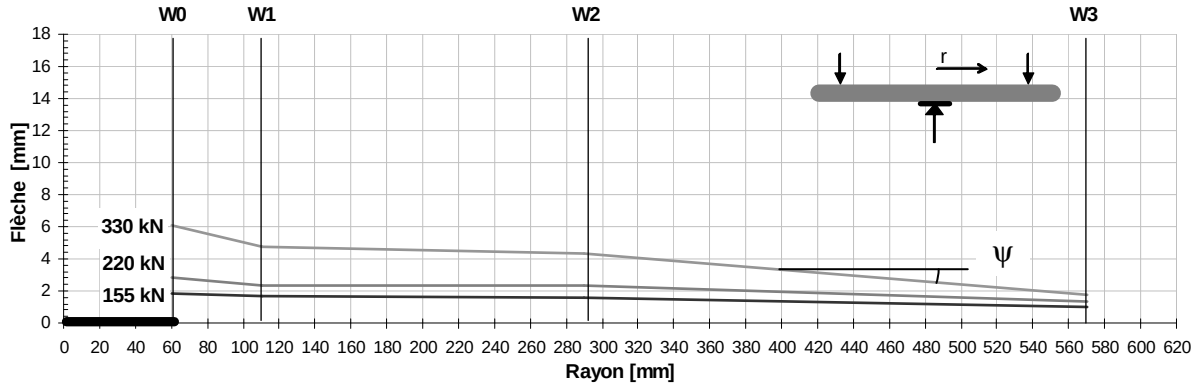

Fig. 29 : Déformation moyenne de la dalle B1-03 à plusieurs niveaux de charge.

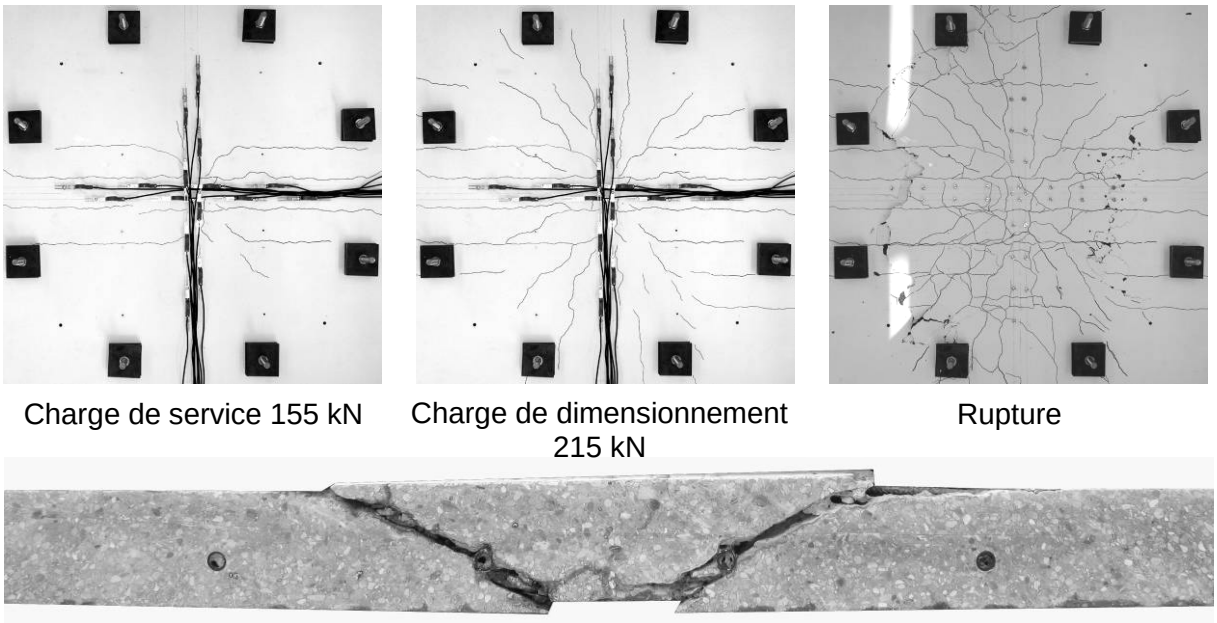

Charge de service 155 kN | Charge de dimensionnement 215 kN | Rupture

Fig. 30 : Fissuration à plusieurs niveaux de charge et fissures internes de la dalle B1-03.

3.2.4. Dalle B1-04

Caractéristiques :

- Béton B1 sans fibres f_{cm} = 90 MPa
- Armature longitudinale supérieure : ϕ10 s = 100 mm ρ = 0.87 %
- Précontrainte : 2 x 4 x 180 kN σ_{cp} = 4.84 MPa

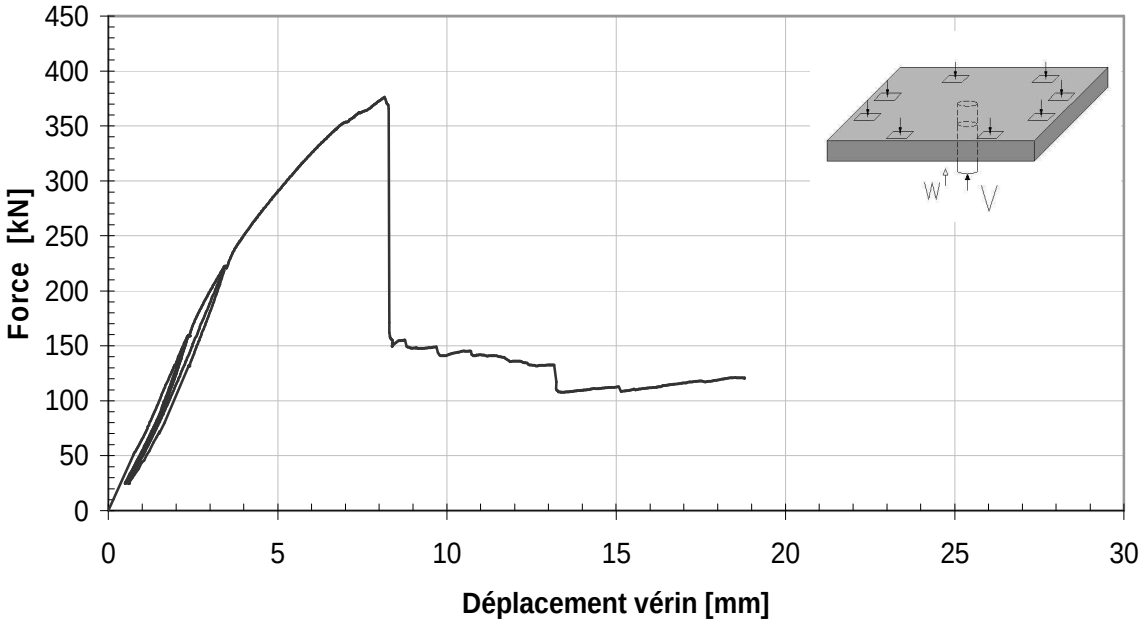

Fig. 31 : Courbe force – déplacement du vérin de la dalle B1-04.

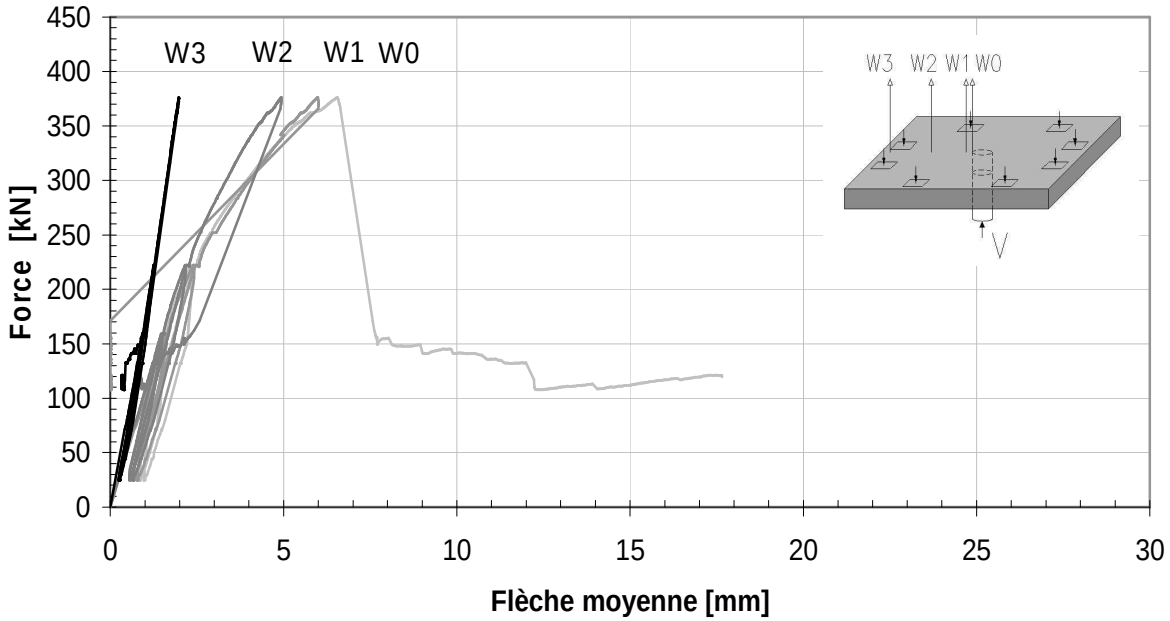

Fig. 32 : Courbes force – flèche moyenne de la dalle B1-04.

Force maximale V_{test} [kN]	Flèche au centre W_0 [mm]	Rotation ψ [‰]
376	**6.6**	**10.5**

Tab. 8 : Résultats principaux de l'essai de la dalle B1-04.

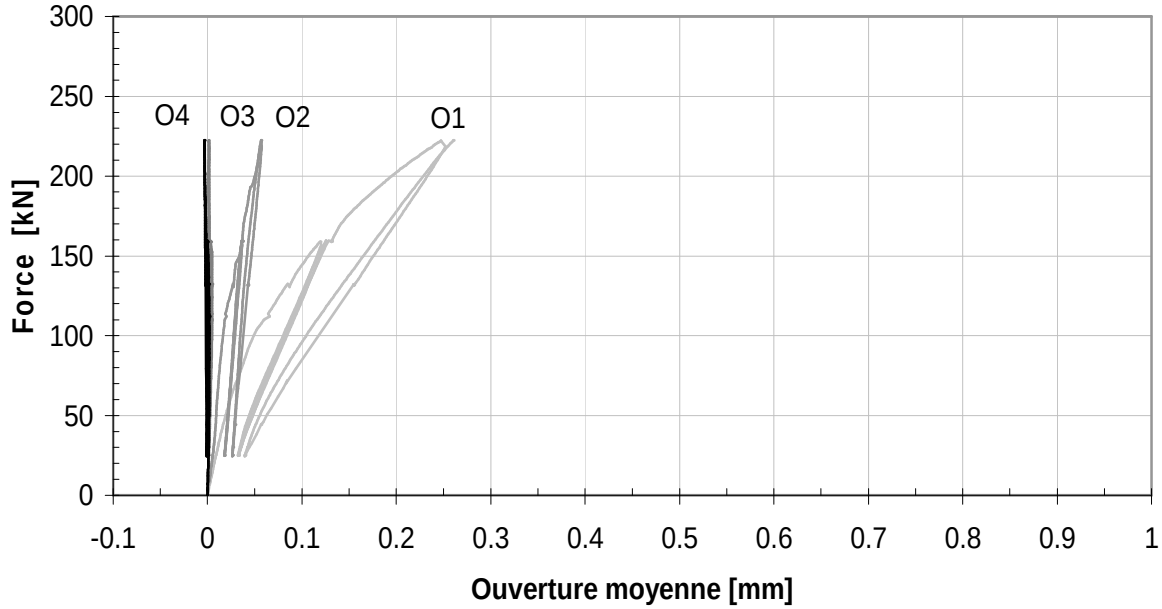

Fig. 33 : Courbes force – ouverture moyenne des fissures de la dalle B1-04.

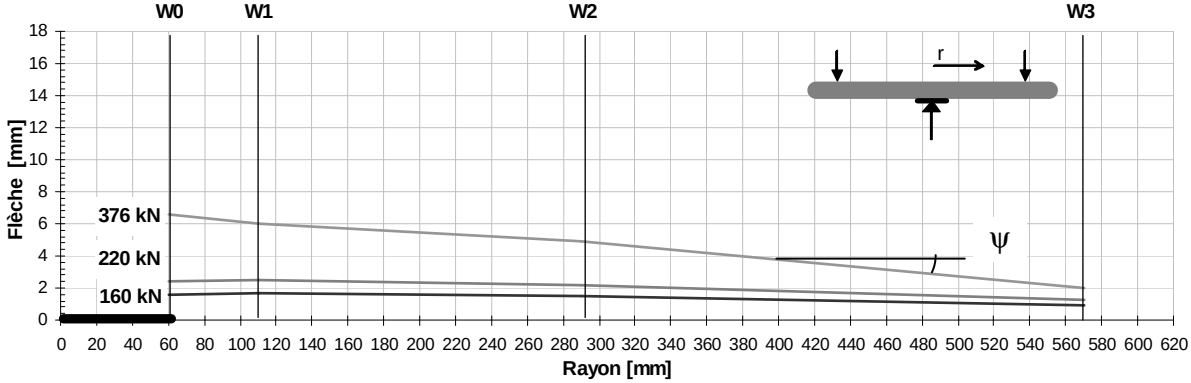

Fig. 34 : Déformation moyenne de la dalle B1-04 à plusieurs niveaux de charge.

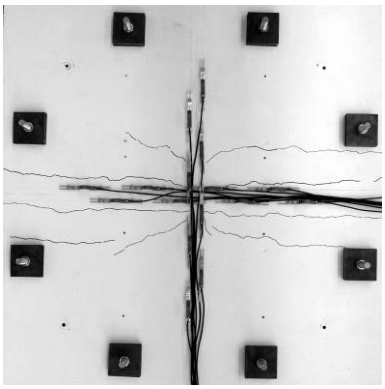

Charge de service 160 kN

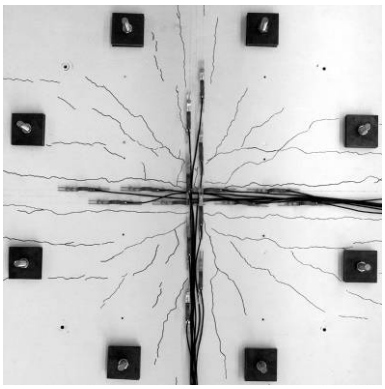

Charge de dimensionnement 220 kN

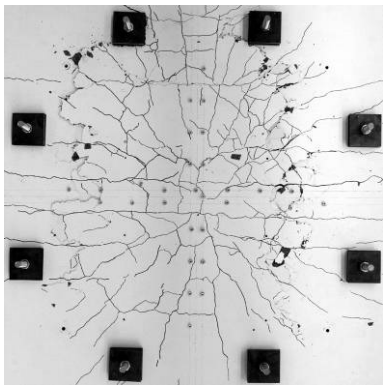

Rupture

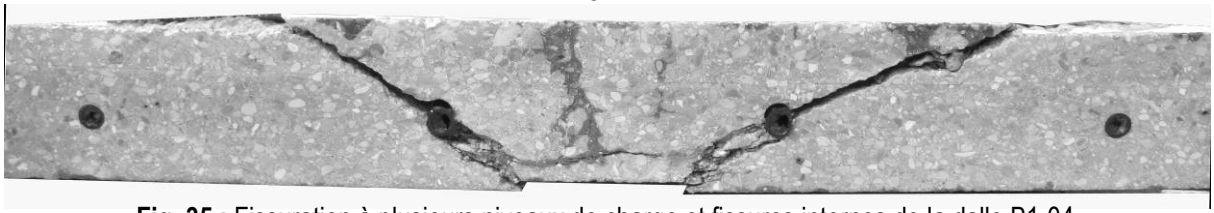

Fig. 35 : Fissuration à plusieurs niveaux de charge et fissures internes de la dalle B1-04.

3.2.5. Dalle B1-05

Caractéristiques :

Béton B1 sans fibres f_{cm} = 99 MPa
Armature longitudinale supérieure : ϕ8 s = 100 mm (ρ = 0.56 %)

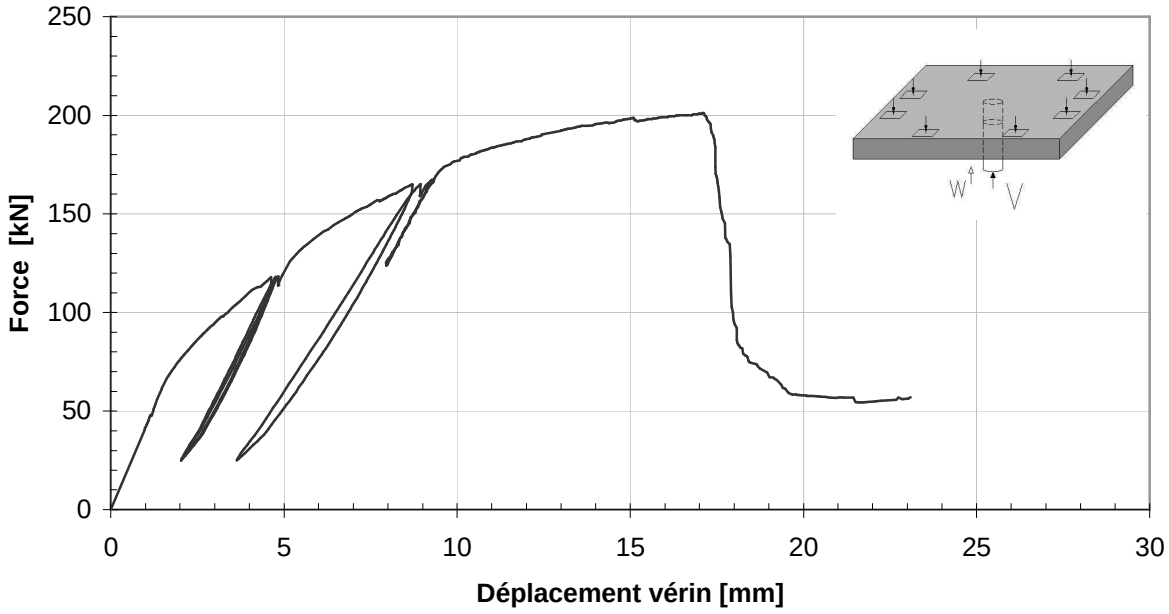

Fig. 36 : Courbe force – déplacement du vérin de la dalle B1-05.

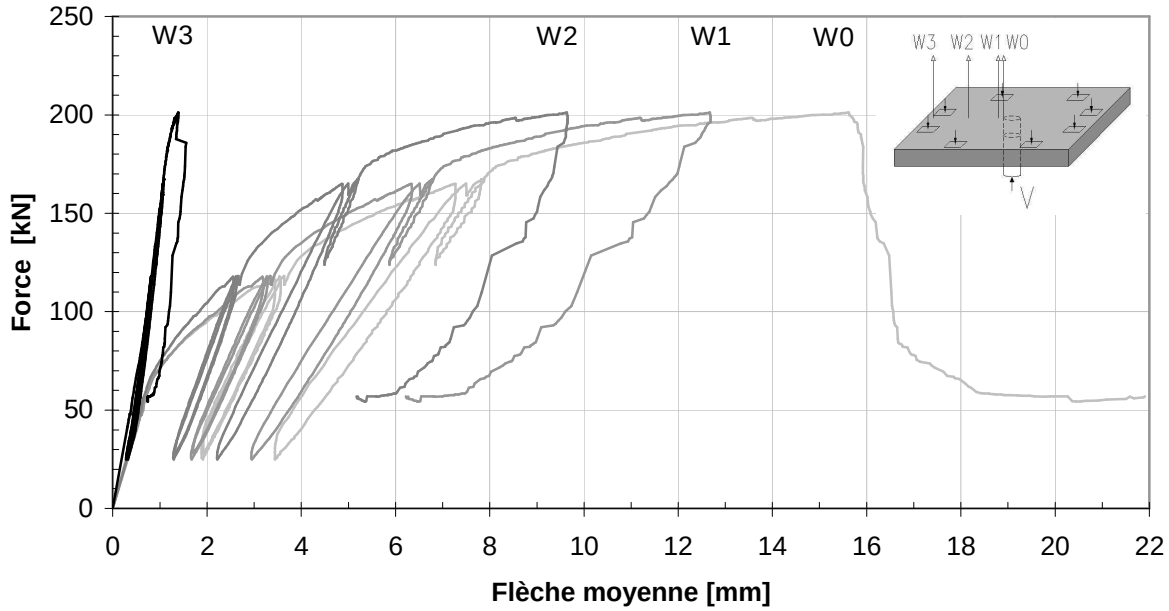

Fig. 37 : Courbes force – flèche moyenne de la dalle B1-05.

Force maximale V_{test} [kN]	Flèche au centre W_0 [mm]	Rotation ψ [‰]
201	**15.6**	**28.8**

Tab. 9 : Résultats principaux de l'essai de la dalle B1-05.

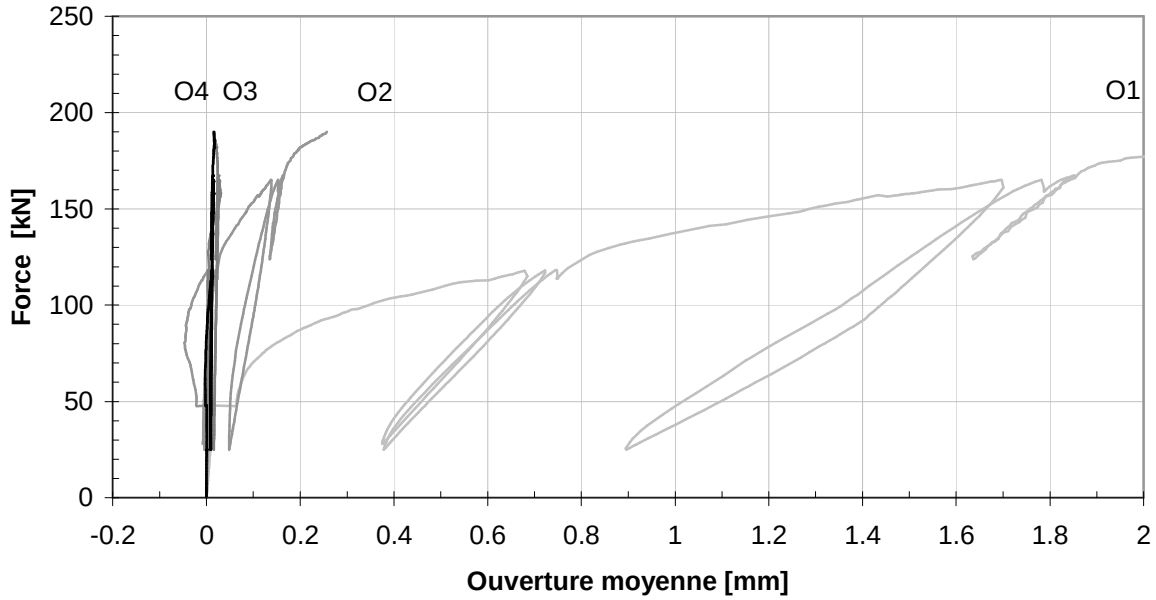

Fig. 38 : Courbes force – ouverture moyenne des fissures de la dalle B1-05.

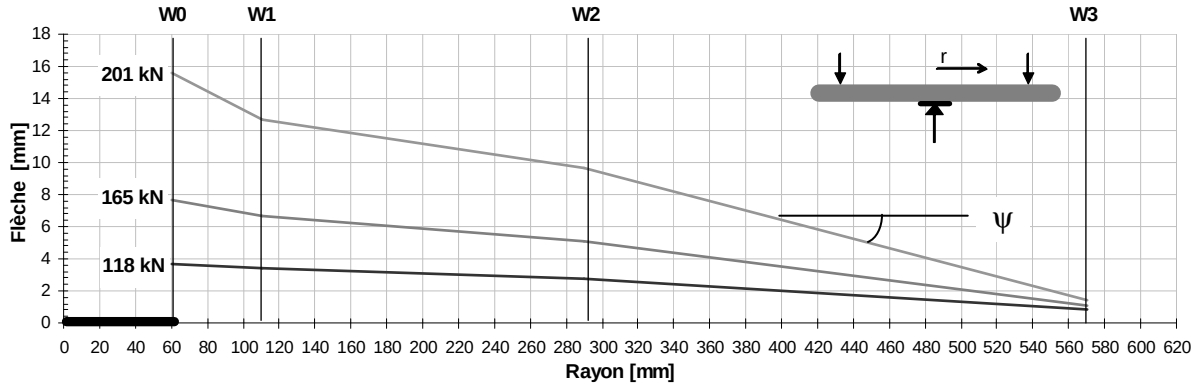

Fig. 39 : Déformation moyenne de la dalle B1-05 à plusieurs niveaux de charge.

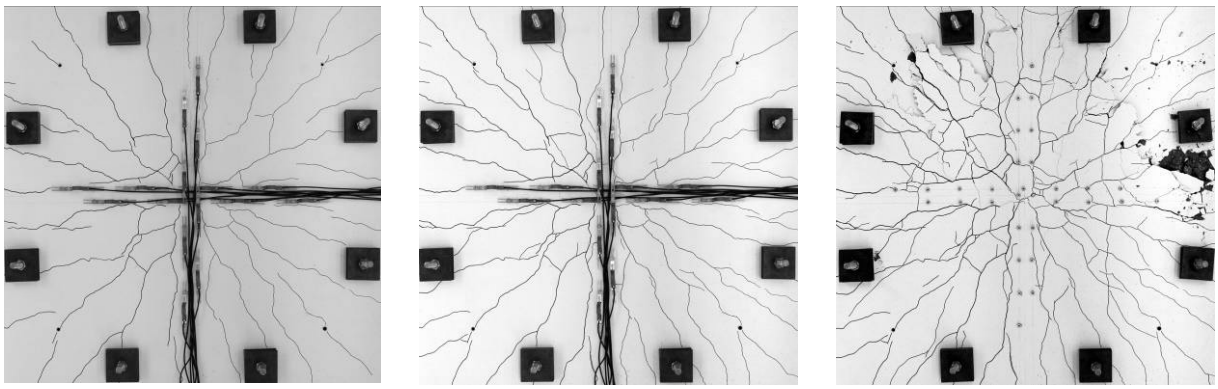

Charge de service 118 kN | Charge de dimensionnement 165 kN | Rupture

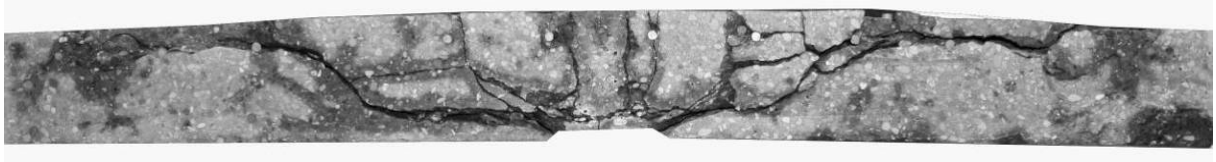

Fig. 40 : Fissuration à plusieurs niveaux de charge et fissures internes de la dalle B1-05.

3.2.6. Dalle B1-06

Caractéristiques :

- Béton B1 sans fibres f_{cm} = 99 MPa
- Armature longitudinale supérieure : ϕ12 s = 100 mm (ρ = 1.26 %)

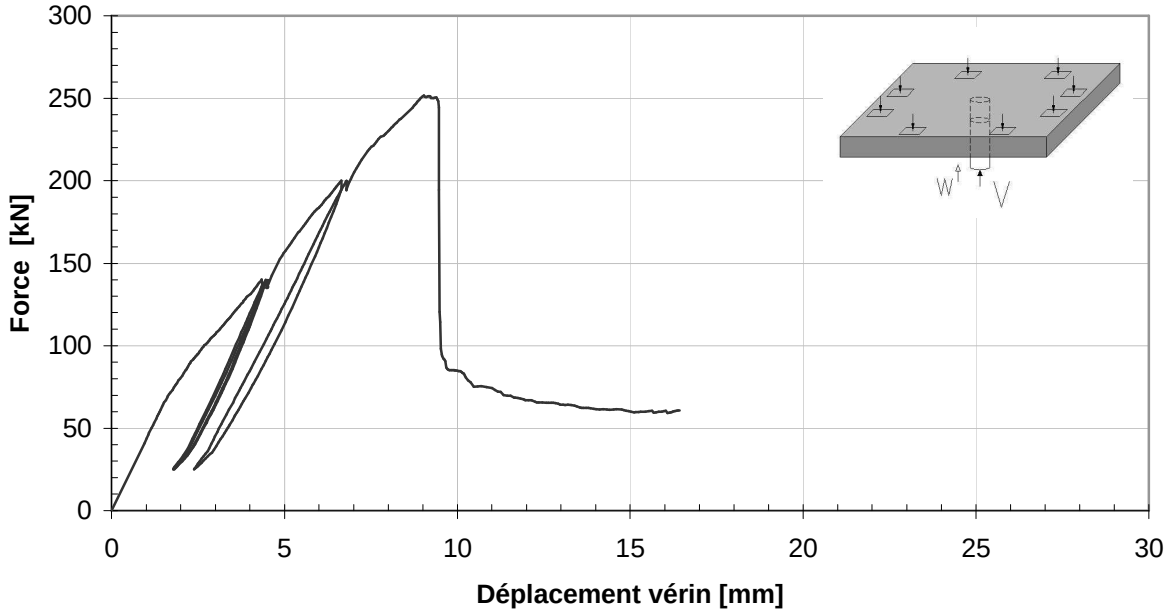

Fig. 41 : Courbe force – déplacement du vérin de la dalle B1-05.

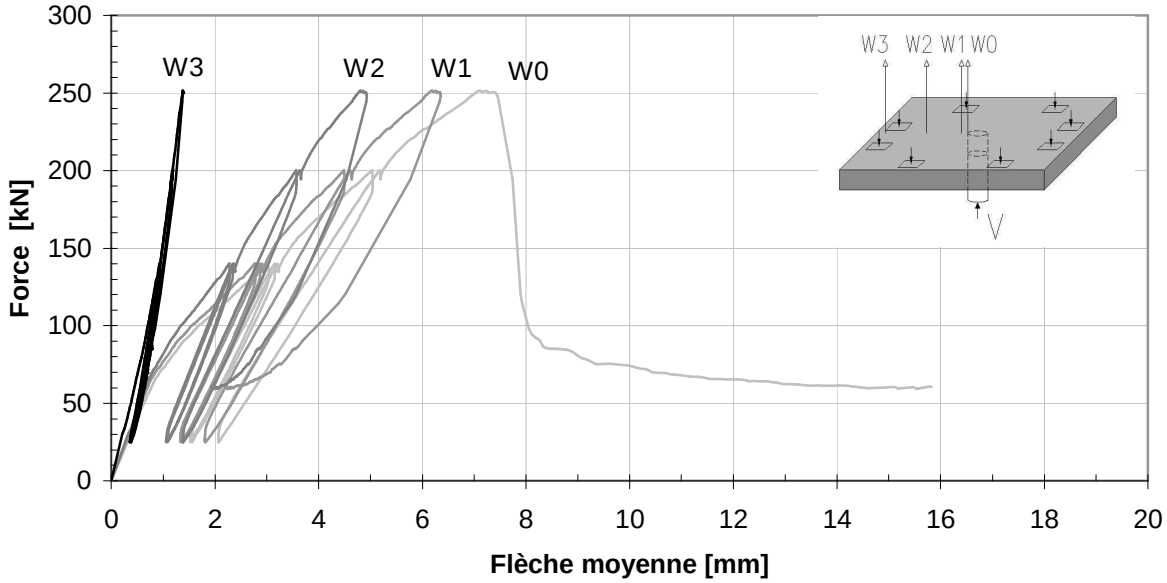

Fig. 42 : Courbes force – flèche moyenne de la dalle B1-05.

Force maximale V_{test} [kN]	Flèche au centre W_0 [mm]	Rotation ψ [‰]
252	**7.1**	**12.5**

Tab. 10 : Résultats principaux de l'essai de la dalle B1-05.

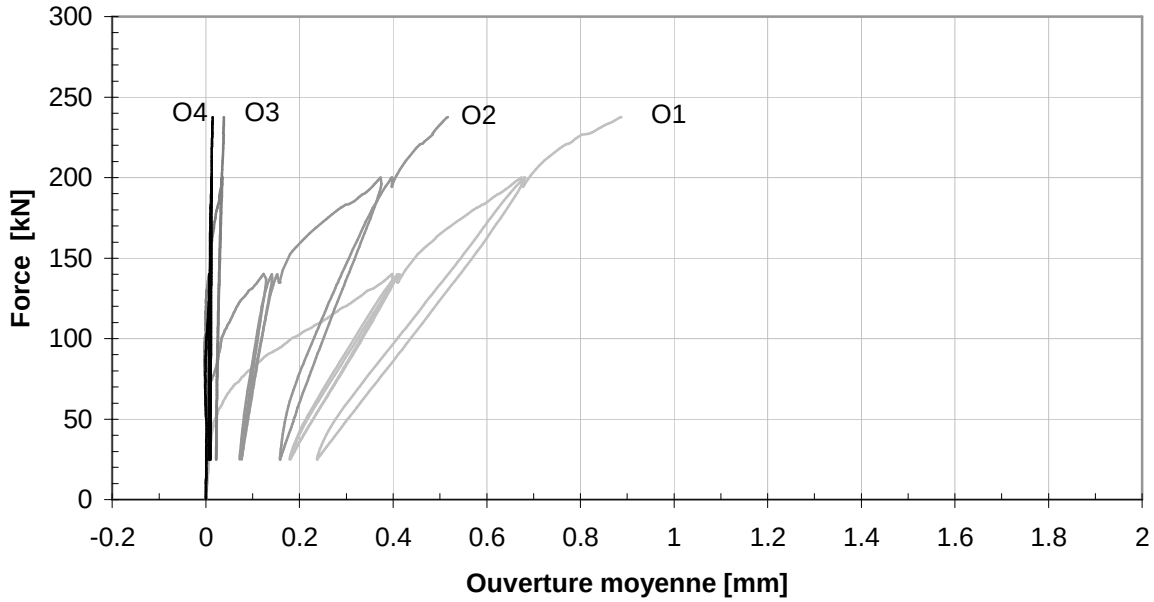

Fig. 43 : Courbes force – ouverture moyenne des fissures de la dalle B1-06.

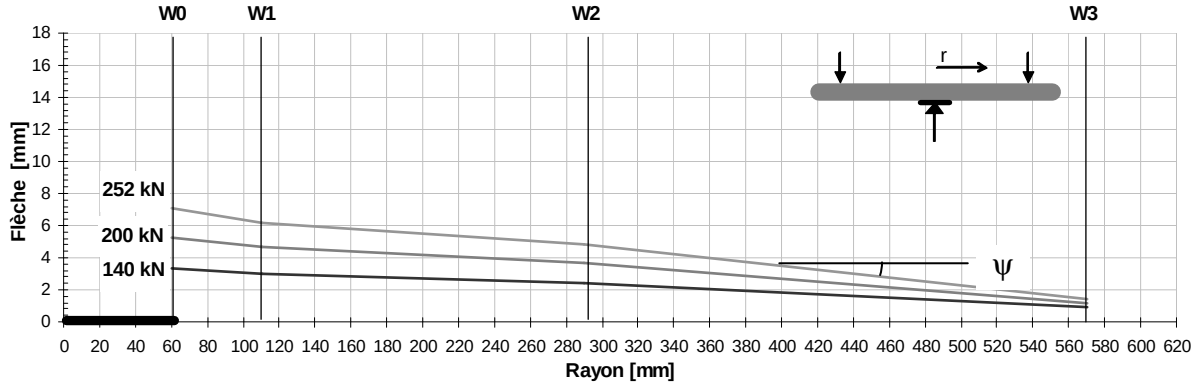

Fig. 44 : Déformation moyenne de la dalle B1-06 à plusieurs niveaux de charge.

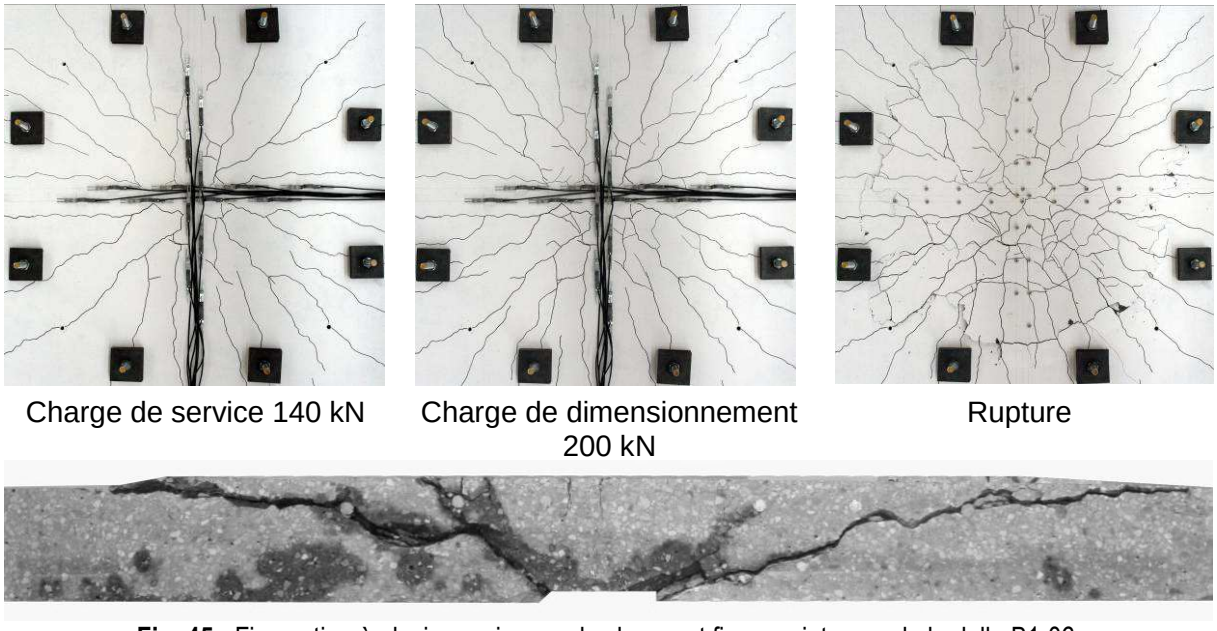

Charge de service 140 kN | Charge de dimensionnement 200 kN | Rupture

Fig. 45 : Fissuration à plusieurs niveaux de charge et fissures internes de la dalle B1-06.

3.2.7. Dalle B2-01

Caractéristiques :

- Béton B2 (20 kg/m^3) f_{cm} = 106 MPa
- Armature longitudinale supérieure : ϕ10 s = 100 mm (ρ = 0.87 %)

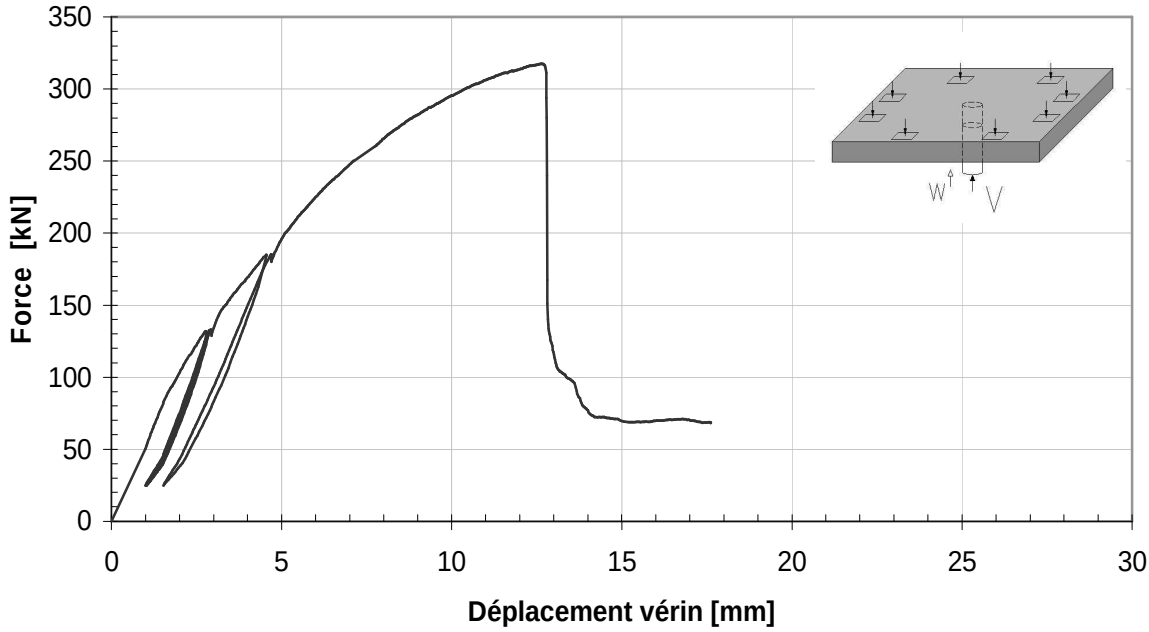

Fig. 46 : Courbe force – déplacement du vérin de la dalle B2-01.

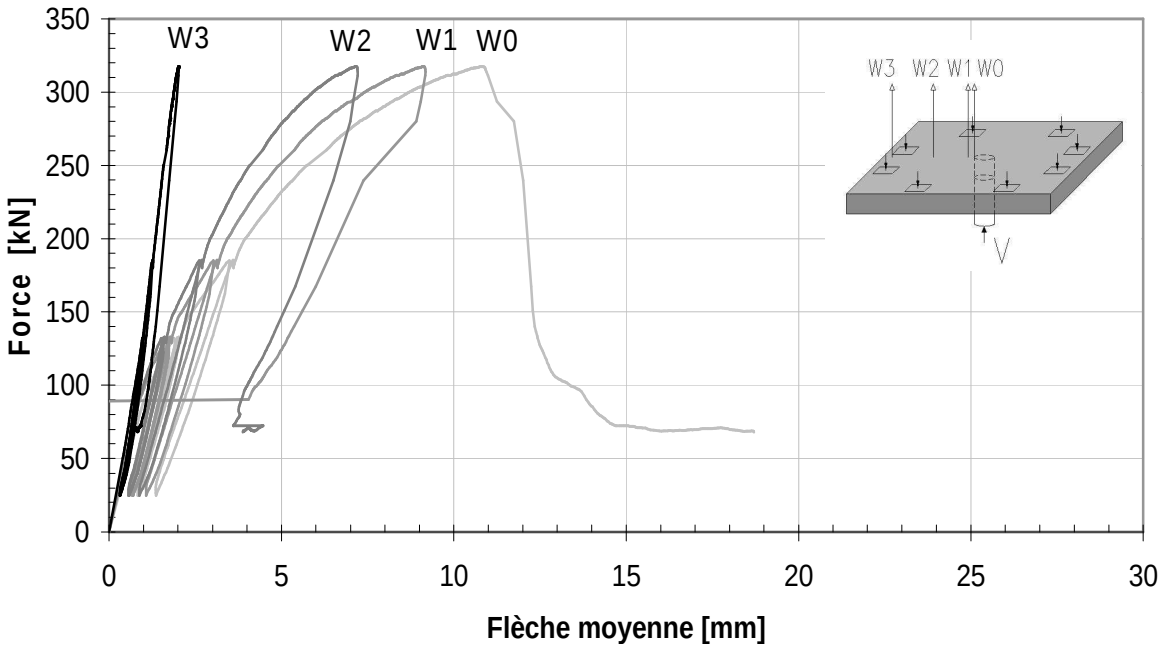

Fig. 47 : Courbes force – flèche moyenne de la dalle B2-01.

Force maximale V_{test} [kN]	Flèche au centre W_0 [mm]	Rotation ψ [‰]
318	**10.8**	**18.3**

Tab. 11 : Résultats principaux de l'essai de la dalle B2-01.

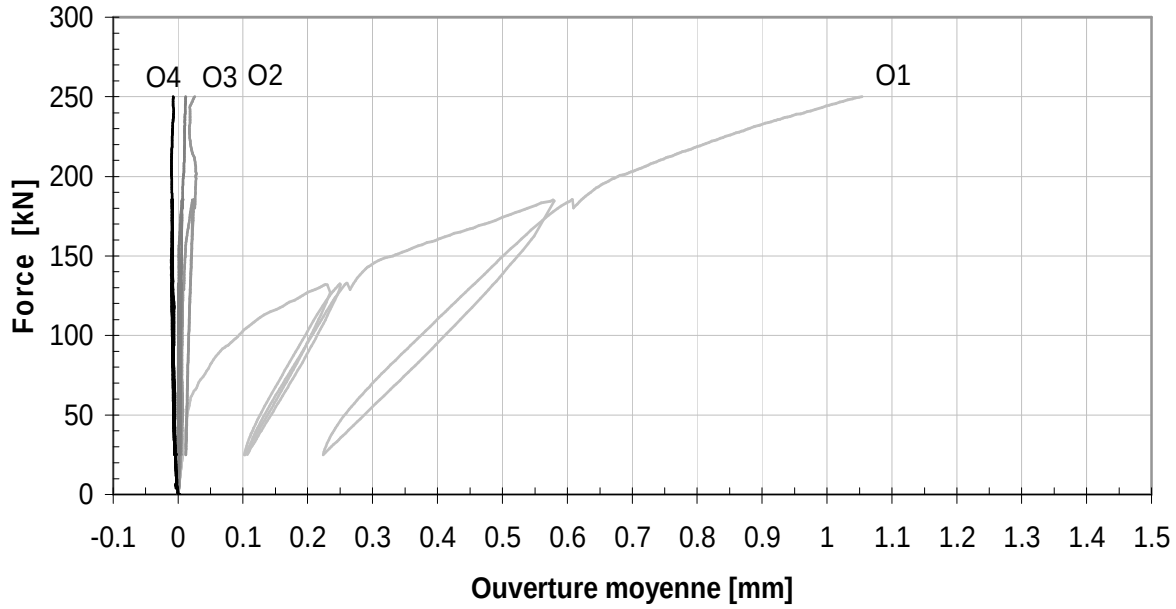

Fig. 48 : Courbes force – ouverture moyenne des fissures de la dalle B2-01.

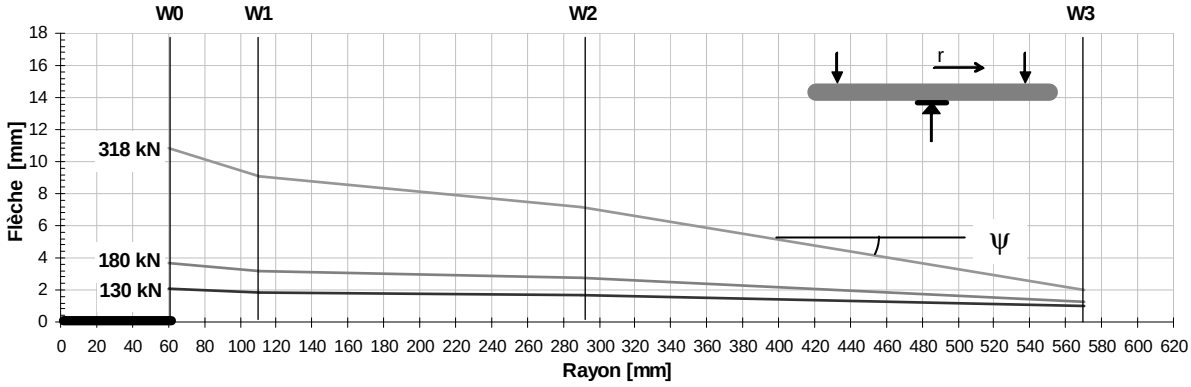

Fig. 49 : Déformation moyenne de la dalle B2-01 à plusieurs niveaux de charge.

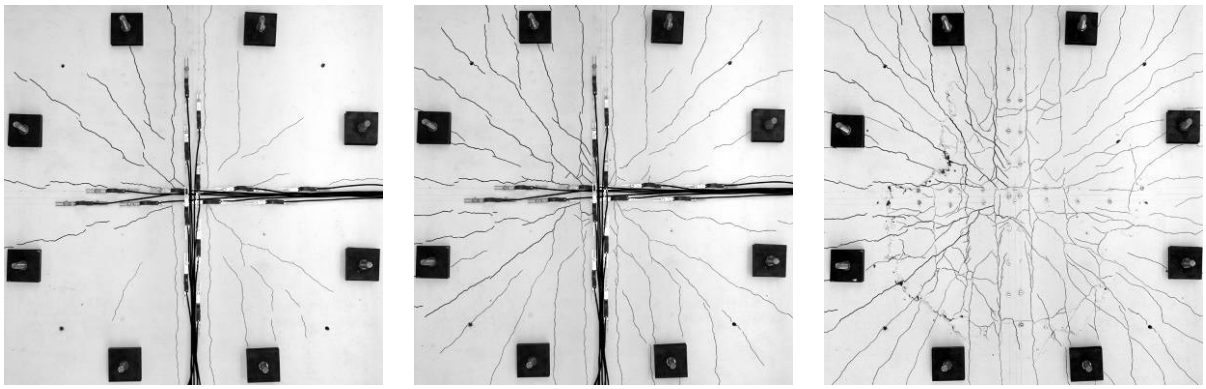

Charge de service 130 kN | Charge de dimensionnement 180 kN | Rupture

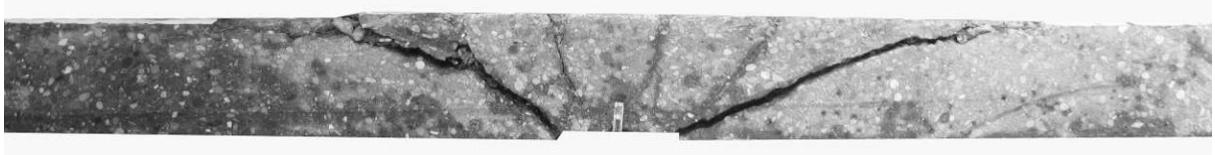

Fig. 50 : Fissuration à plusieurs niveaux de charge et fissures internes de la dalle B2-01.

3.2.8. Dalle B3-01

Caractéristiques :

- Béton B3 (40 kg/m^3) f_{cm} = 102 MPa
- Armature longitudinale supérieure : ϕ10 s = 100 mm (ρ = 0.87 %)

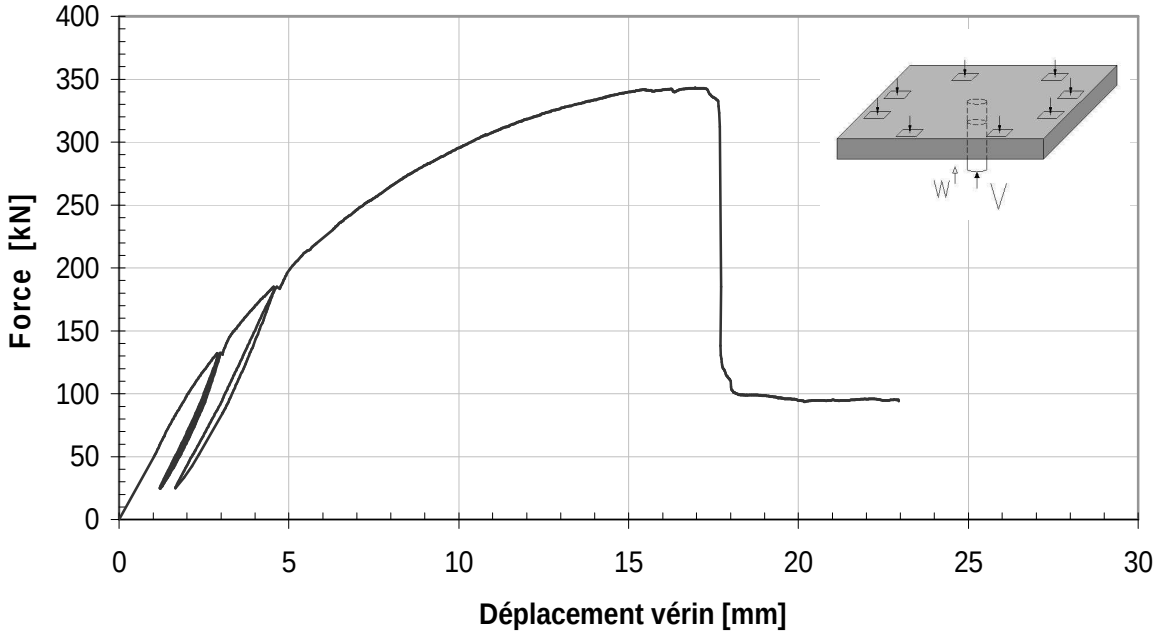

Fig. 51 : Courbe force – déplacement du vérin de la dalle B3-01.

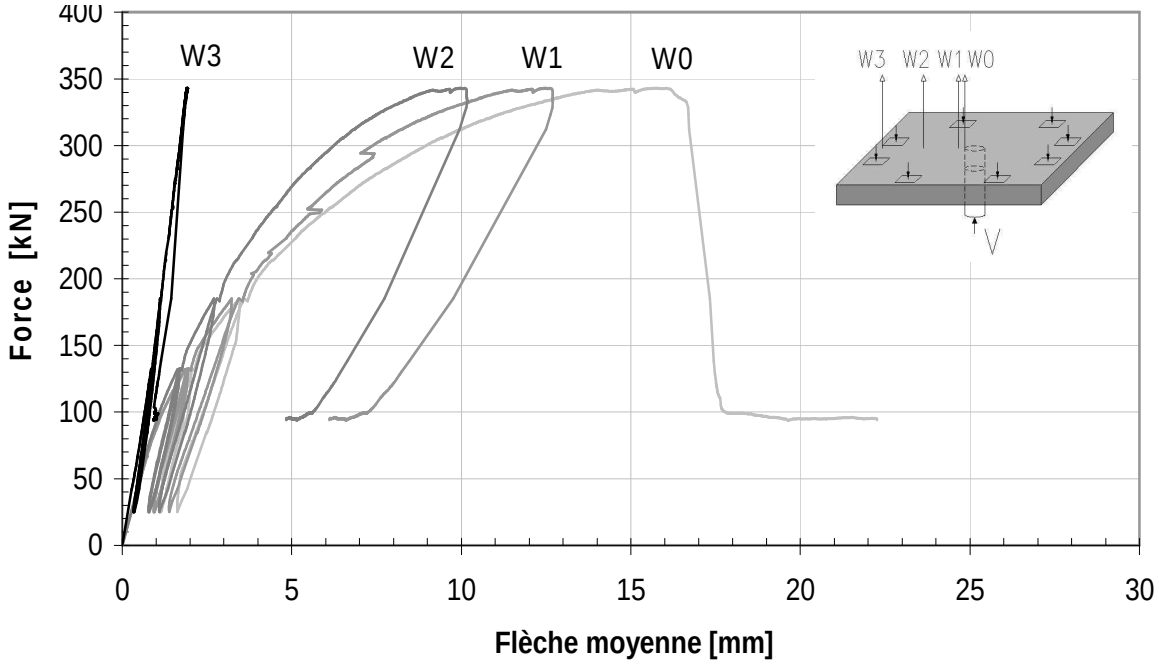

Fig. 52 : Courbes force – flèche moyenne de la dalle B3-01.

Force maximale V_{test} [kN]	Flèche au centre W_0 [mm]	Rotation ψ [‰]
343	**15.7**	**28.7**

Tab. 12 : Résultats principaux de l'essai de la dalle B3-01.

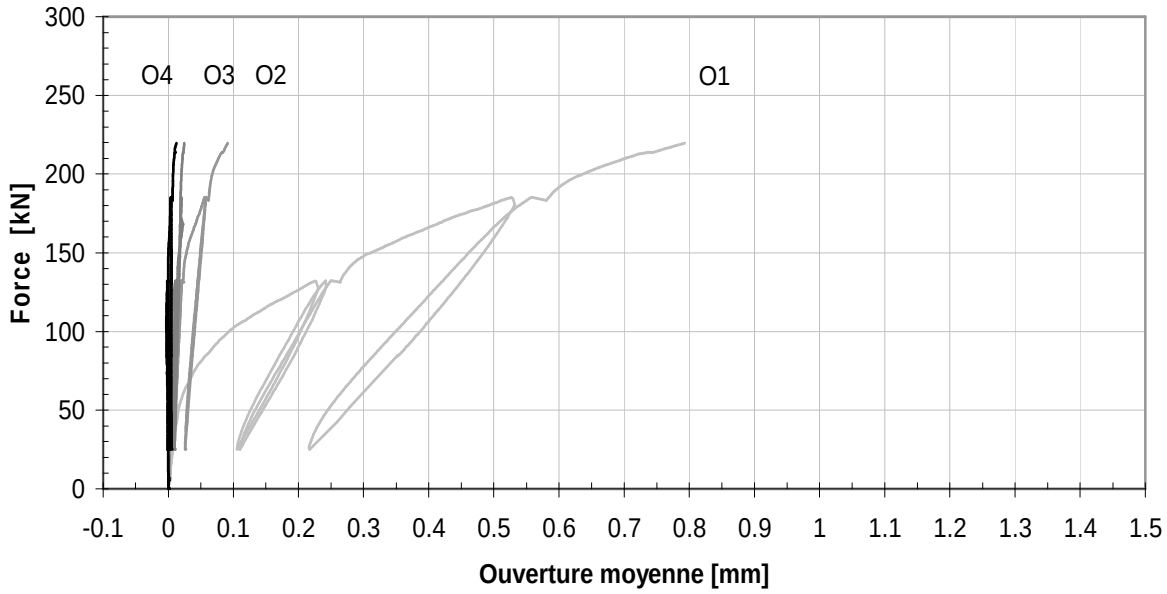

Fig. 53 : Courbes force – ouverture moyenne des fissures de la dalle B3-01.

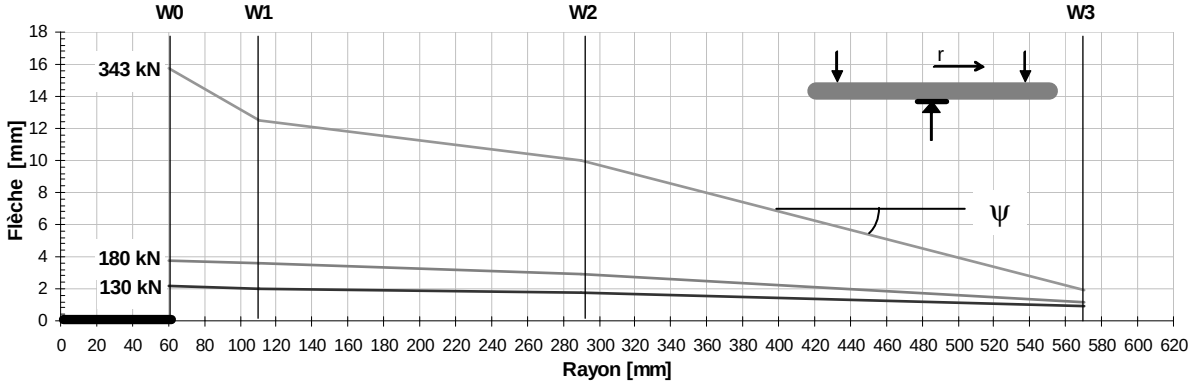

Fig. 54 : Déformation moyenne de la dalle B3-01 à plusieurs niveaux de charge.

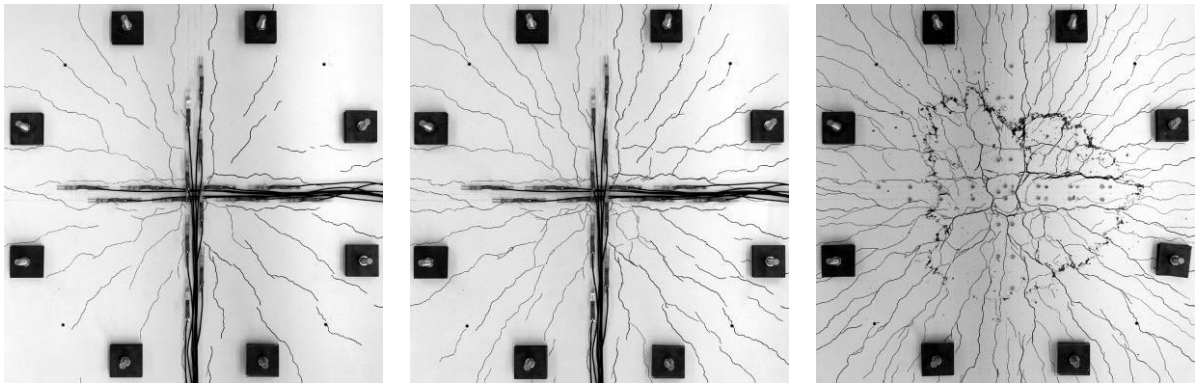

Charge de service 130 kN | Charge de dimensionnement 180 kN | Rupture

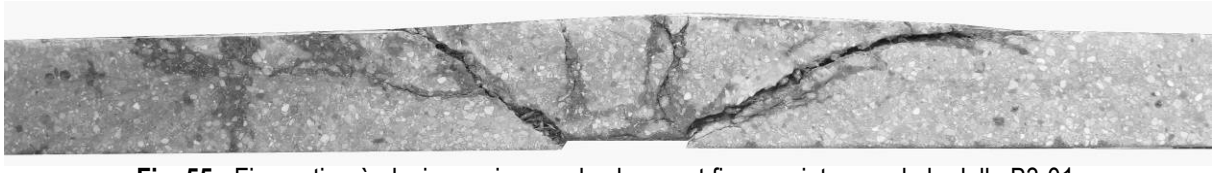

Fig. 55 : Fissuration à plusieurs niveaux de charge et fissures internes de la dalle B3-01.

3.2.9. Dalle B3-02

Caractéristiques :

- Béton B3 (40 kg/m^3) f_{cm} = 103 MPa
- Armature longitudinale supérieure : ϕ10 s = 100 mm ρ = 0.87 %
- Précontrainte : 2 x 2 x 180 kN $\sigma_{cp,0}$ = 2.42 MPa

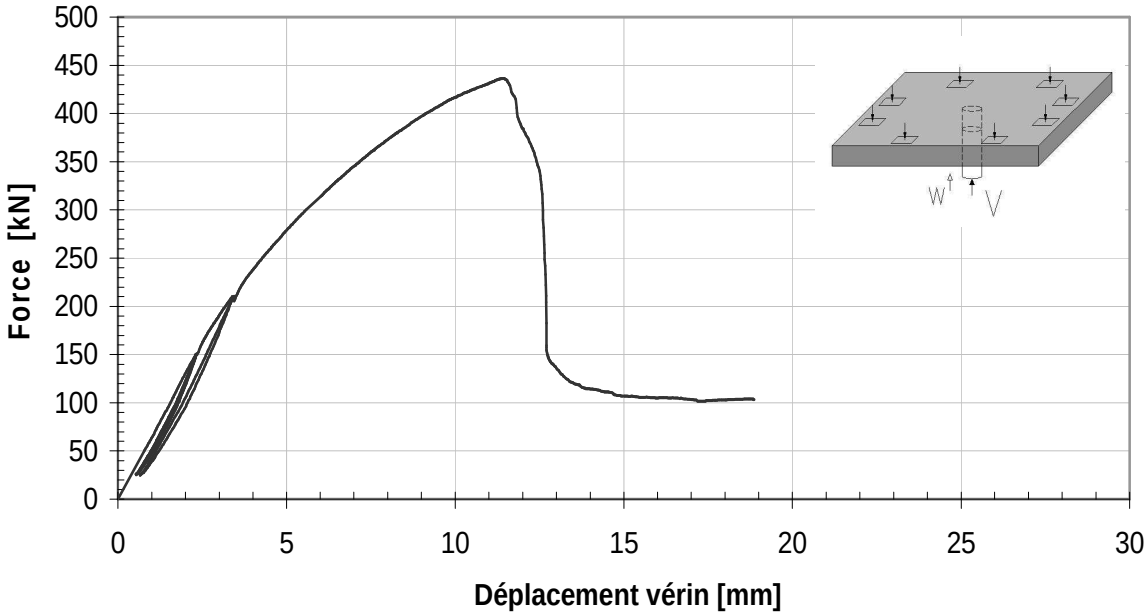

Fig. 56 : Courbe force – déplacement du vérin de la dalle B3-02.

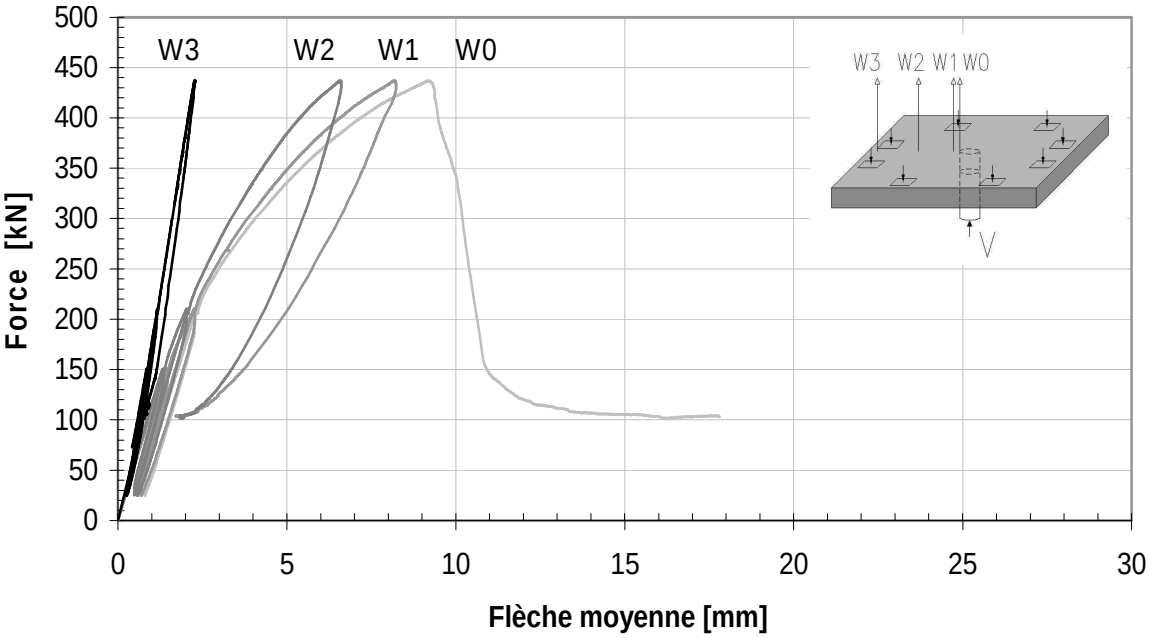

Fig. 57 : Courbes force – flèche moyenne de la dalle B3-02.

Force maximale V_{test} [kN]	Flèche au centre W_0 [mm]	Rotation ψ [‰]
437	**9.2**	**15.4**

Tab. 13 : Résultats principaux de l'essai de la dalle B3-02.

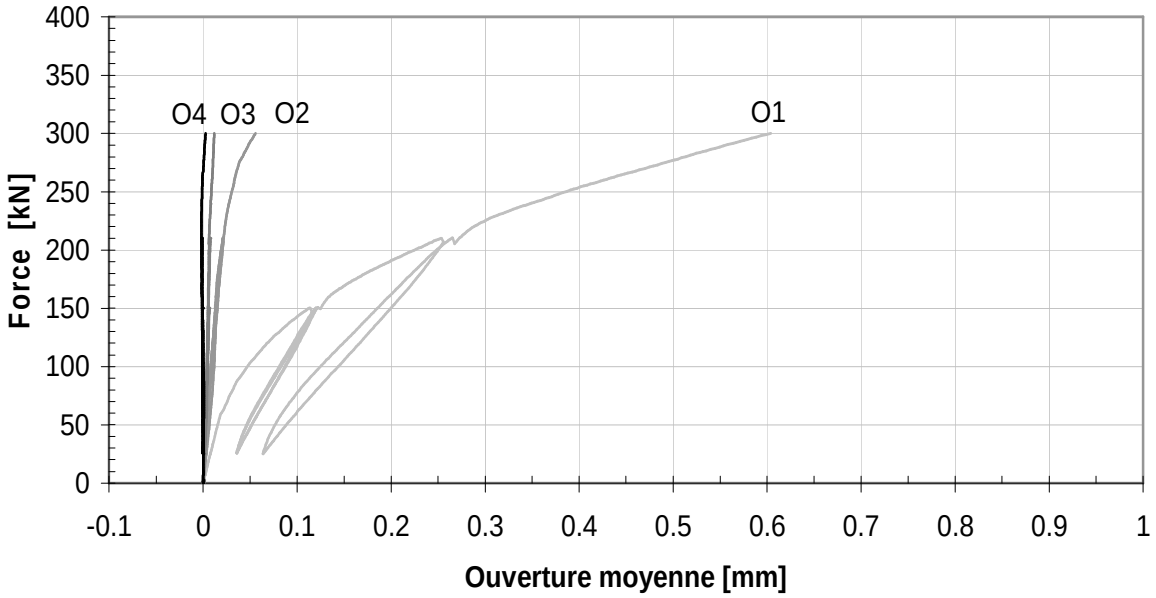

Fig. 58 : Courbes force – ouverture moyenne des fissures de la dalle B3-02.

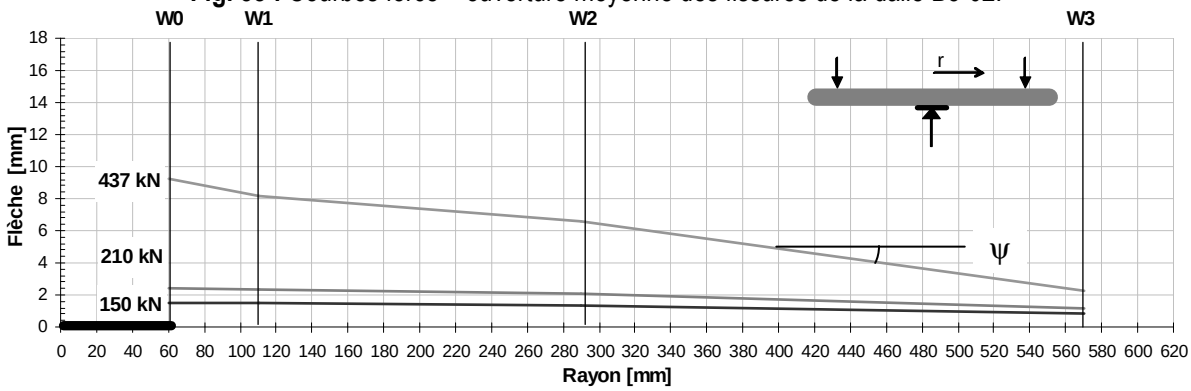

Fig. 59 : Déformation moyenne de la dalle B3-02 à plusieurs niveaux de charge.

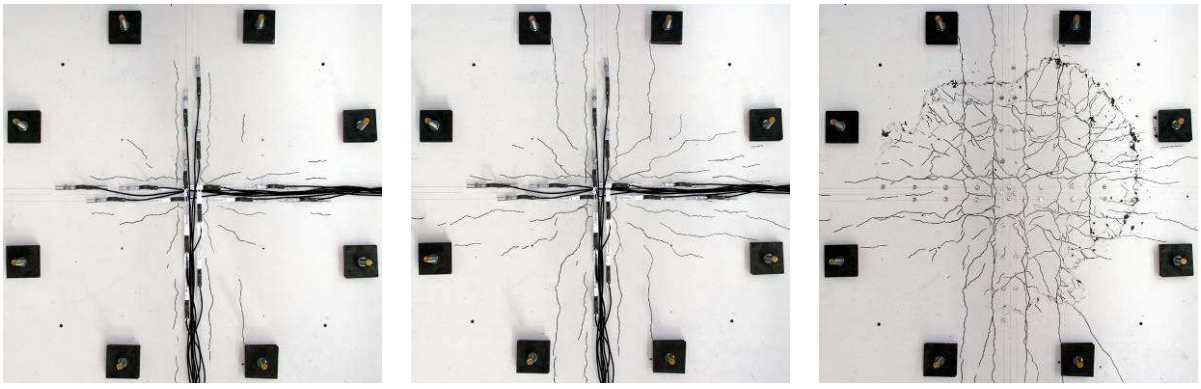

Charge de service 150 kN | Charge de dimensionnement 210 kN | Rupture

Fig. 60 : Fissuration à plusieurs niveaux de charge et fissures internes de la dalle B3-02.

3.2.10. Dalle B3-03

Caractéristiques :

- Béton B3 (40 kg/m^3) f_{cm} = 100 MPa
- Armature longitudinale supérieure : ϕ10 s = 100 mm ρ = 0.87 %
- Précontrainte : 2 x 4 x 135 kN $\sigma_{cp,0}$ = 3.63 MPa

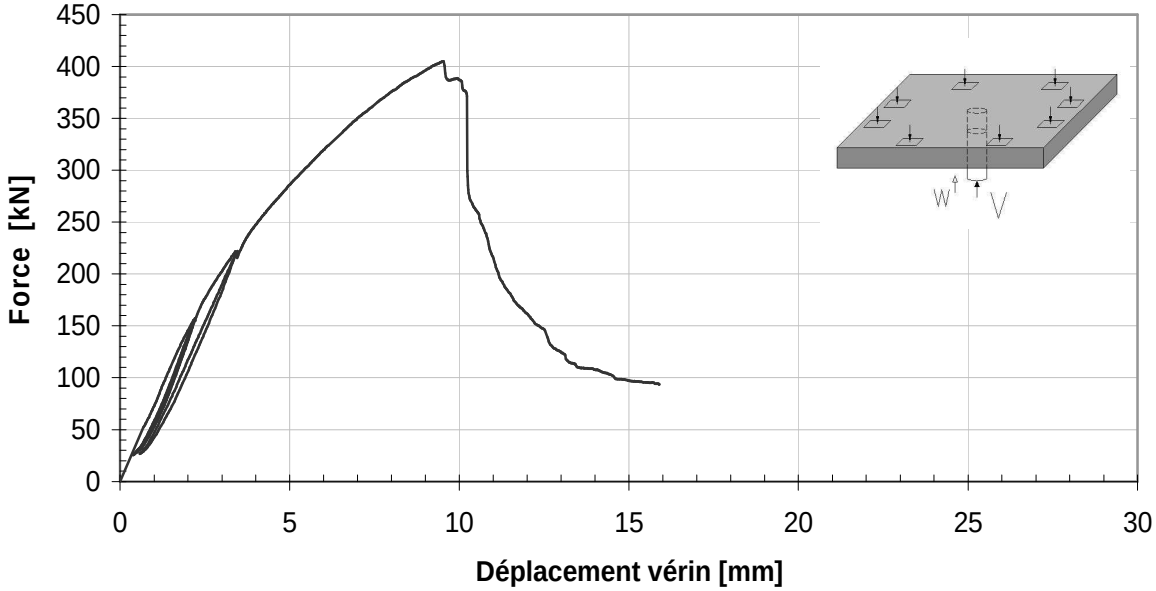

Fig. 61 : Courbe force – déplacement du vérin de la dalle B3-03.

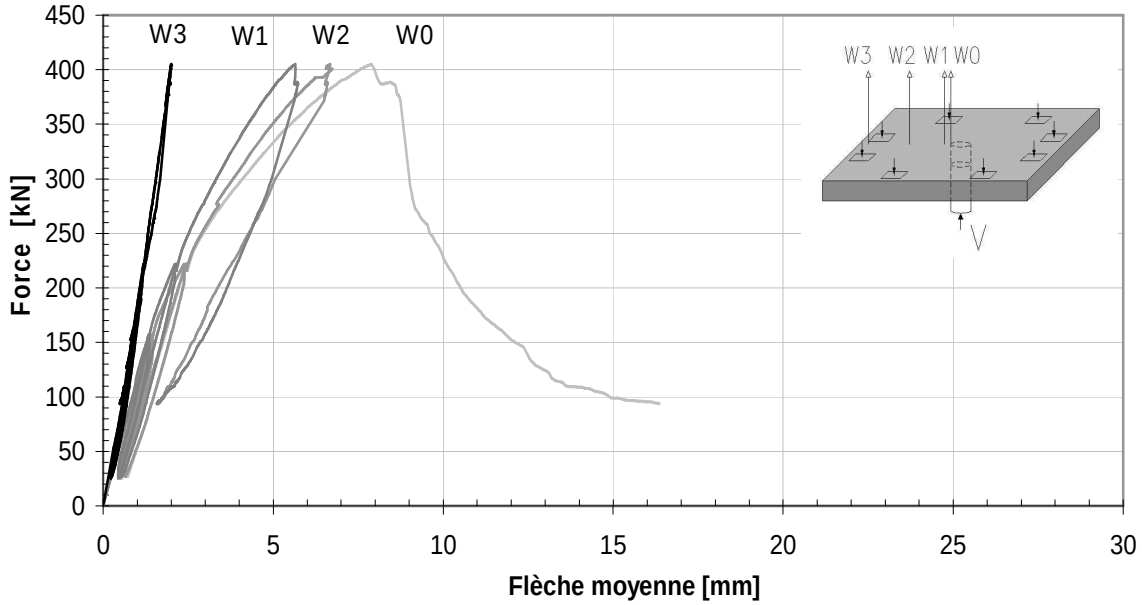

Fig. 62 : Courbes force – flèche moyenne de la dalle B3-03.

Force maximale V_{test} [kN]	Flèche au centre W_0 [mm]	Rotation ψ [‰]
405	**7.9**	**13.4**

Tab. 14 : Résultats principaux de l'essai de la dalle B3-03.

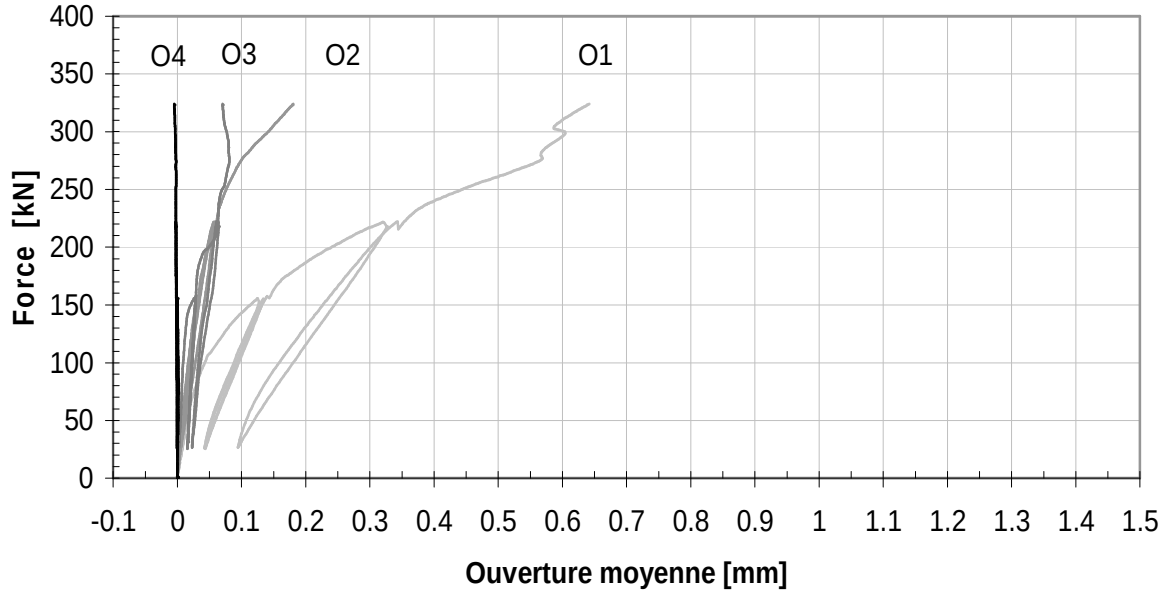

Fig. 63 : Courbes force – ouverture moyenne des fissures de la dalle B3-03.

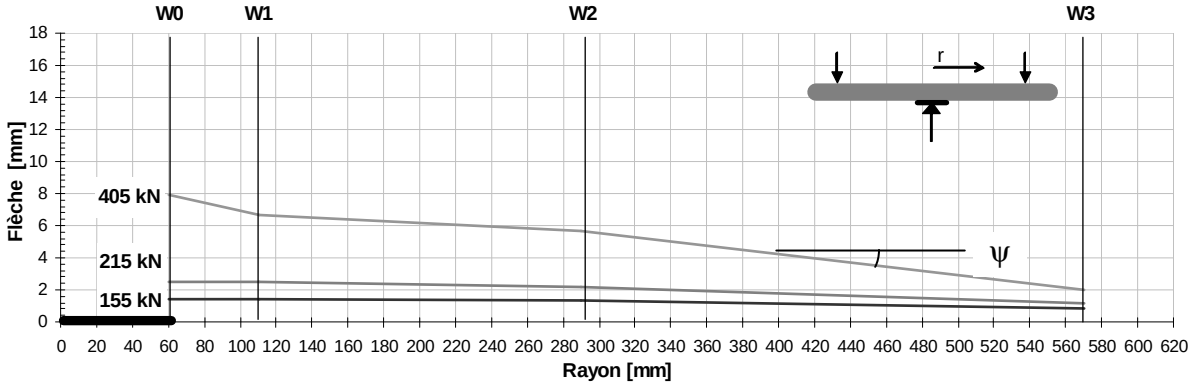

Fig. 64 : Déformation moyenne de la dalle B3-03 à plusieurs niveaux de charge.

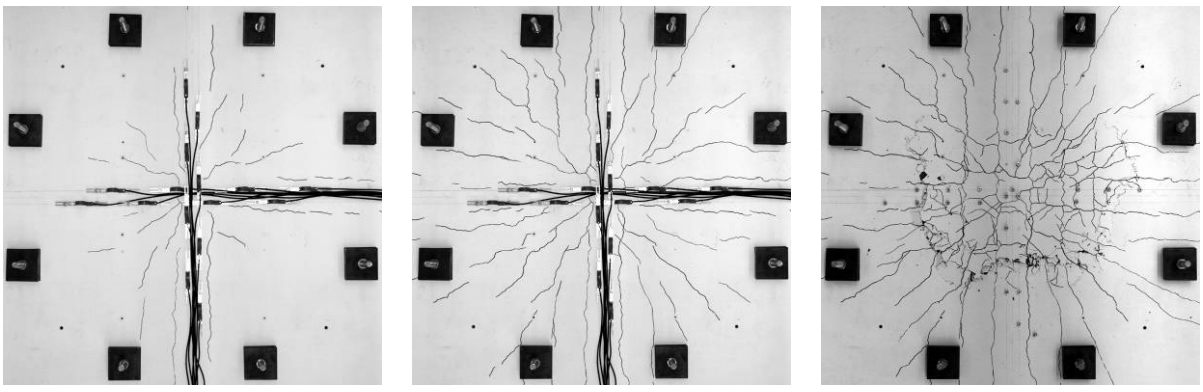

Charge de service 155 kN | Charge de dimensionnement 215 kN | Rupture

Fig. 65 : Fissuration à plusieurs niveaux de charge et fissures internes de la dalle B3-03.

3.2.11. Dalle B3-04

Caractéristiques :

- Béton B3 (40 kg/m^3) f_{cm} = 98 MPa
- Armature longitudinale supérieure : ϕ10 s = 100 mm ρ = 0.87 %
- Précontrainte : 2 x 4 x 180 kN σ_{cp} = 4.84 MPa

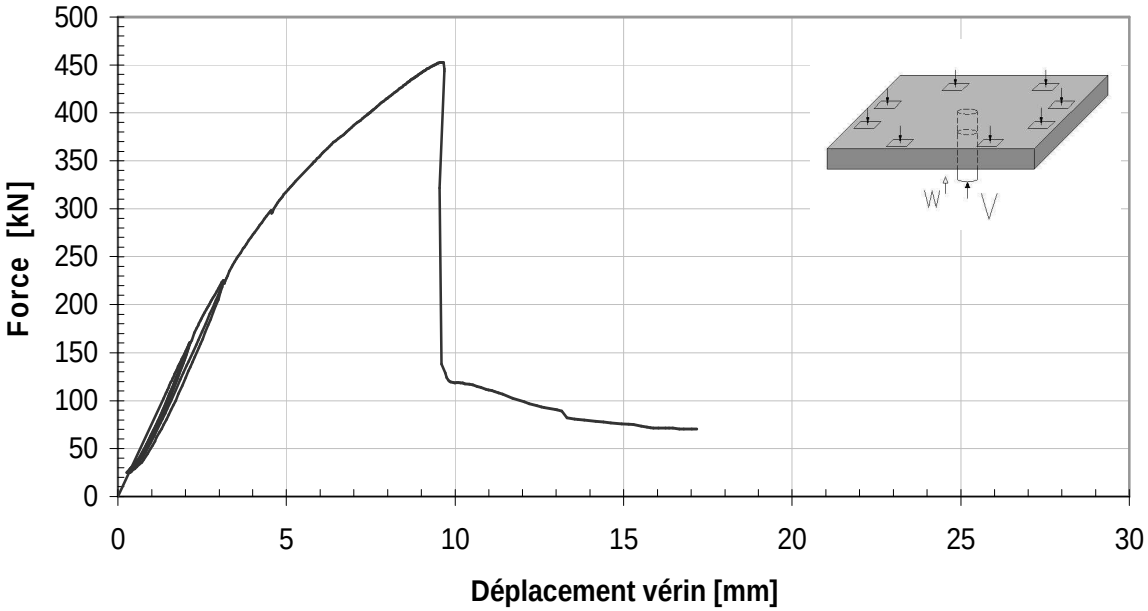

Fig. 66 : Courbe force – déplacement du vérin de la dalle B3-04.

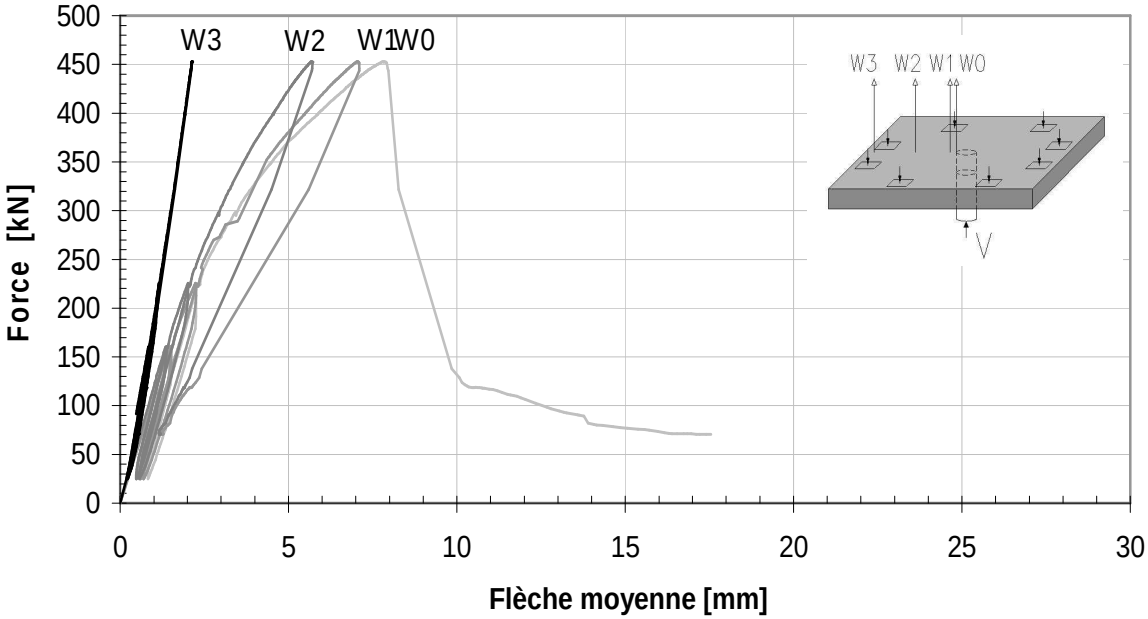

Fig. 67 : Courbes force – flèche moyenne de la dalle B3-04.

Force maximale V_{test} [kN]	Flèche au centre W_0 [mm]	Rotation ψ [‰]
453	**7.8**	**12.6**

Tab. 15 : Résultats principaux de l'essai de la dalle B3-04.

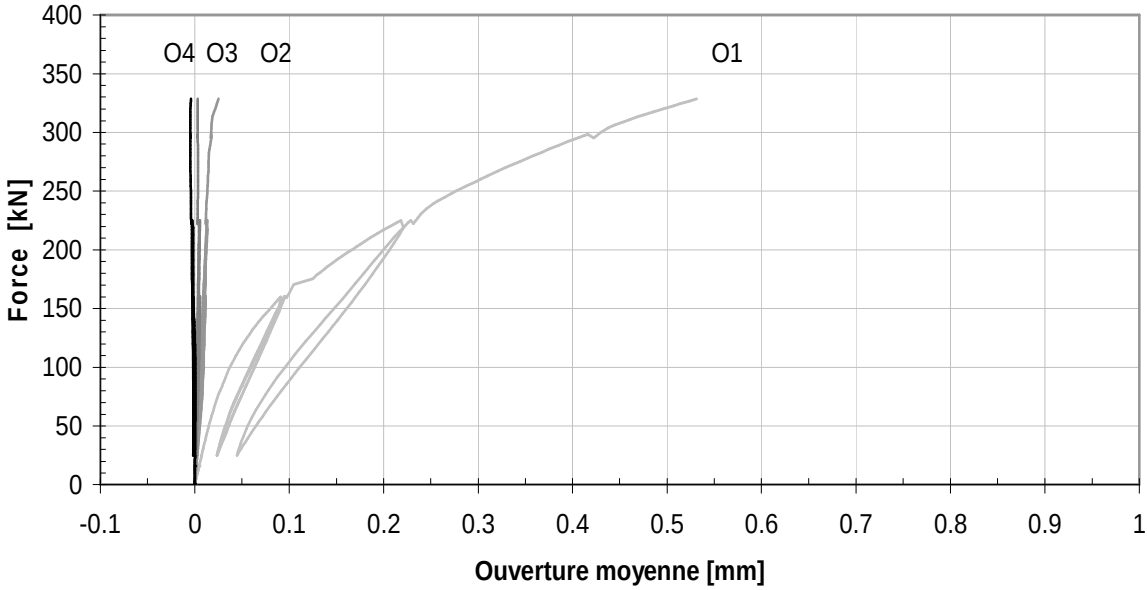

Fig. 68 : Courbes force – ouverture moyenne des fissures de la dalle B3-04.

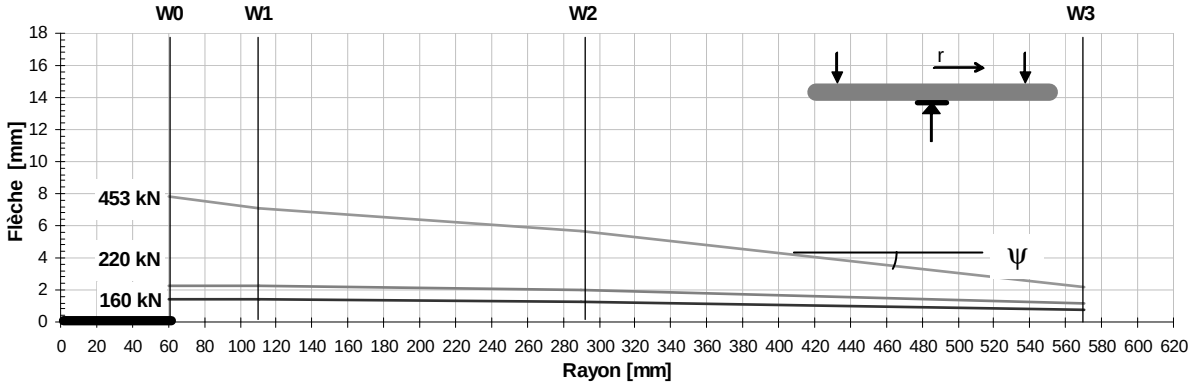

Fig. 69 : Déformation moyenne de la dalle B3-04 à plusieurs niveaux de charge.

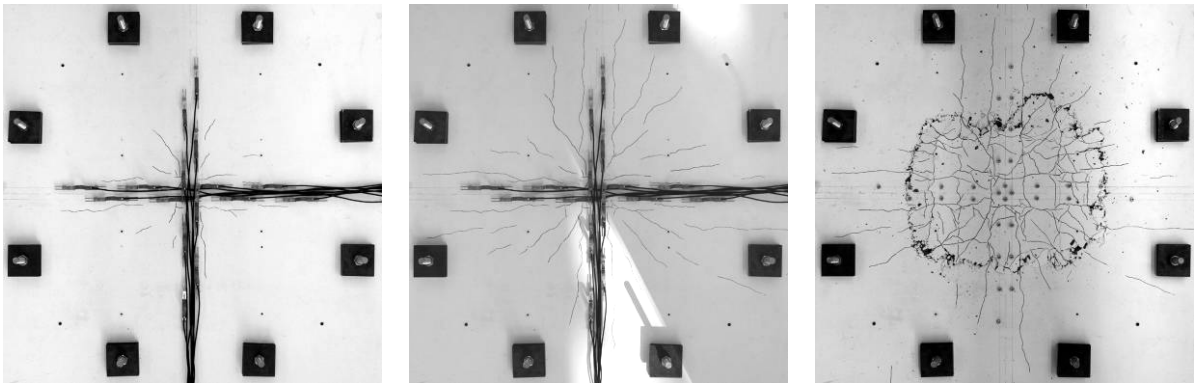

Charge de service 160 kN | Charge de dimensionnement 220 kN | Rupture

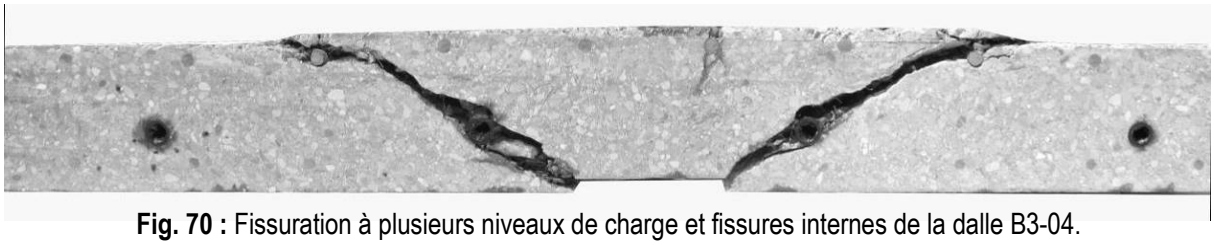

Fig. 70 : Fissuration à plusieurs niveaux de charge et fissures internes de la dalle B3-04.

3.2.12. Dalle B3-05

Caractéristiques :

- Béton B3 (40 kg/m^3) f_{cm} = 108 MPa
- Armature longitudinale supérieure : ϕ8 s = 100 mm (ρ = 0.56 %)

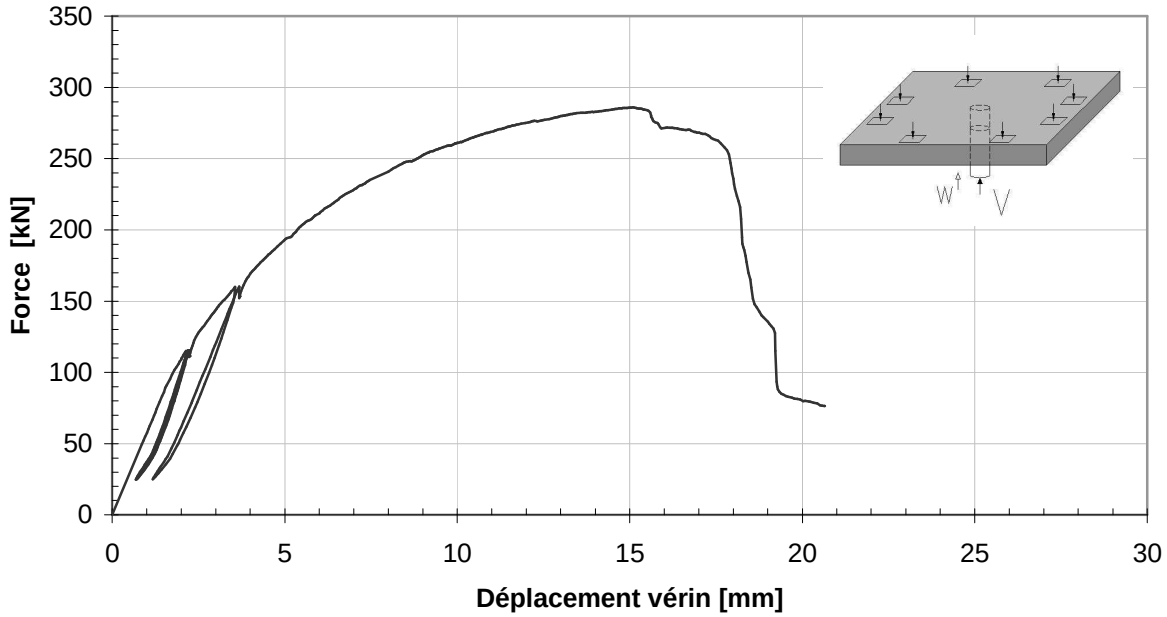

Fig. 71 : Courbe force – déplacement du vérin de la dalle B3-05.

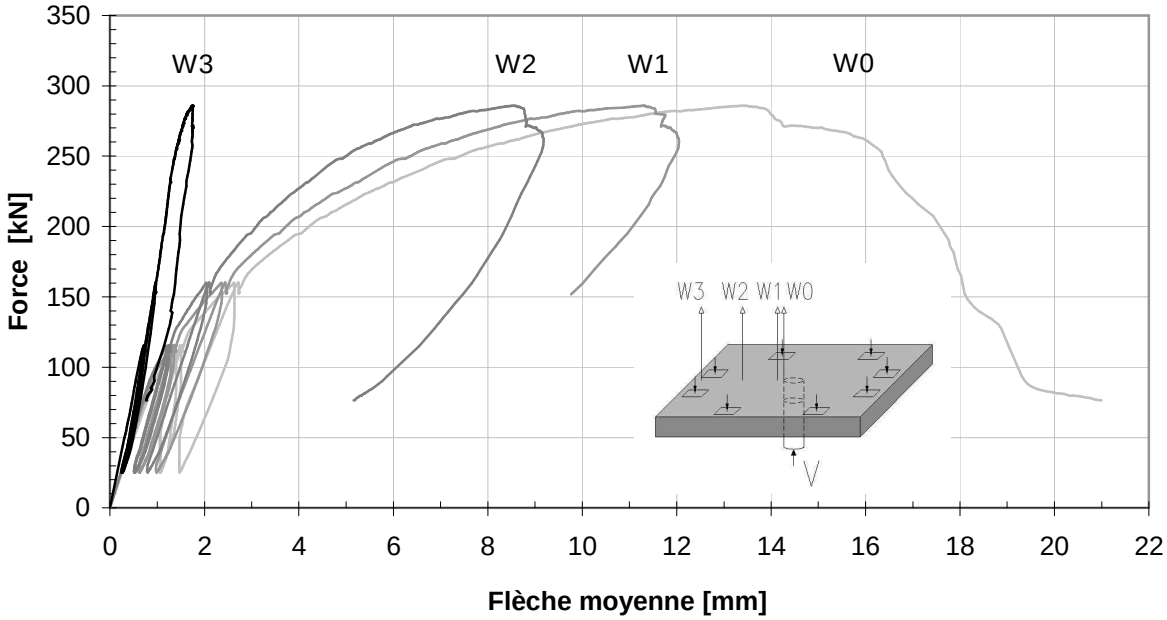

Fig. 72 : Courbes force – flèche moyenne de la dalle B3-05.

Force maximale V_{test} [kN]	Flèche au centre W_0 [mm]	Rotation ψ [‰]
286	**13.4**	**28.1**

Tab. 16 : Résultats principaux de l'essai de la dalle B3-05.

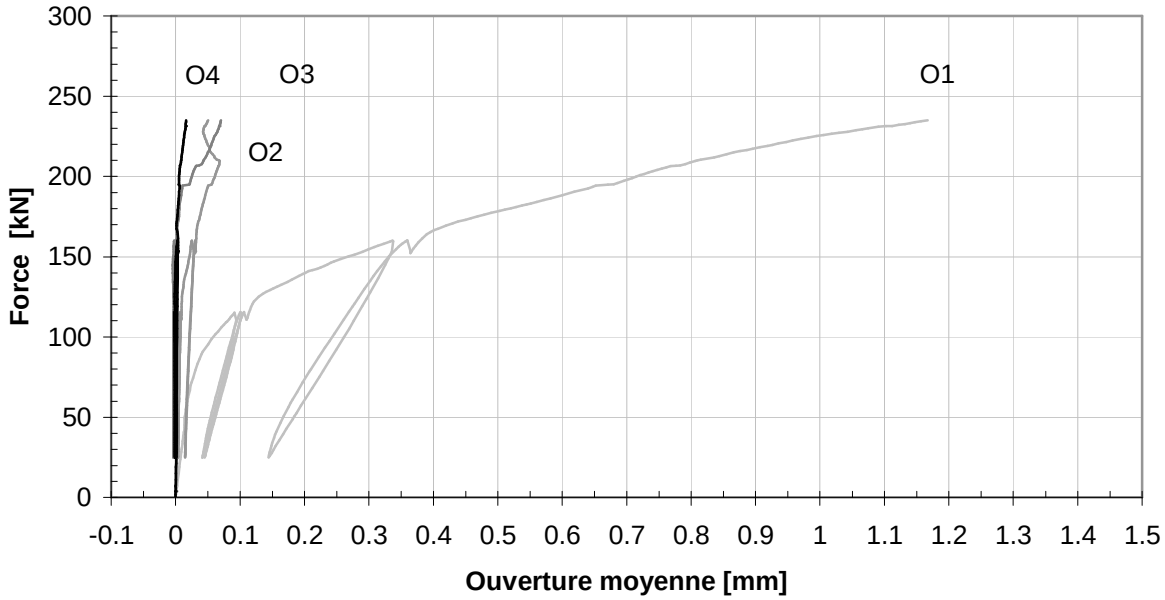

Fig. 73 : Courbes force – ouverture moyenne des fissures de la dalle B3-05.

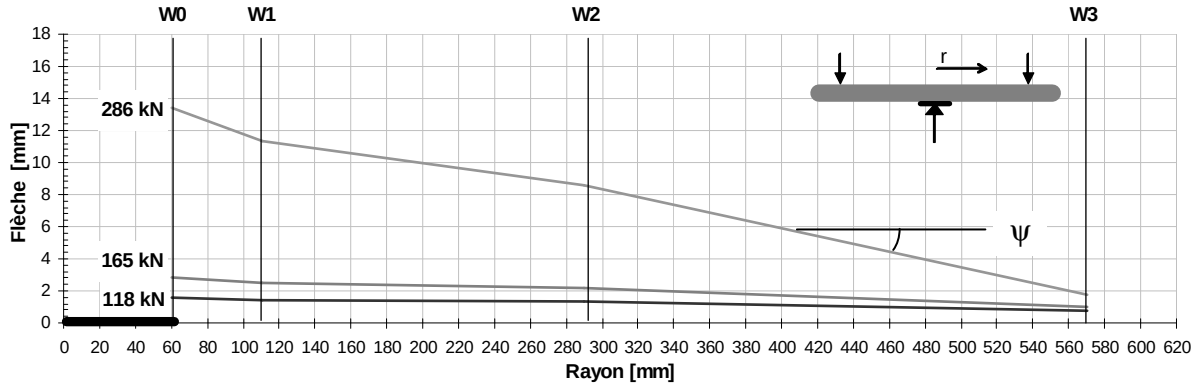

Fig. 74 : Déformation moyenne de la dalle B3-05 à plusieurs niveaux de charge.

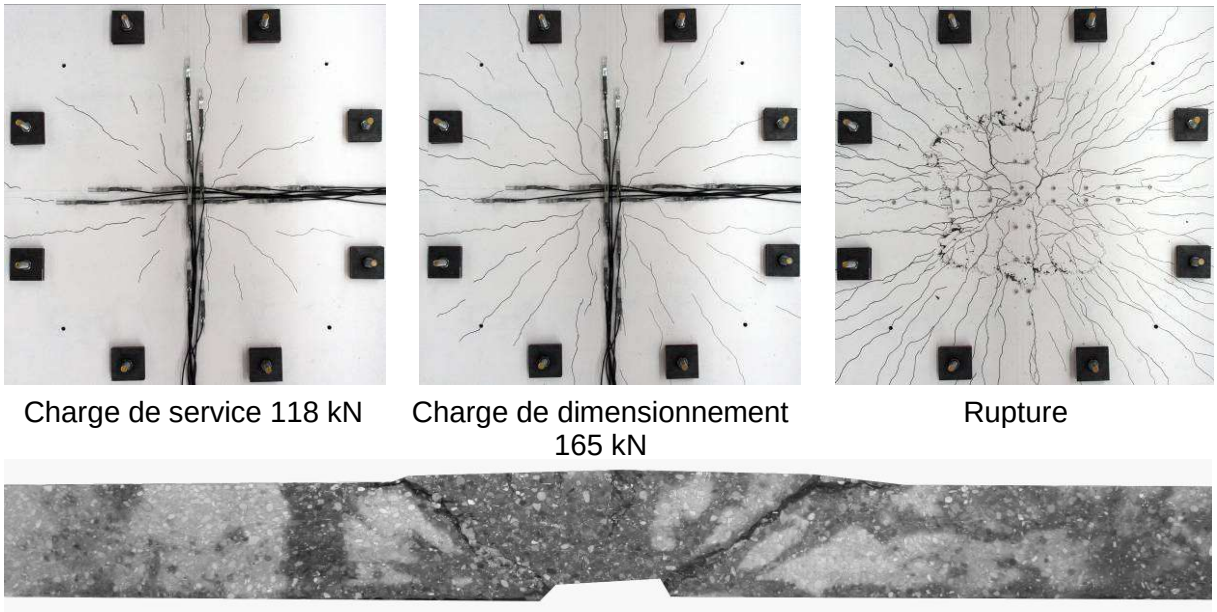

Charge de service 118 kN | Charge de dimensionnement 165 kN | Rupture

Fig. 75 : Fissuration à plusieurs niveaux de charge et fissures internes de la dalle B3-05.

3.2.13. Dalle B3-06

Caractéristiques :

- Béton B3 (40 kg/m^3) f_{cm} = 108 MPa
- Armature longitudinale supérieure : ϕ12 s = 100 mm (ρ = 1.26%)

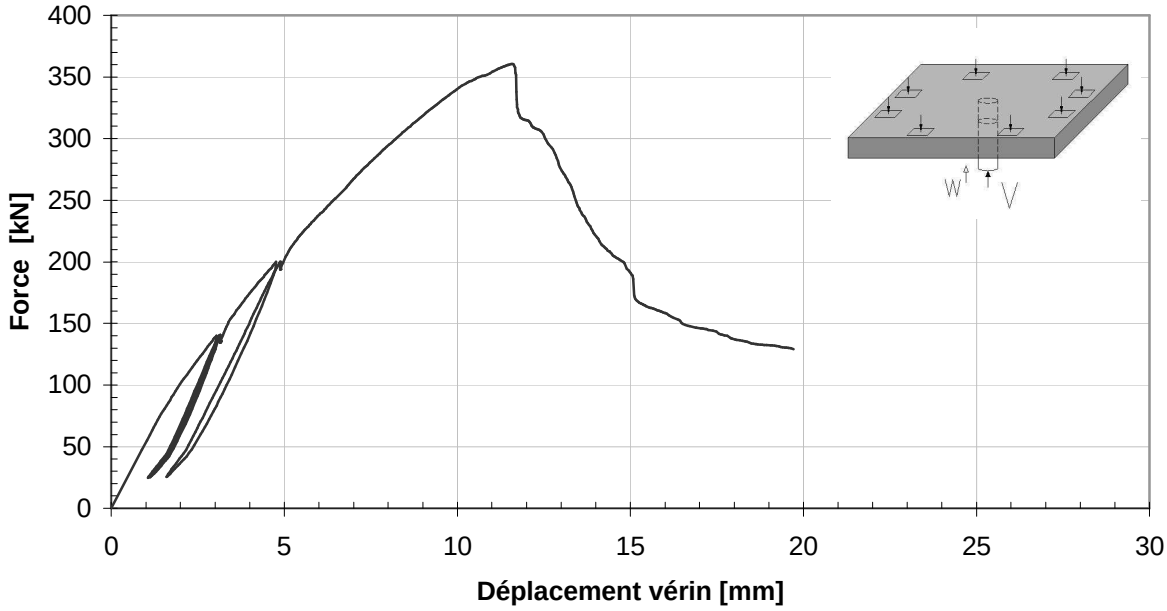

Fig. 76 : Courbe force – déplacement du vérin de la dalle B3-05.

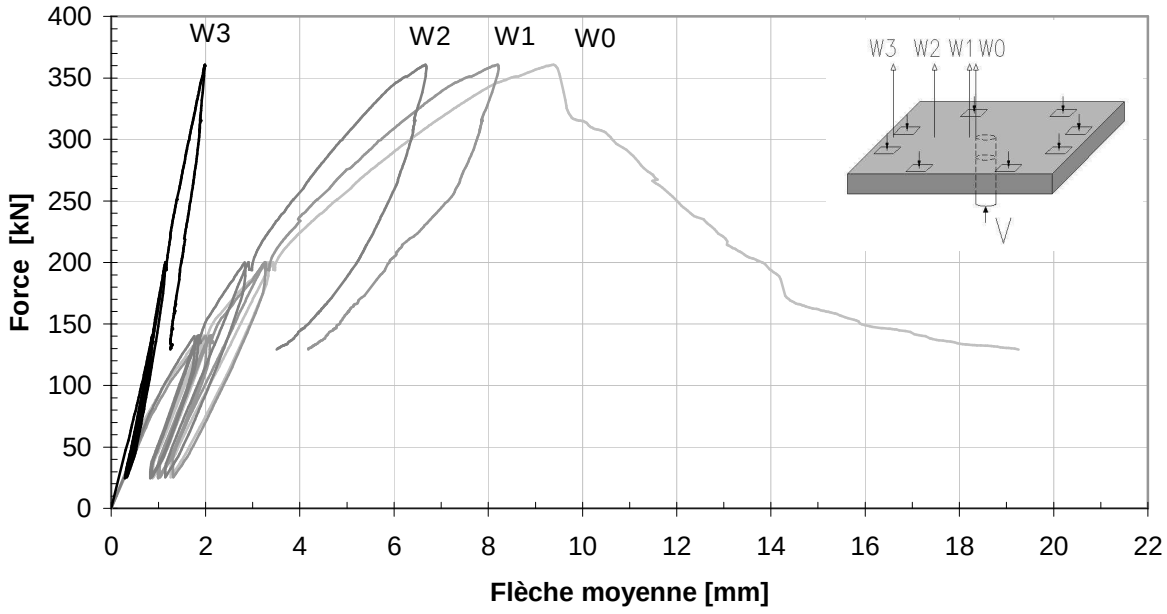

Fig. 77 : Courbes force – flèche moyenne de la dalle B3-05.

Force maximale V_{test} [kN]	Flèche au centre W_0 [mm]	Rotation ψ [‰]
361	**9.4**	**16.7**

Tab. 17 : Résultats principaux de l'essai de la dalle B3-05.

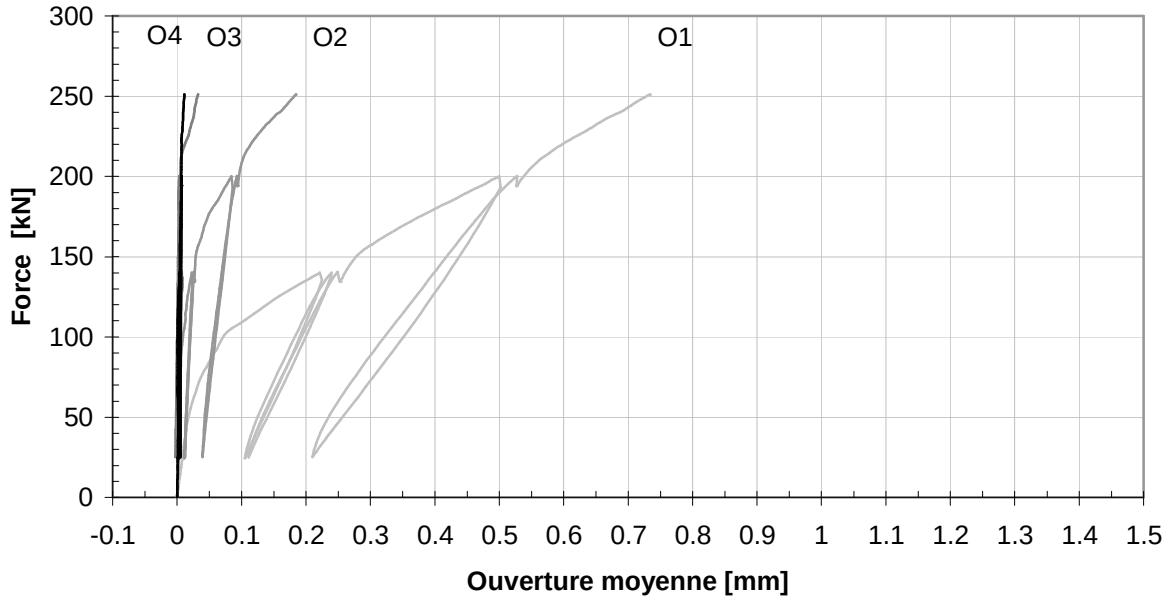

Fig. 78 : Courbes force – ouverture moyenne des fissures de la dalle B3-06.

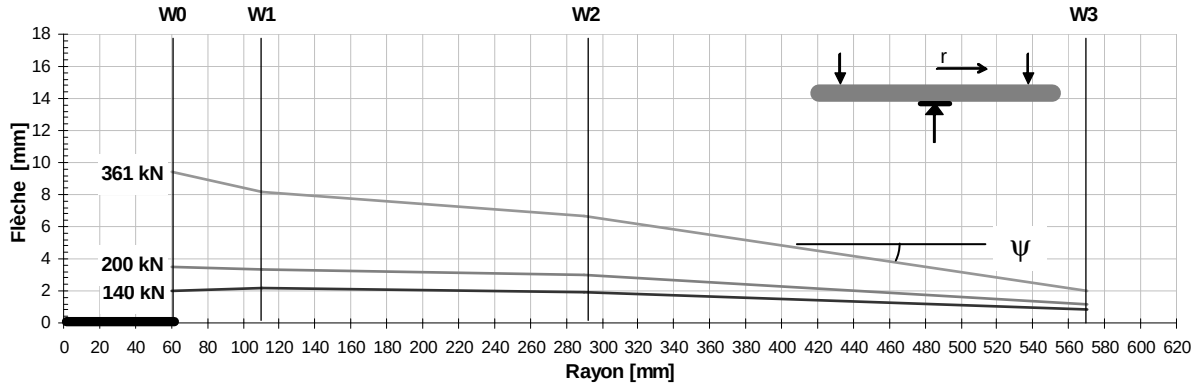

Fig. 79 : Déformation moyenne de la dalle B3-06 à plusieurs niveaux de charge.

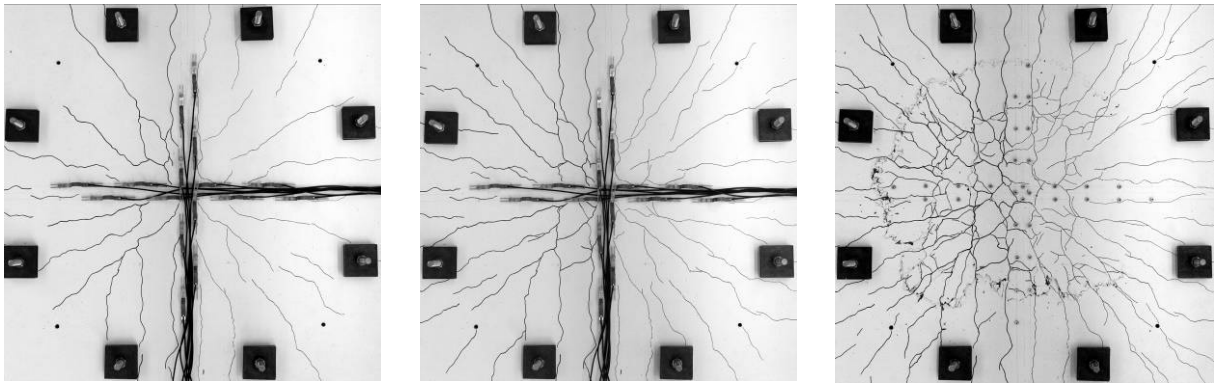

Charge de service 140 kN

Charge de dimensionnement 200 kN

Rupture

Fig. 80 : Fissuration à plusieurs niveaux de charge et fissures internes de la dalle B3-06.

3.2.14. Dalle B4-01

Caractéristiques :

- Béton B4 (60 kg/m^3) f_{cm} = 100 MPa
- Armature longitudinale supérieure : ϕ10 s = 100 mm (ρ = 0.87 %)

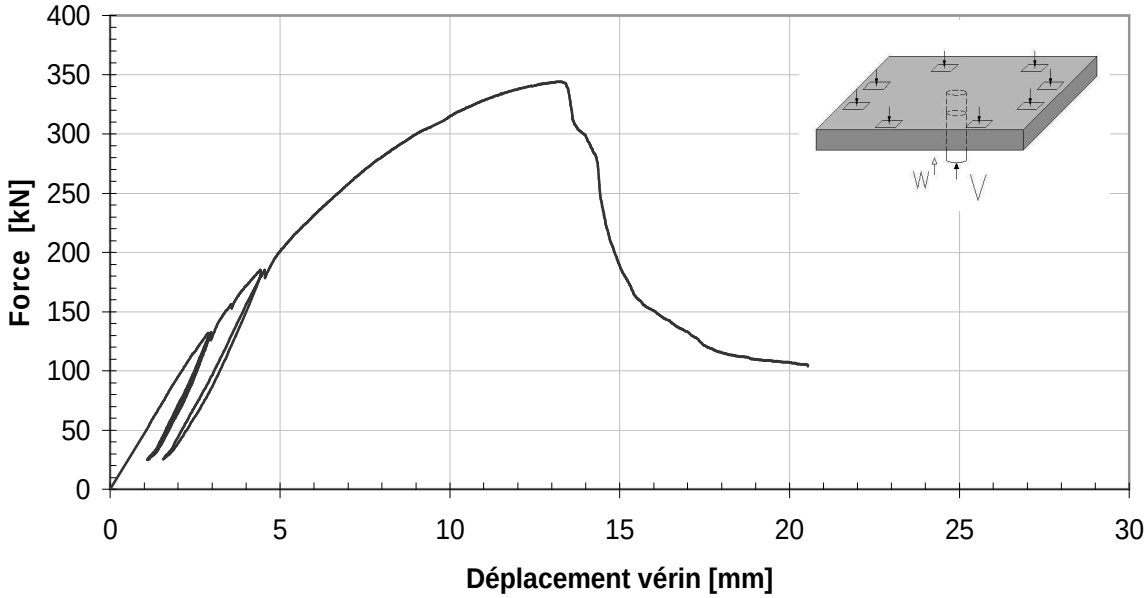

Fig. 81 : Courbe force – déplacement du vérin de la dalle B4-01.

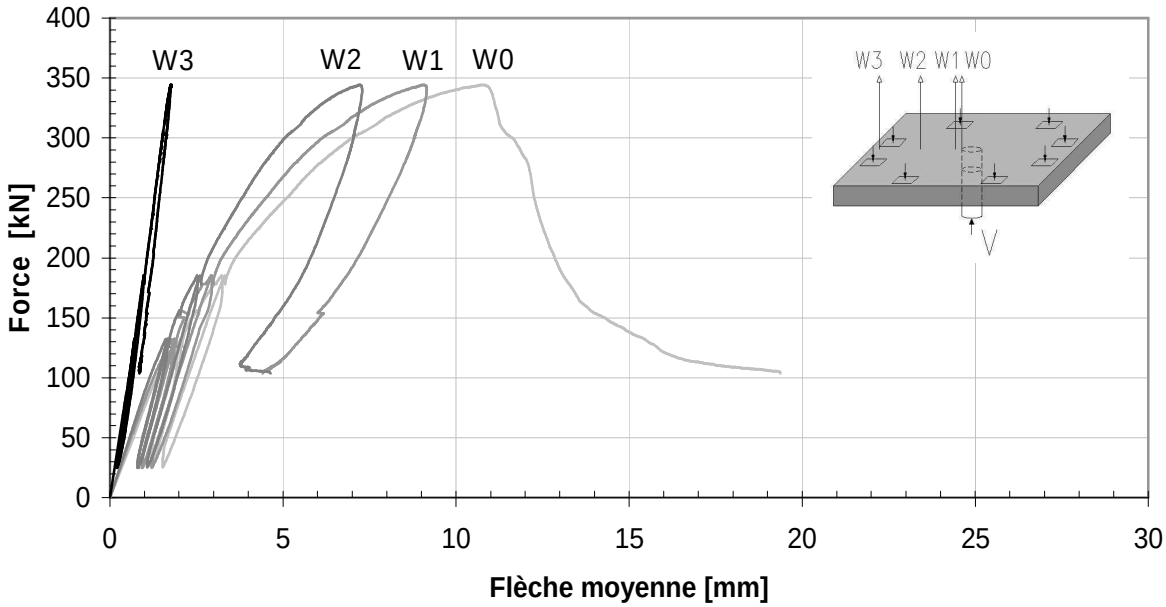

Fig. 82 : Courbes force – flèche moyenne de la dalle B4-01.

Force maximale V_{test} [kN]	Flèche au centre W_0 [mm]	Rotation ψ [‰]
337	**10.8**	**19.3**

Tab. 18 : Résultats principaux de l'essai de la dalle B4-01.

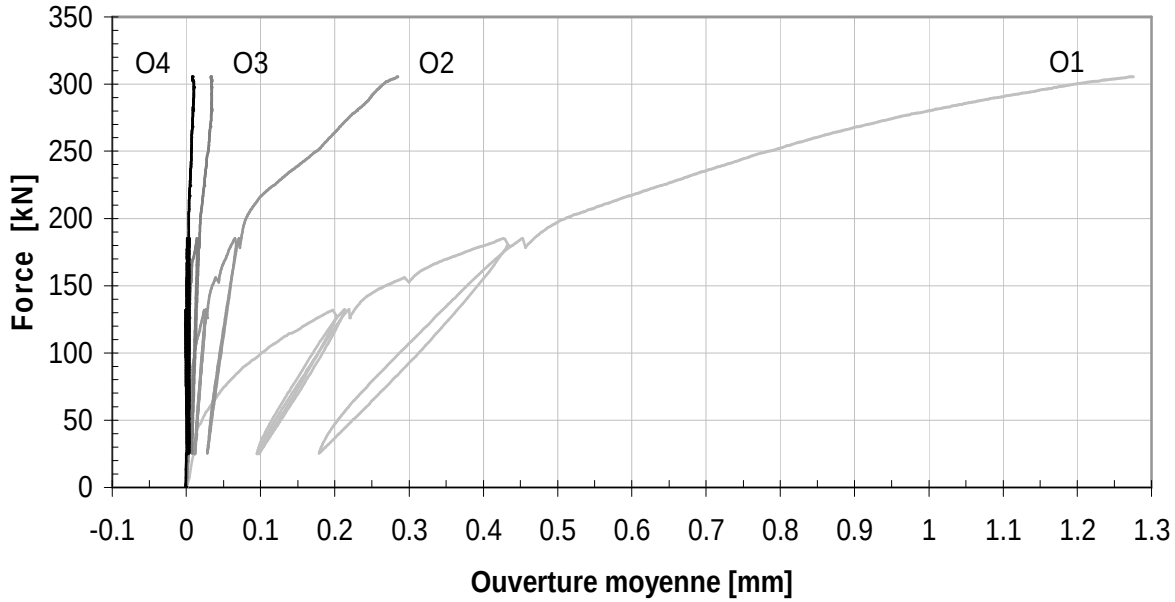

Fig. 83 : Courbes force – ouverture moyenne des fissures de la dalle B4-01.

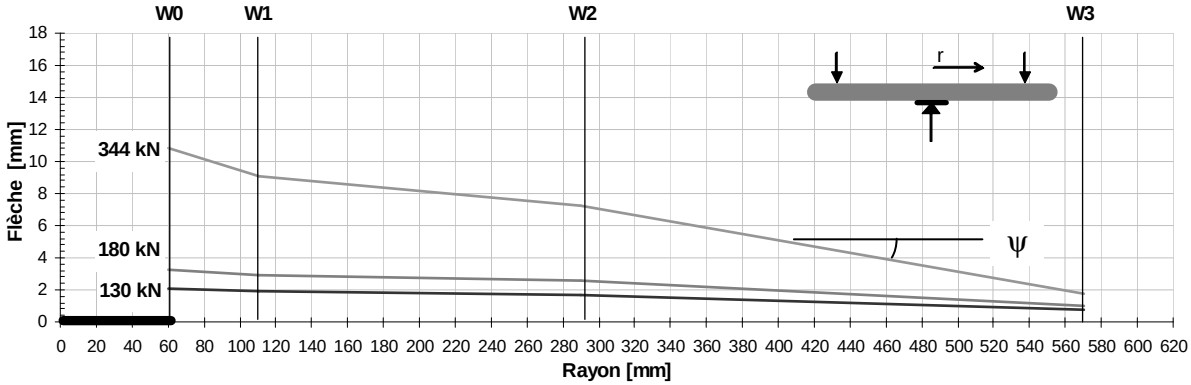

Fig. 84 : Déformation moyenne de la dalle B4-01 à plusieurs niveaux de charge.

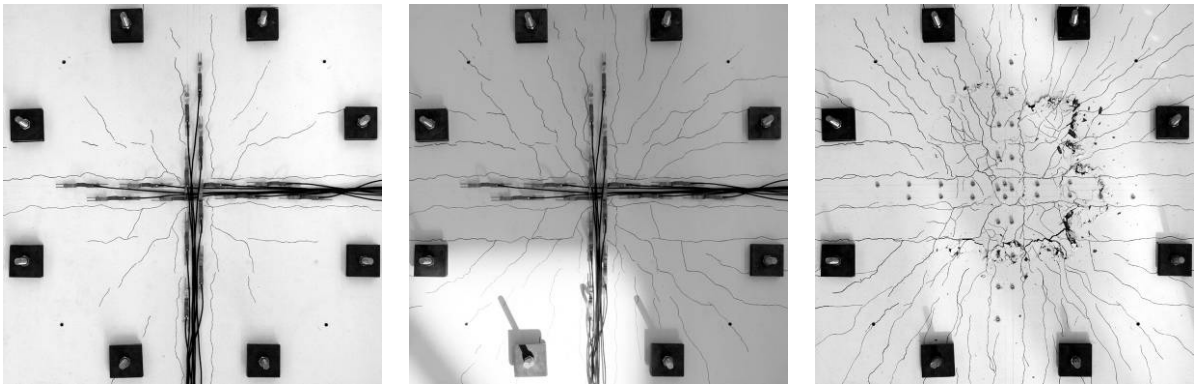

Charge de service 130 kN | Charge de dimensionnement 180 kN | Rupture

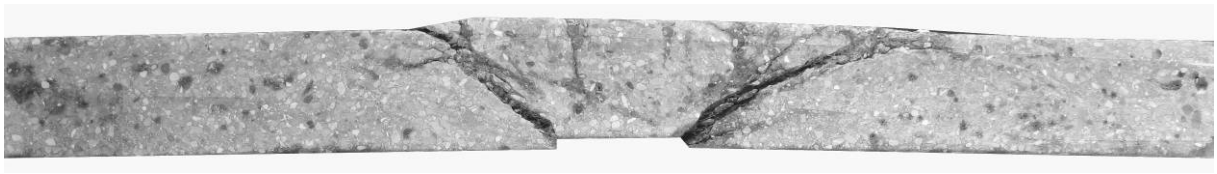

Fig. 85 : Fissuration à plusieurs niveaux de charge et fissures internes de la dalle B4-01.

3.2.15. Dalle B5-01

Caractéristiques :

- Béton B5 (80 kg/m^3) f_{cm} = 105 MPa
- Armature longitudinale supérieure : ϕ10 s = 100 mm (ρ = 0.87 %)

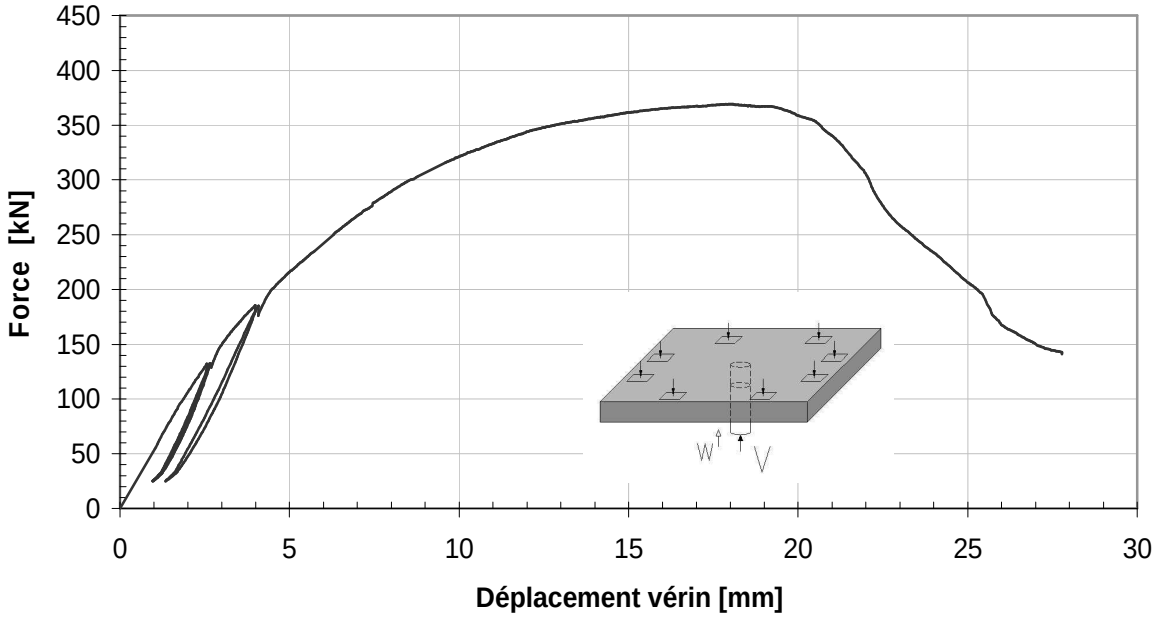

Fig. 86 : Courbe force – déplacement du vérin de la dalle B5-01.

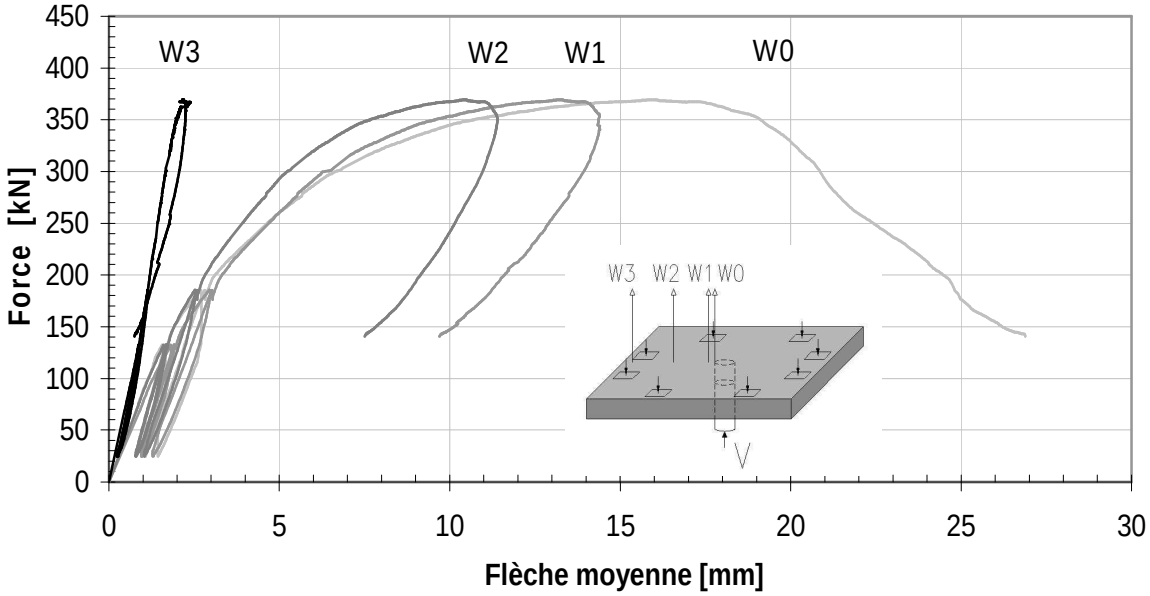

Fig. 87 : Courbes force – flèche moyenne de la dalle B5-01.

Force maximale V_{test} [kN]	Flèche au centre W_0 [mm]	Rotation ψ [‰]
369	**16.0**	**29.5**

Tab. 19 : Résultats principaux de l'essai de la dalle B5-01.

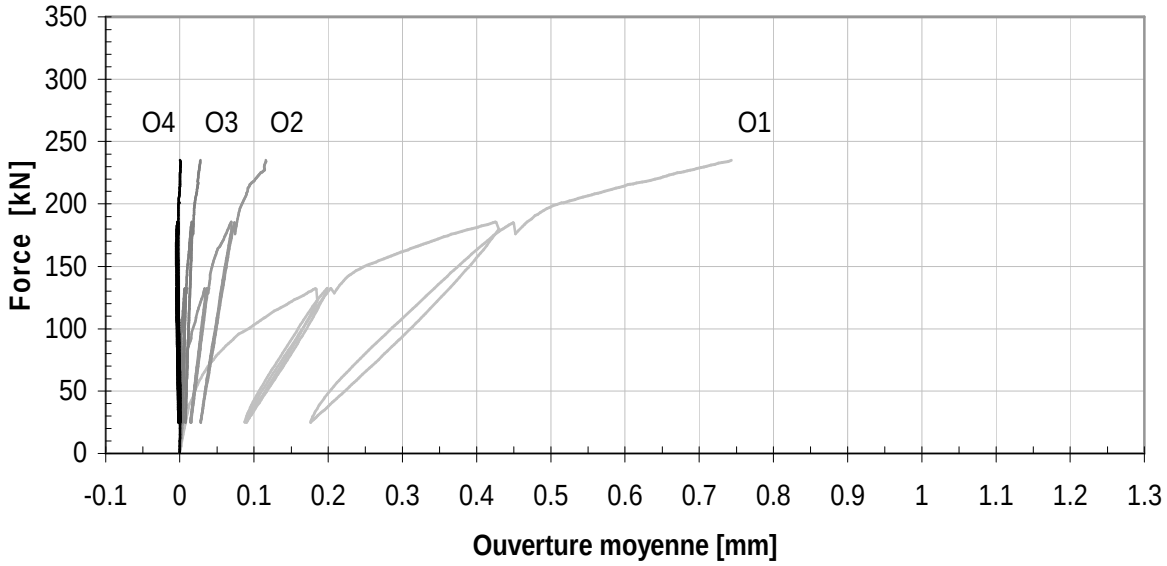

Fig. 88 : Courbes force – ouverture moyenne des fissures de la dalle B5-01.

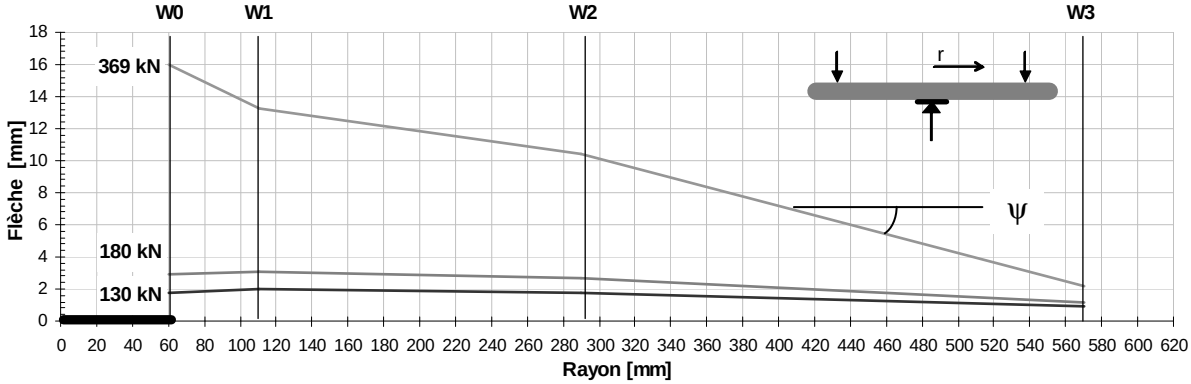

Fig. 89 : Déformation moyenne de la dalle B5-01 à plusieurs niveaux de charge.

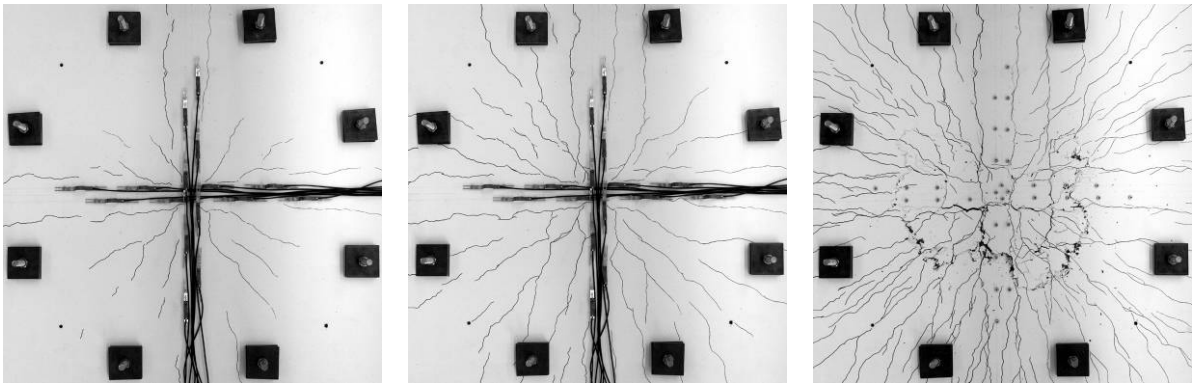

Charge de service 130 kN | Charge de dimensionnement 180 kN | Rupture

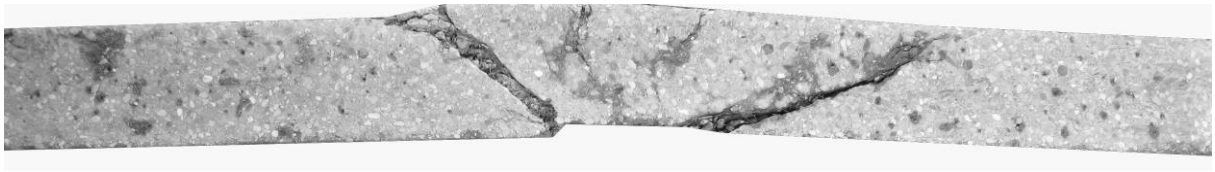

Fig. 90 : Fissuration à plusieurs niveaux de charge et fissures internes de la dalle B5-01.

3.2.16. Dalle B5-02

Caractéristiques :

- Béton B5 (80 kg/m^3) f_{cm} = 105 MPa
- Armature longitudinale supérieure : ϕ10 s = 100 mm ρ = 0.87 %
- Précontrainte : 2 x 2 x 180 kN $\sigma_{cp,0}$ = 2.42 MPa

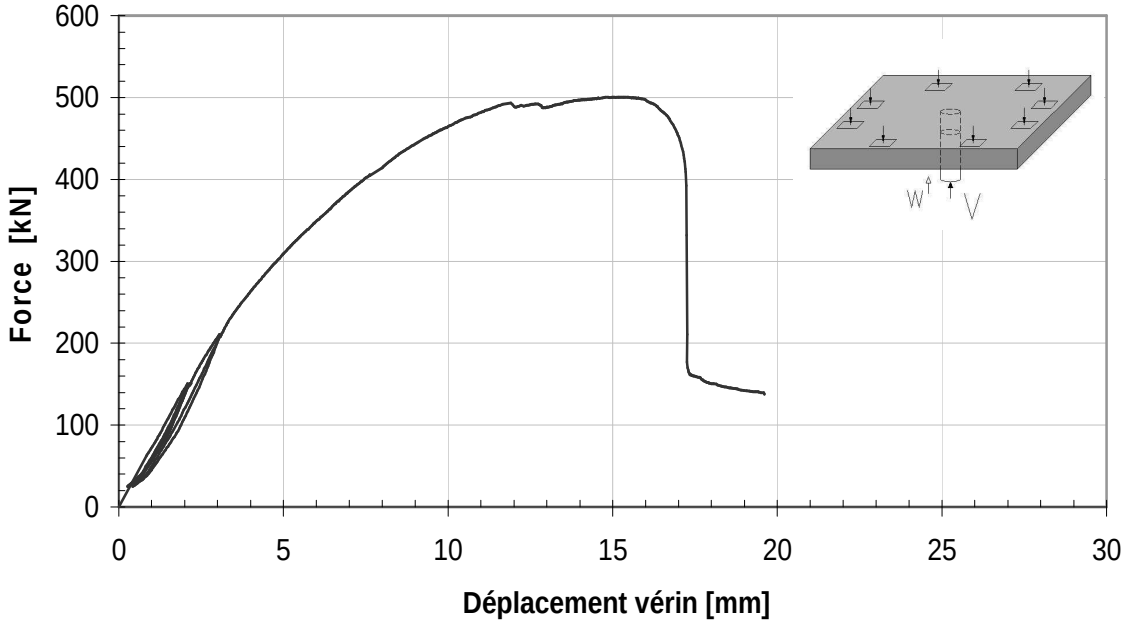

Fig. 91 : Courbe force – déplacement du vérin de la dalle B5-02.

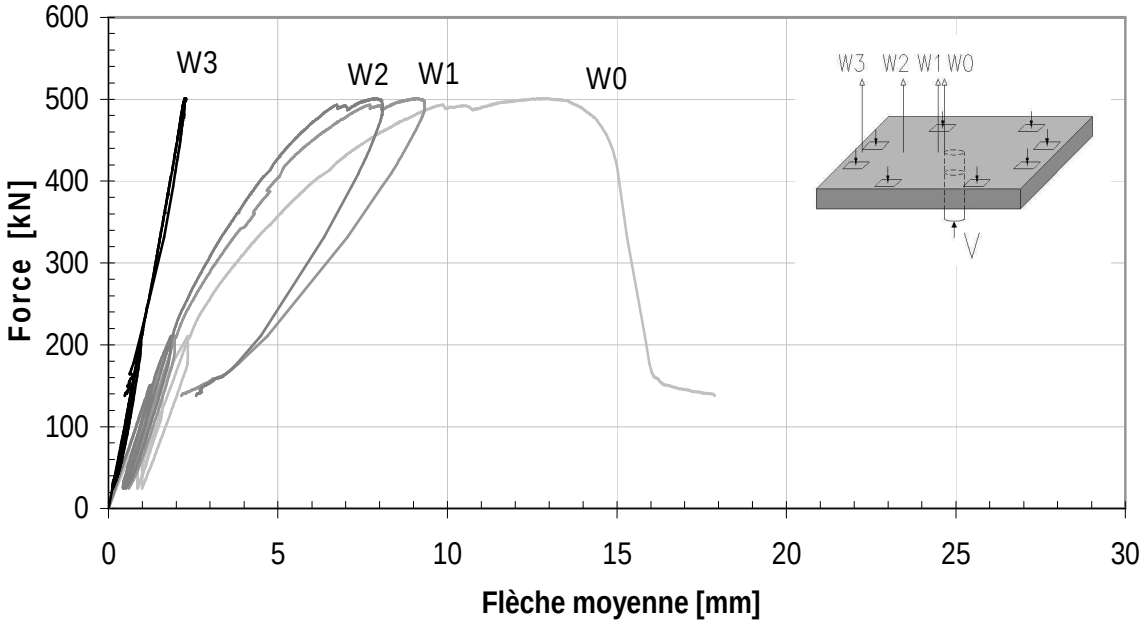

Fig. 92 : Courbes force – flèche moyenne de la dalle B5-02.

Force maximale V_{test} [kN]	Flèche au centre W_0 [mm]	Rotation ψ [‰]
501	**12.8**	**20.1**

Tab. 20 : Résultats principaux de l'essai de la dalle B5-02.

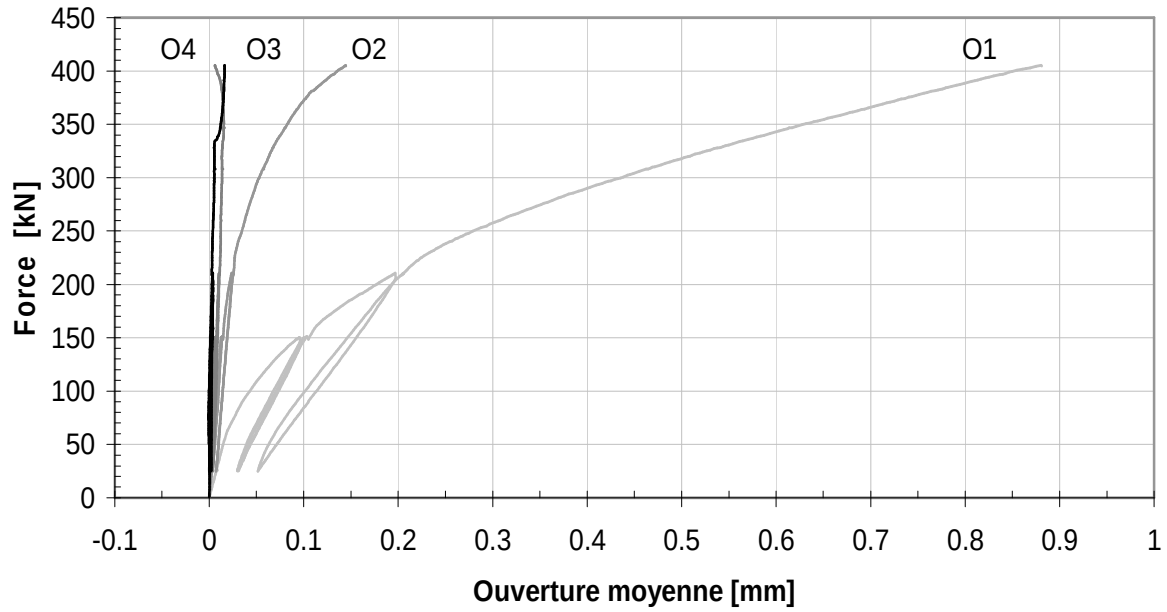

Fig. 93 : Courbes force – ouverture moyenne des fissures de la dalle B5-02.

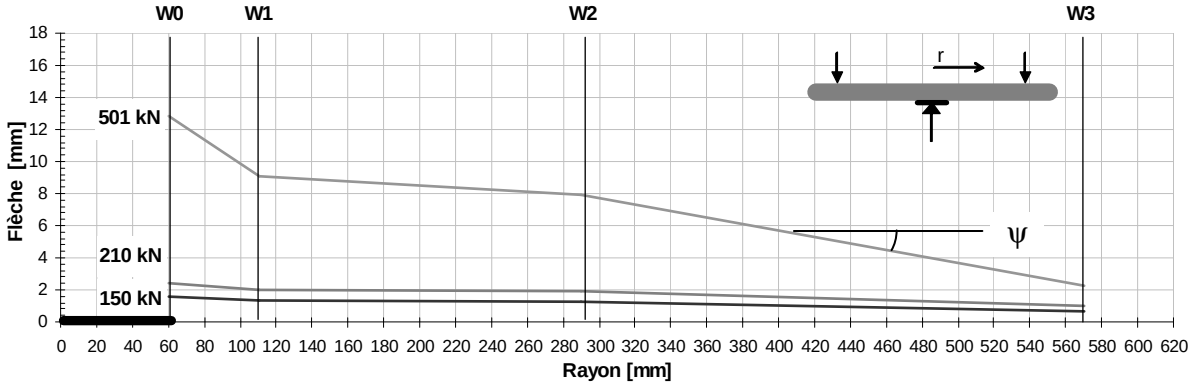

Fig. 94 : Déformation moyenne de la dalle B5-02 à plusieurs niveaux de charge.

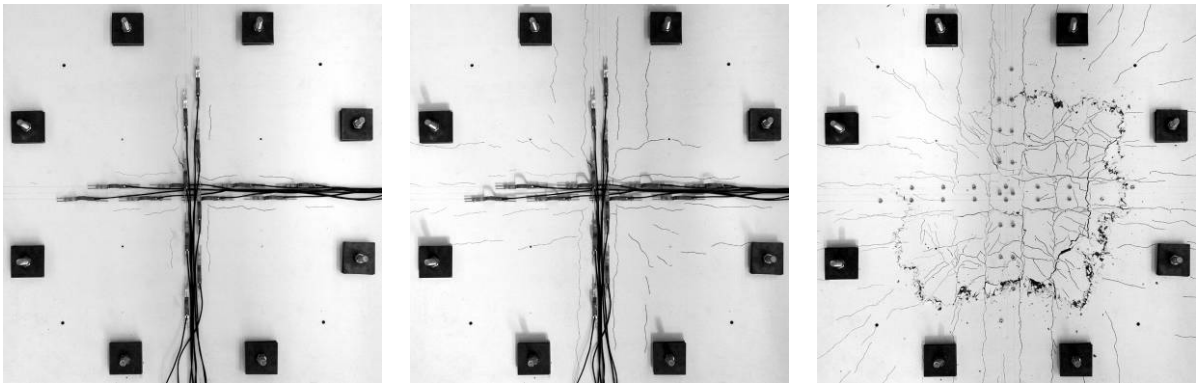

Charge de service 150 kN | Charge de dimensionnement 210 kN | Rupture

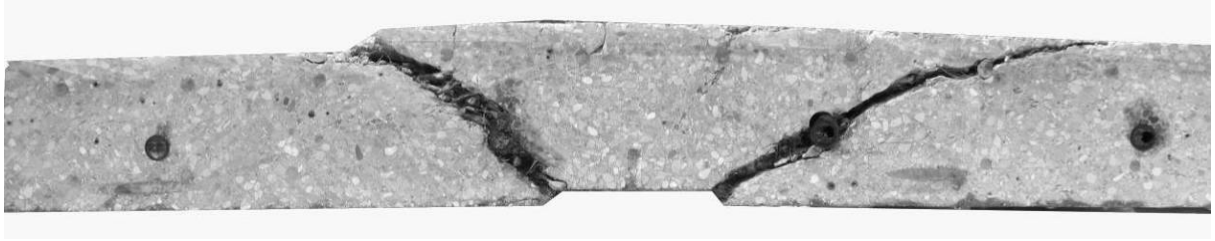

Fig. 95 : Fissuration à plusieurs niveaux de charge et fissures internes de la dalle B5-02.

3.2.17. Dalle B5-03

Caractéristiques :

- Béton B5 (80 kg/m^3) f_{cm} = 107 MPa
- Armature longitudinale supérieure : ϕ10 s = 100 mm ρ = 0.87 %
- Précontrainte : 2 x 4 x 135 kN $\sigma_{cp,0}$ = 3.63 MPa

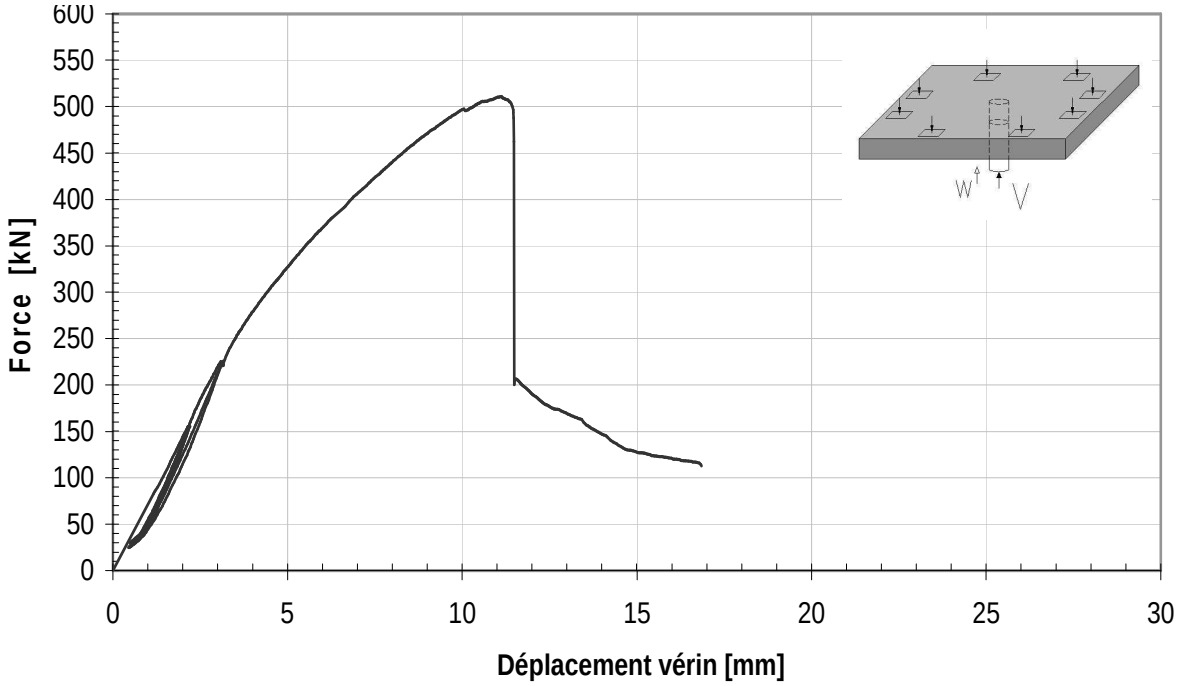

Fig. 96 : Courbe force – déplacement du vérin de la dalle B5-03.

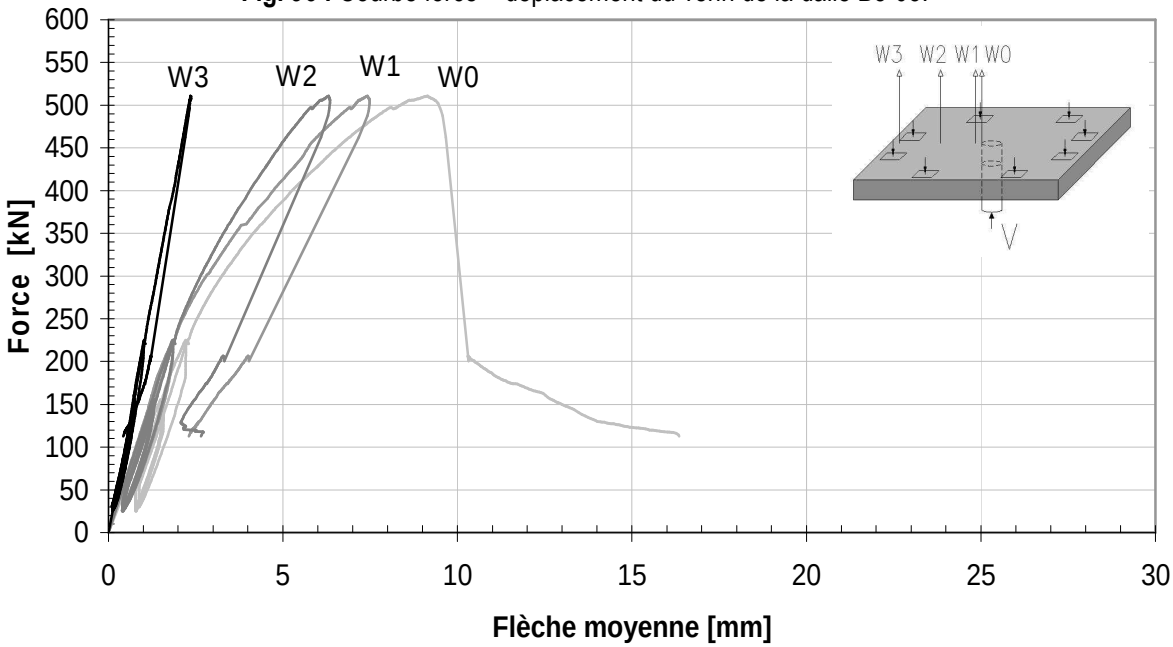

Fig. 97 : Courbes force – flèche moyenne de la dalle B5-03.

Force maximale V_{test} [kN]	Flèche au centre W_0 [mm]	Rotation ψ [‰]
511	**9.1**	**14.2**

Tab. 21 : Résultats principaux de l'essai de la dalle B5-03.

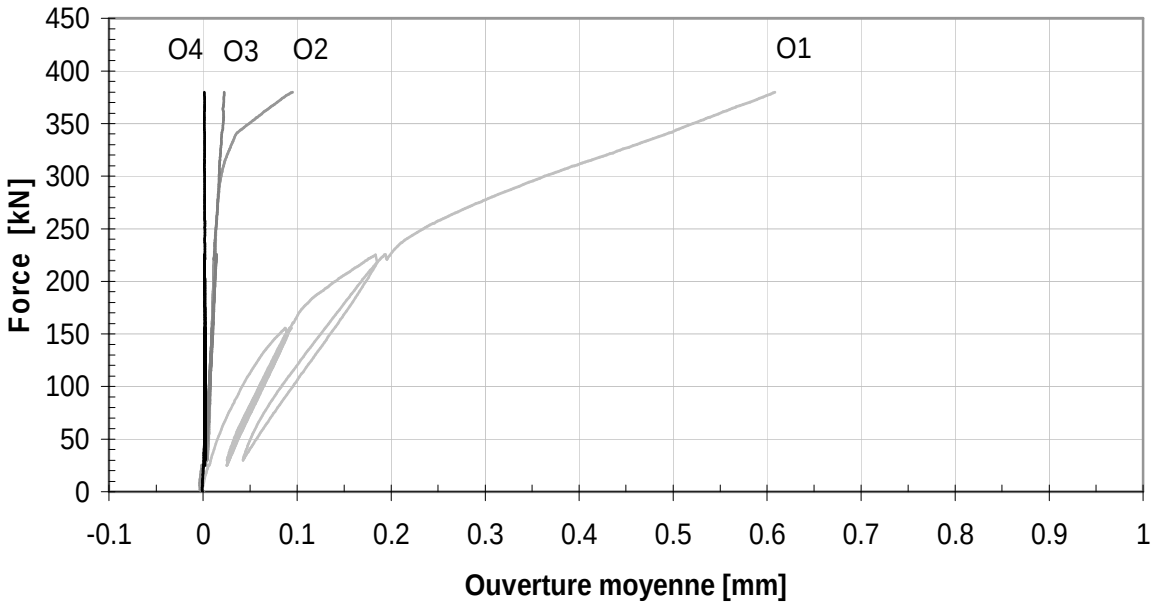

Fig. 98 : Courbes force – ouverture moyenne des fissures de la dalle B5-03.

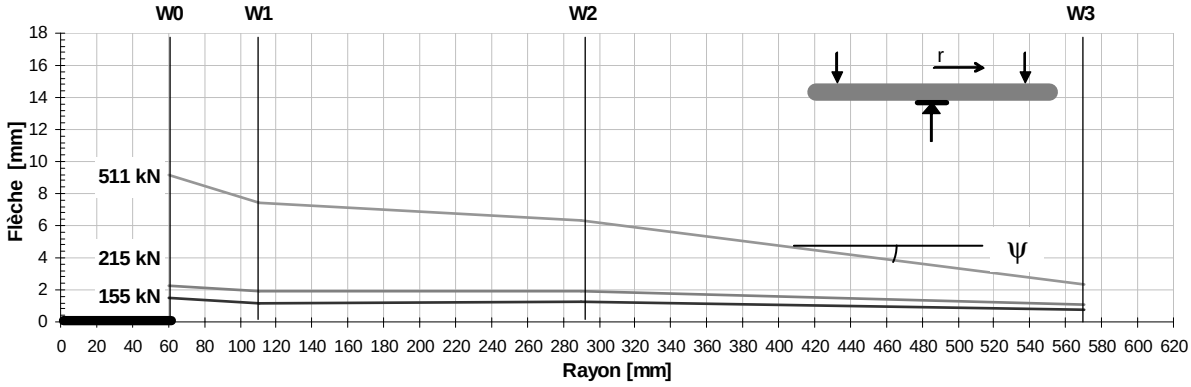

Fig. 99 : Déformation moyenne de la dalle B5-03 à plusieurs niveaux de charge.

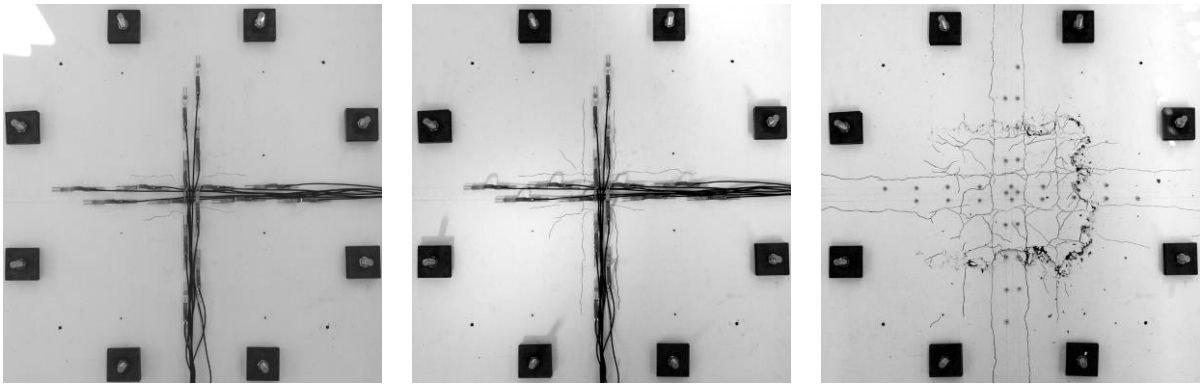

Charge de service 155 kN | Charge de dimensionnement 215 kN | Rupture

Fig. 100 : Fissuration à plusieurs niveaux de charge et fissures internes de la dalle B5-03.

3.2.18. Dalle B5-04

Caractéristiques :

- Béton B5 (80 kg/m^3) f_{cm} = 107 MPa
- Armature longitudinale supérieure : ϕ10 s = 100 mm ρ = 0.87 %
- Précontrainte : 2 x 4 x 180 kN $\sigma_{cp,0}$ = 4.84 MPa

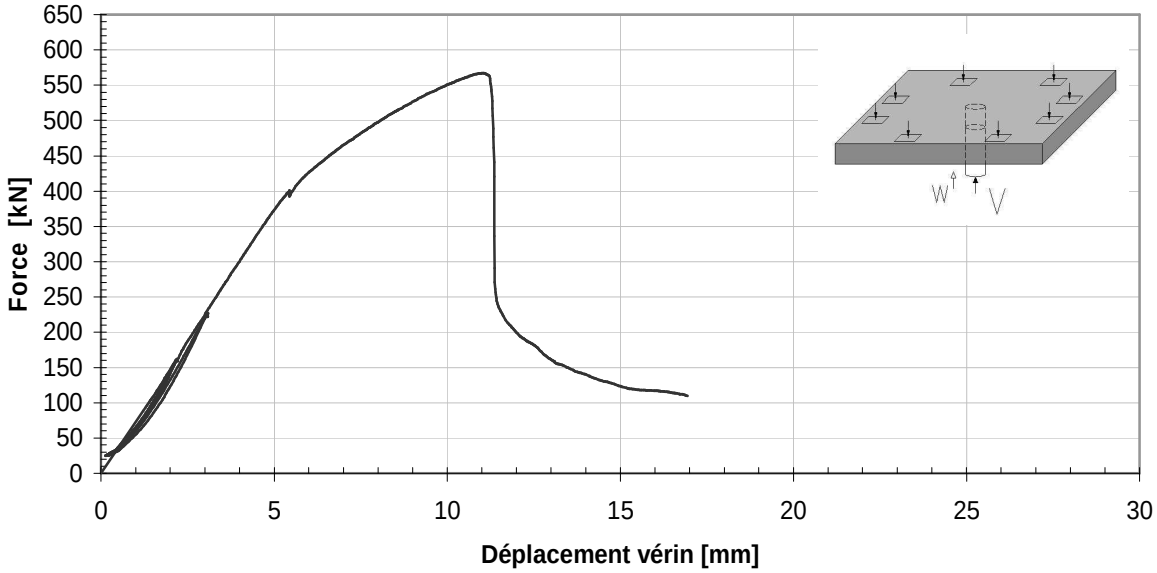

Fig. 101 : Courbe force – déplacement du vérin de la dalle B5-04.

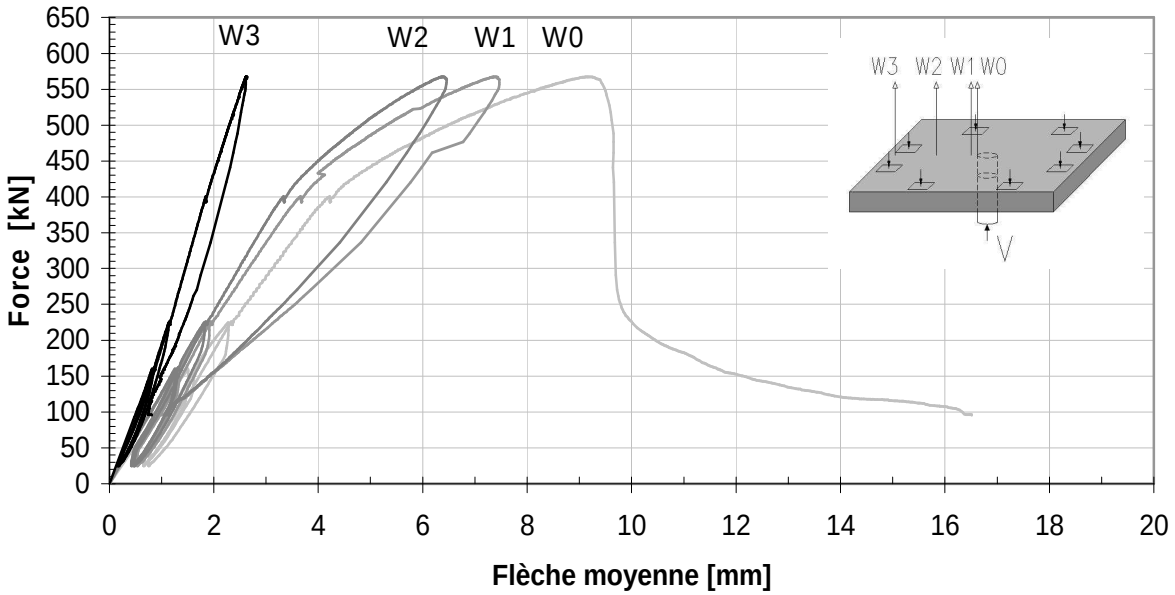

Fig. 102 : Courbes force – flèche moyenne de la dalle B5-04.

Force maximale V_{test} [kN]	Flèche au centre W_0 [mm]	Rotation ψ [‰]
567	**9.2**	**12.6**

Tab. 22 : Résultats principaux de l'essai de la dalle B5-04.

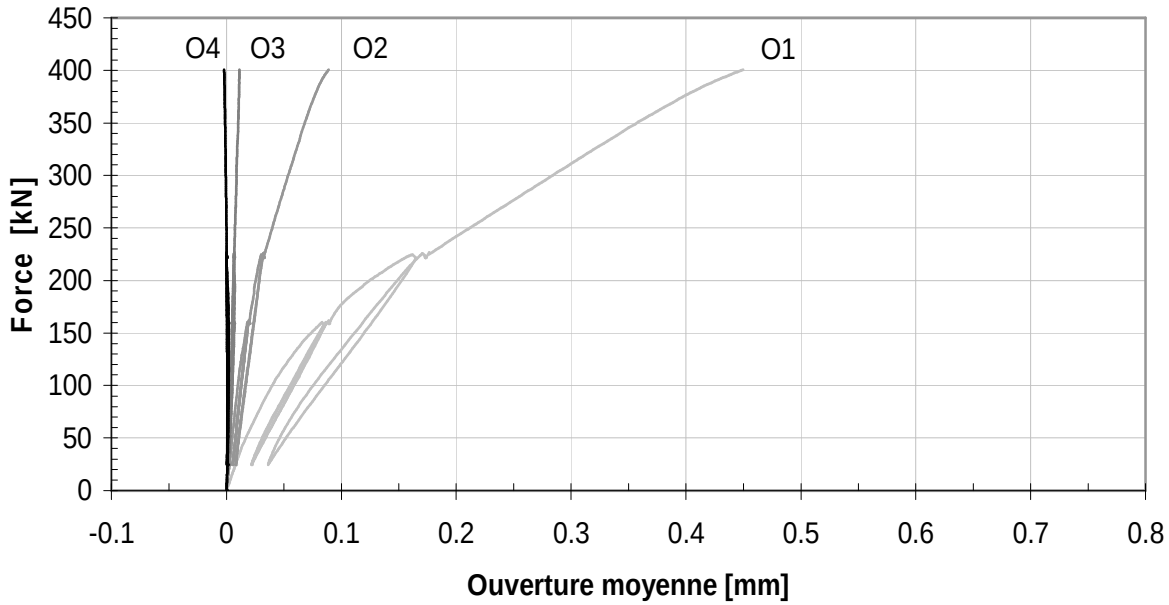

Fig. 103 : Courbes force – ouverture moyenne des fissures de la dalle B5-04.

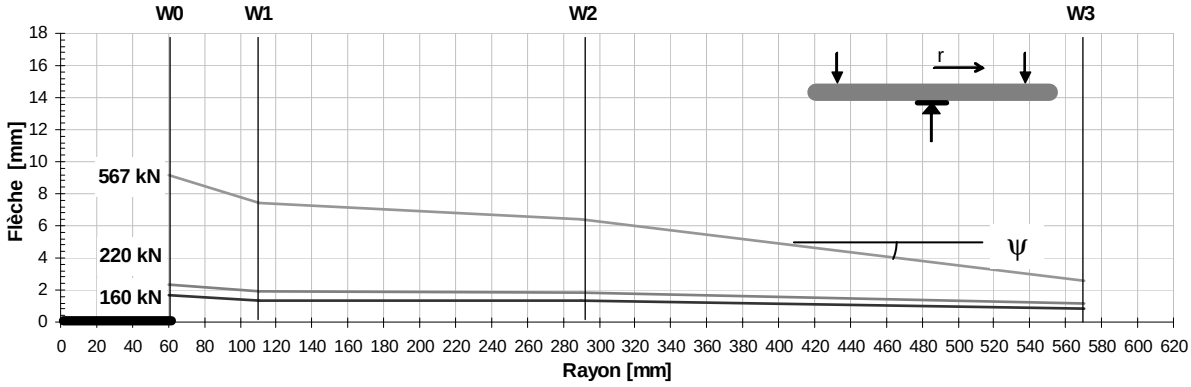

Fig. 104 : Déformation moyenne de la dalle B5-04 à plusieurs niveaux de charge.

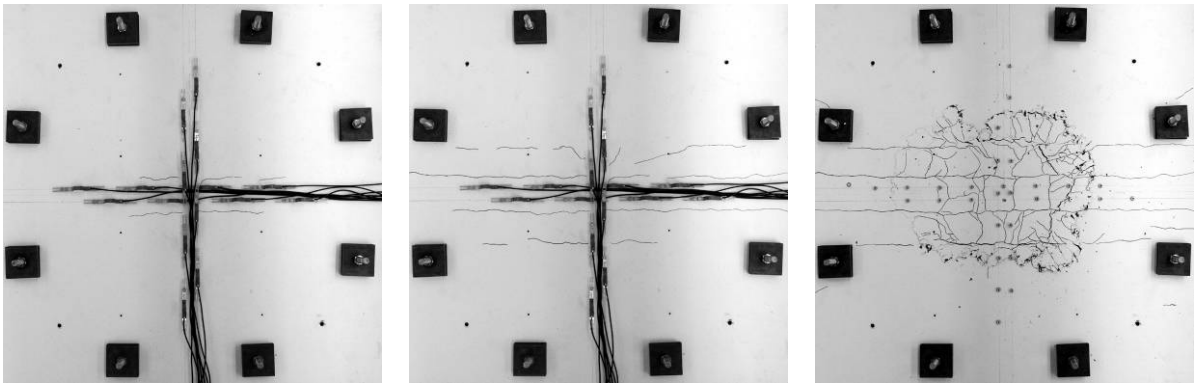

Charge de service 160 kN | Charge de dimensionnement 220 kN | Rupture

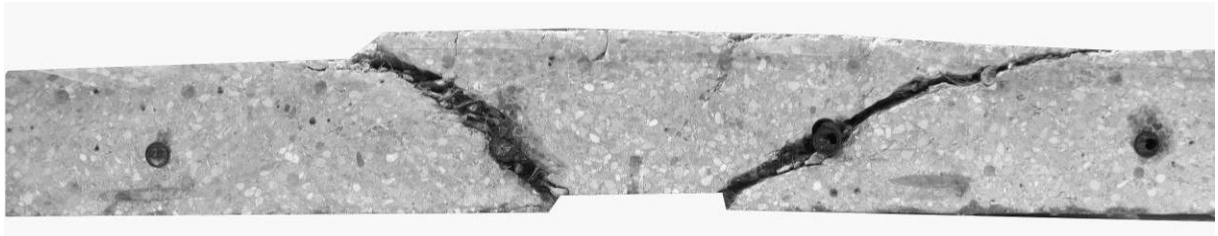

Fig. 105 : Fissuration à plusieurs niveaux de charge et fissures internes de la dalle B5-04.

3.2.19. Dalle B5-05

Caractéristiques :

- Béton B5 (80 kg/m^3) f_{cm} = 107 MPa
- Armature longitudinale supérieure : ϕ8 s = 100 mm (ρ = 0.56%)

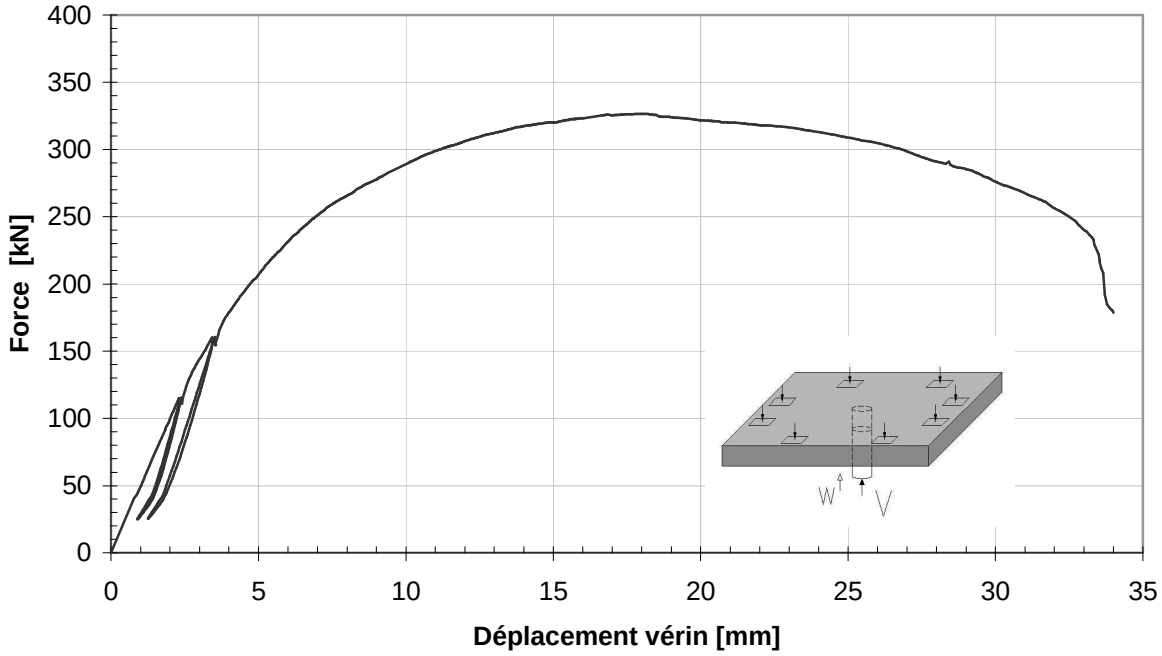

Fig. 106 : Courbe force – déplacement du vérin de la dalle B5-05.

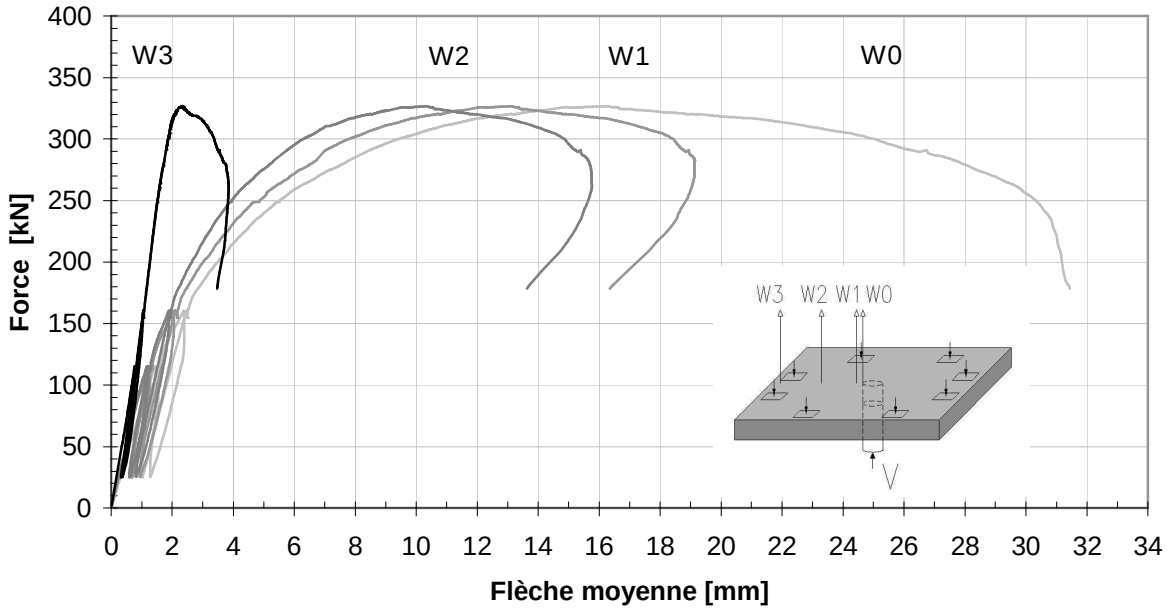

Fig. 107 : Courbes force – flèche moyenne de la dalle B5-05.

Force maximale V_{test} [kN]	Flèche au centre W_0 [mm]	Rotation ψ [‰]
327	**16.2**	**29.6**

Tab. 23 : Résultats principaux de l'essai de la dalle B5-05.

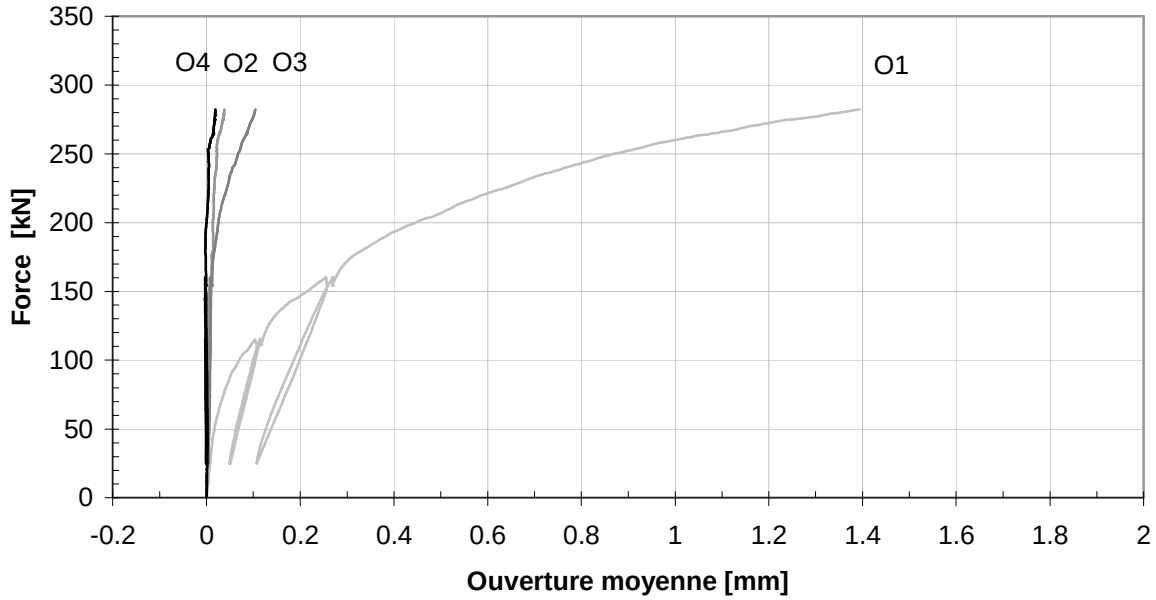

Fig. 108 : Courbes force – ouverture moyenne des fissures de la dalle B5-05.

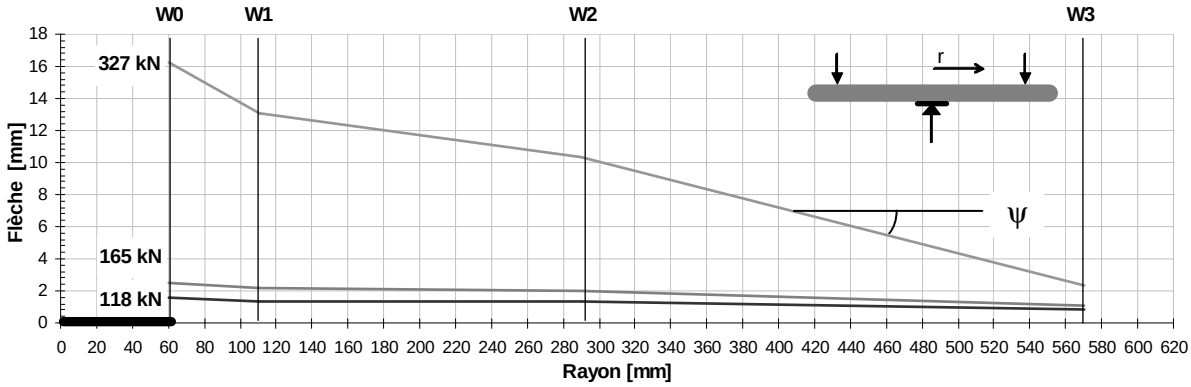

Fig. 109 : Déformation moyenne de la dalle B5-05 à plusieurs niveaux de charge.

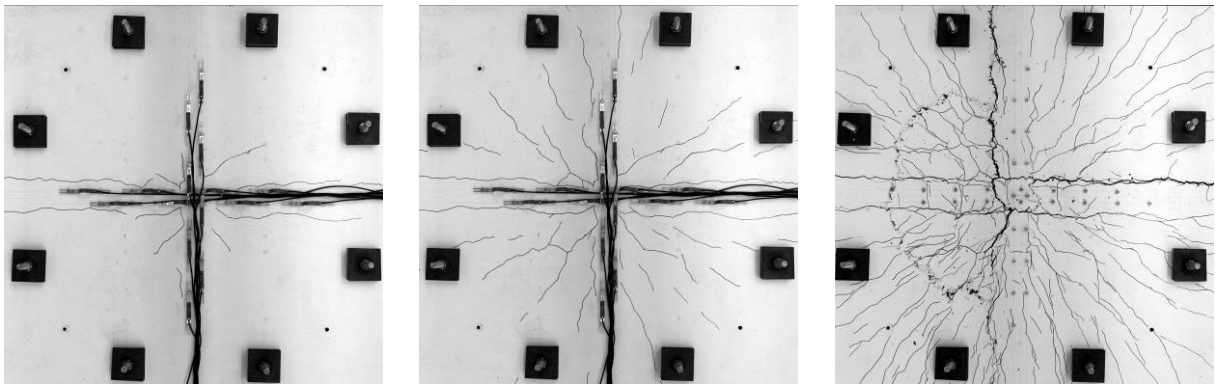

Charge de service 118 kN | Charge de dimensionnement 165 kN | Rupture

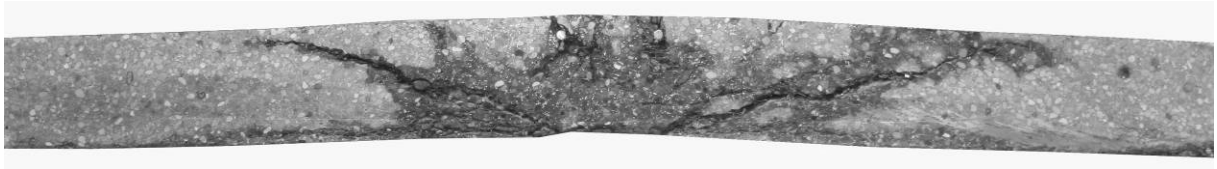

Fig. 110 : Fissuration à plusieurs niveaux de charge et fissures internes de la dalle B5-05.

3.2.20. Dalle B5-06

Caractéristiques :

Béton B5 (80 kg/m^3) f_{cm} = 107 MPa
Armature longitudinale supérieure : ϕ12 s = 100 mm (ρ = 1.26%)

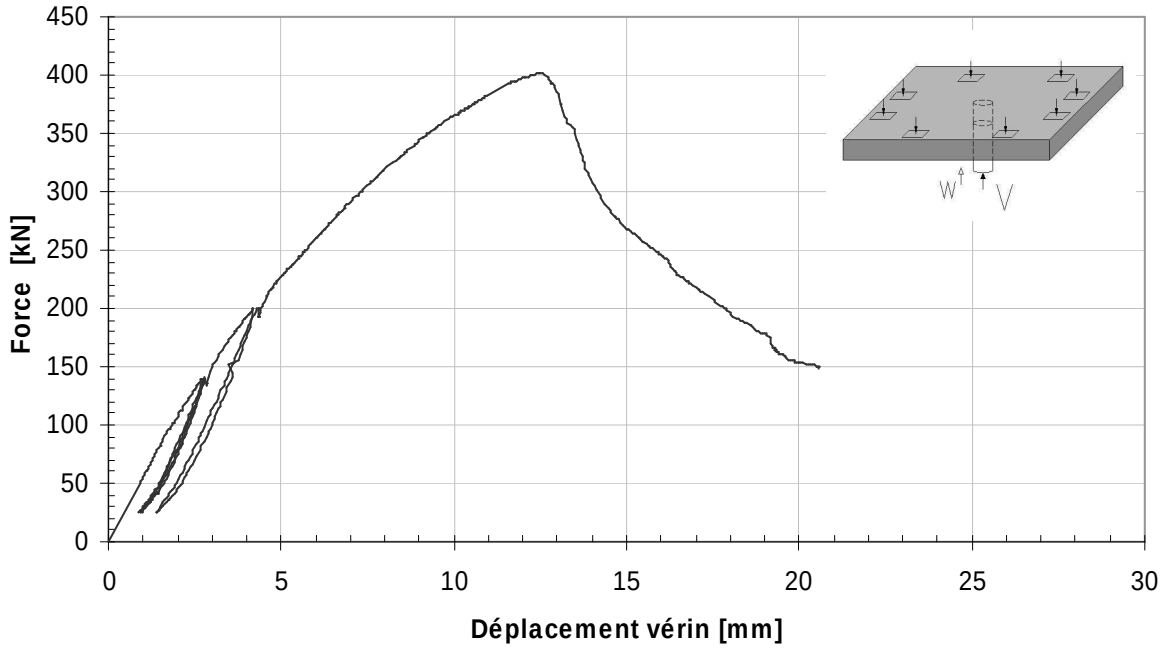

Fig. 111 : Courbe force – déplacement du vérin de la dalle B5-06.

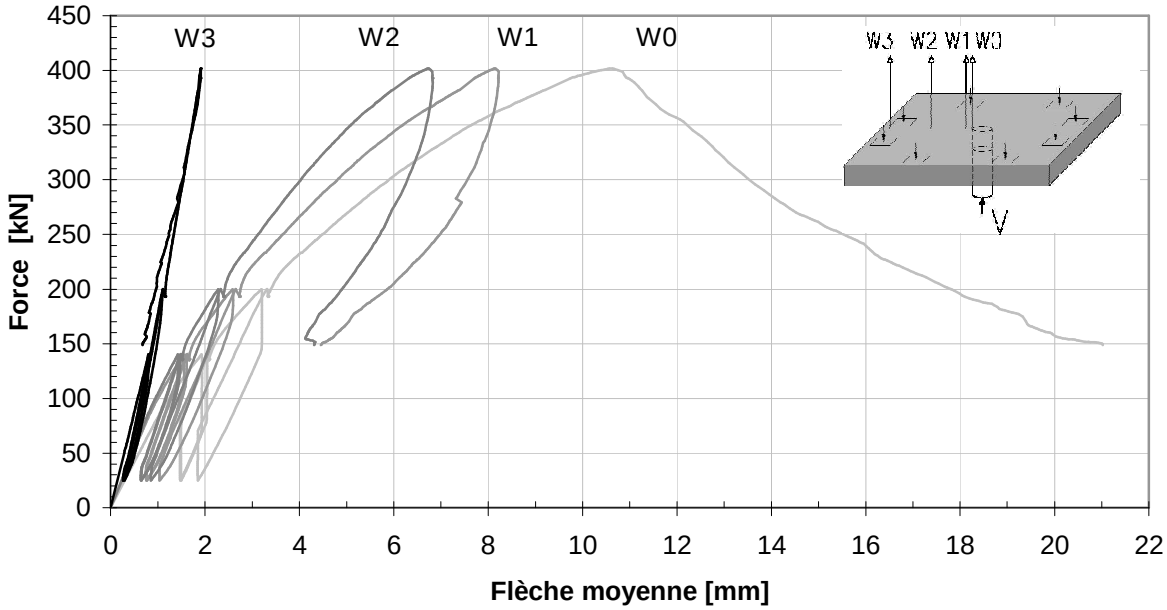

Fig. 112 : Courbes force – flèche moyenne de la dalle B5-06.

Force maximale V_{test} [kN]	Flèche au centre W_0 [mm]	Rotation ψ [‰]
327	**10.6**	**29.6**

Tab. 24 : Résultats principaux de l'essai de la dalle B5-06.

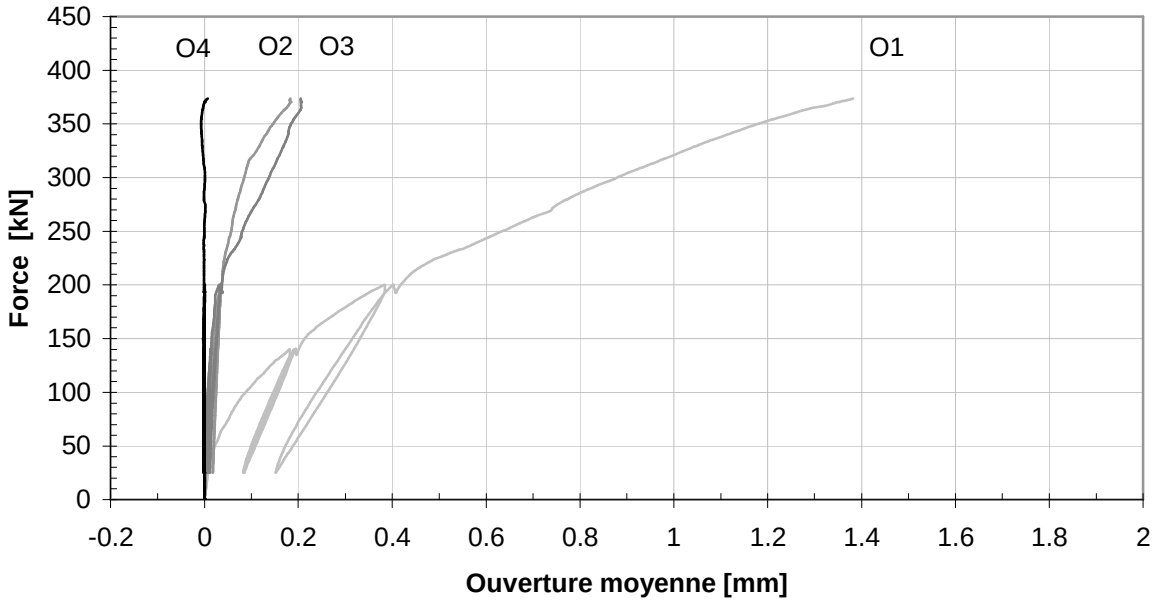

Fig. 113 : Courbes force – ouverture moyenne des fissures de la dalle B5-06.

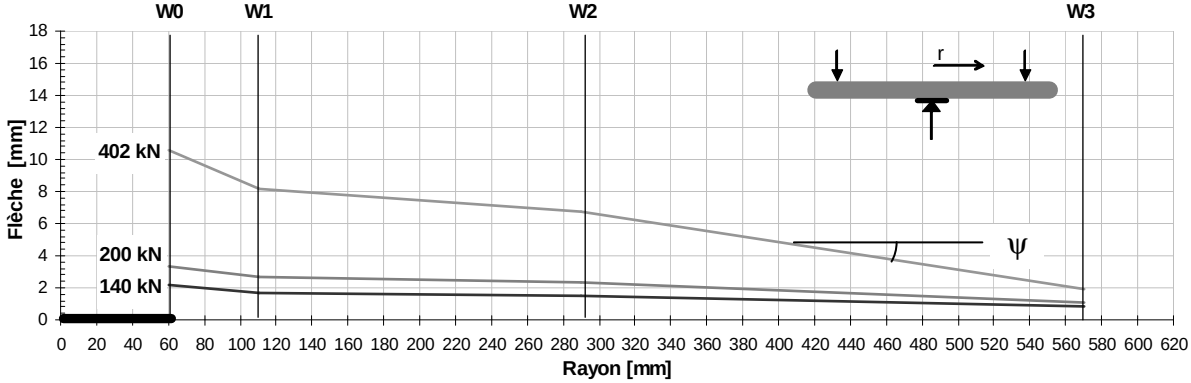

Fig. 114 : Déformation moyenne de la dalle B5-06 à plusieurs niveaux de charge.

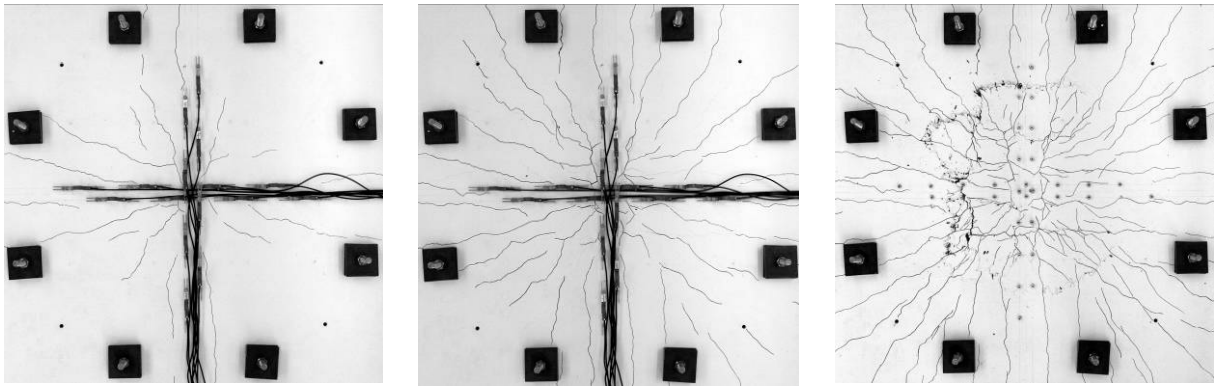

Charge de service 140 kN | Charge de dimensionnement 200 kN | Rupture

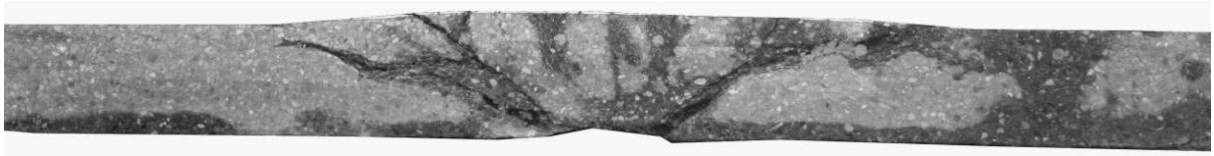

Fig. 115 : Fissuration à plusieurs niveaux de charge et fissures internes de la dalle B5-06.

3.3. Comparaison des résultats

Les 20 dalles sont analysées selon les trois variables, le taux de précontrainte, le taux d'armature et le dosage en fibres métalliques. Afin de rendre les graphiques plus transparents, les cycles de chargement - déchargement n'ont pas été tracés. Le comportement d'un élément en béton armé et/ou précontraint est caractérisé par trois phases successives : linéaire élastique non-fissuré (stade I), élastique fissuré (stade II), domaine plastique (stade III) [10].

La résistance au poinçonnement τ_R se définit de la manière suivante :

$$\tau_{test} = \frac{V_{test}}{u \cdot d_m} \qquad (3.2)$$

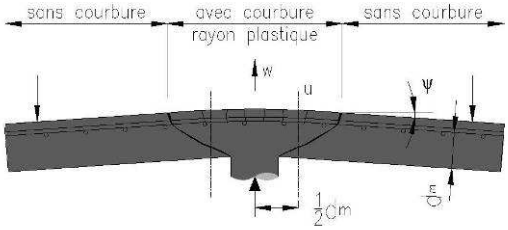

Fig. 116 : Paramètres du mécanisme de rupture.

Où u représente le périmètre de contrôle situé à une distance de $0.5d_m$ de la surface du poinçon conformément à la norme Suisse SIA 262 [26].

Dénomination	Dosage en fibres [kg/m^3]	Force maximale V_{test} [kN]	Résistance au poinçonnement τ_{test} [MPa]	Flèche au centre W_0 [mm]	Rotation de la dalle ψ [‰]
Série 01 : ρ_s = 0.87% / $\sigma_{cp,0}$ = 0 MPa					
B1-01	0	262	4.42	11.3	21.1
B2-01	20	318	5.35	10.8	18.3
B3-01	40	343	5.78	15.7	28.7
B4-01	60	337	5.68	10.8	19.3
B5-01	80	369	6.22	16.0	29.5
Série 02 : ρ_s = 0.87% / $\sigma_{cp,0}$ = 2.42 MPa					
B1-02	0	294	4.95	5.8	8.6
B3-02	40	437	7.35	9.2	15.4
B5-02	80	501	8.43	12.8	20.1
Série 03 : ρ_s = 0.87% / $\sigma_{cp,0}$ = 6.63 MPa					
B1-03	0	330	5.55	6.1	9.2
B3-03	40	405	6.82	7.9	13.4
B5-03	80	511	8.60	9.1	14.2
Série 04 : ρ_s = 0.87% / $\sigma_{cp,0}$ = 4.84 MPa					
B1-04	0	376	6.34	6.6	10.5
B3-04	40	453	7.62	7.8	12.6
B5-04	80	567	9.55	9.2	12.6
Série 05 : ρ_s = 0.56% / $\sigma_{cp,0}$ = 0 MPa					
B1-05	0	201	3.39	15.6	28.8
B3-05	40	286	4.82	13.4	28.1
B5-05	80	327	5.50	16.2	29.6
Série 06 : ρ_s = 1.26% / $\sigma_{cp,0}$ = 0 MPa					
B1-06	0	252	4.24	7.1	12.5
B3-06	40	361	6.07	9.4	16.7
B5-06	80	402	6.77	10.6	29.6

Tab. 25 : Récapitulatifs des résultats principaux.

3.3.1. Comparatif en fonction du taux de précontrainte

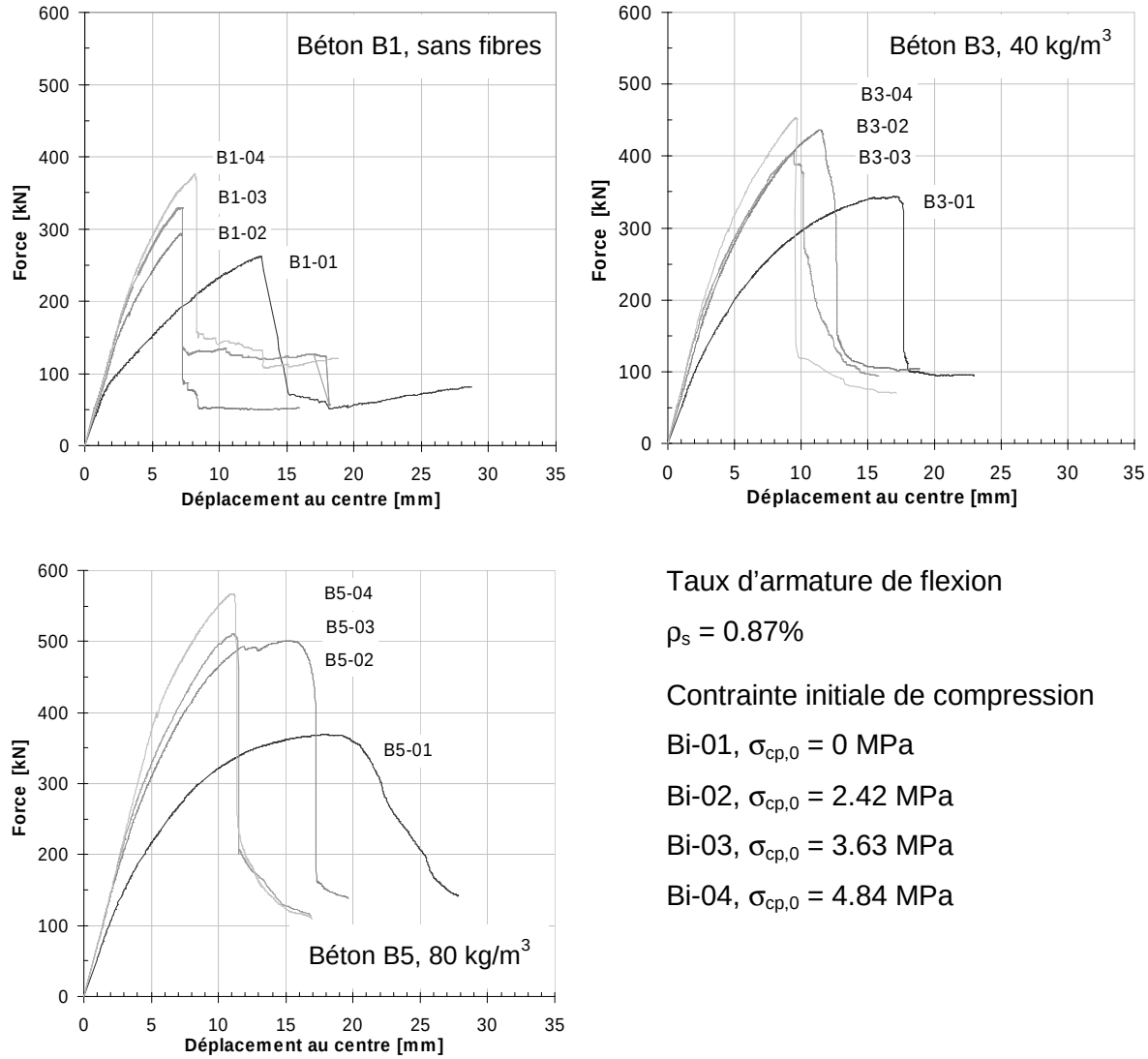

Fig. 117 : Courbes comparatives force – déplacement en fonction du taux de précontrainte.

Les essais montrent que la charge de ruine au poinçonnement est inversement proportionnelle au déplacement. Ce résultat est remarqué dans de nombreuses études traitant du poinçonnement [11]. En stade homogène non-fissuré les dalles précontraintes sont plus rigides. Les dalles non précontraintes subissent une importante baisse de rigidité une fois le moment de fissuration atteint, à une charge comprise entre 90 et 100 kN. Les dalles précontraintes ont une modification de rigidité plus progressive due à l'effort normal permettant de mieux contrôler le développement de la fissuration.

Une fois le niveau de fissuration atteint, la rigidité est influencée de façon significative par le taux de précontrainte. Le point de rupture, pour les dalles ne comportant pas d'effort normal, se situe dans la phase d'écoulement des aciers d'armature, ceci se remarque par le plateau où la charge augmente peu avant la ruine. Hormis la dalle et B5-02, les dalles précontraintes n'ont pas de plateau plastique avant la rupture. Pour ces éléments la rupture par poinçonnement est brutale sans signes annonciateurs (déformations importantes). Globalement, le comportement est similaire entre les trois série de béton B1, B3 et B5.

3.3.2. Comparatif en fonction du taux d'armature

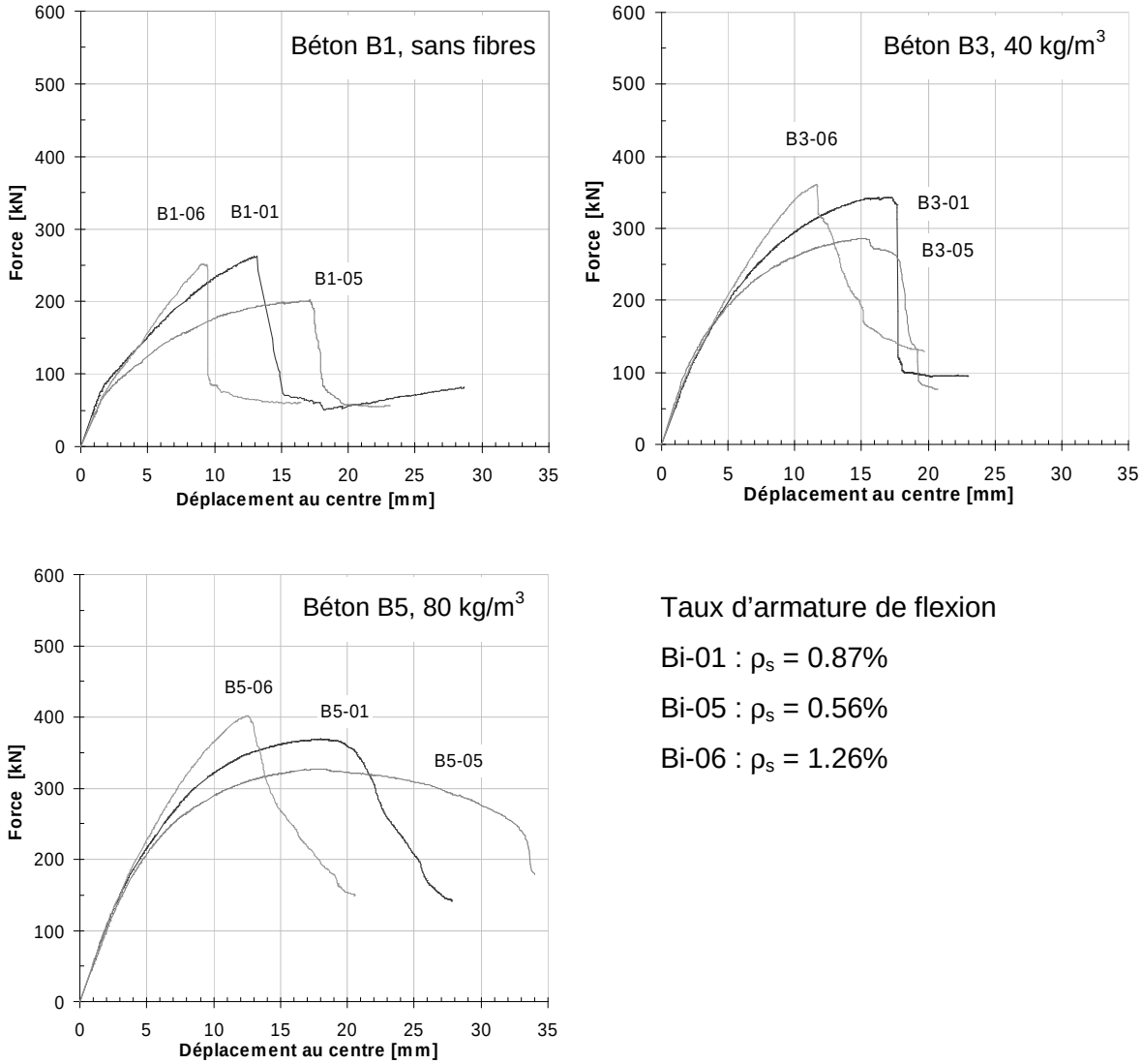

Fig. 118 : Courbes comparatives force – déplacement en fonction du taux d'armature passive.

En stade homogène non-fissuré il n'y a quasiment pas de différence de rigidité entre les différents taux d'armature. Une fois le niveau de fissuration atteint, la rigidité est directement influencée par la quantité d'armature. Le point de rupture des dalles comportant un taux de 0.56 et 0.87% se situe dans la phase d'écoulement des aciers d'armature, ceci se remarque par le plateau où la charge augmente peu avant la ruine. Pour les dalles comportant un taux de 1.26%, les points de rupture se trouvent avant, voire au début de la plastification de l'armature de flexion. Globalement, le comportement est similaire entre les trois série de béton B1, B3 et B5.

3.3.3. Comparatif en fonction du dosage en fibres

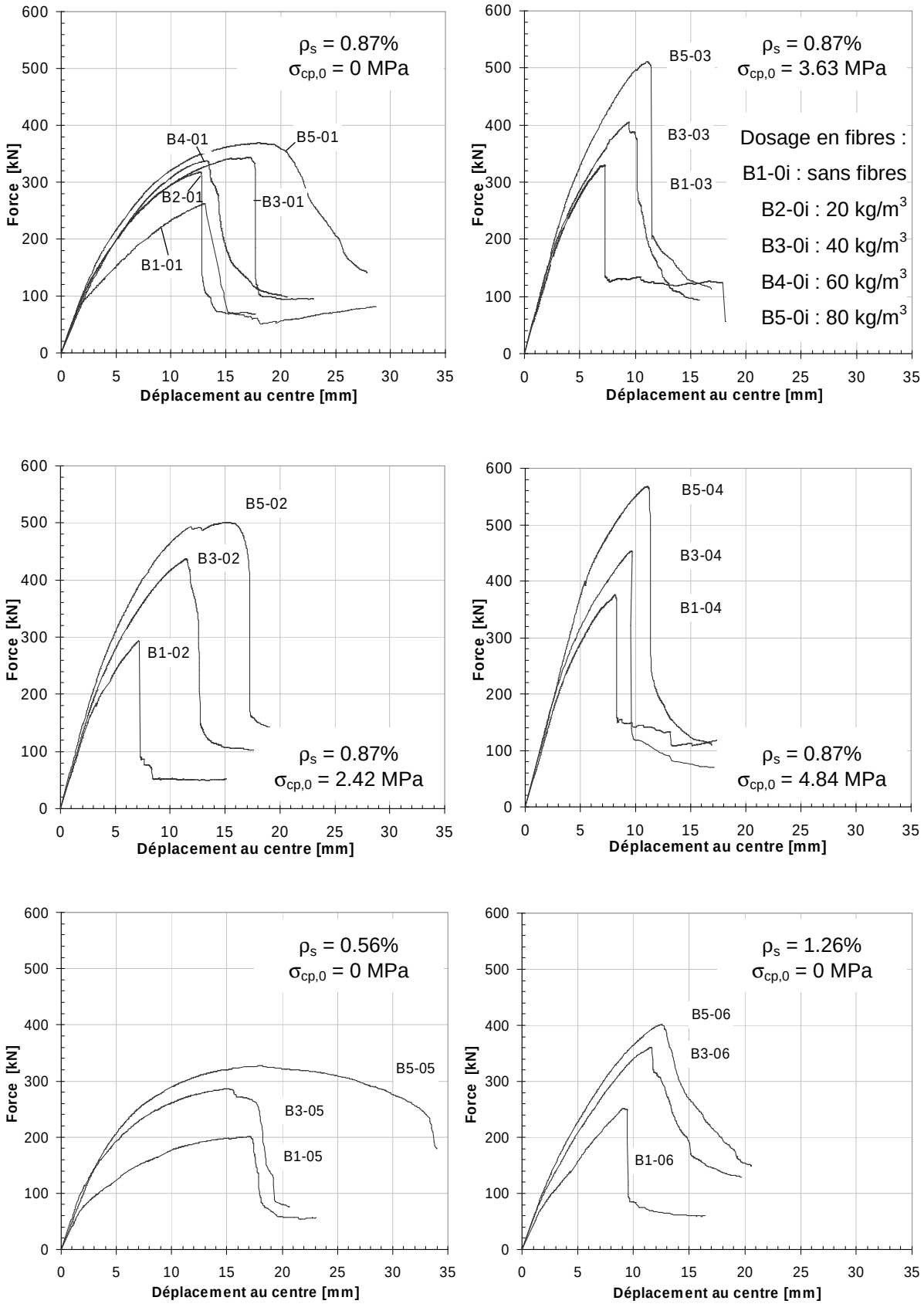

Fig. 119 : Courbes comparatives force – déplacement en fonction du dosage en fibres.

La rigidité des éléments est quasiment identique jusqu'au point de fissuration. Le stade I est influencé principalement par le module d'élasticité du béton. Or celui-ci varie peu entre les différents types de béton. Une fois la charge de fissuration atteinte, les éléments en béton sans fibres connaissent une modification marquée de rigidité. Les dalles en béton à fibres présentent quant à elles une modification de rigidité plus progressive, qui s'explique par un meilleur contrôle du développement de la fissuration, cet effet est particulièrement marqué pour les dalles munies uniquement d'une armature passive.

Le point de rupture pour les dalles ne comportant pas de précontrainte se situe dans le stade II ou stade III, suivant le taux d'armature de flexion. Le plateau plastique est très marqué pour les éléments B3-01, B5-01, B1-05, B3-05 et B5-05. Ces cinq dalles subissent d'importantes déformations avant la rupture. La dalle B5-05 présente une ruine par flexion avec un poinçonnement à la fin du domaine plastique. Les fibres permettent d'augmenter sensiblement la charge de ruine au poinçonnement. L'augmentation de résistance par rapport aux dalles en béton sans fibres, s'échelonne respectivement entre 20 et 40% pour la série 01 et entre 40 et 60% pour la série 05 et 06, en fonction du dosage en fibres. Hormis les dalles B5-01 et B5-05, les déformations à la ruine sont quasiment constantes entre les éléments. En revanche, la chute de résistance est beaucoup moins brutale pour les éléments en BFHP.

Les dalles précontraintes ont un point de rupture qui se situe en stade II, voire en début de stade III, en fonction de l'intensité de l'effort normal. Hormis la dalle B5-02, il n'y a pas de plateau plastique marqué. Pour tous ces éléments, la ruine par poinçonnement se produit de manière brutale. Additionnées à la précontrainte, les fibres permettent d'augmenter la résistance. Ceci se vérifie pour les trois degré de précontrainte. L'augmentation de résistance par rapport aux dalles sans fibres, s'échelonne respectivement entre 50 et 70% pour la série 02 et entre 20 et 55% pour les séries 03 et 04 en fonction de la quantité de fibres. Quant à l'augmentation de déformations à la ruine, elle n'est pas proportionnelle à l'augmentation de la résistance et s'échelonne, par rapport aux dalles sans fibres, pour la série 02 entre 60 et 115%, pour la série 03 entre 30 et 55% et pour la série 04 entre 20 et 35%, en fonction du dosage en fibres métalliques.

De manière générale, l'ajout de fibres au BHP permet d'augmenter la rigidité en stade fissuré ainsi que la charge de ruine. La déformabilité à la rupture est semblable pour les éléments non précontraints hormis les dalles B5-01 et B5-05 qui subissent un long domaine plastique. Par contre, superposées à une précontrainte, l'ajout de fibres a permis de gagner en déformabilité à la ruine. La fissuration est mieux répartie et les ouvertures sont plus fines.

3.3.4. Synthèse des résultats

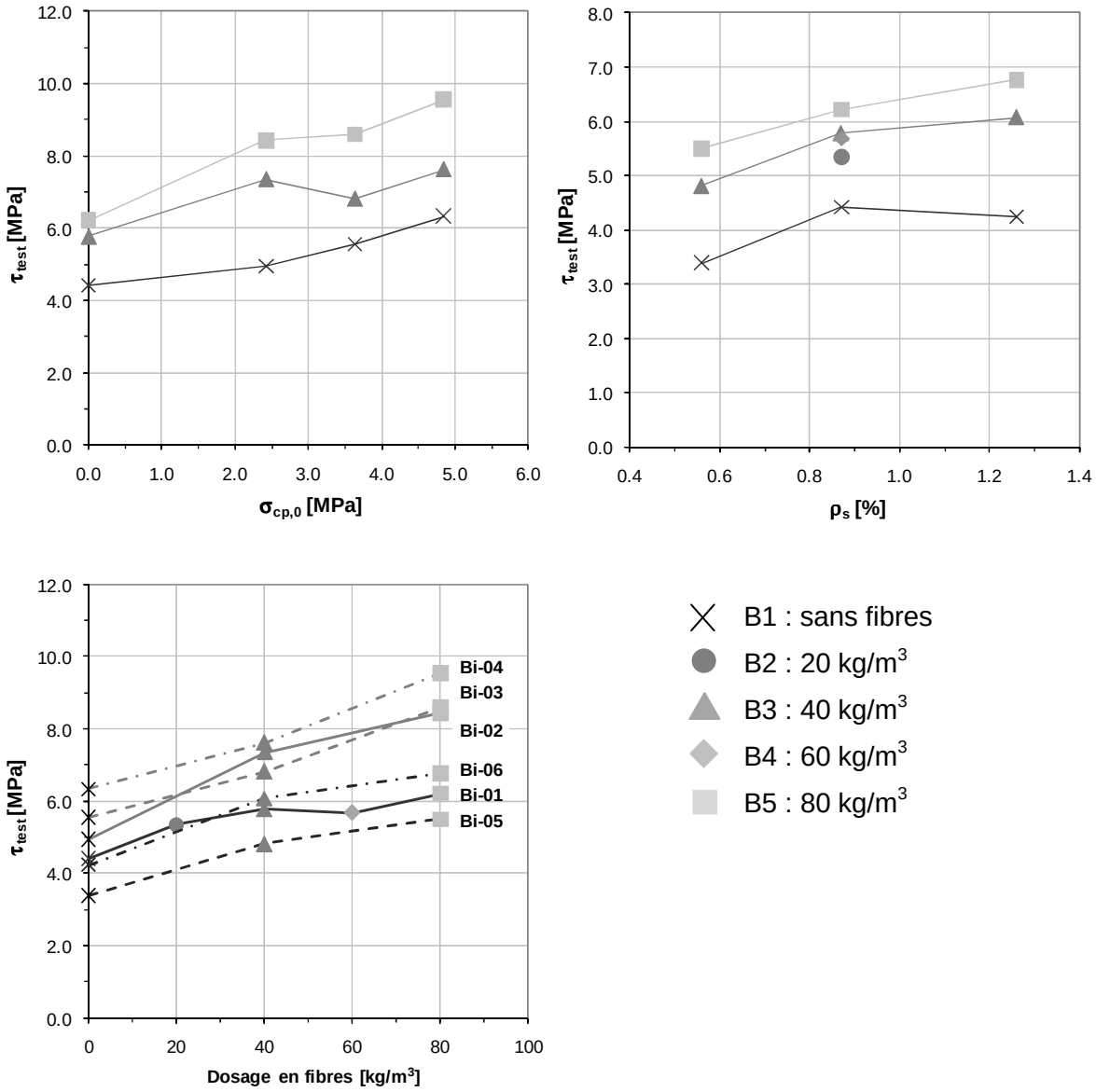

Fig. 120 : Synthèse des résultats en fonction des paramètres d'essai.

L'évolution de la résistance au poinçonnement en fonction du taux de précontrainte et du taux d'armature n'est pas une fonction linéaire. Pour des dosages en fibres faibles de l'ordre de 20 à 40 kg/m^3, l'effet sur la résistance au poinçonnement est important. Ceci s'explique par le comportement fortement hyperstatique des dalles où les fibres même en petite quantité produisent un apport mécanique important [31].

La résistance au poinçonnement est influencée par le dosage en fibres métalliques pour les trois taux d'armature et les trois taux de précontrainte testés.

Remerciements

L'Ecole d'ingénieurs et d'architectes de Fribourg a mené, durant les années 2006 à 2008, le projet de recherche "Bétons à hautes performances renforcés de fibres métalliques". Ce projet a bénéficié du soutien matériel et financier de différentes institutions, fonds de recherche et entreprises :

- Office fédéral de la formation professionnelle et de la technologie OFFT
  Agence pour la promotion de l'innovation CTI
- Cemsuisse (industrie du ciment) Forschungsaufträge
- Fonds de recherche RA&D de l'Ecole d'ingénieurs et d'architectes de Fribourg
- Holcim (Schweiz) AG
- Bekaert (Schweiz) AG
- Sika (Schweiz) AG
- Element SA, produits en béton

Nous tenons à remercier très sincèrement ces institutions et entreprises pour leur soutien de nos recherches.

Les études théoriques et expérimentales ont été suivies par une commission d'accompagnement de Cemsuisse. Nous tenons à remercier les membres de cette commission (Dr. Heiner Widmer, Didier Aeby, Blaise Fleury, Dr. Claude Pilloud, Miriam Runke) pour leur conseil et leur participation active à nos travaux.

Dans l'analyse des différents problèmes, nous avons pu profiter des conseils précieux des professeurs Eugen Brühwiler et Aurelio Muttoni de l'Ecole Polytechnique Fédérale de Lausanne et de leurs collaborateurs que nous remercions.

Nos remerciements vont également aux différents membres de notre Ecole qui ont soutenu nos travaux, en particulier le professeur André Oribasi, les collaborateurs scientifiques Patrick Buchs, Marino Grisanti, Jérôme Nicolet, Yanis Schaller et les collaborateurs techniques Arthur Perroud et Lukas Habegger.

Références

[1] AFGC. *Recommandations pour l'emploi des bétons auto-plaçant*. Paris, 2008.

[2] AÏTCIN, Pierre-Claude. *Bétons haute performance*. Paris : Eyrolles, 2001.

[3] BUCHS, Patrick, *Réfection du pont sur la Broye à Salavaux – Etude expérimentale*, Projet de diplôme, Document interne EIA-FR, Fribourg, 2003.

[4] BARON, Jacques et al. *Les bétons, Bases de données pour leur formulation*. Paris : Eyrolles, 1999.

[5] CASANOVA, Pascal. *Bétons renforcés de fibres métalliques du matériau à la structure*. Paris : Presses du Laboratoire Central des Ponts et Chaussées, 1996.

[6] D 0182; Documentation. *Construction en béton - Introduction à la norme SIA 262*. Zürich : Société suisse des ingénieurs et architectes, 2003.

[7] D 0192; Documentation. *Construction en béton – Exemples de dimensionnement selon la norme SIA 262*. Zürich : Société suisse des ingénieurs et architectes, 2004.

[8] D 0223; Documentation. *Nouveaux acquis de la recherche sur les ponts*. Zürich : Société suisse des ingénieurs et architectes, 2007.

[9] D 0226; Documentation. *Sécurité structurale des Parkings couverts*. Zürich : Société suisse des ingénieurs et architectes, 2008.

[10] FALKNER, Horst / TEUTSCH, Manfred. XI Stahlfaserbeton – Anwendungen und Richtlinie, *BetonKalender*, Berlin : Ernst & Sohn, 2006.

[11] FAVRE, Renaud et al. *Traité de génie civil de l'EPFL Volume 8 : Dimensionnement des structures en béton*. Lausanne : Presses polytechniques et universitaires romandes, 1997

[12] GUANDALINI, Stephano. *Poinçonnement symétrique des dalles en béton armé*. Thèse N°3380, Ecole Polytechnique Fédérale de Lausa nne, 2005.

[13] HILLEMEIER, Bernd et al. IX Spezialbetone, *BetonKalender*, Berlin : Ernst & Sohn, 2006.

[14] HOLCIM (Suisse) SA. *Guide pratique*, 4ème édition, 2004.

[15] HOLCIM (Suisse) SA. *Le béton autocompactant*, 1ère édition, 2005.

[16] HOLSCHEMACHER, Klaus et al. X Faserbeton, *BetonKalender*, Berlin : Ernst & Sohn, 2006.

[17] LARRARD (de), François. *Structures granulaires et formulations des bétons*. Paris : Presses du Laboratoire Central des Ponts et Chaussées, 2000.

[18] MARTI, Peter et al. Harmonized test procedures of steel fiber-reinforced concrete, *ACI Materials Journal*, 1999, V.96, n°6, pages 676 à 685.

[19] MUTTONI A., FERNANDEZ RUIZ M., Shear Strength of Members without Transverse Reinforcement as Function of Critical Shear Crack Width, *ACI Structural Journal,* 2008, V.105, n°2, pages 163 à 172.

[20] MUTTONI, Aurelio. Punching Shear Strength of Reinforced Concrete Slabs without transverse Reinforcement, *ACI Structural Journal,* 2008, V.105, n°4, pages 440 à 450.

[21] NAAMAN A., REINHARDT H., *Fiber reinforced concrete - Current needs for successful implementation*, International RILEM Workshop "Fiber Reinforced Concrete from Theory To practice", Bergamo, 2004.

[22] NAAMAN A., REINHARDT H., *Fourth International Workshop on - High Performance Fiber Reinforced Cement Composites*, RILEM, Ann Arbor USA, 2003.

[23] NF EN 14'651+A1, Norme européenne version française. *Méthode d'essai du béton de fibres métalliques – Mesurage de la résistance à la traction par flexion (limite de proportionnalité (LOP), résistance résiduelle)*. Paris : AFNOR, 2007.

[24] NICOLET J, SUTER R., *Bétons à hautes performances renforcés de fibres métalliques – Refends parasismiques, Rapport d'essai*, Ecole d'ingénieurs et d'architectes de Fribourg, 2007.

[25] PFYL, Thomas. *Tragverhalten von Stahlfaserbeton*, Dissertation n°15005, ETH Zürich, 2003.

[26] PFYL T., MARTI P., *Versuche an stahlfaserverstärkten Stahlbetonelementen*, Institut für Baustatik und Konstruktion, ETH Zürich, 2001.

[27] RILEM TC 162-TDF, *Test and design methods for steel fibre reinforced concrete: Uni-axial tension test for steel fibre reinforced concrete*. Bagneux : RILEM, 2000.

[28] RILEM TC 162-TDF, *Test and design methods for steel fibre reinforced concrete : bending test.* Bagneux : RILEM, 2002.

[29] RILEM TC 162-TDF, *Test and design methods for steel fibre reinforced concrete: sigma-epsilon-design method*. Bagneux : RILEM, 2003.

[30] ROSENBUSCH J., TEUTSCH M. S*hear design with sigma-epsilon-method*, Bagneux RILEM Publications, 2003.

[31] ROSSI, Pierre. *Les bétons de fibres métalliques*, Paris : Presses de l'Ecole Nationale des Ponts et Chaussée, 1998.

[32] ROSSI, Pierre. *Le développement industriel des bétons de fibres métalliques*, Paris : Presses de l'Ecole Nationale des Ponts et Chaussées, 2002.

[33] SCHNUTGEN B., VANDEWALLE L. *Test and Desing Methods for Steel Fibre Reinforced Concrete*, RILEM TC 162-TDF Workshop, 2003.

[34] SIKA Schweiz AG, *Bréviaire du béton*, 2007.

[35] SN 505-262, Norme suisse. *Construction en béton*. Zürich : Société suisse des ingénieurs et architectes, 2003.

[36] SN 505-262/1, Norme suisse. *Construction en béton – Spécifications complémentaires*. Zürich : Société suisse des ingénieurs et architectes, 2003.

[37] SN 562 162/6, Recommandation. *Béton renforcé de fibres métalliques*. Zürich : Société suisse des ingénieurs et architectes, 1999.

[38] SN EN 12'350-7 :2000, Norme européenne version suisse. *Essais sur béton frais - partie 7 : Détermination de la teneur en air – Méthode de la compressibilité*, Zürich, Société suisse des ingénieurs et architectes, 2000.

[39] SUTER R., BUCHS P. *Béton à hautes performances renforcé de fibres métalliques : Synthèse des études expérimentales menées de 2001 à 2005. Rapport de synthèse*, Ecole d'ingénieurs et d'architectes de Fribourg, 2005.

[40] SUTER R., BUCHS P. *Voussoirs préfabriqués en béton à fibres - Etude expérimentale en vue d'une optimisation de l'armature, Rapport de synthèse,* Ecole d'ingénieurs et d'architectes de Fribourg, 2005.

[41] SUTER R., BROYE A. *Bétons renforcés de fibres synthétiques et métalliques*, *Rapport d'étude*, Ecole d'ingénieurs et d'architectes de Fribourg, 2006.

[42] SUTER R., MOREILLON L. *Bétons à hautes performances renforcés de fibres métalliques – Technologie des bétons, Rapport d'essai*, Ecole d'ingénieurs et d'architectes de Fribourg, 2009.

[43] SUTER R., MOREILLON L. *Bétons à hautes performances renforcés de fibres métalliques – Dalles nervurées préfabriquées, Rapport d'essai*, Ecole d'ingénieurs et d'architectes de Fribourg, 2009.

[44] SUTER R., MOREILLON L. *Bétons à hautes performances renforcés de fibres métalliques – Poinçonnement de dalles, Rapport d'essai*, Ecole d'ingénieurs et d'architectes de Fribourg, 2009.

[45] SUTER R., MOREILLON L. *Bétons à hautes performances renforcés de fibres métalliques, Rapport de synthèse*, Ecole d'ingénieurs et d'architectes de Fribourg, 2009.

[46] SUTER R., NICOLET J. *Béton renforcé de fibres - Etude comparative entre fibres synthétiques et métalliques, Rapport d'étude*, Ecole d'ingénieurs et d'architectes de Fribourg, 2007.

[47] SUTER R., NICOLET J. *Bétons à hautes performances renforcés de fibres métalliques – Etude de la composition de bétons à fibres C70/85 destinés à la préfabrication, Rapport d'essai*, Ecole d'ingénieurs et d'architectes de Fribourg, 2007.

[48] VAZ RODRIGUES, Rui. *Shear strength of reinforced concrete bridge deck slabs*. Thèse N°3739, Ecole Polytechnique Fédérale de Lausa nne, 2007.

[49] WALTHER R., MIEHLBRADT M. *Traité de génie civil de l'EPFL Volume°7 : Dimensionnement des structures en béton – Bases et technologie*. Lausanne : Presses polytechniques et universitaires romandes, 1999.

A-3 Punching shear of thin UHPFRC slabs

Lionel MOREILLON
Robert LE ROY
René SUTER

1. Description de l'étude expérimentale

1.1. Eléments d'essai

Le programme expérimental est composé de 22 dalles carrées de 960 mm de côté soumises à un chargement concentré. L'étude est divisée en dix séries d'essais (Tableau 2.1) dont les numéros se rapportent à la date de coulage, pour une même quantité de fibres.
Les principaux paramètres sont :

- l'épaisseur des dalles, variant de 30 à 80 mm,
- le dosage en fibres, variant de 1 à 2%,
- le taux d'armature passive, variant de 0 à 2% environ,
- l'arrangement de l'armature passive

Les dalles comportent 8 ouvertures de diamètre 45 mm permettant le passage des tiges d'appuis. Les huit ouvertures sont placées sur un cercle de diamètre 878 mm de diamètre. Trois arrangements d'armature différents ont été mis en œuvre et sont représentés dans la Figure 1-1. Pour les schémas A et B, l'armature est composée de treillis spéciaux à mailles carrées avec un espacement de 100 mm, le diamètre des barres varie en fonction du taux d'armature. Le schéma A est caractérisé par un positionnement du treillis où le centre de la dalle coïncide avec le centre d'une cellule alors que, pour le schéma C, le centre de la dalle coïncide avec une intersection des barres d'armature. Le schéma B comporte trois barres nervurées ou lisses, écartées de 50 mm, placées au centre dans les deux directions.

L'excentricité moyenne des barres par rapport à la face tendue est de 15 mm pour les dalles d'une épaisseur de 30 mm et de 20 mm pour les dalles d'une épaisseur de 40 mm, 60 mm et 80 mm. Le positionnement précis des armatures est assuré par des distanceurs en plastique placés sur le deuxième lit d'armature.

Le taux d'armature est calculé de la manière suivante :

$$\rho = \frac{A_s}{d \cdot b} \qquad \text{avec} \quad b = 960 \text{ mm}$$

La dénomination des éléments d'essai comprend le dosage en fibres V_f, l'épaisseur de la dalle h et le taux d'armature ρ.

BCV_V_f_h_ρ

Appendix 3

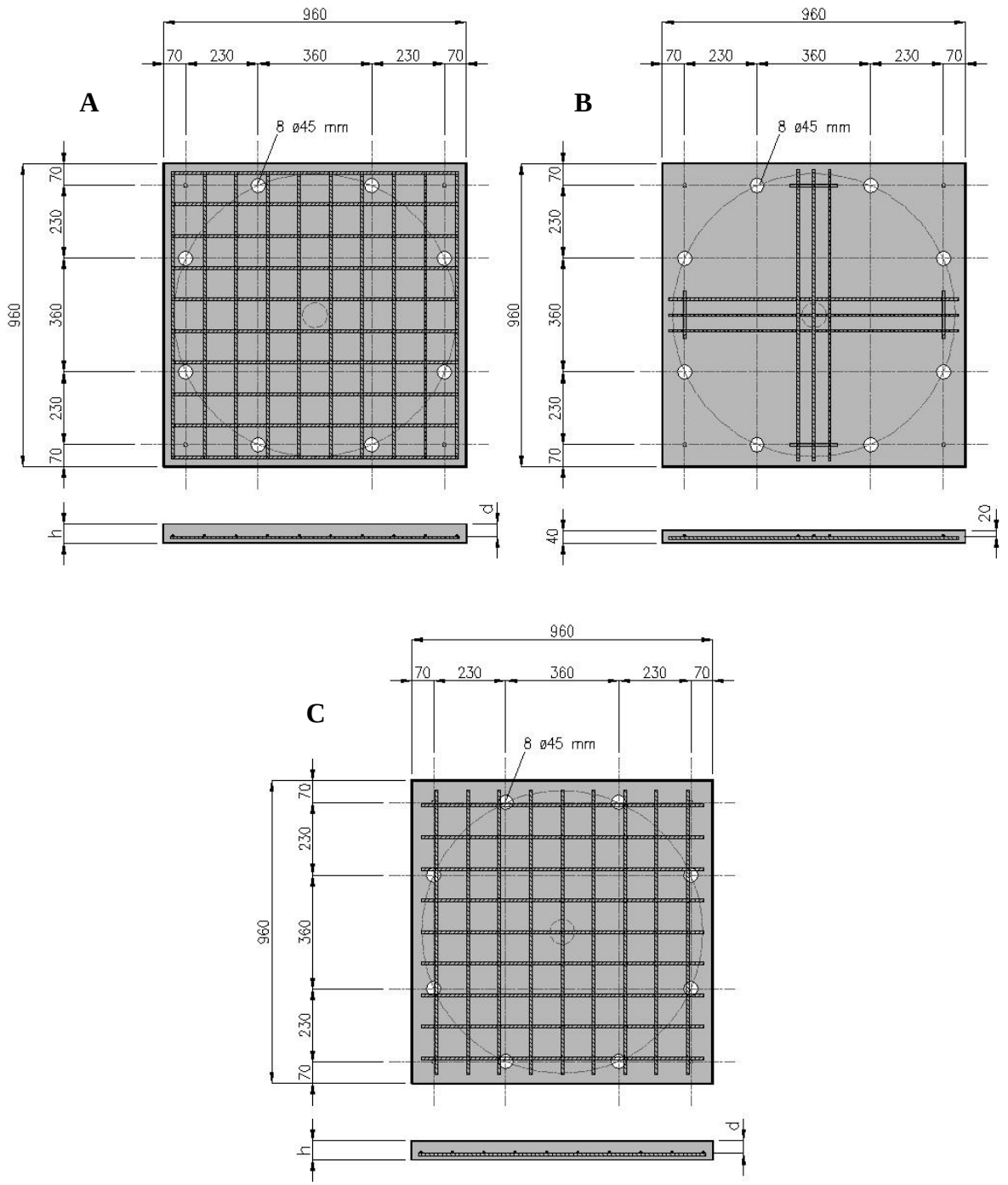

Figure 1-1 : Géométrie des dalles et arrangement des armatures

Tableau 1-1 : Caractéristiques des éléments d'essai

Série	V_f [%]	Dénomination	h [mm]	ϕ / s [mm]	d [mm]	ρ [%]	Arrangement réf. fig. 2-1
1	2	BCV-2%_30_0	30	sans armatures			
		BCV-2%_40_0	40				
		BCV-2%_60_0	60				
		BCV-2%_80_0	80				
2	2	BCV-2%_30_1.36	30	ϕ5 #100	15	1.36	A
		BCV-2%_40_1.02	40	ϕ5 #100	20	1.02	
		BCV-2%_60_1.00	60	ϕ7 #100	40	1.00	
		BCV-2%_80_1.10	80	ϕ9 #100	60	1.10	
3	1	BCV-1%A_30_0	30	sans armatures			A
		BCV-1%A_40_1.02	40	ϕ5 #100	20	1.02	
		BCV-1%A_60_2.05	60	ϕ10 #100	40	2.05	
		BCV-1%A_80_1.10	80	ϕ9 #100	60	1.10	
4	2	BCV-2%_40_R	40	ϕ10 #50 R*	20	1.49	B
		BCV-2%_40_S		ϕ10 #50 S**	20	1.77	
5	1	BCV-1%_40_R	40	ϕ10 #50 R*	20	1.49	B
		BCV-1%_40_S		ϕ10 #50 S**	20	1.77	
6	2	BCV-2%_60_1.49	60	ϕ9 #100	40	1.49	C
		BCV-2%_80_1.77	80	ϕ12 #100	60	1.77	
7	1	BCV-1%A_30_2.67	30	ϕ7 #100	15	2.67	A
		BCV-1%A_80_1.96	60	ϕ12 #100	60	1.96	
8	2	BCV-2%_60_1.66	60	ϕ9 #100	40	1.66	A
9	2	BCV-1%A_60_1.49	60	ϕ9 #100	40	1.49	C

* RB = barres nervurées ** SB = barres lisses

1.2. Réalisation des éléments d'essai

Les éléments d'essai des séries 1 à 5 ont été réalisés par Creabeton Matériaux SA à Einigen. En usine de préfabrication, le béton BCV a été réalisé avec un malaxeur conique *Kniele* d'une capacité de 450 litres (Figure 1-2). Les dalles des séries 6 à 9 ont été réalisées au sein du laboratoire des Structures de l'EIA-FR. En laboratoire, le BCV a été réalisé avec un malaxeur *Zyklos* d'une capacité de 150 litres.

Toutes les dalles ont été exécutées de manière identique, le BFUP a été coulé à l'aide d'une benne verseuse au milieu du coffrage en une seule étape et en assurant un écoulement continu (Figure 1-3). Les dalles ont été décoffrées après 24 heures et enrobées dans une feuille de plastique et ensuite stockées à l'intérieur de la halle de préfabrication et/ou du laboratoire.

Figure 1-2 : Malaxeur Kniele et coffrages des dalles

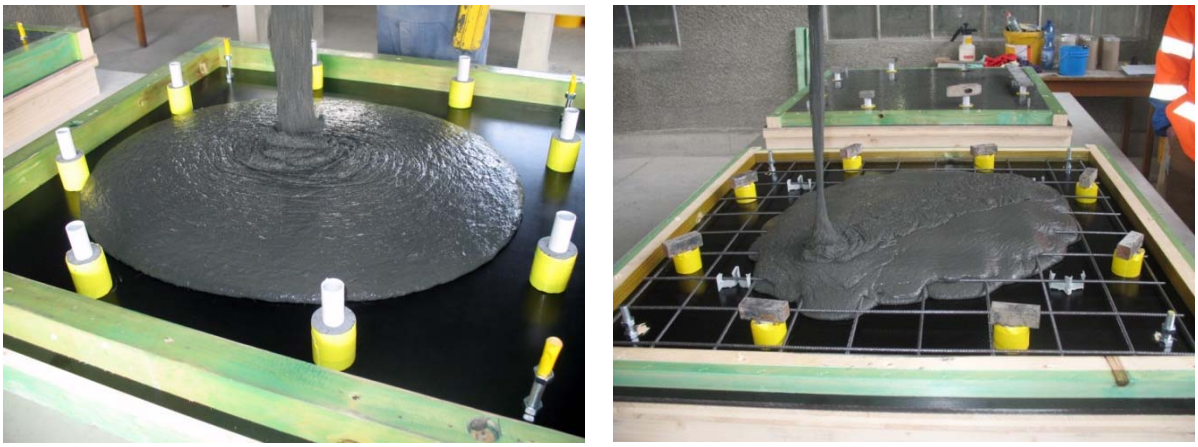

Figure 1-3 : Coulage des dalles sans et avec armature

1.3. Dispositif d'essai

Les essais de charge ont été réalisés au sein du laboratoire de Structure de l'EIA-FR sur un banc d'essai spécialement conçu pour cette étude. La dalle est chargée au centre par un vérin hydraulique surmonté d'un poinçon en acier de diamètre 80 mm. Elle est retenue en 8 points par des tiges filetées M20 ancrées au cadre en acier. Le système d'appui décrit un cercle de diamètre 878 mm (*Figure 1-4*). Les points d'appuis sont pourvus de rotules axiales laissant libres la rotation (Figure 1-5). Les essais sont contrôlés en déplacement par un système d'asservissement servo-électronique de la firme *Walter & Biai*. Le chargement est effectué à une vitesse de 0.02 mm/s représentant un chargement quasi-

statique. La force est appliquée par incréments jusqu'à la rupture. Les incréments de charge sont fixés en fonction de l'épaisseur des dalles. A chaque palier, l'évolution de fissuration est relevée.

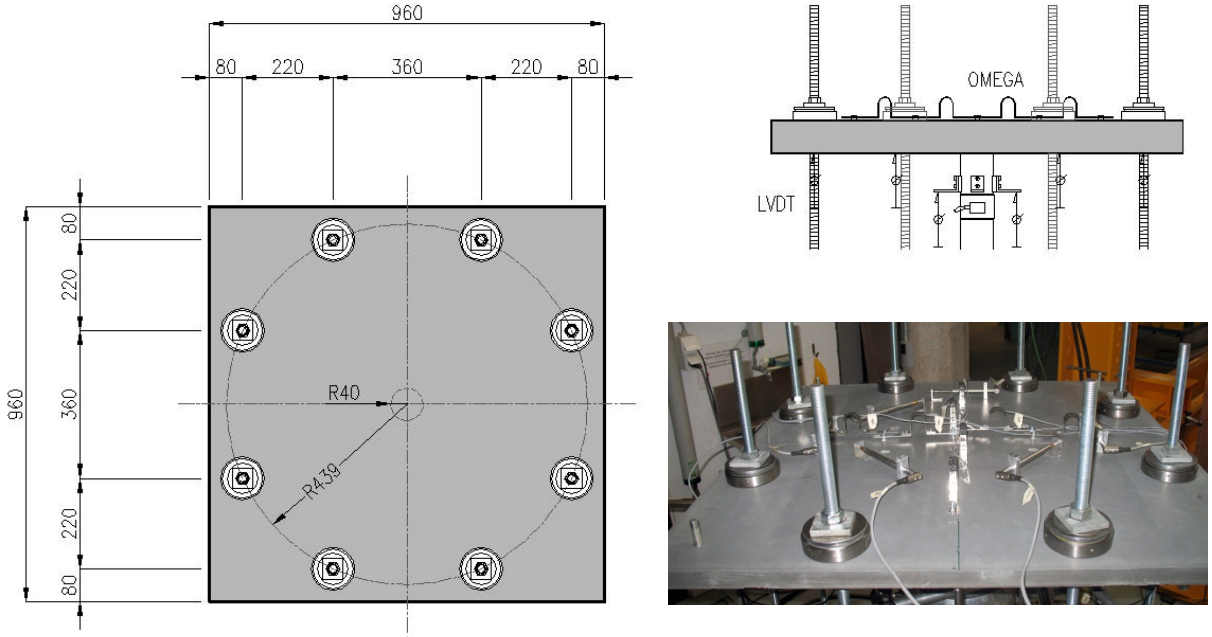

Figure 1-4 : Configuration des essais de poinçonnement

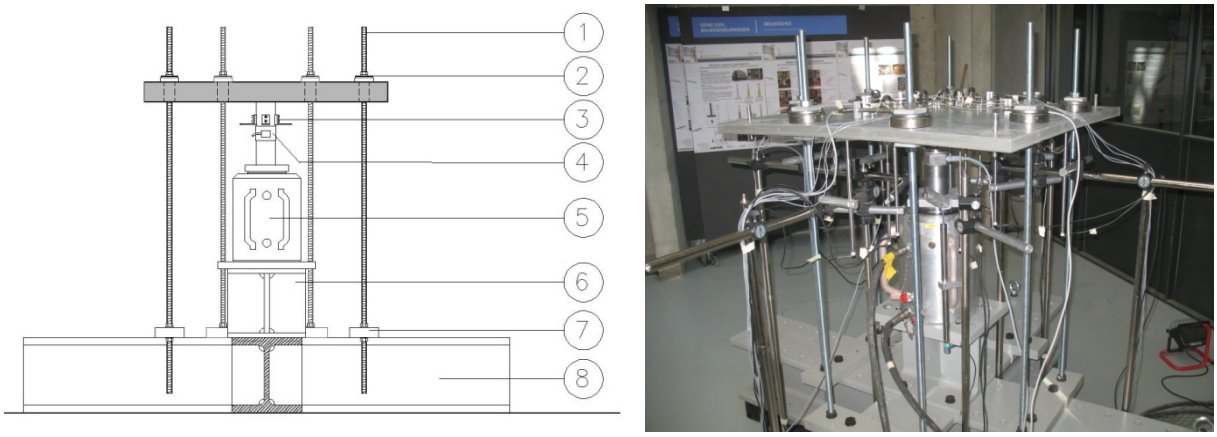

Figure 1-5 : Dispositif d'essai, schéma et vue d'ensemble

1 tiges filetées M20 8.8
2 rotules axiales *SKF GX 40 F*
3 poinçon en acier ϕ80 mm
4 cellule de force *HBM* 500 kN
5 Vérin *Bieri* 1000 kN/160 mm
6 profilé de support HEB 300
7 plaques d'ancrage 400 x 100 x 40 mm
8 croix de support HEM 280

1.4. Mesures et observations

Le système de mesure comprend 31 capteurs disposés sur chaque élément d'essai. Une cellule de force *HBM C6A* 500 kN est placée entre le vérin et le poinçon pour le suivi de l'évolution de la force appliquée. Douze capteurs *LVDT* permettent de mesurer les flèches à différents points de la dalle. Douze capteurs de déformations de type *TML Omega* sont placés sur la face tendue de la dalle suivent les allongements des axes. Six capteurs *LVDT* placés sur la face tendue de la dalle permettent de mesurer l'ouverture des lignes de rupture. Tous les capteurs sont reliés à un système d'acquisition de type *HBM spider 8* et gérer par le programme *HBM Catman*. La vitesse d'acquisition est fixée à 1 Hz (1 mesure par seconde). A chaque palier de charge, l'évolution de fissuration est relevée.

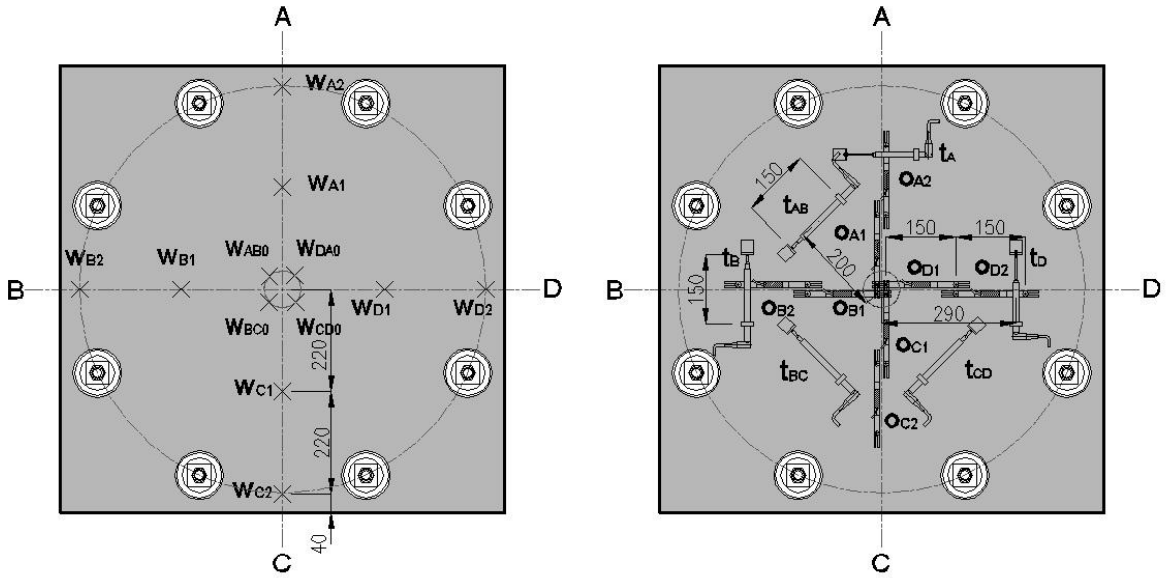

Figure 1-6 : Disposition des instruments de mesures

Figure 1-7 : Vues de la disposition des capteurs, face inférieure, face supérieure

2. Propriétés des matériaux

2.1. Compositions des BFUP

Le Béton Composite Vicat (BCV®) est développé par le groupe Vicat. Il appartient à la famille des BFUP selon la définition des recommandations provisoires de l'Association Française de Génie Civil (AFGC) [1]. Le BCV a une granulométrie optimisée comprise entre 0-3 mm et un rapport E/L inférieur à 0.2 obtenu par l'utilisation de fluidifiants puissants. A l'état frais, le BCV est un béton auto-plaçant. Le dosage en fibres est adapté aux caractéristiques en traction recherchées. Le BCV a déjà fait l'objet de réalisations remarquables telles que le passage supérieur PS34 sur l'autoroute A51

Dans le cadre de cette étude, le BCV® Structure est employé avec différents dosages et types de fibres. Les deux compositions suivantes sont analysées dans le cadre de cette étude :

BCV 1%A fibres métalliques, dosage V_f = 1% (79 kg/m^3),

BCV 2% fibres métalliques, dosage V_f = 2% (158 kg/m^3).

Tableau 2-1 : *Composition théorique des BFUP analysés*

BCV®		**1%A**	**2%**
Premix [kg/m^3]	Béton composite Vicat Type : *BCV® Structure*	2'090	
Adjuvant [kg/m^3]	Fluidifiant *Sika® ViscoCrete®-20 HE Krono*	21.4	
Eau [litres/m^3]		215	
Ajout [kg/m^3]	Fibres en acier *Sodetal* 12.7/0.175 mm	79	52
	Fibres en acier *Sodetal* 20.0/0.300 mm	-	106

2.2. Caractéristiques en compression

La résistance en compression f_c est déterminée sur des cylindres ϕ110 x 220 mm ainsi que des cubes de 100 mm de côté pour les séries 2 et 3. L'âge entre les différentes séries est différent et correspond à l'âge des essais sur les dalles. Le module d'élasticité E_c est défini sur des cylindres ϕ110 x 220 mm en fixant une contrainte supérieure de 50 MPa correspondant environ au tiers de la résistance en compression sur cube, en accordance avec la norme SIA 262/1.

Tableau 2-2 : Récapitulatif des essais de compression

Série	V_f [%]	Age [j]	Densité [kg/m^3]	E_{cm} [GPa]	f_{cm} [MPa]	$f_{cm,cube}$ [MPa]
1	2	63	2519* *18***	41.1 *0.4*	143 *2.7*	-
2	2	71	2535 *50*	43.4 *0.7*	156 *5.0*	158 *4.1*
3	1	74	2482 *19*	45.7 *0.5*	157 *3.5*	140 *4.2*
4	2	187	2551 *38*	49.9 *1.9*	169 *9.5*	-
5	1	186	2450 *20*	44.8 *0.8*	158 *5.7*	-

* valeur moyenne, ** écart type

2.3. Caractéristiques en traction par flexion

Pour des éléments minces, les recommandations provisoires BFUP de l'AFGC [1-2] préconisent des essais de flexion sur prismes d'épaisseur égale à la structure analysée. L'épaisseur réduite influence notablement l'orientation des fibres par conséquent la réponse mécanique du matériau. Les résultats de ces essais sont ensuite traités par une méthode inverse simplifiée dans le but d'obtenir une loi de comportement en traction pour le dimensionnement.

Par rapport aux recommandations [1-2] qui conseillent un essai de flexion 4 points, les BFUP ont été caractérisés par un essai de flexion 3 points développé dans le cadre d'une thèse à l'EPFL [12] (Figure 2-2). Les prismes ont une longueur de 600 mm pour une largeur de 200 mm, l'épaisseur h varie en fonction de l'élément de structure analysé. Les prismes sont sciés dans des plaques de dimensions 500 x 600 x h mm coulés de manière identique aux dalles d'essai (Figure 2-1). Les prismes sont testés sur une portée de 500 mm. L'évolution de la force, la flèche au centre et l'allongement de la face tendue sont mesurés par des capteurs inductifs.

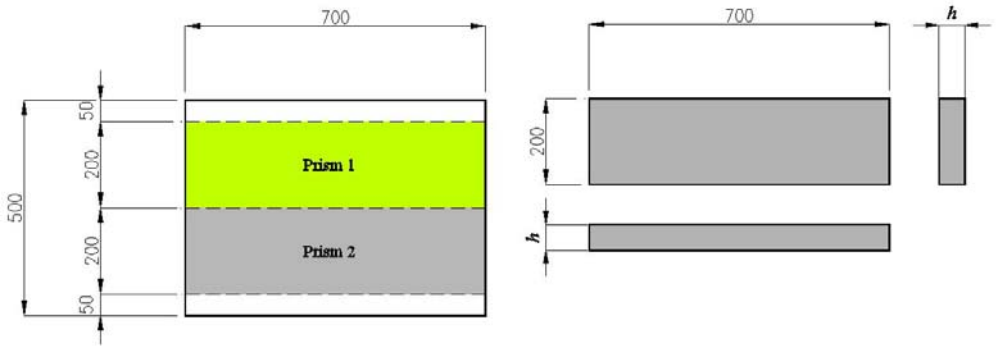

Figure 2-1 : Géométrie des spécimens

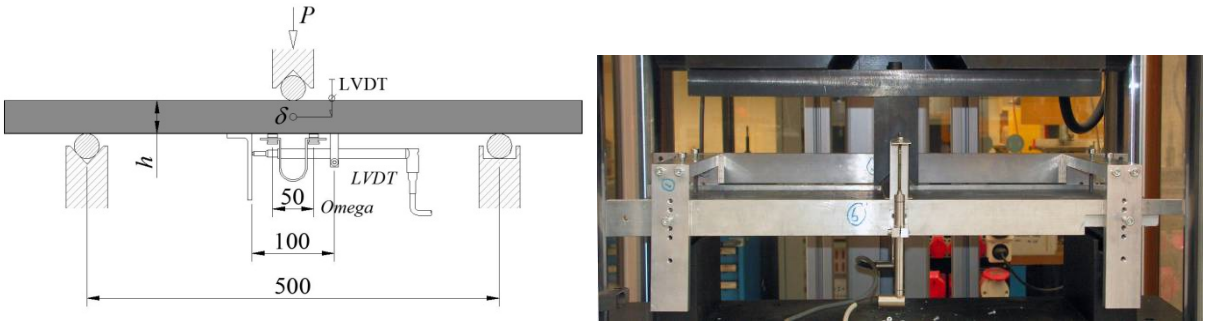

Figure 2-2 : Essai de flexion 3-points sur les prismes

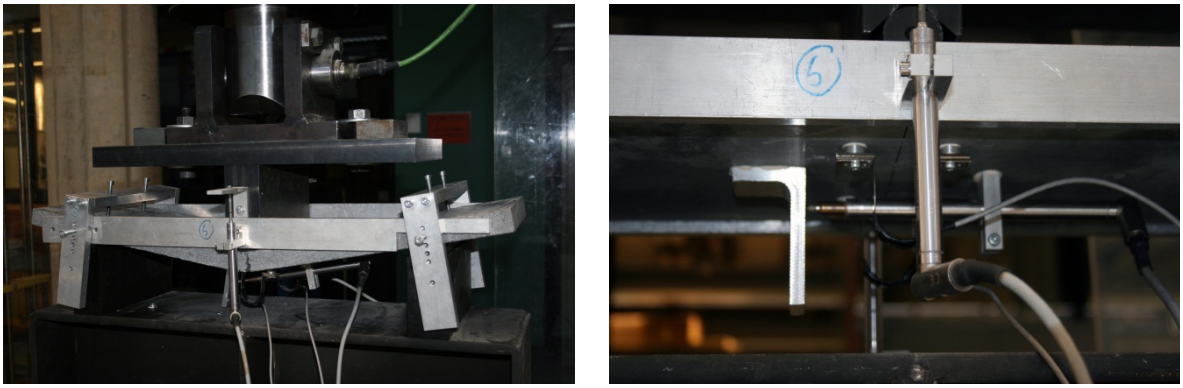

Figure 2-3 : Vues du système de mise en charge et de mesures

La contrainte équivalente de traction par flexion σ_{eq} est définie en admettant une distribution élastique des contraintes. Cette manière de procéder permet de comparer les résultats entre les différentes épaisseurs.

$$\sigma_{eq} = \frac{3 \cdot P \cdot L}{2 \cdot b \cdot h^2} \qquad (2\text{-}1)$$

Appendix 3

BCV 1%A

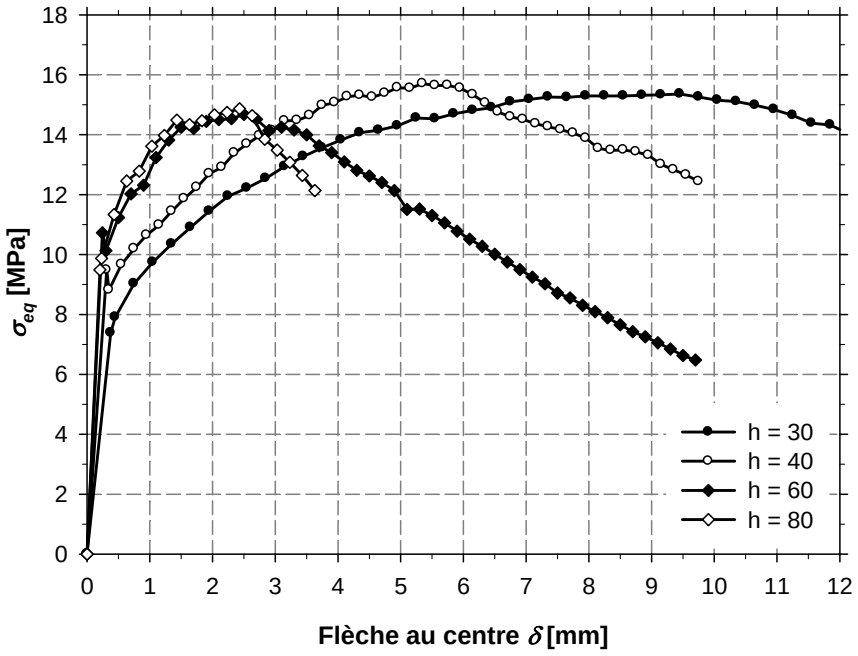

Figure 2-4 : Courbes moyennes des essais de flexion sur prismes, BCV_1%A

Tableau 2-3 : Récapitulatif des essais de flexion sur prismes, BCV_1%A

h [mm]	σ_{fiss} [MPa]	δ_{fiss} [mm]	E_{flex} [GPa]	F_u [kN]	f_u [MPa]	δ_u [mm]
30	7.39	0.38	27.8	3.59	15.5	8.2
40	9.50	0.31	76.6	6.75	15.6	5.4
60	10.7	0.3	117	14.5	15.1	2.5
80	9.48	0.21	156	26.20	15.4	2.4

BCV 2%

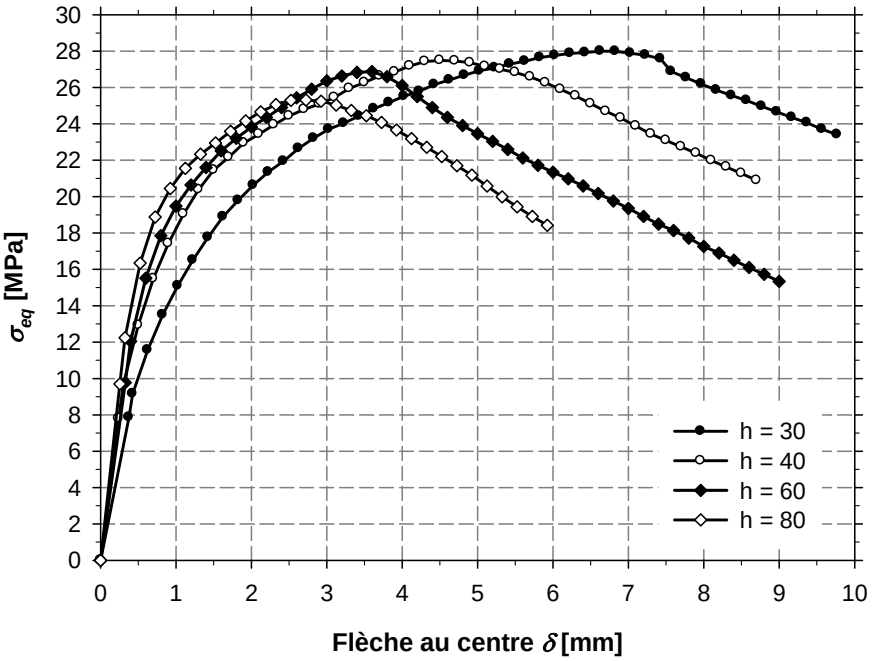

Figure 2-5 : Courbes moyennes des essais de flexion sur prismes, BCV_2%

Tableau 2-4 : Récapitulatif des essais de flexion sur prismes, BCV_2%

h [mm]	σ_{fiss} [MPa]	δ_{fiss} [mm]	E_{flex} [GPa]	F_u [kN]	f_u [MPa]	δ_u [mm]
30	7.88	0.329	27.6	5.61	28.2	6.6
40	7.81	0.241	54.5	11.8	27.9	4.5
60	9.74	0.327	76.7	26.8	27.1	3.6
80	9.70	0.256	126	43.3	25.7	2.7

La résistance équivalente en traction par flexion du BCV 1%A se situent entre 15 et 16 MPa indépendamment de l'épaisseur des prismes. Alors que pour le BCV 2%, la résistance équivalente en traction par flexion varie entre 25 à 28 MPa et augmente avec la diminution de l'épaisseur. Ceci provient des fibres longues qui s'orientent de manière préférentielle dans les éléments minces.

Les résultats des essais de flexion sont ensuite traités avec la méthode inverse proposée pour les éléments minces dans les recommandations BFUP de l'AFGC [1-2] dans le but de déterminer une loi de comportement en traction pour le dimensionnement (Figure 2-6). Les différents calculs sont décrits plus détails dans le rapport traitant de la caractérisation du BCV [xx].

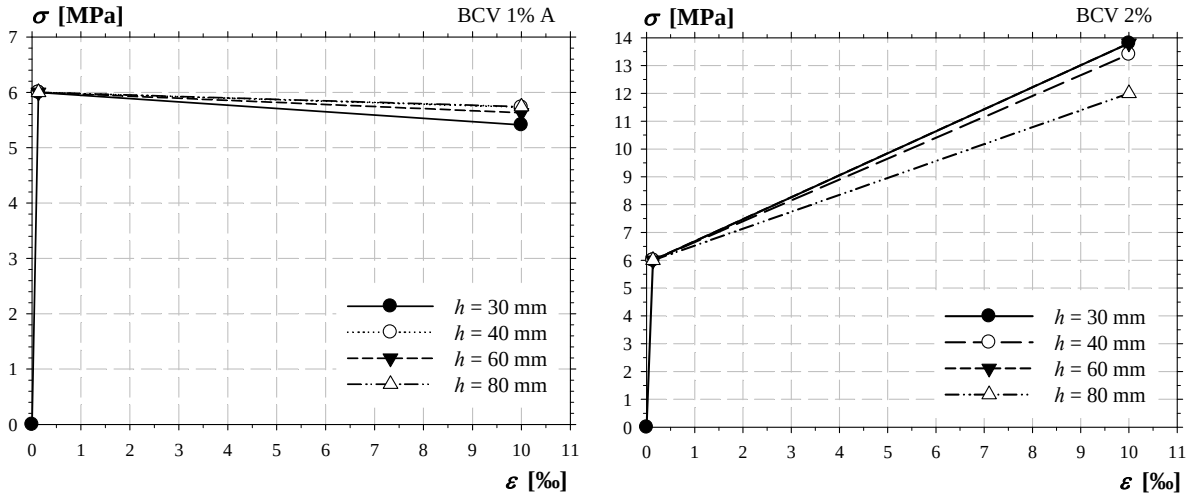

Figure 2-6 : Lois de comportement déterminées au moyen de la méthode inverse proposée dans [2]

2.4. Propriétés des aciers d'armature

Les caractéristiques mécaniques des aciers d'armature ont été déterminées au sein du laboratoire des Structures de l'EIA-FR. Les essais sont réalisés sur 4 barres d'une longueur de 600 mm pour chaque diamètre en accord avec les normes ISO 15'630 parties 1 et 3 "Aciers pour l'armature et la précontrainte du béton – Méthode d'essai".

Tableau 2-5 : Récapitulatif des essais de traction sur les aciers d'armature

Diamètre [mm]	E_s [GPa]	$f_{s0,2}$ [MPa]	f_u [MPa]	ε_u [%]
5	201	623	645	3.60
7	205	546	585	3.43
9	202	556	599	3.52
10	203	557	599	3.80
12	200	504	599	8.24

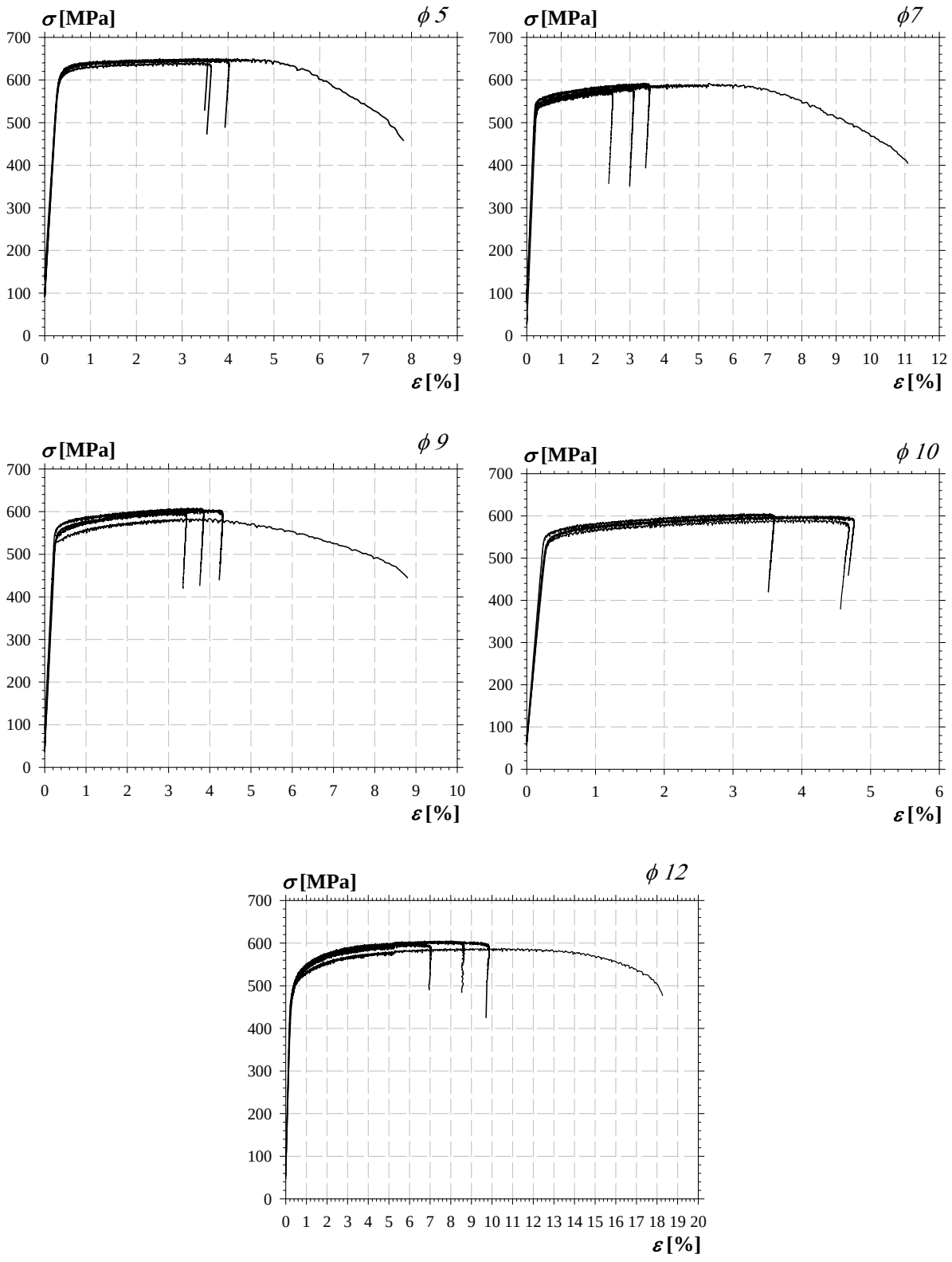

Figure 2-7 : Courbes contrainte-allongement des armatures passives

3. Résultats

Les résultats des essais de flexion et poinçonnement sur les dalles en BFUP effectués au laboratoire de Structures de l'EIA-FR sont présentés de la manière suivante.

Dans une première paire de graphiques sont présentées les relations force/flèche au centre et force/rotation des différentes dalles d'essai. Les rotations des axes AC et BD sont calculées de la manière :

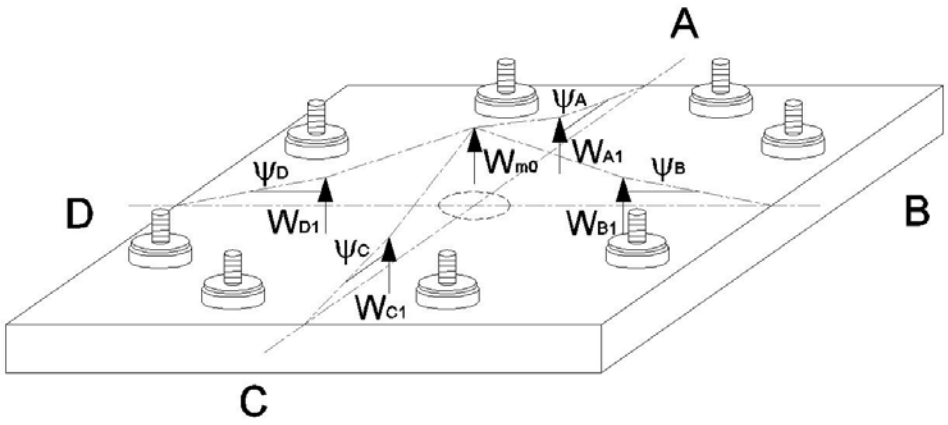

Figures 3-1 : Schéma explicatif du calcul des rotations des axes AC et BD

Dans une deuxième paire de photos sont présentés le relevé de la fissuration à la rupture des faces tendue et comprimée.

La troisième photo donne une image de la fissuration interne des dalles. Toutes les dalles dont la rupture s'est faite par poinçonnement ou par flexion/poinçonnement ont été sciées à travers le centre afin d'observer l'allure des fissures internes de poinçonnement.

Dans une quatrième paire de graphiques sont présentées les relations force/allongement dans les directions tangentielles. Ces allongements mesurés par des capteurs LVDT disposés perpendiculairement aux directions principales et sous un angle de 45°, permettent de déterminer les ouvertures des fissures radiales.

Dans une cinquième paire de graphiques sont présentées les relations force/allongement dans les directions radiales. Ces allongements mesurés par des capteurs du type Omega disposés dans les directions principales permettent de déterminer les ouvertures des fissures tangentielles.

Dans une sixième paire de graphiques sont présentées les relations force/flèche pour tous les points situés sur les axes principaux. Ces flèches mesurées par des capteurs LVDT donnent une image de la déformée dans les deux directions des dalles d'essai.

3.1. Série 1

3.1.1. Dalle BCV_2%_30_0%

Béton : BCV 2% de fibres
Epaisseur : 30 mm
Sans armature passive

a)

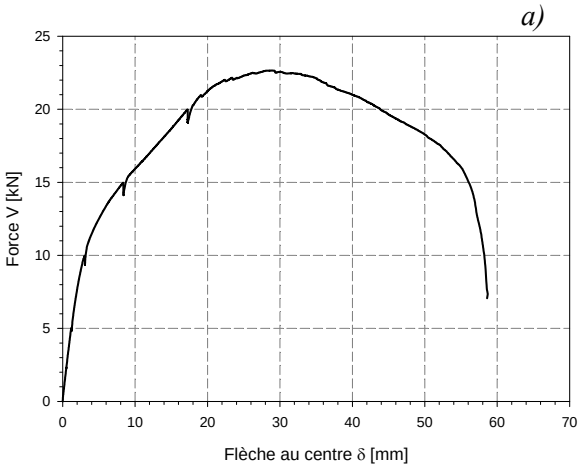

a) Relation force-flèche

b)

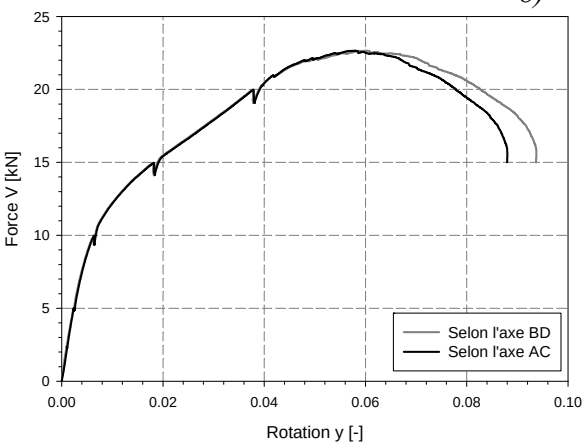

b) Relation force- rotation

c)

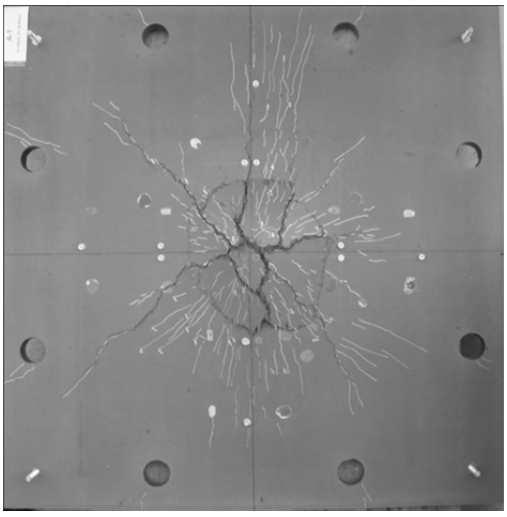

c) Fissuration de la face tendue

d)

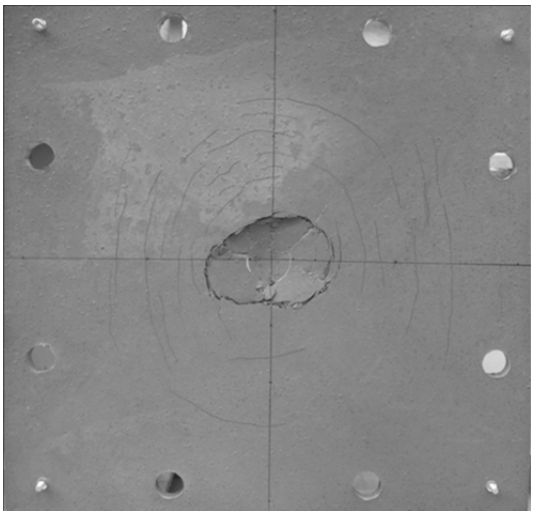

d) Fissuration de la face comprimée

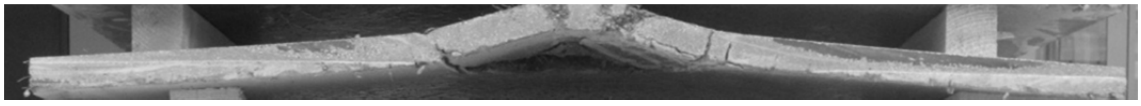

e) Vue de la fissuration interne après découpe de l'élément

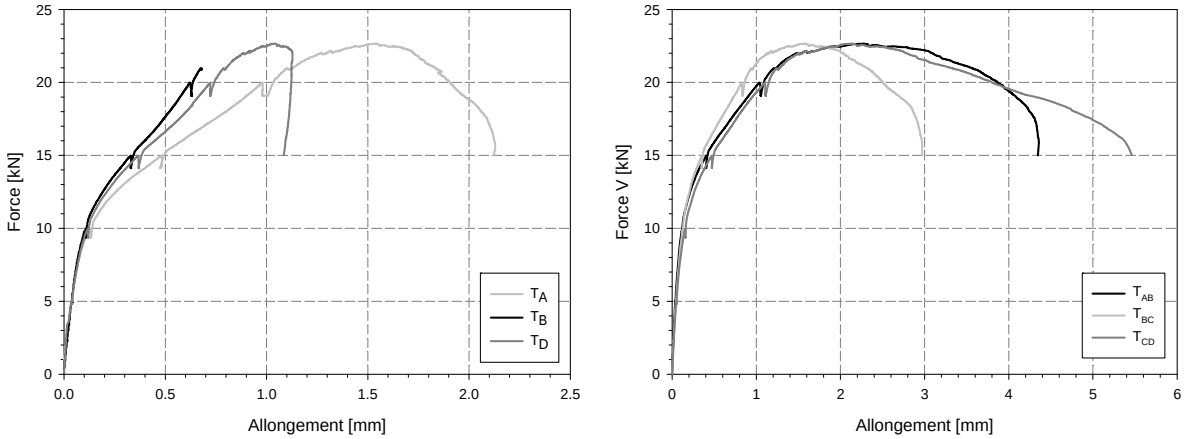

f) Relation force-allongements des capteurs tangentiels

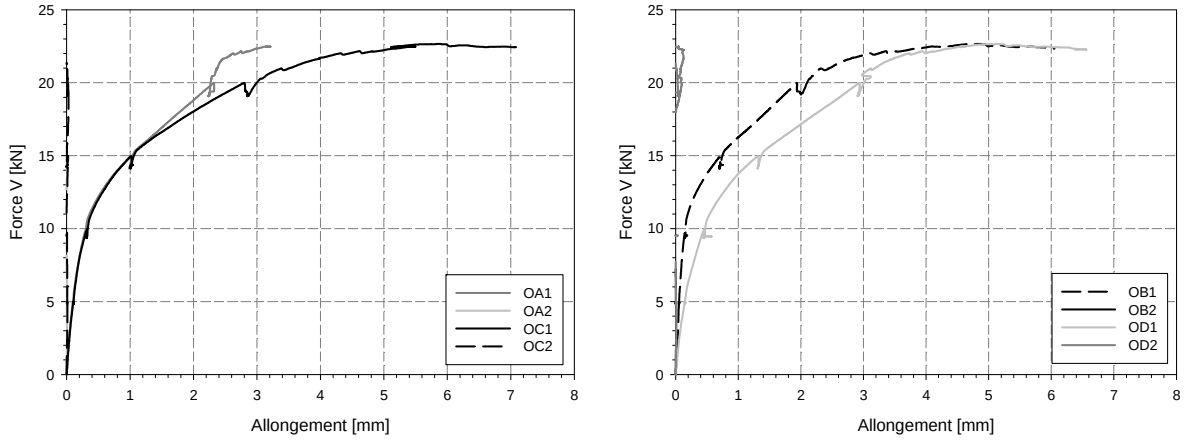

g) Relation force-allongements des capteurs radiaux

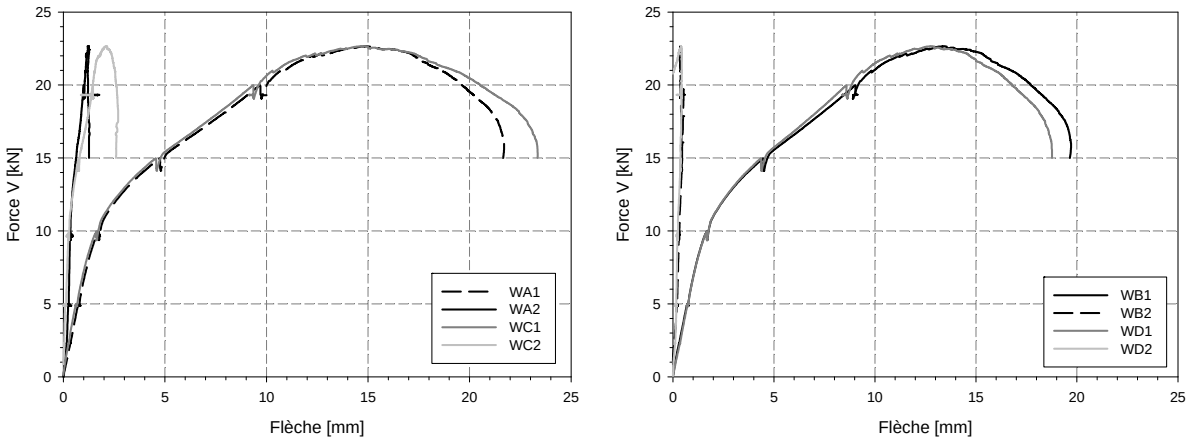

h) Relation force-flèches

Figures 3-2 : Résultats des essais - Dalle BCV_2%_30_0%

3.1.2. Dalle BCV_2%_40_0%

Béton : BCV 2% de fibres
Epaisseur : 40 mm
Sans armature passive

a)

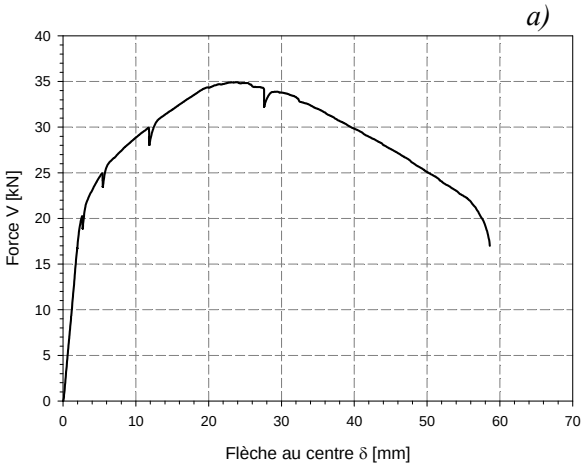

a) Relation force-flèche

b)

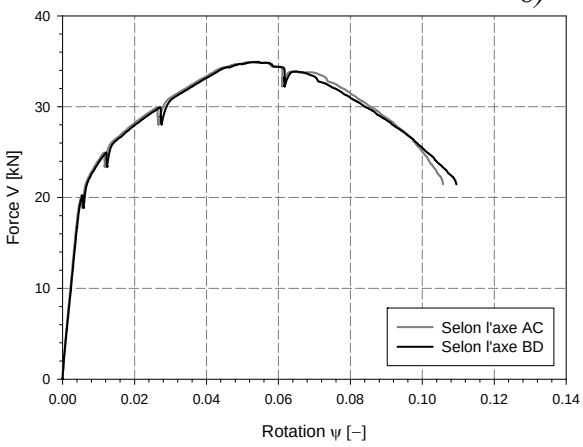

b) Relation force- rotation

c)

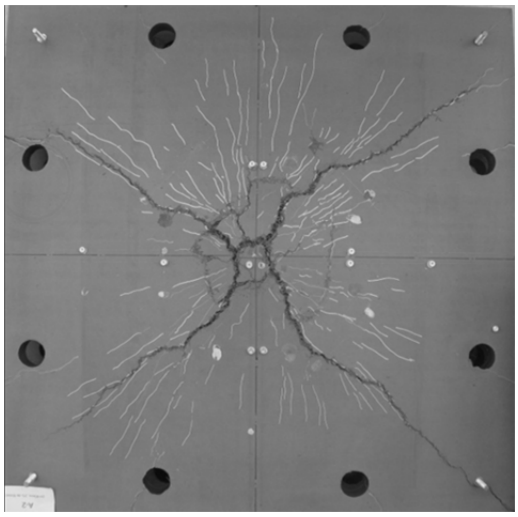

c) Fissuration de la face tendue

d)

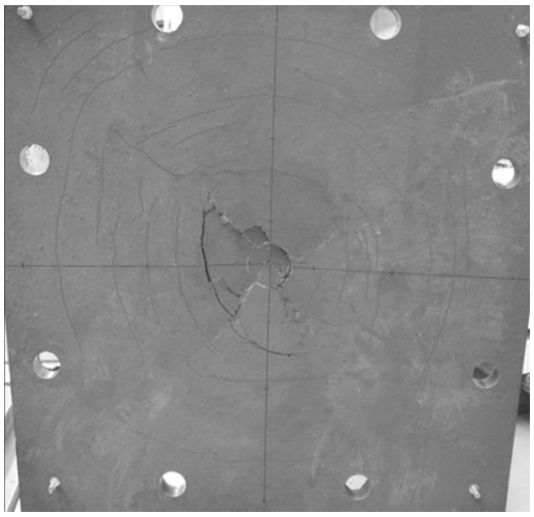

d) Fissuration de la face comprimée

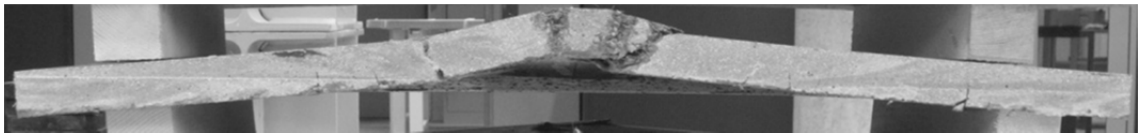

e) Vue de la fissuration interne après découpe de l'élément

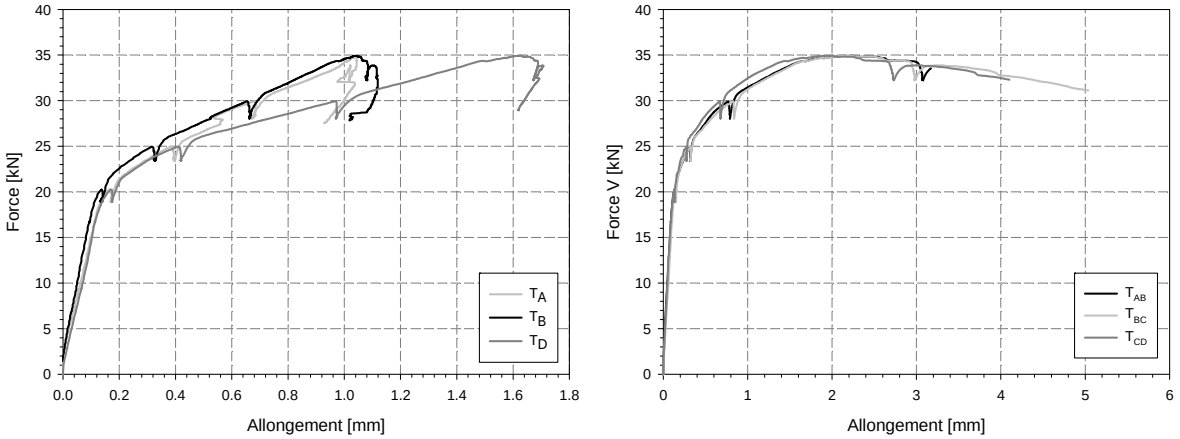

f) Relation force-allongements des capteurs tangentiels

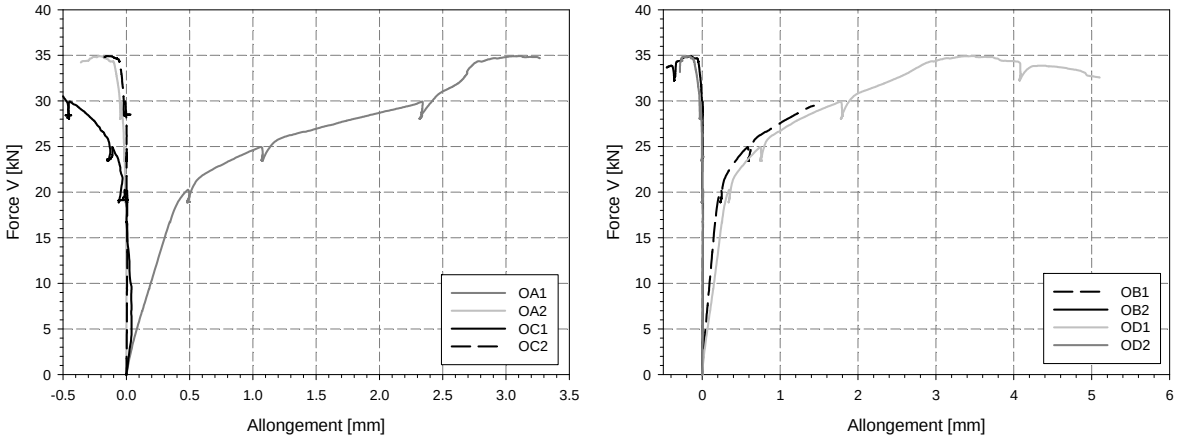

g) Relation force-allongements des capteurs radiaux

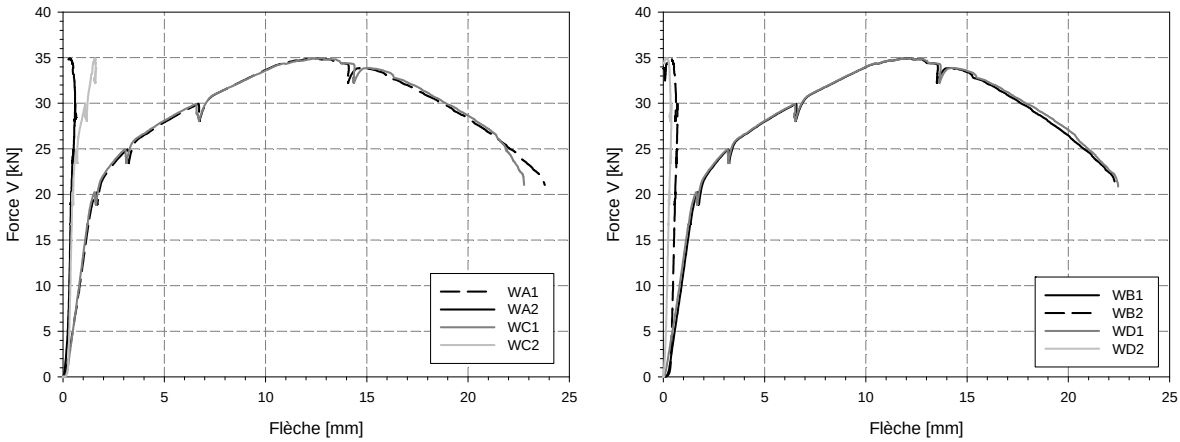

h) Relation force-flèches

Figures 3-2 : Résultats des essais - Dalle BCV_2%_40_0%

3.1.3. Dalle BCV_2%_60_0%

Béton : BCV 2% de fibres
Epaisseur : 60 mm
Sans armature passive

a)

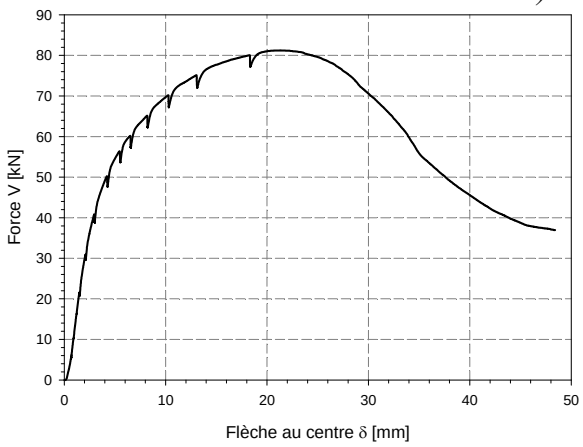

a) Relation force-flèche

b)

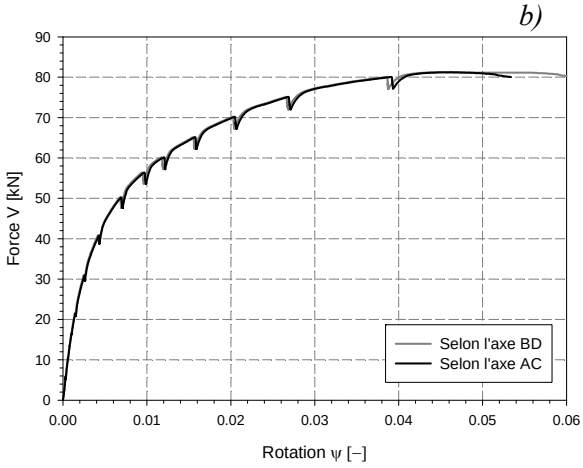

b) Relation force- rotation

c)

c) Fissuration de la face tendue

d)

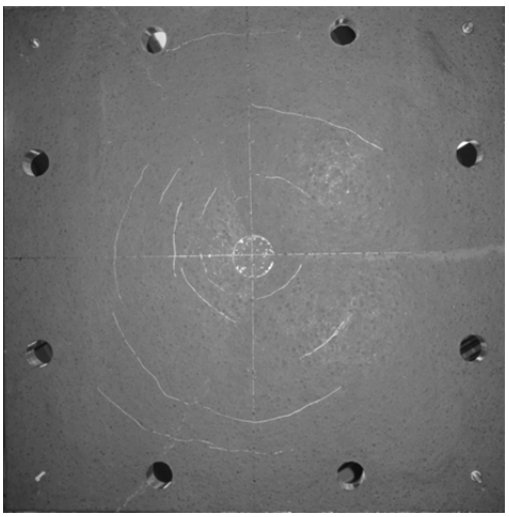

d) Fissuration de la face comprimée

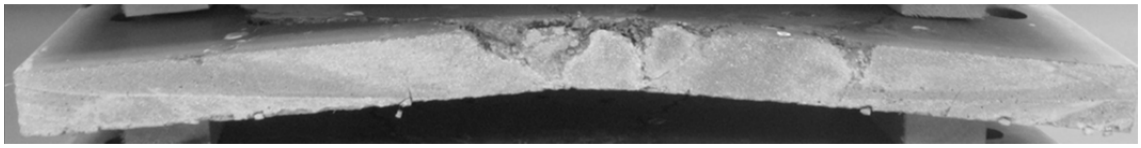

e) Vue de la fissuration interne après découpe de l'élément

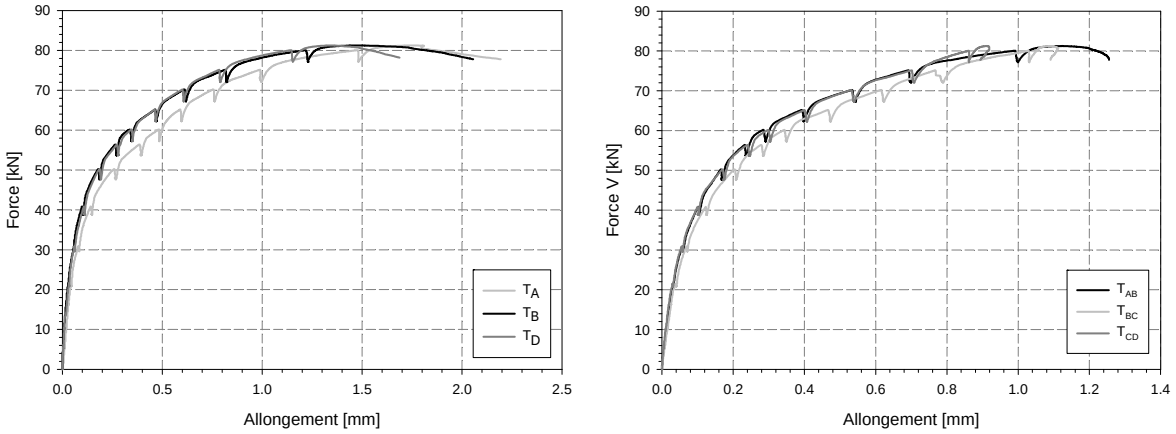

f) Relation force-allongements des capteurs tangentiels

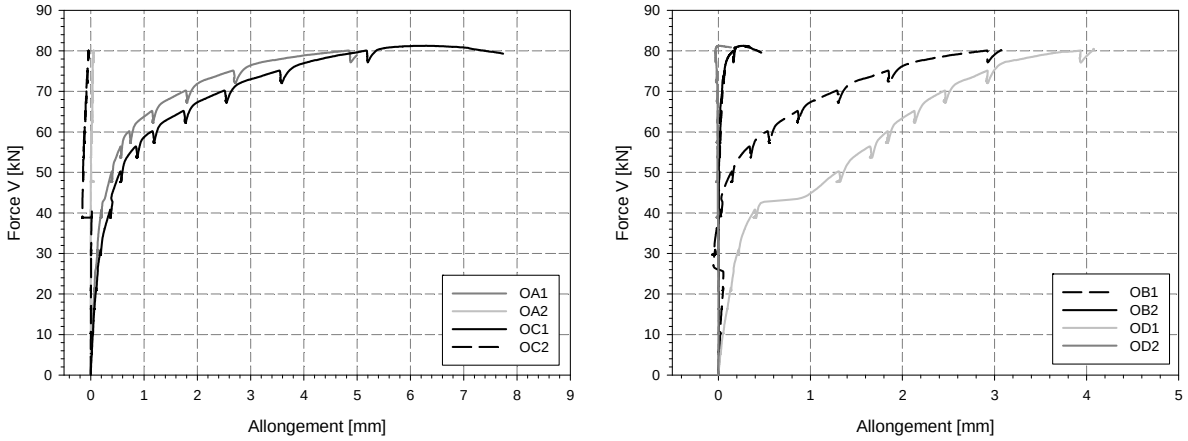

g) Relation force-allongements des capteurs radiaux

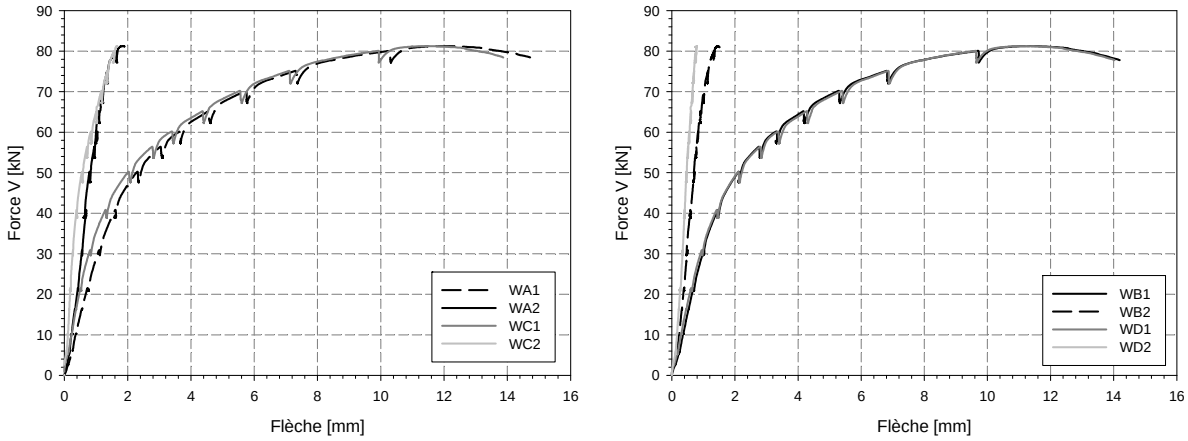

g) Relation force-flèches

Figures 3-3 : Résultats des essais - Dalle BCV_2%_60_0%

3.1.4. Dalle BCV_2%_80_0%

Béton : BCV 2% de fibres
Epaisseur : 80 mm
Sans armature passive

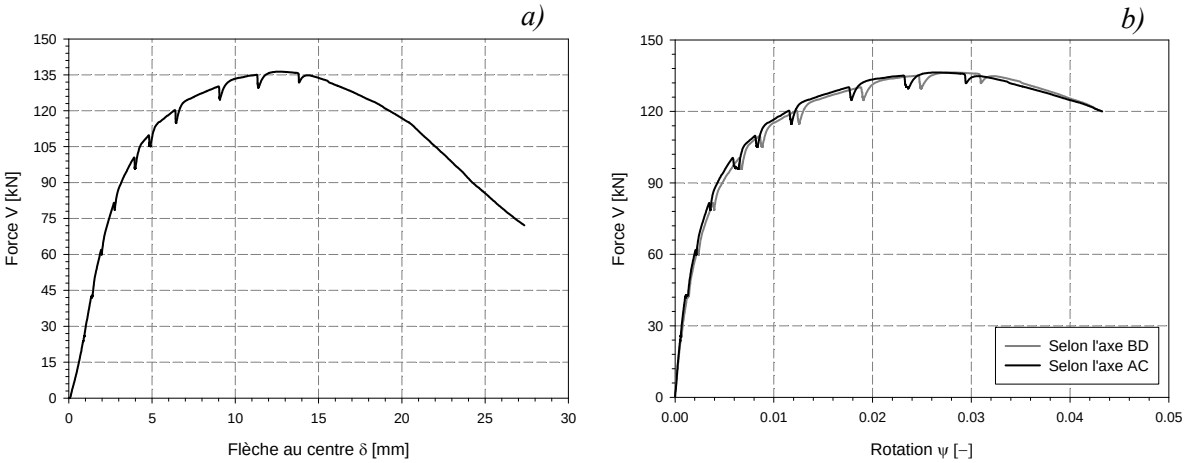

a) Relation force-flèche b) Relation force- rotation

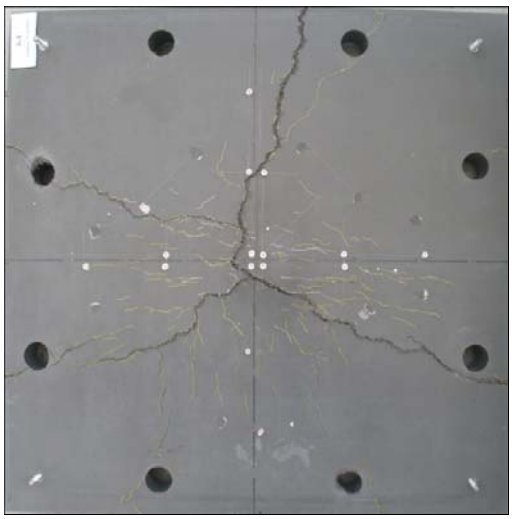

c) Fissuration à la rupture de la face tendue

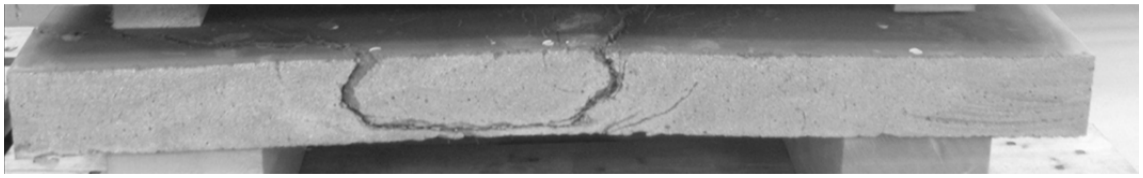

d) Vue de la fissuration interne après découpe de l'élément

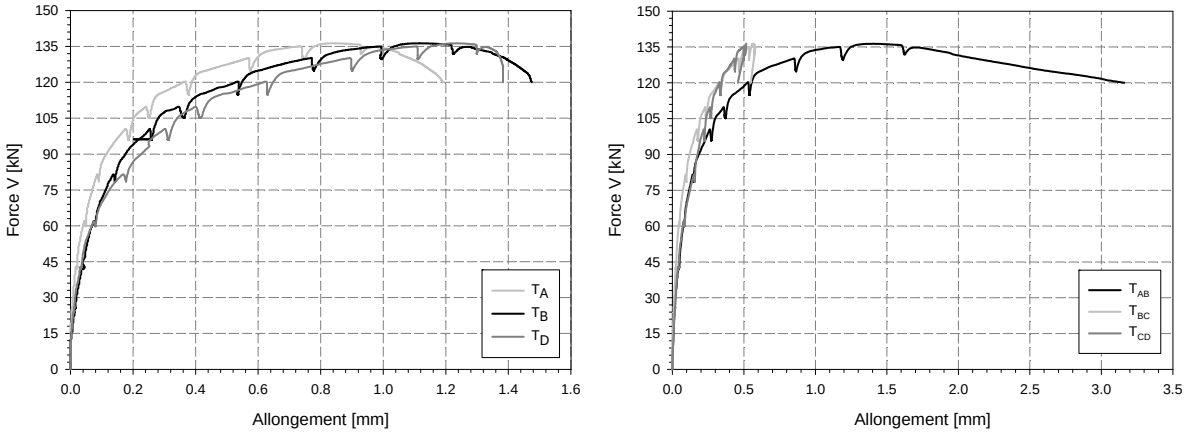

e) Relation force-allongements des capteurs tangentiels

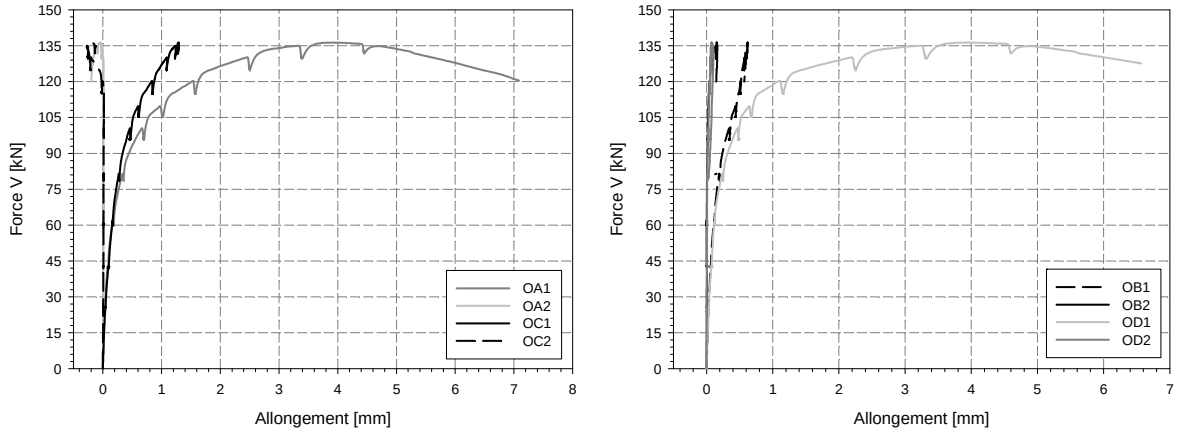

f) Relation force-allongement des capteurs radiaux

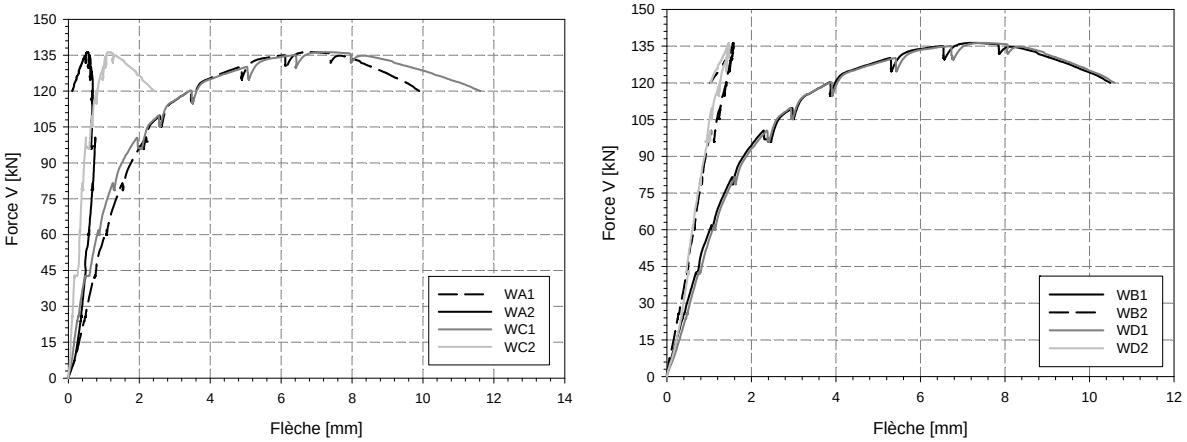

g) Relation force-flèches

Figures 3-4 : Résultats des essais - Dalle BCV_2%_80_0%

3.2. Série 2

3.2.1. Dalle BCV_2 %_30_1.36%

Béton : BCV 2% de fibres
Epaisseur : 30 mm
Taux d'armature : Ø5 #100, ρ_s = 1.36%

a)

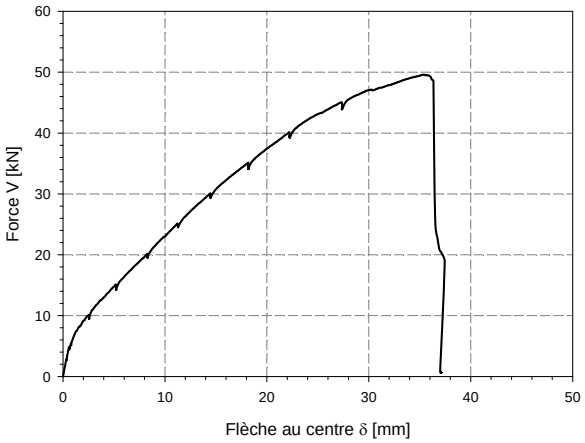

a) Relation force-flèche

b)

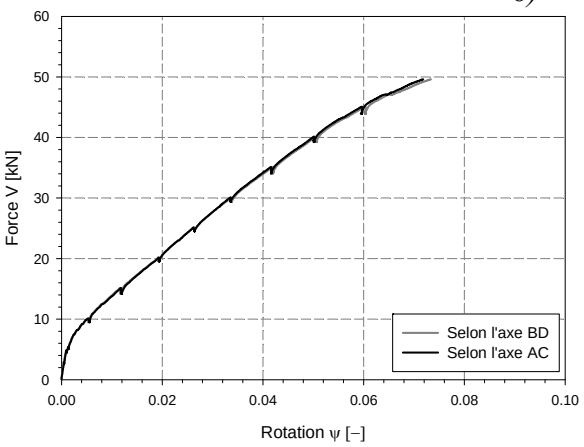

b) Relation force- rotation

c)

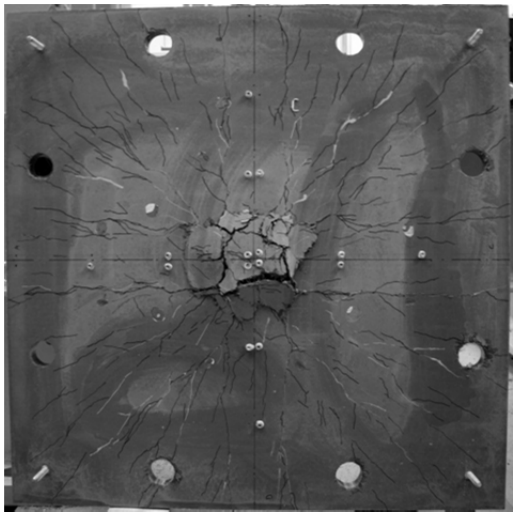

c) Fissuration de la face tendue

d)

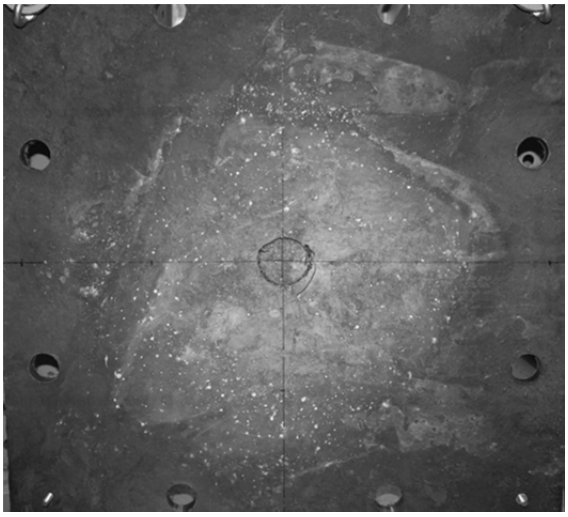

d) Fissuration de la face comprimée

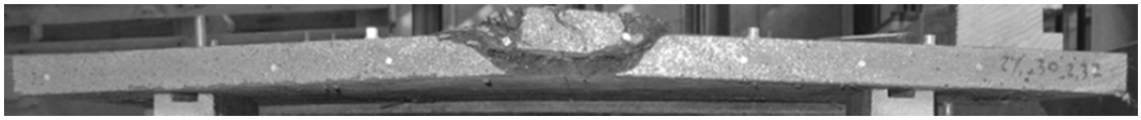

e) Fissuration interne dans la partie centrale

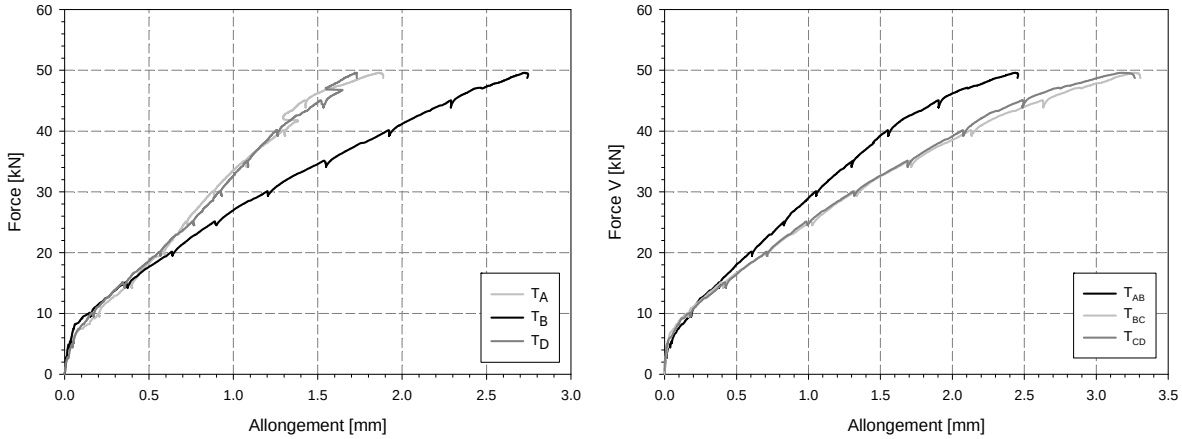

f) Relation force-allongements des capteurs tangentiels

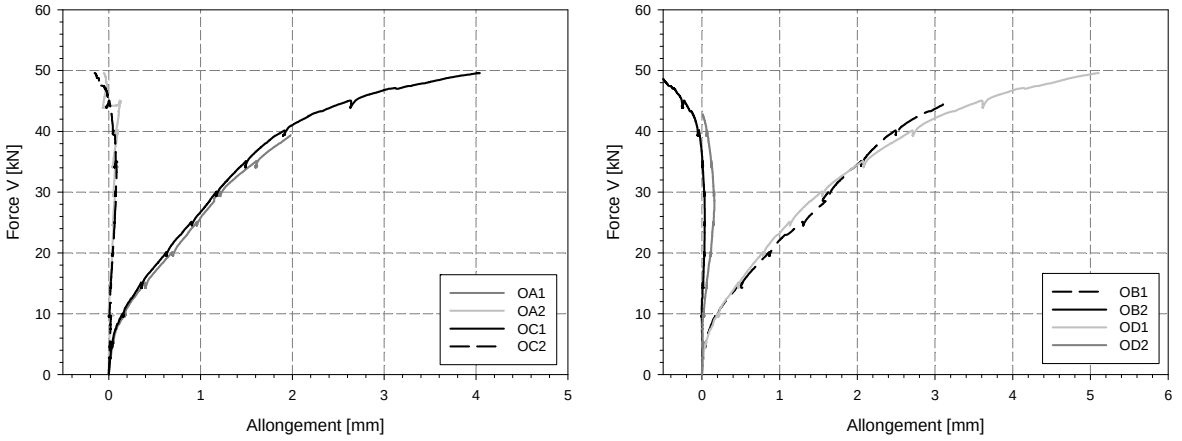

g) Relation force-allongements des capteurs radiaux

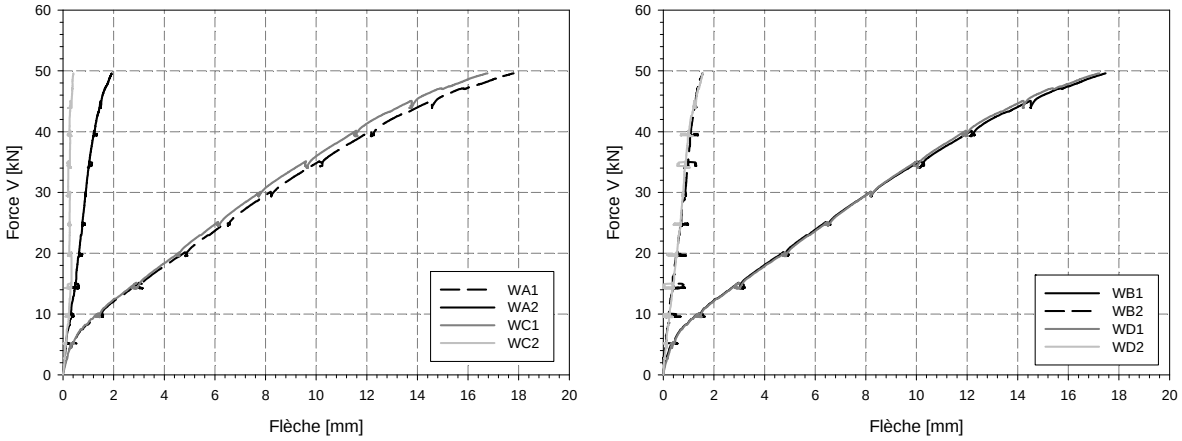

h) Relation force-flèches

Figures 3-5 : Résultats des essais - Dalle BCV_2%_30_1.36%

3.2.2. Dalle BCV_2 %_40_1.02%

Béton : BCV 2% de fibres
Epaisseur : 40 mm
Taux d'armature : Ø5 #100, ρ_s = 1.02%

a)

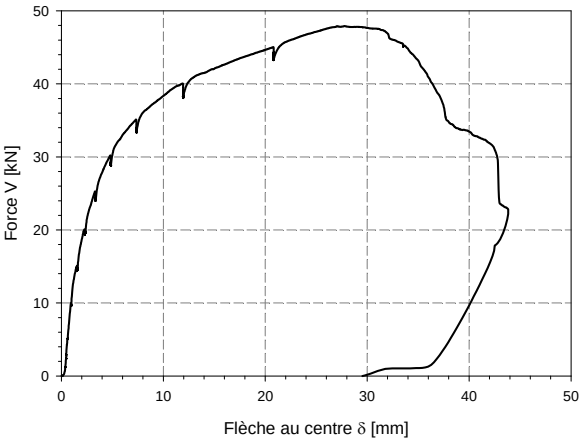

a) Relation force-flèche

b)

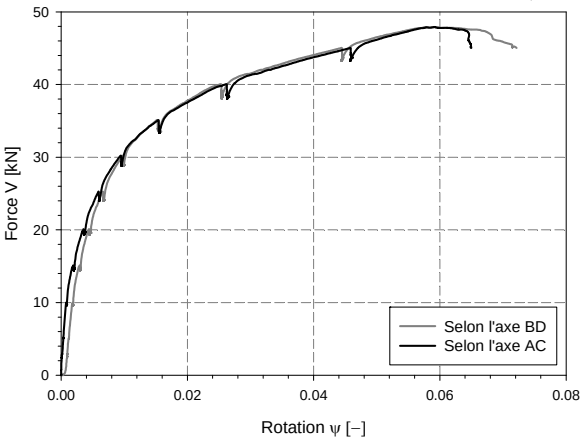

b) Relation force- rotation

c)

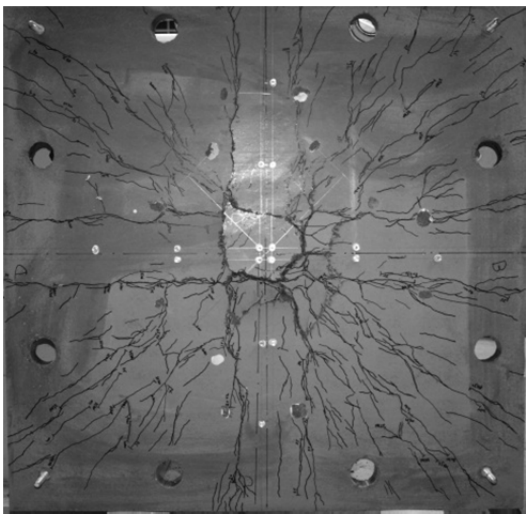

c) Fissuration de la face tendue

d)

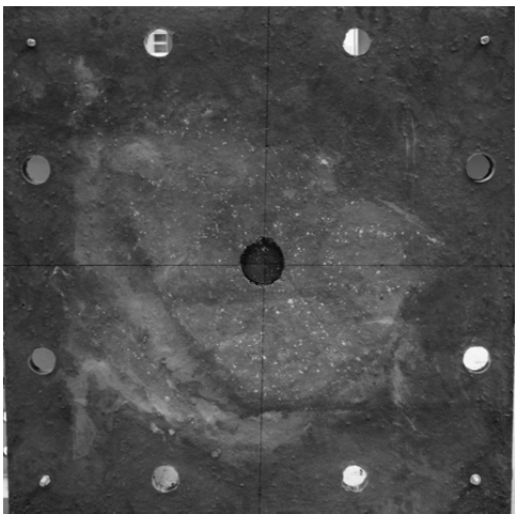

d) Fissuration de la face comprimée

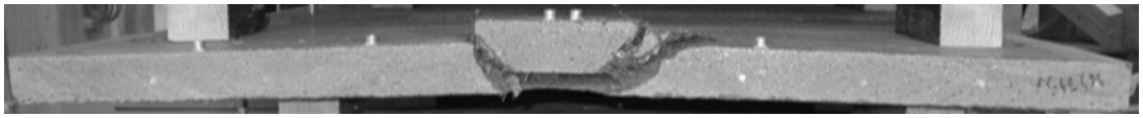

e) Fissuration interne dans la partie centrale

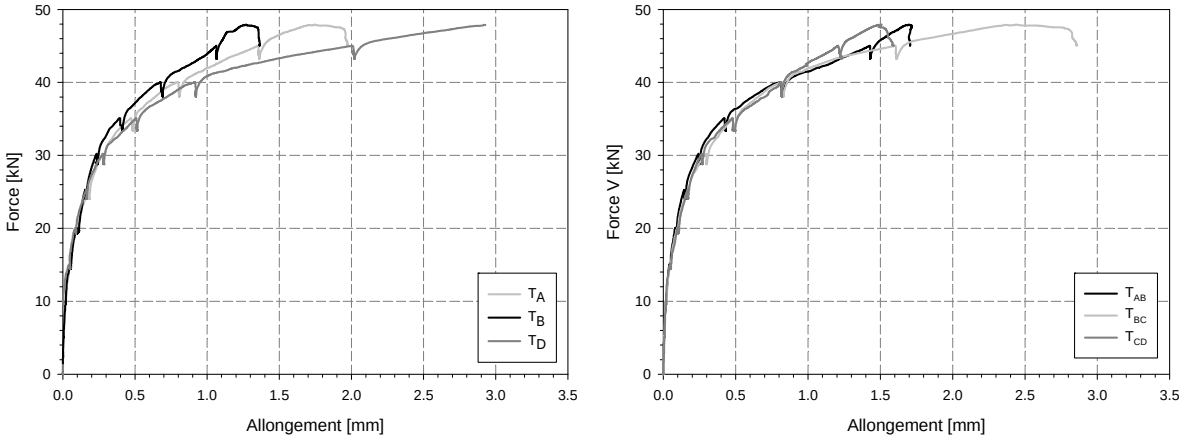

f) Relation force-allongements des capteurs tangentiels

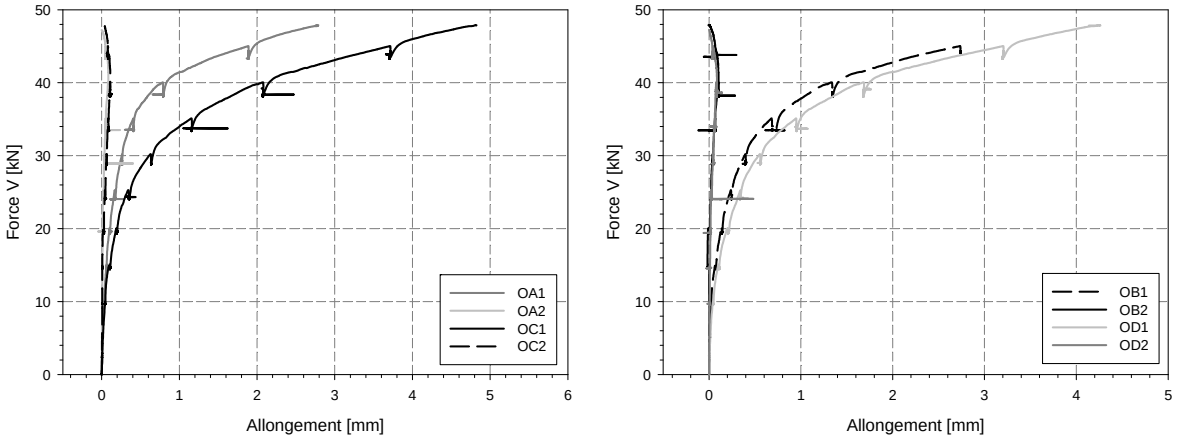

g) Relation force-allongements des capteurs radiaux

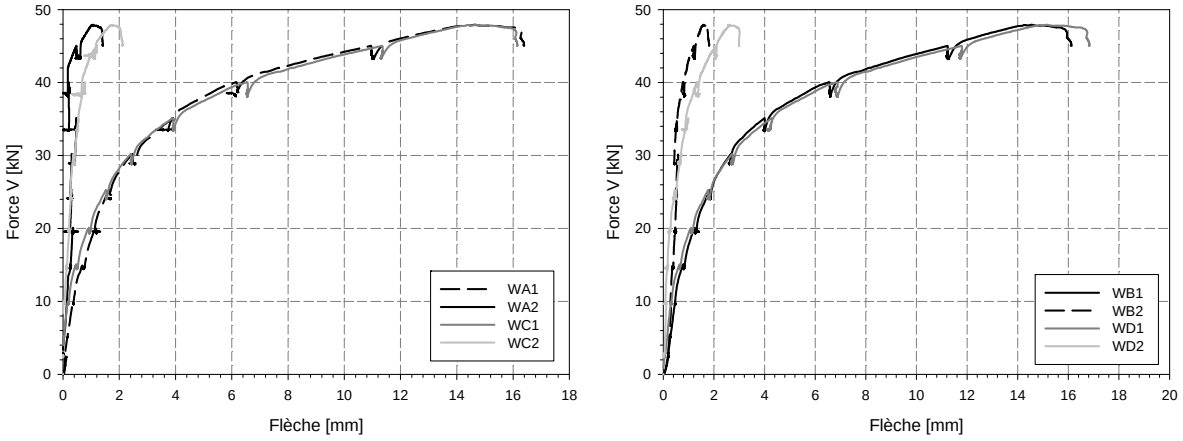

h) Relation force-flèches

Figures 3-6 : Résultats des essais - Dalle BCV_2%_40_1.02%

3.2.3. Dalle BCV_2 %_60_1.00%

Béton : BCV 2% de fibres
Epaisseur : 60 mm
Taux d'armature : Ø7 #100, ρ_s = 1.00%

a)

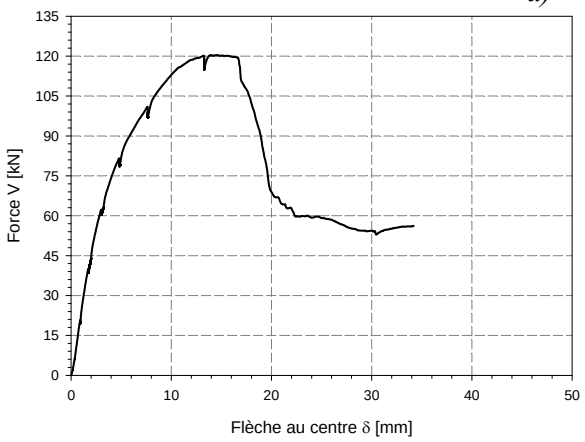

a) Relation force-flèche

b)

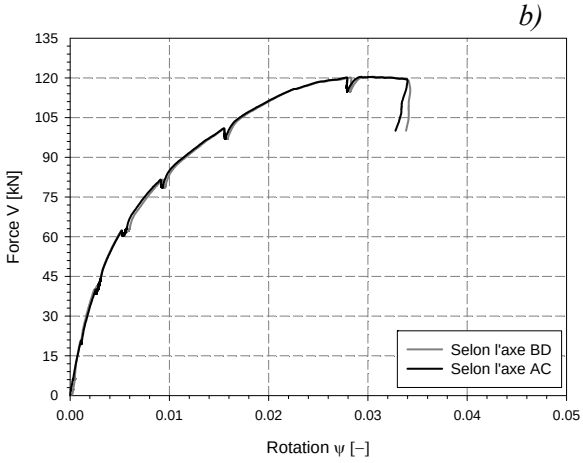

b) Relation force- rotation

c)

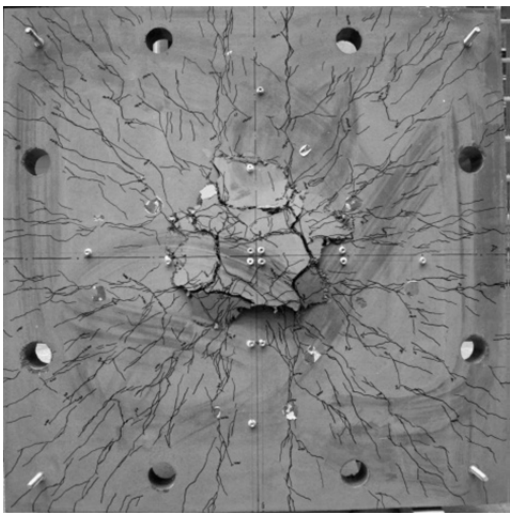

c) Fissuration de la face tendue

d)

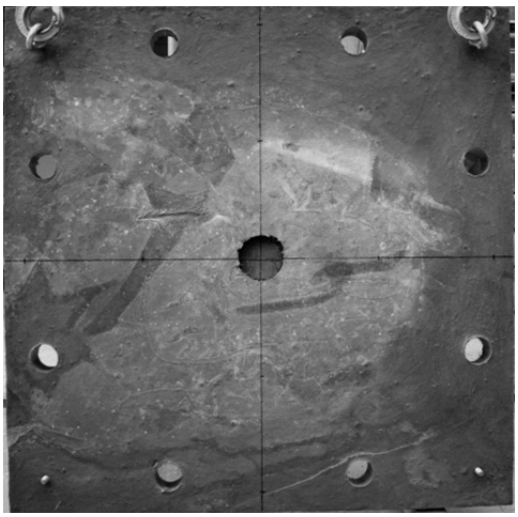

d) Fissuration de la face comprimée

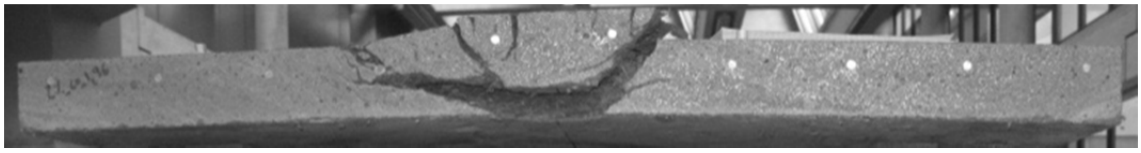

e) Vue de la fissuration interne après découpe de l'élément

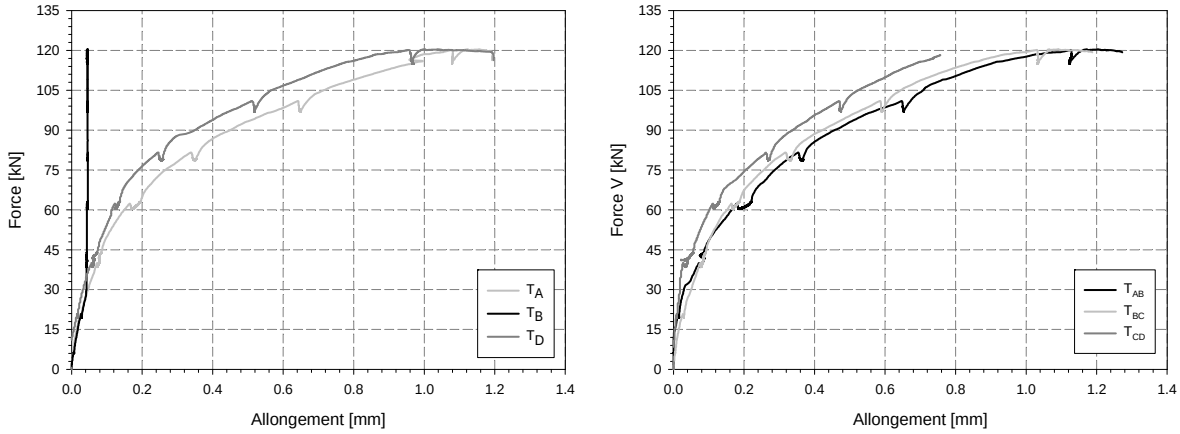

f) Relation force-allongements des capteurs tangentiels

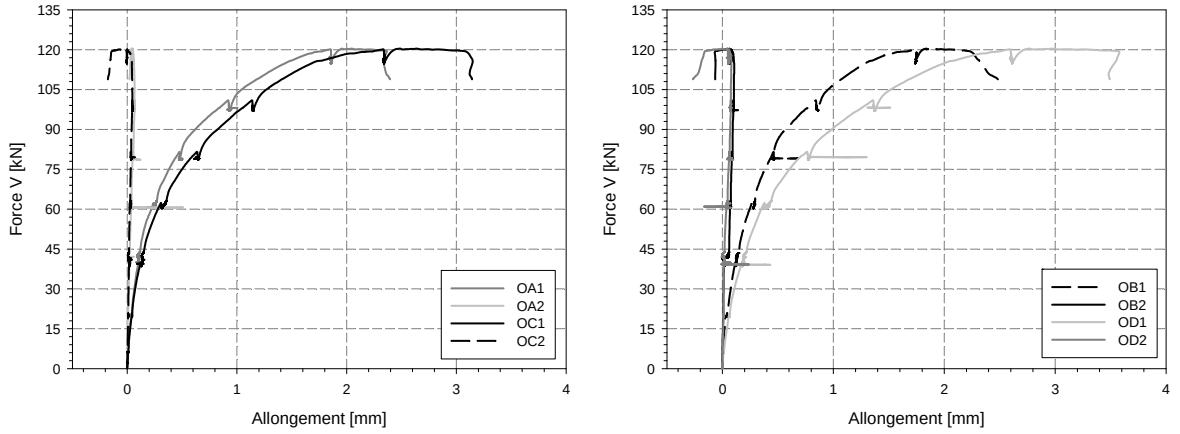

g) Relation force-allongements des capteurs radiaux

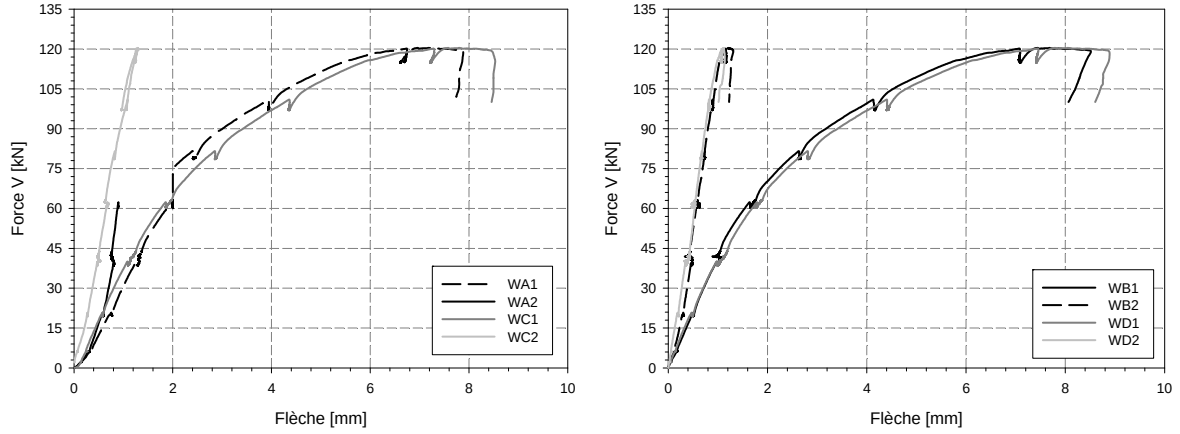

h) Relation force-flèches

Figures 3-7 : Résultats des essais - Dalle BCV_2%_60_1.00%

3.2.4. Dalle BCV_2 %_80_1.10%

Béton : BCV 2% de fibres
Epaisseur : 80 mm
Taux d'armature : Ø9 #100, ρ_s = 1.10%

a)

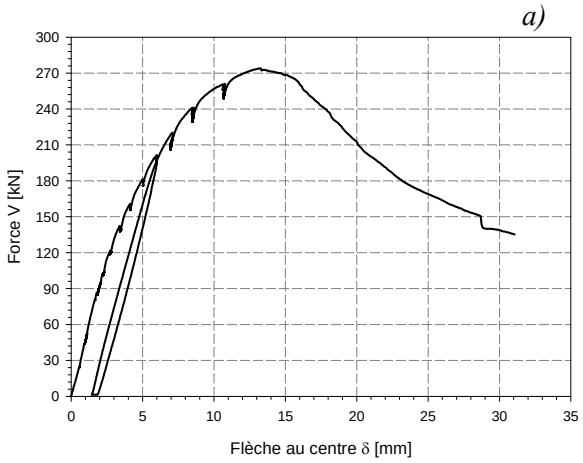

a) Relation force-flèche

b)

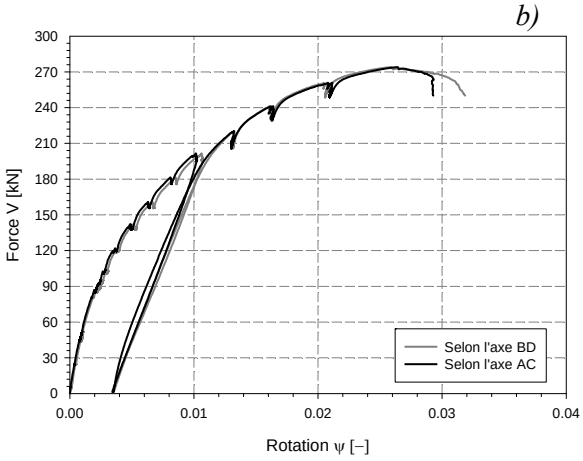

b) Relation force- rotation

c)

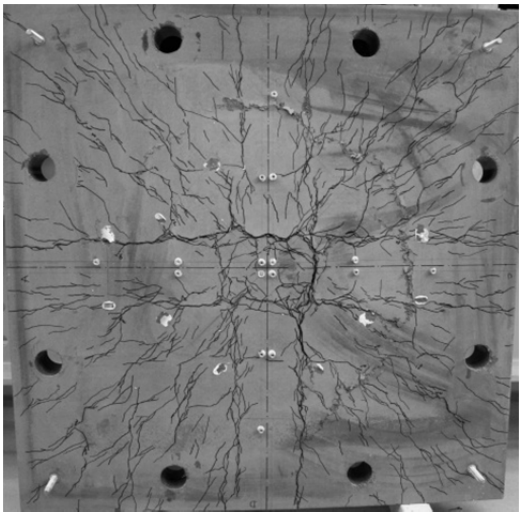

c) Fissuration de la face tendue

d)

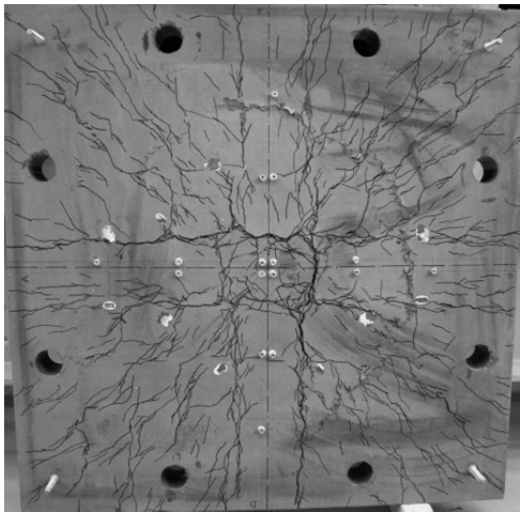

d) Fissuration de la face comprimée

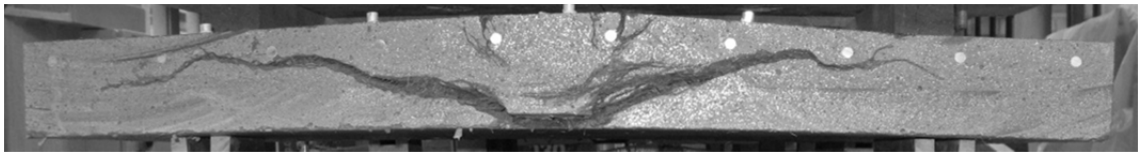

e) Vue de la fissuration interne après découpe de l'élément

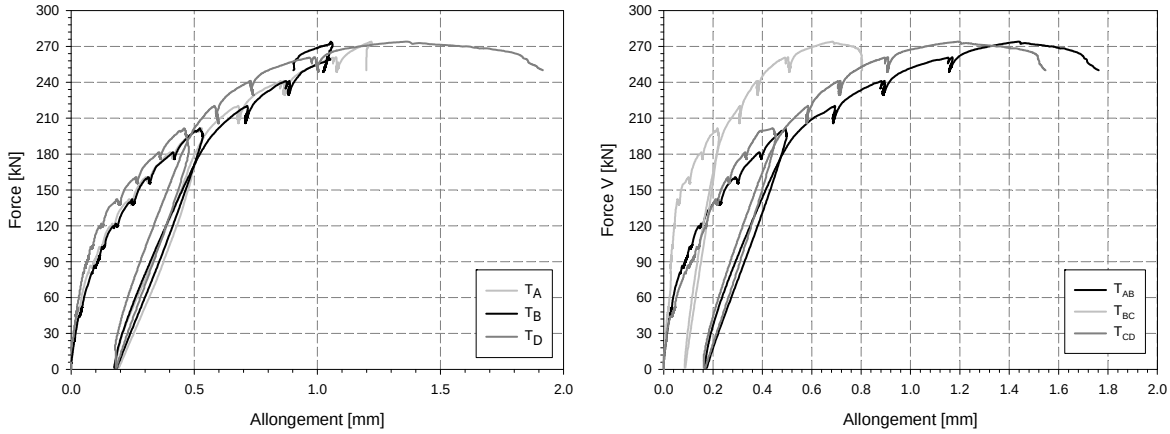

f) Relation force-allongements des capteurs tangentiels

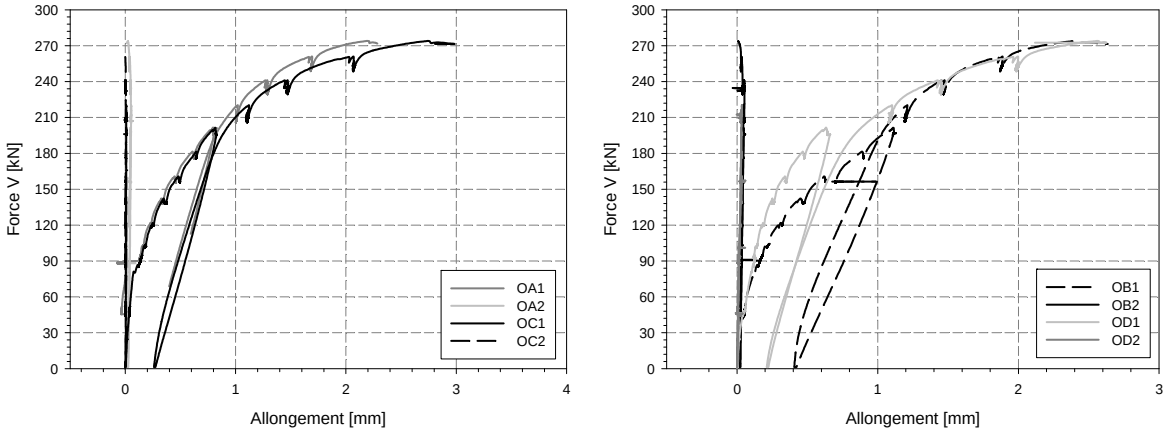

g) Relation force-allongements des capteurs radiaux

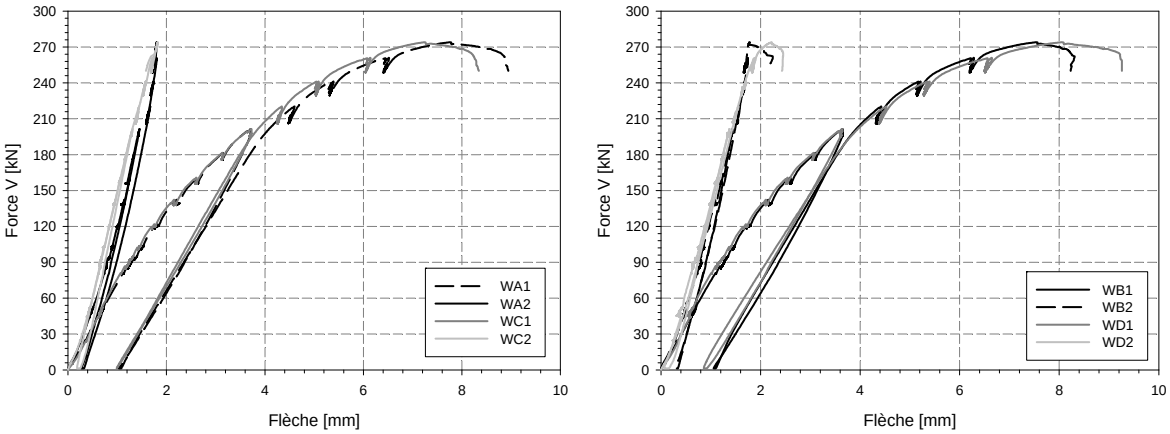

h) Relation force-flèches

Figures 3-8 : Résultats des essais - Dalle BCV_2%_80_1.10%

3.3. Série 3

3.3.1. Dalle BCV_1%A_30_0%

Béton : BCV 1% de fibres
Epaisseur : 30 mm
Pas d'armature passive

a)

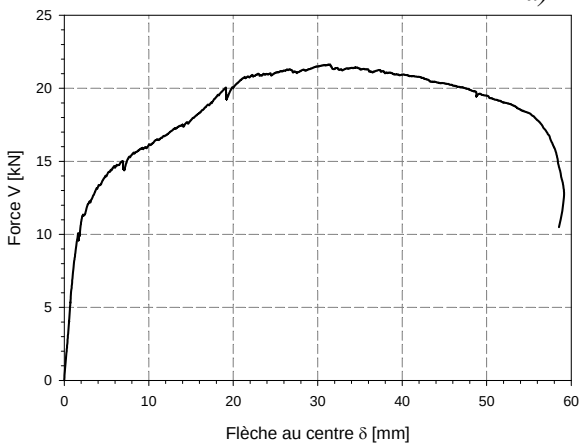

a) Relation force-flèche

b)

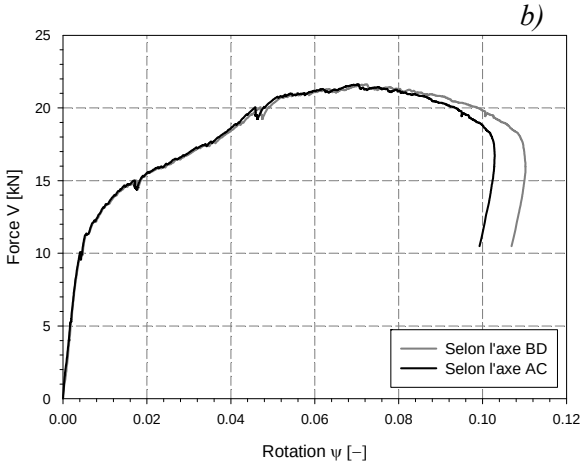

b) Relation force- rotation

c)

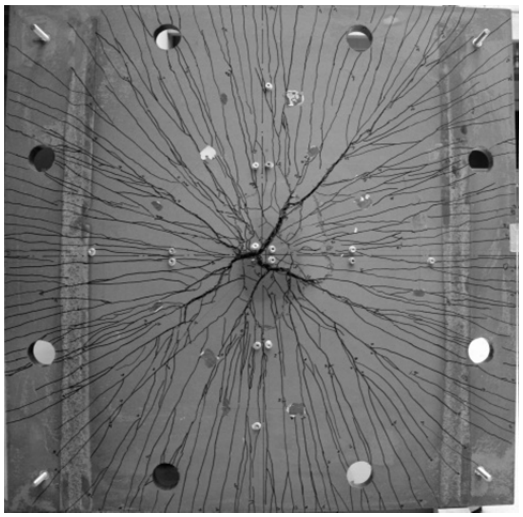

c) Fissuration de la face tendue

d)

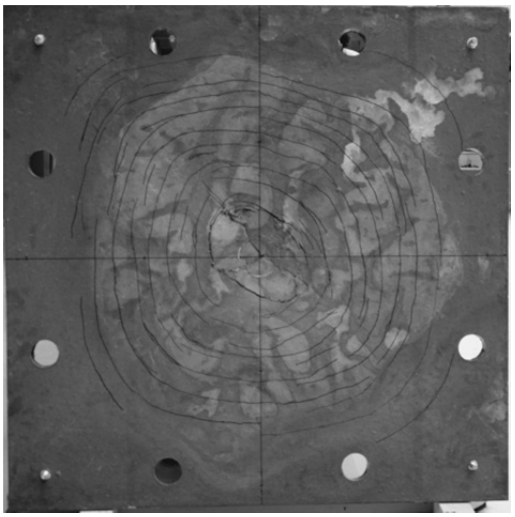

d) Fissuration de la face comprimée

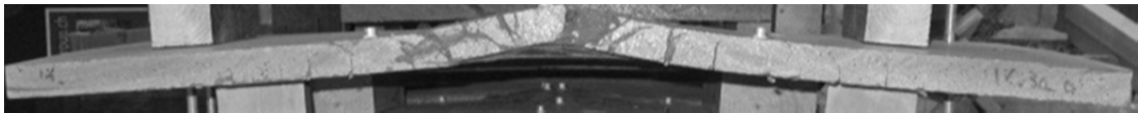

e) Vue de la fissuration interne après découpe de l'élément

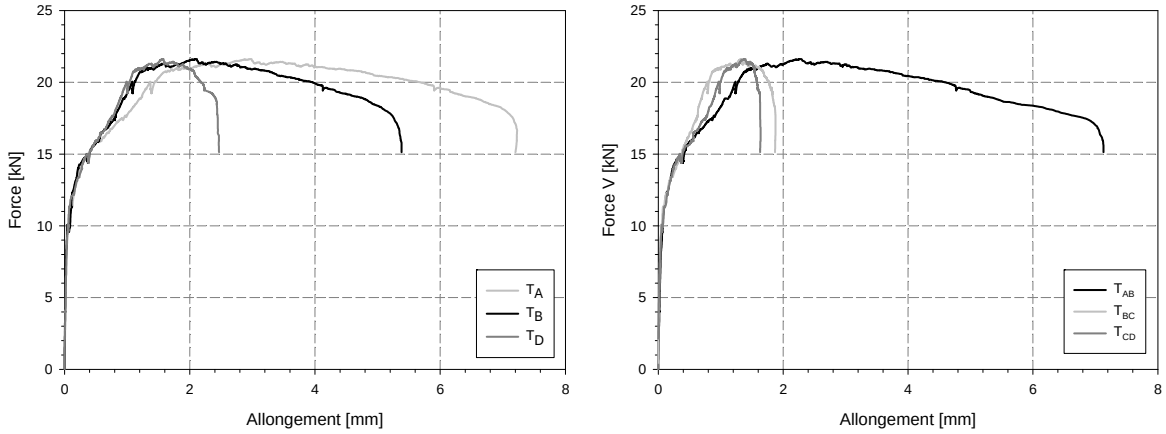

f) Relation force-allongements des capteurs tangentiels

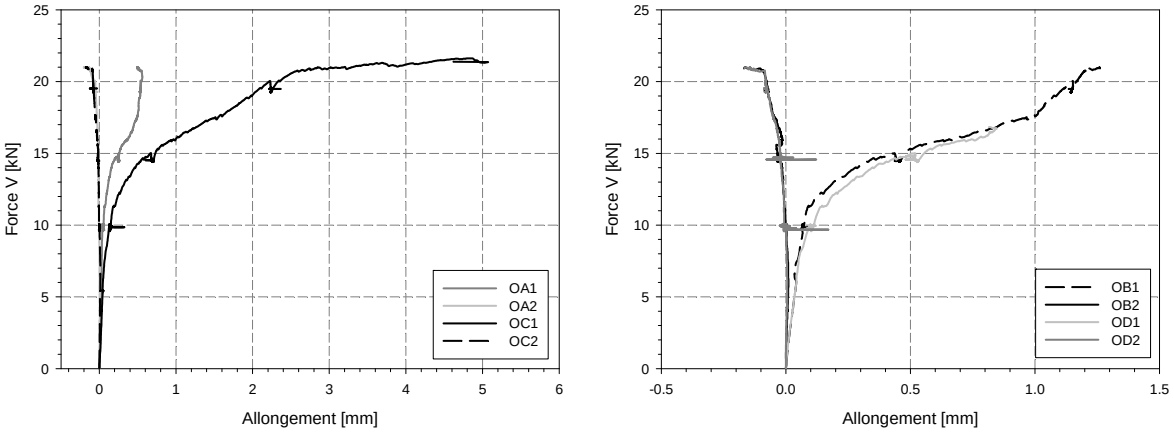

g) Relation force-allongements des capteurs radiaux

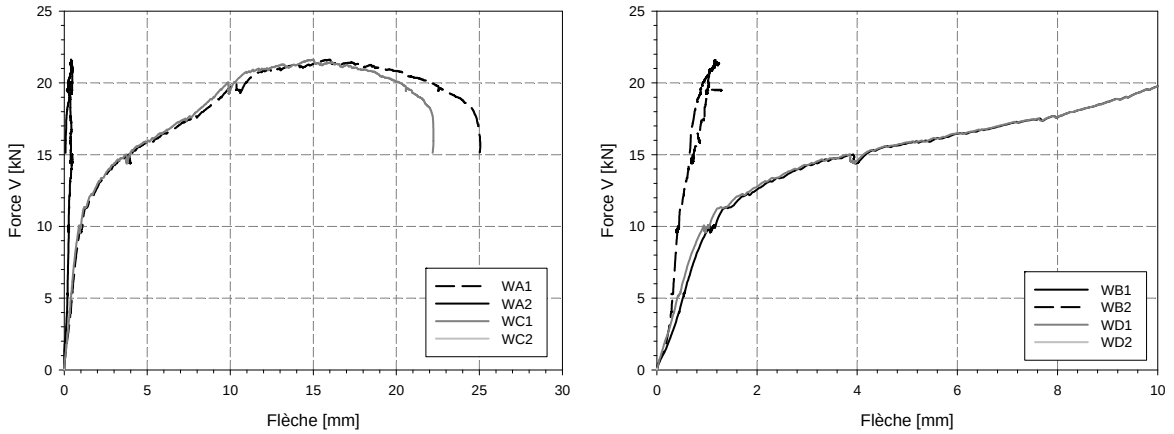

h) Relation force-flèches

Figures 3-9 : Résultats des essais - Dalle BCV_1%A_30_0%

3.3.2. Dalle BCV_1%A_40_1.02%

Béton : BCV 1% de fibres
Epaisseur : 30 mm
Taux d'armature : Ø5 #100 ρ_s = 1.02%

a)

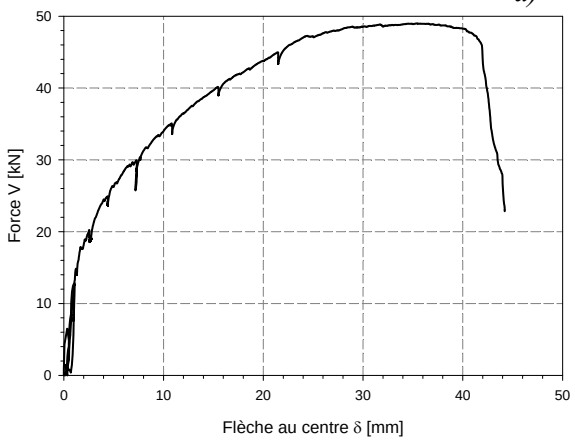

a) Relation force-flèche

b)

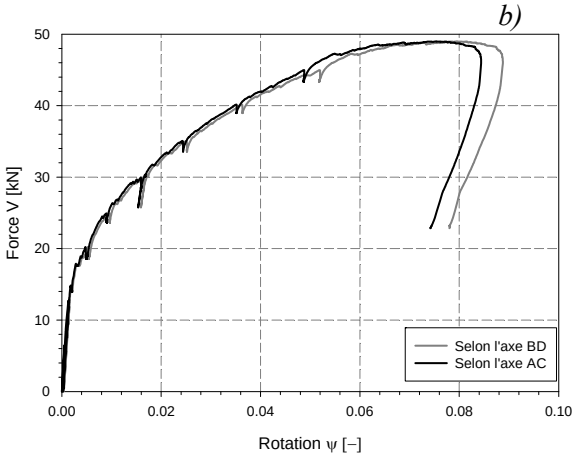

b) Relation force- rotation

c)

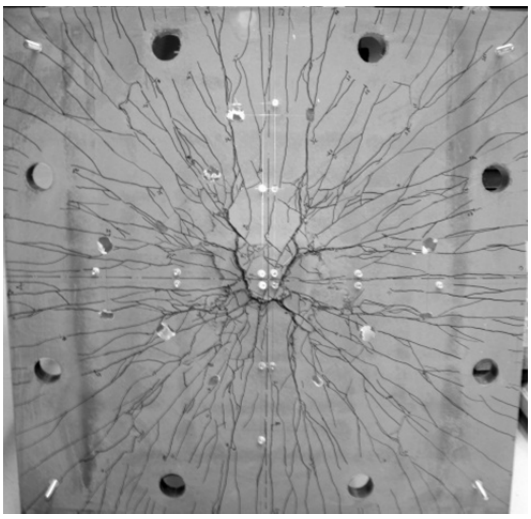

c) Fissuration de la face tendue

d)

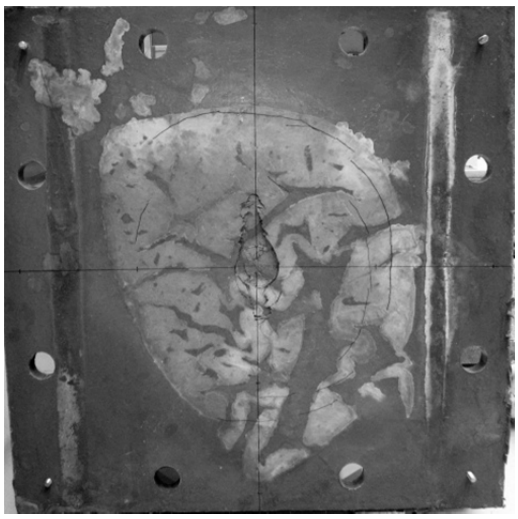

d) Fissuration de la face comprimée

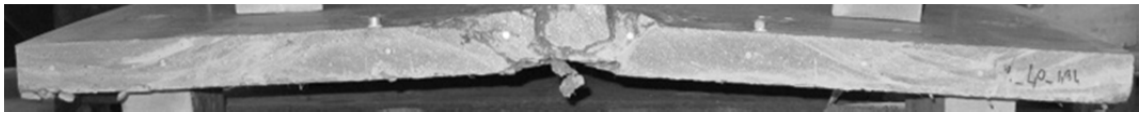

e) Fissuration interne dans la partie centrale

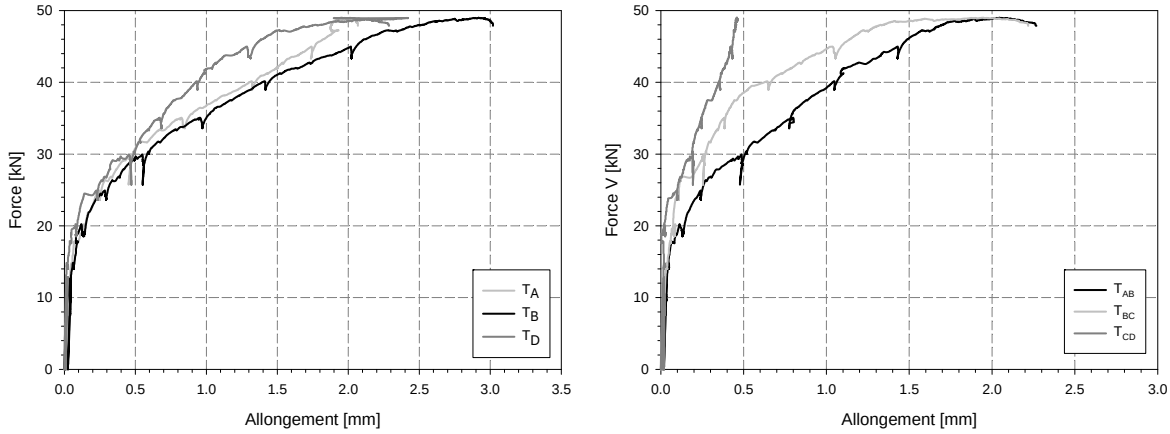

f) Relation force-allongements des capteurs tangentiels

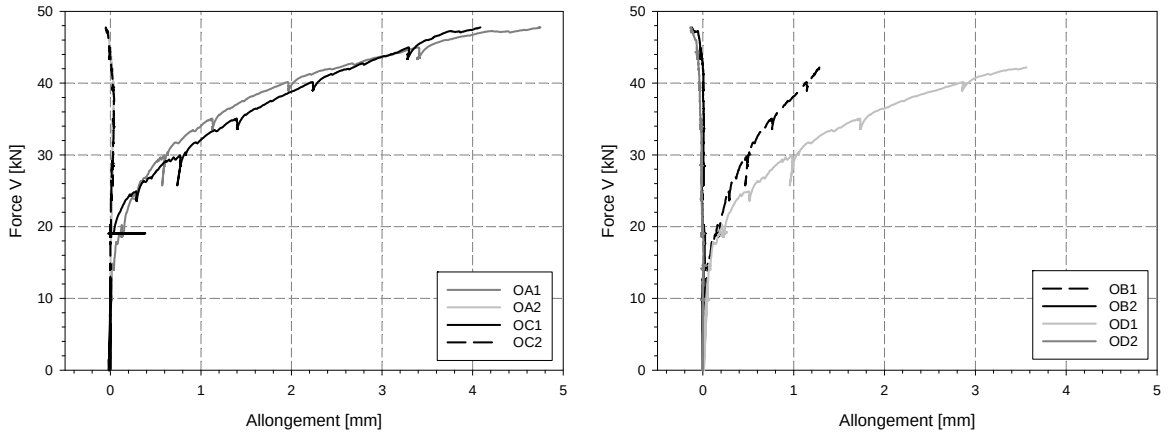

g) Relation force-allongements des capteurs radiaux

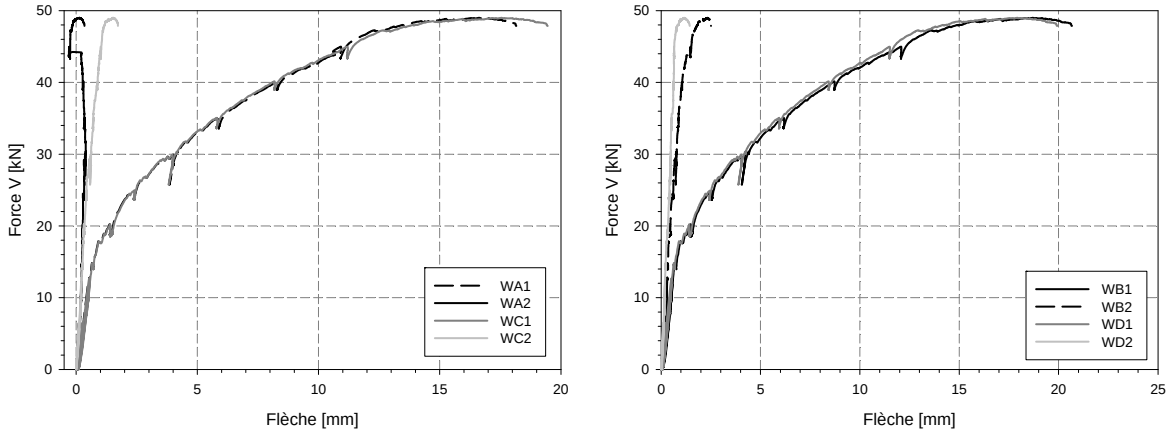

h) Relation force-flèches

Figures 3-10 : Résultats des essais - Dalle BCV_1%A_40_1.02%

3.3.3. Dalle BCV_1%A_60_2.05%

Béton : BCV 1% de fibres
Epaisseur : 60 mm
Taux d'armature : Ø10 #100, ρ_s = 2.05%

a)

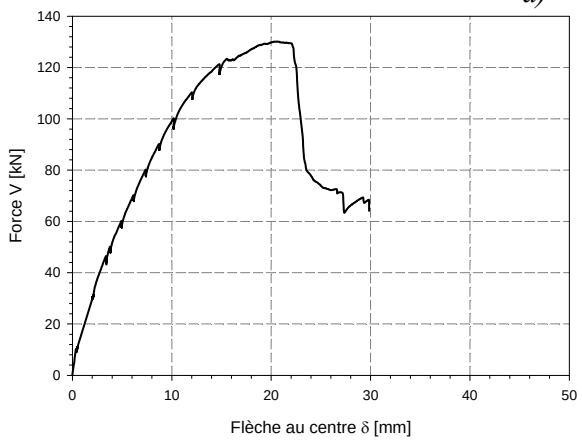

a) Relation force-flèche

b)

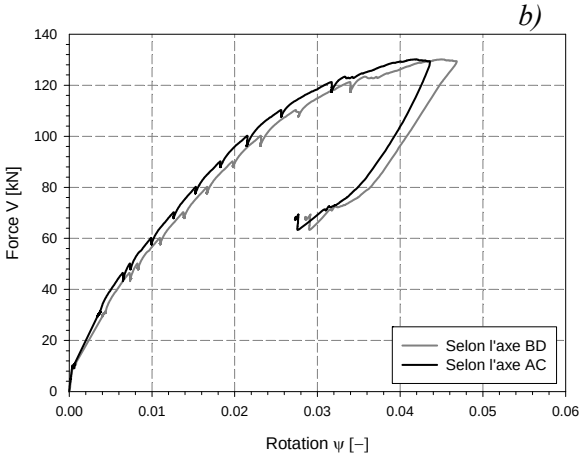

b) Relation force- rotation

c)

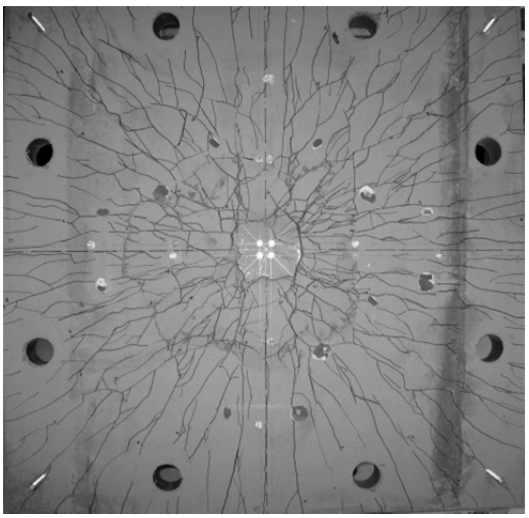

c) Fissuration de la face tendue

d)

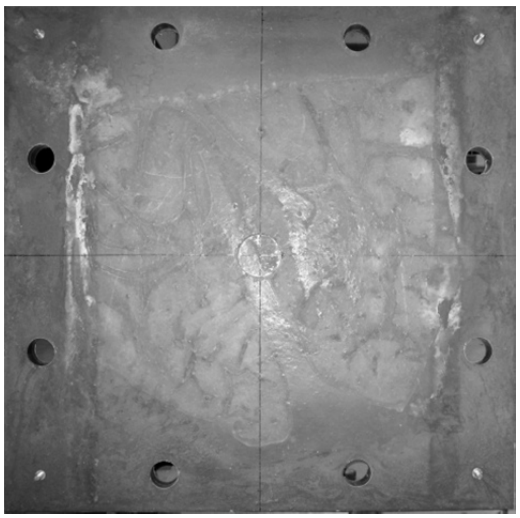

d) Fissuration de la face comprimée

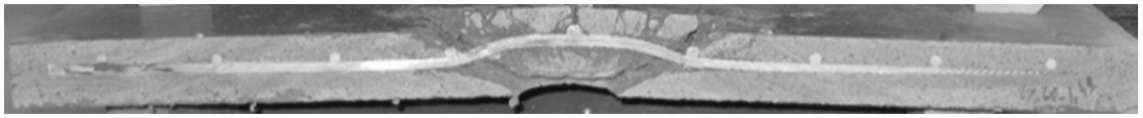

e) Vue de la fissuration interne après découpe de l'élément

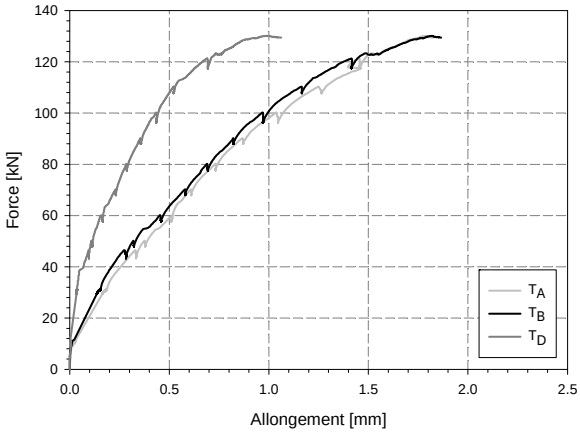

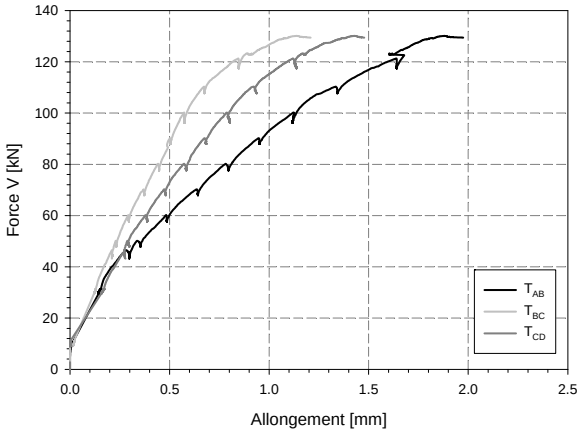

f) Relation force-allongements des capteurs tangentiels

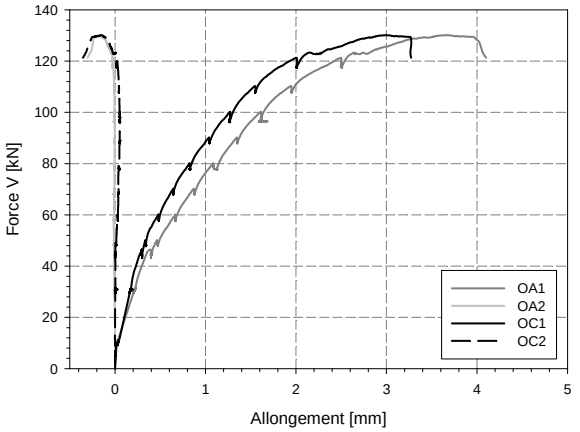

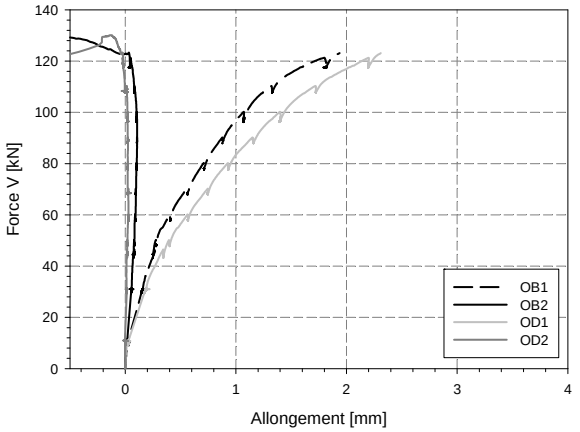

g) Relation force-allongements des capteurs radiaux

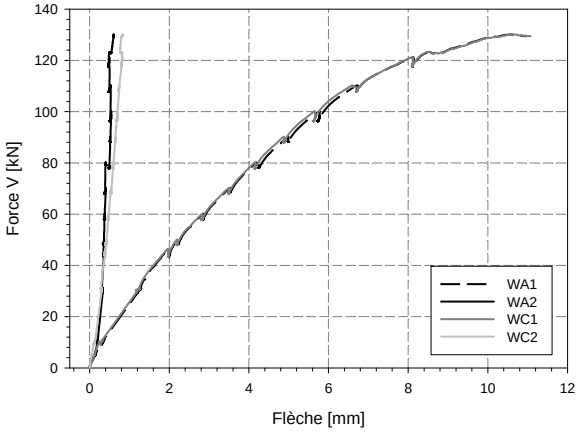

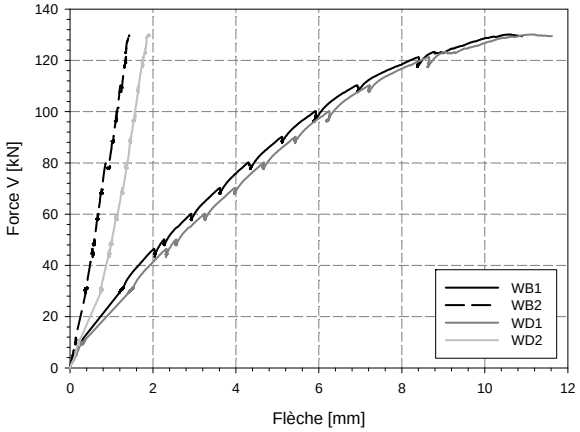

h) Relation force-flèches

Figures 3-11 : Résultats des essais - Dalle BCV_1%A_60_2.05%

3.3.4. Dalle BCV_1%_80_1.10%

Béton : BCV 1% de fibres
Epaisseur : 80 mm
Armature : Ø9 #100, ρ_s = 1.10%

a)

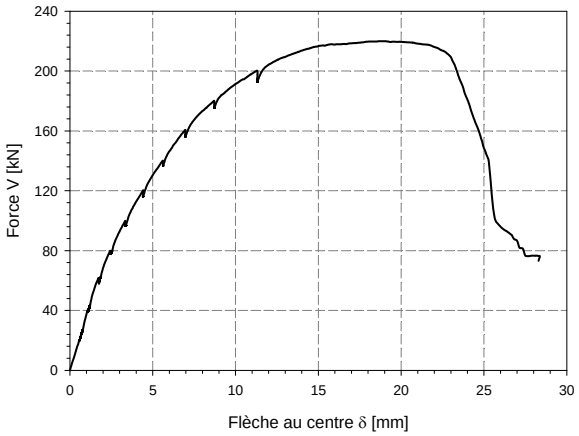

a) Relation force-flèche

b)

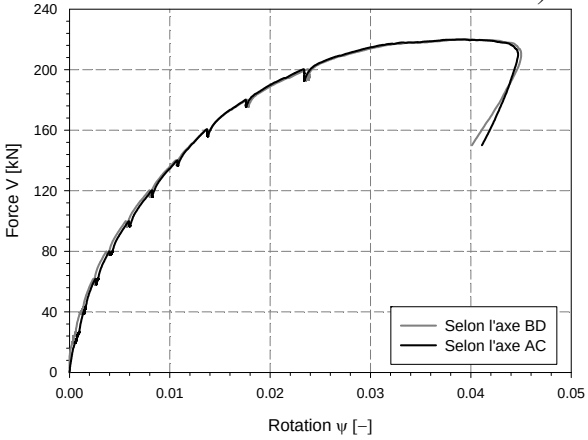

b) Relation force- rotation

c)

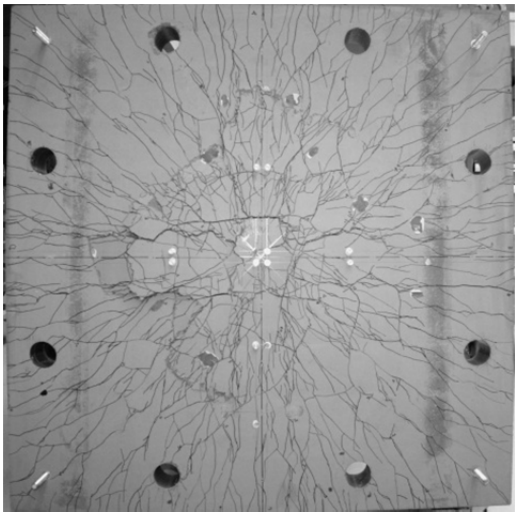

c) Fissuration de la face tendue

d)

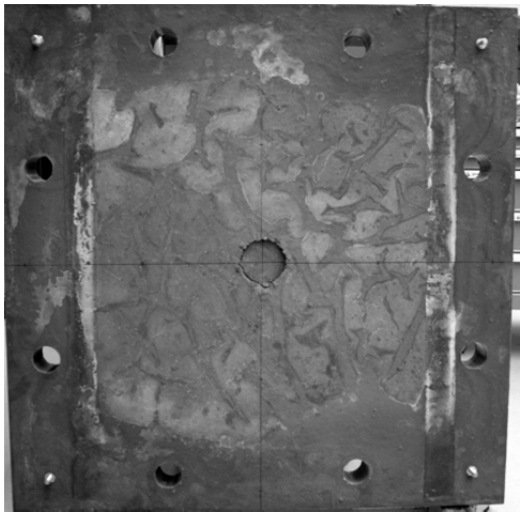

d) Fissuration de la face comprimée

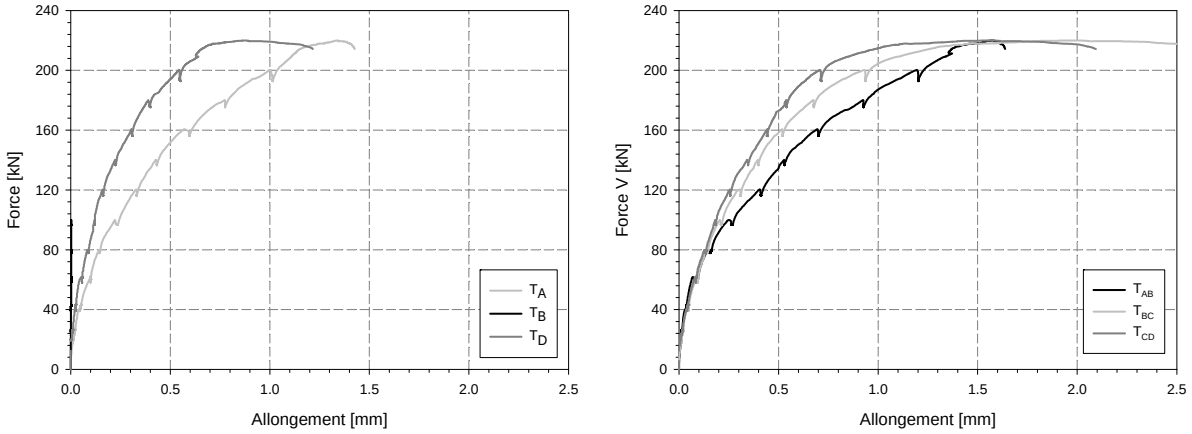

d) Relation force-allongements des capteurs tangentiels

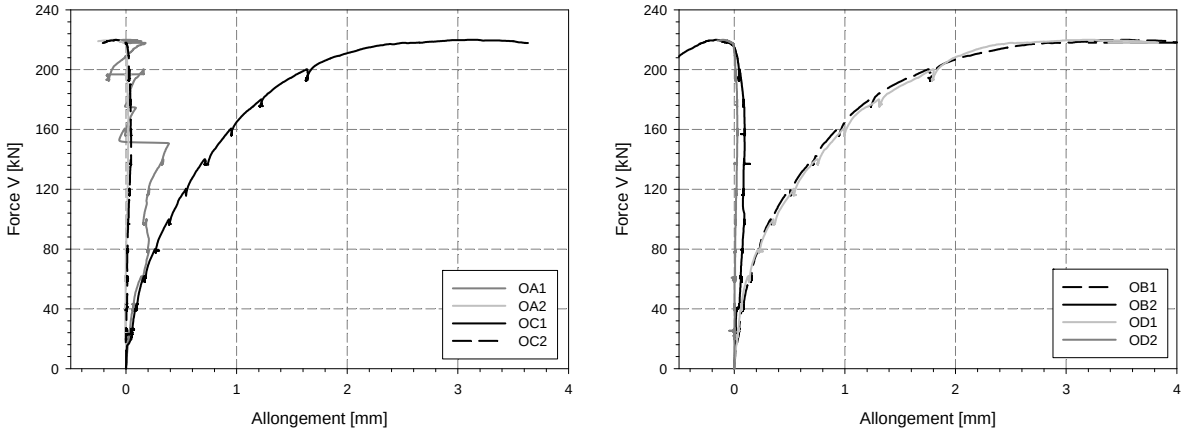

e) Relation force-allongements des capteurs radiaux

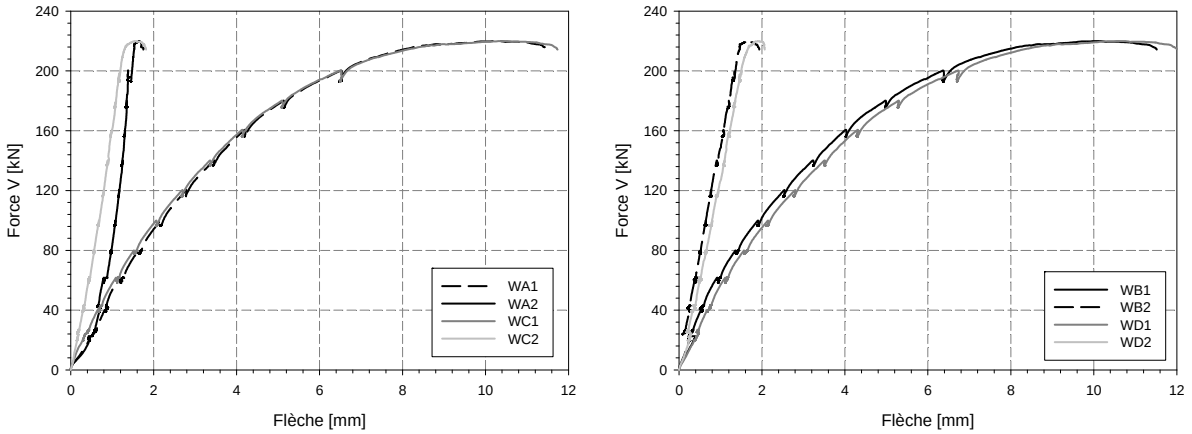

f) Relation force-flèches

Figures 3-12 : Résultats des essais - Dalle BCV_1%_80_1.10%

3.4. Série 4

3.4.1. Dalle BCV_1%A_40_RB

Béton : BCV 1% de fibres
Epaisseur : 40 mm
Type d'armatures : Ø10 #50, nervurées

a)

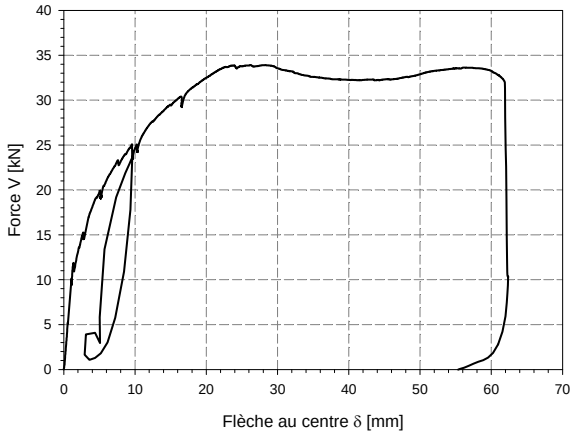

a) Relation force-flèche

b)

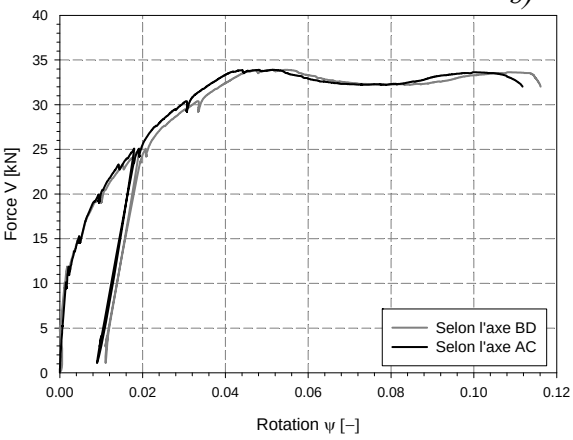

b) Relation force- rotation

c)

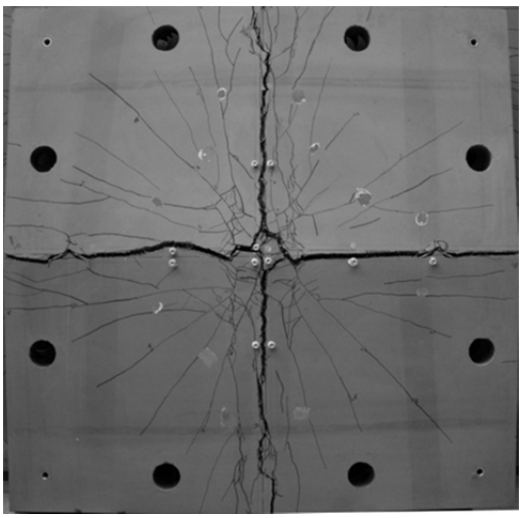

c) Fissuration de la face tendue

d)

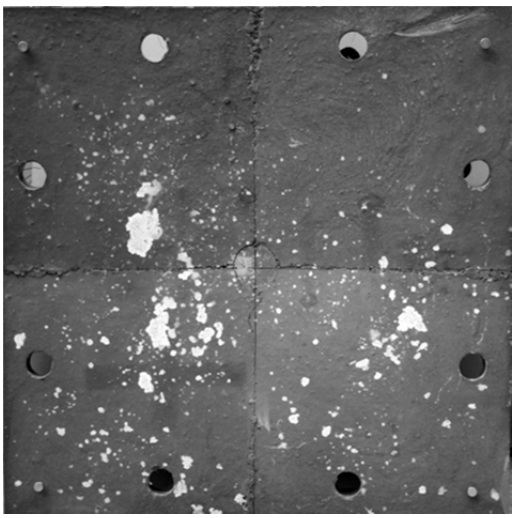

d) Fissuration de la face comprimée

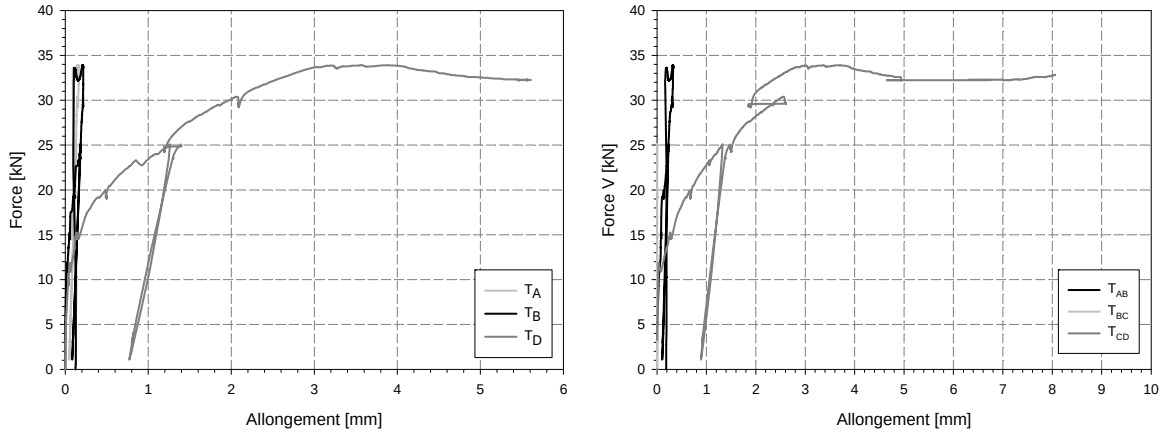

d) Relation force-allongements des capteurs tangentiels

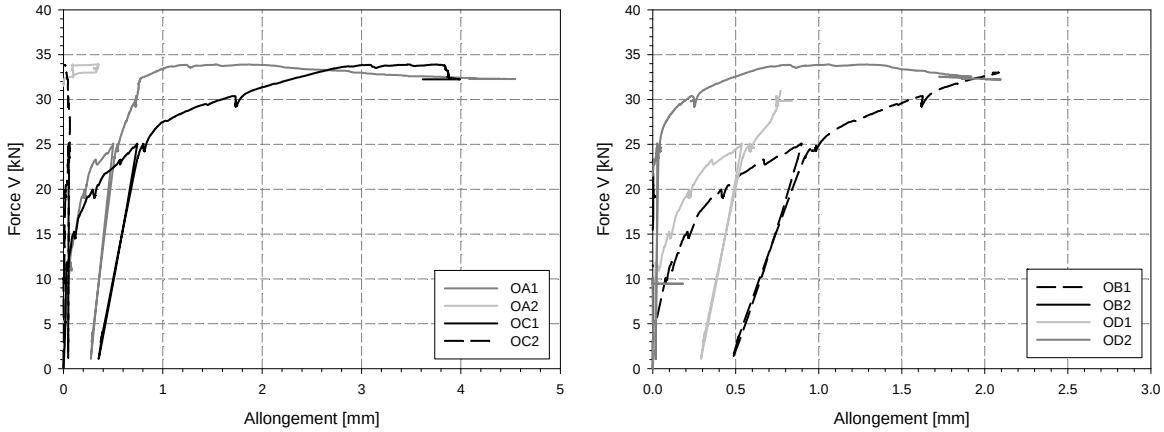

e) Relation force-allongements des capteurs radiaux

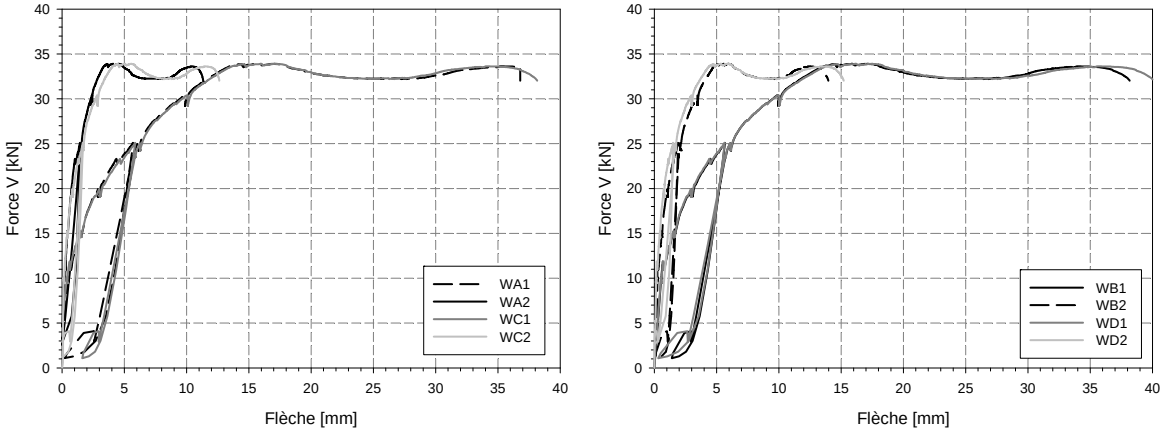

f) Relation force-flèches

Figures 3-13 : Résultats des essais - Dalle BCV_1%A_40_RB

3.4.2. Dalle BCV_1%A_40_SB

Béton : BCV 1% de fibres
Epaisseur : 40 mm
Type d'armatures : Ø10 #50, lisses

a)

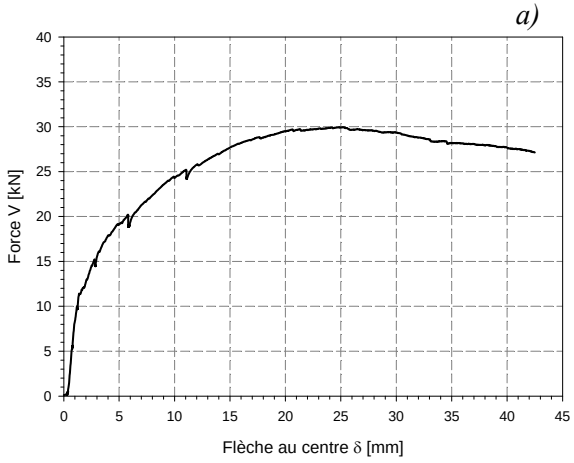

a) Relation force-flèche

b)

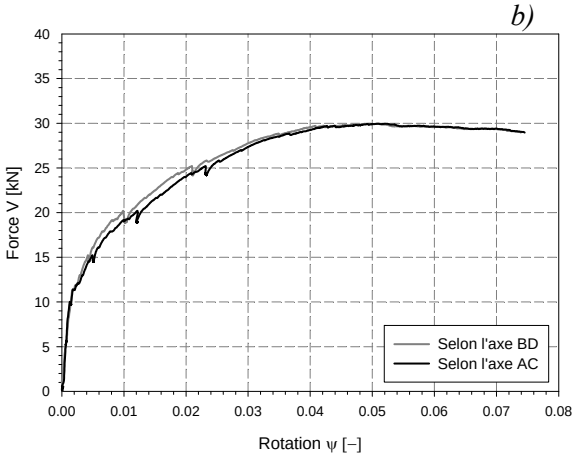

b) Relation force- rotation

c)

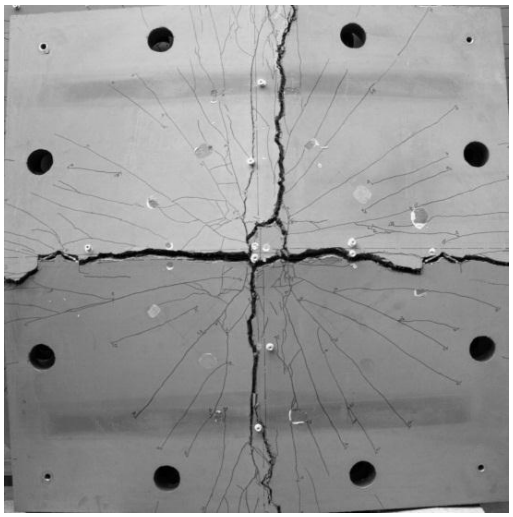

c) Fissuration de la face tendue

d)

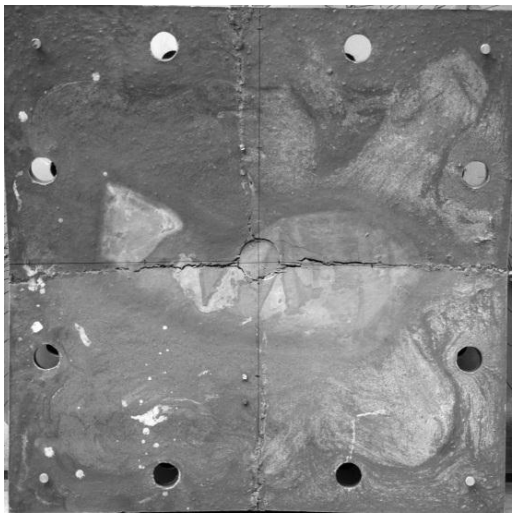

d) Fissuration de la face comprimée

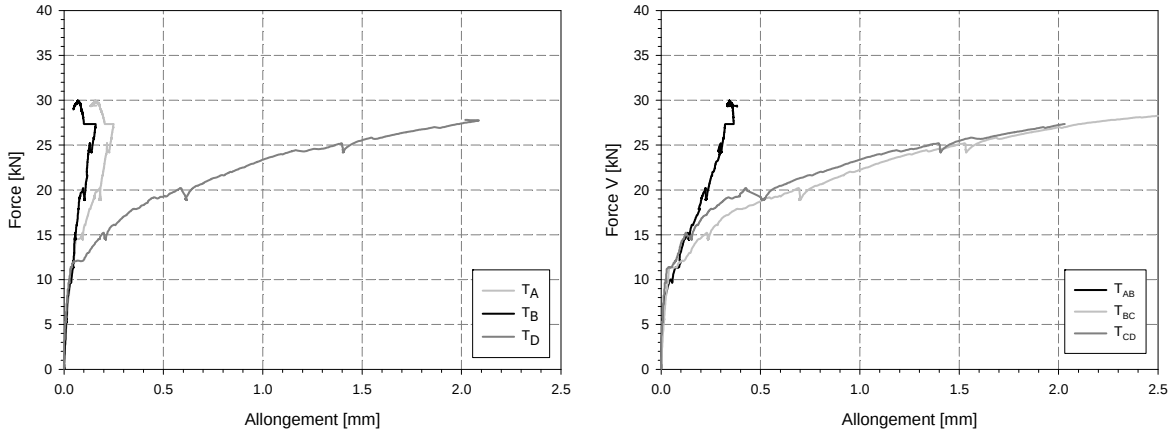

e) Relation force-allongements des capteurs tangentiels

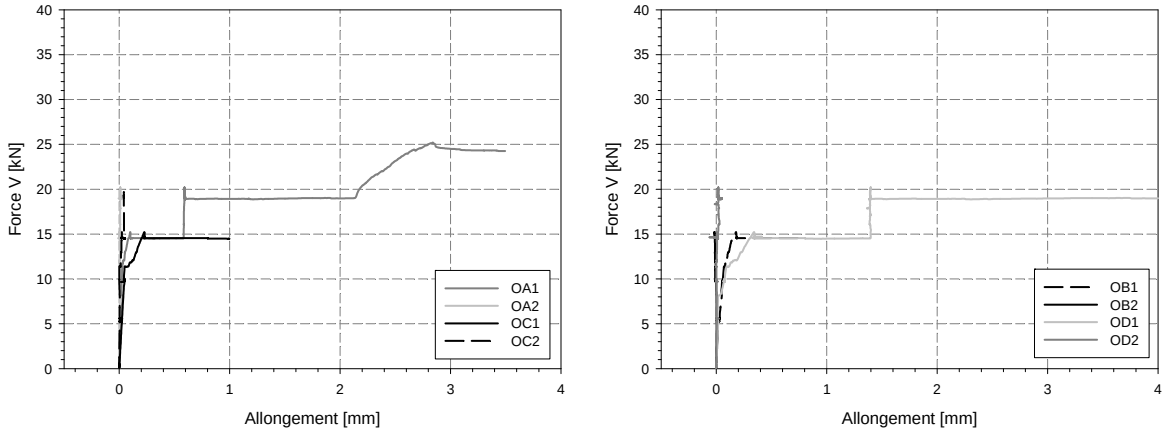

f) Relation force-allongements des capteurs radiaux

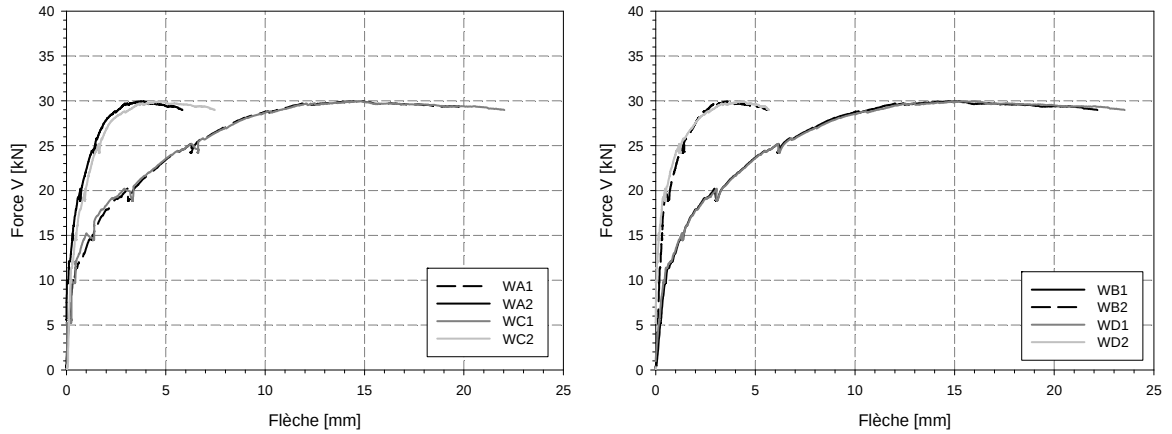

g) Relation force-flèches

Figures 3-14 : Résultats des essais - Dalle BCV_1%A_40_SB

3.5. Série 5

3.5.1. Dalle BCV_2%_40_RB

Béton : BCV 2% de fibres
Epaisseur : 40 mm
Type d'armatures : Ø10 #50, nervurées

a)

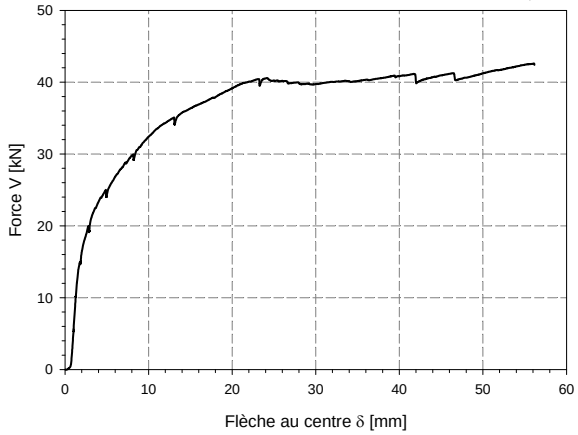

a) Relation force-flèche

b)

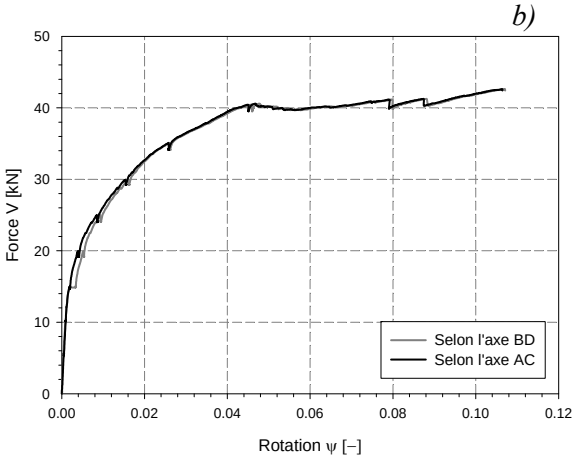

b) Relation force- rotation

c)

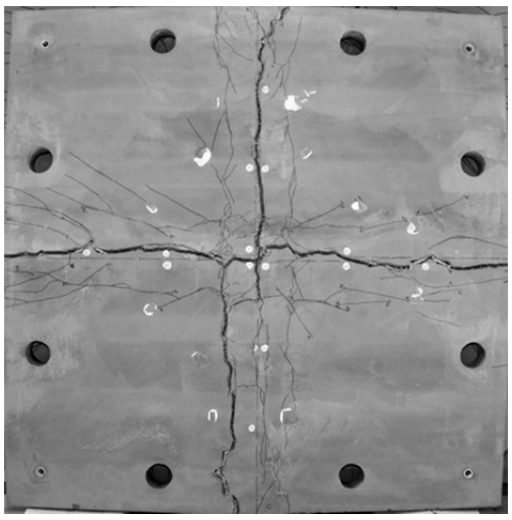

c) Fissuration de la face tendue

d)

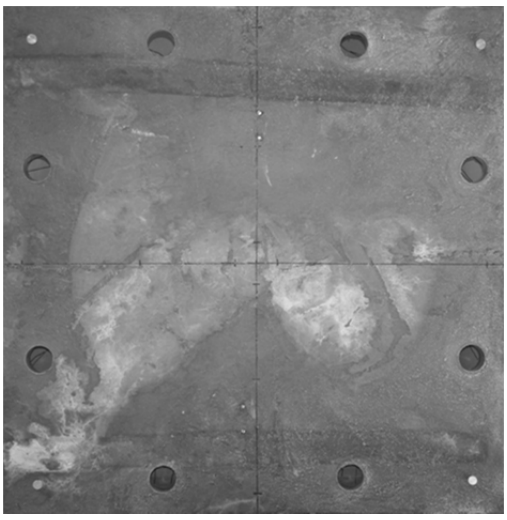

d) Fissuration de la face comprimée

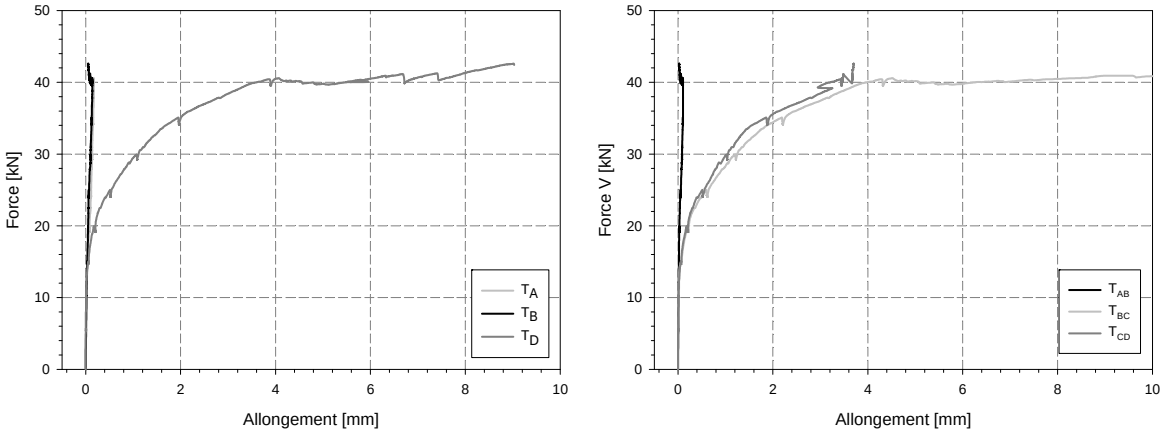

e) Relation force-allongements des capteurs tangentiels

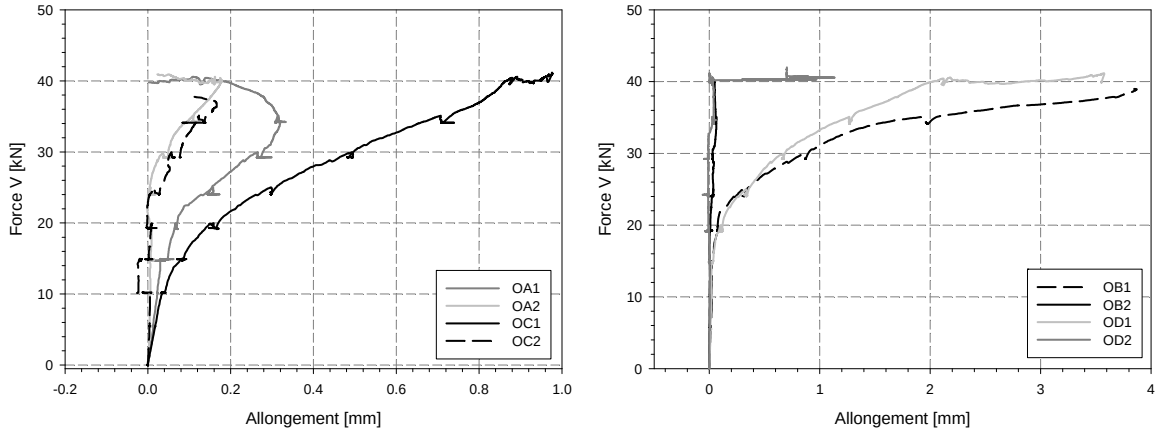

f) Relation force-allongements des radiaux

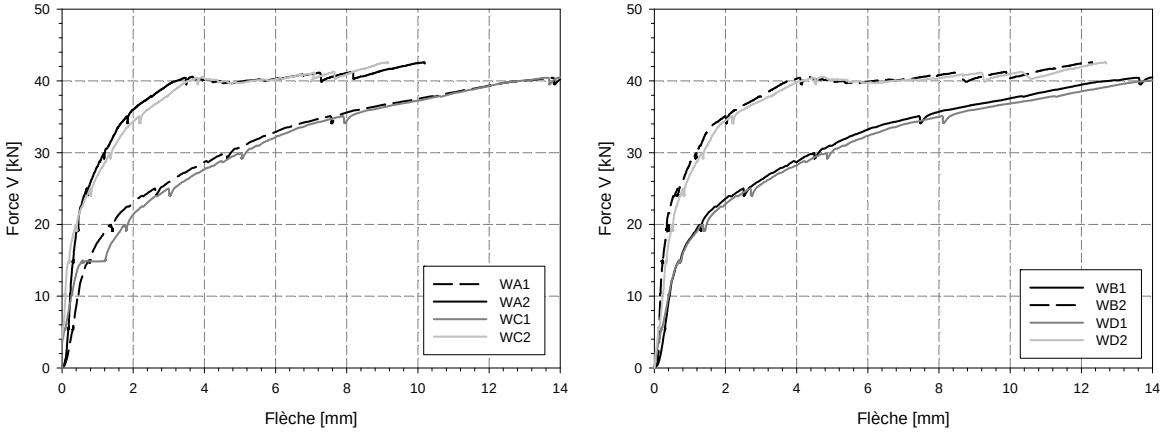

g) Relation force-flèches

Figures 3-15 : Résultats des essais - Dalle BCV_2%_40_RB

3.5.2. Dalle BCV_2%_40_SB

Béton : BCV 2% de fibres
Epaisseur : 40 mm
Type d'armatures : Ø10 #50, lisses

a)

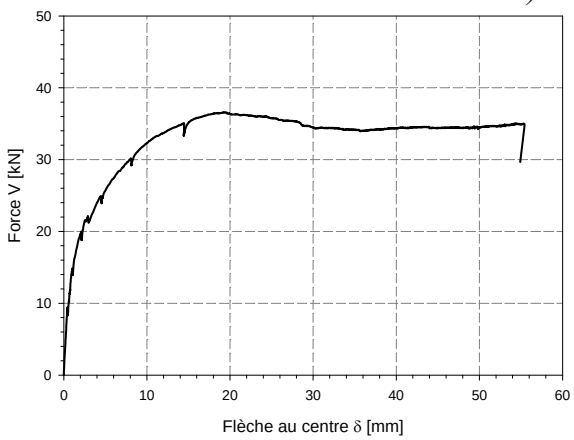

a) Relation force-flèche

b)

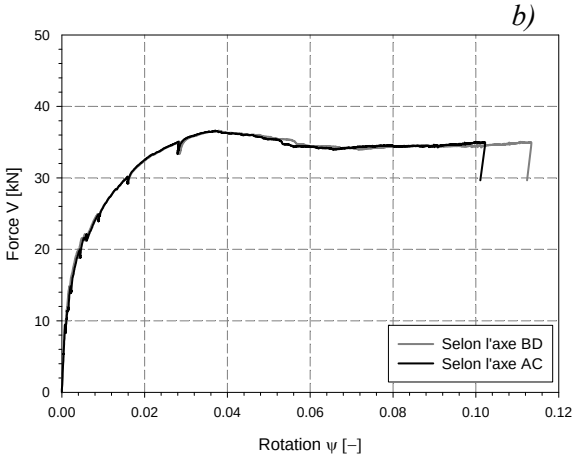

b) Relation force- rotation

c)

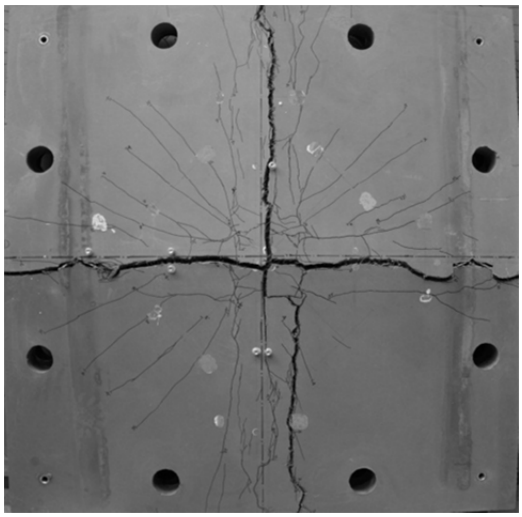

c) Fissuration de la face tendue

d)

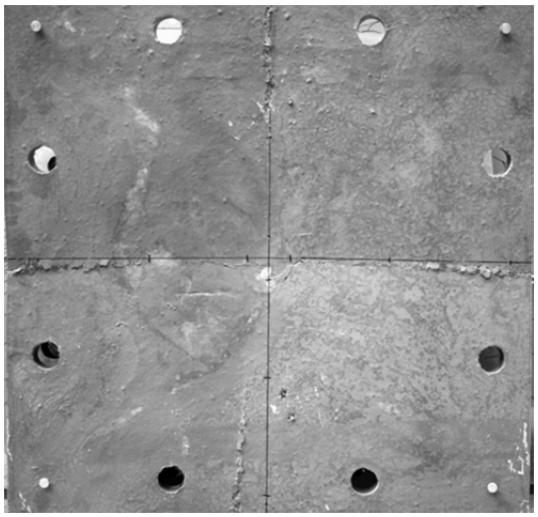

d) Fissuration de la face comprimée

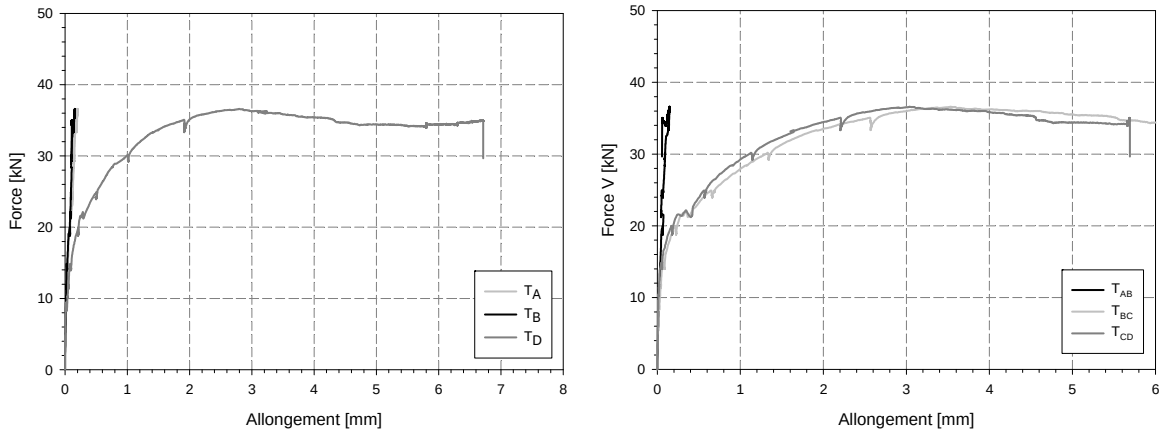

e) Relation force-allongements des capteurs tangentiels

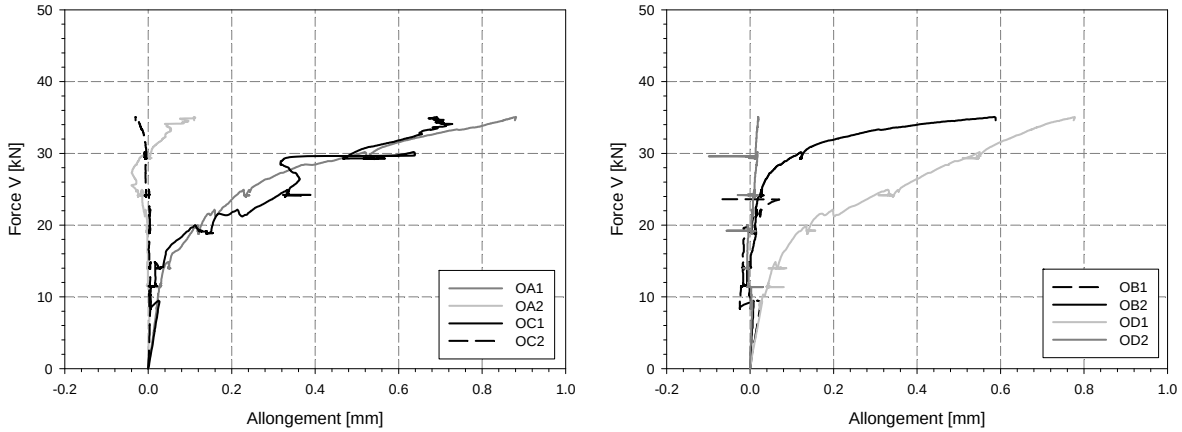

f) Relation force-allongements des capteurs radiaux

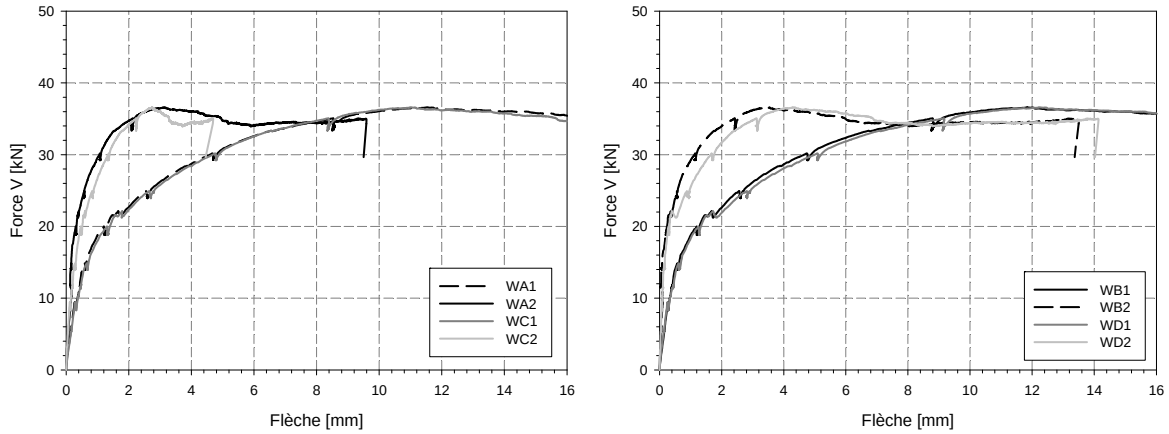

g) Relation force-flèches

Figures 3-16 : Résultats des essais - Dalle BCV_2%_40_RB

3.6. Série 6

3.6.1. BCV_2%_60_1.49%

Béton : BCV 2% de fibres
Epaisseur : 60 mm
Type d'armatures : Ø9 #100, ρ_s = 1.49%

a)

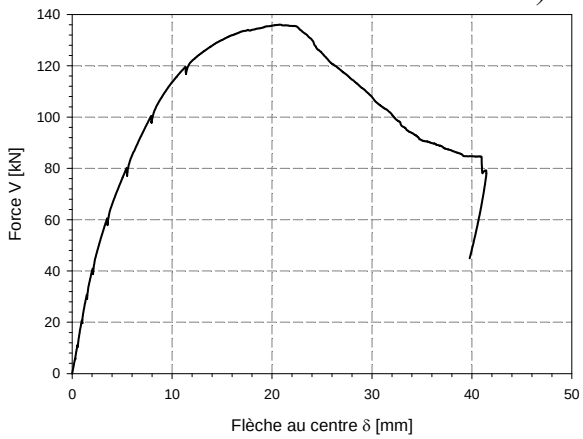

a) Relation force-flèche

b)

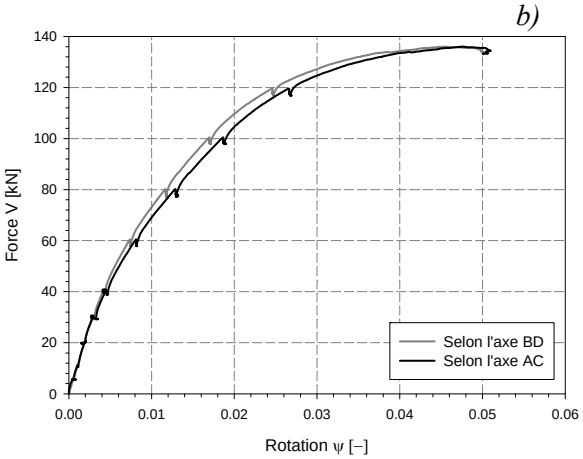

b) Relation force- rotation

c)

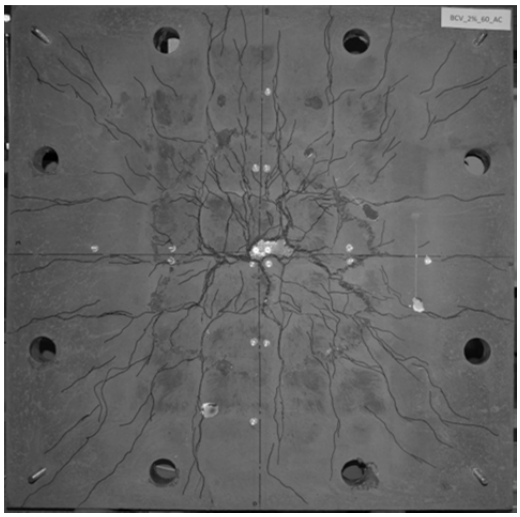

c) Fissuration de la face tendue

d)

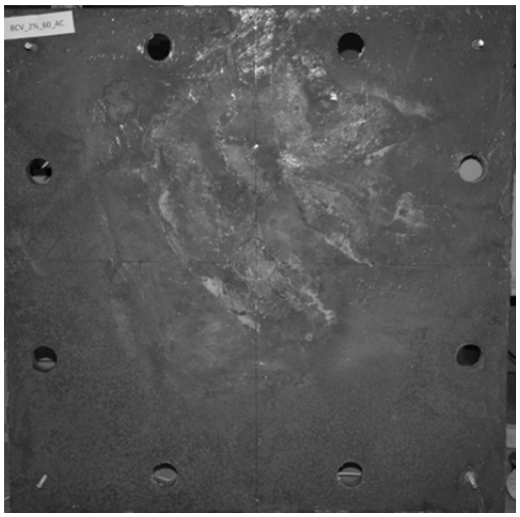

d) Fissuration de la face comprimée

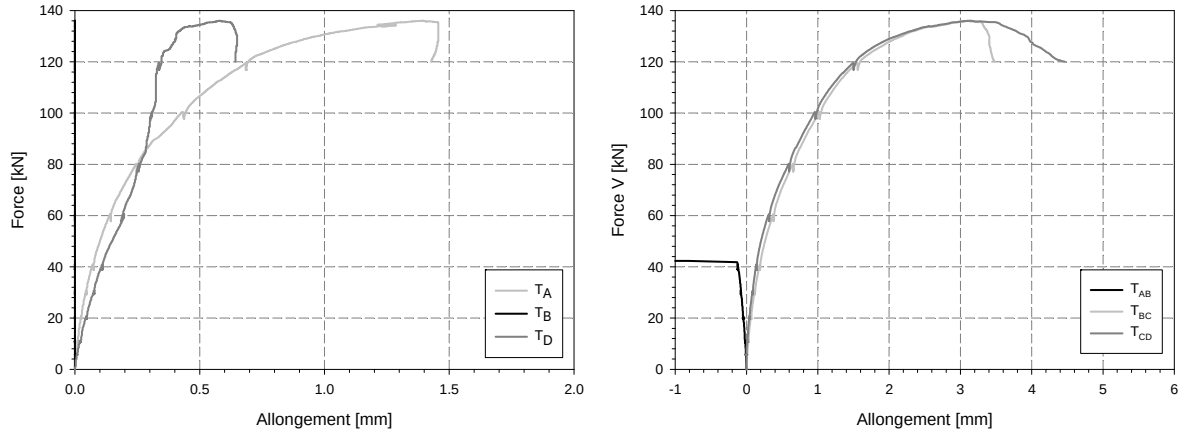

e) Relation force-allongements des capteurs tangentiels

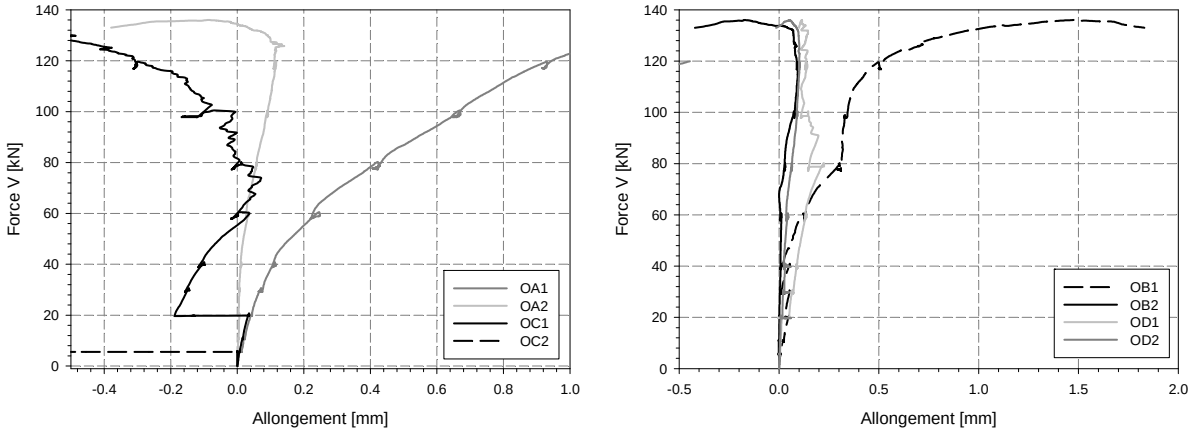

f) Relation force-allongements des capteurs radiaux

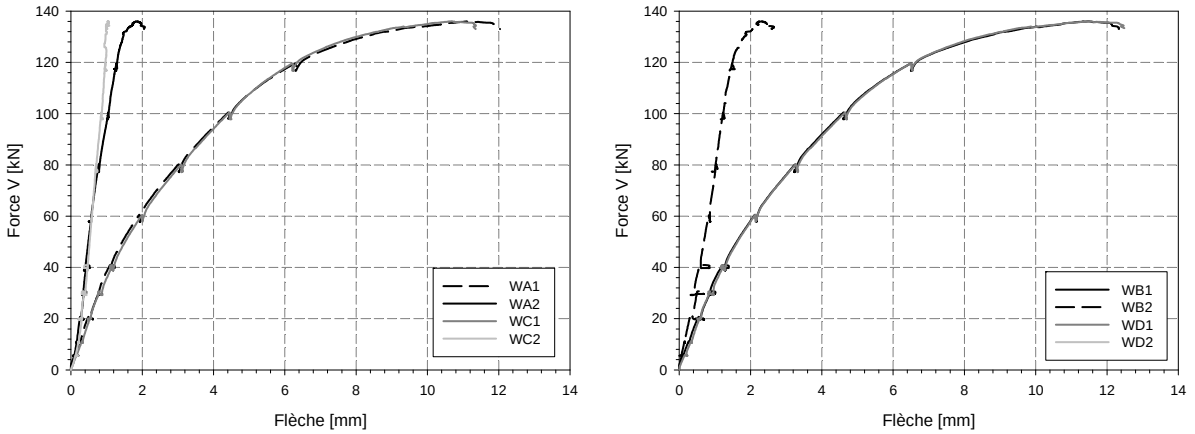

g) Relation force-flèche

Figures 3-17 : Résultats des essais - Dalle BCV_2%_60_1.49%

3.6.2. BCV_2%_80_1.77%

Béton : BCV 2% de fibres
Epaisseur : 80 mm
Type d'armatures : Ø12 #100, ρ_s = 1.77%

a)

a) Relation force-flèche

b)

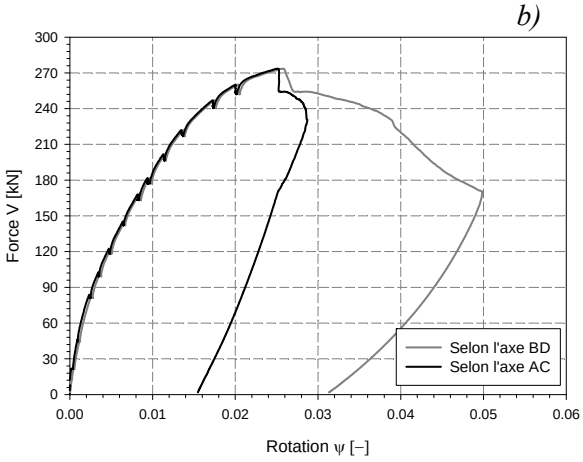

b) Relation force- rotation

c)

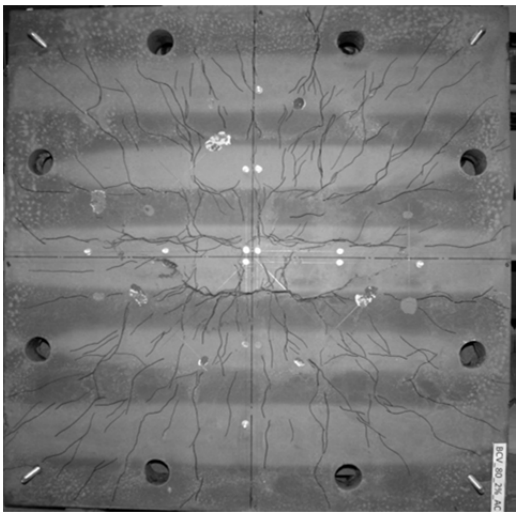

c) Fissuration de la face tendue

d)

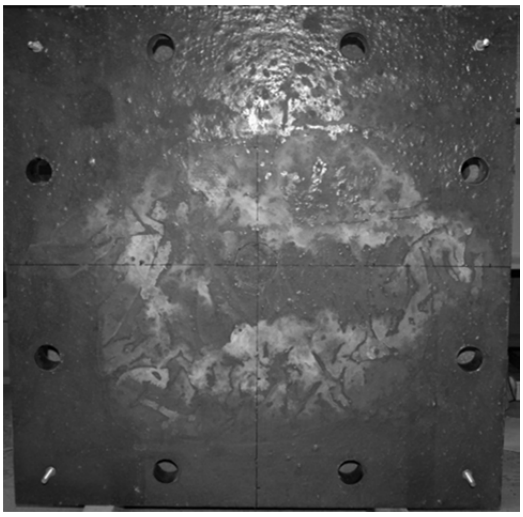

d) Fissuration de la face comprimée

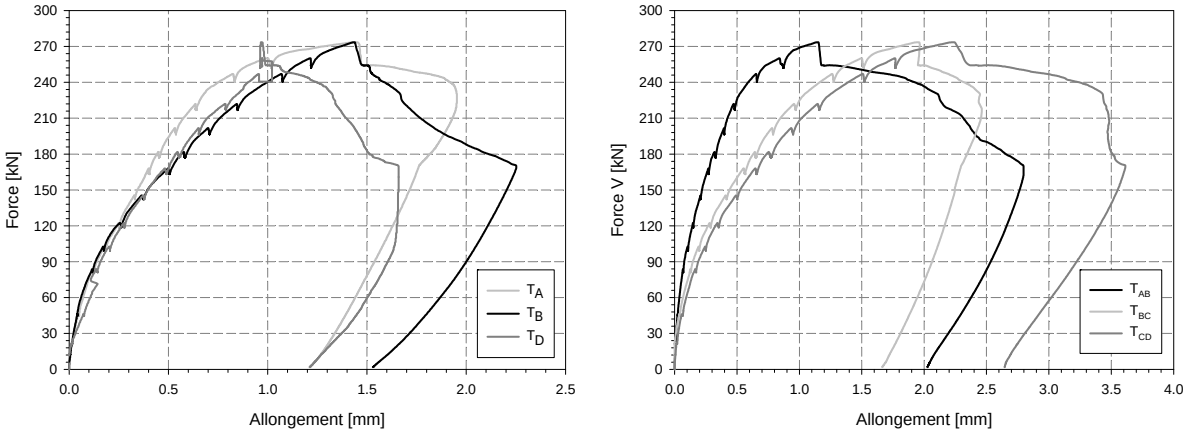

e) Relation force-allongements des capteurs tangentiels

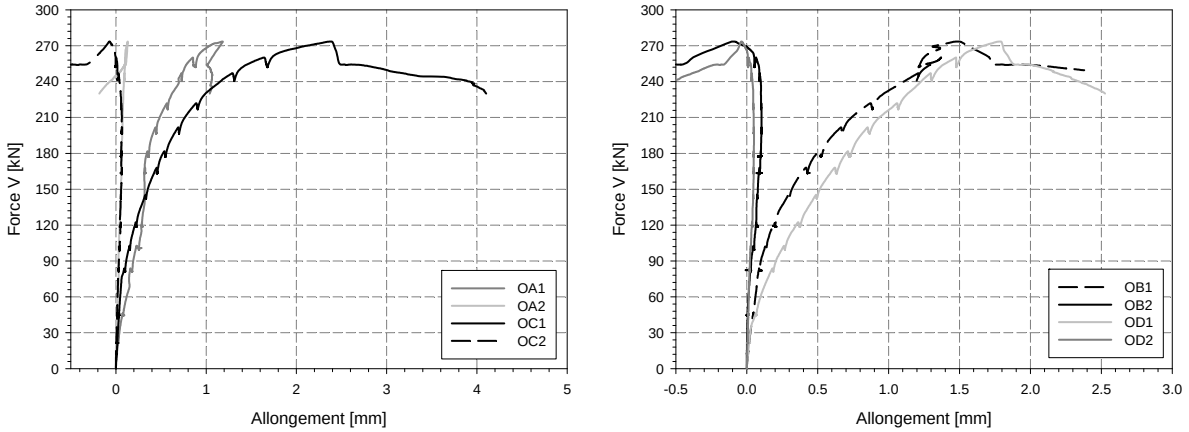

f) Relation force-allongements des capteurs radiaux

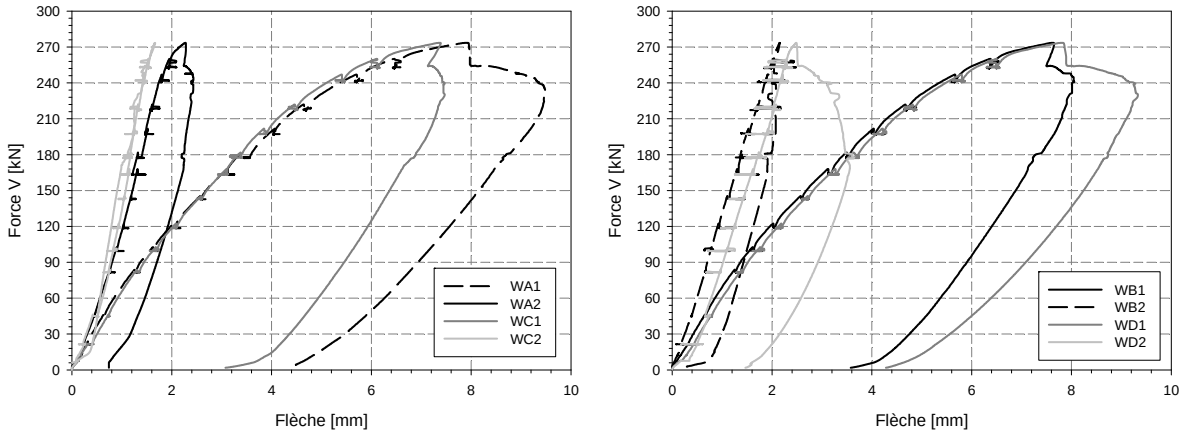

g) Relation force-flèche

Figures 3-18 : Résultats des essais - Dalle BCV_2%_80_1.77%

3.7. Série 7

3.7.1. BCV_1% _30_2.67%

Béton : BCV 1% de fibres
Epaisseur : 30 mm
Type d'armatures : Ø7 #100, ρ_s = 2.67%

a)

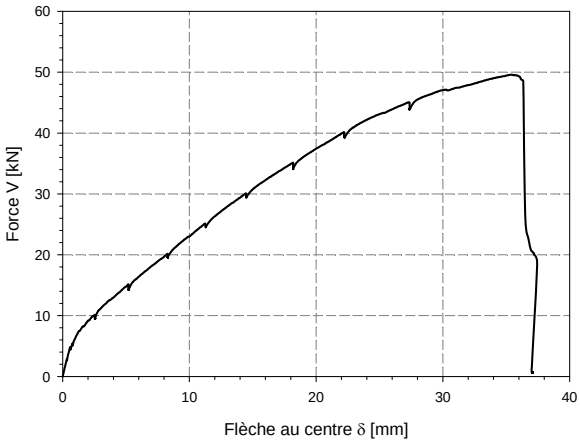

a) Relation force-flèche

b)

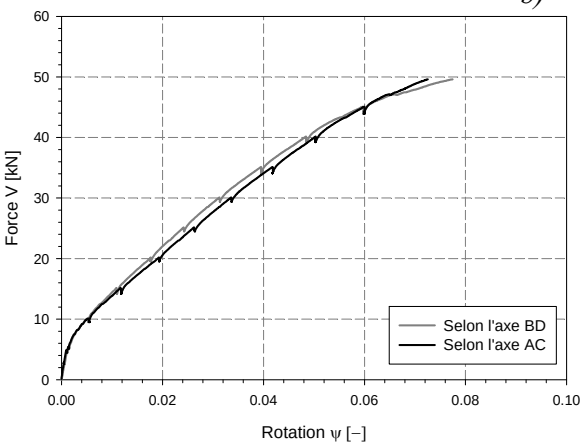

b) Relation force- rotation

c)

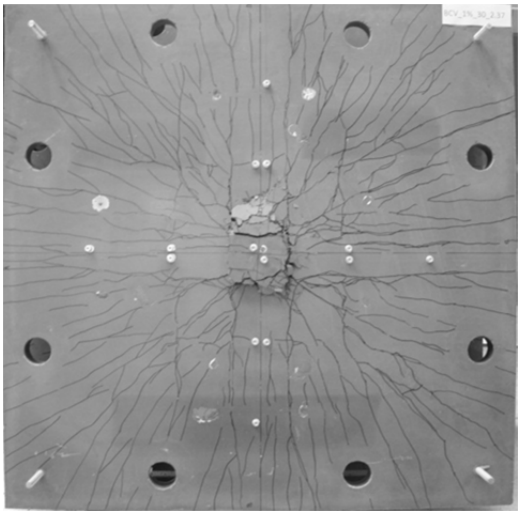

c) Fissuration de la face tendue

d)

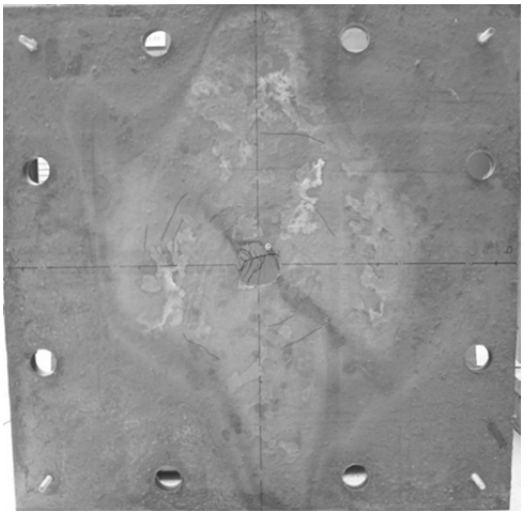

d) Fissuration de la face comprimée

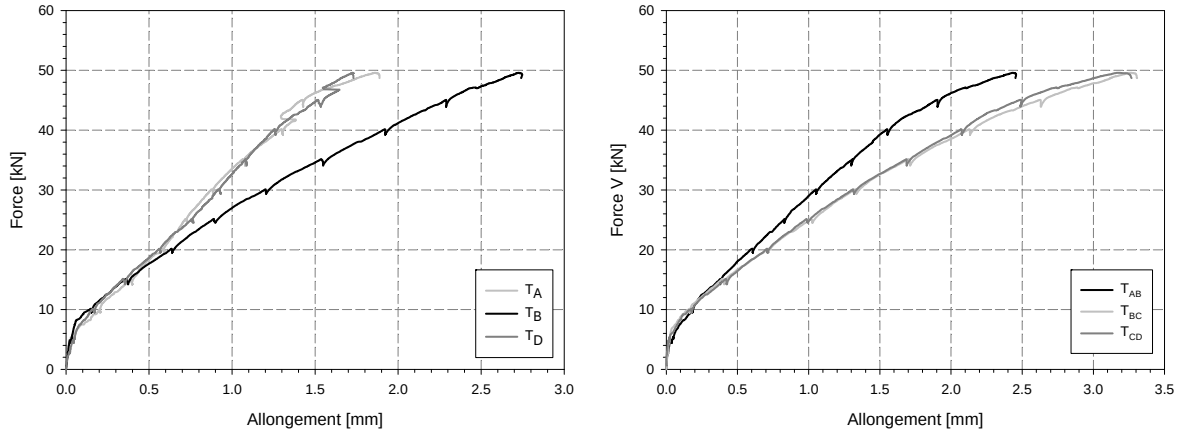

e) Relation force-allongements des capteurs tangentiels

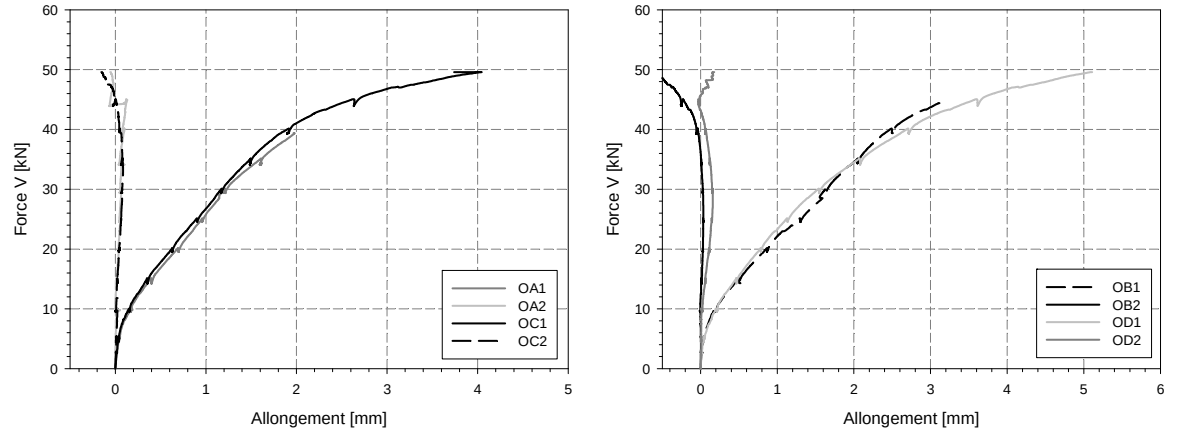

f) Relation force-allongements des capteurs radiaux

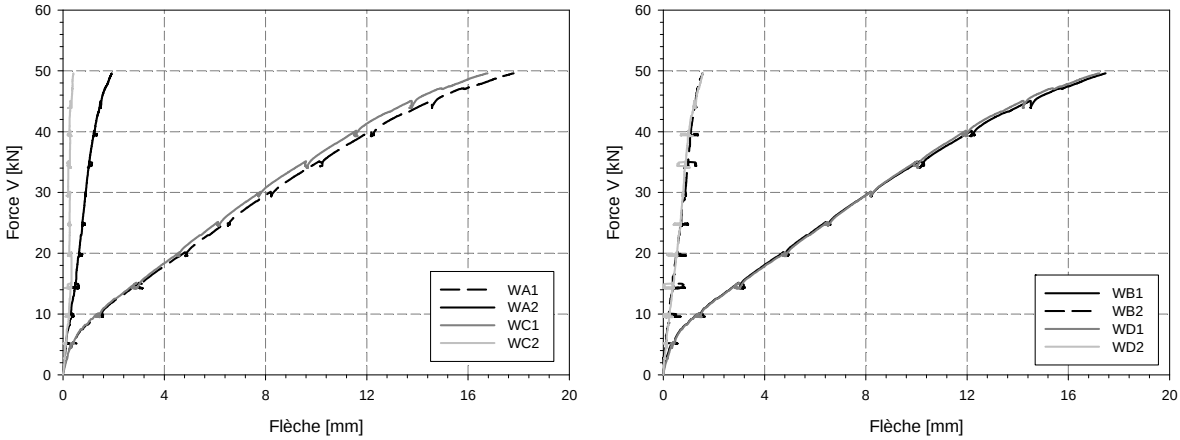

g) Relation force-flèche

Figures 3-19 : Résultats des essais - Dalle BCV_1%_30_2.67%

3.7.2. BCV_1%_80_1.96%

Béton : BCV 1% de fibres
Epaisseur : 80 mm
Type d'armatures : Ø12 #100, ρ_s = 1.96%

a)

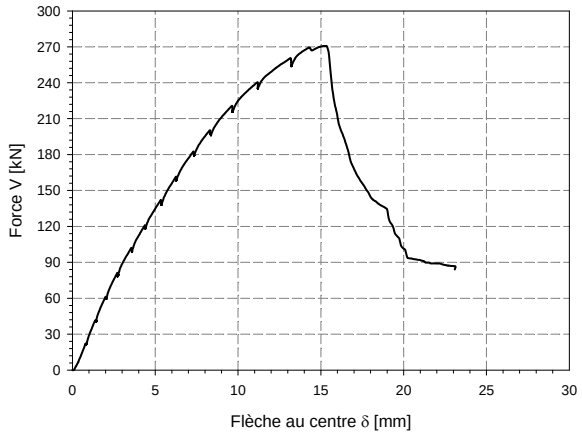

a) Relation force-flèche

b)

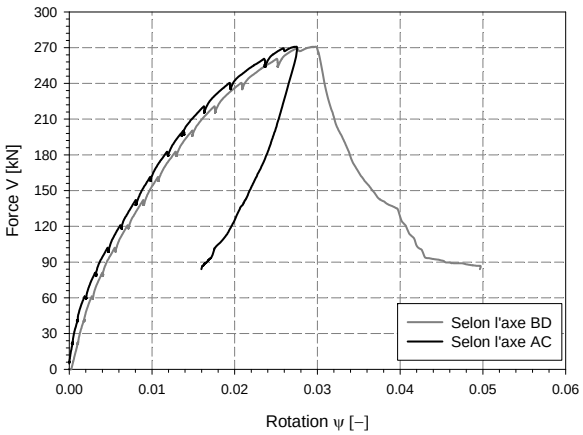

b) Relation force- rotation

c)

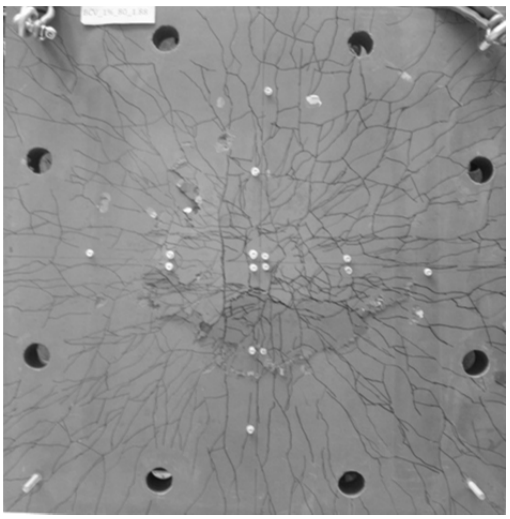

c) Fissuration de la face tendue

d)

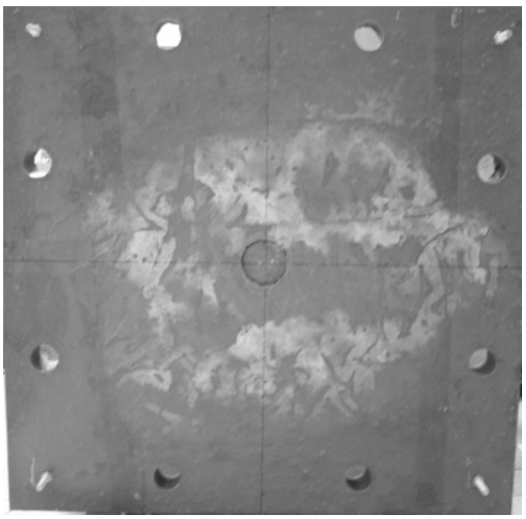

d) Fissuration de la face comprimée

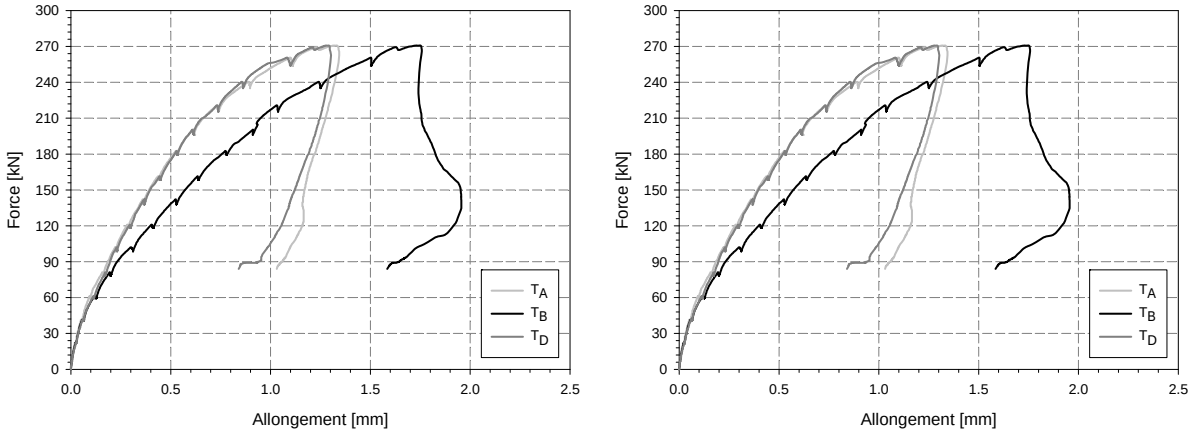

e) Relation force-allongements des capteurs tangentiels

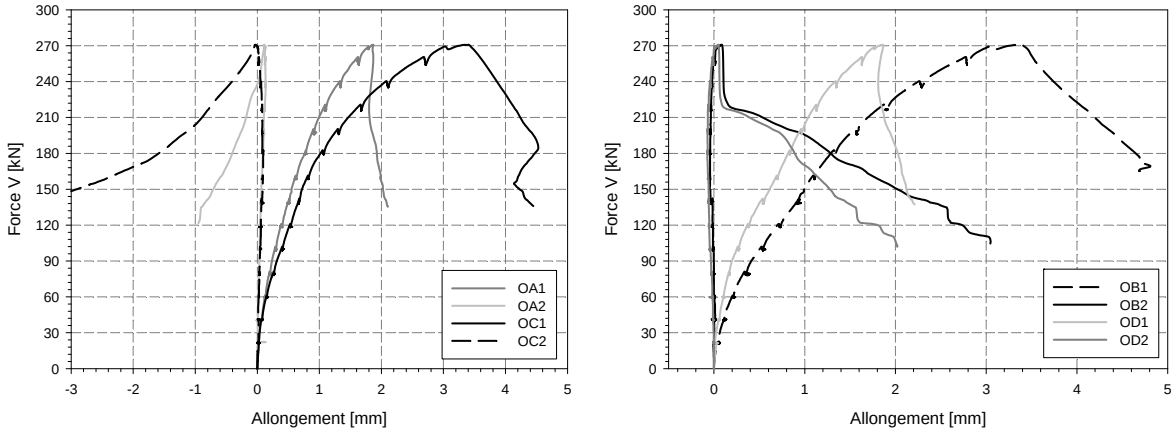

f) Relation force-allongements des capteurs radiaux

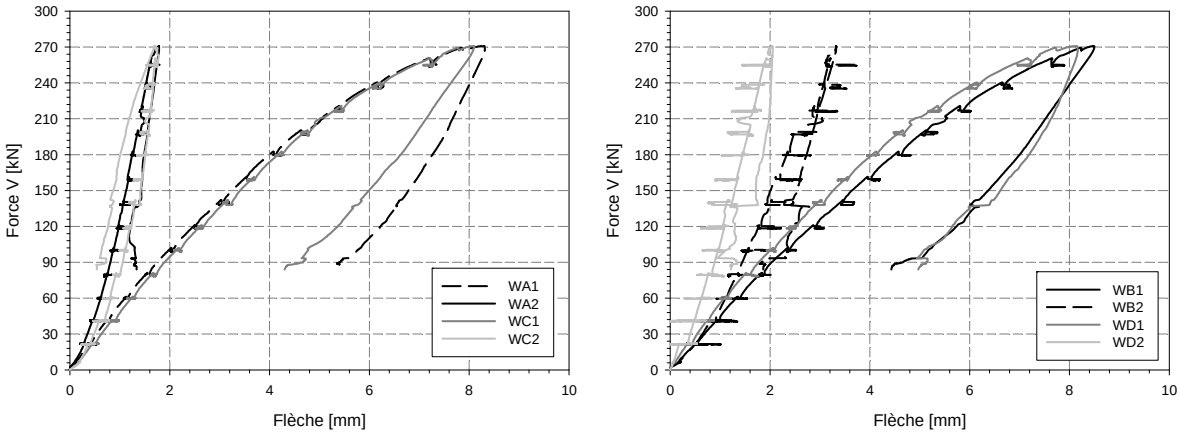

g) Relation force-flèche

Figures 3-20 : Résultats des essais - Dalle BCV_1%_80_1.96%

3.8. Série 8

3.8.1. BCV_2%_60_1.66%

Béton : BCV 1% de fibres
Epaisseur : 60 mm
Type d'armatures : Ø9 #100, ρ_s =1.96

a)

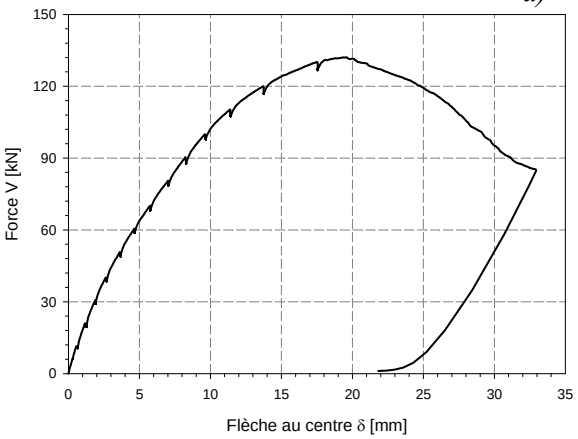

a) Relation force-flèche

b)

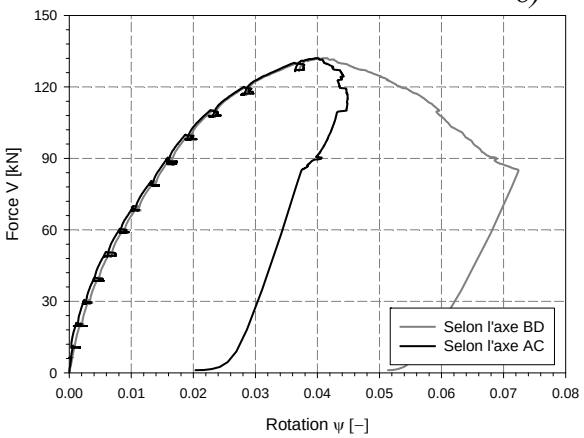

b) Relation force- rotation

c)

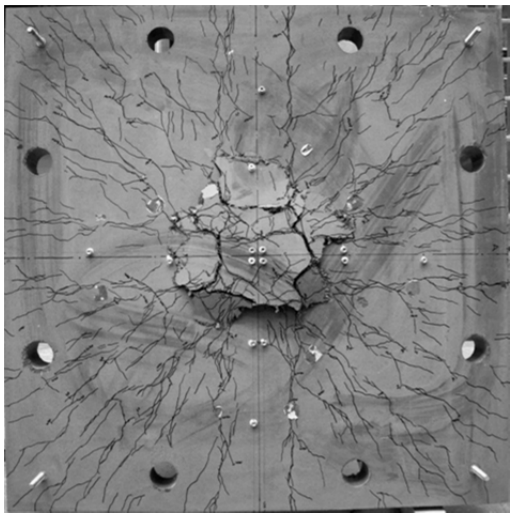

c) Fissuration de la face tendue

d)

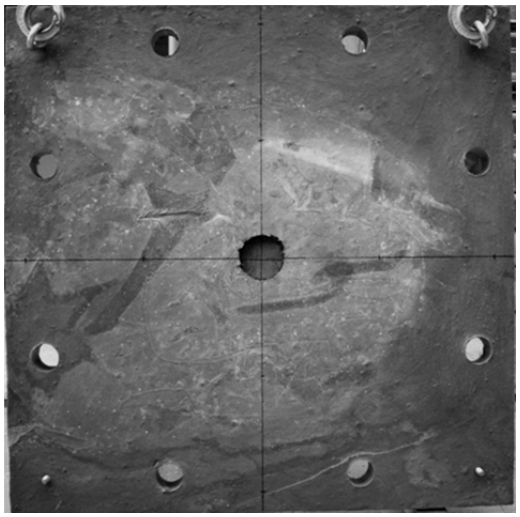

d) Fissuration de la face comprimée

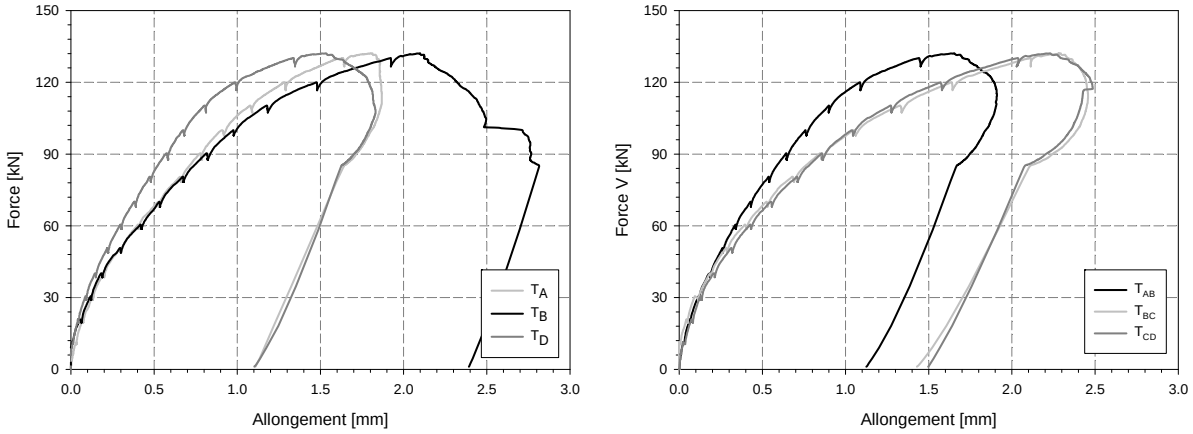

e) Relation force-allongements des capteurs tangentiels

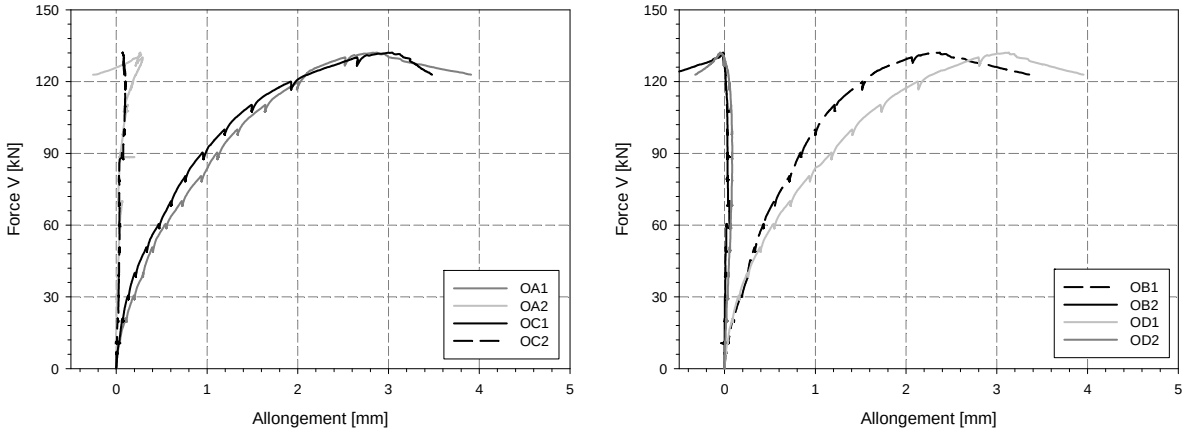

f) Relation force-allongements des capteurs radiaux

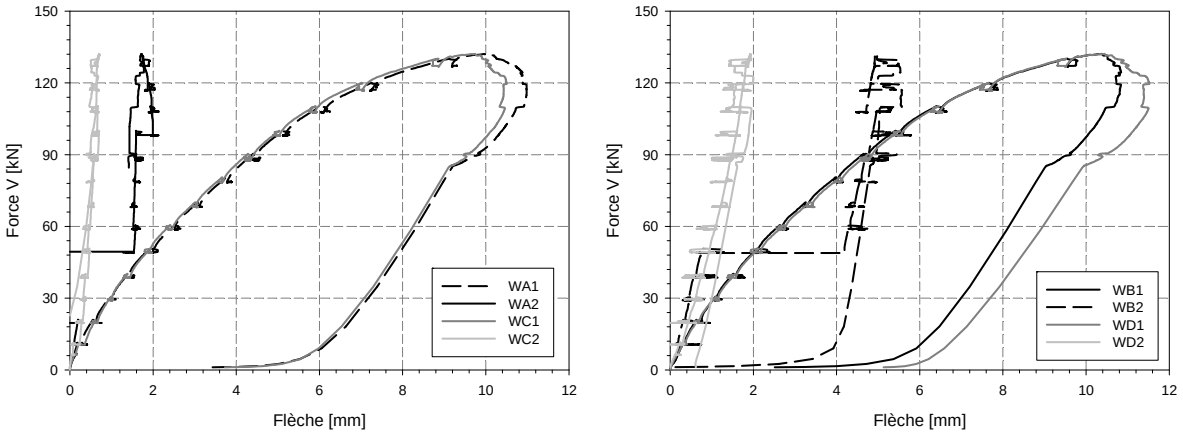

g) Relation force-flèche

Figures 3-21 : Résultats des essais - Dalle BCV_2%_60_1.66%

3.9. Série 9

3.9.1. BCV_1%_60_1.49%

Béton : BCV 1% de fibres
Epaisseur 60 mm
Type d'armatures : Ø9 #100, ρ_s =1.49

a) *b)*

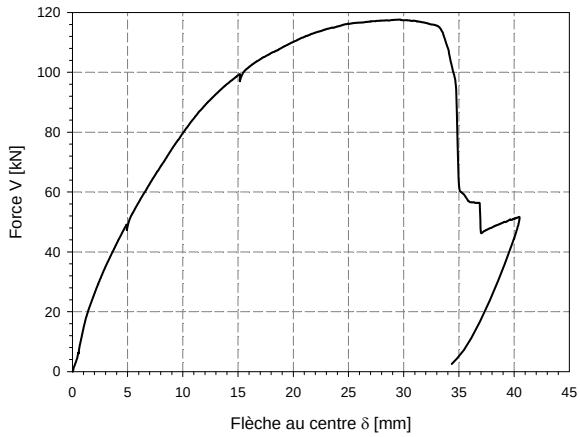

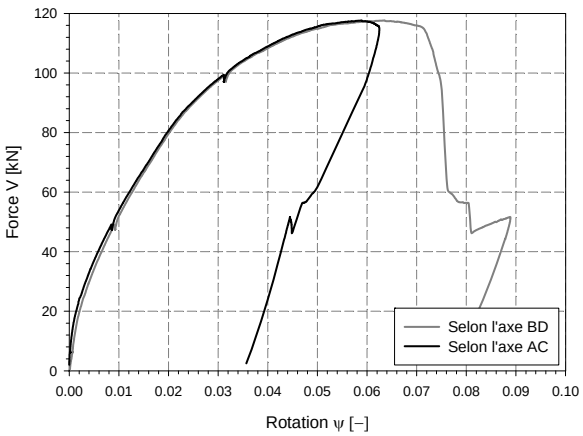

a) Relation force-flèche *b) Relation force- rotation*

c) *d)*

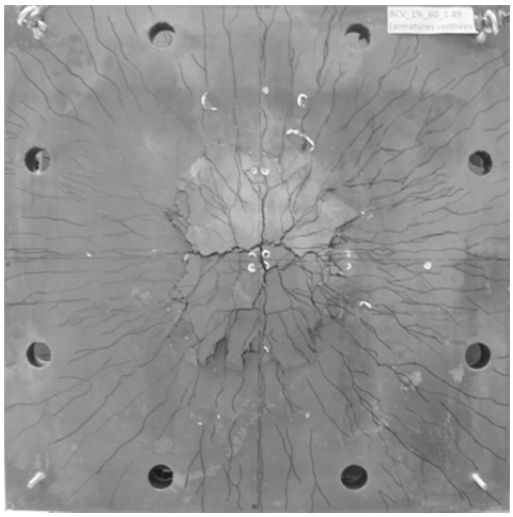

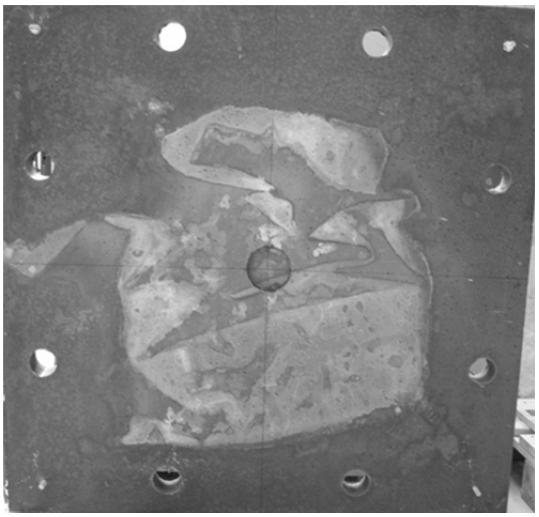

c) Fissuration de la face tendue *d) Fissuration de la face comprimée*

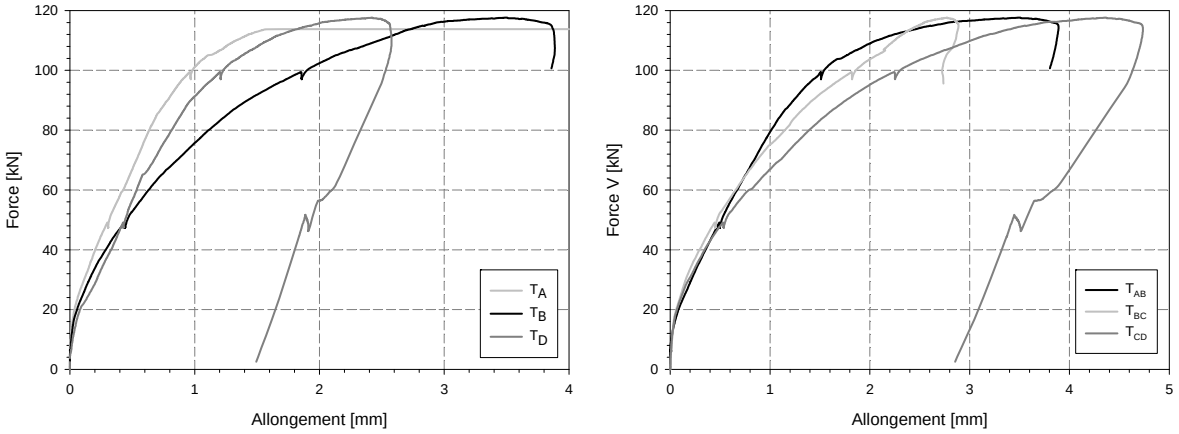

e) Relation force-allongements des capteurs tangentiels

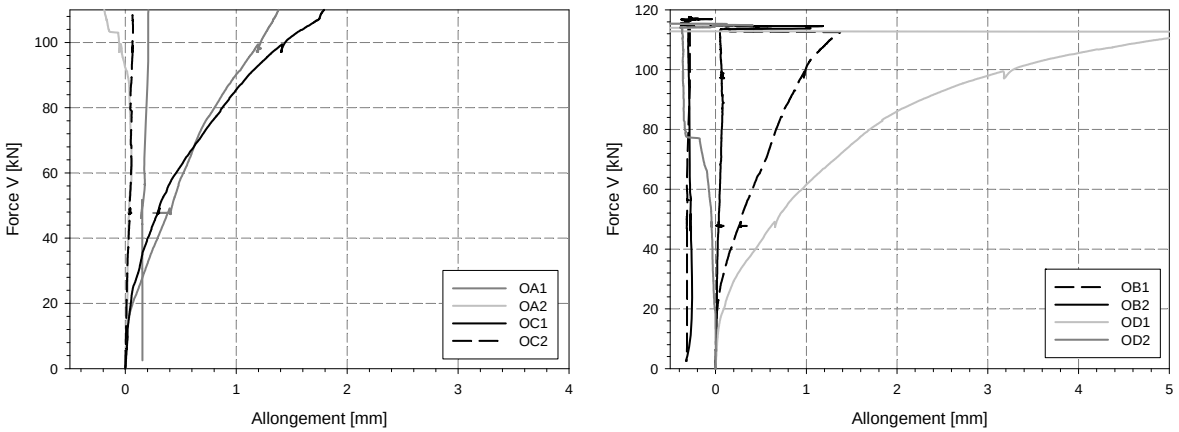

f) Relation force-allongements des capteurs radiaux

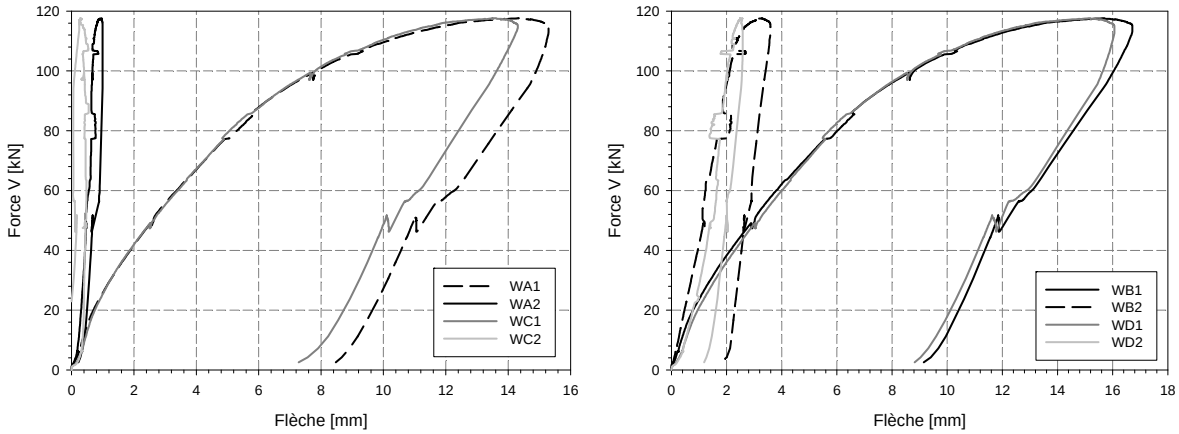

g) Relation force-flèches

Figures 3-22 : Résultats des essais - Dalle BCV_2%_60_1.66%